PROCEEDINGS

The 5th IEEE/IFToMM International Conference on Reconfigurable Mechanisms and Robots

August 12-14, 2021, Toronto, Canada

Fengfeng (Jeff) Xi
Jian S. Dai
Xilun Ding
Volkert van der Wijk

IEEE

IFToMM

Ryerson University

Fengfeng (Jeff) Xi • Jian S. Dai • Xilun Ding • Volkert van der Wijk

Editors

Proceedings of the 5th IEEE/IFToMM International Conference on Reconfigurable Mechanisms and Robots

Editors

Fengfeng (Jeff) Xi
Department of Aerospace Engineering
Ryerson University

Xilun Ding
School of Mechanical Engineering and
Automation
Beihang University

Jian S. Dai
Mechanisms and Robotics
King's College London

Volkert van der Wijk
Department of Precision and
Microsystems Engineering (PME) -
Mechatronic System Design
Delft University of Technology

Table of Contents

Section 1 Reconfigurable Mechanisms and Robots

Section 2 Variable Topology and Morphing Mechanisms

Section 3 Origami and Bio-inspired Mechanisms

Optimizing Cable-Routing for Reconfigurable Cable-Driven Parallel Robots

Utkarsh A. Mishra[1], Stéphane Caro[2,★] and Marc Gouttefarde[3]

[1] Indian Institute of Technology Roorkee, Uttarakhand 247667, India
umishra@me.iitr.ac.in
[2] CNRS, Laboratoire des Sciences du Numérique de Nantes, UMR CNRS 6004,
1, rue de la Noë, 44321 Nantes, France
stephane.caro@ls2n.fr
[3] LIRMM, Univ Montpellier, CNRS, Montpellier, France
marc.gouttefarde@lirmm.fr

Abstract. Reconfigurable cable-driven parallel robots have proved to be very effective in tasks involving complex and cluttered environments. This paper presents a methodology for determining an appropriate cable routing between the cable exit points and the winches. The cable exit points are defined beforehand and the pulleys can be discretely positioned on the robot frame. A six-degree-of-freedom (6-DOF) reconfigurable cable-driven parallel robot is used as an illustrative example. The locations and connections between all pulleys are obtained based on structural and mechanical constraints, mainly imposed by the pulleys. Two specific cases are studied and the optimal configuration for each case is presented in an illustrative and quantitative manner.

Keywords: Cable-Driven Parallel Robots, Cable Routing, Optimization

1   Introduction

Cable-Driven Parallel Robots (CDPRs) have gained a lot of popularity in a wide range of applications. In such robots, cables are used to manipulate a Moving Platform (MP) and connect it to a fixed base frame. Hereafter, the connection points between the cables and the base frame will be referred to as exit points. The use of cables instead of rigid links to make the MP move brings to CDPRs several advantages such as low inertia, very large workspace, and a higher payload to weight ratio as compared to their serial and parallel counterparts. Various tasks like large scale 3D printing [1], rehabilitation mechanisms [5], transfer robots for the elderly [6], rescue robots [7] as well as large-scale telescopes [10] have exploited these advantages. However, there are some potential drawbacks associated with CDPRs. Due to the use of a significant number of cables, the probability of collisions between the cables and the surrounding environment increases. Furthermore, the static equilibrium of the MP is influenced by the non-rigid nature of the cables as they can pull, but not push on the MP.

★ Address all correspondance to this author.
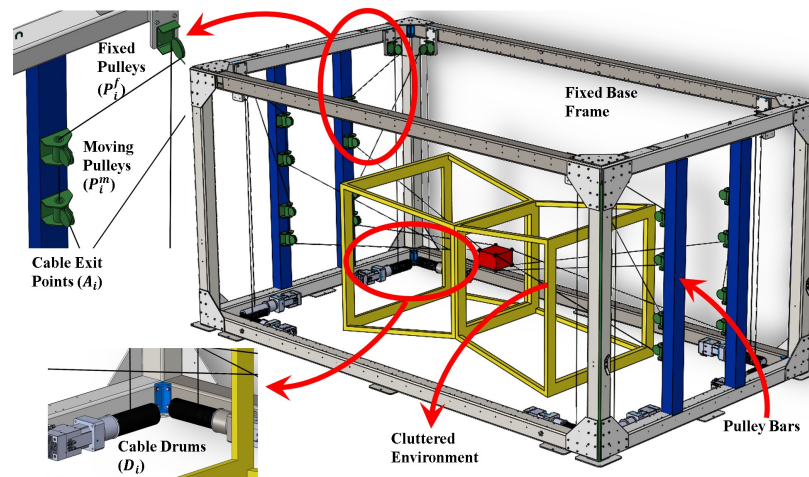
Fig. 1: A Reconfigurable Cable-Driven Parallel Robot evolving in a cluttered environment

Generally, the design of a CDPR is such that the layout of the cable exit points is fixed [4]. In such a case, the CDPR can hardly operate efficiently in a cluttered environment where it is not entirely possible to avoid cable collisions. Using multiple CDPRs working together in a single environment might resolve this issue, but significantly increases the complexity and cost of the process. Keeping all these issues in mind, the idea of reconfiguration with fixed base frame was explored in [2] and extended in [3] to allow the possibility of multiple task-specific configurations in a large workspace. For relatively small workspaces, CDPRs with mobile base frames [8,9] have been proposed. Such CDPRs are referred to as Reconfigurable CDPRs (RCDPRs), and the presented work primarily deals with such robots with fixed base frames. In this context, the algorithm proposed in [3] efficiently determines the cable exit positions on the base frame based on the required task constraints using a graph-based formulation. It allows one to find suitable cable layouts for the RCDPR while minimizing the number of reconfigurations and optimizing some performance functions. However, the authors did not study the management of the cable routing between the cable exit points and the winches. The cable being routed over multiple pulleys and each cable having multiple segments, it becomes very likely that the cable routing from the exit points to the winch drums is infeasible, violating pulley physical constraints and collision conditions.

In this paper, we explore the possibilities of optimizing cable routing for RCDPRs. While most previous works have contributed to reconfiguration planning, the methodology of connecting winch drums to the cable exit points obtained from the reconfiguration planner has not been addressed. Cable routing configurations might not always be feasible when physical constraints of the pulley are taken into concern. Furthermore, as each cable is segmented into multiple parts, the occurrence of cable collisions become more likely. Considering such constraints, an objective function is formulated in

this paper to provide a feasible and optimal routing configuration. Two case studies are discussed with a cluttered environment inspired from authors' previous works [2, 3]. First, the MP moves inside a lattice. Then, the MP moves outside the lattice. Symmetry is used to simplify the problem and resulting configurations are calculated using ®MATLAB and represented with ®SOLIDWORKS models.

The modeling of the manipulator and the associated nomenclature are discussed in Section 2. Section 3 describes all the constraints considered for the determination of the cable routing. Section 4 formulates the problem statement as an integer optimization problem. Section 5 gives the results obtained using the proposed approach. Those results are discussed in Section 6. Conclusions and future work are drawn in Section 7.

2   Problem Formulation and Parametrization

Let us consider a 6-DOF fully-constrained RCDPR with 8 cables. Its ith closed loop is shown in Fig. 2, $i = 1, \ldots, 8$. The frame $\mathscr{F}_b$ of origin O is attached to the base. The frame $\mathscr{F}_p$ of origin P is attached to the MP. The figure shows drums D_i's (position vector $\mathbf{d}_i$), fixed pulleys P_i^f's (position vector $\mathbf{p}_i^f$), positioned directly above each of the drums and movable pulleys P_i^m (position vector $\mathbf{p}_i^m$). The cable anchor points, B_i's ($\mathbf{b}_i$ denotes the position vector of anchor point B_i expressed in $\mathscr{F}_p$), on the moving platform, are connected to each of the corresponding base frame exit pulleys denoted by A_i's. Ideally, based on [3], P_i^m and A_i are located on the same reconfigurable pulley bar. All pulley and drum position vectors are expressed in $\mathscr{F}_b$.
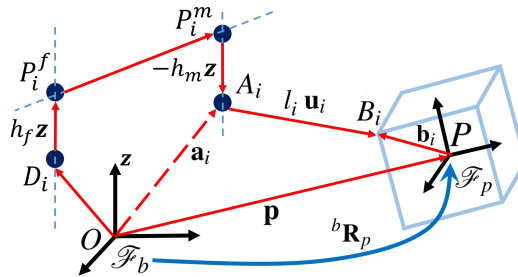
Fig. 2: i^{th}-closed loop of the CDPR

The distances h_f and h_m denote the distances between drum and fixed pulley, and moving pulley and cable exit points, respectively. Their signs are with respect to the direction of the vectors as shown in Fig. 2. Here, h_f is constant for all the drum and fixed pulley pairs, whereas h_m is chosen for each A_i based on a discretized setting where $h_m = z_i \Delta h_m$ and Δh_m is the discretization step along each bar of the RCDPR frame. z_i is an integer bounded by the structural constraints that the moving pulley should remain on the pulley bar.
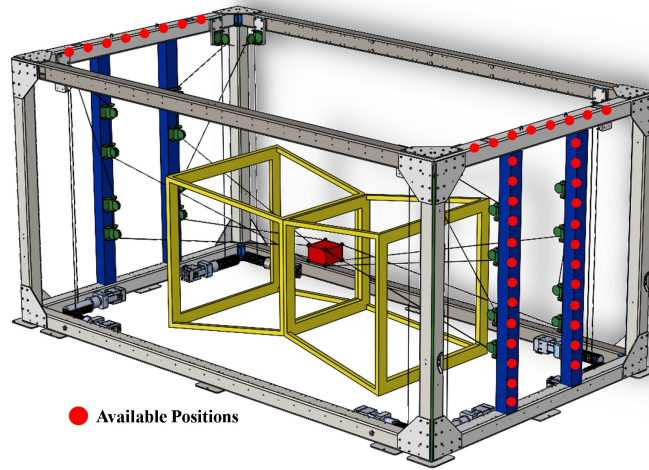
Fig. 3: Possible locations for the pulleys and mobile pulley bars

In Fig. 2, the cable exit points are obtained with the algorithm described in [3]. Hence, we already know A_i corresponding to each of the cable anchor points, B_i. Moreover, this is a direct inference that once we choose a drum, D_i, for a given cable exit point A_i, P_i^f is by default the fixed pulley located over the drum since connecting to any other fixed pulley does not make proper sense.

Given all the required information as stated above, the aim of this work is to find a proper cable routing which abides by all the structural, pulley and collision constraints as well as optimizes the cumulative cable length of all the eight cables. Hereafter, it should be noted that all reconfigurations are discrete and the available positions for each reconfigurable unit (pulley bars and moving pulleys) are discretized as shown in Fig. 3.

3   Constraints

The problem definition gives rise to a number of constraints and for the sake of simplicity, some assumptions are made in order to find a suitable cable routing configuration. The following three types of constraints are considered.

3.1   Structural Constraints

The structural constraints are imposed by the reconfiguration design. The drums, D_i and pulleys above them, P_i^f, are fixed and hence the distance between them is fixed. This reduces the problem to finding an optimal P_i^f for each A_i. Furthermore, a similar constraint is applicable for all the moving pulleys, P_i^m, i.e. the moving pulley should always be above or under the exit point, A_i, the latter being given. Indeed, both the

moving pulley P_i^m and cable exit point A_i are located on the same pulley bar. However, the distance between A_i and P_i^m can vary and is an optimization variable denoted as z_i as defined in Section 2. P_i^m can be above or below A_i. In addition, from Fig. 1, it is apparent that a pulley bar may contain four pulleys, two of which being the exit points and the other two being the moving pulleys. This imposes further constraints that there should not be any overlapping between the A_l-P_l^m and A_u-P_u^m cable segments, where subscripts l and u denote lower and upper respectively.

3.2   Pulley Constraints

Pulleys play a vital role in changing the directions of the cables. The pulleys considered in this work typically have two types of entries and exits (from both top and bottom), namely through the "pulley groove" and the "pulley wheel". These pulleys are accompanied by their own set of structural constraints being restricted by their range of rotation about their axis and imposing rules on cables entering or exiting through the pulley wheel as illustrated in Fig. 4.
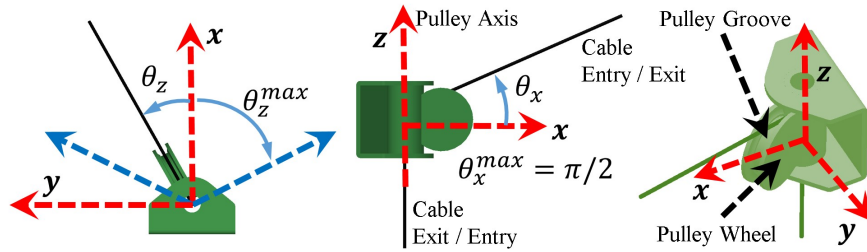
Fig. 4: Pulley-cable constraints

If the cable exits one pulley through wheel and enters another pulley through wheel, then the two pulleys must be co-planar. In such a case, the rotation of the corresponding pulleys and the exit angles between the cable and the pulley is bounded. However, if any of the entry or exit happens through the groove, the co-planarity constraint is not required for that entry or exit.

3.3   Collision Constraints

The cable routing in case of a RCDPR discretizes the cable into multiple segments as compared to a single cable for standard CDPRs. Such segments are generally formed between the cable anchor point on the MP, cable exit point, moving pulley, fixed pulley and the drum. This not only increases the probability of collision between cables but also between two different segments of a single cable. Hence, collisions between all the possible pairs of such segments including pairs belonging to the same cable should

be checked. Apart from collision between cables, all the segments should also avoid collisions with the environment obstacles as well as the MP itself.

4   Methodology

The problem formulation as described in Section 2 has two different settings to be optimized. First, a suitable drum D_i has to be chosen for every A_i and then the position of the moving pulleys as determined by z_i has to be optimized such that all the constraints are satisfied. Now, as the complete setting is discrete, an integer optimization based approach is considered and solved using an optimization algorithm. The overall objective function is to minimize the cumulative cable length due to the routing configuration i.e. from the cable exit point to the drum. This results in the following optimization problem:

$$\min_{z_i,\ P_i^f} \sum_{i=1}^{i=8} l_i + \text{secondary objectives}$$

subject to:

1. Cable Constraints:

$$\mathbf{p}_i^m = \mathbf{a}_i + z_i \Delta h_m \mathbf{z}, \quad \mathbf{y}_P = \text{Pulley Normal Axis}$$

$$\left| \frac{\pi}{2} - \cos^{-1}\left(\frac{(\mathbf{p}_i^m - \mathbf{p}_i^f)^T \mathbf{y}_P}{\left\| \mathbf{p}_i^m - \mathbf{p}_i^f \right\|_2} \right) \right| \le \theta_z^{max}$$

2. Collision Constraints: Satisfied

and

$$l_i = \sqrt{(\mathbf{a}_i - \mathbf{p}_i^m)^T (\mathbf{a}_i - \mathbf{p}_i^m)} + \sqrt{(\mathbf{p}_i^m - \mathbf{p}_i^f)^T (\mathbf{p}_i^m - \mathbf{p}_i^f)} + \sqrt{(\mathbf{p}_i^f - \mathbf{d}_i)^T (\mathbf{p}_i^f - \mathbf{d}_i)}$$

$$= |z_i \Delta h_m| + \sqrt{(\mathbf{p}_i^m - \mathbf{p}_i^f)^T (\mathbf{p}_i^m - \mathbf{p}_i^f)} + h_f$$

which directly implies that the absolute value of z_i should be as small as possible. However, the pulley constraints play a vital role in their selection. Apart from the primary cable length objective, various secondary objectives are possible in order to create a more accurate analysis. Examples of such objectives can be minimizing pulley bending and pulley friction loss. Such objective functions are not considered in this section, but briefly discussed in Section 6.

   In order to simplify the number of explorable solutions, we strictly take the advantage of all the possible symmetries in the configuration of the cable exit points with respect to the position of the fixed pulleys. Using the symmetry, the number of optimization variables is reduced by $1/2^k$ for k symmetry planes. some examples of symmetry are shown in Fig. 6. With a reduced number of optimization variables, complete search over all the space of reconfigurations can be performed in order to find the best possible routing. The methodology is illustrated in the form of a flowchart in Fig. 5.
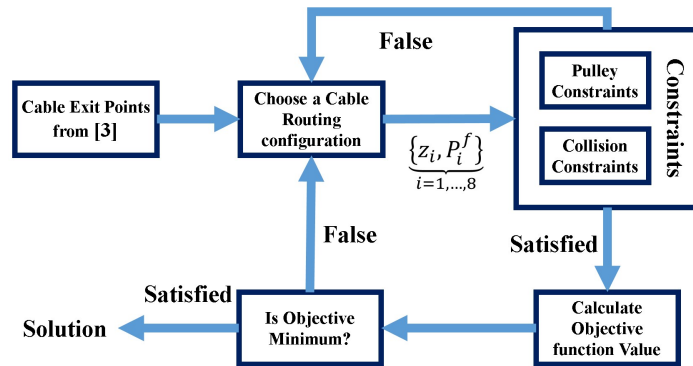
Fig. 5: Methodology to determine cable routing
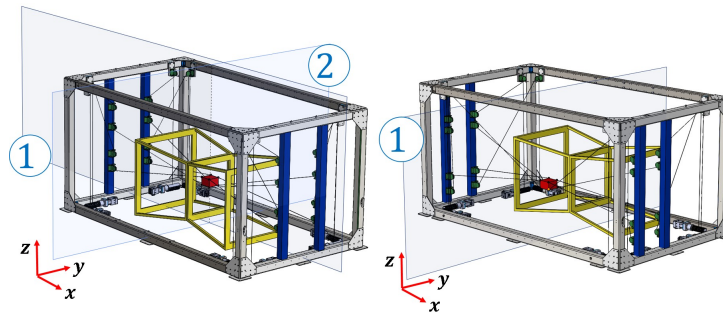
Fig. 6: Two Symmetry Planes

5   Simulation Results

The foregoing methodology is used to the determine the cable routings associated with two configurations of a RCDPR similar to [3]. For the first case, the MP was placed inside the hollow obstacle as shown in Fig. 1 which addresses the tasks of painting and inspecting the obstacle from inside. The configuration is considered first because it addresses usage of all the movable pulleys available for reconfiguration and also allows us to consider two planes of symmetry as in Fig. 6 (left). Whereas in the second case, the MP was placed outside the obstacle as shown in Fig. 7. In this configuration, significant differences are created because of the presence of a single symmetry plane as shown in Fig. 6 (right) and there are some cables for which the exit points are the fixed pulleys themselves. In Fig. 7, two cables are directly connected to the fixed pulleys and hence they do not require the pulley bar which further reduces the number of variables in the cable routing optimization.

The symmetry planes reduced the problem of solving for only one corner, i.e. two fixed pulleys, two moving pulleys and two exit points. The solution is expected to give
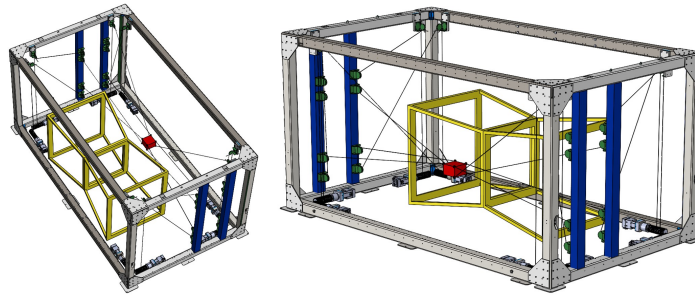
Fig. 7: Optimized cable routing configuration for case 2: when MP is outside (on one side) of the obstacle

values for z_1 and z_2 to determine the position of the moving pulleys w.r.t. exit points and then choose suitable fixed and moving pulley pairs to be connected. The routing solution obtained for one corner is illustrated in Fig. 8 (left) where the respective pulley pairs are (P_1^f, A_2) and (P_2^f, A_1). The values of z_1 and z_2 are -3 and -2 respectively. The negative values mean that the moving pulleys are above the cable exit points based on the parametrization in Fig. 2.

For the second case, based on the symmetry plane, the solution for routing configuration consists of three pulley pairs and the corresponding three z values. One fixed pulley is the exit point and is not included in the optimization process. This is to be noted that all exit points were previously obtained using the algorithm of [3]. The obtained configuration shown in Fig. 8 consists of the pulley pairs (P_1^f, A_2), (P_2^f, A_1) and (P_3^f, A_3). The corresponding values of z_1, z_2 and z_3 are -1, 2 and 2, respectively.
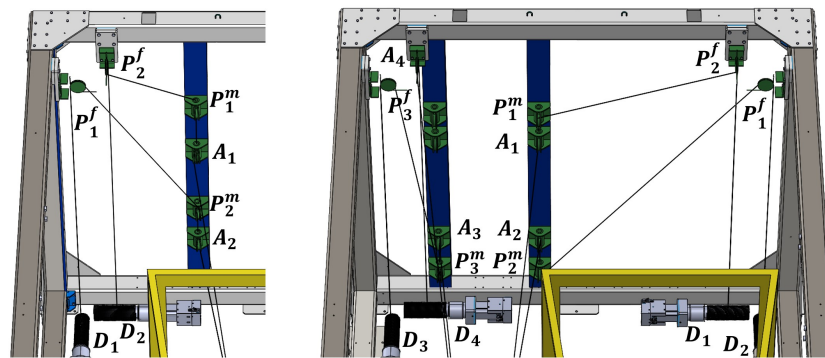
Fig. 8: Optimized cable routing configuration for case 1 (left) and case 2 (right) based on variable reduction with symmetry

Table 1 gives some quantitative results for cases 1 and 2. The reduced number of variables are presented after considering the symmetry planes. The calculations were carried out with an Intel ®i7-7500U CPU@2.70GHz processor.

Table 1: Results for configurations 1 and 2

Parameter	Case 1	Case 2
Original no of optimization variables	16	12
Original no of cable routings	$8! \times 6^8 \approx 68$ billions	$6! \times 4^6 \approx 3$ millions
No. of symmetry planes	2	1
Reduced no of optimization variables	4	6
Reduced no of cable routings	$2! \times 6^2 = 72$	$3! \times 4^3 = 384$
Total Computation Time	31 s	214 s

6   Discussion

The methodology discussed in the present paper is modular and is open to addition of constraints and secondary objectives which will eventually result in a more accurate and practical results. The architecture of the RCDPR is chosen such that the number of pulleys between an exit point and a drum is odd [3].The introduction of multiple number of pulleys play a vital role in introducing various other conditions which should be considered while planning for such robots. Simple pulley rotation constraint is considered in this work but multiple criteria like pulley bending and losses due to pulley friction will definitely play a significant role. While the former can be added directly to the process of optimizing cable routing after the cable exit points are obtained, the latter will modulate the decision on cable tensions (as pulley friction depends on cable tension) as well as affect the choice of the most optimal cable exit points. This will couple static equilibrium, exit point selection and optimal cable routing.

7   Conclusions and Future Work

Cable routing between the winch drum and the cable exit point is an important criterion to be defined for RCDPRs. While RCDPRs are helpful for operation in complex and highly cluttered environments, their performance can be further optimized by considering an optimal cable routing configuration as well. This paper exhibits two cases of planning in RCDPRs as discussed in previous works and introduces an insight on how such cable routing can be performed in an efficient manner. Cable routings are obtained, assessed and illustrated. Future work will deal with experimental studies and introduce more objective functions and constraints in the optimization problems as discussed in Section 6.

References

1. Barnett, E., Gosselin, C.: Large-scale 3D printing with a cable-suspended robot. Additive Manufacturing (2015). https://doi.org/10.1016/j.addma.2015.05.001
2. Gagliardini, L., Caro, S., Gouttefarde, M., Girin, A.: A reconfiguration strategy for reconfigurable cable-driven parallel robots. In: 2015 IEEE International Conference on Robotics and Automation (ICRA). pp. 1613–1620 (2015). https://doi.org/10.1109/ICRA.2015.7139404
3. Gagliardini, L., Caro, S., Gouttefarde, M., Girin, A.: Discrete reconfiguration planning for cable-driven parallel robots. Mechanism and Machine Theory **100**, 313–337 (2016). https://doi.org/https://doi.org/10.1016/j.mechmachtheory.2016.02.014, https://www.sciencedirect.com/science/article/pii/S0094114X16000513
4. Gouttefarde, M., Collard, J., Riehl, N., Baradat, C.: Geometry selection of a redundantly actuated cable-suspended parallel robot. IEEE Transactions on Robotics **31**(2), 501–510 (2015). https://doi.org/10.1109/TRO.2015.2400253
5. Homma, K., Fukuda, O., Sugawara, J., Nagata, Y., Usuba, M.: A wire-driven leg rehabilitation system: Development of a 4-DOF experimental system. In: IEEE/ASME International Conference on Advanced Intelligent Mechatronics, AIM (2003). https://doi.org/10.1109/AIM.2003.1225463
6. Merlet, J.P.: MARIONET, A Family of Modular Wire-Driven Parallel Robots. In: Advances in Robot Kinematics: Motion in Man and Machine (2010). https://doi.org/10.1007/978-90-481-9262-5_6
7. Merlet, J.P., Daney, D.: A portable, modular parallel wire crane for rescue operations. In: Proceedings - IEEE International Conference on Robotics and Automation (2010). https://doi.org/10.1109/ROBOT.2010.5509299
8. Pedemonte, N., Rasheed, T., Marquez-Gamez, D., Long, P., Hocquard, É., Babin, F., Fouché, C., Caverot, G., Girin, A., Caro, S.: FASTKIT: A Mobile Cable-Driven Parallel Robot for Logistics, pp. 141–163. Springer International Publishing, Cham (2020). https://doi.org/10.1007/978-3-030-22327-4_8, https://doi.org/10.1007/978-3-030-22327-4_8
9. Rasheed, T., Long, P., Caro, S.: Wrench-Feasible Workspace of Mobile Cable-Driven Parallel Robots. Journal of Mechanisms and Robotics **12**(3) (01 2020). https://doi.org/10.1115/1.4045423, https://doi.org/10.1115/1.4045423, 031009
10. Su, Y.X., Duan, B.Y., Nan, R.D., Peng, B.: Development of a large parallel-cable manipulator for the feed-supporting system of a next-generation large radio telescope. Journal of Robotic Systems (2001). https://doi.org/10.1002/rob.8102

Design and Development of a Reconfigurable Aircraft Maintenance Robot

M. A. Viraj J. Muthugala, Manuel Vega-Heredia, Nay Htet Lin,
S. M. Bhagya P. Samarakoon, A. A. Hayat, and Mohan R. Elara

Engineering Product Development Pillar, Singapore University of Technology and
Design (SUTD), 8 Somapah Road, Singapore

Abstract. The ability to climb on an aircraft body and move across
different planar surfaces such as wings and fuselage can improve the
productivity of an aircraft maintenance robot. This paper proposes a
novel design of a reconfigurable aircraft maintenance robot. The pro-
posed robot utilizes vacuum suction to generate the adhesion force re-
quired for climbing on the skin of an aircraft. The reconfiguration ability
of the robot accommodates it to move across different planes. The robot
is incorporated with a maintenance unit that can perform cleaning and
has provisions to attach sensors for inspections. Particulars on the de-
sign and development of the mechanical, electrical, and control systems
of the robot are presented. Experimental results obtained by operating a
prototype of the robot on a segment of an aircraft skin confirmed the ap-
plicability of the proposed reconfigurable robot for aircraft maintenance.

Keywords: Aircraft maintenance, Reconfigurable robotics, Climbing robotics

1 Introduction

The aviation industry has become a major form of transport throughout the
world, and it is rapidly growing. Frequent maintenance and inspection should be
done to ensure the safety of the aircraft. Mainly the cleaning is done with the
aim of maintaining visual appearance, efficiency, and corrosion protection [1].
Aircraft skin should be cleaned to prevent the potential risk of corrosion as well
as the degradation of non-metallic parts such as rubber beading. Typically, air-
craft maintenance work is done by human workers [2]. However, the conventional
methods lack the efficiency of maintenance operations and safety issues for hu-
man workers since human workers need to climb on structures for performing the
tasks. Therefore, robots can be introduced as a solution for the issues associated
with conventional methods.

Ground robotic systems that are used for cleaning and inspection of aircraft
with the aid of various sensors have been developed [3, 4]. Nevertheless, these
robots have limited access to the outer surface of an airplane and not capable of
accessing the top of the wings and fuselage. Therefore, robots should be capable
of attaching to the outer surface of an aircraft without the aid of external support

structures to perform cleaning and inspection. Several mechanisms that enable a robot to climb and navigate in vertical structures have been developed [5–7].

The use of passive suction cups for the adhesion is one of the mechanisms widely used in robots operated on smooth surfaces [7, 8]. However, the adhesion provided by passive suction cups is not reliable in surfaces with dust particles [5,7]. This is the major shortcoming that hinders the usage of passive suction cups for an aircraft maintenance robot. Magnetic adhesion is another one of the widely used adhesion methods for climbing robots used in maintenance and inspection applications [7, 9]. The adhesion force depends on the ferromagnetic characteristic of a surface. Magnetic adhesion is not applicable for an aircraft inspection robot since the surface of an aircraft is made from non-ferromagnetic materials. Therefore, thrust based adhesion and vacuum based adhesion mechanism are preferred for a robot anticipated for onboard operation in an outer surface of an airplane over the other adhesion mechanisms.

Robots with thrust based adhesion mechanisms use electric duct fans to generate propulsion force required for the adhesion [7]. In this regard, Andrikopoulos et al. [10] proposed a new design of a thrust based climbing robot and studied the variation of the adhesion force requirement with the surface inclination. Robots that use vacuum suction for the adhesion uses active suction mechanisms such as impellers or vacuum pumps. In this regard, White et al. [11] proposed a mobile robot based on vacuum adhesion for inspection of aerostructures. The scope of the work is limited to the development of a navigation algorithm based on sensor fusion. A double frame robot that can walk on the surface of an aircraft using legs fixed with pneumatic suction pads has been proposed for inspections [12,13]. The main focus of the work is on developing controllers and observes for maintaining a stable adhesion force and motion. However, the existing robots designs discussed above are not convenient for continuous operation on the outer surface of an aircraft since the designs of the robots do not facilitate the moving across surfaces with different inclinations (e.g., moving from the wings to the fuselage can be considered).

Reconfigurable designs have open up a new horizon for maintenance and inspection robotics due to their ability of adapting the morphology in accordance to a given context [14]. Therefore, this paper proposes a novel design of a reconfigurable aircraft maintenance robot to mitigate the limitations in state of the art. The robot applies vacuum suction to produce the adhesion force needed for climbing on the outer layer of an aircraft. Reconfigurability of the robot helps the robot to navigate across different planes. The robot is equipped with a maintenance module that can perform cleaning and used to install sensors required for inspection. Section 2 describes the robot's mechanical and electrical design. Reconfiguration and adhesion control are discussed in Section 3. The experiments conducted to validate the design is explained in Section 4. Concluding remarks are given in Section 5.

2 Robot Design

2.1 Mechanical design

The Computer-Aided Design (CAD) model of the proposed robot is depicted in Fig. 1. The robot consists of two main modules, module 1 and module 2, which have similar hardware components. Each of these main modules contains four drive wheels powered by DC motors. Wheels in a side of the robot are synchronously operated, yielding to a skid steering drive mechanism for the locomotion of the robot on a surface. Wheels are made with a rubber layer to improve the grip on the surface of an aircraft. Furthermore, the rubber wheels minimize possible damages caused to the surface of an aircraft by the robot locomotion. Module 1 and module 2 of the robot are connected through an active hinge actuated through a servo motor. The actuation of the hinge is responsible for the reconfiguration required for moving across two different planes.

The robot utilizes vacuum suction to climbing on the outer surface of an aircraft. Each module consists of nine suction cups in this regard. The suction cups are designed to have accordions to provide adaptability to the curvature of the surface.This adaptability ensures the safe adhesion of the robot to the curve surface of an aircraft body without causing substantial air leakages. The vacuum suction required for the adhesion is created through two external vacuum pumps (EVE-TR-M-2.3-12V-DC) on the ground. The vacuum chambers of module 1 and module 2 of the robot are independently connected to the vacuum pumps through hoses. Each vacuum pump is capable of producing a maximum of 78 kPa
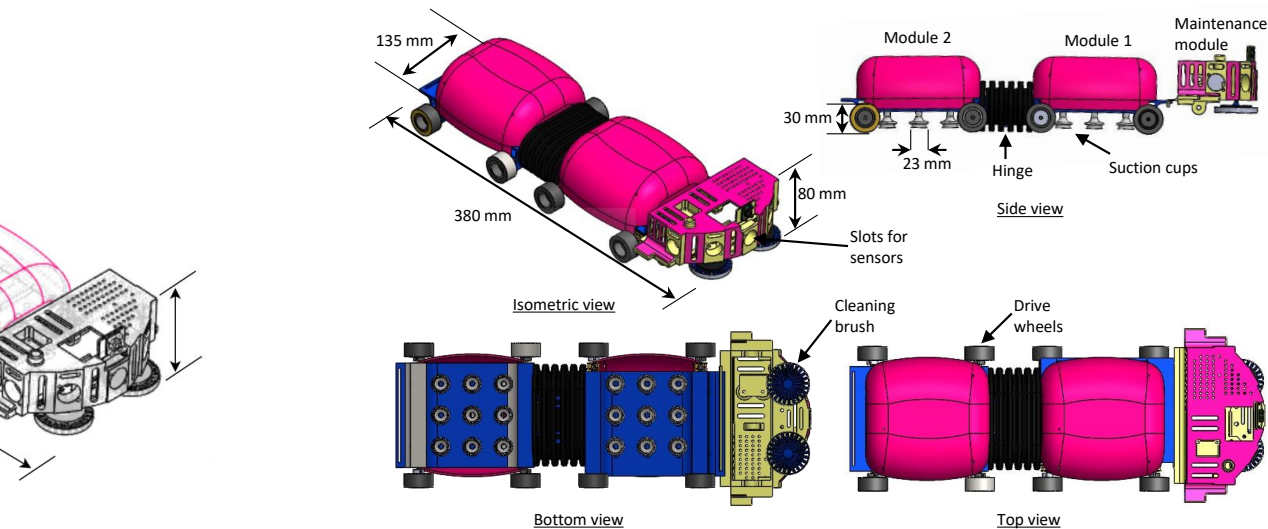
Fig. 1. Design of the robot.

Apart from these two modules, the robot design of the robot has been incorporated with a maintenance module. The maintenance module has a brushing system that can scrub the grimy outside surface of an aircraft. Two DC motors are attached to the brushing mechanism for the actuation. Furthermore, the service module has been designed with provision to install sensors required for inspections, such as cameras and other non-destructive testing equipment. This service module is fixed to the front of the robot ahead of module 1. The ability to install sensors and inbuilt cleaning mechanisms improves the overall functionality and usage for aircraft maintenance.

2.2   Electrical design

The circuit diagram of the robot is depicted in Fig. 2 The robot is powered by a 12 V external power source connected to the robot. The Main Controller (MC) is a microcontroller (Arduino Mega 2560). MC is responsible for managing all the local functionality of the robot, such as locomotion and cleaning motor controlling, vacuum controlling, reconfiguration, and sensor handling. Teleportation commands to the robot are sent by an external Personal Computer (PC) through a Universal Serial Bus (USB) connection attached to MC.

The DC motors responsible for the locomotion ('LM1', 'LM2', 'LM3', 'LM4', 'RM1', 'RM2', 'RM3', and 'RM4') are controlled through the motor drivers, 'MD 2' and 'MD 3' fixed inside the respective module. The motors, 'CM1' and 'CM2' in the maintenance module, are operated through the motor driver, 'MD4'. RoboClaw 2x7A dual-channel motor drivers are used for 'MD2', 'MD3', and 'MD4'. A
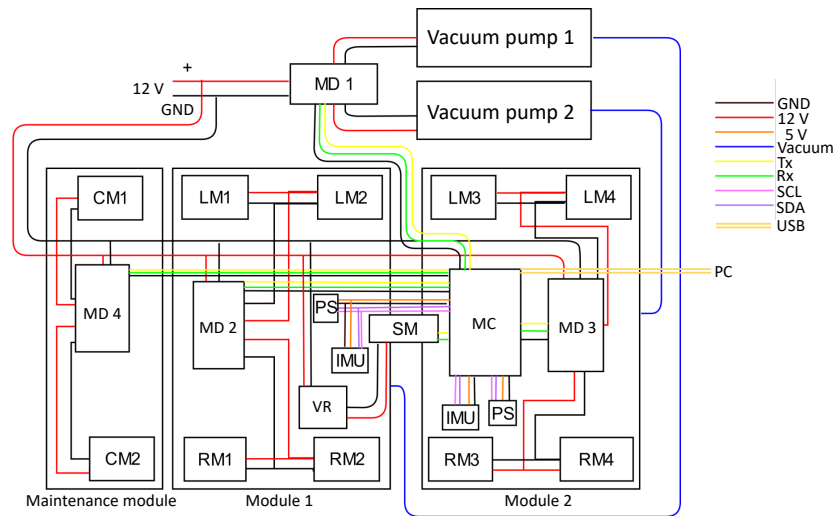
Fig. 2. Electrical design of the robot.

that produce the adhesion force. This motor driver and the vacuum pumps are externally placed on the ground. All the motor drivers are connected to MC through a Transistor-Transistor Logic (TTL) serial communication link for controlling.

A HerkuleX DRS-0101 smart Servo Motor (SM) is used to actuate the hinge for reconfiguration. SM is supplied a 7.4 V by using a Voltage Regulator (VR). MC is communicated with SM using a TTL serial connection. Module 1 and 2 each consist of an Inertial Measurement Unit (IMU) to estimate the robot's orientation in 3D space. BNO055 absolute orientation sensor is used in this regard. An AMS5915 Pressure Sensor (PS) is installed in each vacuum chamber to measure the pressure difference. These sensors are communicated with MC through I2C protocol. The inspection sensors to be installed the maintenance module are expected to have wireless. A 12 V DC terminal is available in the maintenance module to power up the inspection sensors.

3   Robot control

3.1   Reconfiguration

The moving across different planes is performed with reconfiguration through the active hinge placed between module 1 and module 2 of the robot. During the initiation of the reconfiguration, the vacuum suction of a block is deactivated. Then the hinge is actuated to change the inclination of the module (vacuum deactivated one) from the current plane to a new plane while the other block (vacuum activated one) is firmly attached to the surface. Similarly, the adhesion of the two modules is alternated, and the hinge actuator is operated stepwise until the robot entirely moves to the new plane. The design facilitates hinge reconfiguration in the range of -90° to 90°. The main steps of moving across two planes when the new plane is positively inclined and negatively inclined are explained in Fig. 3 and Fig. 4, respectively.

3.2   Adhesion control

The pressure difference required for the safe adhesion of the robot in a surface inclined with theta is formulated considering the static equilibrium of forces acting on the robot (see Fig. 5). It should be noted that the possible forces applied on the robot due to the vacuum hoses and wires have not been considered in the analysis. The adhesion force, F_A acting on the robot due to the negative pressure, P can be found from (1), where A is the area of the suction cups.

$$F_A = PA \tag{1}$$

Then, the friction force, F_F acting on the robot, is obtained from (2) based on $N = F_A + mg\cos\theta$ and $F_F = \mu N$, where μ is the coefficient of friction.

$$F_F = \mu(PA + mg\cos\theta) \tag{2}$$
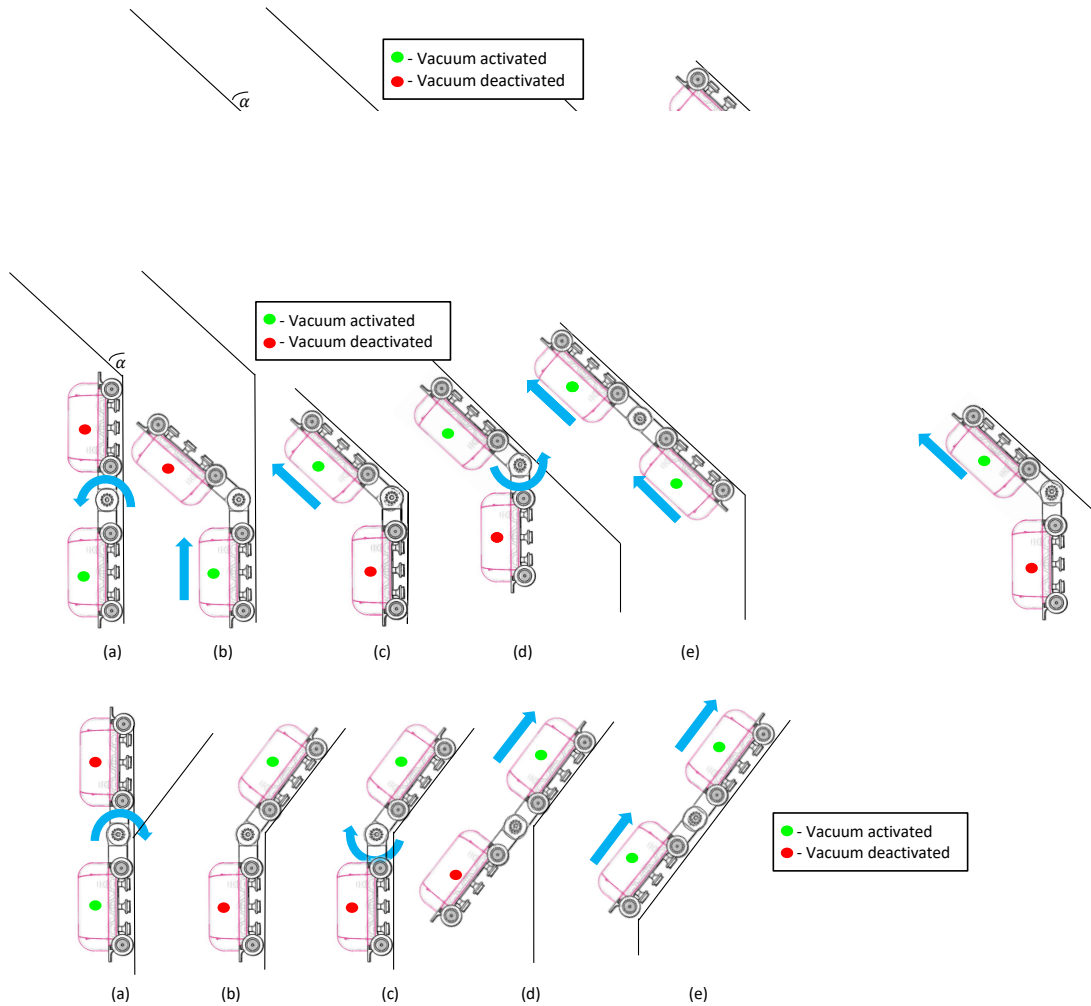
Fig. 4. Moving across two planar surfaces with the aid of reconfiguration, if new plane is negatively inclined. (a): Activating the reconfiguration to lean module 1 on the new surface, (b): Activating the vacuum of module 1 when module 1 reaches the other surface, (c): Lifting the module 2 from the surface through reconfiguration while deactivating the vacuum of module 2, (d): When module 2 aligns with the new surface stop reconfiguration and start the forward locomotion by module 1, and (e): When module 2 is completely lean on new surface, the vacuum of module 2 is also activated, and start moving on new surface.

To avoid the falling off, $F_F > mg \sin \theta$ that yields to the condition (3).

$$P > \frac{mg}{A} \left(\frac{\sin \theta}{\mu} - \cos \theta \right) \tag{3}$$
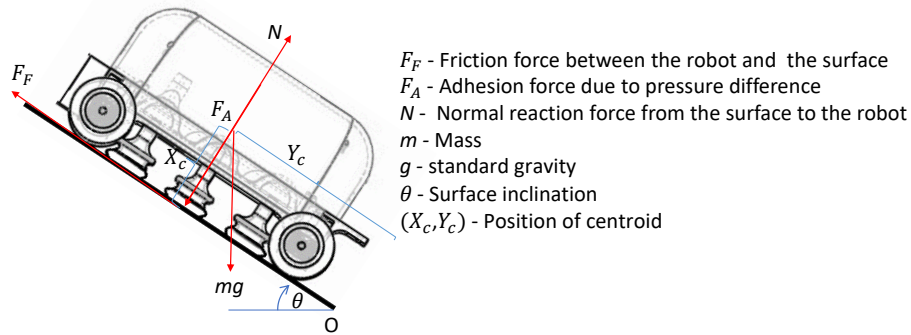
Fig. 5. Forces acting on the robot.

The condition for avoiding the overturning can be formulated as in (4) by taking moments around 'O'.

$$P > \frac{mg}{A}(\frac{X_c}{Y_c}\sin\theta - \cos\theta) \tag{4}$$

The vacuum pressure should always be maintained to satisfy the conditions given in (3) and (4) in a given situation. On the other hand, excessive adhesion force increases the frictional forces and makes locomotion difficult for the robot. Furthermore, operating the robot above a constant threshold reduces energy efficiency. Therefore, the vacuum pressure is adapted per the inclination angle. The inclination of the surface is estimated based on the IMU reading, and the required vacuum pressure is calculated. Subsequently, the power of the vacuum pumps is altered through a closed-loop pressure controller. The fuzzy logic based closed-loop pressure controller proposed in [15] for a vacuum-based wall cleaning robot is adapted in this regard.

4   Experiments

A prototype of the robot has been developed for validating the proposed design features. Experiments were conducted inside a laboratory setting using a section of an aircraft's skin. Experimenting with the robot prototype is shown in Fig. 6. The robot was teleoperated through the PC during the experiments.

In the first part of the experiment, the climbing ability of the robot was verified by moving the robot on top of the aircraft skin in the vertical direction as shown in Fig. 6(a). The robot was successful in climbing and safely attaching to the surface. The adaptation of the suction cups to the curvature is essential for sustaining the vacuum without heavy leakages. Thus, the pressure difference of the vacuum was logged to test the adaptability of the accordion design. The variation of the pressure difference during the moving on the curvature is depicted in Fig. 7. No sudden drops of the pressure could be observed, confirming that there were no sudden air leakages due to improper sealing of the suction

(a)   (b)   (c)
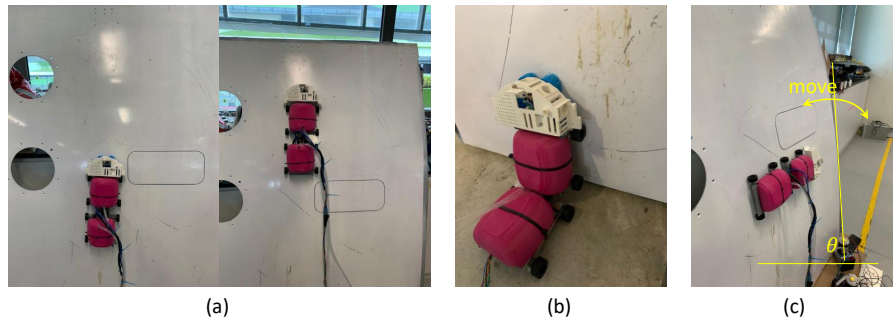
Fig. 6. Experimenting with the prototype of the robot. (a): Moving in vertical curvature, (b): Reconfiguration, (c): Testing the vacuum pressure adaptation.

cups. Thus, the results validate the ability of the suction cups adaptation to the surface curvature.

A scenario of the reconfiguration to moving from ground to the segment of the aircraft skin is shown in Fig. 6(b). This scenario is almost similar to moving from a wing to the fuselage of an aircraft. The robot was capable of reconfiguring the inclination of the new surface (i.e., aircraft skin) from the existing surface (i.e., ground) through actuating the hinge motor. This observation verifies the usability of the reconfiguration for moving across different planes.

In the situation shown in Fig. 6 (c), the robot was placed on the middle of the aircraft skin facing the longitudinal axis of the robot horizontally. The robot was placed in this way to avoid the inclination variation caused due to
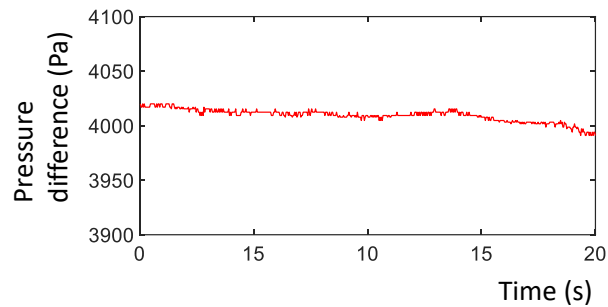
Fig. 7. Variation of the pressure difference when robot moving on the vertical curvature.

conditions for the safe adhesion derived under Section 3.2. Thus, the experiment confirms the ability to adapt the vacuum pressure per inclination of the surface.

Table 1. The observed average pressure for different inclinations.

Inclination	30°	60°	90°	120°	150°
Pressure (Pa)	2010	2144	4003	4870	4418

5   Conclusions

Robotics solutions are demanded for handling routine aircraft maintenance operations. The ability to climb and moving across different planes, such as moving from a wing to the fuselage, could improve the productivity of an aircraft maintenance robot. Therefore, a reconfigurable aircraft maintenance robot that can climb and move across different planes has been designed.

The salient features of the proposed design can be summarized follows. Vacuum suction power is used to produce the adhesion force required to climbing on an aircraft's skin. The suction cups are designed with accordions to firmly seal them in a curved surface. The reconfiguration of the robot is designed to facilitate the adaptation to the change of inclination of two surfaces. A pressure controller is also deployed to adjust the vacuum pressure per the inclination of the surface.

A prototype of the robot has been developed, and experiments have been conducted to evaluate the features of the proposed reconfigurable robot design. The experimental results confirm the validity of the above-mentioned salient features of the robot. Even though the experiments were conducted in a laboratory setting, the robot was operated on a segment of an aircraft's skin, where the surface conditions experienced by the robot are similar to real world setting. Thus, the outcomes of the experiments ascertain the real-world applicability to a greater extent. Nevertheless, the scope of the experimental test runs was limited due to the size limitations of the available segment of the aircraft's skin. Experimenting with the proposed reconfigurable robot on an aircraft in a maintenance hangar is expected to be conducted in the future. At this stage, the robot has to be tele-operated for main actions such as reconfiguration and locomotion. Therefore, the developments of algorithms for autonomous reconfiguration and navigation are proposed for future work.

Acknowledgements

References

1. Longmuir, M., Ahmed, N.A.: Commercial aircraft exterior cleaning optimization. Journal of Aircraft 46(1), 284–290 (2009)
2. Samaranayake, P.: Current practices and problem areas in aircraft maintenance planning and scheduling–interfaced/integrated system perspective. In: Proceedings of the 7th Asia-Pacific Conference in Industrial Engineering and Management Systems. pp. 2245–2256 (2006)
3. Leiva, J.R., Villemot, T., Dangoumeau, G., Bauda, M.A., Larnier, S.: Automatic visual detection and verification of exterior aircraft elements. In: 2017 IEEE International Workshop of Electronics, Control, Measurement, Signals and their Application to Mechatronics (ECMSM). pp. 1–5. IEEE (2017)
4. Bauda, M.A., Grenwelge, A., Larnier, S.: 3d scanner positioning for aircraft surface inspection (2018)
5. Nansai, S., Mohan, R.E.: A survey of wall climbing robots: recent advances and challenges. Robotics 5(3), 14 (2016)
6. Chu, B., Jung, K., Han, C.S., Hong, D.: A survey of climbing robots: Locomotion and adhesion. International journal of precision engineering and manufacturing 11(4), 633–647 (2010)
7. Schmidt, D., Berns, K.: Climbing robots for maintenance and inspections of vertical structures—a survey of design aspects and technologies. Robotics and Autonomous Systems 61(12), 1288–1305 (2013)
8. Deneke, C., Schlosser, C., Mehler, S., Schüppstuhl, T.: Positioning ndt sensors with a mobile robot for efficient aircraft inspections. In: 7th International Symposium on NDT in Aerospace, Bremen (Germany) (2015)
9. Muthugala, M.A.V.J., Le, A.V., Cruz, E.S., Rajesh Elara, M., Veerajagadheswar, P., Kumar, M.: A self-organizing fuzzy logic classifier for benchmarking robot-aided blasting of ship hulls. Sensors 20(11), 3215 (2020)
10. Andrikopoulos, G., Papadimitriou, A., Brusell, A., Nikolakopoulos, G.: On model-based adhesion control of a vortex climbing robot. In: 2019 IEEE/RSJ International Conference on Intelligent Robots and Systems (IROS). pp. 1460–1465. IEEE (2019)
11. White, T.S., Alexander, R., Callow, G., Cooke, A., Harris, S., Sargent, J.: A mobile climbing robot for high precision manufacture and inspection of aerostructures. The International Journal of Robotics Research 24(7), 589–598 (2005)
12. Wang, C., Gu, J., Li, Z.: Switching motion control of the climbing robot for aircraft skin inspection. In: 2019 IEEE International Conference on Fuzzy Systems (FUZZ-IEEE). pp. 1–6. IEEE (2019)
13. Wu, X., Wang, C., Hua, S.: Adaptive extended state observer-based nonsingular terminal sliding mode control for the aircraft skin inspection robot. Journal of Intelligent & Robotic Systems pp. 1–12 (2019)
14. Samarakoon, S.M.B.P., Muthugala, M.A.V.J., Elara, M.R., Kumaran, S.: Toward pleomorphic reconfigurable robots for optimum coverage. Complexity 2021 (2021)
15. Muthugala, M.A.V.J., Vega-Heredia, M., Mohan, R.E., Vishaal, S.R.: Design and control of a wall cleaning robot with adhesion-awareness. Symmetry 12(1), 122 (2020)

Kinetostatic Analysis of a Reconfigurable 4-rRUU Manipulator Using Davies Method

Rodrigo Cerqueira de Campos, Paulo Rossi, Estevan Hideki Murai, and
Henrique Simas

Universidade Federal de Santa Catarina, Florianópolis SC 88040-900, Brazil,
`rodrigo.c.campos@posgrad.ufsc.br`
`paulo.rossi@posgrad.ufsc.br`

Abstract. The kinetostatic modeling represents an essential evaluation in parallel manipulator design, especially when dealing with complicated geometry reconfigurable parallel manipulators. Analytical models aid the design engineer in identifying any necessary modifications. This paper proposes a kinetostatic model of the 4-DoF 4-rRUU rPM, which is based on the natural coordinates system to calculate the position kinematics and Davies' method to compute the statics of such a manipulator. Adopting basic points and unity vectors embedded in the PM's rigid links, it is possible to compute every joint position employing the Newton-Raphson numerical method. The joints' positions calculation presented a mean error of 0.00118%. Ultimately, with the achieved results, one can formulate the magnitude vector regarding the operational forces and moments through the screw theory, as Davies' method exposes, which produced consistent output values concerning the given torques. Finally, some conclusions and future works are discussed.

Keywords: parallel robot, Schönflies motion, natural coordinates, screw theory, Davies' method

1 Introduction

Compared with their serial counterparts with open-loop topologies, parallel manipulators (PMs) have the fixed base connected towards the moving platform through at least two kinematic limbs, resulting in multi-loop architectures. Such a PM structure, whose stiffness is inherently better, makes it feasible to mount all actuators on the base, reducing the inertial mass, reaching higher operational velocities and accelerations, and dynamic performance. Traditional PMs have consistent topology, number of degrees of freedom (DoFs), and mobility characteristics, and these properties bound the PM's adaptability [11].

The reconfigurable PMs (rPMs) attracted much research attention. PMs are tempting alternatives for reconfiguration due to their legs' high modularization. Reconfigurable machines, in general, can be described as mechanisms that have two main characteristics, namely, the ability to transform their topology from one to another and the changeable mobility. Reconfiguration can be classified

into geometrical and topological reconfiguration, and the former means adjusting limbs' components size or orientation without rearranging them [4]. This paper will analyze a rPM capable of geometrical reconfiguration.

Both kinematic and static analysis are crucial steps in the PMs' design and significantly impact their applications. With the kinetostatic model, it is possible to know the PM performance indices and optimize them. Throughout this process, the designer can better adjust the machine to the demanded task [3].

Huang [3] proposed a new rPM by using an existing spatial overconstrained parallel mechanism. The author developed the kinematic model through the loop-closure equation and the dynamic one using the Lagrange formulation; computational software simulations have been done to validate obtained models. Jingjun [4] presented a n-4R rPM family adequated to geometrical reconfiguration and studied these multiple candidates' configurations concerning n limbs number, resulting in similar kinematic performances and also same DoF characteristics. Ye [11] investigated a new rPM based on a metamorphic spherical variable-axis joint in which phase changes can switch between different DoFs types, and then evaluates the machine kinematic performance and optimization.

The PM's static model definition requires the previous calculated kinematic model. One powerful method to compute the statics is through the well-known Davies' method, which was based on graph theory and screw theory, to describe the topology and joints' geometric features, respectively [5]. Golin [2] developed a cooperative robotic system kinestatic model, using the Kirchhoff laws adaptation as exposed by the Davies' method. Muraro [7] presented the kinetostatic model of a cable-actuated robot for bedridden patients applications. The author solved the kinematics analytically, and the statics was solved employing Davies' method.

Inspired by the recent developments and importance concerning the kinetostatic analysis and to overcome the mentioned PMs' limitations, this paper will provide the kinetostatic analysis of the 4-rRUU rPM proposed by [8]. This analysis is based on the natural coordinate system (NC). This method calculates the position kinematics through a combination of Cartesian components and unity vectors embedded in the rigid bodies [10]. Furthermore, to determine the statics, it was used Davies' method. This paper is organized as follows: in Sect. 2 the details concerning the 4-rRUU rPM family and its architecture itself is described. Sect. 3 calculates the inverse kinematic problem analytically adopting the NC system. Sect. 4 formulates the static model according to Davies' method. Finally, in Sect. 5 some conclusions and future works are discussed.

2   4-rRUU rPM Description

The rPM studied in this paper, henceforth known as 4-rRUU rPM (where the "rR" means reconfigurable revolute joint), was studied by Nayak [8]. This parallel architecture has 4-DoF 3T1R motion. Fig. 1 illustrates a 4-rRUU rPM variation topology (known as coupled architecture in this paper) which has similar structural and kinematic characteristics as 4-rRUU rPM studied by Nayak [8]. This
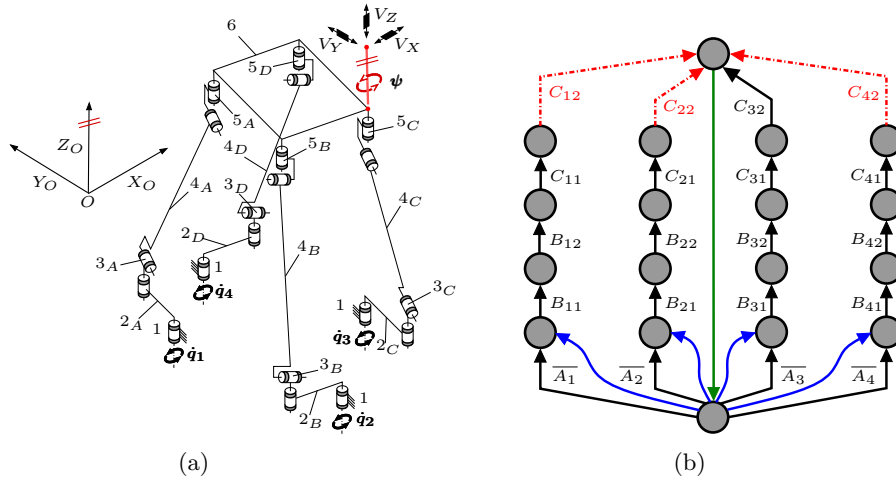
Fig. 1: (a) Coupled architecture, and (b) its directed graph representation.

figure shows the coupled architecture functional representation, illustrating all possible movements (V_X, V_Y, V_Z, ψ) and its directed graph representation.

Schönflies or 3T1R motion can perform three translations along the oriented Cartesian axes and one rotation around a specific axis, in that case, illustrated in Fig. 1, the Z axis. This topology has coupled motions, i.e., its operational velocities or end-effector velocities, depend on four actuated joints $V_k = V_k(\dot{q}_1, \dot{q}_2, \dot{q}_3, \dot{q}_4)$, $k = X, Y, Z$, in addition to $\psi = \psi(\dot{q}_1, \dot{q}_2, \dot{q}_3, \dot{q}_4)$. Coupled architecture must respect some connecting conditions to perform its motion. Namely, the first, the second, and the last revolute joints of each limb must have their axes parallel. Furthermore, the limbs' topology can be more satisfactory described as $4 - \overline{R} \parallel R \perp R \parallel R \perp R$, where the symbol $\parallel$ means that the joints are parallel or $\perp$ orthogonal to each other. The overline and numeral four represent the actuated joint and the total number of limbs, respectively.

The 4-rRUU rPM has its practical representation illustrated in Fig. 2, where both studied operation modes are presented. It can be seen that this figure shows different topologies compared to Fig. 1. First, one can notice that the functional representation as illustrated in Fig. 1 possesses five joints in each limb, while the 4-rRUU rPM in Fig. 2 have six joints. Although, the revolute joint located on the motor fixed on the base should be locked to select one specific operation mode. This modification leads the practical and functional representations to be the same. Additionally, the limbs' position and orientation changed, and the consecutive revolute joints with perpendicular axes in all limbs were considered universal joints. The 4-rRUU rPM has its limbs turned 90° in one direction. In Fig. 2a for example, the limbs are turned in such a manner that all actuated joints axes intersect in one point, which is the reference frame $O - XYZ$.

Naturally, this kind of modification can also alter the kinematic characteristics. Rotating the limbs in 90° as Fig. 2a illustrates will include one more constraint in the moving platform, since the last revolute joints have their axes
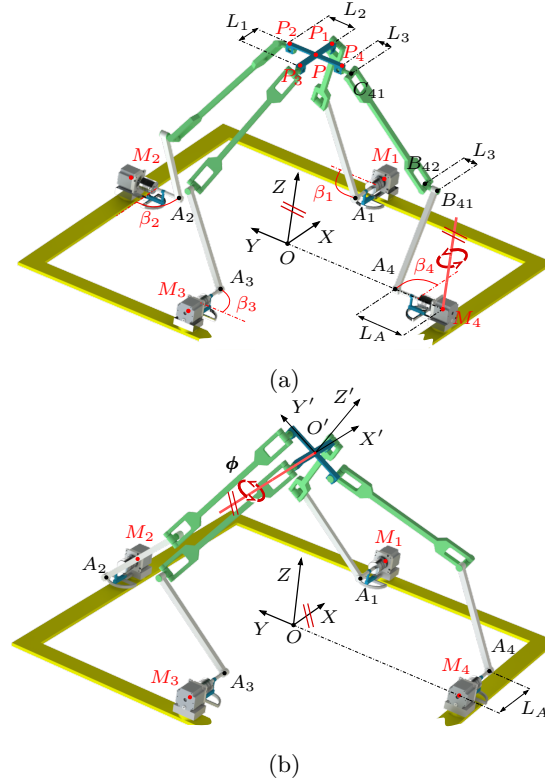
Fig. 2: (a) 4-rRUU rPM analyzed trivial, and (b) non-trivial situations.

intersecting at the same point. Thus, the axes are not parallel anymore, resulting in the mobility decrease in one degree, turning into a 3-DoF 3T motion. Fig. 2b in turn, also have their limbs rotated comparing to Fig. 1. However, in that case, the last revolute joint axes are not intersecting. In fact, the last revolute joints of limbs 1 and 3 intersect, notwithstanding, all last revolute joints axes are parallel similarly as Fig. 1. This fact leads to the same Schönflies motion type, with the rotational motion around the X axis in that case.

These motion type differences lead to the 4-rRUU rPM reconfigurable property. All actuated revolute joints (rR) are pivotable along with the Z axis by an angle β_i, where $i = 1, 2, 3, 4$ indicating each limb, and this actuated joints rotational motion leads to different operation modes. Nayak [9] studied the operation modes of the 4-rRUU rPM, describing two distinct operation modes. The first case concerns the arbitrarily oriented actuated joints' axes; furthermore, this operation mode depends on the design parameters and carries a mixed motion type. The second case regards the same orientation for opposite actuated revolute joint axes ($\beta_1 = \beta_3$ and $\beta_2 = \beta_4$); here, there are three trivial solutions where the first two are independent of the design parameters and actuated variables. Additionally, there exist two more non-trivial solutions for the second

case. This paper will consider only the situations that have not mixed motion type. Studying design parameters is not the focus of this paper.

It is essential to say that the β_i angles variation is done through manual intervention, i.e., the technician should choose the desired β_i angle for every joint and then lock it for the manipulator's correct operation. Tab. 1 shows a scheme for all 4-rRUU rPM operation modes. Examining first and second trivial

Table 1: 4-rRUU rPM operation modes.

Case	Actuated pairs orientation	Output forces
1	Arbitrarily oriented	Mixed motion type
2 - Trivial 1	$\beta_1 = \beta_3$ and $\beta_2 = \beta_4$	3-DoF 3T, upside-down
2 - Trivial 2	$\beta_1 = \beta_3$ and $\beta_2 = \beta_4$	3-DoF 3T, upright
2 - Trivial 3	$\beta_1 = \beta_3$ and $\beta_2 = \beta_4$	Mixed motion type
2 - Non-trivial 1	$\beta_1 = \beta_3 = \beta_2 - 90° = \beta_4 - 90°$	4-DoF 3T1R, upside-down
2 - Non-trivial 2	$\beta_1 = \beta_3 = \beta_2 - 90° = \beta_4 - 90°$	4-DoF 3T1R, upright

situations, the motion type is addressed as 3-DoF 3T motion. In the first trivial situation, the moving platform is upside-down (with the Z' axis illustrated in Fig. 2a pointing in the opposite direction of the Z axis). In the second trivial situation, the motion type is also a 3-DoF 3T, where the moving platform is in an upright position (with the Z' axis pointing in the same direction of the Z axis). It is of note that in some particular conditions for case 2, the solutions are not trivial, namely when $\beta_1 = \beta_3 = \beta_2 - 90° = \beta_4 - 90°$.

For these conditions, there are two more non-trivial situations, and both of them have Schönflies motion. Similar to the earlier mentioned two trivial situations, the first non-trivial situation has the moving platform in an upside-down position, and the second one in an upright position. The rotational motion is along with the moving reference frame X' axis, and this axis is oriented by an angle $\beta_2 = \beta_4$ concerning the X axis for both cases. Since the kinetostatic solutions of situations when the moving platform is in upright or upside-down positions are basically the same, this paper will consider only the moving platform upright position situations. Thus, referring to Tab. 1 this paper will evaluate the second condition for both trivial (Fig. 2a) and non-trivial (Fig. 2b) situations. Specifically, for the trivial situation, the adopted angles are $\beta_i = 90°$, moreover, $\beta_1 = \beta_3 = 90°$ and $\beta_2 = \beta_4 = 0°$ angles are adopted for non-trivial situation.

3   Inverse Kinematic Analysis

Multibody systems kinematic analysis is generally achieved geometrically through a vector-loop equation. This method was successfully applied by several authors, such as [6] who analyzed the stiffness of a 5-DoF PM. It presents, however, two major drawbacks. First, along with the procedure, all passive joint variables are eliminated. These passive joint variables are necessary to perform the static analysis. Second, the high degree of nonlinearity of the governing equations results in a complex computer implementation [10]. In order to overcome the mentioned drawbacks, inverse kinematics was developed through NC.

Let $\mathbf{M_i}$ be a point of the axis of rotation of the ith limb's motor. Through Fig. 2, the coordinates $\mathbf{M_i}$ may be obtained from the dimensions of the fixed frame. Hence, the coordinates of joints A_i can be calculated with simple trigonometry relations, as stated by Eq. 1.

$$\mathbf{A_i} = \begin{bmatrix} x_{M_i} + (i-2)L_A sin(\beta_i) \\ y_{M_i} + (2-i)L_A cos(\beta_i) \\ z_{M_i} \end{bmatrix}_{i=1,3} \text{, and } \mathbf{A_i} = \begin{bmatrix} x_{M_i} + (i-3)L_A cos(\beta_i) \\ y_{M_i} + (i-3)L_A sin(\beta_i) \\ z_{M_i} \end{bmatrix}_{i=2,4} \text{, (1)}$$

where L_A is the length of the link connecting the motor to joint A_i, and z_{M_i} is the height of the axis of the motor relative to O. For the analyzed cases, $z_{M_i} = 0$.

Since in the inverse kinematics the desired position of the moving platform $\mathbf{P}(x_p, y_p, z_p)$ is known, it is possible to calculate the coordinates of joints C_{i1}. First defining $\mathbf{G_i}$ as the C_{i1} joint position with respect to P_i or C_{i2} (P_i and C_{i2} points coincide), one can state the following equations for each limb:

$$\mathbf{G_1} = \begin{bmatrix} L_3 sin\beta_2 & L_3 cos\beta_2 & 0 \end{bmatrix}^\mathsf{T}, \mathbf{G_2} = \begin{bmatrix} -L_3 cos\beta_2 & L_3 sin\beta_2 & 0 \end{bmatrix}^\mathsf{T},$$
$$\mathbf{G_3} = \begin{bmatrix} -L_3 sin\beta_2 & -L_3 cos\beta_2 & 0 \end{bmatrix}^\mathsf{T}, \text{ and } \mathbf{G_4} = \begin{bmatrix} L_3 cos\beta_2 & -L_3 sin\beta_2 & 0 \end{bmatrix}^\mathsf{T}. \quad (2)$$

Also adopting $V = \begin{bmatrix} L_1 cos(\alpha) & L_2 sin(\alpha) & 0 \end{bmatrix}^\mathsf{T}$ and $\alpha = \frac{\pi}{2}(i-1)$ it is feasible to compute $\mathbf{C_{i1}}$ through Eq. 3 for the trivial situation. For the non-trivial situation, it is necessary to compute the coordinates of the C_{i1} joints considering the angle ϕ of the moving platform concerning the fixed frame, as presented by Eq. 4.

$$\mathbf{C_{i1}} = \mathbf{P} + V + \mathbf{G_i} = \begin{bmatrix} x_p \\ y_p \\ z_p \end{bmatrix} + \begin{bmatrix} L_1 cos(\alpha) \\ L_2 sin(\alpha) \\ 0 \end{bmatrix} + \mathbf{G_i}; \quad (3)$$

$${}^{O'}\mathbf{C_{i1}} = V + \mathbf{G_i}, \text{ and } \mathbf{C_{i1}} = \mathbf{P} + R_z(\beta_2)R_x(\phi) \cdot {}^{O'}\mathbf{C_{i1}},$$
$$\mathbf{C_{i1}} = \begin{bmatrix} x_p \\ y_p \\ z_p \end{bmatrix} + \begin{bmatrix} cos(\beta_2) & -sin(\beta_2)cos(\phi) & sin(\beta_2)sin(\phi) \\ sin(\beta_2) & cos(\beta_2)cos(\phi) & -cos(\beta_2)sin(\phi) \\ 0 & sin(\phi) & cos(\phi) \end{bmatrix} \cdot \begin{bmatrix} L_1 cos(\alpha) \\ L_2 sin(\alpha) \\ 0 \end{bmatrix} + \mathbf{G_i}. \quad (4)$$

${}^{O'}\mathbf{C_{i1}}$ and $\mathbf{C_{i1}}$ represent the C_{i1} joint position regarding the moving reference frame O' and fixed reference frame O, respectively. R_z and R_x are rotation matrices around the Z and X axis, and $\beta_2 = \beta_4$ are the 2 and 4 motors' angles. In Eq. 4, there are two rotation matrices (R_z and R_x) pre-multiplied according to the moving reference frame, resulting in the O' coordinate system orientation regarding O. Finally, multiplying the obtained result by V and adding the $\mathbf{G_i}$ and $\mathbf{P}$ coordinates, one can achieve the C_{i1} position concerning O.

At this point, there are two unknowns for each limb for both trivial and non-trivial situations. First, the A and C joints positions have already been calculated. In the trivial situation, the A joint coordinate x_A and the B joint coordinate x_B are equal for limbs 1 and 3. Additionally, y_A is equal to y_B for limbs 2 and 4. It should be noted that there is an offset distance between B_{i1} and B_{i2}, represented as L_3 in Fig. 2a. This offset distance must be considered when computing the position kinematics. Therefore, let B_{i1} be in the same plane

of joint A_i and B_{i2} considering the offset L_3. Similarly for joints C_i, C_{i2} is coincident to P_i, and C_{i1} considers the offset L_3. The remaining two unknowns for the trivial situation are $y_{B_{i1}}$ and $z_{B_{i1}}$ for limbs 1 and 3, and $x_{B_{i1}}$ and $z_{B_{i1}}$ for limbs 2 and 4. Considering the non-trivial situation, x_A and x_B are equal for all limbs, and then the two unknowns are the y_B and z_B. Through natural coordinates modeling, it is possible to achieve Eq. 5.

$$(\mathbf{B_{i1}} - \mathbf{A_i}) \cdot (\mathbf{B_{i1}} - \mathbf{A_i}) = L_{AB}^2, \text{ and } (\mathbf{C_{i1}} - \mathbf{B_{i2}}) \cdot (\mathbf{C_{i1}} - \mathbf{B_{i2}}) = L_{BC}^2. \quad (5)$$

Since Eq. 5 is nonlinear, it is not possible to solve them analytically. Hence, the Newton-Raphson numerical method is adopted to solve this system of equations. It should be noted that this architecture presents position redundancy, which means that the same position of the moving platform can be achieved by different orientations of each limb. The redundancy occurs because of the existing different operation modes, as described in Sect. 2. This redundancy, however, only occurs if the motor input angle changes the quadrant of operation. In order to guarantee that the numerical method will converge to a specific position, the numerical algorithm must limit the range of convergence.

In the trivial situation, the first, second, and fourth motors' inputs (q_1, q_2, q_4) are restricted to lay into the first quadrant, i.e., $0° \leq q_1, q_2, q_4 \leq 90°$. While q_3 is limited to the second quadrant, $90° \leq q_3 \leq 180°$. Additionally, regarding the studied position for non-trivial situation as Fig. 2b shows, q_1 and q_3 are restricted to the first $0° \leq q_1 \leq 90°$ and second $90° \leq q_3 \leq 180°$ quadrants, respectively. Defining these quadrants for first and third motor input angles solves the system completely. It is not necessary to restrict the quadrants for q_2 and q_4 since there are no position redundancy when q_1 and q_3 are restricted in this manner.

The method described in this section was developed using Python, and the results were validated through a CAD model of the 4-rRUU rPM. The validation process considered fifteen different moving platform positions and presented an average difference of $0.001612mm$, with a standard deviation of $0.003288mm$. The maximum, minimum, and mean percentage error was 0.00387%, 0.000028%, and 0.00118%, respectively. The presented deviation between the CAD and NC results is negligible and does not compromise the analysis precision.

4 Static Analysis Through Davies' Method

The static analysis of a mechanism is generally based on a system of equilibrium equations. The static equilibrium depends on the existence of external actions to the input links generated by actuators [1]. This paper aims to determine the output forces through the moving platform for a set of torque inputs from the motors. Further details of the employed Davies' method can be found in [1].

For the static analysis of the 4-rRUU rPM, the external forces acting on the moving platform and the torques generated by the motors must be internalized. The equilibrium equations are achieved from a directed graph representation of the mechanism, presented by Fig. 1b. The dashed red, black, blue, and green lines represent the chords, branches, torques generated by the motors, and the

external load applied to the moving platform. The number of cuts k is equal to the number of edges, minus the number of independent loops. Let C be the total number of constraints imposed by the joints. The cutset matrix Q is composed of k rows and C columns. Each element q_{ij} of the Q matrix may take on the values of 0, -1 or +1, following the pattern presented by Eq. 6.

$$q_{ij} = \begin{cases} 0, \text{if cut } i \text{ does not include edge } j; \\ +1, \text{if cut } i \text{ and edge } j \text{ shares the same direction}; \\ -1, \text{if cut } i \text{ and edge } j \text{ have opposite directions.} \end{cases} \quad (6)$$

Let λ be the number of DoFs of the workspace. The wrench \$ of a joint is a $\lambda \times C_{joint}$ matrix, where C_{joint} represents the number of constraints imposed by the joint, in which each column contains the λ unit action coordinates of the restraint action [1]. Each column of \$ represents the unit screw of a reaction force and can be determined individually. Hence, the first column of \$ is the reaction force's unit screw in the x direction, and the second column is the reaction force's unit screw in the y direction, and so on. The unit screw of a reaction force is defined as $\$_\psi = \begin{bmatrix} \vec{S} & \vec{S_0} \times \vec{S} \end{bmatrix}^\mathsf{T}$. Where $\vec{S}$ is a unit directional vector, which describes the direction of the axis of rotation of a joint, $\vec{S_0}$ is a position vector of any point belonging to the axis of rotation and ψ is a determined reaction force.

For each joint, the vector $\vec{S_0}$ is constructed with the results achieved from the position kinematics equations described in Sect. 3. The axis of rotation for joints A_i, B_{i1} and C_{i2} are constant, regardless of the moving platform's position. Hence, the vectors $\vec{S}$ for the aforementioned joints can be constructed manually by inspecting Fig. 2a and Fig. 2b. It can be seen that for the trivial case, the direction of the rotation axis for joints A_i, B_{i1} and C_{i2} are the same for each limb and are shown as follows: $\vec{S} = \begin{bmatrix} 1 & 0 & 0 \end{bmatrix}^\mathsf{T}$, for limbs 1 and 3, and $\vec{S} = \begin{bmatrix} 0 & 1 & 0 \end{bmatrix}^\mathsf{T}$, for limbs 2 and 4. For the non-trivial case, all axes are oriented to the x direction. Hence, vector $\vec{S}$ for the same joints are given by: $\vec{S} = \begin{bmatrix} 1 & 0 & 0 \end{bmatrix}^\mathsf{T}$.

The rotation axis for joints B_{i2} and C_{i1} may change their direction as the moving platform translates. Let $\vec{S_{B_{i2}}}$ be the unit direction vector for joints B_{i2} and C_{i1}, and $\vec{B_{i2}C_{i1}}$ be the vector along link $B_{i2}C_{i1}$, which can be determined by the position kinematics. Since $\vec{B_{i2}C_{i1}}$ and $\vec{S_{B_{i2}}}$ are always orthogonal, their dot product is always equal to zero as Eq. 7 shows.

In the trivial case, one can see from Fig. 2a that joint B_{i2} axis of rotation changes its direction in the YZ plane for limbs 1 and 3. Hence, the x coordinate of $\vec{S_{B_{i2}}}$ is always equal to zero. After expanding the dot product exhibited in Eq. 7, it is possible to achieve the first vector presented in this equation. The same process applied to limbs 2 and 4 is also calculated by this equation. In the non-trivial case, it can be seen from Fig. 2b that joint B_{i2} axis of rotation changes its direction in the YZ plane for all limbs. Hence, $\vec{S_{B_{i2}}}$ is determined only by the first vector presented in Eq. 7 where the x axis coordinate is null.

$$\vec{B_{i2}C_{i1}} \cdot \vec{S_{B_{i2}}} = 0 \Rightarrow \begin{cases} \vec{S_{B_{i2}}} = \begin{bmatrix} 0 & -\frac{z_{B_{i2}C_{i1}}}{y_{B_{i2}C_{i1}}} & z_{B_{i2}C_{i1}} \end{bmatrix}^\mathsf{T}, \text{for i=1, i=3}; \\ \vec{S_{B_{i2}}} = \begin{bmatrix} -\frac{z_{B_{i2}C_{i1}}}{x_{B_{i2}C_{i1}}} & 0 & z_{B_{i2}C_{i1}} \end{bmatrix}^\mathsf{T}, \text{for i=2, i=4.} \end{cases} \quad (7)$$

Finally, a joint wrench matrix can be assembled by joining each reaction unit wrench. For a joint that restricts every possible motion ($C_{joint} = 6$), its wrench would be presented as follows: $\$ = \begin{bmatrix} \$_{F_x} & \$_{F_y} & \$_{F_z} & \$_{T_x} & \$_{T_y} & \$_{T_z} \end{bmatrix}$.

As stated above, the external forces must be internalized. The wrench that represents the external load, $\$_{F_{load}}$, can be obtained by the same procedure as the joints. The wrenches can be bound together in a single unit action matrix, A_D. As presented by Eq. 8, the A_D matrix is assembled by positioning first the chord wrenches, and afterwards the branches. The network action matrix A_N establishes the relationship between the wrenches grouped in A_D with the k cuts defined in the cutset matrix Q. Each row of Q represents which wrenches belong to that respective row, considering its sign (positive or negative). A systematic approach to build the A_N matrix is presented by Eq. 9.

$$A_D = \begin{bmatrix} \$_{C_1} & \$_{C_2} & \$_{C_4} & \$_{A_1} & \$_{B_1} & \$_{A_2} & \$_{B_2} & \$_{A_3} & \$_{B_3} & ... & \$_{C_3} & \$_{A_4} & \$_{B_4} & \$_{F_{load}} \end{bmatrix}; \qquad (8)$$

$$A_N = \begin{bmatrix} [A_D]_{\lambda,C} \cdot diag\{[Q_1]_{1,C}\} \\ [A_D]_{\lambda,C} \cdot diag\{[Q_2]_{1,C}\} \\ \vdots \\ [A_D]_{\lambda,C} \cdot diag\{[Q_k]_{1,C}\} \end{bmatrix}. \qquad (9)$$

Let $[\Psi]_{C,1}$ be the action magnitude vector, composed of all mechanism's reaction forces. The cutset law states that the sum of all wrenches belonging to the same cut must be equal to zero. Hence, the matrix $[A_N]_{\lambda k,C}$ multiplied by $[\Psi]_{C,1}$ is equal to zero, namely: $[A_N][\Psi] = [\overrightarrow{0}]$. This equation is only solvable if matrix A_N is square. However, for an overconstrained mechanism, there is a required number of known variables $C_n = C - \lambda k$ to fully define the mechanism.

In order to solve the statics, it is necessary to identify both known (primary) and unknown (secondary) variables. This paper considers that the torque applied by each motor is known. Ultimately, it is feasible to divide the network action matrix in a primary A_{N_p} and secondary A_{N_s} network action matrices. The magnitude vector Ψ is also divided in the same manner as follows:

$$[A_{N_s}][\Psi_s] = -[A_{N_p}][\Psi_p]. \qquad (10)$$

The static analysis method presented in this section was developed for both trivial and non-trivial situations in Python. Even though the number of known variables does not match the C_n number, i.e., the A_{N_s} matrix is not square, the problem is solvable by the least-squares solution approach. This method computes the **x** vector that approximately solves the system of equations in the form of $\mathbf{Ax} = \mathbf{b}$ and can be implemented through the *numpy.linalg.lstsq* python package. Table 2 presents the adopted torque input of each actuator and the resulting output forces for each situation.

Table 2: Static analytical model results.

Case	Input torques $[Nm]$	Output reactions
Trivial	$T_{A1} = 15$, $T_{A2} = -30$, $T_{A3} = 15$, $T_{A4} = -30$	$F_x = 116.92N$, $F_y = 72.59N$, $F_z = -232.32N$
Non-trivial		$F_x = -336.71N$, $F_y = 398.10N$, $F_z = -54.62N$, $T_x = -41.51Nm$

5   Conclusions

This paper developed the static analysis of a rPM based on screw theory and Davies' method. The 4-rRUU PM's inverse kinematics was modeled through NC, which result in a system of nonlinear equations. These equations were solved through the Newton-Raphson numerical method, presenting a mean error of 0.00118% concerning the designed CAD model. The results achieved were used to perform the rPM's static analysis under two configurations yielding an analytical model. The conducted static analysis produced consistent results regarding the applied input torques. For future works, the results obtained from the inverse position kinematics and static analysis will be used to perform a stiffness analysis of the 4-rRUU rPM to establish its suitability in several applications better. Furthermore, one can validate the achieved results by static analysis employing a different method such as the numerical finite element analysis.

References

1. Davies, T.: The 1887 committee meets again, freedom and constraint (2000)
2. Golin, J.F., Frantz, J.C., Simas, H.: Kinestatic analysis of serial-parallel cooperative robotic systems. In: 23rd ABCM International Congress of Mechanical Engineering, pp. 1–7 (2015)
3. Huang, G., Zhang, D., Tang, H., Kong, L., Song, S.: Analysis and control for a new reconfigurable parallel mechanism. International Journal of Advanced Robotic Systems **17**(5), 1729881420931,322 (2020)
4. Jingjun, Y., Zhixiang, D., Yan, X.: Kinematics analysis of n-4R reconfigurable parallel mechanisms. In: Advances in Reconfigurable Mechanisms and Robots II, pp. 275–285. Springer (2016)
5. Laus, L., Simas, H., Martins, D.: Machine efficiency determined using graph and screw theories with application in robotics. Mechanism and Machine Theory **148**, 103,748 (2020)
6. Lian, B., Sun, T., Song, Y., Jin, Y., Price, M.: Stiffness analysis and experiment of a novel 5-DoF parallel kinematic machine considering gravitational effects. International Journal of Machine Tools and Manufacture **95**, 82–96 (2015)
7. Muraro, T., Simas, H., Martins, D.: Kinematic and static analysis of the cable-driven spatial mechanism for bedridden patients. Intl Cong Mech Eng **23** (2015)
8. Nayak, A., Caro, S., Wenger, P.: Kinematic analysis and design optimization of a 4-rRUU parallel manipulator. In: Advances in Mechanism and Machine Science Proceedings of the 15th IFToMM World Congress on Mechanism and Machine Science (2019)
9. Nayak, A., Caro, S., Wenger, P.: Operation modes and workspace of a 4-rRUU parallel manipulator. In: IFToMM World Congress on Mechanism and Machine Science, pp. 649–657. Springer (2019)
10. Xu, X., Luo, J., Feng, X., Peng, H., Wu, Z.: A generalized inertia representation for rigid multibody systems in terms of natural coordinates. Mechanism and Machine Theory **157**, 104,174 (2021)
11. Ye, W., Chai, X., Zhang, K.: Kinematic modeling and optimization of a new reconfigurable parallel mechanism. Mechanism and Machine Theory **149**, 103,850 (2020)

A Novel Construction Method for the Type Synthesis of Variable-DOF Mechanisms

Xianwen Kong

Heriot-Watt University, Edinburgh EH14 4AS UK,
X.Kong@hw.ac.uk,
WWW home page: http://home.eps.hw.ac.uk/~xk5/

Abstract. This paper proposes a novel construction method for the type synthesis of variable-DOF mechanisms. Using the proposed method, variable-DOF mechanisms can be obtained in two steps: The first step is to construct multi-DOF overconstrained mechanisms using compositional overconstrained mechanisms, and the second step is to obtain variable-DOF mechanisms by removing a link from each multi-DOF overconstrained mechanism obtained in the first step. An 8-link variable-DOF planar mechanism is obtained using this method, which has less number of links than the existing variable-DOF multi-loop planar mechanisms. Motion mode analysis of an example 8-link variable-DOF planar mechanism shows that it has one 2-DOF motion mode and seven 1-DOF motion modes.

Keywords: Variable-DOF mechanism, Type synthesis, Construction method, Overconstrained mechanism, Motion mode

1 Introduction

Variable-DOF (or kinematotropic) mechanisms [1–13] are a class of reconfigurable mechanisms. Several approaches have been proposed for the type synthesis of variable-DOF single-loop spatial mechanisms [3–7, 9, 11] and parallel mechanisms [10, 12–14, 16]. In addition to method by intuition [1], mathematical methods [2, 3, 9–11, 15, 16], construction methods [4, 5, 7] have also been proposed.

Several variable-DOF multi-loop planar mechanisms, such as the 12-link Wunderlich mechanism [1] and 10-link Kovalev mechanism [2], have been proposed. However, the number of variable-DOF multi-loop planar mechanisms proposed so far is very limited. This paper is to extend the construction approach to the type synthesis of variable-DOF mechanisms and to reveal an 8-link variable-DOF multi-loop planar mechanism with fewer number of links than the Wunderlich mechanism [1] and Kovalev mechanism.

This paper is organized as follows. In Section 2, a novel construction method for the type synthesis of variable-DOF mechanisms is proposed, and the construction of a novel variable-DOF 8-link planar mechanism is presented. The motion modes of the novel variable-DOF 8-link planar mechanism are identified in Sections 3. Finally, conclusions are drawn.

Since this paper focuses on the type synthesis of variable-DOF mechanisms, link interference is ignored in this paper and will be addressed in the future.

2   A novel construction method for the type synthesis of variable-DOF mechanisms

Unlike the construction methods for the type synthesis of variable-DOF mechanisms in which joints are added to an overconstrained mechanism [4, 5, 7, 12], a novel construction method for the type synthesis of variable-DOF mechanisms in which a link is removed is proposed from an overconstrained mechanism in this section to complement the existing construction methods.

Using this novel construction method, variable-DOF mechanisms can be obtained in two steps:

Step 1: Construct multi-DOF overconstrained mechanisms using compositional overconstrained mechanisms. For example, a 5-link 3-RR planar parallelogram is composed of two identical links ($A_1A_2A_3$ and $B_1B_2B_3$ in Fig. 1(a) or $A_1'A_2'A_3'$ and $B_1'B_2'B_3'$ in Fig. 1(b)) connected with three RR links ($A_1B_1 = A_2B_2 = A_3B_3$ in Fig. 1(a) or $A_1'B_1' = A_2'B_2' = A_3'B_3'$ in Fig. 1(b)) of equal link lengths. Here R denotes a revolute joint. By assembling two 1-DOF planar 5-link 3-RR parallelograms (Figs. 1(a) and 1(b)) in such a way that links A_2B_2 and $A_2'B_2'$ coincide and the joint axes of R joints A_2 and B_2 are collinear with the joint axes of R joints A_2' and B_2' respectively, we can obtain a 2-DOF 9-link planar mechanism (Fig. 1(c)).
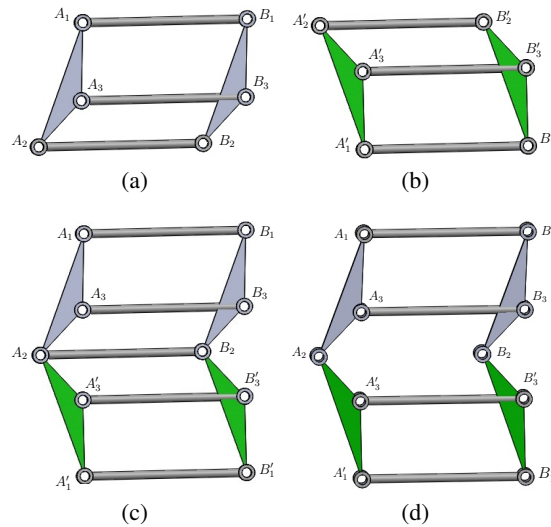
Fig. 1. Construction of a variable-DOF mechanism: (a) 5-link 3-RR planar parallelogram I, (b) 5-link 3-RR planar parallelogram II, (c) A 2-DOF 9-link planar mechanism, and (d) An 8-link variable-DOF planar mechanism.

Step 2: Obtain variable-DOF mechanisms by removing a link from each multi-DOF overconstrained mechanism constructed in Step 1. For example, by removing the common link (A_2B_2) from the 2-DOF 9-link planar mechanism in Fig. 1(c), we can

obtain a variable-DOF 8-link planar mechanism (Fig. 1(d)). From the construction of the mechanism, one can observe that this mechanism has a 2-DOF motion mode. In addition, the DOF of the mechanism obtained using traditional mobility formulas for planar mechanisms is one. Therefore, this mechanism should have at least one 1-DOF motion mode.

In addition to the above 8-link variable-DOF planar mechanism, a number of new variable-DOF planar and spatial mechanisms can be obtained using the above construction approach.

From a ν-loop overconstrained mechanism constructed using n_U compositional overconstrained mechanisms, a $(\nu - n_U + 1)$-loop variable-DOF mechanism can be obtained. In the above example, a 3-loop variable-DOF mechanism (Fig. 1(d)) is obtained from a 4-loop overconstrained mechanism (Fig. 1(c)) constructed using two compositional overconstrained mechanisms.

3   Motion mode analysis of an 8-link variable-DOF planar mechanism

In this section, we will reveal all the motion modes of the novel 8-link variable-DOF mechanism obtained in Section 2.

3.1   Geometric description of the 8-link variable-DOF planar mechanism

The link parameters of the 8-link variable-DOF planar mechanism (Fig. 2) are:
$a_1 = A_1A_2 = B_1B_2$, $a_2 = A_1A_3 = B_1B_3$, $\alpha = \angle A_2A_1A_3 = \angle B_2B_1B_3$, $a_1' = A_1'A_2' = B_1'B_2$, $a_2' = A_1'A_3' = B_1'B_3'$, $\alpha' = \angle A_2A_1'A_3' = \angle B_2B_1'B_3'$, and $A_1B_1 = A_3B_3 = A_1'B_1' = A_3'B_3' = L_1$. In this paper, we focus on 8-link variable-DOF mechanisms with $\alpha \neq 0$ and $\alpha' \neq 0$.

For the example 8-link variable-DOF planar mechanism in this paper, $a_1 = a_1' = 80$, $a_2 = a_2' = 15\sqrt{10}$, $\alpha = \alpha' = atan(1/3)$, and $L_1 = 100$.

3.2   Kinematic equations

For the purpose of simplification and without loss of generality, four coordinate systems are established. The coordinate system $O - XY$ is attached to the link $A_1A_2A_3$ with O being coincident with A_1 and the X-axis passing through A_2. The coordinate system $O_B - X_BY_B$ is attached to the link $B_1B_2B_3$ with O_B being coincident with B_1 and the X_B-axis passing through B_2. The coordinate system $O' - X'Y'$ is attached to the link $A_1'A_2'A_3'$ with O' being coincident with A_1' and the X'-axis passing through A_2'. The coordinate system $O_B' - X_B'Y_B'$ is attached to the link $B_1'B_2B_3'$ with O_B' being coincident with B_1' and the X_B'-axis passing through B_2. Let ϕ (θ and ξ) denote the angle between the X_B-axis (link A_1B_1, link A_3B_3) and $X-$axis measured anti-clockwise, and ϕ' (θ' and ξ') be the angle between the X_B'-axis (link $A_1'B_1'$, link $A_3'B_3'$) and $X'-$axis measured clockwise.
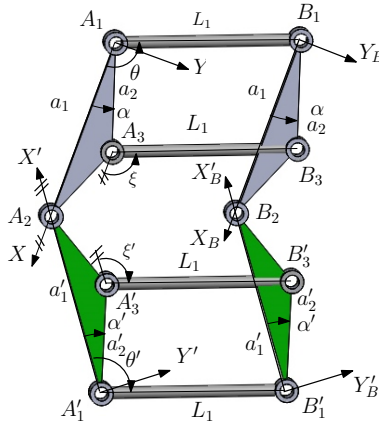
Fig. 2. Link parameters of the 8-link variable-DOF planar mechanism.

The loop closure equations of loops $A_1B_1B_3A_3A_1$, $A_1B_1B_2B'_1A'_1A_2A_1$ and $A'_1B'_1B'_3A'_3A'_1$ written in complex form are

$$
\begin{cases}
(L_1e^{i\theta} + a_2e^{i(\phi+\alpha)} - a_2e^{i\alpha})(L_1e^{-i\theta} + a_2e^{-i(\phi+\alpha)} - a_2e^{-i\alpha}) = (L_1e^{i\xi})(L_1e^{-i\xi}) \\
(L_1e^{i\theta} + a_1e^{i\phi} - a_1)(L_1e^{-i\theta} + a_1e^{-i\phi} - a_1) \\
= (L_1e^{i\theta'} + a'_1e^{i\phi'} - a'_1)(L_1e^{-i\theta'} + a'_1e^{-i\phi'} - a'_1) \\
(L_1e^{i\theta'} + a'_2e^{i(\phi'+\alpha')} - a'_2e^{i\alpha'})(L_1e^{-i\theta'} + a'_2e^{-i(\phi'+\alpha')} - a'_2e^{-i\alpha'}) = (L_1e^{i\xi'})(L_1e^{-i\xi'})
\end{cases}
$$

i.e.,

$$
\begin{cases}
2L_1a_1(C\phi - 1)C\theta + 2L_1S\theta S\phi a_1 - 2C\phi a_1^2 + L_1^2 + 2a_1^2 = \\
2L_1a'_1(C\phi' - 1)C\theta' + 2L_1S\theta'S\phi'a'_1 - 2C\phi'^2a'_1 + L_1^2 + 2a'^2_1 \\
2a_2(((C\phi - 1)C\theta + S\theta S\phi)L_1C\alpha \\
-L_1S\phi C\theta S\alpha + (C\phi - 1)(L_1S\theta S\alpha - a_2)) = 0 \\
2a'_2(((C\phi' - 1)C\theta' + S\theta'S\phi')L_1C\alpha' \\
-L_1S\phi'C\theta'S\alpha' + (C\phi' - 1)(L_1S\theta'S\alpha' - a'_2)) = 0
\end{cases}
\tag{1}
$$

where $S*$ and $C*$ denote $\sin *$ and $\cos *$ respectively.

To simplify the motion mode analysis of the 8-link variable-DOF planar mechanism. Let L_2 denote the distance between A_2 and B_2. Equation (1) can be turned into a set of four equations.

$$
\begin{cases}
2L_1a_1(C\phi - 1)C\theta + 2L_1S\theta S\phi a_1 - 2C\phi a_1^2 + L_1^2 + 2a_1^2 = L_2^2 \\
2a_2(((C\phi - 1)C\theta + S\theta S\phi)L_1C\alpha \\
-L_1S\phi C\theta S\alpha + (C\phi - 1)(L_1S\theta S\alpha - a_2)) = 0 \\
2L_1a'_1(C\phi' - 1)C\theta' + 2L_1S\theta'S\phi'a'_1 - 2C\phi'a'^2_1 + L_1^2 + 2a'^2_1 = L_2^2 \\
2a'_2(((C\phi' - 1)C\theta' + S\theta'S\phi')L_1C\alpha' \\
-L_1S\phi'C\theta'S\alpha' + (C\phi' - 1)(L_1S\theta'S\alpha' - a'_2)) = 0
\end{cases}
\tag{2}
$$

The motion mode analysis of the 8-link variable-DOF planar mechanism can be obtained by solving Eq. (2). The 3rd and 4th equations of Eq. (2) can be obtained from

the 1st and 2nd equations by replacing a_1, a_2, α, ϕ and θ with a'_1, a'_2, α', ϕ' and θ' respectively. To solve Eq. (2), we can first solve the following two subsets of Eq. (2), including Eq. (3) composed of the 1st and 2nd equations and Eq. (4) composed of the 3rd and 4th equations, and then combine these solutions to obtain solutions to Eq. (2).

$$\begin{cases} 2L_1a_1(C\phi - 1)C\theta + 2L_1S\theta S\phi a_1 - 2C\phi a_1^2 + L_1^2 + 2a_1^2 = L_2^2 \\ 2a_2(((C\phi - 1)C\theta + S\theta S\phi)L_1C\alpha \\ \quad -L_1S\phi C\theta S\alpha + (C\phi - 1)(L_1S\theta S\alpha - a_2)) = 0 \end{cases} \tag{3}$$

$$\begin{cases} 2L_1a'_1(C\phi' - 1)C\theta' + 2L_1S\theta'S\phi'a'_1 - 2C\phi'a_1'^2 + L_1^2 + 2a_1'^2 = L_2^2 \\ 2a'_2(((C\phi' - 1)C\theta' + S\theta'S\phi')L_1C\alpha' \\ \quad -L_1S\phi'C\theta'S\alpha' + (C\phi' - 1)(L_1S\theta'S\alpha' - a'_2)) = 0 \end{cases} \tag{4}$$

3.3 Solutions to Eq. (3)

Rewriting Eq. (3) as a set of linear equations in $S\theta$ and $S\theta$, we have

$$\begin{cases} RC\theta + SS\theta + Q = 0 \\ UC\theta + VS\theta + W = 0 \end{cases} \tag{5}$$

where $R = 2L_1a_1(C\phi - 1)$, $S = 2L_1S\phi a_1$, $Q = -2C\phi a_1^2 + L_1^2 - L_2^2 + 2a_1^2$, $U = a_2((C\phi - 1)L_1C\alpha - L_1S\phi S\alpha)$, $V = a_2(S\phi L_1C\alpha + (C\phi - 1)L_1S\alpha)$, and $W = -a_2^2(C\phi - 1)$.

The determinant of the coefficient matrix of the above equation is

$$\Delta = RV - US = 4L_1^2a_1a_2S\alpha(C\phi - 1) \tag{6}$$

Therefore, solutions to Eq. (5) can be classified into two classes, including solutions with $C\phi - 1 = 0$ and solutions with $C\phi - 1 \neq 0$.

Solutions with $C\phi - 1 = 0$ In the case of $C\phi - 1 = 0$, we have $S\phi = 0$. The second equation in Eq. (5) is met. The first equation in Eq. (5) leads to

$$L_2 = L_1 \tag{7}$$

In this case, θ can have any value.

Solutions with $C\phi - 1 \neq 0$ Solving Eq. (5) for $C\theta$ and $S\theta$, we obtain

$$\begin{cases} C\theta = (SW - VQ)/\Delta \\ S\theta = -(RW - UQ)/\Delta \end{cases} \tag{8}$$

The substitution of Eq. (8) into $C^2\theta + S^2\theta = 1$ yields

$$2a_2^2L_1^2(C\phi - 1)(-L_2^4 + (e_0C\phi + e1)L_2^2 + e_2C^2\phi + e_3C\phi + e_4) = 0 \tag{9}$$

where $e_0 = 4a_1a_2C\alpha - 4a_1^2$, $e_1 = -4a_1a_2C\alpha + 2L_1^2 + 4a_1^2$, $e_2 = 8C\alpha a_1^3 a_2 - 4a_1^4 - 4a_1^2 a_2^2$, $e_3 = 8L_1^2 C\alpha^2 a_1^2 - 4L_1^2 C\alpha a_1 a_2 - 16C\alpha a_1^3 a_2 - 4L_1^2 a_1^2 + 8a_1^4 + 8a_1^2 a_2^2$, and $e_4 = -8L_1^2 C\alpha^2 a_1^2 + 4L_1^2 C\alpha a_1 a_2 + 8C\alpha a_1^3 a_2 - L_1^4 + 4L_1^2 a_1^2 - 4a_1^4 - 4a_1^2 a_2^2$.

If $L_2 = L_1$, Eq. (9) becomes

$$(C\phi - 1)^2 [f_0 C\phi + f_1] = 0 \tag{10}$$

where

$$f_0 = 2a_1 a_2 C\alpha - a_1^2 - a_2^2$$

$$f_1 = 2L_1^2 C^2 \alpha - 2a_1 a_2 C\alpha - 2L_1^2 + a_1^2 + a_2^2$$

Eq. (10) is then reduced to a linear equation in $C\phi$

$$f_0 C\phi + f_1 = 0 \tag{11}$$

If $L_2 \neq L_1$, Eq. (9) is reduced to a equation in $C\phi$ and L_2^2 as

$$-L_2^4 + (e_0 C\phi + e_1)L_2^2 + e_2 C^2 \phi + e_3 C\phi + e_4 = 0 \tag{12}$$

The solutions to Eq. (3) of the 8-link variable-DOF planar mechanism are summarized in Table 1.

Table 1. Solutions to Eq. (3).

No	Case	ϕ	θ
I	$L_2 = L_1$	0	Any value
II		$\begin{cases} C\phi = -f_1/f_0 \\ S\phi = (1 - C^2\phi)^{1/2} \end{cases}$ where $f_0 = 2a_1 a_2 C\alpha - a_1^2 - a_2^2$ and $f_1 = 2L_1^2 C^2 \alpha - 2a_1 a_2 C\alpha - 2L_1^2 + a_1^2 + a_2^2$.	$\begin{cases} C\theta = (SW - VQ)/\Delta \\ S\theta = -(RW - UQ)/\Delta \end{cases}$ where $\Delta = 4L_1^2 a_1 a_2 S\alpha(C\phi - 1)$, $R = 2L_1 a_1 (C\phi - 1)$, $S = 2L_1 S\phi a_1$, $Q = -2C\phi a_1^2 + L_1^2 - L_2^2 + 2a_1^2$, $U = a_2((C\phi - 1)L_1 C\alpha - L_1 S\phi S\alpha)$, $V = a_2(S\phi L_1 C\alpha + (C\phi - 1)L_1 S\alpha)$, $W = 2a_2^2(C\phi - 1)$.
III		$\begin{cases} C\phi = -f_1/f_0 \\ S\phi = -(1 - C^2\phi)^{1/2} \end{cases}$	
IV	$L_2 \neq L_1$	$-L_2^4 + (e_0 C\phi + e_1)L_2^2 + e_2 C^2\phi + e_3 C\phi + e_4 = 0$ where $e_0 = 4a_1 a_2 C\alpha - 4a_1^2$, $e_1 = -4a_1 a_2 C\alpha + 2L_1^2 + 4a_1^2$, $e_2 = 8C\alpha a_1^3 a_2 - 4a_1^4 - 4a_1^2 a_2^2$, $e_3 = 8L_1^2 C\alpha^2 a_1^2 - 4L_1^2 C\alpha a_1 a_2 - 16C\alpha a_1^3 a_2 - 4L_1^2 a_1^2 + 8a_1^4 + 8a_1^2 a_2^2$, and $e_4 = -8L_1^2 C\alpha^2 a_1^2 + 4L_1^2 C\alpha a_1 a_2 + 8C\alpha a_1^3 a_2 - L_1^4 + 4L_1^2 a_1^2 - 4a_1^4 - 4a_1^2 a_2^2$.	

3.4   Solutions to Eq. (4)

Similarly, there are four solutions to Eq. (4). These four solutions, I', II', III' and IV', can be obtained from the four solutions to Eq. (3) in Table 1 by replacing a_1, a_2, α, e_i, f_i, ϕ and θ with a'_1, a'_2, α', e'_i, f'_i, ϕ' and θ' respectively.

3.5   Motion mode analysis of the 8-link variable-DOF planar mechanism

By combining the solutions, I, II, III and IV, to Eq. (3) and the solutions, I', II', III' and IV', to Eq. (4), we can obtain that there are six solutions to Eq. (2): I-I', I-II', I-III', I'-II, I'-III, and IV-IV'. The first five solutions can be readily obtained, while elimination of L_2 is required to obtain the sixth solution IV-IV'. As detailed in the remaining of this section, one can obtain all the motion modes of a 8-link variable-DOF planar mechanism from these solutions. All the motion modes of the example 8-link variable-DOF planar mechanism are shown as a point, straight line or curve in the $\phi - \phi'$ plane (Fig. 3). Eight configurations, including one in each of the motion modes, of the example 8-link variable-DOF planar mechanism are illustrated in Fig. 4, where link $A'_1 B'_1$ is selected as the frame of the mechanism.
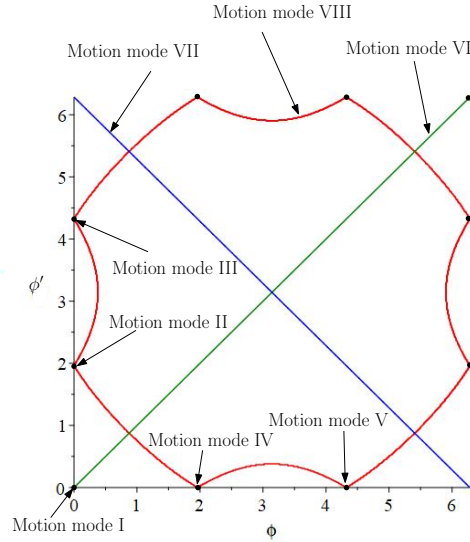
Fig. 3. Eight motion modes the example variable-DOF 8-link planar mechanism in ϕ-ϕ' space.

Solution I-I' represents motion mode I of the 8-link variable-DOF planar mechanism. In motion mode I (Fig. 4(a)), we have $\phi = \phi' = 0$. Loops A_1-B_1-B_3-A_3 and A'_1-B'_1-B'_3-A'_3 are both parallelograms, and the mechanism has two DOF with θ and θ' as independent joint variables.

Solutions I-II' (Fig. 4(b)) and I-III' (Fig. 4(c)) represent motion modes II and III of the 8-link variable-DOF planar mechanism. In these motion modes, $\phi = 0$, and ϕ' is a
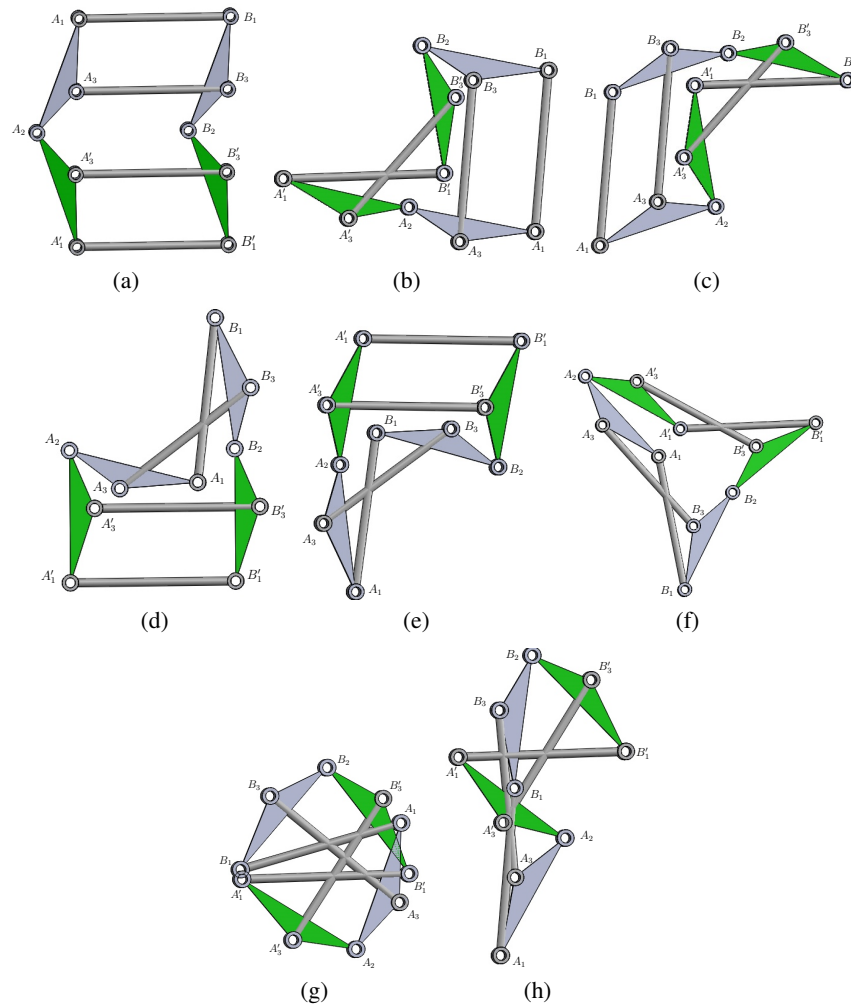
Fig. 4. The example 8-link variable-DOF planar mechanism in: (a) Motion mode I; (b) Motion mode II; (c) Motion mode III; (d) Motion mode IV; (e) Motion mode V; (f) Motion mode VI; (g) Motion mode VII; and (h) Motion mode VIII;

non-vanishing constant. Loop A_1-B_1-B_3-A_3 is a parallelogram while loop A'_1-B'_1-B'_3-A'_3 is an anti-parallelogram. Joints A'_1, B'_1, B'_3 and A'_3 lose their DOF. The mechanism has one DOF with θ as an independent joint variable.

Solutions I'-II (Fig. 4(d)) and I'-III (Fig. 4(e)) represent motion modes IV and V of the 8-link variable-DOF planar mechanism. In these motion modes, $\phi' = 0$, and ϕ is a non-vanishing constant. Loop A'_1-B'_1-B'_3-A'_3 is a parallelogram while loop A_1-B_1-B_3-A_3 is an anti-parallelogram. Joints A_1, B_1, B_3 and A_3 lose their DOF. The mechanism has one DOF with θ' as an independent joint variable. .

Solution IV-IV′ (Figs. 4(f), 4(g), 4(h)) leads to at least one 1-DOF motions mode, in which loops A_1-B_1-B_3-A_3 and A'_1-B'_1-B'_3-A'_3 are both anti-parallelograms. For this solution, we have

$$\begin{cases} -L_2^4 + (e_0 C\phi + e_1)L_2^2 + e_2 C^2\phi + e_3 C\phi + e_4 = 0 \\ -L_2^4 + (e'_0 C\phi' + e'_1)L_2^2 + e'_2 C^2\phi' + e'_3 C\phi' + e'_4 = 0 \end{cases} \tag{13}$$

Eliminating L_2 from Eq. (13), we obtain a nonlinear equation in $C\phi$ and $C\phi'$ as

$$\sum_{i=1}^{4}\sum_{j=1}^{4-i} h_{i,j} C^i\phi C^j\phi' = 0 \tag{14}$$

where $h_{0,4} = -e_2'^2$, $h_{1,3} = -e_0 e'_0 e'_2$, $h_{0,3} = -e_1 e'_0 e'_2 - 2e'_2 e'_3$, $h_{2,2} = e_0^2 e'_2 + e_2 e_0'^2 + 2e_2 e'_2$, $h_{1,2} = 2e_0 e_1 e'_2 - e_0 e'_0 e'_3 - e_0 e'_1 e'_2 + e_3 e_0'^2 + 2e_3 e'_2$, $h_{0,2} = e_1^2 e'_2 - e_1 e'_0 e'_3 - e_1 e'_1 e'_2 + e_4 e_0'^2 + 2e_4 e'_2 - 2e'_2 e'_4 - e_3'^2$, $h_{3,1} = -e_0 e_2 e'_0$, $h_{2,1} = e_0^2 e'_3 - e_0 e_3 e'_0 - e_1 e_2 e'_0 + 2e_2 e'_0 e'_1 + 2e_2 e'_3$, $h_{1,1} = 2e_0 e_1 e'_3 - e_0 e_4 e'_0 - e_0 e'_0 e'_4 - e_0 e'_1 e'_3 - e_1 e_3 e'_0 + 2e_3 e'_0 e'_1 + 2e_3 e'_3$, $h_{0,1} = e_1^2 e'_3 - e_1 e_4 e'_0 - e_1 e'_0 e'_4 - e_1 e'_1 e'_3 + 2e_4 e'_0 e'_1 + 2e_4 e'_3 - 2e'_3 e'_4$, $h_{4,0} = -e_2^2$, $h_{3,0} = -e_0 e_2 e'_1 - 2e_2 e_3$, $h_{2,0} = e_0^2 e'_4 - e_0 e_3 e'_1 - e_1 e_2 e'_1 + e_2 e_1'^2 - 2e_2 e_4 + 2e_2 e'_4 - e_3^2)$, $h_{1,0} = 2e_0 e_1 e'_4 - e_0 e_4 e'_1 - e_0 e'_1 e'_4 - e_1 e_3 e'_1 + e_3 e_1'^2 - 2e_3 e_4 + 2e_3 e'_4$, and $h_{0,0} = e_1^2 e'_4 - e_1 e_4 e'_1 - e_1 e'_1 e'_4 + e_4 e_1'^2 - e_4^2 + 2e_4 e'_4 - e_4'^2$.

There must be at least one motion mode corresponding to Solution IV-IV′, and the number of 1-DOF motion modes associated with Solution IV-IV′ depends on the link parameters of the variable-DOF planar mechanism. For the example 8-link variable-DOF planar mechanism, Eq. (14) has the following three solutions:

$$\phi = \phi' \tag{15}$$

$$\phi = 2\pi - \phi' \tag{16}$$

and

$$C^2\phi - 1160C\phi'C\phi + 841C^2\phi' + 1798C\phi + 1798C\phi' - 2518 = 0 \tag{17}$$

Equations (15), (16) and (17) lead to 1-DOF motion modes VI (Fig. 4(f)), VII (Fig. 4(g)) and VIII (Fig. 4(h)) of the example 8-link variable-DOF planar mechanism.

In summary, an 8-link variable-DOF planar mechanism has one 2-DOF motion mode and at least five 1-DOF motion modes. The example 8-link variable-DOF mechanism has one 2-DOF motion mode and seven 1-DOF motion modes (Fig. 3).

4   Conclusions

A novel two-step construction method for the type synthesis of variable-DOF mechanisms has been proposed. An 8-link variable-DOF mechanism has been obtained, which has less number of links than the existing variable-DOF multi-loop planar mechanisms. This 8-link variable-DOF planar mechanism with $\alpha \neq 0$ has one 2-DOF motion mode and at least five 1-DOF motion modes. An example 8-link variable-DOF planar mechanism that has one 2-DOF motion mode and seven 1-DOF motion modes has been identified.

This paper enriches the methods for the type synthesis of variable-DOF mechanisms and the types of variable-DOF mechanisms.

Acknowledgments

References

1. Wohlhart, K.: Kinematotropic linkages. *Recent Advances in Robot Kinematics*, J. Lenarcic and V. Parenti-Castelli (Eds). Kluwer Academic, Dordrecht, The Netherlands, pp. 359–368 (1996).
2. Kovalev, M.D.: Geometric theory of hinge mechanisms. *Izvestiya RAN Seriya Matematicheskaya*, 58(1), pp. 45–70 (1994).
3. Galletti, C., Fanghella, P.: 2001, "Single-loop kinematotropic mechanisms," *Mechanism and Machine Theory*, Vol.36, pp. 743–761.
4. Kong, X., Pfurner, M.: Type synthesis and reconfiguration analysis of a class of variable-DOF single-loop mechanisms. *Mechanism and Machine Theory*, **85**, pp. 116–128 (2015).
5. Pfurner, M., Kong, X.: Algebraic analysis of a new variable-DOF 7R mechanism. In Philippe Wenger and Paul Flores, editors, *New Trends in Mechanism and Machine Science, Theory and Industrial Applications*, pp.71–79, Springer (2016).
6. He, X., Kong, X., Chablat, D., Caro, S., Hao, G.: Kinematic analysis of a single-loop reconfigurable 7R mechanism with multiple operation modes. *Robotica*, Vol.32, pp. 1171–1188 (2014).
7. Kong, X.: A variable-DOF single-loop 7R spatial mechanism with five motion modes. *Mechanism and Machine Theory* **120**, pp. 239–249 (2018).
8. Feng, H., Chen, Y., Dai, J.S., Gogu, G.: Kinematic study of the general plane-symmetric Bricard linkage and its bifurcation variations. *Mechanism and Machine Theory*, 116, pp. 89–104 (2017).
9. Lopez-Custodio, P.C., Rico, J.M., Cervantes-Sánchez, J.J., Perez-Soto, G.I.: Reconfigurable mechanisms from the intersection of surfaces. *Journal of Mechanisms and Robotics*, 8(2), 021029 (2016).
10. Fanghella, P., Galleti, C., Gianotti, E.: Parallel robots that change their group of motion. *Advances in Robot Kinematics*, Springer, pp. 49–56 (2006).
11. Liu, K., Yu, J. and Kong, X.: Synthesis of multi-mode single-loop Bennett-based mechanisms using factorization of motion polynomials. Mechanism and Machine Theory, Vol. 155, 104110 (2021).
12. Kong, X.: Type synthesis of variable degree-of-freedom parallel manipulators with both planar and 3T1R operation modes. *Proceedings of ASME 2012 International Design Engineering Technical Conferences & Computers and Information in Engineering Conference*, DETC2012-70621, August 12-15, 2012, Chicago, USA (2012).
13. Zeng, Q, Ehmann, KF, Cao, J: Design of general kinematotropic mechanisms. *Robotics and Computer-Integrated Manufacturing*, 38, pp. 67–81 (2016).
14. Coste, M., Demdah, K.M.: Extra modes of operation and self motions in manipulators designed for Schoenflies motion. *Journal of Mechanisms and Robotics*, 7 (4), 041020 (2015).
15. Nurahmi, L., Caro, S., Wenger, P., Schadlbauer, J., Husty, M.: Reconfiguration analysis of a 4-RUU parallel manipulator. *Mechanism and Machine Theory*, 96, pp.269–289 (2016).
16. Kong, X: Classification of a 3-RER parallel manipulator based on the type and number of operation modes. *ASME Journal Mechanisms Robotics*, 13(2): 021013 (2021).

A novel kinematic performance index and its application in the optimum design of a 4-DOF parallel manipulator

Hao Ye [1,2] and Jun Wu [1,2,✉]

[1] State Key Laboratory of Tribology and Institute of Manufacturing Engineering, Department of Mechanical Engineering, Tsinghua University, Beijing 100084, China
[2] Ultra-precision Manufacturing Equipment and Control, Beijing 100084, China
✉ jhwu@mail.tsinghua.edu.cn

Abstract. Based on the requirements of the driving torque and velocity of the motor, this paper presents the local motor payload index (LMPI) and the local motor velocity index (LMVI), which have the advantages of clear physical meaning and mathematical differentiability compared with other indexes based on singular value. In order to transform the local index to the global index, the worst-best subsampling method is proposed, which selects the worst local index of the best taskspace as the global index of the overall workspace. This transformation method is more suitable for the requirements of reasonable taskspace of the mechanism, and reflects the lower performance limit of the mechanism. Based on LMPI, LMVI and the transformation method, the global motor requirement index (GMRI) is proposed and applied to the optimum design of a novel 4-DOF parallel manipulator. The results show that the boundary of the appropriate parameter space selected according to GMRI is clear, which is conducive to the selection of the structural parameters and actuated motors.

Keywords: kinematic evaluation, parallel manipulator, optimum design, global index, motor requirement.

1   Introduction

Parallel manipulator (PM) is a kind of mechanism with the kinematic closed chain. Compared with the serial manipulator, the research shows that the PM has some advantages of high speed, high stiffness and high precision [1] and has been used in high-speed pick-and-place manipulator [2], machine tool [3] and spray robot [4].

The evaluation of kinematic performance is an important issue of performance comparison [5], actuation modes selection [6] and optimum design [7] about the PM. Some indexes are proposed to evaluate the kinematic performance of PMs [8], generally based on singular values of Jacobian matrix: (i) the local velocity index (LVI) and the local payload index (LPI) [9] are determined by the maximum (minimum) singular values, represent the maximum (minimum) ratio of 2-norm of the input-output torque (velocity) of the mechanism; (ii) the manipulability index (MI) [10] is determined by the product of singular values, represents the volume ratio of the distribution region of input and output torque (velocity) of the mechanism; (iii) the conditioning index (CI) [11,12]

is determined by the ratio of the maximum and minimum singular values and is a good measure of the manipulator's distance singularity and kinematic accuracy. In addition, the global dexterity index (GDI) [13], the global isotropy index (GII) [14] and other comprehensive indexes based on the above indexes have also been applied in PM.

These indexes mentioned above have been well used in PMs, but there are still few limitations: (1) these kinematic indexes generally ignores the information beyond singular values in Jacobian matrix, and cannot be corresponding to the actual physical entity; (2) Generally a simple combination of the workspace index (WSI) or other local indexes is used as the global comprehensive kinematic index and used for parameter optimization [14], which lacks clear physical significance.

For the limitation (1), the pressure angle [15] and the transmission efficiency of torque (velocity) [16] are paid attention to, the local transmission index (LTI) is obtained and used in optimum design of PM [17,18]. Different from the above physical parameters, this paper decouples the payload (velocity) performance of different motors to retain the information of singular vectors in Jacobian matrix, and proposes the local motor payload index (LMPI) and the local motor velocity index (LMVI). for the limitation (2), the worst-best subsampling method is proposed, which selects the worst local index of the best taskspace as the global index of the overall workspace. The global motor payload index (GMPI) and the global motor velocity index (GMVI) are obtained by this method and synthesized into the global motor requirement index (GMRI). Finally, the optimum design of a novel 4-DOF PM, PRPS-2PRS, is realized based on GMRI and the results show that the appropriate parameter space selected according to GMRI is conducive to the selection of the structural parameters and actuated motors.

2 Kinematic Performance Evaluation Index

For each n-DOF non-redundant manipulator, the relationship between the pose of the end-effector (EE) and the displacements of the active joint can be expressed as

$$q = f(\theta), \theta = f^{-1}(q) \tag{1}$$

where $\theta = [\theta_1, \theta_2, \dots, \theta_n]^T$ is the displacement of active joints，$q = [q_1, q_2, \dots, q_n]^T$ denotes the generalized coordinates of EE, $f(\cdot)$ and $f^{-1}(\cdot)$ are the forward and inverse kinematics which can be analytical or non-analytical. Taking the time derivative of (1):

$$\dot{q} = J_f \dot{\theta}, \dot{\theta} = J_i \dot{q} \tag{2}$$

where $J_f \in \mathbb{R}^{n \times n}$ is the forward Jacobian matrix, $J_i = J_f^{-1}$ is the inverse Jacobian matrix. When J_f (J_i) does not exist, the corresponding pose is defined as forward (inverse) singular pose of the manipulator.

2.1 Local Motor Payload Index & Local Motor Velocity Index

The local motor payload index (LMPI) and the local motor velocity index (LVPI) are proposed to describe the requirement of driving torque and velocity and measure the payload and velocity transmission performance of the PM in this section.

The relationship between the driving torque provided by motors and the payload acting on the EE can be expressed by virtual work principle

$$\boldsymbol{\tau}^{\mathrm{T}}\boldsymbol{\delta\theta} = \boldsymbol{f}^{\mathrm{T}}\boldsymbol{\delta q_{out}} \tag{3}$$

where $\boldsymbol{\delta\theta} \in \mathbb{R}^n$ represents the virtual displacement of the actuated joint, $\boldsymbol{\delta q_{out}} \in \mathbb{R}^6$ represents the virtual displacement of EE including three virtual rotations and three virtual translations, $\boldsymbol{\tau} \in \mathbb{R}^n$ is the driving force or torque, $\boldsymbol{f} = [\boldsymbol{f}_v^{\mathrm{T}} \quad \boldsymbol{f}_\omega^{\mathrm{T}}]^{\mathrm{T}} \in \mathbb{R}^6$ is the payload including external force $\boldsymbol{f}_v$ and torque $\boldsymbol{f}_\omega$ in the EE. $\boldsymbol{\delta q_{out}}$ can be rewritten as

$$\boldsymbol{\delta q_{out}} = \boldsymbol{A}\boldsymbol{\delta q} \tag{4}$$

where $\boldsymbol{\delta q} \in \mathbb{R}^n$ is the virtual displacement corresponding to the generalized coordinates $\boldsymbol{q}$, and $\boldsymbol{A} \in \mathbb{R}^{6 \times n}$ is the transformation matrix between $\boldsymbol{\delta q}$ and $\boldsymbol{\delta q_{out}}$. According to (4) and (3), $\boldsymbol{\tau}$ can be determined as

$$\boldsymbol{\tau} = \boldsymbol{J}_i^{-\mathrm{T}}\boldsymbol{A}^{\mathrm{T}}\boldsymbol{f} \tag{5}$$

which represents the relationship between the driving torque and the payload of the EE in this specific pose of the manipulator. Similar to (3) and (4), the relationship between the driving velocity and the required velocity of the EE can be expressed as:

$$\dot{\boldsymbol{q}}_{out} = \boldsymbol{A}\dot{\boldsymbol{q}}, \dot{\boldsymbol{\theta}} = \boldsymbol{J}_i\dot{\boldsymbol{q}} \tag{6}$$

where $\dot{\boldsymbol{q}}_{out} = [\dot{\boldsymbol{q}}_v^{\mathrm{T}} \quad \dot{\boldsymbol{q}}_\omega^{\mathrm{T}}]^{\mathrm{T}} \in \mathbb{R}^6$, $\dot{\boldsymbol{q}}_v$ and $\dot{\boldsymbol{q}}_\omega$ are the velocity and angular velocity of the EE respectively. It is assumed that $\boldsymbol{f}$ and $\dot{\boldsymbol{q}}_{out}$ are distributed in

$$\left\|\boldsymbol{\Lambda}_f\boldsymbol{f}\right\|_2 \leq \kappa_f, \left\|\boldsymbol{\Lambda}_v\dot{\boldsymbol{q}}_{out}\right\|_2 \leq \kappa_v \tag{7}$$

where $\boldsymbol{\Lambda}_f = diag(\lambda_f\boldsymbol{I}_3, \boldsymbol{I}_3)$, $\boldsymbol{\Lambda}_v = diag(\lambda_v\boldsymbol{I}_3, \boldsymbol{I}_3)$, $\boldsymbol{I}_j$ is the j-order identity matrix, λ_f represents the weight ratio of force and torque applied to EE, the unit is m, λ_v represents the weight ratio of velocity and angular velocity in the EE and the unit is m^{-1}. Since the virtual work of the EE in all directions should be equivalent, $\boldsymbol{\Lambda}_v$ and $\boldsymbol{\Lambda}_f$ are inverse matrix of each other, $\lambda_v = \lambda_f^{-1}$ is the reciprocal of characteristic length of the EE. Thus, $\boldsymbol{\Lambda}_f\boldsymbol{f}$ represents the normalized payload torque of the EE with the unit is N · m and $\boldsymbol{\Lambda}_v\dot{\boldsymbol{q}}_{out}$ can be expressed as the normalized angular velocity of the EE in the manipulator with the unit is rad/s.

Since the larger the required range of driving torque is, the higher the requirement for the motor is, the required maximum driving torque of the j-th motor, $\tau_{j,max}$, can measure the payload transmission performance of the manipulator in the direction of the j-th motor, and is defined as

$$\tau_{j,max} \triangleq max(|\tau_j|), s.t. \left\|\boldsymbol{\Lambda}_f\boldsymbol{f}\right\|_2 \leq \kappa_f \tag{8}$$

where $\tau_j = \boldsymbol{e}_j^{\mathrm{T}}\boldsymbol{\tau}$ and $\boldsymbol{e}_j$ is the j-th column of the identity matrix. Similarly, the required maximum velocity of the j-th motor, $\dot{\theta}_{j,max}$, can measure the force transmission performance of the manipulator in the direction of the j-th motor, and is defined as

$$\dot{\theta}_{j,max} \triangleq max\left(\left|\dot{\theta}_j\right|\right), s.t. \|\boldsymbol{\Lambda}_v \dot{\boldsymbol{q}}_{out}\|_2 \leq \kappa_v \tag{9}$$

Based on Cauchy-Schwarz inequality and (5), $\tau_{j,max}$ can be determined as

$$\tau_{j,max} = max\left(\boldsymbol{e}_j^{\mathrm{T}}\boldsymbol{J}_i^{-\mathrm{T}}\boldsymbol{A}^{\mathrm{T}}\boldsymbol{\Lambda}_f^{-1}\boldsymbol{\Lambda}_f \boldsymbol{f}\right) = \left\|\boldsymbol{e}_j^{\mathrm{T}}\boldsymbol{J}_i^{-\mathrm{T}}\boldsymbol{A}^{\mathrm{T}}\boldsymbol{\Lambda}_f^{-1}\right\|_2 \kappa_f \tag{10}$$

Based on Lagrange multiplier method, the constrained optimization problem (9) can be transformed into

$$L = \dot{\theta}_j^{\mathrm{T}}\dot{\theta}_j + \lambda(\kappa_v^2 - \|\boldsymbol{\Lambda}_v \dot{\boldsymbol{q}}_{out}\|_2^2) = \dot{\boldsymbol{q}}^{\mathrm{T}}\boldsymbol{L}_1\dot{\boldsymbol{q}} + \lambda(\kappa_v^2 - \dot{\boldsymbol{q}}^{\mathrm{T}}\boldsymbol{L}_2\dot{\boldsymbol{q}}) \tag{11}$$

where $\boldsymbol{L}_1 = \boldsymbol{J}_i^{\mathrm{T}}\boldsymbol{e}_j\boldsymbol{e}_j^{\mathrm{T}}\boldsymbol{J}_i$, $\boldsymbol{L}_2 = \boldsymbol{A}^{\mathrm{T}}\boldsymbol{\Lambda}_v^{\mathrm{T}}\boldsymbol{\Lambda}_v\boldsymbol{A}$. Since $\boldsymbol{A}$ represents the transformation matrix between $\dot{\boldsymbol{q}}$ and $\dot{\boldsymbol{q}}_{out}$ and the terms of $\dot{\boldsymbol{q}}$ are independent of each other, $\boldsymbol{A}$ must be a column full rank matrix. Similarly, $\boldsymbol{\Lambda}_v$ is a nonsingular matrix. Thus, $\boldsymbol{L}_2$ is invertible. The necessary conditions for obtaining the extreme value in (11) must be satisfied:

$$(\boldsymbol{L}_2^{-1}\boldsymbol{L}_1 - \lambda)\dot{\boldsymbol{q}} = \boldsymbol{0},\ \kappa_v^2 = \dot{\boldsymbol{q}}^{\mathrm{T}}\boldsymbol{L}_2\dot{\boldsymbol{q}} \tag{12}$$

Thus, when λ is an eigenvalue of $\boldsymbol{L}_2^{-1}\boldsymbol{L}_1$ and $\dot{\boldsymbol{q}}$ is the corresponding eigenvector, $\dot{\theta}_j$ obtains the extreme value. In matrix theory, the geometric multiplicities of the nonzero characteristic roots of $\boldsymbol{BC}$ coincide with those of $\boldsymbol{CB}$[19], so λ can be obtained as

$$\lambda = \boldsymbol{e}_j^{\mathrm{T}}\boldsymbol{J}_i\boldsymbol{L}_2^{-1}\boldsymbol{J}_i^{\mathrm{T}}\boldsymbol{e}_j, 0 \tag{13}$$

when $\boldsymbol{B} = \boldsymbol{L}_2^{-1}\boldsymbol{J}_i^{\mathrm{T}}\boldsymbol{e}_j$ and $\boldsymbol{C} = \boldsymbol{e}_j^{\mathrm{T}}\boldsymbol{J}_i$. Thus, $\dot{\theta}_{j,max}$ can be determined as

$$\dot{\theta}_{j,max} = \sqrt{max(\dot{\boldsymbol{q}}^{\mathrm{T}}\boldsymbol{L}_1\dot{\boldsymbol{q}})} = \sqrt{max(\dot{\boldsymbol{q}}^{\mathrm{T}}\lambda\boldsymbol{L}_2\dot{\boldsymbol{q}})} = \sqrt{max(\lambda)}\,\kappa_v = \sqrt{\boldsymbol{e}_j^{\mathrm{T}}\boldsymbol{J}_i\boldsymbol{L}_2^{-1}\boldsymbol{J}_i^{\mathrm{T}}\boldsymbol{e}_j}\kappa_v \tag{14}$$

It is reasonable to use the average value of $\tau_{j,max}$ and $\dot{\theta}_{j,max}$ in all drive directions to represent the comprehensive payload and velocity transmission performance of the manipulator. According to (10) and (14), the local motor payload index (LMPI) and the local motor velocity index (LVPI) can be defined as the comprehensive required range of driving torque and velocity under the normalized unit payload and angular velocity:

$$\eta_1 = \sum_{j=1}^n \frac{1}{n}\left\|\boldsymbol{e}_j^{\mathrm{T}}\boldsymbol{J}_i^{-\mathrm{T}}\boldsymbol{A}^{\mathrm{T}}\boldsymbol{\Lambda}_f^{-1}\right\|_2,\quad \eta_2 = \sum_{j=1}^n \frac{1}{n}\sqrt{\boldsymbol{e}_j^{\mathrm{T}}\boldsymbol{J}_i\boldsymbol{L}_2^{-1}\boldsymbol{J}_i^{\mathrm{T}}\boldsymbol{e}_j} \tag{15}$$

where η_1 is the LMPI and η_2 is the LMVI. It is noted that the unit of $\tau_{j,max}$ is N·m which is consistent with κ_f. Thus, the index LMPI is a unitless number independent of the size of the mechanism. Similarly, the index LMVI also is a unitless number.

2.2 Compare with Other Local Kinematic Indexes

The kinematic indexes based on Jacobian matrix generally can be represented graphically by ellipsoid as the blue area in Fig. 1. The index LVI and LPI can be regarded as the length of the longest axis, as the navy-blue line in Fig. 1, or the shortest axis. MI is the volume of the ellipsoid and the indexes related to CI is roughly the ratio of longest and shortest axis.
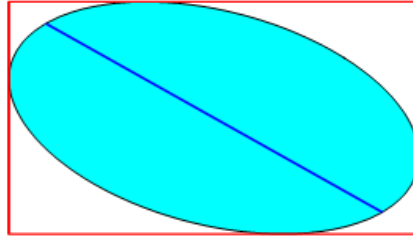
Fig. 1. Geometric expression of different indexes

Generally, these kinematic indexes are related to the shape and size of the velocity or torque ellipsoid, but not its orientation, due to the driving torque or velocity considered as entire piece such as the norm. In fact, each actuated motor is physically decoupled with others, and the performance this motor required cannot be replaced by other, which shows that the performance of the manipulator should be related to the orientation of the ellipsoid. LMPI and LMVI are to consider the maximum driving torque and velocity of each motor separately, and then synthesize these in all motors as the length of red rectangle in Fig. 1 effected by the orientation of ellipsoid, which satisfies that each motor is decoupled from others. In addition, the non-differentiability of singular values will bring difficulties to other indexes in the subsequent analysis, LMPI and LMVI.

2.3 Worst-Best Subsampling Method

In this section, worst-best subsampling method is proposed and used for transforming the local kinematic index to the global kinematic index. In previous research, the average value of local index in the workspace was generally used as the global [5,11]:

$$\bar{\eta}(V) = \int \eta dV / \int 1 dV \tag{16}$$

where η is the local index, $\bar{\eta}(V)$ is the global index in the workspace V. But sometimes, (16) is not reasonable since the local index of torque and velocity represents the driving requirement of motors, and the requirement is determined by the worst position in the evaluated workspace, rather than the average value of all positions. Thus, the more reasonable global index should be the worst local index in the evaluated workspace:

$$\bar{\eta}(V) = \text{worst}\{\eta \ in \ V\} \tag{17}$$

For the selection of the evaluated workspace, researchers generally set it as the overall workspace V_{all} or specific taskspace V_{work}, which has the advantage of convenient calculation and clear practical significance, but it is not completely suitable with the

actual situation. In fact, it still has the limitation as mention in the introduction: the index cannot reflect the size of the workspace and generally needs to be combined with WSI and other indexes to describe the comprehensive performance of the mechanism, which lacks clear physical significance.

In fact, the manipulator needs to provide the range of motion for each degree of freedom at the EE as the taskspace, and the size of taskspace is more important than the specific pose distribution. Therefore, this paper suggests to look for all workspaces consistent with the scope of the taskspace V_{work} in the overall workspaceV_{all}, and select the workspace with the best performance as the evaluated workspace:

$$\bar{\eta} = best\{\text{worst}\{\eta\ in\ V_{work} + \Delta\}, V_{work} + \Delta \subseteq V_{all}\ \} \tag{18}$$

where $V_{work} + \Delta$ represents the workspace obtained by the translation Δ from V_{work}. Thus, this method only depends on the selection of the required size about taskspace with definite physical meaning. For the same size about taskspace V_{work}, the change of structure parameters would lead to the change of the size about the overall workspace V_{all}, whose influence can be reflected in (18). Thus, the global index transformed by this method, can describe the comprehensive performance of the mechanism, including the influence of the workspace and the local index, without combining any other indexes.

This transformation method shown in (18), can be regarded as two subsampling shown in Fig. 2: the subsampling window size is equal to the size of V_{work} in the first subsampling and the worst point would be selected; the best point would selected in the second subsampling while the window is the whole space. Thus, this method is defined as worst-best subsampling method. In Fig. 2, the number in each square is the local index, and the smaller the index, the better the performance. ∞ means that the corresponding point is outside V_{all}. The size of V_{work} is 2×2. Based on the worst-best subsampling method, the global motor payload index (GMPI) and the global motor velocity index (GMVI) are determined by LMPI and LMVI respectively.
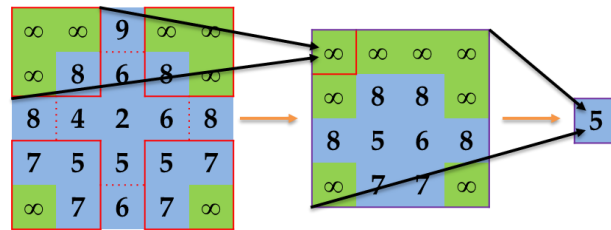
Fig. 2. Worst-best subsampling method (n=2)

2.4   Global Motor Requirement Index (GMRI)

The global motor requirement index (GMRI) is proposed to describe the motor requirement including driving torque and velocity of the PM in this section.

Since the GMPI (LMPI) and the GMVI (LMVI) are the unitless indexes, they can be directly added and calculated as a comprehensive index. Therefore, the global motor requirement index (GMRI) can be defined as their weighted average value:

$$\bar{\eta}_0 = \kappa\bar{\eta}_1 + \bar{\eta}_2 \tag{19}$$

where $\bar{\eta}_0$, $\bar{\eta}_1$ and $\bar{\eta}_2$ are GMRI, GMPI and GMVI respectively. When the payload $\boldsymbol{f}$ in the EE is in the ellipsoid $\left\|\boldsymbol{\Lambda}_f\boldsymbol{f}\right\|_2 \leq \kappa_f$, the velocity $\dot{\boldsymbol{q}}_{out}$ of the EE is in the ellipsoid $\|\boldsymbol{\Lambda}_v\dot{\boldsymbol{q}}_{out}\|_2 \leq \kappa_v$, $\tau_0 = \kappa_f\eta_1$ is the comprehensive maximum driving torque, $v_0 = \kappa_v\eta_2$ is the comprehensive maximum driving velocity. Based on (19), it is reasonable to the influence of $\bar{\eta}_1$ and $\bar{\eta}_2$ in $\bar{\eta}_0$ should be proportional to τ_0 and v_0 since they all represent the ratio of the torque to the velocity in the motor requirement:

$$\kappa = \kappa_f/(\kappa_\lambda\kappa_v) \tag{20}$$

where $\kappa_\lambda = (60T_d)/(2\pi n_d)$ is the ratio between unit angular velocity and torque at the motor, T_d (N $\cdot$ m) is the rated torque, n_d (r $\cdot$ min^{-1}) is the rated speed. The LMRI and the GMRI still are unitless numbers and represent the local and global requirements of motor performance including driving torque and velocity.

3 Optimum design of <u>PRPS</u>-2<u>PRS</u> PM

3.1 System Architectures

A novel 4 degree of freedom (DOF) PM, <u>PRPS</u>-2<u>PRS</u>, is proposed for friction stir welding, in which each chain is connected to the base and the EE by prismatic (P) joint and spherical (S) joint respectively. All P joints in these three limbs are actuated.

Fig. 3 shows the schematic diagram where A_i (i=1,2,3) represent the center of the P joints and B_i is the center of S joint. The fixed coordinate system $\{O - xyz\}$ is attached to the base and O is zero position of P joint in A_2. The x axis is vertical to the plane $A_1A_2A_3$, the y axis is along A_2A_3, and the z axis satisfies the right-hand rule. A body fixed coordinate system $\{O' - XYZ\}$ is attached to the EE with the origin O' being foot of perpendicular of B_1 on the line B_2B_3. The Y axis is along $O'B_3$, the X axis is vertical to the plane $B_1B_2B_3$, and the Z axis satisfies the right-hand rule. For limb A_iB_i, the same rules can be followed to define the body-fixed coordinate system $\{A_i - x_iy_iz_i\}$. The rotational axis of revolute (R) joint is parallel to the z axis, the v axis is constrained in the xOy plane. O' in line B_2B_3 is also constrained in plane xOy, and $x_{O'}$ and $y_{O'}$ where are the x and y coordinates of point O' can be used to describe the translational DOFs of the PM. The orientation of $\{O' - XYZ\}$ with respect to $\{O - xyz\}$ can be described by two Euler angles θ_z and θ_y associated with the rotations about the z and y axis, i.e.

$$\boldsymbol{R} = Rot(\theta_z, z) \cdot Rot(\theta_y, y) \tag{21}$$

The orientation of limb A_iB_i with respect to $\{O - xyz\}$:

$$\boldsymbol{R_1} = Rot(\varphi_1, y), \boldsymbol{R_2} = Rot(\varphi_2, z), \boldsymbol{R_3} = Rot(\varphi_3, z) \tag{22}$$

where φ_i is rotational angle of R joint in limb A_iB_i.
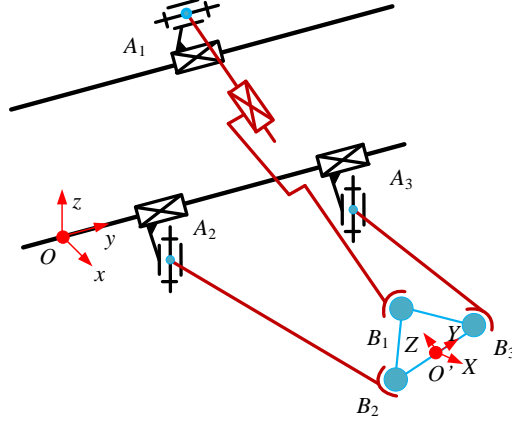
Fig. 3. Schematic diagram of the 4-DOF PM

3.2 Inverse Position & Velocity Analysis

The closed-loop constraint equation can be written as

$$\boldsymbol{r_{ai}} + \boldsymbol{R_i} l_i \boldsymbol{e_1} = \boldsymbol{P_{li}}, i = 1,2,3 \tag{23}$$

where $\boldsymbol{P_{li}} = \boldsymbol{r_{O'}} + \boldsymbol{R} \boldsymbol{r'_{bi}}$, $\boldsymbol{r_{O'}} = [x_{O'} \quad y_{O'} \quad 0]^\mathrm{T}$, $\boldsymbol{r_{ai}}$ are the position of A_i in $\{O - xyz\}$, l_i is the length of $A_i B_i$, and $\boldsymbol{r'_{bi}}$ is the position of B_i in $\{O' - XYZ\}$. Let y_{Ai} is the y coordinate of A_i in $\{O - xyz\}$. In the inverse kinematics, $\boldsymbol{R}$ and $\boldsymbol{r_{O'}}$ are given while l_1 and y_{Ai} needed to be solved. (35) can be rewritten as

$$y_{A1} = \boldsymbol{e_2^\mathrm{T}} \boldsymbol{P_{l1}}, l_1 = |z_1|, \varphi_1 = \arg(z1)$$

where $z_1 = \left(\boldsymbol{e_1^\mathrm{T}} - j\boldsymbol{e_2^\mathrm{T}}\right)\boldsymbol{P_{l1}} + jd$, d is the distance from point A_1 to the y axis, j is imaginary unit, and $\arg(\cdot)$ is the argument of a complex number. φ_2 and φ_3 also can be determined as

$$l_i \cos(\varphi_i) = \boldsymbol{e_1^\mathrm{T}}(\boldsymbol{P_{li}} - \boldsymbol{A_i}), i = 2,3 \tag{24}$$

Both φ_2 and φ_3 have two solutions. Thus, the inverse kinematics has four solutions. In practical application, it is expected that the two prismatic joints in limbs $A_2 B_2$ and $A_3 B_3$ have enough distance to avoid collision. Therefore, φ_2 and φ_3 are given by $0 \leq \varphi_2, -\varphi_3 \leq \pi/2$ and can be expressed as

$$\begin{aligned} \varphi_i &= k_{\varphi i} \arccos\left(\boldsymbol{e_1^\mathrm{T}}(\boldsymbol{P_{li}} - \boldsymbol{A_i})/l_i\right) \\ y_{Ai} &= y_{O'} + v_{Bi} cos\theta_z - l_i sin\varphi_i \end{aligned}, i = 2,3 \tag{25}$$

where $k_{\varphi 2} = -k_{\varphi 3} = 1$, v_{B2} and v_{B3} are the v coordinate of B_2 and B_3 in $\{O' - XYZ\}$. The distance from point B_1 to the v axis is w_{B1}. Taking the time derivative of (23) leads to

$$\dot{y}_{A1} \boldsymbol{e_2} + \widehat{\boldsymbol{\omega}}_1 \boldsymbol{R_1} l_1 \boldsymbol{e_1} + \boldsymbol{R_1} \dot{l}_1 \boldsymbol{e_1} = \dot{\boldsymbol{P}}_{l1} \tag{26}$$

$$\dot{y}_{Ai}\boldsymbol{e_2} + \widehat{\boldsymbol{\omega}}_i\boldsymbol{R}_i l_i\boldsymbol{e_1} = \dot{\boldsymbol{P}}_{li}, i = 2,3 \tag{27}$$

where $\dot{\boldsymbol{P}}_{li} = \dot{\boldsymbol{r}}_{O'} + \widehat{\boldsymbol{\omega}}\boldsymbol{R}\boldsymbol{r}'_{bi}$, and $\boldsymbol{\omega}$ is the angular velocity of the EE, $\widehat{\boldsymbol{\omega}}$ represents the screw matrix of $\boldsymbol{\omega}$ where the symbol $\widehat{(\cdot)}$ has the similar meaning in other expression, $\boldsymbol{\omega}_i$ is the angular velocity of limb A_iB_i, $\boldsymbol{\omega_1} = \dot{\varphi}_1\boldsymbol{e_2}, \boldsymbol{\omega_2} = \dot{\varphi}_2\boldsymbol{e_3}, \boldsymbol{\omega_3} = \dot{\varphi}_3\boldsymbol{e_3}$. Taking dot product $\boldsymbol{R_1}\boldsymbol{e_i}(i = 1,2,3)$ on both sides of (26) leads to

$$\dot{y}_{A1} = \boldsymbol{e_2^{\mathrm{T}}}\dot{\boldsymbol{P}}_{l1}, \dot{l}_1 = \boldsymbol{e_1^{\mathrm{T}}}\boldsymbol{R_1^{\mathrm{T}}}\dot{\boldsymbol{P}}_{l1}, \dot{\varphi}_1 = -\boldsymbol{e_3^{\mathrm{T}}}\boldsymbol{R_1^{\mathrm{T}}}\dot{\boldsymbol{P}}_{l1}/l_1 \tag{28}$$

$\dot{y}_{Ai}$ and $\dot{\varphi}_\iota(i = 2,3)$ are determined by (27) as

$$\dot{y}_{Ai} = \boldsymbol{e_1^{\mathrm{T}}}\boldsymbol{R_i^{\mathrm{T}}}\dot{\boldsymbol{P}}_{li}, \dot{\varphi}_\iota = -\boldsymbol{e_1^{\mathrm{T}}}\dot{\boldsymbol{P}}_{li}/(l_i \sin\varphi_i) \tag{29}$$

Based on (28) and (29), the velocity of parameters can be expressed as

$$\dot{\boldsymbol{\theta}}_s = \boldsymbol{J_s^{\mathrm{T}}}\dot{\boldsymbol{q}}, \boldsymbol{q} = \left[x_{O'}, y_{O'}, \theta_y, \theta_z\right]^{\mathrm{T}}, \dot{\boldsymbol{\theta}}_s = [y_{A1}, y_{A2}, y_{A3}, l_1]^{\mathrm{T}} \tag{30}$$

Assume the lead of screw is p, $\boldsymbol{\theta} = \frac{2\pi}{p}\dot{\boldsymbol{\theta}}_s$ is displacement vector of motors. The Jacobian matrix and the transformation matrix $\boldsymbol{A}$ can be expressed as

$$\boldsymbol{J}_i = \boldsymbol{J_f^{-1}} = \frac{2\pi}{p}\boldsymbol{J_s^{\mathrm{T}}}, \boldsymbol{A} = [\boldsymbol{e_1}, \boldsymbol{e_2}, -sin\theta_z\boldsymbol{e_3}, cos\theta_z\boldsymbol{e_3}, \boldsymbol{e_4}]^{\mathrm{T}} \tag{31}$$

3.3   Optimum Design by GMRI

The simulated annealing (SA) is used to optimize the mechanism parameters to minimize the corresponding GMRI in this section. SA is a heuristic random search optimization algorithm based on Monte Carlo method [20]. The method simulates the physical process of heating materials and then slowly lowering the temperature to achieve the lowest energy. This notion of slow cooling implemented in SA is interpreted as a slow decrease in the probability of accepting worse solutions as the solution space is explored. Accepting worse solutions allows for a more extensive search for the global optimal solution. Pseudocode of SA is shown in Algorithm 1.

Algorithm 1 Simulated Annealing

Input: $\boldsymbol{s_0}$: initial state; T_0: initial state; T_{min}: the lowest limit of temperature;
Output: $\boldsymbol{s_{best}}$: (approximate) optimal state;
1: set $\boldsymbol{s_{best}} \leftarrow \boldsymbol{s_0}, T \leftarrow T_0$
2: while $T > T_{min}$ do
3:    $\boldsymbol{s} \leftarrow \boldsymbol{s_{best}}$;
4:    for $k \leftarrow 0$ to k_{max} do
5:       $\boldsymbol{s_{new}} \leftarrow$ neighbor$(\boldsymbol{s}, T)$;
6:       if random$(0,1) < \exp\left(\left(E(\boldsymbol{s_{best}}) - E(\boldsymbol{s_{new}})\right)/T\right)$ then $\boldsymbol{s_{best}} \leftarrow \boldsymbol{s_{new}}$;
7:    $T \leftarrow \alpha T$; ▷ where α is decay factor

According to the symmetry of the PRPS-2PRS, l, v, w and d can be used to represent the structural parameters: $l = l_2 = l_3, v = -v_{B2} = v_{B3}, w = w_{B1}$.

The footprint of mechanism is constrained to limit the size of the PM. The length along y axis is determined by the guide, and the height of manipulator only limited by the height of place. Thus, the length along x axis mainly determines the footprint, which can be roughly equal to the value of l. For the same V_{work}, the larger the mechanism, the better the kinematic index according to (18). Thus, limiting the maximum of l is consistent with the given l. Thus, the problem of the optimized ratio between the parameters can be express as:

$$\min \bar{\eta}_0(s), s = [\lambda_d, \lambda_v, \lambda_w], s.t. \mathbf{0} \prec \mathbf{s} \prec \mathbf{1} \tag{32}$$

where $\lambda_d = d/l, \lambda_v = v/l, \lambda_w = w/l$. The other parameters hidden in (9) are set to:

$$p/l = 0.01, \lambda_f = 0.15, \kappa = 8000$$
$$V_{work}: \Delta(\theta_y) = 60°, \Delta(\theta_z) = 40°, \Delta(x_{o'})/l = 0.25 \tag{33}$$

where $\Delta(\cdot)$ is the range of variable. It can be found that $\bar{\eta}_0$ selected by SA decreases with some volatility in the iteration, and the convergence trend is obvious and stable as shown in Fig. 4(a). Finally, the optimized ratio between the parameters $s^* = [\lambda_d^*, \lambda_v^*, \lambda_w^*]$ converge to $[0.2200, 0.2082, 0.1216]$ and the corresponding GMRI is 355.033. The global index $\bar{\eta}_0$ in neighborhood of s is shown in Fig. 4 (b), where it can be found that GMRI is the most sensitive to v and rises sharply when $\lambda_d > \lambda_d^*$ or $\lambda_w < \lambda_w^*$ while rises slowly in another part, which makes the boundary of reasonable parameters space and the turning in the optimal structural parameters clear. It is conducive to the selection of the structural parameters and actuated motors.
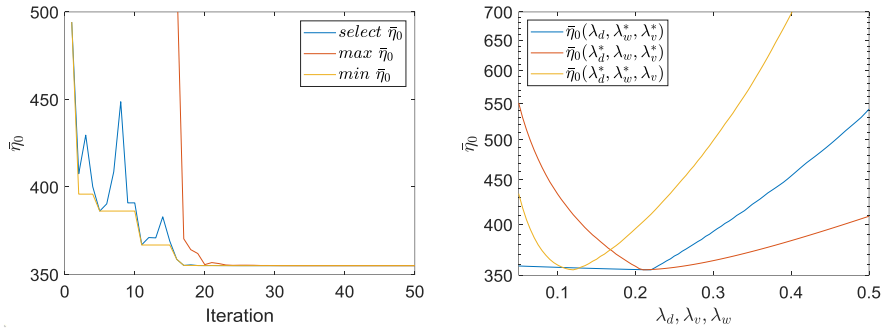

Fig. 4. (a) $\bar{\eta}_0$ iterative curve   (b) $\bar{\eta}_0$ in neighborhood of s^*

4   Conclusion

GMRI is proposed and applied in the optimum design of the parallel manipulator in this paper, including:

(a) LMPI and LMVI are proposed based on the required driving torque and velocity

of the motor, which retain the orientation information of toque/velocity ellipsoid and have the clear physical meaning and mathematical differentiability;

(b) the worst-best subsampling method is proposed to transform the local index to the global index, which is more suitable for the required reasonable taskspace of the mechanism and does not need to combine with other index in the comprehensive performance evaluation;

(c) based on (a) and (b), GMRI is proposed and the effectiveness is validated by the optimum design of a novel 4-DOFs parallel manipulator, PRPS-2PRS.

References

1. Wu J, Yu G, Gao Y, Wang L P.: Mechatronics modeling and vibration analysis of a 2-DOF parallel manipulator in a 5-DOF hybrid machine tool. Mechanism and Machine Theory 121, 430-445(2018)
2. Xie F, Liu X J.: Design and Development of a High-Speed and High-Rotation Robot With Four Identical Arms and a Single Platform. Journal of Mechanisms and Robotics 7(4), 041015(2015).
3. Ye H, Wang D, Wu J, et al: Forward and inverse kinematics of a 5-DOF hybrid robot for composite material machining. Robotics and Computer-Integrated Manufacturing 65, 101961(2020).
4. Wu J, Gao Y, Zhang B B, Wang L P: Workspace and dynamic performance evaluation of the parallel manipulators in a spray-painting equipment. Robotics and Computer Integrated Manufacturing, 44, 199-207(2017)
5. My C A, Bohez E L J: A novel differential kinematics model to compare the kinematic performances of 5-axis CNC machines. International Journal of Mechanical Sciences 163, 105117(2019).
6. Zhang Z K, Wang L P, Shao Z F: Improving the kinematic performance of a planar 3-RRR parallel manipulator through actuation mode conversion. Mechanism and Machine Theory 130, 86-108(2018).
7. Zhao Y, Mei J, Jin Y, et al: A new hierarchical approach for the optimal design of a 5-dof hybrid serial-parallel kinematic machine. Mechanism and Machine Theory 156, 104160 (2021).
8. Patel, S., Sobh, T: Manipulator Performance Measures - A Comprehensive Literature Survey. J Intell Robot Syst 77, 547–570 (2015)
9. Liu X J, Wang J, Pritschow G: Performance atlases and optimum design of planar 5R symmetrical parallel mechanisms. Mechanism and Machine Theory, 41(2), 119-144(2006).
10. Li Y, Xu Q: Kinematics and dexterity analysis for a novel 3-DOF translational parallel manipulator. 2005 IEEE International Conference on Robotics and Automation, IEEE, 2955–2960(2005).
11. Jin Y, Bi Z, Higgins C, et al: Optimal design of a new parallel kinematic machine for large volume machining. Advances in Reconfigurable Mechanisms and Robots I. Springer, 343-354(2012).

12. Salisbury J K, Craig J J: Articulated hands: Force control and kinematic issues. The International journal of Robotics research, 1(1), 4-17(1982).
13. Mazare M, Taghizadeh M, Najafi M R: Kinematic analysis and design of a 3-DOF translational parallel robot. International Journal of Automation and Computing, 14(4), 432-441(2017).
14. Puglisi L J, Saltaren R J, Moreno H A, et al: Dimensional synthesis of a spherical parallel manipulator based on the evaluation of global performance indexes. Robotics and Autonomous Systems, 60(8), 1037-1045(2012).
15. Takeda Y, Funabashi H, Ichimaru H: Development of spatial in-parallel actuated manipulators with six degrees of freedom with high motion transmissibility. JSME International Journal Series C Mechanical Systems, Machine Elements and Manufacturing, 40(2), 299-308(1997).
16. Wang J, Wu C, Liu X J: Performance evaluation of parallel manipulators: Motion/force transmissibility and its index. Mechanism and Machine Theory, 45(10), 1462-1476(2010).
17. N. M. Bajaj and A. M. Dollar: Kinematic Optimization of a Novel Partially Decoupled Three Degree of Freedom Hybrid Wrist Mechanism. 2018 IEEE International Conference on Robotics and Automation, IEEE, 6953-6960(2018).
18. Ophaswongse C, Agrawal S K: Optimal Design of a Novel 3-DOF Orientational Parallel Mechanism for Pelvic Assistance on a Wheelchair: An Approach Based on Kinematic Geometry and Screw Theory. IEEE Robotics and Automation Letters 5(2), 3315-3322(2020).
19. Flanders H.: Elementary divisors of AB and BA. Proceedings of the American Mathematical Society 2(6), 871-874(1951).
20. L. Ingber: Adaptive simulated annealing (ASA): Lessons learned. Control and Cybernetics 25(1), 33–54(1996).

Mass equivalence of four-bar linkages for the design of reconfigurable force-balanced mechanisms

Volkert van der Wijk

Faculty of Mechanical, Maritime, and Materials Engineering, Department of Precision and Microsystems Engineering, Mechatronic System Design, Delft University of Technology, Mekelweg 2, 2628 CD Delft, The Netherlands
`v.vanderwijk@tudelft.nl`

Abstract. In this paper the mass equivalence of four-bar linkages is investigated, which is the characteristic that the mass of the complete linkage can be modeled dynamically equivalent with one or more equivalent masses in one or more points in the linkage. For a general spatial or planar four-bar linkage this results in a model with two equivalent masses, one in a point in each of two opposite links. Since a four-bar consists of two sets of opposite links, its mass can be modeled with two different mass equivalent models and therefore there exists a mass equivalent point in each of the four links. It is shown how these four mass equivalent points can be used for designing a balanced linkage with a floating four-bar linkage that can be reconfigured into four different compositions, depending on which equivalent points are applied as joints to connecting links. It is also shown that when the four-bar linkage becomes a parallelogram, the four mass equivalent points become mass equivalent lines, allowing smooth reconfiguration to numerous positions along the links.

Keywords: mass equivalent model, four-bar linkage, force balance, parallelogram, reconfigurable

1 Introduction

Modeling the mass of mechanism elements with equivalent masses has shown to be a fruitful approach in statics and dynamics for long time. In robotics it is commonly used for deriving the balance conditions of closed loop mechanisms, modeling the mass of the moving platform or of one link in each closed loop in order to obtain open-loop chains [11, 2] or for finding optimally balanced solutions [3].

Mass equivalent modeling has also shown fruitful in the synthesis of (complex) balanced linkages where a single mass model can represent a variety of multi-degree-of-freedom (multi-DoF) mass equivalent linkages, which then can be exchanged with one another without affecting the force balance. Examples have been shown of mass equivalent dyads [5], mass equivalent triads [6], and

mass equivalent pantographs [10], which are also applied for constructing balanced focal linkages [8] and for balancing the Peaucellier-Lipkin straight-line linkage [9]. This synthesis approach also allows a relatively simple way to derive the force balance conditions of complex linkages [7].

This paper is focussed on the mass equivalence of a general (spatial or planar) four-bar linkage of which the mass can be modeled with a single mass model. Without paying notice to it, Dobrovolskii [4] already made use of the mass equivalent points of the planar 4R four-bar linkage by applying a pantograph to these points to trace the center of mass of the linkage. In this paper the mass equivalence of the four-bar linkage is investigated in dept. First the mass equivalent points of the general four-bar linkage are obtained and subsequently they are applied for the design of a reconfigurable mechanism with a floating four-bar linkage that can be reconfigured in four different compositions without affecting the force balance. The last part presents the specific situation that the general four-bar linkage has become a planar parallelogram in which mass equivalent lines allow smooth reconfiguration to a wide variety of poses.

2   Mass Equivalent Points for Force Balance

In Fig. 1 a force-balanced linkage of 7 elements is presented. It consists of a floating four-bar linkage $B_0 B_1 B_2 B_3$ and links $A_0 A_1$ and $A_2 A_3$ of which A_0 and A_3 are pivots with the base link $A_0 A_3$ and A_1 and A_3 are connected with a joint in points R_1 and R_3, respectively. R_1 and R_3 are points in links $B_0 B_1$ and $B_2 B_3$, respectively, located at a distance r_1 and r_3, respectively, from the joint as illustrated and are mass equivalent points of the four-bar, as will become clear later. This linkage can also be observed as a four-bar linkage $A_0 A_1 A_2 A_3$ of which
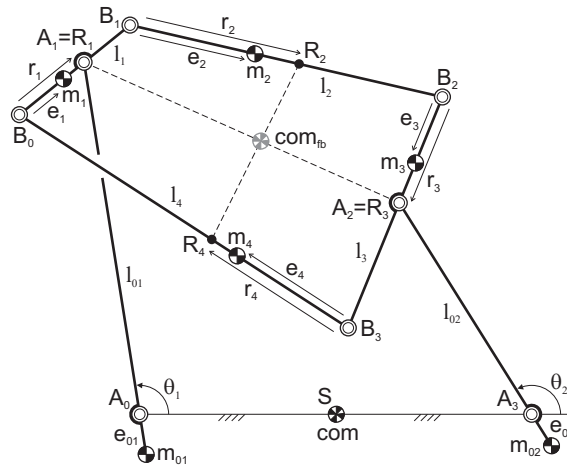

Fig. 1. Force-balanced reconfigurable linkage with common CoM in S for any pose, based on a floating four-bar $B_0 B_1 B_2 B_3$ that is connected to the base with two links.

the coupler link has been replaced with the floating four-bar linkage $B_0 B_1 B_2 B_3$. All the joints can be considered spherical joints, allowing spatial motions in all directions, but they can also be considered as universal or revolute joints in any desired combination. When all the joints would be revolute pairs with their axes of rotation parallel, then Fig. 1 would show a 2-DoF planar linkage with the DoFs θ_1 and θ_2 as illustrated.

Each link i of the floating four-bar has a length l_i and a mass m_i of which the link center-of-mass (CoM) is located at a distance e_i from the link joint as illustrated. Links $A_0 A_1$ and $A_2 A_3$ have a length l_{01} and l_{02}, respectively, and a mass m_{01} and m_{02}, respectively, located at a distance e_{01} and e_{02}, respectively, from the base joints as illustrated. These link masses act also as countermasses in order to balance the complete linkage such that the common CoM of all the links is in a fixed point S in the base for any pose or motion of the linkage.

To calculate the conditions for which the common CoM of all the links is in S, the floating four-bar linkage can be modeled mass equivalently as shown in Fig. 2. The mass of link $B_1 B_2$ is modeled with an equivalent mass $m_2^a = m_2(1 - \frac{e_2}{l_2})$ in B_1 and $m_2^b = m_2 \frac{e_2}{l_2}$ in B_2 while the mass of link $B_3 B_0$ is modeled similarly with equivalent masses $m_4^a = m_4(1 - \frac{e_4}{l_4})$ in B_3 and $m_4^b = m_4 \frac{e_4}{l_4}$ in B_0. With these equivalent masses the links $B_1 B_2$ and $B_3 B_0$ can be eliminated, resulting in two independend parts of the linkage.

The common CoM of m_1, m_2^a, and m_4^b in link $B_0 B_1$ is defined as point R_1 while the common CoM of m_3, m_2^b, and m_4^a in link $B_2 B_3$ is defined as point R_3 of which their locations are calculated as:

$$r_1 = \frac{m_1 e_1 + m_2^a l_1}{m_1 + m_2^a + m_4^b}, \quad r_3 = \frac{m_3 e_3 + m_4^a l_3}{m_3 + m_4^a + m_2^b} \tag{1}$$
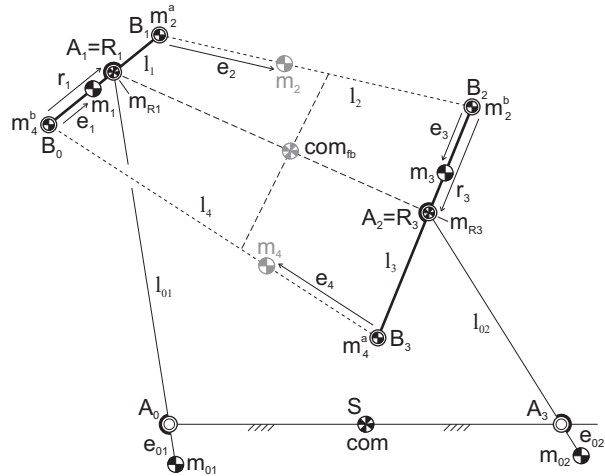

Fig. 2. Equivalent mass model of the floating four-bar linkage with equivalent masses m_{R1} and m_{R3} in mass equivalent points R_1 and R_3, respectively.

R_1 and R_3 are mass equivalent points of the floating four-bar, which means that the motion of the floating four-bar mass $m_{fb} = m_1 + m_2 + m_3 + m_4$ can be modeled mass equivalently with an equivalent mass $m_{R_1} = m_1 + m_2^a + m_4^b$ in point R_1 and an equivalent mass $m_{R_3} = m_3 + m_4^a + m_2^b$ in point R_3. With these equivalent masses, the two separate parts of the model in Fig. 2 must be balanced individually. Therefore A_1 must be located in R_1 and A_2 must be located in R_3 to have the floating four-bar balanced about A_1 and A_2. Subsequently the CoMs of links A_0A_1 and A_2A_3 need to fulfill the balance conditions:

$$e_{01} = \frac{(m_1 + m_2^a + m_4^b)l_{01}}{m_{01}}, \quad e_{02} = \frac{(m_3 + m_4^a + m_2^b)l_{02}}{m_{02}} \tag{2}$$

with which the common CoM of the left part of the linkage model in Fig. 2 is in A_0 and the common CoM of the right part of the linkage model is in A_3 for any pose and motion. Since A_0 and A_3 are base pivots, the common CoM of the complete linkage is in a stationary point in the base as well, which is in point S.

For the balance conditions (1) and (2) the linkage in Fig. 1 is force balanced for any possible variation. Figure 3 shows, for instance, a variation in which the floating four-bar linkage is inverted and the base joints A_0 and A_3 are in a single point. This linkage is force balanced with the common CoM in this single base point for any pose.

It is possible to follow the same procedure to find the mass equivalent points R_2 and R_4 of the floating four-bar, which are located in links B_1B_2 and B_3B_0, respectively, at distances r_2 and r_4 from the link joint, respectively, as illustrated in Fig. 1. In this case the mass of link B_0B_1 is modeled with equivalent masses $m_1^a = m_1(1 - \frac{e_1}{l_1})$ and $m_1^b = m_1 \frac{e_1}{l_1}$ located in B_0 and B_1, respectively, and the mass of link B_2B_3 is modeled with equivalent masses $m_3^a = m_3(1 - \frac{e_3}{l_3})$ and $m_3^b = m_3 \frac{e_3}{l_3}$ located in B_2 and B_3, respectively. The location of points R_2 and
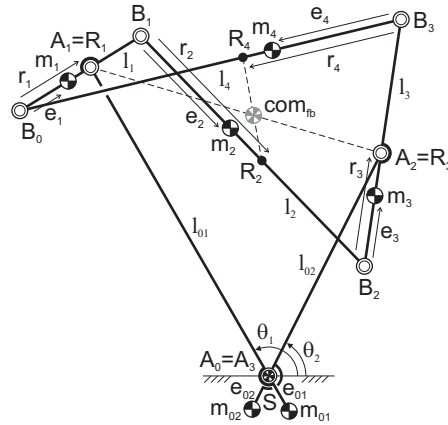

Fig. 3. Force-balanced linkage with inverted floating four-bar and the base pivots in a single point, a variation of the design in Fig. 1.

R_4 in their link then is found with:

$$r_2 = \frac{m_2 e_2 + m_3^a l_2}{m_2 + m_3^a + m_1^b}, \quad r_4 = \frac{m_4 e_4 + m_1^a l_4}{m_4 + m_1^a + m_3^b} \tag{3}$$

It is interesting to note that the line through R_1 and R_3 and the line through R_2 and R_4 intersect at the common CoM of the floating four-bar for any pose. It is also interesting that for force balance the floating four-bar could be mounted on links $A_0 A_1$ and $A_2 A_3$ in four different ways, for instance as well by placing joint A_1 in R_4 and joint A_2 in R_2 as illustrated in Fig. 4c. This results in a model with an equivalent mass $m_{R_4} = m_4 + m_1^a + m_3^b$ located in A_1 and an equivalent mass $m_{R_2} = m_2 + m_3^a + m_1^b$ located in A_2. For force balance the CoMs of links $A_0 A_1$ and $A_2 A_3$ then need to fulfill the balance conditions:

$$e_{01} = \frac{(m_4 + m_1^a + m_3^b) l_{01}}{m_{01}}, \quad e_{02} = \frac{(m_2 + m_3^a + m_1^b) l_{02}}{m_{02}} \tag{4}$$

3   Reconfiguration to Four Force-balanced Compositions

With the four mass equivalent points, it is possible to mount the floating four-bar in four different ways on the supporting links $A_0 A_1$ and $A_2 A_3$, as illustrated in Fig. 4. However, since the equivalent masses of the floating four-bar m_{R_1}, m_{R_2}, m_{R_3}, and m_{R_4} are not equal in general, this has influence on the design of the supporting links which then also have different balance conditions for each of the four configurations, which already becomes clear by comparing Eqs. (2) and (4) of the configurations in Fig. 4a and 4c. In this section three different cases are presented for the floating four-bar to be reconfigured from one composition to another without affecting the balanced design by dismounting and reassembling it onto A_1 and A_2.

3.1   Case 1, one reconfiguration possibility of R_1 to R_4 and R_3 to R_2

To reconfigure the linkage from Fig. 4a to Fig. 4c such that force balance is maintained implies that the balance conditions for the supporting links, Eqs. (2) and (4), must be equal. Since this reconfiguration consists of mounting joints A_1 and A_2 in either R_1 and R_3 or R_4 and R_2, respectively, the additional balance condition for which force balance is maintained follows also from the equivalent four-bar masses that need to be equal with $m_{R_1} = m_{R_4}$ and $m_{R_3} = m_{R_2}$, which can be written as:

$$m_1 + m_2^a + m_4^b = m_4 + m_1^a + m_3^b \tag{5}$$
$$m_3 + m_4^a + m_2^b = m_2 + m_3^a + m_1^b$$

and which results in the single force balance condition:

$$m_1^b + m_2^a - m_3^b - m_4^a = 0 \tag{6}$$

or after substitution:

$$m_1 \frac{e_1}{l_1} + m_2 (1 - \frac{e_2}{l_2}) - m_3 \frac{e_3}{l_3} - m_4 (1 - \frac{e_4}{l_4}) = 0 \tag{7}$$

3.2   Case 2, one reconfiguration possibility of R_1 to R_2 and R_3 to R_4

Similarly as for case 1, it is possible to reconfigure the linkage from Fig. 4a to Fig. 4d such that force balance is maintained without modifying the supporting links. This reconfiguration consists of mounting joints A_1 and A_2 in either R_1 and R_3 or R_2 and R_4, respectively. The additional balance condition for which force balance is maintained follows from the equivalent four-bar masses that need to be equal with $m_{R_1} = m_{R_2}$ and $m_{R_3} = m_{R_4}$, which can be written as:

$$m_1 + m_2^a + m_4^b = m_2 + m_3^a + m_1^b \tag{8}$$
$$m_3 + m_4^a + m_2^b = m_4 + m_1^a + m_3^b$$
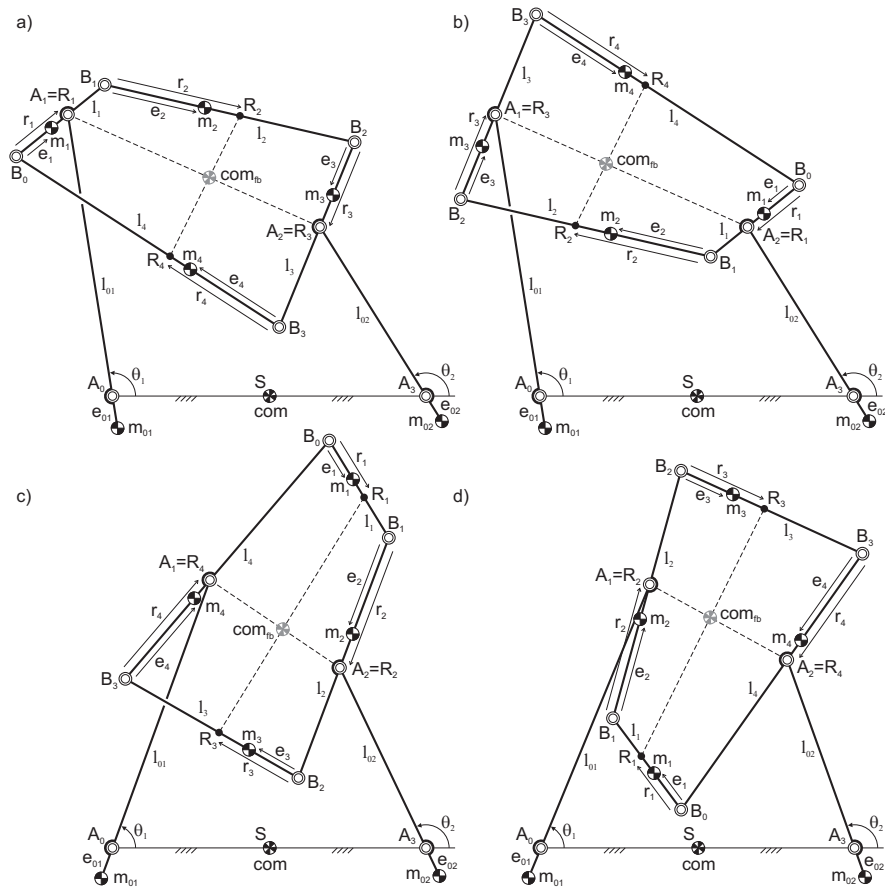
Fig. 4. Four different ways of mounting the floating four-bar on the supporting links A_0A_1 and A_2A_3 for balance. Reconfiguration of the linkage from one composition to another is possible without affecting the force balance.

and which results in the single force balance condition:

$$m_1^a - m_2^b - m_3^a + m_4^b = 0 \qquad (9)$$

or after substitution:

$$m_1(1 - \frac{e_1}{l_1}) - m_2\frac{e_2}{l_2} - m_3(1 - \frac{e_3}{l_3}) + m_4\frac{e_4}{l_4} = 0 \qquad (10)$$

3.3   Case 3, independent reconfiguration to any R_i

To reconfigure the floating four-bar linkage from any composition to any other composition in Fig. 4 while maintaining force balance it is required that all equivalent masses of the floating four-bar are equal, i.e. $m_{R_1} = m_{R_2} = m_{R_3} = m_{R_4}$. From this it is derived that both the balance condition of case 1, Eq. (7), and of case 2, Eq. (10), need to hold at the same time. It has been numerically verified that these conditions result in realistic, natural, and practical designs.

4   Reconfigurable Parallelogram Linkage

It is interesting to discover the specialities of the linkage when the floating four-bar linkage is constructed as a planar parallelogram with $l_1 = l_3$ and $l_2 = l_4$ as shown in Fig. 5. Instead of the ability of all the joints being of any type - spherical, universal, or revolute - as in Fig. 1, here the joints in B_0, B_1, B_2, and B_3 must have revolute pairs to obtain a planar parallelogram $B_0B_1B_2B_3$. The
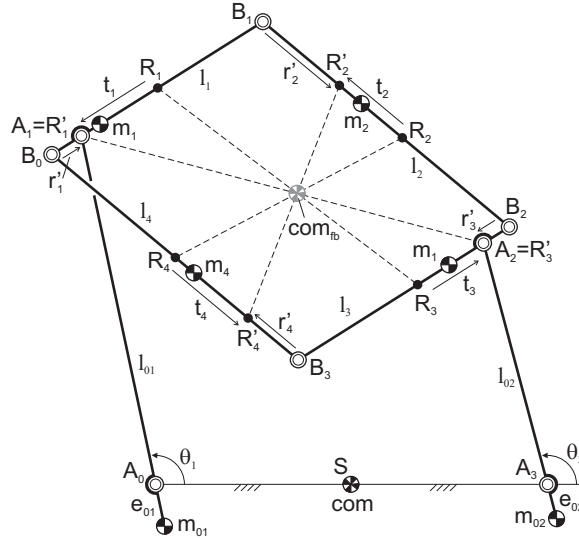
Fig. 5. Force-balanced reconfigurable linkage with CoM in S for any pose, based on a floating parallelogram connected to the base with supporting links A_0A_1 and A_2A_3.

other joints A_0, A_1, A_2, and A_3 can still be of any type such that the planar parallelogram can be moved spatially.

Since the parallelogram is known for its properties of similarity [1], caused by opposite links moving synchronously and referred to as a pantograph, it can be modeled mass equivalently not solely in a single mass equivalent point in each link as for the general four-bar linkage, but in infinitely many points along each link. These points R_i' are located at distances r_i' from the indicated link joint and can be described with distances t_i from the initial mass equivalent points R_i as illustrated. With r_1 and r_3 calculated as in Eq. 1, the locations of R_1' and R_3' can be described with:

$$r_1' = r_1 - t_1 = \frac{m_1 e_1 + m_2^a l_1}{m_1 + m_2^a + m_4^b} - t_1 \tag{11}$$

$$r_3' = r_3 - t_3 = \frac{m_3 e_3 + m_4^a l_3}{m_3 + m_4^a + m_2^b} - t_1 \frac{m_1 + m_2^a + m_4^b}{m_3 + m_4^a + m_2^b}$$

in which the relation between t_1 and t_3 is determined with $m_{R_1} t_1 = m_{R_3} t_3$ such that the line through R_1' and R_3' intersects with the CoM of the parallelogram. With r_2 and r_4 calculated as in Eq. 3, the positions of R_2' and R_4' can be found similarly with:

$$r_2' = r_2 - t_2 = \frac{m_2 e_2 + m_3^a l_2}{m_2 + m_3^a + m_1^b} - t_2 \tag{12}$$

$$r_4' = r_4 - t_4 = \frac{m_4 e_4 + m_1^a l_4}{m_4 + m_1^a + m_3^b} - t_2 \frac{m_2 + m_3^a + m_1^b}{m_4 + m_1^a + m_3^b}$$

in which the relation between t_2 and t_4 is determined with $m_{R_2} t_2 = m_{R_4} t_4$. Instead of defining the mass equivalent points, these equations can be said to define the mass equivalent lines of the parallelogram linkage.

By mounting joints A_1 and A_2 to R_1' and R_3', respectively, and having these points slide along the links following conditions (11), the reconfigurable force balanced linkage in Fig. 6 is obtained. In fact there can be real slider elements in R_1' and R_3' of which the mass can be included in m_{R_1} and m_{R_3} for balance. The linkage is force balanced not only for any pose and motion of the linkage with R_1' and R_3' fixed in their link, but also for any pose and motion of R_1' and R_3' along their link, gaining an additional DoF.

While in Fig. 6 the two slider elements are not mechanically constrained to move synchronously according the conditions of Eq. (11), in Fig. 7 a solution for this is presented with two additional links which intersect in the CoM of the parallelogram where they have a common revolute pair. One link is parallel to links $B_0 B_1$ and $B_2 B_3$ and has joints with links $B_1 B_2$ and $B_3 B_0$ while the other link is connected with sliders to the revolute joints in R_1' and R_3' and hence maintains the condition between the two points. Also the mass of these additional elements can be included for force balance of the complete linkage. It is interesting to note that for $r_1' + r_3' = l_1$, leading to $t_1 = \frac{(r_1 + r_3 - l_1) m_{R_3}}{m_{R_1} + m_{R_3}}$, in Eqs. (11) the line through R_1' and R_3' is parallel to links $B_1 B_2$ and $B_3 B_0$.

Also for the floating parallelogram the four different ways for reconfiguration as shown in Fig. 4 are possible, following the same conditions as presented for each case in the previous section. Altogether this leads to a wide variety of possible reconfigurable designs for which force balance is maintained. In the
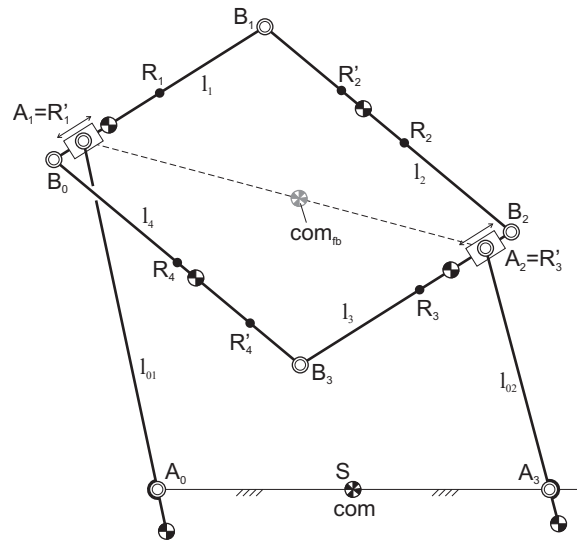

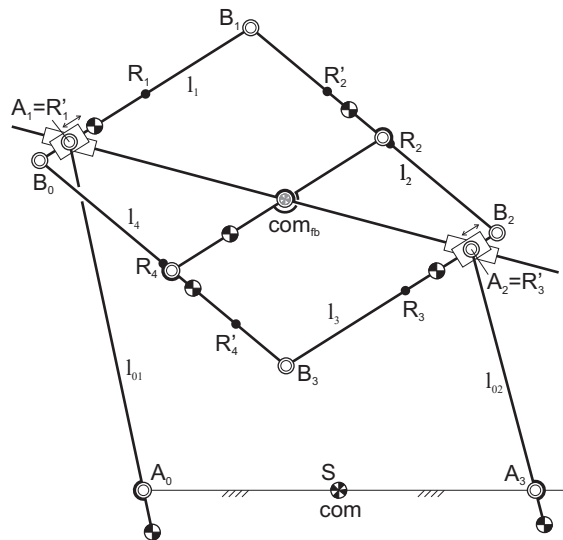**Fig. 6.** Force-balanced reconfigurable linkage solution with sliders in R'_1 and R'_3.

Fig. 7. Force-balanced reconfigurable linkage solution where the sliders in R'_1 and R'_3 are mechanically constrained by additional elements to move proportionally.

solution of Fig. 7 the link through R_1' and R_3' could also be considered as a kind of coupler link of the four-bar linkage $A_0A_1A_2A_3$ mounted with sliders in A_1 and A_2. Hence the linkage in Fig. 7 could be regarded a way to balance such four-bar linkage with a sliding coupler link. Finding other and even better means to synchronize the motions of the two sliders in R_1' and R_3' may be an interesting target for further studies, e.g. investigating solutions with cables and pulleys along the four-bar links.

5   Conclusions

In this paper the mass equivalent models of a general four-bar linkage were presented. It was shown that there is a mass equivalent point in each of the four links and that these points can be applied for the design of force-balanced linkages that can be reconfigured into four different compositions without affecting the balance. It was also shown that when the general four-bar linkage is reduced to a planar parallelogram, the mass equivalent points become mass equivalent lines, allowing smooth reconfiguration to a wide variety of configurations without affecting the force balance.

References

1. Artobolevskii, I.I.: Mechanisms for the Generation of Plane Curves. Pergamon Press (1964)
2. Baradat, C., Arakelian, V., Briot, S., Guegan, S.: Design and prototyping of a new balancing mechanism for spatial parallel manipulators. Mechanical Design (2008)
3. Chaudhary, H., Saha, S.K.: Balancing of shaking forces and shaking moments for planar mechanisms using the equimomental systems. Mechanism and Machine Theory **43**, 310–334 (2008)
4. Dobrovol'skii, V.V.: On the motion of the center of mass of a four-bar linkage. Mechanisms **3**, 233–234 (1968)
5. Van der Wijk, V.: Mass equivalent dyads. In: S. Bai and M. Ceccarrelli (eds.), Recent Advances in Mechanism Design for Robotics **MMS 33**, 35–45 (2015). Springer.
6. Van der Wijk, V.: Mass equivalent triads. Proceedings of the 14th IFToMM World Congress in Mechanism and Machine Science p. OS13.131/DOI 10.6567 (2015)
7. Van der Wijk, V.: Force balance conditions of complex parallel mechanisms with mass equivalent modeling. In: Husty, M. and Hofbaur, M. (eds.), New Trends in Medical and Service Robots 2016 **MMS 48**, 275–287 (2018). Springer Int. Publishing.
8. Van der Wijk, V.: Mass equivalent pantographs for synthesis of balanced focal mechanisms. In: Lenarčič, J. and Merlet, J.-P. (eds.), Advances in Robot Kinematics 2016 **4**, 1–10 (2018). Springer Int. Publishing.
9. Van der Wijk, V.: Shaking force balance of the peaucellier-lipkin straight-line linkage. In: Kecskemethy A., Geu Flores F., Carrera E., Elias D. (eds), Interdisciplinary Applications of Kinematics (IAK 2018) **MMS 71**, 177–184 (2019). Springer
10. Van der Wijk, V., Herder, J.L.: On the addition of degrees of freedom to force-balanced linkages. Proceedings of the 19th CISM-IFToMM Symposium on Robot Design, Dynamics, and Control pp. 2012–025 (2012)
11. Wu, Y., Gosselin, C.M.: On the dynamic balancing of multi-dof parallel mechanisms with multiple legs. Mechanical Design **129**, 234–238 (2007)

Reconfigurable Parallel Mechanisms: A Classification and Review

Dongming Gan[1] and Jian S. Dai[2]

[1] Polytechnic Institute, Purdue University, West Lafayette IN 47907, USA
[2] School of Natural and Mathematical Sciences, King's College London,
University of London, London WC2R2LS, UK
dgan@purdue.edu, jian.dai@kcl.ac.uk

Abstract. Reconfigurable parallel mechanisms have attracted much interests in the research field due to their same advantages with traditional parallel mechanisms and adaptability to various application needs. There are many different designs and reconfiguration methods developed in the literature but no systematic review yet to have a better understanding of their design methodology. This paper aims at reviewing and classifying existing works on reconfiguration parallel mechanisms to provide a systematic picture of this class of mechanisms. The main contribution lies on a systematic classification of reconfigurable parallel mechanisms by defining their main reconfiguration focus on geometric constraints explained by the screw-based modified mobility criterion. The review tries to differentiates existing design concepts including singularity-based reconfiguration, reconfiguration through reconfigurable platforms and bases, through reconfigurable links and joints, and through lockable joints.

Keywords: Reconfigurable Parallel Mechanism, Review, Screw Theory

1 Introduction

Parallel mechanisms can date back to 1928 when James E. Gwinnett designed an entertainment platform used an actually spherical parallel mechanism [1]. Following that, parallel mechanisms have been widely studied in the past decades [2]. The representative parallel mechanism, Stewart-Gough platform [3, 4], has six degrees of freedom and led to many variants and applications [5–8]. Because of the advantages of simpler forward position analysis, mechanical assembly, larger workspace, simpler singularity and control, and wider applications in industries, parallel mechanisms with less than six degrees of freedom attracted much interests with many applications including manufacturing for high precision machining [9–13], camera orienting devices [14], robotic joints [15–17], robotic surgery [18], and human joint rehabilitation [19].

Thus, parallel mechanisms with less than six DOFs are the trend due to their advantages stated above. However, traditional parallel mechanisms have fixed number of DOFs and motion types once designed. To meet the changing market requirements, there is a desired target to generate parallel mechanisms with changed mobility to adapt to different application scenarios. Based on the 2016 US Robotics Road Map of

Robot in Manufacturing section [20], the 5/10/15 years goal is to achieve ability to set up, configure and program basic assembly line operations for new products with a specified industrial robot arm, tooling and auxiliary material handling devices in under 24/8/1 hours. This reflects the industry's need from the traditional mass product case to one-off product system with rapid customized production change. This general context motivates the development of reconfigurable parallel mechanisms as high precision machines and devices that can reconfigure their mobility and motion types to adapt to different application needs.

In the literature, many different reconfigurable parallel mechanisms have been developed and will be classified and reviewed in the following sections. The aim is to reveal their reconfiguration strategies to provide references for future development.

2 Reconfiguration Principles

Different reconfiguration strategies have been developed in the literature. To explain their mobility change principles, the screw-based modified Grubler-Kützbach criterion will be used and reviewed first in section 2.1 followed by the illustrations of reconfigurable principles in section 2.2.

2.1 The Screw-based Modified Grubler-Kützbach Criterion

The screw-based mobility analysis is a widely applied method in many novel parallel mechanisms. In general, the analysis starts from setting up limb motion-screw system and their reciprocal screws to form the limb constraint-screw system. The union of all limb provides the total constraints to the platform, as platform constraint-screw system which can be decomposed into common constraints and other constraints [21]:

$$\langle S^r \rangle = \langle S^r_1, S^r_2, \dots, S^r_n \rangle = \langle S^c \rangle + \langle S^r_c \rangle = \langle S^c \rangle + \{S^r_c\} + \langle S^r_v \rangle \tag{1}$$

where multiset $\langle S^r \rangle$ represents the total constraint on the platform by all limbs, which generally contains common and redundant constraints. Multiset $\langle S^c \rangle$ represents the common constraint on the platform that is supplied by every limb. Multiset $\langle S^r_c \rangle$ represents the portion of the total constraint that is not included in $\langle S^c \rangle$. $\{S^r_c\}$ is the largest linearly independent set of wrenches in $\langle S^r_c \rangle$. The remaining wrenches make up the virtual constraint multiset $\langle S^r_v \rangle$.

Then, the modified Grubler-Kützbach criterion [22] is given

$$m = d(n - g - 1) + \sum_{i=1}^{g} f_i + v - v_{local} \tag{2}$$

where mobility m is calculated for n bodies connected by g joints, each with f_i degrees of freedom. d refers to the mechanism motion system dimension and can be obtained by $d = 6\text{-dim}(S_c)$ where $\text{dim}(S_c)$ gives the dimension of the common constraint S_c. Variable v is the number of virtual constraints and is equal to $\text{card}\langle S^r_v \rangle$. The local mobility of each limb affects the platform mobility and can be obtained by checking if there exist redundant wrenches in every limb constraint system, it follows that

$$v_{local} = \sum_{i=1}^{l} v_{bi} = \sum_{i=1}^{l} (\text{card}\langle \boldsymbol{S}_i \rangle - \dim(\boldsymbol{S}_i)) \tag{3}$$

where v_{bi} is the number of local degrees of freedom of limb i, $\text{card}\langle \boldsymbol{S}_i \rangle$ gives the cardinal number of the multiset $\langle \boldsymbol{S}_i \rangle$, which is always greater than or equal to the dimension of S_i which is the motion-screw system of the ith limb.

By changing any parameters in (2), the mechanism mobility will be changed. This can give a general guideline on developing reconfigurable parallel mechanisms through reconfiguring the mobility parameters. Inversely, this paper uses the modified criterion to explain existing reconfigurable principles by linking their mobility strategy with a specific parameter in (2) as discussed below.

2.2 Reconfiguration Principles

The mobility of a parallel mechanism is determined by the topology of the mechanism including limbs, joints, links and their arrangement in the assembly. The key outcome from the limb to the platform is their geometric constraints which intrinsically determine the mobility and motion of the platform. Based on this, to make a parallel mechanism reconfigurable, the key is to make the geometric constraint changeable to the platform. In the literature, many methods have been developed and an early method focused on designs that the joints and links can be disassembled and reassembled into different parallel mechanisms for different mobility [23–26]. This shows one way to meet the application requirement of changing the platform for different motion types. However, this is not a desired way as reassembling will cause extra effort on assembly, recalibration, and setup. Thus, majority of the recent literature work follows the way that a parallel mechanism can reconfigure its mobility and motion type without disassembling the design, which is also the focus of this review. Based on the literature, it can be mainly divided into four different categories which represent five different methodologies in designing reconfigurable parallel mechanisms that can reconfigure but without disassembling as shown in Fig. 1.
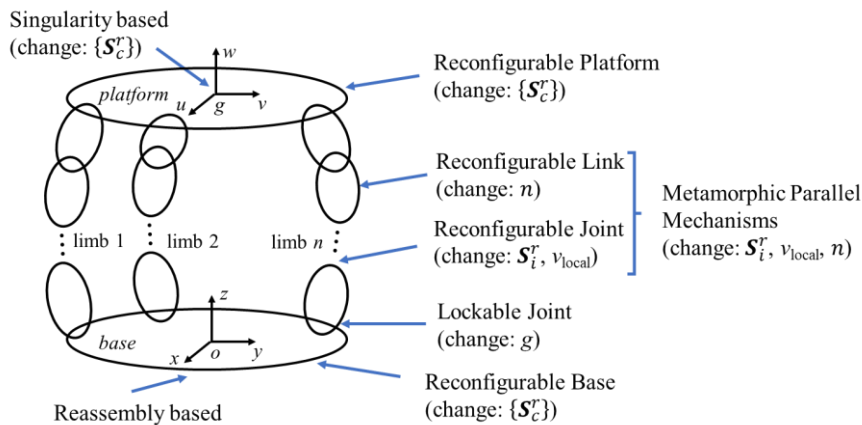

Fig. 1. Parallel Mechanism Reconfiguration Principles

Based on singularity analysis, it was found that some parallel mechanisms could change their mobility and motion types after passing special singular configurations. This resulted in the method of designing reconfigurable parallel mechanisms based on singularities which change the dependency of geometric constraints from all limbs in $\{S_c^r\}$. This method is a kind of passive way since it is associated with a particular configuration and the parallel mechanism experiences singularity in the transition which is not preferred in control. Other four methods are more active on reconfiguration including reconfigurable platforms, reconfigurable bases, lockable joints and metamorphic parallel mechanisms that use link coincidence and reconfigurable joint method. In general, they all actively control the joint directions and their contribution in the limb to the platform geometric constraints. By reconfiguring the platform, the arrangement of the connecting joints between the platform and the limbs will be reconfigured, resulting in the platform constraint $\{S_c^r\}$ change and mobility reconfiguration. This method needs a linkage platform which can be complex for both design and application. The reconfigurable base method uses similar idea with the reconfigurable platform but introducing linkage bases. The lockable joint method changes the joint effectiveness (number of joints, g, in the modified Grubler-Kützbach criterion) by locking and unlocking its motion to make the limb and platform constraint reconfigurable. Theoretically, every parallel mechanism can be reconfigurable through this method by adding actuators to lock the joints. This freedom and wide possibility also make the method not easily or systematically applicable. Moreover, this method doesn't reconfigure the geometric constraint but the effective number of joints (g), which is not preferred in mechanism design and synthesis seeking more on geometric constraints. Metamorphic parallel mechanisms show a promising way to develop reconfigurable parallel mechanisms by changing joint directions and contribution to the limb geometric constraints through link coincidence (number of links, n) or joint reconfiguration (S_i^r, v_{local}). This method theoretically is in line with geometric constraint-based mechanism design and synthesis, and practically are flexible with local joint or link reconfiguration within the limbs.

3 Classification and Review

In the following, existing literature work will be reviewed and classified for each method to reveal more information and discussions.

3.1 Singularity based Reconfiguration

One of the cases of singularity-based reconfiguration is to have bifurcated configurations through constraint singularities [27]. Kinematotropic mechanisms were the earliest mechanisms that the permanent mobility could be changed after passing through the singular configurations [28]. Following the study of single-loop and multi-loop kinematotropic mechanisms, parallel mechanisms with bifurcated motion were constructed [29]. Those early work paved one way of making reconfigurable parallel mechanisms through constraint singularities and has been followed in the literature. Based on the workspace property, this class of reconfigurable parallel mechanisms can be classified into two different types. One of them is that through constraint sin-

gularity, the two different operation modes can be switched and work effectively in the whole actuation range or workspace of the mechanism. For example, a family of parallel mechanisms that have multiple operation modes were presented in [30, 31]. The parallel mechanisms can be either pure rotational or pure translational in the whole workspace after some limb tuning at the constraint singular configuration. Possible operation modes of the 3-UPU parallel mechanism were revealed based on the geometric constraint using Study parameters [32]. A systematic synthesis was proposed in [33] on designing reconfigurable parallel mechanisms with bifurcated motion through constraint singularities and a number of those reconfigurable parallel mechanisms were obtained.

The second type is that the two operation modes or bifurcated motion have complementary sharing of the whole workspace of the mechanism which means the platform shows one motion in one part of the workspace but cannot reach the other part which belongs to another motion branch. Most of the reconfigurable parallel mechanisms based on constraint singularity belong to this type. It shows that the workspace of each of the operation modes is smaller than the whole workspace but they can be useful in particular applications, for example, a parallel mechanism with changed motion on two different directions for machine tool applications was proposed [34]. It decoupled the machining workspace on two directions to avoid conflict on the machined object. Similarly, a family of parallel mechanisms with bifurcated Schoenflies motion was found in [35] and two of them were further analyzed in [36]. Using linear transformations, new 2T1R parallel mechanisms with a bifurcated rotation motion on two orthogonal directions [37] were synthesized and constraint singularity [38] and mechanism connectivity were also investigated. It was found that bifurcated motion occurs when the mechanism reaches mobility less than 3 in a metamorphic parallel mechanism [39] that covers a wide range of mobility change. At the same time, inspired from an origami fold, [40] proposed a metamorphic parallel mechanism with ability of performing orientation switch via the constraint singular configuration. Branch motions of a class of 3-*PUP* parallel mechanisms [41] were investigated and one of the bifurcated branch motions was a screw motion while the other was a pure rotation. When the platform falls into one motion branch it cannot move to another with complementary workspace. Recently, a systematic quaternion-based method was presented to investigate multi-operation modes of reconfigurable parallel mechanisms [42] and a new kinematotropic parallel mechanism that could reconfigure into operation modes with 1 through 3 DOFs was designed [43]. The constraint-singularity based operation modes of reconfigurable parallel mechanisms were also extended to various applications as ankle exoskeleton [44], walking robot [45], and 3D printing [46].

In addition to constraint singularities, through both Type 1 [47] and Type 2 [48] singularities, parallel mechanisms can be also reconfigured between different motion types. This is more obvious about the complementary workspace sharing since the operation modes exist in different workspace zones separated by the singularity loci. For example, the 3-PRS parallel mechanism [49] had different motion types within different workspace zones separated by singularity surfaces and reconfiguration can

be realized through special trajectory planning [50] and variable actuation modes [51, 52] other than through the constraint singularity configurations.

In general, this class of reconfigurable parallel mechanisms show an interesting property of parallel mechanisms on mobility and constraint change. But they are not practically preferable by experiencing singularity and singularity-close configurations which can cause control disfunction and extra actuators are needed. Moreover, most of them work in separated workspace zones for different operation modes resulting in very small workspace since parallel mechanisms have already very small workspace due to their multi-loop structures.

3.2   Reconfigurable Platform and Reconfigurable Base based Reconfiguration

Reconfigurable Platform. Traditionally, the platform of parallel mechanisms is a single rigid body and all the connecting joints between the platform and limbs have fixed arrangement on the platform. A creative way of developing reconfigurable parallel mechanisms is to introduce linkage platforms which can change the connecting joints' relative directions on the platform to change the combined limb constraints to the platform. In [53], the Bennett linkage, Bricard linkage, an 8-bar linkage and a 12-bar linkage were used as the platform of a parallel mechanism as in Fig. 2(a). The linkage configuration change will change the last limb joint configuration on the platform, thus changing the constraint to the platform without passing by singularity configurations. A similar reconfigurable parallel mechanism using the Bricard linkage was also proposed and built to have reconfigured motion between pure rotation, pure translation and planar motion [54] while another design was applied for a walking robot to adapt to flat and stair walking phases [55]. A general method using screw theory to transferability of limb constraints to the platform motion was proposed and extended to parallel mechanisms with n-bar reconfigurable platforms [56] as in Fig. 2(b). So far only those few mechanisms have been proposed in the literature using reconfigurable platforms mainly through some symmetric linkages, like the Bricard linkage.
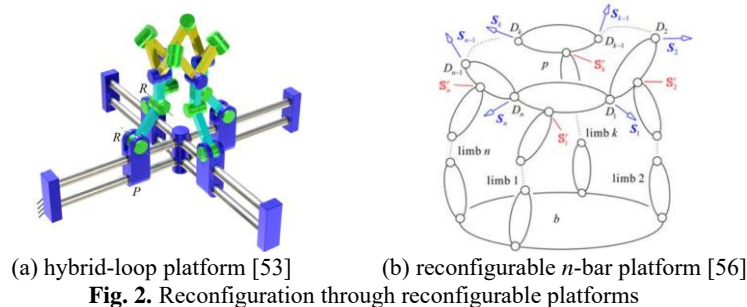
(a) hybrid-loop platform [53]   (b) reconfigurable n-bar platform [56]
Fig. 2. Reconfiguration through reconfigurable platforms

Reconfigurable Base. Existing work on reconfigurable base mainly tried to reconfigure limb configuration with respect to the base, which is different with the reconfigurable linkage-based platform method. In [57], the prismatic joints were designed to sit on an intermediate platform which could change the prismatic joints' position with respect to the main mechanism base. The design didn't change the mechanism's mo-

bility or output motion but the kinematics and dynamics property. Similarly, pantographic linkages were used to reconfigure the base of a spherical 3-RRR parallel mechanism to change its rotation center to adapt to different surgery cases in craniotomy [58]. Recently, an over-constrained intermediate platform was designed to change the prismatic joints' configuration as actuators in a reconfigurable 3-PUU parallel mechanism with potential application in manufacturing [59].

In summary, those types of reconfigurable parallel mechanisms based on reconfigurable platforms or bases have not been studied much and the method is generally complex to apply. A reconfigurable platform is also complex from the application, design, modelling and control point of view since the whole mechanism has more multi-loops than traditional parallel mechanisms but they may show good properties in specific applications, like the surgery case in [58].

3.3 Metamorphic Parallel Mechanisms

Metamorphic parallel mechanisms are believed very promising considering their theoretical geometric constraint-based model and practically flexible local reconfiguration tuning. This class of reconfigurable parallel mechanisms focuses on the link and joint reconfiguration principles.

Reconfigurable Link based Reconfiguration. One method to design reconfigurable mechanisms is to change the number of links by link coincidence and self-locking as in [60–63]. It was used in proposing metamorphic mechanisms in the study of decorative carton folds and reconfigurable packaging [61]. Based on this concept, a metamorphic multi-fingered hand with an articulated palm by link coincidence of a spherical five bar linkage was invented [60]. A general approach for self-locking analysis was proposed in [62] while various joint types were explained and used in kinematic representations of metamorphic pop-up paper mechanisms in [63]. Based on the link coincidence of a four-bar linkage, different motion branches were obtained and used in reconfiguring parallel mechanisms by varying the limb constraints between forces and wrenches [64]. This reconfigurable linkage method was then extended to other three designs for reconfigurable parallel mechanisms [65]. Following those, reconfigurable close-loop kinematic chains including five bars [66–68] and six bar [69] were developed with corresponding reconfigurable parallel mechanisms synthesized as two examples in Fig. 3.
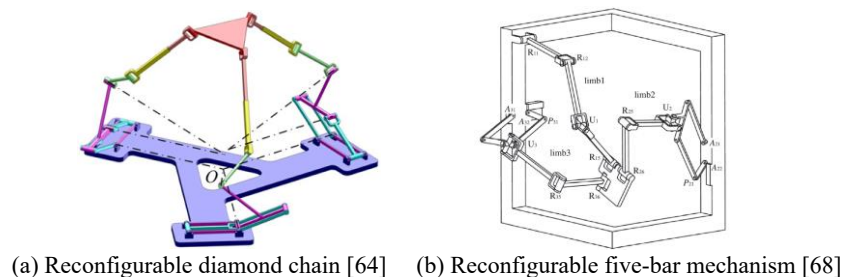

(a) Reconfigurable diamond chain [64]   (b) Reconfigurable five-bar mechanism [68]
Fig. 3. Reconfigurable link-based reconfiguration

This method has the function of changing the joint contribution to the limb through link coincidence but existing work mainly focused on changing the effective number of links and joints. More work can be devoted to explore how the joint directions can be changed through link reconfiguration to eventually change the geometric constraints. The method of reconfigurable joints shows more flexibility and applicability in synthesizing metamorphic parallel mechanisms through direct joint property change as discussed below.

Reconfigurable Joint based Reconfiguration. By applying geometric constraints to change joint property, mobility and motion types of parallel mechanisms can be changed. This has been an active method recently in designing reconfigurable parallel mechanisms. Variable topologies of kinematic joints and their topological reconfiguration was presented in [70]. Based on a patented reconfigurable Hooke (rT) joint as in Fig. 4(a), various metamorphic parallel mechanisms [22, 39, 71, 72] were designed and a systematic synthesis method based on screw theory was introduced [73]. Similarly, a metamorphic parallel mechanism with ability of performing phase change and orientation switch was proposed by introducing a metamorphic kinematic pair [40] and a class of metamorphic parallel mechanisms [74] was designed using a variable-axis (vA) joint [75] which can reconfigure among three different mobility as in Fig. 4(b). Following this direction, a reconfigurable revolute joint was invented and a 3-rRPS metamorphic parallel mechanism was designed to have reconfigured motions between pure rotation and 1T2R motion (one translation and two rotation) [76]. Singularity and various operation modes of this mechanism was systematically explored with respect to different rR joint configurations [77]. The design methodology of reconfiguring joints' property has been recently extended to new joints, including a modified rT joint [78] as in Fig. 4(c), a variable topology joint [79] and a reconfigurable axis (rA) joint [80] as in Fig. 4(d). Those led to many new reconfigurable parallel mechanisms based on the joints' constraint change.
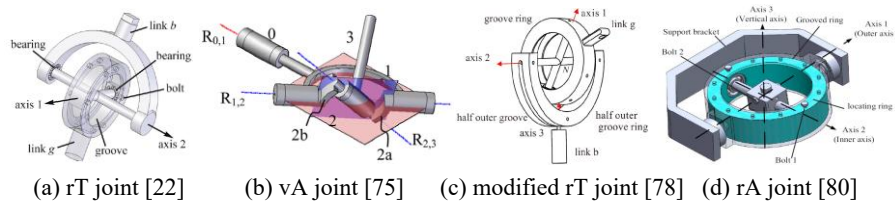
(a) rT joint [22]   (b) vA joint [75]   (c) modified rT joint [78]   (d) rA joint [80]
Fig. 4. Reconfiguration joints

The reconfigurable joint method touches the core of geometric constraints in the limbs and mechanisms by varying the joint relative directions. Comparing with reconfigurable platform method and reconfigurable link method in changing the joint contribution, this method directly goes to the joint property change. Its local joint reconfiguration also brings flexibility in parallel mechanism reconfiguration by avoiding affecting other links or joints or whole mechanism configuration change as needed in the singularity-based methods. It also shows alinement with traditional synthesis methods based on joint modules for parallel mechanisms. Thus, it's easy to apply

existing parallel mechanism theory for synthesizing and designing novel reconfigurable parallel mechanisms.

3.4   Lockable Joint based Reconfiguration

The last method is lockable joint based reconfiguration. This is not included in the reconfigurable joint method of metamorphic parallel mechanisms since it does not reconfigure the joints to have changeable geometric constraints. Instead, it changes the effective number (n) of conventional kinematic joints in the limb system through which it changes the output motion and constraint of the limb to the platform. Thus, this is a different method and theoretically, it can be applied for any mechanism by adding lockable joints. Existing literature designs are classified by the type of the joints locked as revolute (R) joints, prismatic (P) joints and both of them in one mechanism. Universal (U) joints and spherical (S) joints are treated as combined R joints.

Lockable R joints. Most of the reconfigurable mechanisms using lockable joints were based on lockable R joints, including the early work on a planar 3-RRR parallel mechanism with redundant actuators in the first two R joints in each limb [81]. By locking different ones, it can reconfigure into 2-DOF and 3-DOF mechanisms. On the same mechanism, a parallelogram was introduced to the first R joint in the planar 3-RRR NaVARo robot which could reconfigure into 8 actuation modes through a double clutch design [82, 83]. By rotating an extra R joint between the limb and the base to tune the limb configuration, a hybrid parallel mechanism can reconfigure its kinematics performance [84]. With lockable 12 actuators associated with 12 of the 20 R joints in a four-limb parallel mechanism, a reconfigurable mobile parallel robot was designed that could operate as an equivalent rolling robot or quadruped robot [85]. The needs of lockable R joints also led to new lockable designs through cavities or grooves [86–89] and general synthesis method in developing reconfigurable parallel mechanisms [54].

In addition to locking single R joint, locking one of the revolute axes in a U joint or S joint was also investigated with new designs. By locking one axis of the U joints in a 3-UPS parallel mechanism [90], the parallel mechanism could reconfigure between 3-DOFs and 6-DOFs which were used in planning the motion of the platform through transition among them. An S joint with two lockable R joints was designed which enabled a 3-CPS parallel mechanism to reconfigure into either pure rotation or pure translation 3-CPU configurations [91, 92]. The method was also extended to a 3-SRU reconfigurable parallel mechanism [93].

Lockable P joints. P joints are common actuated joints in parallel mechanisms and are easily lockable. [94] presented a 6-DOF reconfigurable parallel mechanism which reconfigured its mobility from 3 through 6 by locking a number of the six actuated prismatic joints on the base. By adding extra limbs with lockable P joints, a reconfigurable parallel mechanism was developed in [95] which enhances the stiffness of the platform through static redundancy at different configurations through locking and unlocking the P joints. This method was recently extended to a 9-SPS reconfigurable parallel mechanism with enhanced stiffness within the workspace [96].

Lockable R and P joints. By locking both or between R and P joints, new reconfigurable parallel mechanisms were developed. In [97], both the R and P joints were lockable to reconfigure a 3-RPRP spherical parallel mechanism into 10 different spherical mechanism modes including 2 symmetrical and 8 asymmetrical ones. The combined locking of P and R joints in a parallelogram limb structure, a reconfigurable parallel mechanism was able to reconfigure into 5 operation modes including one pure translation and four 2T1R modes [98]. Along this direction by combined P and R joint locking, 7 symmetrical and 25 asymmetrical configurations with mobility from 0 through 6 were obtained with a 3-PXPS reconfigurable parallel mechanism [99]. By locking between a P joint and a R joint in each limb, [100, 101] demonstrated new reconfigurable parallel mechanisms.

In general, joint locking-based reconfiguration is a relatively easy way to develop reconfigurable parallel mechanisms based on the rich knowledge of traditional parallel mechanism research. This has attracted much interests as shown above and may lead to new practical applications.

3.5 Summary of the classification and references

The above classifications are summarized in Table 1 below to have a systematic view of the reconfiguration categories and corresponding mechanisms and works.

Table 1. Summary of the reconfiguration parallel mechanisms

Reconfiguration Principles (Constraint change)	Classifications	References
Singularity-based (change: $\{S_c^r\}$)	Constraint-singularity based shared workspace	[30 − 33]
	Constraint-singularity based Complementary workspace	[29, 34 − 46]
	Type 1 singularity based	[47]
	Type 2 singularity based	[48 − 52]
Reconfigurable platform and base (change: $\{S_c^r\}$)	Reconfigurable platform	[53 − 56]
	Reconfigurable base	[57 − 59]
Metamorphic Parallel Mechanisms (change: S_i^r, v_{local}, n)	Reconfiguration links (change: n)	[60 − 69]
	Reconfigurable joints (change: S_i^r, v_{local})	[22,39,40,70 − 80]
Lockable joints (change: g)	Lockable R joints	[54, 81 − 89]
	Lockable U/S joints	[90 − 93]
	Lockable P joints	[94 − 96]
	Lockable R and P joints	[97 − 101]

Conclusions

This paper reviewed and classified reconfigurable parallel mechanisms through their reconfiguration principles. Seven different categories were concluded including singularity based, reassembly based, and reconfigurations through reconfigurable platforms, bases, links, joints and lockable joints. The paper focused on geometric constraint principles which were linked and explained by the screw-based modified Grubler-Kützbach criterion. While singularity-based reconfiguration was an early developed concept, recent work focused more on reconfigurable and lockable joint methods due to their modularity and local operability in the limbs. The paper grouped reconfigurable links and joints as methods in developing metamorphic parallel mechanisms which were a branch of reconfigurable parallel mechanisms. The reconfigurable joint method was also differentiated with lockable joint method as the former focused on geometric change of the joint while the latter mainly changed the effective number of joints through locking and unlocking. Both the two methods are promising to develop modular reconfigurable units for future reconfigurable parallel mechanisms with practical applications.

References

1. Bonev, I.: The True Origins of Parallel Robots, http://www.parallemic.org/Reviews/Review007.html.
2. Merlet, J.P.: Parallel Robots. Springer Science & Business Media (2005).
3. Gough, V.E.: Automobile stability, control, and tyre performance. Proc. Automob. Div. Inst. Mech. E. 171, 392–394 (1956).
4. Stewart, D.: A platform with six degrees of freedom. Proc. IMechE. 180, 371–385 (1965).
5. Dai, J.S., Kerr, D.R.: Six-component contact force measurement device based on the Stewart platform. Proc. Inst. Mech. Eng., Part C J. Mech. Eng. Sci. 214, 687–697 (2000).
6. Dasgupta, B., Mruthyunjaya, T.S.: The Stewart platform manipulator: a review. Mech. Mach. Theory. 35, 15–40 (2000).
7. Gan, D., Liao, Q., Dai, J.S., Wei, S., Seneviratne, L.D.: Forward displacement analysis of the general 6-6 Stewart mechanism using Gröbner bases. Mech. Mach. Theory. 44, (2009).
8. Gan, D., Liao, Q., Dai, J.S., Wei, S., Seneviratne, L.D.: Forward displacement analysis of a new 1CCC-5SPS parallel mechanism using Gröbner theory. Proc. Inst. Mech. Eng. Part C J. Mech. Eng. Sci. 223, 1233–1241 (2009).
9. Siciliano, B.: The Tricept robot: Inverse kinematics, manipulability analysis and closed-loop direct kinematics algorithm. Robotica. 17, 437–445 (1999).
10. Xie, F.G., Liu, X.J.: Design and development of a high-speed and high-rotation robot with four identical arms and a single platform. ASME J. Mech. Robot. 7, 041015_1–12 (2015).
11. Neumann, K.-E.: Robot, US patent 4732525, (1988).
12. Gan, D., Dai, J.S., Dias, J., Umer, R., Seneviratne, L.: Singularity-free workspace aimed optimal design of a 2T2R parallel mechanism for automated fiber placement. J. Mech. Robot. 7, (2015).
13. Gan, D., Dai, J.S., Dias, J., Seneviratne, L.: Forward kinematics solution distribution and

analytic singularity-free workspace of linear-actuated symmetrical spherical parallel manipulators. J. Mech. Robot. 7, (2015).

14. Gosselin, C., St-Pierre, E., Gagné, M.: on the Development of the Agile Eye: Mechanical Design, Control Issues and Experimentation. IEEE Rob. Autom. Mag. 3, 29–37 (1996).

15. Vishcher, P., Clavel, R.: Argos: A Novel 3-dof Parallel Wrist Mechanism. Int. J. Rob. Res. 19, 5–11 (2000).

16. Hofschulte, J., Seebode, M., Gerth, W.: Parallel Manipulator Hip Joint for a Bipedal Robot. Climbing Walk. Robot. 601–609 (2004).

17. Cui, L., Dai, J.S.: Posture, workspace, and manipulability of the metamorphic multifingered hand with an articulated palm. ASME J. Mech. Robot. 3, 021001 (2011).

18. Kuo, C.-H., Dai, J.S.: Kinematics of a Fully-Decoupled Remote Center-of- Motion Parallel Manipulator for Minimally Invasive Surgery. ASME J. Med. Devices. 6, 021008 (2012).

19. Dai, J.S., Zhao, T., Nester, C.: Sprained Ankle Physiotherapy Based Mechanism Synthesis and Stiffness Analysis of Rehabilitation Robotic Devices. Robot. Auton. Robot. 16, 207–218 (2004).

20. US Robotics Roadmap and the National Robotics Initiative 2.0. (2016).

21. Dai, J.S., Huang, Z., Lipkin, H.: Mobility of overconstrained parallel mechanisms. J. Mech. Des. Trans. ASME. 128, 220–229 (2006).

22. Gan, D., Dai, J.S., Liao, Q.: Mobility change in two types of metamorphic parallel mechanisms. J. Mech. Robot. 1, 1–9 (2009).

23. Kumar, S.G., Nagarajan, T., Srinivasa, Y.G.: Characterization of reconfigurable Stewart platform for contour generation. Robot. Comput. Integr. Manuf. 25, 721–731 (2009).

24. Sarabandi, S., Grosch, P., Porta, J.M., Thomas, F.: A Reconfigurable Asymmetric 3-UPU Parallel Robot. 2018 Int. Conf. Reconfigurable Mech. Robot. ReMAR 2018 - Proc. (2018).

25. Zhang, D., Lang, S.Y.T.: Stiffness modeling for a class of reconfigurable PKMs with three to five degrees of freedom. J. Manuf. Syst. 23, 316–327 (2004).

26. Dash, A.K., Chen, I.M., Yeo, S.H., Yang, G.: Task-oriented configuration design for reconfigurable parallel manipulator systems. Int. J. Comput. Integr. Manuf. 18, 615–634 (2005).

27. Zlatanov, D., Bonev, I.A., Gosselin, C.M.: Constraint singularities of parallel mechanisms. Proc. - IEEE Int. Conf. Robot. Autom. 1, 496–502 (2002).

28. Wohlhart, K.: Kinematotropic Linkages. Recent Adv. Robot Kinemat. 359–368 (1996).

29. Fanghella, P., Galletti, C., Giannotti, E.: PARALLEL ROBOTS THAT CHANGE THEIR GROUP OF MOTION Single-loop Kinematotropic Chains. Adv. Robot Kinemat. 49–56 (2006).

30. Kong, X.: Type synthesis of 3-DOF parallel manipulators with both a planar operation mode and a spatial translational operation mode. J. Mech. Robot. 5, (2013).

31. Kong, X., Gosselin, C.M., Richard, P.L.: Type synthesis of parallel mechanisms with multiple operation modes. J. Mech. Des. Trans. ASME. 129, 595–601 (2007).

32. Walter, D.R., Husty, M.L., Pfurner, M.: A complete kinematic analysis of the SNU 3-UPU parallel robot. 331–346 (2009).

33. Zeng, Q., Ehmann, K.F., Cao, J.: Design of general kinematotropic mechanisms. Robot. Comput. Integr. Manuf. 38, 67–81 (2016).

34. Refaat, S., Hervé, J.M., Nahavandi, S., Trinh, H.: Two-mode overconstrained three-DOFs rotational-translational linear-motor-based parallel-kinematics mechanism for machine tool applications. Robotica. 25, 461–466 (2007).

35. Li, Q., Herv, J.M.: Short Papers of Schoenflies Motion. IEEE Trans. Robot. 25, 158–164 (2009).

36. Chen, Q., Li, Q., Wu, C., Hu, X., Huang, Z.: Mobility analysis of 4-RPRPR and 4-RRRPR parallel mechanisms with bifurcation of schoenflies motion by screw theory. Proc. 2009 ASME/IFToMM Int. Conf. Reconfigurable Mech. Robot. ReMAR 2009. 279–284 (2009).

37. Gogu, G.: Maximally regular T2R1-Type parallel manipulators with bifurcated spatial motion. J. Mech. Robot. 3, 1–8 (2011).

38. Gogu, G.: Bifurcation in constraint singularities and structural parameters of parallel mechanisms. Meccanica. 46, 65–74 (2011).

39. Gan, D., Dai, J.S., Liao, Q.: Constraint analysis on mobility change of a novel metamorphic parallel mechanism. Mech. Mach. Theory. 45, (2010).

40. Zhang, K., Dai, J.S., Fang, Y.: Topology and constraint analysis of phase change in the metamorphic chain and its evolved mechanism. J. Mech. Des. Trans. ASME. 132, (2010).

41. Gan, D., Dai, J.S.: Geometry constraint and branch motion evolution of 3-pup parallel mechanisms with bifurcated motion. Mech. Mach. Theory. 61, (2013).

42. Liu, K., Kong, X., Yu, J.: Operation mode analysis of lower-mobility parallel mechanisms based on dual quaternions. Mech. Mach. Theory. 142, 103577 (2019).

43. P.C., L.-C., A., M., J.S., D.: A Kinematotropic Parallel Mechanism Reconfiguring Between Three Motion Branches of Different Mobility. Adv. Mech. Mach. Sci. 73, 2611–2620 (2019).

44. Nurahmi, L., Caro, S., Solichin, M.: A novel ankle rehabilitation device based on a reconfigurable 3-RPS parallel manipulator. Mech. Mach. Theory. 134, 135–150 (2019).

45. Liu, Y., Li, Y., Yao, Y. an, Kong, X.: Type synthesis of multi-mode mobile parallel mechanisms based on refined virtual chain approach. Mech. Mach. Theory. 152, 103908 (2020).

46. Nurahmi, L., Putrayudanto, P., Wei, G., Agrawal, S.K.: Geometric Constraint-Based Reconfiguration and Self-Motions of a Four-CRU Parallel Mechanism. J. Mech. Robot. 13, (2021).

47. Bonev, I., Briot, S., Wenger, P., Chablat, D.: Changing Assembly Modes without Passing Parallel Singularities in Non-Cuspidal 3-RPR Planar Parallel Robots. In: Second International Workshop on Fundamental Issues and Future Research Directions for Parallel Mechanisms and Manipulators. pp. 1–6. , Montpellier, France (2008).

48. Pagis, G., Bouton, N., Briot, S., Martinet, P.: Enlarging parallel robot workspace through Type-2 singularity crossing. Control Eng. Pract. 39, 1–11 (2015).

49. Nurahmi, L., Caro, S., Wenger, P.: Operation Modes and Singularity analysis of 3-PRS Parallel Manipulators with different arrangements of P-joints. In: Proceedings of the ASME 2015 International Design Engineering Technical Conference and Computers and Information in Engineering Conference. pp. 1–10. , Boston, USA (2015).

50. Wenger, P.: Cuspidal and noncuspidal robot manipulators. Robotica. 25, 677–689 (2007).

51. Arakelian, V., Briot, S., Glazunov, V.: Increase of singularity-free zones in the workspace of parallel manipulators using mechanisms of variable structure. Mech. Mach. Theory. 43, 1129–1140 (2008).

52. Caro, S., Chablat, D., Hu, Y.: Algorithm for the actuation mode selection of the parallel manipulator navaro. Proc. ASME Des. Eng. Tech. Conf. 5B, 1–10 (2014).

53. Zeng, Q., Ehmann, K.F.: Design of parallel hybrid-loop manipulators with kinematotropic property and deployability. Mech. Mach. Theory. 71, 1–26 (2014).

54. Kong, X., Jin, Y.: Type Synthesis of 3-DOF multi-mode translational/spherical parallel mechanisms with lockable joints. Mech. Mach. Theory. 96, 323–333 (2016).

55. Xu, Y., Liang, Z., Liu, J.: A New Metamorphic Parallel Leg Mechanism with Reconfigurable Moving Platform. Math. Probl. Eng. 2020, (2020).

56. Kang, X., Dai, J.S.: Relevance and Transferability for Parallel Mechanisms with Reconfigurable Platforms. J. Mech. Robot. 11, 1–9 (2019).

57. Zhang, D., Shi, Q.: Novel design and analysis of a reconfigurable parallel manipulator using variable geometry approach. Adv. Intell. Soft Comput. 124, 447–457 (2011).

58. Essomba, T., Hsu, Y., Sandoval Arevalo, J.S., Laribi, M.A., Zeghloul, S.: Kinematic Optimization of a Reconfigurable Spherical Parallel Mechanism for Robotic-Assisted Craniotomy. J. Mech. Robot. 11, 1–14 (2019). https://doi.org/10.1115/1.4044411.

59. Huang, G., Zhang, D., Tang, H., Kong, L., Song, S.: Analysis and control for a new reconfigurable parallel mechanism. Int. J. Adv. Robot. Syst. 17, 1–20 (2020).

60. Dai, J.S., Wang, D.: Geometric analysis and synthesis of the metamorphic robotic hand. J. Mech. Des. Trans. ASME. 129, 1191–1197 (2007). https://doi.org/10.1115/1.2771576.

61. Dai, J.S., Rees Jones, J.: Mobility in ivietamorphic iviechanisms of foldable/erectable kinds. J. Mech. Des. Trans. ASME. 121, 375–382 (1999).

62. Leonesio M. Bianchi G., M.P.: A general approach for Self-locking Analysis in Closed Kinematic Chains. (2007).

63. Winder, B.G., Magleby, S.P., Howell, L.L.: Kinematic representations of pop-up paper mechanisms. J. Mech. Robot. 1, 1–10 (2009).

64. Ye, W., Fang, Y., Zhang, K., Guo, S.: A new family of reconfigurable parallel mechanisms with diamond kinematotropic chain. Mech. Mach. Theory. 74, 1–9 (2014).

65. Ye, W.I., Fang, Y., Guo, S.: Reconfigurable parallel mechanisms with three types of kinematotropic chains. 2015 IFToMM World Congr. Proceedings, IFToMM 2015. (2015).

66. Ye, W., Fang, Y., Zhang, K., Guo, S.: Mobility variation of a family of metamorphic parallel mechanisms with reconfigurable hybrid limbs. Robot. Comput. Integr. Manuf. 41, 145–162 (2016).

67. Tian, C., Fang, Y., Guo, S., Qu, H.: A class of reconfigurable parallel mechanisms with five-bar metamorphic linkage. Proc. Inst. Mech. Eng. Part C J. Mech. Eng. Sci. 231, 2089–2099 (2017).

68. Ye, W., Fang, Y., Guo, S.: Design and analysis of a reconfigurable parallel mechanism for multidirectional additive manufacturing. Mech. Mach. Theory. 112, 307–326 (2017).

69. Tian, C., Fang, Y., Guo, S., Qu, H.: Structure synthesis of reconfigurable parallel mechanisms with closed-loop metamorphic linkages. Proc. Inst. Mech. Eng. Part C J. Mech. Eng. Sci. 232, 1303–1316 (2018).

70. Kuo, C.H., Yan, H. Sen: On the mobility and configuration singularity of mechanisms with variable topologies. J. Mech. Des. Trans. ASME. 129, 617–624 (2007).

71. Gan, D., Dai, J.S., Dias, J., Seneviratne, L.D.: Variable motion/force transmissibility of a metamorphic parallel mechanism with reconfigurable 3T and 3R motion. J. Mech. Robot. 8, 1–9 (2016).

72. Gan, D., Dai, J.S., Dias, J., Seneviratne, L.: Constraint-plane-based synthesis and topology variation of a class of metamorphic parallel mechanisms. J. Mech. Sci. Technol. 28, (2014).

73. Gan, D., Dai, J.S., Caldwell, D.G.: Constraint-based limb synthesis and mobility-change-aimed mechanism construction. J. Mech. Des. Trans. ASME. 133, (2011).

74. Ye, W., Chai, X., Zhang, K.: Kinematic modeling and optimization of a new reconfigurable parallel mechanism. Mech. Mach. Theory. 149, 103850 (2020).

75. Zhang, K., Dai, J.S., Fang, Y.: Geometric constraint and mobility variation of Two 3SvPS v metamorphic parallel mechanisms. J. Mech. Des. Trans. ASME. 135, 1–8 (2013).

76. Gan, D., Dias, J., Seneviratne, L.: Unified kinematics and optimal design of a 3rRPS metamorphic parallel mechanism with a reconfigurable revolute joint. Mech. Mach. Theory. 96, 239–254 (2016).

77. Nurahmi, L., Gan, D.: Reconfiguration of a 3-(rR)PS Metamorphic Parallel Mechanism Based on Complete Workspace and Operation Mode Analysis. J. Mech. Robot. 12, 1–15 (2020).

78. Wei, J., Dai, J.S.: Reconfiguration-aimed and manifold-operation based type synthesis of metamorphic parallel mechanisms with motion between 1R2T and 2R1T. Mech. Mach. Theory. 139, 66–80 (2019).

79. Ma, K., Ma, H., Tian, H.: Kinematic analysis of a novel 2-PrRS-PR(P)S metamorphic parallel mechanism. Adv. Mech. Eng. 11, 1–15 (2019).

80. Li, D., Jia, P., Li, J., Zhang, D., Kong, X.: Constraint and Mobility Change Analysis of Rubik's Cube-inspired Reconfigurable Joints and Corresponding Parallel Mechanisms. Chinese J. Mech. Eng. (English Ed. 33, (2020).

81. Fisher, R., Podhorodeski, R.P., Nokleby, S.B.: Design of a reconfigurable planar parallel manipulator. J. Robot. Syst. 21, 665–675 (2004).

82. Rakotomanga, N., Chablat, D., Caro, S.: Kinetostatic performance of a planar parallel mechanism with variable actuation. In: Advances in Robot Kinematics: Analysis and Design. pp. 311–320 (2008).

83. Chablat, D., Jha, R., Caro, S.: A framework for the control of a parallel manipulator with several actuation modes. IEEE Int. Conf. Ind. Informatics. 0, 190–195 (2016).

84. Coppola, G., Zhang, D., Liu, K.: A 6-DOF reconfigurable hybrid parallel manipulator. Robot. Comput. Integr. Manuf. 30, 99–106 (2014).

85. Tian, Y., Zhang, D., Yao, Y.A., Kong, X., Li, Y.: A reconfigurable multi-mode mobile parallel robot. Mech. Mach. Theory. 111, 39–65 (2017).

86. Riabtsev, M., Petuya, V., Urízar, M., Macho, E.: Design and analysis of an active 2-DOF lockable joint. Mech. Based Des. Struct. Mach. 0, 1–25 (2020).

87. Riabtsev, M., Petuya, V., Riera, A., Urízar, M.: An active/passive joint for reconfiguration applications. In: Mechanisms and Machine Science. pp. 133–140 (2020).

88. Riabtsev, M., Petuya, V., Riera, A., Macho, E.: Design of an active reconfigurable 2R joint. Mech. Mach. Sci. 73, 1423–1429 (2019).

89. Li, D., Li, C., Zhang, Z., Kong, X.: Block Adjacency Matrix Method for Analyzing the Configuration Transformations of Metamorphic Parallel Mechanisms. In: Proceedings of the ASME Design Engineering Technical Conferences & Computers and Information in Engineering Conference. pp. 1–9 (2014).

90. Grosch, P., Di Gregorio, R., López, J., Thomas, F.: Motion planning for a novel

reconfigurable parallel manipulator with lockable revolute joints. Proc. - IEEE Int. Conf. Robot. Autom. 4697–4702 (2010).

91. Carbonari, L., Callegari, M., Palmieri, G., Palpacelli, M.C.: A new class of reconfigurable parallel kinematic machines. Mech. Mach. Theory. 79, 173–183 (2014).

92. Palpacelli, M.C., Carbonari, L., Palmieri, G., Callegari, M.: Analysis and Design of a Reconfigurable 3-DoF Parallel Manipulator for Multimodal Tasks. IEEE/ASME Trans. Mechatronics. 20, 1975–1985 (2015).

93. Carbonari, L., Costa, D., Palmieri, G., Palpacelli, M.C.: Reconfigurability analysis of a class of parallel kinematics machines. J. Mech. Robot. 11, 1–8 (2019).

94. KONYA, B., PLITEA, N.: THE DYNAMICS OF A NEW RECONFIGURABLE PARALLEL ROBOT. ACTA Tech. NAPOCENSIS Ser. Appl. Math. Mech. 55, 859–868 (2012).

95. Moosavian, A., Xi, F.: Design and analysis of reconfigurable parallel robots with enhanced stiffness. Mech. Mach. Theory. 77, 92–110 (2014).

96. You, J., Xi, F., Shen, H., Wang, J., Yang, X.: A novel Stewart-type parallel mechanism with topological reconfiguration: Design, kinematics and stiffness evaluation. Mech. Mach. Theory. 162, 104329 (2021).

97. Li, R., Zhao, J., Fan, D., Liang, S., Song, S., Bai, S.: Design and Workspace Analysis of Reconfigurable 3-RPRP Spherical Parallel Mechanisms. 2018 Int. Conf. Reconfigurable Mech. Robot. ReMAR 2018 - Proc. (2018).

98. Chablat, D., Kong, X., Zhang, C.: Kinematics, workspace, and singularity analysis of a parallel robot with five operation modes. J. Mech. Robot. 10, 1–12 (2018).

99. Rong, Y., Zhang, X.C., Qu, M.K.: Unified inverse dynamics for a novel class of metamorphic parallel mechanisms. Appl. Math. Model. 74, 280–300 (2019).

100. Ibarreche, J.I., Hernández, A., Petuya, V., Urízar, M.: A methodology to achieve the set of operation modes of reconfigurable parallel manipulators. Meccanica. 54, 2507–2520 (2019). https://doi.org/10.1007/s11012-019-01081-5.

101. Li, D., Guo, S., Qu, H.: A novel multiple working modes parallel mechanism with variable workspace. Proc. Inst. Mech. Eng. Part C J. Mech. Eng. Sci. 234, 211–224 (2020).

Matrix Representation of a Metamorphic VGTM

Yinjun Zhao[1,2], Fengfeng Xi[3], Yingzhong Tian[1,2*], Long Li[1,2]

[1] School of Mechatronic Engineering and Automation, Shanghai University,
[2] Shanghai Key Laboratory of Intelligent Manufacturing and Robotics,
Shanghai 200444, China
[3] Department of Aerospace Engineering, Ryerson University, Toronto ON M5B 2K3, Canada
*Corresponding author email: troytian@shu.edu.cn

Abstract. In this paper, a metamorphic method is adopted to model a planar variable geometry truss manipulator (VGTM) which is designed for topology reconfiguration while maintaining the structural stability. Through locking the lengths of some variable-length limbs, this VGTM can be changed to have three distinctive topologies: 1-, 2- and 3-DOF. If the 3-DOF topology is taken as the basic configuration, the 1- and 2-DOF topology can be expressed as a metaphoric transformation from it. Though the 1-DOF and 2-DOF topology are both under-actuated, it is shown that the two topologies can be utilized to control a full 3 DOF motion of the VGTM by using multi-step topology switching. Further discussion is carried out to show that the 2-DOF topology is driven by internal actuation, while the 1-DOF topology is driven by external actuation. When the two topologies are integrated with skins to cover the VGTM, the 2-DOF topology will be combined with a passive skin and the 1-DOF topology will be combined with an active skin.

Keywords: Planar Metamorphic VGTM; Adjacent Matrix; Motion Control through Reconfiguration

1 Introduction

Variable geometry truss manipulators (VGTMs) are a kind of manipulators that are composed of variable-length members connected by revolute (R) or spherical (S) joints under tension or compression forces [1]. Due to their high stiffness to weight ratio, structural simplicity, and shape adaptability, VGTMs have been applied to a wide range of applications including long robot arms [2], hyper-redundant manipulators [3] [4], flight simulators [5], morphing wings [6] [7], space devices [8] and civil engineering structures [9].

The common design method of variable geometry truss comes from the perspective of truss structures, i.e., replacing the truss members with telescopic bars, some being actuated by linear actuators according to the degree of freedom (DOF) of the truss units. Usually, a modular design [7] method is applied to develop a large and complex VGTM system based on several basic modules.

For applications in aerospace, weight is one of the main concerns. There are currently two schemes considered to address this problem. One is to integrate the actuation elements with the VGTMs from the point of view of smart materials and struc-

tures [10]. However, this solution is limited by the current materials due to low force magnitude, short motion range, slow response time, high nonlinearity and unproven reliability. Hence, it is challenging to apply this solution to real engineering applications that require long motion ranges and large loads.

The second solution comes from the perspective of mechanism design. With the introduction of reconfigurable/metamorphic mechanisms, VGTMs can be developed as underactuated systems to achieve full degrees-of-freedom of motion through multi-step topology switching [6]. The overarching concept is to maintain a VGTM as a determinate truss structure in the course of topology transformation by using lockable prismatic joints. Xi *et al* proposed several planar and spatial designs of reconfigurable/metamorphic VGTMs for aerospace applications [6] [11] [12]. Recently, they applied a compliant parallel mechanism to enclose a VGTM and form a complete morphing mechanism [4].

Although lockable mechanisms still need to be actuated, these devices give rise to small driving forces and simple control functions. Different from actuators, lockable members can be designed to achieve compact size and lightweight. There are a variety of principles and devices that can realize the locking function of a moving pair [13]. For aerospace applications, Xi *et al* proposed a lockable P joint [14] constructed by a self-circulating hydraulic cylinder and a multifunctional valve. Aghili *et al* designed a cylindrical lockable joint [15] for reconfigurable space robots using the friction locking principle and controlled by an electromagnetic switch.

By locking and releasing specific P joints, metamorphic VGTM can realize the reconfiguration of different topological structures, including statically determinate truss structures, statically indeterminate truss structures, and single- or multi-DOF mechanisms. To facilitate the morphing control, we need to develop a mathematical representation. In this paper, we propose to use a topological graph along with the adjacency matrix proposed by Dai *et al.* [16] [17] for this development. We summarize three different topologies to realize a full 3-DOF control for various planar motion cases while maintaining the structural rigidity.

2   A Metamorphic Variable Geometry Truss Mechanism

A Statically Indeterminate Truss   A VGTM   A 3-RPR Parallel Mechanism
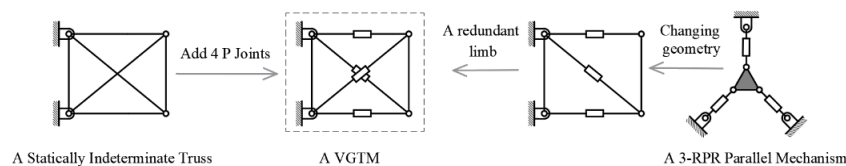
Fig. 1.   A planar 3-DOF VGTM derived from a truss or a parallel mechanism

In this section, we introduce a planar metamorphic VGTM consisting of 4 RPR limbs. First, we describe a general variable geometry truss using a basic module and explain the design principle of the corresponding mechanism. Then, we analyze the reconfigurable topologies by using the metamorphic principle of member-decreasing that corresponds to locking specific P joints.

 The said VGTM module is derived from an indeterminate truss shown on the left side of Fig. 1. By replacing all the truss members with telescopic bars, this truss unit will be able to change its geometric shape. Of all the truss members, some will be

actuated and the others will be lockable. By locking and actuating different truss members, the structure of the truss unit can be altered.

To relate this movable truss unit to a mechanism, it is expressed as a determinate unit which can be equated to a 3-DOF RPR parallel mechanism, as shown on the right side of Fig. 1. By adding a redundant RPR limb, this unit becomes an indeterminate system, i.e. redundant. The mobility and structural stability of the two configurations can be determined by the Grübler-Kutzbach formula [18] and the truss stability equation, respectively.

For this VGTM module, the P joints, i.e. telescopic bars, can be locked to merge adjacent links. By locking different P joints, we will have different truss topologies as listed in Fig. 2. In total, the VGTM module has $C_4^1 + C_4^2 + C_4^3 + C_4^4 = 16$ topologies, classified by five DOFs. In Fig. 2, a locked prismatic joint will degenerate to a link represented by a line.
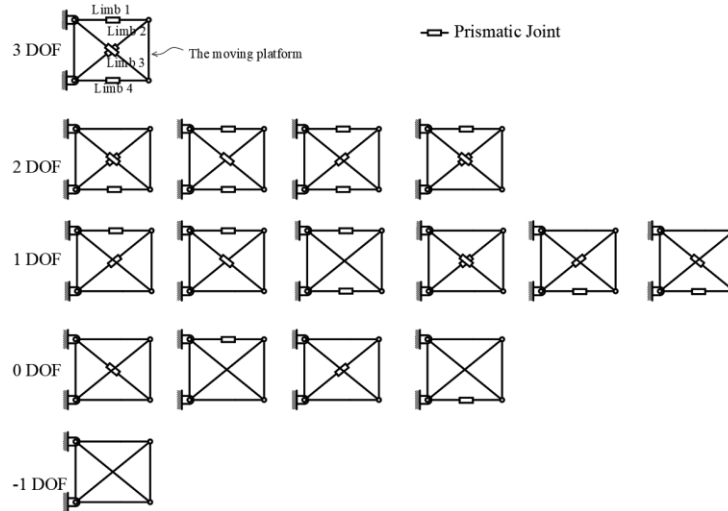

Fig. 2. Mobility and Configurations of the Metamorphic VGTM (The switching of the topology is realized by merging the adjacent telescopic links connected by lockable P joints).

From Fig. 2, we can see that when P joints are free, the VGTM unit has 3 DOFs. When one P joint is locked and the two corresponding links are merged, 2-DOF configurations are obtained. When two P joints are locked, 1-DOF configurations are attained. When three or four P joints are locked, the mechanism will turn into a truss structure. The 0 DOF label in Fig. 2 indicates that the truss is a statically determinate truss called isostatic, and the -1 DOF indicates that the truss has 1 degree of static indeterminacy, called hyperstatic.

The relation between a truss and a mechanism is that the former has the mobility $M \leq 0$ with no actuation and the latter has the mobility ($M > 0$) with actuation. For structural morphing, we need both but the two are in conflict. To resolve this problem we need to design some P joints as active and the others as passive yet lockable. A design method was put forward in [11] for this purpose through configuration optimization according to the specific requirement of a given application. In the next section, we explain three designs corresponding to 1, 2 and 3 DOFs listed in Fig. 2, while the last two represent the VGTM unit at two stationary configurations.

3   Matrix Representation and Transformation of Topologies for Motion Control

There are numerous ways to realize the required motions of the VGTM unit from the perspective of mechanisms. Since our study is focused on trusses, our approach is to ensure that the VGTM unit remains as an isostatic topology to withstand loads during structural morphing. In what follows, we describe three designs for three DOFs and model the topology transformation using matrix representation.
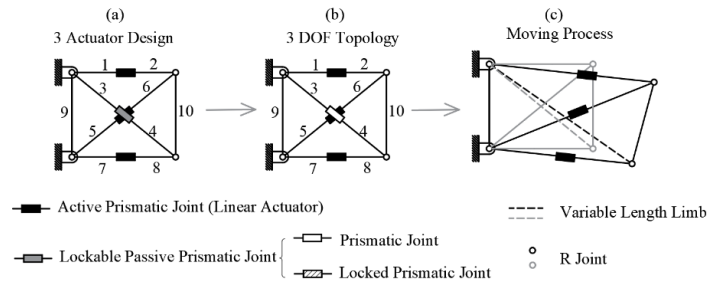
3.1   3-DOF Topology

Fig. 3.   Use a 3-DOF topology to achieve 3 DOF control

For the 3-DOF topology, we need to assemble three actuators on the VGTM unit as shown in Fig. 3(a) to fully control the 3-DOF motion as shown in Fig. 3 (b) and (c). This is the most common design, i.e., the number of the actuators equals the mobility of the VGTM. The only difference is that there is a redundant limb with variable length and a lockable P joint to constrain the mechanism when locked. During the morphing process, the redundant limb is released and does not provide any kinematic constraints (Fig. 3(c)). When the mechanism is in a static state, this limb is locked to switch the truss unit from an isostatic topology to a hyperstatic topology.

Since the 3-DOF topology is the most basic configuration, we treat it as an initial configurations. As indicated in Fig. 3(a), there are in total ten links. In light of the metamorphic theory [16], the adjacency matrix can be written as

$$\mathbf{A_0}_{10\times10} = \begin{bmatrix} 1 & P & R & 0 & 0 & 0 & 0 & 0 & R & 0 \\ P & 2 & 0 & 0 & 0 & R & 0 & 0 & 0 & R \\ R & 0 & 3 & P & 0 & 0 & 0 & 0 & R & 0 \\ 0 & 0 & P & 4 & 0 & 0 & 0 & R & 0 & R \\ 0 & 0 & 0 & 0 & 5 & P & R & 0 & R & 0 \\ 0 & R & 0 & 0 & P & 6 & 0 & 0 & 0 & R \\ 0 & 0 & 0 & 0 & R & 0 & 7 & P & R & 0 \\ 0 & 0 & 0 & R & 0 & 0 & P & 8 & 0 & R \\ R & 0 & R & 0 & R & 0 & R & 0 & 9 & 0 \\ 0 & R & 0 & R & 0 & R & 0 & R & 0 & 10 \end{bmatrix}, \tag{1}$$

where number $1, 2, 3, \cdots, 10$ indicate the link number, R and P stand for the prismatic joint and revolute joint, respectively.

The matrix of Eq. (1) contains the information about the link numbers and their connectivities. The rows and columns of the matrix follow the link numbers in sequence. Element *i, j* of the adjacency matrix represents the connectivity between the *i*th link and *j*th link. If the two links are connected, the element is denoted by the joint type, P or R. If the two links are not connected, the element is assigned 0.
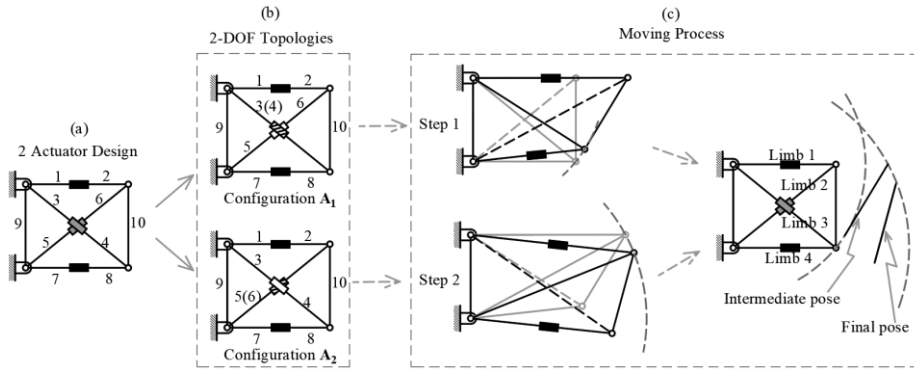
3.2 2-DOF Topology

Fig. 4. Use two 2-DOF topologies to achieve 3 DOF control

For the 2-DOF topology, we need to assemble two actuators on the top and bottom limb of the VGTM unit as shown in Fig. 4(a). The two diagonal limbs are designed with passively lockable joints. Fig. 4(b) shows two permissibly isostatic configurations [12], by locking each passive joint, denoted by $\mathbf{A_1}$ and $\mathbf{A_2}$, respectively. A traditional 2-DOF mechanism would only be able to control 2 DOFs of the moving platform. However, our VGTM 2-DOF module can control 3 DOFs of the moving platform by switching between the two isostatic configurations as shown in Fig. 4(c). During structural morphing, two actuators on the top and bottom will provide the first two forces and the first two motions; a locked P joint (diagonal) will provide the third force and a free P joint (diagonal) will provide the third motion. In this case, there are in total nine links. In light of the metamorphic theory [16], the adjacency matrix for $\mathbf{A_1}$ can be written as

$$\mathbf{A_1}_{9\times9} = \begin{bmatrix} 1 & P & R & 0 & 0 & 0 & 0 & R & 0 \\ P & 2 & 0 & 0 & R & 0 & 0 & 0 & R \\ R & 0 & 3 & 0 & 0 & 0 & R & R & R \\ 0 & 0 & 0 & 5 & P & R & 0 & R & 0 \\ 0 & R & 0 & P & 6 & 0 & 0 & 0 & R \\ 0 & 0 & 0 & R & 0 & 7 & P & R & 0 \\ 0 & 0 & R & 0 & 0 & P & 8 & 0 & R \\ R & 0 & R & R & 0 & R & 0 & 9 & 0 \\ 0 & R & R & 0 & R & 0 & R & 0 & 10 \end{bmatrix}. \tag{2}$$

Since the 2-DOF configuration is obtained through locking one P joint from the 3-DOF configuration $\mathbf{A_0}$, an elementary matrix describing the metamorphic transformation from $\mathbf{A_0}$ to $\mathbf{A_1}$ can be written as

$$\mathbf{A_1} = (\mathbf{E_4 U_{3,4}})\mathbf{A_0}(\mathbf{E_4 U_{3,4}})^\mathbf{T}, \tag{3}$$

where

$$\mathbf{U_{3,4} \atop 10\times10} = \begin{bmatrix} 1 & 0 & 0 & 0 & 0 & 0 & 0 & 0 & 0 & 0 \\ 0 & 1 & 0 & 0 & 0 & 0 & 0 & 0 & 0 & 0 \\ 0 & 0 & 1 & 1 & 0 & 0 & 0 & 0 & 0 & 0 \\ 0 & 0 & 0 & 1 & 0 & 0 & 0 & 0 & 0 & 0 \\ 0 & 0 & 0 & 0 & 1 & 0 & 0 & 0 & 0 & 0 \\ 0 & 0 & 0 & 0 & 0 & 1 & 0 & 0 & 0 & 0 \\ 0 & 0 & 0 & 0 & 0 & 0 & 1 & 0 & 0 & 0 \\ 0 & 0 & 0 & 0 & 0 & 0 & 0 & 1 & 0 & 0 \\ 0 & 0 & 0 & 0 & 0 & 0 & 0 & 0 & 1 & 0 \\ 0 & 0 & 0 & 0 & 0 & 0 & 0 & 0 & 0 & 1 \end{bmatrix}, \mathbf{E_4 \atop 9\times10} = \begin{bmatrix} 1 & 0 & 0 & 0 & 0 & 0 & 0 & 0 & 0 & 0 \\ 0 & 1 & 0 & 0 & 0 & 0 & 0 & 0 & 0 & 0 \\ 0 & 0 & 1 & 0 & 0 & 0 & 0 & 0 & 0 & 0 \\ 0 & 0 & 0 & 0 & 1 & 0 & 0 & 0 & 0 & 0 \\ 0 & 0 & 0 & 0 & 0 & 1 & 0 & 0 & 0 & 0 \\ 0 & 0 & 0 & 0 & 0 & 0 & 1 & 0 & 0 & 0 \\ 0 & 0 & 0 & 0 & 0 & 0 & 0 & 1 & 0 & 0 \\ 0 & 0 & 0 & 0 & 0 & 0 & 0 & 0 & 1 & 0 \\ 0 & 0 & 0 & 0 & 0 & 0 & 0 & 0 & 0 & 1 \end{bmatrix}. \tag{4}$$

The above matrix operation contains two steps. The first step is to apply the U-elementary matrix operation passing the connectivity of link 4 to link 3. The second step is to apply the E-element matrix to remove link 4 which is annexed to link 3.

Please note that in the process of matrix calculation, the link number in the diagonal line needs to be replaced with 0. Besides, the addition calculation generated in the matrix operation follows the following rules: $0+R=R$, $0+P=P$, $R+P=0$, $R+R=0$, $P+P=0$.

Similarly, the adjacency matrix for configuration $\mathbf{A_2}$ can be expressed as

$$\mathbf{A_2 \atop 9\times9} = \begin{bmatrix} 1 & P & R & 0 & 0 & 0 & 0 & R & 0 \\ P & 2 & 0 & 0 & R & 0 & 0 & 0 & R \\ R & 0 & 3 & P & 0 & 0 & 0 & R & 0 \\ 0 & 0 & P & 4 & 0 & 0 & R & 0 & R \\ 0 & R & 0 & 0 & 5 & R & 0 & R & R \\ 0 & 0 & 0 & 0 & R & 7 & P & R & 0 \\ 0 & 0 & 0 & R & 0 & P & 8 & 0 & R \\ R & 0 & R & 0 & R & R & 0 & 9 & 0 \\ 0 & R & 0 & R & R & 0 & R & 0 & 10 \end{bmatrix}. \tag{5}$$

The elementary matrix operation from $\mathbf{A_0}$ to $\mathbf{A_2}$ gives

$$\mathbf{A_2} = (\mathbf{E_6 U_{5,6}})\mathbf{A_0}(\mathbf{E_6 U_{5,6}})^\mathbf{T}, \tag{6}$$

where

$$\mathbf{U}_{5,6} \atop 10\times10 = \begin{bmatrix} 1 & 0 & 0 & 0 & 0 & 0 & 0 & 0 & 0 & 0 \\ 0 & 1 & 0 & 0 & 0 & 0 & 0 & 0 & 0 & 0 \\ 0 & 0 & 1 & 0 & 0 & 0 & 0 & 0 & 0 & 0 \\ 0 & 0 & 0 & 1 & 0 & 0 & 0 & 0 & 0 & 0 \\ 0 & 0 & 0 & 0 & 1 & 1 & 0 & 0 & 0 & 0 \\ 0 & 0 & 0 & 0 & 0 & 1 & 0 & 0 & 0 & 0 \\ 0 & 0 & 0 & 0 & 0 & 0 & 1 & 0 & 0 & 0 \\ 0 & 0 & 0 & 0 & 0 & 0 & 0 & 1 & 0 & 0 \\ 0 & 0 & 0 & 0 & 0 & 0 & 0 & 0 & 1 & 0 \\ 0 & 0 & 0 & 0 & 0 & 0 & 0 & 0 & 0 & 1 \end{bmatrix}, \mathbf{E}_{6} \atop 9\times10 = \begin{bmatrix} 1 & 0 & 0 & 0 & 0 & 0 & 0 & 0 & 0 & 0 \\ 0 & 1 & 0 & 0 & 0 & 0 & 0 & 0 & 0 & 0 \\ 0 & 0 & 1 & 0 & 0 & 0 & 0 & 0 & 0 & 0 \\ 0 & 0 & 0 & 1 & 0 & 0 & 0 & 0 & 0 & 0 \\ 0 & 0 & 0 & 0 & 1 & 0 & 0 & 0 & 0 & 0 \\ 0 & 0 & 0 & 0 & 0 & 0 & 1 & 0 & 0 & 0 \\ 0 & 0 & 0 & 0 & 0 & 0 & 0 & 1 & 0 & 0 \\ 0 & 0 & 0 & 0 & 0 & 0 & 0 & 0 & 1 & 0 \\ 0 & 0 & 0 & 0 & 0 & 0 & 0 & 0 & 0 & 1 \end{bmatrix}. \tag{7}$$

Eqs. (3) and (6) reveal that the two 2-DOF topologies ($\mathbf{A_1}$, $\mathbf{A_2}$) are both transformed from the basic configuration $\mathbf{A_0}$. This will help the reader to understand a two-step approach to realize the 3 DOFs of the moving platform even with two actuators. For a given pose of the moving platform, the final lengths of all four limbs can be determined using the inverse kinematics. In the first step, configuration $\mathbf{A_1}$ is used to move the first diagonal limb to the final length while locking the second diagonal limb. In the second step, the configuration $\mathbf{A_2}$ is used to move the second diagonal limb to the final length along with two active limbs (1, 4) reaching the final lengths. When all four limbs get to their final lengths, the desired pose is achieved. Since each configuration is isostatic, it is easy for the reader to understand that this mechanism ensures the structural stability during morphing.

One interesting point of this topology is that the pose for the intermediate state after the first step is not unique. One can determine the workspace for each of the two configurations, respectively. Any pose within its workspace can be selected. Furthermore, the order of configuration switching is interchangeable. For a full 3 DOF pose control, one can have two reconfiguration paths: $\mathbf{A_0} \rightarrow \mathbf{A_1} \rightarrow \mathbf{A_2}$ or $\mathbf{A_0} \rightarrow \mathbf{A_2} \rightarrow \mathbf{A_1}$.
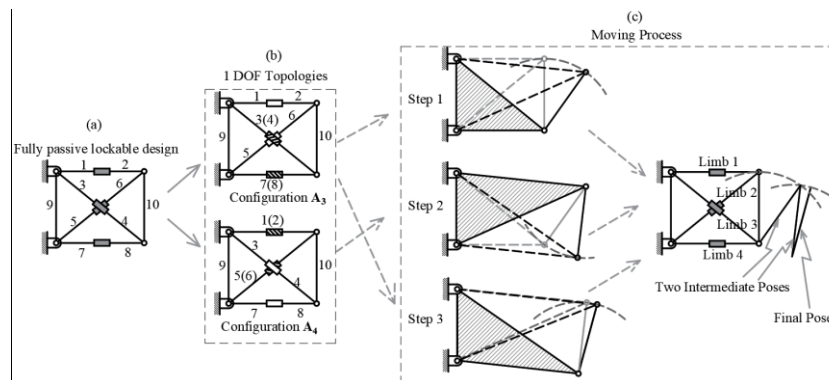
3.3 1-DOF Topology

Fig. 5. Use two 1-DOF topologies to achieve 3 DOF control

For the 1-DOF topology, the VGTM unit is designed with four passively lockable joints as shown in Fig. 5(a). By locking the P joint on limb 3 and 4 (diagonal) and the

P joint on limb 7 and 8 (bottom), as shown in the top of Fig. 5(b), the bottom triangle truss becomes isostatic so as to withstand loads. This configuration is denoted by $\mathbf{A_3}$. There are in total eight links after locking two P joints. The adjacency matrix of $\mathbf{A_3}$ can be expressed as

$$\mathbf{A_3}_{8\times8} = \begin{bmatrix} 1 & P & R & 0 & 0 & 0 & R & 0 \\ P & 2 & 0 & 0 & R & 0 & 0 & R \\ R & 0 & 3 & 0 & 0 & R & R & R \\ 0 & 0 & 0 & 5 & P & R & R & 0 \\ 0 & R & 0 & P & 6 & 0 & 0 & R \\ 0 & 0 & R & R & 0 & 7 & R & R \\ R & 0 & R & R & 0 & R & 9 & 0 \\ 0 & R & R & 0 & R & R & 0 & 10 \end{bmatrix} \tag{8}$$

The 1-DOF configuration can be viewed through locking one more P joint from the 2-DOF configuration $\mathbf{A_1}$ or two P joints from the 3-DOF configuration $\mathbf{A_0}$, hence the corresponding elementary matrix can be given as

$$\mathbf{A_3} = (\mathbf{E_8 U_{7,8}})\mathbf{A_1}(\mathbf{E_8 U_{7,8}})^{\mathbf{T}} = (\mathbf{E_8 U_{7,8} E_4 U_{3,4}})\mathbf{A_0}(\mathbf{E_8 U_{7,8} E_4 U_{3,4}})^{\mathbf{T}} \tag{9}$$

where

$$\mathbf{U_{7,8}}_{9\times9} = \begin{bmatrix} 1 & 0 & 0 & 0 & 0 & 0 & 0 & 0 & 0 \\ 0 & 1 & 0 & 0 & 0 & 0 & 0 & 0 & 0 \\ 0 & 0 & 1 & 0 & 0 & 0 & 0 & 0 & 0 \\ 0 & 0 & 0 & 1 & 0 & 0 & 0 & 0 & 0 \\ 0 & 0 & 0 & 0 & 1 & 0 & 0 & 0 & 0 \\ 0 & 0 & 0 & 0 & 0 & 1 & 0 & 0 & 0 \\ 0 & 0 & 0 & 0 & 0 & 0 & 1 & 1 & 0 \\ 0 & 0 & 0 & 0 & 0 & 0 & 0 & 1 & 0 \\ 0 & 0 & 0 & 0 & 0 & 0 & 0 & 0 & 1 \end{bmatrix}, \mathbf{E_8}_{8\times9} = \begin{bmatrix} 1 & 0 & 0 & 0 & 0 & 0 & 0 & 0 & 0 \\ 0 & 1 & 0 & 0 & 0 & 0 & 0 & 0 & 0 \\ 0 & 0 & 1 & 0 & 0 & 0 & 0 & 0 & 0 \\ 0 & 0 & 0 & 1 & 0 & 0 & 0 & 0 & 0 \\ 0 & 0 & 0 & 0 & 1 & 0 & 0 & 0 & 0 \\ 0 & 0 & 0 & 0 & 0 & 1 & 0 & 0 & 0 \\ 0 & 0 & 0 & 0 & 0 & 0 & 1 & 0 & 0 \\ 0 & 0 & 0 & 0 & 0 & 0 & 0 & 0 & 1 \end{bmatrix} \tag{10}$$

Similarly, configurations $\mathbf{A_4}$ is achieved by locking the other two P joints as shown in the bottom of Fig. 5(b), and its adjacency matrix can be given as

$$\mathbf{A_4}_{8\times8} = \begin{bmatrix} 1 & R & 0 & R & 0 & 0 & R & R \\ R & 3 & P & 0 & 0 & 0 & R & 0 \\ 0 & P & 4 & 0 & 0 & R & 0 & R \\ R & 0 & 0 & 5 & R & 0 & R & R \\ 0 & 0 & 0 & R & 7 & P & R & 0 \\ 0 & 0 & R & 0 & P & 8 & 0 & R \\ R & R & 0 & R & R & 0 & 9 & 0 \\ R & 0 & R & R & 0 & R & 0 & 10 \end{bmatrix} \tag{11}$$

The elementary matrix operation gives

$$\mathbf{A}_4 = (\mathbf{E}_2\mathbf{U}_{1,2})\mathbf{A}_2(\mathbf{E}_2\mathbf{U}_{1,2})^{\mathbf{T}} = (\mathbf{E}_2\mathbf{U}_{1,2}\mathbf{E}_6\mathbf{U}_{5,6})\mathbf{A}_0(\mathbf{E}_2\mathbf{U}_{1,2}\mathbf{E}_6\mathbf{U}_{5,6})^{\mathbf{T}} \qquad (12)$$

where

$$
\mathbf{U}_{1,2} = \begin{bmatrix}
1 & 1 & 0 & 0 & 0 & 0 & 0 & 0 & 0 \\
0 & 1 & 0 & 0 & 0 & 0 & 0 & 0 & 0 \\
0 & 0 & 1 & 0 & 0 & 0 & 0 & 0 & 0 \\
0 & 0 & 0 & 1 & 0 & 0 & 0 & 0 & 0 \\
0 & 0 & 0 & 0 & 1 & 0 & 0 & 0 & 0 \\
0 & 0 & 0 & 0 & 0 & 1 & 0 & 0 & 0 \\
0 & 0 & 0 & 0 & 0 & 0 & 1 & 0 & 0 \\
0 & 0 & 0 & 0 & 0 & 0 & 0 & 1 & 0 \\
0 & 0 & 0 & 0 & 0 & 0 & 0 & 0 & 1
\end{bmatrix}_{9\times9}, \mathbf{E}_2 = \begin{bmatrix}
1 & 0 & 0 & 0 & 0 & 0 & 0 & 0 & 0 \\
0 & 0 & 1 & 0 & 0 & 0 & 0 & 0 & 0 \\
0 & 0 & 0 & 1 & 0 & 0 & 0 & 0 & 0 \\
0 & 0 & 0 & 0 & 1 & 0 & 0 & 0 & 0 \\
0 & 0 & 0 & 0 & 0 & 1 & 0 & 0 & 0 \\
0 & 0 & 0 & 0 & 0 & 0 & 1 & 0 & 0 \\
0 & 0 & 0 & 0 & 0 & 0 & 0 & 1 & 0 \\
0 & 0 & 0 & 0 & 0 & 0 & 0 & 0 & 1
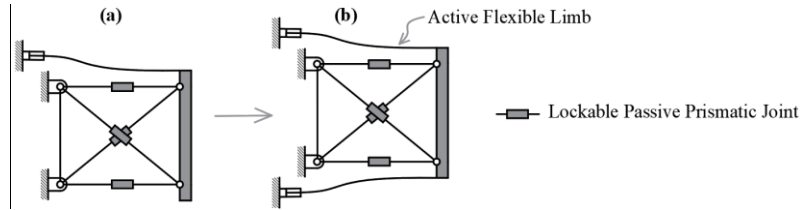\end{bmatrix}_{8\times9} \qquad (13)
$$

Fig. 6.   Fully passive metamorphic VGTM driven by flexible limbs

Since the 1-DOF configurations are completely composed of passive limbs, the actuation will have to be supplied externally. Our approach is to cover the passive VGTM by active skins, either single side (top or bottom) or double sides (both top and bottom), as shown in Fig. 6. With this design, the 3 DOFs of the VGTM can be fully controlled through a 3-step approach, as shown in Fig. 5(c). Essentially, each 1-DOF configuration provides one motion, and repetition of three times in an alternate fashion will result in a full 3 DOF motion control.

Similarly to the 2-DOF configuration, the intermediate poses after the first two steps need to be determined based on the forward kinematics, as shown in Fig. 5(c) [12]. In general, a single actuation is sufficient for motion. However, double actuation will offer a better transmission efficiency of the driving forces in different configurations. Furthermore, the order of configuration switching is interchangeable. For a full 3 DOF pose control, one can have two reconfiguration paths: $\mathbf{A_0} \rightarrow \mathbf{A_3} \rightarrow \mathbf{A_4} \rightarrow \mathbf{A_3}$ or $\rightarrow \mathbf{A_0} \rightarrow \mathbf{A_4} \rightarrow \mathbf{A_3} \rightarrow \mathbf{A_4}$.

4   Conclusions

In this paper, a class of planar VGTMs is studied under five categories, with the first three being movable (1, 2, 3-DOF) and the last two being stationary (0, -1 DOF). The metamorphic theory is applied to model the three movable topologies in terms of adjacency matrix and E/U element matrix. The 3-DOF topology is taken as the basic configuration, and the 1/2-DOF topology can be expressed as a metaphoric transformation from it. Though the 1-DOF and 2-DOF topology are both under-actuated, it is shown that the two topologies can be utilized to control a full 3 DOF motion of the VGTM by using respective multi-step approaches. Furthermore, the relation between a truss for loading and a mechanism for motion is delineated. The purpose of utilizing

the underactuated systems is to fulfill the required shape morphing motion while maintaining the needed structural stability. Further discussion is carried out to show that the 2-DOF topology is driven by internal actuation, while the 1-DOF topology is driven by external actuation. When the two topologies are integrated with skins to cover the VGTM, the 2-DOF topology will be combined with a passive skin and the 1-DOF topology will be combined with an active skin.

References

[1] J.M. Porta, F. Thomas, Closed-form position analysis of variable geometry trusses, Mechanism and Machine Theory, 109 (2017) 14-21.

[2] P.C. Hughes, W.G. Sincarsin, K.A. Carroll, Trussarm--A Variable-Geometry-Truss Manipulator, Journal of Intelligent Material Systems Structures, 2 (2) (1991) 148-160.

[3] G.S. Chirikjian, J.W. Burdick, A hyper-redundant manipulator, IEEE Robotics Automation Magazine, 1 (4) (1994) P.22-29.

[4] Y. Tian, Y. Zhao, L. Li, G. Yuan, F. Xi, Design and Analysis of a Multi-Segment Shape Morphing Mechanism, Journal of Mechanisms Robotics, 13 (2) (2020) 1-24.

[5] C. Sultan, M. Corless, R.E. Skelton, Tensegrity Flight Simulator, Journal of Guidance Control Dynamics, 23 (6) (2012) 1055-1064.

[6] A. Moosavian, F. Xi, S.M. Hashemi, Design and Motion Control of Fully Variable Morphing Wings, Journal of aircraft, 50 (4) (2013) 1189-1201.

[7] A.D. Finistauri, F. Xi, Type synthesis and kinematics of a modular variable geometry truss mechanism for aircraft wing morphing, 2009 ASME/IFToMM International Conference on Reconfigurable Mechanisms and Robots, 2009.

[8] K. Miura, H. Furuya, K. Suzuki, Variable geometry truss and its application to deployable truss and space crane arm, Acta Astronautica, 12 (7-8) (1985) 599-607.

[9] G. Senatore, P. Duffour, P. Winslow, C. Wise, Shape control and whole-life energy assessment of an 'infinitely stiff' prototype adaptive structure, Smart Materials and Structures, 27 (1) (2018) 015022.

[10] J.H. Glenn, Self-Deploying Trusses Containing Shape-Memory Polymers, Nasa Tech Briefs, 32 (5) (2008) p.54,56.

[11] J. Wang, Y. Zhao, F. Xi, Y. Tian, Design and analysis of a configuration-based lengthwise morphing structure, Mechanism and Machine Theory, 147 (2020) 103767.

[12] F. Xi, Y. Zhao, J. Wang, W. Wang, Y. Tian, Two Actuation Methods for a Complete Morphing System Composed of a VGTM and a Compliant Parallel Mechanism, Journal of Mechanisms and Robotics, (2021) 1-39.

[13] M. Plooij, G. Mathijssen, P. Cherelle, D. Lefeber, B. Vanderborght, Lock Your Robot: A Review of Locking Devices in Robotics, IEEE Robotics and Automation Magazine, 22 (1) (2015) 106-117.

[14] A. Moosavian, M. Rizoiu, F. Xi, Design of a Multifunctional Flow Control Valve for Self-Circulating Hydraulic Cylinders, Journal of Pressure Vessel Technology, 139 (2) (2017) 025001.

[15] F. Aghili, K. Parsa, Design of a Reconfigurable Space Robot with Lockable Telescopic Joints, 2006 IEEE/RSJ International Conference on Intelligent Robots and Systems, 2006 4608-4614.

[16] J.S. Dai, J.R. Jones, Matrix Representation of Topological Changes in Metamorphic Mechanisms, Journal of Mechanical Design, 127 (4) (2005) 837-840.

[17] D. Wang, J. Dai, Theoretical foundation of metamorphic mechanism and its synthesis, Chinese Journal of Mechanical Engineering, 43 (8) (2007) 32-42.

[18] K.H. Hunt, Kinematic geometry of mechanisms, The Clarendon Press, New York, 1978.

Hybridization Through Modularity: Exploring Complex Modes of Locomotion with a "Bag of Robotic Modules"

Yuanmeng Huang[1], Jonathan Miller[1], Upinder Kaur[1], Yubing Han[1], Ram M.S. Ramdas[2], Shashank Priya[2], and Richard M. Voyles[1]

[1] Purdue University, West Lafayette, IN, USA,
`huan1368@purdue.edu, mill2459@purdue.edu, kauru@purdue.edu,`
`rvoyles@purdue.edu`
[2] Pennsylvania State University, State College, PA, USA,
`sup103@psu.edu, rxs1279@psu.edu`

Abstract. Exploration of complex environments is still a challenge for real-world applications of robots. Robots that rely on locomotion modes such as wheels and treads are designed for relatively flat engineered and non-engineered surfaces and may not be suitable for operating in complex environments. Robots with hybrid modes of locomotion, such as tread/limb and tread/limb/serpentine hybrids have evolved for more aggressive and complex terrains. A problem with these highly hybridized locomotion modes is the lengthy trial-and-error process often required to develop and iterate a successful design and compatible gait strategy. We have begun using modular robotic components to quickly develop and swap modules to meet a variety of locomotion scenarios. This paper presents the development of a novel suite of modular robot components to explore locomotion strategies for some very different environments: underground corrugated drain tile and a cow's digestive chamber. The variety of robotic modules within our "bag of tricks" – some conventional and some custom-built – allow us to rapidly discover novel hybrid locomotion schemes that may not be obvious. From "wheg"-like steerable wheel/limb hybrids for drain tiles to novel buoyancy control configurations for the cow rumen, we describe the benefits of modular robots for rapid prototyping of hybrid gaits.

Keywords: modular robot, hybridized locomotion mode, buoyancy gait

1 Introduction

Exploration of inaccessible and unknown environments with robotic sensors remains a challenge in real-world applications. An example is emergency response, wherein the goal is generally to explore with cameras and sensors so human teleoperators can infer where survivors are trapped. Many such robots have been developed for various niches in this field, but only a few have received widespread use, largely because of the difficulty of locomoting through such chaotic environments. Wheels provided easy mobility around the perimeter of emergencies and

in special circumstances [1] [2], but focus quickly shifted to tracked vehicles for deconstructed environments. Tracked vehicles enhance traction and stability and several commercial examples have evolved for general purpose use [3] [4] [5]. Still, tracked vehicles did not gain widespread application in complex terrains until the iRobot Packbot hybridized tracks and limbs [6]. The Packbot adds a simple, one-degree-of-freedom (DoF) "flipper" to the tracked locomotion, dramatically enhancing locomotion capability. Since then, additional hybrid locomotion modes have begun to proliferate through extensions of tread/limb hybrids [7] [8], hybrids that employ snake-like locomotion with high-DoF [9] [10], and other tread/limb/serpentine hybrids [11] [12] [13].

However, a problem with these hybridized systems has been the highly optimized and specialized designs that are costly and expertise-intensive to design. These systems are often subject to failures and cumbersome to operate due to their novel, "one-off" designs. In pursuit of the development of a wide variety of disparate miniature robotic systems, we have begun to standardize the suite of actuation modules for interchangeable use. This *familiarity through modularity* allows for more robust designs of the modules to propagate and enhances system robustness and usability, in turn. It also allows for broader and quicker exploration of the hybrid locomotion space and the resulting complexity of locomotion "gaits" that must be co-developed with the hardware. While this paper is not focused on emergency response, the expertise developed and lessons learned on those prior examples, to evolve our modular and reconfigurable system, are employed to new domains of hybrid mechanisms.

The core components that form the basis of our "Bag of Modules" are from the MOTHERSHIP (Modular Omnidirectional Terrain Handler for Emergency Response, Serpentine and Holonomic for Instantaneous Propulsion) [14] and CRAWLER (Cylindrical Robot for Autonomous Walking and Lifting for Emergency Response) [15] robots. Both of these use hybrid locomotion gaits – at the meter-scale and centimeter scale, respectively – but were developed using specialized designs. Inspired by our own work on modular real-time systems [16] we combined these diverse size scales into a common modular suite that allows the rapid prototyping of hybrid locomotion solutions to the demands of different scenarios and problems.

To highlight the benefits of modularity and interoperability, we examine two completely different applications with radically different forms of hybrid locomotion that share some modules. A new modular robot called DAUGHTERSHIP (Directional Active Underwater Gait Hybrid with Tiny Energy Reserves for Sensing Health, Inactivity and Productivity) is being developed for *in vivo* sensing of animal health in the complex, stratified liquid environment of the cow stomach. This *animal agrobot* employs a novel form of buoyancy-based locomotion to control orientation and translation of the sensor-laden DAUGHTERSHIP. Additionally, a drain tile locomotion *crop agrobot* is described to explore the soil microbiome, deep below the surface of Midwestern farms.

The contributions of this paper are:

– A bag of heterogeneous modules for rapid prototyping of hardware/software co-design techniques for hybrid locomotion gaits is proposed.
– A novel hybrid buoyancy gait for orientation and translation control in liquid environments is proposed that resulted from the demonstration.

2   Suite of Configurable Robot Modules

An eclectic suite of modular components has evolved and allows a great deal of design creativity. Due to space limitations, we describe the mini-modules in this section, detailing their locomotion and functionalities. The resulting modular configurations consist of mechanically linked steering and propulsion modules.

2.1   2-DoF Articulating Joint

With the omnidirectional characteristic enabled by the coincidentally and orthogonally placed components, this articulating joint consists of two major units: the central ring as shown in Fig.1(a) and interconnecting cable-driven housings as shown in Fig.1(b). The four posts on the outer side of the central ring enable the mounting of the housings on both sides. The coupling method between the ring and cables offers two DoF to this modular robot. Two sets of cable-driven cylinders were placed in this articulating joint, and each of them can be individually controlled by a 6 volt DC motor. The cylinders, in tandem with a cable-driven system, are designed to accommodate the actuators for the mechanisms used in each module. When assembled with a central ring, each cylinder provides one DoF, and the torque required to control the cylinders is 351 mNm. The total weight of the articulating joint is only 77 grams (dimensions: 33mm diameters, 130 mm total length). All actuators are contained within the cylinders to facilitate rotation of the joint and movement of the modular attachments. The rotation at each DoF is activated through a cable system which provides sufficient torque for movement. Full rotation from -60 °to 60 °can be attained.
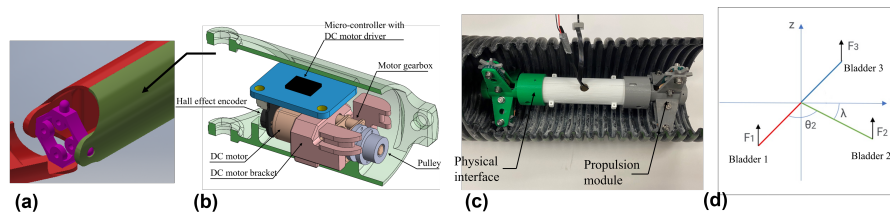

Fig. 1. Structure of articulating joint and subterranean robot. (a) The central ring design (b) The articulating joint cut-section view. (c) The subterranean robot drive through pipeline. (d) Shows the angles with respect to the buoyancy robot structure.

2.2   Wheg-Like Propulsion Module

The design of the propulsion module consists of a system of three idler gears meshing with a central worm gear, as shown in Fig.1(c). The mechanism divides one motor input into three shaft outputs and these shafts supply the relatively high torque to navigate the rough terrain we are attempting. A single worm gear divides the motor rotation among the three radially-spaced gear trains with the use of perpendicular gear meshing. Secondly, these gears are not back-drive-able, but provide the desired torque advantage. The output wheel of each gear train is a rimless multi-spoked wheel, like a Wheg [17], that engages the corrugations of the pipe with gearing traction. This wheel/leg hybrid design enables the robot to fit into corrugations in the tubing and provide enough traction to overcome large obstacles.

2.3   Buoyancy-Control Propulsion Module

This buoyancy module was developed consisting of three bladders, shown as Fig.1(d). Bladder 3 was connected orthogonally to link 2. Bladders 1 and 2 were on both sides of articulating joint. Works like ocean gliders, this module can change its buoyancy center by changing the weight of the bladders through injecting and extracting water, which will allow up-and-down movement through the water. Meanwhile, by combining the articulating joint, this buoyancy module can adjust its gesture until it comes to its static equilibrium.

2.4   Inch-Worm Propulsion Module

Peristaltic actuation is an important form of locomotion in the natural world. Earthworms and other insects (such as nematodes) use peristaltic actuation to either powerfully enlarge granular media or gently grapple fragile tissues. Hence, this peristaltic actuation is highly valuable in a reconfigurable context. Our collaborators at Penn State developed the inch-worm propulsion module described here. In Fig.2(a) a worm robot for solid surfaces is illustrated with multiple segments and its gait cycle (Fig.2(c)). The longitudinal peristaltic module uses an asymmetric frictional outer surface to inch forward, and one of the three actuation units actuates at a time. The pull force of the inch-worm module depends on the materials of interaction. When the elastomeric sheet interacts with soft silicone, as shown in Fig.2(d), the peak propulsion force is up to 10 N.

3   Example Problem Scenarios for Robotic Sensing

3.1   In Vivo Sensing of Rumen Digestive State

A cow's digestive chamber, or rumen, is a large organ wherein the feed is digested and converted by bacteria into proteins and energy through fermentation. The liquid in the rumen is a highly stratified environment with a thick mat of feed on the top, followed by fluid with suspended particles, but it is stirred occasionally
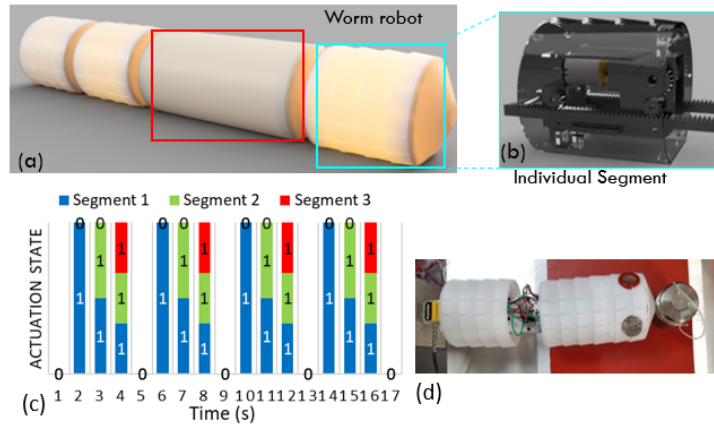
Fig. 2. Inch Worm propulsion module, (a) multi-segment robot with articulating joint (red) and peristaltic module (cyan) (b) individual longitudinal peristaltic segment, (c) actuation gait of worm robot, and (d) module drawbar test.

by contraction. The volume of the rumen is 184 liters and the lining is populated with colonies of micro-organisms that aid in digestion of the food. In order to monitor the digestion and rumen health, animal nutritionists are using boluses to take measurements of rumen environment such as volatile fatty acids (VFA), pH, temperature, etc. However, boluses are stationary sensor packs settled at the bottom of the rumen which fails to capture the health changes occurring at various levels of this highly complex environment. An in-vivo explorer robot with locomotion capabilities can overcome this limitation, creating a new dimension of understanding of the function of the rumen and its correlation with the overall health of the animal.

3.2 Subterranean Exploration of the Soil Microbiome

Underground agricultural drain pipes are corrugated plastic pipes used for insuring the soil of the farmland remains free of excess water. They are essential for farming yet often face issues associated with blockage due to weeds and debris falling in. They are mostly laid straight with few T-intersections. Inspection robots are needed in such an environment to sense gas and water content to monitor the nutrients in runoff as well as to identify any blockage. However, these toothed pipelines have proved to be difficult terrain for wheeled robots. Thus, hybridization of wheels and limbs (e.g. gears) helps to improve the performance of locomotion. Some hybrid robots, like leg-wheeled hybrid robots and wheeled-tracked hybrid robots, represent the next step in hybridization as they combine wheels, tracks, and limbs to develop a giant leap in mobility.

4   Hybrid Locomotion Gaits

The hybrid locomotion modules enable the robot to display a better performance in an amphibious environment. By mounting it with different modules, this modular robot can achieve a wide variety of motions and gaits corresponding to the module's design for use in a given environment.

4.1   Motion Analysis of Buoyancy Modules

In the buoyancy robot, the angles between links are geometrically related. As shown in Fig. 1(d), let θ_1 and θ_2 be the rotation angles around Pitch axis and Yaw axis, respectively. Let ϕ_1, ϕ_2, and ϕ_3 be the angles between the three links and the vertical plane (YOZ plane). Based on the mechanism, link 2 and link 3 are normal to each other. The sum of θ_1, ϕ_1, and ϕ_2 equals to π. Thus, θ_1, ϕ_1, ϕ_2, and ϕ_3 can be calculated with the equations (1) and (2).

$$\phi_2 + \phi_3 = 90° \tag{1}$$

$$\phi_1 + \phi_2 + \theta_1 = 180° \tag{2}$$

Let F_1, F_2, and F_3 represent the buoyancy force of these three buoyancy bladders. Let r_1, r_2, and r_3 be the lengths of the three links. Let λ be the angle between link2 and the horizontal plane (XOY plane). The value of $\phi_i s$ depends upon the frame of reference and the given value of θ_1. To match the simplified simulation, ϕ_2 is a fixed angle. When at a neutral buoyant state, the bladders provide upwards buoyancy force equaled to gravity to this robot. The steady-state equilibrium can be expressed as:

$$\sum \tau = r_i(\theta_1, \theta_2, \lambda, \phi_1, \phi_2, \phi_3) \times F_i \tag{3}$$

The equation suggests that equilibrium is decided by the angle of articulating joint and buoyancy force of each bladder when other parameters are constant. In this situation, λ can be calculated as:

$$\tan \lambda = \frac{F_3 \sin \phi_3 - F_2 \sin \phi_2 + F_1 \cos \theta_2 \sin \phi_1}{-F_1 \sin \theta_2 \sin \phi_1} \tag{4}$$

When θ_1 and θ_2 are fixed, changing the mass of the robot yields the unbalance between gravity and buoyancy force, which becomes the power source of the robot's movement. In this scenario, any transformation of this robot will cause the stable orientation shift, causing the robot to settle into a new stable position.

4.2   Novel Buoyancy Gaits

In the simplest case, the concept of a "buoyancy gait" is more about the change of orientation. In its neutrally buoyant state, any changes to the robot's gesture will cause movements that disrupt its condition. The altitude of the three

bladders automatically adjusts to keep the equilibrium as the robot makes gestures. Meanwhile, by carefully shaping the bladders – using them as hydrofoils – changes can be made not only on orientation but on the lateral position. However, all the activities are happening inside the ruminal cavity, which is undergoing periodic contractions. It had not been determined if these "gaits" will counteract the effects of the contractions, but capturing the currents caused by these contractions – effectively "riding the waves," is the next step. For this paper, we focus only on motion in the still fluids between contractions, as this is when we want to sense the strata of the rumen.

According to equation (3), F_i is the only parameter that can influence the robot's locomotion once the θ_1 and θ_2 are settled. The buoyancy gait of this modular robot is correlated with its bladders' buoyancy force changes. If the masses of these three bladders proportionally reduce or increase during a certain process, the buoyancy gait for the robot will be either vertically floating or vertical sinking, ideally. However, this vertical movement is not stable due to the influence of water flows generated by robot motion, and achieving a precisely proportional mass changing may also be a challenge for encoders. Thus, adjusting the masses for three bladders with keeping the robot in a neutral configuration has been a new solution for controlling the robot's orientation. According to equation (4), when the robot suspends inside the water with constant weight and fixed rotation angles, attitude is affected by three buoyancy forces. In order to keep the final total water content unaltered, when water is separately pumped from or injected into the bladders, the robot will have motions to keep its balance due to the unbalance between gravity and buoyancy force. The final depth of the robot is immobile due to the constant nature of gravity, but the joint position will be adjusted in order to facilitate a stable configuration at the stable depth. In the same way as F_i parameter, parameters θ_1 and θ_2 are factors that can influence the robot's attitude. Varying rotation angles lead the robot to have different postures as well as predictable motions which can be calculated by the steady-state equilibrium. Also, bladders with oblate shapes functioning like flippers can improve the performance on the orientation control by utilizing the fluid's characteristics.

4.3   Adaptive Cyclic Pattern Generator for Subterranean Steering

Like a subway tube, the drain tile provides a guide way to steer the robot along the length of the buried pipe as the Wheg propulsion units propel it forward or backward. However, some sections of the buried drain tile may have "Y-" and "T-intersections." Placing the articulating joint between two propulsion modules enables the subterranean robot to make selective turns to visit different parts of the field. This combination of articulating joint and propulsion modules requires coordination of both the front and rear drive modules. In general, the two propulsion modules are in sync – running at the same frequency and in phase – and driven by a single central pattern generator (CPG) [18] that keeps the individual Whegs from conflicting with one another. But when turning with the articulating joint in the center, the front propulsion module begins to cross the

corrugations at an angle, elongating the spatial frequency of Wheg engagements with the corrugations. The CPG, then, uses steering commands to shift the frequency of the steering module in relation to the rear module.

A CPG also controls the inch-worm gait for the non-liquid agRobot locomotor, as indicated in Fig 2(c). The inch-worm peristaltic CPG is not adaptive, as steering does not impact the propulsion sequence.

5   Experimental Results

A transparent water container (dimensions: 584mm length, 432mm width, and 305mm height) was used as the underwater environment. Two fixed cameras captured the top view and side view. Initially, the robot stays neutrally buoyant without any disturbance. The joint angle was controlled, and the rotation angles θ_1, θ_2 were subsequently measured when the robot floated to its equilibrium orientation in the water. Fig. 3 showed the buoyancy motion at various rotation angles in the experiment.

Initially, the robot was suspended underwater with neutral buoyancy when θ_1 equals 160°. Maintaining θ_1 as a fixed rotation angle we then assigned different rotation angles to θ_2 (150°, 160°, 170°, 180°) to observe the locomotion of the buoyancy module. Since θ_1 was fixed, no significant gestures change can be observed from the top view. Thus, the result of buoyancy gaits was presented by the rotation angle captured from the side view. There were two variables in this experiment, mass (F_i) and rotation angle (θ_2), and we tested them separately. Based on the fixed angle of θ_2, we changed the weight of three bladders but kept the total weight unchanged. For rotation angle testing, we kept each bladder's weight constant but let the robot settle to the given angle and captured their neutral state. According to Fig. 3(a) and Fig. 3(b), the gesture of the robot was changed when each bladder mass was changed under the circumstance of unchanged total weight and fixed θ_2 angle. From the figures, as we properly reduced the weight for link 1 but increased the same for link 3, bladder 1 was visibly elevated. According to Fig. 3(c)-(f), based on the unchanged weight of bladders, the robot's gesture was changed due to different rotation angle θ_2. Table 1 presents the results of both the predicted angles from the simulation and the actual angles we obtained from the experiments.

Table 1. Angles of robot joints from simulation and test

θ_2 angle	predicted λ	actual λ
150°	60°	66°
160°	52°	53°
170°	48°	50°
180°	38°	40°

Results showed the ability of this simulation to predict the orientation for a real underwater robot even though the environment for this modular robot
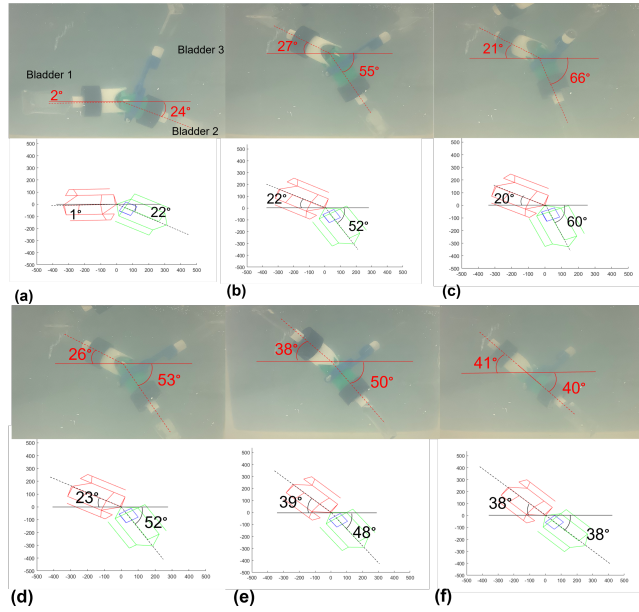
Fig. 3. (a) Neutral state of buoyancy robot ($\theta_2 = 160°$) (b) Neutral state of buoyancy robot with adjusted bladder mass ($\theta_2 = 160°$). (c)-(f) Neutral state of buoyancy robot given different θ_2 angles.

is complicated and there exists variance between the simulation and measured orientation angles.

6   Conclusions and Future work

This paper proposed a suite of modular robot components for the rapid prototyping and testing of hybrid forms of locomotion in highly specialized environments. This work introduced the advantages of using a modular robot with hybrid gaits in the field of robotics. A pipeline traversing modular robot with "wheg" locomotion was built with an adaptive CPG-based gait controller. The robot can move forward through and around corners in corrugated drain pipe. This modular robot has a compact structure, low production cost, and high controllability. We also presented the novel hybridized buoyancy gait. We have proven the effectiveness of the novel gaits that were co-developed with the system in simulated and real-world experiments. Furthermore, these robots are adaptable to complex working environments and capable of quickly switching modules to meet varieties of requirements. Because of the modular design of this robot, it can be quickly repaired by replacing the same modules, which increases the feasibility of the robot in practical application. The further study will focus on exploring buoyancy force control. Soft materials will be considered for our future research and we aim to embed sensors on the soft material to enrich the robot's functionality.

References

1. A. Morris, D. Ferguson, Z. Omohundro, D. Bradley, D. Silver, C. Baker, W. Whittaker (2006). "Recent developments in subterranean robotics." Journal of Field Robotics, 23(1), 35-57.
2. J. Abouaf, "Trial by fire: teleoperated robot targets Chernobyl," in IEEE Computer Graphics and Applications, vol. 18, no. 4, pp. 10-14, July-Aug. 1998.
3. "Bomb Disposal Robot - QinetiQ." https://www.qinetiq.com/en-us/capabilities /robotics-and-autonomy/talon-medium-sized-tactical-robot (acc: Apr. 13, 2021).
4. R. R. Murphy, J. Kravitz, K. Peligren, J. Milward and J. Stanway, "Preliminary report: Rescue robot at Crandall Canyon, Utah, mine disaster," 2008 IEEE International Conference on Robotics and Automation, 2008, pp. 2205-2206.
5. M.J. Micire (2008), "Evolution and field performance of a rescue robot." J. Field Robotics, 25: 17-30.
6. "PackBot - ROBOTS: Your Guide to the World of Robotics." https://robots.ieee.org/robots/packbot/ (accessed Apr. 06, 2021).
7. T. Yoshida, K. Nagatani, S. Tadokoro, T. Nishimura, and E. Koyanagi, "Improvements to the rescue robot quince toward future indoor surveillance missions in the Fukushima Daiichi nuclear power plant," in Springer Tracts in Advanced Robotics, 2014, vol. 92, pp. 19–32
8. W. A. Lewinger, C. M. Harley, R. E. Ritzmann, M. S. Branicky and R. D. Quinn, "Insect-like Antenna Sensing for Climbing and Tunneling Behavior in a Biologically-inspired Mobile Robot," IEEE Intl. Conf. on Rob. and Auto., 2005, pp. 4176-4181.
9. J. Whitman, N. Zevallos, M. Travers and H. Choset, "Snake Robot Urban Search After the 2017 Mexico City Earthquake," IEEE Intl. Symp. on Safety, Security, and Rescue Robotics (SSRR), 2018, pp. 1-6
10. R. Ariizumi and F. Matsuno, "Dynamic Analysis of Three Snake Robot Gaits," in IEEE Transactions on Robotics, vol. 33, no. 5, pp. 1075-1087, Oct. 2017
11. J. T. Lane and R. M. Voyles, "A 2-D tread mechanism for hybridization in USAR robotics," IEEE Intl. Symp. on Safety, Security, and Rescue Robotics (SSRR), 2016.
12. A. Masayuki, T. Takayama and S. Hirose, "Development of "Souryu-III": connected crawler vehicle for inspection inside narrow and winding spaces," IEEE/RSJ Intl. Conf. on Intelligent Robots and Systems (IROS), 2004, pp. 52-57 vol.1.
13. J. Borenstein and A. Borrell, "The OmniTread OT-4 serpentine robot," IEEE Intl. Conf. on Robotics and Automation, 2008, pp. 1766-1767.
14. J. Huff, S. Conyers and R. Voyles, "MOTHERSHIP — A serpentine tread/limb hybrid marsupial robot for USAR," IEEE Intl. Symp. on Safety, Security, and Rescue Robotics (SSRR), 2012, pp. 1-7
15. R. M. Voyles and R. Godzdanker, "Side-Slipping Locomotion of a Miniature, Reconfigurable Limb/Tread Hybrid Robot," IEEE Intl. Wkshp. on Safety, Security and Rescue Robotics, 2008, pp. 58-64
16. Y Cui, RM Voyles, JT Lane, A Krishnamoorthy, MH Mahoor, "A mechanism for real-time decision making and system maintenance for resource constrained robotic systems through ReFrESH," in Autonomous Robots 39 (4), 487-502, 2015.
17. A. S. Boxerbaum, J. Oro and R. D. Quinn, "Introducing DAGSI Whegs™: The latest generation of Whegs™ robots, featuring a passive-compliant body joint," IEEE Intl. Conf. on Robotics and Automation, 2008, pp. 1783-1784.
18. B. R. Tietz, R. W. Carnahan, R. J. Bachmann, R. D. Quinn and V. SunSpiral, "Tetraspine: Robust terrain handling on a tensegrity robot using central pattern generators," IEEE/ASME Intl. Conf. on Adv. Intell. Mecha., 2013, pp. 261-267.

Concept and Modeling of a Discrete Variable Stiffness Actuator Based on a Reconfigurable Parallel-Beam Flexure Mechanism

Jiaming Fu[1], Lianxi Zheng[2], and Dongming Gan[1*]

[1] Purdue University, West Lafayette, IN 47907, USA
dgan@purdue.edu
[2] Khalifa University, Abu Dhabi, 127788, UAE

Abstract. Variable stiffness actuators (VSAs) are one of the effective solutions in developing collaborative robots with intrinsic safety for physical human-robot interaction. This paper presents a novel compact variable stiffness actuator based on a reconfigurable parallel-beam flexure mechanism, named reconfigurable beam VSA (RBVSA). The RBVSA is composed of two mechanisms: stiffness adjustment and stiffness transmission. The main structure of the stiffness adjustment mechanism is an integrated centrosymmetric four compliant branch mechanism with each branch a parallel-beam flexure mechanism. The primary principle of stiffness change is to change the cross-sectional properties of the parallel beam segment in a discrete manner. This is realized by a block inserting method through a bistable mechanism equipped with a push-pull electromagnet module. The key structures of the stiffness transmission mechanism are four lever pin-slot connections that transmit torque to drive the flexure frame to rotate. Using the superposition method, two theoretical models are proposed to model the stiffness modes. The stiffness change relationship with various design parameters is investigated using the developed models and validated by finite element analysis (FEA). Based on these results, the optimal parameters and configurations of the RBVSA are determined to realize a large span of stiffness adjustment.

Keywords: variable stiffness actuator, parallel beam flexure, discrete variable stiffness, stiffness modeling, compliant mechanisms

1 Introduction

Most traditional industrial robots' actuators are powerful but rigid, so they have to work separately from humans. However, people hope that robots could complete more tasks on our behalf. Therefore, the development's pace of collaborative robots (co-robots) has been accelerated[1].

For co-robots, the most important thing is to ensure the safety of humans during human-robot interaction[2, 3]. One of the common solutions is to use a variable stiffness actuator (VSA) at the joints of the co-robot. The basic design principle of VSA is to change the stiffness of elastic modules, such as springs and gear sets[4], located between the input shaft and output shaft. There are multiple ways to achieve this goal.

The most popular method is to change the effective length of the elastic modules [5–10], which could simplify the structure design and implement process. Changing the transmission ratio[11–14] between the output of the actuator and elastic modules is also a feasible method, but the effective load may be limited. Some VSAs also use the antagonistic approach to change the pretension of the spring[15–18], which may cause energy loss. In addition, changing the cross-sectional area[19, 20] is also an effective method to adjust the stiffness of elastic modules .

So far, the majority of VSAs that have been published change the stiffness continuously, however, it is not always necessary to have the continuous stiffness. Representative stiffness levels are enough to deal with most of the interaction scenarios and needs. In this case, designing compact and simple structured VSAs [21–24] that can adjust stiffness discretely is an innovative perspective. It only needs a few different stiffness modes, and even only two modes of low stiffness and high stiffness for some cases. Following this motivation, we designed a new VSA, named RBVSA, which achieved discrete variable stiffness by changing the cross-sectional area property of a reconfigurable beam. The function of variable stiffness is mainly implemented by an integrated center symmetrical four-compliant-branch mechanism. The advantage of RBVSA is that it can balance the force and minimize the parasitic movement. The structure of each branch adopts the parallel-beam flexure mechanism. Compared with a single leaf spring, the parallel-beam flexure mechanism could reduce the lateral bending and improve the transmission efficiency of torque. A block can be inserted or pulled out into the cavity of this flexure to increase or decrease its stiffness. This mechanism can be implemented by a compliant bistable switch mechanism [25] equipped with a push-pull electromagnet module through power-on and power-off to eject or insert the block.

Compared with the existing VSAs, the RBVSA possess the following advantages: First, the structure is relatively simple and compact, and no motors are needed besides the driving motor, which reduces the complexity of the controller. Second, low energy consumption is needed for the stiffness change. The push-pull electromagnet module needs low power to energized when performing variable stiffness tasks. Last but not least is its fast response on stiffness change. The electromagnet module can complete the variable stiffness rapidly after being activated. Compared with using servo motors, RBVSA will significantly improve the efficiency of the system.

The paper is structured as follows. Section 2 introduces the mechanical design of the RBVSA, and the concept implemented for adjusting the stiffness. Section 3 establishes theoretical models of stiffness variations. Section 4 compares FEA and theoretical models while Section 5 summarizes the work.

2 Concept of the Design

2.1 Stiffness adjustment mechanism

As shown in Fig. 1, the RBVSA is composed of two units: a stiffness adjustment mechanism and a stiffness transmission mechanism. In order to balance the force and

minimize the parasitic movement, an integrated centrosymmetric four-compliant-branch mechanism is used as the carrier of the stiffness adjustment mechanism. The structure of each branch adopts the parallel-beam flexure mechanism (the Flexure). Compared with a single leaf spring, it can reduce lateral bending, thereby improving the torque transmission efficiency. The RBVSA achieves discrete variable stiffness by changing the cross-sectional area property. The specific method is to insert or pull out a block into the cavity of the Flexure to increase and decrease its stiffness. This mechanism is implemented by a compliant bistable switch mechanism equipped with a push-pull electromagnet module. The frame of the bistable mechanism is compliant, and the block in the middle is made of aluminum alloy, which is consistent with the Flexure. A pin puller is installed at the bottom of the block, which is composed of a magnet.
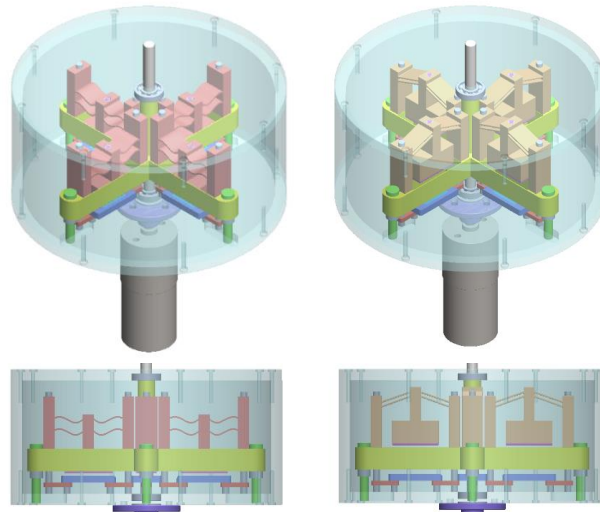

Fig. 1. Discrete stiffness change of the proposed RBVSA: (a) in 'on' mode; (b) in 'off' mode

As illustrated in Fig.2, when the electromagnet located under the cavity of the Flexure is powered off, it will be attracted by the pin puller. At this time, the block is pulled into the cavity of the Flexure by the magnetic attraction force, and the system will be in the on mode. When the electromagnet is powered on, it will generate the same pole as the pin puller and repel the pin puller. In this case, the block is ejected from the Flexure cavity and the system will switch to off mode. The electromagnet is fixed on an electromagnet holder, which is made of compliant material. The electromagnet holder is connected to two electromagnet holder links through the rotating pivot located at both ends of the electromagnet holder. The electromagnet holder links are connected to the Flexure by rotating shafts located at both ends of the cavity. The bistable switch mechanism is also connected to the Flexure through the same pivot. This way could minimize the interference of the bistable switch mechanism and electromagnet module connected to the Flexure on the deformation of the Flexure when the system is operating. When the Flexure has a large deformation, the block cannot be inserted or pulled

out smoothly. Therefore, the RBVSA can only achieve offline variable stiffness but cannot achieve online variable stiffness.
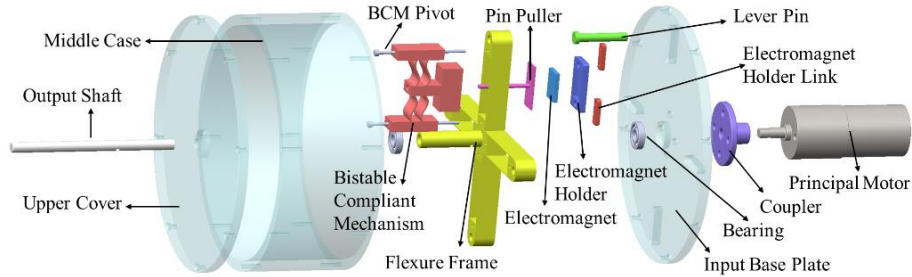

Fig. 2. Exploded view of the RBVSA

2.2 Stiffness transmission mechanism

As shown in Fig.2, the shaft of the principal drive motor is coupled with the input base plate at the bottom of the RBVSA through a coupler and generates a torque T to drive the entire case to rotate. As in Fig. 3, the torque T is equivalent to the moment M at the center of the base plate, which drives the flexure frame to rotate through four lever pins. The effect of moment M on the lever pin can be treated as four times of a force F multiple the length of lever arm L, and the direction is perpendicular to L and tangent to the lever pin. The lever pin is inserted into the guide slot on the base plate. When the flexure frame is bent, it can translate in the slot to ensure that the force F is always perpendicular to L and tangent to the lever pin. Since the force component along the L direction is small, it could be ignored. The flexure frame is connected to the output shaft by bolts, and the output shaft is connected to the load simultaneously.
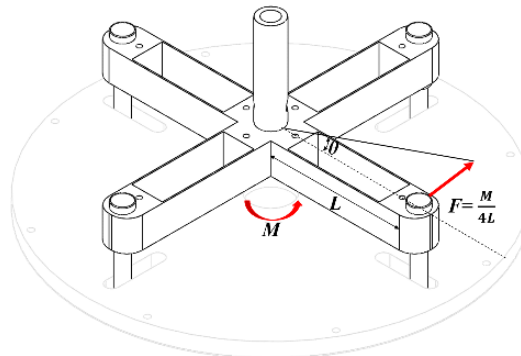

Fig. 3. Schematic diagram of the load analysis

3 The Stiffness Modelling

As shown in Fig. 4, a quarter of the flexure frame could be regarded as a variable stiffness parallel-beam flexure to analyze. There is a hollow beam L with a block in the

center in an *x-y* coordinate system: the *x*-axis direction is horizontal along the long axis of the beam to the right and the *y*-axis is perpendicular to the x-axis and downward; meanwhile, the *z*-axis could be ignored since the beam is regarded only working on the *x-y* plane.
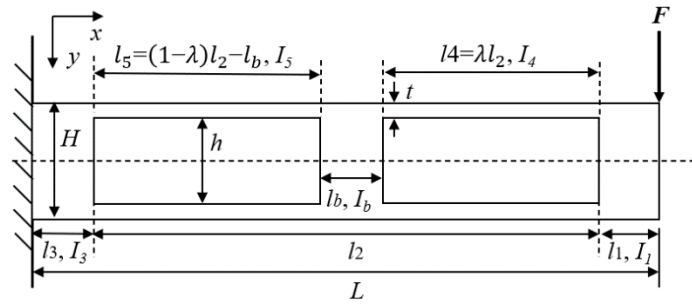

Fig. 4. Free body diagram of the RBVSA in on mode

3.1 On Mode

For the on mode, a block is added in the middle of the Flexure as in Fig. 4. Supposing that the left end of the beam is fixed to the wall, and a downward force *F* perpendicular to the x-axial direction is applied to the right end. In this model, parasitic error motions [26] in the *x*-axis direction will be ignored, because its value is too small compared with the deflection in the *y*-direction.

The height of the Flexure is *H* and the height of the cavity is *h*. Then the thicknesses of the leaf springs in l_4 and l_5 are $t=(H-h)/2$. The width *b* of the beam is not marked in the figure and it is perpendicular to the surface of the paper. Receptively, the moment of inertia I_1 and I_4 of the solid parts and compliant parts are

$$I_1 = \frac{H^3 b}{12} \tag{1}$$

$$I_4 = \frac{t^3 b}{12} \tag{2}$$

To get the result as accurately as possible, we will compute the deflection of the beam segment-by-segment and then superpose the results together. The deflection of all segments will be calculated one by one and apply them to the right end of the beam to get its maximum deflection on y-direction. Therefore, the beam is divided into five segments in this case, where l_1, l_b and l_3 are compliant bodies with the moment of inertia I_1, I_b and I_3 respectively, which are equal to I_1 in the previous section. The segments l_4 and l_5 are parallel-beam mechanisms that are considered as two parallel leaf springs with the moment of inertia I_4 and I_5 which are identical. Segment l_2 is equal to the sum of l_4, l_b and l_5. Although most of the deflection will be generated by the compliant segments, solid segments should not be omitted, since they have a certain thickness in real

applications whose deformation will significantly impact the accuracy of the model. For the convenience of analysis and modeling, we can parameterize l_4 and make it be λl_2, then l_5 is equal to $(1-\lambda)l_2-l_b$.

The calculation process of the deflection and stiffness of the flexure is: First, segments l_2 and l_3 are considered as rigid, and only the segment l_1 is compliant. At this time, the left end of l_2 can be regarded as fixed on the wall, and the right end of l_1 is affected by the downward force F. We can get the deflection angle θ_1 and the deflection δ_1 of l_1. For segment l_1, although the deflection angle θ_1 is calculated, it does not affect the deflection of the right end of l_1. Next, treat the other parts as rigid bodies, and only the compliant segment l_4 is considered. At this time, the left end of l_4 can be seen as fixed on the wall, and the right end of l_4 is affected by both the downward force F and the bending moment Fl_1 from segment l_1. The deflection angle θ_2 of segment l_4 can be obtained by simplification and calculation based on the parallel guided mechanism theory [27, 28], which will be transmitted to the right end of L through l_1 making then end with a deflection $\delta_2 + \theta_2 l_1$. The deflection and deflection angle of the rest of segments can be obtain by the same method. Finally, by accumulating all the deflection acting on the right end of L, the maximum deflection δ_y and deflection angle θ_y of the Flexure and its stiffness k_θ can be calculated below. It is worth mentioning that the total stiffness of the RBVSA is the sum of the four branches.

$$
\delta_y = \underbrace{\frac{Fl_1^3}{3EI_1}}_{\delta_1} + \underbrace{\frac{F(\lambda l_2)^3}{24EI_4}}_{\delta_2} + \underbrace{\frac{Fl_b^2}{3EI_b} + \frac{F(l_1+\lambda l_2)l_b^2}{2EI_b}}_{\delta_3} + \underbrace{\frac{F[(1-\lambda)l_2-l_b]^3}{24EI_5}}_{\delta_4} + \underbrace{\frac{Fl_3^3}{3EI_3} + \frac{F(l_1+l_2)l_3^2}{2EI_3}}_{\delta_5} +
$$

$$
\underbrace{\frac{t^2}{6h^2}\left(\frac{Fl_1(\lambda l_2)}{EI_4} + \frac{F(\lambda l_2)^2}{2EI_4}\right)}_{\theta_2} l_1 + \underbrace{\left(\frac{Fl_b^2}{2EI_b} + \frac{F(l_1+\lambda l_2)l_b}{EI_b}\right)}_{\theta_3}(l_1 + \lambda l_2) +
$$

$$
\underbrace{\frac{t^2}{6h^2}\left(\frac{F(l_1+\lambda l_2+l_B)[(1-\lambda)l_2-l_b]}{EI_5} + \frac{F[(1-\lambda)l_2-l_b]^2}{2EI_5}\right)}_{\theta_4}(l_1 + \lambda l_2 + l_B) + \underbrace{\left(\frac{Fl_3^2}{2EI_3} + \frac{F(l_1+l_2)l_3}{EI_3}\right)}_{\theta_5}(l_1 +
$$

$$
l_2) \tag{3}
$$

$$
\theta_y = \frac{\delta_y}{L} \tag{4}
$$

$$
k_\theta = \sum_i^{n=4} k_i = \frac{M}{\theta_y} \tag{5}
$$

3.2 Off Mode

In order to decrease the stiffness of the Flexure, the block is removed from the middle of the beam through the bistable mechanism, switching to the off mode. In this case, we can still use the equations of the on mode, but just make $l_b = 0$ and $\lambda = 1$. Then, l_5 will be 0 and l_4 will be equal to l_2 in Eq. (3)

3.3 A Heuristic Theoretical Model

Based on the analysis of large amounts of data, we summed up a heuristic model which was added compensation of the rigid whole beam model to the hollow parallel

beam. There is no theoretical derivation, but this simplified model is proved to be relatively accurate comparing with the theoretical models shown in section 3.1.

For the off mode, we can compute the deflection of all compliant segments and add those deflection of the whole beam as a rigid body; then to get deflection angle and stiffness.

There will be certain restrictions that will be discussed in the next section.

For the on mode, the entire two-hollow beam could be regarded as connected by two beams that comes from off mode. Therefore, segment l_b is divide into two segments from its intermediate cross-section. At first, calculate the deflection and angle of the left Flexure. Next, superimpose the deflection of the right Flexure to obtain the maximum deflection. Then calculate the deflection angle θ_{sip} and stiffness k_{sip} of the entire beam as

$$\theta_{sip} = \underbrace{\frac{Fl_5^3}{24EI_5L} + \frac{F\,(l_3+l_5+\frac{l_b}{2})^3}{3EI_bL}}_{\delta_{l_5}/L} + \underbrace{arc\,\tan\left(\frac{\delta_{l_5}}{l_3+l_5+\frac{l_b}{2}}\right)}_{\theta_{l_5}} \frac{(l_1+l_4+\frac{l_B}{2})}{L} + \frac{Fl_4^3}{24EI_4L} + \frac{F\,(l_1+l_4+\frac{l_b}{2})^3}{3EI_bL}$$

(6)

$$k_{sip} = \frac{M}{\theta_{sip}}$$

(7)

4 Theoretical Model Validation with FEA Simulation

4.1 FEA Simulation Setup

In ANSYS, the 3-D model of the RBVSA is simplified for clear illustration and low computation load. Aluminum alloy is used as the material of the Flexure and the blocks, while the other parts are alloy steel. Their Young's modulus are E_{Al} = 71 GPa and E_{steel} = 200 GPa, respectively. A moment M that is equivalent to the torque from the driving motor is applied to the shaft connected to the base plate, and at the same time, the center of the Flexure is fixed. The lever pin can rotate relative to the beam or translate in the slot.

Fig. 5 shows the FEA simulation of RBVAS under different configurations. In this simulation, we set $l_1 = l_3 = 8$ mm, $l_2 = 30$ mm, $H = B = 10$ mm, $h = 9.2$ mm, $l_b = 12$ mm, $M = 2$ Nm, and the animation ratio to 1:1. Fig. 5(a) shows that under the off mode, the deflection angle of the RBVSA is 3.85° and the stiffness is 0.52 Nm/°. Fig. 5(b) illustrates that in the two blocks on mode, the deflection angle of the RBVSA is 0.45° and the stiffness is 4.42 Nm/°. Obviously, under the same external force, the beam in on mode has less deformation and greater stiffness than in off mode. Fig. 5(c) presents that in all four blocks on mode, the deflection angle of the RBVSA is 0.23° and the stiffness is 8.58 Nm/°. This is close to twice the stiffness in two blocks on mode. Fig. 5(d) shows that in the four blocks on mode. When $\lambda = 0.15$, the deflection angle of the RBVSA is 1.34° and the stiffness is 1.49 Nm/°. Compared with the block located in the middle of the beam, the stiffness of the RBVSA is smaller in this case.
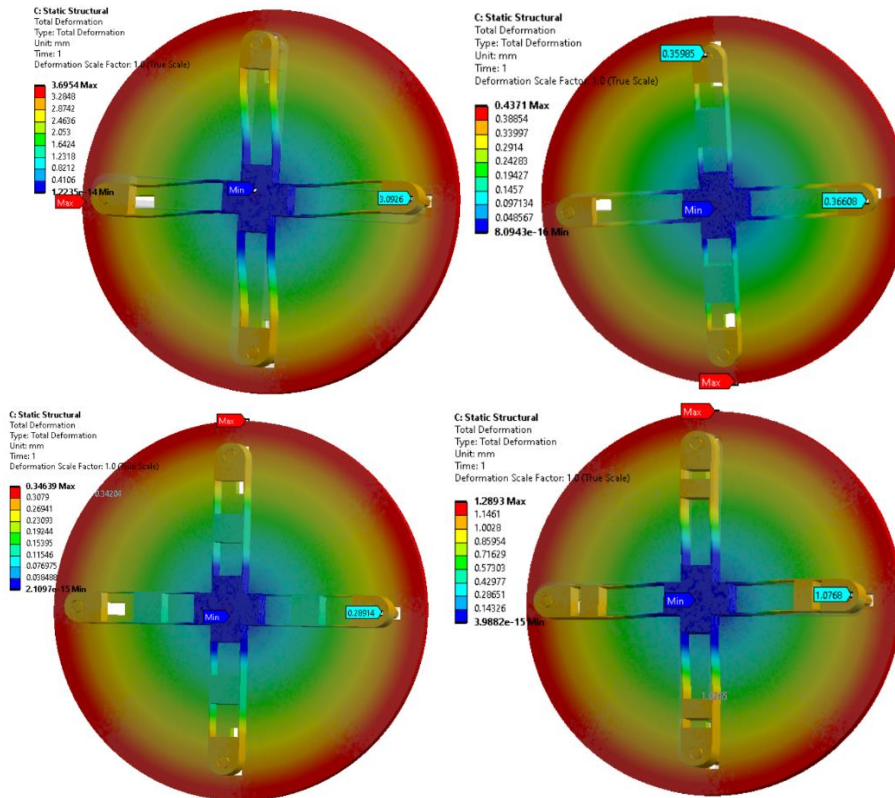
Fig. 5. FEA simulation under different configurations: (a) off mode; (b) two blocks on mode; (c) four blocks on mode; (d) four blocks on mode in the eccentric position

4.2 Model Validation by Comparing with FEA for Various Design Parameters

In order to validate the accuracy of the above theoretical model and find the optimal parameter configuration of the RBVSA, we control the variables to make the width b of the beam, the length l_2 of the parallel-beam segment, and its thickness t as independent variables. In addition, the proportion λ of the length of l_4 and the proportion l_b/L of the block's length of the whole beam will be also considered. Through FEA simulation and MATLAB calculation, the data of deflection and stiffness are collected under different moments. For the convenience of analysis and comparison, we normalize the existing parameters. For example, h/H could represent the thickness ratio of the leaf spring that help determine the thickness of the leaf spring. The smaller value of h/H means the leaf spring will be thicker, and its stiffness will rise. l_2/L represents the compliance ratio, which is useful for finding appropriate the length of parallel beam segments. The larger value of this ratio means the greater proportion of the compliance segment to the total length, which will reduce the stiffness. b/L represents the thickness ratio of the beam that help determine the thickness of the beam. The lower value of this

ratio means the beam will be thinner, accompanying the decrease in stiffness. λ reflects the position change of the block in the cavity of the beam, which assists in determining the proper position of the block. When λ is approaching to 0.5, this means that the block is close to the center of the cavity, so the beam can obtain greater stiffness. If λ approaches 0, it indicates that the block is close to the end of the cavity, so the beam can obtain smaller stiffness. l_b/L reflects the size change of the block in the center of the cavity that is useful for seeking the optimal block length. When this value decreases, the stiffness of the beam will be reduced as well.

In the following FEA results, if there are no special instructions, several parameters are unchanged: $L = 46$ mm, $l_1 = l_3 = 8$ mm, $l_2 = 30$ mm, $H = B = 10$ mm, $h = 9.2$ mm, $\lambda = 1$, $l_b = 0$, $M = 2$ Nm. Fig.6(a) and (b) illustrate the relationship between h/H and the deflection angle and the stiffness where the value of h is various. The result is consistent with the theory; when h/H increases, the deflection angle also increases but the stiffness decreases. We found that the error of k_A and k_{sip} with respect to the FEA becomes bigger as the value of h/H is smaller, but the theoretical model has satisfactory performance when h/H is greater than 0.5, which is in commonly used range in the application. Fig.6(c), (d) present the variation tendency of B/L, where the value of B is various. When b/L becomes larger, the deflection angle will be smaller, but the stiffness will be bigger. In this model, the error of k_A and k_{sip} comparing with FEA are all less than 10%. Fig.6(e), (f) show the relationship between λ and the deflection angle and the stiffness where λ will change from 0 to 0.5 and l_b will be 6 mm. When λ becomes larger, the deflection will reduce while the stiffness increases. The plot of λ changing from 0.5 to 1 is symmetrical with from 0 to 0.5. In these cases, the errors of k_A and k_{sip} with respect to FEA are all below 8%. Fig.6(g), (h) elucidate the variation tendency of l_b/L. Here, l_b will increase from 0 to 30 mm and λ will be smaller passively. When the value of l_b/L is higher, the deflection angle is smaller as the stiffness grows. In these cases, the maximum error between k_{sip} and FEA reaches -41%, and the maximum error of k_A archives 36%. However, if l_b/L is smaller than 0.7, the errors will be always smaller than 10%, which indicate the model is feasible. When l_b/L is 0, it means that the RBVSA is in off mode and there is no block in the cavity. When $l_b/L = 1$, it means that the Flexure becomes a solid cantilever beam, and the stiffness will reach 100 times compared with off mode. Fig.6(i) and (j) illustrate the relationship between M and the deflection angle and the stiffness. When M increases, the deflection angle becomes larger, but the stiffness remains unchanged because stiffness is a property of the system itself. Once the parameters of RBVSA are being determined, it does not change with adjustment in external forces.
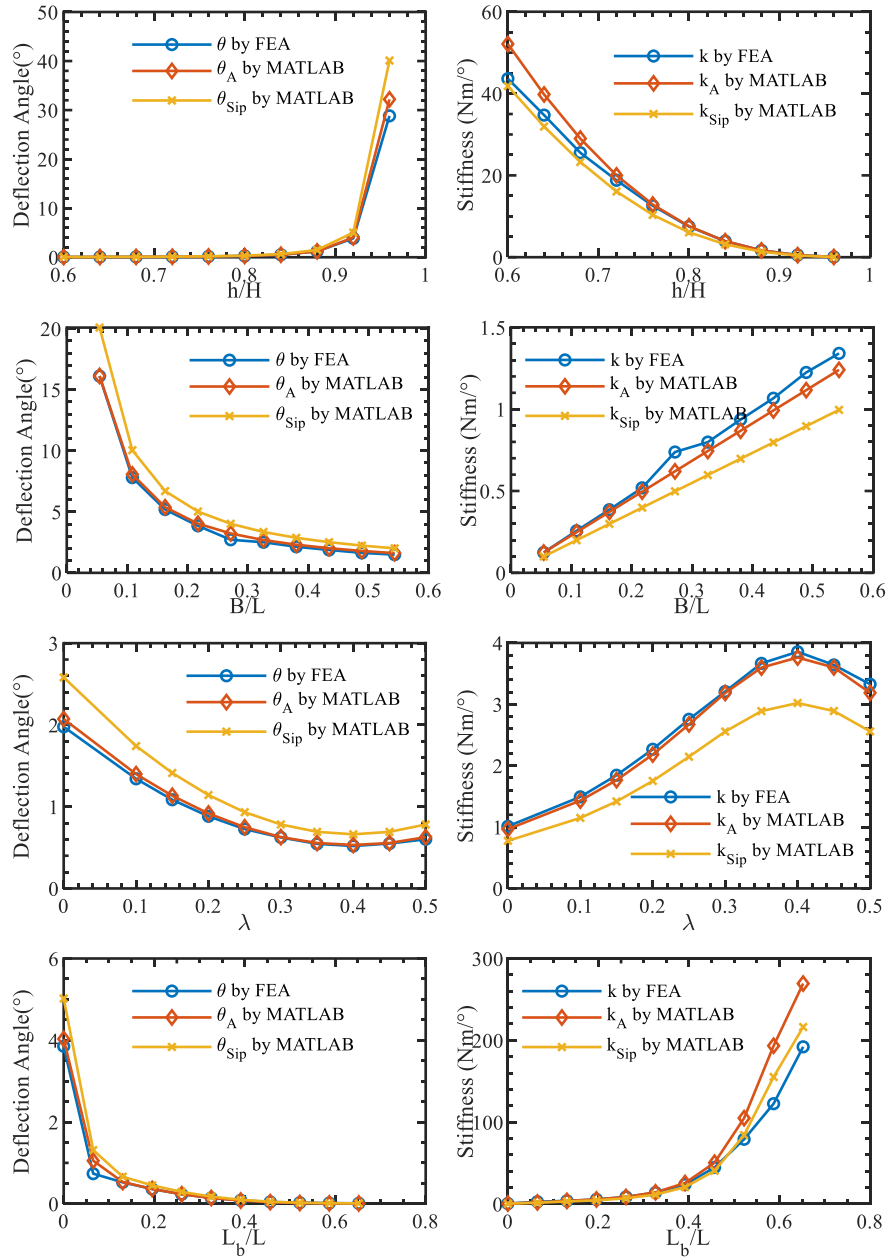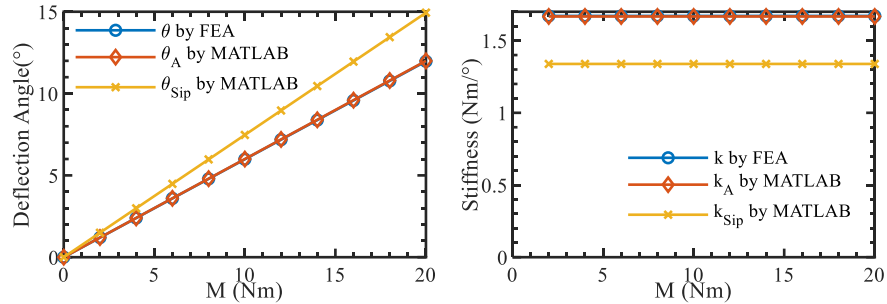
Fig. 6. Comparison of the FEA (k, θ), theoretical value (k_A, θ_A) and the value of the simplified model (k_{sip}, θ_{sip}): (a) h/H vs deflection angle; (b) h/H vs stiffness; (c) b/L vs deflection angle (d) b/L vs stiffness; (e) λ vs deflection angle; (f) λ vs stiffness; (g) l_b/L vs deflection angle; (h) l_b/L vs stiffness; (i) M vs deflection angle; (j) M vs stiffness

Considering the small error and high stiffness variation range, we selected the optimal configuration for the RBVSA from current data: $L = 46$ mm, $l_1 = l_3 = 8$ mm, $l_2 = 30$ mm, $H = B = 10$ mm, $h = 9.2$ mm, $\lambda = 0.15$, $l_b = 21$. When $M = 2$ Nm and it is in off model, the deflection angle of the RBVSA is 3.85° and the stiffness is 0.52 Nm/°. When the RBVSA is in on model, its deflection angle is 0.04° and the stiffness is 44.60 Nm/°. This means that the RBVSA could achieve 86 times the stiffness change within 7% of the error. Other main specifications of the RBVSA are shown in Table. 1, following which a prototype is being built.

Table 1. Main specifications of the RBVSA

Parameters	Values	Units
Outer diameter of the RBVSA	12	cm
Hight of the RBVSA	6	cm
Effective length of the parallel beam	3	cm
Thickness of the flexure frame	4	mm
Range of stiffness variation	0.52 ~ 44.60	Nm/°
Range of deflection	0 ~ 38.5	°

5   Conclusions

This paper proposes a new discrete variable stiffness actuator concept, which is designed to adapt to the mechanical design of variable stiffness robots and aim to realize safe human-robot interaction. The principle of stiffness variation is to change the cross-sectional area properties of the hollow beam structure by using a bistable switch mechanism. The stiffness adjustment mechanism and transmission mechanism of RBVSA

were illustrated, respectively. Based on the superposition principle, a mathematical model for calculating the deflection and stiffness of the beam section by section. Two cases of off mode and on mode are compared to show how the stiffness changes. The model is also further simplified to a heuristic model. The results of the theoretical model and its simplified version were calculated by MATLAB and with the corresponding FEA data using the controlled variable method. This model can achieve high accuracy in the range of commonly used applications. The error of the model only becomes larger under higher stiffness. In addition, different configurations of the RBSAP in FEA simulation are also presented. Based on the existing data, the optimal parameters of the RBVSA are determined. Its stiffness change rate can achieve 86, which is an innovative breakthrough. Next, additional data will be collected to optimize its parameters. Besides, we will construct prototypes to compare and analyze experiments, FEA, and theoretical results. The improvements on the structural design of RBVSA will also be conducted to achieve outstanding performance.

Acknowledgement

References

1. KNUDSEN, M., KAİVO-OJA, J.: Collaborative Robots: Frontiers of Current Literature. J. Intell. Syst. Theory Appl. 3, 13–20 (2020).
2. Bi, Z.M., Luo, M., Miao, Z., Zhang, B., Zhang, W.J., Wang, L.: Safety assurance mechanisms of collaborative robotic systems in manufacturing, (2021)
3. Gan, D., Tsagarakis, N.G., Dai, J.S., Caldwell, D.G., Seneviratne, L.: Stiffness design for a spatial three degrees of freedom serial compliant manipulator based on impact configuration decomposition. J. Mech. Robot. 5, 11002-1-11002–10 (2013).
4. Li, X., Chen, W., Lin, W.: Design of a structure-controlled variable stiffness actuator based on rotary flexure hinges. Proc. - IEEE Int. Conf. Robot. Autom. 45–50 (2017).
5. Xie, Z., Qiu, L., Yang, D.: Analysis of a novel variable stiffness filleted leaf hinge. Mech. Mach. Theory. 144, 103673 (2020).
6. Wu, J., Wang, Z., Chen, W., Wang, Y., Liu, Y.H.: Design and Validation of a Novel Leaf Spring-Based Variable Stiffness Joint with Reconfigurability. IEEE/ASME Trans. Mechatronics. 25, 2045–2053 (2020).
7. Xu, Y., Guo, K., Sun, J., Li, J.: Design, modeling and control of a reconfigurable variable stiffness actuator. Mech. Syst. Signal Process. 160, 107883 (2021).
8. Liu, H., Zhu, D., Xiao, J.: Conceptual design and parameter optimization of a variable stiffness mechanism for producing constant output forces. Mech. Mach. Theory. 154, 104033 (2020).
9. Xu, Y., Guo, K., Li, J., Li, Y.: A Novel Rotational Actuator With Variable Stiffness Using S-shaped Springs. IEEE/ASME Trans. Mechatronics. (2020).
10. Choi, J., Hong, S., Lee, W., Kang, S., Kim, M.: A robot joint with variable stiffness

using leaf springs. IEEE Trans. Robot. 27, 229–238 (2011).

11. Usman, M., Raza, A.: Development of adjustable stiffness actuator by varying lever arm length. J. Chinese Inst. Eng. Trans. Chinese Inst. Eng. A. 40, 651–658 (2017).

12. Shao, Y., Zhang, W., Ding, X.: Configuration synthesis of variable stiffness mechanisms based on guide-bar mechanisms with length-adjustable links. Mech. Mach. Theory. 156, 104153 (2021).

13. Tsagarakis, N.G., Sardellitti, I., Caldwell, D.G.: A new variable stiffness actuator (CompAct-VSA): Design and modelling. Presented at the December 6 (2011)

14. Jafari, A., Tsagarakis, N.G., Caldwell, D.G.: A novel intrinsically energy efficient actuator with adjustable stiffness (AwAS). IEEE/ASME Trans. Mechatronics. 18, 355–365 (2013).

15. Petit, F., Chalon, M., Friedl, W., Grebenstein, M., Albu-Schäffer, A., Hirzinger, G.: Bidirectional antagonistic variable stiffness actuation: Analysis, design & implementation. In: Proceedings - IEEE International Conference on Robotics and Automation. pp. 4189–4196 (2010)

16. Malosio, M., Spagnuolo, G., Prini, A., Molinari Tosatti, L., Legnani, G.: Principle of operation of RotWWC-VSA, a multi-turn rotational variable stiffness actuator. Mech. Mach. Theory. 116, 34–49 (2017).

17. Chang, H., Kim, S.J., Na, Y., Park, J., Kim, J.: Development and control of a variable stiffness actuator using a variable radius gear transmission mechanism. In: IEEE International Conference on Intelligent Robots and Systems. pp. 4749–4755. Institute of Electrical and Electronics Engineers Inc. (2017)

18. Schiavi, R., Grioli, G., Sen, S., Bicchi, A.: VSA-II: A novel prototype of variable stiffness actuator for safe and performing robots interacting with humans. In: Proceedings - IEEE International Conference on Robotics and Automation. pp. 2171–2176 (2008)

19. Choi, J., Park, S., Lee, W., Kang, S.C.: Design of a robot joint with variable stiffness. In: Proceedings - IEEE International Conference on Robotics and Automation. pp. 1760–1765 (2008)

20. Schimmels, J.M., Garces, D.R.: The Arched Flexure VSA: A compact variable stiffness actuator with large stiffness range. In: Proceedings - IEEE International Conference on Robotics and Automation. pp. 220–225. Institute of Electrical and Electronics Engineers Inc. (2015)

21. Awad, M.I., Gan, D., Cempini, M., Cortese, M., Vitiello, N., Dias, J., Dario, P., Seneviratne, L.: Modeling, design & characterization of a novel Passive Variable Stiffness Joint (pVSJ). In: IEEE International Conference on Intelligent Robots and Systems. pp. 323–329. Institute of Electrical and Electronics Engineers Inc. (2016)

22. Hussain, I., Albalasie, A., Awad, M.I., Gan, D.: Modeling, identification, and control of a discrete variable stiffness actuator (DVSA). Actuators. 8, (2019).

23. Awad, M.I., Gan, D., Hussain, I., Az-Zu'Bi, A., Stefanini, C., Khalaf, K., Zweiri, Y., Dias, J., Seneviratne, L.D.: Design of a novel passive binary-controlled variable stiffness joint (BpVSJ) towards passive haptic interface application. IEEE Access. 6, 63045–63057 (2018).

24. Awad, M.I., Hussain, I., Gan, D., Azzu'bi, A., Stefanini, C., Khalaf, K., Zweiri, Y., Taha, T., Dias, J., Seneviratne, L.: Passive discrete variable stiffness joint (PDVSJ-II):

Modeling, design, characterization, and testing toward passive haptic interface. J. Mech. Robot. 11, (2019).

25.   Zirbel, S.A., Tolman, K.A., Trease, B.P., Howell, L.L.: Bistable Mechanisms for Space Applications. PLoS One. 11, e0168218 (2016).

26.   Awtar, S., Slocum, A.H., Sevincer, E.: Characteristics of beam-based flexure modules. J. Mech. Des. Trans. ASME. 129, 625–639 (2007).

27.   Awtar, S., Sevincer, E.: Elastic Averaging in Flexure Mechanisms: A Muliti-Beam Parallelogram Flexure Case-Study. Presented at the January 1 (2006)

28.   Awtar, S., Shimotsu, K., Sen, S.: Elastic averaging in flexure mechanisms: A three-beam parallelogram flexure case study. J. Mech. Robot. 2, (2010).

Stiffness Modeling and Sensitivity Analysis of a 1T2R Parallel Manipulator

Zenghui Chong[1], Fugui Xie[1,2*], Xin-Jun Liu[1,2*]and Jinsong Wang[1]

[1] The State Key Laboratory of Tribology, Department of Mechanical Engineering (DME), Tsinghua University, Beijing 100084, China
xiefg@mail.tsinghua.edu.cn (Fugui Xie)
xinjunliu@mail.tsinghua.edu.cn (Xin-Jun Liu)
[2] Beijing Key Lab of Precision/Ultra-precision Manufacturing Equipments and Control, Tsinghua University, Beijing 100084, China

Abstract. The stiffness of a parallel manipulator has significant effects on the quality and efficiency in polishing or machining. In this paper, a stiffness modeling method of a 1T2R parallel polishing manipulator is presented and a stiffness sensitivity index is proposed subsequently. To establish the stiffness model quickly and accurately, the matrix structural analysis method is utilized and the stiffness matrix of each element is identified through finite element analysis. Based on the virtual experiment, the stiffness matrices of elements with arbitrary nodes are identified. The explicit stiffness model of the manipulator is derived through stiffness matrix integration. By comparing with the FEA model, the established model is verified and the distribution of stiffness in the workspace is demonstrated. To identify the main source of the compliance, the local and global stiffness sensitivity indices are proposed. By analyzing the distribution of the stiffness sensitivity index, the vital elements in stiffness improvement are identified. The proposed stiffness modeling method and stiffness sensitivity index can be used in the design and analysis of other parallel manipulators.

Keywords: Stiffness Modeling, Stiffness Sensitivity Analysis, Parallel Manipulator, Matrix Structural Analysis

1   Introduction

Due to the potential advantages of low inertia, high stiffness, compact structures and quick response, parallel manipulators have attracted attention from both academia and industry [1-3]. There are some successful applications of parallel manipulators like Tricept [4] and Sprint Z3 tool head [5] in the field of aerospace machining, automobile, etc. As one of the vital performances, stiffness of a manipulator characterizes the resistance to the deformations caused by an external force or torque. In the field of processing, accuracy and efficiency are closely related to the stiffness of the manipulator [6]. Therefore, it is important to establish the stiffness model to estimate the stiffness performance during the design stage or application stage of a parallel manipulator.

The stiffness modeling approaches can be mainly classified into three categories: the finite element analysis method, the virtual joint modeling method, and the matrix structural analysis method. The finite element method divides the model into smaller and simpler connected elements and the FEA method is relatively accurate [7]. However, this requires the aid of commercial FEA software and the FEA model has to be re-meshed for different poses, resulting in high computational costs. Therefore, the FEA method is more suitable in stiffness verification in the final design stage rather than stiffness evaluation through the entire workspace [8].

The virtual joint approach has been widely used in analytical parametric analysis of parallel manipulators based on Jacobian matrix and Hooke's Law [8]. The concept of the "virtual joint" is introduced to express the bending and torsional compliance of the joints/limbs. However, the stiffness of the virtual spring is hard to identify since the cross-section of the parts would be arbitrary. Besides, when the base is lightweight, neglecting the compliance of the base may result in considerable deviation [9].

Matrix structural analysis is established based on stiffness matrix integration of standard elements such as beam, shell and solid elements [10]. Normally, the shape of elements is considered as standard shape and the stiffness matrix of the elements can be approximately derived [11]. Therefore, the stiffness matrix would not be accurate enough for all parts since the shape would be irregular. In Ref. [12], the method to identify the stiffness matrix based on finite element analysis is proposed. By employing this method, the accurate stiffness matrix can be derived for parts with arbitrary shapes. For elements with multiple nodes, the presented work in Ref. [9] is inspiring. When the compliance of the base and platform is taken into consideration, the accuracy of the stiffness model can be further improved. In this paper, the stiffness matrix will be identified through commercial FEA software. By integrating the stiffness matrix under different poses, the stiffness model can be established quickly with sufficient accuracy.

In the field of accuracy assurance, sensitivity analysis is widely used to identify vital error sources [13]. In the design procedure of a parallel manipulator, the element that influence the overall stiffness most is expected to be identified as well. By doing this, the stiffness can be further improved. In the stiffness analysis of a parallel manipulator, the sensitivity analysis method is rarely presented [14]. In this paper, an index to analytically evaluate the stiffness sensitivity of each element will be proposed.

The rest of this paper is organized as follows: In Sect. 2, the stiffness modeling is carried out based on element stiffness matrix identification. The distribution of stiffness in the workspace is presented. In Sect. 3, a stiffness sensitivity index is proposed and the stiffness sensitivity of each element is analyzed. Section 4 concludes the paper.

2 Stiffness modeling of the manipulator

2.1 Structure description

In Ref. [15], a hybrid mobile robot is proposed to accomplish the polishing task of large-scale wind turbine blades. In application, the stiffness of the manipulator will influence the effect of polishing. Therefore, the stiffness performance will be the focus of the paper and the 1T2R parallel manipulator will be the object. The CAD model and

kinematic scheme of the 1T2R parallel manipulator are shown in Fig. 1. The end-effector (the polishing tool) is connected with the base through three identical RCU limbs and actuated by three ball screw drives. The pose of the end effector can be expressed by (z, φ, θ), z is the z-coordinate of point o' in the global coordinate system $\Re : o - xyz$. (φ, θ) is the direction of $o'z'$ under the description of Tilt-and-Torsion (T&T) angles. The azimuth angle and the tilt angle are defined as $\varphi \in \left[0, 360° \right)$ and $\theta \in \left[0, 180° \right)$, respectively [15].

(a)   (b)
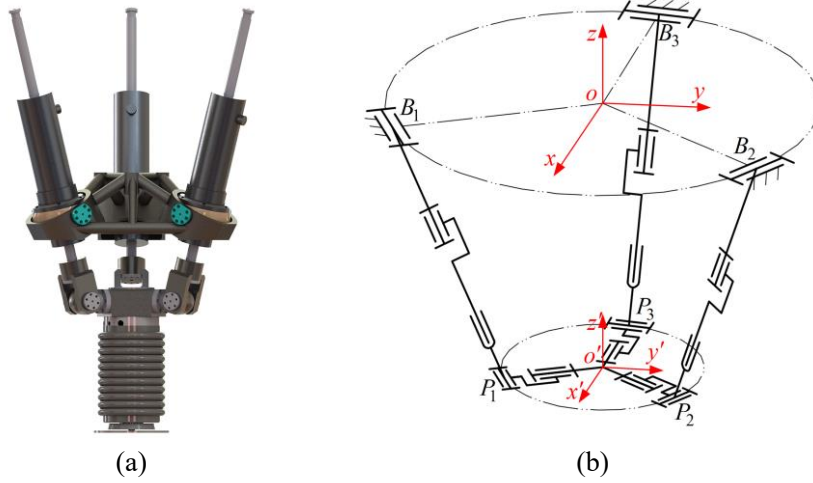
Fig. 1. The 1T2R parallel manipulator: (a) CAD model; (b) kinematic scheme

2.2   Element stiffness matrix identification

In stiffness modelling, the parallel manipulator can be divided into many spatial beam elements. Each part within the limb can be treated as a spatial beam element with two end nodes. However, for this parallel manipulator, the base and the platform are connected to three kinematic chains. For these two parts, the two node stiffness matrix is unable to describe the actual stiffness characteristics. In this paper, the base and platform will be treated as a beam element with four end nodes.

The end nodes of two-node element are i and j; the displacements of node i in the element coordinate system is $\bar{\boldsymbol{\delta}}_i = \begin{bmatrix} \bar{x}_i & \bar{y}_i & \bar{z}_i & \bar{\alpha}_i & \bar{\beta}_i & \bar{\gamma}_i \end{bmatrix}^{\mathrm{T}}$ and the nodal force vectors is $\bar{\boldsymbol{F}}_i = \begin{bmatrix} F_{ix} & F_{iy} & F_{iz} & M_{ix} & M_{iy} & M_{iz} \end{bmatrix}$. The expression is similar for node j. Based on the relationship between the force and the corresponding displacement, the following equation can be derived:

$$\begin{bmatrix} \bar{\boldsymbol{F}}_i \\ \bar{\boldsymbol{F}}_j \end{bmatrix} = \bar{\boldsymbol{k}}^e \begin{bmatrix} \bar{\boldsymbol{\delta}}_i \\ \bar{\boldsymbol{\delta}}_j \end{bmatrix} = \begin{bmatrix} \bar{\boldsymbol{k}}_{ii} & \bar{\boldsymbol{k}}_{ij} \\ \bar{\boldsymbol{k}}_{ji} & \bar{\boldsymbol{k}}_{jj} \end{bmatrix} \begin{bmatrix} \bar{\boldsymbol{\delta}}_i \\ \bar{\boldsymbol{\delta}}_j \end{bmatrix} \tag{1}$$

In order to derive the element stiffness matrix precisely, the finite element analysis is employed. The method to carry out virtual experiment is shown in Fig. 2. In virtual experiment, one node will be fixed and external force or moment will be applied on the other nodes.
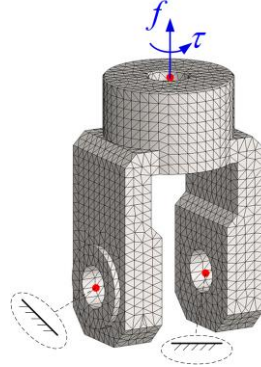

Fig. 2. FEA model for stiffness matrix identification

The nodal translational and rotational displacements can be obtained in the finite element software through the identification algorithm proposed in Ref. [14]. In one group of virtual experiments, there are 6 tests and concentrated force vectors $\bar{F}_k$ $(k = 1, \cdots, 6)$ can be expressed as:

$$\begin{bmatrix} \bar{F}_1 & \bar{F}_2 & \cdots & \bar{F}_6 \end{bmatrix} = \begin{bmatrix} 1 & 0 & 0 & 0 & 0 & 0 \\ 0 & 1 & 0 & 0 & 0 & 0 \\ \vdots & \vdots & \vdots & \vdots & \vdots & \vdots \\ 0 & 0 & 0 & 0 & 0 & 1 \end{bmatrix} = I \tag{2}$$

When node j is fixed and external force matrix (a unit diagonal matrix) is applied on node i, Eq. (1) can be written as:

$$\begin{bmatrix} I \\ T_{i,j} I \end{bmatrix} = \begin{bmatrix} \bar{k}_{ii} & \bar{k}_{ij} \\ \bar{k}_{ji} & \bar{k}_{jj} \end{bmatrix} \begin{bmatrix} \bar{\delta}_{Ti} \\ 0 \end{bmatrix} \tag{3}$$

where $T_{i,j}$ is the matrix to transform the force matrix I from node i to node j, and $\bar{\delta}_{Ti}$ is the displacement matrix of node i. Then $\bar{k}_{ii}$ and $\bar{k}_{ji}$ can be derived. Similarly, when node i is fixed and external forces are applied on node j, $\bar{k}_{ij}$ and $\bar{k}_{jj}$ can be identified.

For an element with multiple end nodes, the stiffness equation can be expressed as:

$$\begin{bmatrix} \bar{F}_1 \\ \vdots \\ \bar{F}_n \end{bmatrix} = \bar{k}^e \begin{bmatrix} \bar{\delta}_1 \\ \vdots \\ \bar{\delta}_n \end{bmatrix} = \begin{bmatrix} \bar{k}_{11} & \cdots & \bar{k}_{1n} \\ \vdots & \ddots & \vdots \\ \bar{k}_{n1} & \cdots & \bar{k}_{nn} \end{bmatrix} \begin{bmatrix} \bar{\delta}_1 \\ \vdots \\ \bar{\delta}_n \end{bmatrix} \tag{4}$$

In order to identify the stiffness matrix of an element with n end nodes, n groups of virtual experiments will be carried out. In group virtual experiment 1, node n is clamped and external force matrix (a unit diagonal matrix) is applied on node 1. In group virtual experiment i ($i \geq 2$), node i-1 is clamped and external force matrix is applied on node i. then the equations to identify the stiffness matrix can be written as:

$$\bar{k}^e = \begin{bmatrix} I & \cdots & 0 & \cdots & 0 \\ 0 & \cdots & \vdots & \cdots & 0 \\ 0 & \cdots & T_{i,i-1}I & \cdots & \vdots \\ \vdots & \cdots & I & \cdots & 0 \\ 0 & \cdots & 0 & \cdots & T_{n,n-1}I \\ T_{1,n}I & \cdots & \vdots & \cdots & I \end{bmatrix} \begin{bmatrix} \bar{\delta}_{1,T_1} & \cdots & \bar{\delta}_{i,T_1} & \cdots & \bar{\delta}_{n,T_1} \\ \bar{\delta}_{1,T_2} & \cdots & \vdots & \cdots & \bar{\delta}_{n,T_2} \\ \bar{\delta}_{1,T_3} & \cdots & 0 & \cdots & \vdots \\ \vdots & \cdots & \bar{\delta}_{i,T_i} & \cdots & \bar{\delta}_{n,T_{n-2}} \\ \bar{\delta}_{1,T_{n-1}} & \cdots & \bar{\delta}_{i,T_{i+1}} & \cdots & 0 \\ 0 & \cdots & 0 & \cdots & \bar{\delta}_{n,T_n} \end{bmatrix}^{-1} \tag{5}$$

where $T_{i,i-1}$ is the matrix used to transform the force matrix I from node i to node i-1 based on the theorem of equivalent force systems and $\bar{\delta}_{i,T_1}$, $\bar{\delta}_{i,T_i}$, and $\bar{\delta}_{i,T_n}$ are the displacement matrices of nodes 1, i and n in the ith group virtual experiment, respectively.

2.3   Stiffness matrix integration

In the global coordinate system, the displacements and force vectors of each node can be expressed as:

$$\delta_i = T\bar{\delta}_i = \begin{bmatrix} R & 0 \\ 0 & R \end{bmatrix} \bar{\delta}_i \tag{6}$$

$$F_i = T\bar{F}_i = \begin{bmatrix} R & 0 \\ 0 & R \end{bmatrix} \bar{F}_i \tag{7}$$

where R is the coordinate transformation matrix from the element coordinate system to the global coordinate system.

The relationship between nodal displacements and force vectors for an element with two nodes in the global coordinate system can be written as:

$$\begin{bmatrix} F_i \\ F_j \end{bmatrix} = k^e \begin{bmatrix} \delta_i \\ \delta_j \end{bmatrix} = \begin{bmatrix} T & 0 \\ 0 & T \end{bmatrix} \bar{k}^e \begin{bmatrix} T & 0 \\ 0 & T \end{bmatrix}^{\mathrm{T}} \begin{bmatrix} \delta_i \\ \delta_j \end{bmatrix} \tag{8}$$

Then, the global stiffness matrix can be obtained by integrating all the element stiffness matrices in the global coordinate system. The following equation can be obtained:

$$K = \sum_{i=1}^{N} k_i^e \tag{9}$$

where elements with joint connection require treatment of DOF condensation and $\boldsymbol{K}$ is the stiffness matrix of the parallel manipulator.

The stiffness model of the parallel manipulator in the global coordinate system is:

$$\boldsymbol{F} = \boldsymbol{KU} \tag{10}$$

where $\boldsymbol{F}$ is the external load vector of all nodes and $\boldsymbol{U}$ is the displacement vector.

By applying boundary condition and external load, the stiffness of the manipulator can be derived.

2.4   Simulation validation and stiffness distribution

In order to verify the established stiffness model, the FEA software (ANSYS) analysis is applied to several typical configurations. The pose of the manipulator is represented as (z, φ, θ). The linear stiffness of reference point o' in the global coordinate system obtained by theoretical and FEA models is listed in table 1. It can be concluded that the variation tendency of the theoretical values is similar to that of the FEA values and the errors are in an acceptable range (within 10%), which indicates the validation of theoretical stiffness model. After verifying the theoretical stiffness model by means of FEA model, the distribution of stiffness in the prescribed workspace can be analyzed explicitly.

Table 1. Comparison between linear stiffness of theoretical and FEA model

Linear stiffness		(250,0°,0°)	(300,0°,30°)	(350,90°,30°)
x-directional (N/μm)	Theoretical	2.25	0.72	0.60
	FEA	2.44	0.76	0.64
	Divergence	7.72%	5.89%	5.56%
y-directional (N/μm)	Theoretical	2.24	1.89	0.64
	FEA	2.44	2.01	0.68
	Divergence	8.03%	5.79%	5.45%
z-directional (N/μm)	Theoretical	256.02	18.16	37.29
	FEA	238.91	17.42	34.18
	Divergence	-6.72%	-4.24%	-9.09%

The distribution of linear stiffness k_x, k_y and k_z and the angular stiffness k_{rx}, k_{ry} and k_{rz} in the global coordinate system $\Re : O - xyz$ when z=-350mm is demonstrated in Fig. 3 .It can be found out that: 1) The values of k_x and k_{ry} get larger when $\varphi =180°$ while the values of k_y and k_{rx} get larger when $\varphi =0°$; 2) The distribution of k_z is symmetrical about $\varphi =60°$, 180° and 300° and the value of k_z gets its maximum when $\varphi=\theta=0°$; 3) The distribution of k_{rz} is symmetrical about $\varphi =0°$, 120° and 240° and the value of k_{rz} gets its maximum when $\varphi=\theta=0°$.
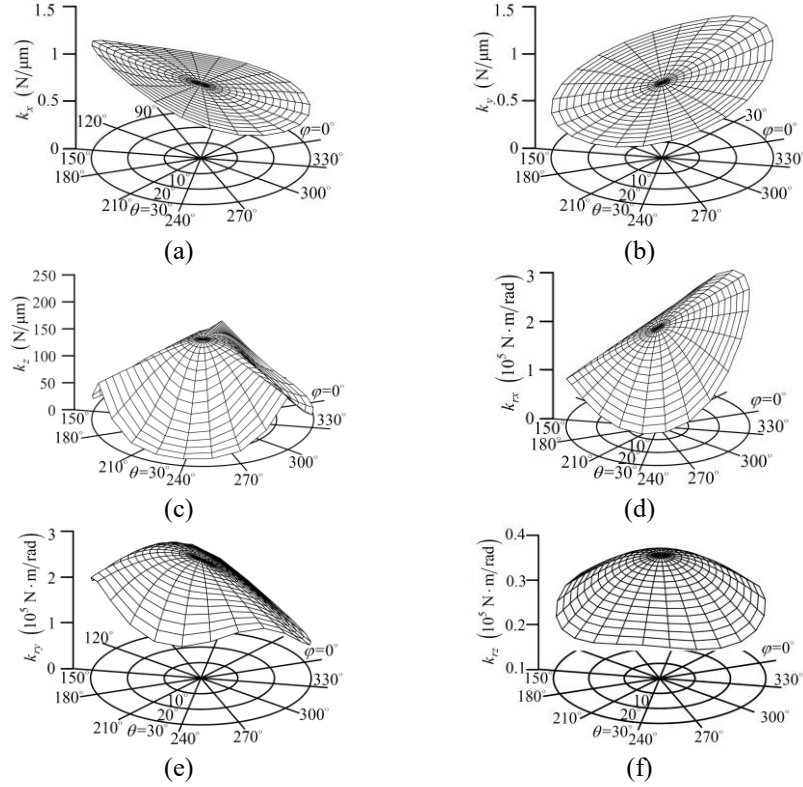
Fig. 3. Stiffness distribution in the global coordinate system (z=-350mm)

3 Stiffness sensitivity analysis

3.1 Definition of stiffness sensitivity index

Inspired by the commonly used objective function in topology optimization, the mean compliance of the manipulator can be expressed as:

$$C = \boldsymbol{F}^{\mathrm{T}}\boldsymbol{U} = \boldsymbol{U}^{\mathrm{T}}\boldsymbol{K}\boldsymbol{U} = \sum_{i=1}^{N}\boldsymbol{u}_i^{\mathrm{T}}\boldsymbol{k}_i^e\boldsymbol{u}_i = \sum_{i=1}^{N}C_i \tag{11}$$

where $\boldsymbol{u}_i$ is the displacement vector of the ith element and C_i is the compliance of the ith element.

From Eq. (11), it can be concluded that the mean compliance of the manipulator is the total compliance of each element. Therefore, the stiffness of the manipulator is more sensitive to an element with greater compliance.

Considering that the stiffness of the manipulator is pose dependent, the stiffness index will be calculated at a certain pose first. The local stiffness sensitivity index (LSSI) of element i can be defined as follow:

$$LSSI_i = \frac{C_i}{C} = \frac{\boldsymbol{u}_i^{\mathrm{T}} \boldsymbol{k}_i^e \boldsymbol{u}_i}{\boldsymbol{U}^{\mathrm{T}} \boldsymbol{K} \boldsymbol{U}} \tag{12}$$

The index embodies the compliance contribution of element i to the overall compliance of the manipulator at a certain pose. An element possesses higher $LSSI_i$ indicates that the overall stiffness is more sensitive to this element and the stiffness of this element should be the focus if the stiffness of the manipulator is expected to be higher. Under the assumption of linear elasticity and small deformation, it can be concluded that this index is determined by the direction rather than the magnitude of applied external load. Besides, the following equation can be obtained:

$$\sum_{i=1}^{N} LSSI_i = 1 \tag{13}$$

In order to analyze the sensitivity of an element comprehensively, the global stiffness sensitivity indices (GSSI) over the workspace are introduced as follow:

$$GSSI_i = \frac{\int_W LSSI_i \, dW}{\int_W dW} \tag{14}$$

where W denotes the workspace of the parallel manipulator.

3.2 Sensitivity analysis for the parallel manipulator

To identify the vital compliance sources among all elements for the parallel manipulator, sensitivity analysis is conducted in this section. As shown in Fig. 4, the manipulator is divided into the base, the platform, the motor base, motor, screw, nut, U-shape part (within the U joint), spherical part (within the U joint), flange of the platform.
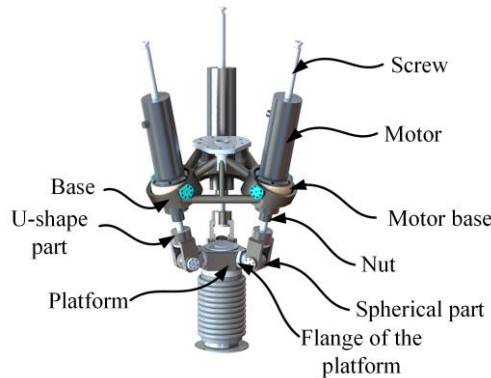

Fig. 4. Structure of the 1T2R manipulator

In polishing, the main external load is the normal force, which goes along the z'-axis. In this section, the external load is set as the unit force along the z'-axis. The LSSI and GSSI are presented in Fig. 5.
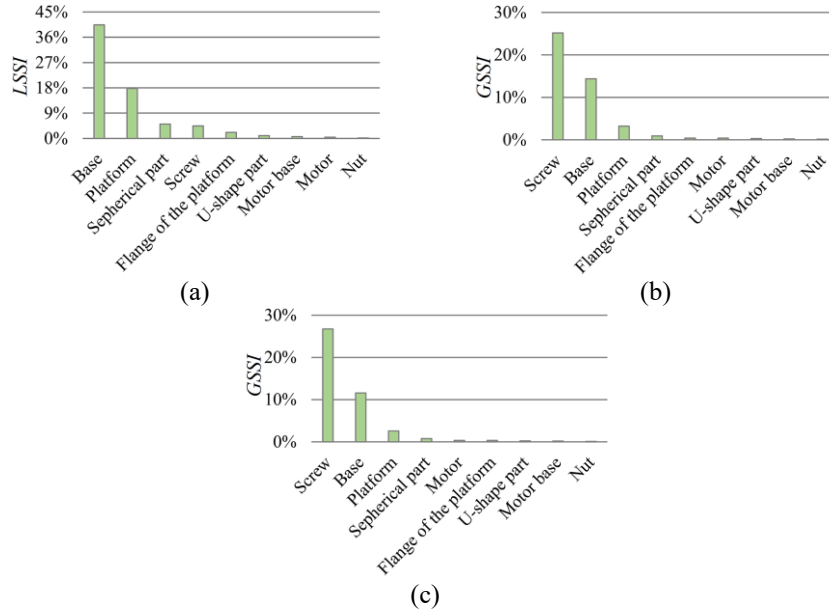
(a)

(b)

(c)

Fig. 5. Distribution of LSSI or GSSI: (a) z=-300mm, θ=0 ; (b) z=-300mm, $\varphi \in \left[0,\ 360°\right)$, $\theta \in \left[0,\ 30°\right]$; (c) $z \in \left[-300,\ -400\right]$mm, $\varphi \in \left[0,\ 360°\right)$, $\theta \in \left[0,\ 30°\right]$

Of note is that the same elements within different limbs possess the same index value and they are not distinguished with each other in Fig.5. Based on Fig. 5 (a), it can be found that the lightweight base and platform have significant influence on the overall stiffness of the manipulator. Therefore, it is necessary to establish the stiffness model considering the base and platform. From the distribution of GSSI, the screw in the limbs is the main source of the compliance and the total compliance proportion of the three screws exceeds 75%. If the stiffness of the manipulator is expected to be further improved, the screw should be the focus.

4   Conclusion

In this paper, a stiffness modeling method for the 1T2R parallel manipulator is presented. The FEA is employed to identify the stiffness matrix of each element for higher accuracy. By integrating the stiffness matrix at different pose, the analytical stiffness model of the manipulator is established. The established theoretical stiffness model is validated through comparison with FEA model and the stiffness distribution in the prescribed workspace is investigated and presented. To identify the element that influence the overall stiffness most, a local stiffness sensitivity index which characterizes the compliance contribution of one element, is proposed. On this basis, the global sensitivity stiffness index is defined. By analyzing the distribution of the two indices, the main source of the compliance is identified, and the screw should be the focus in further stiffness improvement. The presented work is helpful and can be utilized as a guide in the design and analysis of other parallel manipulators.

References

1. Liu, X. J., Bi, W. Y., Xie, F. G.: An energy efficiency evaluation method for parallel robots based on the kinetic energy change rate. Science China Technological Sciences, 62(6), 1035-1044 (2019).
2. Xie, Z. H., Xie, F. G., Liu, X. J., Wang, J. S., Shen, X.: Parameter optimization for the driving system of a 5 degrees-of-freedom parallel machining robot with planar kinematic chains. Journal of Mechanisms and Robotics, 11(4), 041003 (2019).
3. Codourey, A.: Dynamic modeling of parallel robots for computed-torque control implementation. The International Journal of Robotics Research, 17(12), 1325-1336 (1998).
4. Xi, F., Zhang D., Xu Z., Mechefske, C.M.: A comparative study on tripod units for machine tools, International Journal of Machine Tools and Manufacture, 43(7), 721–730 (2003).
5. Chen, X., Liu, X. J., Xie, F.G., Sun, T.: A Comparison Study on Motion/Force Transmissibility of Two Typical 3-DOF Parallel Manipulators: The Sprint Z3 and A3 Tool Heads. International Journal of Advanced Robotic Systems, 11(1),57458 (2014).
6. Xie H. , Li W. L., Zhu D. H., Yin Z. P., Ding H.: A systematic model of machining error reduction in robotic grinding. IEEE/ASME Transactions on Mechatronics, 25(6), 2961-2972 (2020).
7. Wu, J., Wang, J.S., Wang, L.P., Li, T.M., You, Z.: Study on the stiffness of a 5-DOF hybrid machine tool with actuation redundancy, Mechanism and Machine Theory, 44, 289–305 (2009).
8. Sun, T., Lian, B.B., Song, Y.M.: Stiffness analysis of a 2-dof over-constrained rpm with an articulated traveling platform. Mechanism and Machine Theory, 96, 165-178 (2016).
9. Yu, G., Wang, L., Wu, J., Wang, D., Hu, C.: Stiffness modeling approach for a 3-dof parallel manipulator with consideration of nonlinear joint stiffness. Mechanism and Machine Theory, 123, 137-152 (2018).
10. Pashkevich, A., Klimchik, A., Chablat, D.: Enhanced stiffness modeling of manipulators with passive joints, Mechanism and Machine Theory, 46, 662–679 (2011).
11. Cammarata, A.: Unified formulation for the stiffness analysis of spatial mechanisms, Mechanism and Machine Theory, 105, 272–284 (2016).
12. Klimchik, A., Pashkevich, A., Chablat, D.: Cad-based approach for identification of elastostatic parameters of robotic manipulators. Finite Elements in Analysis and Design, 75(6), 19-30 (2013).
13. Luo, X., Xie, F. G., Liu, X. J., Lie, J.: Error modeling and sensitivity analysis of a novel 5-degree-of-freedom parallel kinematic machine tool. Proceedings of the Institution of Mechanical Engineers Part B Journal of Engineering Manufacture, 233, 1637-1652 (2018).
14. Han, L., Zhang, D., Tian, Y., Wang, F., Xiao, H.: Static stiffness modeling and sensitivity analysis for geared system used for rotary feeding. Proceedings of the Institution of Mechanical Engineers Part C: Journal of Mechanical Engineering Science, 228, 1431-1443 (2014).
15. Chong, Z. H., Xie, F. G., Liu, X. J., Wang, J. S. Niu, H. F.: Design of the parallel mechanism for a hybrid mobile robot in wind turbine blades polishing. Robotics and Computer-Integrated Manufacturing, 61, 101857 (2020).

Reconfiguration of Two Novel Plane- and Line-Symmetric Sarrus-Extended Reconfigurable Mechanisms

Ruiqin Wang[1] and Jian S. Dai[2]

[1] Tianjin University, Tianjin, 300072, PR China
[2] King's College London, Strand, London WC2R 2 LS, UK
`jian.dai@kcl.ac.uk, wruiqin@foxmail.com`

Abstract. This paper proposes two novel Sarrus-extended reconfigurable mechanisms via adding revolute joint to each limb of Sarrus linkage. The two mechanisms are assembled by the limbs with line and plane symmetry, respectively. Reconfiguration of the two mechanisms is revealed in the context of reciprocity of screws separately. Firstly, in light of the inherent geometric property of the mechanisms under the general configuration, the mechanisms reveal four distinct motion branches: a Sarrus linkage, two planar 4R linkages, and an overconstrained 6R linkage. Among the evolved motion branch, motion characteristic of the two mechanisms is illustrated under the specific configuration. Further, the specific configuration of the two mechanisms is identified to be singular, respectively. The two mechanisms under the singular configuration possess the characteristics of deployability and kinematotropy. The results show that the proposed mechanisms have the ability to reconfigure their branches and change their configurations. Finally, both of the proposed mechanisms extend the motion characteristic of the original Sarrus linkage.

Keywords: Reconfigurable mechanism, Sarrus linkage, Reconfiguration, Motion branch, Screw theory.

1   Introduction

Reconfigurable mechanisms have maintained their fascination to researchers, which are developed based on kinematotropic linkages [1] and metamorphic mechanisms [2] in the 1990s. Different from traditional mechanisms with fixed degree of freedom (DOF), reconfigurable mechanisms can change their configurations to fulfill variable tasks and meet various working requirements. With the thriving progress of cross-disciplinary science and technology, the studies about the reconfigurable mechanisms were obviously increased, especially the design approaches to achieving reconfiguration.

An intuitive approach was presented to obtain different reconfigurable mechanisms via integrating and merging existing linkages as the source of design. The pioneering construction works were mainly classified into the Bennett-based linkages [3, 4] and the Bricard-related linkages [5, 6]. The former contributed to create new reconfigurable mechanisms by combining several Bennett linkages, and further removing the

2

common links or joints. The latter was obtained by devising certain symmetric properties. Recently, the explorations of distinct incorporated types of linkages were recently revealed. Pfurner et al. [7] presented a class of single-loop 7-link mechanisms based on the concatenation of the Bennett and the overconstrained RPRP mechanisms. Guo et al. [8] proposed a series of spatial overconstrained linkages by combining Bennett linkages. Chai and Dai [9] put forward three novel metamorphic and reconfigurable linkages by combining Waldron's double-Bennett hybrid linkage and Bricard linkages.

Another design approach for creating reconfigurable mechanisms is to insert joint into classical linkages. A class of variable-DOF reconfigurable mechanisms were proposed by inserting two joints to an overconstrained mechanism [10]. Song et al. [11] created a novel 6R metamorphic mechanism by inserting two revolute joints to a Bennett mechanism. Kang et al. [12, 13] proposed a class of novel Schatz-inspired metamorphic mechanisms via adding a revolute joint to Schatz linkage. Further, the design approach was extended via inserting the reconfigurable joint to mechanisms. With the novel reconfigurable Hooke (rT) joint [14], the variable-axis (vA) joint [15], a variable revolute (vR) joint, and the lockable joint [16], various reconfigurable mechanisms were constructed to enrich the field of reconfigurable mechanisms.

Among the reconfigurable mechanisms, Sarrus linkage [17] is a typical spatial 6R mechanism that composed of two sets of three adjacent parallel axes. It converted circular motion to linear motion, and further is extended to utilize in potential applications, such as deployable structures [18], robotic arm [19]. By adding revolute joint to Sarrus linkage can generate several reconfigurable mechanisms. He et al. [20] presented a novel reconfigurable 7R mechanism with multiple operation modes via adding a revolute joint to Sarrus linkage. Tang et al. [21] presented a novel 8R metamorphic mechanism by inserting two revolute joints to Sarrus linkage. In 2018, Xiu et al. [22] presented a Sarrus-like overconstrained eight-bar linkage for the first time with one extra revolute joint in each limb.

Inspired by the above works, two novel Sarrus-extended reconfigurable mechanisms are proposed by inserting a revolute joint to each limb of the Sarrus linkage. The two limbs are integrated with two types: line symmetry and plane symmetry. The paper is organized as follows. Section 2 presents the geometry of the two mechanisms. Section 3 gives the reconfiguration of the plane-symmetric Sarrus-extended reconfigurable mechanism. In Section 4, the reconfigurability of the line-symmetric Sarrus-extended reconfigurable mechanism is illustrated in detail. The conclusions in Section 5 end the paper.

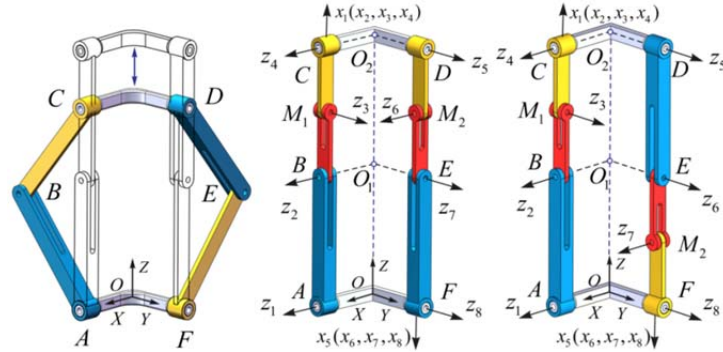## 2   Geometry of Two Novel Sarrus-Extended Mechanisms

Fig. 1. Two Sarrus-extended mechanisms from original Sarrus mechanism (a) Original mechanism (b) plane symmetry (c) line symmetry

Inspired by the pioneer works, two novel Sarrus-extended reconfigurable mechanisms are proposed via inserting a revolute joint to each limb of the Sarrus linkage as seen in Fig. 1. The mechanisms are integrated by a base AF, a moving platform CD, and two identical limbs, composed of joints A, B, C, M_1 and D, E, F, M_2, respectively. When the two identical limbs are integrated with plane symmetry, the plane-symmetric mechanism is seen in Fig. 1(b). Alternatively, the line-symmetric mechanism is integrated by the limbs with line symmetry as seen in Fig. 1(c).

To facilitate the analysis, a coordinate frame O-XYZ is attached to the base AF as follows: the X-axis is aligned with the axis of joint A, the Y-axis is along the axis of joint F and the Z-axis is set following the right-handed rule.

Hence, the geometrical parameters of the plane symmetric mechanism are shown in Fig. 1(b) with the conditions that

$$a_{12} = a_{78} = \mathrm{a}, a_{23} = a_{34} = a_{56} = a_{67} = \mathrm{a}/2, a_{45} = a_{81} = 0$$

$$\begin{cases} \alpha_{12} = \alpha_{78} = 0, \alpha_{23} = \alpha_{45} = \alpha_{56} = \alpha_{81} = \pi/2 \\ \alpha_{34} = \alpha_{67} = -\pi/2 \end{cases} \quad (1)$$

$$\begin{cases} d_1 = d_5 = \mathrm{a}/2 \\ d_2 = d_3 = d_4 = d_6 = d_7 = d_8 = 0 \end{cases}$$

The geometrical parameters of the line symmetric mechanism are written as

$$a_{12} = a_{56} = \mathrm{a}, a_{23} = a_{34} = a_{67} = a_{78} = \mathrm{a}/2, a_{45} = a_{81} = 0$$

$$\begin{cases} \alpha_{12} = \alpha_{56} = 0, \alpha_{23} = \alpha_{45} = \alpha_{67} = \alpha_{81} = \pi/2 \\ \alpha_{34} = \alpha_{78} = -\pi/2 \end{cases} \quad (2)$$

$$\begin{cases} d_1 = d_5 = \mathrm{a}/2 \\ d_2 = d_3 = d_4 = d_6 = d_7 = d_8 = 0 \end{cases}$$

where $a_{i(i+1)}$ is the normal distance between axes z_i and z_{i+1}, $\alpha_{i(i+1)}$ is twist angle from z_i and z_{i+1} positively about axis x_i, and d_i is normal distance between axes

4

x_{i-1} and x_i positively about axis z_i, θ_i is rotation angle from x_{i-1} to x_i positively about axis z_i, $a > 0$ based on the geometric conditions.

3 Reconfiguration of The Plane-Symmetric Reconfigurable Mechanism

In this section, motion characteristics of the plane-symmetric Sarrus-extended reconfigurable mechanism are unveiled due to the unique geometry.
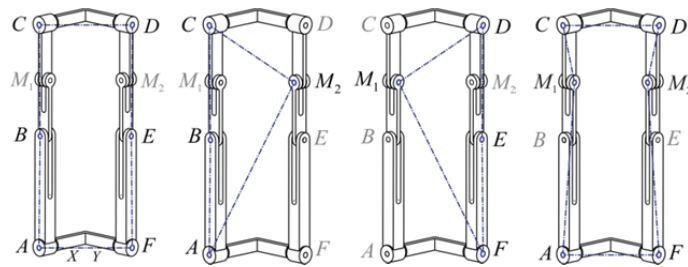

Fig. 2. Four motion branches evolved from the general configuration (a) Motion branch MB_1 (b) Motion branch MB_2 (c) Motion branch MB_3 (d) Motion branch MB_4

Figure 2 shows a general configuration of the plane-symmetric Sarrus-extended reconfigurable mechanism, the moving platform CD is parallel to the base AF, and the axes of joints A and F intersect at point O, the points O_1 and O_2 are the intersections of joints B, E and C, D, respectively. According to the unique axes disposition of the mechanism, it can move to four motion branches by passing this transitory position.

In the first motion branch MB_1, the mechanism turns into a Sarrus linkage as shown in Fig. 2(a), composed of the effective joints A to F. The second motion branch MB_2 in Fig. 2(b) is a planar 4R linkage composed of the effective joints A, B, C, and M_2. Symmetrically, the third motion branch MB_3 in Fig. 2(c) is also a planar 4R linkage composed of the effective joints D, E, F, and M_1. The fourth motion branch MB_4 in Fig. 2(d) is a plane-symmetric 6R linkage composed of the effective joints A, M_1, C, D, M_2, and F. Based on the geometrical parameters, the evolved linkage is identified to be an overconstrained 6R linkage.
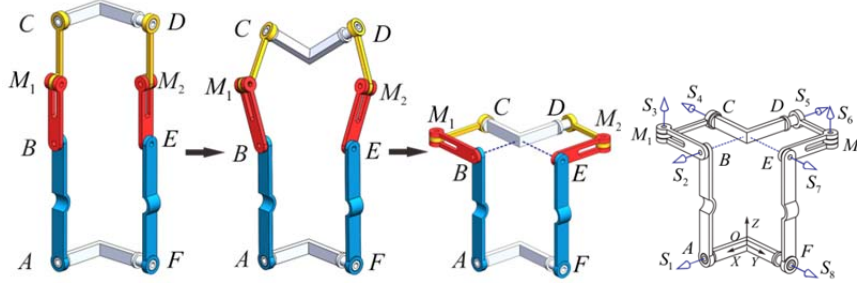
Fig. 3. Concomitant motion in branches MB$_1$ and MB$_4$ and its resultant specific configuration

Among the evolved motion branches MB$_1$ and MB$_4$, the concomitant motion of the mechanism is given in Fig. 3, and then a specific configuration is obtained. The axes of joints B and C are collinear with the joint axes D and E, respectively. A global reference frame O-XYZ is located at the intersection point of joint axes A and F, the X-axis is aligned with the axis of joint A, and the Y-axis is along with the orientation of joint axis F.

The single loop mechanism can be supposed to be a parallel mechanism with two limbs $\mathbb{S}_{l1}$ and $\mathbb{S}_{l2}$ composed of joints A, B, C, M$_1$ and D, E, F, M$_2$, respectively.

$$\mathbb{S}_{l1} = \begin{cases} \boldsymbol{S}_1 = \left(1,0,0,0,0,0\right)^{\mathrm{T}} \\ \boldsymbol{S}_2 = \left(1,0,0,0,a,0\right)^{\mathrm{T}} \\ \boldsymbol{S}_3 = \left(0,0,1,-a/2,-a/2,0\right)^{\mathrm{T}} \\ \boldsymbol{S}_4 = \left(0,-1,0,a,0,0\right)^{\mathrm{T}} \end{cases}, \quad \mathbb{S}_{l2} = \begin{cases} \boldsymbol{S}_5 = \left(-1,0,0,0,-a,0\right)^{\mathrm{T}} \\ \boldsymbol{S}_6 = \left(0,0,1,a/2,a/2,0\right)^{\mathrm{T}} \\ \boldsymbol{S}_7 = \left(0,1,0,-a,0,0\right)^{\mathrm{T}} \\ \boldsymbol{S}_8 = \left(0,1,0,0,0,0\right)^{\mathrm{T}} \end{cases} \quad (3)$$

The mechanism constraint-screw system composed of $\mathbb{S}_{l1}^r$ and $\mathbb{S}_{l2}^r$ is reciprocal to motion-screw system derived as

$$\mathbb{S}_{l1}^r = \begin{cases} \boldsymbol{S}_{11}^r = \left(1,0,0,0,a,a/2\right)^{\mathrm{T}} \\ \boldsymbol{S}_{12}^r = \left(0,0,1,0,0,0\right)^{\mathrm{T}} \end{cases}, \quad \mathbb{S}_{l2}^r = \begin{cases} \boldsymbol{S}_{21}^r = \left(0,1,0,-a,0,-a/2\right)^{\mathrm{T}} \\ \boldsymbol{S}_{22}^r = \left(0,0,1,0,0,0\right)^{\mathrm{T}} \end{cases} \quad (4)$$

The total constraint-screw multiset of the mechanism combines the two basis sets,

$$\left\langle \mathbb{S}^r \right\rangle = \mathbb{S}_{l1}^r \uplus \mathbb{S}_{l2}^r \quad (5)$$

Hence, the mobility m can be calculated from the modified Grübler-Kutzbach mobility criterion [23-25] as:

$$m = \sum_{i=1}^g f_i - 6l + \mathrm{card}\left\langle \mathbb{S}^r \right\rangle - \dim \mathbb{S}^r \quad (6)$$

where g is the number of joints, f_i is the degree of freedom of the i th joint, l expresses the number of independent loops, $\mathrm{card}\left\langle \mathbb{S}^r \right\rangle$ represents the cardinal number of the constraint-screw multiset, and $\dim \mathbb{S}^r$ denotes the dimension of the constraint-screw system.

6

Thus, $l=1$, $\text{card}\langle \mathbb{S}^r \rangle =4$, $\dim \mathbb{S}^r =3$. According to Eqs. (5) and (6), the mobility is $m=8-6\times 1+4-3=3$.

Taking the reciprocal of $\langle \mathbb{S}^r \rangle$ gives the platform CD motion-screw system $\mathbb{S}_f$ with the basis,

$$\mathbb{S}_f = \begin{cases} \boldsymbol{S}_{f1} = (1,0,0,0,a,0)^{\text{T}} \\ \boldsymbol{S}_{f2} = (0,1,0,-a,0,0)^{\text{T}} \\ \boldsymbol{S}_{f3} = (0,0,1,-a/2,-a/2,0)^{\text{T}} \end{cases} \tag{7}$$

It demonstrates that $\boldsymbol{S}_{f1}$ gives a rotation about the X-axis with position vector $\boldsymbol{r} = (0,0,a)^{\text{T}}$, $\boldsymbol{S}_{f2}$ presents a rotation along the Y-axis with position vector $\boldsymbol{r} = (0,0,a)^{\text{T}}$ and $\boldsymbol{S}_{f3}$ expresses a rotation along the Z-axis with position vector $\boldsymbol{r} = (-a/2,-a/2,0)^{\text{T}}$. Thus, the platform CD under the configuration has three rotational DOFs.
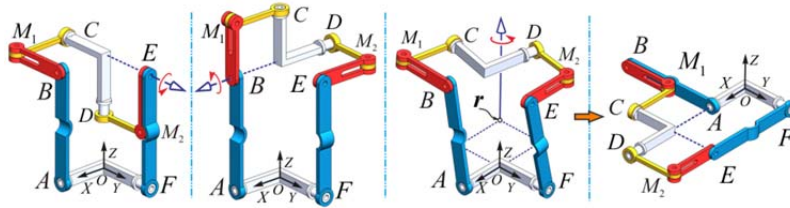
Fig. 4. Three motion branches of the mechanism under the special configuration (a) Branch 1 (b) Branch 2 (c) Branch 3 (d) Flattened configuration

Figure 4 displays three motion branches. When the moving platform CD rotates around collinear axes of joint C and E, it reconfigures to motion branch 1 as shown in Fig. 4(a). Similarly, Figure 4(b) gives branch 2 when the platform rotates about the collinear axes of joints B and D. As shown in Figs 4(c) and 4(d), a flattened configuration is obtained in branch 3 by rotating about the Z-axis with position vector $\boldsymbol{r}$.

In addition, when the mechanism moves out of this configuration in an arbitrary motion branch, the rank of the constraint-screw system increases and the mobility decreases. Hence, the specific configuration of the mechanism is singular referring to [26-28]. The proposed mechanism under this singular configuration possesses the characteristic of kinematotropy.

Figures 2 to 4 demonstrate the reconfiguration of the plane-symmetric Sarrus-extended reconfigurable mechanism. Further, in the evolved motion branch, the specific configuration is demonstrated based on screw theory, which provide distinct motion branches.

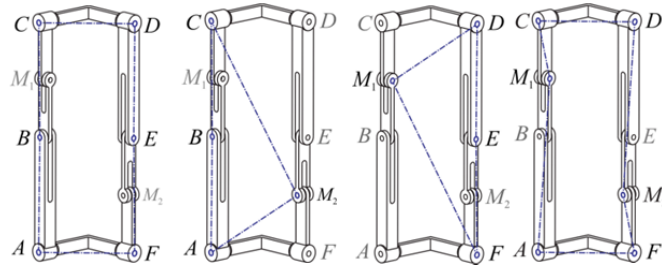# 4   Reconfiguration of The Line-Symmetric Reconfigurable Mechanism

Fig. 5. Four motion branches evolved from the unique joint axes disposition (a) Motion branch MB$_1$ (b) Motion branch MB$_2$ (c) Motion branch MB$_3$ (d) Motion branch MB$_4$

Similarly, as shown in Fig. 5, a novel line-symmetric Sarrus-extended reconfigurable mechanism is composed of two limbs with line symmetry. And the mechanism under this general configuration can reconfigure four motion branches: motion branch MB$_1$ is a Sarrus linkage in Fig. 5(a) and motion branches MB$_2$ and MB$_3$ are two planar 4R linkages in Figs. 5(b) and (c) and an overconstrained 6R linkage in motion branch MB$_4$ as seen in Fig. 5(d).
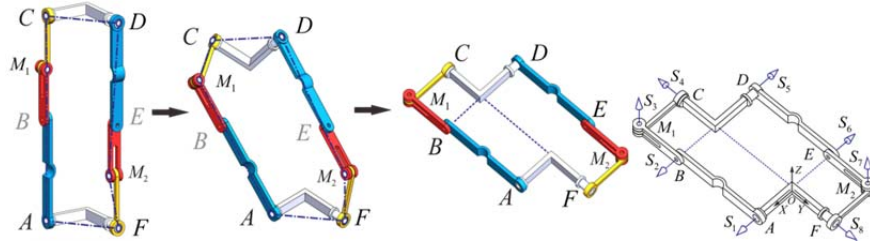
Fig. 6. The reconfiguration evolved from motion branch MB$_4$ and its resultant specific configuration

Figure 6 gives reconfiguration of the mechanism in motion branch MB$_4$, and then a flattened configuration is revealed. Similarly, the mechanism constraint-screw system composed of $\mathbb{S}_{l1}^r$ and $\mathbb{S}_{l2}^r$ is reciprocal to motion-screw system derived as

$$\mathbb{S}_{l1}^r = \begin{Bmatrix} \boldsymbol{S}_{11}^r = \left(1,0,0,0,0,3a/2\right)^{\mathrm{T}} \\ \boldsymbol{S}_{12}^r = \left(0,1,0,0,0,a/2\right)^{\mathrm{T}} \end{Bmatrix}, \quad \mathbb{S}_{l2}^r = \begin{Bmatrix} \boldsymbol{S}_{21}^r = \left(1,0,0,0,0,-a/2\right)^{\mathrm{T}} \\ \boldsymbol{S}_{22}^r = \left(0,1,0,0,0,-a/2\right)^{\mathrm{T}} \end{Bmatrix} \quad (8)$$

Thus, $l=1$, $\mathrm{card}\langle \mathbb{S}^r \rangle = 4$, $\dim \mathbb{S}^r = 3$. According to Eqs. (5) and (6), the mobility is $m = 8 - 6 \times 1 + 4 - 3 = 3$.

Taking the reciprocal of $\langle \mathbb{S}^r \rangle$ gives the platform CD motion-screw system $\mathbb{S}_f$ with the basis,

$$\mathbb{S}_f = \begin{cases} \boldsymbol{S}_{f1} = (1,0,0,0,0,0)^{\mathrm{T}} \\ \boldsymbol{S}_{f2} = (0,1,0,0,0,0)^{\mathrm{T}} \\ \boldsymbol{S}_{f3} = (0,0,0,0,0,1)^{\mathrm{T}} \end{cases} \tag{9}$$

This provides a translation along the Z-axis and two rotations about the X-axis and the Y-axis separately. Thus, the platform CD under the configuration has three DOFs.
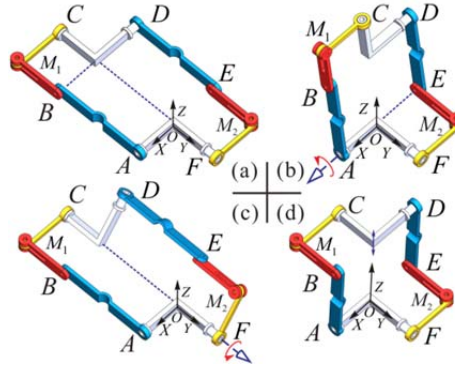

Fig. 7. Three motion branches of the mechanism under the special configuration (a) Original configuration (b) Branch 1 (c) Branch 2 (d) Branch 3

Figure 7 displays three motion branches in accord with three DOFs. When the moving platform CD rotates around collinear axes of joint B and D, it moves to motion branch 1 as shown in Fig. 7(b). Similarly, Figure 7(c) gives branch 2 when the platform rotates about the collinear axes of joints C and F. In addition, branch 3 is obtained by translating along the Z-axis as seen in Fig. 7(d). Similarly, the specific configuration of the mechanism is identified to be singular. The motion characteristic of the proposed mechanism under this singular configuration is kinematotropic.

Similarly, Figures 5 to 7 demonstrate the reconfiguration of the line-symmetric Sarrus-extended reconfigurable mechanism. Among the evolved motion branches, the mechanism can reconfigure a flattened configuration where all the links lie on the same plane. This indicates the structure deployability due to the special geometric arrangement such that the mechanism can be fully expanded and fully folded.

5   Conclusions

In this paper, two novel Sarrus-extended reconfigurable mechanisms are presented by inserting a revolute joint to each limb of the Sarrus linkage. Based on the assembling manners of the two limbs, the plane- and line-symmetric Sarrus-extended reconfigurable mechanisms are identified by the distinct geometry. In terms of the specific axes disposition, the two mechanisms under the general configuration can reconfigure four distinct motion branches: a Sarrus linkage, two planar 4R linkages, and an overconstrained 6R linkage. Among the evolved motion branch, motion characteristic of the specific configuration is investigated based on screw theory. Further, the specific

configuration of the two mechanisms is identified to be singular, respectively. Both of the proposed mechanisms have the ability to change their configurations, including a flattened configuration where all the links lie on the same plane. This indicates the structure deployability due to the special geometric arrangement. In addition, the two mechanisms under the singular configuration possess the characteristic of kinematotropy. Finally, both of the proposed mechanisms extended the motion characteristics of the original Sarrus linkage. The work in this paper contributes to the design and analysis of new reconfigurable mechanisms.

References

1. K. Wohlhart. Kinematotropic Linkages, In: J. Lenarčič and V. Parenti-Castelli (Eds.) Recent Advances in Robot Kinematics, pp. 359-368 Springer Netherlands, Dordrecht(1996).
2. J. S. Dai, J. Rees Jones. Mobility in Metamorphic Mechanisms of Foldable/Erectable Kinds. Journal of Mechanical Design, 121(3), 375-382 (1999).
3. M. Goldberg. New five-bar and six-bar linkages in three dimensions. Transactions of ASME, 65, 649-661 (1943).
4. K. Wohlhart. Merging two general goldberg 5R linkages to obtain a new 6R space mechanism. Mechanism and Machine Theory, 26(7), 659-668 (1991).
5. J. Phillips. Freedom in Machinery: Volume 2, Screw Theory Exemplified Cambridge University Press, (1984).
6. J. E. Baker, H. Min. On spatial networks of overconstrained linkages. Mechanism and Machine Theory, 21(5), 427-437 (1986).
7. M. Pfurner, X. Kong, C. Huang. Complete kinematic analysis of single-loop multiple-mode 7-link mechanisms based on Bennett and overconstrained RPRP mechanisms. Mechanism and Machine Theory, 73, 117-129 (2014).
8. H. Guo, X. Song, L. Li, Z. Deng, R. Liu, J. Geng. Type synthesis of deployable single-loop overconstrained linkages based on Bennett linkages. Mechanism and Machine Theory, 120, 1-29 (2018).
9. X. Chai, J. S. Dai. Three Novel Symmetric Waldron–Bricard Metamorphic and Reconfigurable Mechanisms and Their Isomerization. Journal of Mechanisms and Robotics, 11(5), (2019).
10. X. Kong, M. Pfurner. Type synthesis and reconfiguration analysis of a class of variable-DOF single-loop mechanisms. Mechanism and Machine Theory, 85, 116-128 (2015).
11. Y. Song, X. Ma, J. S. Dai. A novel 6R metamorphic mechanism with eight motion branches and multiple furcation points. Mechanism and Machine Theory, 142, 103598 (2019).
12. X. Kang, H. Feng, J. S. Dai, H. Yu. High-order based revelation of bifurcation of novel Schatz-inspired metamorphic mechanisms using screw theory. Mechanism and Machine Theory, 152, 103931 (2020).
13. X. Kang, X. Ma, J. S. Dai, H. Yu. Bifurcation variations and motion-ruled-surface evolution of a novel Schatz linkage induced metamorphic mechanism. Mechanism and Machine Theory, 150, 103867 (2020).
14. D. Gan, J. S. Dai, Q. Liao. Constraint analysis on mobility change of a novel metamorphic parallel mechanism. Mechanism and Machine Theory, 45(12), 1864-1876 (2010).

10

15. K. Zhang, J. S. Dai, Y. Fang. Topology and Constraint Analysis of Phase Change in the Metamorphic Chain and Its Evolved Mechanism. Journal of Mechanical Design, 132(12), (2010).

16. C. Zhao, H. Guo, R. Liu, Z. Deng, B. Li. Design and Kinematic Analysis of a 3RRlS Metamorphic Parallel Mechanism for Large-Scale Reconfigurable Space Multifingered Hand. Journal of Mechanisms and Robotics, 10(4), (2018).

17. P. Sarrus. Note Sur la Transformation des Mouvements Rectilignes Alternatifs, en Mouvements Circulaires, et Reciproquement, Comptes. Rendus. Acad. Sci., Paris, 36, 1036 (1853).

18. S. Lu, D. Zlatanov, X. Ding, R. Molfino, M. Zoppi. Novel Deployable Mechanisms With Decoupled Degrees-of-Freedom. Journal of Mechanisms and Robotics, 8(2), (2015).

19. S.-J. Kim, D.-Y. Lee, G.-P. Jung, K.-J. Cho. An origami-inspired, self-locking robotic arm that can be folded flat. Science Robotics, 3(16), eaar2915 (2018).

20. X. He, X. Kong, D. Chablat, S. Caro, G. Hao. Kinematic analysis of a single-loop reconfigurable 7R mechanism with multiple operation modes. Robotica, (2014).

21. Z. Tang, P. Qi, J. S. Dai. Mechanism design of a biomimetic quadruped robot. Industrial Robot: An International Journal, 44(4), 512-520 (2017).

22. H. Xiu, K. Wang, G. Wei, L. Ren, J. S. Dai. A Sarrus-like overconstrained eight-bar linkage and its associated Fulleroid-like platonic deployable mechanisms. Proceedings of the Institution of Mechanical Engineers, Part C: Journal of Mechanical Engineering Science, 234(1), 241-262 (2020).

23. K. H. Hunt. Kinematic geometry of mechanisms Oxford University Press, USA, (1978).

24. Z. Huang, Q. C. Li. General Methodology for Type Synthesis of Symmetrical Lower-Mobility Parallel Manipulators and Several Novel Manipulators. The International Journal of Robotics Research, 21(2), 131-145 (2002).

25. J. S. Dai, Z. Huang, H. Lipkin. Mobility of Overconstrained Parallel Mechanisms. Journal of Mechanical Design, 128(1), 220-229 (2004).

26. D. Zlatanov, I. A. Bonev, C. M. Gosselin. In: Proceedings 2002 IEEE International Conference on Robotics and Automation (Cat. No.02CH37292), vol. 1, pp. 496-502 vol.1. (2002).

27. Q. C. Li, J. M. Herve. Parallel Mechanisms With Bifurcation of Schoenflies Motion. IEEE Transactions on Robotics, 25(1), 158-164 (2009).

28. S. Yang, Y. Li. Classification and analysis of constraint singularities for parallel mechanisms using differential manifolds. Applied Mathematical Modelling, 77, 469-477 (2020).

Optimal Design of a 6-DOF Reconfigurable Parallel Mechanism

Pengda Ye[1], Jingjing You[1], Xin Qiu[1], Shuai Xu[1], Yu Ru[1]

[1] College of Mechanical and Electronic Engineering, Nanjing Forestry University, Nanjing 210037, China
youjingjing251010@njfu.edu.cn

Abstract. Aiming at obtaining a larger workspace volume, a novel six degrees of freedom (6-DOF) reconfigurable parallel mechanism (RPM) is designed, and its structure parameters and driving modes are optimized. A kind of triple compound spherical joint and a kind of metamorphic prismatic joint are designed, and 81 driving modes are realized by switching actuated and passive modes. Based on the interval analysis theory, an interval discretization method (IDM) involving the prediction and correction of workspace is proposed to determine the workspaces of parallel mechanisms. Then an accurate and reliable method of the workspace volume calculation is put forward by introducing the critical interval multiplier. The structure parameters and driving modes of 2-2-2 configuration are optimized. The results show that: (i) the side length of the moving platform has no effect on the workspace volume; (ii) the workspace volume after reconstruction increases by about 2.80 times than that before reconstruction; and (iii) the reverse layout of actuated prismatic joints of the mechanism is more restrictive to the workspace volume than the identical layout. The research conclusions lay a theoretical foundation for practical applications.

Keywords: Reconfigurable Parallel Mechanism, Interval Discretization method, Optimal Design.

1 Introduction

With the development of science and technology and the advancement of the industrial revolution, the demand for multi-functional mechanisms in modern production operations is increasing [1]. Mechanisms with a fixed degree of freedom (DOF) and a single operation mode are limited by its own structure, and it is difficult to meet the requirements of different tasks and working conditions. Therefore, the reconfigurable parallel mechanism (RPM) has attracted widespread attention from domestic and foreign scholars [2,3].

Compared with the parallel mechanism with a single motion form, RPM can realize the change of the motion form, thereby improving the motion performance of the parallel mechanism. Workspace is one of the important indexes to measure the motion performances of parallel mechanisms, and its size directly affects the application fields

of parallel mechanisms [4,5]. In order to obtain a larger workspace, some scholars optimized the structure parameters of parallel mechanisms. Liu et al. [6] proposed a new type of 2TIR parallel mechanism, determined the reachable position workspace of the moving platform through the discrete point search method, and optimized the structure parameters of the mechanism. Ye et al. [7] proposed a novel parallel manipulator with remote center of motion for minimally invasive surgery, determined the workspace using a discrete point search method, and improved the global performance by optimal design. Li et al. [8] proposed a novel 2-2 PRUR parallel mechanism, and reasonable structure parameters are obtained by optimizing workspace with the principle of maximizing scattered points. However, the ideas of these workspace calculation methods are essentially point discretization. The boundary of the point discrete workspace is not smooth, and its volume is difficult to evaluate, so it is not very suitable for optimal design.

In view of these, some scholars proposed some methods to determine the workspace based on the interval analysis. Chablat et al. [9] analyzed the workspaces of two 3-DOF translational parallel mechanisms (namely, the Orthoglide and the UraneSX mechanisms) based on the interval analysis to find the largest regular dextrous workspace. FarzanehKaloorazi et al. [10] proposed an interval-based approach in order to obtain the obstacle-free workspace of parallel mechanisms, where the mechanical stroke of actuators, collision between limbs and obstacles, and limb interference were taken into account. Ye et al. [11] designed two 10 limbs parallel mechanisms (i.e., 10-6 and 10-5 configurations), and the position and orientation workspaces were studied by interval analysis method. However, there have been few study conducted on the workspace prediction. This paper adds the process of the workspace prediction on the basis of Ref. [11], which further improves the numerical behavior of the algorithm. Generally speaking, the method of increasing the workspace mostly adopts optimization design, while the method of increasing the workspace through the reconstruction is rarely studied [12-14]. This paper presents a new 6-DOF RPM (namely 9-3 RPM), and optimizes its structure parameters and driving modes to obtain a larger workspace volume. This mechanism was invented by our research group [15], and realized the reconstruction by switching the working modes of the metamorphic prismatic joints, thereby improving its ability to adapt to working conditions.

The remaining paper is organized as follows. Section 2 describes the structure model and reconstruction principle of the 9-3 RPM in detail. Section 3 elaborates the interval discretization method (IDM) and the principle of the workspace volume calculation. Section 4 optimizes the structure parameters and driving modes of the 9-3 RPM. Conclusions are drawn in Sec. 5.

2   Configuration Description

The 9-3 RPM is composed of a hollow cubic fixed platform, a triangular moving platform, nine general spherical joints, three triple compound spherical joints, nine metamorphic prismatic joints, and other component parts, as shown in Fig. 1. The nine general spherical joints are connected to the fixed platform, and the three triple compound

spherical joints are connected to the moving platform. In the initial state, the geometric center of the fixed platform coincides with the geometric center of the moving platform, and the orientations of the fixed and moving platforms are the same. When the metamorphic prismatic joints are driven, the pose (position and orientation) of the moving platform changes, thereby realizing the movement of the moving platform.

As shown in Fig. 2, in order to reduce the coupling degree of the mechanism, a triple compound spherical joint is designed [16], which is mainly composed of the first-layer joint, the second-layer joint, the third-layer joint and the central column. The central column is connected with the moving platform, and the first-, second-, and third-layers joints are connected with the metamorphic prismatic joints. The three-layers joints all have three mutually perpendicular rotation axes, and the rotation axes always intersect at the point B_i (i=1, 2, 3).

As shown in Fig. 3, in order to realize the reconfiguration of the mechanism, a metamorphic prismatic joint that can switch the actuated and passive modes is designed, which is mainly composed of a follower rod, an inner sleeve, an outer sleeve and a conversion sleeve [17]. The follower rod and the inner sleeve are in a sliding connection, and the inner sleeve and the outer sleeve are in a threaded connection. As explained in detail in Ref. [17], two working modes of this kind of prismatic joint can be switched from one to another by means of simple manual operations, as follows:

(i) *Actuated mode*: Being activated when its follower rod and conversion sleeve are fitted together by means of a specially designed bolt-nut device and the outer sleeve is driven by an external torque.

(ii) *Passive mode*: Being activated when its follower rod and conversion sleeve are not fitted together and there is no driving torque exerted on the outer sleeve.
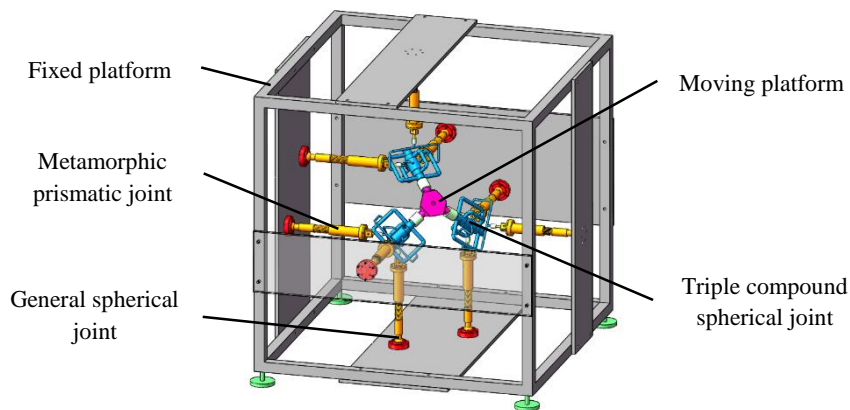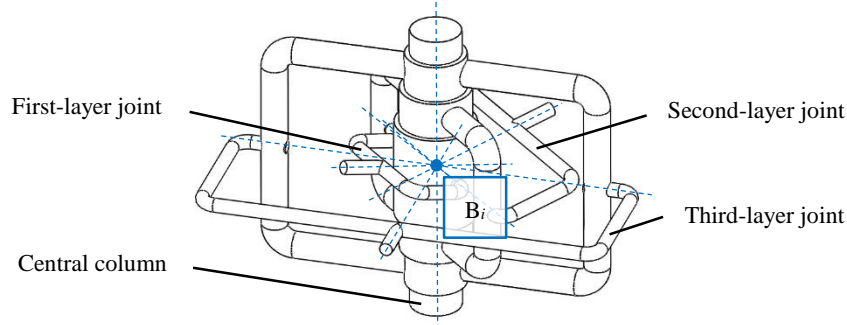

Fig. 1. Structure model of 9-3 RPM

Fig. 2. Structure model of triple compound spherical joint
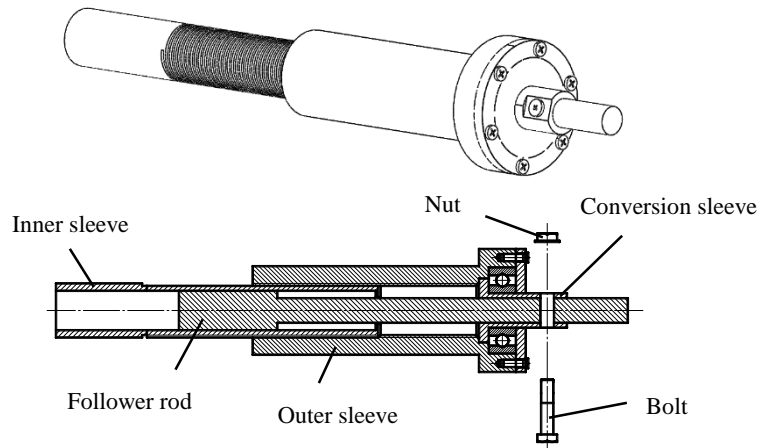

Fig. 3. Three-dimensional and cross-sectional views of metamorphic prismatic joint

3   Workspace Determination Based on Interval Analysis

3.1   Interval Discretization Method

The general idea of the algorithm can be summed up as the combination of the forward prediction and the inverse correction. The procedure of IDM contains seven steps that are organized gradationally as follows.

Initialization: (i) establish a fixed coordinate frame attached to the fixed platform and a moving coordinate frame attached to the moving platform of a parallel mechanism; (ii) determine that the inputs are the lengths of the limbs or the rotation angles of the revolute joints and the outputs are the pose of the moving platform; and (iii) set the preset intervals of the inputs ($[\mathbf{L}]$) and the preset interval width of the outputs (ε).

Step 1: According to the analytic forward kinematic (AFK) of a parallel mechanism, substituting $[\mathbf{L}]$ into the expressions of the AFK, the predicting region of the reference

point of the moving platform can be obtained, which contains the actual workspace. This process is called the workspace prediction.

Step 2: Based on the geometric constraint relationship of a parallel mechanism, the expressions of the analytic inverse kinematic (AIK) are derived.

Step 3: According to the results of the workspace prediction in *Step 1*, the initial box of the workspace is given. The initial box is substituted into the expressions obtained in *Step 2*, then the calculation values of the input intervals ($[l]_k$ ($k=0, 1, …, n$)) are obtained (where the subscript k denotes the kth calculation value of the input interval and n denotes the number of the interval bisection).

Step 4: Comparing $[l]_k$ and $[L]$, there are three probable conditions:
- For all inputs, if $[l]_k \subseteq [L]$, the box which lies inside the workspace is stored in the internal interval set (W_{in});
- For at least one input, if $[l]_k \cap [L] = \varnothing$, the box which lies outside the workspace is stored in the external interval set (W_{out});
- Other conditions indicate that the box is located at the workspace boundary, and the box is stored in the boundary interval set (W_{bou}), then empty the search interval set (S).

Step 5: The interval width (ε_k) of the box in W_{bou} is calculated. Comparing ε_k and ε, there are two probable conditions:
- If $\varepsilon_k \leq \varepsilon$, go to *Step 7*;
- If $\varepsilon_k > \varepsilon$, all boxes in W_{bou} will get bisected. The intervals in W_{bou} are divided into two sub-intervals, and several sub-boxes composed of sub-intervals are generated and stored in S.

Step 6: Empty W_{bou} and substitute the sub-boxes in S into the expressions obtained in *Step 2* in turn, then $[l]_k$ are obtained and go back to *Step 4*.

Step 7: According to W_{in}, W_{out}, and W_{bou} obtained in *Step 4*, all boxes are portrayed by the straight-line frame to constitute the workspace of a parallel mechanism.

3.2 Principle of Workspace Volume Calculation

For the three-dimensional (3D) position workspace, the interval discrete workspace is composed of a large number of 3D boxes. Figure 4 shows the schematic diagram of a single 3D box in the interval discrete workspace, and the volume of a single 3D box can be presented as
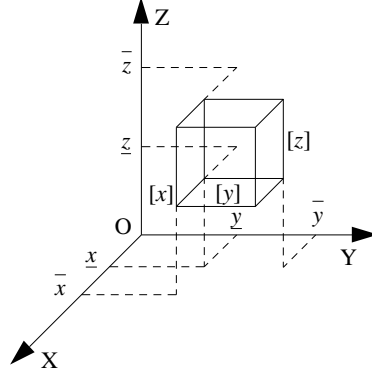
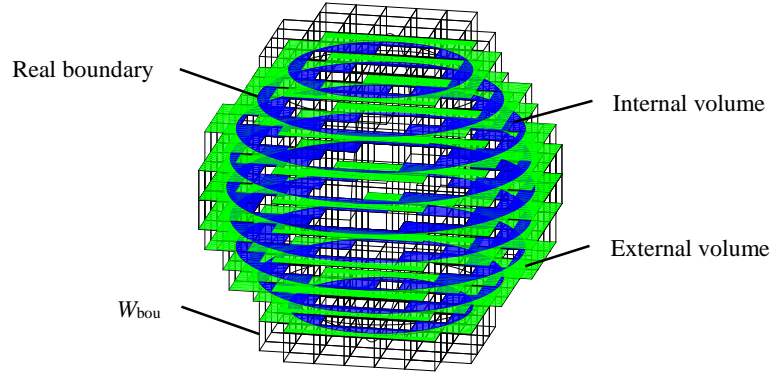**Fig. 4.** A single 3D box in the interval discrete workspace

Fig. 5. Real boundary and W_{bou} of 3D boxes

$$V_{\text{single}} = \left(\overline{x} - \underline{x}\right) \times \left(\overline{y} - \underline{y}\right) \times \left(\overline{z} - \underline{z}\right) \tag{1}$$

where $\overline{\bullet}$ and $\underline{\bullet}$ denote the upper and lower bounds of the interval $[\bullet]$, respectively.

Therefore, the volume of the interval discrete workspace can be regarded as the sum of volumes of all 3D boxes in W_{in} and W_{bou}. However, the 3D boxes in W_{bou} are not fully inside the workspace. In other words, part of the boxes in W_{bou} is inside the workspace and the other part is outside, as shown in Fig. 5. In order to obtain the more accurate workspace volume, the critical interval multiplier λ_{V} is introduced here, and λ_{V} is set equal to 0.5, which represents the ratio of the internal volume to the external volume of boxes in W_{bou}. The volume calculation formula of the interval discrete workspace is defined as

$$V = V_{W_{\text{in}}} + \lambda_{\text{V}} V_{W_{\text{bou}}} \tag{2}$$

where $V_{W\text{in}}$ and $V_{W\text{bou}}$ represent the volumes of W_{in} and W_{bou}, respectively.

4 Optimal Design

4.1 Parameter Optimization

In order to optimize geometric parameters of the 9-3 RPM and obtain a larger workspace volume, the workspace volumes are calculated when geometric parameters vary, so as to analyze the influence of geometric parameters on the workspace volume. This paper does not consider the singularity of the mechanism, which will be studied in another paper. The number of actuated prismatic joints is nine and the strokes of the limbs are all set from 15 mm to 35 mm. Figure 6 shows the volumes of the zero-orientation position workspace with full actuation under different geometric parameters, where N denotes the distance between the geometric center of the triple compound spherical joint and the geometric center of the fixed platform in the initial state and L denotes the initial lengths of the limbs. Meaningfully, the workspace volume is the maximum near at L=24 mm, and the distance between the geometric centers of the triple compound spherical joints has no effect on the workspace volume.
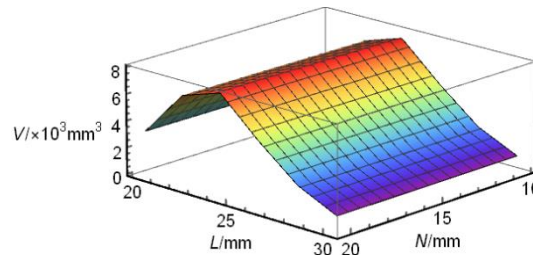
Fig. 6. Workspace volumes under different geometric parameters

4.2 Actuation Optimization

According to the three triple compound spherical joints, the nine metamorphic prismatic joints can be divided into three groups, i.e., the first group is P_1, P_2, and P_3, the second group is P_4, P_5, and P_6, and the third group is P_7, P_8, and P_9, where P_j (j=1, 2, …, 9) represents the jth metamorphic prismatic joint. In this section, the number of actuated prismatic joints is set to 6, so there are three passive prismatic joints. The 81 6-DOF driving modes can be classified into two categories: (i) 2-2-2 configuration, which means two metamorphic prismatic joints in each group are chosen as the actuators (totally including 27 driving modes, as listed in Table 1, where symbols "√" and "×" represent that the metamorphic prismatic joint is in the actuated mode and passive mode, respectively); and (ii) 3-2-1 configuration, which means three, two, one metamorphic prismatic joint in each group is chosen as the actuator, respectively (totally including 54 driving modes). Due to the space limitation, only the driving modes of the 2-2-2 configuration are optimized here, and the 3-2-1 configuration will be studied in another paper.

As can be seen from Table 1, the driving mode number <0> represents the mechanism with 9 actuated prismatic joints where the redundancy is equal to 3. Figure 7

shows the workspace volumes of different driving modes from Table 1. The red solid line represents the workspace volume of <0>, which is equal to 6.3524×10^3 mm^3. We find that the workspace volume of <0> is less than or equal to that of other driving modes, which indicates that redundant actuation will not increase the workspace volume of the mechanism. Obviously, the driving mode of <6> has the largest workspace volume equaling to 17.7900×10^3 mm^3, and the workspace volumes of <16> and <20> are the same as that of <0>. From the analysis of the layouts of the actuated prismatic joints, the actuated prismatic joints of <6> are all identical layout along the x-, y-, and z-axes directions.

Table 1. Driving modes of 2-2-2 configuration

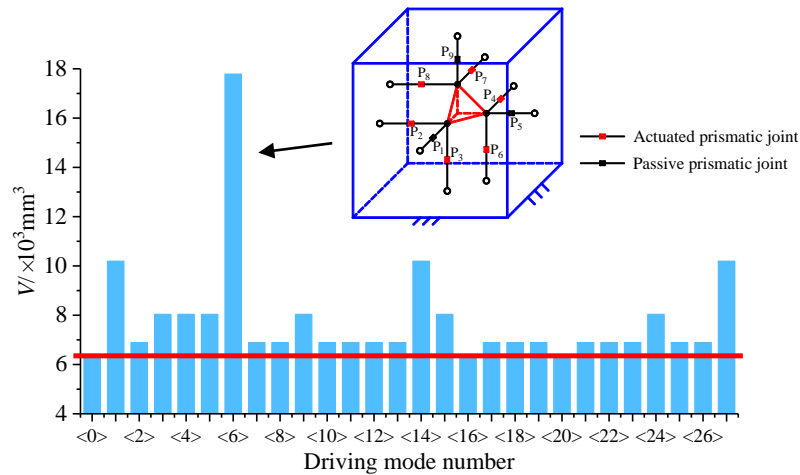| Driving mode number	The first group			The second group			The third group		
	P_1	P_2	P_3	P_4	P_5	P_6	P_7	P_8	P_9
<0>	√	√	√	√	√	√	√	√	√
<1>	×	√	√	×	√	√	×	√	√
<2>	×	√	√	×	√	√	√	×	√
<3>	×	√	√	×	√	√	√	√	×
<4>	×	√	√	√	×	√	×	√	√
<5>	×	√	√	√	×	√	√	×	√
<6>	×	√	√	√	×	√	√	√	×
<7>	×	√	√	√	√	×	×	√	√
<8>	×	√	√	√	√	×	√	×	√
<9>	×	√	√	√	√	×	√	√	×
<10>	√	×	√	×	√	√	×	√	√
<11>	√	×	√	×	√	√	√	×	√
<12>	√	×	√	×	√	√	√	√	×
<13>	√	×	√	√	×	√	×	√	√
<14>	√	×	√	√	×	√	√	×	√
<15>	√	×	√	√	×	√	√	√	×
<16>	√	×	√	√	√	×	×	√	√
<17>	√	×	√	√	√	×	√	×	√
<18>	√	×	√	√	√	×	√	√	×
<19>	√	√	×	×	√	√	×	√	√
<20>	√	√	×	×	√	√	√	×	√
<21>	√	√	×	×	√	√	√	√	×
<22>	√	√	×	√	×	√	×	√	√
<23>	√	√	×	√	×	√	√	×	√
<24>	√	√	×	√	×	√	√	√	×
<25>	√	√	×	√	√	×	×	√	√
<26>	√	√	×	√	√	×	√	×	√
<27>	√	√	×	√	√	×	√	√	×

Fig. 7. Workspace volumes of different driving modes

5   Conclusions

(1) A new 6-DOF RPM is invented, which is mainly composed of a kind of triple compound spherical joint whose rotation centers always intersect at one point and a kind of metamorphic prismatic joint that can switch actuated and passive modes.

(2) Using the interval analysis, a workspace determination method including the workspace prediction and the workspace correction, namely IDM, is proposed, and a method of workspace volume calculation is given based on interval boxes.

(3) Based on the goal of the larger workspace volume, the structure parameters and driving modes are optimized. The results show that: (i) the workspace volume of the 9-3 RPM is not affected by the side length of the moving platform; (ii) the workspace volume after reconstruction increases by about 2.80 times than that before reconstruction; and (iii) compared with the reverse layout of actuated prismatic joints of the 9-3 RPM, the identical layout is more conducive to obtaining a larger workspace volume. The research conclusions are of great significance to the further researches and development applications of the 9-3 RPM.

Acknowledgment

References

1. Jiansheng Dai, Xilun Ding, Huijun Zou, Fundamentals and categorization of metamorphic mechanisms. Chinese Journal of Mechanical Engineering 41(6), 7-12 (2005).
2. Jun Wei, Jiansheng Dai, Lie group based type synthesis using transformation configuration space for reconfigurable parallel mechanisms with bifurcation between spherical motion and planar motion. ASME Journal of Mechanical Design 142(6), 063302 (2020).
3. Wei Ye, Xinxue Chai, Ketao Zhang, Kinematic modeling and optimization of a new reconfigurable parallel mechanism. Mechanism and Machine Theory 149, 103850 (2020).
4. Pengda Ye, Jingjing You, Xin Qiu, Linkang Wang, Chenggang Li, Yu Ru, Status and development trend of motion performance in parallel robot. Journal of Nanjing University of Aeronautics & Astronautics 52(3), 363-377 (2020).
5. Hao Li, Yuru Zhang, Dangxiao Wang, Comparative analysis of optimization algorithms in workspace optimization of parallel mechanisms. Journal of Mechanical Engineering 46(13), 61-67 (2010).
6. Jichen Liu, Mengli Wu, Mingxi Wang, Bowen Tian, Cheng Yu, Hengjia Zhu, Kinematic analysis and dimension optimization of a 2T1R parallel mechanism. Journal of Machine Design 37(12), 71-81 (2020).
7. Wei Ye, Zhentao Xie, Qinchuan Li, Kinematics analysis and performance optimization of a parallel manipulator for minimally invasive surgery. Journal of Mechanical Engineering 56(19), 103-112 (2020).
8. Dian Li, Sheng Guo, Guanyu Huang, Fuqun Zhao, Kinematic analysis and workspace optimization of a novel 2-2 PRUR parallel mechanism. Journal of Beijing University of Aeronautics and Astronautics 43(10), 2011-2020 (2017).
9. D. Chablat, Ph. Wenger, F. Majou, J. P. Merlet, An interval analysis based study for the design and the comparison of three-degrees-of-freedom parallel kinematic machines. The International Journal of Robotics Research 23(6), 615-624 (2004).
10. MohammadHadi FarzanehKaloorazi, Mehdi Tale Masouleh, Stephane Caro, Collision-free workspace of parallel mechanisms based on an interval analysis approach. Robotica 35(8), 1747-1760 (2017).
11. Pengda Ye, Jingjing You, Xin Qiu, Linkang Wang, Yu Ru, Forward displacement analysis and workspace of ten links Stewart derivative parallel mechanism. Mechanical Science and Technology for Aerospace Engineering. http://doi.org/10.13433/j.cnki.1003-8728.20200220.
12. Weizhong Zhang, Jinping Li, Min Ye, Chao Yang, Multi-objective optimization of dimensional synthesis for 2-PUR-PSR parallel manipulator. Transactions of the Chinese Society for Agricultural Machinery 51(11), 403-410 (2020).
13. Zhongzhe Chi, Dan Zhang, Lian Xia, Zhen Gao, Multi-objective optimization of stiffness and workspace for a parallel kinematic machine. International Journal of Mechanics and Materials in Design 9, 281-293 (2013).
14. Guanyu Huang, Sheng Guo, Dan Zhang, Haibo Qu, Hongyan Tang, Kinematic analysis and multi-objective optimization of a new reconfigurable parallel mechanism with high stiffness. Robotica 36(2), 187-203 (2018).
15. Chenggang Li, Hongtao Wu, Jingjing You, Redundant parallel six-axis accelerometer and measuring method: China (201010249900.1[P]) 2013 4.
16. Xin Qiu, Jingjing You, Linkang Wang, Libing Zhu, Pengda Ye, A kind of triple compound universal joint: China (201920682793.8[P]) 2020 2.
17. Jingjing You, Xin Qiu, Linkang Wang, Pengda Ye, A kind of convertible master-slave output prismatic joint: China (201910559216.4[P]) 2019 6.

Kinematics and Stability Analysis of a Reconfigurable Parallel Bionic Mobile Robot (RPBMBot)

MI Wenbo[1] MA Chunsheng[1] and LI Ruiqin[1*]

([1] North University of China, Taiyuan 030051, China)
*liruiqin@nuc.edu.cn

Abstract. This paper presents a reconfigurable parallel bionic mobile robot (RPBMBot for short), which can be used in space exploration, disaster relief and rescue applications that include complex terrain. Combining the concept of bionics, the mobile platform and the parallel bionic torso are configured. The kinematics analysis and workspace calculation of the reconfigurable parallel mechanism are carried out using finite screw theory. The mathematical model and stability analysis of the mobile robot's center of gravity are established. The relationship between the center of gravity of the mechanism and the stability margin is solved. This provides a theoretical basis for the drive optimization scheme of mobile robots.

Keywords: RPBMBot, Reconfiguration, Mobile robot, Kinematics, Stability margin

1   Introduction

Mobile robots are a typical representative of intelligent robots and are currently one of the most active research fields. In recent years, more and more reconfigurable parallel mechanisms have been applied to mobile robots to enhance the terrain adaptability of mobile robots. For the kinematics research of parallel mechanism, in addition to traditional methods, the finite screw method has also attracted the attention of many scholars. Screw theory has a concise form and generality of mathematics. It has been deeply and widely used in many scientific fields, especially in the field of mechanism [1]. Sun et al [2] proposed finite and instantaneous screw theory in robotic mechanism. Guo et al [3] presents an optimization-driven planning framework for WHLR with parallel Stewart mechanism by abstracting the robot as a deformable bounding box. It will improve the obstacle negotiation ability of the high degree-of-freedoms robot. Zhang et al [4] proposed an optimal trajectory planning method based on an improved dolphin swarm algorithm to balance localization uncertainty and energy efficiency, such that a minimum total cost trajectory is obtained for wheeled mobile robots. Wang et al [5] proposed an omni-directional mobile robot based on four Mecanum wheels. The mechanical system of the mobile robot is made up of three separable layers so as to simplify its combination and reorganization. Luo et al [6] designed a novel reconfigurable hybrid wheel-track mobile robot (RHMBot) based on a Watt II six-bar linkage, it can provide three locomotion modes as wheel mode, tracked mode, and climbing and roll-over mode. Because the bionic mobile robot draws on the motion characteristics of animals in nature, it has a wide range of applications in the field of multi-legged mobile robots. Qu et al [7] designed a kind of wheel-leg hybrid agricultural quadruped robot, which can achieve walking, dynamic wheel moving, and roller-skating. Spröwitz et al [8] present Oncilla robot, a novel mobile, quadruped legged locomotion machine. This large-cat sized, 5.1 kg robot is one of a kind of a recent, bioinspired legged robot class designed with the capability of model-free locomotion control. Suzuki et al [9]

presented an experimental validation of the cross-coupled sensory feedback control using a developed quadruped robot.

An important evaluation index of a mobile robot is its motion stability. Skonieczny et al [10] presented a novel center-of-gravity (CoG) control algorithm, designed to increase rover mobility over step obstacles. Teng et al [11] present an improved method of constructing CPGs and successfully solve the problem which the quadruped robot can't lift it hind limbs from the ground during a walk gait locomotion. Zhang et al [12] proposed a metamorphic quadruped robot with a moveable trunk. Through trunk twisting, the stability margin of the quadruped robot can be increased compared with that of a quadruped robot with a rigid trunk. Agheli et al [13] provided a method for analyzing and comparing the stable workspace of scalable hexapod robots incorporating the FFSM as the stability margin. Using the presented method for analyzing the stable workspace of scalable hexapod robots, the workspace and the stability of SHeRo are analyzed under different external loading conditions. Zhu et al [14] proposed an arbitrary gait pattern generation algorithm which is effective and have good performance on stability of the robot. Jia et al [15] presented a stability criterion for the motion of quadruped robots with dynamic gaits running over irregular terrain. The traditional zero-moment point (ZMP) is improved to analyze the motion on irregular terrain precisely for dynamic gaits.

This paper presents a reconfigurable parallel bionic mobile robot (RPBMBot for short), which can switch between wheeled walking mode and wheel-footed walking mode, and has good adaptability to complex terrain. Combined with the concept of bionics to design the configuration of the mobile platform and the reconfigurable parallel bionic torso, and use the finite spin theory to analyze the kinematics and calculate the workspace of the reconfigurable parallel mechanism, and establish a mathematical model of the center of gravity of the mobile robot. The relationship between the trajectory of the center of gravity of the mechanism and the stability margin are solved, and the trajectory of the center of gravity is combined to propose an optimization plan for the center of gravity adjustment.

2 Configuration Design of RPBMBot

2.1 Overall configuration

The configuration of the mobile robot is shown in Fig. 1. The parallel drive system is used as a bionic waist to connect the front and rear of the robot. The parallel drive system is equipped with a disc-shaped center of gravity adjustment device to adjust the center of gravity of the waist in real time. To prevent the waist posture change from affecting the center of gravity deviation of the whole vehicle, two independently driven wheels are installed symmetrically at the front and rear of the body. The center of gravity can be adjusted by changing the position of the support triangle when the mechanism is in wheel-footed motion, so as to maintain the stability of the robot.
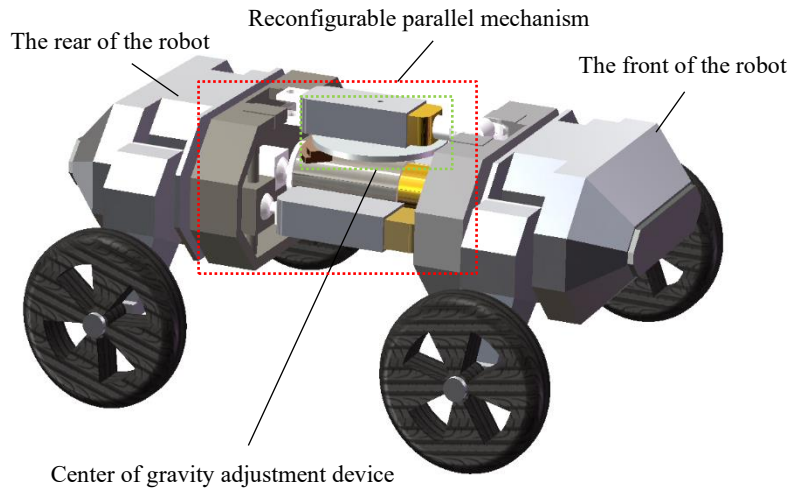
Fig. 1. Overall configuration of RPBMBot.

2.2 2-SPR/UP(vA)/SPS reconfigurable parallel mechanism

The 2-SPR/UP(vA)/SPS parallel mechanism is composed of a static platform, a moving platform, two SPR limbs, UP(vA) limb and SPS limb, as shown in Fig. 2.
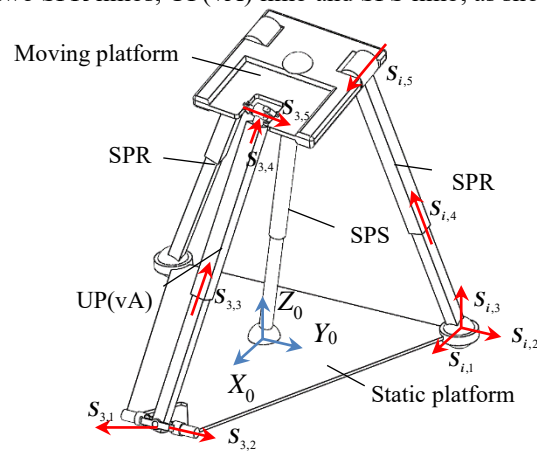

Fig. 2. 2-SPR/UP(vA)/SPS parallel mechanism

The variable axis kinematic pair is abbreviated as vA pair, which is a kinematic pair containing two variable axes. It can be switched to two different forms by rotating the axis. Wei et al [16] conducted related research on this kinematic pair. As shown in Fig. 3(a), when the two axes of the vA pair are in a coincident state, they can be treated as an R pair, called R phase; as shown in Fig. 3(b), when the two axes of the vA pair are in a vertical state, Can be treated as U pair, called U phase. Corresponding to the two configurations of vA, the mechanism also has two configurations of R phase and U phase. The moving platform of the 2-SPR/UP(vA)/SPS parallel mechanism can change

its DOF in the two forms of the vA pair. When the vA pair is located at R phase, the mechanism has 3 DOF, i.e. two rotations around X_0 axis and Y_0 axis, respectively and one translation along Z_0 axis; when the vA pair is located at U phase, the mechanism has 4 DOF, which are two rotations around X_0 axis and Y_0 axis and two translations along Y_0 axis and Z_0 axis, respectively.
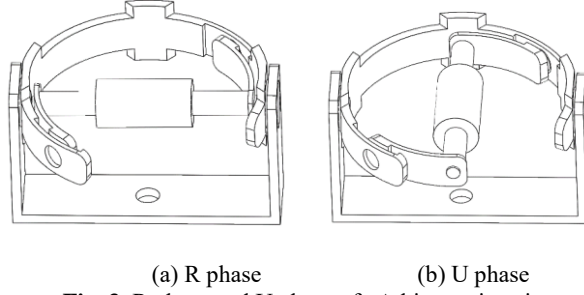
(a) R phase   (b) U phase
Fig. 3. R phase and U phase of vA kinematic pair

3   Kinematics of 2-SPR/UP(vA)/SPS Parallel Mechanism

3.1   Forward kinematics of 2-SPR/UP(vA)/SPS parallel mechanism

In kinematic analysis, when the mechanism is reconstructed to R phase. As shown in Fig. 2, the kinematic equations of the ith limb is expressed as

$$\boldsymbol{S}_{f,i} = 2\tan\frac{\theta_{i,5}}{2}\begin{pmatrix} s_{i,5} \\ r_{i,5}\times s_{i,5} \end{pmatrix}\Delta t_{i,4}\begin{pmatrix} 0 \\ s_{i,4} \end{pmatrix}\Delta 2\tan\frac{\theta_{i,3}}{2}\begin{pmatrix} s_{i,3} \\ r_{i,3}\times s_{i,3} \end{pmatrix}\Delta 2\tan\frac{\theta_{i,2}}{2}\begin{pmatrix} s_{i,2} \\ r_{i,2}\times s_{i,2} \end{pmatrix}\Delta 2\tan\frac{\theta_{i,1}}{2}\begin{pmatrix} s_{i,1} \\ r_{i,1}\times s_{i,1} \end{pmatrix} \quad i=1,2 \tag{1}$$

$$\boldsymbol{S}_{f,i} = 2\tan\frac{\theta_{i,5}}{2}\begin{pmatrix} s_{i,5} \\ r_{i,5}\times s_{i,5} \end{pmatrix}\Delta 2\tan\frac{\theta_{i,4}}{2}\begin{pmatrix} s_{i,4} \\ r_{i,4}\times s_{i,4} \end{pmatrix}\Delta t_{i,3}\begin{pmatrix} 0 \\ s_{i,3} \end{pmatrix}\Delta 2\tan\frac{\theta_{i,2}}{2}\begin{pmatrix} s_{i,2} \\ r_{i,2}\times s_{i,2} \end{pmatrix}\Delta 2\tan\frac{\theta_{i,1}}{2}\begin{pmatrix} s_{i,1} \\ r_{i,1}\times s_{i,1} \end{pmatrix} \quad i=3 \tag{2}$$

where, $\boldsymbol{S}_{f,i}$ denotes the current pose of the end-effector of the ith limb. $\theta_{i,k}$ (k=1,2,3,5 when $i=1,2$, k=1,2,4,5 when $i=3$) is the rotational angle of the kth joint in the ith limb. $\left[\boldsymbol{S}_{i,k}^{\mathrm{T}}\left(\boldsymbol{r}_{i,k}\times\boldsymbol{s}_{i,k}\right)^{\mathrm{T}}\right]^{\mathrm{T}}$ is the axis of the kth joint in the ith limb. $\boldsymbol{t}_{i,4}$ (i = 1,2) and $\boldsymbol{t}_{i,3}$ ($i=3$) are the translational distances. $\left(\mathbf{0} \quad \boldsymbol{s}_{i,3}^{\mathrm{T}}\right)^{\mathrm{T}}$ are the unit screws of the P joints.

Since all the limbs share the same moving platform, the kinematic equation of mechanism can be formulated as

$$\boldsymbol{S}_{f,i} = \boldsymbol{S}_{f,1} = \boldsymbol{S}_{f,2} = \boldsymbol{S}_{f,3} \tag{3}$$

It can be written into simultaneous equations. In total, there are 12 unknown parameters. The number of scalar equations resulted from Eq. (3) is 12. Therefore, the unknown joint parameters can be computed by solving the equations. Finally, the finite motion of the mechanism is obtained by Eq. (1) or Eq. (2).

3.2 Inverse Kinematics of 2-SPR/UP(vA)/SPS Parallel Mechanism

The UP(VA) limbs and the SPR limb share the same moving platform. The inverse kinematics problem of the mechanism can be divided into three inverse kinematics problems of limbs. The kinematic equation of the ith limb can be written as

$$S_{f,i} = f(\theta_{i,1}, \ \theta_{i,2}, \ \theta_{i,3}, \ t_{i,4}, \ \theta_{i,5}) \qquad i = 1, 2 \tag{4}$$

$$S_{f,i} = f(\theta_{i,1}, \ \theta_{i,2}, \ t_{i,3}, \ \theta_{i,4}, \ \theta_{i,5}) \qquad i = 3 \tag{5}$$

The current pose of the moving platform is known in the inverse kinematics problem. The finite motion of the moving platform from the initial pose to the current pose can be expressed by the finite screw as

$$S_{f,i} = 2\tan\frac{\theta_i}{2}\begin{pmatrix} s_i \\ r_i \times s_i \end{pmatrix} + t_i\begin{pmatrix} 0 \\ s_i \end{pmatrix} \tag{6}$$

Substituting Eq. (4) into Eq. (6), yields

$$s_i = f_s(\theta_{i,1}, \ \theta_{i,2}, \ \theta_{i,3}, \ \theta_{i,5}), \qquad \tan\frac{\theta_i}{2} = f_\theta(\theta_{i,1}, \ \theta_{i,2}, \ \theta_{i,3}, \ \theta_{i,5})$$

$$r_i = f_r(\theta_{i,1}, \ \theta_{i,2}, \ \theta_{i,3}, \ t_{i,4}, \ \theta_{i,5}), \qquad t_i = f_t(\theta_{i,1}, \ \theta_{i,2}, \ \theta_{i,3}, \ t_{i,4}, \ \theta_{i,5}) \tag{7}$$

Similarly, substituting Eq. (5) into Eq. (6), yields

$$s_i = f_s(\theta_{i,1}, \ \theta_{i,2}, \ \theta_{i,4}, \ \theta_{i,5}), \qquad \tan\frac{\theta_i}{2} = f_\theta(\theta_{i,1}, \ \theta_{i,2}, \ \theta_{i,4}, \ \theta_{i,5})$$

$$r_i = f_r(\theta_{i,1}, \ \theta_{i,2}, \ t_{i,3}, \ \theta_{i,4}, \ \theta_{i,5}), \qquad t_i = f_t(\theta_{i,1}, \ \theta_{i,2}, \ t_{i,3}, \ \theta_{i,4}, \ \theta_{i,5}) \tag{8}$$

The analytical solutions of all joint parameters are finally obtained by solving Eqs. (7)~(8) using vector and polynomial method.

3.3 Workspace of 2-SPR/UP(vA)/SPS Parallel Mechanism

The position workspace of the mechanism is considered. The position vector of the center of moving platform before the movement of the kth R joint in the ith limb is known as r_0. The distance vector generated by the kth R joint in the kth limb is expressed as

$$d_{i,k} = \left(\exp(\theta_{i,k}\tilde{s}_{i,k}) - E_3\right)\left(r^{k-1} - r_{i,k}\right) \tag{9}$$

Similarly, the distance vector generated by the P joint in the ith limb is given as

$$d_{i,3} = t_{i,4}s_{i,4}, \qquad i = 1, 2 \quad \text{or} \quad d_{i,3} = t_{i,3}s_{i,3}, \qquad i = 3 \tag{10}$$

The position of the ith limb generated by all the joints can be calculated as

$$d_i = \sum_{k=1}^{5} d_{i,k}, \qquad i = 1, 2 \quad \text{or} \quad d_i = \sum_{k=1}^{4} d_{i,k}, \qquad i = 3 \tag{11}$$

d_i can be regarded as a function of joint parameters. Hence, the position workspace of the ith limb can be obtained as

$$\{d_i\} = \left\{ f\left(\theta_{i,1}, \theta_{i,2}, \theta_{i,3}, t_{i,4}, \theta_{i,5}\right) \middle| \begin{array}{c} t_{i,4} \in \left[t_{i,4}^{\mathrm{L}}, t_{i,4}^{\mathrm{U}}\right] \\ \theta_{i,k} \in \left[\theta_{i,k}^{\mathrm{L}}, \theta_{i,k}^{\mathrm{U}}\right], k = 1, 2, 3, 5 \end{array} \right\}, i = 1, 2 \tag{12}$$

$$\{\boldsymbol{d}_i\} = \left\{ f\left(\boldsymbol{\theta}_{i,1}, \boldsymbol{\theta}_{i,2}, \boldsymbol{t}_{i,3}, \boldsymbol{\theta}_{i,4}, \boldsymbol{\theta}_{i,5}\right) \middle| \begin{array}{c} \boldsymbol{t}_{i,3} \in \left[\boldsymbol{t}_{i,3}^{\mathrm{L}}, \boldsymbol{t}_{i,3}^{\mathrm{U}}\right] \\ \boldsymbol{\theta}_{i,k} \in \left[\boldsymbol{\theta}_{i,k}^{\mathrm{L}}, \boldsymbol{\theta}_{i,k}^{\mathrm{U}}\right], k=1,2,4 \end{array} \right\}, i=3 \qquad (13)$$

Finally, the position workspace of the mechanism is computed by the intersection of the position space of each limb as

$$\{\boldsymbol{d}\} = \{\boldsymbol{d}_1\} \cap \{\boldsymbol{d}_2\} \cap \{\boldsymbol{d}_3\}$$

When the mechanism is reconstructed into U phase, the kinematics analysis is the same as above. Thus, the solution process has be omitted.

4 Stability of RPBMBot

4.1 Center of gravity of the mechanism

When the mechanism is in non-wheeled motion, the motion generated is quadrupedal motion, that is, walking gait is generated by waist and head and tail motion. In this process, in order to ensure the stability of its motion process, the center of gravity needs to be analyzed.

In the process of center of gravity analysis, we first divide the weight of the robot into five areas, $\boldsymbol{i}=(1,2,3,4)$ and corresponding to the five color blocks as shown in Fig. 4, it is approximately considered that the quality of each area is uniform. The landing locations of the four wheels of the robot are $\boldsymbol{i}=(1,2,3,4)$.
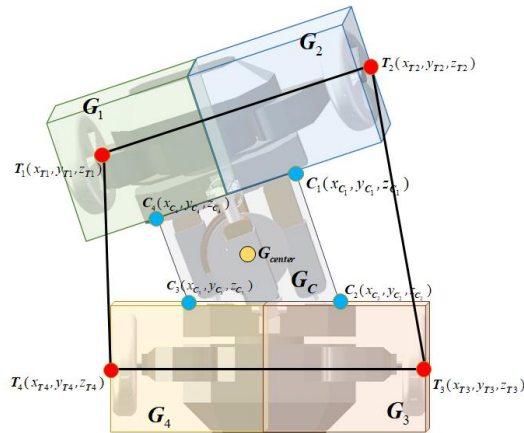
Fig. 4. Schematic diagram of center of gravity

The area $\boldsymbol{G}_C$ of the robot is equipped with a center of gravity adjustment device. The offset of the center of gravity in the X-axis and Y-axis directions of the $\boldsymbol{G}_C$ area is Δx_{Center} and Δy_{Center}. From the geometric relationship, it can be seen that the coordinates of $\boldsymbol{G}_{Center}$ projected on the ground are $(\Delta x_{Center}, \Delta y_{Center}, \boldsymbol{0})$, where:

$$\begin{cases} x_{center} = \dfrac{\sum_{i=1}^{3} x_{C_i}^2 \, y_{C_{i+1}} + x_4^2 \, y_1 - \sum_{i=1}^{3} x_{C_{i+1}}^2 \, y_{C_i} - x_1^2 \, y_4 + \sum_{i=1}^{3} x_{C_i} \, x_{C_{i+1}} \, y_{C_{i+1}} + x_4 \, x_1 \, y_1 - \sum_{i=1}^{3} x_{C_i} \, y_{C_i} \, y_{C_{i+1}} - x_4 \, y_1 \, y_4}{3\left(\sum_{i=1}^{3} x_{C_i} \, y_{C_{i+1}} + x_4 \, y_1 \sum_{i=1}^{3} x_{C_i} \, y_{C_{i+1}} - x_1 \, y_4\right)} + \Delta x_{center} \\[2em] y_{center} = \dfrac{\sum_{i=1}^{3} x_{C_{i+1}} \, y_{C_i}^2 + x_4 \, y_1^2 - \sum_{i=1}^{3} x_{C_{i+1}} \, y_{C_i}^2 - x_1 \, y_4^2 + \sum_{i=1}^{3} x_{C_i} \, y_{C_i} \, y_{C_{i+1}} + x_4 \, y_4 \, y_1 - \sum_{i=1}^{3} x_{C_i} \, x_{C_{i+1}} \, y_{C_i} - x_4 \, x_1 \, y_4}{3\left(\sum_{i=1}^{3} x_{C_i} \, y_{C_{i+1}} + x_4 \, y_1 \sum_{i=1}^{3} x_{C_i} \, y_{C_{i+1}} - x_1 \, y_4\right)} + \Delta y_{center} \end{cases}$$

(14)

Then the coordinate of the robot's center of gravity **CoG** projected on the ground is **CoG'**, where:

$$\begin{cases} x_{CoG} = \dfrac{\sum_{i=1}^{4} G_i \, x_{Ti} + G_C \, x_{center}}{\sum_{i=1}^{4} G_i + G_C} \\[2em] y_{CoG} = \dfrac{\sum_{i=1}^{4} G_i \, x_{Ti} + G_C \, x_{center}}{\sum_{i=1}^{4} G_i + G_C} \end{cases}$$

(15)

4.2 Stability Margin of RPBMBot

As shown in Fig. 5, taking the lifting of the right front wheel as an example, when it is lifted, the support boundary closest to the center of gravity is $T_1 T_3$. The specific value of the stability margin index d_{min} can be obtained by the following formula:

$$d_{min} = \frac{\left| A\, x_{CoG} + B\, y_{CoG} + C \right|}{\sqrt{A^2 + B^2}}$$

(16)

where, $A = y_{T3} - y_{T2}$, $B = x_{T2} - x_{T3}$, $C = x_{T3} y_{T2} - x_{T2} y_{T3}$.
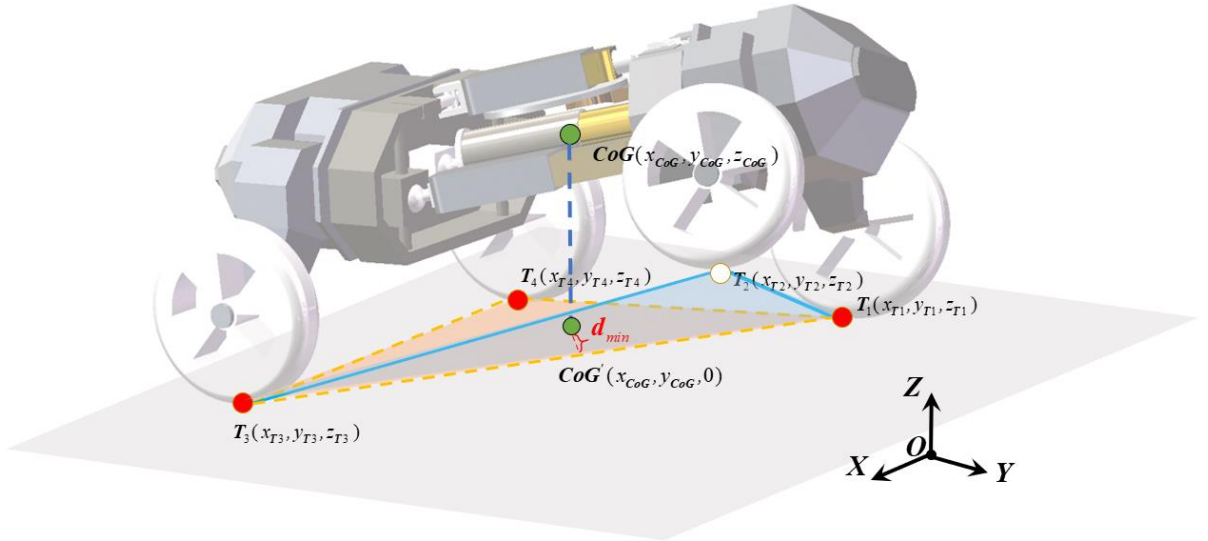
Fig. 5. Stability margin of the RPBMBot

4.3 Center of Gravity Trajectory and Stability Margin

When the robot is moving in a non-wheeled state, it can be regarded as a quadruped-like robot. When the quadruped robot is walking, once the foot touches the ground as a support phase, it will not be able to move during the next motion cycle. The robot's support polygon will also be fixed during one leg lift until it is lifted the next time. Therefore, in order to prevent the robot from overturning during the movement, the robot's travel range, movement efficiency and climbing ability will be greatly affected. However, during the movement of the robot, the robot's wheel movement, waist posture adjustment and the movement of the center of gravity adjustment plate can maintain the stability of the robot's center of gravity while ensuring the amplitude and distance of the leg lift phase.

In the process of adjusting the center of gravity, the change rule of the stability margin $d_{\min}$ of the robot with the coordinate $(x_{CoG}, y_{CoG}, 0)$ of the center of gravity projection of the robot can be established during a leg raising process of the robot, as shown in Fig. 6.
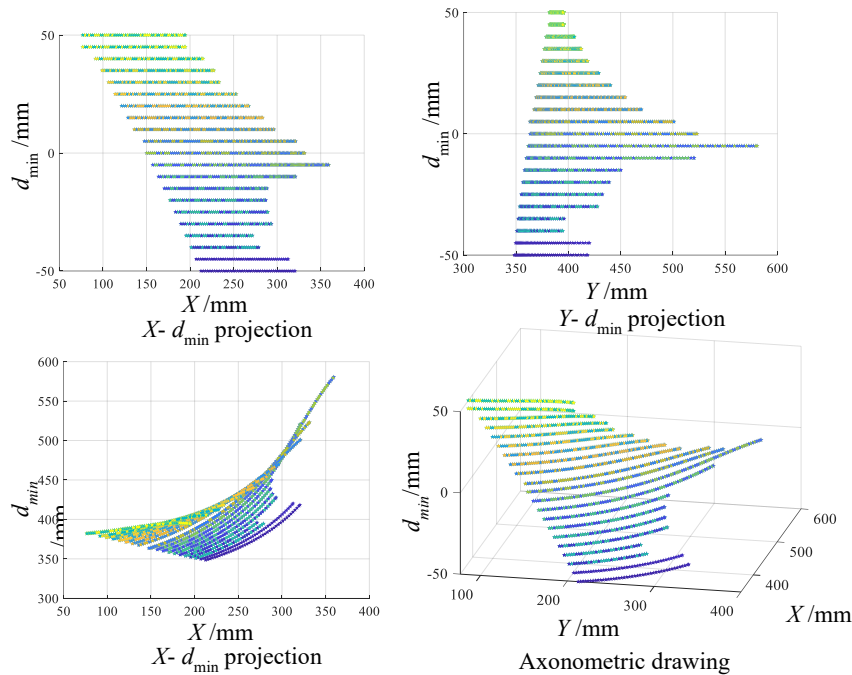
Fig. 6. Trajectory of center of gravity and stability margin

when the stability margin is set unchanged, the mechanism has many kinds of attitudes corresponding to it. These attitudes corresponding to a certain stability margin are named the attitude group. During the adjustment process, an optimal adjustment method needs to be found, that is, a set of optimal attitudes needs to be selected from the target stability margin attitude group, and then adjusted.

5   Conclusion

A reconfigurable parallel bionic mobile robot (RPBMot) is presented, which can adapt to a variety of complex terrains through gait switching. Kinematic models are developed to drive the parallel mechanism to move. The robot's center of gravity coordinate solution method and stability margin calculation scheme are established. The relationship between the trajectory of the center of gravity and the stability margin provides a theoretical basis for the further drive optimization of the mobile robot.

Acknowledgements

References

1. Dai JS.: Historical relation between mechanisms and screw theory and the development of finite displacement screws. Journal of Mechanical Engineering 51(13), 13-26 (2015). (in Chinese)
2. Sun T, Yang S, Lian B.: Finite and instantaneous screw theory in robotic mechanism. Singapore: Springer (2020).
3. Guo F, Wang SK, Yue BK, et al.: A deformable configuration planning framework for a parallel wheel-legged robot equipped with lidar. Sensors (Basel) 20(19), 5614_1-21 (2020).
4. Zhang XL, Huang Yu, Rong YM, et al.: Optimal trajectory planning for wheeled mobile robots under localization uncertainty and energy efficiency constraints. Sensors (Basel) 21(2), 335_1-26 (2021).
5. Qian J, Zi B, Wang DM, et al.: The design and development of an omni-directional mobile robot oriented to an intelligent manufacturing system. Sensors (Basel) 17(9), 2073_1-16 (2017).
6. Luo ZR, Shang JZ, Wei GW, et al.: A reconfigurable hybrid wheel-track mobile robot based on Watt II six-bar linkage. Mechanism and Machine Theory 128, 16-32 (2018).
7. Qu MK, Wang HB, Rong Yu.: Design of 6-DOF parallel mechanical leg of wheel-leg hybrid quadruped robot. Transactions of the Chinese Society of Agricultural Engineering 33(11), 27-37 (2017). (in Chinese)
8. Spröwitz AT, Tuleu A, Ajallooeian M, et al.: Oncilla Robot: A versatile open-source quadruped research robot with compliant pantograph legs. Frontiers in Robotics and AI 5:67_1-18 (2018).
9. Suzuki S, Kano T, Ijspeert AJ, et al.: Sprawling quadruped robot driven by decentralized control with cross-coupled sensory feedback between legs and trunk. Frontiers in Neurorobotics 14, 607455_1-8 (2021).
10. Skonieczny K, D'Eleuterio, GMT.: Improving mobile robot step-climbing capabilities with center-of-gravity control. ASME International Design Engineering Technical Conferences & Computers & Information in Engineering Conference, Montreal, Quebec, Canada, 1531-1538 August 15-18 (2010).

11. Teng L, Wu XM, Chen WH, et al.: Center of gravity balance approach based on CPG algorithm for locomotion control of a quadruped robot. IEEE/ASME International Conference on Advanced Intelligent Mechatronics, Wollongong, Australia, 325-329 July 9-13 (2013).

12. Zhang CS, Zhang C, Dai JS.: Stability margin of a metamorphic quadruped robot with a twisting trunk. ASME Journal of Mechanisms and Robotics 11(6), 064501_1-13 (2019).

13. Agheli M, Qu L, Nestinger SS.: SHeRo: Scalable hexapod robot for maintenance, repair, and operations. Robotics and Computer-Integrated Manufacturing 30(5), 478-488 (2014).

14. Zhu YG, Guo T, Liu Q, et al.: A study of arbitrary gait pattern generation for turning of a bio-inspired hexapod robot. Robotics and Autonomous Systems 97, 125-135 (2017).

15. Jia Y, Luo X, Han BL, et al.: Stability criterion for dynamic gaits of quadruped robot. Applied Sciences 8, 2381_1-25 (2018).

16. Ye W, Chai XX, Zhang KT.: Kinematic modeling and optimization of a new reconfigurable parallel mechanism. Mechanism and Machine Theory 149, 103850_1-18 (2019).

A new type of 6-DOF parallel mechanism with a single driver

Yundou Xu[1,2], Yiming Zhang[1], Xiaoyu Pang[1], Fengfeng Xi[3], Yongsheng Zhao[1,2]

[1] Parallel Robot and Mechatronic System Laboratory of Hebei Province, Yanshan University, Qinhuangdao 066004, China
[2] Key Laboratory of Advanced Forging and Stamping Technology and Science of Ministry of National Education, Yanshan University, Qinhuangdao 066004, China
[3] Department of Aerospace Engineering, Ryerson University, Toronto, Canada
ydxu@ysu.edu.cn

Abstract. In this paper, a new type of 6-DOF parallel mechanism with a single driver is proposed. It is formed by adding a SPS driving branch to the previous 6SPS mechanism, and the prismatic joint of the original 6SPS mechanism are controlled by a lockable joint. This mechanism can realize 6-DOF output of the moving platform through multiple adjustments of the only driving branch. For this method, control strategies are discussed along with kinematic analysis, and the correctness of the kinematic model is validated by simulation software. It is very suitable for pose adjustment occasions with the requirements of low real-time and high loading capacity.

Keywords: parallel mechanism, single actuation, Under-actuated.

1   Introduction

According to the relationship between the number of inputs N and the number of degrees of freedom (DOFs) M, parallel mechanisms can be divided into normal parallel mechanisms ($N=M$), redundantly actuated parallel mechanisms ($N>M$) and under-actuated parallel mechanisms ($N<M$). Under-actuated mechanisms need to be balanced by external forces and can only be used in very few special cases. At present, the majority of parallel equipments use normal parallel mechanisms, and a minority of equipments use redundantly actuated parallel mechanisms to improve the loading capacity [1-4]. For example, Ska is made up of about 3000 parabolic antennas with 15m diameter aperture [5]. If a single antenna format adjustment system can realize six degree of freedom pose adjustment with single or two drives, it can not only greatly save the manufacturing cost, but also reduce the coordination difficulty of manual adjustment of multiple branches at the same time. At present, spacecraft docking, aircraft parts assembly and other pose adjustment systems mostly use the traditional 6-DOF parallel mechanism 6SPS [6]. Six drives are used to realize the pose adjustment of parts. If single or few drives are used to realize the expected pose adjustment, the manufacturing and maintenance costs can be reduced. When the base of working

platform such as lifting platform is in an inclined state, an effective leveling scheme currently adopted is two rotational and one translational DOFs parallel mechanism 3RPS [7], which can realize the leveling of the base of the work platform by three drives. If a single drive can be used to realize the leveling, the complexity of the system and the cost of manufacturing and maintenance will be reduced. For the normal parallel mechanisms, the more the input number of the mechanism, the higher the equipment cost. If the input number is less than the number of DOFs of the mechanism and the original multiple DOFs of the mechanism can still be achieved independently, the manufacturing cost of the equipment will be greatly reduced, which has very important scientific research significance and practical application value. Some scholars have proposed a type of fewer input and more output parallel mechanisms [8]. This kind of mechanisms use fewer inputs to achieve multiple outputs of the moving platform. However, these outputs are dependent and it cannot achieve the independent outputs of multiple DOFs. This type of mechanisms can only be used in some specific occasions that do not require multiple independent outputs. In reference [9], a planar 3-DOF morphing wing mechanism with two drivers based on lockable kinematic joints is proposed. In reference [10], a spatial 6-DOF morphing wing mechanism with four drivers and four passive driving branches is proposed. Except for the above-mentioned reports, there are few reports on the parallel mechanisms that have multiple independent DOFs with fewer drivers. Therefore, this paper will propose a 6-DOF parallel mechanism with a single driver and analyze its forward and inverse kinematics.

2   Description of the 6-DOF parallel mechanism with a single driver

The structure of the 7SPS parallel mechanism is shown in Fig. 1, which includes a base, a moving platform, six passive branches with the same SPS kinematic structure and an active branch of the SPS kinematic structure. The upper and lower end of each branch (passive and active) are connected to the moving platform and the base through a spherical joint, respectively. A controllable clutch is installed on the prismatic joint for each of the six passive branches, which can be locked or released. A driver is installed on the prismatic joint of the active branch.
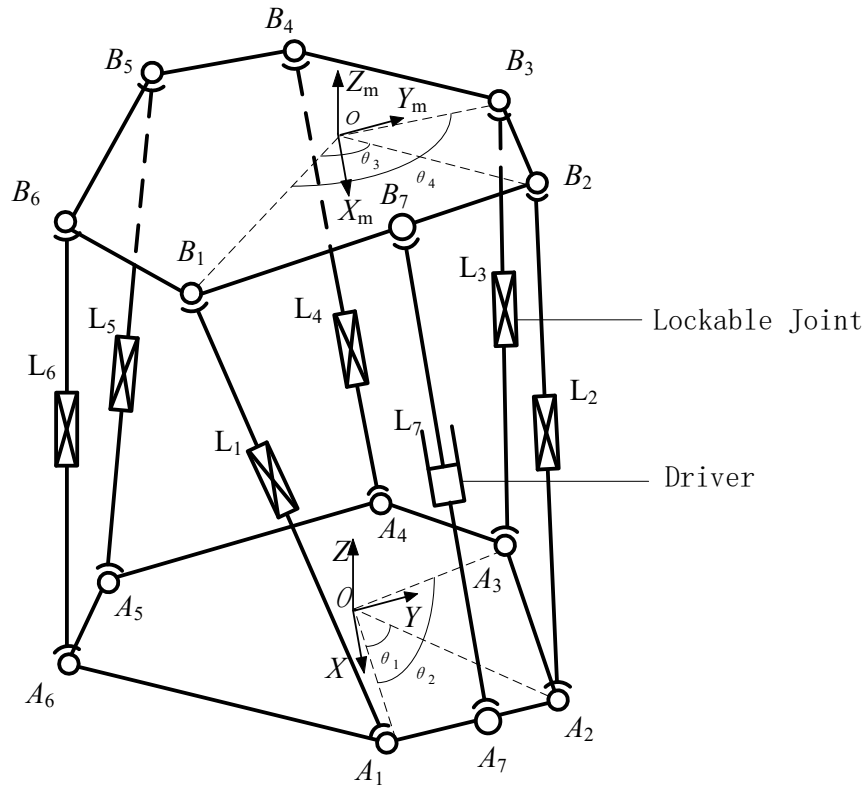
Fig. 1. The 6-DOF parallel mechanism with a single driver

3   Finite pose control of the moving platform

According to the desired pose of the moving platform and based on the inverse kine-matics solution of the original 6SPS parallel mechanism, the required length l_i of each kinematic branch (active and passive) can be calculated. Then five of the six passive branches are locked, and the active branch is actuated to control the free passive branch to the final length. As shown in Fig. 1, for example, in the first step, release the clutch on the first branch L_1, and lock the other five branches L_2 to L_6. By control-ling the length of the active branch L_7, the first branch can reach its final position. In the second step, release the clutch on the second branch L_2, and lock the clutches on the other five branches, again control the active branch to move the second branch to reach its final position. Likewise, the position control of six passive branches of the original parallel mechanism can be realized by repeating the same process six times, and the finite pose of the six DOF moving platform can be fully realized.

4   Kinematic algorithm

The kinematic model of the mechanism is established for pose control. As shown in Fig. 1, the global coordinate system is fixed at the center point O of the base, and the moving coordinate system is located at the center point o of the moving platform. The coordinates of centers of each S joint can be expressed as:

$$\boldsymbol{A}_i = \begin{cases} \boldsymbol{A}_1 = [& R & 0 & 0 &]^T \\ \boldsymbol{A}_2 = [& R\cos\theta_1 & R\sin\theta_1 & 0 &]^T \\ \boldsymbol{A}_3 = [& R\cos\theta_2 & R\sin\theta_2 & 0 &]^T \\ \boldsymbol{A}_4 = [& R\cos(\theta_1+\theta_2) & R\sin(\theta_1+\theta_2) & 0 &]^T \\ \boldsymbol{A}_5 = [& R\cos(2\theta_2) & R\sin(2\theta_2) & 0 &]^T \\ \boldsymbol{A}_6 = [& R\cos(\theta_1+2\theta_2) & R\sin(\theta_1+2\theta_2) & 0 &]^T \\ \boldsymbol{A}_7 = [& R\cos(\pi/36) & R\sin(\pi/36) & 0 &]^T \end{cases} \quad (1)$$

$$\boldsymbol{B}_i = \begin{cases} \boldsymbol{B}_1 = [& r\cos(-\pi/4) & r\sin(-\pi/4) & 0 &]^T \\ \boldsymbol{B}_2 = [& r\cos(-\pi/4+\theta_3) & r\sin(-\pi/4+\theta_3) & 0 &]^T \\ \boldsymbol{B}_3 = [& r\cos(-\pi/4+\theta_4) & r\sin(-\pi/4+\theta_4) & 0 &]^T \\ \boldsymbol{B}_4 = [& r\cos(-\pi/4+\theta_3+\theta_4) & r\sin(-\pi/4+\theta_3+\theta_4) & 0 &]^T \\ \boldsymbol{B}_5 = [& r\cos(-\pi/4+2\theta_4) & r\sin(-\pi/4+2\theta_4) & 0 &]^T \\ \boldsymbol{B}_6 = [& r\cos(-\pi/4+\theta_3+2\theta_4) & r\sin(-\pi/4+\theta_3+2\theta_4) & 0 &]^T \\ \boldsymbol{B}_7 = [& R\cos(\pi/24) & R\sin(\pi/24) & 0 &]^T \end{cases} \quad (2)$$

where A_i and B_i represent the center point of the S joints within the SPS branch connecting the moving platform and base respectively, r represents the radius of the circumcircle of the moving platform, R represents the radius of the circumcircle of the base, θ_1 represents the angle between $\boldsymbol{OA}_1$ and $\boldsymbol{OA}_2$, θ_2 represents the angle between $\boldsymbol{OA}_1$ and $\boldsymbol{OA}_3$, θ_3 represents the angle between $\boldsymbol{oB}_1$ and $\boldsymbol{oB}_2$, θ_4 represents the angle between $\boldsymbol{oB}_1$ and $\boldsymbol{oB}_3$.

When the position $[Px\ Py\ Pz]^T$ and orientation $(\alpha\ \beta\ \gamma)$ expressed by XYZ Euler angles are given for the pose of the moving platform, the inverse kinematics solution of the original 6SPS parallel mechanism is needed to calculate the target length l_i of the six passive branches.

First, taking the target length l_1 of branch L_1 and initial lengths of branches L_2~L_6 as inputs, solve the forward kinematic solution of the original 6SPS parallel mechanism to obtain position and orientation of the moving platform after the first driving motion, here the numerical iteration method is used to solve this problem [11]. Then calculate the length l_{71} of L_7 according to the inverse kinematic solution of the entire parallel mechanism. Under the action of the given input l_{71} of the active branch L_7, branch L_1 can reach its expected position l_1.

Similarly, the inputs l_{7i} of the active branch L_7 to control branches L_2~L_6 reach their expected positions l_i can be obtained in sequence.

A specific numerical example is given to illustrate the kinematic algorithm below.

A set of geometrical parameters are given as follows: r=500mm, R=670mm, θ_1=$\pi/18$, θ_2=$2\pi/3$, θ_3=$7\pi/12$, θ_4=$2\pi/3$. The target pose of the moving platform is given as Table 1.

Table 1. The target pose of the moving platform

P_x (mm)	P_y (mm)	P_z (mm)	α (rad)	β (rad)	γ (rad)
0	0	550	0	0	0

Through the inverse kinematic solution of the parallel mechanism, the expected length of each kinematic branch is calculated and given in Table 2.

Table 2. The expected length of each kinematic branch

l_1 (mm)	l_2 (mm)	l_3 (mm)	l_4 (mm)	l_5 (mm)	l_6 (mm)
726.3873	755.4683	726.3873	755.4683	726.3873	755.4683

According to the above-mentioned principle, the length of each passive branch and that of the active branch can be calculated respectively for six times, and is shown in Table 3.

Table 3. The length of each branch in each adjustment

	l_1 (mm)	l_2 (mm)	l_3 (mm)	l_4 (mm)	l_5 (mm)	l_6 (mm)	l_7(mm)
Initial length	689.303	719.884	689.303	719.884	689.303	719.884	528.713
Target length	726.3873	755.4683	726.3873	755.4683	726.3873	755.4683	576.227
First time	726.3873	719.884	689.303	719.884	689.303	719.884	552.247
Second time	726.3873	755.4683	689.303	719.884	689.303	719.884	575.344
Third time	726.3873	755.4683	726.3873	719.884	689.303	719.884	582.507
Fourth time	726.3873	755.4683	726.3873	755.4683	689.303	719.884	575.569
Fifth time	726.3873	755.4683	726.3873	755.4683	726.3873	719.884	568.774
Sixth time	726.3873	755.4683	726.3873	755.4683	726.3873	755.4683	576.227

After each adjustment, the position and orientation of the moving platform is calculated as Table 4.

Table 4. The position and orientation of the moving platform after each adjustment

	P_x (mm)	P_y (mm)	P_z (mm)	α (rad)	β (rad)	γ (rad)
Initial position	0	0	500	0	0	0
Target position	0	0	550	0	0	0
First time	-13.086	-11.7696	508.506	-0.02255	- 0.02727	-0.0174
Second time	-27.657	-2.40005	516.222	0.003755	-0.046423	-0.0001
Third time	-10.729	-8.30731	525.247	0.038178	-0.051396	-0.0187
Fourth time	-11.995	-25.7687	532.889	0.040443	0.019276	-0.0004
Fifth time	-15.849	-8.09838	541.853	0.028824	0.013128	-0.0175
Sixth time	0	0	550	0	0	0

5   Simulation analysis

The simulation model of the mechanism is established as shown in Fig. 2, and the driver is added in the L_7 branch, while the clutches are added in the L_1-L_6 branches. When a passive branch needs to be released, its clutch will be set invalid. For example, at the first adjustment, the clutch on L_1 branch is set invalid, and L_2-L_6 will still be locked by a fixed value. According to the input l_7 of the active branch given in Table 3, the moving platform can reach the target pose finally. Fig 3 shows the length variation of each branch in the entire motion process, which is consistent with the data in Table 3. This verifies the correctness of our kinematic model.
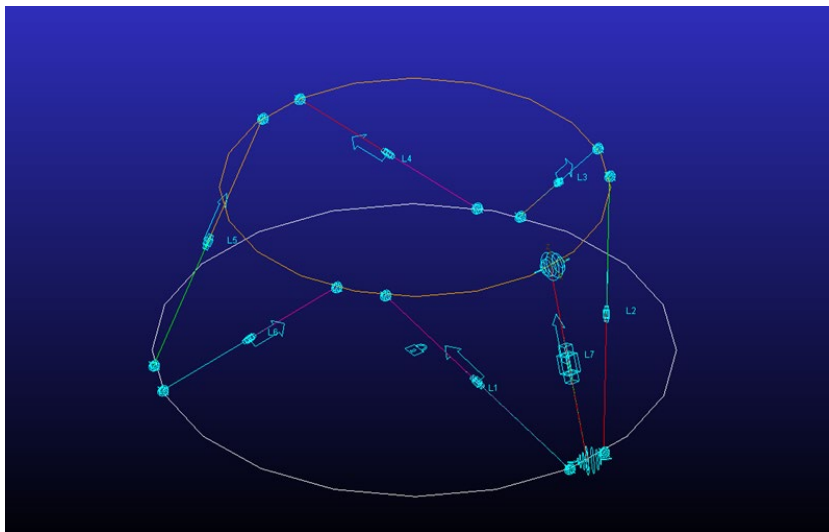
Fig. 2. Simulation model
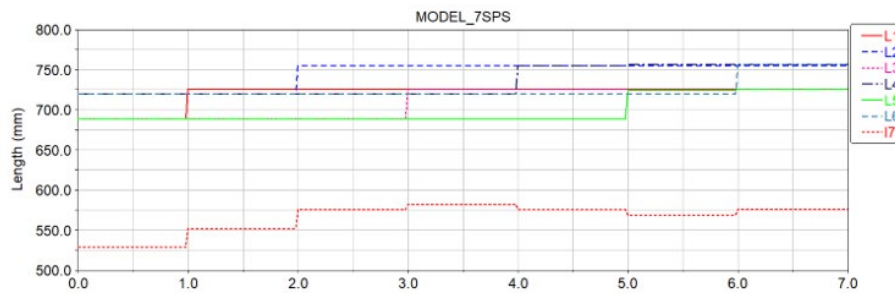
Fig. 3. The length variation of each branch in the whole motion process

6   Conclusion

A new type of 6-DOF parallel mechanism 7SPS with a single driver is proposed, which can realize the finite motion of the original mechanism. This is achieved by adjusting the active branch six times, corresponding to the individual control of six passive branches in sequence. The kinematics algorithm for the proposed mechanism is analyzed, and the results are verified by the simulation. This new type of mechanism only uses a single driver to obtain the 6-DOF outputs, which can greatly reduce the cost of equipment. At the final configuration, it has seven branches support the moving platform together. This forms a statically indeterminate system and the loading capacity can be improved compared with the original 6-DOF parallel mechanism. This mechanism is suited for heavy-load pose adjustment that requires to be implemented in slow pace.

References

1. W. Shang, S. Cong: Nonlinear Adaptive Task Space Control for A 2-DOF Redundantly Actuated Parallel Manipulator. Nonlinear Dyn 59, 61-72 (2010).
2. L. Xu, X. Chai, Q. Li: Design and Experimental Investigation of a New 2R1T Overconstrained Parallel Kinematic Machine with Actuation Redundancy. Journal of Mechanisms and Robotics 11(3), 1 (2019).
3. C. Wang, Y. Fang, S. Guo: Multi-objective optimization of a parallel ankle rehabilitation robot using modified differential evolution algorithm, Chinese Journal of Mechanical Engineering 28(4), 702-715 (2015).
4. A. Müller, T. Hufnagel: Model-Based Control of Redundantly Actuated Parallel Manipulators in Redundant Coordinates. Robotics and Autonomous Systems 60, 563-571 (2012).
5. S. Min，B. Yun: Structural Modelling and System Simulation Analysis of SKA Radio Telescope Dish. Radio Communications Technology 45(04), 431-436 (2019).
6. N. Duan: Research on Parallel Mechanism Designed For the Docking and Attitude Adjustment Process of Large Components. Machine Design & Research 30(05), 34-37 (2014).
7. T. Liu: Statics study of automatic leveling lifts based on 3-RPS with equivalent spherical hinge. Journal of Yanshan University 41(03), 230-234 (2017).
8. H. Shen, X. Zhu, D. Zhang, J. Deng, L. Dai: The design methodology for fewer input–more output parallel mechanisms. Mechanism and Machine Theory 104, 43-58 (2016).
9. J. Wang, Y. Zhao, F. Xi, Y. Tian: Design and analysis of a configuration-based lengthwise morphing structure. Mechanism and Machine Theory 147, 103767(2020).
10. A. Moosavian, F. Xi: Design and motion control of fully variable morphing wings. Journal of aircraft 50(4), 1189-1201 (2013).
11. Y. Kim, H. Shi, N. Dagalakis: Design of a six-DOF motion tracking system based on a Stewart platform and ball-and-socket joints. Mechanism and Machine Theory 133, 84-94 (2019).

A Novel Reconfigurable Hybrid Kinematics Five-axis Machine Tool

Abdur Rosyid [a], Bashar El-Khasawneh [a,b,1], Cesare Stefanini [a,c]

[a] Khalifa University Center for Autonomous Robotic Systems (KUCARS), Khalifa University of Science and Technology, Abu Dhabi, United Arab Emirates
[b] Mechanical Engineering Department, Khalifa University of Science and Technology, Abu Dhabi, United Arab Emirates
[c] Biomedical Engineering Department, Khalifa University of Science and Technology, Abu Dhabi, United Arab Emirates

Abstract. Hybrid kinematics machines have been developed to combine the advantages of serial and parallel kinematics machines. This paper proposes a novel 3T2R hybrid kinematics machine for machining application consisting of a novel reconfigurable 3T PKM and a decoupled 2R PKM. By locking/reconfiguration of some joints, the novel reconfigurable PKM can be transformed to four topologies with eight configurations in order to attain certain kinematic properties while keeping its 3T mobility. Either the proximal or intermediate prismatic joints of the reconfigurable PKM can be actuated. Some of the configurations are orthogonal (cube) configurations having a workspace bounded by a box and some other configurations are non-orthogonal which provides more flexibility to the machine to perform a machining task to a large workpiece/structure in various positions with respect to the machine.

Keywords: Reconfigurable Machine, Reconfigurable Mechanism, Hybrid Mechanism, Parallel Kinematics Machine, 3T2R, Machining.

1 Introduction

In the machining of large structures such as airplane wings and fuselage, the machine should have good reachability (workspace) and good stiffness-to-weight ratio across its workspace to perform the required machining tasks with an acceptable accuracy. Serial kinematics machines (SKMs) have been earlier used to perform machining tasks on large structures. However, the SKMs have some typical drawbacks such as accumulating joint errors, low stiffness at extended arm configurations, and low dynamics. To overcome those drawbacks, parallel kinematics machines (PKMs) such as hexapods have been developed to perform the tasks. Nevertheless, such PKMs typically have very limited (translational and rotational) workspace.

---

[1] Corresponding author - Email: `bashar.khasawneh@ku.ac.ae`

Recently, several hybrid kinematics machines (HKMs) consisting of parallel modules and serial modules have been developed to combine the advantages of SKMs (e.g., large workspace) and PKMs (e.g., high stiffness-to-weight ratio, non-accumulating joint errors, and high dynamics). Among the interesting classes of HKMs are 3T2R HKMs which provide three translational and two rotational degrees of freedom (DOFs) in their task space, and therefore they are capable to perform five-axis machining tasks. Many existing 3T2R HKMs were built by employing 3T PKMs with linear actuators since the use of linear actuators usually provides larger workspace. In this case, such PKMs can be classified into two categories: 1) those with active prismatic joints in the middle of the legs, i.e., active struts, and 2) those with active prismatic joints in the beginning of the legs, i.e., active sliders. Many of the existing HKMs using the 3T PKMs with active struts and active sliders simply use serial <u>RR</u> wrists at the final position of the manipulators in addition to the 3T PKMs. In this case, the parallel modules serve as translators while the serial <u>RR</u> wrists provide the required 2R mobility. Furthermore, some of those manipulators use serial <u>PP</u> links in the beginning of the kinematic chain to provide large translational workspace. However, all these existing machines only have single, fixed configurations, although some of them offer modularity. To provide more flexibility and wider applicability, recently reconfigurable PKMs have been proposed and developed. A reconfigurable mechanism is a mechanism which can change its configuration to attain certain kinematic properties such as mobility, workspace, or properties of the workspace. A reconfigurable mechanism can be designed by using several ways including reassembly (assembly and disassembly) [1], switching the active/passive modes of some joints [2], singularity passing [3], platform reconfiguration [4], joint locking [5], link coincidence [6], and joint reconfiguration [7 - 9].

This work proposes a 3T2R HKM which consists of a novel, reconfigurable 3T parallel module and 2R parallel module. Both the parallel mechanisms are then connected serially, hence it is called an HKM. While many reconfigurable PKMs are aimed at changing their mobility by the reconfiguration, the reconfigurable PKM proposed in this work keeps its mobility unchanged but changes its workspace and properties of the workspace. The remainder of this paper is organized as follows. First, the topology and reconfigurability of the 3T parallel module is discussed. Second, the topology of the 2R parallel module is presented. Finally, some conclusions are provided.

2 Topology and Reconfiguration

The topology of the proposed HKM was designed by considering the following requirements. First, *mobility*. It is required that the manipulator can provide five DOFs to perform a five-axis machining task. The five DOFs should be 3T2R, i.e. three orthogonal translations and two rotations about two orthogonal axes. This mobility is in particular necessary when the workpiece is fixed, i.e., not to be moved during the machining process. Second, *reconfigurability*. The machine should be reconfigurable to adapt to variation of workpiece size, geometry, machining direction and reach. Third, *modularity*. The 3T2R mechanism which consists of two modules can be transformed to 3T mechanism. Such modularity is also a kind of reconfigurability. Fourth, *practicality and cost*. Among ways to make the reconfigurable machine practical and cost-efficient is a con-

sistent placement of the actuators. In other words, in all the configurations of the reconfigurable machine, the placement of the actuators should not be changed. As a result, a minimum number of actuators can be used. Fifth, *extensibility to a mobile robot*. The HKM is going to be used in the future as a mobile robot for machining application. Consequently, the proposed design should be able to be easily extended or integrated with a mobile base/platform.

2.1 DOF distribution

To meet the aforementioned requirements, it is possible to employ either a purely parallel 3T2R mechanism or a hybrid 3T2R mechanism. It is then decided to employ hybrid kinematics in order to combine the advantages of both serial and parallel kinematics topologies as discussed earlier. In this case, it is possible to have any DOF distribution as listed in Table 1. The SKM module can be either in the beginning or final position.

Table 1. Possible DOF distribution of the 3T2R HKM

Number and distribution of DOFs	Types of DOFs
3-DOF PKM + 2-DOF SKM/PKM	PPP (3T) PKM + RR SKM/PKM
	PPR (2T1R) PKM + PR SKM/PKM
	PRR (1T2R) PKM + PP SKM/PKM
4-DOF PKM + 1-DOF SKM	PPPR (3T1R) PKM + R SKM
	PPRR (2T2R) PKM + P SKM

Furthermore, it is decided to use linear actuators for the PKM module, which can be either in the beginning (active sliders) or in the middle (active struts). As mentioned earlier, this is because the linear actuators provide larger translational workspace.

Among the available options, the PPP (3T) PKM + RR SKM/PKM topology is selected. This is because it is easier to achieve the modularity which enables the transformation between 3T and 3T2R mobility. The former mobility can be easily achieved by dismantling the RR module from the machine. On the other hand, the latter mobility is achieved by attaching the RR module. The HKM is achieved by serially connecting a PPP PKM to an RR PKM. The PPP PKM provides the 3T mobility whereas the RR PKM provides the 2R mobility.

Furthermore, either serial RR or parallel RR module is possible to use. The latter option is selected as theoretically the parallel module offers some advantages associated with a parallel mechanism such as high stiffness-to-weight ratio, non-accumulating joint errors, etc.

In a nutshell, this HKM topology has the following advantages:

- The two modules provide clear separation between translations and rotations. The first module only gives translations whereas the second module only gives rotations.
- With this arrangement, each module does not have mixed DOFs. Hence, the Jacobian-based performance measures will be easily evaluated (and optimized) with sound meaning. However, the evaluation of the whole manipulator indeed still mixes the DOFs.

- With this arrangement, the manipulator can be transformed from five-axis to three-axis by removing the 2R module and attaching the tool directly to the 3T module.
- The use of PKM (instead of SKM) for the second module, i.e. serially connecting a PKM to another PKM, is expected to offer the advantages of PKM such as higher stiffness and accuracy due to the closed loop kinematics.

2.2 Topology of the 3T reconfigurable PKM

The proposed HKM can be reconfigured into several configurations based on the type of machining required (whether it is stationary or mobile and the direction of the machining) and how the workpiece looks like. Hence, this reconfigurable machine can adapt to various machining types and workpiece shapes. Fig. 1 shows the proposed HKM at one of its configurations. The machine consists of a base structure, a reconfigurable 3T PKM, and a 2R PKM rigidly connected to the moving platform of the 3T PKM. A tool spindle is mounted on the moving platform of the 2R PKM. The reconfigurable 3T PKM has three limbs. When none of its joints is locked, limb 1 has P//R⊥P⊥R joint topology in which the rotation axes of both the R joints are parallel, limb 2 has PUPS joint topology, and limb 3 has PUPU joint topology. Symbols // and ⊥ are used in this paper to indicate parallelism and perpendicularity between two adjacent joints, respectively.
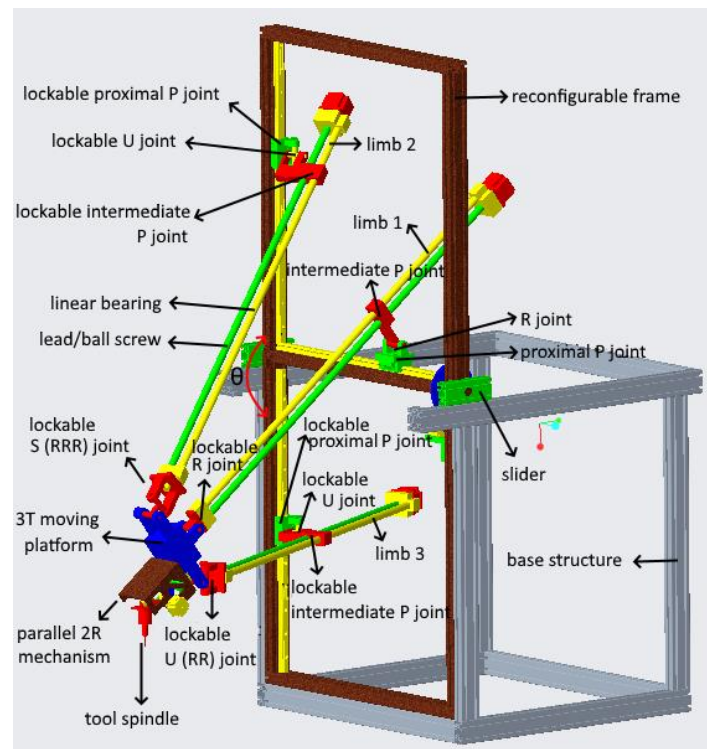
Fig. 1. The proposed HKM at one of its configurations

The 3T PKM can be transformed into several configurations as shown in Table 2 and illustrated in Fig. 2. The reconfiguration is performed by changing the angle θ, which is an angle made by the two reconfigurable frames, and changing the joint topology of the limbs by locking or reconfiguring some joints. With the goal to limit the reconfiguration to 3T mobility, the proposed reconfigurable 3T PKM can be transformed to four joint topologies, as shown in Table 2, and eight configurations, as shown in Fig. 2. Term "orthogonal" is used in this paper to indicate that all the three frames of the reconfigurable 3T PKM are perpendicular to each other. This is achieved when the angle θ is 90 degrees. When the angle θ is not 90 degrees, the configuration is called "non-orthogonal". It is intentional that only two frames are reconfigurable to change the 3T mechanism from orthogonal to non-orthogonal topologies, with the following reasons: 1) minimizing the number of frames to be reconfigured, and accordingly minimizing the number of actuator required for the reconfiguration from orthogonal topology to non-orthogonal topology as well as increasing the reliability of the whole mechanism, 2) making the mechanism frame have a good fit with the base structure which is going to be integrated with a mobile base/platform, and 3) making the mechanism easier to be retracted and extended with respect to the base structure. It is worth-mentioning that the reconfigurable PKM can also be transformed to 3T1R topologies as shown in Table 3, but this is not the aim of the machine and hence such topologies are excluded. The 3T1R DOF is the highest DOF possible to be achieved by the reconfigurable PKM as limb 1 constrains rotations about two axes.

Some limb topologies involve the use of lockable or reconfigurable joints which can be either lockable/reconfigurable U joints, lockable/reconfigurable S joints, or lockable/reconfigurable P joints. Some reconfigurable joints have been developed. References [7, 8] presented reconfigurable U joints whereas [10] presented a reconfigurable S joint. To transform a P joint into a fixed link, one can simply lock it at a certain link length.

Limb 1 can be transformed to a P//R⊥P joint topology by locking/constraining the distal P joint. The joint topology P//R⊥P⊥R can be achieved in limb 2 and limb 3 by locking/constraining one R joint in all the U lockable/reconfigurable joints. The joint topology P//R⊥P⊥U of limb 2 and limb 3 can be achieved by locking/constraining one R joint in all the proximal U lockable/reconfigurable joints. The joint topology PUU of limb 2 and limb 3 can be achieved by unlocking/freeing the U lockable joints while locking/constraining the passive intermediate P joints, whereas the joint topology UPU of limb 2 and limb 3 can be achieved by unlocking/freeing the U lockable joints while locking (fixing) the passive proximal P joints. The lockable/reconfigurable S joint in limb 2 can be transformed to a U joint by locking/constraining the R joint having rotation axis parallel with the limb. It should be noticed that each of the upper and lower limbs can be called either limb 2 or limb 3.

Table 2. Several configurations of the reconfigurable 3T PKM

Limb	Topology 1	Topology 2	Topology 3	Topology 4
1	P//R⊥P⊥R	P//R⊥P⊥R	P//R⊥P	P//R⊥P
2	P//R⊥P⊥R	P//R⊥P⊥R	P//R⊥P⊥U or P//R⊥PS	P̲UU/ P̲US or UP̲U/UP̲S
3	P//R⊥P⊥R	P//R⊥P⊥U	P//R⊥P⊥U	P̲UU or UP̲U

Table 3. Some non-3T configurations of the reconfigurable PKM

Limb 1	Limb 2	Limb 3	Mobility
P//ṞP̱R	P//ṞP̱U or P//ṞPS	P//ṞP̱U	3T1R (X, Y, Z, and rotation about X)
P//ṞP̱R	PUU or UPU	PUU or UPU	3T1R (X, Y, Z, and rotation about X)

Topology 1. In this topology, the angle θ is 90 degrees whereas the joint topology is orthogonal 3PRPR. Either the proximal P joints or the intermediate P joints can be actuated. This joint topology includes three configurations as follow:

Configuration 1. This is a retracted, orthogonal configuration, as shown in Fig. 2(a), that is suitable for stationary machining inside the base structure. In other words, it is suitable for stationary machining with a workpiece having a size smaller than the machine volume, i.e. the volume of the base structure of the machine.

Configuration 2. This is an extended, orthogonal configuration, as shown in Fig. 2(b), that is suitable for mobile, front machining with limited-height workpiece. In other words, the main advantage of this configuration is suitability for mobile machining with a workpiece not taller than the height of the machine. The direction of the machining can be either downward (vertical) or horizontal. These two directions can be achieved by different placement of the 2R module. The former configuration is achieved by placing the 2R module under the 3T moving platform so that the 2R module is facing downward. The latter configuration is achieved by placing the 2R module on the side of the 3T moving platform so that the 2R module is facing to the front side.

Configuration 3. This is an orthogonal configuration, as shown in Fig. 2(c), in which the moving frame is tilted to face to the front. As a result, this configuration is suitable for front machining in which the height of workpiece is more than the height of the base structure of the machine.

| (a) | (b) | (c) |
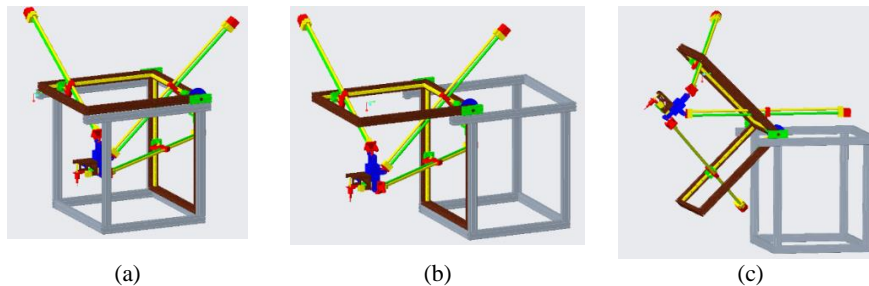
Fig. 2. Orthogonal configurations of the HKM: (a) Configuration 1, (b) Configuration 2, and (c) Configuration 3.

Topology 2. This topology is achieved by changing the angle θ to be larger than 90 degrees but less than 180 degrees, i.e., 90 degrees < θ < 180 degrees, whereas the joint topology is 2PRPR – 1PRPU, as shown in Fig. 3(a). This configuration is called the *configuration 4*, which is a non-orthogonal configuration. In this configuration, either the proximal P joints or the intermediate P joints can be actuated. Only the joint topo-

logy of limb 3 in this topology is different from that in the topology 1. The use of U joint instead of R joint as the last joint in limb 3 in this topology is due to the fact that the base frames of the PKM, i.e. the X, Y, and Z' axes, in this topology is not axisymmetric. A PKM is geometrically axisymmetric if it has an identical angle between any two adjacent limb base frames.

Topology 3. This topology is also achieved by changing the angle θ to be larger than 90 degrees but less than 180 degrees, i.e., 90 degrees < θ < 180 degrees, whereas the joint topology is 1PRP – 2PRPU, as shown in Fig. 3(b). This configuration is called the *configuration 5*, which is a non-orthogonal configuration. In this configuration, either the proximal P joints or the intermediate P joints can be actuated.

(a)   (b)

(c)   (d)   (e)
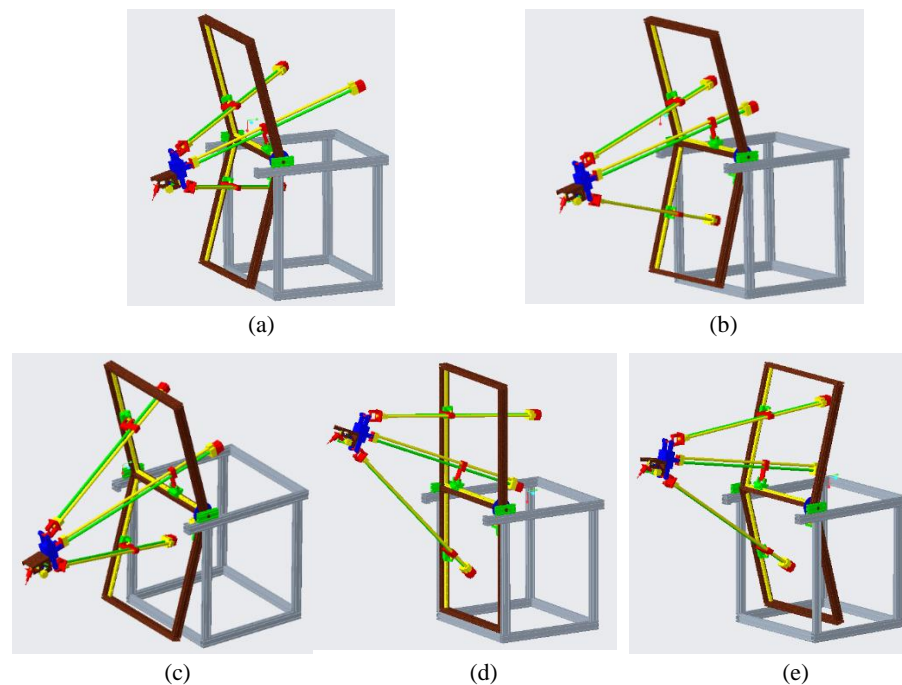
Fig. 3. Non-orthogonal configurations of the HKM: (a) Configuration 4, (b) Configuration 5, (c) Configuration 6, (d) Configuration 7, and (e) Configuration 8

Topology 4. In this topology, the angle θ is either between 90 and 180 degrees (i.e., 90 degrees < θ < 180 degrees), equal to 180 degrees, or more than 180 degrees. The joint topology of limb 1 is PRP whereas the joint topology of limb 2 and limb 3 is either 2PUU or 2UPU. In the former joint topology, the proximal P joints are actuated. In the latter joint topology, the intermediate P joints are actuated. It is also possible to add one more R joint to the other two R joints at the distal end of either limb 2 or limb 3 to create an S joint without changing the mobility of the mechanism. This is achieved by arranging the three R joints orthogonal to each other. This joint topology includes the following three configurations:

Configuration 6. This is a non-orthogonal configuration in which the angle θ is larger than 90 degrees but less than 180 degrees. For example, θ = 150 degrees, as shown in Fig. 3(c). This is suitable for mobile, front machining with tall workpiece. The mechanism's reconfigurable frames occupy some of the space in front of the machine.

Configuration 7. This is a non-orthogonal configuration in which the angle θ is 180 degrees as shown in Fig. 3(d). This is a T configuration as the three axes form a rotated letter T. This is also suitable for mobile, front machining with tall workpiece. The mechanism's reconfigurable frames do not occupy any space in front of the machine. In this configuration, if the passive P joints are fixed, a motion toward the vertical base of the mechanism is achieved by translating the active P joints in a transversal direction normal to the motion direction. Given a limited span of the vertical axes, i.e. the base axes of limb 2 and limb 3, this would result in a shorter workspace in the direction normal to the vertical base, i.e. in the horizontal direction.

Configuration 8. This is a non-orthogonal configuration in which the angle θ is more than 180 degrees, as shown in Fig. 3(e). This is also suitable for front machining with tall workpiece. The mechanism's reconfigurable frames do not occupy any space in front of the machine.

2.3 Placement of actuators and the resulting 3T configurations

There are two feasible scenarios in the placement of linear actuators: 1) actuators are placed at the proximal P joints, 2) actuators are placed at the intermediate P joints. For practicality and cost efficiency, the placement of actuators across the whole configurations should be consistent. With the actuation applied to either the proximal or intermediate P joints across the whole configurations, only three actuators are required to be installed. The resulting topologies in the four architectures (with underline indicates actuated joints) are described in Table 4. It can be seen that only the topology 4 results in two different topologies due to different actuator placements. The limb joint topologies in the other three topologies remain the same despite of the different actuator placements, with only different letters being underlined which indicate the actuator placement. In both the actuator placement scenarios, the torque demand for the actuators is expected to be relatively low due to the parallel kinematics.

Table 4. Resulting configurations corresponding to two different actuator placements

	Actuators at proximal P joints	Actuators at intermediate P joints
Topology 1	3P̲RPR	3PRP̲R
Topology 2	2P̲RPR – 1P̲RPU	2PRP̲R – 1PRP̲U
Topology 3	1P̲RP – 2P̲RPU or	1PRP̲ – 2PRP̲U or
	1P̲RP – 1P̲RPS - 1P̲RPU	1PRP̲ – 1PRP̲S - 1PRP̲U
Topology 4	1P̲RP - 2P̲UU or	1PRP̲ - 2UP̲U or
	1P̲RP - 1P̲US - 1P̲UU	1PRP̲ - 1UP̲U - 1UP̲S
	(two intermediate P joints changed to fixed-length links)	(two proximal P joints changed to fixed points)

2.4 Topology of the 2R PKM

The determination of 2R PKM topology candidates is based on the following design constraint: "The PKM wrist should use only R joints. The use of P, C, S, and H joints is not allowed." This design constraint is provided for the following reasons: 1) to create as small space as possible for the 2R module because longer or larger space of the 2R module will reduce the effective workspace of the machine, 2) to require simple actuation mechanism, and 3) to provide as minimum joint errors as possible.

After comparing between some topology candidates, the selected topology is an overconstrained, decoupled 2R PKM using R joints only as depicted in Fig. 4. This 2R PKM has R̲R̲ – R̲RR topology. This mechanism was firstly proposed by Gosselin and Caron [11] and is listed by Gogu [12] under the class of 2-DOF parallel wrists.

Fig. 5(a) shows the basic implementation of this mechanism. The mechanism has three links with two actuated R joints. In order to further increase the stiffness, double-bar links are used in two links as shown Fig. 5(b). Consequently, this also needs two more R bearings. The dimension and detail geometry of the links of the 2R PKM were optimized to maximize the tilting range. The optimized 2R PKM has a tilting range of -90 to 90 degrees for both rotations.
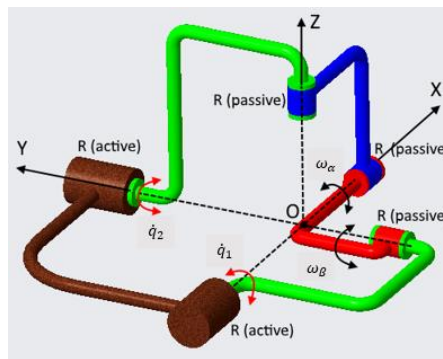
Fig. 4. The R̲R̲-R̲RR PKM schematic, with $\dot{q}_1$ and $\dot{q}_2$ denote the velocities of the actuated joints whereas ω_α and ω_β denote the angular velocities of the end-effector

(a)   (b)
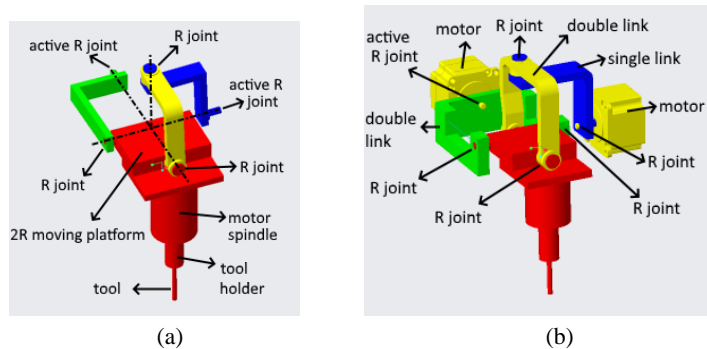
Fig. 5. (a) Basic implementation of the RR-RRR PKM with single-bar links, and (b) implementation of the RR-RRR PKM with two double-bar links

3 Conclusions

A 3T2R machine tool consisting of a novel reconfigurable 3T PKM and a 2R PKM was proposed. The proposed reconfigurable 3T PKM can be transformed to four topologies with eight configurations, which are suitable for machining with various reach, workspace, and directions. Most interestingly, these topologies include orthogonal (cube) and non-orthogonal topologies, each with its advantages. A decoupled 2R PKM with some double-bar links to increase its stiffness was also proposed to be serially connected to the reconfigurable 3T PKM to compose a 3T2R HKM capable of performing five-axis machining. The dimension and detail geometry of the links of the 2R module were optimized to provide an optimal tilting range. The 2R module can be removed to transform the 3T2R machine to a 3T machine.

References

1. Z. M. Bi and L. Wang, Optimal design of reconfigurable parallel machining systems, *Robotics and Computer-Integrated Manufacturing*, 25 (2009), pp. 951-961.
2. D. Tosi, G. Legnani, N. Pedrocchi, P. Righettini, and H. Giberti, Cheope: A new reconfigurable redundant manipulator, *Mechanism and Machine Theory*, 45 (4) (2010), pp. 611-626.
3. K. Wohlhart, Kinematotropic linkages, In: J. Lenarcic, V. P. Castelli (eds), *Advances in Robot Kinematics*, Springer, Dordrecht, 1996, pp. 359 368.
4. Q. Zeng and K. F. Ehmann, Design of parallel hybrid loop manipulators with kinematotropic property and deployability, *Mechanism and Machine Theory*, 71 (2014), pp. 1-26.
5. P. Grosch, R. Di Gregorio, J. López, and F. Thomas, "Motion planning for a novel reconfigurable parallel manipulator with lockable revolute joints", Proceedings on 2010 IEEE International Conference on Robotics and Automation, IEEE (2010), 3-7 May, 2010, Anchorage, AK, 4697 4702.
6. W. Ye, Y. Fang, K. Zhang, and S. Guo, Mobility variation of a family of metamorphic parallel mechanisms with reconfigurable hybrid limbs, *Robotics and Computer-Integrated Manufacturing*, 41 (2016), pp. 145-162.
7. D. M. Gan, J. Dai, J. Dias, and L. D. Seneviratne, Reconfigurability and unified kinematics modeling of a 3rTPS metamorphic parallel mechanism with perpendicular constraint screws, *Robotics and Computer-Integrated Manufacturing*, 29 (2013), pp. 121–128.
8. M. C. Palpacelli, L. Carbonari, G. Palmieri, and M. Callegari, Analysis and Design of a Reconfigurable 3 DoF Parallel Manipulator for Multimodal Tasks, IEEE/ASME Transactions on Mechatronics, 20 (4) (2015), pp. 1975 1985.
9. D. M. Gan, J. Dias, and L. D. Seneviratne, Unified Kinematics and Optimal Design of a 3 rRPS Metamorphic Parallel Mechanism with a Reconfigurable Revolute Joint, *Mechanism and Machine Theory*, 96 (part 2) (2016), pp. 239 254.
10. T-F. Tang and J. Zhang, Conceptual design and comparative stiffness analysis of an Exechon-like parallel kinematic machine with lockable spherical joints, *International Journal of Advanced Robotic Systems*, July-August 2017, pp. 1–13, DOI: 10.1177/1729881417724134.
11. C. M. Gosselin and F. Caron, Two-Degree-of-Freedom spherical orienting device, US Patent: 5966991, 1999.10.19, 1999.
12. G. Gogu, *Structural Synthesis of Parallel Robots, Part 4: Other Topologies with Two and Three Degrees of Freedom*, Edition 1, Springer, Netherlands, 2009.

Configuration Optimization for Improved Tip-over Stability of a Modular Reconfigurable Mobile Manipulator

Tao Song [1], Jiang-Tao Peng[1] and Heng-Yu Li[2]

[1] Key Laboratory of Intelligent Manufacturing and Robotics, School of Mechatronics, Engineering and Automation, Shanghai University, HC206, No. 99, Road Shangda, Shanghai 200444, China

[2] School of Mechatronic Engineering and Automation, Shanghai University, 99 Shangda Road, Shanghai, China

songtao43467226@shu.edu.cn

Abstract. A method is presented for configuration optimization to improve the tip-over stability of a modular reconfigurable mobile manipulator (MRMM). The said MRMM consists of a modular reconfigurable robot (MRR) mounted on a mobile platform. The MRR in different configurations creates different wrenches onto the mobile platform, leading to different tip-over moments of the MRMM. The underlying problem is how to find one optimal configuration of MRR to reconfigure under a given application that would improve the system's tip-over stability. Firstly, all the permissible configurations are identified through an enumeration method. Then, the feasible configurations are determined based on application-oriented workspace classifications. At last, two workspace indices, Vertical Reach and Horizontal Reach, are used to obtain the optimal configuration. For verification, the tip-over stability computation of MRMM with two indices, tip-over moment and stable region ratio, are carried out. The results of three cases, i.e. vertical, horizontal and general 3D space applications, show that the proposed method can be used to obtain optimal configuration for improving MRMM's tip-over stability.

Keywords: Tip-Over Stability, Modular Reconfigurable Mobile Manipulator, Modular Reconfigurable Robot

1   Introduction

A modular reconfigurable mobile manipulator (MRMM) integrates a mobile platform with an onboard modular reconfigurable robot (MRR) [1]. This combination offers the dexterous manipulation capability from the manipulator as well as the mobility from the mobile platform [2]. Since MRR can form a new system enabling new functionalities by disconnecting and reconnecting modules in different configurations, the MRMM inherits this feature to adapt new applications without the need of acquiring a new manipulator [3]. In the past few decades, research has been carried out for modular

mobile platforms including design approaches for obtaining orientation capability [1], kinematics and dynamics analysis [4], tip-over stability analysis [5, 6], control [7], path, trajectory planning [8, 9], and configuration optimization for calibration [10] as well as structural design [11] and updating method [12].

For traditional mobile manipulators, the tip-over instability can be induced by reaction forces and moments from the manipulator onto the mobile platform. The instability problem caused by this dynamic effect poses a great concern for the safety of robot operation. The issue of tip-over stability has been studied for decades , and many criteria were proposed to measure the stability margin of a mobile system, e.g. center of gravity, static stability margin, zero moment point (ZMP) , longitudinal stability margin [13], dynamic stability margin [14], tumble stability judgment [15], leg-end supporting moment[16], force-angle stability (FA) [17], foot-rotation indicator (FRI) [18], moment-height stability [19], stability pyramid, and tip-over moment (TOM) [10].

With these criteria, a number of path planning and guidance control methods were proposed. Qiang et al. proposed a method of ZMP path planning using a stability potential field to control the manipulator to maintain the stability of the whole system while moving along a given trajectory [20]. Hatanol et al. studied the ZMP-based stability of a mobile manipulator in transient states [21]. Lee et al. proposed an online compensation scheme for rollover prevention of mobile manipulators based on the invariance control framework with the gradient of ZMP [22]. Peters et al. presented a method to control the Sample Return Rover's reconfigurability to enhance system tip-over stability with FA criterion [23]. Talke et al. developed an autonomous tip-over prevention behavior for a mobile robot using a FA stability measure [24]. Choi et al. provided an asymptotically stabilizing controller that integrates fully-actuated and under-actuated phases of walking with FRI criterion [25].

For configuration optimization, Jason et al. presented a task-based optimization method to maximize the number of attractive regions and minimize the number of repellent regions [26]. Jan et al. proposed an optimization method for reconfiguration planning of handling systems. With this method, a fixed number of configurations is optimally selected from the entire configuration space and simultaneously allocated to a set of handling tasks in a most energy efficient way [27]. Bo et al. proposed a task-oriented configuration optimization method to obtain a lattice distortable reconfigurable robot which has enough workspace reachability and structural strength to perform a specific task [28]. Liu proposed a novel configuration optimization method for reconfigurable manipulators using genetic algorithms and Dijkstra algorithms. This method combines a minimum task execution time with minimum energy consumption [29]. Saleh et al. proposed a memetic algorithm approach to optimize a serial modular and reconfigurable robot which can generate multiple solutions to the inverse kinematics problem for any given spatial task [10].

So far, the configuration optimization to improve the MRMM's tip-over stability has not been fully studied. The challenge lies in the configuration space of the MRR. In this paper, one methodology is presented to study this problem. The underlying problem for this study is to identify an optimal configuration with the most tip-over stability of the MRR mounted on a mobile platform.

2   Problem Formulation

The MRR under this study is mounted on a mobile platform. The MRR consists of a number of joint modules and link modules. Each joint module can be manually reconfigured to provide the rotation about one of three axes of module's body coordinate system. Successive modules are connected to each other by attaching one end of the link module to one of the flat faces of the previous joint module which can form a serial manipulator. Fig. 1 (a) and (b) show one configuration with three revolute joint modules and three link modules.

(a)

(b)
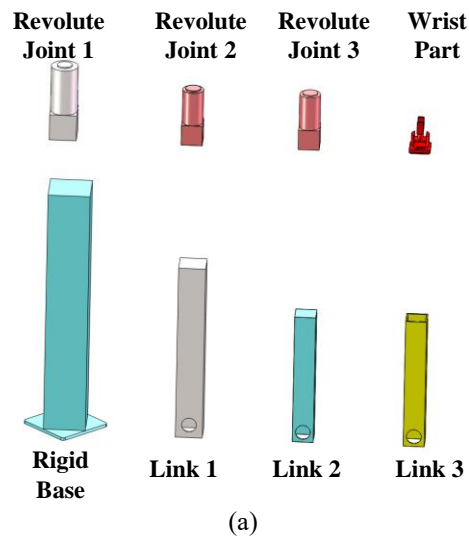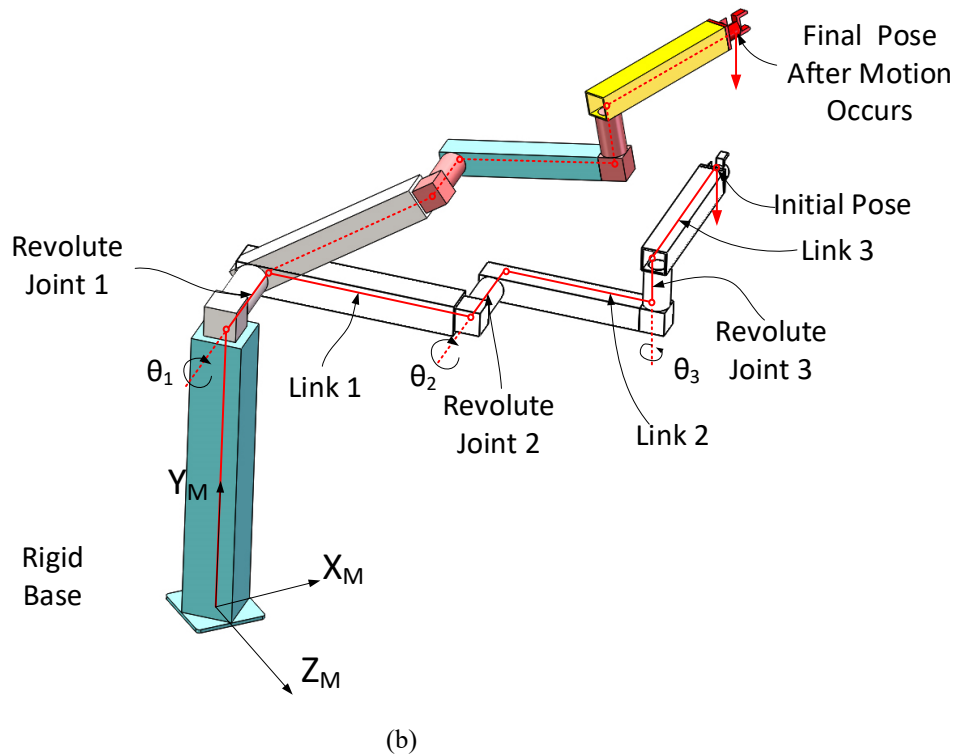
Fig. 1. (a) Joint and link modules, (b) Assembled MRR

The tip-over stability analysis is to determine an optimal configuration that can provide the most stable MRMM system for a given application. In Fig. 2, a search method for optimal configuration is proposed as follows:

1) For given joint modules and link modules, all the permissible configurations (PCs) of a MRR will be found using an enumeration algorithm [3].

2) For all PCs, the feasible configurations (FCs) will be identified by application-oriented workspace classifications.

3) For all FCs, the optimal configuration will be determined based on the workspace indices.
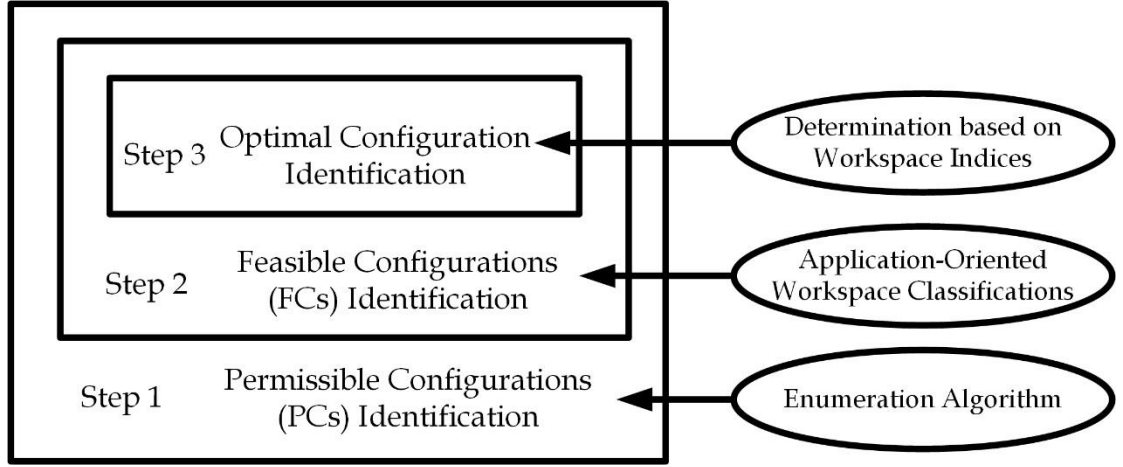
Fig. 2. Optimization process to improve MRMM's tip-over stability

3 Methodology

3.1 MRR Modeling

Kinematically, MRR can be modeled as [10]:

$$\mathbf{X} = f(\mathbf{q}, {}^{C}\mathbf{g}), \quad \mathbf{q_i} = (\theta_i, s_i), \quad {}^{C}\mathbf{g_i} = (x_i, y_i, z_i, \alpha_i, \beta_i, \gamma_i)^{T}, \quad i = 1, \dots, n \qquad (1)$$

where $\mathbf{X}$ is a vector representing the MRR's pose, i.e., $\mathbf{X} = (x, y, z, \alpha, \beta, \gamma)^{T}$ with the first three components representing the end-effector's position and the last three ones representing the pitch, roll and yaw (PRY) angles of the end-effector; $\mathbf{q_i}$ is the joint variable for the ith joint with θ_i for a revolute joint and s_i for a prismatic joint; ${}^{C}\mathbf{g_i}$ is a set of kinematic parameters for setting up a joint-link module at an initial configuration, with $(x_i, y_i, z_i)^{T}$ representing its position and $(\alpha_i, \beta_i, \gamma_i)^{T}$ for its orientation with respect to the global coordinates. Superscript C is a configuration index and subscript i is a joint-link module index. By selecting the configurations of these modules, the overall structure of the MRR is reconfigured.

For reconfiguration purpose, the initial configuration set-up (ICSU) is defined for a MRR by including a static rotation matrix ${}^{C}\mathbf{R}_{si}$ and a static body vector ${}^{C}\mathbf{b}_{si}$, which can be obtained from ${}^{C}\mathbf{g_i}$,

$$\text{ICSU}_i = ({}^{C}\mathbf{b}_{si}, {}^{C}\mathbf{R}_{si}) = f'({}^{C}\mathbf{g_i}) \qquad (2)$$

where

$$ {}^{C}\mathbf{R}_{si} = \mathbf{R}_x(\alpha_i)\mathbf{R}_y(\beta_i)\mathbf{R}_z(\gamma_i) \qquad (3)$$

$$^C\mathbf{b}_{si} = x_i\overrightarrow{\mathbf{X_I'}} + y_i\overrightarrow{\mathbf{Y_I'}} + z_i\overrightarrow{\mathbf{Z_I'}} \tag{4}$$

Where $\mathbf{R}_x(\alpha_i)$, $\mathbf{R}_y(\beta_i)$ and $\mathbf{R}_z(\gamma_i)$ are the rotation matrices according to the PRY angles, respectively, and $\overrightarrow{\mathbf{X_I'}}$, $\overrightarrow{\mathbf{Y_I'}}$ and $\overrightarrow{\mathbf{Z_I'}}$ are the three unit-vectors of the local frame attached to the ith joint. A conventional robot manipulator usually has its fixed ICSU, while a MRR's ICSU changes each time after reconfiguration. Based on [10], the kinematic formulation involves a static part and a motion part. As shown in Fig. 3, the static part ($^C\mathbf{R}_{s(i-1)i}$, $^C\mathbf{b}_{si}$) is defined according to the ICSU as indicated in Eq. (2), and the motion part ($\mathbf{R}_{mi}$, $\mathbf{b}_{mi}$) represents the movement of either joint or link $\mathbf{q}_i$. The total translation $\mathbf{b}_i'$ and rotation $\mathbf{R}_{(i-1)i}$ of the ith link can be given as:

$$^C\mathbf{R}_{(i-1)i} = {}^C\mathbf{R}_{s(i-1)i}\mathbf{R}_{mi} \tag{5}$$

$$^C\mathbf{b}_i' = {}^C\mathbf{b}_{si} + \mathbf{b}_{mi} \tag{6}$$

Where $\mathbf{R}_{mi}$ and $\mathbf{b}_{mi}$ are the rotation matrices and body vectors, respectively, which are functions of the joint variables $\mathbf{q}_i$ in Eq.(1), and their calculations are equivalent to Eqs. (3) and (4). The end-effector's pose can be expressed with respect to the global reference frame by

$$^C\mathbf{p}_{n+1} = \sum_{i=0}^{n} {}^C\mathbf{R}_{oi}{}^C\mathbf{b}_i' \tag{7}$$

$$^C\mathbf{R}_{on} = \prod_{i=1}^{n} {}^C\mathbf{R}_{(i-1)i} \tag{8}$$

Where $^C\mathbf{b}_i'$ is the link body vector in the local frames, which is transformed to the global frame by multiplying the orientation matrix $^C\mathbf{R}_{oi}$ and then summed to obtain the position of the end effector, as given in Eq. (7); $^C\mathbf{R}_{(i-1)i}$ represents the rotation matrix between two adjacent link body frames, which is sequentially multiplied together to determine the orientation of the end-effector, as given in Eq. (8).

The separation of the static part and dynamic part of the rotation matrix in Eq. (5) allows the use of Zero Reference Plane (ZRP). Under ZRP, all modules can be set up uniformly with respect to the global coordinates for each configuration, i.e. previously mentioned ICSU. This would alleviate some burdens when required to re-generate the robot kinematics and dynamics equations after reconfiguration. At ZRP meaning that no joint motion is applied, the following can be obtained.

$$^C\mathbf{R}_{s0i} = {}^C\mathbf{R}_{s0(i-1)}{}^C\mathbf{R}_{s(i-1)i} \tag{9}$$

Where $^C\mathbf{R}_{s0i}$ is the static rotation matrix of the ith module that is set up with respect to the global frame at ZRP; $^C\mathbf{R}_{s0(i-1)}$ is the static rotation matrix of the (i-1)th module with respect to the global frame at ZRP. Then, $^C\mathbf{R}_{s(i-1)i}$ needed for Eq. (5) can be derived as

$$^{C}\mathbf{R}_{s(i-1)i} = {}^{C}\mathbf{R}_{s0(i-1)}^{T}\,{}^{C}\mathbf{R}_{s0i} \qquad (10)$$

Eq. (10) is the basic formulation for the robot kinematics and dynamics based on ZRP.
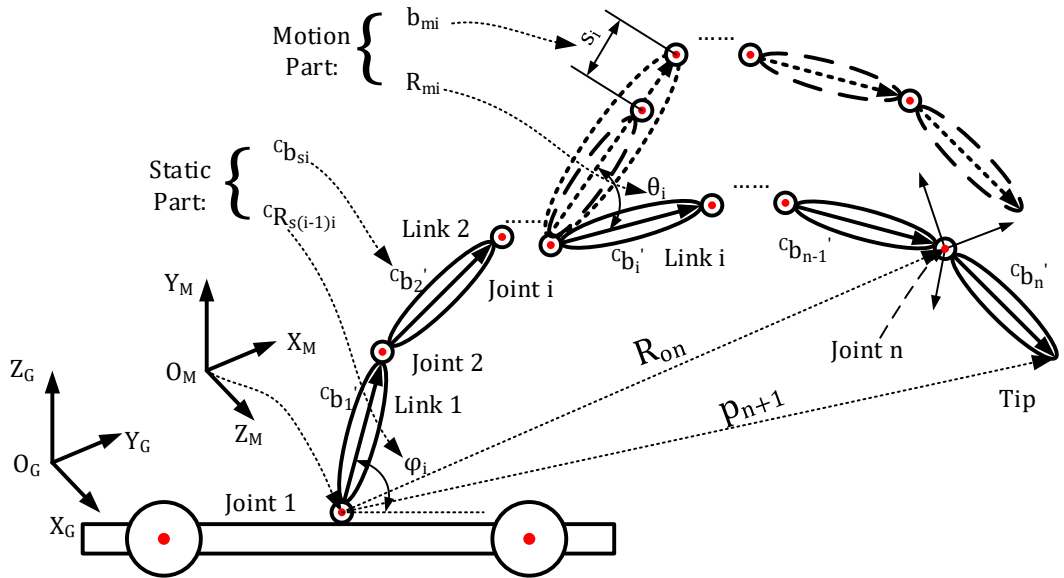
Fig. 3. Manipulator kinematic modeling with static and motion parts

3.2 Configurations Enumeration

A configuration space is referred to as the number of PCs that can be realized using the robot modules of a MRR without violating physical constraints. The basic structure of the MRR under study follows that of a traditional industrial robot manipulator. The first three joint-link modules form a main body for positioning and the last three joints form a wrist for orientation. This study is only focused on the first three modules. Based on the joint-link modules shown in Fig. 1, the total number of feasible configurations for the first three joint and link modules would be $6^6 = 46656$. However, through isomorphism analysis, deletion of collinear modules and consideration of physical limits, a three DOFs MRR yields 14 FCs for spatial motions, as listed in Table 1. All these FCs and their workspaces are shown in Appendix as well. In Table 1, and these axes are the initial axes set up according to the global frame at ZRP. It is noted that Conf. 11 y-x-z-x-z-x is the commonly used industrial PUMA robot configuration.

Table 1. Enumerated Feasible MRR spatial configurations – axes arrangement

Conf. #	Joint 1 axis	Link 1 axis	Joint 2 axis	Link 2 axis	Joint 3 axis	Link 3 axis
1	x	z	x	z	y	x
2	x	z	y	x	y	x
3	z	x	y	x	y	x
4	z	x	-z	x	y	x
5	x	z	-y	x	y	x
6	z	x	-y	x	y	x
7	y	x	-z	x	y	x
8	x	z	y	x	z	x
9	y	x	y	x	z	x
10	z	x	y	x	z	x
11	y	x	z	x	z	x
12	y	x	-y	x	z	x
13	z	x	-y	x	z	x
14	y	x	-z	x	z	x

3.3 Application-Oriented Workspace Classifications

To find an optimal configuration in FCs, three general applications are considered. The first one is that the tip of MRMM works in a vertical plane. Such applications include drilling or riveting of flat or curved panels, such as aircraft fuselage. The second one is that the tip of MRMM works in a horizontal plane. These applications include grinding, welding and painting of large components, such as train roofs. The third one is that the tip of MRMM works in a general 3D space, with application including part handling or assembling.

For 14 FCs listed in Appendix, their workspace shapes are computed and shown in the last column that can be classified according to the above-mentioned three applications. The first class is the vertical doughnut shape which is suited for vertical plane application. The second class is the horizontal doughnut shape which is suited for horizontal plane application. The last class is hemisphere or hemi-ellipsoid shape which is suited for 3D space applications.

The first class includes Conf. 1 and Conf. 4. In this case, the axes of adjacent joint 1 and 2 are all along the same direction, i.e. Joint 1 and 2 in Conf. 1 both along the x direction while Joint 1 and 2 in Conf. 4 both along the z direction. Since these axes are not in parallel with the horizontal direction, their workspaces are of doughnut shape in the vertical direction. The second class is similar to the first class which includes Conf. 9 and Conf. 12. The axes of Joint 1 and 2 of these two configurations are both along the y direction, i.e. along vertical direction. Their workspaces are of doughnut shape in the horizontal direction. The last class includes all the rest, i.e. Conf. 2, 3, 5, 6, 7, 8, 10, 11, 13 and 14. For those, the axes of Joint 1 and Joint 2 are not along the same direction, which makes their workspaces more like a hemisphere or hemi-ellipsoid shape.

Table 2. Workspace Classifications and Indices

Workspace Classifications	Conf. #	VR (mm)	HR (mm)
Vertical Plane Application	1	1621.4	1621.4
	4	1562.6	1562.6
Horizontal Plane Application	9	1420.1	1621.4
	12	1205.9	1562.6
	2	1614.2	1614.2
	3	1614.2	1614.2
	5	1570	1570
	6	1570	1570
3D Space Application	7	1282.7	1621.4
	8	1562.6	1562.6
	10	1621.4	1621.4
	11	1393.1	1614.2
	13	1621.4	1621.4
	14	1341.6	1570

Vertical Reach (VR)

Horizontal Reach (HR)
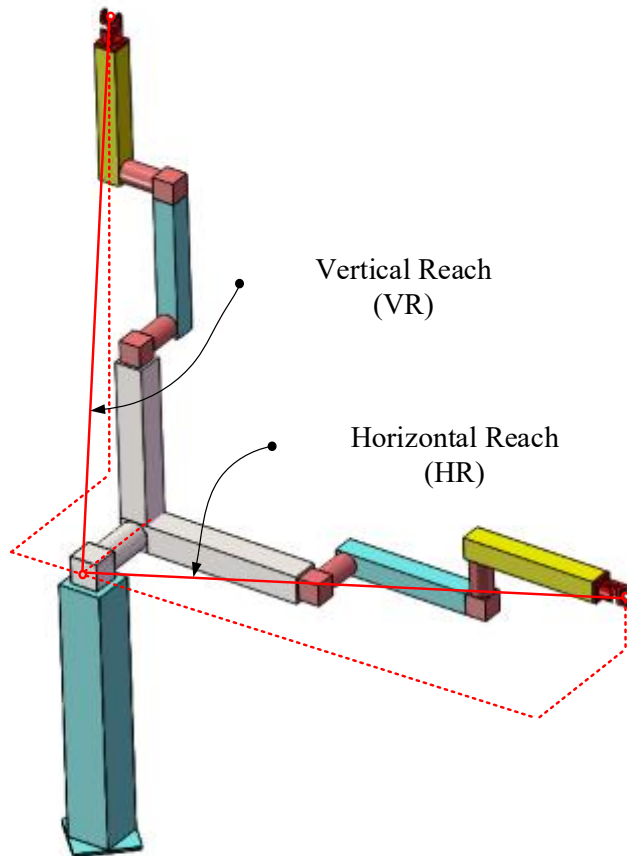
Fig. 4. VR and HR

3.4 Determination based on Workspace Indices

Since the workspace of MRR is a main performance index that is closely related to the tip-over problem, two indices describing the workspace characteristics are introduced. Taking Conf. 1 shown in Fig. 4 as an example, one important index is Vertical Reach (VR), i.e. the highest position which the manipulator can reach. The other one is Horizontal Reach (HR), i.e. the farthest position which the manipulator can reach. VR and HR of all feasible configurations are listed in Table 2. These two indices play a key role in determining an optimal configuration for a given task. If these two indices are longer, it means the workspace is bigger. Based on the former research [10], for static case, long HR may mean more tip-over moment if the manipulator tip moves to the outside of the mobile platform. For dynamic case, long HR or VR may mean less tip-over stability with the same joint speed and acceleration. For tip payload case, long HR or VR means long arm of force, which may lead to less tip-over stability. The method proposed here is configuration optimization with these two workspace indices. After application-oriented workspace classifications, the configuration corresponding to the short HR and VR combination will be assigned as an optimal one. The short HR and VR will also result in small workspace, which will reduce reachability, the mobility of mobile platform which can be solved by a linear guide rail module between the mobile platform and MRR.

4 Tip-over Stability Verification

4.1 Tip-Over Stability Modeling

For the tip-over analysis of a traditional mobile manipulator, two criteria are used: tip-over moment (TOM) and stable region ratio (SRR) [10, 30]. This method is based on the dynamic interaction of the manipulator with the mobile platform. These criteria are now applied for MRMM as well.
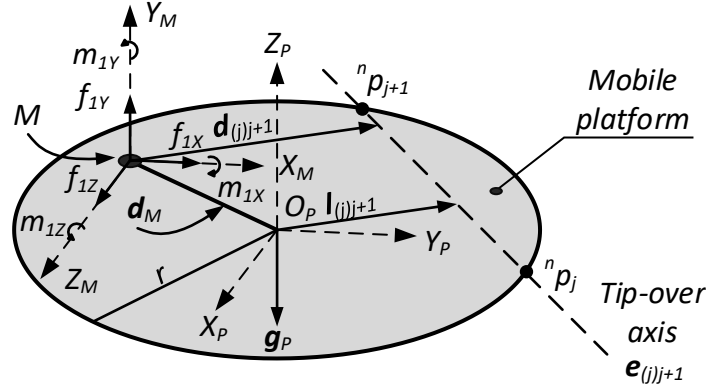
Fig. 5. Forces and moments on a mobile platform

Fig. 5 depicts the underlying problem. In this figure, the ellipse represents a mobile platform on which the afore-mentioned MRR is mounted. A local coordinate frame $\{X_P, Y_P, Z_P\}$ is attached to the center of gravity of the platform at point O_P. $\mathbf{g}_P$ is the vector of the gravitational force of the mobile platform and m_P is its mass. The mass of the MRR is m_r. It is mounted at point M to which the MRR's base coordinate frame $\{X_M, Y_M, Z_M\}$ is attached. The reaction wrench, denoted by $-{}^C\mathbf{w}_1$, is acting on point M from the MRR onto the mobile platform. This wrench has three force components ${}^C\mathbf{f}_M = [f_{1X}, f_{1Y}, f_{1Z}]^T$ and three moment components ${}^C\mathbf{m}_M = [m_{1X}, m_{1Y}, m_{1Z}]^T$, i.e. $-{}^C\mathbf{w}_1 = [{}^C\mathbf{f}_M{}^T, {}^C\mathbf{m}_M{}^T]^T$.

When tip-over occurs, the mobile platform rolls about a tip-over axis formed by two adjacent wheels. Two vectors ${}^n\mathbf{p}_j$ and ${}^n\mathbf{p}_{j+1}$ represent two adjacent wheels of the mobile platform, forming a tip-over axis $\mathbf{e}_{j(j+1)}$. $\mathbf{d}_M$ is the vector from the origin O_P to point M, representing the mounting position of the MRR. $\mathbf{d}_{j(j+1)}$ is a vector from point M to the tip-over axis $\mathbf{e}_{j(j+1)}$, while $\mathbf{l}_{j(j+1)}$ is a vector from O_P to the tip-over axis $\mathbf{e}_{j(j+1)}$. TOM about the tip-over axis $\mathbf{e}_{j(j+1)}$ can be derived considering all the afore-mentioned forces and moments as [10]

$$
{}^C\text{TOM}_{j(j+1)} = {}^C\mathbf{m}_M \cdot \mathbf{e}_{j(j+1)} + \left({}^C\mathbf{f}_M \times \mathbf{d}_{j(j+1)}\right) \cdot \mathbf{e}_{j(j+1)} + \left(\mathbf{g}_P \times \mathbf{l}_{j(j+1)}\right) \cdot \mathbf{e}_{j(j+1)} \quad (11)
$$

Based on Eq. (11), it can be seen that the size of mobile platform, the number of wheels, the mass of mobile platform, the placement of the manipulator and accessory will definitely affect the tip-over stability. These factors have already been discussed in [10, 30]. Generally, for a n-wheel mobile manipulator, there are n tip-over axes, i.e. n ${}^C\text{TOM}_{i(i+1)}$ values. The maximum ${}^C\text{TOM}_{i(i+1)}$ value represents the largest tip-over moment that the system has around the axis $\mathbf{e}_{i(i+1)}$. If this maximum ${}^C\text{TOM}_{i(i+1)}$ is positive, the system will tip over. If this maximum one is negative, the system is stable with a tip-over moment margin of $|{}^C\text{TOM}_{i(i+1)}|$. As mentioned before, except these factors, the configuration of MRR affects the tip-over stability as well. For this reason, our

study is to find one configuration that has the maximum tip-over moment margin or minimum tip-over moment for a set of given tasks.

For a selected configuration of MRR, the actual workspace volume can be obtained after mounting the MRR on the mobile platform. This obtained workspace is denoted by $^{C}v_{W}$, and the tip-over stability region is denoted by $^{C}v_{S}$. A stable region ratio (^{C}SRR) is introduced as $^{C}\text{SRR} = {}^{C}v_{S}/{}^{C}v_{W}$, which normalizes $^{C}v_{S}$ against $^{C}v_{W}$. The second objective of this study is to identify a configuration that has the maximum SRR with which the system can remain stable as much in workspace as possible.

The search method proposed in Fig. 2 is implemented using a workspace-based approach to determine an optimal configuration. For simplicity, the mobile platform, joint modules, link modules, payload are set the same for all FCs, so are the motion parameters including joint ranges, speeds and accelerations. In this case, the study of tip-over stability of the MRMM is bounded to the configuration of MRR.

As mentioned above, search over all FCs would be time consuming. An effective approach would be application-oriented workspace classifications. The first step is to classify the FCs into three classes according to the workspaces. Secondly, the two workspace indices, VR and HR, are used to further narrow down the selected classes. As analyzed in the previous research [10], the tip-over mostly occurs when the manipulator reaches the workspace boundary. Based on this, the selected configurations can be further sorted out from the FCs. Finally, an optimal configuration will be identified from the selected configuration space by the two criteria: tip-over moment (TOM) and stable region ratio (SRR).

In this section, the proposed method is applied for three applications, vertical, horizontal and 3D, respectively. For the first two applications, three cases are simulated: static, dynamic and tip force cases. For the last application, two situations are simulated: static and dynamic cases.

In static case, all joints' speed and acceleration are equal to 0. In dynamic case, based on the conclusions in [10], TOM and SRR will be computed as follows: the joint speeds of all revolute joints are set to $175°/s$ in two directions, and the joint accelerations are set to $200°/s^{2}$ in two directions. In this case, 5 kg payload at the tip is also included.

In tip force case, the force vector will be chosen based on workspace and application. For example, the horizontal tip force will be introduced into simulation if a MRMM works on a vertical plane, with applications including drilling or riveting of fuselage. The vertical tip force will be introduced if a MRMM works on a horizontal plane, with applications including grinding and welding. TOM and SRR of all configurations will be computed and compared to obtain the most stable configuration.

4.2 Vertical Plane Application

For the vertical plane application, through the above analysis, the selected class only includes Conf. 1 and 4. Comparing the workspace indices listed in Table 2, HR and VR of Conf. 4 are shorter than those of Conf. 1. With the method given in Sec. 3.2, it can be predicted that the MRMM system in Conf. 4 has a higher tip-over stability margin. For validation, the dynamics simulation is carried out.

The simulation results of these two configurations in three cases are listed in Table 3 and IV. In static case, the MRMM system is stable with a certain TOM margin in these two configurations and SRR results are both 100%. In dynamic case, the TOM results show that the MRMM systems in two configurations are unstable and the one in Conf. 4 is more stable than the one in Conf. 1. SRR results are consistent with TOM. Conf. 1's SRR is smaller than Conf. 4's which means that the MRMM with MRR in Conf. 4 is more stable than the one in Conf. 1. In tip force case, the TOM and SRR results show that system in Conf. 4 is more stable than the one in Conf. 1 as well.

As figures listed in Appendix shown, it can be found that Conf. 1's axes of Joint 1 and 2 are in the same direction, while Conf. 4's axes of Joint 1 and 2 are in the opposite direction. With the offset caused by motor length, it leads to that the tip and link CG positions of Conf. 1 is a little further than that of Conf. 4 from the origin point under the same joint angles. Based on [10], in static case, the conclusion has already been obtained that tip-over instability correlates with the horizontal positions of link CGs and the manipulator's tip. In view of this, the system with MRR in Conf. 4 is more stable than the one in Conf. 1 in static case. In dynamic case, the tip and link CG position difference also makes Conf. 1's linear velocity and acceleration bigger than Conf. 4's under the same joint speeds and accelerations, which in turn makes the system with MRR in Conf. 4 more stable than the one in Conf. 1. In tip-force case, this difference means that a longer arm of force for Conf. 1 would cause a bigger tip-over moment.

In view of this, conclusions can be drawn. For vertical plane application, the MRMM system with MRR in Conf. 4 is optimal. The result of dynamics calculation is in coordination with the result obtained with proposed method. Since SRR of Conf. 4 is not equal to 100% in dynamic case, for tip-over safety, the system should decrease joint speeds and accelerations.

Table 3. TOM and SRR results of static and dynamic case for vertical plane application

| Conf. # | Static | | Dynamic | | | |
	TOM ($N \cdot m$)	SRR (%)	J1-J3 speed (m/s)	J1-J3 acc. (m/s^2)	TOM ($N \cdot m$)	SRR (%)
1	-31.94	100	[175, 175, -175]	[200, 200, 200]	252.02	97.5
4	-88.76	100	[175, -175, -175]	[-200, 200, -200]	150.40	98.6

Table 4. TOM and SRR results of tip force case for vertical plane application

Conf. #	Tip force	TOM ($N \cdot m$)	SRR (%)
1	[500, 0, 0]	18.93	98.5
	[-500, 0, 0]	18.93	98.5
	[0, 0, 500]	18.93	99.8
	[0, 0, -500]	6.15	99.9
4	[500, 0, 0]	-23.32	100
	[-500, 0, 0]	-36.10	100

[0, 0, 500]	-23.32	100
[0, 0, -500]	-23.32	100

4.3 Horizontal Plane Application

For the horizontal plane application, through the above analysis, the selected class only contains Conf. 9 and 12. Comparing the data as shown in Table 2, HR and VR of Conf. 12 are shorter than those of Conf. 9 simultaneously. With the method proposed, it can be predicted that the MRMM system in Conf. 12 has a higher tip-over stability margin. The simulation results of these two configurations are listed in Table 5 and 6. It can be found that, in static and tip-force cases, the systems are both stable. As shown in Table 2, the difference of these two configurations is the direction of joint 2's axis. The one of Conf. 9's is along the positive direction while the one of Conf. 12's is along the minus direction. This difference makes the workspace of Conf. 9 stand higher than that of Conf. 12, but this difference does not affect the horizontal positions of tip or CG i.e. not affecting tip-over stability of system in static or tip-force case.

In dynamic case, the horizontal components of force caused by joint speeds and accelerations are the same. Since Conf. 9's arm of force in vertical direction is longer, the tip-over moment is bigger. It should be noted that, in real applications, the vertical height of the system is fixed according to the work-piece, so the height difference between Conf. 9 and 12 will be made up by an extra linear lifting platform. The aforementioned difference will no longer exist. In other words, the stability of MRMM in Conf. 9 and 12 are nearly the same.

Table 5. TOM and SRR results of static and dynamic case for horizontal plane application

Conf. #	Static		Dynamic			
	TOM ($N \cdot m$)	SRR (%)	J1-J3 speed (m/s)	J1-J3 acc. (m/s^2)	TOM ($N \cdot m$)	SRR (%)
9	-361.45	100	[175, 175, -175]	200, 200, 200	75.25	97.7
12	-361.45	100	[175, -175, -175]	-200, 200, -200	-181.26	100

Table 6. TOM and SRR results of tip force case for horizontal plane application

Conf. #	Tip force	TOM ($N \cdot m$)	SRR (%)
9	[0, 500, 0]	176.9	79.6
	[0, -500, 0]	41.62	99.3
12	[0, 500, 0]	176.9	79.6
	[0, -500, 0]	41.62	99.3

In view of this, conclusions can be drawn. For horizontal plane application, the stability of MRMM system with MRR in Conf. 12 has better tip-over stability than the one in

Conf. 9. The result of dynamics calculation is in correlation with the result obtained with the proposed method. To improve the stability, the operation height should be kept as low as possible.

4.4 3D Space Application

For 3D space applications, the selected class includes the rest ten configurations. The VR of Conf. 7 is the smallest, but its HR of Conf. 7 is the biggest. It means that the workspace of Conf. 7 is short in vertical direction but long in horizontal direction. The second smallest VR is Conf. 14 and its HR is the second smallest as well. The smallest HR is Conf. 8, while its VR is the third smallest. Overall, Conf. 14 may have the highest tip-over stability, since the distances in both directions are smaller.

The simulation results are listed in Table 7. In static and dynamic cases, it can be found that the tip-over stability difference of these ten configurations is very small. In static case, the horizontal position change of different configurations' CG is small which makes tip-over stability nearly the same. It can be obtained from Table 2 that Conf. 14's VR and HR are shorter than most of others. MRR in Conf. 14 cannot reach far positions in either vertical or horizontal direction, and this will decrease TOM. It improves the stability of system.

In view of these conclusions can be drawn. For 3D space applications, the stability of MRMM system with MRR in Conf. 14 is optimal. The result of dynamics calculation is in correlation with the result obtained with the proposed method.

Table 7. TOM and SRR results of static and dynamic case for horizontal plane application

| Conf. # | Static | | Dynamic | | | |
	TOM ($N \cdot m$)	SRR (%)	J1-J3 speed (m/s)	J1-J3 acc. (m/s^2)	TOM ($N \cdot m$)	SRR (%)
2	-359.07	100	[175, 175, 175]	[-200, -200, -200]	87.30	99.3
3	-359.07	100	[175, 175, 175]	[-200, -200, -200]	87.30	99.3
5	-361.28	100	[175, 175, -175]	[200, 200, -200]	65.80	99.5
6	-361.28	100	[175, 175, -175]	[-200, -200, 200]	65.80	99.5
7	-359.42	100	[175, -175, 175]	[-200, -200, -200]	9.88	99.9
8	-359.37	100	[175, 175, -175]	[-200, -200, 200]	10.51	99.9
10	-359.34	100	[175, 175, 175]	[200, 200, 200]	16.42	99.9
11	-358.85	100	[175, -175, -175]	[200, 200, 200]	9.95	99.8
13	-359.34	100	[175, 175, 175]	[200, 200, 200]	16.42	99.9
14	-360.63	100	[175, -175, 175]	[-200, -200, 200]	-4.81	100

5 Conclusions

In this paper, a method for determining the optimal configuration of MRR is proposed for a MRMM in order to improve the system's tip-over stability. The proposed method is of three steps. First, the permissible configurations are found using an enumeration algorithm. An application-oriented workspace classification is carried out to obtain feasible configurations for different applications. At last, two workspace indices, VR and HR, are used for configuration optimization. The optimal configuration can improve tip-over stability of MRMM. With proposed method, three cases including the vertical/horizontal plane application and 3D space applications are investigated. It is found that for vertical and horizontal plane application, Conf. 4 and 12 are the optimal one respectively, and for 3D space applications, Conf. 14 is the optimal configuration. Simulations on different cases are carried out for method validation. The results show that the proposed method can greatly facilitate the determination of an optimal configuration for MRMM for a given application that can guarantee an improved tip-over stability.

Acknowledgment

Reference

1 A. Ananiev, I. Kalaykov, B. Iliew, 2002, "An approach to the design of lightweight reconfigurable robot arm for a mobile platform," Proceedings of the 33rd ISR (International Symposium on Robotics), October, Vol. 7.

2 Yoshio Yamamoto, Xiaoping Yun, 1999,"Unified analysis on mobility and manipulability of mobile manipulators," Robotics and Automation, Proceedings. IEEE International Conference on, Vol. 2, pp. 1200-1206.
DOI: 10.1109/ROBOT.1999.772525

3 Richard Phillip Mohamed, 2015,"Kineto-Elastic Analysis of Modular Robot Systems with Component Model Updating," PhD thesis, Ryerson University, Toronto, Canada.

4 Yongchao Wang, Guilin Yang, Liang Liu, 2016, "Configuration-independent kinematics for modular mobile manipulators," Information and Automation (ICIA), IEEE International Conference on, IEEE.
DOI: 10.1109/ICInfA.2016.7832004

5 Yugang Liu, Guangjun Liu, 2010, "Interaction analysis and online tip-over avoidance for a reconfigurable tracked mobile modular manipulator negotiating slopes," IEEE/ASME Trans Mechatron, Vol. 15, no. 4, pp. 623–635.
DOI: 10.1109/TMECH.2009.2031174

6 Yugang Liu, Guangjun Liu, 2010,"Interaction analysis and posture optimization for a reconfigurable tracked mobile modular manipulator negotiating slopes," Robotics and Automation (ICRA), IEEE International Conference on, IEEE.
DOI: 10.1109/ROBOT.2010.5509986

7 Ahmad Saleh, Hongwei Zhang, Guangjun Liu, 2013,"Multiple working mode control of door-opening with a mobile modular and reconfigurable robot," IEEE/ASME Transactions on Mechatronics, Vol. 18, no. 3, pp. 833-844.
DOI:10.1109/TMECH.2012.2191301

8 Saleh Ahmad, Guangjun Liu, 2010, "A door opening method by modular re-configurable robot with joints working on passive and active modes," Robotics and Automation (ICRA), IEEE International Conference on, IEEE, pp. 1480-1485.
DOI: 10.1109/ROBOT.2010.5509162

9 Jiajun Li, Jianguo Tao, Liang Ding, Haibo Gao, Zongquan Deng, Kerui Xia, 2015,"Twisting door handles and pulling open doors with a mobile manipulator," Robotics and Biomimetics (ROBIO), IEEE International Conference on, IEEE, pp. 686-691.
DOI: 10.1109/ROBIO.2015.7418848

10 Lin, Y., Xi, F. Mohamed, R., and Tu, X., "Calibration of Modular Reconfigurable Robots Based on a Hybrid Search Method," ASME Journal of Manufacturing Science and Engineering, Vol. 132, No. 6, 061002, 2010.
DOI: 10.1115/1.4002586

11 Mohamed, R., Xi, F., and Finistauri, D., "Module-Based Static Structural Design of a Modular Reconfigurable Robot," ASME Journal of Mechanical Design, Vol. 132, No. 1, 014501, 2010.
DOI: 10.1115/1.4000639

12 Mohamed, R., Xi, F., and Chen, T.Y., "Pose-Based Structural Dynamic Model Updating Method for Serial Modular Robots," Mechanical Systems and Signal Processing, V. 85, pp. 530-555, 2017.
DOI: 10.1016/j.ymssp.2016.08.026

13 Robert B. Mcghee, Geoffrey I. Iswandhi, 1979, "Adaptive locomotion of a multi-legged robot over rough terrain," IEEE transactions on systems, man, and cybernetics, Vol. 9, no. 4, pp. 176-182.
DOI: 10.1109/TSMC.1979.4310180

14 Ben Sheng Lin, Shin-Min Song, 2001,"Dynamic modeling, stability, and energy efficiency of a quadrupedal walking machine," Journal of Robotic Systems, Vol. 18, no. 11, pp. 657-670.
DOI: 10.1002/rob.8104

15 KanYoneda, Shigeo Hirose, 1997,"Three-Dimensional Stability Criterion of Integrated Locomotion and Manipulation," J. of Robotics and Mechatronics, Vol. 9, no. 4, pp. 267-274.

16 Debao Zhou, K. H. Low, Teresa Zielinska, 2000,"A stability analysis of walking robots based on leg-end supporting moment," Robotics and Automation, IEEE International Conference on, IEEE, no. 3, pp. 2834-2839.
DOI:10.1109/ROBOT.2000.846457

17 Papadopoulos E.G., Rey D.A., 1996, "A new measure of tip-over stability margin for mobile manipulators," Robotics and Automation. Proceedings., IEEE International Conference on, Vol. 4, pp. 3111–3116, Minneapolis, MN.
DOI: 10.1109/ROBOT.1996.509185

18 Ambarish Goswami, 1999, "Postural stability of biped robots and the foot-rotation indicator (FRI) point," The International Journal of Robotics Research, Vol. 18, no. 6, pp. 523-533.
DOI: 10.1177/02783649922066376

19 S. Ali A. Moosavian, Khalil Alipour, 2006, "Stability evaluation of mobile robotic systems using moment-height measure," Robotics, Automation and Mechatronics, IEEE Conference on, IEEE.
DOI: 10.1109/RAMECH.2006.252730

20 Qiang Huang, Kazuo Tanie, Shigeki Sugano, 2000, "Coordinated motion planning for a mobile manipulator considering stability and manipulation," The International Journal of Robotics Research, Vol.19, no.8, pp.732-742.
DOI: 10.1177/02783640022067139

21 M. Hatanol, H. Obara, 2003, "Stability evaluation for mobile manipulators using criteria based on reaction," SICE Annual Conference, IEEE, no.2, pp. 2050-2055.

22 Sohee Lee, Marion Leibold, Martin Buss, Frank C. Park, 2012, "Online stability compensation of mobile manipulators using recursive calculation of ZMP gradients," Robotics and Automation (ICRA), IEEE International Conference on, IEEE, pp. 850-855.
DOI:10.1109/ICRA.2012.6225203

23 Steven C. Peters, Karl Iagnemma, 2006, "An analysis of rollover stability measurement for high-speed mobile robots," Robotics and Automation, ICRA, Proceedings IEEE International Conference on, IEEE, pp. 3711-3716.
DOI: 10.1109/ROBOT.2006.1642269

24 Kurt Talke, Leah Kelley, Patrick Longhini, Garret Catron, 2014, "Tip-over prevention through heuristic reactive behaviors for unmanned ground vehicles," Space and Naval Warfare Systems Center Pacific San Diego Ca, Vol. 9084, 90840L.
DOI: 10.1117/12.2049667

25 Jun Ho Choi, J. W. Grizzle, 2005, "Planar bipedal walking with foot rotation," American Control Conference, Proceedings of the 2005, IEEE, pp. 4909-4916.
DOI: 10.1109/ACC.2005.1470773

26 Jason A. Kereluk, M. Reza Emami, 2017, "Task-based optimization of reconfigurable robot manipulators," Advanced Robotics, 31(16), pp. 836–850.
DOI: 10.1080/01691864.2017.1362995

27 Jan B., Marco L., Yukio T., Burkhard C., 2017, "Optimization of the reconfiguration planning of
handling systems based on parallel manipulators with delta-like architecture," IEEE Robotics and Automation Letters, 2(3), pp. 1802-1808.
DOI: 10.1109/LRA.2017.2705286

28 Bo Yin, Zhenning Liang, Xin Dai, Jinqiu Mo, Shigang Wang, 2016, "Task-oriented configuration optimization of a lattice distortable reconfigurable robot," J Mechanical Engineering Science, 230(9), pp.1532–1543.

DOI: 10.1177/0954406215576061

29 Xinyu Liu, Bo Dong, Keping Liu, Yuanchun Li, 2016, "Configuration optimization method of reconfigurable manipulator based on Dijkstra algorithm," 4th International Conference on Sensors, Measurement and Intelligent Materials, Atlantis Press, pp.296-302.
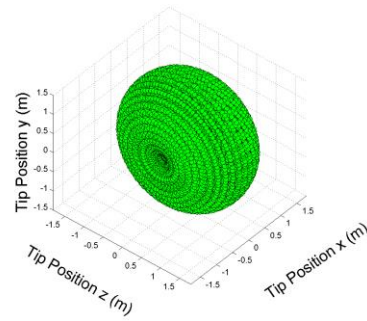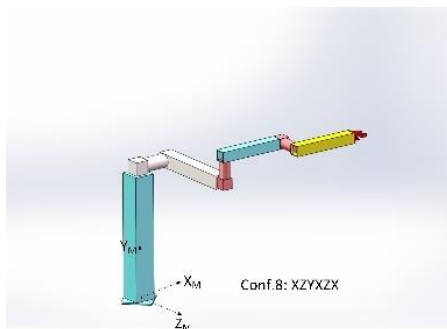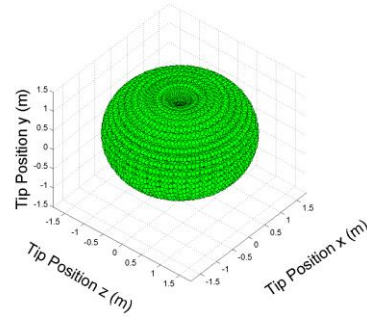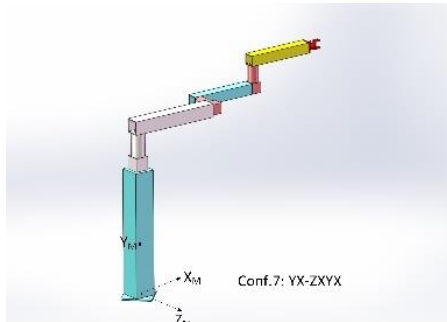DOI: 10.2991/icsmim-15.2016.56

30 Tao Song, Fengfeng (Jeff) Xi, Shuai Guo, Yu Lin, 2016, "Optimization of a Mobile Platform for a Wheeled Manipulator," ASME. J. Mechanisms Robotics, Vol. 8, no. 6, pp. 061007-061007-14.
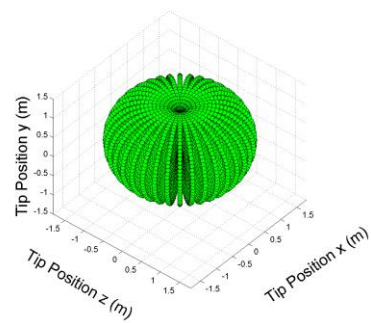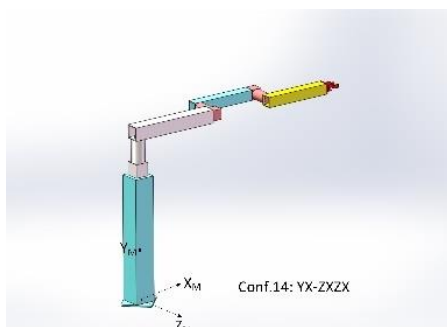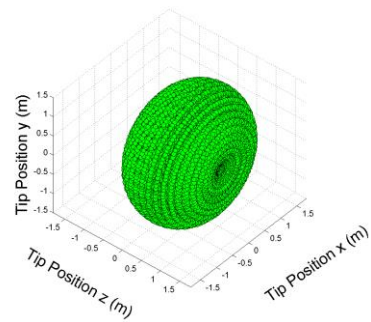DOI:10.1115/1.4033855.

Appendix:

Conf.3: ZXYXYX

Conf.4: ZX-ZXYX

Conf.5: XZ-YXYX

Conf.6: ZX-YXYX

Conf.11: YXZXZX

Conf.12: YX-YXZX

Conf.13: ZX-YXZX

Conf.14: YX-ZXZX
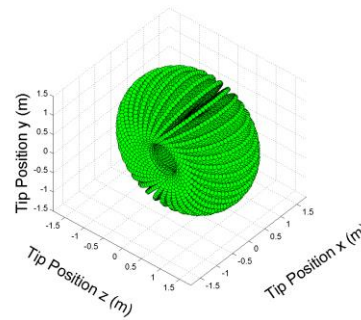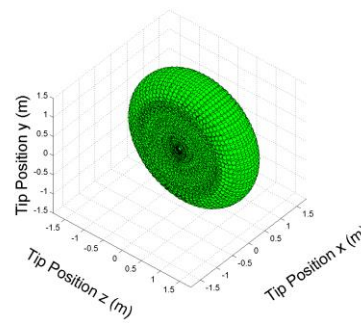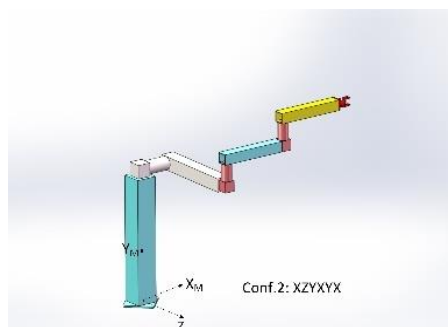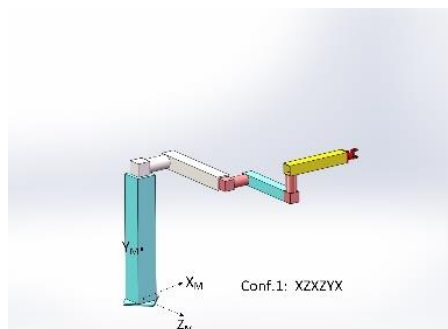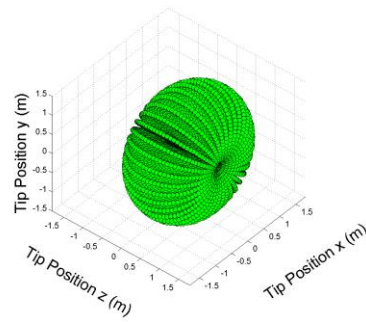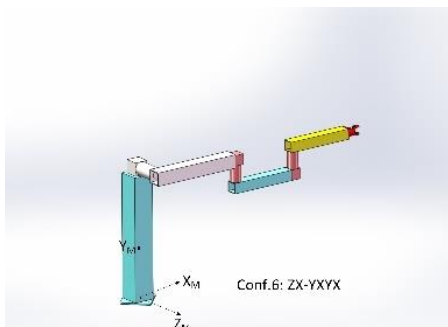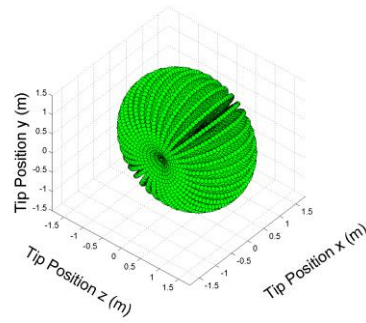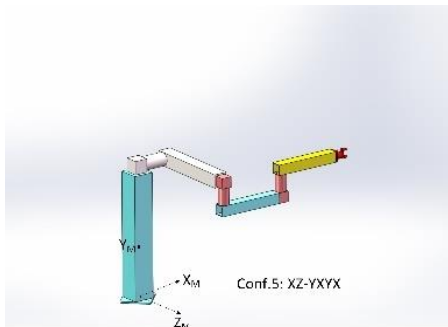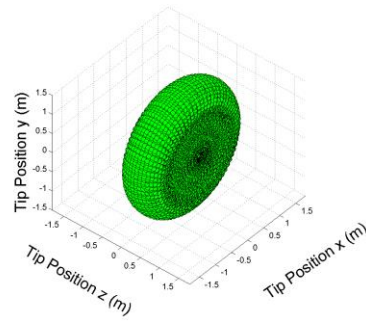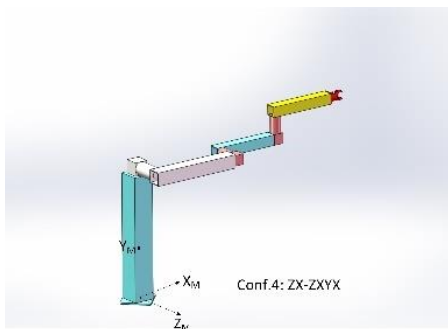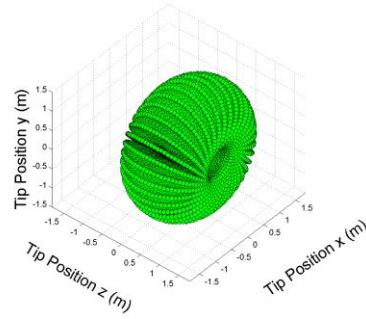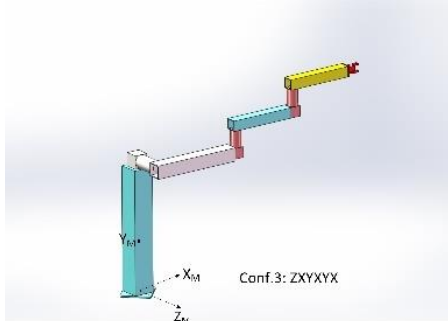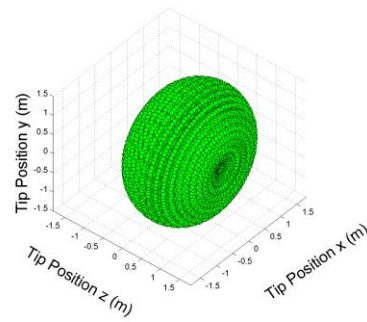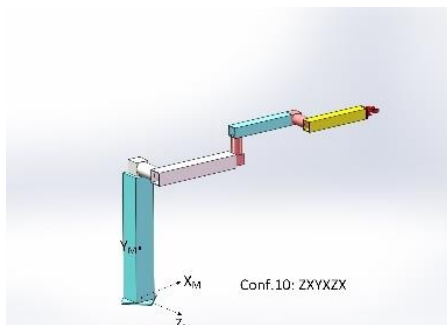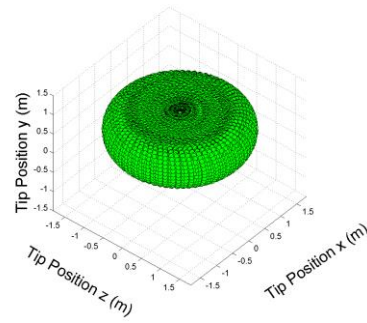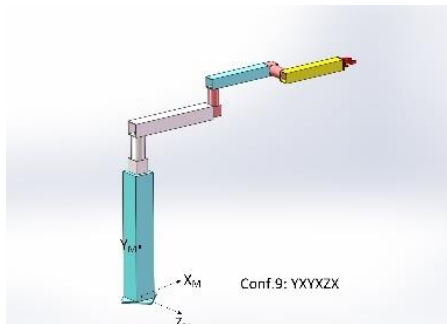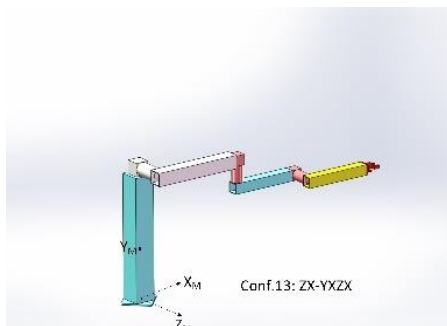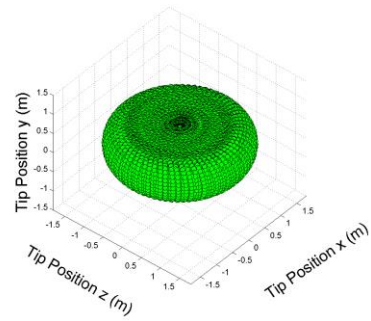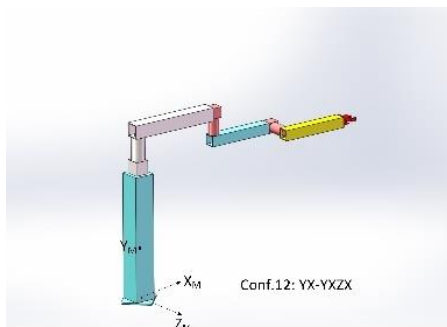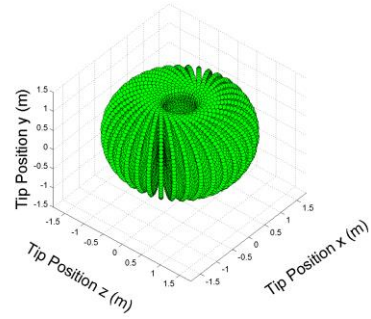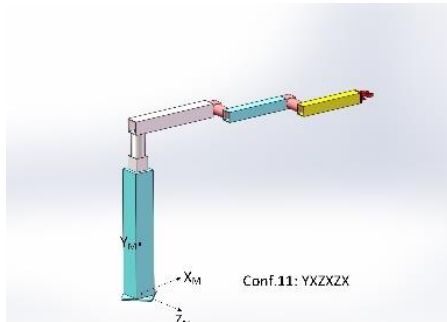
Design and analysis of a portable six-wheeled mobile robot with a reconfigurable body and self-adaptable climbing obstacle mechanism

Zhen Song[1], Zirong Luo[1*], Guowu Wei[2*] and Jianzhong Shang[1]

[1] College of Mechatronic Engineering and Automation, National University of Defense Technology, Changsha 410073, PR China

[2] School of Science, Engineering and Environment, University of Salford, Salford M5 4WT, United Kingdom

Abstract. This paper presents the design and development of a portable six-wheeled mobile robot with a reconfigurable body and self-adaptable climbing obstacle mechanism. Through body reconfiguration, this robot can provide three locomotion states as high-posture, low-posture, and folded state. When moving on a slope, the robot maintains the low-posture to prevent it from turning over; when moving in rough terrain, the robot transits to the high-posture to prevent the chassis from touching the ground. The robot also has the ability of self-adaptive climbing in unstructured environments. Mechanical design of the proposed robot is introduced, and kinematic and dynamic on obstacle crossing are addressed. In addition, experiments on land walking and obstacle climbing are conducted for verifying the structural and operational parameters design.

Keywords: Reconfigurable robot, mobile robot, Self-adaptive climbing mechanism, kinematic and dynamic.

1   Introduction

Frequent natural and man-made disasters seriously threaten the security and stability of human society [1, 2]. Whether the rescuers can detect the location of the trapped people in time is related to the life and safety of the trapped people. Mobile robots have been widely used for life detection in unstructured and rugged environments, which requires the robot to have excellent terrain adaptability and obstacle climbing ability [3, 4]. Therefore, it is of great value and significance to develop a ground mobile robot with a simple structure, high energy efficiency, and outstanding obstacle climbing ability and terrain adaptability [5, 6].

A suspended articulated frame can improve the ability of wheeled robot to adapt to unstructured environment. Examples of wheeled robots with suspended articulated frames are the rocker-bogie type rovers developed for Mars exploration, Spirit and Sojourner [7]. The two rocker-bogie mechanisms on each side of the robots maintain all

---

* Corresponding authors

the wheels in contact with the ground, even in presence of uneven terrain and obstacles. However, the suspended articulated frames complicate the mechanical structure of the robot and exhibit limitations in adapting to a complex terrain with high obstacles and steep slopes [8].

Legged robots are the most suitable for unstructured environments due to their capability to overcome obstacles and irregularities. Some robots move with rotating legs, which can reduce the complexity of the leg architecture and, consequently, control complexity whilst preserving good obstacle climbing ability. These robots include the RHex [9], the Loper [10], the ASGUARD [11] and so on. But robot with rotating legs is continuously subjected to shocks and vibrations during the movement, which is not conducive to the robot's carrying of mission equipment such as cameras.

However active locomotion concepts using additional motorized degrees of freedom combined with walking wheels can be more efficient in very rough terrain, for examples, the MULE [12], the Hybtor [13] and the Hylos [14]. Such mechanisms allow the robots to actively control the position of the centre of gravity with respect to the contact points with ground, thereby enhancing their stability and traction. But they are mostly a hybrid wheel-legged type with many degrees of freedom (DOFs), which add complexity to the control system and extend control and power resources [15].

Inspired by the above research, we propose a portable six-wheeled robot with a reconfigurable body, which does not rely on complex perception and control and has the ability of self-adaptable obstacle climbing. This robot has good obstacle climbing ability and has a broad application prospect in disaster rescue detection, mine clearance and explosive disposal detection.

2 Mechanism design of a portable six-wheeled mobile robot with a reconfigurable body

As illustrated in Fig. 1(a), the reconfigurable six-wheeled robot consists of a two-wheeled front body, a Sarrus-variant mechanism and a four-wheeled rear body with two rocker arms. The front body and rear body are the carriers that accommodate the batteries, transmission system and control system. The front body is driven by two walking wheels independently, two sets of obstacle-crossing wheels mounted on the adaptive climbing rocker arms are symmetrically distributed on both sides of the rear body. The front body and the rear body are connected by the Sarrus-variant mechanism, providing the relative rotation and foldability between the two bodies. The front body and the rocker arms on both sides constitute the three rocker arms of the robot that can rotate relative to the robot. The robot can realize the transformation among the three locomotion states as the low-posture state (see Fig. 1(b)), the high-posture state (see Fig. 1(c)), and the folded state (see Fig. 1(d)) through the Sarrus-variant mechanism. When moving on a slope (see Fig. 1(e)), the robot works at the low-posture state to lower the center of gravity; when moving on rough terrain (see Fig. 1(f)), the robot transforms into the high-posture state to raise the center of gravity to prevent the robot chassis from contacting the ground; when encountering a staircase (see Fig. 1(g)), the robot also works at the high-posture state, and climbs the stairs by continuously flipping

the rocker arms; when the robot needs to be carried, the robot folds up to reduce its size as shown in Fig. 1(d).
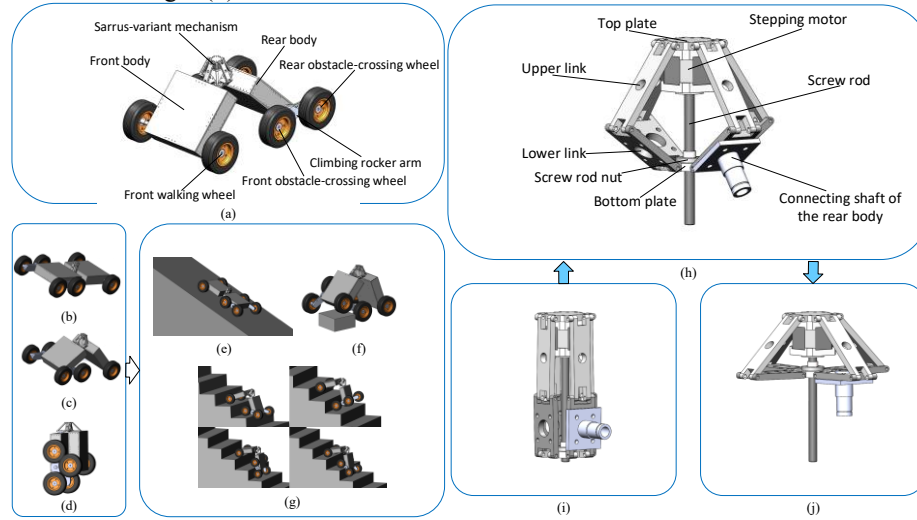

Fig. 1. Mechanical structure of the robot and the Sarrus-variant mechanism.

Reconfigurability of the robot's locomotion states is implemented by the Sarrus-variant mechanism. As shown in Fig. 1(h), the Sarrus-variant mechanism is a mechanical linkage device with one degree of freedom to realize the mutual conversion between limited circular motion and linear motion [16]. The stepper motor drives the nut to reciprocate linearly on the screw rod, which is converted to the relative rotational motion of the front and rear body, so that the robot movement posture can be adjusted (see Fig.1(b) to Fig. 1(d)) according to the changing environment.

As illustrated in Fig. 2, the adaptively climbing rocker and arm obstacle-crossing wheel system consists of a parallel-axis gear train and a rocker arm planetary epicyclic gear train. The secondary gear of the parallel-axis gear train and the center gear of the epicyclic gear train rotate synchronously, sharing the same shaft. Then the robot can climb over obstacles by turning the climbing rocker arms.
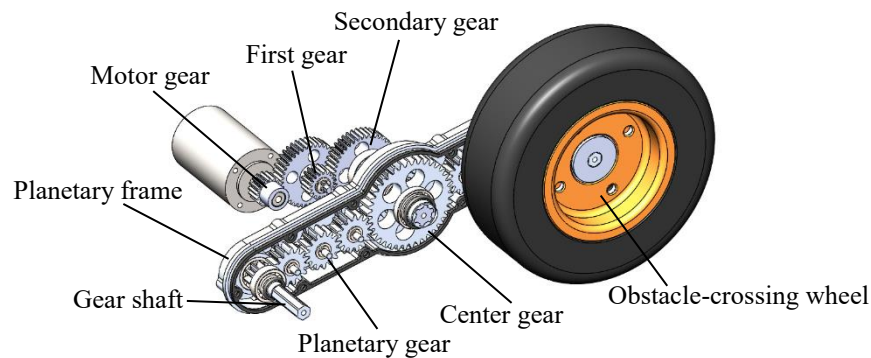

Fig. 2. Structure of the adaptively climbing rocker arm and obstacle-crossing wheel system.

3 Geometric, dynamic and stability analysis of robot obstacle crossing

The obstacle crossing process of the robot is shown in Fig. 3. Before encountering the obstacle, the robot first transforms itself into the high-posture state. When the robot moves forward horizontally on flat ground, the rocker arm does not turn over (see Fig. 3(a)). After encountering the obstacle, the front walking wheels pull the robot's front body to climb over the obstacle, relying on the friction force between the wheels and the obstacle (see Fig. 3(b)). Then the robot continues to move forward (see Fig. 3(c)) until the front obstacle-crossing wheels are against the obstacle, and the climbing rocker arms on both sides turn over and push the robot body forward (see Fig. 3(d)). When the rear obstacle-crossing wheels contact the edge of the obstacle (see Fig. 3(e)), the robot climbs the obstacle under the common traction of the six wheels (see Fig. 3(f)).
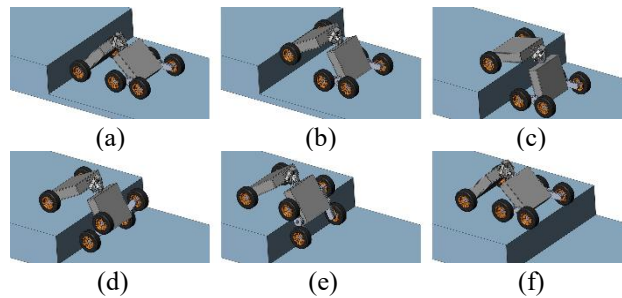
Fig. 3. Robot obstacle climbing process.

Based on the aforementioned mechanical design and the obstacle crossing process of the robot, it can be found that whether the robot can climb the obstacle is related to the reconfiguration of the Sarrus-variant mechanism. To climb obstacles, the robot must meet the requirements of geometric passing capability, dynamic passing capabilty and stability at the same time. In geometrics, the robot must have geometric passing ability, the robot cannot interfere and collide with obstacles in the process of obstacle crossing. In dynamics, the front walking wheels can lift the front body along the vertical surface of the obstacle, and the climbing rocker arms can support the rear body by overturning. In terms of stability, the robot will not overturn when crossing obstacles. Therefore, in order to reveal the relation between configurations of the Sarrus-variant mechanism and the obstacle crossing process of the robot, the geometric, dynamic and stability models of the robot's obstacle crossing process are established.

3.1 Geometric analysis of robot obstacle crossing

When the robot climbs over the obstacle, it should avoid the contact between the robot body and the obstacle. Even if contact occurs, it should have the mechanism of disengagement, so that the robot has good geometric passing ability.
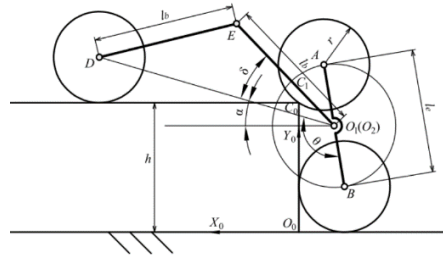
Fig. 4. The critical state of the robot obstacle crossing

Figure 4 shows the critical state of the robot obstacle-crossing as shown in phase (e) in Fig. 3. The rocker arm turns over and puts the rear obstacle-crossing wheel on the edge of the obstacle. At the time both the rear obstacle-crossing wheels and the front obstacle-crossing wheels are in contact with the obstacle.

In order to ensure that the robot's rear body will not contact with the edge of the obstacle when the robot's rocker arm is overturned, and the rear obstacle-crossing wheel can climb on the upper surface of the obstacle, the coordinate y_{C1} of point C_1 must be greater than the coordinate y_{C0} of point C_0. The geometric passing capability condition of robot obstacle crossing can be expressed as the function $G(\delta)$

$$G(\delta) = y_{C_1} - y_{C_0} = r\sin\delta\cos\alpha + r\cos\delta\sin\alpha - 2l_b\cos\delta\sin\alpha + r > 0 \tag{1}$$

3.2 Dynamic passing capability analysis of robot obstacle crossing

In addition to geometric factors, the robot must satisfy certain dynamics conditions. The stress condition of the robot in the obstacle-crossing phase (a) and phase (c) are shown in Figure. 5. In phase (a), under the joint action of the friction between the front wheel and the obstacle, and the output torque of the rear motor, the robot lifts the front body and keeps the front walking wheels in contact with the vertical surface of the obstacle. If the robot can't lift its front body, it cannot climb the obstacle. In phase (c), the robot front obstacle-crossing wheel just touches the vertical surface of the obstacle. The robot is about to support the rear body by turning the rocker arm, and pull the robot's front body by the friction between the front walking wheel and the upper surface of the obstacle, so that the robot can climb over the obstacle.
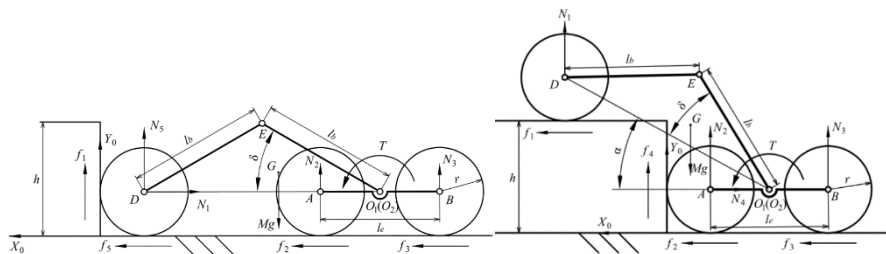

Fig. 5. The stress condition of the robot in the obstacle-crossing phase (a) and phase (c)

Based on the analysis of the stress condition of the robot in phase (a), only when $N_3 > 0$, the robot can climb along the vertical surface of the obstacle, instead of turning the rocker arms. And in phase (c), only when $N_1 > 0$, the robot rocker arms can overturn and prop up the rear body and continue to push the robot to climb over the obstacle instead of overturning. So the dynamic condition of robot's obstacle crossing can be expressed as the function $F_1(\delta)$ and $F_2(\delta)$

$$F_1(\delta) = N_3 = \frac{mg}{4} + \left(\frac{r}{l_e} - \frac{\mu}{2} - \frac{ri_{73}}{l_e}\right)\frac{\left(3m_{fb} + m_{rb} + 8m_w\right)gl_b\cos\delta}{4\left(ri_{73} + \mu(r + 2l_b\cos\delta)\right)} \quad (2)$$

$$F_2(\delta) = N_1 = \frac{\dfrac{mgl_e}{4(1 - 1/i_{73})} - \dfrac{\sqrt{(l_b\cos\delta)^2 - \left(\dfrac{h}{2}\right)^2}\left(3m_{fb} + m_{rb} + 8m_w\right)g}{4} + \dfrac{\left(m_{fb} + m_{rb}\right)hg\sin\delta}{8\cos\delta}}{\dfrac{l_e}{2(1 - 1/i_{73})} + \mu(h - r) - 2\sqrt{(l_b\cos\delta)^2 - \left(\dfrac{h}{2}\right)^2}} \quad (3)$$

In summary, only when the structural parameters of the robot satisfy $F_1(\delta) > 0$ and $F_2(\delta) > 0$ at the same time, the robot has the dynamic passing capability for obstacle crossing.

3.3 Motion stability analysis of robot obstacle crossing

In the obstacle crossing phase (d), the robot is most prone to overturn. As shown in Fig. 6, in this phase, the stability condition is verified if the center of mass vertical projection lies between the contact points of the front walking wheels and the front obstacle-crossing wheels with the obstacle upper surface and ground (C_1 and C_2).
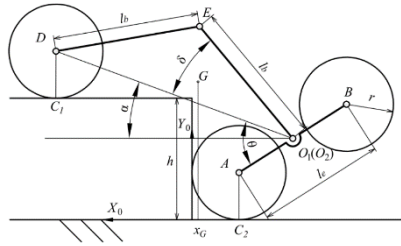

Fig. 6. Static stability condition of the robot in obstacle-crossing phase (d)

The stability condition of robot obstacle crossing can be expressed by the function $S(\delta)$

$$S(\delta) = \frac{\sqrt{(2l_b\cos\delta)^2 - h^2}\left(3m_{fb} + m_{rb} + 8m_w\right)}{4m} - \frac{\left(m_{fb} + m_{rb}\right)hl_b\sin\delta}{4ml_b\cos\delta} - \frac{l_e}{2} > 0 \quad (4)$$

4 Numerical simulation and parametric study

In the previous section, we established the geometric model $G(\delta)$, dynamic model $F_1(\delta)$, $F_2(\delta)$ and stability model $S(\delta)$ of the robot obstacle crossing. It can be seen that the obstacle crossing capability of the six-wheeled robot is closely related to the robot's structure and operation parameters. Given the robot's front body mass $m_{fb} = 3.6$ kg, rear body mass $m_{rb} = 2$ kg, front and rear body length $l_b = 240$ mm, walking wheel mass $m_w = 0.55$ kg and radius $r = 77.5$ mm, climbing rocker arm length $l_e = 210$ mm and mass $m_a = 1.6$ kg, the dynamic model $F_1(\delta)$ is only related to the friction coefficient between the wheel and the ground and obstacle surface, the dynamic model $F_2(\delta)$ is also related to the friction coefficient and the obstacle height, and the geometric model $G(\delta)$ and stability model $S(\delta)$ are only related to the obstacle height.

Only when $G(\delta) > 0$, $F_1(\delta) > 0$, $F_2(\delta) > 0$ and $S(\delta) > 0$ are satisfied at the same time, the robot can cross the obstacle of height h. Based on this, we can optimize the structure and operation parameters of the robot and control the pitch angle δ of the robot's rear body to realize the crossing of obstacles with different heights.

According to the parameters given above, numerical simulations are presented to verify the above derivations. As shown in Fig. 7, the maximum obstacle crossing height h_{max} of the robot changes with the pitch angle δ of the robot rear body, when $G(\delta) = 0$, $F_1(\delta) = 0$, $F_2(\delta) = 0$ and $S(\delta) = 0$ respectively. The shadowed parts in the figures are the feasible regions of δ where the robot satisfies the obstacle crossing conditions of geometrics, dynamics and stability respectively.
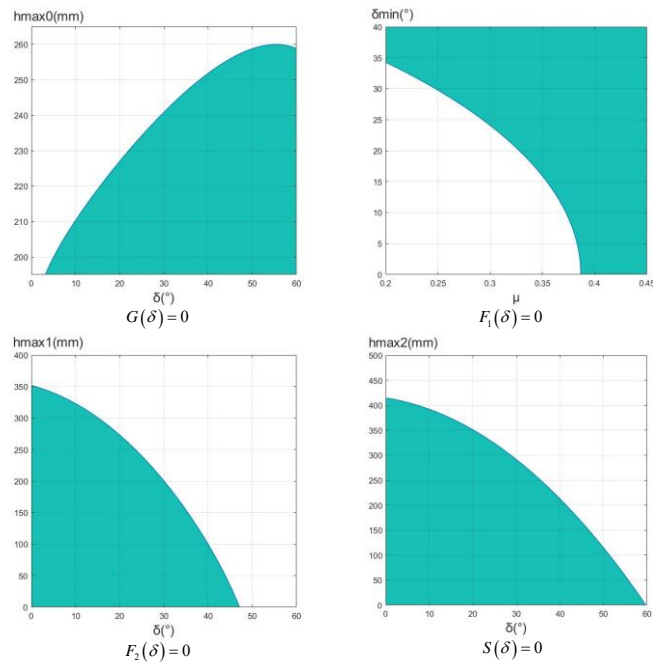

Fig. 7. The feasible regions of the pitch angle δ of the robot rear body

5 Prototype development and field tests

Based on the theoretical analysis presented above, a physical prototype of the proposed robot was developed as shown in Fig. 8. The robot can be transformed into three locomotion states as aforementioned, i.e. the high-posture state in Fig. 8(a), the low-posture state in Fig. 8(b) and the folded state in Fig. 8(c).
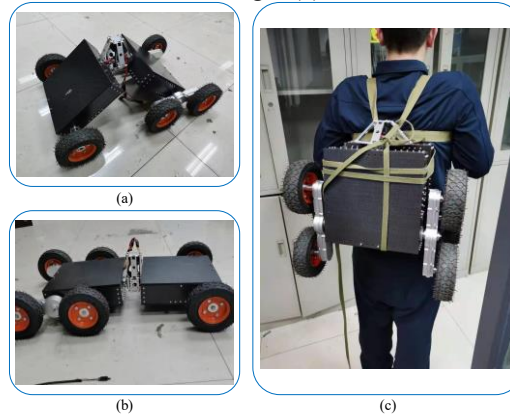

(a)

(b)   (c)

Fig. 8. Physical prototype of the proposed mobile robot.

Based on the prototype, a series of field tests were carried out to check and verify the performance of the proposed mobile robot.

The experiment of robot climbing over the 200 mm high vertical obstacle is carried out. As shown in Fig. 9, when the rear body pitch angle δ is equal to 30°, the robot can climb a vertical obstacle with a height of 200 mm.

Fig. 9. The experiment of the robot climbing 200 mm vertical obstacle.

As shown in Fig. 10, when the rear body pitch angle δ is equal to 30°, the experiment of robot climbing 140mm high continuous steps is carried out. The robot's front walking wheels always keep in contact with the step surface during the movement, and the climbing rocker arms on both sides of the robot continuously flip to push the robot to climb the steps.
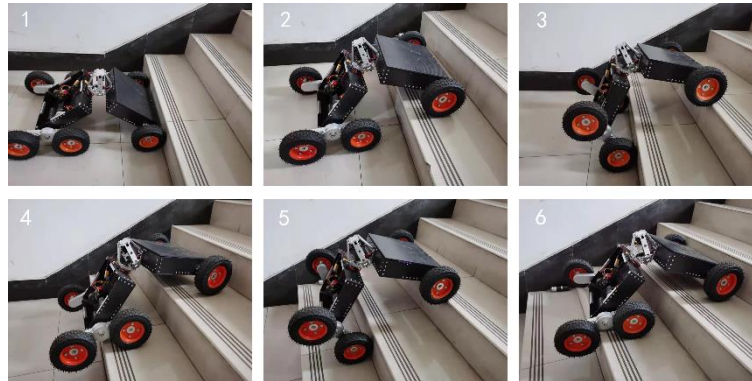
Fig. 10. The experiment of robot climbing a continuous staircase.

The tests conducted here shows the fact that the robot developed based on the proposed design principles has the distinctive obstacle-crossing capability and terrain adaptability.

6   Conclusions

This paper for the first time proposed and developed a portable six-wheeled mobile robot with a reconfigurable body and self-adaptable climbing obstacle mechanism. The robot is divided into two car bodies, which are connected by the Sarrus-variant mechanism. The robot can climb over obstacles by turning the rocker arms on both sides of its body, and can also adjust its posture through the Sarrus-variant mechanism to adapt to different terrain environments.

The mechanical design of the proposed mobile robot was presented. Further, through the analysis of obstacle performance of the robot from geometrics, dynamics, and stability, the relationship between the robot obstacle climbing ability and the structural operation parameters was characterized and illustrated. Through numerical simulation, the feasible region of the robot rear body pitch angle δ under different friction conditions and facing different height obstacles was obtained.

Based on the above design structure, an experimental prototype was developed, and field tests were subsequently carried out to prove the design concept, feasibility, maneuverability and multiple locomotion of the proposed mobile robot. The test results indicate that the robot can reconfigure itself to adapt to different terrains and to climb obstacles of different heights.

Further research will be focused on the development of an automatic navigation system (the first prototype is radio-controlled by a human operator) and an energy optimal path planning method to make the robot perform more tasks and more efficiently with limit energy supply.

References

1. S. Tadokoro, "On Robotic Rescue Facilities for Disastrous Earthquakes -From the Great Hanshin-Awaji (Kobe) Earthquake," *Journal of Robotics Mechatronics,* vol. 9, 1997.
2. J. Casper and R. R. Murphy, "Human-robot interactions during the robot-assisted urban search and rescue response at the World Trade Center," *IEEE Transactions on Systems Man Cybernetics Part B Cybernetics A Publication of the IEEE Systems Man Cybernetics Society,* vol. 33, no. 3, p. 367, 2003.
3. A. Meghdari, H. N. Pishkenari, A. L. Gaskarimahalle, S. H. Mahboobi, and R. Karimi, "A Novel Approach for Optimal Design of a Rover Mechanism," *Journal of Intelligent Robotic Systems,* vol. 44, no. 4, pp. 291-312, 2005.
4. K. Nagatani, A. Yamasaki, K. Yoshida, and T. Adachi, "Development and Control Method of Six-Wheel Robot with Rocker Structure," in *Safety, Security and Rescue Robotics, 2007. SSRR 2007. IEEE International Workshop on*, 2007.
5. Y. Zhu, Y. Fei, and H. Xu, "Stability Analysis of a Wheel-Track-Leg Hybrid Mobile Robot," *Journal of Intelligent Robotic Systems,* 2017.
6. F. O. Michaud *et al.*, "Multi-Modal Locomotion Robotic Platform Using Leg-Track-Wheel Articulations," *Autonomous Robots,* vol. 18, no. 2, pp. 137-156, 2005.
7. R. A. Lindemann and C. J. Voorhees, "Mars Exploration Rover mobility assembly design, test and performance," in *IEEE International Conference on Systems*, 2006.
8. D. Kim, H. Hong, H. S. Kim, and J. Kim, "Optimal design and kinetic analysis of a stair-climbing mobile robot with rocker-bogie mechanism," *Mechanism Machine Theory,* vol. 50, no. none, pp. 90-108, 2012.
9. R. Altendorfer, N. Moore, H. Komsuoglu, M. Buehler, and D. E. Koditschek, "RHex: A Biologically Inspired Hexapod Runner," *Autonomous Robots,* vol. 11, no. 3, pp. 207–213, 2001.
10. S. D. Herbert, A. Drenner, and N. Papanikolopoulos, "Loper: A quadruped-hybrid stair climbing robot," in *IEEE International Conference on Robotics & Automation*, 2008.
11. K. J. Waldron, M. Eich, F. Grimminger, and F. Kirchner, "Adaptive compliance control of a multi-legged stair-climbing robot based on proprioceptive data," *Industrial Robot,* vol. 36, no. 4, pp. 331-339, 2009.
12. T. Heimfarth, J. P. D. Araujo, and J. C. Giacomin, "Unmanned Aerial Vehicle as Data Mule for Connecting Disjoint Segments of Wireless Sensor Network with Unbalanced Traffic," in *IEEE International Symposium on Object/component-oriented Real-time Distributed Computing*, 2014.
13. I. L. Aarne Halme, Sami Salmi, "Development of WorkPartner-robot - Design of actuating and motion control system," 1999.
14. C. Grand, F. Benamar, and F. Plumet, "Motion kinematics analysis of wheeled-legged rover over 3D surface with posture adaptation," *Mechanism Machine Theory,* vol. 45, no. 3, pp. 477-495, 2010.
15. R. Siegwart, P. Lamon, T. Estier, M. Lauria, and R. Piguet, "Innovative design for wheeled locomotion in rough terrain," *Robotics Autonomous Systems,* vol. 40, no. 2-3, pp. 151-162, 2000.
16. G. Chen, S. Zhang, and G. Li, "Multistable Behaviors of Compliant Sarrus Mechanisms," *Journal of Mechanisms Robotics,* vol. 5, no. 2, p. 021005, 2013.

Central Pattern Generator Inspired Crawling Gait in Tensegrity Robots

Shashank Sarvan[1], Keshab Patra[1] and Anirban Guha[1]

[1] Department of Mechanical Engineering, Indian Institute of Technology Bombay, India
`anirbanguha1@gmail.com`

Abstract. Tensegrity structures have well-accepted applications in the area of static structure for their low self-weight to weight carrying ratio. However, their dynamic characteristics, particularly their capabilities for robotics applications have been less explored. This is perhaps because the complex interactions of forces among its members, interaction with external perturbation and highly non-linear dynamics leads to considerable difficulty in design of a suitable control system. Instead of using a nonlinear dynamics-based method, this paper explores a stochastic search-based method to find an optimized set of cable actuations for periodic motion generations for a tensegrity structure. A triangular prism based tensegrity with only three struts has been chosen. A biological Central Pattern Generator inspired periodic motion generation strategy was implemented. Simulated annealing was used for parameter identification. It was found that even a simple sinusoid implemented at three cables was able to produce a crawling gait, albeit with considerable ground scraping. The speed was large enough for practical applications.

Keywords: Tensegrity, Gait Generation, Central Pattern Generator, Simulated Annealing

1   Introduction

Conventional robots are built of rigid links and joints [1]. They often suffer from the problem of weight. High structural stiffness makes also makes them prone to damage besides introducing safety concerns while interacting with a human. Tensegrity structures are likely to address these drawbacks of conventional robots. Tensegrity is a self-standing, prestressed, easily deformable, lightweight structure. A set of tensile components i.e. strings or cables interacts with a set of compressive components i.e. bars or struts to define a stable volume in space and forms a tensegrity structure [2]. The shape of the tensegrity structure can be changed by varying the length of string or changing the length of the strut or varying the length of both. Varying the length of a string is comparatively easy as compared to strut. Change of lengths of a string results in movement of the structure which can be utilized for motion generation. Tensegrity structure-based locomotion generation was first proposed by Kanchanasaratool and Williamson [3]. They introduced a passive non-linear particle dynamic model for the path following

problem. Jager and Skelton [4] suggested a linearization of a nonlinear dynamic model for 2D tensegrity structure. Several models based on nonlinear dynamics are available for overly simplified tensegrity structures. The applicability of a similar model for a complex tensegrity system is a challenge.

In this paper, a stochastic search-based approach has been used for a 3-strut tensegrity structure to find possible periodic patterns of actuation for gait generation. It uses simple periodic motions inspired by Central Pattern Generators (CPG) and a modified version of simulated annealing [5] for parameter estimation for string actuation. Then the optimized parameter has been implemented in NASA Tensegrity Robotics Toolkit (NTRT) Simulator.

2 Stochastic Search Methods for Gait Generation

When one turns towards nature for the successful gaits it has created in various organisms, be it horses, snakes, or even humans, there is one striking feature that is common among all of them: periodic motion. Throughout a gait cycle, different parts go through a contraction/expansion and return to a normal state during different phases and with different frequencies. It does seem that a complex motion like human walking would require a lot of computation (brain activity) and sensing to successfully perform the motion. Surprisingly, this is not the case.

The solution to the problem boils down to figuring out a control strategy that achieves the goal. The tensegrity structure can be considered as the plant. The main structures used in this study are the 3-bar tensegrity structures.

2.1 Central Pattern Generator (CPG)

CPGs are a group of neurons that bring about a lot of rhythmic movements like walking, chewing, breathing, etc. invertebrates. They do not require sensory feed-back to function, however, they can fine-tune themselves based on external input. For example, the act of walking on the smooth ground does not require much feedback, but when the terrain is uneven or the body is carrying a load, sensory feedback can help fine-tune the movement. These rhythmic signals do not originate from the brain. And when these rhythmic signals are coupled with motor neurons, we get the motion as we know it.

It is not hard to imagine the tensegrity structure under a similar light with the strings acting like muscles and the rods as the skeletal system. There is however one major difference, that is the lack of vertical symmetry in tensegrities. This does play a role in the kind of motion we see as an output. In one gait cycle, a specific string may have to go through multiple contractions/relaxations with a different phase or frequency compared to other strings. Hence to keep things as general as possible, each string that was actuated had a clock/sinusoid that was independent of the others. The basic actuation function took the form

$$f(t) = l_0 + A \sin(\omega t + \phi) \tag{1}$$

Where $f(t)$ is cable actuation, l_0 initial string length, A amplitude, ω angular frequency, ϕ phase.

2.2 Simulated Annealing

To make a tensegrity move, the only thing left is to decide on the right value for the variables in equation (1). An optimization algorithm is required for selecting these parameters and evaluating them based on some criteria (reward policies).

In this study, a modified version of simulated annealing described in the NTRT Repository [6] is chosen. The algorithm first generates a search space / first generation S_0 of size n. Each $s \epsilon S_0$ is a set that defines all the parameters of the actuated strings in a tensegrity structure. For example, if it is decided that 3 strings will be actuated in a structure and each string had the variables as defined in equation (1); then $s = [a_1, \omega_1, \phi_1, a_2, \omega_2, \phi_2, a_3, \omega_3, \phi_3,]$. The members of s are randomly generated numbers picked uniformly in $[0,1]$.

After S_0 has been generated, each one of the n members is tested in the NTRT Simulation Environment. Their performance is evaluated using the reward policy $R(s)$. The best performing k sets become the next generation S_1. As the members of S_1 have already been defined, only small tweaks are made in s. About 30 percent of the value in each set are replaced with new ones chosen uniformly and randomly from $[0,1]$. This is called the mutation step. After this, the members of S1 are simulated again and the process repeats itself. After a defined number of tests, the process stops and the set s which has the highest score up to that point is the most optimized parameter set. The process schematic is shown in Fig. 1.
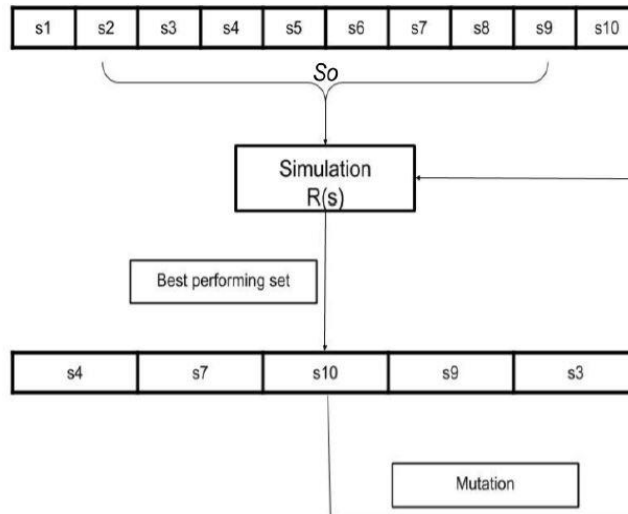

Fig. 1. Simple diagram of the simulated annealing process

2.3   Implementation for Crawling Motion of 3 Bar Tensegrity

The basic 3-bar tensegrity (Fig. 2) was chosen as the model for the implementation. The height of the tensegrity is 200 cm, the side of the base triangle is 90 cm and the strut length, L is 206 cm. For stability purposes, the structure was flipped on its side by 90 degrees as shown in Fig. 3. The nodes are numbered from 1-6 in black and the three cables chosen for actuation are numbered a, b and c in red shown in Fig. 3.
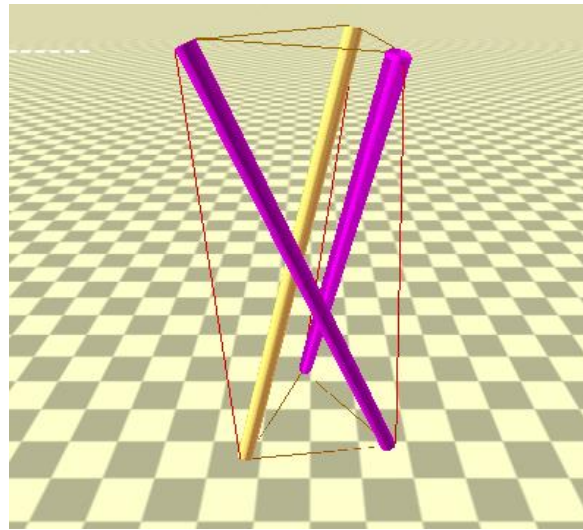

Fig. 2. 3 strut tensegrity before rotation
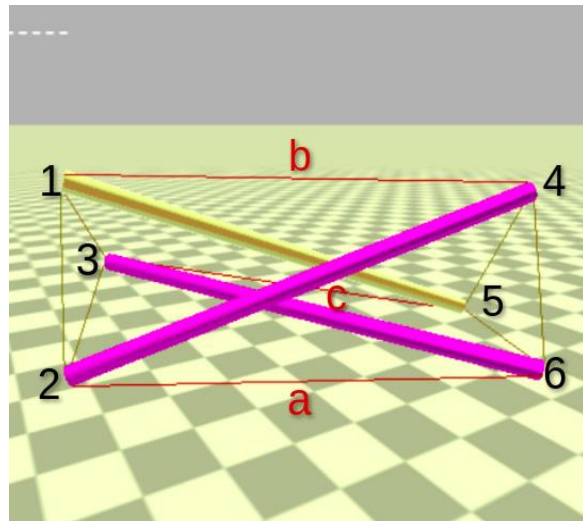
Fig. 3. 3 strut tensegrity(rotated) with labels

Actuation Parameters

The strings a, b and c (Fig. 3) connecting the left and right triangles form the chosen set of actuators. These strings were chosen intuitively, expecting them to be the primary source of forwarding motion. Another reason why a smaller set of actuators were chosen was to keep the number of parameters smaller thereby reducing the computations required.

$$l(t) = \begin{cases} 1.3l_0 & if\ f(t) \geq\ 1.3l_0 \\ f(t) \\ 0.7l_0 & if\ f(t) \leq\ 0.7l_0 \end{cases} \tag{2}$$

$$f(t) = l_0 + A\sin(\omega t + \emptyset) \tag{3}$$

Here l_0 is the initial string length, A is the amplitude, ω is the angular frequency and $\emptyset$ is the phase.

Table 1. Parameter Ranges (L=206 cm)

Parameter	Lower Bound	Upper Bound
Amplitude (A)	0.08L	0.35L
Frequency (ω)	0.3 Hz	10 Hz
	-π	π

Reward Policy

Each set of controller parameters were simulated for 100 seconds. The displacement between the initial Center of Mass (CoM) and the position of the CoM at the end of the simulation was calculated. This was assigned as a reward. The reason for choosing such a reward function is as follows:

1. In the long run, when trying to find a set of parameters that make the structure move in a line, the set that covers the maximum displacement will be the one that moves closest along a straight line.
2. Some sets of parameters created rapid motions which covered a lot of distance but they moved irregularly or in circles which is undesired. Hence total distance traveled is not a good measure.

Results

The optimization was run through a simulated annealing process. The number of random samples generated for the first generation was 200, the best performing 30 based on the reward policy mentioned in the previous section were chosen to become the next generation. The parameters in the new generation were mutated randomly and then

tested once again. A total of 400 such tests were conducted. The set of parameters that the search converged to is given in Table 2.

Table 2. Result Set (L= 206 cm)

String	Amplitude	Frequency (rad/s)	Phase
a	0.31L	1.43	0.01
b	0.18L	0.84	-1.27
c	0.24L	5.34	0.40

The structure had two discernible stages of motion, a contraction and an expansion, as shown in Fig. 4. The structure traveled at an average speed of $3.9 \times 10^{-2} \frac{L}{s} = 8.2\ cm/s$. The path traversed is given in Fig. 5.
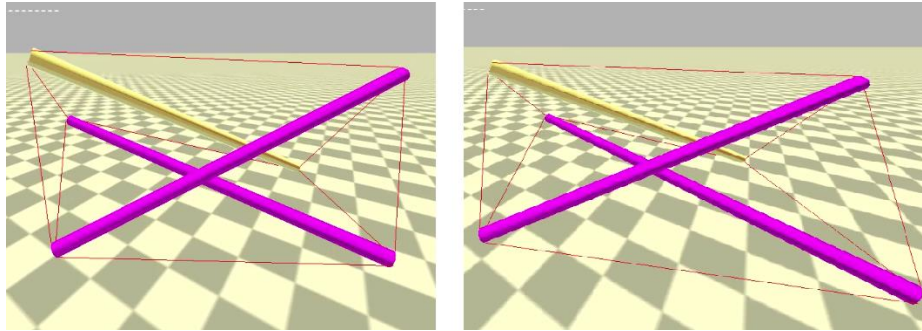
Fig. 4. Stages of crawling of 3 bar tensegrity, left: contracted phase, right: expanded phase.
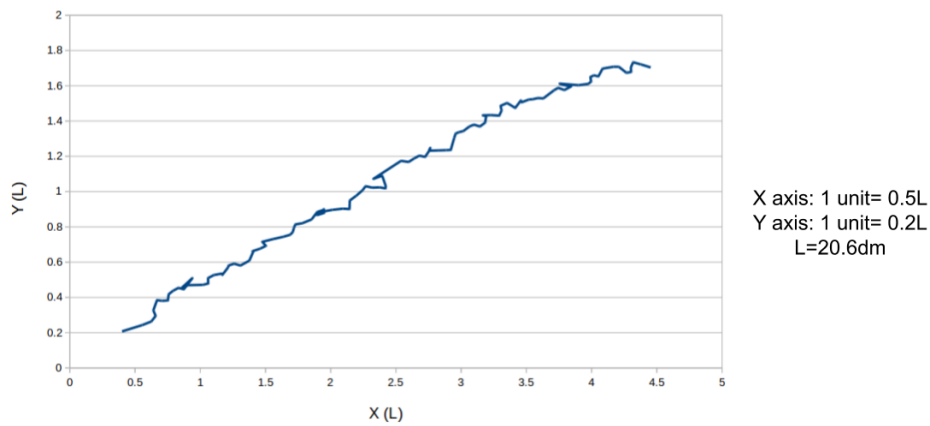

Fig. 5. The trajectory of CoM of tensegrity on the X-Y plane

3   Conclusion

The result shows that a simple feedforward controller can be used to move a tensegrity structure by actuating only a few of the strings. The speed is large enough for practical use. The computational complexity of the controller is low and so is the hardware complexity. It is a general method and can be used to obtain similar results for tensegrities of any configuration. However, in order to make it scalable to tensegrity structures with a much higher number of struts and cables, it may be necessary to explore pattern generators based on multiple sinusoids.

There are certain drawbacks to this approach. As the motion is dependent on crawling, it leads to scraping of the end nodes resting on the ground. This leads to vibrations, wear and tear. Different surface properties like friction and surface irregularities might render the motion useless. The reward policy fell short in some cases like, many unstable motions were not penalized and the ground scraping was not also penalized.

It is possible that a more robust search algorithm, larger sample set, and higher number of generations with an appropriate reward policy can arrive at a better solution. The actuation was done using a single sinusoidal. Although it was effective for simple crawling structures, multiple sinusoids may be suitable for more complex motions. A Fourier series based motion generator will be implemented in future for generating more complex motions and hopefully avoiding ground scraping.

References

1. J. Kasac, D. Majetic and D. Brezak, "Global positioning of robot manipulators with mixed revolute and prismatic joints," *IEEE Transactions on Automatic Control,* vol. 51, no. 6, pp. 1035-1040, 2006.

2. A. Pugh, An Introduction to Tensegrity, California: University of California Press, 1976.

3. N. Kanchanasaratool and D. Williamson, "Modelling and control of class NSP tensegrity structures," *International Journal of Control,* vol. 75, no. 2, pp. 123-139, 2002.

4. B. De Jager and R. Skelton, "Input-output selection for planar tensegrity models," *IEEE Transactions on Control Systems Technology,* vol. 13, no. 5, pp. 778-785, 2005.

5. "GitHub repository: NTRT," [Online]. Available: https://github.com/NASA-Tensegrity-Robotics-Toolkit/NTRTsim. [Accessed 24 September 2019].

6. A. Iscen, A. Agogino, V. SunSpiral and K. Tumer, "Controlling tensegrity robots through evolution," in *Proceedings of the 15th annual conference on Genetic and Evaluationary computation*, Amsterdam The Netherlands, 2013.

Motion/Force Transmission Performance Analysis of a Reconfigurable Single-Driven 3-RRR Planar Parallel Mechanism

Xiang Li, Ruiqin Li*, Hui Li and Fengping Ning

North University of China, Taiyuan 030051, Shanxi, China
*liruiqin@nuc.edu.cn

Abstract. This paper focuses on the transmission performance (TP) of the reconfigurable single-driven 3-RRR planar parallel mechanism (PPM). The method used to define the input transmission index (ITI) and output transmission index of the reconfigurable single-drive 3-RRR PPM is known as power coefficient. The method of changing the initial input angle is applied to single-drive 3-RRR PPM to realize mechanism reconfiguration. To reveal the influence of the reconfiguration on TP of mechanism, a set of mechanism parameters is given as numerical example and the local transmission index of different configuration are calculated. The studies show that the ITI is related to the cosine of the inverse pressure angle and sine of the transmission angle of each limb and link. Reconfiguration has a great influence on the good transmission workspace (GTW) and appropriate reconfigurable angle can significantly increase the GTW range.

Keywords: 3-RRR, Planar Parallel Mechanism (PPM), Single-driven, Reconfiguration, Transmission Performance

1 Introduction

Reconfigurable mechanisms have varying configurations, variable numbers of mobility and movement performance and can achieve multi-function operation, thus it is widely used in many fields [1-6]. The control system of single-driven mechanism is simple and doesn't rely on sensors and can significantly reduce the energy consumption when driving continuously. Therefore, the reconfigurable single-driven mechanism has important application value.

3-RRR planar parallel mechanism (PPM) is a typical PPM, and its kinematic and dynamic performance has been studied [7-13]. Some scholars constrained PPMs as planar linkages and study the synthesis problem [14-15]. Bai [16] proposed a linkage synthesis method of 1-DOF PPM by constraining 3-RRR PPM with parallelogram mechanism. This 1-DOF planar linkages can visit up to 10 poses. Li [17] calculated the coupler curve and orientation of the reconfigurable single-driven 3-RRR PPM by numerical solution.

In this paper, the motion/force transmission performance (TP) of single-driven 3-RRR PPM is studied, and the input transmission index (ITI) and output transmission

index (OTI) of the driver at different positions are deduced. A method to reconfigure the mechanism by changing the initial input angle is proposed. The influence of the reconfiguration on the TP is analyzed by numerical examples. This paper provides experience on the selection of drive position of reconfigurable single-driven mechanism and the improvement of TP of reconfigurable single-driven mechanism.

2   Motion/Force Transmission Performance

Fig. 1 shows the single-driven 3-RRR PPM. A_i, B_i, C_i (i=1, 2, 3) are revolute joints of the ith limb. G and H are revolute joints of limb 2 to constrain limb 1 and limb 3. θ_{i0} represents the initial angle of the ith limb. O_B-$X_BY_BZ_B$ is the fixed coordinate system at B_2. The 3-RRR PPM has three original moving links, but B_1C_1 and B_3C_3 are constrained by C_1G and C_3H, respectively, and become a 1-DOF mechanism. When B_2C_2 is rotated by θ_j, the input angle $\theta=\theta_{20}+\theta_j$, where j represents the jth orientation of the mechanism. When the mechanism is located at the initial orientation, j=0.
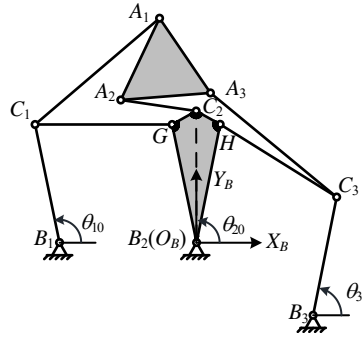

Fig.1. Single-driven 3-RRR PPM

The permitted twist screw/subspace (PTS) $\{\mathbf{T}_{P1}\}$ of limb 1 is expressed as

$$\{\mathbf{T}_{P1}\} = \begin{cases} \boldsymbol{S}_{Tp11} = (0 \quad 0 \quad 1; \quad y_{B_1} \quad -x_{B_1} \quad 0) \\ \boldsymbol{S}_{Tp12} = (0 \quad 0 \quad 1; \quad y_{C_1} \quad -x_{C_1} \quad 0) \\ \boldsymbol{S}_{Tp13} = (0 \quad 0 \quad 1; \quad y_{A_1} \quad -x_{A_1} \quad 0) \end{cases} \tag{1}$$

where $x_{B_1}, y_{B_1}, x_{C_1}, y_{C_1}, x_{A_1}, y_{A_1}$ represent the coordinates of B_1, C_1, A_1, respectively, and their values don't affect the solution of reciprocal screw.

The constraint wrench screw/subspace (CWS) $\{\mathbf{W}_{C1}\}$ of limb 1 is reciprocal to $\{\mathbf{T}_{P1}\}$.

$$\{\mathbf{W}_{C1}\} = \begin{cases} \boldsymbol{S}_{Wc11} = (0 \quad 0 \quad 1; \quad 0 \quad 0 \quad 0) \\ \boldsymbol{S}_{Wc12} = (0 \quad 0 \quad 0; \quad 1 \quad 0 \quad 0) \\ \boldsymbol{S}_{Wc13} = (0 \quad 0 \quad 0; \quad 0 \quad 1 \quad 0) \end{cases} \tag{2}$$

If B_1 is the driving joint of limb 1, the input twist screw (ITS) $\boldsymbol{S}_{I1}$=$\boldsymbol{S}_{Tp11}$, and the transmission wrench screw (TWS) $\boldsymbol{S}_{T1}$ of limb 1 is obtained as

$$\$_{T1} = \$_{Wall} = \left(\frac{x_{A_1} - x_{C_1}}{y_{A_1} - y_{C_1}} \quad 1 \quad 0 \; ; 0 \quad 0 \quad \frac{x_{C_1} \cdot y_{A_1} - x_{A_1} \cdot y_{C_1}}{y_{A_1} - y_{C_1}} \right) \tag{3}$$

Obviously, $\$_{T1}$ is a pure force along the $A_1 C_1$.

Similarly, the PTS $\{T_{P2}\}$ and $\{T_{P3}\}$, the CWS $\{W_{C2}\}$ and $\{W_{C3}\}$ and the TWS of $\$_{T2}$ and $\$_{T3}$ of limb 2 and limb 3 can be obtained respectively.

The TWS of limb 2 and 3 and the CWS of limb 1 do no work on the output twist screw (OTS) $\$_{O1}$, so $\$_{O1}$ is the reciprocal screw of $\$_{T2}$, $\$_{T3}$ and $\{W_{C1}\}$

$$\$_{O1} = \left(0 \quad 0 \quad 1 ; \quad \frac{M_1}{P_1} \quad -\frac{N_1}{P_1} \quad 0 \right) \tag{4}$$

where

$$\left|\begin{aligned}
M_1 &= x_{A_2} y_{A_3} y_{C_2} - x_{C_2} y_{A_2} y_{A_3} - x_{A_3} y_{A_2} y_{C_3} + x_{C_3} y_{A_2} y_{A_3} - x_{A_2} y_{C_2} y_{C_3} + x_{C_2} y_{A_2} y_{C_3} \\
&\quad - x_{C_3} y_{A_3} y_{C_2} + x_{A_3} y_{C_2} y_{C_3} \\
N_1 &= x_{A_2} x_{A_3} y_{C_2} - x_{A_3} x_{C_2} y_{A_2} - x_{A_2} x_{A_3} y_{C_3} + x_{A_2} x_{C_3} y_{A_3} - x_{A_2} x_{C_3} y_{C_2} + x_{C_2} x_{C_3} y_{A_2} \\
&\quad - x_{C_2} x_{C_3} y_{A_3} + x_{A_3} x_{C_2} y_{C_3} \\
P_1 &= x_{A_2} y_{A_3} - x_{A_3} y_{A_2} - x_{A_2} y_{C_3} + x_{A_3} y_{C_2} - x_{C_2} y_{A_3} + x_{C_3} y_{A_2} + x_{C_2} y_{C_3} - x_{C_3} y_{C_2}
\end{aligned}\right. \tag{5}$$

Obviously $\$_{O1}$ pitch is 0, which is pure rotation.

In the same way, the OTS of limb 2 and limb 3 can be obtained respectively

$$\$_{O2} = \left(0 \quad 0 \quad 1 ; \quad \frac{M_2}{P_2} \quad -\frac{N_2}{P_2} \quad 0 \right) \tag{6}$$

$$\$_{O3} = \left(0 \quad 0 \quad 1 ; \quad \frac{M_3}{P_3} \quad -\frac{N_3}{P_3} \quad 0 \right) \tag{7}$$

where

$$\left|\begin{aligned}
M_2 &= x_{A_1} y_{A_3} y_{C_1} - x_{C_1} y_{A_1} y_{A_3} - x_{A_3} y_{A_1} y_{C_3} + x_{C_3} y_{A_1} y_{A_3} - x_{A_1} y_{C_1} y_{C_3} + x_{C_1} y_{A_1} y_{C_3} \\
&\quad - x_{C_3} y_{A_3} y_{C_1} + x_{A_3} y_{C_1} y_{C_3} \\
N_2 &= x_{A_1} x_{A_3} y_{C_1} - x_{A_3} x_{C_1} y_{A_1} - x_{A_1} x_{A_3} y_{C_3} + x_{A_1} x_{C_3} y_{A_3} - x_{A_1} x_{C_3} y_{C_1} + x_{C_1} x_{C_3} y_{A_1} \\
&\quad - x_{C_3} y_{A_3} y_{C_1} + x_{A_3} y_{C_1} y_{C_3} \\
P_2 &= x_{A_1} y_{A_3} - x_{A_3} y_{A_1} - x_{A_1} y_{C_3} + x_{A_3} y_{C_1} + x_{C_3} y_{A_1} - x_{C_3} y_{C_1} - y_{A_3} y_{C_1} + y_{C_1} y_{C_3}
\end{aligned}\right. \tag{8}$$

$$\left|\begin{aligned}
M_3 &= x_{A_1} y_{A_2} y_{C_1} - x_{C_1} y_{A_1} y_{A_2} - x_{A_2} y_{A_1} y_{C_2} + x_{C_2} y_{A_1} y_{A_2} - x_{A_1} y_{C_1} y_{C_2} + x_{C_1} y_{A_1} y_{C_2} \\
&\quad - x_{C_2} y_{A_2} y_{C_1} + x_{A_2} y_{C_1} y_{C_2} \\
N_3 &= x_{A_1} x_{A_2} y_{C_1} - x_{A_2} x_{C_1} y_{A_1} - x_{A_1} x_{A_2} y_{C_2} + x_{A_1} x_{C_2} y_{A_2} - x_{A_1} x_{C_2} y_{C_1} + x_{C_1} x_{C_2} y_{A_1} \\
&\quad - x_{C_2} y_{A_2} y_{C_1} + x_{A_2} y_{C_1} y_{C_2} \\
P_3 &= x_{A_1} y_{A_2} - x_{A_2} y_{A_1} - x_{A_1} y_{C_2} + x_{A_2} y_{C_1} + x_{C_2} y_{A_1} - x_{C_2} y_{C_1} - y_{A_2} y_{C_1} + y_{C_1} y_{C_2}
\end{aligned}\right. \tag{9}$$

2.1 The Revolute Joint B_1 Acts as the Driver

Fig. 2 shows that limb 1 is driven by B_1. ω_1 is the angular velocity at B_1. f_{1-1} represents a vector along A_1C_1. v_{1-1} represents the velocity vector of C_1. $\$_{I1}$ is ITS. $\$_{T1-1}$ is TWS. $\$_{O1-1}$ represents OTS. r_{1-1} and r_{2-1} represent intersections of the common perpendicular of $\$_{T1-1}$ and $\$_{O1-1}$ with $\$_{T1-1}$ and $\$_{O1-1}$ respectively. φ_{1-1} is the inverse pressure angle (IPA) of limb 1. ψ_{1-1} is the transmission angle (TA) of limb 1.
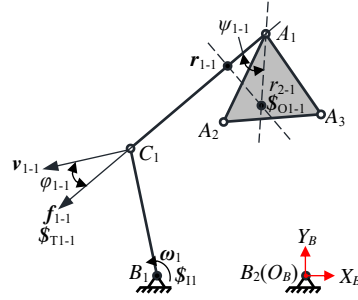
Fig. 2. Limb 1 driven by B_1

Power coefficient is used to define the transmission performance index [18], and ITI λ_{11} of limb 1 driven by B_1 is

$$\lambda_{11} = \frac{\left| \boldsymbol{S}_{T1-1} \circ \boldsymbol{S}_{I1} \right|}{\left| \boldsymbol{S}_{T1-1} \circ \boldsymbol{S}_{I1} \right|_{max}} = \frac{\left| \boldsymbol{f}_{1-1} \square \boldsymbol{v}_{1-1} \right|}{\left| \boldsymbol{f}_{1-1} \square \boldsymbol{v}_{1-1} \right|_{max}} = \cos \varphi_{1-1} \tag{10}$$

The OTI η_{11} of limb 1 is

$$\eta_{11} = \frac{\left| \boldsymbol{S}_{T1-1} \circ \boldsymbol{S}_{O1-1} \right|}{\left| \boldsymbol{S}_{T1-1} \circ \boldsymbol{S}_{O1-1} \right|_{max}} \tag{11}$$

$\left| \boldsymbol{S}_{T1-1} \circ \boldsymbol{S}_{O1-1} \right|$ can be represented as

$$\left| \boldsymbol{S}_{T1-1} \circ \boldsymbol{S}_{O1-1} \right| = \left| \omega_1 f_{1-1} [(h_1 + h_2) \cos \beta - d \sin \beta] \right| \tag{12}$$

where ω_1 and f_{1-1} are module of ω_1 and f_{1-1}. h_1 and h_2 represent pitch of $\$_{T1-1}$ and $\$_{O1-1}$ respectively. d is the distance between r_{1-1} and r_{2-1}. β is the angle of $\$_{T1-1}$ and $\$_{O1-1}$. According to Fig. 2, β is always 90°, thus Eq. (12) can be expressed as

$$\left| \boldsymbol{S}_{T1-1} \circ \boldsymbol{S}_{O1-1} \right| = \left| \omega_1 f_{1-1} d \right| \tag{13}$$

$\left| \boldsymbol{S}_{T1-1} \circ \boldsymbol{S}_{O1-1} \right|_{max}$ can be represented as

$$\left| \boldsymbol{S}_{T1-1} \circ \boldsymbol{S}_{O1-1} \right|_{max} = \left| \omega_1 f_{1-1} d_{max} \right| \tag{14}$$

where d_{max} represents by the distance A_1 and $\$_{O1-1}$. Therefore, Eq. (11) can be written as

$$\eta_{11} = \frac{\left| \boldsymbol{S}_{T1-1} \circ \boldsymbol{S}_{O1-1} \right|}{\left| \boldsymbol{S}_{T1-1} \circ \boldsymbol{S}_{O1-1} \right|_{max}} = \frac{d}{d_{max}} = \left| \sin \psi_{1-1} \right| \tag{15}$$

From Eq. (4), we can know the coordinate of $\$_{O1-1}$, and the coordinate of A_1 can be calculated [17]. From Eq. (3), we can know the axis direction of $\$_{T1-1}$, and Eq. (15) can be solved through geometric relation.

Local transmission index (LTI) γ_{11} of limb 1 driven by B_1 is

$$\gamma_{11} = \min\{\lambda_{11},\ \eta_{11}\} \tag{16}$$

If to analyze the TP of limb 2 driven by B_1, the TP of link $B_1C_1GB_2$ driven by B_1 is first analyzed, which causes limb 2 to move. Then the TP of limb 2 is analyzed. Finally, the two indexes are multiplied together to be the index of limb 2 driven by B_1.

Fig. 3 shows limb 2 driven by B_1. $\$_{O1\text{-}2}$ represents OTS of limb 2. $\$_{T1\text{-}12}$ is TWS of link $B_1C_1GB_2$. $\varphi_{1\text{-}12}$ is IPA of link $B_1C_1GB_2$. $\psi_{1\text{-}12}$ is TA of link $B_1C_1GB_2$. $\$_{T1\text{-}2}$ is TWS of limb 2. $\varphi_{1\text{-}2}$ is IPA of limb 2. $\psi_{1\text{-}2}$ is TA of limb 2.
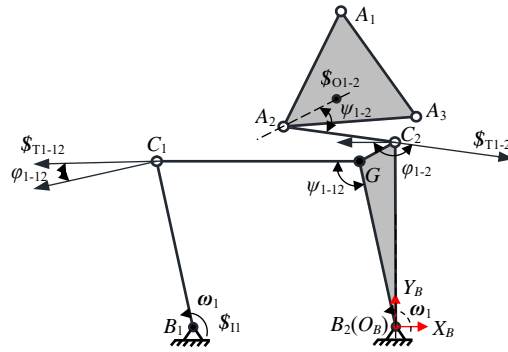
Fig. 3. Limb 2 driven by B_1

According to the above analysis. Similarly, ITI λ_{12} of limb 2 driven B_1 is

$$\lambda_{12} = \lambda_{1-12} \times \lambda_{1-2} = \left|\cos\varphi_{1-12}\Box\cos\varphi_{1-2}\right| \tag{17}$$

OTI η_{12} of limb 2 driven B_1 is

$$\eta_{12} = \eta_{1-12} \times \eta_{1-2} = \left|\sin\psi_{1-12}\Box\sin\psi_{1-2}\right| \tag{18}$$

Therefore, LTI γ_{12} of limb 2 driven B_1 is

$$\gamma_{12} = \min\{\lambda_{12},\ \eta_{12}\} \tag{19}$$

The method for analyzing the TP of limb 3 driven by B_1 is similar to that of limb 2. Limb 3 is driven by B_1 through link $B_1C_1GB_2$ and $B_2HC_3B_3$.

Fig. 4 shows limb 3 driven by B_1. $\$_{O1\text{-}3}$ represents OTS of limb 3. $\$_{T1\text{-}23}$ is TWS of link $B_2HC_3B_3$. $\varphi_{1\text{-}23}$ is IPA of link $B_2HC_3B_3$. $\psi_{1\text{-}23}$ is TA of link $B_2HC_3B_3$. $\$_{T1\text{-}3}$ is TWS of limb 3. $\varphi_{1\text{-}3}$ is IPA of limb 3. $\psi_{1\text{-}3}$ is TA of limb 3.

ITI λ_{13} of limb 3 driven B_1 is

$$\lambda_{13} = \lambda_{1-12} \times \lambda_{1-23} \times \lambda_{1-3} = \left|\cos\varphi_{1-12}\Box\cos\varphi_{1-23}\Box\cos\varphi_{1-3}\right| \tag{20}$$

OTI η_{13} of limb 3 driven B_1 is

$$\eta_{12} = \eta_{1-12} \times \eta_{1-23} \times \eta_{1-3} = \left|\sin\psi_{1-12}\Box\sin\psi_{1-23}\Box\sin\psi_{1-3}\right| \tag{21}$$

LTI γ_{13} of limb 3 driven B_1 is

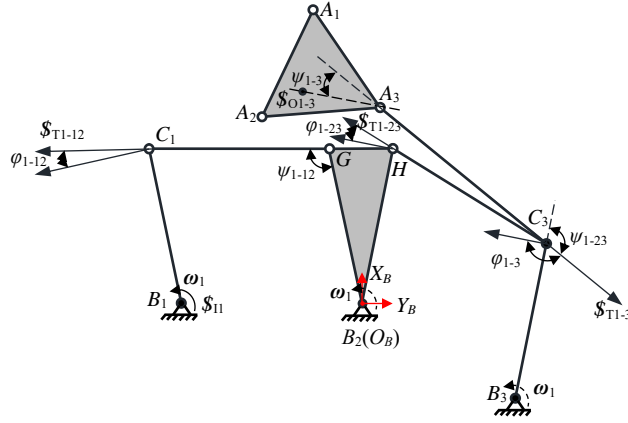$$\gamma_{13} = \min\{\lambda_{13},\ \eta_{13}\} \tag{22}$$

Fig. 4. Limb 3 driven by B_1

2.2 The Revolute Joint B_2 Acts as the Driver

Similarly, when B2 is the driver, ITI λ_{22} of limb 2 is the cosine of the IPA $\varphi_{2\text{-}2}$ of limb 2

$$\lambda_{22} = \left|\cos\varphi_{2-2}\right| \tag{23}$$

OTI η_{22} of limb 2 is the sine of the TA $\psi_{2\text{-}2}$ of limb 2

$$\eta_{22} = \left|\sin\psi_{2-2}\right| \tag{24}$$

LTI γ_{22} of limb 2 is

$$\gamma_{22} = \min\left\{\lambda_{22},\ \eta_{22}\right\} \tag{25}$$

ITI λ_{21} of limb 1 is the product of the cosine of the IPA $\varphi_{2\text{-}12}$ of link $B_1C_1GB_2$ and the IPA $\varphi_{2\text{-}1}$ of limb1

$$\lambda_{21} = \lambda_{2-12} \times \lambda_{2-1} = \left|\cos\varphi_{2-12}\Box\cos\varphi_{2-1}\right| \tag{26}$$

OTI η_{21} of limb 1 is the product of the sine of TA $\psi_{2\text{-}12}$ of link $B_1C_1GB_2$ and the TA $\psi_{2\text{-}1}$ of limb1

$$\eta_{21} = \eta_{2-12} \times \eta_{2-1} = \left|\sin\psi_{2-12}\Box\sin\psi_{2-1}\right| \tag{27}$$

LTI γ_{21} of limb 1 is

$$\gamma_{21} = \min\left\{\lambda_{21},\ \eta_{21}\right\} \tag{28}$$

ITI λ_{23} of limb 3 is the product of the cosine of the IPA $\varphi_{2\text{-}23}$ of link $B_2HC_3B_3$ and the IPA $\varphi_{2\text{-}3}$ of limb3

$$\lambda_{23} = \lambda_{2-23} \times \lambda_{2-3} = \left|\cos\varphi_{2-23}\Box\cos\varphi_{2-3}\right| \tag{29}$$

OTI η_{23} of limb 3 is the product of the sine of the TA $\psi_{2\text{-}23}$ of link $B_2HC_3B_3$ and the TA $\psi_{2\text{-}3}$ of limb 3

$$\eta_{23} = \eta_{2-23} \times \eta_{2-3} = \left|\sin\psi_{2-23}\Box\sin\psi_{2-3}\right| \tag{30}$$

LTI γ_{23} of limb 3 is

$$\gamma_{23} = \min\left\{\lambda_{23},\ \eta_{23}\right\} \tag{31}$$

2.3 The Revolute Joint B_3 Acts as the Driver

ITI λ_{33} of limb 3 is the cosine of the IPA $\varphi_{3\text{-}3}$ of limb 3

$$\lambda_{33} = \left| \cos \varphi_{3-3} \right| \tag{32}$$

OTI η_{33} of limb 3 is the sine of the TA $\psi_{3\text{-}3}$ of limb 3

$$\eta_{33} = \left| \sin \psi_{3-3} \right| \tag{33}$$

LTI γ_{33} of limb 3 is

$$\gamma_{33} = \min \left\{ \lambda_{33}, \ \eta_{33} \right\} \tag{34}$$

ITI λ_{32} of limb 2 is the product of the cosine of the IPA $\varphi_{3\text{-}23}$ of link $B_2HC_3B_3$ and the IPA $\varphi_{3\text{-}2}$ of limb 2

$$\lambda_{32} = \lambda_{3-23} \times \lambda_{3-2} = \left| \cos \varphi_{3-23} \square \cos \varphi_{3-2} \right| \tag{35}$$

OTI η_{32} of limb 2 is the product of the sine of the TA $\psi_{3\text{-}23}$ of link $B_2HC_3B_3$ and the TA $\psi_{3\text{-}2}$ of limb 2

$$\eta_{32} = \eta_{3-23} \times \eta_{3-2} = \left| \sin \psi_{3-23} \square \sin \psi_{3-2} \right| \tag{36}$$

LTI γ_{32} of limb 2 is

$$\gamma_{32} = \min \left\{ \lambda_{32}, \ \eta_{32} \right\} \tag{37}$$

ITI, λ_{31}, of limb 1 is the product of the cosine of the IPA $\varphi_{3\text{-}23}$ of link $B_2HC_3B_3$, the IPA $\varphi_{3\text{-}12}$ of link $B_1C_1GB_2$ and the cosine of IPA $\varphi_{3\text{-}1}$ of limb 1

$$\lambda_{31} = \lambda_{3-23} \times \lambda_{3-12} \times \lambda_{3-1} = \left| \cos \varphi_{3-23} \square \cos \varphi_{3-12} \square \cos \varphi_{3-1} \right| \tag{38}$$

OTI η_{31} of limb 1 is the product of the sine of the TA $\psi_{3\text{-}23}$ of link $B_2HC_3B_3$, the sine of the TA $\psi_{3\text{-}12}$ of link $B_1C_1GB_2$ and the sine of TA $\psi_{3\text{-}1}$ of limb 1

$$\eta_{31} = \eta_{3-23} \times \eta_{3-12} \times \eta_{3-1} = \left| \sin \psi_{3-23} \square \sin \psi_{3-12} \square \sin \psi_{3-1} \right| \tag{39}$$

LTI, γ_{31}, of limb 1 is

$$\gamma_{31} = \min \left\{ \lambda_{31}, \ \eta_{31} \right\} \tag{40}$$

It can be seen that the motion/force TP of the mechanism is related to the cosine of IPA and sine of TA of each limb and each link. When selecting the position of the driver, the limb with fewer power transmission times should be selected as far as possible to avoid energy loss. Therefore, B_2 should be selected as the driver in this paper.

3 Reconfiguration Method and Transmission Performance Analysis of the 3-RRR PPM

Fig. 5 shows the mechanism reconfigured. θ_{RE} is the reconfiguration angle, which's the angle between B_1G_1 and B_1C_1. θ_{RE0} is the initial reconfiguration angle. An arc guide rail with a center of B_1 and a radius of B_1C_1 is fixed on the C_1 of B_1C_1. G_1 can be fixed after sliding θ_{RE} along the arc guide rail, so as to change the initial reconfiguration angle θ_{RE0}. At this time, $\theta_{RE0}=\theta_{10}+\theta_{RE}$, the parallelogram of constraint B_1C_1 becomes $B_1G_1G_2B_2$. Each time θ_{RE} is changed, a reconfiguration of the mechanism is realized. The mechanism can be reconfigured by adding arc guide rail on different original moving parts, and several new mechanisms can be obtained by this method.
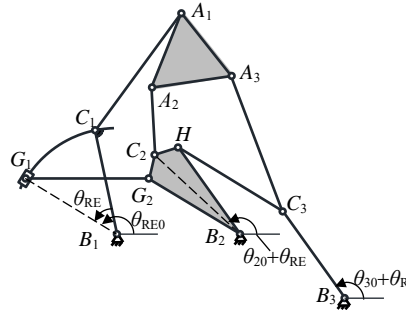
Fig. 5. Kinematic diagram of the reconfiguration mechanism

According to the analysis in Section 2, the motion/force TP of the mechanism is only related to the IPA of the limb and link. After the mechanism is reconfigured, the motion/force TP can be obtained only by recalculating IPA of each limb and link. See the literature [17] for specific calculation methods.

4   Case Study

As shown in Fig. 1, the design parameters and the motion parameters of the mechanism are shown in Table 1.

Table 1. The design parameters and the motion parameters of the mechanism

Design parameters	a_{01}	$[-17.03\ \ 102.34]^T$	c_{01}	$[-74.24\ \ 53.84]^T$	b_1	$[-63\ \ 0]^T$
	a_{02}	$[-34.84\ \ 65.03]^T$	c_{02}	$[-0.21\ \ 60]^T$	b_2	$[0\ \ 0]^T$
	a_{03}	$[6.37\ \ 68.25]^T$	c_{03}	$[64.40\ \ 20.74]^T$	b_3	$[52.63\ \ -34.63]^T$
Motion parameters	$\theta_{10}\ /(°)$	101.79				
	$\theta_{20}\ /(°)$	90.2				
	$\theta_{30}\ /(°)$	78.63				

Note: a_{01}, a_{02}, a_{03}, c_{01}, c_{02}, c_{03}, b_1, b_2 and b_3 represent the coordinates of A_1, A_2, A_3, C_1, C_2, C_3, B_1, B_2 and B_3, respectively, in the fixed coordinate system at the initial position.

The curves of γ_{11}, γ_{12} and γ_{13} changing with input angles driven by B_1, B_2 and B_3 respectively are shown in Fig. 6. The mechanism is in good transmission workspace (GTW) when γ_{11}, γ_{12} and γ_{13} are all greater than 0.7. As shown in Fig. 6, there are no GTW in the entire work cycle.

The mechanism was reconfigured by changing θ_{RE}. When θ_{RE} =-15°, LTI of each limb is shown in Fig. 7. As shown in Fig. 9(a), when $\theta_j \in [-10.8°,\ 17.2°]$, mechanism is in GTW. As shown in Fig. 9(b), when $\theta_j \in [-19.5°,\ 20.7°]$, mechanism is in GTW. As shown in Fig. 9(c), when $\theta_j \in [-15.4°,\ 15°]$, the mechanism is in GTW. GTW accounted for 7.78%, 11.17% and 8.44% of the total movement space, respectively.

When $\theta_{RE} = 15°$, LTI of each limb driven is shown in Fig. 8. Fig. 8 shows that there are no GTW in the entire work cycle.
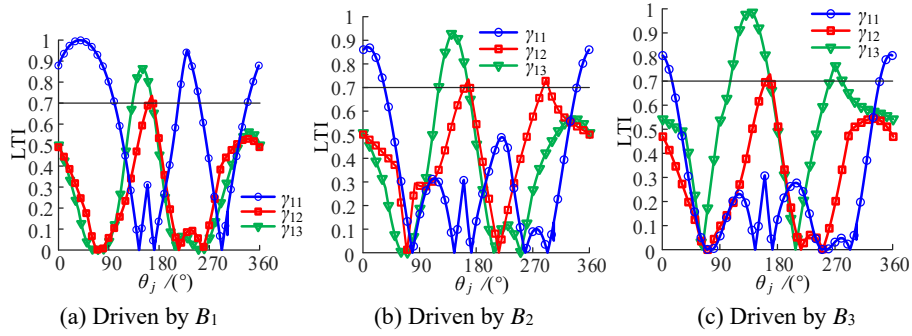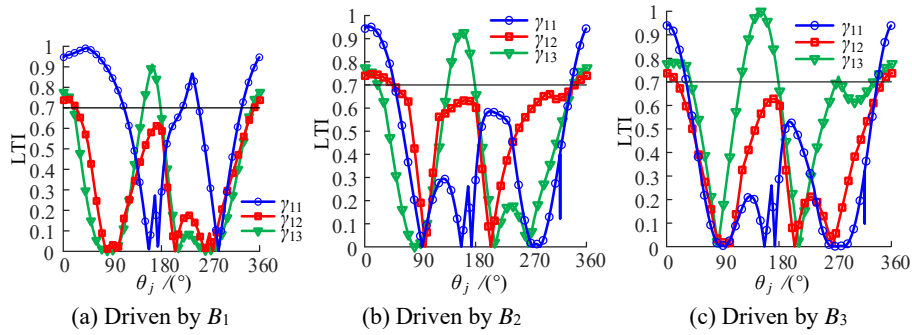

(a) Driven by B_1 (b) Driven by B_2 (c) Driven by B_3

Fig. 6. LTI of each limb

(a) Driven by B_1 (b) Driven by B_2 (c) Driven by B_3

Fig. 7. LTI of each limb ($\theta_{RE} = -15°$)

(a) Driven by B_1 (b) Driven by B_2 (c) Driven by B_3
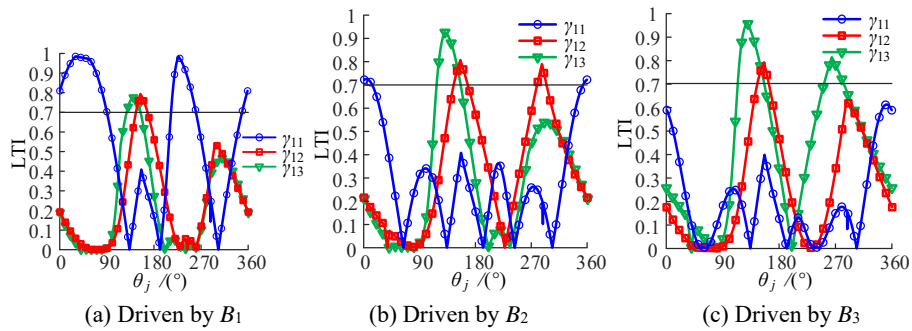
Fig. 8. LTI of each limb ($\theta_{RE} = 15°$)

Fig. 7 and Fig. 8 show that the reconfiguration has a great influence on the motion/force TP of the mechanism, and the appropriate reconfiguration angle can significantly increase the range of GTW of the mechanism.

5   Conclusion

The motion/force TP formula of the single-driven 3-RRR PPM was derived by power coefficient. The formulas show that the motion/force TP of the single-driven 3-RRR PPM is only related to the cosine of IPA and sine of TA of each limb and link.

The numerical results show that GTW range of the single-driven 3-RRR PPM is related to the power transmission times of the mechanism. In other words, the driver with more power transmission times does necessarily reduce the GTW range of the mechanism.

A method is proposed to realize the reconfiguration by changing the initial angle. The numerical results show that the reconfiguration has a great influence on the motion/force TP of the mechanism, and GTW range can be significantly increased if the reconfiguration angle is suitable, on the other hand, the mechanism may lose GTW.

Nomenclature

TP: Transmission performance   PPM: Planar parallel mechanism
ITI: Input transmission index   OTI: Output transmission index
PTS: Permitted twist screw/subspace   CWS: Constraint wrench screw/subspace
ITS: Input twist screw   TWS: Transmission wrench screw
LTI: Local transmission index   OTS: Output twist screw
IPA: Inverse pressure angle   TA: Transmission angle
GTW: Good transmission workspace

Acknowledgements

References

1. Li ZY., Bai SP.: A novel revolute joint of variable stiffness with reconfigurability. Mech Mach Theory 133, 720-736 (2019).
2. Zhang T., Qi P., Dai JS.: Mechanism design of a biomimetic quadruped robot. Industrial Robot: An International Journal 44(4), 512-520 (2017).
3. Zhan CZ., Dai JS.: Continuous static gait with twisting trunk of a metamorphic quadruped robot. Mech Sci 9(1), 1-14 (2018).
4. Zhang CZ., Dai JS.: Trot gait with twisting trunk of a metamorphic quadruped robot. J Bionic Eng 15, 971-981 (2018).
5. Tian HB., Ma HW., Ma K.: Method for configuration synthesis of metamorphic mechanisms based on functional analyses. Mech Mach Theory 123, 27-39 (2018).

6. Anderson PL., Mahoney AW., Webster RJ.: Continuum reconfigurable parallel robots for surgery: shape sensing and state estimation with uncertainty. IEEE Robot Autom Let 2(3), 1617-1624 (2017).

7. Can E., Stachel H.: A planar parallel 3-RRR robot with synchronously driven cranks. Mech Mach Theory 79, 29-45 (2014).

8. Cervantes-Sánchez JJ., Rico-Martínez JM., Brabata-Zamora IJ., et al.: Optimization of the translational velocity for the planar 3-RRR parallel manipulator. J Braz Soc Mech Sci 38(6), 1659-1669 (2016).

9. Liu S., Qiu ZC., Zhang XM.: Singularity and path-planning with the working mode conversion of a 3-DOF 3-RRR planar parallel manipulator. Mech Mach Theory 107, 166-182 (2017).

10. Wu XY., Bai SP.: Analytical determination of shape singularities for three types of parallel manipulators. Mech Mach Theory 149, 103812 (2020).

11. Zhang XC., Zhang XM.: A comparative study of planar 3-RRR and 4-RRR mechanisms with joint clearances. Robot Cim-Int Manuf 40, 24-33 (2016).

12. Li RQ., Dai JS.: Crank conditions and rotatability of 3-RRR planar parallel mechanisms. Sci China Technol Sc 52(12), 3601-3612 (2009).

13. Zhang ZK., Wang LP., Shao ZF.: Improving the kinematic performance of a planar 3-RRR parallel manipulator through actuation mode conversion. Mech Mach Theory 130, 86-108 (2018).

14. Chung WY.: Synthesis of two four-bar in series for body guidance. MATEC Web of Conferences 95, 04006 (2017).

15. Suárez-Velásquez HA., Cervantes-Sánchez JJ., Rico-Martínez JM.: Synthesis of a novel planar linkage to visit up to eight poses. Mech Based Des Struc 46(6), 781-799 (2018).

16. Bai SP, Li ZY., Li RQ.: Exact synthesis and input–output analysis of 1-DOF planar linkages for visiting 10 poses. Mech Mach Theory 143, 103625 (2020).

17. Li X., Li RQ., Li H., et al.: A numerical solution of coupler curve and orientation for reconfigurable single-driven 3-RRR planar parallel mechanism. Acta Armam 42(5), 1074-1082(2021).

18. Wang JS., Wu C., Liu XJ.: Performance evaluation of parallel manipulators: Motion/force transmissibility and its index. Mech Mach Theory 45, 1462-1476 (2010).

A New Anthropomorphic Robot for Fastening in Wing-box

Jiefeng Jiang[1], Fengfeng(Jeff) Xi[2], Jingjing You[3], Qunxing Xue[2]

[1] Qianjiang College, Hangzhou Normal University, Hangzhou, Zhejiang 310036, China
[2] Department of Aerospace Engineering, Ryerson University, Toronto, ON M5B 2K3, Canada
[3] College of Mechanical and Electronic Engineering, Nanjing Forestry University, Nanjing, Jiangsu 210037, China
jiangjf@hznu.edu.cn

Abstract. The fastener installation in the wing-box faces with narrow space, and it has to be done manually at present. Automatic fastening assembly using a robot undoubtedly is an appropriate solution. However, the existing robots can not meet the assembly requirements in the wing-box. We develop a new anthropomorphic robot with multiple links to perform the inner fastening. It has five degrees of freedom, a prismatic joint, a 360 degree rotated joint, and three revolute joints. S-shape link is designed for the compact requirement and the dimensions are constrained based on the cross-section of human arm. Stable frame structure is set up for the robot through the rear door frame and the bridge beam. Finally, the control system and program are presented for moving and positioning, and which is verified by the experiments.

Keywords: Wing-box fastening, Anthropomorphic robot, S-shape link, Stable frame, Control system.

1 Introduction

In the aircraft assembly process, riveting and bolt joints are the most widely used connection methods, such as each Airbus 340 plane has 900,000 rivets and 700,000 bolts [1] used. The installation of these fasteners is the most laborious part of the assembly. With the improvement of modern assembly level, multifunction automatic riveting machines have undertaken a large number of tasks, such as hole making, riveting and bolt connection [2]. But it generally requires the working space to be open and the assembly object to be fixed. An industrial robot has been applied in aircraft drilling and riveting [3,4], as an intelligent tool with greater flexibility than automatic riveting machines.

Due to its poor openness, the wing-box is the most difficult part of the aircraft assembly. There are lots of bolted or riveted installation works between the skin and the main load-bearing structural parts (beams, ribs). When the first side skin had assembled, another side becomes more difficult, because the collar or nut installation has to be conducted in the wing-box with the narrow space, and it has to be done manually. Since manual labor has size constraints, the efficiency is low, and there

may be assembly quality instability, it urgently needs automation. Automatic fastening assembly using a robot undoubtedly is an appropriate solution. Some studies [5-9] applied a commercial 6R industrial robot to integrate the assembly systems for the fastener installation by developing the end effector, using visual or force sensing sensors in control, which are mainly used for external assembly operations. Others [10-13] developed Cartesian linear robot or SCARA robotic system for the installation of bolt and screw, which are also fit to the external fastening occasion. However, for the narrow internal assembly situation of wing-box, the existing industrial robots are obviously not applicable.

For the narrow inner working, there are some bionic robots, such as the snake robot [14]. Wright et al.[15] designed a hyper-redundant serial-linkage snake robot, which suited to the locomotion in the pipe network [16]. OC Robotics company [17] developed a non-destructive inspection snake-arm robot system for confined and difficult-to-access areas in aircraft structure. Yao et al.[18] fabricated a prototype of a snake arm robot with 8 degrees of freedom for wing-box inner gluing, deburring, and residue removal. Though the snake robot is flexible due to many freedoms, its control is complex. Also its load-bearing capacity at the end is confined because of the long cantilever and more flexibility. So the snake robot is more fitted to vision inspection and simple works inside, and the snake robot for inner fastening assembly has not appeared in current publishing.

Since previous inner fastening was conducted manually in the wing-box, we also can consider the humanoid robot. There are lots of humanoid robots, such as DLR's Justin [19], Boston Dynamics Atlas [20], Yaskawa Motoman [21]. These robots always have the trunk and limbs like a human, also have complex hand and fingers. They generally can grab and grip the tool, are employed to simulate humans to do some works. But it is complex for the control and lower efficiency if they engage in the industrial operation.

At present, the existing industrial robots, snake robots, humanoid robots can not meet the fastening assembly requirements in the wing-box. So we use the anthropomorphic concept, develop a new robot with one prismatic joint and four revolute joints to accomplish the positioning of the end tool at the fastening site. The compact structure of S-shape link is designed and the stable frame structure is set up. Practical control system is established to implement the program for robotic motion.

2   Inner fastening requirement and robotic design concept

The length of a wing in a large aircraft is generally more than 10 meters. Here, a section of the wing-box in the wingspan direction is selected as the research model, as shown in Fig. 1. In this research, we consider the second assembly surface on the wing-box to be plane with the non-obvious curvature in the section. On the fastening plane of the wing-box model, there is an elliptical process hole located approximately at the middle position of the Z direction. It is used for human's arm entering into the wing-box deeply to work handed the fastening tool. During manual fastener installation, depending on human experience, the tool is held to the general position,

and the initial contact force feedback leads to the judgement of whether the sleeve and nut align with the bolt tail. After manual adaptive adjustment, human operates the tool finally to complete the collar or nut installation. If automation is used to replace the manual assembly, an anthropomorphic robotic arm needs to be designed first. It can go through the process hole enter into the wing-box and reach each local assembly site under automatic control. The detailed fastening behavior is conducted by the special fastening tool. In addition, the robot can also move along the direction of the wingspan covering the whole wing.
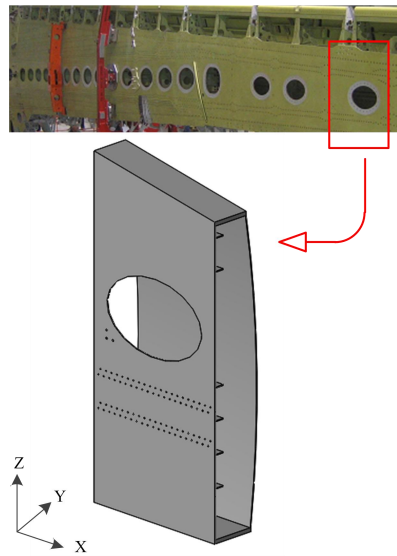
Fig. 1. Model of wing-box section
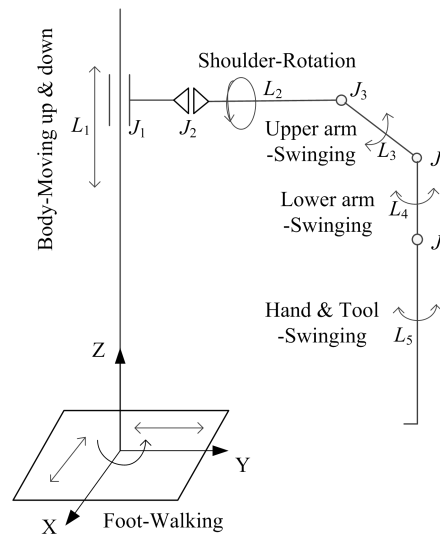
Fig. 2. Robotic concept of anthropomorphic motion

The anthropomorphic concept of the robot is presented in Fig. 2. There is a chassis with the plane motion freedoms, corresponding to human walking, which is used to determine the initial position of the robot relative to the wing-box. A prismatic pair (J_1) is designed in the up and down direction, corresponding to the human crouching and standing, to meet the requirements of the wing height direction, and drive the rear arm links to enter into wing-box through the process hole. To imitate the role of human shoulder, we innovatively designed a rotated shaft link (L_2) to adapt the circumference range (360 degrees) of assembly work, by driving the rear arms rotation around the process hole. At the end of the shoulder, there is a revolute joint (J_3) to drive the upper arm (L_3), corresponding to human forearm. The upper arm connects with the lower arm (L_4) by revolute joint (J_4), and the lower arm connects with the hand and tool (L_5) using another revolute joint (J_5). These three joints have the parallel revolute axis, which actuate three links swinging in some angle range, driving the tool end to reach every local fastening site. As shown in Fig. 2, in principle, the linkage robot with the combination of prismatic and revolute joints can simulate the human various actions for robotic end effector positioning and inner fastening.

Based on the above design concept, we consider the robotic motion process. Once the initial position of the chassis with the wing-box is determined, the chassis would be locked. The following actions are mainly implemented by the robotic joint's movement. The diagram, Fig. 3, presents several poses of the robotic motion, according to the work requirements. Fig. 3(a) shows the beginning of the arm links entering into the wing-box. Through the moving of the prismatic joint and the swinging of the revolute joints, the arms entirely enter into the wing-box, and the end of the tool reaches the fastening site at bottom, as seen in Fig. 3(b). Fig. 3(c) presents the end reaches another assembly position by the swinging of revolute joints. Then, the shaft of link 2 rotates 180 degrees, the tool end arrives the fastening site above the elliptical process hole, as shown in Fig. 3(d).
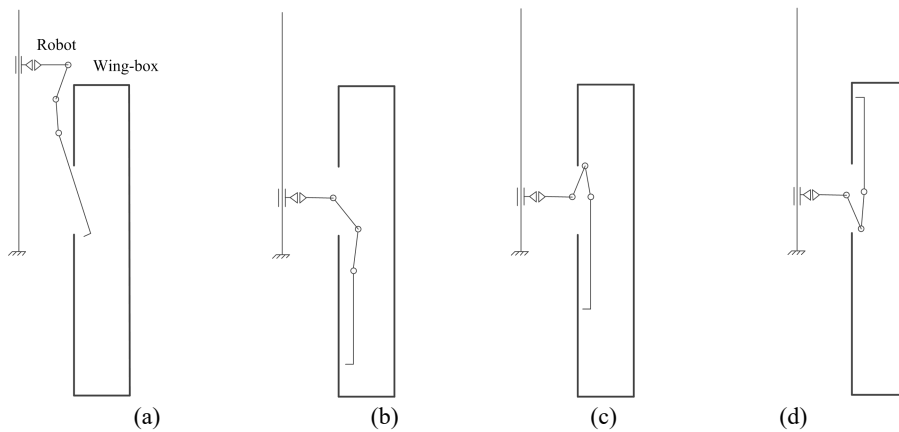
Fig. 3. Four typical poses

3   Robotic mechanical structure and transmission

3.1   Arm link layout and shape design

The mechanism of the fastening robot has been designed theoretically, the next problem is the design of the robotic detail structures. We first consider the arm links because of its critical role in the robot. As we know that link 3, 4 and 5 work in the wing-box suffering the narrow space constraints, sometimes they are facing to pass through the process hole of the inner rib. So the arm units should be designed as compact as possible.

Fig. 4 shows the layout of link 3, 4, and 5, which is an unfolded state for presenting the arrangement relationship. The heavy lines represent the links, the S shape of link 3 and 4 for upper arm and lower arm are skillfully designed. The bend place of the S shape link can accommodate the driving motor and corresponding transmission in two sides, not adding the dimension in the transverse direction. At the revolute joint, the

upper and lower arms overlap by the planes of the end of S shape link, and they are arranged for the appropriate layout.
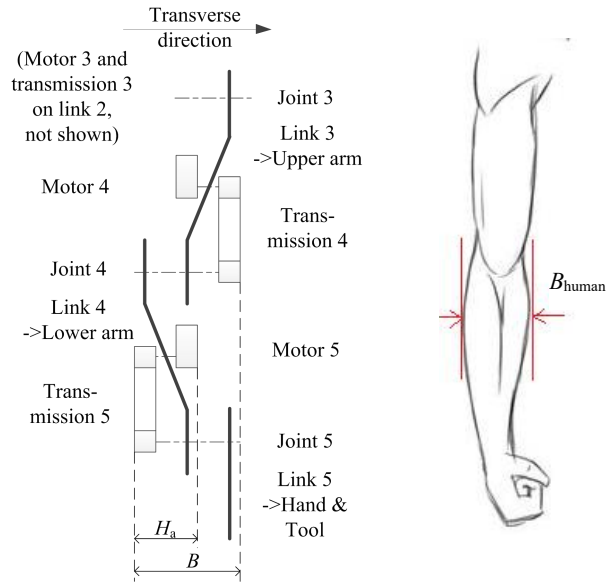

Fig. 4. Arm link layout vs human arm

Assuming that there are three columns, a middle motor column and two side transmission columns. If the height of a unit of arm (two columns) is defined by H_a, the whole breadth (three columns) of the layout in the transverse direction, B, is almost equivalent to 1.5 times of H_a.

$$B = 1.5H_a \tag{1}$$

Since the initial design concept of operation space in the wing-box is fit to human arms, here the whole dimension can be limited to less than the breadth of human wrist, B_{human}.

$$B \leq B_{human} \tag{2}$$

Combining the Eq.(1) and (2), the arm height, H_a, can be constrained as:

$$H_a \leq (2/3)B_{human} \tag{3}$$

If the breadth of a human arm is 135 mm, we should design the height of the arm link to be less than 90 mm.

The S-shape structure of the arm link is designed in three dimension, shown in Fig. 5. The arm link is a skew-symmetric structure in the length direction, convex platforms at both ends are used to connect with other links, the holes in details are ignored. In the height direction, except for the middle plate (h), the stiffeners (w) are

6

applied to improve the stiffness of the arm link. The formed "well" is used to accommodate the motor or mechanical transmission.
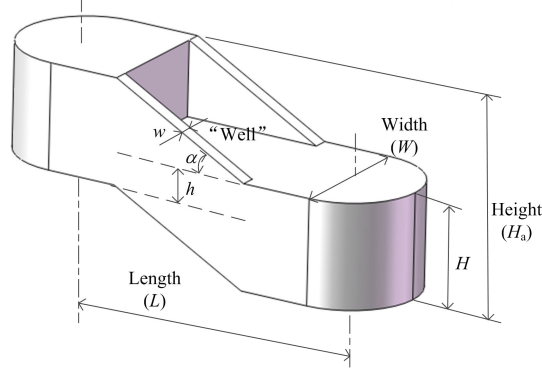
Fig. 5. 3D structure of S-shape arm link

For the dimensions of S shape link, the height of the arm (H_a) is just limited. Here, we consider the appropriate width (W) for the arm link according to the character of the structure, in addition, it should be less than the thickness of human wrist, T_{human}.

$$W \leq T_{human} \tag{4}$$

The length (L) is confirmed based on the workspace, which is less than the inner thickness of wing-box, $T_{wing-box}$.

$$L \leq T_{wing-box} \tag{5}$$

Except for length, height and width of the arm, there are several parameters to be determine, the middle plane thickness h, the convex platform height H, the stiffener width w, and the oblique angle α. Based on the consideration of structural rationality and the dimension relationship, the parameters are completely chosen and determined. The detail dimensions of S-shape arm are listed in Table 1.

Table 1. Detail dimension of S-shape arm link

S-shape arm link	Length L/mm	Height H_a/mm	Width W/mm	Convex platform height H/mm	Middle plane thickness h/mm	Stiffener width w/mm	Oblique angle α/°
Detail dimension	110	88	50	50	12	6	30

3.2   Frame structure and transmission

After designing the arm links, the whole frame of the robot is considered fully as the mounting base of the links. First, the chassis of the robot manipulator is designed in

the form of a wheeled cart, which is supported by three points of universal wheel. It meets the requirement of the motion in the direction of the wing-span to adapt to different sections of the wing, which also fits to adjust the initial position of the robot relative to one section of the wing-box.
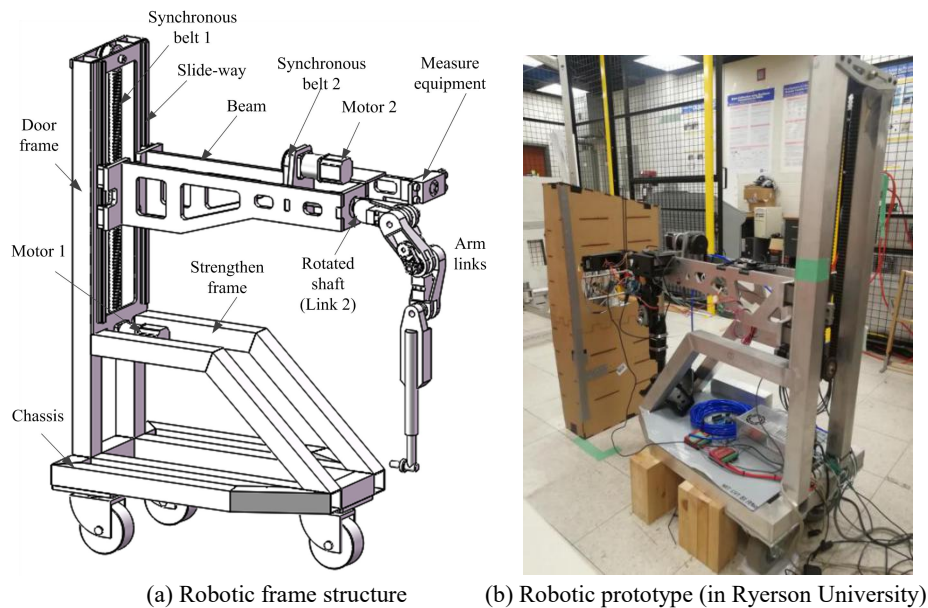

(a) Robotic frame structure   (b) Robotic prototype (in Ryerson University)

Fig. 6. Robot for fastening in wing-box

On the chassis, the door frame and strengthen frame are mounted, and the slide-ways for the robot's up and down movement are installed on the back of door frame. The chassis and the frames are welded by square tube, as shown in Fig. 6(a). Because the robotic arms are going out of the front of the chassis for working, in order to form the counterweight and improve whole structural stability, the door frame is placed at the rear of the chassis. At the same time, the bridge beam is arranged as a bridge to connect the door frame and the shoulder. The bridge beam mainly consists of two hollowed-out plates with sufficient rigidity. The shoulder is designed as a typical mechanical shaft structure to obtain 360° rotation, and mounted at the end of the bridge beam. The arm links are jointed at the end of the rotated shaft. Finally, the prototype of fastening robot is fabricated as shown in Fig. 6(b) (in Ryerson University).

In addition to the chassis, there are five motion degrees of freedom on the robot. For translated moving joint, the stepper motor with a reducer is employed, the bridge beam is clamped on the synchronous belt, and supported and guided by the slide-way. For the rotation of the shoulder, also the stepper motor and synchronous belt are applied to drive the rotated shaft. Similarly, the three swing degrees of freedom of the robot arm links are implemented by the steering engines and synchronous belts.

8

4   Robotic control

The hardware devices of robotic control system mainly include PC, controllers, power drivers, motors. It is mainly used to drive robotic joints to move or rotate. In addition, the measurement feedback devices consist of a camera and four ultrasonic sensors, they are used to determine the initial position of the robot and the wing-box. The whole robot control system is shown in Fig. 7.
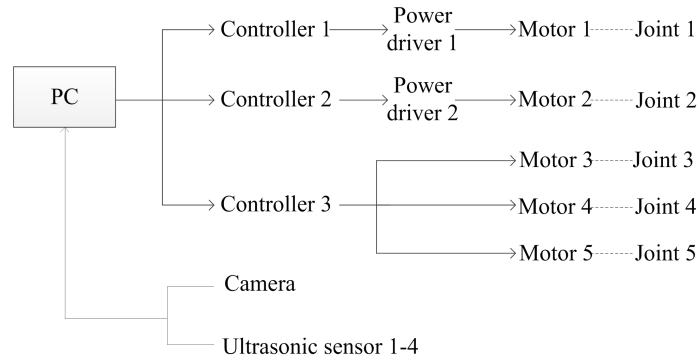

Fig. 7. Control system

Robot control program are written based on MATLAB platform. The functional modules are shown in Fig. 8. The program of measurement module is used to process the images collected by the camera, to measure the distance between the robot and the wing-box through the ultrasonic sensors. It provides the initial pose of the robot relative to the wing-box. Based on the known digital model, the obstacle avoidance motion planning of the robot is carried out, and the motion control program of the robot is generated. The control program is used for the robot to enter the wing-box through the process hole, complete the movement and positioning of different fastening positions in the wing-box.
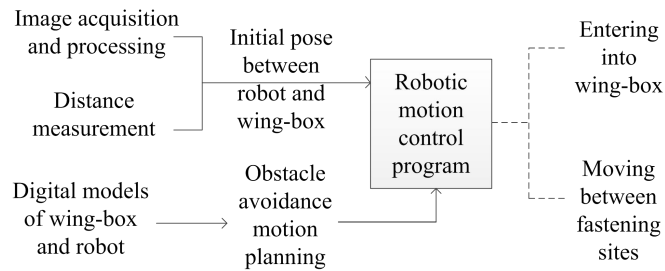
Fig. 8. Control program

By using above control system, the experiments of robotic motion are carried out. It indicate that the new robot can smoothly enter into the wing-box, and the end tool can locate at the local fastening site.

5 Conclusions

Based on the process requirement of automatic fastening in wing-box. A new anthropomorphic robot are carried out. A prismatic pair is employed to fit the links entering into the wing-box. A rotated shaft like the shoulder is designed creatively to meet the circumferential positioning around the process hole. And three links are used for the detail positioning to fastening site.

S-shape arm links are cleverly designed and reasonably arranged, and the critical dimensions are determined by comparison with human's elbow. Stable frame structure is developed, and the transmissions used synchronous belts are employed. The practical control system and program algorithm are established to implement the experiments of robotic moving and positioning.

Acknowledgements

References

1. Jiang, J., Bi, Y., Dong, H., Ke, Y.: Influence of interference fit size on hole deformation and residual stress in hi-lock bolt insertion. Proc IMechE Part C: J Mechanical Engineering Science 228(18), 3296-3305 (2014).
2. Chen, X., Tian, W., Xue, H.: Automatic riveting technology and its development in aircraft digital assembly. Aviation manufacturing technology 2016(5), 52-56 (2016). (in Chinese)
3. Gray, T., Orf, D., Adams, G.: Mobile automated robotic drilling, inspection, and fastening. SAE Paper, 012338 (2013).
4. Xi, F., Yu, L., Tu, X.: Framework on robotic percussive riveting for aircraft assembly automation. Advances in Manufacturing 1(2), 112-122 (2013).
5. Muller R., Horauf L., Vette M.: Robot guided bolt tensioning tool with adaptive process control for the automated assembly of wind turbine rotor blade bearings. Production Engineering - Research and Development 8, 755-764 (2014).
6. Duan, X., Wang, Y., Liu, Q.: Manipulation robot system based on visual guidance for sealing blocking plate of steam generator, Journal of Nuclear Science and Technology 53(2), 281-288 (2016).
7. Jiang, J., Bi, Y.: Design of robotic end effector for hi-lock nut automated installation, Manufacturing Technology and Tools 2019(8), 73-76 (2019). (in Chinese)

10

8. Liu, M., Liang, X., Wang, C., Wang, J.: A Robotic Hi-Lite Bolts/Collars Assembly System and Control Strategy. Proceedings of the 2017 IEEE International Conference on Robotics and Biomimetics, Macau SAR, China (2017).

9. Nozu, K., Shimonomura, K.: Robotic bolt insertion and tightening based on in-hand object localization and force sensing. Proceedings of the 2018 IEEE/ASME International Conference on Advanced Intelligent Mechatronics, Auckland, New Zealand (2018).

10. Chu, B., Jung, K., Ko, K.H., Hong, D.: Mechanism and analysis of a robotic bolting device for steel beam assembly. International Conference on Control, Automation and Systems 2010, Gyeonggi-do, Korea (2010).

11. Jiang, W., Zhou, Z.: Fuzzy control-based bolt tightening for power cable maintenance robot. Industrial Robot: An International Journal 45(4), 561-571 (2018).

12. Ali, M.A.H., Alshameri, M.A.: An intelligent adjustable spanner for automated engagement with multi-diameter bolts/nuts during tightening/loosening process using vision system and fuzzy logic. The International Journal of Advanced Manufacturing Technology 101, 2795-2813 (2019).

13. Visumatic Industrial Products Company, http://www.visumatic.com/fix/fixed_robotics_systems, 2010.

14. Transeth, A.A., Pettersen, K.Y., Liljeback, P.: A survey on snake robot modeling and locomotion. Robotica 27, 999-1015 (2009).

15. Wright, C., Buchan, A., Brown, B., et al.: Design and Architecture of the Unified Modular Snake Robot. 2012 IEEE International Conference on Robotics and Automation, RiverCentre, Saint Paul, Minnesota, USA (2012).

16. Rollinson, D., Choset, H.: Pipe network locomotion with a snake robot. Journal of Field Robotics 33(3), 322-336 (2016).

17. OC Robotics Company, http://www.ocrobotics.com/ case-studies/aerospace, 2017.

18. Yao, Y.B., Du, Z.C., Wei, Z.Q.: Research on snake-arm robot assembly system. Aviation manufacturing technology 2015(21), 26-30 (2015). (in Chinese)

19. Bidot, J., Karlsson, L., Lagriffoul, F., Saffiotti, A.: Geometric backtracking for combined task and motion planning in robotic systems. Artificial Intelligence 247, 229-265 (2017).

20. Kuindersma, S., Deits, R., Fallon, M., et al.: Optimization-based locomotion planning, estimation, and control design for the atlas humanoid robot. Autonomous Robot 40, 429-455 (2016).

21. Dharmara, K., Monfared, R.P., Ogun, P.S., Jackson, M.R.: Robotic assembly of threaded fasteners in a non-structured environment. The International Journal of Advanced Manufacturing Technology 98, 2093-2107 (2018).

Multi-mode Mobile Robot Based on Eccentric Paddle Mechanism of High Step-climbing Capacity: Design, Analysis and Performance Evaluation

Yi Sun[1], Longteng Zhang[2], Min Wang[3], Jiheng Ding[4], Wenchuan Jia[5], Huayan Pu[6] and Jun Luo[7]

[1-6] School of Mechanical and Electrical Engineering and Automation, Shanghai University, Shanghai 200444, China
[7] State Key Laboratory of Mechanical Transmission, Chongqing University, Chongqing 400044, China
phygood_2001@shu.edu.cn

Abstract. To improve climbing performance of the robot in complex environments, we propose a 2-DOF ePaddle-based reconfigurable robot of high step-climbing capacity. Climbing strategies of the robot under the circle-wheeled mode (CW), passive-paddle-wheeled mode (PPW) and active-paddle-legged mode (APL) are investigated. Determinants for success in climbing is discussed by establishing the climbing posture models and analyzing the margin of slippage. Simulation and experimental results reveal that paddle's motion can significantly improve the climbing performance to avoid slipping. The robot is capable of climbing over 280 mm and 300mm step under PPW and APL respectively, which is 2 times and 2.14 times the wheel radius. And compared with the APL, the robot under the PPW takes greatly lower power consumption to climb over obstacle with a lower margin of slippage.

Keywords: Reconfigurable mechanism, 2-DOF ePaddle, wheel-legged robots, step-climbing strategies.

1 Introduction

Based on the uncertainty and variability of environmental factors, single-mode mobile robots have been unable to satisfy the requirements of compound motion. Researchers have developed multi-modal robots adapting to the multi-topography, including wheel-legged hybrid and wheel-legged transformation robots.

Wheel of the wheel-legged hybrid robot is located at the end of the leg, controlled by independent drives. This type of robot good at step-climbing. Octal Wheel [1] robot has a special propulsion mechanism composed of the wheel and arm. This wheel-arm mechanism can also be found in Epi.q-1 [2]. The actuator of Shrimp Rover [3] consists of the wheel and self-adjustable linkages to maintain the dynamic stability. Bjelonic et al. equipped the quadruped ANYmal [4] with four non-steerable torque control wheels towards stable and dynamic locomotion. Similar to these robots

are ATHLETE [5], PAW [6], Momaro [7], WLR [8], etc. Moreover, wheels and legs of some robots are independent. ALDURO [9] only has wheels on the rear legs and front legs which are driven by joints. Wheel-legged [10] robot has two 3-DOF front legs actuated by air pressure, and two rear wheels driven independently.

The wheel-legged transformation robots generally adopt deformable mechanisms for switching between wheels and legs. They simplify the structure and control system greatly. PEOPLE-II [11] can transform between wheeled and legged mode by mounting two crossbars on each wheel. Quattroped [12] is equipped with eight semi-circular wheels and unfolds two semicircles as wheels or folds each other as legs to achieve the mode transformation. Liu et al. proposed an amphibious robot [13] that uses a large-diameter wheel-leg mechanism composed of three wheeled plates. A wheel-legged robot [14] designed by Sun et al. is capable of finishing the wheel-legged conversion in a short period of time. Bai et al. proposed a wheel-legged robot based on multi-four-bar linkage transformable mechanisms [15] similar to WheeLeR [16]. In addition, some robots whose rims are missing or incomplete mainly rely on gait planning to achieve the wheeled rolling or legged walking. Whegs [17] has four rimless wheels consisting of three struts and achieves a squat-like tripod gait.

We have previously developed the 3-DOF eccentric paddle mechanism (ePaddle) [18-20] and proposed five locomotion gaits [18]. Robot-stair interaction modes and feasible postures were presented in [19], which proved the robot can climb up the stair under the help of paddles. Structure of original 3-DOF ePaddle is complex and its climbing sequences are complex and redundant [20]. Therefore, we propose a 2-DOF ePaddle of the same step-climbing capacity but with only two actuated degrees of freedom. The fabricated prototype robot has multiple modes, including the circle-wheeled mode (CW), the passive-paddle-wheeled mode (PPW) and the active-paddle-legged mode (APL).

2 Design of the ePaddle-based Robot

2.1 Multi-mode Mobile Robot Based on ePaddle Modules

The robot proposed is composed of two 2-DOF ePaddle modules, two auxiliary wheels, a body carrying a controller and a power supply, as shown in Fig. 1. The ePaddle module realizes the wheel-legged transformation. It has two independent degrees of freedom, namely the rotation of wheel and the deflection of paddle rod. The two rear auxiliary wheels help to maintain stability of the robot.

In the CW as shown in Fig. 1(a), tires always be in contact with ground and rolling as wheels. Normally, the paddle rod is fully retracted into wheeled shell to avoid the interference of paddle-ground. Under the PPW, as shown in Fig. 1(b), the wheel actively rotates and the paddle rod passively swings. The robot is lifted by the paddle gradually. In APL as shown in Fig. 1(c), the paddle rod extends out of wheeled shell to the longest length and its motion is coordinated with rotation of the wheel to achieve a legged-climbing similar to legged robots. Four 2-DOF ePaddle modules can forms a quadruped robot as illustrated in Fig. 1(d).
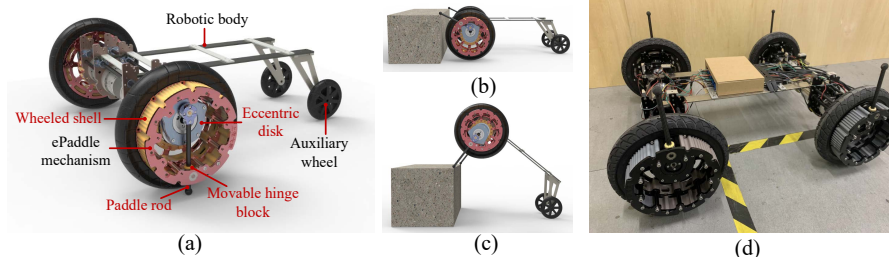
Fig. 1. CAD model of the 2-DOF ePaddle-based robot in (a) CW, (b) PPW, and (c) APL modes. (d) A 2-DOF ePaddle-based quadruped robot.

2.2 Design of the 2-DOF ePaddle

As shown in Fig. 2(a), 2-DOF ePaddle is composed of wheeled shell, eccentric disk, rotating disk, paddle-leg, movable hinge block and joint actuators. The eccentric disk is located at the same center of the wheeled shell. The rotating disk is fixed in the eccentric disk and the paddle shaft is fixed on the rotating disk. The paddle rod slides through the linear bearing which is in the movable hinge block and swings around the shaft smoothly. The joint actuator composes of a reducer, motor, driver and encoder, and its angular position, velocity can be controlled by its embedded controller.
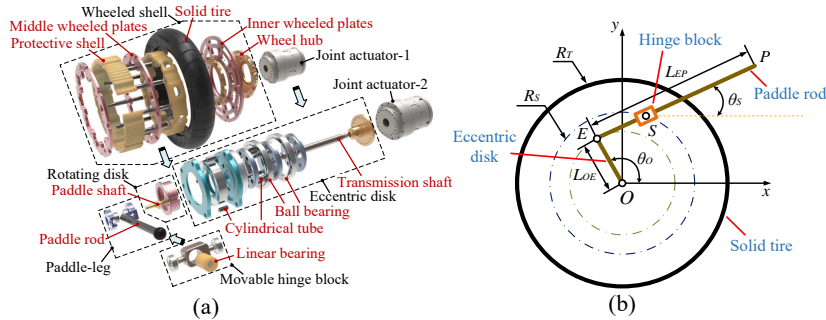
Fig. 2. Mechanism design of the 2-DOF ePaddle. (a) Componets. (b) Geometrical representation.

2.3 Kinematics of the ePaddle

The posture of the 2-DOF ePaddle, as shown in Fig. 2(b), can be determined by the angular positions of the wheel joint and the paddle joint, θ_O and θ_S, respectively by

$$\theta_S = \operatorname{atan}2\left(y_S - y_E, x_S - x_E\right) \tag{1}$$

and

$$P = \left[x_P, y_P\right]^T = \left[x_E + L_{EP}\cos\theta_S, y_E + L_{EP}\sin\theta_S\right]^T \tag{2}$$

where P is the endpoint of the paddle rod, $E = [x_E, y_E]^T$, $S = [x_S, y_S]^T$ are the position of the paddle rod and movable hinge block, respectively, L_{OE} is the eccentricity, L_{EP} is the length of the paddle rod.

3   Mathematical Modeling of Step-climbing

3.1   Step-climbing Strategy

The proposed robot has three step-climb strategies. The first one is CW, which is similar as a traditional wheeled robot, as shown in Fig. 3(a).

In PPW as shown in Fig. 3(b), only the wheel is actuated, and paddle rod swings passively with the traction of wheeled shells. When wheels are slipping, paddle rods swing in the air until contacting with the step. Then, the robot is gradually lifted to climb steps by the paddles. Robot in PPW has high stability as wheeled vehicles and high step-climbing capability as legged robot.

APL helps the robot to climb up even higher steps as shown in Fig. 3(c), where the paddle rod fully extends out of the wheeled shell and rotate at the same angular velocity with the wheel. In this mode the robot can be lifted at a place much higher than that in CW and PPW modes as illustrated in Fig.3(c).
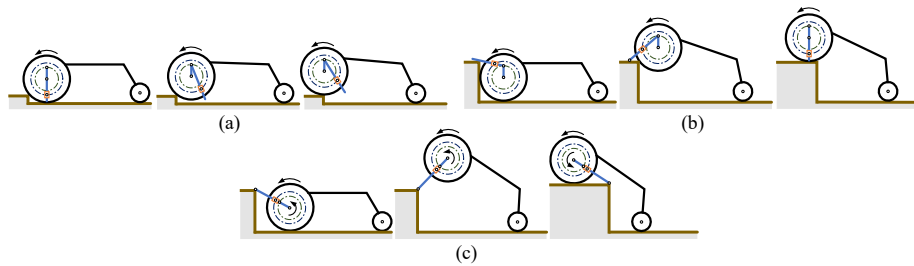
Fig. 3. Schematic diagram of step-climbing strategies. (a) CW. (b) PPW. (c) APL.

3.2   Determinants for Success in Climbing
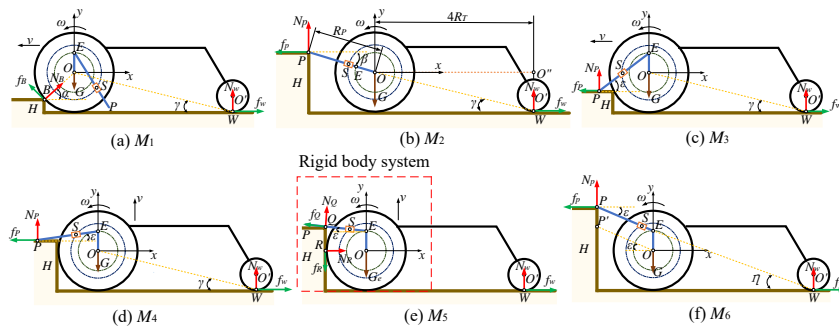
Fig. 4. Step-climbing posture model. (a) CW. (b) APL. (c-f) PPW.

The prerequisite of step-climbing is that the paddle or wheel is in contact with the step without slipping, which is determined by the normal force and friction force at the contact point. The following geometric constraints need to be satisfied:

$$D = F_f - F_m \geq 0 \tag{3}$$

where D is the margin of slippage, F_f is the obtained maximum friction force, F_m is the required traction force. Positive value of D means the robot will not slip.

As shown in Fig. 4(a), ePaddle modules are treated as a rigid body system to establish a static equilibrium model of CW, which is presented as:

$$
\begin{cases}
\sum F_x = f_B \sin\alpha - N_B \cos\alpha - f_W = 0 \\
\sum F_y = f_B \cos\alpha + N_B \sin\alpha - G + N_W = 0 \\
\sum M_O = f_B R_T - N_W L_{OW} \cos\gamma - f_W L_{OW} \sin\gamma = 0
\end{cases}
\tag{4}
$$

where N_B, f_B and N_W, f_W are the normal force and friction force at the corner contact point B and the auxiliary wheel-ground contact point W, respectively, G is the gravity force of the robot, R_T is the radius of the tire, α is the angle between OB and x axis, M_O is the resultant moment at point O, γ is the angle between OW and x axis, and H is the height of the obstacle.

The mathematical equations of APL shown in Fig. 4(b) is obtained as:

$$
\begin{cases}
\sum F_x = f_P - f_W - mR_P\omega^2 \cos\beta = 0 \\
\sum F_y = N_P + N_W - G - mR_P\omega^2 \sin\beta = 0 \\
\sum M_O = N_P R_P \cos\beta - f_P R_P \sin\beta - N_W L_{OW} \cos\gamma - f_W L_{OW} \sin\gamma = 0
\end{cases}
\tag{5}
$$

where N_P and f_P are the normal force and friction force between paddle's tip and obstacle at point P, R_P is the maximum radius of gyration, m is the weight of the robot, ω is the angular velocity of the ePaddle, β is the angle between OP and x axis.

Based on the contact position of the paddle-step and the moving direction of the robot, we establish four typical models of step-climbing under the PPW, as shown in Fig. 4(c-f). In particular, the robot takes point P as the center to make a variable-speed circular motion in M_6. In order to simplify the model, we equivalent point P to P', and the centripetal force is carried by the virtual paddle OP'.

For example, for the robot at Posture M_3:

$$
\begin{cases}
\sum F_x = f_P - f_W = 0 \\
\sum F_y = N_P + N_W - G = 0 \\
\sum M_O = N_P L_{EP} \cos\varepsilon + f_P R_T \sin\varepsilon - N_W L_{OW} \cos\gamma - f_W L_{OW} \sin\gamma = 0
\end{cases}
\tag{6}
$$

where ε is the angle between EP and x axis. Similarly, static equilibrium model of the robot in PPW at Posture M_4, M_5, and M_6 can be granted in the same way.

Determinants for success in climbing then can be found by solving these equations.

3.3   Climbing Path

As shown in Fig. 5(a-c), we take the position change of the wheel center O, represented by W, P and A, as the climbing path of the robot in three step-climbing strategies. (1) CW (W_1-W_2-W_3). (2) PPW (P_1-P_2-P_3-P_4-P_5): The wheel moves vertically from P_1 to P_3 along the side of step, where P_1-P_2 and P_2-P_3 are corresponding to M_4 and M_5 respectively. When the wheel reaches the upper surface of the step Z, it rotates around point Q to P_4, corresponding to M_3. (3) APL (A_1-A_3-A_4): The wheel rotates around the point P from A_1 to A_3.

It means that the robot has finished climbing when the wheel center passes the position W_2, P_4, and A_2. Time consumed is denoted by T and angular velocity is ω.
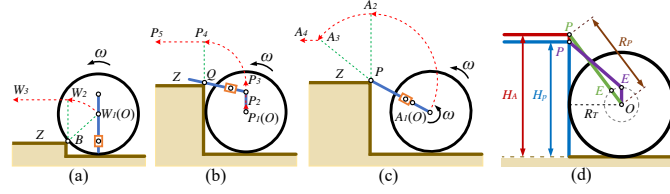
Fig. 5. The diagram of the climbing path in climbing strategies. (a) CW. (b) PPW. (c) APL. (d) The theoretical limit height of step-climbing.

4 Simulation and Experiment

4.1 Simulation Analysis

As shown in Fig. 5(d), the theoretical limit height of climbing can be expressed by

$$H_P = R_T + L_{OE} + \sqrt{L_{EP}^2 - R_T^2} \tag{7}$$

$$H_A = R_T + \sqrt{R_P^2 - R_T^2} \tag{8}$$

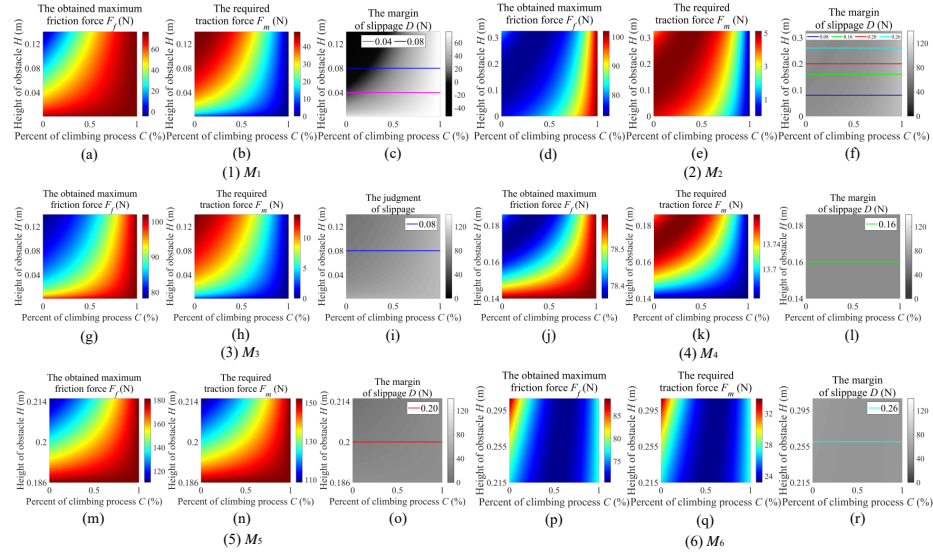where H_P and H_A are the limit height under the PPW and APL, respectively.

Fig. 6. Simulation results of F_f, F_m and D in step-climbing. (1) CW. (2) APL. (3-6) PPW. (a, d, g, j, m, p) The relation between F_f and C, H. (b, e, h, k, n, q) The relation between F_m and C, H. (c, f, i, l, o, r) The relation between D and C, H.

Fig. 6 shows the simulation results of F_f, F_m and D with respect to C and H respectively, using dimensions of the prototype robot in Table 1, where C is the percentage of climb process, which satisfies:

$$C = G(T, H) \cdot T \tag{9}$$

where $G(T, H)$ is the functional expression of T and H at the W_2, A_2, P_4, P_3 and P_2.

As shown in Fig. 6(a-c), D reaches 0 when H equals 0.04m, which means this height is the highest steps that a robot can climbs up in CW. Comparing with results shown in Fig. 6(d-f), maximal climbable height increased significantly in the APL.

According to Fig. 6(g-r), optimal climbing postures for climbing steps of different heights under the PPW can be determined, as shown in Fig. 7(a). (1) $H = 0\text{-}0.14$m: the robot climbs steps with M_3. (2) $H = 0.14\text{-}0.186$m: the robot moves upward along the step with M_4, and switches to M_3 when $OZ = 0$. (3) $H = 0.186\text{-}0.215$m: the posture is switched from M_5 to M_4 when $OZ = 0.046$m, and then similar to the second type. (4) $H = 0.215\text{-}0.308$m: the robot climbs steps with M_6.
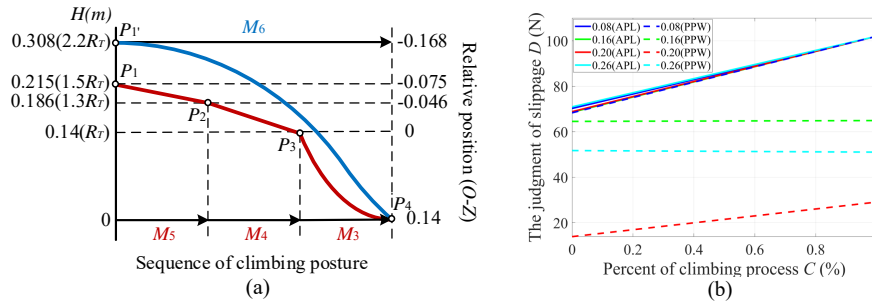
Fig. 7. The Inferences from simulation results of climbing strategy. (a) Posture sequence under the PPW. (b) Comparison of step-climbing performance under the PPW and APL.

Table 1. Robot specifications.

Item		Symbol	Value
ePaddle-based robot	Length		560mm
	Width (front)		556mm
	Width (rear)		230mm
	Height (body)		204mm
	Weight	m	17.3kg
	Distance (OW)	L_{OW}	580mm
	Distance (EW)	L_{EW}	590mm
	Correction factor	k	0.35
ePaddle mechanism	Radius (wheeled)	R_T	140mm
	Radius (legged)	R_P	232mm
	Length (paddle rod)	L_{EP}	186mm
	Eccentricity	L_{OE}	46mm
	Weight	m_e	15.3kg
	Angular velocity	ω	0.06rad/s
	Friction coefficient	k_T	0.45
	Friction coefficient	k_P	0.6
	Joint actuator	Reduction ratio	80
		Continuous torque	56Nm
		Continuous speed	25rpm
Auxiliary wheel	Radius		60mm
	Friction coefficient	k_W	0.3

To compare the climbing performance in PPW and APL, we take the margin of slippage D as the comparison index, and select four different obstacle heights of 0.08m, 0.16m, 0.20m and 0.26m corresponding to posture models of the PPW. As shown in Fig. 7(b), the climbing performance in APL is better than that in PPW (i.e., the larger the D, the higher the success rate of climbing). The normal force is greatly reduced when the robot moves vertically upwards, resulting in a reduction in effective friction force, as indicated by the experiments at $H = 0.20$m.

4.2 Prototype fabrication

The prototype robot as shown in Fig. 8(a) has specifications listed in Table 1. Fig. 8(b) shows its controller network. The PC sends commands to and receives feedbacks from actuators at a sampling rate of 2Hz, while the joint actuator runs its position PID loop at a sampling rate of 1000Hz.

(a) (b)
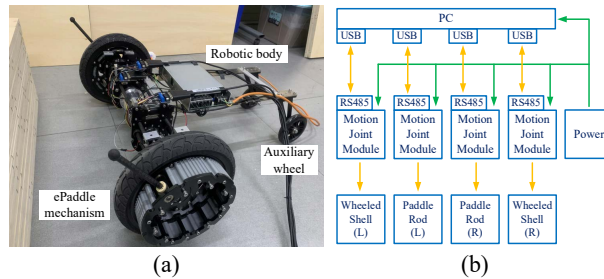
Fig. 8. The prototype of the robot. (a) 2-DOF ePaddle-based robot. (b) Control system.

4.3 Experimental Verification

Fig. 9 shows robots moving in CW, where alder wood boards of 10mm heigh was used to set up steps of different heights. As shown in Fig. 10(a,b), the robot can climb the step of 40mm in CW, but slips for step higher than 50mm.

Experiments in PPW as shown in Fig. 10(c,d) confirmed that the robot can climb steps up to 200mm or 280mm height (namely 1.42 times and 2.0 times the wheel radius), which agree with theoretical prediction in Fig. 6(c-f).

The robot can climb the step of 300mm height (2.14 times the wheel radius) in APL as shown in Fig. 10(e), confirming again that the paddle is useful in climbing, which makes up for the shortcomings of traditional wheeled robots.
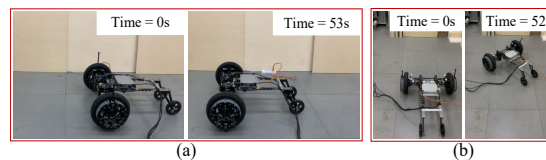

(a) (b)

Fig. 9. Experiments on the basic motion. (a) Wheeled rolling. (b) Steering.
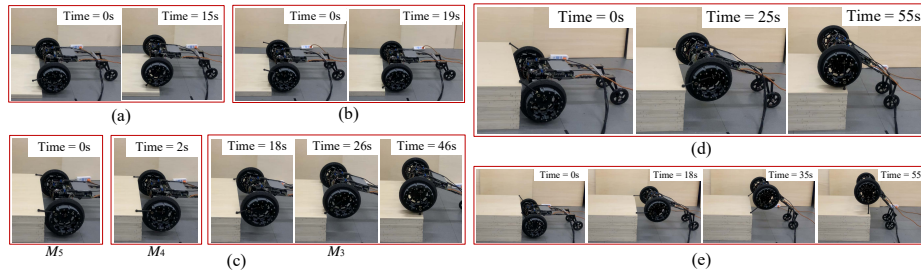
Fig. 10. Experiments on step-climbing. (a, b) Climbing steps of 0.04m and 0.05m in CW. (c, d) Climbing steps of 0.20m and 0.28m in PPW. (e) Climbing step of 0.30m in APL.

As shown in Fig 11(a,b), the power consumption of the PPW reaches a peak in the initial stage of climbing, and gradually decreases, while the APL shows a trend of increasing first and then decreasing. Compared with results in APL, the average power consumed in PPW is greatly reduced, as shown in Fig. 11(c).
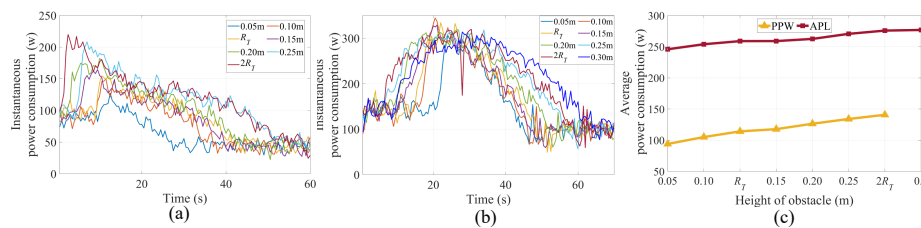

Fig. 11. Power consumption for robot to climb different steps. (a) PPW. (b) APL. (c)Average power consumption in PPW and APL.

5 Conclusion

In this paper, a multi-mode mobile robot based on 2-DOF ePaddle is proposed, which has a high step-climbing capacity thanks to the wheel-paddle motion coordination. Climbing strategies of the robot under the CW, PPW and APL are analyzed by establishing kinematics models. The robot can easily climb over an obstacle of 2 times and 2.14 times its wheel radius under the PPW and APL, respectively. And the power consumption of PPW is more advantageous than that of APL.

In our future study, more robots based on the 2-DOF ePaddle will be considered to further improve the maneuverability of the robots on rough terrains.

References

1. Takita, Y., Shimoi, N., Date, H.: Development of a wheeled mobile robot "octal wheel" realized climbing up and down stairs. In: Proc. IEEE/RSJ Int. Conf. Intell. Robots Syst., Sendai, Japan (2004).

2. Quaglia, G., Maffiodo, D., Franco, W., Appendino, S., Oderio, R.: The Epi.q-1 hybrid mobile robot. Int. J. Robot. Res. 29(1), 81-91(2010).

3. Estier, T., Crausaz, Y., Merminod, B., Lauria, M., Piguet, R., Siegwart, R.: An innovative space rover with extended climbing abilities. In: Proc. Space Robot., Albuquerque, USA (2000).

4. Bjelonic, M. et al.: Keep rolling'—Whole-body motion control and planning for wheeled quadrupedal robots. IEEE Robot. Autom. Lett. 4(2), 2116–2123 (2019).

5. Wilcox, B., Litwin, T., Biesiadecki, J., Matthews, J., Heverly, M., Morrison, J.: ATHLETE: A cargo handling and manipulation robot for the moon. J. Field Robot. 24(5), 421-434 (2007).

6. Smith, J., Sharf, I., Trentini, M.: PAW: A hybrid wheeled-leg robot. In: Proc. IEEE Int. Conf. Robot. Autom., pp. 4043-4048 (2006).

7. Schwarz, M., Rodehutskors, T., Schreiber, M., Behnke, S.: Hybrid driving-stepping locomotion with the wheeled-legged robot Momaro. In: Proc. IEEE Int. Conf. Robot. Autom., pp. 5589-5595, Stockholm, Sweden (2016).

8. Li, X., Zhou, H., Feng, H., Zhang, S., Fu, Y.: Design and Experiments of a Novel Hydraulic Wheel-legged Robot (WLR). In: Proc. IEEE/RSJ Int. Conf. Intell. Robots Syst., pp. 3292-3297, Madrid, Spain (2018).

9. Hiller, M., Germann, D., Morgado de Gois, J. A.: Design and control of a quadruped robot walking in unstructured terrain. In: Proc. IEEE Int. Conf. Control Appl., vol. 2, pp. 916-921, Taipei, Taiwan (2004).

10. Lacagnina, M., Muscato, G., Sinatra, R.: Kinematics dynamics and control of a hybrid robot wheeleg. Robot. Auton. Syst. 45(3), 161-180 (2003).

11. Okada, T., Botelho, W., Shimizu, T.: Motion analysis with experimental verification of the hybrid robot PEOPLER-II for reversible switch between walk and roll on demand. Int. J. Robot. Res. 29, 1199-1221 (2010).

12. Chen, S., Huang, K., Chen, W., Shen, S., Li, C., Lin, P.: Quattroped: A leg–wheel transformable robot. IEEE/ASME Trans. Mechatron. 19(2), 730-742 (2014).

13. Liu, J., and Yang, J.: Design and mode switching of wheel-leg adaptable amphibious robot. In: Proc. 2nd Asia-Pacific Conf. Intell. Robot Syst., pp. 270-274, Wuhan (2017).

14. Sun, T., et al.: A transformable wheel-legged mobile robot: Design, analysis and experiment. Robot. Auton. Syst. 98, 30-41 (2017).

15. Bai, L., et al.: An optional passive/active transformable wheel-legged mobility concept for search and rescue robots. Robot. Auton. Syst. 107, 145-155 (2018).

16. Zheng, C., Lee, K.: WheeLeR: Wheel-Leg Reconfigurable Mechanism with Passive Gears for Mobile Robot Applications. In: Proc. Int. Conf. Robot. Autom., pp. 9292-9298, Montreal (2019).

17. Schroer, R., Boggess, M., Bachmann, R., Quinn, R., Ritzmann, R.: Comparing cockroach and Whegs robot body motions. In: Proc. IEEE Int. Conf. Robot. Autom., vol.4, pp. 3288-3293, New Orleans, LA, USA (2004).

18. Sun, Y., et al.: Modeling the rotational paddling of an ePaddle-based amphibious robot. In: Proc. IEEE/RSJ Int. Conf. Robots Syst., pp. 610-615, Vilamoura (2012).

19. Pu, H. et al.: Optimized non-reciprocating legged gait for an eccentric paddle mechanism. Robot. Auton. Syst. 103, 83-92 (2018).

20. Sun, Y., et al.: Modeling paddle-aided stair-climbing for a mobile robot based on eccentric paddle mechanism. In: Proc. IEEE/RSJ Int. Conf. Intell. Robot. Syst., pp. 4153-4158, Hamburg, Germany (2015).

Error compensation for water jet cutting robot based on MDH and POE exponential product models

Haijun Xie[1]，Shijin Zhang[2] ，Kenji Yoshigoe[3] and Yue Zhao[2]*

[1] Shanghai Key Lab of Intelligent Manufacturing and Robotic, School of Mechatronic Engineering and Automation, Shanghai University, Shanghai, 200072, China
[2] School of Software, Northwestern Polytechnical University, Taicang, Jiangsu, 215400, China
[3] Department of Electrical Engineering and Computer Science, Embry-Riddle Aeronautical University, Daytona Beach FL, 32114, USA
* Corresponding author, Yue Zhao: `yxzhao01@nwpu.edu.cn`

Abstract. Currently, there is limited freedom for the five-axis water jet cutting machine tool in the market, while the industrial robot has more flexibility. Therefore, for the present study, the combination of robot and water jet technology was selected. The industrial robot has high repeated-positioning accuracy and low absolute-positioning accuracy, which cannot meet the requirements of precision machining. Therefore, it is important to conduct the precision compensation of the robot. In order to deal with this concern, two error models, namely, the MDH model and the global POE exponential product model, were established, followed by a comparison of the two models and their selection. A platform for measuring the data of the ball-bar instrument was constructed, and the correction parameters of the two models were obtained using MATLAB simulation solution. Finally, the trial cutting was performed prior to and after the calibration. The calibration of the two models could meet the requirements, and the calculation time of the global exponential product model was shorter when the optimization rates were close to each other.

Keywords：Water jet, Industrial robot, Precision compensation, MDH and POE model.

1   Introduction

In recent years, with the emergence of the new age of Industrial Revolution 4.0, the industrial field has been moving toward a higher level of intelligence, which has brought opportunities for the development of high-energy beam processing technology.Water jet cutting is a branch of high energy beam. Owing to the multi-degree freedom of the industrial robot and the flexibility of the robot itself, the combination of robot and water jet cutting technology was selected for use in the present study to meet the cutting requirements of complex workpieces. Fig. 1(a) presents the schematic diagram of the manipulator holding the water jet cutting head. Since water jet processing is accompanied by the use of consumables, the robot body was mounted inversely on the walking frame, as depicted in Fig. 1(b). In the figure,

framework *R* represents the coordinate system of the base of the robot body and framework *M* represents the coordinate system of the machine tool.

The most of the robots in the market exhibit the characteristic of high repeatable positioning accuracy and low absolute positioning accuracy[1], which renders it difficult to meet high-precision processing requirements. Therefore, the absolute positioning accuracy of the robot must be compensated to meet the accuracy requirements of machining.
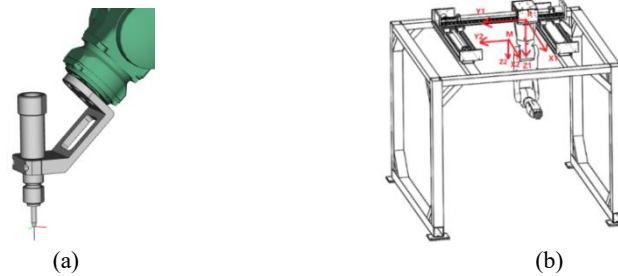

(a)   (b)

Fig. 1.   (a) Combination of robot hand-holding water jet cutting head   (b) Schematic diagram of robot body inversion

The complete process of robot kinematics calibration is generally divided into the following four steps: error modeling, pose measurement, parameters identification, and compensation. Certain scholars have conducted extensive research on robot accuracy compensation. The modeling is based mainly on the MDH model and the POE exponential product model, along with the methods improved upon these models. He S et al. employed the multi-point constraint method to calibrate the 6-axis industrial robot and compared the results obtained using this method with the three parameter identification methods to demonstrate the effectiveness of their parameter identification method[2]. Ping Yang et al. measured the plane roundness error using a double-ball ball instrument, substituted the collected data into the MDH error model to optimize the geometric parameters, and eventually, the calibration results were observed using a laser interferometer[3]. Le Ma et al. integrated the error terms from seven aspects into a unified error formula, and introduced higher-order polynomials in which the normalized joint variables were considered the parameters of the polynomials; thus, the error model was established[4]. Jorge Santolaria et al. used an angular displacement sensor to measure the actual value of the joint rotation angle. A laser tracker was employed to measure the actual pose of the end actuator. Subsequently, the corresponding relationship between the joint angle error and the pose error was sought. After least-square iteration, the compensation value of the method was obtained[5]. Jorge Santolaria et al. completed the calibration of the CPA dot method for a six-axis industrial robot using a laser tracker[6]. Morris R. Driels and Uday S. Pathre first derived the Jacobian matrix based on the DH parameters and then applied it to the error compensation of the PUMA560 robot[7]. In the process of calibration, a few interference factors are inevitably introduced, such as environmental noise and measurement error, which would lead to the failure of algorithm convergence or low accuracy of the calibration algorithm. Therefore, to improve the efficiency and stability of the algorithm, Nguyen Van Toan and Phan Bui

Khoi proposed the singular value decomposition exponential product model least square algorithm, which was not quite sensitive to the impact of environmental noise[8]. Mao Chentao et al. utilized the unique characteristics of the MDH model to transform the kinematics calibration problem into a separable non-linear least squares problem, which was further categorized into two sub-problems – the linear least squares problem and a simplified problem involving only non-linear parameters. The optimal structural parameters were determined through an iterative solution, and the method was subsequently applied to ABB 2600 robot[9]. Xiangdong Yang et al. established the exponential product model and the corresponding differential motion error model for the robot based on the spinor theory and the mathematical basis of Lie algebra, and also verified these models through simulation and experimentation[10].

The first portion of the report is the introduction section which discusses the combined background of robot and water knife, to study the research results reported by previous scholars in a problem-oriented way. The second portion of the present report is mainly focused on explaining the establishment of the MDH and POE exponential product error models in detail. The third portion of the report briefly expounds on data measurement and the optimization algorithm used for parameter identification. The fourth portion discusses the simulation and the experiment. The fifth portion provides the conclusion.

2 Establishment of the error model

Robot modeling is based mainly on the MDH model and the exponential product model. MDH model is an improvement of the original DH model, in which a coordinate system has to be established for each joint successively, and the DH parameters are obtained based on the relationship among the coordinate systems. The global exponential product model considers only the custom base coordinate system and the end coordinate system. The global exponential product model is a kind of absolute modeling approach that involves customization of the base coordinate system as the absolute reference frame for each joint.

2.1 MDH error model

The establishment of the coordinate system for the robot joint is illustrated in Fig. 2(a). Table 1 presents the DH parameters.
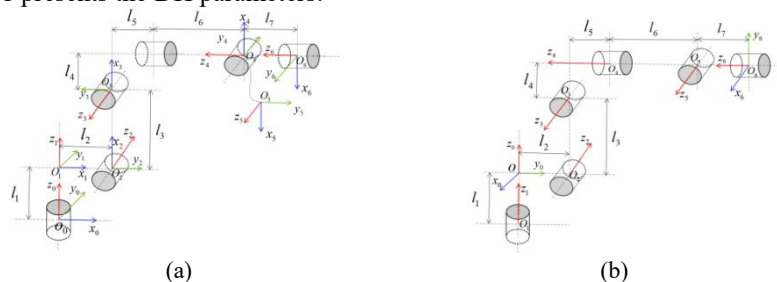

(a)   (b)

Fig. 2. (a) The establishment of the robot joint coordinate system based on the MDH model (b) The establishment of the robot model based on the POE exponential product theory

Table 1. Parameter table corresponding to the MDH model

	d	a	alpha	theta	beta
1	L1	L2	0	0	0
2	0	L3	-90	-90	0
3	0	L4	180	0	DELTA
4	-(L5+L6)	0	-90	0	0
5	0	0	-90	180	0
6	0	0	0	0	0

Table 2. The spiral scale of the POE model

	b	w	v
1	[0,0,-L1]	[0,0,1]	[0,0,0]
2	[0,L2,0]	[-1,0,0]	[0,0,-L2]
3	[0,L2,L3]	[1,0,0]	[0,-L3,L2]
4	[0,L2+L5,L3+L4]	[0,-1,0]	[-(L3+L4),0,0]
5	[0,L2+L5+L6,L3+L4]	[1,0,0]	[0,-(L3+L4),(L2+L5+L6)]
6	[0,L2+L5+L6+L7,L3+L4]	[0,-1,0]	[-(L3+L4),0,0]

As inferred from the DH model, the adjacent two joints only required translation and rotation around the *X*-axis and then around the *Z*-axis to enable the first joint in the adjacent joint to rematch the next joint completely. However, when the adjacent link is approximately parallel, the adjacent joints are unable to rejoin after the DH transformation and the coupling of the series robot amplifies to the end actuator, which would cause the conformation of the end actuator to mutate. S. Hayati and M. Mirmirani have proposed a method to add a rotation angle β_i that rotates around the *y*-axis such that the small changes do not cause large disturbances, thereby resolving the singular phenomenon of DH modeling[11]. On the basis of the modified DH model, the transformation relationship of the adjacent link in the MDH model is represented below:

$$^{i-1}T_i = Rot\ (x_{i-1},\alpha_{i-1}) \bullet Trans\ (x_{i-1},a_{i-1}) \bullet Rot\ (z_i,\theta_i) \bullet Trans\ (z_i,d_i)$$

$$= \begin{bmatrix} c\theta_i & -s\theta_i & 0 & a_{i-1} \\ c\alpha_{i-1}s\theta_i & c\theta_i c\alpha_{i-1} & -s\alpha_{i-1} & -d_i s\alpha_{i-1} \\ s\alpha_{i-1}s\theta_i & s\alpha_{i-1}c\theta_i & c\alpha_{i-1} & d_i c\alpha_{i-1} \\ 0 & 0 & 0 & 1 \end{bmatrix}$$

(2-1)

The manufacturing and assembly error, as well as the changes in the external environment or load, result in the difference in the robot nominal value and its actual value, which manifests as the deviation among the four parameters, namely, the length *a* of the link, the twisting angle *α* of the link, the offset direction *d* of the link, and the joint angle *θ*. The joint angle is controlled according to the pulse emitted by the encoder, and is, therefore, an error parameter that could be eliminated through artificial compensation.

According to the differential kinematics theory of the robots, the adjacent link transformation matrix takes the total derivative of the five parameters, as presented in the equation (2–2):

$$d^{i-1}T_i = \frac{\partial^{i-1}T_i}{\partial\theta_i}\Delta\theta_i + \frac{\partial^{i-1}T_i}{\partial d_i}\Delta d_i + \frac{\partial^{i-1}T_i}{\partial a_{i-1}}\Delta a_{i-1} + \frac{\partial^{i-1}T_i}{\partial\alpha_{i-1}}\Delta\alpha_{i-1}$$

$$d^{i-1}T_i = (D_\theta\Delta\theta_i + D_d\Delta d_i + D_a\Delta a_{i-1} + D_\alpha\Delta\alpha_{i-1})\bullet^{i-1}T_i = \delta^{i-1}T_i \bullet^{i-1}T_i$$

(2-2)

where

$$D_\theta = \begin{bmatrix} -s\theta_i & -c\theta_i & 0 & 0 \\ c\alpha_{i-1}c\theta_i & -c\alpha_{i-1}s\theta_i & 0 & 0 \\ s\alpha_{i-1}c\theta_i & s\alpha_{i-1}s\theta_i & 0 & 0 \\ 0 & 0 & 0 & 0 \end{bmatrix}, \quad D_d = \begin{bmatrix} 0 & 0 & 0 & 0 \\ 0 & 0 & 0 & -s\alpha_{i-1} \\ 0 & 0 & 0 & c\alpha_{i-1} \\ 0 & 0 & 0 & 0 \end{bmatrix}, \quad D_\alpha = \begin{bmatrix} 0 & 0 & 0 & 0 \\ -s\alpha_{i-1}s\theta_i & -s\alpha_{i-1}c\theta_i & -c\alpha_{i-1} & -d_ic\alpha_{i-1} \\ c\alpha_{i-1}s\theta_i & c\alpha_{i-1}c\theta_i & -s\alpha_{i-1} & -d_is\alpha_{i-1} \\ 0 & 0 & 0 & 0 \end{bmatrix}, \quad D_a = \begin{bmatrix} 0 & 0 & 0 & 1 \\ 0 & 0 & 0 & 0 \\ 0 & 0 & 0 & 0 \\ 0 & 0 & 0 & 0 \end{bmatrix}$$

$\delta^{i-1}T_i$ represents the bias transformation matrix of the adjacent link.

$$\delta^{i-1}T_i = \begin{bmatrix} -s\theta_i\Delta\theta_i & -c\theta_i\Delta\theta_i & 0 & \Delta a_{i-1} \\ c\alpha_{i-1}c\theta_i\Delta\theta_i - s\alpha_{i-1}s\theta_i\Delta\alpha_{i-1} & -s\alpha_{i-1}c\theta_i\Delta\alpha_{i-1} - c\alpha_{i-1}s\theta_i\Delta\theta_i & -c\alpha_{i-1}\Delta\alpha_{i-1} & -s\alpha_{i-1}\Delta d_i - d_ic\alpha_{i-1}\Delta\alpha_{i-1} \\ c\alpha_{i-1}s\theta_i\Delta\alpha_{i-1} + s\alpha_{i-1}c\theta_i\Delta\theta_i & c\alpha_{i-1}c\theta_i\Delta\alpha_{i-1} - s\alpha_{i-1}s\theta_i\Delta\theta_i & -s\alpha_{i-1}\Delta\alpha_{i-1} & c\alpha_{i-1}\Delta d_i - d_is\alpha_{i-1}\Delta\alpha_{i-1} \\ 0 & 0 & 0 & 0 \end{bmatrix}$$

On the basis of the above differential transformation mechanism of the robot, the error model of the end actuator relative to the robot base could be established. If the degree of freedom of the serial robot is *n*, then the transformation relationship between the end of the robot and the base of the robot may be expressed as equation (2–3) :

$$^0T_n + d\,^0T_n = \prod_{i=0}^{n-1}(^iT_{i+1} + d\,^iT_{i+1}) \tag{2-3}$$

The above formula may be expanded using the Taylor series. Since it is a differential transformation, the magnitude of a single differential part is relatively small and, therefore, the high-order of the differential part may be ignored to simplify the calculation. Therefore, Taylor expansion was applied to retain the first-order differential part, as presented in equation (2–4):

$$^0T_n + d\,^0T_n = {}^0T_n + \sum_{i=0}^{n-1}(^0T_1\cdots^{i-1}T_i \bullet d\,^iT_{i+1} \bullet^{i+1}T_{i+2}\cdots^{n-1}T_n) \tag{2-4}$$

$$d\,^0T_n = \left[\sum_{i=0}^{n-1}{}^0T_i\delta^iT_{i+1}\,^0T_i^{-1}\right]{}^0T_n, \quad d\,^0T_n = \delta^0T_n\bullet^0T_n \tag{2-5}$$

Next, the differential transformation relationship between the end of the robot and the base of the robot is as follows:

$$\delta^0T_n = \sum_{i=0}^{n-1}{}^0T_i\delta^iT_{i+1}\,^0T_i^{-1} \tag{2-6}$$

2.2 POE exponential product model

Fig. 2(b) depicts the exponential product model of the six-axis robot and Table 2 presents the corresponding rotation table of the exponential product model.

The exponential product model proposed by Brocket undertakes a global perspective[12]. The base frame of the robot is *S* and the tool coordinate system is *H*. In general, the measurement system cannot be coincident with the base system of the robot. If the measurement system is denoted as *M*, the forward kinematics model of the robot is transformed into:

$$g = g_{MS}(0)\exp(\hat{\xi}_1 q_1)\exp(\hat{\xi}_2 q_2)\cdots\exp(\hat{\xi}_n q_n)g_{SH}(0) \tag{2-7}$$

where, $g_{MS}(0)$ represents the transformation of the robot from *S* to *M* when the robot is at position zero; the $g_{SH}(0)$ represents the transformation from *H* to *S* when the robot is at position zero and $\hat{\xi}_i$ represents the joint spinor of the *i-th* joint.

The global POE exponential product model is represented by Equation (2–7), while Equation (2–8) represents the total differentiation of the forward kinematics model of the exponential product.

$$\delta g g^{-1} = \left(\frac{\partial g}{\partial \xi_{MS}} \delta \xi_{MS} + \frac{\partial g}{\partial q} \delta q + \frac{\partial g}{\partial \xi} \delta \xi + \frac{\partial g}{\partial \xi_{SH}} \delta \xi_{SH} \right) g^{-1}$$

(2-8)

Here, $\delta \xi_{MS}$ denotes the error of the transformation coordinate system, $\delta \xi_{SH}$ denotes the error of the end actuator, and $q = [q_1, q_2, \cdots q_n]^T, \xi = [\xi_1, \xi_2, \cdots \xi_n] \in \Re^{6n}$.

The size of the end actuator is obtained by calibrating the tool coordinate system of the robot itself, and the angle error may be regarded as a source of the coordinate error of the spinor of each joint. Therefore, these two terms may be omitted as both the terms would result in the Jacobian matrix disrank. Since it is essential to obtain the accurate error of the transformation matrix between the measurement coordinate system and the robot base system, the identification of ξ_{MS} and ξ might greatly improve the feasibility of the experiment.

$$\delta g g^{-1} = \left(\frac{\partial g}{\partial \xi_{MS}} \delta \xi_{MS} + \frac{\partial g}{\partial \xi} \delta \xi \right) g^{-1}$$

(2-9)

The right side of the equal sign represents the pose errors of the end actuator caused by the kinematics parameters $\delta \xi_{MS}$ and ξ in the base scale system, where $\delta \xi$, $\delta \xi_{MS}$ respectively represent the joint spin coordinate errors and the initial pose transformation spin coordinate errors. The left side of the equal sign, $\delta g g^{-1} \in se(3)$, represents the deviation from the actual pose of the end actuator to the nominal pose in basis coordinate system, which can be expressed as:

$$\delta g g^{-1} = (g_a - g_n) g_n^{-1} = g_a g_n^{-1} - I_4$$

(2-10)

Further derivation[13] may be represented as:

$$\delta g g^{-1} = \log(g_a g_n^{-1})$$

According to the adjoint change mapping relation of the exponential product[14], one obtains:

$$Ad_g\left(\hat{\xi}\right) = g \hat{\xi} g^{-1} = \begin{bmatrix} R & p \\ 0 & 1 \end{bmatrix} \begin{bmatrix} \hat{\omega} & \upsilon \\ 0 & 0 \end{bmatrix} \begin{bmatrix} R & p \\ 0 & 1 \end{bmatrix}^{-1}$$

(2-11)

The above equation may be transformed into the following equation:

$$\begin{aligned}
\left[\delta g g^{-1} \right]^\vee &= \left[\left(\delta \exp(\hat{\xi}_{MS}) \right) \exp(-\hat{\xi}_{MS}) \right]^\vee + \\
Ad &\left(\exp(\hat{\xi}_{MS}) \right) \left[\left(\delta \exp(\hat{\xi}_1 q_1) \right) \exp(-\hat{\xi}_1 q_1) \right]^\vee + \\
Ad &\left(\exp(\hat{\xi}_{MS}) \exp(\hat{\xi}_1 q_1) \right) \left[\left(\delta \exp(\hat{\xi}_2 q_2) \right) \exp(-\hat{\xi}_2 q_2) \right]^\vee + \cdots + \\
Ad &\left(\exp(\hat{\xi}_{MS}) \prod_{i=1}^{n-1} \exp(\hat{\xi}_i q_i) \right) \left[\left(\delta \exp(\hat{\xi}_n q_n) \right) \exp(-\hat{\xi}_n q_n) \right]^\vee
\end{aligned}$$

(2-12)

$$\left[\left(\delta \exp(\hat{\xi}_i q_i) \right) \exp(\hat{\xi}_i q_i) \right]^\vee = \left(q_i I_6 + \frac{4 - \theta_i \sin\theta_i - 4\cos\theta_i}{2\|\omega_i\|^2} \Omega_i + \right.$$

where

$$\left. \frac{4\theta_i - 5\sin\theta_i + \theta_i \cos\theta_i}{2\|\omega_i\|^3} \Omega_i^2 + \frac{2 - \theta_i \sin\theta_i - 2\cos\theta_i}{2\|\omega_i\|^4} \Omega_i^3 + \frac{2\theta_i - 3\sin\theta_i + \theta_i \cos\theta_i}{2\|\omega_i\|^5} \Omega_i^4 \right) \delta\xi_i = A_i \delta\xi_i$$

(2-13)

and

$$\Omega_i = \begin{bmatrix} \hat{\omega}_i & 0 \\ \hat{v}_i & \hat{\omega}_i \end{bmatrix}, \quad \theta_i = \|\hat{\omega}\| q_i, \quad \|\hat{\omega}_i\| = \sqrt{(\omega_{i,1}^2 + \omega_{i,2}^2 + \omega_{i,3}^2)}$$

$$\left[\left(\delta \exp(\hat{\xi}_{MS} q_{MS}) \right) \exp(-\hat{\xi}_{MS} q_{MS}) \right]^\vee = A_{MS} \delta\xi_{MS}$$

where, A_{MS} is A_i in the same form of expression, which will not be repeated here. Therefore, the error model based on the global exponential product formula and the orientation measurement method is obtained as follows:

$$J_i = \begin{cases} A_{MS} \\ Ad\left(\exp(\hat{\xi}_{MS}) \prod_{k=1}^{i-1} \exp(\hat{\xi}_k q_k) \right) A_i, 1 \leq i \leq n \end{cases}$$

(2-14)

3   Data measurement and parameter identification

The instrument used for measuring data was Renishaw QC20-W ball-bar. The construction of the experimental platform included two steps. The first step was alignment, as illustrated in figures A and B for Fig. 3. Number 1 in Figure A represents the bar on the seat, and this bar could move along the direction of the bar with a certain margin under the illustrated state. Number 2 in Figure A represents the smooth ball used for alignment. Number 3 in Figure A is the magnet and Number 4 in Figure A is the clamping lock. When the seat is near the smooth ball, the magnet drives rod 1 to move upward through suction, thereby reaching the state illustrated in the right picture B. At this time, the horizontal rotation of the ball causes the rod to be fixedly attached to the ball in a horizontal state, indicating that the rod on the seat is in a vertical state. When the lock is locked, rod 1 on the seat would become stuck and fixed.
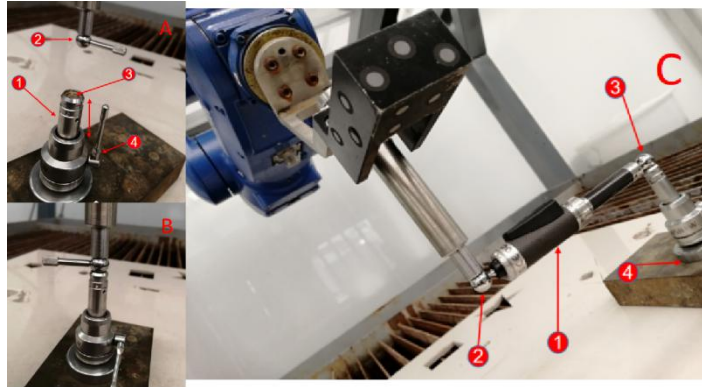
Fig. 3.   Ball-bar alignment chart and installation diagram of robot end ball-bar instrument

The seat of the ball-bar was placed approximately 150 mm away from the robot's end actuator, and the robot's end position was moved to the position just right to it. The ball-bar instrument was lightly mounted between the actuator and the seat, as depicted in figure C for Fig. 3. Number *1* represents the ball-bar instrument, number *2* is a small ball that may be moved with a small displacement, number *3* is a fixed-end ball, and number *4* is the point where the seat is connected to the platform surface. The platform must have a certain weight of the iron material so that the seat-down magnet is adsorbed on the platform surface, thereby not allowing the seat to move easily. The

hardware part of the ball-bar was then constructed. Next, the supporting ball-bar instrument software was used, which relied on Bluetooth to connect with the ball-bar instrument within the effective connection distance of approximately *1* meter. After programming, the robot was allowed to perform circular motions and the data was collected by the software.

The most commonly used method for parameter identification is the least square algorithm, the standard form of which is as follows:

$$\Delta X = (J^T J)^{-1} J^T \Delta P$$

(3-1)

The least-square algorithm presents the characteristics of fast convergence and small computation. When the matrix $J^T J$ is close to the singularity, this leads to irreversibility or becomes an ill-conditioned matrix, because of which the parameter error solved by the least square method is wrong and the method is not stable. The damped least square algorithm (L-M algorithm), therefore, introduced the damping factor into the least square algorithm. The L-M algorithm combines the advantages of the gradient descent method and the Newton method.

$$\Delta X = (J^T J + \lambda I)^{-1} J^T \Delta P$$

(3-2)

where, λ represents damping factor.

4   Simulation and Experiment

As illustrated in Fig. 4(a), a six-axis robot model was established using MATLAB software. A circular arc was drawn in MATLAB, with the green line representing the target trajectory, the blue line representing the trajectory prior to calibration, and the red line representing the trajectory after the calibration, as illustrated in Fig. 4(b). It may be observed that the accuracy of the trajectory after calibration was improved greatly.

(a)   (b)
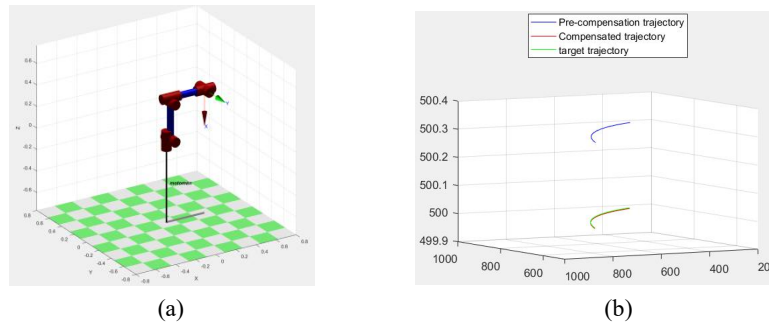
Fig. 4.   (a) The six-axis robot model established using MATLAB   (b) Arc trajectories prior and after calibration

The joint pulse and the actual measured values at the end of the robot were the input, and the joint pulse was converted into the joint angle radian value, based on which, the nominal value of the end-actuator of the robot could be obtained. The difference between the nominal value and the measured value is the error value. Fig. 5(a) depicts the error curve prior to and after the calibration based on the MDH model. The

collection points comprised 100 groups of points, the running time was 13 s, and the optimization rate was 86.201%. It may be observed from the figure that the average error prior to calibration was approximately 3 mm, while the maximum error was close to 6 mm. The maximum error is obviously the error in the periphery of the robot's workspace. The four dotted lines depicted in the figure represent the upper and the lower boundaries of the error curve prior to and after the calibration, respectively, and the residual error of the calibration curve could be reduced to less than 1 mm. Fig. 5(b) presents the error curve based on the POE exponential product model prior to and after the calibration, where the sequence points comprised 100 groups of points. However, the running time was only 3 s, and the optimization rate was 85.495%, which appears to be slightly less compared to that for the MDH model. However, the running time is much faster than that for the MDH model. Table 3(a) and Table 3(b) present the modified parameters of the MDH model and the POE model, respectively. Under the condition of an optimal close rate, selecting the POE model would be a better choice.

(a)   (b)
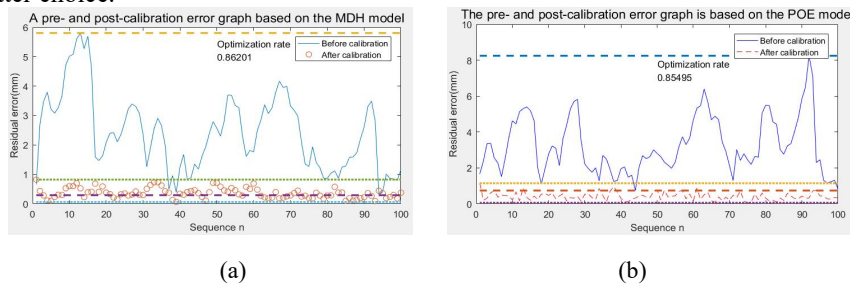
Fig. 5. (a) The error curve prior and after the calibration based on the MDH model   (b) The error curve prior and after the calibration based on the POE model

Table 3.   (a) The MDH model parameter correction table   (b) The POE model parameter correction table

(a)   (b)

MDH compensation parameter table

	Δα	Δa	Δd	Δθ	Δβ
1	-1.1698e-04	-1.5671	-0.7548	2.5457e-05	NaN
2	2.0012e-04	1.2853	0.6508	0.0019	NaN
3	0.0015	-0.5481	0.6508	-5.2437e-04	0.0011
4	-6.7462e-04	0.0701	7.9469e-06	0.0014	NaN
5	-0.0010	0.0669	-0.1170	1.4306e-04	NaN
6	0.0196	0.1323	0.1239	0.0113	NaN

POE compensation parameter table

	Δξ1	Δξ2	Δξ3	Δξ4	Δξ5	Δξ6	Δξt
1	-3.6208e-05	-0.0025	0.0014	1.5559e-04	0.0020	9.8620e-05	2.2857e-04
2	5.4532e-04	1.7822e-04	-1.6557e-04	0.0025	6.8656e-06	0.0021	-0.0027
3	-5.0262e-04	-0.0075	0.0021	0.0017	3.9541e-04	0.0021	8.4761e-05
4	-0.0344	0.0278	0.1598	-2.5893	2.3125	-2.2063	-2.4920
5	0.0719	-0.0287	1.3816	0.2449	1.5618	-0.1016	0.5212
6	0.0317	-0.1420	3.1621	-0.7452	3.7262	-1.0203	1.5488

The abrasive water cutting head was fixed mechanically on the end flange of the robot to cut the ceramic tile, as illustrated in Fig. 6(a). The cutting-down graphics are depicted in Fig. 6(b). The figure presents the two manifestations of the same object cut prior to and after the compensation; the performance prior to compensation is similar to the top view of the shape of the egg and the cutting-down graphic after the compensation is similar to the comparison circle. Indeed, there would be a cut out of a gap, although it does not alter the effect prior to and after the compensation; the dollar coin is used as a reference in the left image and the figure on the right presents the

difference prior to and after the compensation. It may be observed that the deviation of the cutting effect prior to and after the compensation was approximately 1 mm.
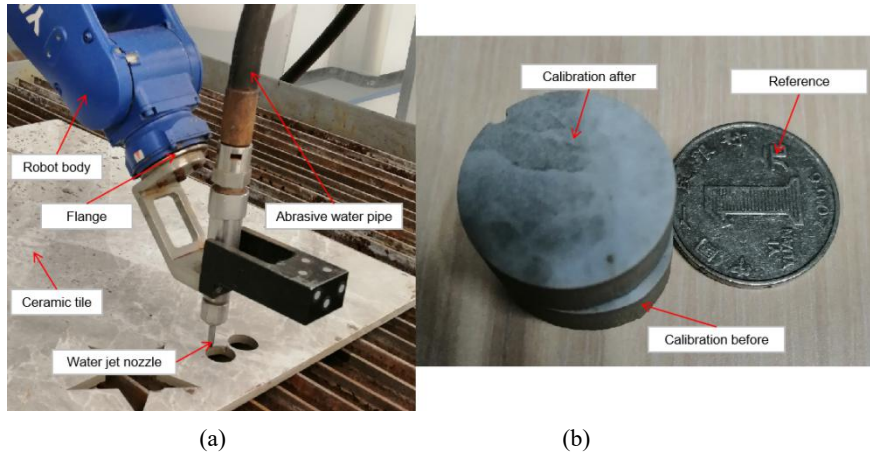

(a)

(b)

Fig. 6. (a) Physical picture of water cutting robot (b) The cutting physical image before and after calibration based on POE model

5   Conclusion

On the basis of the simulation and experiment results, the MDH model and the POE model were compared after the calibration, and it was revealed that both the models presented a good optimization effect with quite similar optimization rates. However, from the perspective of time-consumption of the optimization process, the POE model consumed much less time compared to the MDH model. In regard to the final cutting effect, the combination of robot and water jet cutting technology is a completely feasible concept.

Acknowledgement

References

1. 邓永刚. 工业机器人重复定位精度与不确定度研究[D].天津大学,2014.

2. He S, Ma L, Yan C, Lee C-H, Hu P. Multiple location constraints based industrial robot kinematic parameter calibration and accuracy assessment[J]. International Journal of Advanced Manufacturing Technology, 2019,102 (5-8).

3. Ping Yang, Zhiguang Guo, Yangbo Kong. Plane kinematic calibration method for industrial robot based on dynamic measurement of double ball bar[J].Precision Engineering, 2020, 62:265-272.

4. Le Ma, Patrick Bazzoli, Patrick M. Sammons, et al. Modeling and calibration of high-order joint-dependent kinematic errors for industrial robots[J].Robotics and Computer-Integrated Manufacturing,2018, 50:153-167.

5. Jorge Santolaria, Javier Conte, Marcos Pueo, et al. ROTATION ERROR MODELING AND IDENTIFICATION FOR ROBOT KINEMATIC CALIBRATION BY CIRCLE POINT METHOD[J].Metrology and Measurement Systems, 2014, 21(1):85-98.

6. Jorge Santolaria,Javier Conte,Manuel Ginés. Laser tracker-based kinematic parameter calibration of industrial robots by improved CPA method and active retroreflector[J]. The International Journal of Advanced Manufacturing Technology,2013,66(9-12).

7. Morris R. Driels,Uday S. Pathre. Robot manipulator kinematic compensation using a generalized jacobian formulation[J]. Journal of Robotic Systems,1987,4(2).

8. Nguyen Van Toan,Phan Bui Khoi. A svd-least-square algorithm for manipulator kinematic calibration based on the product of exponentials formula[J]. Journal of Mechanical Science and Technology,2018,32(11).

9. Mao Chentao,Chen Zhangwei,Li Shuai,Zhang Xiang. Separable Nonlinear Least Squares Algorithm for Robust Kinematic Calibration of Serial Robots[J]. Journal of Intelligent & Robotic Systems,2020,101(1).

10. Xiangdong Yang, Liao Wu, Jinquan Li, et al. A minimal kinematic model for serial robot calibration using POE formula[J].Robotics and Computer-Integrated Manufacturing, 2014, 30(3):326-334.

11. S.Hayati, M.Mirmirani. Improving the absolute positioning accuracy of robot manipulators[J].Journal of Robotic Systems, 1985 ,112 (2) :397–413.

12. Brockett R.W.Robotic Manipulators and the Product of Exponentials Formula[C].Mathematical theory of Networks and Systems.New York:Spring-Verlag,1984.120-129.

13. He R，Li X，Shi T，et al. A kinematic calibration method based on the product of exponentials formula for serial robot using position measurements[J].Robotica，2014，33(6):1-19.

14. 戴建生. 旋量代数与李群李代数[M].北京：高等教育出版社，2014.

Integrated Modular Solution for Task Oriented Manipulator Configuration Design

Anubhav Dogra, Sakshay Mahna, Srikant Sekhar Padhee, and Ekta Singla

Indian Institute of Technology Ropar, Rupnagar, Punjab, India 140001
`2016mez0019@iitrpr.ac.in`, `2018csb1119@iitrpr.ac.in`,
`sspadhee@iitrpr.ac.in`, `ekta@iitrpr.ac.in`

Abstract. Modular and reconfigurable robotic systems have been designed to provide a customized solution for the non-repetitive tasks to be performed in a constrained environment. Customized solutions are normally extracted from task-based optimization of the possible manipulator configurations but the solution are not integrated, for providing the modular compositions directly. In this work, in the first phase, a strategy of finding unconventional optimal configurations with minimal number of degrees-of-freedom are discussed based upon the prescribed working locations and the cluttered environment. Then, in the second phase, design of the modular and reconfigurable architecture is presented which can adapt these unconventional robotic parameters. Rather than generating and evolving the modular compositions, a strategy is presented through which the unconventional optimal configurations can be mapped directly to the modular compositions. The generated modular composition is validated using Robot Operating System for the motion planning between the prescribed working locations in a given cluttered environment.

Keywords: Modular Library, Reconfigurable Manipulators, Configuration Synthesis, Robot Operating System, Task-Based Designs.

1 Introduction

Providing the robotic solutions for the custom tasks needs time and cost-effective customizable systems. These robotic systems should be adaptable to all the variations of the prescribed tasks and the constrained working locations where the standard robotic configurations cannot work. These tasks may belong to industry such as pick and place works in highly cluttered environments, in servicing or maintenance sectors, or in health care sectors [12]. Given an environment and the working locations, a robotic solution strategy has been provided by the various researchers - using modularity and reconfiguability, but is never integrated. Attention is required to provide a modular solution which can directly give the modular configurations based upon the prescribed task [7]. Configuration synthesis has been explored by many reseachers in recent years providing different frameworks considering various factors such as reachability, kinematic

and dynamics performances, obstacle avoidance, path planning etc. Campos et. al [3] presented configuration synthesis for reachability in 3D space with obstacle avoidance using Sketch synthesis system and used HEBI actuators for their modular configurations. Icer et. al. [8] uses evolutionary algorithms to generate possible modular compositions and to find their best modular composition for given task and environment. Similar work is presented by Liu et. al. [10] for optimizing modular composition in static environment, also considering energy efficiency, cycle time and few performance metrics. Kereluk et. al. [9] developed a reconfigurable 12-Degree-of-Freedom (DoF) manipulator and optimizes the number of joints to be active or locked for the prescribed task. Stravopodis et. al. [14] presented 3-DoF modular design with psuedo joint and optimizes the configuration for a recitlinear task using Genetic Algorithm. Whitman et. al. [17] presented a motion planner which also synthesizes the manipulator for required tasks which includes elimination of the joints to reduce the DoF if required. Along with that, various modular designs has been presented in literature to provide the customized solutions and can be seen in [4, 11, 18, 16, 13, 7]

These solutions are majorly explored on the basis of generating modular compositions from a given set of modules and then checking the configurations if able to work or not on the prescribed tasks. Alongside, the configurations are explored mostly for a fixed DoF system and standard parameters. In this paper, we have presented: 1. An optimal and unconventional configuration synthesis of the manipulator along with minimizing the number of DoF required for the prescribed working locations and a cluttered environment. 2. Design of a modular library which can adapt to the unconventional parameters in the optimal configurations. 3. Integration of optimal synthesis with modular compositions, which provides the optimal modular sequence having two variants of the modules as Heavy (H) and Light (L).

The paper is organized as follows. Section 2 defines the approach and methodology for the optimal configuration synthesis in a given environment and specified working locations. Section 3 presents the design of each unit of the module and its features. Section 4 shows the rules of assembling different configurations considering the designed modules, and composition possibilites. Section 5 discusses about the outcomes of the approach, with the conclusion of the work in last section.

2   Optimal Configuration Synthesis: Minimized DoF Approach

The objective of minimizing number of DoF is considered in this paper to determine the best possible configuration of a manipulator to do a specific set of tasks. A nested bi-level optimization problem has been formulated, in which first level is used to compute the DoF of the manipulator and the second level provides the optimal robotic parameters. Binary search method is applied for the computation of DoF as a unidirectional search problem during optimization at the upper level [12]. Algorithm 1 shows the steps of computation, where k_l and

k_u are the lower and the upper limits of the element number in the given array, say A. A contains k number of elements as $\{A_0,\ A_1,\ A_2,\ \ldots,\ A_{k-1}\}$. f is the

---

Algorithm 1: Binary search algorithm to initialize DoF for configuration synthesis

---

   Result: n=DoF
   initialization: k_l= 0; k_u= $k - 1$;
   while $k_l \leq k_u$ **do**
      m = floor($(k_l + k_u)$ / 2); n=A[m];
      if $f \leq T$ **then**
         | k_u= $m - 1$;
      else
         | k_l= $m + 1$;
      end
   end

---

optimization objective function value and n is the number of DoF. The result from the outer problem of binary search goes into the (inner) lower level and iterations occur accordingly with respect to the function value.

2.1   Constrained Optimization Formulation

The desired manipulator is required to reach the set of Task Space Locations (TSLs) in a cluttered environment. Thus optimization problem is formulated to design an optimal configuration with minimum number of DoF which can reach to the TSLs avoiding obstacles. $P_d = [x_d,\ y_d,\ z_d]$ is considered as desired position vector, and $O_d = [\alpha_d,\ \beta_d,\ \gamma_d]$ as the desired orientation vector of the end-effector frame or last frame. Thus, for N number of TSLs, the objective function can be derived as the error between the desired and the current pose.

$$P_{error} = \sum_{i=1}^{N}[(x_{id} - x_{ia})^2 + (y_{id} - y_{ia})^2 + (z_{id} - z_{ia})^2]; \tag{1}$$

$$O_{error} = \sum_{i=1}^{N}[(\alpha_{id} - \alpha_{ia})^2 + (\beta_{id} - \beta_{ia})^2 + (\gamma_{id} - \gamma_{ia})^2]; \tag{2}$$

$$f(\mathbf{x}) = |\sqrt{P_{error}}| + |\sqrt{O_{error}}|; \tag{3}$$

Here, subscript a denotes actual parameters of position and orientations computed through homogenous transformations at the current design variables as

$$T_n^0 = T_1^0\ T_2^1 \ldots T_n^{n-1}. \tag{4}$$

The configuration of a manipulator is defined by a set of Denavit-Hartenberg (DH) parameters, which are all considered as variables in this study. For N number of TSLs in a Cartesian space, the manipulator with same robotic parameters

is required to reach all TSLs. Thus, the total number of design variables would be $(3 + N) * n$ as $[a_i, \ \alpha_i, \ d_i, \ \theta_{ij}]$, where $i \ \in \ 1 : n$, and $j \ \in \ 1 : N$.

To avoid collisions with obstacles, the obstacles and the links are assumed as triangulated meshes. Each link is assumed to be a parallelopiped with a certain width. The minimum distance (D) between the two meshes is computed and treated as a constraint. Collision check is done amoung links and between the links and the obstacles. Value of the D becomes negative when there is collision between the meshes. Thus nonlinear inequality constraint can be written as

$$g_{ij}(\mathbf{x}) = -D_{ij} - \delta \leq 0; \ i \in 1 : n, \ j \in 1 : N \tag{5}$$

where δ can be used as a safety margin to avoid just touching of links with the obstacles. Thus the optimization model can be written as.

To Minimize:

$$f(\mathbf{x}) = |\sqrt{P_{error}}| + |\sqrt{O_{error}}|; \tag{6}$$

with design variables vector,

$$\mathbf{x} = [a_i, \alpha_i, d_i, \theta_{ij}]^T, for \ i \in 1 : n, j \in 1 : N. \tag{7}$$

Subjected to:

$$a_i^l \leq a_i \leq a_i^u, \tag{8}$$

$$\alpha_i^l \leq \alpha_i \leq \alpha_i^u, \tag{9}$$

$$d_i^l \leq d_i \leq d_i^u, \tag{10}$$

$$\theta_{ij}^l \leq \theta_{ij} \leq \theta_{ij}^u, \tag{11}$$

$$-D_{ij} - \ \delta \leq \ 0 \tag{12}$$

3   Modular Architecture

The presented modular library [7] mainly consists of link modules and joint modules. The joint module is designed to incorporate the actuator and its adjustment in terms of connection with other modules and the required arrangement of twist angles. It consists of mainly 3 components as shown in Fig. 1, an actuator, an unconventional twist unit, and two casings for input and output section of the actuator. To design the modular joint assembly, *KA-Series* actuators from *Kinova* [2] are used in this work. Specifications of both the actuators are provided in Table 1. ϵ is the parameter which defines the capacity of the designed modules to pick up the the number of modules of its kind. This study was done by the authors based on worst-torque analysis of the modular assemblies in [7]. Link modules are passive modules to provide structural aspects to a manipulator. Two kinds of links are designed as shown in Fig. 1 (d). One type has the parallel connection ports and the other has perpendicular.

Table 1. Technical specifications of actuators

Quantity	KA-75+	KA-58
Weight (kg)	0.57	0.357
No load speed (rpm)	12.2	20.3
Nominal torque (Nm)	12	3.6
Maximum torque (Nm)	30.5	6.8
ϵ	3	3
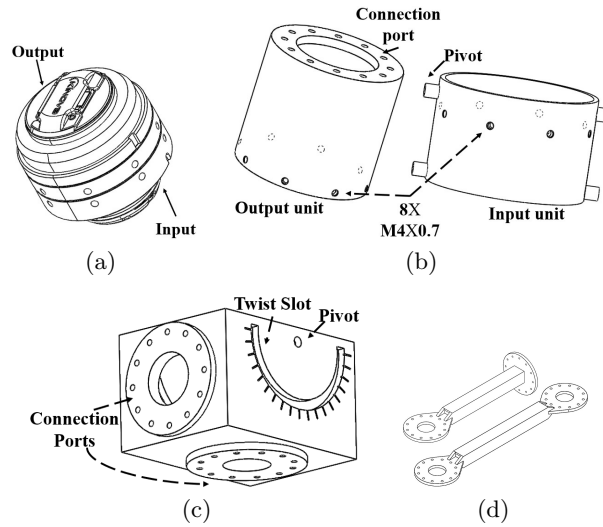
Fig. 1. Modular library containing (a) actuator, (b) actuator casings (c) Adaptive twist unit, (d) Link modules.

Adaptive twist unit is designed to incorporate the twist angles adjustments between two adjacent frames according to *DH* convention. The twist adjustment can be done in two ways. One is the angle between the two adjacent intersecting joint axes, another is an angle between two adjacent skew joint axis. In this design, pivotal extension from the input unit of casing is assembled with pivot of twist adjusting unit, see Fig. 1. The twist unit has a semi-circular slot with resolution of $10°$ ranges from 0 to $+90°$ and $-90°$ in both clockwise and anticlockwise direction as shown in Fig. 1 (c). The input unit can rotate about pivotal axis in the twist unit to adjust the twist angle. Besides, there are two connection ports provided orthogonal to each other and are provided with 12 holes with resolution of $30°$ to adjust twist angle.

Two casings are designed for an actuator for each of its sides. The input casing is to be assembled with input section of actuator, which is relatively fixed. Thus, it has two pivotal extensions, as shown in Fig. 1 (b), which are assembled with

the twist unit. The output casing is to be assembled with the output section which rotates with respect to the input section. On each of the casing, there are eight tapped holes which are used to fix these casings onto the actuator. Output casing has 12 threaded holes. These 12 holes gives the resolution of 30° when assembling other modules to it.

Post analysis of the design of the modules including validations, modular assembly combinations and possibilities, worst torque analysis are not given in this paper, and can be checked in authors work in [6, 7].

4   Modular Composition based upon Optimal Configuration

The proposed modular components can be assembled together to get the required custom configuration, even with unconventional twist angles. As there are two sizes of actuators used, two variants of modules are considered in the modular library as Heavy (H) and Light (L). For futher assembly simpilifications, four modular subassemblies (units) are proposed based upon the connection ports on the joint modules, as shown in Fig. 2. These are valid for both 'H and 'L' variant of the joint modules. These can be enumerated as, 'H^k' associated to Heavy (H) modules and 'L^k' associated to Light (L) modules, where $k \in 1 : 4$.
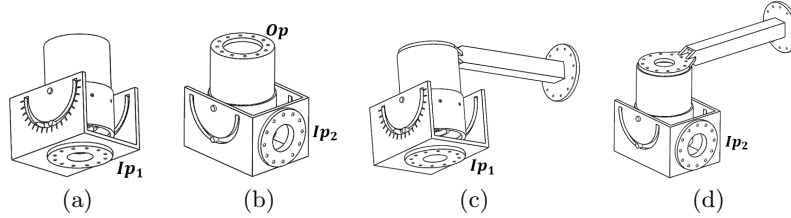
Fig. 2. The 4 types of modular units are as (a) H^1 or L^1, (b) H^2 or L^2, (c) H^3 or L^3 and (d) H^4 or L^4

1. 'H^1' or 'L^1' is used when a joint module is to be connected through Ip_1.
2. 'H^2' or 'L^2' represents the corresponding joint module connected through Ip_2.
3. 'H^3' or 'L^3' is used when a joint module is connected through Ip_1 and it is having a link module attached at Op.
4. 'H^4' or 'L^4' represents a joint module connected through Ip_2 and having a link module at Op.

In this work, it has been assumed that the base modules or the first joint axis will always be 'H^1'or 'H^3' depending upon the spatial or planar case.

4.1 Optimal Robotic Parameters to Modular Sequence and Combinations

The desired custom configuration can be realized by assembling the modules even without considering the DH parameters, using modular units sequence as desired. But the DH parameter approach provides a direct solution rather than trying out different combinations of modular units. DH parameters possess the information of number of degrees-of-freedom (DoF) and relationship between the adjacent joint frames in terms of the position and the orientation. As per the discussions in section 4, modular configurations are formed using four modular units. Therefore, first step of the process is to interpret a given set of DH parameters and convert them into modular units sequence i.e. in terms of H^k or L^k. Along with that, unconventional twist parameters are to be incorporated within these modular units, if any. The algorithm to convert DH parameters into modular unit sequence works upon the following points, these are valid for both H and L variants.

1. If $a \neq 0$ in the *DH* table, use H^3 or H^4, else use H^1 or H^2.
2. If $a = 0 \cap \alpha \neq 0$ in the *DH* table, twist is given by rotating actuator casings about the pivotal axis in the adaptive twist unit of joint module.
3. If $a \neq 0 \cap \alpha \neq 0$ in the *DH* table, twist is given using Ip_1 or Ip_2 connections ports of the joint module and H^3 or H^4 are used.
4. If $d \neq 0$ in the *DH* table, H^1 or H^2 are used.

Through this, the prescribed DH parameters are converted into the modular unit sequence. To incorporate the different variants of the modular units (H or L), a strategy is proposed based upon the worst-torque analysis done by the authors in [7] to assemble the sequence.

1. Fix link 1: H^k and link n: L^k.
2. Connect $H^k \rightarrow H^k$ or $H^k \rightarrow L^k$.
3. $L^k \rightarrow L^k$.
4. Refer ϵ for maximum number of each module carrying by the parent module in Table 1

Now considering this, for a given DoF and the value of ϵ, there can be many possiblities of the combinations of the H and L modules. For e.g. 3-DoF configuration can be realized using $[L^k - L^k - L^k;\ H^k - L^k - L^k;\ H^k - H^k - L^k;\ H^k - H^k - H^k]$ combinations of modules. As maximum 4 number of H modules can be assembled in series, same is applicable to L, thus for a given DoF, the number of possible combinations can be deduced from

$$C_n = 5 - |n - 4|, \quad n = DoF \tag{13}$$

Therefore, for number of DoF = {2, 3, 4, 5, 6, 7, 8}, number of combinations comes out to be {3, 4, 5, 4, 3, 2, 1}. Selection of the modular assembly composition from the set of possible compositions becomes important so as to accomplish the task efficiently. This can be done using dynamic performance parameters such

as minimized energy or torque required for the particular task. The selected modular composition is then modelled in a unified way for the motion planning and control of the realized modular manipulator through Robot Operating System (ROS).

5   Results and Discussions

Constrained optimization as discussed in section 2.1, is integrated with the modular units selection, formation of modular sequence.
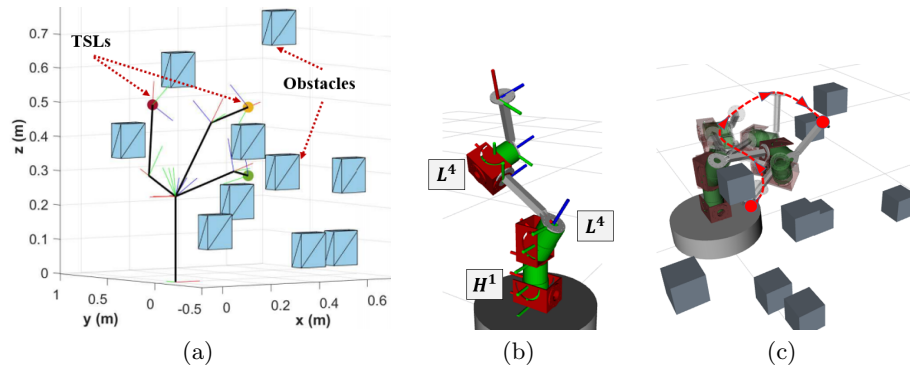

(a)   (b)   (c)

Fig. 3. (a) 3-DoF optimal configuration reaching all 3-TSLs avoiding obstacles, (b) 3-DoF modular composition based upon synthesized configuration, (c) Motion planning between the TSLs of the modular composition using ROS.

Table 2. Optimal robotic parameters (DH) based upon the prescribed TSLs and cluttered environment.

i	a_i (m)	α_i (rad)	d_i (m)	θ_{i1} (rad)	θ_{i2} (rad)	θ_{i3} (rad)
1	0	1.0367	0.25	2.6063	2.336	1.4483
2	0.3	1.0624	0	2.1362	2.8469	0.2030
3	0.3	0	0	1.7242	2.0784	0.6573

A test case is shown here to validate the algorithm discuss above. As shown in Fig. 3 (a), 10 obstacles are used as triangulated mesh cubes of sides 0.1 m each. These boxes are placed in a Cartesian space to make the environment cluttered. Three TSLs are choosen for reachbility in between the boxes at (0.3,

0, 0.5), (0.3, 0, 0.3) and (0.1, 0.5, 0.5)[1]. The desired orientation parameters can be given in Euler angles format. Optimization problem in the inner loop, is solved by using Sequential Quadratic Program (SQP) with *fmincon* function in MATLAB R2021a. Collision constraints are treated as nonlinear inequality constraints for this problem, with $\delta = 0.005$, and lower and upper limits on the design parameters are treated as bounds. Iterations are started with 5-DoF as per binary search algorithm, but eventaully converged down to 3-DoF configuration to reach the prescribed working locations within the obstacles, as shown in Fig. 3 (a). Table 2 shows the corresponding DH parameters of the optimal configuration and joint values for all the TSLs.

As briefed in section 4, the optimal parameters can be realized using modular architecture and modular units. The parameters are reduced to $H^1 - L^4 - L^4$ using given set of rules in section 4.1, as shown in Fig. 3 (b). For the validation of the 3-DoF modular configuration, a Unified Robot Description Format (URDF) of the configuration is generated automatically to use it for the motion planning of the robot between the working locations avoiding obstacles. This has been implemented in Robot Operating System platform using Moveit [5]. Moveit uses a joint limited Jacobian based numerical solution for the inverse kinematics called as TracIK [1] and Open Motion Planning Library (OMPL) [15] for the motion planning of the end-effector of the manipulator under the constrained environment. The motion of the end-link of the 3-DoF configuration from working location 2 to 3 is implemented using this, as shown in Fig. 3 (c). This validates that the modular configuration is not only able to reach the working locations but also able to plan the motion between each task space location.

6   Conclusion

Mapping of the optimal configuration synthesis of the manipulator to the modular composition with minimal number of DoF and considering unconventional parameters is presented in this paper. A nested bi-level constrained optimization problem is formulated with-respect-to prescribed working locations and given cluttered environment to synthesize a serial configuration with minimal number of DoF. A modular library is presented which can adapt to the unconventional robotic parameters to provide custom solutions based upon the user requirements. A strategy is presented to map the optimal unconventional configuration into the modular assembly with assembly possibilites and that is the novelty of the proposed intregrated solution. A unified way of modeling and control of modular composition is presented using ROS, that validates the reachability and motion planning between the TSLs in a cluttered environment.

References

1. Beeson, P., Ames, B.: Trac-ik: An open-source library for improved solving of generic inverse kinematics. In: 2015 IEEE-RAS 15th International Conference on

---

[1] All dimensions are in meters.

Humanoid Robots (Humanoids), pp. 928–935. IEEE (2015)

2. Campeau-Lecours, A., Lamontagne, H., Latour, S., Fauteux, P., Maheu, V., Boucher, F., Deguire, C., L'Ecuyer, L.J.C.: Kinova modular robot arms for service robotics applications. In: Rapid Automation: Concepts, Methodologies, Tools, and Applications, pp. 693–719. IGI Global (2019)

3. Campos, T., Inala, J.P., Solar-Lezama, A., Kress-Gazit, H.: Task-based design of ad-hoc modular manipulators. In: 2019 International Conference on Robotics and Automation (ICRA), pp. 6058–6064. IEEE (2019)

4. Chen, I.M., Yim, M.: Modular robots. In: Springer Handbook of Robotics, pp. 531–542. Springer (2016)

5. Coleman, D., Sucan, I., Chitta, S., Correll, N.: Reducing the barrier to entry of complex robotic software: a moveit! case study. arXiv preprint arXiv:1404.3785 (2014)

6. Dogra, A., Padhee, S.S., Singla, E.: Optimal architecture planning of modules for reconfigurable manipulators. Robotica pp. 1–15 (2021)

7. Dogra, A., Sekhar Padhee, S., Singla, E.: An optimal architectural design for unconventional modular reconfigurable manipulation system. Journal of Mechanical Design **143**(6) (2021)

8. Icer, E., Hassan, H.A., El-Ayat, K., Althoff, M.: Evolutionary cost-optimal composition synthesis of modular robots considering a given task. In: Intelligent Robots and Systems (IROS), 2017 IEEE/RSJ International Conference on, pp. 3562–3568. IEEE (2017). DOI 10.1109/iros.2017.8206201

9. Kereluk, J.A., Emami, M.R.: Task-based optimization of reconfigurable robot manipulators. Advanced Robotics **31**(16), 836–850 (2017). DOI 10.1080/01691864. 2017.1362995

10. Liu, S.B., Althoff, M.: Optimizing performance in automation through modular robots. In: 2020 IEEE International Conference on Robotics and Automation (ICRA), pp. 4044–4050. IEEE (2020). DOI 10.1109/icra40945.2020.9196590

11. Mohamed, R.P., Xi, F.J., Chen, T.: A pose-based structural dynamic model updating method for serial modular robots. Mechanical Systems and Signal Processing **85**, 530–555 (2017)

12. Singh, S., Singla, A., Singla, E.: Modular manipulators for cluttered environments: A task-based configuration design approach. Journal of Mechanisms and Robotics **10**(5), 051,010 (2018). DOI 10.1115/1.4040633

13. Singh, S., Singla, E.: Realization of task-based designs involving dh parameters: a modular approach. Intelligent Service Robotics **9**(3), 289–296 (2016)

14. Stravopodis, N., Moulianitis, V.: Rectilinear tasks optimization of a modular serial metamorphic manipulator. Journal of Mechanisms and Robotics **13**(1) (2020)

15. Şucan, I.A., Moll, M., Kavraki, L.E.: The Open Motion Planning Library. IEEE Robotics & Automation Magazine **19**(4), 72–82 (2012). DOI 10.1109/MRA.2012. 2205651

16. Valente, A.: Reconfigurable industrial robots: A stochastic programming approach for designing and assembling robotic arms. Robotics and Computer-Integrated Manufacturing **41**, 115–126 (2016). DOI 10.1016/j.rcim.2016.03.002

17. Whitman, J., Choset, H.: Task-specific manipulator design and trajectory synthesis. IEEE Robotics and Automation Letters **4**(2), 301–308 (2018). DOI 10.1109/lra.2018.2890206

18. Yun, A., Moon, D., Ha, J., Kang, S., Lee, W.: Modman: An advanced reconfigurable manipulator system with genderless connector and automatic kinematic modeling algorithm. IEEE Robotics and Automation Letters **5**(3), 4225–4232 (2020). DOI 10.1109/lra.2020.2994486

Design of an electrorheological clutch with compound working mode for reconfigurable underactuated gripper

Yi Sun[1], Juncheng Xiao[1] and Huayan Pu[1]

[1] School of Mechanical and Electrical Engineering and Automation, Shanghai University, Shanghai 200444, China

Abstract: This paper introduced a kind of electrorheological clutch for reconfigurable underactuated gripper. It can work in shear mode and compression-shear mode. The maximum clutch torque can reach 2.34Nm, and the compression-shear mode torque is twice that of the shear mode torque, indicating that the compression-shear mode can effectively improve the clutch output torque.

Keywords: Reconfigurable Under-actuated Gripper, Electrorheological Clutch, Shear Mode, Compression-shear Mode.

1   Introduction

Electrorheological (ER) fluid is a kind of smart material that its dynamic shear stress shows a parabolic change under an external electric field[1]. ER fluid has been widely used in clutches [2], dampers [3], and robots [4]. Three working modes, such as shear mode, flow mode, and compression mode are possible for an ER fluid based clutches[5] and first one are most common. For example, the ERIK, an electrorheological clutch device designed by Yamamoto et al. for strength training, used a concentric cylinder structure and takes advantage of the shear effect of the electrorheological fluid to switch between the brake and clutch, achieving constant load and constant speed motion [6]. An electrorheology actuator for rehabilitation training robot developed by Davidson et al. adopts a composite structure of multilayer cylinder and single-layer parallel plate, which can achieve a maximum torque output of 1.1Nm at 1500V [7]. An electrorheological clutch designed by Olszak et al. adopts a parallel disc structure with an achievable torque density of 0.78 kN/m² [8].

It has been reported that by performance of an ER clutch can be further improved by combining the shear mode with other working mode. For example, when the ER fluid between parallel plates is compressed, the force response is greater than that working only in shear mode [9]. Tian et al. found that in the compression mode [10], the shear yield stress of the electrorheological fluid was more than 100 times that of the pure shear mode. In addition, several clutches based on magnetorheological (MR) fluid working in compound modes has been designed. For example, the MR clutch designed by Sarkar et al., can achieve a clutch torque in the compression-shear mode 5 times that in the shear mode when the magnetic field intensity is 200 kA/m [11]. In the MR clutch designed by Wang et al., when the compression clearance is 1mm and the working current is 1A, the clutch torque in the compression-shear mode is 17.9 times that in the

shear mode [12]. Since the ER fluid and MR fluid have similar rheological properties, it is speculated that the output torque of an ER clutch in compression shear mode may be greater than that in shear mode as well.

To verify this hypothesis, an ER clutch with compound working modes is designed. The output torque of the clutch is tunable by applying electric field on the ER fluid, and to further improve tunable range of the output torque, the clutch can work in shear mode or in compression-shear mode. This clutch can be used in a reconfigurable under-actuated gripper for distributing desired torques among gripper joints according to manipulation postures of the gripper.

2 Concept design of reconfigurable underactuated gripper

2.1 Overview of the gripper

The reconfigurable under-actuated gripper as illustrated in Fig.1(a) has a body and two omnidirectional fingers. Each of the omnidirectional fingers has two degrees of freedom. The first one is a linear motion achieved by a timing belt along the finger as shown in Fig.1(b), and the second one if the rotation of a cylinder roller along the finger as shown in Fig.1(c). By coordinating motion of the two omnidirectional fingers, the gripper can work in clamping, pull-in, and twisting modes, as shown in Fig. 1(a), Fig. 1(b) and Fig.1(c), respectively. In the clamping mode, the two omnidirectional fingers clamp and hold the object. In the pull-in mode, the object is pulled in or pushed out by the timing belts. In the twisting mode, the object is lifted or lowered by rotating the rollers.

(a) Clamping mode   (b) Pull-in mode   (c) Twisting mode
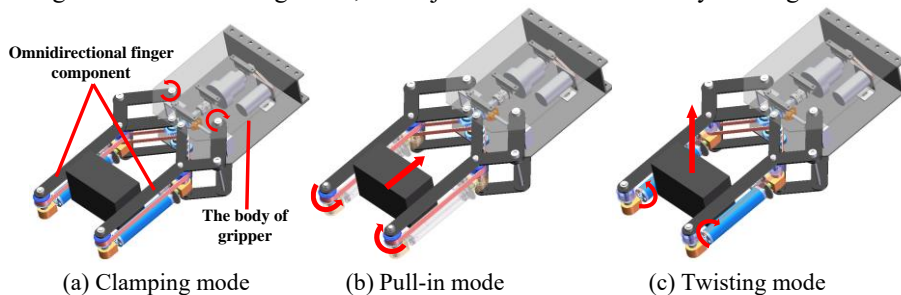
Fig. 1. Working modes of the reconfigurable gripper.

2.2 Design of the drive chain of the gripper

To realize the reconfigurable gripper, a transmission chain of reconfigurability is required. Fig. 2 demonstrates the conceptual design of the transmission chain in clamping mode and pull-in mode. In the clamping mode as shown in Fig.2(a), the output torque of the ER clutch is distributed through the worm gear assembly to the bevel gears, which drive the parallel rods to open or close the finger tips. In the pull-in mode as shown in Fig.2(b), the output torque of the ER clutch is divided into two paths, which

go through the timing belts of the left finger and the right finger respectively. By carefully design the spur gear assembly, the two timing belts always move in the same direction and consequently push objects into or out of the palm. The rollers used in the twisting mode are driven by miniature motors integrated in the rollers.

An ER clutch is designed to switch the working mode of the transmission chain by tuning its output torque. The bearing capacity of the clamping and the pull-in mode are of the most importance for evaluating design of the clutch.

(a) Clamping mode   (b) Pull-in mode
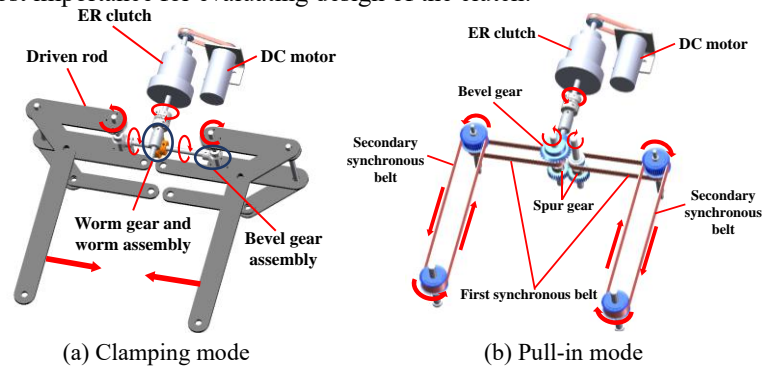
Fig. 2. The transmission chain of the clutch in clamping mode and pull-in mode.

3   Design of ER clutch

3.1   Prototype design of the clutch

Fig. 3(a) shows its cross-section view of the ER clutch which consists of an ER transmission mechanism, a compression mechanism, and a planetary gear row. The ER transmission mechanism is composed of several parallel plate electrodes. Half of these plate electrodes are stator electrodes which are fixed on the clutch chassis, while the others that are mounted on a rotating shaft outputting to the planetary gear are rotor electrodes. Voltage applied on those plate electrodes determines engagement state of the ER transmission mechanism. As voltage increases, ER fluid becomes "stiffer" and therefore bears more torque between the stator and rotor electrodes. The planetary gear is used to widen tunable range of the output torque of the clutch. The compression mechanism driven by tightening manually the compression bolts is used to extrude the ER fluid between plate electrodes in the clutch for evaluating the possibility of increasing torque output by means of compression. Miniature pressure sensor is used to measure pressure in the clutch. Two copper rings, shafts and several metal chassis part are used to introduce exciting voltage from the power supply to the plates electrodes. Other parts are make of plastic for electrical isolation.

3.2 Engagement states of the ER clutch

The output torque of the clutch can be tuned according to the engagement states of the ER transmission mechanism, as show in Fig.3(b). When the ER transmission mechanism is fully engaged, the input torque of the clutch T_i, equals to the output torque T_o, namely:

$$T_i = T_o \tag{1}$$

When the ER transmission mechanism is partially engaged, it satisfies:

$$T_o = (\frac{z_1}{z_2} + 1)T_d \tag{2}$$

where T_d is the shear torque generated by the ER transmission mechanism, T_o the output torque, z_1 is the number of ring gear teeth of the planetary gear, and z_2 is the number of center gear teeth of the planetary gear.

(a) Cross-section view of ER clutch   (b) Transmission path of ER clutch
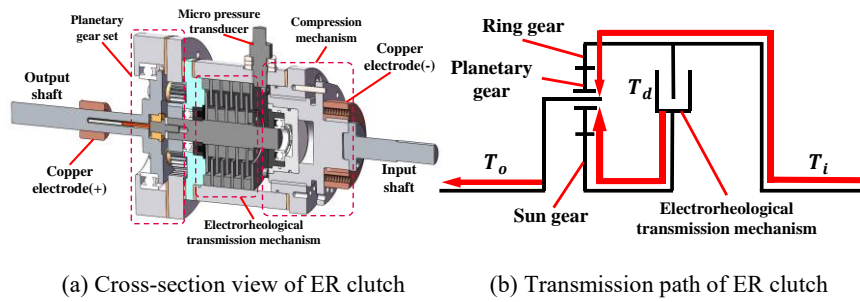
Fig. 3. Clutch torque transmission path and structure.

4 Mathematical modeling of clutch torque

4.1 Rheological property of the ER fluid

Fig. 4 shows test result of the rheological property of the ER fluid (MW-GERF0201 series produced by Ningbo Maiwei Technology Co., Ltd.) used in our research.
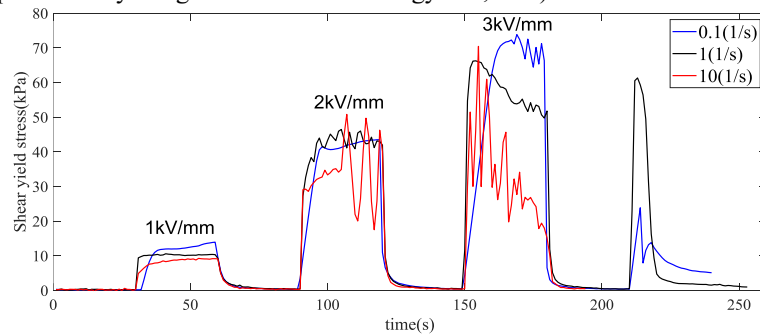
The zero-electric field viscosity μ_0 of the ER fluid is 6.028 Pas. The yield strength of the ER fluid was measured at shear rates of 0.1(1/s), 1(1/s) and 10(1/s). The loading electric field intensities are 1kV/mm, 2kV/mm and 3kV/mm, respectively. The results show that the shear yield stress is a binary expression for the electric field intensity E and the shear rate $\dot{\gamma}$.

The current rheological model for electrorheological fluids is based on the Bingham model, which needs to be modified to take into account the interaction between the electric field strength and the shear rate:

$$\begin{cases} \tau = \mu_0\dot{\gamma}, \;\; E = 0 \\ \tau = aE^b\dot{\gamma}^c + mE(\dot{\gamma})^n + \mu_0\dot{\gamma}, \;\; E > 0 \end{cases} \tag{3}$$

The electric field intensity E, shear rate $\dot{\gamma}$ and shear yield stress τ were substituted into the equation, and the undetermined coefficients were solved by MATLAB. The model was obtained as follows:

$$\begin{cases} \tau = 0.006\dot{\gamma}, \;\; E = 0 \\ \tau = 67.72E^{1.06}\dot{\gamma}^{-0.27} - 52.80E(\dot{\gamma})^{-0.33} + 0.006\dot{\gamma}, \;\; E > 0 \end{cases} \tag{4}$$

The fitting coefficient R^2 is 0.9354.

4.2   Modeling clutch torque in shear mode

The plate electrodes bear torque of the clutch due to shear stress between the stator electrodes and the rotor electrodes and between the chassis and the rotor electrodes. The former one can be modeled using elementary disc clutches between the rotor the stator electrodes as show in Fig.5. The other one can be modeled using elementary cylinder clutches as shown in Fig. 6.
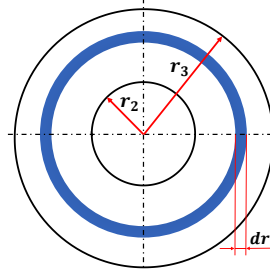
Fig. 5. Simplified model of parallel disc clutch.

The simplified model of the parallel disc clutch is shown in Fig. 5, where the inner diameter of the driving disc and the outer diameter of the driven disc are r_2 and r_3, respectively. The torque acting on an elementary disc dr on the plate electrodes, dT, is:

$$dT = rdF = r\tau dA = 2\pi r^2 \tau dr \tag{5}$$

Once the electric field is applied, two sources of the shear stress of the ER fluid contribute to bearing capacity of the clutch. One is the shear stress caused by viscosity of the ER fluid, and the other one is the shear yield stress caused by the interaction between the electric field and the shear rate:

$$\tau = \tau_{E,\dot\gamma} + \mu_0 \frac{(\omega_a - \omega_p)r}{h} \tag{6}$$

where, ω_p is the rotation speed of the passive plate, ω_a is the rotation speed of the active plate, and h is the gap of the plates. Take the boundary conditions $r = r_2$ and $r = r_3$. The shear rate is distributed linearly between r_2 and r_3, so the calculation is simplified and the average value of the shear rate is taken as the global shear rate of the torus. When there are n groups of parallel plates, the disc clutch torque T_p is:

$$T_p = \frac{2(2n-1)\pi\tau(r_3^3 - r_2^3)}{3} = K_P\tau \tag{7}$$

where K_P is a constant related to dimensions of the clutch, which unit is mm^3.
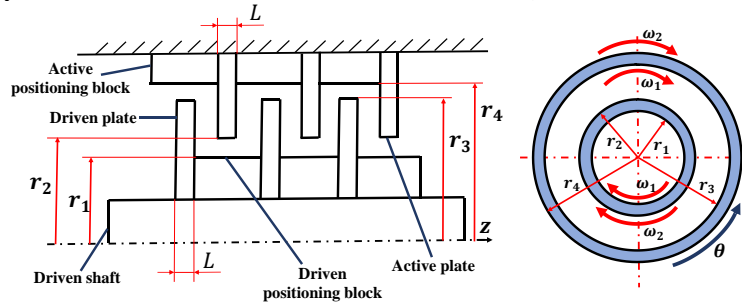
Fig. 6. Simplified model of concentric cylinder clutch.

The simplified model of the concentric cylinder clutch is shown in Fig. 6, where r_1 is the outer diameter of the driven positioning block, r_2 is the inner diameter of the driving disc, r_3 is the outer diameter of the driven disc, r_4 is the inner diameter of the active positioning block, and L is the main and the width of the driven disc.

The cylindrical coordinate system (θ, r, z) is selected and the infinitesimal radius r between the driven positioning block and the driving disk is taken to obtain the momentum equation of the rotating shear flow as follows:

$$\frac{\partial \tau}{\partial r} + \frac{2\tau}{r} = 0 \tag{8}$$

Calculate the angular velocity of the fluid between r_1 and r_2 according to equations (6) and (8):

$$\omega_r = \frac{1}{\eta_0}\left(-\frac{c_1}{2r^2} - \tau_{E,\dot\gamma}\ln r\right) + c_2 \tag{9}$$

c_1 and c_2 are integral constants. Take the boundary conditions, $r=r_1$, $r=r_2$, $\omega_r=\omega_1$, $\omega_r=\omega_2$. For the transfer torque of the infinite element radius, there are:

$$T = 2\pi r^2 L\tau \tag{10}$$

Combining equations (6), (8), (9) and (10), the shear torque T_1 between the driven positioning block and the driving disc is obtained:

$$T_1 = \frac{4\pi\tau_2 L r_1^2 r_2^2 \ln\left(\frac{r_2}{r_1}\right)}{r_2^2 - r_1^2} \tag{11}$$

where τ_2 is the shear stress of an electrorheological fluid at radius r_2. Similarly, the expression of the shear torque between the driven plate and the driving cylinder is:

$$T_2 = \frac{4\pi r_4 L r_3^2 r_4^2 \ln\left(\frac{r_4}{r_3}\right)}{r_4^2 - r_3^2} \tag{12}$$

where τ_4 is the shear stress of an electrorheological fluid at radius r_4. When there are n groups of pole plates, the total torque of the concentric cylinder clutch is:

$$T_c = n(T_1 + T_2) = T(K_C, \tau_2, \tau_4) \tag{13}$$

where K_C is a structure constant, unit is mm^3. Combined with the friction torque T_f and equation (2), it can be obtained that the shear torque T in shear mode is an expression about K_P, K_C, τ, τ_2 and τ_4:

$$T = \left(\frac{z_1}{z_2} + 1\right)(T_p + T_c) + T_f = T(K_P, K_C, \tau, \tau_2, \tau_4) + T_f \tag{14}$$

Table 1. Structure parameters of the clutch

Parameters	r_1	r_2	r_3	r_4	n	L	z_1	z_2	T_f
Value	9mm	10mm	15mm	16mm	5	1mm	72	36	0.15Nm

According to dimension parameters listed in Table 1, the constants K_P and K_C are calculated. Combined with equations (4) and (14), the shear torque T is can be expressed by the electric field intensity E and shear rate $\dot{\gamma}$:

$$T = 11.143E^{1.06}\dot{\gamma}^{-0.27} - 8.678E(\dot{\gamma})^{-0.33} + 0.001\dot{\gamma} + 0.15 \tag{15}$$

4.3 Modeling clutch torque in compression-shear mode

In the compression-shear mode, the electrorheological fluid's electro-induced yield stress τ_E is given by Tao et al. [13]:

$$\tau_E = \tau^0 + KP \tag{16}$$

where τ^0 is the shear yield stress of the material at zero pressure, and P is the compression stress, K is the proportional coefficient. Substitute equation (16) into equation (14) to obtain the torque expression of the compression-shear mode as follows:

$$T = 11.143E^{1.06}\dot{\gamma}^{-0.27} - 8.678E(\dot{\gamma})^{-0.33} + 0.001\dot{\gamma} + 0.1653KP + 0.15 \tag{17}$$

5 Experiment verification

5.1 Test bench

A test bench as shown in Fig. 7 was fabricated where a magnetic powder brake provides the load for the clutch and a servo motor (Panasonic's MSMF series) drives the clutch. Output torque of the clutch was measured by a torque sensor. A carbon brush is installed below the input shaft and output shaft of the clutch, and an adjustable high-voltage DC power supply is used to supply power to the clutch.
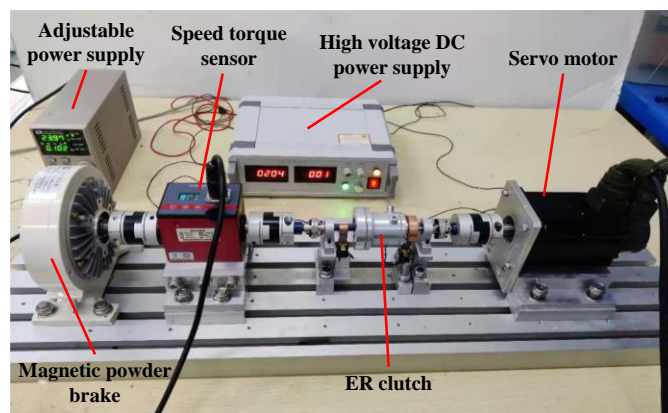
Fig. 7. Test bench for measuring ER clutch output torque.

5.2 Experiment results in the shear mode

Fig. 8 shows the experimental results of the clutch in the shear mode driven at the experimental speed of 10 - 40rpm. The voltage ranges from 0V to 1.6kV and the corresponding field intensity ranges from 0-1.6kV/mm. The magenta curve is the theoretical model corresponding to each speed, and the triangle marks represent the actual clutch output torque at each speed.

In all the experiments, the output torque increases with increasing of the exciting voltage. The maximum output torque was 1.14Nm which was observed at speed of 10rpm with a 1.6kV exciting voltage. However, theoretical predicted output torque is 2.86Nm. There is a big difference between the experimental and the theoretical predicted results. It might because unexpected breakdown of the ER fluid happened in the clutch due to discharge of the electrodes caused by tiny burr on the surface of plate electrodes.
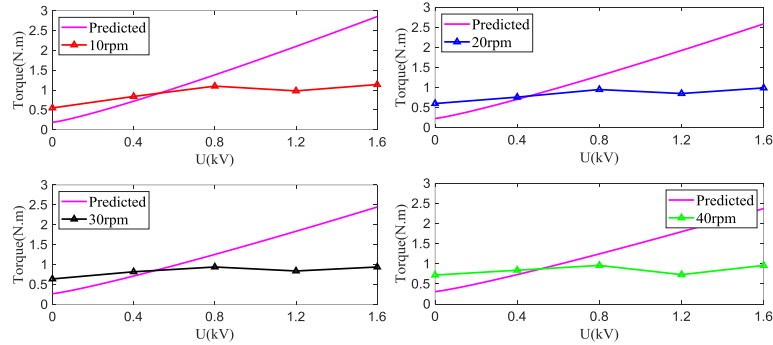
Fig. 8. Output torque of clutch in shear mode.

5.3 Analysis of results in compression-shear mode

Fig. 9 shows the torque and voltage distribution in compression-shear mode at 10 rpm. Compared with the shear mode, the clutch torque is significantly improved when the compression stress reaches 7.2kPa, and the clutch torque reaches the maximum value of 2.34Nm under the voltage of 1200V, which is more than twice that of the shear mode in the same conditions. It confirmed that pre-compression of the ER fluid can increase the shear yield stress. In addition, it is also found in the experiment that the breakdown voltage of the compression shear mode is lower than the breakdown voltage of the shear mode, because the current density of the ER fluid during the pre-compression period increases, resulting an increased electric field as discussed in [14].
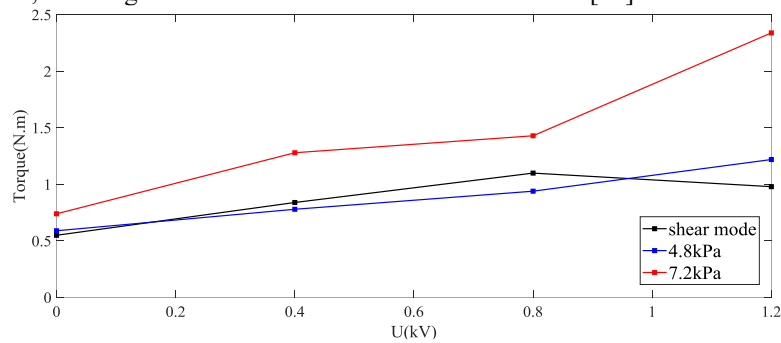
Fig. 9. Output torque of clutch in compression-shear mode(10rpm).

6 Conclusion

An ER clutch capable of operating in shear mode and compression-shear mode was designed for potential usage in reconfigurable underactuated gripper. The output torque of the clutch was modeled by considering rheological property of the ER fluid as well as structure of the clutch. Experiment results on the output torque confirmed that the

clutch can output more than twice torque in compression-shear mode than that in shear mode.

Judging from the current results, the predicted value of the theoretical model in the shear mode is quite different from the experimental value, and the compressive stress that the device can currently load is limited, which is not enough to determine the quantitative relationship between the coefficient K and the electric field E. Later, the device will be optimized to improve further the output performance of the clutch.

References

1. W. M. Winslow, "Induced fibration of suspensions," *Journal of Applied Physics*, vol. 20, no. 12, pp. 1137-1140, 1950.
2. Chris A. Papadopoulos, "Brakes and clutches using ER fluids," *Mechatronics*, vol. 8, no. 7, pp. 719-726, 1998.
3. H.Q. Gong, L M King, "Experimental Investigations on Tension and Compression Properties of an Electro-Rheological Material," *Journal of Intelligent Material Systems and Structures*, vol, 7, no. 1, pp. 89-96, 1996.
4. D. J. Brookfield and Z. B. Dlodlo, "Robot torque and position control using an electrorheological actuator," *Proceedings of the Institution of Mechanical Engineers, Part I: Journal of Systems and Control Engineering*, vol. 212, no. 3, pp. 229-238, 1998.
5. Y. Yamamoto, K. Koyanagi, Y. Kimura, M. Koyanagi and T. Oshima, "Verification of device modes of a strength training machine using an electrorheological fluid brake," *2014 IEEE/SICE International Symposium on System Integration.* IEEE, 2015.
6. J. Davidson and H. I. Krebs, "An Electrorheological Fluid Actuator for Rehabilitation Robotics," *IEEE/ASME Transactions on Mechatronics*, vol. 23, no. 5, pp. 2156-2167, 2018.
7. M. Yoshikawa, K. Boku and T. Nakamura, "High Speed Switching Control of 1DOF Manipulator Using ER Clutch," *Electro-Rheological Fluids and Magneto-Rheological Suspensions*, pp. 68-73, 2011.
8. A. Olszak, K. Osowski, P. Motyl, G. Mędrek, J. Zwolak, A. Kęsy, Z. Kęsy and S.-B. Choi , "Selection of Materials Used in Viscous Clutch with ER Fluid Working in Special Conditions," *Frontiers in Materials*, vol. 6, no. 139, 2019.
9. M. Nilsson, and N. G. Ohlson, "An Electrorheological Fluid in Compression Mode," *Journal of Intelligent Material Systems and Structures*, vol. 11, no. 7, pp. 545-554, 2000.
10. Y. Tian, M. Zhang, X. Zhu, Y. Meng and S. Wen, "Ultrahigh yield stress in a general electrorheological fluid under compression," *Smart Materials and Structures*, vol. 19, no. 3, 2010.
11. C. Sarkar and H. Hirani, "Theoretical and experimental studies on a magnetorheological brake operating under compression plus shear mode," *Smart Materials and Structures*, vol. 22, no. 11, p. 115032, 2013.
12. H. Y. Wang and C. Bi, "Study of a magnetorheological brake under compression-shear mode," *Smart Materials and Structures*, vol. 29, no. 1, 2019.
13. R. Tao, Y. C. Lan and X. Xu, "Structure-enhanced yield shear stress in electrorheological fluids," *International Journal of Modern Physics B*, vol. 16, no. 17-18, 2002.
14. M. L. Zhang, T. Yu, J. L. Jiang, X. L. Zhu and S. Z. Wen, "Compression Enhanced Shear Yield Stress of Electrorheological Fluid," *Chinese Physics Letters*, vol. 26, no. 4, 2009.

Design and Optimization of a Hybrid Air-land Robot for Nuclear Power Plant Inspection

Pengfei Lu[1], Qingqing Wei[2], Yaobin Tian[1], ZixinTang[2],

Shuiqing Jiang[2], Kun Xu[1*], Xilun Ding[1]

[1] Beihang University, Beijing 100191, China
{xk007&lupfi&ybtian&xlding}@buaa.edu.cn
[2]Beijing Institute of Spacecraft System Engineering, Beijing, China
ago126@126.com,zxtang@163.com,weiqingqing51@sina.com

Abstract. Nuclear power generation is taking up an increasing share of the world's total power generation. To ensure safety during operation, robots are usually used for periodic inspection tasks. However, due to the complex terrain structure in nuclear power plant, the robot is required to have better terrain adaptability. Traditional robots with a single moving form are not competent for these inspection tasks. Therefore, this paper proposes a variable configuration of multi-mode robot in land and air, which has the locomotion forms of flight, walking, rolling and the function for collision protection. Firstly, through the comparison of various air movement forms and ground movement forms, the layout of the whole mechanism is determined. Then the overall endurance time model of the system is established, and parameters such as the size of the robot are optimized to obtain the optimal endurance time. Finally, the multi-mode conversion process of the robot is analyzed and verified by simulation.

Keywords: Air-land robot, multi locomotion forms, mechanism design and optimization, dynamic simulation

1 Introduction

Nuclear energy is the only energy that can almost fully replace fossil fuels, and it is also one of the important methods to realize sustainable energy development [1]. However, the potential threat of radiation leaks can't be ignored. To ensure safety while the power station is running, regular maintenance for internal equipment is necessary. Robots has high security and they are usually easy to use. As a result, they are widely used in nuclear power plants [2-3].

However, the internal environment of nuclear power plants is complex with the characteristics of narrow space, slopes, and complicated pipeline [4]. For example, wheeled robots can only move on flat ground [5-6]. Flying robots can reach target quickly, but they have high energy consumption [7-8]. Legged robots can walk on small obstacles, but they are slow and consume more energy compared with wheeled robots. As a result, the robot with multi locomotion forms are necessary.

Research into hybrid robots with multi locomotion forms has been developed recently. These robots are usually composed of a land locomotion form and an air locomotion form. For example, some studies combine fixed-wing aircraft with ground rolling [9-10]. Some studies combine multi-rotor flight with ground movement [11-13]. Robot HyTAQ can roll on the obstacle terrain using the power provided by the flying part by adding a cylindrical cage shell to quadrotor aircraft [12]. The robot Flying STAR designs the fixed arms of the quadrotor into a foldable form, with wheels attached to the ends [13]. There are also studies that combine foot movements with flight. For example, Leonardo combines biped walking and multirotor. Its leg motor and propeller work together to maintain balance and posture [14]. Yash Mulgaonkar et al. present the flying monkey which has three main capabilities: walking, grasping, and flight [15]. The DUCK robot combines a quadcopter with passive-dynamic legs to create a versatile system that can fly and walk [16].

However, the robots in the above research usually combine the two kinds of locomotion forms, and do not have collision protection. In this article, a novel hybrid air-land robot is designed for equipment inspection in nuclear power plants. Through the reconfigurable mechanism design, the legs of the robot can be switched in different configurations [17], and then a variety of movement forms can be realized. The robot has the locomotion form of flying, walking and rolling. In walking mode, the legs are like quadruped mammals. While in flying mode, the legs can fold to make a circle which protects the middle coaxial propeller and external equipment. Besides, this circle can also be used to roll on ground with the same actuation as walking mode.

The article is organized as follows. The mechanism design of the robot and hardware system is derived in next section. Section III talks about the mechanism optimization. section IV introduces the method of multi-mode conversion and simulation. In the last, section V gives the conclusions.

2 Design of the robot

The mechanism design goal is to achieve the locomotion forms of flying, rolling and walking. The collision safety is also needed because of the narrow space in nuclear power station. At the same time, the robot had to be low in weight to increase its work time without recharging.

2.1 Mechanism Design of the Robot

In aerial mode, the coaxial propeller is chosen to get lift because it has higher lift in the same area compared to multi rotor copter and single rotor helicopter. To reduce structural complexity, the coaxial propeller is attached to a coaxial brushless motor directly. The motor axis can be changed by parallelogram link.

As shown in Fig.2, the parallelogram link is driven by two servo motor. One is using to control pitch angle and the other controls roll angle. The roll servo motor is attached to brushless motor so that the roll angle will remain unchanged when pitch angle changes. The rigid body which houses the controllers, the batteries and the communication system is located below the servo motor.

For land mode, the robot has four legs, each of which has 3 degrees of freedom and is driven by three servo motors. The mechanism of legs is like quadruped mammals. In order to fold into two layers of rings, the leg link is designed as a circular arc.
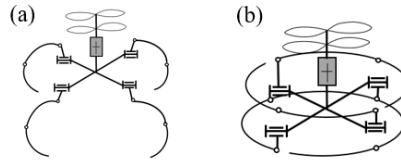

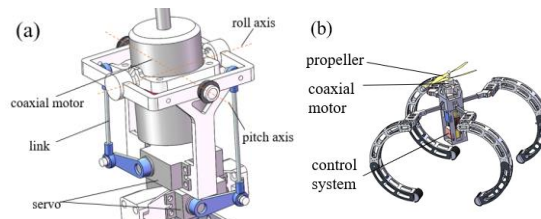**Fig. 1.** The mechanism of the robot: (a)leg expanded state; (b)leg fold state

Fig. 2. Design of the robot: (a) The connecting rod mechanism is used for motor attitude adjustment; (b) Overall structure of robot.

2.2 Working modes of the Robot
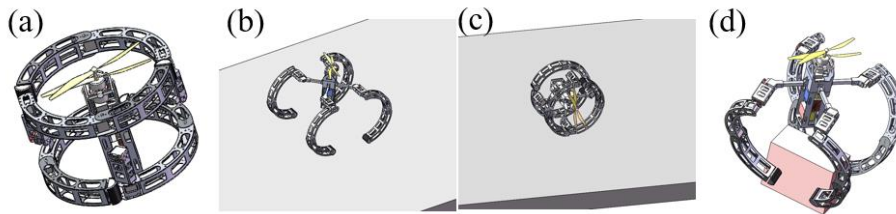
Fig. 3. Working modes of the robot: (a)flying; (b) crawling; (c) rolling; (d)grabbing an object.

As shown in Fig.3, the robot has three locomotion forms, flying, walking and rolling. In flying mode, the coaxial rotor in the middle of the body will produce lift. The axis of lift can be changed to produce attitude control torque. In walking mode, the mechanism of legs is the same as quadruped robots with 12 degrees of freedom. Consequently, it will be able to move like quadruped robots. In rolling mode, the axis of rotors is parallel to ground surface. Circular legs contacts with ground and the leg joints rotate to produce forward torque.

2.3 Hardware and Control systems

The robot is equipped with a flight controller Pixracer R15 which integrates attitude sensors and the MCU STM32F427. Besides, a STM32F103 microcontroller board is chosen to control leg servos. We use coaxial brushless motors (CRM2212,

KV1400) to drive the propeller. The block diagram for the hardware is shown in Fig. 4.
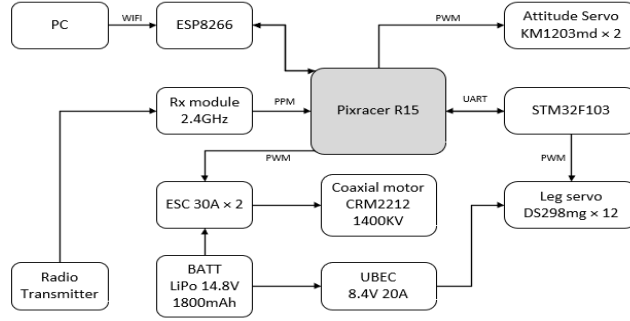
Fig. 4. Hardware of the robot

3 Mechanism optimization of the robot

For both air and ground mobile platforms, the addition of new movement modes brings additional load. The increase in mass affects the performance of multiple movement modes at the same time, or even the inability to move in one mode. Therefore, it is necessary to carry on the overall modeling analysis to the robot design. With the addition of additional robotic legs, flight endurance will be significantly affected. To get as long working time as possible, the total power of hybrid flying-walking system in flying mode will be calculated to optimize endurance time.

As a result, the design optimization process will change the following variables freely:
Propeller diameter D_p, Brushless motor constant K_V, Battery capacity C_b.

The following items will be set to constraints:
Brushless motor maximum voltage U_{max}, Servo motor torque τ_s.

3.1 Weight of the Robot

To calculate the overall mass, the robot is divided into two parts. The total weight of the robot W is the sum of the flying part W_{air} and the legged part W_{land}.

$$W = W_{air} + W_{land} \tag{1}$$

The weight of flying part includes body frame W_{af}, equipment of control system W_{ad} and battery W_{batt}.

$$W_{air} = W_{af} + W_{ad} + W_{batt} \tag{2}$$

For legged part, the frame weight W_{lf} is calculated as the radius of the leg multiplied with 0.045 kg/m which is the weight of an arc carbon fiber structure whose radius is 1m. The mass of the robot's leg drive system and control system are calculated into the flight section.

$$W_{land} = W_{lf} + W_{ld} \tag{3}$$

$$W_{lf} = k_m R \tag{4}$$

The weight of servo motors is

$$W_{ld} = N_s w_s \tag{5}$$

where N_s denotes the num of servos and w_s denotes weight of single servo.

3.2 Propeller performance

According to [18] and [19], the thrust T and torque M generated by a single propeller is expressed as

$$T = C_T \rho \left(\frac{N}{60}\right)^2 D_p^4 \tag{6}$$

$$M = C_M \rho \left(\frac{N}{60}\right)^2 D_p^5 \tag{7}$$

where C_T and C_M denote thrust and torque coefficient respectively. ρ is density of air. N is the speed of propeller (RPM). D_P is the diameter of propeller.

$$C_T \approx 0.25\pi^3 \lambda \zeta^2 B_p K_0 \frac{\varepsilon \arctan \dfrac{H_p}{\pi D_p} - \alpha_0}{\pi A + K_0} \tag{8}$$

$$C_M \approx \frac{1}{8A} \pi^2 C_d \varsigma^2 \lambda B_p^2 \tag{9}$$

$$C_d \approx C_{fd} + \frac{\pi A K_0^2}{e} \frac{\left(\varepsilon \arctan \dfrac{H_p}{\pi D_p} - \alpha_0\right)^2}{\left(\pi A + K_0\right)^2} \tag{10}$$

From [20], the current and voltage of motor is

$$\left\{ \begin{aligned} I_m &= \frac{\pi M K_V U_{m0}}{30(U_{m0} - I_{m0} R_m)} + I_{m0} \\ U_m &= I_m R_m + \frac{U_{m0} - I_{m0} R_m}{K_V U_{m0}} N \end{aligned} \right. \tag{11}$$

The total power in hover can be written as

$$P = U_m I_m \tag{12}$$

3.3 Flight endurance time

According to the definition of battery power density, the total weight of battery is

$$W_{batt} = \frac{C_b U_b}{1000 g \rho_b} \tag{13}$$

When the aircraft hovers, the propeller thrust is equal to the total weight of the aircraft.

According to Equation (1-12), the total power consumption of the hovering robot can be calculated, and then the hovering time can be obtained as

$$t_{hover} = \frac{1000 C_b U_b}{P_{hover}} \tag{14}$$

3.4 Constraints

In the process of robot flight, part of propeller force should be reserved for attitude adjustment. So, the maximum thrust that the flight system can provide is greater than the body weight. The maximum thrust can be written as

$$T_{max} = \beta T \tag{15}$$

where β is coefficient.

At the same time, the voltage of brushless motor U_{max} in the maximum thrust is limited by the battery voltage U_b. The motor constraint is

$$U_{max} \leq U_b \tag{16}$$

where U_{max} can be get from (6-10) and (11)

For the legged part, the choice of servo motor is mainly limited by the driving torque required by the joint. Considering the light mass and slow walking speed of the robot, the inertial force during the walking process is ignored, and only the static torque under the action of gravity is considered.

Servo motors is usually divided into different types according to size such as are micro, medium and large. As a result, the mass m_s is not continuous. According to the required joint torque value τ_s, we need to choose different size of servo motors.

$$m_s = \begin{cases} m_{s1}, \tau_s < T_1 \\ m_{s2}, T_1 \leq \tau_s < T_2 \\ m_{s3}, \tau_s > T_2 \end{cases} \tag{17}$$

3.5 Optimization

The parameters in A-D are listed in the table I.

Table 1. Parameters for flight endurance optimization

parameter	Value	Units
W_{af}	0.5	N
W_{ad}	2.94	N

k_m	0.175	kg/m
N_s	12	--
ρ	1.293	Kg/m^3
U_{m0}	10	V
I_{m0}	0.5	A
R_m	0.201	Ω
U_b	12.6	V
ρ_b	0.084	g/mAh
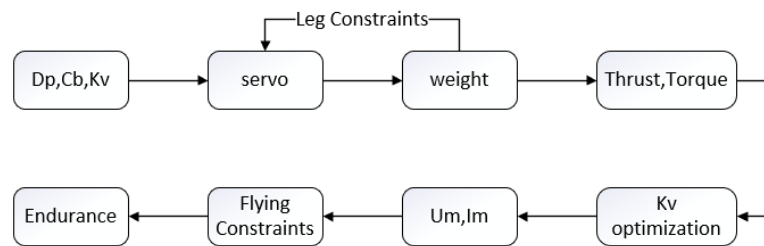
Fig. 5. Flight endurance calculation process

For calculation process, enter a set of parameters to be optimized first, and then pass the mass of the body through Equations (1-5). The mass of the servo motor should be selected according to the restriction (17). Then, according to the total mass, the pulling force of the hovering propeller can be obtained, and parameters such as propeller speed and torque can be calculated through Equation (6-10). To reduce the number of parameters to be optimized, motor KV value optimization is carried out in the next step. After selecting the optimal KV value, voltage, current and power parameters can be obtained through Equation (11-12). Finally, the endurance time is calculated according to Equation (13-14).
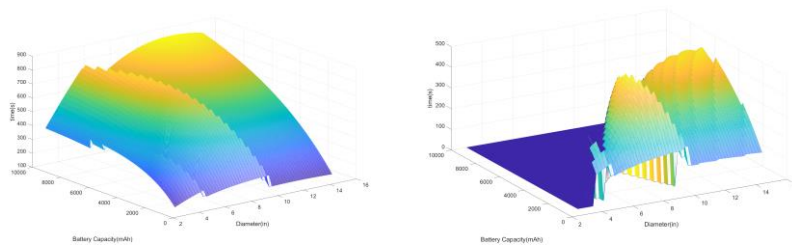
Fig. 6. Flight endurance optimization results: (left)without constraints; (right)with constraints.

It can be seen from the curved figure that with the increase of the diameter of the blade and the battery capacity, the endurance time increases. However, due to the two jumps in the mass of the servo motor, there are also two sudden decreases in the endurance time as the diameter of the propeller increases. According to the optimization results, an 8-inch propeller, a 1800mAh battery, and a 1400kV motor were selected.

The overall weight of the robot is around 1020g, the outer diameter is 252mm, and the body height is 222mm.

4 Control and simulation of the robot

4.1 Transition Process

In walking mode, the legs are in expanded state and they can be landing gears for flying. The legs adjust the body attitude to horizontal to make take-off easier with feedback of attitude sensors. As a result, it will be able to take-off on terrains or slopes.

The axis direction in flying and rolling mode is perpendicular to each other. To transfer to rolling mode, the robot should rolling-over 90 degrees. The coaxial rotors are using in this procedure to produce overturning torque as shown in Fig.7.
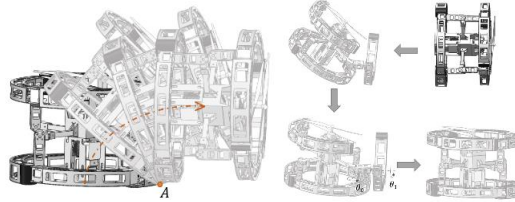
Fig. 7. Transition process of the robot

The conversion process from rolling to flying is shown in the figure above. The robot generates the tilting torque to through the outward swing of the hip joint and knee joint, which makes the robot complete the turnover.

4.2 Control System for Multi-mode Locomotion

The flight controller is a PID controller. For rolling mode, the rolling motion of the robot is realized through the alternating hind swing of the leg joints. In walking mode, the robot walks in a TROT gait.

4.3 Simulation in Gazebo

To verify the feasibility of each motion function of the robot and whether the parameters of the selected hardware system meet the requirements, a simulation model is built in Gazebo, a dynamic simulation environment, and each locomotion mode is simulated.
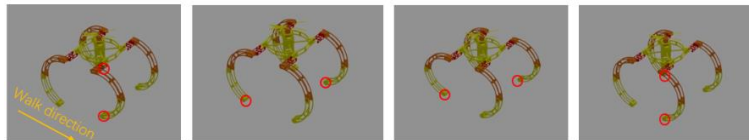
Fig. 8. Simulation of the robot: the robot walks in a TROT gait for one cycle, with the red circles indicating that the leg is in the swing phase.

The simulation of the robot rolling process is shown in Fig. 9. The fuselage is rolled forward through the swing of the touching leg in turn.
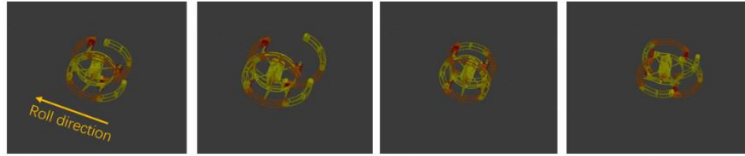
Fig. 9. Roll simulation of the robot: the robot rolls forward by swinging the joint on the ground
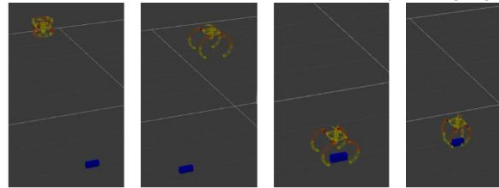
Fig. 10. fly and grab simulation: the robot completes a process of spreading, landing, grabbing and taking off

Figure 10 shows the process of a flight operation task of the robot. After arriving at the target point in the folded state, the robot unfurls its robotic legs and drops to altitude. Then use the legs to grasp the object and fly away.

5   Conclusion

This paper presented a novel hybrid air-land robot which combines coaxial UAV and quadruped robot. It has 3 movement modes, flying, rolling, crawling and it has the function of grabbing and collision protection. The robot can be used in flight mode when it needs to fly over large obstacles in the factory, or when it needs to quickly reach a target point. Through rolling mode, the robot can move at a faster speed on flat ground or slope, saving energy consumption. When the robot faces rough terrain, it can pass smoothly by legged movement.

In this study, the mechanism of multi-mode robot is designed and analyzed. Based on the overall quality analysis and flight energy consumption modeling of the robot, the flight and crawl combined system's endurance model was established, and then parameters such as size were optimized to obtain the longest endurance time as possible. Finally, the feasibility of each movement form of the robot is simulated and verified through the dynamic simulation software. However, at present, the robot can only switch modes manually, and each mode cannot switch automatically in the face of changing environment.   This will be our future work.

Acknowledgement

References

1. Author, F.: Arti Petti, David, and Herring, J Stephen. Nuclear Energy R&D Imperative 3: Enable a Transition Away from Fossil Fuel in the Transportation and Industrial Sectors. United States: N. p., 2010. Web.
2. Nagatani, Keiji , et al. "Emergency response to the nuclear accident at the Fukushima Daiichi Nuclear Power Plants using mobile rescue robots." Journal of Field Robotics (2012).
3. Heyer, C. "Human-robot interaction and future industrial robotics applications." Intelligent Robots and Systems (IROS), 2010 IEEE/RSJ International Conference on IEEE, 2010.
4. Dong, Pengfei, et al. "Design and control of a tracked robot for search and rescue in nuclear power plant." 2016 International Conference on Advanced Robotics and Mechatronics (ICARM) IEEE, 2016.
5. White, J. , H. Harvey , and K. Farnstrom . "Testing of mobile surveillance robot at a nuclear power plant." IEEE International Conference on Robotics & Automation IEEE, 1987.
6. Kiyoshi, et al. "Development of a radiation-proof robot." Advanced Robotics (2002).
7. Ding, Xilun , et al. "A Review of Aerial Manipulation of Small-scale Rotorcraft Unmanned Robotic Systems." Chinese Journal of Aeronautics 32.01(2018):203-217.
8. Cai, Guowei , J. Dias , and L. Seneviratne . "A Survey of Small-Scale Unmanned Aerial Vehicles: Recent Advances and Future Development Trends." Unmanned Systems 2.02(2014):175-199.
9. Bachmann, By, and R. Joseph. "A hybrid vehicle for aerial and terrestrial locomotion." Dissertations & Theses - Gradworks (2009).
10. Daler, Ludovic, et al. "A Flying Robot with Adaptive Morphology for Multi-Modal Locomotion." 2013 IEEE/RSJ International Conference on Intelligent Robots and Systems IEEE, 2014.
11. Kawasaki, Koji, et al. "MUWA: Multi-field universal wheel for air-land vehicle with quad variable-pitch propellers." (2013).
12. Kalantari, Arash, and M. Spenko. "Design and experimental validation of HyTAQ, a Hybrid Terrestrial and Aerial Quadrotor." Robotics and Automation (ICRA), 2013 IEEE International Conference on IEEE, 2013.
13. Meiri, Nir, and D. Zarrouk. "Flying STAR, a Hybrid Crawling and Flying Sprawl Tuned Robot." 2019 International Conference on Robotics and Automation (ICRA) IEEE, 2019.
14. This Birdlike Robot Uses Thrusters to Float on Two Legs, www.wired.com/story/this-birdlike-robot-uses-thrusters-to-float-on-two-legs/. 2019
15. Mulgaonkar, Yash, et al. "The Flying Monkey: a Mesoscale Robot that can Run, Fly, and Grasp." IEEE International Conference on Robotics & Automation IEEE, 2016.
16. Pratt, Christopher J. , and K. K. Leang . "Dynamic underactuated flying-walking (DUCK) robot." IEEE International Conference on Robotics & Automation IEEE, 2016:3267-3274.
17. Dai J S , Zoppi M , Kong X . Advances in Reconfigurable Mechanisms and Robots I[M]. Springer London, 2012.
18. B. A. Moffitt et al., "Validation of vortex propeller theory for UAV design with uncertainty analysis," in Proc. 46th AIAA Aerosp. Sci. Meeting Exhib., 2008, Art. no. 2008-406.
19. M. P. Merchant and L. S. Miller, "Propeller performance measurement for low Reynolds number UAV applications," in Proc. 44th AIAA Aerosp. Sci. Meeting Exhib., 2006, Art. no. 1127:2006.
20. Shi D, Dai X, Zhang X, et al. A Practical Performance Evaluation Method for Electric Multicopters[J]. IEEE/ASME Transactions on Mechatronics, 2017, 22(3):1337-1348.

Design of vector-thrust propelled legged platform with reconfigurable closed-chain leg mechanisms

Chaoran Wei, Jianxu Wu and Yanan Yao

School of Mechanical, Electronic and Control Engineering, Beijing Jiaotong University, Beijing 100044, PR China
18116023@bjtu.edu.cn, 13116343@bjtu.edu.cn, yayao@bjtu.edu.cn

Abstract. With the increasing research on legged robots, simple walking ability can no longer meet the needs of tasks. In order to reduce the dependence of legged platform on ground frictional force, a vector-thrust propelled closed-chain legged platform (VCLP) with reconfigurable leg mechanism was proposed, and the VCLP can walk in passive motion mode. Considering the demand of mobility, we adopted the reconfigurable approach for trajectory flexibility. The VCLP can accelerate without slipping and surmount obstacles adhesively on a relatively slippery ground. On the basis of kinematics analysis, the reconfigurable design of the leg mechanism was proposed and the adjusted trajectory parameters were analyzed. For the whole platform, the reconfigurable assignments and strategies were analyzed to satisfy the different obstacle-surmounting requirements. The dynamic simulations were performed to testify the walking performance and the passive obstacle-surmounting capability. The research of VCLP improved the ability of accelerating with low friction coefficient, getting rid of muddy ground and climbing extreme obstacles by means of vector thrust propulsion.

Keywords: Vector-thrust propelled, Closed-chain mechanism, Variable topologies.

1 Introduction

At present, legged robots[1–3] have been used in different occasions, such as BigDog [4] and AlphaDog [5] are quadruped robots which can walk in the wild. Bigdog had 16 active joints driven by hydraulic actuators, and it was used in US army for coordinated operations. ANYmal [6, 7] designed by ETH Zurich is an electric-powered quadruped robot with series elastic actuators (SEAs). It was developed to perform work for humans under extreme conditions.

To simplify the drive and control system in a multi-legged arrangement, the closed-chain leg mechanism with comparatively fewer DoFs has shown great potential [8–10]. However, the restrictive influence of fixed foot trajectory on the platform's ability to overcome obstacles cannot be ignored [11]. In order to improve the adaptability of the closed-chain legged platform to terrain, the reconfigurable Theo Jansen linkage [12] and Klann mechanism [13] have effectively improved the trajectory flexibility. A

hexapod robot [14] with the hybrid-driven mechanism performs the turning gait by adjusting the link lengths.

By reconfigurable design of the leg mechanism [15], the ability of overcoming obstacles had been improved. However, when the platform is crossing obstacles or accelerating, it is necessary to ensure that there is sufficient frictional force between the feet and the ground to provide the traction. If the friction coefficient is insufficient, it will cause the foot to slip, making it difficult to continue the task. Inspired by the way of vehicle getting rid of obstacles, when the vehicle is in the mud or climbing a slope with a large angle, the wheel slips frequently and requires thrust traction to get out of trouble. Unlike active movement, if the legged units adopt a passive movement mode (such as wheels) and uses vector thrust as the driving force, the frictional force between the foot and the ground only needs to overcome the joint friction of the leg mechanism.

In this paper, we proposed a VCLP that replaced the torque output of the motor with vector thrust propulsion. To further improve the ability to climb slopes and steps, we designed a closed-chain mechanism with variable topologies structures on the basis of passive motion. The VCLP can adapt to various complex terrains by generating a variety of different foot trajectories.

2 Mechanism design and analysis

2.1 Leg mechanism design

In order to improve the adaptability to the terrain and as much as possible not to increase the inertial force of the leg mechanism, we developed a leg mechanism with reconfigurable trajectory. In a single leg mechanism, six links are included. Among them, there are three two-pair links and three three-pair links. They are all connected by rotating pairs, which is shown in Fig.1.

In the past, the optimized design of the closed-chain leg mechanism tends to increase the height of the swing phase to adapt to different terrains, and increase the straightness of the support phase to improve the walking stability. The VCLP can generate different foot trajectories to cross different obstacles through the reconfigurable design. Therefore, the optimization design of the leg mechanism is focused on increasing the straightness of the support phase when driving on flat ground. Thereby reducing the fluctuation of the center of mass to $\Delta h / l \leq 2\%$. In order to reduce the impact on the ground, the touchdown angle should be reduced to $\varphi \leq 10°$. By using the sequence quadratic program [29], the trajectory parameters with the obtained optimal solutions are: $\Delta h = 4.3$ mm, $l = 335$ mm, $\varphi = 9.1°$ and the straightness of the supporting phase is $\Delta h / l = 1.2\%$, where Δh is the vertical displacement fluctuation, l is the supporting phase length, and φ is the touchdown angle, which is shown in Fig.3.
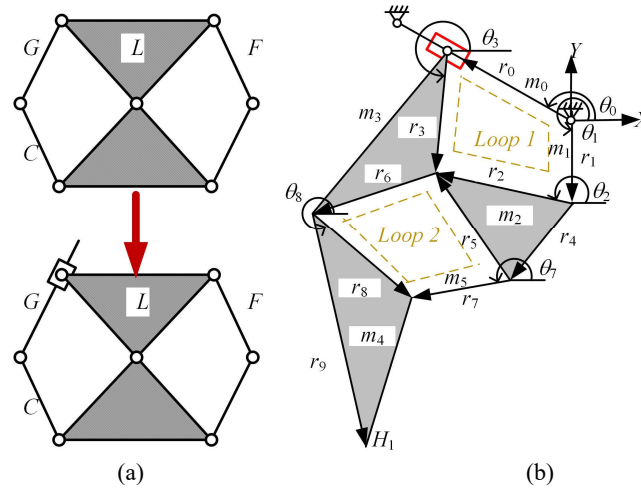
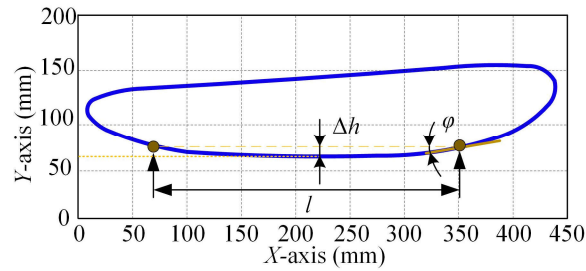Fig. 1. Schematic diagram of leg mechanism.

Fig. 2. Closed-chain foot trajectory.

Affected by fixed geometric dimensions and loops of the closed-chain leg mechanism, the foot trajectory is unchangeable, which makes it difficult to balance the stride length and the height of the leg. Therefore, we develop a reconfigurable design for the closed-chain leg mechanism. Considering that if the size of swing link of leg mechanism is changed, the drive motor for reconfigurable design will be installed on the swing link. As a result, the swing inertia force of the leg mechanism will increase. However, if the size of r_0 is adjustable and the drive motor is arranged on the body, the motor will not swing with the movement of the leg mechanism.

For a single legged unit, the each leg adopts the same leg structure. Therefore, the foot trajectory is the same, and eight legs moves in a phase difference. In a single support period, the foot trajectory can be divided into a support phase and a swing phase. By adjusting the size of r_0, the size can be gradually reduced from 220mm to 140mm as shown in Fig.3. The length of the supporting phase can be reduced from 335mm to 255mm, and the step length is reduced, which is convenient for approaching the obstacle with the split step. The touchdown angle increases from 9.1 degrees to 23 degrees, and the increase of touchdown angle facilitate the foot trajectory to fit the slope.
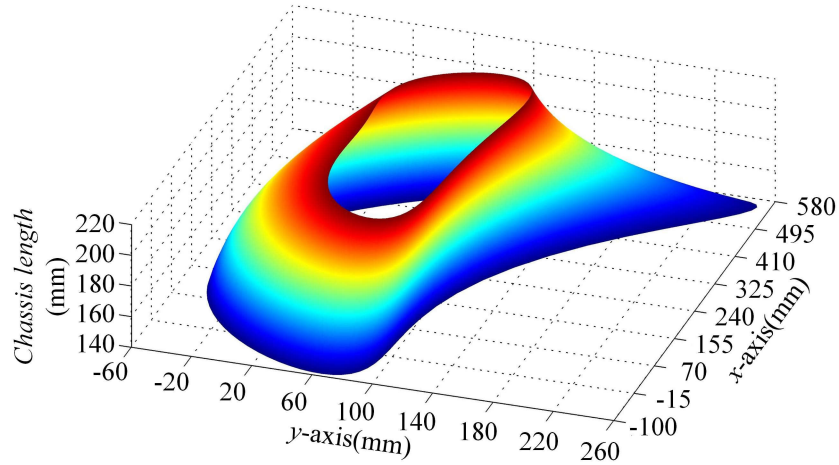
Fig. 3. Reconfigurable foot trajectory.

2.2 The whole platform design

The VCLP was designed based on the closed-chain leg mechanism. In order to realize the passive movement ability without mechanism self-locking, we use the eight legs as a legged unit, and realize the movement by the phase difference of the crank as shown in Fig.4.
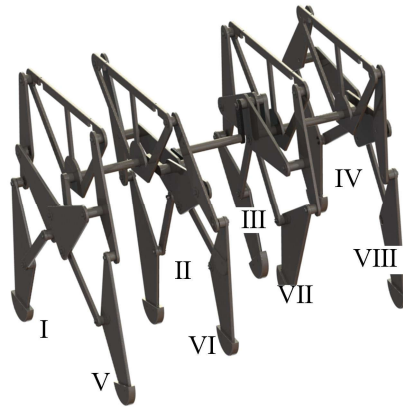
Fig.4. Single legged unit.

As shown in Fig.5, the platform is composed of four legged units, with two turbo-jets as the coupling power source, instead of the form that each legged unit needs to be arranged with a motor. While reducing the weight of the whole platform, the width of a single legged unit has been reduced by 40%. The thrust direction of the turbofan

engine is controlled by a servo, and the range of the angle between thrust direction and chassis is ±20°, so as to achieve the way of vector thrust propulsion.
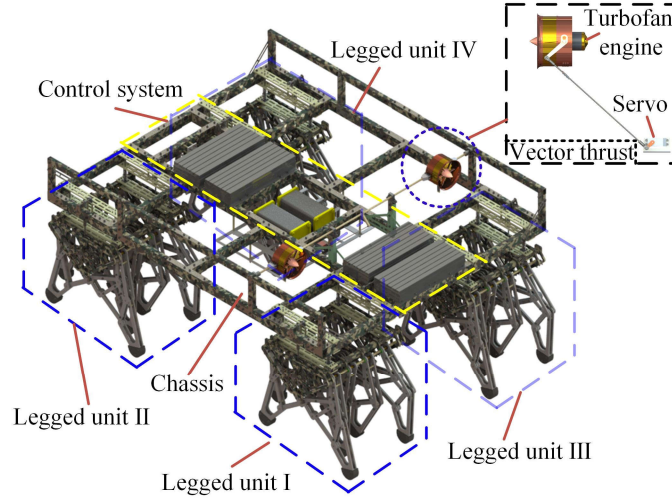
Fig. 5. Layout design of VCLP.

3   Terrain adaptability

The existing active walking of closed-chain legged platforms usually adopt a high torque motor arranged at the crank to realize the walking ability. The ground frictional force not only provides the traction of platform acceleration, but also need to overcome the joint frictional force. The VCLP we proposed can be driven by vector thrust, the ground frictional force is only needed to overcome joint friction, which is shown in Fig.6. Obviously, the platform with vector thrust propulsion is less dependent on the ground friction coefficient (that is, $f_{ai} >> f_{pi}$), in which f_{ai} and f_{pi} represent the frictional force required in active and passive movement mode respectively. Even in some extreme terrain conditions, vector thrust can be used to increase ground friction.

The required ground frictional force in the active motion mode is shown in Eq. (1-6), where a represents the acceleration of the platform and μ_1 represents the friction coefficient at the joint.

$$f_{a1} = (k_1 + k_2 + k_3 + k_4 + k_5)/\sqrt{x_H^2 + y_H^2}) + 32\sum_{i=0}^{5} m_i a \tag{1}$$

The intermediate variables are as follows:

$$k_1 = \mu_1 g(\sum_{i=0}^{1} m_i + m_3)\sqrt{r_1^2 + \frac{4}{9}r_4^2 + \frac{1}{9}r_5^2 + \frac{4}{3}r_1 r_4 \cos(\theta_1 - \theta_4)} \tag{2}$$

6

$$k_2 = \mu_1 g (\sum_{i=0}^{1} m_i + m_3) \sqrt{\frac{2}{3} r_1 r_5 \cos(\theta_1 - \theta_5) + \frac{4}{9} r_4 r_5 \cos(\theta_4 - \theta_5)} \tag{3}$$

$$k_3 = \mu_1 g \sum_{i=0}^{3} m_i \sqrt{r_1^2 + r_4^2 + 2 r_1 r_4 \cos(\theta_1 - \theta_4)} \tag{4}$$

$$k_4 = \mu_1 g (\sum_{i=0}^{3} m_i + m_5) \sqrt{x_H^2 + y_H^2 + \frac{1}{9} r_9^2 + \frac{1}{9} r_8^2} \tag{5}$$

$$k_5 = \mu_1 g (\sum_{i=0}^{3} m_i + m_5) \sqrt{\sum_{i=8}^{9} (-1)^i \frac{2}{3} r_i (x_H \cos\theta_i + y_H \sin\theta_i) - \frac{2}{9} r_8 r_9 \cos(\theta_8 - \theta_9))} \tag{6}$$

When the leg mechanism is walking in passive motion mode, the required ground frictional force is as shown in Eq. (7).

$$f_{p1} = 64 \mu_1 g (m_0 + m_3 + \sum_{i=0}^{1} m_i + 2 \sum_{i=0}^{3} m_i + m_4) \tag{7}$$
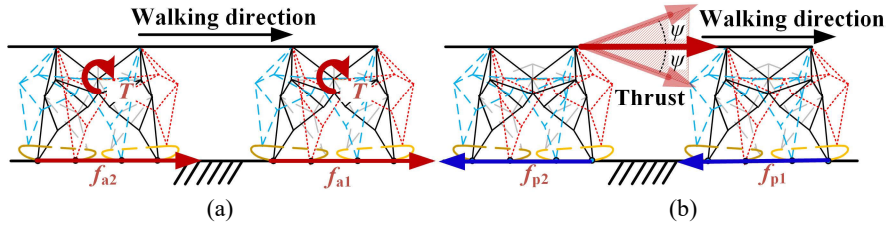
Fig.6. (a) active movement, (b) passive movement
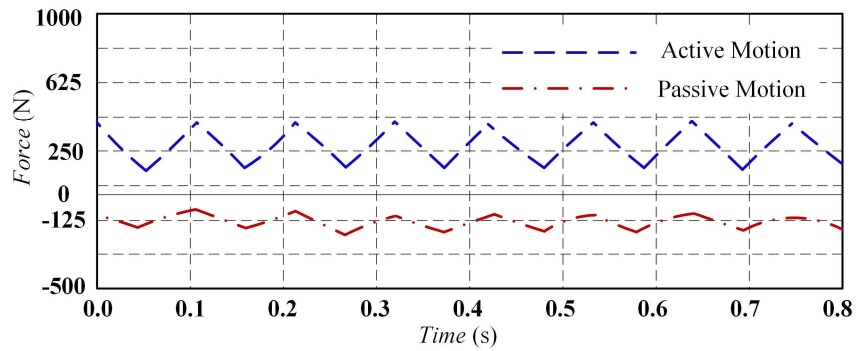
Fig.7. Numerical comparison of ground frictional force

As shown in Fig. 7, when the VCLP is walking at an acceleration of 0.18m/s2, the value of f_{ai} is approximately twice that of f_{pi}. And as the acceleration increases, this ratio will continue to rise. When the VCLP is walking at a constant speed in passive mode, the minimum ground friction coefficient for the VCLP without slipping is 0.098. When the friction is insufficient, the pressure on the ground can be increased by adjusting the direction ψ of the thrust, thereby increasing the friction. In practical applications, when the ground is slippery or soft, the passive movement mode is obviously more suitable. In other words, the walking performance of the VCLP has been improved by the change of contact mechanism between foot and ground.

4   Simulation analysis

As shown in Fig. 8, in order to verify the obstacle-surmounting ability of VCLP, we established a simulation model in Adams^{TM}. The drive motor is no longer arranged at the crank of the leg mechanism, the vector thrust is applied to the chassis and the legged unit moves in passive mode. In terms of climbing slopes, we verify the performance of the platform with a 40° slope. By adjusting the length of r_0 from the initial value of 220mm to 140mm, it can be seen that the platform can overcome obstacles successfully. In the process of passive motion of the platform, the rotation speed and torque of the passive motion crank have been shown in Fig. 9. The rotation speed of the crank fluctuates between 300°/s and 375°/s. At the same time, the torque of the crank was also fluctuates synchronously between 9500N·mm and 10400N·mm.
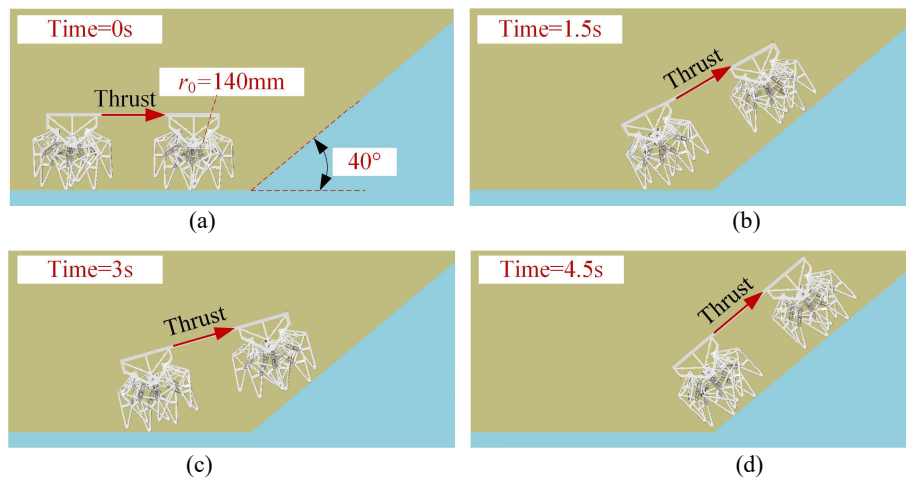
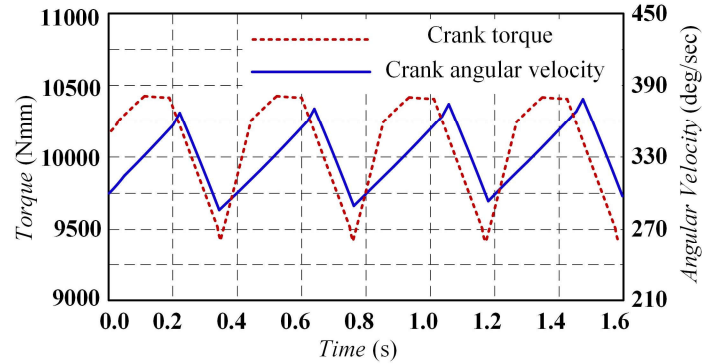Fig.8. Climbing slope simulation.

8

Fig.9. Crank torque and angular velocity.

5 Conclusion

This paper proposes a new type of closed-chain leg platform, which uses vector thrust as the driving force, combined with the design of a variable topology leg mechanism, thereby enhancing the platform's terrain adaptability. The layout of the platform and the configuration of the appropriate power source are introduced. Based on kinematic analysis, the original foot trajectory was obtained and optimized design. Through the variable topology design of the leg mechanism, a series of foot trajectories are obtained. The dependence of the platform on the relatively slippery ground under two different motion modes is analyzed. When the VCLP is walking at an acceleration of 0.18m/s^2, the value of f_{ai} is approximately twice that of f_{pi}. And as the acceleration increases, this ratio will continue to rise. When the VCLP is walking at a constant speed in passive mode, the minimum ground friction coefficient for the VCLP without slipping is 0.098. In the simulation, we verify the performance of the platform with a 40° slope. This verifies the feasibility of the passive obstacle-surmounting mode of the legged platform with vector propulsion and the improvement of platform performance through the design of the variable topology mechanism.

References

1. Tenreiro Machado, J. A., Silva. M.: An overview of legged robots, MME 2006 International symposium on mathematical methods in engineering, 1 (40) 2006.
2. Nansai, S., Rojas, N., Elara, M. R., Sosa, R., Iwase, M.: A novel approach to gait synchronization and transition for reconfigurable walking platforms, Digit. Commun. Net. 1 (2) (2015) 141–151.
3. Wu, J. X., Yao, Y. A., Ruan, Q., Liu, X. P.: Design and optimization of a dual quadruped vehicle based on whole close-chain mechanism, Proc. Inst. Mech. Eng. Part C J. Mech. Eng. Sci. 231 (19) (2017) 3601–3613.

4. Raibert, M., Blankespoor, K., Nelson, G., Playter, R.: BigDog, the rough-terrain quadruped robot. IFAC Proceedings Volumes, 41 (2) 10822–10825 (2008).
5. Raibert, M.: Alphadog, the rough-terrain robot. In: Adaptive Mobile Robotics, pp. 07-07 (2012).
6. Fankhauser, P., Hutter, M.: ANYmal: a unique quadruped robot conquering harsh environments. Research Features, (126) 54-57 (2018).
7. Hwangbo, J., Lee, J., Dosovitskiy, A., et al.: Learning agile and dynamic motor skills for legged robots. Science Robotics, 4(26) (2019).
8. Fedorov, D., and Birglen, L.: Design of a Self-Adaptive Robotic Leg Using a Triggered Compliant Element. IEEE Robotics and Automation Letters, 2(3) 1444–1451 (2017).
9. Birglen, L., Ruella, C.: Analysis and Optimization of One-Degree of Freedom Robotic Legs. Journal of Mechanisms and Robotics, 6(4) 041004 (2014).
10. Shin, S. Y., Deshpande, A. D., Sulzer, J.: Design of a Single Degree-of-Freedom, Adaptable Electromechanical Gait Trainer for People With Neurological Injury. Journal of Mechanisms and Robotics, 10(4) 044503 (2018).
11. Wu, J. X., Yao, Y. A., Li, Y. B., et al.: Design and Analysis of a Sixteen-Legged Vehicle With Reconfigurable Close-Chain Leg Mechanisms. Journal of Mechanisms and Robotics, 11(5) DOI: 10.1115/1.4044003 (2019).
12. Nansai, S., Rojas, N., Elara, M. R., Sosa, R., Iwase, M.: On a Jansen leg with multiple gait patterns for reconfigurable walking platforms. Advances in Mechanical Engineering, 7 (3) doi:10.1177/1687814015573824 (2015).
13. Sheba, J. K., Elara, M., Martínez-García, E., Tan-Phuc, L.: Trajectory generation and stability analysis for reconfigurable klann mechanism based walking robot. Robotics, 5 (3) 13 (2016).
14. Wang, Z. R., Dong, E. B., Xu, M., Yang, J.: Circling turning locomotion of a new multiple closed-chain-legs robot with hybrid-driven mechanism. Advanced Robotics, 29 (24) 1637–1648 (2015).
15. Wu, J. X., Yang, H., Li, R. M., Ruan, Q., Yan, S.Z., Yao, Y. A.: Design and analysis of a novel octopod platform with a reconfigurable trunk. Mechanism and Machine Theory, (156) 104134 (2021).

Reconfigurable Deployable Plane-symmetric Bricard-like Mechanism Based on Angulated Elements

Ran Liu[1], Yan-an Yao[2*], Xilun Ding[1]

[1] School of Mechanical Engineering and Automation, Beihang University, Beijing 100191, China
[2] School of Mechanical, Electronic and Control Engineering, Beijing Jiaotong University, Beijing 100044, China
liuran@buaa.edu.cn

Abstract. This paper presents a novel reconfigurable deployable plane-symmetric Bricard-like mechanism based on four angulated elements (AEs). The reconfigurable AE/dual-AE units are designed by considering layers and sizes of links. Then a reconfigurable plane-symmetric Bricard-like mechanism (RPBM) based on two AE units and one dual-AE unit connected by spatial RRR (R denotes revolute) chains is constructed for the first time. And the RPBM can reach two different transition configurations, through which it can switch between three motion modes, including the prism deployable mode I, the prism deployable mode II and the Bricard turnover mode. Further, two kinds of two-layer prism deployable mechanisms based on RPBMs and spatial RRR chains are constructed. Finally, the multi-layer prism deployable mechanisms based on RPBMs is presented, which shows the potential of RPBM in the construction of reconfigurable/deployable polyhedral mechanisms.

Keywords: Reconfigurable Mechanism, Deployable Mechanism, Plane-symmetric Bricard, Angulated Element, Spatial RRR Chain

1   Introduction

Deployable mechanisms (DMs) have received much attention in applications of architecture and aerospace due to their adaptability to limited space and specific tasks [1, 2]. The design method of DMs based on scissor-like elements was early attempted by Pinero [3] in the design of a movable theatre and then developed by Escrig [4] by taking the link length into consideration. Hoberman [5] modified the straight link into angulated, and constructed Hoberman sphere based on angulated elements (AEs). You and Pellegrino [6] later generalized AEs to construct planar DMs. Kiper et al. [7] proposed a design method for deployable polyhedral mechanisms with AEs based on the principle of Cardan motion. Bai et al. [8] synthesized planar and spatial DMs based on straight elements and AEs. Dai et al. [9] proposed a mobility analysis method for ball DMs with AEs based on mechanism decomposition and screw system analysis.

Besides planar deployable units like AE, spatial overconstrained linkages are also adopted to construct DMs. Since the appearance of the first spatial overconstrained

linkage, a 6R linkage called Sarrus [10], a series of 6R linkages have been discovered and developed. Among them, Bricard is a remarkable one with six various cases [11], including the line-symmetric, the plane-symmetric, the trihedral cases and three mobile octahedra cases. Therefore, DMs based on Bricard linkages are diversity. And Chen et al. [12, 13] investigated the twofold-symmetric and the threefold-symmetric Bricard linkages that can be folded into bundles. Lyu et al. [14] proposed the bundle folding type III Bricard linkage. Guest et al. [15] presented a deployable ring based on the plane-symmetric Bricard linkage. Qi et al. [16] made large DMs based on plane-symmetric Bricard linkages. Planar AEs and spatial single-loop overconstrained linkages each has its own advantages, but few DMs have both functions of these two units.

In order to make DMs more flexible and adaptable, some reconfigurable DMs have emerged. Wei and Dai [17] proposed a group of reconfigurable deployable Platonic mechanisms for the first time with variable revolute (R) joints. Wang and Kong [18] proposed a construction method for multimode deployable polyhedron mechanisms based on spatial single-loop deployable linkages.

In our previous work [19], a family of reconfigurable deployable Bricard-like mechanism of four Bricard cases based on scissor-like elements, AEs and spatial RRR chains was presented. As an extension, we propose a reconfigurable plane-symmetric Bricard-like mechanism (RPBM) with only AEs connected by spatial RRR chains in this paper. It can switch between three motion modes through two transition configurations. And based on RPBMs, the construction of multi-layer prism DMs is introduced.

This paper is organized as follows. Section 2 describes the design of reconfigurable AE and dual-AE units. Section 3 presents a RPBM with AEs connected by spatial RRR chains. Multi-layer prism deployable mechanisms based on RDPMs is constructed in Section 4. Section 5 concludes the paper.

2 Reconfigurable AE/dual-AE units

The AE is a basic planar deployable unit, parameters of which satisfy that $\gamma_1 = \gamma_2 \neq \pi$, $|a_0 o_0| = |b_0 o_0|$, $|d_0 o_0| = |c_0 o_0|$, as shown in Fig. 1. Based on structure features of the AE that contains a couple of unequal diagonal angles, the reconfigurable AE/dual-AE units are developed to be used in reconfigurable mechanisms.
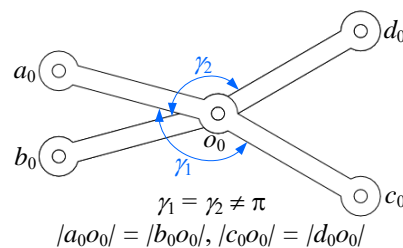

$$\gamma_1 = \gamma_2 \neq \pi$$
$$|a_0 o_0| = |b_0 o_0|, \ |c_0 o_0| = |d_0 o_0|$$

Fig. 1. Diagram of the AE

According to the unequal diagonal angles $\angle a_0 o_0 b_0$ and $\angle d_0 o_0 c_0$ of the AE, a reconfigurable AE unit is designed by dividing the structure into four layers, as shown in Fig.

2. Links A_0J_0, B_0J_0', B_0O_0 and A_0O_0 form a planar prismatic-revolute-revolute-revolute (PRRR) mechanism which can reach two transition configurations. In transition configuration I, as shown in Fig. 2(d), nodes A_0, O_0 and B_0 are collinear, thus node O_0 can rotate inward or outward, as shown in Fig. 2(c) and (f). Similarly, when nodes D_0, O_0 and C_0 are collinear, nodes O_0 can also rotate inward or outward relative to axis D_0C_0, which is denoted as transition configuration I', as shown in Fig. 2(e). In configuration II, as shown in Fig. 2(g), nodes A_0 and B_0 coincide, the PRRR mechanism is degenerated into two rigid bars with a rotation motion, as shown in Fig. 2(h).
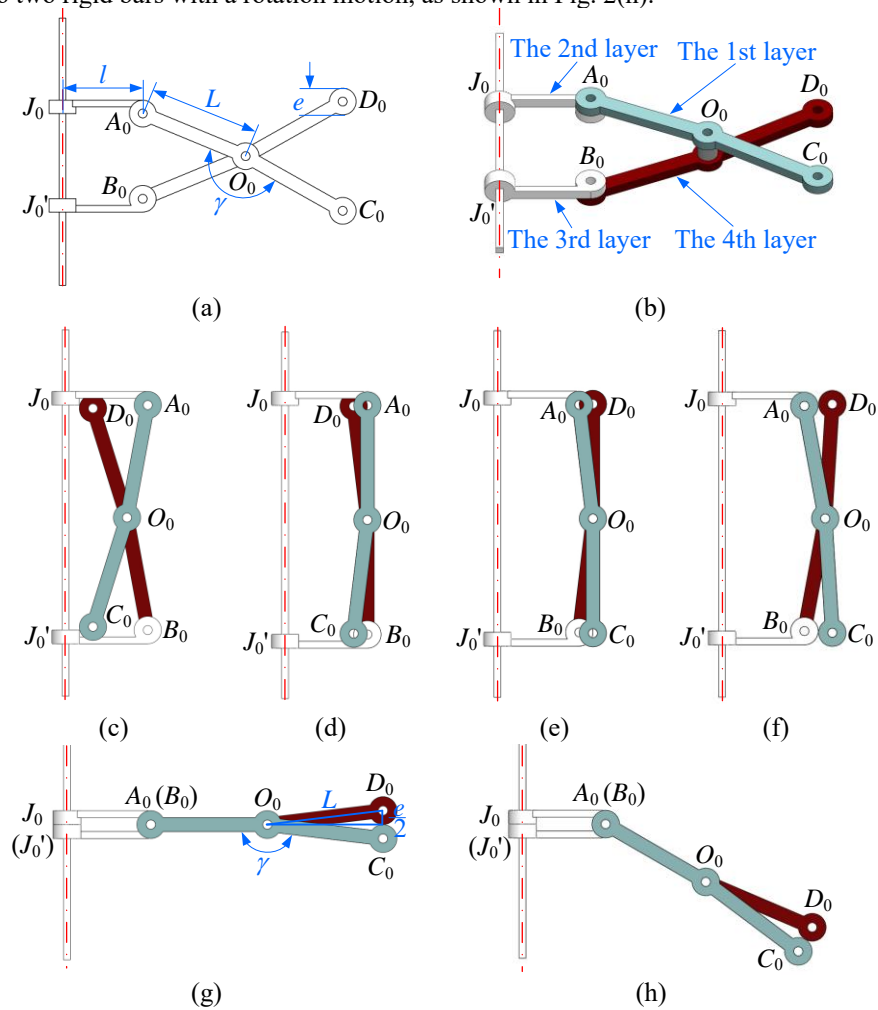
Fig. 2. Reconfigurable AE unit: (a) diagram, (b) structure design, (c) PRRR mode I, (d) transition configuration I, (e) transition configuration I', (f) PRRR mode II, (g) transition configuration II, (h) rotation mode

In all states of the reconfigurable AE unit, the distance from O_0 to J_0J_0' varies by the rotation of R joints at nodes A_0 and B_0, which makes the unit realize the capability of

folding and deploying. The link lengths of the unit are set as $|A_0O_0| = |B_0O_0| = |C_0O_0| = |D_0O_0| = L$, $|A_0J_0| = |B_0J_0'| = l$, the diameter of each node is e, and then the link angle γ is derived as shown in Eq. (1).

$$\gamma = \pi - \arcsin \frac{e}{2L} \tag{1}$$

Based on a pair of symmetrically arranged AEs, a reconfigurable dual-AE unit is built, as shown in Fig. 3. This unit is also constructed with four layers, which provides conditions for the coincidence of nodes A and B to reach the transition configuration, as shown in Figs. 3(b) and (c). When nodes A and B coincide with each other, the dual-AE is also degenerated into two rigid bars connected by a R joint (Fig. 3(d)). And parameters of this unit are consistent with those of the reconfigurable AE unit.

(a)　(b)　(c)　(d)
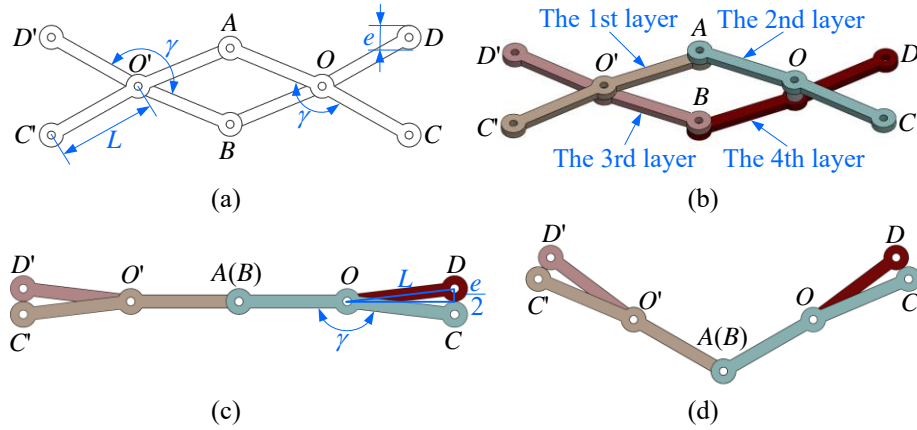
Fig. 3. Reconfigurable dual-AE unit: (a) diagram, (b) scissor-like deployable mode, (c) transition configuration, (d) rotation mode

3　Construction of the RPBM

By connecting two reconfigurable AE units and a reconfigurable dual-AE unit with three groups of two parallel spatial RRR chains, the RPBM is constructed, as shown in Fig. 4. In each spatial RRR chain, two links have the same length that is denoted as l, the first and the third R joints are connected with AE/dual-AE units, while the second R joint is perpendicular to the other two, and it corresponds to the R joint with axis of u_1, u_3 or u_5 of the Bricard linkage, as shown in Fig. 4(b). Then the virtual R joint in the midpoint of A_iB_i ($i = 1, 2, 4$) can be viewed as the R joints with axis of u_2, u_4 or u_6 of the Bricard linkage, and when nodes A_i and B_i coincide, R joints at nodes A_i (B_i) will be the real R joints of the Bricard linkage.

In the RPBM, as shown in Fig. 4, two parallel spatial RRR chains and two AEs connected to them form a Sarrus-like 8R linkage ($A_1J_1A_4O_4B_4J_1'B_1O_1$, $D_1J_2D_2O_2C_2J_2'C_1O_1$, $D_3J_3D_4O_4C_4J_3'C_3O_3$). Dai et al. [20] revealed that this linkage has two DOFs, where one motion is the rotation around axis J_jJ_j' ($j = 1, 2, 3$) and the other

is the translation along axis J_jJ_j'. When A_i and B_i do not coincide, the RPBM is a triangular prism, and $\angle J_j$ ($\angle J_j' = \angle J_j$) is determined by the lengths of J_1J_2, J_2J_3 and J_3J_1, that is the rotation motion around axis J_jJ_j' is determined by the translation motion along axis J_jJ_j', the RPBM has only one DOF. When nodes A_i and B_i coincide, the translation motion along axis J_jJ_j' is lost, and the RPBM degenerates into a Bricard linkage with a single DOF. However, when the reconfigurable AE/dual-AE is in its transition configuration, the RPBM is in the singular position and has two DOFs.
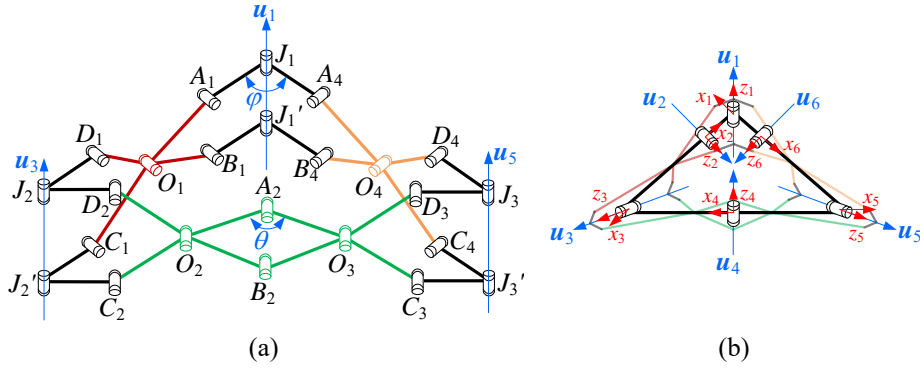
Fig. 4. Diagram of the RPBM: (a) the RPBM. (b) the plane-symmetric Bricard linkage

The coordinate system of links of the Bricard linkage is established, as shown in Fig. 4(b), where z_k (k = 1, 2, 3, 4, 5, 6) is the axis along the kth R joint, x_k is the axis along the common normal direction from axes z_{k-1} to z_k. The D-H parameters are defined as follows: the link length $a_{k(k+1)}$ is the common normal distance from z_k to z_{k+1} along x_{k+1}; the twist $\alpha_{k(k+1)}$ is the rotation angle from z_k to z_{k+1} about x_{k+1}; the offset R_k is the common normal distance from x_k to x_{k+1} along z_k. Link lengths of angulated elements and spatial RRR chains are respectively denoted by L and l. $\angle A_1J_1A_4$ equals to $\angle B_1J_1'B_4$ is denoted by φ, $\angle O_2A_2O_3$ is denoted by θ. Then geometric parameters of the Bricard linkage contained in the Bricard-like mechanism are shown in Eqs. (2) to (4), which satisfy the conditions of the plane-symmetric Bricard linkage with special twist angles.

$$a_{12} = a_{61} = l, a_{23} = a_{34} = a_{45} = a_{56} = l + L\left(\sin\frac{\theta}{2} + \sin\left(\frac{\theta}{2} - \arcsin\frac{e}{2L}\right)\right) \quad (2)$$

$$\alpha_{12} = \alpha_{34} = \alpha_{56} = \frac{\pi}{2}, \alpha_{23} = \alpha_{45} = \alpha_{61} = \frac{3\pi}{2} \quad (3)$$

$$R_1 = R_2 = R_3 = R_4 = R_5 = R_6 = 0 \quad (4)$$

Corresponding to the PRRR mode I, transition configuration I', PRRR mode II, transition configuration II, rotation mode of the reconfiguration AE unit, the RPBM can switch between prism deployable mode I, prism deployable mode II and Bricard turnover mode through two transition configurations.

3.1 Prism deployable mode I

The 3D model of the RPBM in prism deployable mode I is shown in Fig. 5. In this mode, the mechanism has the highest size at the transition configuration I', and the motion transition appears at $\theta = 2\arcsin(e/2L)$. Then through this transition configuration, the mechanism changes to an isosceles triangular prism.
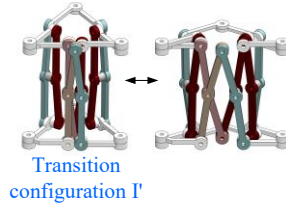

Transition
configuration I'

Fig. 5. Prism deployable mode I of the RPBM

3.2 Prism deployable mode II

In prism deployable II, as shown in Fig. 6, the RPBM stays as a regular triangular prism, and the size of the prism changes as the contraction and deployment of AEs, the height of the mechanism is obtained in Eq. (5). To avoid the link interference, the range of the θ in this mode is limited to $[2\arcsin(e/2L), \pi]$. The mechanism has the highest size in the transition configuration I' as $2L + e$, and when nodes A_i and B_i coincide, the height of the RPBM is contracted to the smallest as $2e$, thus the deployable ratio of the mechanism in this mode is $L/e + 1/2$. Then the mechanism transforms into transition configuration II.

$$h = 2L\cos\left(\frac{\theta}{2} - \arcsin\frac{e}{2L}\right) + e \tag{5}$$

Transition
configuration I'

Transition configuration II
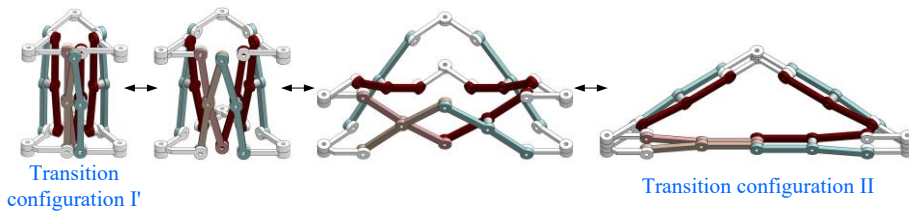
Fig. 6. Prism deployable mode II of the RPBM

3.3 Bricard turnover mode

In the Bricard turnover mode, as shown in Fig. 7, nodes A_i and B_i coincide with each other, each AE of the RPBM degenerated as a rigid bar with the length of $\sqrt{L^2 - e^2/4} + L$. And taking the links of the spatial RRR chain into consideration, the link length of the plane-symmetric Bricard linkage is $a_{12} = a_{61} = l$, $a_{23} = a_{34} = a_{45} = a_{56} = \sqrt{L^2 - e^2/4} + L + l$. In order to avoid the link interference of the RPBM in the turnover

motion, design parameters of the mechanism, including e, l and L, should satisfy the condition in Eq. (6).

$$\frac{e}{L+\sqrt{L^2-\dfrac{e^2}{4}}} < \frac{l}{\sqrt{4\left(L+l+\sqrt{L^2-\dfrac{e^2}{4}}\right)^2-l^2}} \tag{6}$$

The inputs of the rotation angle θ at node $A_2(B_2)$ is described in Fig. 7, and the transition configuration II appears at $\theta = \pi$, $\varphi = 2\arcsin((l + L + \sqrt{L^2-e^2/4})/(2l + L + \sqrt{L^2-e^2/4}))$. From the transition configuration, the RPBM can realize the infinite turnover motion, and the eight positions described in Fig. 7 is only several remarkable positions in a circle of turnover process.
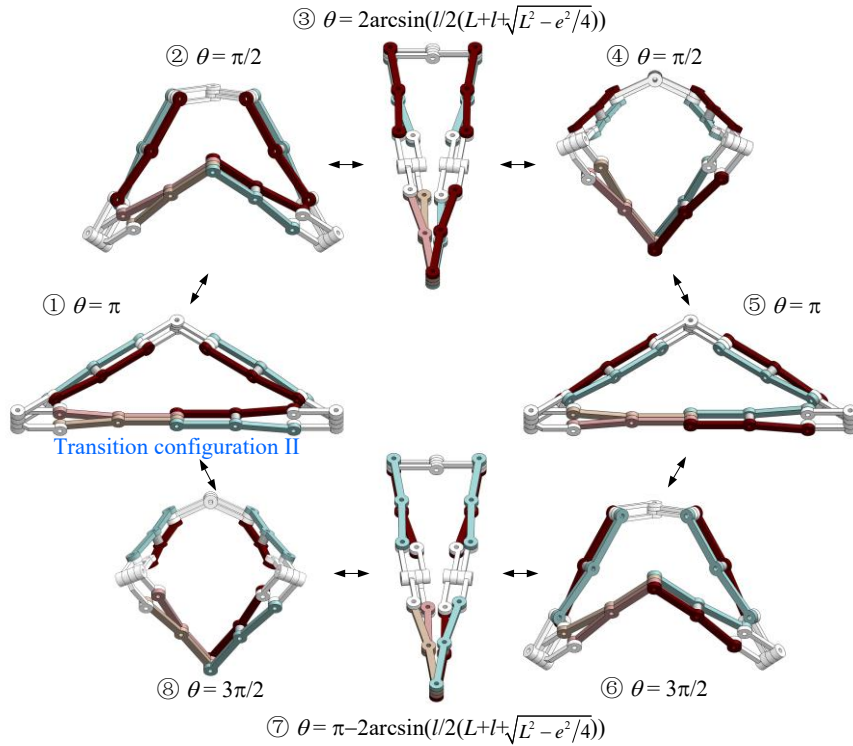
Fig. 7. Bricard turnover mode of the RPBM

4   Multi-layer prism DMs based on RPBMs

The proposed RPBM can also be used as a basic unit to construct DMs. Two identical RPBMs can be connected by three spatial RRR chains, in which the first and the third

R joints are articulated with RPBMs at node A_i or B_i. And there are two construction styles of the two-layer prism DMs, one is to connect the spatial RRR chains to the outmost layer of the AEs of the RPBM, while the other is to the innermost layer of the AEs of the RPBM, which is shown as the first and the last two RPBMs in Fig. 8.

By using the two construction styles of the RPBMs with spatial RRR chains, the multi-layer prism DMs is constructed, as shown in Fig. 8. Based on the three motion modes of the RPBM, the multi-layer prism DMs can realize four motion modes, including the prism deployable mode I, the prism deployable mode II, the Bricard turnover mode I and the Bricard turnover mode II. It can switch between the four motion modes through two transition configurations, and the multi-layer prism DM has a single DOF except for being in transition configurations.

Prism deployable mode I

Bricard turnover mode I

Bricard turnover mode II

Transition configuration II

Prism deployable mode II

Transition configuration I'
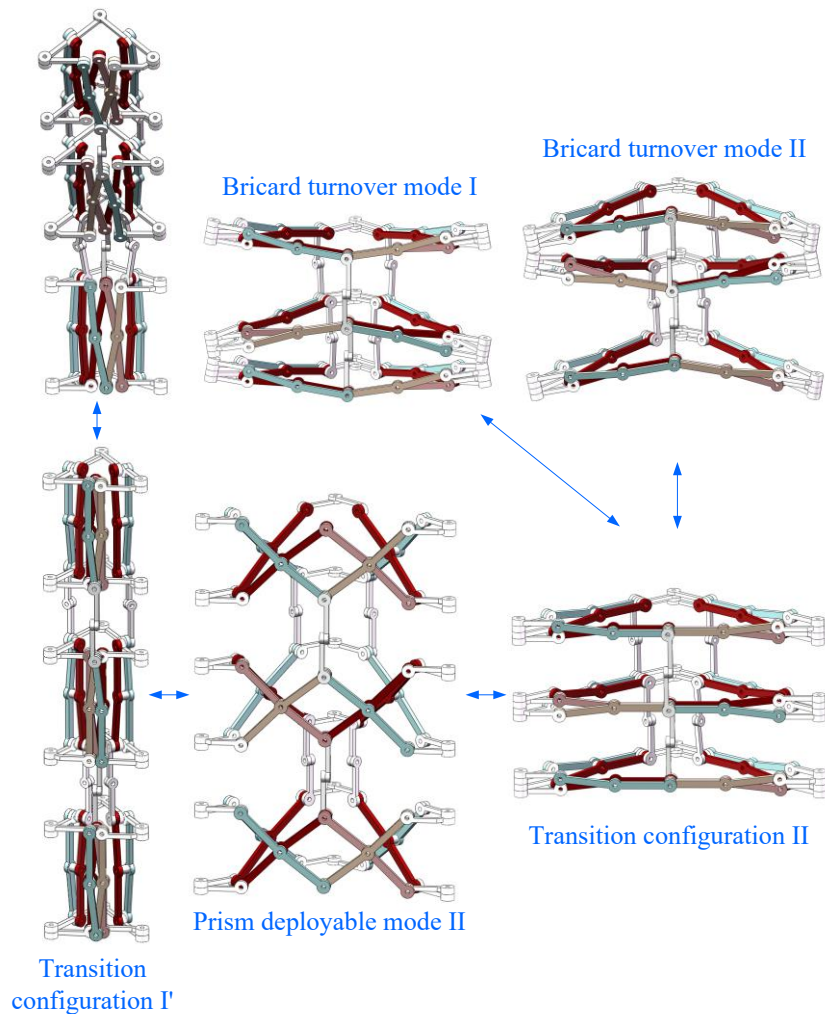
Fig. 8. Multi-layer prism deployable mechanism based on RPBMs

5 Conclusions

A RPBM composed of four AEs is proposed for the first time in this paper. The reconfigurable AE/dual-AE units are designed by considering sizes and layers of links. The obtained RPBM can switch between the prism deployable mode I, the prism deployable mode II and the Bricard turnover mode. Further, the multi-layer prism DMs are constructed based on RPBMs connected by spatial RRR chains, which can switch between four motion modes through two transition configurations. For both the RPBM and prism DMs based on RPBMs, the mechanism is always in a plane-symmetric state during the motion process.

In the future, the proposed RPBM can be used as a unit to construct polyhedral DMs due to its excellent folding performance and diversity motion modes.

References

1. Puig, L., Barton, A., Rando, N.: A review on large deployable structures for astrophysics missions. Acta Astronautica 67, 12–26 (2010).
2. Hanaor, A. Levy, R.: Evaluation of deployable structures for space enclosures. International Journal of Space Structures 16(4), 211–229 (2001).
3. Pinero, E.P.: Project for a mobile theatre. Architectural Design 12(1), 154–155 (1961).
4. Escirg, F.: Expandable space structures. International Journal of Space Structures 1(2), 79–91 (1985).
5. Hoberman, C.: Reversibly expandable doubly-curved truss structure. Patent 4942700, USA, 1990.
6. You, Z., Pellegrino, S.: Foldable bar structures. International Journal of Solids Structures 34(15), 1825–1847 (1997).
7. Kiper, G., Söylemez, E., Kisisel, A.U.Ö.: A family of deployable polygons and polyhedral. Mechanism and Machine Theory 43, 627–640 (2008).
8. Bai, G.C., Liao, Q.Z., Li, D.L., Wei, S.M.: Synthesis of scaling mechanisms for geometric figures with angulated-straight elements. Proceedings of the Institution of Mechanical Engineers Part C-Journal of Mechanical Engineering Science 227 (12), 2795–2809 (2013).
9. Dai, J.S., Li, D.L., Zhang, Q.X., Jin, G.G.: Mobility analysis of a complex structured ball based on mechanism decomposition and equivalent screw system analysis. Mechanism and Machine Theory 39 (4), 445–458 (2004).
10. Sarrus, P.T.: Note sur la transformation des mouvements rectilignes alternatifs, en mouvements circulaires, et reciproquement. Académie des Sciences 36, 1036–1038 (1853).
11. Chen,Y.: Design of structural mechanisms. Doctor of Philosophy Dissertation, University of Oxford, London (2003).
12. Chen, Y., You, Z.: Two-fold symmetrical 6R foldable frame and its bifurcations. International Journal of Solids and Structures 46, 4504–4514 (2009).
13. Chen, Y., You, Z., Tarnai, T.: Threefold-symmetric Bricard linkages for deployable structures. International Journal of Solids and Structures 42, 2287–2301 (2005).
14. Lyu, S.N., Zlatanov, D., Zoppi, M., Ding, X.L., Chirikjian, G.S., Guest, S.D.: Bundle folding type III Bricard linkages. Mechanism and Machine Theory 144, 1–14 (2020).
15. Viquerat, A.D., Hutt, T., Guest, S.D.: A plane symmetric 6R foldable ring. Mechanism and Machine Theory 63, 73-88 (2013).

16. Qi, X.Z., Huang, H.L., Miao, Z.H., Li, B., Deng, Z.Q.: Design and mobility analysis of large deployable mechanisms based on plane-symmetric Bricard linkage. Transactions of the ASME-Journal of Mechanical Design 139 (2), 022302 (2017).
17. Wei, G.W., Dai, J.S.: Reconfigurable and deployable platonic mechanisms with a variable revolute joint. In: Advances in Robot Kinematics, pp. 485–495. Springer, Cham (2014).
18. Wang, J.Y., Kong, X.W.: A novel method for constructing multi-mode deployable polyhe-dron mechanisms using symmetric spatial compositional units. Transactions of the ASME-Journal of Mechanisms and Robotics 11, 020907 (2019).
19. Liu, R., Li, R.M., Yao, Y.A.: Reconfigurable deployable Bricard-like mechanism with an-gulated elements. Mechanism and Machine Theory 152, 103917 (2020).
20. Tang, Z., Qi, P., Dai, J.: Mechanism design of a biomimetic quadruped robot. Industrial Robot: An International Journal 44 (4), 512–520 (2019).

Cobots for Covid: Modular Robot Design for Human Safety with Regard to Evolving Pandemics Phases

Jonathan Heidegger[1], Byung Wook Kim[1], Haoguang Yang[1], Mythra V. Balakuntala[1], Abigayle E. Moser[1,3], Shijie Zhu[2], Qizhong Li[2], Ali Doosttalab[1], Jhon J. Quiñones[1], Antonio Esquivel-Puentes[1], Tanya Purwar[1], Yu Chen[2], Hanyu Liu[2], Gangtie Zheng[2], Robin R. Murphy[5], Victor M. Castaño[4], Luciano Castillo[1], Nina Mahmoudian[1], and Richard M. Voyles[1]

[1] Purdue University, West Lafayette, IN 47907, USA,
{jheidegg, kim2986, yang1510, mbalakun, rvoyles}@purdue.edu
[2] Tsinghua University, Beijing 100084, China
[3] Iowa State University, Ames, IA 50011, USA
[4] Universidad Nacional Autonoma de Mexico, Coyoacan, 04510 Mexico City, Mexico
[5] Texas A&M University, College Station, TX 77843, USA

Abstract. This paper discusses the application of a modular collaborative robot designed to aid in the fight against COVID-19 in increasing safety for essential workers and students. We identify three main phases of a pandemic in onset, quarantine, and reopening which affect the demands and requirements placed on robots. The international team proposed a series of robotic modules that were deployed in hospitals, quarantine facilities, and classrooms, to be a telepresence for doctors, disinfects surfaces with UVC, disinfects air with a novel Bernoulli filter design, respectively. From these deployments we propose key benefits to a modular approach when designing robots for the current pandemic and future emergency responses.

1 Introduction

During the Ebola outbreak of 2014, robots were proposed as a logical technology for reducing risk to human caregivers. Despite the efforts of co-authors Voyles and Murphy and the White House Office of Science and Technology Policy [7][2], few thought robots were ready. Six years later, with the appearance of COVID-19, robots have blossomed onto the scene as a viable solution in many countries to protect humans from the spread of pandemic disease [20][25]. Throughout the COVID-19 pandemic, more than 200 different robots have been deployed for human safety [21] in every aspects, from the in-take of patients at emergency rooms to the monitoring of social distancing [27].

However, as the pandemic has progressed through three distinct phases we have identified: surge phase, quarantine phase, and re-opening phase, the needs for human protection have evolved, as well as the businesses and human populations most affected. The clinical, logistics, and educational sectors have all been

impacted by the phases of the COVID-19 pandemic [25]. In nearly every country, hospital workers were an obvious front-line concern as patient loads surged with the spread of the virus [26]. Robots became headline news [1] by enabling physical separation between sick people and vulnerable healthcare workers through remote teleoperation [27]. But as governments and societies practice quarantine policies, the term "essential workers" has generalized to include relatively low-paid cashiers and delivery personnel [22]. These workers, during the quarantine phase, were more numerous, harder to protect, with social contact with other people inevitable. Keeping a safe indoor environment for human interaction thus become top priority [18], where disinfection robots are involved [24][28]. Finally, the re-opening phase is characterized by enticing customers to return to businesses to help re-open the local economy. With the "essential worker" concept fading as the economy and social interaction revive, robots are required to work with non-worker humans around, which necessitates the adoption of "collaborative robots" (cobots) [12]. Specifically, education at both the university and K-12 levels became a hot-button topic [18] during the re-opening phase in the U.S.. Despite low levels of infections and symptoms among school-age children and teenagers, many students were reluctant to return to school. In light of this, we consider the education sector as a high-impact opportunity to address human-safe cleaning robots.

To be sure, these phases are not necessarily sequential nor are they orderly. Many regions experienced recurring and oscillating phases and thus shifts in needs. This shift in workplace needs has been a key obstacle to pandemic robot adoption. At Purdue, with clear need for the disinfection of empty rooms at the Purdue Village Quarantine Facility and full rooms of students – albeit, socially-distanced – in classes, a modular solution was preferred to spread development effort. As the main force in response to the pandemic shifts from hospitals to essential businesses, and further to schools and communities, the potential applications of robots increase [20]. While these robots service each fragmented application segments, they unveil critical challenges in keeping up with the shifting requirements during sporadic public safety events [17], [19]. Specifically, we deduced three main challenges from literature as:

1. Lack of cost and effort efficiency. The effectiveness of deployed robots in contrast to the cost and effort invested is low;
2. Lack of robot's adaptability to evolving situations and changing demands;
3. Lack of robot's readiness for similar future emergencies.

A potential solution to overcoming these challenges is to make robots modular. When responding to evolving low-incidence high-consequence events, such as the COVID-19 pandemic, modular robots are favored over application-specific robots due to their expansible capabilities - gained by swapping the functional modules [6]. This in turn presents advantages in operator familiarity, confidence in the systems, and reduced time and cost for emergency response [19], [9].

In response to the COVID-19 pandemic, our modular development and deployment of robots provide multi-modal services and unveil two key findings on modularity. Firstly, modularity reduces the effort to develop and deploy robots,

thereby allowing robots to fight a pandemic in the early stages and the following phases. Secondly, modularity decreases the cost needed to develop a robot that can adapt to requirements and demands to increase worker safety throughout all three phases of the pandemic.

2 Hardware Components

Our proposed modular design of the robot for COVID-19 response consists of five parts: a common omnidirectional mobile base, a Ultraviolet band-C (UVC) light disinfection module, an air filtration module, a medical care package, and a disinfectant spraying module, as shown in Fig. 1. The modules are added modularly onto the base to achieve multimodal disinfection and services, driven by specific application requirements. Specifically, the UVC and disinfectant spray apply to surface disinfection without occupants, and the Bernoulli air filtration module disinfects the indoor air to block transmission between occupants at their presence. In addition to the generic disinfection services, this robotic system is capable of hosting a medical care package that is speciallized to clinical care of the COVID-19 patients in quarantine. The dual-use of the robotic system circumvents rebuilding the entire robot for every specific scenarios, thus reduces the effort and cost of deployment and improves user familiarity.
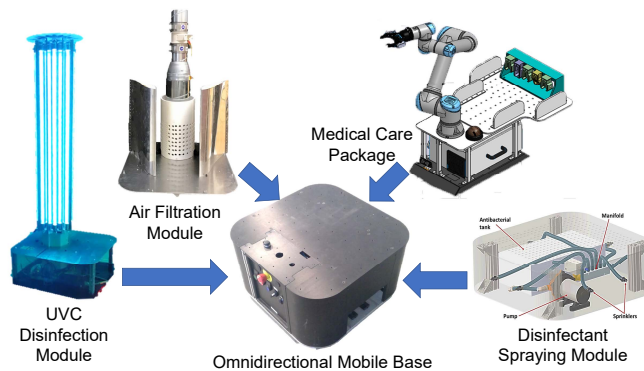
Fig. 1.   Functional modules of the robot in response to the COVID-19 pandemics.

2.1 Holonomic Base as the Foundation of Mobility

For maneuvering the disinfection payloads, the robot consists of a common omnidirectional holonomic base with 4 powered caster wheels driven by 8 motors. The robotic base uses odometer and LiDAR sensors to support autonomous map navigation and dynamic obstacle avoidance in Robot Operating System (ROS) [28]. An operational space controller [13] overcomes overactuation, generating desired motion of the robot with decoupled three degrees of freedom,

and outputs wheel odometry as a byproduct. This foundation lowers constraints on path planning for modular designs such as a directional air filtration unit, or the direction agnostic UVC module. The choice to use the holonomic base which were already in use in other non-COVID projects, allowed for software and hardware to be developed modularly from a known interface and experience during the surge phase of the pandemic. The uniform software and hardware of the robotic system between different disinfection and operation types, enabled faster deployments thanks to the operator familiarity with the modules.

2.2   Bernoulli Air Filtration Module

When dealing with the reopening phase of the pandemic robotic solutions were looked for to aid in the protection of environments with people actively working or learning. The Bernoulli Air Filtration Module [28] is designed to reduce the number of Infections Bioaerosol droplets which range from 0.1 to 10 μm in diameter, which can suspend in air for hours, pose a major threat for horizontal transmission through inhalation when reopening. The Bernoulli module employs a novel design of air filtration system to increase the effectiveness of indoor air filtration when used with a mobile robot. The Bernoulli air filtration module brings medical-grade air treatment—a combination of particle filtration (a High Efficiency Particulate Air (HEPA) filter) and internal UV disinfection—to public indoor spaces, aiming to inactivate infectious bioaerosol droplets. Since the disinfection component is shielded and does not pose irritation to occupants, the module is suitable for disinfecting occupied indoor space, where transmission through air is a significant risk such as in classrooms and offices.

The filtration efficiency of the module, measured in percentage of the captured particles, is higher than 99.3% for particles larger than 0.3 μm, with capacity of 2.5 m^3/minute air. The flow tract design of the Bernoulli module, i.e. the AeroMINE™(Motionless, INtegrated Extraction) technology, originates from wind energy applications [14]. The filter design features low turbulance and large swept air volume to trap contaminants, facilitated by the motion of the filter when carried by the holonomic base. Using a pair of mirrored perforated airfoils and a perforated cylindrical tower, a low pressure zone is created between the airfoils which helps to drive the surrounding air into the intake of the system. The air is then driven by an axial fan in the cylinder through the HEPA filter, thus achieves high flow rate and efficiency, low turbulance air filtration.

2.3   UVC Disinfection Module

As infectious droplets are emitted by virus carriers, they start to precipitate onto surfaces, which causes surface contamination and therefore poses risk of community spread. As a result, regular surface disinfection is required by pandemic prevention regulations, which calls for a direct method of killing the pathogen on surfaces. The UVC with wavelength of 254 nm is proven to be germicidal [16], and has been applied in hospitals. However, UVC is also harmful for humans under direct exposure [10], which necessitates the automation of unattended

UVC disinfection process through robots. The proposed UVC disinfection module consists of eight mercury vapor bulbs installed on a tower for illuminating the surrounding walls and floors, 360 degrees around. A stop-and-move scheme is adopted for the robot, to apply illumination dosage more uniformly around the target facility. The surface dosage at a certain indoor spot is thus achieved based on the location of each stopping location of the robot and their corresponding dwell times, as illustrated in Section 3.1.

2.4   Disinfectant Spraying Module

Spraying disinfectants is a hospital-proven measure of epidemic prevention [23]. However, since it is a labor-intensive job performed by staffs, and disinfectants usually cause some form of irritation to human body, and the contaminated surfaces poses risks of infections, the staffs are exposed to two-fold hazard risks without extensive protection. We therefore propose a novel nanoparticle disinfectant solution and micro-spray system that, when combined with an autonomous mobile robotic base, can run either pre-scheduled or teleoperated.

The module features a three gallon tank containing antimicrobial solution. The nozzles system features a diaphragm pump connected to a manifold to split the flow into several nozzles, to produce a disinfectant cone-shaped mist with an average droplets size of $\sim 50\,\mu$m. The micro-droplet cloud from the nozzle can cover a radius of up to $2.25\,$m in the surrounding area of the robot. To enhance coverage in corners and hard-to-reach areas, an Electrostatic Spray Deposition (ESD) unit is also added.

2.5   Medical Care Module

The medical care module consists of a Universal Robots UR5 arm and a suite of tools for assessing the health of patients. The considered health assessment tasks of the medical care module are taking body temperature, operating the stethoscope, and ultrasound diagnosis, since they cover the common symptoms used in infection screening (fever, coughing, etc.), and provides valuable observations of the patient's organs. As a result, an infrared thermometer, a electronic stethoscope, and an ultrasound probe are included as end-effector tools of the robotic arm. The tools are mounted on 3D-printed adapters to suit the grabbing gesture of the gripper on the robotic arm, and stored in a toolbox for on-demand access of the arm. The module is also equipped with a speaker and microphone for two-way audio communication.

The tools, when attached to the robotic arm, are associated with their different interaction dynamics. The temperature taking task is contact-free, therefore a visual-servoing approach is adopted to pinpoint the tool with respect to the face of the patient. The stethoscope involves point-wise contact to the patient, while the ultrasound probe involves contact with sliding and gimbaling. Both the stethoscope and ultrasonic examinations require a certain amount of contact force between the probe and the skin of the patient, considering the reception

quality. To accomplish this while ensuring patient safety, a contact force controller is developed to relieve operator burden and prevent patient discomfort. The controller limits the normal force applied at the probe, through measurements from the wrist force sensor on the robotic arm.

3   Software Components

In support the the modules there is also extensive work to develop modular software to meet the demands of the rapidly changing pandemic. The robots share software and with module specific software developed in individual software tasks subroutines. Unifying the modules is the teleoperation modules which must work with the robot base and provide users access to module specific functions.

3.1   Planning objectives of the UVC module

When determining the desired path for the UVC equipped robots we employ simulations to verify the paths effectiveness and plan more optimal paths. The UCV disinfection paths are simulated in Matlab using a ray casting approach to determine sample points on the map to accumulate UVC dosage. This dosage was calculated based on dwell time and UVC power at different distances, which is a 2D simplification of the method discussed in [8]. We gathered experimental data from 8 different points ranging from 10cm to 120cm to produce a exponential function, as shown in Fig. 2(a) to inform UVC lamp dosage. As a reference, surface dosages over 50mJ/cm2 is shown to effectively kill the SARS-CoV-2 virus [5].

Once a path has been verified in Matlab a combination of a UVC Dosimeter and UVC dosage stickers are used to corroborate the simulation. This simulation is limited to 2-D due to two considerations. Firstly, the UVC bulbs are fixed vertically to a tall tower, which promotes uniform exposure on all vertical surfaces. Secondly, the simplicity of 2-D estimates vastly increases the speed of deployment to verify paths without having to expend on site time to test paths which average an hour to complete per path.

3.2   Planning objectives of the Bernoulli Air Filtration Module

A similar approach is being considered with the air filtration robot with applying experimentally gathered particle count data with Computational Fluid Dynamics (CFD) analysis done of a classroom to identify hot spots for the robot to clean. We assume identical spreading pattern of the infectious bioaerosol emitted from each individual occupant. The individual spreading pattern is computed using CFD with a simulated mouth and airflow speed and droplet diameter profile of a cough obtained from [11]. Upon a room with multiple occupants, the spreading of bioaerosol particles from each individual is superimposed as a simplification to circumvent computational-intensive calculation of the CFD, which is infeasible for on-site evaluation. Then, a modified convection-diffusion model [28] is

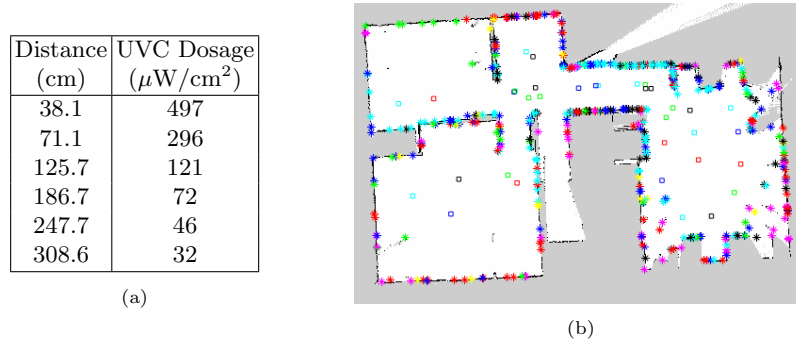| Distance | UVC Dosage |
(cm)	(μW/cm^2)
38.1	497
71.1	296
125.7	121
186.7	72
247.7	46
308.6	32

(a)

(b)

Fig. 2.   (a) UVC dosage measured at various distances and same height level from the module. (b) A result of a simulated UVC disinfection where stars are representative of accumulation points and squares are the robot path points. Accumulation points are color coded based on UVC dosage (Red: <45, Yellow: <50, Green: <60, black: <100, cyan: >100. Unit: mJ/cm^2).

applied to estimate the effect of the air filter on the spread of the particles. The path of the robot during the air filtration task is parameterized by the frontal passing distance and speed of the robot in front of each occupant. The parameters are optimized based on the simulation result to minimize the cumulative particle weights inhaled by each occupant, should one of their neighbors cough.

3.3   Unified Teleoperation User Interface

Although the robot involves certain degree of autonomy in navigation and motion planning, the versatile nature of application scenarios means that a one-fits-all solution does not exist. To move the robot around reliably in all scenarios of interest, a teleoperation interface is thus required for when full autonomous navigation is not well suited such as in unstructured environments. To enhance operator familiarity, the teleoperation interface adopts unified, intuitive, and user-friendly input devices, consisting of a 3-DoF joystick and an optional 6-DoF space mouse. The planar motion of the robotic base is directly controlled by the 3-DoF joystick, while the robotic arm of the medical care module can be controlled by either the joystick (by remapping) or the space mouse, depending on the user preference. Visual feedback is the most intuitive approach to notify the operator about the surroundings of and troubles encountered by the robot. As a result, a frontal chassis camera is set on the robotic base, and an eye-in-hand camera is embedded on the robotic arm facing the gripper (on the medical care module) for the operator to gain situational awareness and monitor robot motion.

Concerning operator workload, network latency and bandwidth limits, the teleoperation approach is an augmentation, rather than substitution, of the existing autonomy. While teleoperation is required for contact-based medical tasks such as ultrasound and stethoscope operations, it is an on-demand component

that augments other automated tasks the robot is capable of. For instance, the robot may need human assistance to recover itself when navigating in confined door thresholds or classrooms, which the on-board path planner is not well optimized for. Given that the robot can still achieve autonomous navigation except in scattered edge cases, a small effort in teleoperation as error correction can widely expand the applicability of the robot.

To make the robot learn from these error correction events, such that human intervention can be further reduced, a model-free learning from demonstration (LFD) framework is proposed [3]. The framework eliminates explicit reward engineering by inferring the reward from the goal states collected from expert demonstrations of the skill. Robot states from the demonstration are extracted to correlate with the success/fail result of the teleoperation. The extracted states are then used to train a classifier which ultimately represents the reward. To accelerate the learning process such that fewer demonstrations are needed before the model converges, a one-shot learning scheme is adopted with further corrections made through coaching. Using a decision tree classifier, the demonstration is semantically segmented into a sequence of actions the robot can perform (via points in this case). The skill parameters are then updated using a self evaluator based on the execution performance to ultimately improve the task performance, thereby locally optimizing cumulative performance [4]. As a result, the LFD framework allows the modular robot to learn ways to overcome unexpected situations from few demonstrations.

3.4   Fleet management

To manage the fleet of robots and monitor their running status, the robot statuses are uploaded onto a centralized database. Each robot transmit four types of information – telemetry, base navigation, motor status, and payload status. These information helps assistance team assess the health status of the robot and determine if maintenance is required. To ease up the inspection of these data, an IoT web dashboard is created using Grafana software. The dashboard provides graphical interface of the historical data that each robot transmitted and sends out alerts through web-hooks when values are abnormal.

4   Deployments and Experiments

To validate the individual modules and the integration of modules, a series of deployments were done in a variety of settings in both the quarantine and reopening phase. Through these deployments, data is gathered to measure the efficacy of individual modules and to gain key insights to improve designs for the future.

4.1   Medical Care Package at Beijing and Wuhan hospitals

To prove the effectiveness of the medical care module, experiments were conducted in hospitals in Wuhan Union Hospital and Beijing Ditan Hospital, as

shown in Fig. 3. These locations were overwhelmed with SARS-CoV-2 patients during the surge and quarantine phases. The robot assisted the doctor in diagnosing patients with the help of an on-site nurse. Using our system, the doctor can chat with the patient as well as see the real-time result of the ultrasound examination remotely. The real-time sound of the patient breathing was picked up by the electrical stethoscope and transmitted to the the doctor. The digitized data was recorded by the doctor for future analysis.
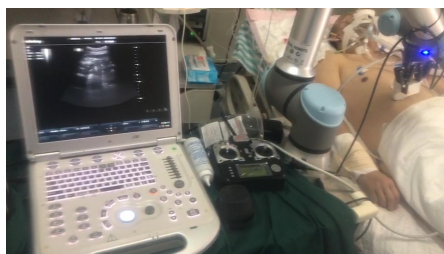
Fig. 3.   The Medical Care Module during a trial in Beijing Ditan hospital. The robot was performing ultrasound diagnosis through augmented teleoperation. The monitor is set up for the assistant nurse, who applies the ultrasound gel, and takes over the robot with a radio control in case of emergency.

A survey was distributed to physicians that participated in the training for robot operation and medical trials, and four valid responses were collected. The survey features subjective evaluations that compares the users' experience with the robot as a telepresence device versus the absence of the robot. The survey evaluates the benefits of the robot when using different input devices for different functions or purposes. The result of the survey is averaged and summarized in Table 1. According to the survey, despite the unified input interface for teleoperation, the operator familiarity and user experience is still negatively related to the complexity of the task. Although the robot physically separates the medical staff from the patients, the ease of use of the robot still needs to be improved.

4.2   UVC module at the Purdue Quarantine Facility

The UVC module has been tested in the quarantine facility at Purdue University. Using the simulations outlined in 3.1 a disinfection path was chosen that complied with reachability and necessary dosage. The paths were verified within the quarantine facility using a combination of an electronic UVC dosimeter and UVC Dosage cards to verify a minimum dosage of 50 mJ/cm2. to corroborate the data collected a deployment with T1 Phage samples placed throughout the room was conducted in a method similar to [15]. With 4 test sites and a control kept in full occlusion we were able to demonstrate an effective cleaning of the room. We can see that in 2 there is an approximately 3 log reduction in phage concentration even in challenging locations with complex shadows such as a gap

Table 1.   Result of the survey on user experience with the robot with medical care module. Items are scored on a 0 − 100 scale, where 0 stands for poor/totally disagree, and 100 stands for good/totally agree.

Items		Scores
Robot ease of control	robotic arm	67.25
	mobile platform	63.25
Human-machine interface	3DoF joystick	56
	6DoF space mouse	53.75
Likelihood of using the robot compared to in-person operation	temperature taking	88
	stethoscope	79.5
	ultrasound	54.25
Reasons contributing to the use of robots	remote operation	91
	improved efficiency	54
	better patient experience	46.75

between the fridge and cabinets (Location 3). The robotic disinfection is effective and takes less time than static UVC that has been used before [16].

Table 2.   Testing UVC illumination effectiveness with T1 phage in culturing broth. Two drops of $5\mu L$ T1 broth are placed on a microscope slide cover at each location. After irradiation, place the cover glass into 10 mL tryptic soy broth (TSB) for virus extraction. Log reduction is calculated via a comparison to the control.

Sample	Concentration (PFU/mL)	Log Reduction	UVC Dosimeter Card Reading (mJ/cm^2)
Onsite control	5.12E+06		
Location 1	1.42E+02	-4.56	128.38
Location 2	1.26E+03	-3.61	132
Location 3	1.04E+04	-2.69	73.53
Location 4	5.22E+02	-3.99	109.53

The actual position of the robot during the UVC disinfection run is recorded in the database, which is later retrieved for validation of the actual dosage. The verification uses the same dosage estimation software as shown in Fig. 2(b), which reveals the underexposure locations due to variations in localization and obstacle positions. The indication of underexposure will guide janitorial staffs for the follow-up spot-cleaning.

4.3   Bernoulli Air Filtration module in Purdue Classrooms

To explore the effectiveness of the Bernoulli robot, experiments within a real classroom setting is carried out as shown in Fig. 4. The purpose of the experiment is to show that (a) airborne particles created by human activities are local to the people's locations, and (b) the motion of the robot does not excite excessive amount of sedimented particles (such that the combination of robotic base with

the air filtration module yields net decrease of airborne particles). As a result, the robot is set to move in a serpentine pattern that passes in front of every occupant as suggested in [28]. Two particle counters (VPC300) are placed on the robot to measure the particle concentration around the robot and its spatial
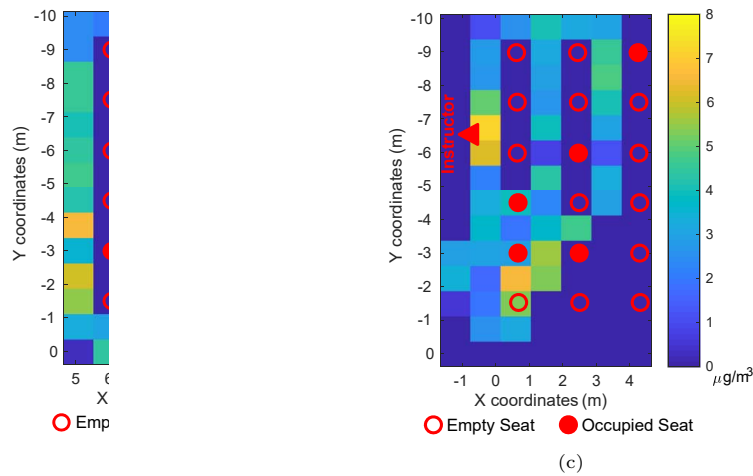

Fig. 4.   (a) Testing the robot with air filtration module in a classroom. (b) Particle concentration map with air filtration off. (c) Particle concentration map with air filtration on.

The measurements from the particle counter are labeled with time, which is correlated with the localization logging of the robot stored on the database. The dosage measurement at discrete locations are then cast and averaged on a grid division of the working area, such that the size of a grid roughly equals to the distance traveled of the robot during a sampling window. Since a larger particle has the capacity of carrying more contaminant, the particle counts at each diameter channel are weighted by their volumes and summed together. The density of the particles are assumed to be the density of water, which yields

the measuring unit of particle concentration being $\mu g/m^3$. The concentration map of the two experiments are shown in Fig. 4b, c. From the concentration map, whether a seat is occupied strongly correlates ($p = 0.003$) with the particle count nearby, which indicates that the airborne particles created by human activities has locality as long as the occupants remain stationary. By comparing the particle counts without and with air filtration, the maximum particle count (grid-averaged) has reduced from $27.01\,\mu g/m^3$ to $12.75\,\mu g/m^3$, while the time-averaged particle count has reduced from $3.66\,\mu g/m^3$ to $3.47\,\mu g/m^3$. This result confirms the effectiveness of the module.

5   Conclusion

During this pandemic we have seen the effects of increased robotic deployment towards the COVID-19 crisis. As the pandemic evolved, different industries made unique demands and induced application-specific robots to be developed. However, the deployed robots - designed for a single purpose - face several limitations such as lacking efficiency, adaptability and future readiness. We address the inefficiency and inflexibility issues by introducing modularity, thereby allowing a single robot to have several different purposes and functions instead of one. The modular robot we developed works by attaching and detaching "modules" from a universal mobile base depending on the task the robot has to complete. From ultrasound and stethoscope measurements to UVC disinfection and air filtration, our modular robot can execute risky tasks without endangering the lives of workers. We evaluated the overall performance for a variety of settings when each module is attached to the uniform navigation base. The successful navigation of the robot using a single mobile base and a unified software illustrates the effort efficient manner of our approach. For every different module test, we didn't have to completely reprogram the robot. In addition, results of the individual module experiments show the effectiveness of task execution. Notably, the air filtration module reduced maximum particle count from $27.01\,\mu g/m^3$ to $12.75\,\mu g/m^3$. In the future, this framework can be extended to incorporate more complex procedures and implement learning from demonstration frameworks, ultimately providing the robot with more flexibility and increased semi-operability.

6   Acknowledgements

References

1. 10 ways robots fight against the covid-19 pandemic (2020). URL `https://www.eu-robotics.net/eurobotics/newsroom/press/robots-against-covid-19.html`

2. Ackerman, E.: Real robots to help fight ebola. IEEE Spectrum (2014). URL https://spectrum.ieee.org/automaton/robotics/medical-robots/real-robots-to-help-fight-ebola

3. Balakuntala, M.V., Kaur, U., Ma, X., Wachs, J., Voyles, R.M.: Learning multimodal contact-rich skills from demonstrations without reward engineering (2021)

4. Balakuntala, M.V., Venkatesh, V.L.N., Bindu, J.P., Voyles, R.M., Wachs, J.: Extending policy from one-shot learning through coaching. In: 2019 28th IEEE International Conference on Robot and Human Interactive Communication (RO-MAN), pp. 1–7 (2019). DOI 10.1109/RO-MAN46459.2019.8956364

5. Biasin, M., Bianco, A., Pareschi, G., Cavalleri, A., Cavatorta, C., Fenizia, C., Galli, P., Lessio, L., Lualdi, M., Tombetti, E., Ambrosi, A., Redaelli, E.M.A., Saulle, I., Trabattoni, D., Zanutta, A., Clerici, M.: Uv-c irradiation is highly effective in inactivating sars-cov-2 replication. Scientific Reports **11**(1), 6260 (2021). DOI 10.1038/s41598-021-85425-w. URL https://doi.org/10.1038/s41598-021-85425-w

6. Brunete, A., Ranganath, A., Segovia, S., de Frutos, J.P., Hernando, M., Gambao, E.: Current trends in reconfigurable modular robots design. International Journal of Advanced Robotic Systems **14**(3), 1729881417710,457 (2017). DOI 10.1177/1729881417710457. URL https://doi.org/10.1177/1729881417710457

7. Bryant, R.: Innovating to fight ebola (2014). URL https://obamawhitehouse.archives.gov/blog/2014/11/17/exploring-opportunities-robotics-aid-disease-outbreaks. Retrieved on Apr 26, 2021

8. Conte, D., Leamy, S., Furukawa, T.: Design and map-based teleoperation of a robot for disinfection of covid-19 in complex indoor environments. In: 2020 IEEE International Symposium on Safety, Security, and Rescue Robotics (SSRR), pp. 276–282 (2020). DOI 10.1109/SSRR50563.2020.9292625

9. Di Lallo, A., Murphy, R., Krieger, A., Zhu, J., Taylor, R.H., Su, H.: Medical robots for infectious diseases: Lessons and challenges from the covid-19 pandemic. IEEE Robotics & Automation Magazine **28**(1), 18–27 (2021). DOI 10.1109/MRA.2020.3045671

10. FDA: UV lights and lamps: Ultraviolet-c radiation, disinfection, and coronavirus (2021). URL https://www.fda.gov/medical-devices/coronavirus-covid-19-and-medical-devices/uv-lights-and-lamps-ultraviolet-c-radiation-disinfection-and-coronavirus

11. Gupta, J., Lin, C.H., Chen, Q.: Flow dynamics and characterization of a cough. Indoor air **19**(6), 517–525 (2009)

12. Holland, J., Kingston, L., McCarthy, C., Armstrong, E., O'Dwyer, P., Merz, F., McConnell, M.: Service Robots in the Healthcare Sector. ROBOTICS **10**(1) (2021). DOI {10.3390/robotics10010047}

13. Holmberg, R., Khatib, O.: Development and control of a holonomic mobile robot for mobile manipulation tasks. The International Journal of Robotics Research **19**(11), 1066–1074 (2000). DOI 10.1177/02783640022067977

14. Houchens, B.C., Marian, D.V., Pol, S., Westergaard, C.H.: A novel energy-conversion device for wind and hydrokinetic applications. In: Fluids Engineering Division Summer Meeting, vol. 59070, p. V004T04A013. American Society of Mechanical Engineers (2019)

15. Jelden, K.C., Gibbs, S.G., Smith, P.W., Hewlett, A.L., Iwen, P.C., Schmid, K.K., Lowe, J.J.: Ultraviolet (uv)-reflective paint with ultraviolet germicidal irradiation (uvgi) improves decontamination of nosocomial bacteria on hospital room surfaces. Journal of Occupational and Environmental Hygiene **14**(6), 456–460 (2017). DOI 10.1080/15459624.2017.1296231. PMID: 28278065

16. Lindblad, M., Tano, E., Lindahl, C., Huss, F.: Ultraviolet-c decontamination of a hospital room: Amount of uv light needed. Burns **46**(4), 842–849 (2020). DOI https://doi.org/10.1016/j.burns.2019.10.004

17. Malik, A.A.: Robots and covid-19: Challenges in integrating robots for collaborative automation (2020)

18. Morawska, L., Milton, D.K.: It Is Time to Address Airborne Transmission of Coronavirus Disease 2019 (COVID-19). Clinical Infectious Diseases **71**(9), 2311–2313 (2020). DOI 10.1093/cid/ciaa939. URL `https://doi.org/10.1093/cid/ciaa939`

19. Murphy, R.R., Adams, J., Gandudi, V.B.M.: Robots are playing many roles in the coronavirus crisis – and offering lessons for future disasters (2020). URL `https://theconversation.com/robots-are-playing-many-roles-in-the\` `-coronavirus-crisis-and-offering-lessons-for-future-disasters-135527`. Retrieved on Mar 29, 2021

20. Murphy, R.R., Gandudi, V.B.M., Amin, T., Clendenin, A., Moats, J.: An analysis of international use of robots for covid-19 (2021)

21. Murphy, R.R., Gandudi, V.B.M., Amin, T., Clendenin, A., Moats, J.: An analysis of international use of robots for covid-19 (2021)

22. Office, D., OECD: The impact of the covid-19 pandemic on jobs and incomes in g20 economies (2020). URL `https://www.ilo.org/global/` `about-the-ilo/how-the-ilo-works/multilateral-system/g20/reports/` `WCMS_756331/lang--en/index.htm`

23. Otter, J., Yezli, S., Perl, T.M., Barbut, F., French, G.: The role of 'no-touch'automated room disinfection systems in infection prevention and control. Journal of Hospital Infection **83**(1), 1–13 (2013)

24. Potenza, A., Kiselev, A., Saffiotti, A., Loutfi, A.: An open-source modular robotic system for telepresence and remote disinfection (2021)

25. Shen, Y., Guo, D., Long, F., Mateos, L.A., Ding, H., Xiu, Z., Hellman, R.B., King, A., Chen, S., Zhang, C., Tan, H.: Robots under covid-19 pandemic: A comprehensive survey. IEEE Access **9**, 1590–1615 (2021). DOI 10.1109/ACCESS.2020. 3045792

26. WHO: Keep health workers safe to keep patients safe (2020). URL `https://www.who.int/news/item/17-09-2020-keep-health-workers-safe\` `-to-keep-patients-safe-who`. Retrieved on Mar 29, 2021

27. Yang, G.Z., J. Nelson, B., Murphy, R.R., Choset, H., Christensen, H., H. Collins, S., Dario, P., Goldberg, K., Ikuta, K., Jacobstein, N., Kragic, D., Taylor, R.H., McNutt, M.: Combating covid-19 – the role of robotics in managing public health and infectious diseases. Science Robotics **5**(40) (2020). DOI 10.1126/scirobotics. abb5589

28. Yang, H., Balakuntala, M.V., Moser, A.E., Quiñones, J.J., Doosttalab, A., Esquivel-Puentes, A., Purwar, T., Castillo, L., Mahmoudian, N., Voyles, R.M.: Enhancing safety of students with mobile air filtration during school reopening from covid-19. In: 2021 IEEE International Conference on Robotics and Automation (ICRA) (2021). URL `https://arxiv.org/abs/2104.14418`

Synchronization control of an actuation redundant system

Gabriel H. Campos[1], Himanshu (Kris) Sharma[2] Fengfeng (Jeff) Xi[3], Puren Ouyang[4]

[1,2,3,4] Ryerson University, Toronto ON M5B 2K3, Canada
gcamposn@ryerson.ca

Abstract. This paper introduces a position domain control method for a redundant actuation mechanism under strict synchronization requirements using error cross-coupling. The sample mechanism consists of two geometrically different parallel kinematic chains coupled together to the same end-effector. The rotation of the end-effector is its single degree of freedom of motion. Redundancy is achieved by actuating each kinematic chain individually in an opposite and interdependent manner to drive the end-effector and share the external load applied on the end-effector platform. The internal loading of the mechanism is a result of three factors: the external force applied to the mechanism, actuator force fighting due to the actuators' opposite motion profiles, and relative position misalignment between chains.

The mechanism's performance can be improved by minimizing the force fighting between the actuators and synchronizing the actuators' trajectory, while the relative position alignment can be further improved by cross coupling the position error. Due to the synchronization requirements, position domain control is used to allow for a master-slave motion scheme, where the motion of the master is used as a reference to the slave. The slave actuator motion is expressed in the position domain using the master motion as its reference to reduce the relative misalignment between the two kinematic chains and to prevent force fighting between the actuators. Additionally, error cross-coupling is implemented on the slave chain to allow the system to operate with minimal misalignment under external disturbances.

Keywords: Position domain control, actuation redundancy, parallel mechanism

1 Introduction

The dynamic capabilities of parallel manipulators can vary significantly throughout their workspace, even if their dynamic models have been optimized for a particular task [1]. The addition of redundancy to a parallel manipulator can help overcome this challenge. Redundancy in parallel kinematic manipulators can be classified into four types, kinematic redundancy, measuring redundancy, static redundancy, and actuation redundancy [2].

Actuation redundancy is often implemented to increase and homogenize the kinematic manipulability and stiffness in a mechanism. Actuation redundancy is achieved in one of two ways, actuating a passive joint or by adding a kinematic chain between the fixed and moving platform [3]. Adding actuation redundancy to a parallel mechanism provides the extra benefit of fault-tolerance which makes them suitable for fail-safe applications [4].

Mechanisms that include permanent active redundant joins are inherently statically indeterminant. This in turn, increases the complexity of the control scheme, where position, velocity, and force must be controlled for each kinematic chain. In addition to the control of each chain, the relative trajectory between chains to balance the load caused by external forces on the system must be synchronized to achieve the desired performance and prevent unnecessary internal loading. Control schemes such as cross-coupled control (CCC) have been proposed to reduce the trajectory error in multi-actuator systems such as in [5], [6]. However, CCC is limited to a variety of systems where determining the coupling gains can be quite complex [7]. Position domain control (PDC) has been developed in recent years to improve the tracking performance of multi-axes system [8]. PDC combines the advantages of directly reducing the tracking error characteristic from CCC and the computation advantages of event-driven control (EDC) such as in [9]. PDC samples the motion of a master axis and uses it as its reference to develop the position domain dynamic model to yield zero tracking error of this axis. Only the tracking error(s) of the slave motion contributes to the overall contour error. The performance benefit of PDC compared to time domain control is attributed to its characteristic of eliminating the trajectory error of the reference chain to the overall trajectory error. The PDC model for a serial robotic system is developed by transforming the dynamic equation from time domain to position domain. The advantage of this control system is that it provides better performance stability since the dynamics are transformed isomorphically and the stability of the position domain control is guaranteed based on Lyapunov method [8], [10]–[17].

PDC has the additional advantage of generalizability to extend its application to other systems, where complexity, objectives, and operation conditions vary from contour tracking performance. The unique feature of position domain control is that the master motion has no effect on the final contour error. Furthermore, this control method has a reasonable computational cost as it benefits from its EDC characteristics but without difficulty in implementation. As proposed in [18], the time domain control can be thought as a special case of the domain control (with a constant virtual unit speed axis). For this reason, it is expected that all existing control systems developed in time domain can be extended to position domain.

The control scheme in this paper was proposed as an improved method to control the synchronized trajectory of redundantly actuated parallel mechanisms where trajectory errors have a detrimental effect on its operation. Position domain control is used to allow for a master-slave motion scheme and error cross-coupling is implemented on the slave chain to allow the system to operate with minimal misalignment under external disturbances. The performance of the control scheme is measured as a reduction on relative position/velocity errors and disproportionate internal loads. The performance

improvement results from a reduction in the uneven force distribution between kinematic branches, actuator force-fighting, and relative position error.

The system was validated by testing it on an existing mechanism design with its kinematics described in [19]. The application of the sample mechanism used for this work is a wing design with a variable winglet cant angle. The mechanism consists of two kinematic branches where the forward (fwd) branch is designated as the master, and the aft branch is the slave, as depicted in **Fig. 1**. A full-size morphing winglet serving as the redundant actuation mechanism was built to replicate the operation of the mechanism. The morphing winglet is designed to change its cant angle during flight between 10˚ to 80˚ to fit the most fuel-efficient configuration during the flight mission [20].
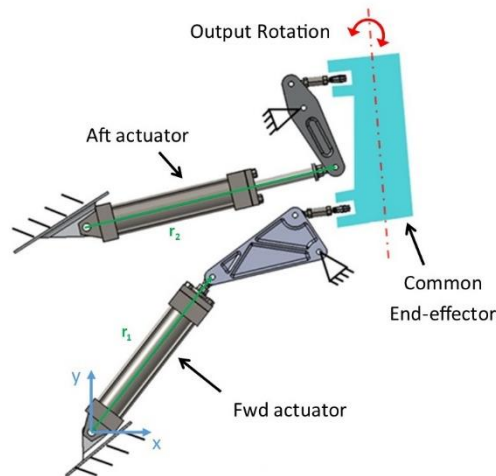
Fig. 1. Wing with a variable cant angle mechanism - 10˚ cant configuration.

2   System description

The mechanism consists of two actuated kinematic chains, each driven by a hydraulic cylinder controlled via a four-way valve. The configuration of the mechanism has been designed to operate under large external loads by distributing the external load between each chain. As described in [19], each closed loop chain consists of two serial loops that work out-of-plane from each other. The forward (fwd) chain consists of the planar loop (on the XY plane), which is connected to the spatial loop (on the XZ plane).

The aft chain is constructed in a similar, but asymmetric, configuration actuated always in opposite direction to the fwd chain. The requirement of opposite chain motion is in part imposed by the space constrain of the dry section of the aircraft wing where the mechanism is enclosed, and the required operation loads and moments of the

mechanism's components. That is, in order to increase the winglet output angle, the prismatic joint in the fwd chain must extend while the prismatic joint in the aft chain must retract. The motion of each chain is not only out-of-plane to each of their respective loops but also it is non-linear in respect to each chain. Finally, each chain is intermediately connected by the output link, which in turns functions as a coupler to the winglet. The output motion of each chain is transferred to the output link and as a result the output link rotates around its own axis of rotation.

The two actuators must be synchronized and share the load exerted on the same winglet. Due to space constraints, the two linkages are geometrically different leading to opposite force profiles for the two actuators. A control method developed in position domain control is proposed to address this complex control problem by combining linkage kinematics with force analysis.

The motion profile of the winglet mechanism is derived from the kinematic model developed in [19] and briefly summarized here for completion. The forward kinematics (FK) for the two chains are modeled with the linear actuator length as the input joint variable, generally:

$$y_M = f_0(\vec{r}_1(x, y)) \tag{1}$$

$$y_S = g_0(\vec{r}_7(x, y)) \tag{2}$$

where y_M and y_S are the stroke lengths for the master and slave actuators, respectively, and $\vec{r}_1$ and $\vec{r}_7$ are the position vectors for the master and slave, respectively. The output angle of the winglet, θ_c, and the angular rate $\dot{\theta}_c$, (obtained FK) are the target variables in the control system.

$$\theta_c = f_1(y_M) = g_2(y_S) \tag{3}$$

$$\dot{\theta}_c = f_2(y_M) = g_2(y_S) \tag{4}$$

The motion trajectory can be plotted to visualize the relative operation of each actuator as a function of the cant angle **Fig. 2**
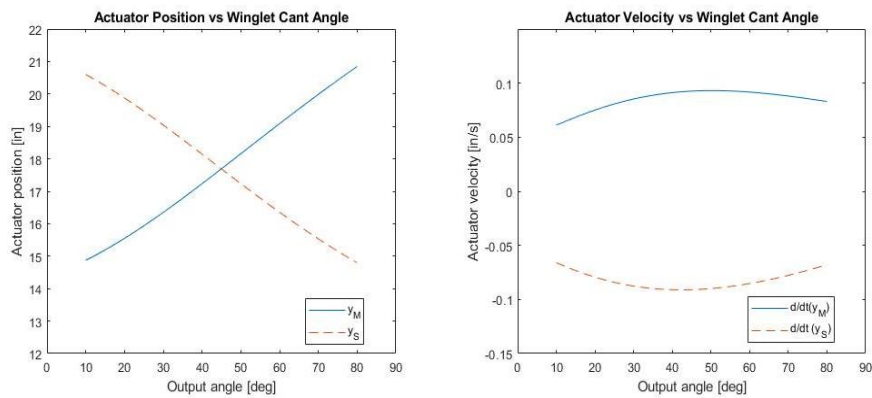
Fig. 2. Actuator trajectory at 1°/s.

The internal force distribution between kinematic chains can be maintain by synchronizing the relative motion between chains, thus preventing undesirable internal loading due to force fighting between actuators and misalignment. The forward chain state assigned as master actuator and the aft chain designated as the slave actuator. By expressing the control problem in position domain, the trajectory error of the leading chain is cancelled out, improving the manipulator's motion trajectory while distributing a large external load constantly acting opposite to the end-effector's motion. The transformation can be seen as a one-to-one mapping from time domain to position domain and is used to transform the dynamics of the slave trajectory:

$$y_S = f(y_M) \tag{5}$$

$$\dot{y}_s = \dot{y}_M y_S' \tag{6}$$

$$\ddot{y}_s = (\dot{y}_M)^2 y_S'' + \ddot{y}_M y_S' \tag{7}$$

The mechanism's misalignment which is used as one of the feedback states in the control system is defined as the difference between the desired relative position of the slave actuator as a function of the master actuator's position, $y_{S_d}(y_M)$, and the measured slave actuator relative position, $y_S(y_M)$. Coupling the slave chain in position domain to its position error output can further reduce the relative trajectory error:

$$\varepsilon_{\text{sync}} = y_{S_d}(y_M) - y_S(y_M) \tag{8}$$

The magnitude and location of the stresses on the mechanism's structure can be used as an upper limit to select the maximum mismatch allowed in the synchronization without any external loads applied. This provides the upper limit for the synchronization error of the mechanism during the motion profile. Ideally, this error should be driven dynamically to zero. The synchronization controller has a set point ($\varepsilon_{\text{sync}}=0$) and treats the misalignment error as a process variable. The settling time can be optimized for the mission's angular rate of the end-effector at about $\omega=1°/s$.

3   Motion control

In practical aerospace applications, due to the large forces experienced during flight and volume and weight restriction, hydraulic system presents a favorable alternative to electromechanical systems by providing highspeed response together with high power density. For this reason, an electrohydraulic system is explored to provide a practical method to implement the mechanism investigated in this research. The modeling requires a more detailed mathematical description of the type of electrohydraulic system, including a mathematical model for the cylinder, and valve before the control system can be analyze and design.

The block diagram, **Fig. 3**, has the master blocks in solid red and the slave blocks in blue to visually differentiate between the feedback block components. The control

block diagram is composed of the master PI position control in parallel with the master PID velocity control. The control architecture for the slave branch also contains the slave PI position control in parallel to the slave velocity control and the PI synchronization error control. The sync error controller is a regulator control in order to minimize any error produced during its trajectory due to external disturbances and/or model uncertainties. The scheduling gains are used to compensate for 1) the non-linearity of the four-way proportional valve at the change between positive and negative fluid flow rate, which gets reflected as a pressure gain drop and 2) the cylinder cross-sectional area difference, between side A and B, due to the shaft of the cylinder.

The unsymmetrical nature of the cylinders created different responses in pressure difference and in turn the forces. Each electrohydraulic actuator has a controller for the master spool position, x_M, composed of the position PI controller in the following form:

$$x_{M,y} = k_{M,x_y}\left(e_{y_M}\right) + k_{M,i_y}\int\left(e_{y_M}\right)dt \tag{9}$$

where the gains are proportional k_x and integral k_i for the position controller. The velocity control for the master branch is given by:

$$x_{M,y'} = k_{M,x_{y'}}\left(e_{y_{M'}}\right) + k_{M,i_{y'}}\int\left(e_{y_{M'}}\right)dt + k_{M,d_{y'}}\frac{d}{dt}\left(e_{y_{M'}}\right) \tag{10}$$

where the proportional, integral and derivative gains are denoted by subscripts x, i and d, with the subscript y' indicating the gains belong to the velocity controller. Thus, combining both controllers in parallel leads to:

$$x_M = \left(k_{M,x_y} + k_{M,i_{y'_M}}\right)e_{y_M} + k_{M,x_y}e_{y_{M'}} + k_{M,i_y}\int e_{y_M}dt + k_{M,d_{y'}}\frac{d}{dt}\left(e_{y_{M'}}\right) \tag{11}$$

In a similar fashion, the spool position for the slave actuator can be written as:

$$x_S = x_{S,y} + x_{S,\dot{y}} + x_\varepsilon \tag{12}$$

The gain schedule is composed of two schedule variables, the cylinder direction, sign(x), and the cylinder's hydraulic fluid flow rate, Q. The proportional gain schedule, k_x is given as

$$k_x = \begin{cases} k_c + k_p x_P k_c & sing(x) > 0 \\ \alpha k_c + k_p x_p k_c & sign(x) < 0 \end{cases} \tag{13}$$

where k_c is the base proportional gain and it is a function of the command analog voltage input, V, to the four-way servo-proportional directional control valve. The coefficient α serves to compensate the cylinder's cross-sectional area difference from the piston side to the shaft side, which results in a force due to pressure difference between the cylinder side A and B. The fluid flow rate is a function of the input variable linearly proportional to the voltage, and the pressure drop gain, k_p, of the valve reflects the valve's pressure difference to the supply pressure. The pressure drop gain is only significant during the change in the flow direction and in the neighborhood of the spool's nominal state with an inversely symmetrical saturated response at x_p as

$$x_P = \begin{cases} g(V) & , \quad x > 0 \\ 0 & , \quad x = 0 \\ -g(V) & , \quad x < 0 \end{cases} \tag{14}$$

The function $g(V)$ can be linearized into 3 different segments to facilitate the gain scheduling,

$$g(V) = \begin{cases} m_1 & , \quad 2.5\% \; signal > V > 0 \\ m_2 & , \quad 5\% \; signal > V > 2.5\% \; signal_1 \\ m_3 = 1 & , \quad V > 5\% \; signal \end{cases} \tag{15}$$

where each segment has a constant slope, m_i, according to the manufacturer's datasheet and validated experimentally. The gain scheduling is blended via real-time control switching states for α, and interpolation for x_p as the function should remain continuous for the entire domain.
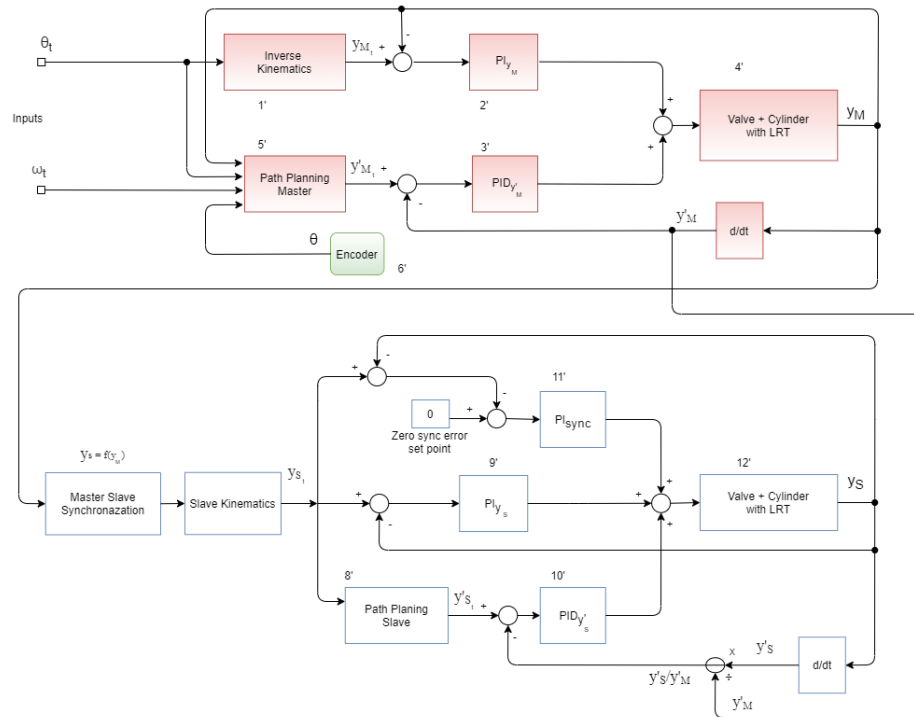
Fig. 3. High level control bock diagram for electromechanical linear actuator winglet prototype

4 Force control and force distribution

The internal loading for this mechanism comprises of the three resulting loads: external load due to aerodynamic loads, loads due force fighting between the actuators and the resulting load from misalignment. For the synchronization control to be in

effect, the dynamic loading model on the mechanism and force distribution model for the actuator is developed and optimized. In order to simulate the aerodynamic loads (External Load) acting on the winglet during flight, the loads can be classified under the two scenarios:

1. Load during morphing (Active Loading)
2. Loads during stationary winglet (Preloading)

Through inspection of aerodynamic loading during a typical mission, the maximum normal load experienced by the winglet was found. This load is essentially the design load the dynamic loading system needs to output during both preloading and active loading scenarios.

The developed setup for the loading system, as shown in **Fig. 4**, of the winglet provides a tensile load using a hydraulic actuator. A shark fin linkage is used to transfer the applied tension from the cable to the winglet and allows for a normal tension force independent of the winglet angle. With a load cell in loop for the acquisition of tension force data, a force controller for the loading mechanism is considered. The objective of this setup is to apply the design load during preloading scenario and maintain that during the morphing motion.
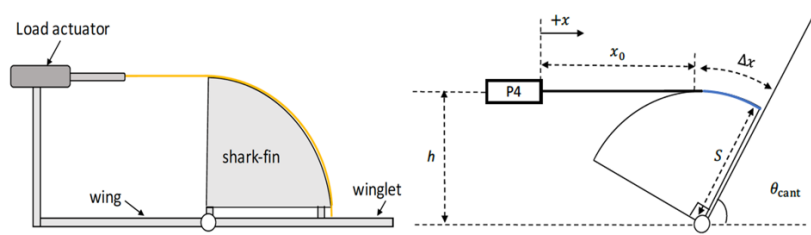
Fig. 4. Dynamic loading setup

To calibrate the loading actuator with the cant module, a position and analysis of the RPRP setup is performed. The position of the linear actuator in terms of the cant angle can be given as:

$$\Delta x = S \times (90° - \theta_{cant}) \times \frac{\pi}{180} \qquad (16)$$

The stoke of the actuator thus becomes:

$$x_{act} = x_0 + S \times (90° - \theta) \times \frac{\pi}{180} \qquad (17)$$

The velocity of the actuator in terms of the angular rate of the cant module:

$$\dot{x}_{act} = -S \times \dot{\theta}_{cant} \qquad (18)$$

The position and velocity of the actuator in terms of the angular rate serves as the constraint for the hydraulic system. As the hydraulic actuator performs the loading through the tension, the velocity of the actuator must be compensated to maintain the required force in accordance with the winglet motion. The force output of the dynamic loading system can be modelled by using a hydraulic plant model that uses a four-way spool valve, a double acting rod cylinder, a constant supply pump and pressure sensors and loadcell. The hydraulic plant for the loading actuator was modelled using the dynamics presented in [21].

The control goal of this system is to improve the input voltage in a way that the force output of the actuator and the resulting tensional load on the winglet can simulate the desired aerodynamic loads despite the existing parametric uncertainties and nonlinearities. Prior to controller design, a few assumptions to assist the control scheme are presented as follows:

Assumption 1: For the desired command $F_{d(t)} \in R^3$, under general operating conditions, the pressures P_A and P_B are all bounded by the supply pressure P_S and the return pressure P_r, i.e. $0 < P_r < (P_A \text{ or } P_B) < P_S$ [22]. Thus, the desired command for the force output must be achievable provided the system's supply and return pressure.

Assumption 2: The valve response is significantly faster than the actuator response. Thus, the valve dynamics can be approximated as a first order system.

Assumption 3: The control function is carried out under steady operating conditions, thus neglecting any transient contributions that may occur due to high – speed operation [23].

Due to the existing nonlinearities, the operating condition for the system varies causing the response to experience oscillations. In order to achieve the desired response for the system and counterbalance the nonlinearity of flow rate vs valve voltage, a PID based MRAC is considered.
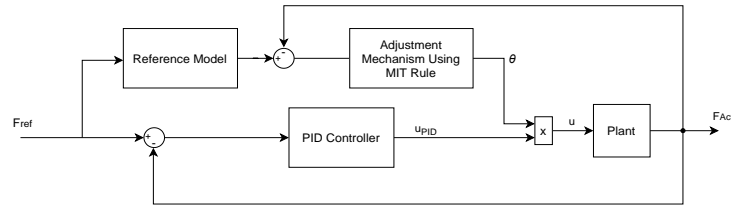
Fig. 5. PID-based Model Reference Adaptive Control Schematic

The adaptation mechanism was designed to adjust the controller input using MIT Rule. The MIT rule uses the negative gradient of the error and the sensitivity derivative of the system in order to adjust the system. The adaptation mechanism for the controller can be expressed as:

$$\theta = (y - y_m)y_m \frac{-\gamma}{s} \tag{19}$$

where γ is the adaptation gain, θ is the adaptation parameter and $(y - y_m)$ is the error between the plant output and the reference model output. The adaptive control design for loading system allows for minimization of loading error under active control and improves performance during turbulence or external disturbance.

The challenge in the PDC for redundant actuation control arises from the effect of external loading on the actuators and resulting force distribution between the actuators. For improved performance with PDC and error coupling, the actuators must counter-balance the force exerted from the winglet loading and the resulting moment. The forces distributions can be developed using static modelling of the redundant system and the geometry of the mechanism can be utilized. **Fig. 6** shows the XY plant view of the fwd chain that can be used to model the force distribution.
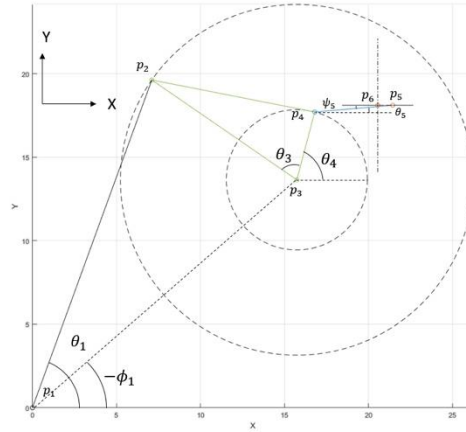
Fig. 6. X-Y plane view
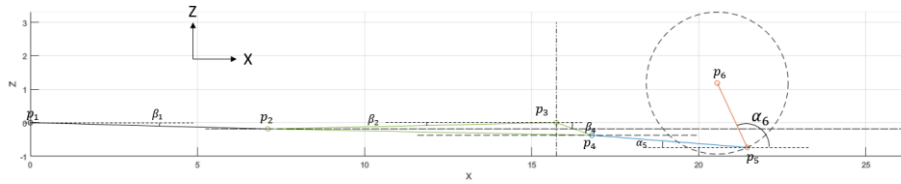
Fig. 7. X-Z Plane View

The first section is the triangular link defined by the points p_2, p_3 and p_4. While the actual link is not planar, it can be projected onto the X-Y plane as the revolute joint on point p_3 rotates along the Z axis. At p_3, the moment balance is

$$F'_{32}(r_2 \cos \beta_2) - F'_{34}(r_3 \cos \beta_4) = 0 \qquad (20)$$

where the angles β_2 and β_4 project the geometry onto the X-Y plane, centered around p_3. These angles are defined as,

$$\beta_2 = \tan^{-1}\left(\frac{p_{2_z} - p_{3_z}}{\sqrt{\left(p_{2_x} - p_{3_x}\right)^2 + \left(p_{2_y} - p_{3_y}\right)^2}} \right) \qquad (21)$$

$$\beta_4 = \tan^{-1}\left(\frac{p_{4_z} - p_{3_z}}{\sqrt{\left(p_{4_x} - p_{3_x}\right)^2 + \left(p_{4_y} - p_{3_y}\right)^2}}\right) \tag{22}$$
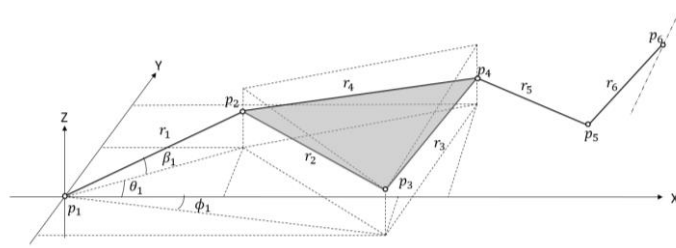
Fig. 8. Close-up of FWD Linkage Mechanism

F'_{32} and F'_{34} are the projected moment forces acting on the triangular link, perpendicular to the projected X-Y images of links r_2 and r_3, respectively. They are defined as,

$$F'_{32} = F'_1 \sin(\theta_4 + \theta_3 - \theta_1) \tag{23}$$

$$F'_{34} = F'_4 \sin(\theta_4 - \theta_5) \tag{24}$$

where the angle θ_1 is the angle between the X-axis and the X-Y plane projection of link r_1 and it is defined as,

$$\theta_1 = \tan^{-1}\left(\frac{p_{2_y} - p_{1_y}}{p_{2_x} - p_{1_x}}\right) \tag{25}$$

θ_3 is the angle between the X-Y plane projections of links r_2 and r_3, which can be found as

$$\theta_3 = \tan^{-1}\left(\frac{p_{2_y} - p_{3_y}}{p_{2_x} - p_{3_x}}\right) - \theta_4 \tag{26}$$
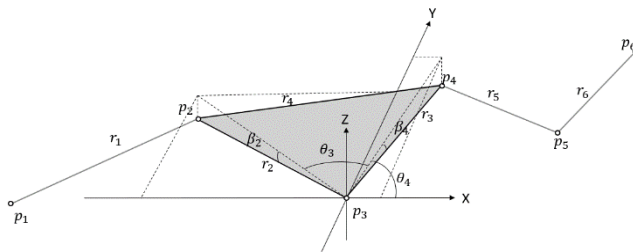
Fig. 9. Projection Angles along XY plane

θ_5 is the angle between the X-axis and the X-Y plane projection of link r_5, defined as

$$\theta_5 = \tan^{-1}\left(\frac{p_{5_y} - p_{4_y}}{p_{5_x} - p_{4_x}}\right) \tag{27}$$

F_1' is the force F_1 projected on the X-Y plane, calculated with p_1 as the origin.

$$F_1' = F_1 \cos\beta_1 \tag{28}$$

where β_1 is the angle between the link r_1 and the X-Y plane, defined as,

$$\beta_1 = \tan^{-1}\left(\frac{p_{2_z} - p_{1_z}}{\sqrt{\left(p_{2_x} - p_{1_x}\right)^2 + \left(p_{2_y} - p_{1_y}\right)^2}}\right) \tag{29}$$

F_1 is the force acting along the actuator link r_1. F_4' is the force F_4 projected in the X-Y plane, calculated with p_4 as the origin.

$$F_4' = F_4 \cos\beta_5 \tag{30}$$

where β_5 is the angle between the link r_5 and the X-Y plane, defined as,

$$\beta_5 = \tan^{-1}\left(\frac{p_{5_z} - p_{4_z}}{\sqrt{\left(p_{5_x} - p_{4_x}\right)^2 + \left(p_{5_y} - p_{4_y}\right)^2}}\right) \tag{31}$$
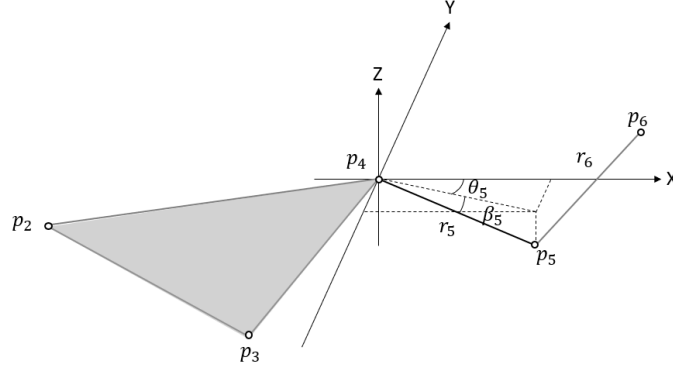
Fig. 10. Toggle and Winglet Angles

F_4 is the force that is transmitted through link r_5. Link r_5 is the smallest link in the chain and is a critical area in the mechanism, and it will be considered independently later. Combining the equations,

$$F_1 \cos\beta_1 \sin(\theta_4 + \theta_3 - \theta_1)(r_2 cos\beta_2) \\ - F_4 cos\beta_5 \sin(\theta_4 - \theta_5)(r_3 cos\beta_4) = 0 \tag{32}$$

Rearranging, the actuator force can be related to F_4.

$$F_1 = F_4 \left(\frac{cos\beta_5}{cos\,\beta_1}\right) \left(\frac{sin(\theta_4 - \theta_5)}{sin(\theta_4 + \theta_3 - \theta_1)}\right) \left(\frac{r_3}{r_2}\right) \left(\frac{cos\beta_4}{cos\beta_2}\right) \tag{33}$$

Next, to find F_4, the second section at p_6 is calculated. There is another moment summation, directly opposing the moment generated by the winglet.

$$M_E k - F_5' r_6 = 0 \tag{34}$$

where F_5' is F_4'' projected normal to link r_5, centered around p_5,

$$F_5' = F_4'' \sin(\alpha_6 - \alpha_5) \tag{35}$$

where the angle α_5 is defined as,

$$\alpha_5 = \tan^{-1}\left(\frac{p_{4_z} - p_{5_z}}{p_{4_x} - p_{5_x}}\right) \tag{36}$$

To find F_4'', F_4 is used again, except projected onto the X-Z plane so that it can be used to calculate the opposing moment generated by the mechanism.

$$F_4'' = F_4 cos\psi_5 \tag{37}$$

where ψ_5 is the angle between link r_5 and the X-Z plane, and it is equal to

$$\psi_5 = \sin^{-1}\left(\frac{p_{5_y} - p_{4_y}}{r_5}\right) \tag{38}$$
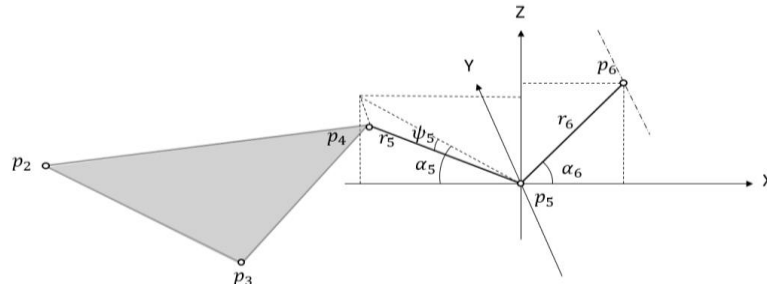
Fig. 11. Projected Toggle and Winglet Angles

F_4 can then be found,

$$F_4 = \frac{M_E k}{cos\psi_5 \sin(\alpha_6 - \alpha_5) r_6} \tag{39}$$

The force in the actuator can then be found by substituting Equation (35) into Equation (33),

$$F_1 = \frac{M_E k}{cos\psi_5 \, sin(\alpha_5 - \alpha_6)\, r_6}\left(\frac{cos\beta_5}{cos\beta_1}\right)\left(\frac{sin(\theta_4 - \theta_5)}{sin(\theta_4 + \theta_3 - \theta_1)}\right)\left(\frac{r_3}{r_2}\right)\left(\frac{cos\beta_4}{cos\beta_2}\right) \tag{40}$$

where M_E is the total winglet moment, $k \in [0,1]$ is a factor that changes the load distribution of the total moment for linkage A and B. For linkage A, the moment is $M_E k$ and for linkage B, the moment is $M_E(1 - k)$. In other words, each chain takes a certain percentage of the load. For the analysis of the force distribution, k was selected at 0.4. Equation (40) shows the output force for the actuator in forward linkage, and a similar distribution can be performed to determine the Aft actuator force.

5   Experimentation and results

The cylinder and valve model presented in this report includes a four-way spool valve with constant pressure supply, Ps =3000 psi, with an unpressurized return pressure Pr=0. The valve is a high performance, servo-proportional directional control valve. The valve is connected to a double-acting, single rod hydraulic linear actuator, which provides a displacement under a load, at a controlled variable velocity. The linear actuator is equipped with an internal LRT used to measure the displacement of the piston, y. The pressure for each side of the cylinder PA and PB is directly measured via pressure transducers. This model is intended to be used for the fwd and aft cylin-ders along with the corresponding FK and synchronization of the cylinders. A similar deri-vation is performed for the tension cylinder used in the dynamic loading rig which applies the external design load to the winglet mechanism.

The model for the hydraulic plant for the dynamic setup incorporates incremental desired force. **Fig. 12** shows the loading response error between the uncontrolled response in comparison to the MRAC controlled response. The error in the uncontrolled response comprises a steady state error alongside some oscillation whereas using a model reference adaptive controlled significantly minimizes the steady error and the oscillation.
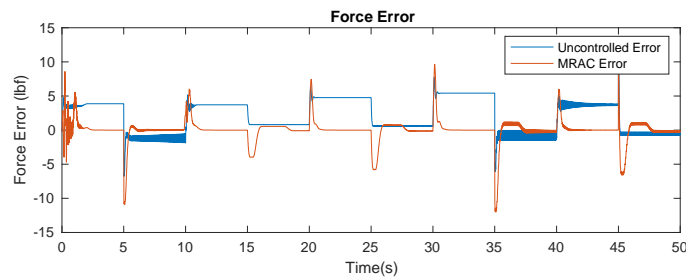
Fig. 12. Tension Load Force Control Error

Fig. 13 shows the parameters of the hydraulic plant with the controller alongside the uncontrolled. It shows the voltage input and the resulting flow rate for the plant alongside the actuator pressures in both chambers of the actuator. Since the desired

response for both the scenarios are similar, the MRAC significantly focuses on minimizing the oscillation that results due to the pressure changes as seen in the pressure distributions.
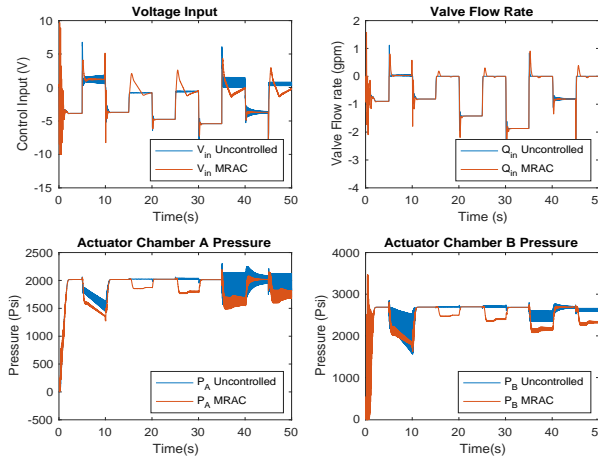

Fig. 13. Loading Plant Parameters

Using the external load from the hydraulic plant, the force distribution for the actuator and the resulting toggle force can be determined. Equation (40) is used to determine the actuator force using the total winglet moment. With varying loading force and the winglet angle, the force distribution allows for determination of the maximum load of both actuator. **Fig. 14** shows the force distribution for both the actuator under an external load for the winglet motion from 45° to 115°. As identified the maximum load is experienced by the AFT actuator with the maximum load of -7318 lbf.
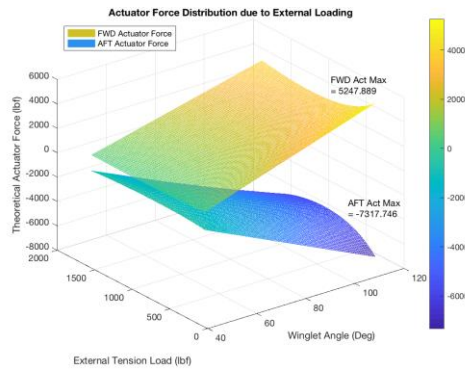
Fig. 14. Actuator Force Distribution due to External Loading

Using the actuator force for the two linkages, the toggle forces can also be determined. **Fig. 15** shows the force distribution on the toggle link due to external force as

the winglet is in motion. The maximum force experience by the aft toggle is at a winglet angle of 45° and maximum external load.
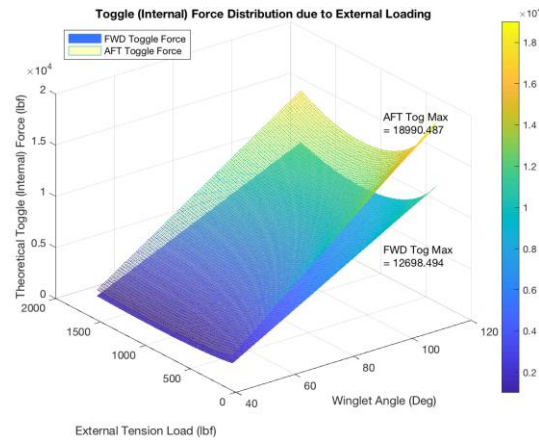
Fig. 15. Toggle force distribution due to external loading

The control system is based on position-velocity closed loop control, where the position of the input link is prioritized over its velocity to guarantee the synchronization requirements. Additionally, the control system is developed in position domain, with the fwd branch states, y_M, $\dot{y}_M$, and $\ddot{y}_M$ as the master subsystem and the aft branch states y_S, y'_s, and y''_S as the slave subsystem in position domain. The system consists of an encoder attached to the output link measuring the cant angle, θ_c, the position sensor on each input link measuring its stroke length, y, a force transducer to measure the force of each cylinder (via pressure differential for a hydraulic actuator) and a loadcell located on the load application point to measure the external force. Additional monitoring sensors consists of strain gauges on key components to measure internal forces (i.e. toggle link).

For the testing with an external load, the load must be applied incrementally, and the internal stresses must be verified to match the FEM analysis. This can be done by installing strain gauges with calibrated data from a tensile test to obtain the actual stresses on key components. Additional verification can be computed by comparing it to the cylinder force which can be calculated from its fluid pressure differential for the hydraulic case and the current for the electromechanically case. For all other magnitudes of mismatch, the stresses can be linearly scaled for further analysis and monitoring.

A full-size prototype was manufactured to validate the control method under realistic loading conditions. The control system was developed in LabVIEW as a real-time, deterministic, controller with FPGA. The full-size prototype consists of the cant mechanism, winglet structure, and dynamic loading test rig (composed of the shark-fin and tension cylinder). The linear actuators of the cant mechanism and tension cylinder are all electrohydraulic, however, the tension cylinder is controlled independently with force feedback. The loading test rig was design as a dynamic loading test rig rather than

a passive system to have the flexibility to test various loads, loading rates and even emulate loading transients related to aerodynamical phenomena.

Following the confirmation of the synchronization requirements, the system was tested under no-load conditions to test the internal forces due to the mechanism's own weight and the relationship to its center of gravity (cg). As expected, at a cant angle of approximately 52˚, the winglet's cg gets behind the axis of rotation thus, changing abruptly the force trend as the winglet cant angle increases from (15˚ to 75˚). Note that, the system is operated during preliminary testing between 15˚ to 75˚ to prevent over-actuation in case of a system error. The reaction forces are solely created by 1) the structural weight of the mechanism and external forces and in a smaller part the by 2) the joint friction and bias cylinder force (due to fluid friction and cross-sectional area difference).

As it can be observed from **Fig. 16** the system mismatch error with a maximum external force applied to the cant does not exceed the error margin and is safe withing its design limits of ±0.06 in**.**
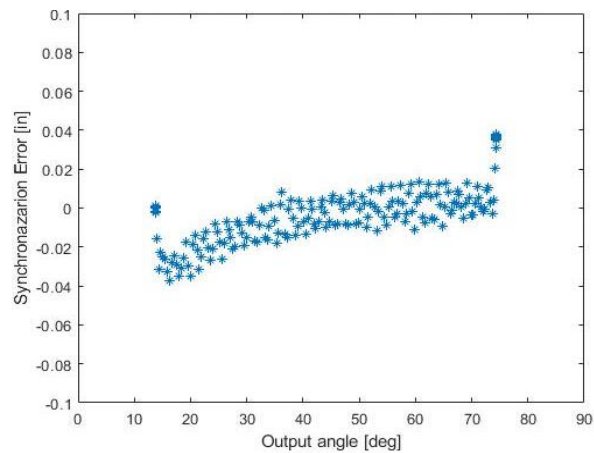
Fig. 16 Mismatch error during the entire trajectory of the winglet during.

6   Conclusion

As presented in this paper, the synchronization scheme for a parallel actuation redundant mechanism can be further improved by modeling the control system in position domain and coupling the error of the slave kinematic chain to its own relative position error. The force distribution model for the actuators, which can be further used to improve the performance by minimizing the force fighting is also considered. The consideration of position domain control alongside error coupling control provides a novel approach for the synchronization control challenge for actuation redundant actuator. By taking advantage of the computational efficiency of position domain control and the synchronization accuracy of coupling the error to a zero setpoint, the control scheme

can be applied to a practical aerospace application, a wing with variable cant angle, as in this paper.

The mismatch during transients at full load, under nominal operation, can be up to ±0.038 in comparison to the nominal trajectory mismatch of ±0.015 in. The mismatch was identified to increase during transient behavior of the master actuator due to the effects of high order dynamics. This results in higher error since the linearization made to calculate the acceleration change during trajectory computation becomes inaccurate and the nonlinearities become significant. This is a direct result of the master-slave actuation as implemented in this work. To lower the error during transients, the subsystem for the master dynamics estimation model can be used to effectively keeping the error closer to zero.

References

[1]   D. Corbel, M. Gouttefarde, O. Company, and F. Pierrot, "Actuation redundancy as a way to improve the acceleration capabilities of 3T and 3T1R pick-and-place parallel manipulators," *J. Mech. Robot.*, vol. 2, no. 4, Aug. 2010, doi: 10.1115/1.4002078.

[2]   A. Moosavian and F. Xi, "Design and analysis of reconfigurable parallel robots with enhanced stiffness," *Mech. Mach. Theory*, vol. 77, pp. 92–110, 2014, doi: 10.1016/j.mechmachtheory.2014.02.005.

[3]   A. Müller, "On the terminology and geometric aspects of redundant parallel manipulators," *Robotica*, vol. 31, no. 1, pp. 137–147, Jan. 2013, doi: 10.1017/S0263574712000173.

[4]   L. Notash and L. Huang, "On the design of fault tolerant parallel manipulators," *Mech. Mach. Theory*, vol. 38, no. 1, pp. 85–101, Jan. 2003, doi: 10.1016/S0094-114X(02)00067-8.

[5]   J. Ling, Z. Feng, D. Yao, and X. Xiao, "Non-linear contour tracking using feedback PID and feedforward position domain cross-coupled iterative learning control," *Trans. Inst. Meas. Control*, vol. 40, no. 6, pp. 1970–1982, Apr. 2018, doi: 10.1177/0142331217695386.

[6]   Z.-Y. Jia, J.-W. Ma, D.-N. Song, F.-J. Wang, and W. Liu, "A review of contouring-error reduction method in multi-axis CNC machining," 2018, doi: 10.1016/j.ijmachtools.2017.10.008.

[7]   Y. S. Shieh, A. C. Lee, and C. S. Chen, "Cross-coupled biaxial step control for CNC EDM," *Int. J. Mach. Tools Manuf.*, vol. 36, no. 12, pp. 1363–1383, Dec. 1996, doi: 10.1016/S0890-6955(96)00039-9.

[8]   T. Dam and P. R. Ouyang, "Contour tracking control in position domain for CNC machines," in *2011 IEEE International Conference on Information and Automation, ICIA 2011*, Jun. 2011, pp. 14–19, doi: 10.1109/ICINFA.2011.5948956.

[9]   K.-E. Åarzén, "A simple event-based PID controller," *IFAC Proc. Vol.*, vol. 32, no. 2, pp. 8687–8692, Jul. 1999, doi: 10.1016/s1474-6670(17)57482-0.

[10]   P. R. Ouyang and T. Dam, "Position domain PD control: Stability and comparison," in *2011 IEEE International Conference on Information and Automation, ICIA 2011*, Jun.

2011, pp. 8–13, doi: 10.1109/ICINFA.2011.5948955.

[11]   P. R. Ouyang, T. Dam, J. Huang, and W. J. Zhang, "Contour tracking control in position domain," *Mechatronics*, vol. 22, no. 7, pp. 934–944, Oct. 2012, doi: 10.1016/j.mechatronics.2012.06.001.

[12]   J. M. Acob, V. Pano, and P. R. Ouyang, "Hybrid PD sliding mode control of a two degree-of-freedom parallel robotic manipulator," *IEEE Int. Conf. Control Autom. ICCA*, pp. 1760–1765, 2013, doi: 10.1109/ICCA.2013.6564907.

[13]   P. R. Ouyang, V. Pano, and T. Dam, "PID position domain control for contour tracking," *Int. J. Syst. Sci.*, vol. 46, no. 1, pp. 111–124, Jan. 2015, doi: 10.1080/00207721.2013.775385.

[14]   P. R. Ouyang, V. Pano, and Y. Q. Hu, "Position domain PD sliding mode control for contour tracking," in *IEEE/ASME International Conference on Advanced Intelligent Mechatronics, AIM*, Aug. 2015, pp. 1020–1025, doi: 10.1109/AIM.2015.7222673.

[15]   P. R. Ouyang, V. Pano, J. Tang, and W. H. Yue, "Position domain nonlinear PD control for contour tracking of robotic manipulator," *Robot. Comput. Integr. Manuf.*, vol. 51, pp. 14–24, Jun. 2018, doi: 10.1016/j.rcim.2017.11.017.

[16]   P. R. Ouyang, M. Kuang, S. Jayasinghe, W. H. Yue, and H. M. Kang, "Adaptive PD-SMC in position domain for contour tracking of hybrid actuated system," in *2017 IEEE International Conference on Mechatronics and Automation, ICMA 2017*, Aug. 2017, pp. 852–857, doi: 10.1109/ICMA.2017.8015927.

[17]   W. H. Yue, V. Pano, P. R. Ouyang, and Y. Q. Hu, "Model-independent position domain sliding mode control for contour tracking of robotic manipulator," *Int. J. Syst. Sci.*, vol. 48, no. 1, pp. 190–199, Jan. 2017, doi: 10.1080/00207721.2016.1173742.

[18]   P. R. Ouyang, M. Kuang, S. Jayasinghe, and W. H. Yue, "Position domain contour tracking control: Theory and controllers," in *Proceedings of the 13th IEEE Conference on Industrial Electronics and Applications, ICIEA 2018*, Jun. 2018, pp. 129–134, doi: 10.1109/ICIEA.2018.8397702.

[19]   F. (Jeff) Xi, A. Moosavian, G. H. Campos, U. (Sana) Choudhuri, C. Z. (John) Sun, and R. Buchkazanian, "Analysis and Control of an Actuation-Redundant Parallel Mechanism Requiring Synchronization," *J. Mech. Robot.*, vol. 12, no. 4, Aug. 2020, doi: 10.1115/1.4045653.

[20]   P. Paudel, "Aerodynamic Aspects in the Development of Morphing Winglet for a Regional Aircraft," Ryerson University, 2015.

[21]   M. A. S. Aboelela, M. E. S. M. Essa, and M. A. M. Hassan, "Modeling and identification of hydraulic servo systems," *Int. J. Model. Simul.*, vol. 38, no. 3, pp. 139–149, 2018, doi: 10.1080/02286203.2017.1405713.

[22]   G. Yang and J. Yao, "High-precision motion servo control of double-rod electro-hydraulic actuators with exact tracking performance," *ISA Trans.*, 2020, doi: https://doi.org/10.1016/j.isatra.2020.03.029.

[23]   N. Manring and R. Fales, *Hydraulic Control Systems*, Second. John Wiley & Sons, Inc., 2016.

A New Reconfigurable Parallel Mechanism for Large Scale Assembly

Harry Anderson[1], Yanqin Zhao[1,2], Yan Jin[1,*] and Colm Higgins[1]

[1] Queen's University Belfast, Belfast BT9 5AH, UK

[2] Tianjin University, Tianjin 300350, China

y.jin@qub.ac.uk

Abstract. New flexible equipment is in urgent needs for the aerospace industry in order to improve machining/assembly efficiency and accuracy. In this paper, a new lockable spherical joint is proposed, which can be used as a revolute joint, a universal joint and a common spherical joint. Based on the proposed lockable spherical joint, a new reconfigurable parallel mechanism (RPM) with large workspace is designed. The RPM has a tripod architecture with lockable joints, and it can be changed to three types of parallel kinematic machines in four motion modes. Mobility analysis based on the screw theory is presented. The new RPM is suitable for many applications, such as machine tools and flexible fixtures.

Keywords: Reconfigurable Parallel Mechanism, Mobility Analysis, Screw Theory.

1   Introduction

Aerospace manufacturing characterized by low volume, large scale and high precision is difficult to automate as there are not much repetitive jobs as in automotive production. Traditional manufacturing equipment used in aerospace is dedicated, expensive and inflexible, and there are still much works manually operated. However, in order to gain competitive edge, aerospace manufacturers are striving to deploy more flexible automation solutions for improving productivity. Robots have been identified as an enabler, though conventional industrial robots are not precise enough to meet aerospace precision requirement. Instead, parallel robots, also called parallel kinematic machines, have shown great potential to provide the solution [1, 2].

Parallel kinematic machines (PKMs) have been applied in the aerospace manufacturing due to their higher stiffness and higher accuracy when compared to serial kinematic machines (SKMs). This has been evidenced by the success applications of Tricept, Z3 head and Exechon in milling and drilling [3-6]. However, aerospace differs from other manufacturing industries in that it consists of large parts in large varieties but in small batches [7, 8]. Furthermore, the existing PKMs used in aerospace manufacturing are mainly used as machine tools, fixed on the ground or simple rails,

which makes the reachable workspace small and working efficiency low. The demand to introduce new flexible technology for large scale assembly in the aerospace becomes very urgent.

One of the most promising areas of research is in reconfigurable machinery. Reconfigurability in manufacturing is a concept which proposes that machinery should be made to be able to adjust and adapt to different tasks quickly and seamlessly. This is all done without the need to change the whole manufacturing system [9]. Any part of the manufacturing system can be targeted and made to be reconfigurable to allow it to work on multiple processes on site and to adjust to future requirements. Usually, the core of reconfigurable machinery is a reconfigurable parallel mechanism (RPM), of which mobility, kinematic stiffness and dynamic performance can be changed by alternating its configurations. There are many methods to achieve reconfigurability, such as modular method [10, 11], constraint-based multi-mode method [12, 13], metamorphic joints/links method [14, 15], and lockable joints method [16]. Among of them, the lockable joints/links method is easy to realize. Palpacelli et al [17-19] proposed a lockable spherical joint, which can be used as a spherical joint, a universal joint, and a revolute joint. However, not all the three revolute joints can be lockable.

To meet different requirements in industrial area, many types of RPMs are proposed. Huang et al [20] proposed a novel RPM based on the spatial multiloop overconstrained mechanism, of which the configuration can be changed by driving a low DOF over-constrained mechanism. It is noted that mobility ability of the proposed RPM keeps unchanged, but its performance can be changed by changing structural parameters. To explore capability in un-established environments, Camacho-Arreguin et al [21] proposed a novel class of RPMs, which can be converted into four types of parallel mechanisms by changing the connection between the platform and limbs. The proposed novel class of RPMs owns good flexibility. However, the aerospace demands large scale assembly besides flexibility in machining. Thus, inspired by the scalable modular multi-agent robotic system for fine manipulation over large workspace [22, 23], a new reconfigurable parallel machine (RPM) is presented, which will provide an alternative solution to the traditional machining technology. A lockable spherical joint is presented, which can be regarded as three revolute joints. Each revolute joint can be lockable. Therefore, the lockable spherical joint can be used as a traditional spherical joint, a universal joint and a revolute joint. The proposed spherical joint enables the new RPM to be converted to three types of parallel kinematic machines in four motion modes. The proposed RPM can translate and rotate in/about three directions, which can meet the requirement of 5-dof machining mobility.

The paper is organized as follows. The new RPM is described in Section 2, followed by mobility analysis in Section 3. Finally, conclusions are drawn in Section 4.

2 Description of a new reconfigurable parallel mechanism

A new RPM with large workspace is shown in Fig. 1. The RPM mainly consists of three limbs and one moving platform. Each limb is actuated by a mobile agent mounted on the guideway. As shown in Fig. 2, the guideway system consists of solid

rail sections with a spur rack and slider rails on either side. In order to avoid the use of batteries and power cables, the guideway system has an embedded power line system with which the mobile actuator can use copper brushes to obtain power. The mobile agent is mainly composed of driven motors, sliders, spacers and copper brushes. Details of guideway and mobile agents can be referred to [22,23].
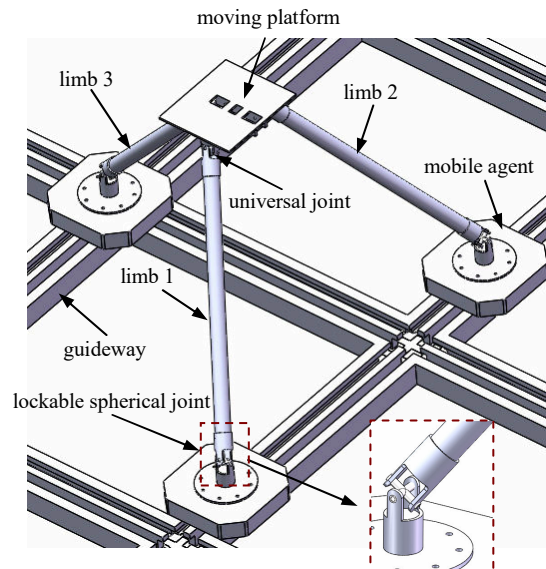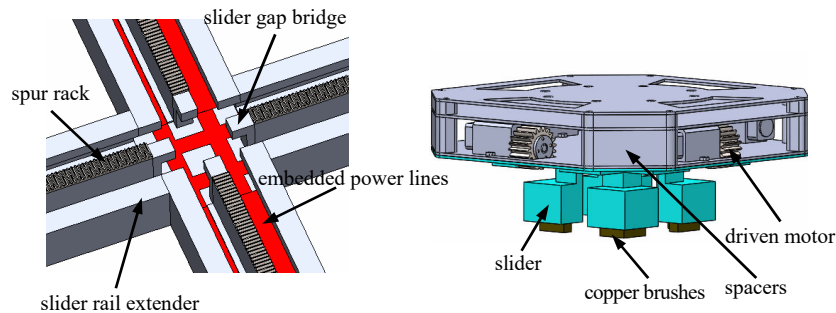

Fig. 1. 3D model of the RPM.

Fig. 2. 3D model of the guideway and mobile agent.

The limb body is connected to the mobile agent by a lockable spherical joint while connected to the moving platform by a universal joint. It is noted that the spherical joint can be decomposed as three orthogonal revolute joints, which are lockable. The lockable spherical joint is realized by two kinds of lockable mechanisms as depicted in Fig. 3. As shown in Fig. 3, there are three lockable mechanisms, which are mounted on the mobile agent, long axis and limb body. It is noted that lockable

mechanisms in the mobile agent and long axis are the same, which can be locked at any configuration. The lockable mechanism mainly consists of a motor, a lead-screw and a nut. When position of the cross axis is adjusted well, the motor will enable the nut move up. One axis of the spherical joint will be disabled when the nut touches the cross axis with certain pressure. The lockable mechanism in the limb body is very different from that in the mobile agent and long axis. As shown, the lockable mechanism mainly consists of a motor, three bevel gears, two lead-screws and two nuts. When a bevel gear is driven by the motor directly, the other two bevel gears will rotate simultaneously. Then the two nuts will translate along the two lead-screws. Once the two nuts touch the long axis with certain pressure, the revolute joint between the limb body and long axis will be disabled.

It can be found from the above discussion that the proposed lockable joint can be locked in each direction. By locking the lockable mechanisms in different locations, we can get different configurations. Mobility analysis will be conducted in the following.
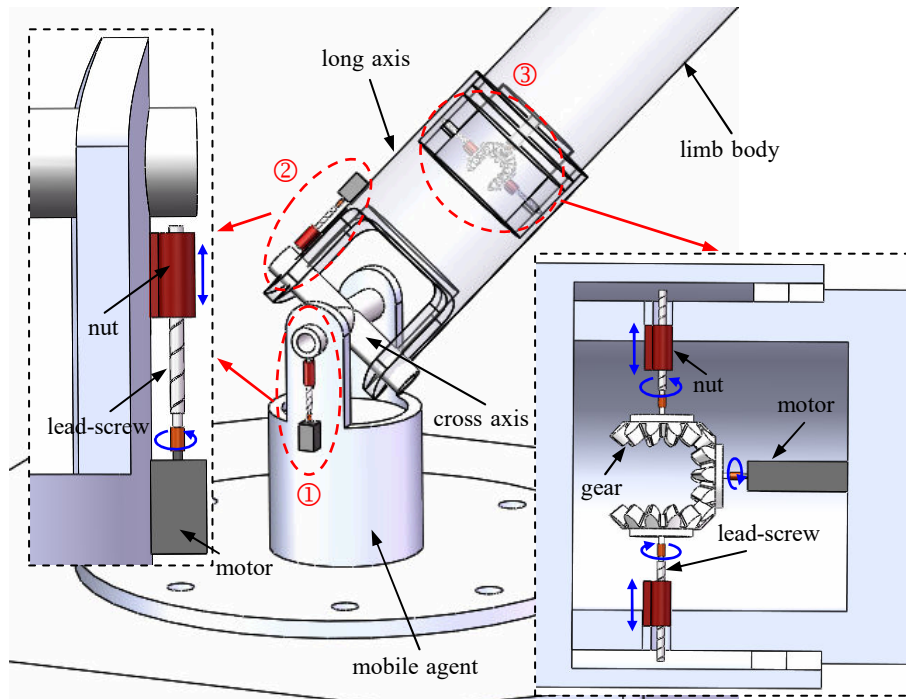
Fig. 3. CAD model of the lockable spherical joint.

3　Degree-of-freedom analysis of the RPM

The schematic diagram of the RPM is depicted in Fig. 4. As demonstrated above, topological structure of each kinematic chain is $\underline{P}SU$, where $\underline{P}$ stands for a linear actuator, S and U represent a spherical joint and a universal joint, respectively. $\boldsymbol{s}_{i1}$ is the

direction of the actuator in the ith kinematic chain, which can be along the x and y axes, respectively. s_{i2}, s_{i3} and s_{i4} are three revolute axes of the spherical joint while s_{i5} and s_{i6} are those of the universal joint in the ith kinematic chain. To make it clear, there exist the following features in the RPM.

- s_{12} and s_{22} are parallel to each other, which are perpendicular to s_{32};
- s_{i3} and s_{i5} are parallel to each other;
- actuator axis s_{11} is parallel to actuator axis s_{21};
- s_{16} and s_{26} are parallel to the v axis while s_{36} is parallel to the u axis.

To facilitate analysis, topological structures of the three kinematic chains are set to be the same. Meanwhile, motion directions of the 1st kinematic chain and the 2nd kinematic chain will keep consistent. This is to say, the 1st kinematic chain and the 2nd kinematic chain will move along the x or y direction simultaneously. However, the 3rd kinematic chain can move in both x and y directions no matter which direction the 1st kinematic chain and the 2nd kinematic chain are in. Therefore, there are 4 motion cases in total. To be specific, topological structure of the RPM becomes a 3-PRS PKM when s_{i2} or s_{i3} are locked. In order to distinguish the two cases, we define the case where s_{i2} is locked as a 3-PRSa PKM and the case where s_{i3} is locked as a 3-PRSb PKM. If the revolute joint at A_i s_{i4} is locked, the topological structure of the RPM is a 3-PUU PKM.
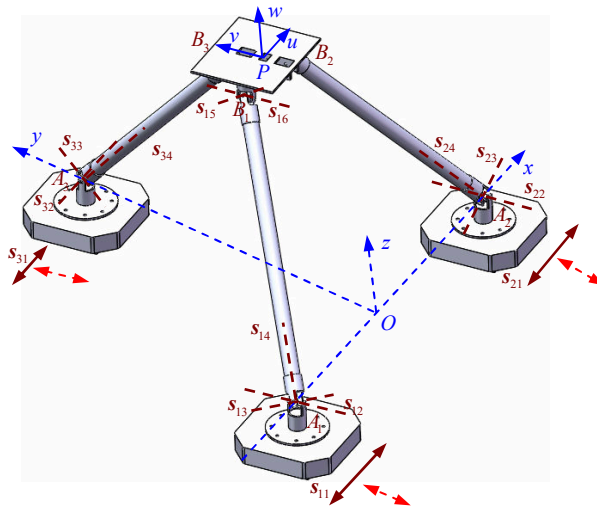
Fig. 4. Schematic diagram of the RPM.

To study the DOF of the mechanism, we can first decompose the mechanism into three kinematic chains connecting the platform with the base and then study the reciprocal screw of each kinematic chain. Finally, derive constraint screws of the platform applied by three kinematic chains, based on which kinematic screws of the platform can be obtained.

6

3.1 Kinematic screws of each kinematic chain

Since the 1st kinematic chain and the 2nd kinematic chain will move in the same direction, we can derive kinematic screws of them by the same procedure.

Schematic diagram and local coordinate system of the kth ($k=1, 2$) kinematic chain is depicted in Fig. 5. The local coordinate system is fixed at point A_k, which is parallel to the global coordinate system $O\text{-}xyz$. Herein, $B_k^{'}$ is the projection of B_k in $x_k z_k$ plane; $A_k B_k^{'}$ is the projective line of $A_k B_k$ in $x_k z_k$ plane; β_k is the angle from line $A_k B_k^{'}$ to line $A_k B_k$; α_k is the angle from x_k axis to line $A_k B_k^{'}$.

Supposing that the three sliders move in the x direction, the Plücker coordinate of slider A_k is

$$\mathcal{S}_{k1} = \begin{pmatrix} 0 & 0 & 0; & 1 & 0 & 0 \end{pmatrix} \tag{1}$$

The spherical joint at A_k can be regarded as three lockable joints, the individual Plücker coordinates of which can be expressed as

$$\mathcal{S}_{k2} = \begin{pmatrix} 0 & 1 & 0; & 0 & 0 & 0 \end{pmatrix}, \quad \mathcal{S}_{k3} = \begin{pmatrix} \sin\alpha_k & 0 & -\cos\alpha_k; & 0 & 0 & 0 \end{pmatrix} \tag{2}$$

$$\mathcal{S}_{k4} = \begin{pmatrix} \cos\beta_k \cos\alpha_k & \sin\beta_k & \cos\beta_k \sin\alpha_k; & 0 & 0 & 0 \end{pmatrix} \tag{3}$$
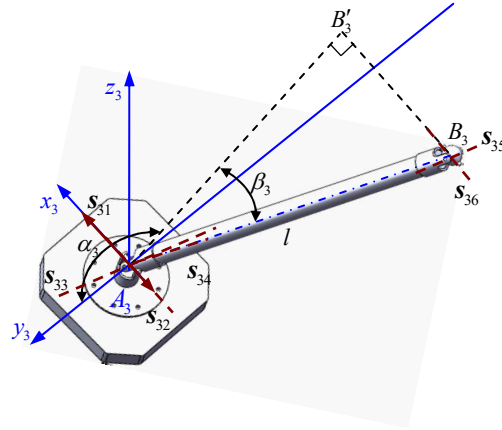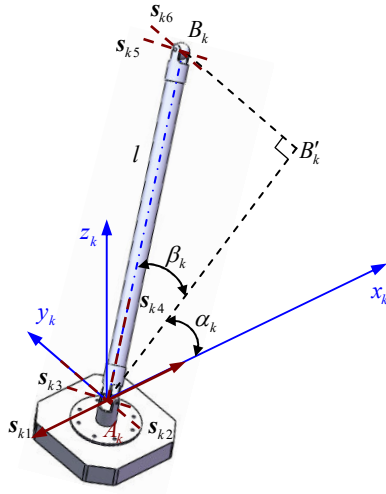
Fig. 5. The kth PSU kinematic chain ($k=1, 2$).　　**Fig. 6.** The 3rd PSU kinematic chain.

The coordinates of B_k are

$$\boldsymbol{r}_{Bk} = \begin{pmatrix} l\cos\beta_k \cos\alpha_k & l\sin\beta_k & l\cos\beta_k \sin\alpha_k \end{pmatrix} \tag{4}$$

where l is the length of each limb.

Then the Plücker coordinates of the two revolute joints at B_k can be denoted as

$$S_{k5} = \left(S_{k5}^1; \quad S_{k5}^0 \right), S_{k6} = \left(S_{k6}^1; \quad S_{k6}^0 \right) \tag{5}$$

where

$$S_{k5}^1 = \left(\sin \alpha_k \quad 0 \quad -\cos \alpha_k \right), S_{k6}^1 = \left(0 \quad 1 \quad 0 \right),$$

$$S_{k5}^0 = r_{Bk} \times S_{k5}^1 = \left(-l \sin \beta_k \cos \alpha_k \quad l \cos \beta_k \quad -l \sin \beta_k \sin \alpha_k \right),$$

$$S_{k6}^0 = r_{Bk} \times S_{k6}^1 = \left(-l \cos \beta_k \sin \alpha_k \quad 0 \quad l \cos \beta_k \cos \alpha_k \right).$$

Therefore, there exist

$$S_{k5} = \left(\sin \alpha_k \quad 0 \quad -\cos \alpha_k; \quad -l \sin \beta_k \cos \alpha_k \quad l \cos \beta_k \quad -l \sin \beta_k \sin \alpha_k \right) \tag{6}$$

$$S_{k6} = \left(0 \quad 1 \quad 0; \quad -l \cos \beta_k \sin \alpha_k \quad 0 \quad l \cos \beta_k \cos \alpha_k \right) \tag{7}$$

As shown in Fig. 6, the local coordinate system of the 3rd kinematic chain is set at point A_3, which is parallel to the global coordinate system O-xyz. Herein, $B_3^{'}$ is the projection of B_3 in $y_3 z_3$ plane; $A_3 B_3^{'}$ is the projective line of $A_3 B_3$ in $y_3 z_3$ plane; β_3 is the angle from line $A_3 B_3^{'}$ to line $A_3 B_3$; α_3 is the angle from y_3 axis to line $A_3 B_3^{'}$.

The Plücker coordinate of slider A_3 is

$$S_{31} = \left(0 \quad 0 \quad 0; \quad 1 \quad 0 \quad 0 \right) \tag{8}$$

The coordinates of B_3 are

$$r_{B3} = \left(-l \sin \beta_3 \quad l \cos \beta_3 \cos \alpha_3 \quad l \cos \beta_3 \sin \alpha_3 \right) \tag{9}$$

Similarly, the spherical joint A_3 can be divided into three orthogonal revolute joints. The individual Plücker coordinates are

$$S_{32} = \left(1 \quad 0 \quad 0; \quad 0 \quad 0 \quad 0 \right), \quad S_{33} = \left(0 \quad \sin \alpha_3 \quad -\cos \alpha_3; \quad 0 \quad 0 \quad 0 \right) \tag{10}$$

$$S_{34} = \left(-\sin \beta_3 \quad \cos \beta_3 \cos \alpha_3 \quad \cos \beta_3 \sin \alpha_3; \quad 0 \quad 0 \quad 0 \right) \tag{11}$$

Then the Plücker coordinates of the two revolute joints at B_3 can be denoted as

$$S_{35} = \left(S_{35}^1; \quad S_{35}^0 \right), S_{36} = \left(S_{36}^1; \quad S_{36}^0 \right) \tag{12}$$

where

$$S_{35}^1 = \left(0 \quad \sin \alpha_3 \quad -\cos \alpha_3 \right), S_{36}^1 = \left(1 \quad 0 \quad 0 \right),$$

$$S_{35}^0 = r_{B3} \times S_{35}^1 = \left(-l \cos \beta_3 \quad -l \sin \beta_3 \cos \alpha_3 \quad -l \sin \beta_3 \sin \alpha_3 \right),$$

$$S_{36}^0 = r_{B3} \times S_{36}^1 = \left(0 \quad l \cos \beta_3 \sin \alpha_3 \quad -l \cos \beta_3 \cos \alpha_3 \right).$$

Therefore, the Plücker coordinates of the two revolute joints at B_3 can be expressed as

8

$$\mathcal{S}_{35} = \begin{pmatrix} 0 & \sin\alpha_3 & -\cos\alpha_3; & -l\cos\beta_3 & -l\sin\beta_3\cos\alpha_3 & -l\sin\beta_3\sin\alpha_3 \end{pmatrix} \quad (13)$$

$$\mathcal{S}_{36} = \begin{pmatrix} 1 & 0 & 0; & 0 & l\cos\beta_3\sin\alpha_3 & -l\cos\beta_3\cos\alpha_3 \end{pmatrix} \quad (14)$$

Based on the discussions above, the followings will be analyzed.

3.2 Degree-of-freedom analysis of the 3-P̲UU PKM

By locking s_{i4}, the kinematic screws of the limb k and limb 3 can expressed as

$$\mathcal{S}_{A_k B_k} = \begin{bmatrix} \mathcal{S}_{k1} \\ \mathcal{S}_{k2} \\ \mathcal{S}_{k3} \\ \mathcal{S}_{k5} \\ \mathcal{S}_{k6} \end{bmatrix}, (k=1,2), \mathcal{S}_{A_3 B_3} = \begin{bmatrix} \mathcal{S}_{31} \\ \mathcal{S}_{32} \\ \mathcal{S}_{33} \\ \mathcal{S}_{35} \\ \mathcal{S}_{36} \end{bmatrix} \quad (15)$$

The reciprocal screws of the three kinematic chains can be derived as

$$\mathcal{S}^r_{A_k B_k} = \begin{pmatrix} 0 & 0 & 0; & \cos\alpha_k & 0 & \sin\alpha_k \end{pmatrix}, \mathcal{S}^r_{A_3 B_3} = \begin{pmatrix} 0 & 0 & 0; & 0 & \cos\alpha_3 & \sin\alpha_3 \end{pmatrix} \quad (16)$$

Therefore, the above three constraint screws applying at the platform can be expressed in the global coordinate system as

$$\mathcal{S}^r_{\text{Platform}} = \begin{bmatrix} \mathcal{S}^r_{A_1 B_1} \\ \mathcal{S}^r_{A_2 B_2} \\ \mathcal{S}^r_{A_3 B_3} \end{bmatrix} \quad (17)$$

Considering the general case where dimension of $\mathcal{S}^r_{\text{Platform}}$ is 3, kinematic screws of the platform can be derived

$$\mathcal{S}_{\text{Platform}} = \begin{cases} \begin{pmatrix} 0 & 0 & 0; & 1 & 0 & 0 \end{pmatrix} \\ \begin{pmatrix} 0 & 0 & 0; & 0 & 1 & 0 \end{pmatrix} \\ \begin{pmatrix} 0 & 0 & 0; & 0 & 0 & 1 \end{pmatrix} \end{cases} \quad (18)$$

As can be seen from Eq. (18), the manipulator can achieve three translations in x, y and z axes. Adopting the same method, we can derive that DOF of 3-P̲UU in all the cases is 3, including translating in x, y and z axes.

For content limitation, only the 3-P̲UU PKM is taken as example. Based on the above analysis, degree-of-freedom of the RPM is listed in Table 1. As can be seen from Table 1, by locking different locked joints, the RPM can realize translation and rotation in/about three axes. Therefore, the RPM can be used as both positional and orientational PKMs with the same set of actuators.

<div align="center">Table 1. Degree-of-freedom of the RPM.</div>

Type	Locked joints	Case 1
		$s_{11}//s_{21}//x$
		$s_{31}//x$
			Case 2
			$s_{11}//s_{21}//x$
			$s_{31}//y$
				Case 3
				$s_{11}//s_{21}//y$
				$s_{31}//y$
					Case 4
					$s_{11}//s_{21}//y$
					$s_{31}//x$

3-<u>P</u>RSa	s_{i2} is locked	translation in x, rotation about x and z	rotation about x, y and z	translation in y, rotation about y and z	rotation about x, y and z
3-<u>P</u>RSb	s_{i3} is locked	translation in x, rotation about x and y	translation in z, rotation about x and y	translation in y, rotation about x and z	rotation about x, y and z
3-<u>P</u>UU	s_{i4} is locked	translation in x, y and z	translation in x, y and z	translation in x, y and z	translation in x, y and z

4   Conclusion

A new reconfigurable parallel manipulator is proposed in this paper. By locking/unlocking corresponding lockable mechanisms, the RPM can be changed into three topological structures, each of which has four motion modes. Mobility analysis shows that the RPM have 5-axis machining capability, which can be used as machine tool and flexible fixtures. Workspace and reconfiguration strategy of the RPM will be studied thoroughly in the near future as well as, error analysis.

References

1. Jin, Y., Lian, B., Price, M., Sun, T., Song, Y.: QrPara: A new reconfigurable parallel manipulator with 5-axis capability. In: Advances in Reconfigurable Mechanisms and Robots, pp. 247-258. Springer, Beijing (2015).
2. Dong, C.L., Liu, H.T., Yue, W., Huang, T.: Stiffness modeling and analysis of a novel 5-DOF hybrid robot. Mechanism and Machine Theory 125, 80-93 (2018).
3. Dong, C.L., Liu, H.T., Huang, T., Chetwynd, D.G.: A screw theory-based semi-analytical approach for elastodynamics of the Tricept robot. Journal of Mechanisms and Robotics 11(3), 031005 (2019).
4. Hennes, N, Staimer, D.: Application of PKM in aerospace manufacturing-high performance machining centers ECOSPEED, ECOSPEED-F and ECOLINER. In: Proceedings of the 4th Chemnitz parallel kinematics seminar, pp. 557-577. 2004
5. Zhang, J., Zhao, Y.Q., Jin, Y.: Kinetostatic-model-based stiffness analysis of Exechon PKM. Robotics and Computer-Integrated Manufacturing 37, 208-220 (2016).

10

6. Bi, Z.M., Jin, Y.: Kinematic modeling of Exechon parallel kinematic machine. Robotics and Computer Integrated Manufacturing 27, 186-193 (2011).

7. Evans, L., Lohse, N., Summers, M.: Intelligent experience based support tools for aerospace manufacturing technology selection. In: 2012 IEEE Aerospace Conference, pp.1-10. IEEE, MT (2012).

8. Aircraft Assembly Manufacturing Improvement Ideas | Chron.com. https://smallbusiness.chron.com/aircraft-assembly-manufacturing-improvement-ideas-81145.html, last accessed 2018/8/24.

9. Rösiö, C., Säfsten, K.: Reconfigurable production system design – theoretical and practical challenges. Journal of Manufacturing Technology Management 24(7), 998-1018 (2013).

10. Yang, G., Chen, I.M., Lim, W.K., Yeo, S.H.: Kinematic design of modular reconfigurable in-parallel robots. Advanced Robotics 10, 83-89 (2001).

11. Bi, Z.M.: Development and control of a 5-axis reconfigurable machine tool. Journal of Robotics 2011, 583072 (2011).

12. Kong, X. Gosselin C.M., Richard P.L.: Type synthesis of parallel mechanisms with multiple operation modes. ASME Journal of Mechanical Design 129, 595-601 (2007).

13. Kong, X.: Type synthesis of 3-dof parallel manipulators with both a planar operation mode and a spatial translational operation mode. Journal of Mechanisms and Robotics 5, 041015 (2013).

14. Gan, D.M., Dai, J.S., Liao, Q.Z.: Constraint analysis on mobility change of a novel metamorphic parallel mechanism. Mechanism and Machine Theory 45(12), 1864-1876 (2010).

15. Zhang, K.T., Dai, J.S., Fang, Y.F.: Topology and constraint analysis of phase change in the metamorphic chain and its evolved mechanism. ASME Journal of Mechanical Design 132(12), 121001 (2010).

16. Moosavian, A., Xi, F.J.: Design and analysis of reconfigurable parallel robots with enhanced stiffness. Mechanism and Machine Theory 77, 92-110 (2014).

17. Palpacelli, M., Carbonari, L., Palmieri, G.: A lockable spherical joint for robotic applications. In: 2014 IEEE/ASME 10th International Conference on Mechatronic and Embedded Systems and Applications (MESA), pp. 1-6. IEEE, Senigallia (2014).

18. Palpacelli, M.C., Carbonari, L., Palmieri, G., Callegari, M.: Analysis and design of a reconfigurable 3-DoF parallel manipulator for multimodal tasks. IEEE/ASME Transactions on Mechatronics 20(4), 1975-1985 (2014).

19. Palpacelli, M.C., Carbonari, L., Palmieri, G.: Details on the design of a lockable spherical joint for robotic applications. Journal of Intelligent and Robotic Systems 81(2), 169-179 (2016).

20. Huang, G., Zhang, D., Zou, Q.: Neural network and performance analysis for a novel reconfigurable parallel manipulator based on the spatial multiloop overconstrained mechanism. International Journal of Aerospace Engineering 2020, 8878058 (2020).

21. Camacho-Arreguin, J., Wang, M., Dong, X., Axinte, D.: A novel class of reconfigurable parallel kinematic manipulators: Concepts and Fourier-based singularity analysis. Mechanism and Machine Theory 153, 103993 (2020).

22. Tavakoli, M., Viegas, C., Sgrigna, L., De Almeida, A.T.: Scala: Scalable modular rail based multi-agent robotic system for fine manipulation over large workspaces. Journal of Intelligent and Robotic Systems 89(3-4), 421-438 (2018).

23. Viegas, C., Tavakoli, M., Lopes, P., Dessi, R., De Almeida, A.T.: SCALA-a scalable rail-based multirobot system for large space automation: design and development. IEEE/ASME Trans. Mechatronics 22, 2208-2217 (2017).

Pseudo rigid body model for nonlinear folding contact-aided compliant mechanism

Angela Nastevska[1][0000-0002-2540-6950] , Brianne Hargrove[2], Mary Frecker[2] and Jovana Jovanova[3][0000-0001-8347-6386]

[1] Kentaur-Impex, Str. 516 no.1, Skopje, Republic of North Macedonia
[2] Penn State University, State College, PA 16801, United States
[3] Delft University of Technology, Mekelweg 5, 2628 CD Delft, Netherlands
`j.jovanova@tudelft.nl`

Abstract. Folding contact-aided compliant mechanisms have the potential for innovative designs tailored for specific applications such as energy absorption, shape morphing, or stress relief. The tailorability relies on multiple variables defining the geometry and superelasticity of the material. The combined effort of the geometry and superelasticity can emphasize certain features in the design, that individually would not be possible. Folding as a concept is very important in origami engineering and requires careful choice in the design variables when it comes to dimensions and material properties. Using finite element analyses for the folding at the level of unit cell as well as the overall structure design has shown to be cumbersome and computationally expensive. Therefore, in this work a segmented pseudo rigid body model that captures the high level of flexibility and the superelasticity of the material is developed. By increasing the number of segments, the model allows the structure to undergo large deformations. The superelastic behavior is introduced with e non-liner function based on the material model. The results from the segmented model are compared with numerical results of the folding contact-aided compliant mechanism.

Keywords: Cellular contact-aided compliant mechanisms, pseudo rigid body model, nonlinear materials, NiTi, superelasticity

1   Introduction

Compliant Mechanisms (CMs) use deformation of flexible members to transform force, motion, and energy. Contact-aided compliant mechanisms are a special class of CMs that incorporate contact surface(s) for non-smooth path generation or tailoring nonlinear structural stiffness [1–5]. Our research group has developed metamaterial-like arrays of contact-aided compliant mechanisms called cellular contact-aided compliant mechanisms (C3M). C3M have been shown to provide improvements over their non-contact counterparts for applications like stress relief [6–8] and energy absorption [9], [10]. We have also demonstrated the benefits of using superelastic and functionally graded materials in C3M in terms of energy absorption [10, 11].

In the literature, various methods have been proposed to model and design CMs under large deformations. Recent developments in topology optimization have used hyperelastic or non-Hookean materials to model the geometric nonlinearity and inelastic behavior of CMs through finite element analysis (FEA) [12–14]. Cellular structures comprised of CMs unit cells have been optimized for a desired compliance with the assumption of a linear displacement profile [15]. There are also FEA models that simulate the nonlinear deflection of compliant beam elements in bending considering Hookean material behavior [16].

Pseudo rigid body models (PRBM) approximate a compliant mechanism with rigid links and torsional springs, and are widely used to account for large deformations in compliant mechanisms, cf. [17]. However, PRBM have been developed only for linear materials. PRBM have been used to model contact-aided compliant mechanisms with nonlinear deflection via contact-aided linear-elastic beams [18]. Using beam theory, analytical and numerical models have demonstrated the selective compliance of curved flexure hinges [19]. However, this approach has considered linear elastic materials under small deformation. Modeling both geometric and material sources of nonlinearity in compliant mechanisms without the use of FEA has yet to be explored.

A particular C3M design consisting of a semicircular arc and contact surface (Fig. 1) was introduced by our group and investigated for large scale shape change applications [20]. This design is called a "folding C3M" due to its similarity to a compliant hinge and ability to experience large folding-like deformations. The design approach relied on finite element analysis to account for both material nonlinearity due to superelasticity and geometric nonlinearity due to large deformations. Parameter variation studies showed that multiple folding C3M units in a metamaterial array improve performance, as does the superelasticty of NiTi material.

When designing the folding C3M, systematic optimization would require many successive finite element analyses, which can become cumbersome and computationally expensive, even when considering only a single unit cell. We seek to address this problem by developing a pseudo rigid body model for the folding C3M which can be computed quickly, facilitating future design optimization. In this paper we propose a method to account for material nonlinearity introduced by superelasticity, while also accounting for geometric nonlinearity introduced by large deformation, in a PRBM of the folding C3M. To the authors' knowledge, there has not been prior work accounting for nonlinear material behavior in PRBM of compliant mechanisms.

The remainder of the paper is organized as follows. First, the folding C3M design is introduced, and the parametric design and the nonlinear stiffness of the cell are discussed. Next, the pseudo rigid body model is described, and the segmentation of the model is introduced. The results for the segmented models for linear and nonlinear NiTi materials are then discussed accordingly. The final section concludes the results and proposes future research.

2 Parametric design of folding C3M

The folding C3M exhibits nonlinear stiffness due to the contact, shown in Fig. 1. It is flexible in one direction (marked in blue) and stiff in the opposite direction (marked in red). The higher flexibility in the first direction of loading is due to the circular beam and the higher stiffness in the opposite direction is due to the contact. The folding C3M has been parametrically designed to enable scalability depending on the application.
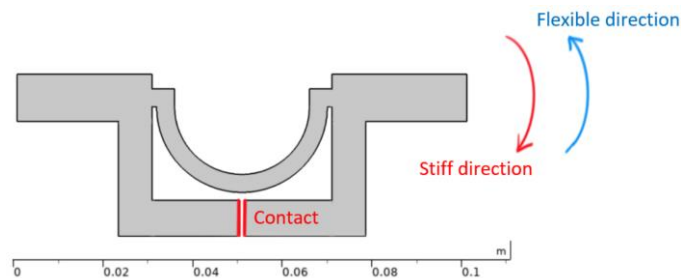

Fig. 1. Design of the folding C3M. Due to the contact one of the folding directions is flexible and the opposite direction is stiff.

The functionality of the folding C3M is shown in Fig. 2. The circular arc acts like a flexure hinge and exhibits large deformation and relatively low stiffness. In the opposite direction of loading, contact is established, and the deformation is constrained. Additionally, after the contact is established the stiffness increases, indicated by the change in slope of the curve pictured in Fig. 2. The results shown on Fig. 2. are for steel AISI 4340 with an out of plane thickness of 1m. Due to the nonlinear stiffness the folding mechanism can be tailored for applications such as shape morphing with large deformations and/or strain energy absorption due to the contact.
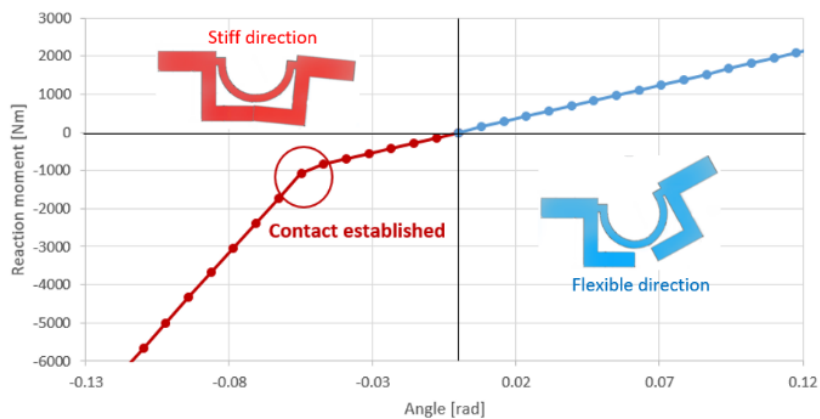
Fig. 2. Loading of folding C3M with an out of plane thickness of 1m made of steel AISI 4340. The nonlinear stiffness characteristic shows the flexibility in one direction and stiffness once the contact is established.

3 Segmented PRBM of folding C3M

The PRBM is a modeling method for simplifying the analysis of compliant mechanisms with nonlinear deflections. The method uses rigid links and springs to model flexible segments, which are then used to predict the relationship between loading and deflection. The arc is considered to be a circular beam with an angle of 180 degrees. It is the most flexible part of the folding C3M, therefore it exhibits the most deformation in the entire structure. A PRBM has been developed for a circular arc compliant mechanism with linear materials in [21], and this model is used as a starting point to analyze the deformation. Here we extend this PRBM to account for nonlinear materials and use it in a segmented approach to better capture nonlinear deformations.

The model shown in Fig. 3 consists of two rigid links with lengths γ_1 and γ_2, and two torsional springs with stiffness K_1 and K_2. The angle ψ in the case of the arc is constant at 180 degrees. As the arc is being deformed due to the applied moment M_0, the displacement angles θ_1 and θ_2 increase. The PRBM parameters were estimated in [21] for different angles ψ with the objective to decrease the error between the PRBM and the beam theory model.
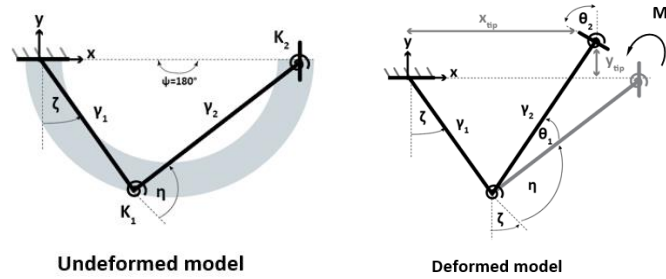
Fig. 3. PRBM for the circular beam loaded with a moment on the tip

By using the optimal values for the PRBM, the deformation of the tip can be estimated. The relationship between the link rotations (θ_1 and θ_2) and the external moment M_o is:

$$\begin{bmatrix} K_1\theta_1 \\ K_2\theta_2 \end{bmatrix} = \begin{bmatrix} 1 \\ 1 \end{bmatrix} [M_o] \tag{1}$$

From Eq. (1) the two angular displacements can be calculated as:

$$\theta_i = \frac{K_i}{M_o} \qquad i = 1,2 \tag{2}$$

where the torsional stiffness K_i is expressed through the values of the nondimensional stiffness coefficients $k_{\theta i}$, where:

$$K_i = k_{\theta i} \frac{EI}{L} \qquad i = 1,2 \tag{3}$$

In Eq. (3) E is the Young's modulus, I is the moment of inertia of the cross section and L is the beam length or the perimeter of the half-circle with radius R.

By combining equations (3) and equations (2) the deformations become:

$$\theta_i = k_{\theta i} \frac{EI}{M_o L} \qquad i = 1,2 \tag{4}$$

In this equation the ratio $\frac{\theta_i}{M_o}$ defined as:

$$\frac{\theta_i}{M_o} = k_{\theta i} \frac{EI}{L} \qquad i = 1,2 \tag{5}$$

shows the relationship between the external input moment M_o and the deformation θ_i.

However, the accuracy of the PRBM is not sufficient for the large deformations exploited in the folding C3M when using only one PRBM to capture the behavior of the arc. We have developed a segmented model where the circular beam is divided into number of continuously connected segments, and the total tip deformation of the arc is a result of the deformations of all the separate segments, i.e., each segment contributes to the final tip position.

The arc is divided into n-segments, each defined by the angle ψ_i as shown in Fig. 4. The segments are assumed to be geometrically identical and the angle of the arc for each segment is $\psi_i = \psi = \pi/n$, where n is the number of segments in the model.
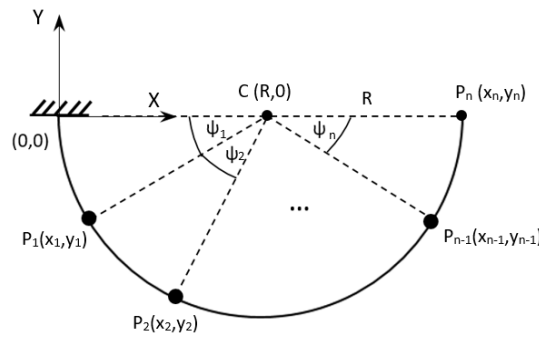
Fig. 4. Segmented circular beam into n number of segments.

Each segment is modelled with a PRBM like the one in Fig. 3, defined by the angle $\psi_i = \pi/n$ with two torsional springs and two rigid links as shown in Fig. 5. The angles ζi and ηi which define the geometry depend on the angle ψ_i and the number of segments.
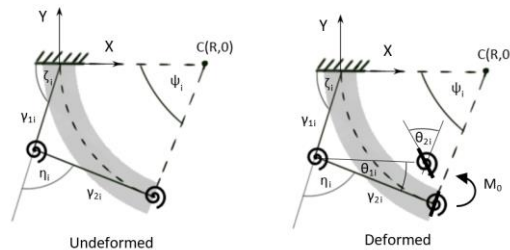
Fig. 5. PRBM for each of the segments

The deformation of the end of each segment is calculated locally as:

$$x_{local,i} = [\gamma_{1i} \sin \zeta_i + \gamma_{2i} \sin(\zeta_i + \eta_i + \theta_{1i})] \cdot \frac{L}{n} \qquad i = 1,2,\ldots,n \qquad (6)$$

$$y_{local,i} = [-\gamma_{1i} \cos \zeta_i - \gamma_{2i} \cos(\zeta_i + \eta_i + \theta_{1i})] \cdot \frac{L}{n} \qquad i = 1,2,\ldots,n \qquad (7)$$

where the angles θ_{1i} and θ_{2i} are the angular deformations of the two torsional springs of the PRBM Eq. (2). The torsional stiffness of the two springs is defined with the nondimensional stiffness coefficients defined in Eq. (3).

The coordinates of the tip point of the arc are the coordinates of the end point of the nth segment in the global coordinate system (X, Y) as shown in Fig. 6a. The deformation of each segment is calculated in its local coordinate system ($x_{local,i}$, $y_{local,i}$). Then each segment is rotated with respect to the previous one in the global coordinate system. The local coordinate system of the first segment is the same as the global one, and the local coordinate systems of the other segments are rotated with respect to this coordinate system as shown in Fig. 6 (a). Additional to the rotation, the local tip deformation of each segment is also translated to the end point of the previous segment after the deformation in the global coordinate system, as shown in Fig. 6 (b).
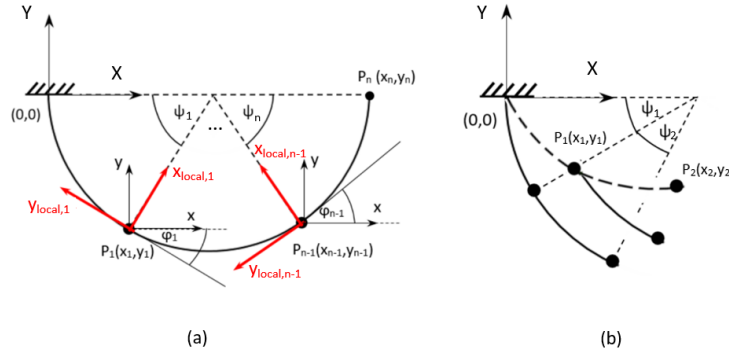
Fig. 6. Local deformation of connected segments

The rotation of the ith segment to the global coordinate system can be calculated using Eq. 8, where it is rotated in the clockwise direction by the angle α_{i-1}.

$$\alpha_{i-1} = -\frac{\pi}{2} - \varphi_{i-1} \qquad i = 1,2,\ldots,n \qquad (8)$$

The angle φ_{i-1} is defined as the tangent angle of the segment curvature at the point P_{i-1}.

$$\varphi_{i-1} = \tan^{-1}\left(\frac{df}{dx}\bigg|_{x_{i-1}}\right) \qquad i = 1,2,\ldots,n \qquad (9)$$

The curvature function $f(x)$ is defined as a semicircle with radius R and center at the point (R,0).

$$f(x) = -\sqrt{R^2 - (x - R)^2} \qquad (10)$$

The orientation of the segments dictates the contribution to the final tip displacement as shown in Fig. 7.
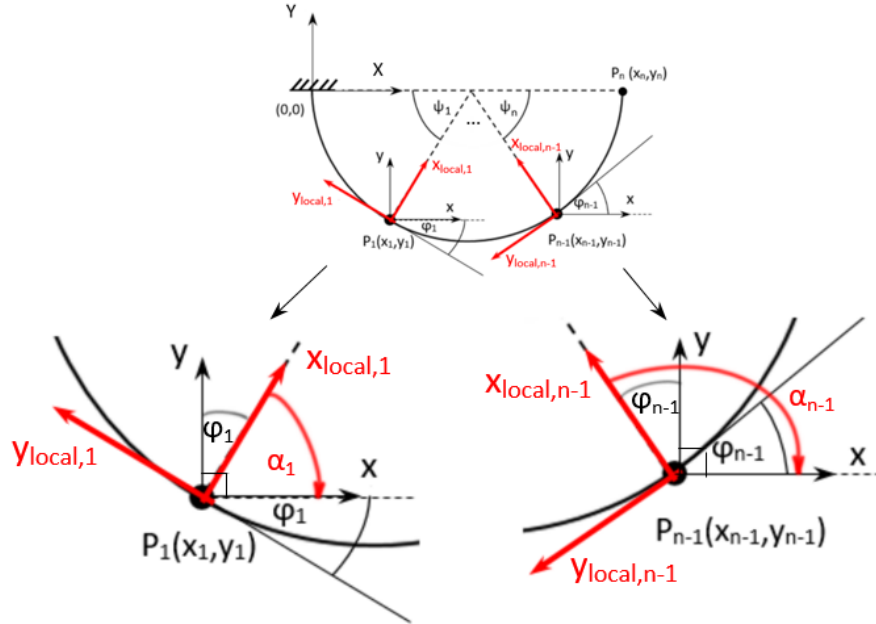

Fig. 7. Segment deformation coordinate transformation

The coordinates of the end point are a sum of the positions of all the other end points in the global coordinate system.

$$x_{tip} = \sum_{i=1}^{n} x_{global,i} \quad i = 1,2,\ldots,n \tag{11}$$

$$y_{tip} = \sum_{i=1}^{n} y_{global,i} \quad i = 1,2,\ldots,n \tag{12}$$

which means that the tip final equations are:

$$x_{tip} = x_{local,1} + \sum_{i=2}^{n} x_{local,i} \cdot \cos\left(\alpha_{i-1} + (i-1) \cdot (-\theta_{1i} - \theta_{2i})\right) + ylocal,_i \cdot \sin\left(\alpha_{i-1} + (i-1) \cdot (-\theta_{1i} - \theta_{2i})\right) \tag{13}$$

$$y_{tip} = y_{local,1} + \sum_{i=2}^{n} -x_{local,i} \cdot \sin\left(\alpha_{i-1} + (i-1) \cdot (-\theta_{1i} - \theta_{2i})\right) + y_{local,i} \cdot \cos\left(\alpha_{i-1} + (i-1) \cdot (-\theta_{1i} - \theta_{2i})\right) \tag{14}$$

Since the (x_i, y_i) values are dimensionless, they need be scaled by the length of the arc L which is the circumference of the half-circle defined by its radius R ($L = R\pi$). The difference in the results for the baseline PRBM with one segment and the segmented model are described in the next section.

4   Segmented PRBM for linear material

The effect of segmentation is explored by considering various numbers of segments and external moment, assuming linear material behavior. The tip displacement was compared with a FEA model solved in COMSOL Multiphysics. The structural mechanics module was used to model the mechanism with the nonlinear structural material module implemented with the fully coupled approach. Automatic physics-controlled mesh was implemented with maximum element size of 3.8E-4 m and minimum element size of 7.6E-7 m. The FEA model is analyzed in 2D with an out of plane thickness of 1m, and the geometric nonlinearity is included. The inner radius of the arc is 15 mm and the thickness is 4 mm. The material is linear with Young's modulus of 70 GPa, and the rectangular cross section has dimensions 1m x 0.004m. The arc in COMSOL Multiphysics is subjected to prescribed rotation at the free end varying from 0 to 2π radians. The reaction moment predicted in COMSOL Multiphysics that correspondents to these angles is an input to the PRBM in Matlab. The values calculated for the loading moment range from 0 to 43449 Nm for this case. At the tip the neutral axis is chosen as the location of interest. Therefore, the radius is set to 17mm and the length of the arc is 0.05 m in the PRBM. Physically the maximum possible rotation of the tip is π radians as shown in Fig. 8. However, for the purpose of the further analysis the model is deformed until 2π rotation and self-collision is not considered.
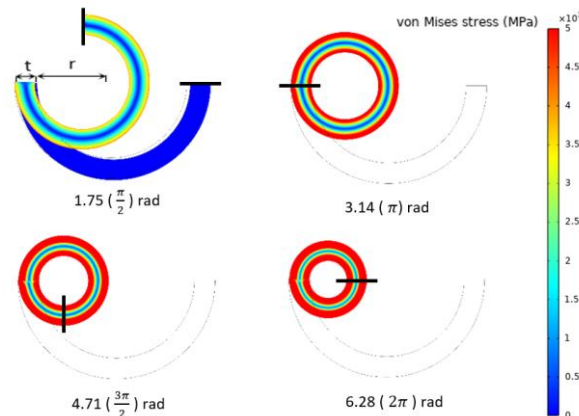
Fig. 8. Position of the tip and stress distribution for different levels of deformations of the folding C3M

In Fig. 9 the position of the tip in the global coordinate system for different number of segments in the segments PRBM is presented, along with the FEA predictions. It is noticeable that the one segment PRBM marked in orange in Fig. 9 overestimates the tip deflection compared to the FEA model. As the number of segments increases the segmented PRBM of the tip deflection is more accurate. The impact of the number of segments on the accuracy of the model depends on the level of deformation. For lower deformations even the model with one segment agrees well with the FEA results. As the deformation increases beyond $\pi/2$ radians the distinction between the baseline

PRBM and the segmented PRBM increases. Although the higher number of segments are more accurate in predicting the position of the tip point of the arc there is not a big difference between different number of segments until the physical maximum deformation of π radians.

After this level of deformation is reached and the deformation approaches the level of 2π radians the results for the higher number of segments changes, especially for the model with two segments which overestimates the tip position for deformation higher that π radians. As the deformation approaches 2π radians the plot shows that by increasing the number of segments the accuracy of the model increases as well. This means that for the scale and rotation needed for folding (the maximal physical deformation of π radians), the segmented model with two segments is a good approximation of the tip deflection.
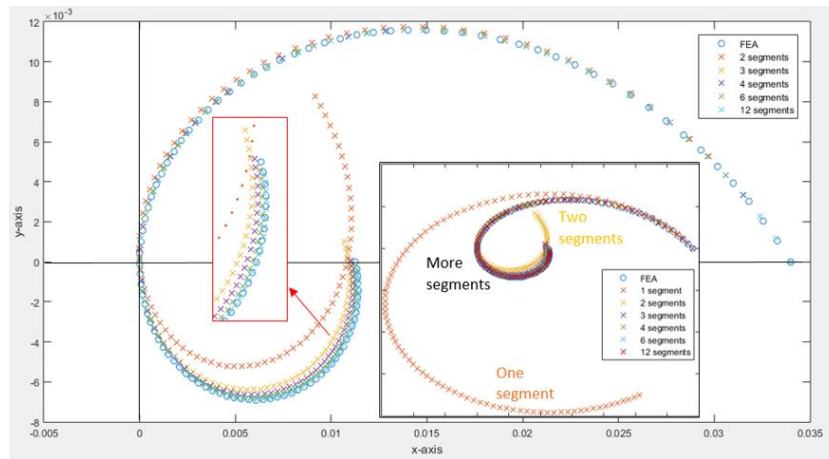
Fig. 9. Segmented model with different number of segments (1 to 12) and FEA tip deflection.

The error between the FEA model and the segmented PRBM with different number of segments is represented in Fig. 10. The error is defined as the distance between the position of the tip measured in the FEA and calculated with the PRBM. If the error between these points is zero, the point from the FEA and PRBM overlap. It can be observed that the results can be divided in three approximate regions. From zero to about 0.5 rad, all of the models, even the one with a single segment, exhibit low error in comparison to the FEA results. As the deformation increases the error of the baseline PRBM with one segment increases drastically. The segmented PRBMs experience an increase in error, with a maximum around 2 rad, after which the error decreases. The error is almost the same for all of the segmented models until the third region of the plot, around 4 rad, where a visible difference in the segmented models is evident, especially for the model with two segments. In this zone the error of the PRBM with two segments is much higher than the other models and approximately linearly increases with the increase of deformation. The error decreases as the number of segments increases although the difference between the PRBMs with more than three segments is lower compared to the model with two segments.
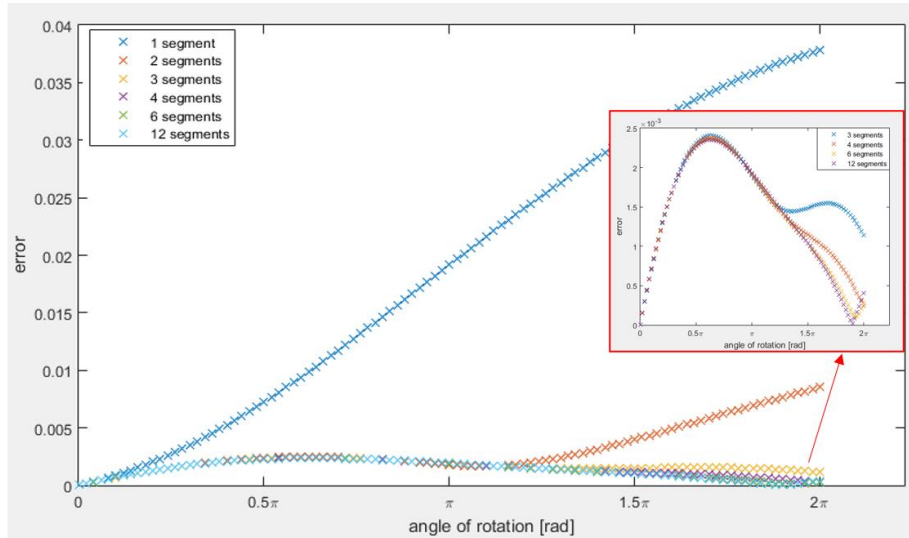
Fig. 10. Error between the FEA numerical results and PRBM for different number of segments.

Mean-squared error (MSE) is calculated over the 2π radian rotation, shown in Table 1.

Table 1. MSE for different segments

Number of segments	MSE
1	5.1145e-04
2	1.4004e-05
3	3.0275e-06
4	2.5778e-06
6	2.4880 e-06
12	2.4839 e-06

The MSE is one order lower for the model with two segments. Additionally, the error decreases as the number of segments increases. The MSE for the models with higher number of segments are two orders lower than the model with one segment.

5   Segmented PRBM for nonlinear material

The segmented PRBM for folding C3Ms has been shown to capture the nonlinearity coming from the large deformations. Another form of nonlinearity beneficial for compliant mechanisms is material nonlinearity. One of the materials that has been used for compliant mechanisms is nickel-titanium (NiTi), a smart material with shape memory effect and superelasticity (SE). The superelastic behavior of NiTi is the one that can be tailored for the benefit of a compliant mechanism design, allowing for up to 10% recoverable elastic deformation due to the phase transformation when the critical stress

is achieved. The multi-linear material model for NiTi developed in [22] is shown in Fig. 11, where is it noticeable that once the critical transformational stress σ_s^{AS} is achieved, the slope of the modulus of elasticity E_{lin} changes to a much lower value denoted with E_{SE}.
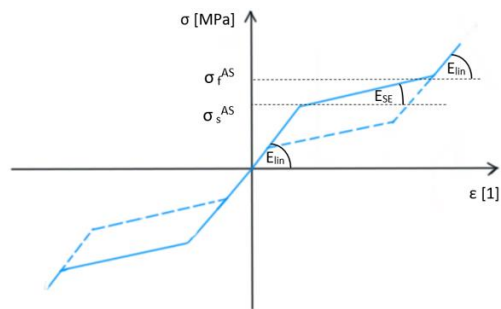
Fig. 11. NiTi material model

To account for the superelastic effect, material nonlinearity must be introduced into the segmented PRBM. In Eq. 4 the angular deformation depends on the moment and the modulus of elasticity E as well. For a linear material E is constant, whereas for the nonlinear model E is a function of the rotation angle. The effective modulus of an arc comprised of superelastic NiTI can be seen in Fig. 12 for a rotation of π radians. Note that this property changes spatially through the thickness.

For the segmented PRBM with nonlinear material, FEA data on effective modulus is used to approximate the nonlinear material behavior. It is assumed that the nonlinear modulus is a function of the stresses based on the material model. Since the stress distribution is not uniform, the average value of the modulus for the whole surface of the arc is used, denoted as the $E_{numerical}$.
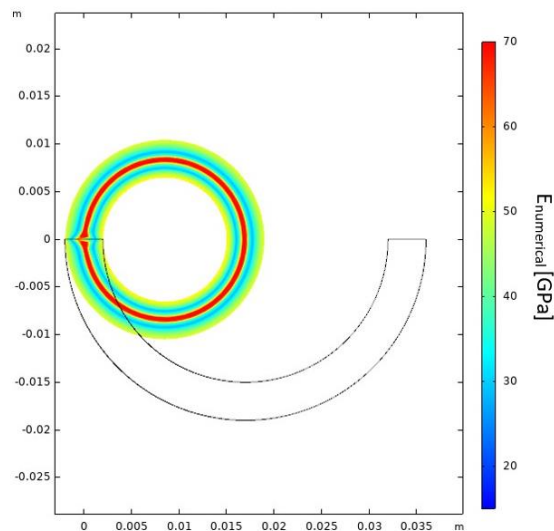
Fig. 12. Spatial distribution of $E_{numerical}$ in COMSOL Multiphysics

The effective modulus of is modelled as nonlinear function, defined in in three zones, based on the superelastic material model. In the first zone the modulus is a constant value E_{lin} until a critical value of the moment M_{cr} is reached, followed by a linearly decreasing modulus $h \cdot E_{lin}$. This decrease reaches a minimum at M_{SE}, after which the modulus adopts a different constant value. This effective modulus of elasticity is represented by Eq. 15 where the value of the modulus for the three previously mentioned zones is defined.

$$E_{eff} = \begin{cases} E_{lin}; for\ M \leq M_{cr} \\ h \cdot E_{lin}; for\ M_{SE} > M > M_{cr} \\ E_{lin} - E_{SE}; for\ M \geq M_{SE} \end{cases} \tag{15}$$

The linear function is defined as:

$$h = \left(1 - \frac{1}{E_{lin} - E_{SE}}\right) \tag{16}$$

M_{cr} and M_{SE} are related with the critical stresses σ_s^{AS} and σ_f^{AS} of the NiTi material model, respectively. The effective modulus functions for two different superelastic materials are shown in Fig. 13. The materials have the same transformation stresses but different values of the two moduli of elasticity. Note that only the loading of the NiTi is considered; the hysteresis that would be present upon unloading is not accounted for in the current approach.
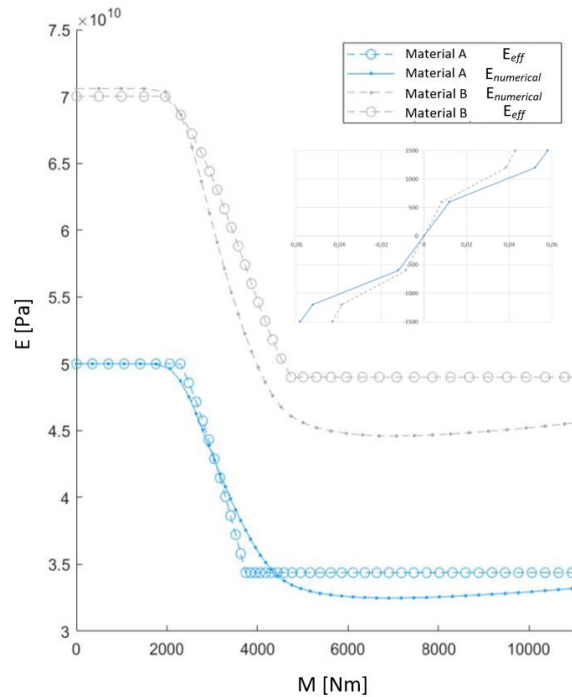
Fig. 13. Model of the nonlinear effective modulus of elasticity for 2 different materials

Fig. 14 shows the results from the nonlinear segmented PRBM for the two materials. The approximation of the nonlinear modulus of elasticity results in satisfactory prediction of the deformation for the two different materials. Additionally, the critical values of the moment are all between the bounds of 2000 and 5000 Nm since all the three curves have the same transformational stresses. Similar to the analysis for the linear material model, the PRBM with one segment has the highest error and the models with segments higher than one exhibit better approximation of the FEA results. Again, the difference between the segmented PRBM results with increasing number of segments is low for the maximal physical deformation. The stress distributions show that for the same deformation, the folding C3M with different superelastic materials exhibit different stresses.
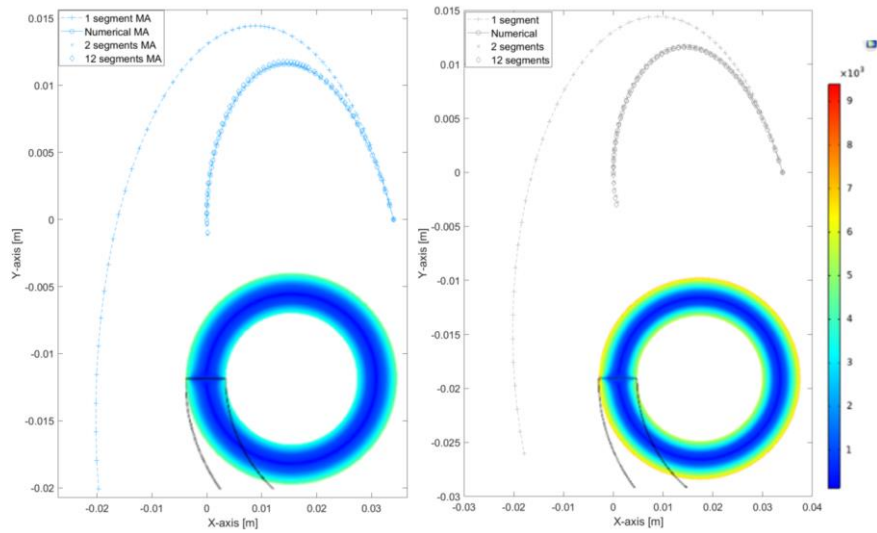
Fig. 14. Segmented model with different number of segments (1, 2 and 12) for the nonlinear functions in Fig 13.

This kind of folding compliant mechanism that can achieve high deformations such as the maximum input rotation of π radians can be beneficial for various origami-inspired and bioinspired structures. Potentially these compliant joints could enable an origami structure to fold from 3D to a 2D structure and vice versa.

In Fig. 15 a potential application of the C3M folding mechanism for a full folding compliant joint in an origami structure is shown. Since the folding C3M analyzed in this paper has the ability to achieve high deformations it could enable the origami structure to achieve a complete fold. Additionally, the shape memory effect of the nonlinear NiTi material implemented in these joints could introduce thermal actuation to enable self-folding origami. The creases need to achieve high rotations in order to achieve the desired fold of the origami structure.
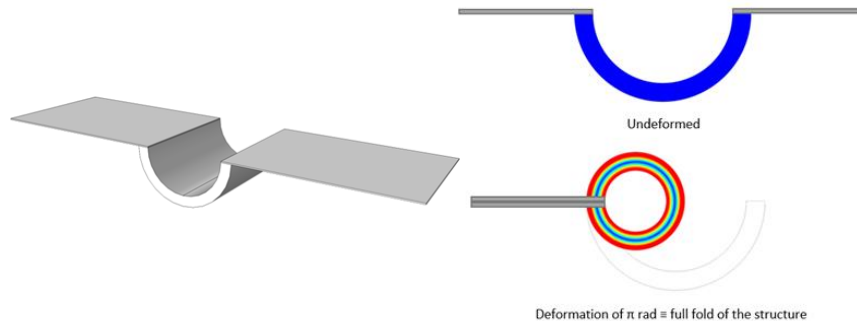
Fig. 15. Joint of an origami structure in 3D, undeformed shape and deformed folding C3M

6 Conclusions

C3Ms have showed great potential in multiple applications including energy absorption and shape morphing. To build on research in this area, a novel design of folding C3M is modelled using nonlinear materials and undergoing large deformations. In this paper a segmented PRBM for a folding C3M is developed by dividing the arc into n number of arcs and making a PRBM for each arc, increasing the overall accuracy of the model. The PRBM is compared to FEA analysis for increasing number of segments. The results show that the error for the PRBM with one segment is the highest, and the error decreases when more segments are introduced. However, the difference between the results for two or more segments is visible only for deformations higher that the maximal expected physical deformation of π radians. This means that for this geometry the segmented model with two segments gives a very good approximation of the tip position. Sensitivity analysis for different values of the radius and thickness of the arc has been carried out. The results show that the model is not sensitive to the radius and thickness of the folding C3M even when they are scaled up with a factor of four. This means that the mechanism can be scaled up or down and tailored to the application needs. The segmented PRB model is then modified to account for a superelastic material. Since the effective elastic modulus depends on the stress, the spatial distribution of this property is not uniform. By approximating the effective modulus with a multi-linear function, the superelastic effect can be adequately captured.

Complex geometry and nonlinear material structures require high amount of computational time if the designs rely only on FEA analysis. Conventional design approaches based on trial and error require a lot of parametric analysis. When the structure undergoes large deformations, nonlinear material and contact, the FEA becomes challenging to solve and time consuming. Introducing this segmented PRBM into optimization is the next step in this research. To capture the effect of the contact member, an additional nonlinear translational spring can be added later to the PRBM. Future work will be focused on design optimization for folding C3M for different applications such as energy absorption, shape morphing, origami engineering, soft grasping.

References

1. N. D. Mankame and G. K. Ananthasuresh, "Synthesis of contact-aided compliant mechanisms for non-smooth path generation," Int. J. Numer. Methods Eng., vol. 69, no. 12, pp. 2564–2605, 2007.
2. N. D. Mankame and G. K. Ananthasuresh, "Topology optimization for synthesis of contact-aided compliant mechanisms using regularized contact modeling," Comput. Struct., vol. 82, no. 15–16, pp. 1267–1290, 2004.
3. J. P. Calogero, M. I. Frecker, Z. Hasnain, and J. E. Hubbard, "Dual optimization of contact-aided compliant mechanisms for passive dynamic shape change," AIAA J., vol. 56, no. 9, pp. 3745–3756, 2018.
4. B. V. S. N. Reddy, S. V. Naik, and A. Saxena, "Systematic synthesis of large displacement contact-aided monolithic compliant mechanisms," J. Mech. Des. Trans. ASME, vol. 134, no. 1, pp. 1–12, 2012.
5. Y. Tummala, A. Wissa, M. Frecker, and J. E. Hubbard, "Design and optimization of a contact-aided compliant mechanism for passive bending," J. Mech. Robot., vol. 6, no. 3, pp. 1–9, 2014.
6. V. Mehta, M. Frecker, and G. A. Lesieutre, "Two-step design of multicontact-aided cellular compliant mechanisms for stress relief," J. Mech. Des. Trans. ASME, vol. 134, no. 12, pp. 1–12, 2012.
7. V. Mehta, M. Frecker, and G. A. Lesieutre, "Stress relief in contact-aided compliant cellular mechanisms," J. Mech. Des. Trans. ASME, vol. 131, no. 9, pp. 0910091–09100911, 2009.
8. S. A. Cirone, G. R. Hayes, B. L. Babcox, M. Frecker, J. H. Adair, and G. A. Lesieutre, "Design of contact-aided compliant cellular mechanisms with curved walls," Artic. J. Intell. Mater. Syst. Struct., vol. 23, no. 16, pp. 1773–1785.
9. J. E. Hyland, M. I. Frecker, and G. A. Lesieutre, "Optimization of honeycomb contact-Aided compliant cellular mechanism for strain energy absorption," in Proceedings of the ASME Design Engineering Technical Conf., 2012, vol. 4, no. PARTS A AND B, pp. 311–320.
10. J. Jovanova, A. Nastevska, and M. Frecker, "Tailoring energy absorption with functional grading of a contact-aided compliant mechanism," Smart Mater. Struct., vol. 28, no. 8, 2019.
11. J. Jovanova, A. Nastevska, and M. Frecker, "Functionally graded cellular contact-aided compliant mechanism for energy absorption," in ASME 2018 Conference on Smart Materials, Adaptive Structures and Intelligent Systems, SMASIS 2018, 2018, vol. 2.
12. P. Kumar, R. A. Sauer, and A. Saxena, "On topology optimization of large deformation contact-aided shape morphing compliant mechanisms," Mech. Mach. Theory, vol. 156, p. 104135, Feb. 2021.
13. L. Liu, J. Xing, Q. Yang, and Y. Luo, "Design of Large-Displacement Compliant Mechanisms by Topology Optimization Incorporating Modified Additive Hyperelasticity Technique," Math. Probl. Eng., vol. 2017, 2017.
14. X. S. Zhang, H. Chi, and Z. Zhao, "Topology optimization of hyperelastic structures with anisotropic fiber reinforcement under large deformations," Comput. Methods Appl. Mech. Eng., vol. 378, p. 113496, May 2021.
15. C. Chu, G. Graf, and D. W. Rosen, "Design for Additive Manufacturing of Cellular Structures," Comput. Aided. Des. Appl., vol. 5, no. 5, pp. 686–696, 2008.
16. A. N. Danun, P. D. Palma, C. Klahn, and M. Meboldt, "Building Block Synthesis of Self-Supported Three-Dimensional Compliant Elements for Metallic Additive Manufacturing," J. Mech. Des. Trans. ASME, vol. 143, no. 5, May 2021.
17. L. L. Howell, Compliant Mechanisms. Wiley, 2001.

18. M. Jin, B. Zhu, J. Mo, Z. Yang, X. Zhang, and L. L. Howell, "A CPRBM-based method for large-deflection analysis of contact-aided compliant mechanisms considering beam-to-beam contacts," Mech. Mach. Theory, vol. 145, p. 103700, Mar. 2020.

19. G. Berselli, F. Parvari Rad, R. Vertechy, and V. Parenti Castelli, "Comparative evaluation of straight and curved beam flexures for selectively compliant mechanisms," in 2013 IEEE/ASME International Conference on Advanced Intelligent Mechatronics: Mechatronics for Human Wellbeing, AIM 2013, 2013, pp. 1761–1766.

20. A. Nastevska and M. Frecker, "Design of Compliant Joints for Large Scale Structures," in ASME Conference on Smart Structures Adaptive Structures and Intelligent Systems, 2020, pp. 1–10.

21. V. K. Venkiteswaran and H. J. Su, "Pseudo-rigid-body models for circular beams under combined tip loads," Mech. Mach. Theory, vol. 106, pp. 80–93, Dec. 2016.

22. F. Auricchio, R. L. Taylor, and J. Lubliner, "SHAPE-MEMORY ALLOYS: macromodelling and numerical simulations of the superelastic behavior Universita' di Roma "Tor Vergata"," Comput. Methods Appl. Mech. Engrg, vol. 146, pp. 281–312, 1997.

Simulation of Scissor-Type Planar Deployable Mechanisms using MeKin2D Subroutines

P. A. Simionescu[0000-0003-0181-7277]

Texas A&M University Corpus Christi, Corpus Christi, TX 78412, USA
pa.simionescu@tamucc.edu

Abstract. Simulations of several linearly, radially, and circularly deployable structures and mechanisms of the scissor type has been performed using the Me-Kin2D package. By calling modular-kinematics subroutines within *do while loops*, complex planar repeatable mechanisms can be simulated easily, and their workspace and other properties assessed.

Keywords: Modular Kinematics, Deployable Structures, Motion Simulation.

1   Introduction

Deployable mechanisms, also known as folding mechanisms, motion structures or deployable structures (Fig. 1), are mechanisms with relatively large number of links and joints which are repeated in a predetermined pattern [1]-[11].

Fig. 1. Examples of scissor-type deployable mechanisms and motion structures.

Although considered tedious to simulate using conventional motion software, many repetitive deployable or foldable mechanisms can be modeled relatively easily using modular kinematic subroutines called inside *do while loops*. In this paper it is shown how the subroutines available in the MeKin2D package [12], [13] can be used to simulate the motion of several planar deployable mechanisms of the scissor type. In these simulations, the input module subroutine(s) are called first, followed by repeatedly calling, inside nested *do while loops*, of expansion module subroutines [14], [15], [16].

The *input module* used in the simulations throughout this paper was the grounded slider **T**, while the *passive modules* used were the **RRR** and **RRT_** dyads - see Fig. 2. In Fig. 2 where an asterisk indicates a potential joint or a powered-joint, while in dashed lines are shown the alternative assembly configurations of the respective dyads.
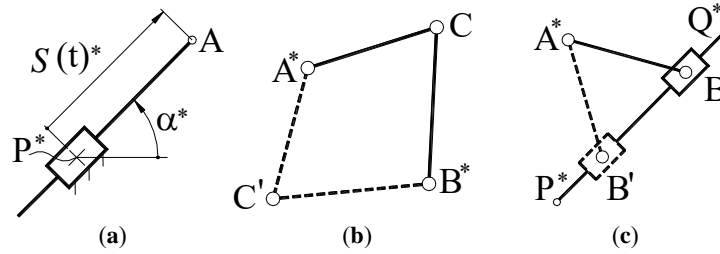
Fig 2. Kinematic modules used in the simulations throughout the paper: (**a**) grounded slider **T**, (**b**) **RRR** dyad, and (**c**) **RRT_** dyad.

(**a**) Given the coordinates x_P and y_P of fixed point P, angle of sliding α and displacement $S(t)$ of the grounded slider **T** in Fig. 3-a, the coordinates of sliding point A are:

$$x_A = x_P + S(t) \cdot cos(\alpha)$$
$$y_A = y_P + S(t) \cdot sin(\alpha) \tag{1}$$

(**b**) Given link lengths AC and BC and the potential-joints coordinates x_A, y_A and x_B, y_B of the **RRR** dyad in Fig. 2-b, the coordinates of joint C are:

$$x_C = x_A + AC \cdot (1 - Q^2)/(1 + Q^2)$$
$$y_C = y_A + 2AC \cdot Q/(1 + Q^2) \tag{2}$$

where

$$Q = (b \pm \sqrt{a^2 + b^2 - c^2})/(a + c)$$
$$a = 2BC \cdot (x_B - x_A)$$
$$b = 2BC \cdot (y_B - y_A)$$
$$c = AC^2 - BC^2 - (x_B - x_A)^2 - (y_B - y_A)^2 \tag{3}$$

(**c**) Given link length AB and the coordinates x_A, y_A, x_P, y_P and x_Q, y_Q of the **RRT_** dyad in Fig. 2-c, the coordinates of joint B are:

$$x_B = x_A + \left(D \cdot d_y \pm sgn(d_y) \cdot d_x \sqrt{AB(d_x^2 + d_y^2) - D}\right)/(d_x{}^2 + d_y{}^2)$$

$$y_B = y_A + \left(-D \cdot d_x \pm |d_y| \sqrt{AB(d_x^2 + d_y^2) - D}\right)/(d_x{}^2 + d_y{}^2) \tag{4}$$

where

$$D = (x_P - x_A)(y_Q - y_A) - (x_Q - x_A)(y_P - y_A)$$
$$d_x = x_Q - x_P \quad \text{and} \quad d_y = y_Q - y_P \tag{5}$$

The double sign ($\pm$) in equations (3) and (4) corresponds to the two assembly modes shown in dashed line in Fig. 2-b and c. The velocity and acceleration equations can be obtained through differentiation of the position equations and are not detailed here.

In the remainder of the paper, the simulation of several scissor-type deployable mechanisms will be presented, accompanied by animations posted on YouTube [17].
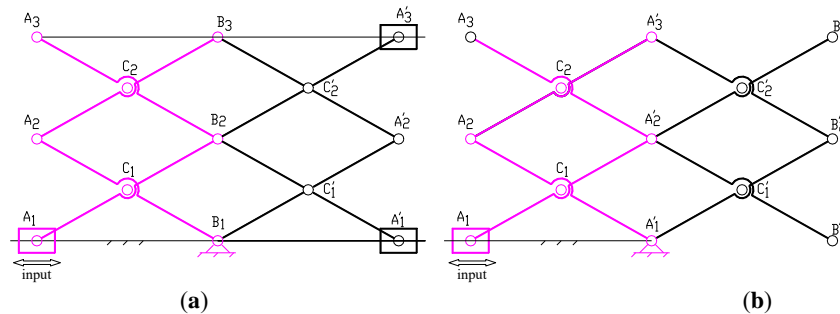
2   Rectilinearly-deployable scissor-type structures

(**a**)   (**b**)

Fig. 3. Rectilinearly-deployable scissor-type motion structures with a grounded slider input modeled (**b**) using **RRR** and **RRT_** dyads and (**a**) using only **RRR** dyads.
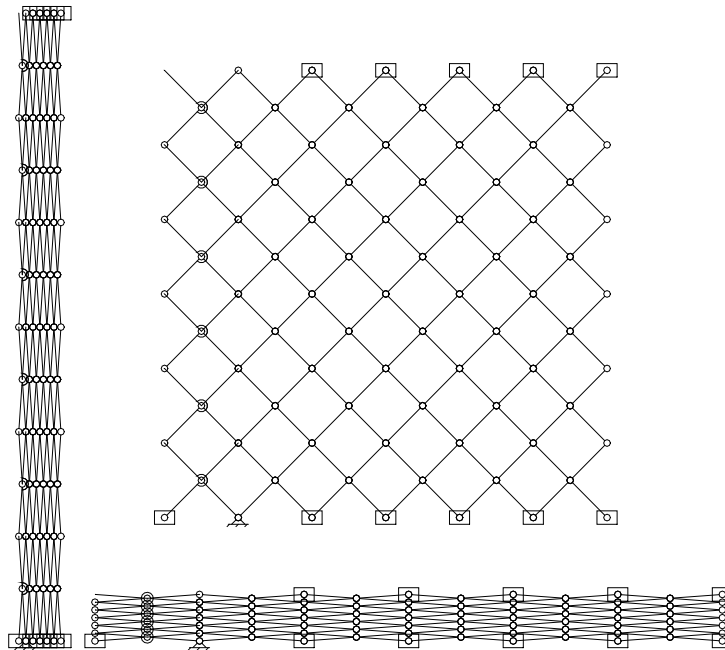
Fig. 4. Deployable scissor structure with 60 cells of the type shown in Fig. 3-a.

Figs. 3 and 4 show two rectilinearly deployable mechanisms of the scissor type, with 4 cells, and the with 60 cells. The motion structure in Fig. 3-a consists of input slider A_1,

amplified with the **RRR** dyad $A_1C_1B_1$. A_2 is offset point of links A_1C_1 and B_2 is offset point of link B_1C_1 of the $A_1C_1B_1$ dyad. The vertical expansion is provided by the **RRR** dyad $A_2B_2C_2$, and of its offset points A_3 and B_3. The horizontal expansion is provided by the **RRR** dyads $B_1C_1'B_2$, $B_2C_2'B_3$ and $C_1'A_2'C_2'$, followed by the **RRT_** dyads $C_1'A_1'$ and $C_2'A_3'$. Line of sliding of the two **RRT_** dyads are A_1B_1 and A_3B_3, respectively. Both the vertical and the horizontal expansions can be programed using *do while loops*, thus allowing for any size lattice to be modeled.

The alternative approach to modeling rectilinearly deployable motion structures like the one in Figs. 3 and 4 is to repeat in the horizontal direction the same vertical expansion with two offset points per dyad as shown in Fig. 3-b.

3 Radially deployable scissor-type structures

Figs. 5, 6 and 7 show radially deployable structures of the Hoberman type. The three-cell motion structure in Fig. 5-top has been simulated similarly to the rectilinearly deployable structure in Fig. 3, starting with a single-row deployable mechanism $A_1C_1B_1$-$A_2C_2B_2$-$A_3C_3B_3$, also known as Hoberman ring. Compared to the rectilinearly deployable motion structure in Fig. 3, links A_1-C_1-B_2 and B_1-C_1-A_2 are angulated rather than straight [9].
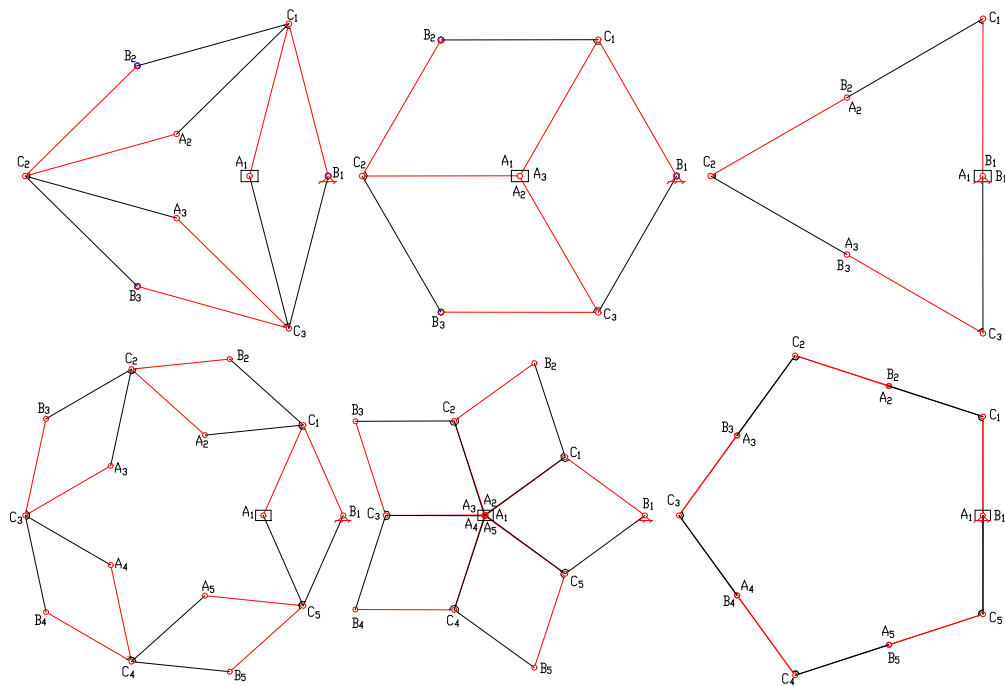

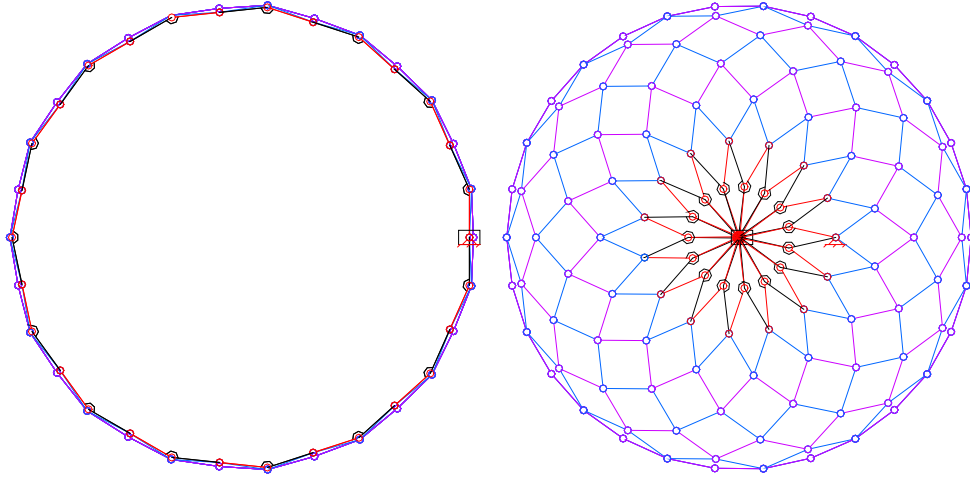**Fig. 5.** Three cell and a five cell Hoberman rings.

Fig. 6. Fully collapsible radially-deployable mechanism based on a Hoberman ring with 15 cells.
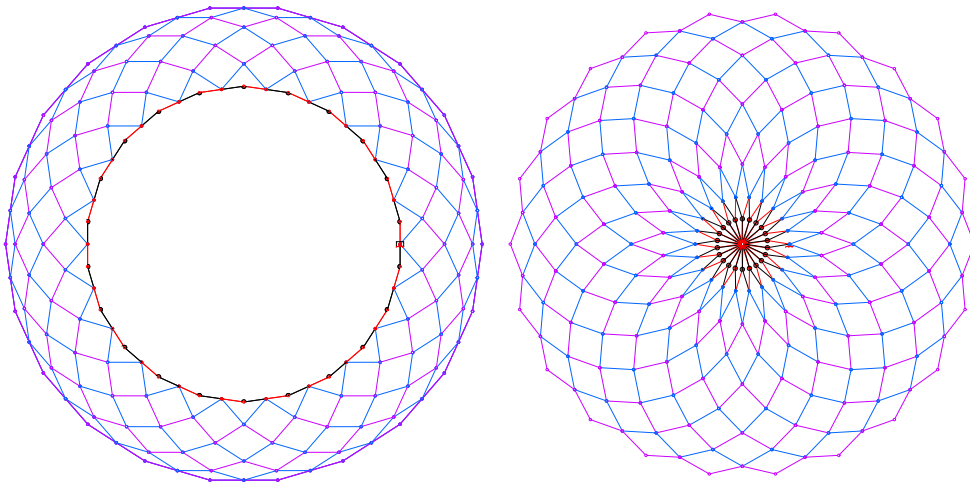

Fig. 7. Partially collapsible deployable mechanism based on a Hoberman ring with 22 cells.

The mechanisms in Figs. 6 and 7 have been obtained by amplifying a Hoberman ring with **RRR** dyads assembled to the outside. In case of the mechanism in Fig. 6 all links have equal length. In case of the mechanism in Fig. 7, the outside dyads have longer links than the original Hoberman ring, and for this reason the structure is not fully collapsible. As shown, the motion structures in Figs. 5, 6 and 7 are overconstrained mechanisms, and they have been simulated by not closing the mechanism at A_1 and B_1 i.e. although they appear to be multiple joints, A_1 and B_1 are perfectly overlapping simple pin joints.

4   Circularly deployable scissor-type structures

If the links of a rectilinearly deployable mechanism like those in Fig. 3 are of two length groups [9], then the resulting structure will deploy circularly - see Figs. 8 and 9. Amplification is possible by adding **RRR** dyads to the outside, as well as to the inside.
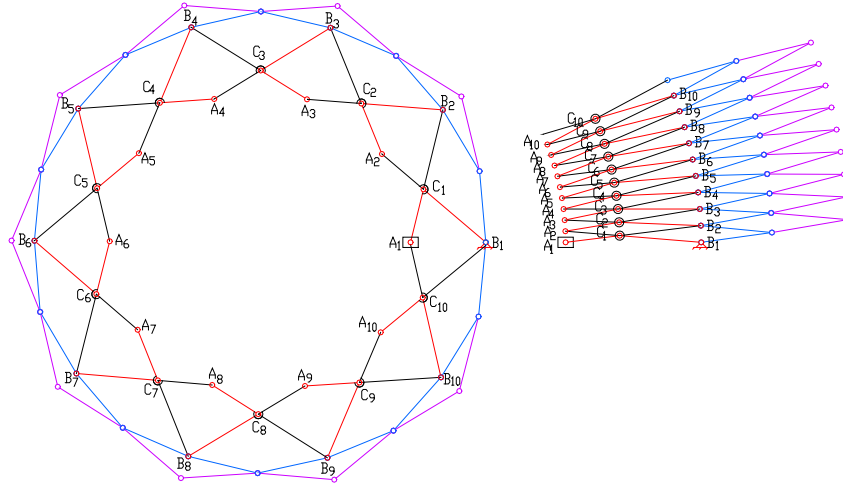

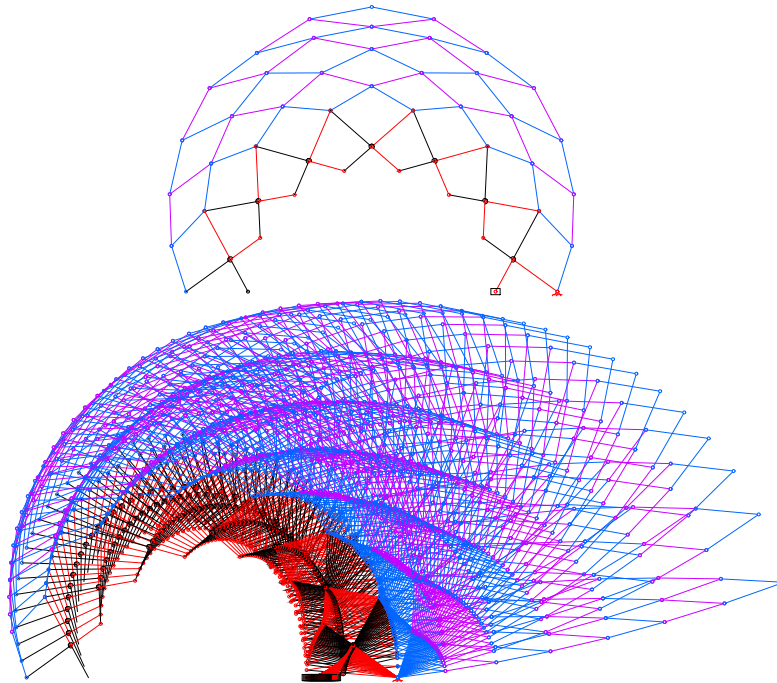**Fig. 8.** Compound circularly deployable structure in its retracted and deployed configurations.

Fig. 9. Semicircular deployable structure also showing its workspace.

Fig. 8 shows a circularly deployable mechanism with three rows of cells. Input is the slider at A_1 which actuates the **RRR** dyad $A_1C_1B_1$ with joint B_1 pined to the ground. Offset points A_2 of link B_1C_1 and B_2 of link A_1C_1 connect to dyad $A_2C_2B_2$ and the pattern is repeated. Outer amplification is done with two rows of **RRR** dyads colored in blue and magenta in Fig. 8. In Fig. 9 it is shown the workspace of a circularly deployable structure amplified to the outside with six rows of **RRR** dyads.

5　Folding pop riveter analysis

The last example discussed in this paper is that of the scissor rivet gun disclosed in [8]. For convenience, the rivet mandrel will be considered the input, while the mandrel guide will be assumed stationary (Fig. 10). The pin-in-slot joints A_1 and A_2 have been modeled as a **R-T** joint combination. C_1 and D_1 are offset points to links A_1B_1 and A_2B_2 of the respective **RRT** dyads. The mechanism is then amplified with the **RRR** dyad $C_1E_1D_1$, and points D_2 and C_2 attached offset to links C_1E_1 and D_1E_1, and the pattern is repeated two more times. The mandrel and the ternary and binary link shapes have been generated automatic by calling specific MeKin2D subroutines.

The simulation program performs both position and velocity calculations, which served to plot (see Fig. 10-b) the handle displacement vs. mandrel displacement and the mechanical advantage of the riveter:

$$F_P/F_{E4} = dy_{E4}/dS \qquad (6)$$

where F_P is the force at the rivet stem, F_{E4} is the force applied by the operator via the handle at joint E_4, and dy_{E4}/dS is the derivative of the handle displacement with respect to mandrel displacement S. As Fig. 10-b shows, the mechanical advantage increases abruptly towards the end of the handle travel, which is beneficial compared to the more commonly used plier-type riveters.
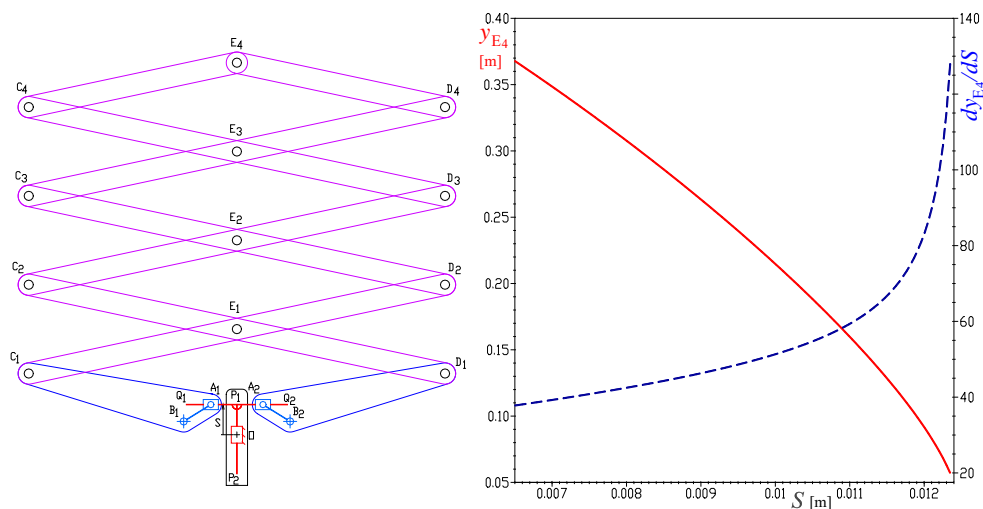

Fig. 10. Scissor riveter mechanism, and plot of the handle displacement (solid line) and mechanical advantage (dashed line) versus mandrel displacement S.

6   Conclusions

Several linearly, radially and circularly deployable scissor-type deployable mechanisms have been simulated relatively easily using modular-kinematics subroutines. Using *do while loops*, complex repetitive deployable mechanisms have been simulated and their kinematic properties assessed. Animations posted on YouTube of these simulations are also provided for a better understanding of the concepts discusses in this paper. Sample source code of mechanism simulations done using MeKin2D subroutines, including of repetitive mechanisms, are available in references [9], [10] and [18].

References

1. Whale, L.: Improvement in fire-escapes, US Pat. 105,280 (1870).
2. Hoberman, C.: Reversibly expandable doubly-curved truss structure, US Pat. 4,942,700 (1990).
3. You, Z., Pellegrino, S.: Foldable bar structures. Intl Journal of Solids and Structures 34(15), 1825-1847 (1997).
4. Kassabian, P.E., You, Z., Pellegrino, S.: Retractable roof structures. Proc. Instn Civ. Engrs Structs & Buildings 134(1), 45–56 (1999).
5. Maden, F., Korkmaz, K., Akgün, Y.: A review of planar scissor structural mechanisms geometric principles and design methods. Arch. Science Rev. 54(3), 246-257 (2011).
6. Zhao, J.-S., Wang, J.-Y., Chu, F., Feng, Z-J, Dai, J.S.: Structure synthesis and statics analysis of a foldable stair, Mechanism and Machine Theory 46(7), 998-1015 (2011)
7. Fenci, G.E., Currie, N.G.R.: Deployable structures classification: A review. International Journal of Space Structures 32(2), 112–130 (2017).
8. Yuan, J.: Folding Rivet Gun. US Des. Pat. D811,185 (2018).
9. Simionescu, P.A., Golfari, N., Constans, E.W.: Planar Motion Structures Modeling and Simulation with MeKin2D Subroutines. Proc. 15th IFToMM World Congr. Springer (2019).
10. Simionescu, P.A.: Kinematics of the RRR, RRT (Passive) and RRRR, RRRT (Active) Linkage-Mechanism Building Blocks with Applications and Reporting of New Findings. ASME Journal Mechanisms Robotics 11(6), 10p (2019).
11. Yang, Y., Liu, H., Zheng, H., Peng, Y., Yu, Y.: Two types of remote-center-of-motion deployable manipulators with dual scissor-like mechanisms. Mechanism and Machine Theory 160(2), 104274 (2021)
12. Simionescu, P.A.: Computer Aided Graphing and Simulation Tools for AutoCAD Users, CRC Press, Boca Raton, USA (2014).
13. Simionescu, P.A.: MeKin2D: Suite for Planar Mechanism Kinematics. ASME 2016 IDETC/CIE Conference, Charlotte, NC, USA, Aug. 21-24, 10p (2016).
14. Kinzel, G.L., Chang, C.: The Analysis of Planar Linkages Using a Modular Approach. Mechanism and Machine Theory, 19(1), 165-172 (1984).
15. Molian, S.: Mechanism Simulation Using Subassemblies. Proc. of the 9th World Congress on the Theory of Machines and Mechanisms, Milan, Italy, 1995, Vol. 4, p. 2594-2596.
16. Hansen, M.R.: A general Method for Analysis of Planar Mechanisms Using a Modular Approach. Mechanism and Machine Theory 31(8), 1155-1166 (1996)
17. YouTube MeKin2D, www.youtube.com/channel/UCeq7sKmlaN1mf1S1UYThpHw, last accessed 2021/04/30.
18. Simionescu, P.A., Mendoza-Diaz, N.V.: Enhancing Computer Programming Skills to Engineering Students Using Mekin2D Modular Kinematics Subroutines. Proc. 2021 ASEE Annual Conference & Exposition, Virtual Meting, July 26-29, Paper ID #33320, 11p (2021).

A Multi-stable Skin for Surface Twist Morphing

Abdulhakim Algmuni[1], Fengfeng (Jeff) Xi[1], and Hekmat Alighanbari[1]

[1] Ryerson University, 350 Victoria St, Toronto, Ontario M5B 2K3, CA
`aalgmuni@ryerson.ca`

Abstract. A new multi-stable skin for surface twist morphing is presented by connecting asymmetric composite patches with both cross-ply and angle-ply. A basic model is presented by connecting two bi-stable composite patches with an aluminum strip in between acting as a transition zone to reduce the interaction between the adjacent patches. A nonlinear finite element method is employed to study the behaviour of the connected patches, and their stable configurations are determined and validated experimentally. The results show a good agreement in terms of the stable shapes and the number of stable states. It is found that the width of the flexible strip is critical to determining the number of stable states, and that for the same flexible strip the angle-ply patch can be selected at different angles to achieve shape morphing in different directions. This study sheds light on the tailoring of bi-stable composite patches that can be used to create a large skin applicable to surface morphing including twist.

Keywords: Multi-stable patches, Flexible strips, Surface twist morphing, Finite element analysis.

1 Introduction

Due to the stiffness deficiency inherent in flexible skins, multi-stable panels have been researched over the last decade as an alternative approach for creating morphing skins to meet both shape change and rigidity requirement. However, it is a daunting task to design a multi-stable panel that can truly approximate a continuous morphing surface by the means of shape switching. A multi-stable panel is usually accomplished by connecting several bi-stable patches in certain form. A bi-stable patch is an asymmetric single patch composite laminate that exhibits two opposite stable configurations. This bi-stability of asymmetric composite patch is caused by the mismatch of the thermal expansion coefficients between layers with different fibre orientations during curing. The alteration between the two stable shapes is called snap-through/snap-back. Apparently, this shape change is discrete, requiring a bending moment or a normal force to switch from a primary stable shape to a secondary one or vice versus.

In the past, extensive research has been carried out on bi-stable composites around the world. After the initial study by Hyer [1-3], many researchers contributed to advancing this research by studying the effects of different parameters on bi-stable laminates. Hamamoto and Hyer [4] incorporated geometric von Kármán nonlinearities in

the Classical Lamination Theory (CLT) and then validated the analysis results experimentally. Hyer and Rousseau [5] started to investigate the models of the arbitrary asymmetric composite laminates. Jun and Hong [6] presented a new formulation including an in-plane shear strain and studied the effects of width-to-thickness ratio (W/T), aspect ratio (AR), and number of layers (n) on the cured shape of asymmetric cross-ply $[0_n/90_n]_T$ and antisymmetric $[0/90]_{n,T}$ ($n = 1,2,...$) family of laminates. Jun and Hong later extended their previous model to studying asymmetric laminates using arbitrary lay-up angles [7]. The results of angle-ply laminates presented two orthogonal in-plane directions and a twisting curvature, unlike cross-ply laminates which only have two normal curvatures κ_x and κ_y. The stable configurations of bi-stable laminates were modelled and successfully predicted by using both analytical approaches and finite element analysis [8-11]. These previous studies did reveal the behaviour of bi-stable shapes but fell short of achieving a continuous multi-stable surface required by real applications. Therefore, an idea has emerged to connect several bi-stable laminates together to form a multi-patch panel that could exhibit multiple stable states.

Technically, this overarching concept falls under the category of laminate tailoring. The first connected multi-patch composite panel was put forward by Potter et al. [12] by connecting two composite laminates side by side. After testing three different compound plates with different laminate orientations, they demonstrated the possibility of tailoring multiple patches of laminates to achieve a large multi-stable panel. This motivated subsequent research including Mattioni et al. [13-14] on analytical modelling of multi patches connected in series; Arrieta et al. [15-16] on the design of a variable stiffness element composite using bi-stable patches; Dai et al. [17-18] on the creation of a multi-stable surface structure jointed by rivets; Cui and Santer [19] on the design of a multi-stable panel connected in series without rivets; Wang et al. [20] on the introduction of a transitional elements between bi-stable patches.

Inspired by the past efforts, we presented a grid-based skin comprising the (2×2) number of bi-stable patches [21]. Our first work showed the feasibility of forming a multi-patch skin in two directions. However, this initial work did not obtain the maximum number of stable shapes. Realizing the cause being the rigid connection between the adjacent bi-stable patches, we investigated a new connection by using flexible strips and achieved a maximum number of stable states [22].

So far, research on multi-stable panels has been focused on cross-ply laminates which cannot withstand surface twist morphing. In this paper, we present a method by connecting bi-stable patches with both cross-ply and angle-ply so that a multi-stable panel can sustain twist morphing. In what follows, the problem under study is defined first and then the method for design and analysis is presented and at the end the results are validated by experiment.

2 Problem Statement

A key issue in the development of a multi-stable composite is the structural connection between bi-stable composite patches. An ideal approach would make these connections

as part of a continuous surface. As mentioned before, all previous multi-patch panels only considered the 0°/90° angles i.e. cross-ply laminates, which are relatively easy to connect experimentally due to the compatibility between laminate angles.

In this study, we extend our previous work [22] to bi-stable patches with a mix of cross-ply and angle-ply. A nonlinear finite element method is applied to predict the stable configurations of connected bi-stable patches. The effect of the width of flexible strips on the stable configurations is investigated. Also, an experimental method is employed to validate the predicted stable configurations of the proposed panels.

3 Design of Multi-stable Patch Composite

It is known from the previous research that an asymmetric composite laminate could take two stable shapes by cooling down from an elevated temperature to the room temperature. If these asymmetric laminates are connected to form a large patch composite, the structure can be assumed to exhibit more than two stable configurations. If n bi-stable patches are connected, theoretically the connected panel should exhibit 2^n stable states. However, the direct connection between these asymmetric composite patches may reduce the number of theoretical stable states due to the interaction between patches at linking edges. To address this problem, a connected multi-patch bi-stable composite is presented with modification of the joint method. In our design, a basic serial multi-stable surface is made of (1×2) composite patches and a flexible strip in between. By introducing this strip in the transition zone between composite patches, each bi-stable patch would be less constrained with the adjacent patches and hence can maintain its own bi-stable shapes. The flexibility of the connection joints between bi-stable patches bears a direct impact on the degree of stability and the number of stable states. Once the material of a flexible joint is selected, then the joint flexibility will depend on the width of the flexible strip.

By referring to Fig. 1, d_s is the total width of a flexible strip. A flexible joint is referred to as the gap between two patches and its width is denoted by d_g where $d_g = d_s - (2 \times d_H)$. d_g is defined by percentage of the side length of a patch. d_H is the overlapping length of the flexible strip with a composite patch, set at $10\ mm$. In our study, the flexible joint width (d_g) will increase until the panel reaches a maximum of stable states. This value directly controls the flexibility of the connection joints. We will use an increment of $10\ mm$ to find an appropriate flexible joint width, d_g, that can achieve a maximum number of stable configurations for the connected surface. Based on our previous work [22], an aluminum shim is employed as a flexible strip.

As shown in Fig. 1, a basic multi-patch surface is made of two bi-stable composite patches, one cross-ply and one angle-ply. They are connected side-by-side by a flexible strip joint. Each composite patch is designed to have two layers of unidirectional T700S-EHM-32 Carbon/Epoxy Prepreg to achieve the behaviour of bi-stability. The cross-ply patch possesses two stable states at 0° and 90°, and the angle-ply patch has two stable states at −45° and 45°. An aluminum alloy shim is placed in between.

The entire panel is $280\ mm \times 140\ mm$ with ($A1$, $A2$) two patches and the two joint sections ($S1$, $S2$), as shown in Fig. 1(a). Because the patches are connected along the y direction, the flexible strip is parallel to the linking edge. The width of each bi-stable patch Ly is constant, while the length of each bi-stable patch is defined by $(Lx - d_g)/2$. The adjacent patches are linked by a lap joint through an overlapping area $d_H = 10\ mm$ on both sides. The sequence of individual patches is defined as ($[A1]_T$, $[A2]_T$) from left to right, as shown in Fig. 1(a).
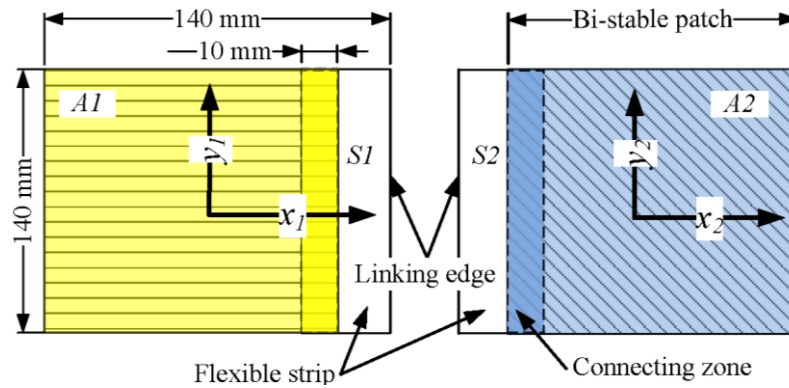
a) Geometry of hybrid patches
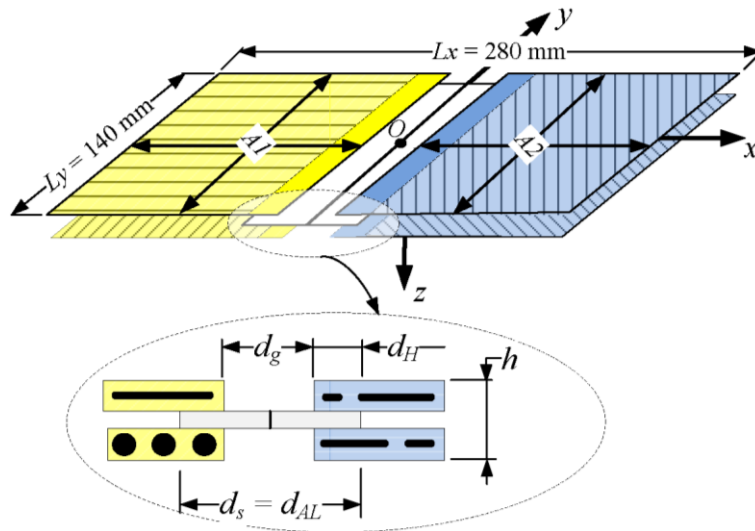
b) Assembly of a serial multi-stable hybrid surface (SMHS)

Fig. 1. Layout of a serial-based multi-stable panel and its coordinate system.

To study the twisting behaviour of the connected composite patches, the asymmetric $[0/90]_T$ and $[-45/45]_T$ laminates are selected first to form serial multi-patch panel, as

shown in Fig. 1. In addition to this panel, three other panels consisting of the $[0/90]_T$ and angle-ply stacking sequences $[\theta/\theta\text{-}90]_T$ ranging θ from 10° to 30° in 10° increments are also investigated. These additional panels are used to explore other twist morphing possibilities on compound surfaces. Table 1 shows four different structural panels that are designed to study the behaviour of a serial connected composite patches for multi-stable twist morphing.

Table 1. The stacking sequence of bi-stable composite patches.

Panel No.	Description	Flexible strip in between ([S1], [S2])	Bi-stable stacking sequence ([A1]$_T$, [A2]$_T$)
1		([AL], [AL])	([0/90]$_T$, [-45/45]$_T$)
2	Cross-ply and angle-ply laminates	([AL], [AL])	([0/90]$_T$, [30/-60]$_T$)
3	$[0/90]_T$ and $[\theta/\theta\text{-}90]_T$	([AL], [AL])	([0/90]$_T$, [20/-70]$_T$)
4		([AL], [AL])	([0/90]$_T$, [10/-80]$_T$)

4 Modelling of Connected Patch Laminates

Modelling starts with panel 1, i.e. with ($[0/90]_T$, $[-45/45]_T$) bi-stable patches and the [AL], [AL] flexible strips, as listed in Table 1. Here AL indicates aluminum. Each composite patch is defined by $\left(Lx - d_g\right)/2$ and Ly, where $Lx = 280\ mm$, $Ly = 140\ mm$. d_g changes from 0 to 20 mm by an increment of $10\ mm$. For example, at $d_g = 0\ mm$, each composite patch is $140\ mm \times 140\ mm$, where the entire panel is $280\ mm \times 140\ mm$. In this case, the two bi-stable composite patches are connected side by side under a rigid connection. When $d_g > 0$, the flexible strip will take an effect. It is assumed that the composite laminates and the aluminum strips are bonded perfectly to form a continuous connection. This means that $S1$ is part of $A1$ and $S2$ part of $A2$, as shown in Fig. 1(a). The material properties of Prepreg composite and aluminum alloy are listed in Table 2.

Table 2. Material properties of CFRP prepreg and Aluminum alloy [23-25].

	Property	$E_{11}\ (GPa)$	$E_{22}\ (GPa)$	$G_{12}, G_{13}\ (GPa)$	v_{12}
Carbon fibre pre-preg (T700S-EHM-32) at $V_f \approx 70\%$	Value	162	15.8	6.85	0.3
	Property	$G_{23}\ (GPa)$	$\alpha_{11}\ (°C^{-1})$	$\alpha_{22}\ (°C^{-1})$	$t_{Ply}\ (mm)$
	Value	5.7	19×10^{-9}	24×10^{-6}	0.152

Aluminum alloy	Property	$E\ (GPa)$	v	$\alpha\ (°C^{-1})$	$t\ (mm)$
Shim 1145-H19	Value	69	0.33	24.5×10^{-6}	0.127

The commercial ABAQUS CAE software is employed to model the panel with the entire side lengths of Lx and Ly as illustrated in Fig. 1(b). The panel is modelled as paired bi-stable patches as shown in Fig. 1(a). Since the patch of model is designed as a regular square panel, it is meshed using four-node-square shell elements (S4R) with six degrees of freedom per node. A mesh refinement study is carried out to determine the accuracy of the FEM solutions. [0/90]$_T$ square laminate models are meshed into 6×6, 10×10, 20×20 and 30×30 corresponding to the total number of degrees of freedom of 49, 121, 441 and 961, respectively. The side length of basic patch on the whole panel is 140 mm. The maximum temperature of the curing cycle for the T700S-EHM-32 prepreg carbon fibre is 135 $°C$. By cooling down the panel from this elevated temperature to the final temperature at 32 $°C$, the panel will be deformed due to the temperature drop of 103 $°C$. Fig. 2 illustrates the convergence history of the maximum out-of-plane displacement.
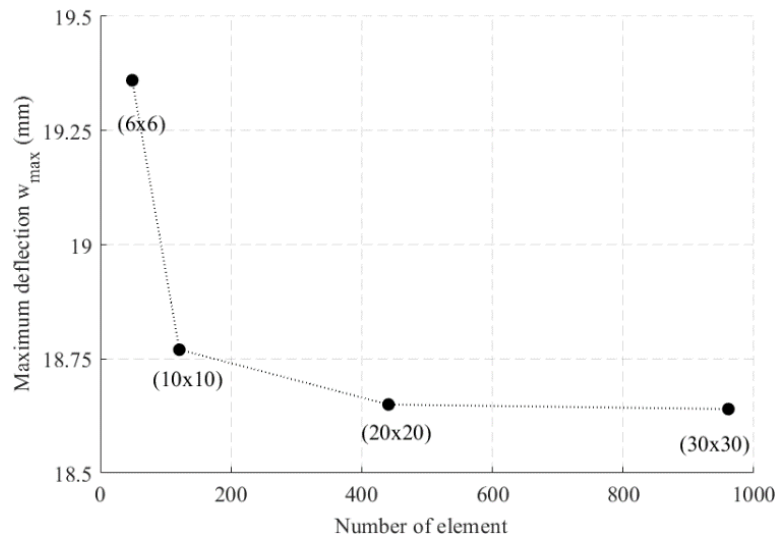

Fig. 2. Maximum out-of-plane displacement for [0/90]$_T$ composite laminate predicted by ABAQUS models with different mesh sizes.

It is clear that the results converge when the mesh density is over 400 elements. In this study, each patch is modelled by 440 four-node-square thick shell elements (S4R). The origin of the coordinate systems (x, y) for this panel is located at the middle point of the linking edge as illustrated in Fig. 1(b). The key in this modelling is the compatibility conditions at the linking edge. To maintain the continuity between the adjacent patches,

the out-of-plane and in-plane displacements as well as the out-of-plane rotations should be the same. Therefore, the entire panel model is assembled by applying multiple point constraints along the linking edge. The panel model with two patches and flexible strips has in total 945 nodes and 5670 degrees of freedom. After cooling the panel down from the maximum temperature to the final temperature at 32 ℃ and restricting the central node of the entire panel, the flat panel is first deformed into the initially preferred state. This stable state is then actuated to switch to another stable state by applying a small point load on the central node of the driving patch, as illustrated in Fig. 3.
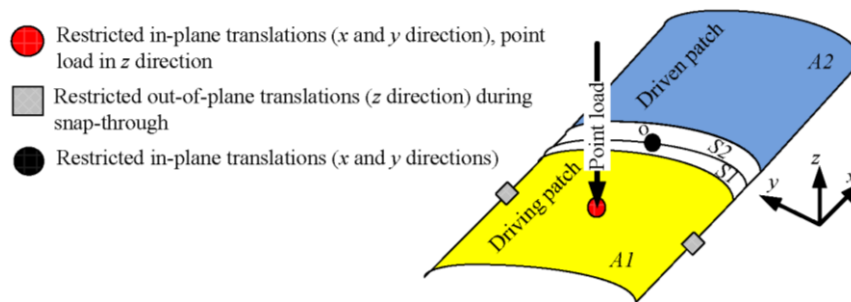
Fig. 3. Boundary conditions and the snap-through driving load on a driving patch for configuration switching.

As shown in Fig. 3, during actuation, the central node of the driving patch should be restricted in the x and y direction, and the middle nodes of the two sides perpendicular to the linking edge need to be fixed in the z direction for a while to avoid unwanted rotations. After removing the load and the constraints while keeping the fixed constraint at the central node of the entire panel, the driving patch will switch to another state, called intermediate state, while the driven patch should remain the same depending on the joint connection.

There are two bi-stable patches in our example, so in total $2^2 = 4$ possible stable shapes. The primary states are indicated by two digits as 0-0 or 1-1. The other two states are indicated by 1-0 and 0-1. Three actuation steps are applied to verify these stable states.

1. Step (a-b): actuate from stable state 0-0 to stable 1-1.
2. Step (a-c): actuate from stable state 0-0 to stable 0-1.
3. Step (a-d): actuate from stable state 0-0 to stable 1-0.

To demonstrate the stability of intermediate states, the patches of the compound panel begin with the primary stable state a) 0-0 corresponding to the global energy minima. Then a snap-through force is applied to the central node of the driving patch at state 0. When the applied force reaches a critical snap-through value, the driving patch at state 0 will switch to the new state 1. In this process, the strain energy of the driven patch will also rise depending on the joint connection. If the driven patch does not snap through to a new state 1, the compound panel has the intermediate state 1-0.

It is shown here that the number of stable configurations of the panel depends on the width of the flexible gap d_g between the patches. To reduce the interaction between the patches so that each patch can maintain its own bi-stable states, we need to increase d_g. In this study, both rigid ($d_g = 0$) and flexible ($d_g > 0$) connections are investigated. We study the effect of the flexible gap on the number of the stable configuration in order to select a reasonable width. Figs. 4-6 illustrate the number of stable states corresponding to the local energy minima for the ([0/90]$_T$, [AL], [AL], [-45/45]$_T$) laminates at $d_g = 0\ mm$, $10\ mm$ and $20\ mm$, respectively.

								Non
a)	0-0 state	b)	1-1 state	c)	0-1 state	d)	1-0 state
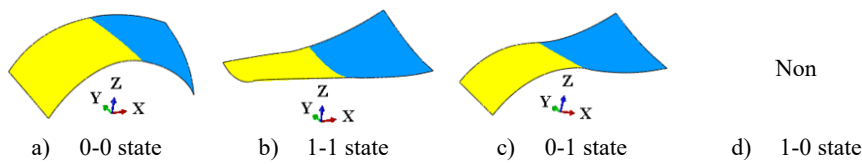
Fig. 4. Stable configurations for panel 1 consisting of ([0/90]$_T$, [AL], [AL], [-45/45]$_T$) patches at $d_g = 0\ mm$.

								Non
a)	0-0 state	b)	1-1 state	c)	0-1 state	d)	1-0 state
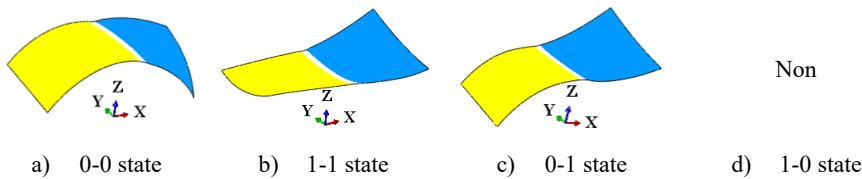
Fig. 5. Stable configurations for panel 1 consisting of ([0/90]$_T$, [AL], [AL], [-45/45]$_T$) patches at $d_g = 10\ mm$.

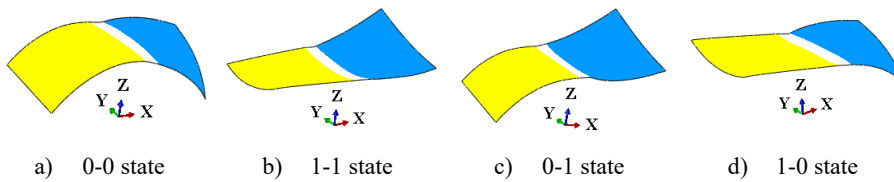|							
a)	0-0 state	b)	1-1 state	c)	0-1 state	d)	1-0 state

Fig. 6. Stable configurations for panel 1 consisting of ([0/90]$_T$, [AL], [AL], [-45/45]$_T$) patches at $d_g = 20\ mm$

Fig. 4 illustrates the stable configurations of panel 1 when the patches are connected side by side under a rigid connection. In this case, the compound panel only shows three stable states a) 0-0, b) 1-1 and c) 0-1, corresponding to three energy minima. The other intermediate state d) 1-0 is a marginal state, which is similar to stable state 0-0.

Now let us move on to consider the effect of flexible connection on the number of stable configurations. By introducing the width of flexible gap (d_g) at $10\ mm$, the intermediate state d) 1-0 is still in a marginal state. This means that the system still has tri-stable states as shown in Fig. 5. By further increasing d_g to $20\ mm$, the panel shows a maximum of 4 stable states as illustrated in Fig. 6. This means that the marginal stable state is now transformed to a new stable state and the behaviours of the two patches are completely decoupled.

Based on the simulation results, the width of flexible joints (d_g) is chosen at $20\ mm$ for designing and testing hybrid multi-stable panels with high twisting curvature. To verify the FE results, the panel 1 and 2 specified in Table 1 are fabricated, tested and compared with the FE results.

5   Experimental Verification and Manufacturing Process

In this section, we start with fabrication of panel 1 as listed in Table 1. Each composite patch is sized by $130\ mm \times 140\ mm$, and the strip between the two patches is $20\ mm \times 140\ mm$. Fig. 7 illustrates the process for fabrication of the panel with ([0/90]$_T$, [AL], [AL], [-45/45]$_T$) at $d_g = 20\ mm$.

a)   Lay-up patch layers and strip layer   b)   Applying vacuum system

c)   Curing process   d)   Production of panel at preferred state
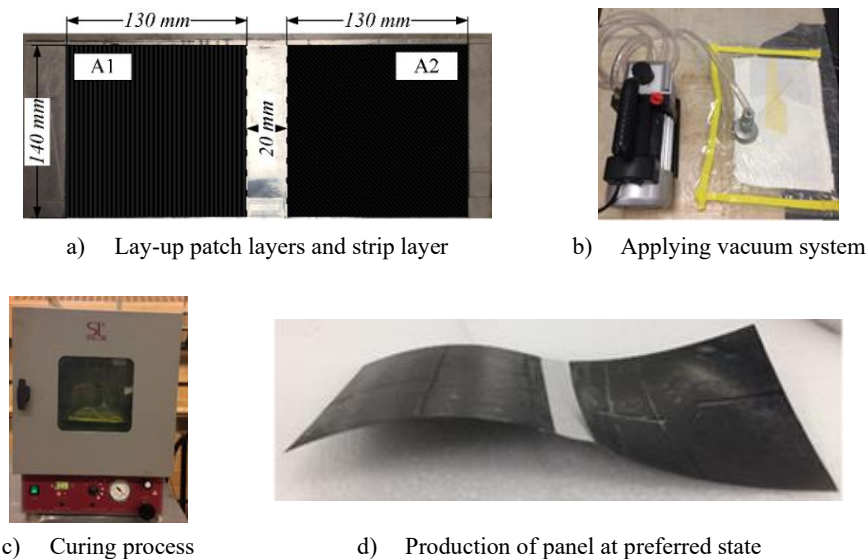
Fig. 7. The manufacturing process of the connected double-patches

All specimens were manufactured by hand layup on a thick metal plate to allow the rigid body motion during the curing process, and then a vacuum bag system was used to provide a consolidating pressure and remove any air bubble trapped between the layers prior to curing. The vacuum system was applied for 10-13 min at the room

temperature. The specimens were then cured in the Shell Lab 1425 Compact Vacuum Drying Oven. The vacuum pressure was maintained at $9 \times 10^4 \ Pa$ throughout the curing period.

The curing cycle for the Rock West 14002-D T700S-EHM-32 Carbon/Epoxy prepreg [23] was modified by adding the curing stage of 90 min at 135 ℃. This total curing process lasted 203-205 min starting at the initial temperature of 32℃, reaching the maximum curing temperature at 135℃ and cooling down to the room temperature. After curing, each multi-stable panel exhibited multiple stable states, which could be switched from the preferred state to another state by applying a small point load on the panel. The experimental tests showed similar shapes to the simulation. Fig. 8 illustrates the physical configurations of the ([0/90]_T, [AL], [AL], [-45/45]_T) laminates compared to the FE prediction at the flexible joint $d_g = 20 \ mm$.
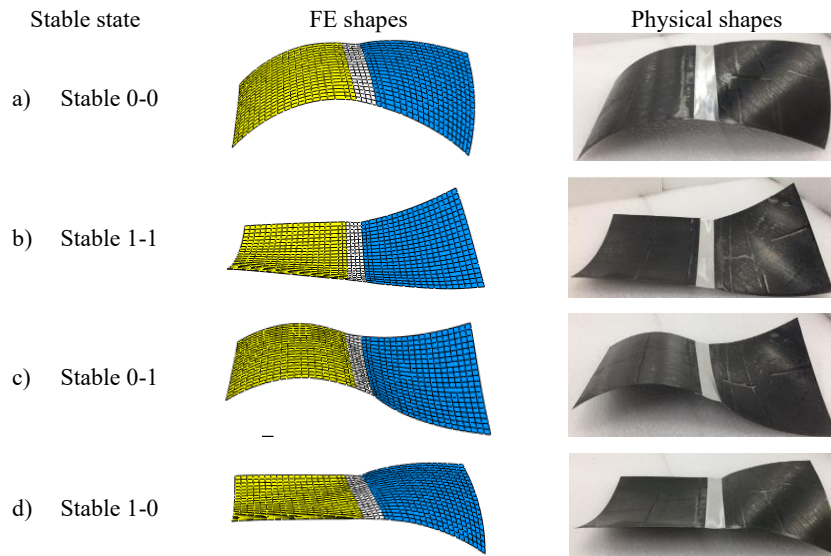
Fig. 8. Stable configurations of panel 1 consisting of ([0/90]_T, [AL], [AL], [-45/45]_T) laminates with $d_g = 20 \ mm$, demonstrating quad-stable behaviour.

In this paper, the FE results are verified by experimental tests qualitatively. Quantitative shape comparison is not necessary for shape determination. As the predicted by the FE model, panel 1 with 20 mm of the flexible gap (d_g) presents a maximum number of 4 stable states. These stable shapes are in a good agreement with the experimental tests.

Furthermore, panel 2 specified in Table 1 was fabricated in the same manner and compared with the simulation results. Panel 2 is made of ([0/90]_T, [AL], [AL], [30/-60]_T) with d_g = 20 mm. As illustrated in Fig. 9, this panel also shows all four stable states by simulation and experiment.
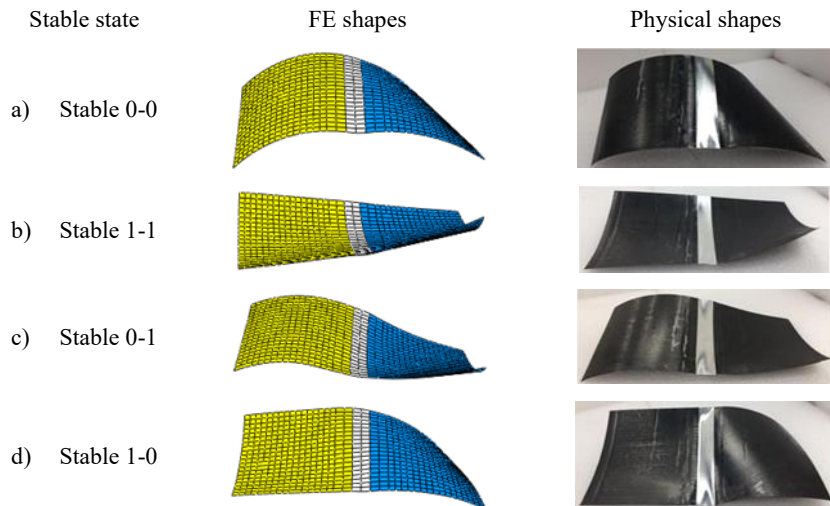
Fig. 9. Stable configurations of panel 2 consisting of ([0/90]$_T$, [AL], [AL], [30/-60]$_T$) laminates with $d_g = 20\ mm$, demonstrating quad-stable behaviour.

It is noted that panel 1 and panel 2 are made of two different angle-ply patches, i.e. -45/45 and 30/-60, respectively, but both having the same 90° difference between the fiber directions of the two stacking composite layers (i.e. orthogonal angle-ply). Since the two panels both exhibit a maximum number of 4 stable states and match the simulation with the experimental results, it indicates that other angle-ply patches can also be designed if they have a 90° difference lay-ups with the same width of the flexible strip, for example, 10/-80, 20/-70, etc. To study other angle plies, panel 3 and 4 as listed in Table 1 are simulated as well. Figs. 10-11 illustrate the predicted shapes of the ([0/90]$_T$, [AL], [AL], [20/-70]$_T$) and the ([0/90]$_T$, [AL], [AL], [10/-80]$_T$) laminates for panel 3 and 4, respectively. Both achieved a maximum of 4 stable states but with an increased width of the flexible strip (d_g = 30mm).
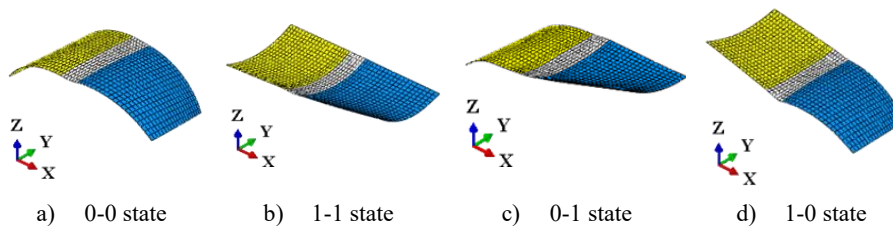

Fig. 10. Stable configurations of panel 3 consisting of ([0/90]$_T$, [AL], [AL], [20/-70]$_T$) laminates using FE model, demonstrating quad-stable behaviour at $d_g = 30\ mm$.
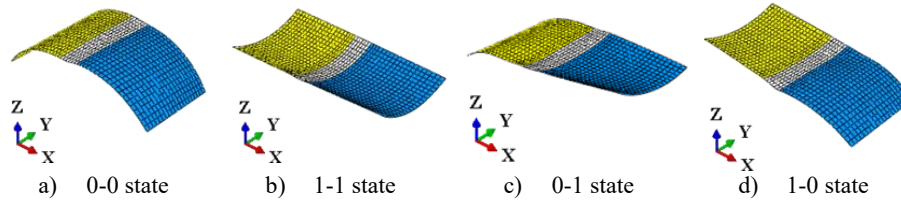
Fig. 11. Stable configurations of panel 4 consisting of ($[0/90]_T$, [AL], [AL], $[10/-80]_T$) laminates using FE model, demonstrating quad-stable behaviour at $d_g = 30\ mm$.

The possibility of selecting different angle-ply patches provides a potential means to design a multi-patch panel with different shape changing directions for more complex shape morphing. From this investigation it further confirms that the connected composite patches need a flexible transition area in between in order to obtain more stable configurations. The flexibility width is affected by the difference of angles between connected patches. As illustrated in Figs.8-9, the reasonable flexible joint width between two connected composite patches could be quantified by $20\ mm$, i.e. $d_g \geq 15\%$ of the side length of composite patch, for angle-ply stacking patches between $30° \leq \theta \leq 60°$. This flexible width needs to increase for angle-ply patches between $30 > \theta > 60$ as illustrated in Figs. 10 and 11. These FE results indicate that the flexible strip width between composite patches with a small twisting curvature should be wider than the patches with a large curvature. For our design, panel 4 ($[0/90]_T$, [AL], [AL], $[10/-80]_T$) laminates results in the smallest twisting curvature. Therefore, the flexible width between composite patches is about 24% of the composite patch length (i.e. d_g is $\approx 25\%$ of side length of composite patch). This design criteria will help to achieve a maximum number of stable configurations, which is equal to 2^n for n connected composite patches.
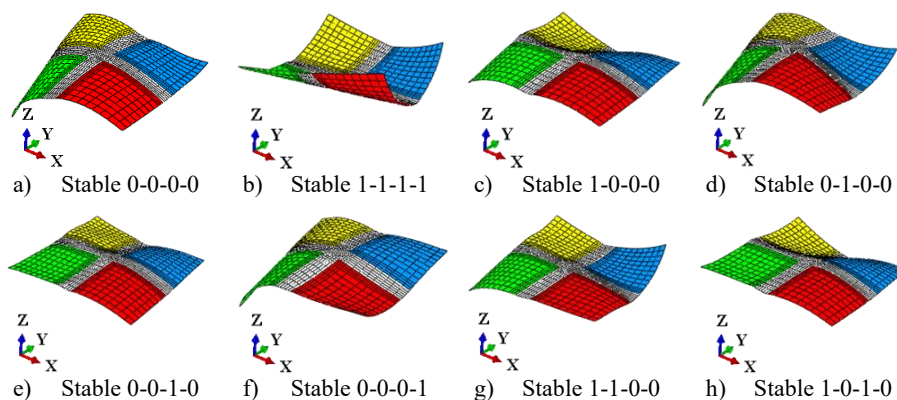
6 Design Grid Composite Patches with Different Angle-Ply

With the understanding described above, we extend this research to simulating a grid-based multi-patch panel with angle-ply. This panel consists of ($[30/-60]_T$, $[-45/45]_T$, $[10/-80]_T$, $[20/-70]_T$) laminates with a flexible gap of $30\ mm$. For simulation, each patch is meshed using 203 four-node-square thick shell elements (S4R). Thus, the model composed of four patches has 870 nodes and 5220 degrees of freedom. The key in this modelling is the boundary conditions among the patches. To maintain the connection between the adjacent patches, the panel model is assembled by applying multiple point constraints to the nodes along the linking edges of all patches. The maximum temperature for curing the prepreg carbon fibres is 135℃. By cooling down the panel from the elevated temperature to a lower temperature 32℃ and restricting the central node of the panel, the initially flat grid panel is first deformed into the preferred stable state 0-1-0-1. This stable configuration is then actuated to another stable state by

applying a small point load on the central node of a driving patch depending on concave/convex patch curvature.

During the actuation, the central node of the driving patch should be restricted in x and y direction, and the middle nodes of the straight sides of the driving patch should be fixed in z direction for a while to help the patch to buckle. By applying a small point force at the central node of the driving patch, the driving patch is subjected to sufficient out-of-plane deformation so that its strain energy reaches the peak point. After removing the load and constraints while keeping the fixed constraint at the central node of the panel, the panel will remain in the new state if the driving patch does not return to the original state.

By looking from the top, the convex or concave shape of a patch is defined by state 0 or state 1, respectively. This patch can change from convex to concave or vice versa. There are four bi-stable composite patches in our design, leading to in total $2^4 = 16$ possible stable shapes, indicated by four digits, such as 0-0-0-0 or 1-1-1-1 for the two primary states. In addition to these two primary states, there are fourteen intermediate states. For example, 1-0-0-1 indicates that the two patches in the first row are in 1, 0, and the other two in the second row are in 0, 1. In this case study, fifteen actuation steps are applied to verify the stability of these states. To demonstrate the stability of intermediate states, the compound panel begins from the primary stable state a) 0-0-0-0 corresponding to a global energy minimum, and then it is subjected to an actuation by applying the snap-force on the central node of the driving patch at state 0. The deformation from the driving patch will be transmitted to the driven patches through the linking-edges. When the applied force reaches a critical snap-force, the driving patch at state 0 will switch to the new state 1, and the strain energy of the driven patches will also rise during this actuation procedure. If the driven patch does not snap through to a new state 1, the compound panel possesses intermediate states corresponding to a local energy minimum. Fig. 12 illustrates the 16 possible stable shapes for the four bi-stable patches of the ([30/-60]$_T$, [-45/45]$_T$, [10/-80]$_T$, [20/-70]$_T$) laminates at 30 mm of flexible gap.

a)   Stable 0-0-0-0   b)   Stable 1-1-1-1   c)   Stable 1-0-0-0   d)   Stable 0-1-0-0

e)   Stable 0-0-1-0   f)   Stable 0-0-0-1   g)   Stable 1-1-0-0   h)   Stable 1-0-1-0

i)   Stable 1-0-0-1   j)   Stable 0-1-1-0   k)   Stable 0-1-0-1   l)   Stable 0-0-1-1

m)   Stable 1-1-1-0   n)   Stable 0-1-1-1   o)   Stable 1-0-1-1   p)   Stable 1-1-0-1
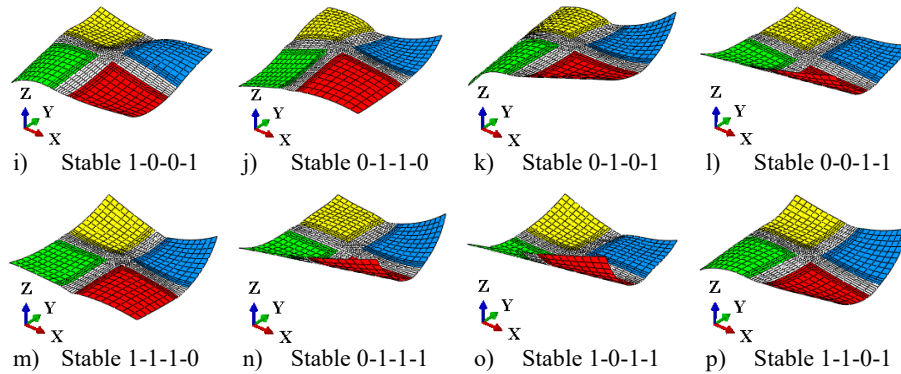
Fig. 12. Sixteen stable predictions of grid connected-four patches with different angle-ply laminates at 30 mm of the flexible joints by FE model.

The grid patch panel consisting of ($[30/-60]_T$, $[-45/45]_T$, $[10/-80]_T$, $[20/-70]_T$) laminates with 30 mm of d_g shows the sixteen stable states, representing the maximum number of stability for four connected twisted bi-stable composite patches. These predicted states prove that the addition of flexible strips as the connecting joints between composite patches helped to reduce the interaction at linking edges. This indicates that a (2×2) grid hybrid patch panel can achieve a maximum of 2^4 stable states at $d_g = 30\ mm$ which is $\approx 25\%$ of side length of the composite patch.

7   Conclusions

The following conclusions can be drawn from this study. 1) A multi-stable panel can be made of cross-ply and angle-ply bi-stable patches. 2) The achievement of a maximum number of stable states depends largely on the width of flexible strips used to connect the adjacent patches. 3) For angle-ply patches, the flexible strip width will depend on the ply angle. A wider width is required for angle-ply patches leading to a small curvature. 4) With a combination of cross-ply and different angle-plies, a more adaptive multi-stable panel can be designed through laminate tailoring to suit realistic surface morphing applications. In the future work, the effect of aerodynamics forces on a multi-stable surface will be investigated as part of loading analysis.

References

1. Hyer, M. W. Some observations on the cured shape of thin unsymmetric laminates. Journal of Composite Materials 1981; 15(2): 175-194.
2. Hyer, M. W. Calculations of the room-temperature shapes of unsymmetric laminates. *Journal of composite material* 1981; 15(6): 296-310.
3. Hyer, M. W. The room-temperature shapes of four-layer unsymmetric cross-ply laminates. *Journal of Composite Materials* 1982; 16 (4): 318-340.

4. Hamamoto, A., and Hyer, M. Non-linear temperature-curvature relationships for unsymmetric graphite-epoxy laminates. *International Journal of Solids and Structures* 1987; 23(7): 919-935.

5. Hyer, M., and Rousseau, C. Thermally induced stresses and deformations in angle-ply composite tubes. *Journal of Composite Materials* 1987; *21*(15): 454-480.

6. Jun, W., and Hong, C. Effect of residual shear strain on the cured shape of unsymmetric cross-ply thin laminates. *Composites Science and Technology* 1990; *38*(1): 55-67.

7. Jun, W., and Hong, C. Cured Shape of Unsymmetric Laminates with Arbitrary Lay-Up Angles. *Journal of Reinforced Plastics and Composites* 1992; *11*(12): 1352-1366.

8. Schlecht, M., Schulte, K., & Hyer, M. W. Advanced calculation of the room-temperature shapes of thin unsymmetric composite laminates. *Composite Structures* 1995; 32(1): 627-633.

9. Ren, L., Parvizi-Majidi, A., Li, Z. Cured shape of cross-ply composite thin shells. *Journal of Composite Materials* 2003; 37(20): 1801-1820.

10. Gigliotti, M., Wisnom, M. R., & Potter, K. D. Loss of bifurcation and multiple shapes of thin [0/90] unsymmetric composite plates subject to thermal stress. *Composites Science and Technology* 2004; 64(1): 109-128.

11. Emam, S., and Inman, D. "A Review on Bistable Composite Laminates for Morphing and Energy Harvesting. *Applied Mechanics Reviews* 2015; 67(6), 060803-1.

12. Potter, D. K., Weaver, M. P. A concept for the generation of out-of-plane distortion from tailored FRP laminates. *Composites Part A: Applied Science and Manufacturing* 2004, 35 (12), 1353-1361.

13. Mattioni, F., Weaver, P., Potter, K., Friswell, M. Analysis of thermally induced multi-stable composites. *International Journal of Solids and Structures* 2008, 45 (2), 657-675.

14. Mattioni, F., Weaver, P., Friswell, M. Multi-stable composite plates with piecewise variation of lay-up in the planform. *International Journal of Solids and Structures* 2009, 46 (1), 151-164.

15. Arrieta, A. F., Kuder, I. K., Waeber, T., Ermanni, P. Variable stiffness characteristics of embeddable multi-stable composites. *Composites Science and Technology* 2014, 97, 12-18.

16. Arrieta, A. F., Kuder, I. K., Rist, M., Waeber, T., Ermanni, P. Passive load alleviation aerofoil concept with variable stiffness multi-stable composites. *Composite Structures* 2014, 116, 235-242.

17. Dai, F., Li, H., Du, S. A multi-stable wavy skin based on bi-stable laminates. *Composites Part A: Applied Science and Manufacturing* 2013, 45, 102-108.

18. Dai, F., Li, H., Du, S. A multi-stable lattice structure and its snap-through behavior among multiple states. *Composite Structures* 2013, 97, 56-63.

19. Cui, Y., Santer, M. M. Highly multi-stable composite surfaces. Composite Structures 2015, 124, 44-54.

20. Wang, J., Nartey, M. A., Luo, Y., Wang, H., Scarpa, F., & Peng, H.-X. Designing multistable structures with enhanced designability and deformability by introducing transition elements. *Composite Structures* 2020, 233, 111580.

21. Algmuni, A., Xi, F., Alighanbari, H. Design and analysis of a grid patch multi-stable composite. *Composite Structures* 2020, 246, 112378

22. Algmuni, A., Xi, F., Alighanbari, H. Flexible joints for a grid-based multi-stable composite morphing skin. *Composite Structures* 2021, 259, 113512.

23. 14002-D Standard modulus unidirectional prepreg (n.d.) Available at: https://www.rock-westcomposites.com/downloads/14002,D_TDS_PROPreg_updated_11-14-17.pdf (07 July 2017).

24. ProfLightningSkunk13 (n.d.). T700SDataSheet - TECHNICAL Data Sheet No CFA-005 T700S DATA Available at: https://www.coursehero.com/file/11225980/T700SDataSheet/ (07 July 2017).
25. 1145-H19 Aluminum alloy (n.d.) Available at: http://www.mat-web.com/search/datasheet_print.aspx?mat-guid=82f3cab027b14d2bb5b09730305a3ba6&n=1 (07 May 2018).

A Planar Shape Transformation Method Based on Non-Crossing Angulated Structural Element

Tao Yang[1], Peng Li[1*], Shun Liu[2*], Yantao Shen[3], and Yunhui Liu[4]

[1] Harbin Institute of Technology, Shenzhen, 518055 Shenzhen, China
[2] Beibu Gulf University, 535011 Qinzhou, China
Corresponding author: `peng.li@hit.edu.cn; ysqliu@126.com`
[3] University of Nevada, Reno, 89557 Reno, NV, USA
[4] The Chinese University of Hong Kong, 999077 Hongkong, China

Abstract. This paper presents two assemblies of non-crossing angulated elements (NCAE) and a shape transformation method to treat planar double-ring mechanisms. Both NCAE assemblies, termed Types I and II NCAE, have a constant subtended angle but different geometric constraints. Using Type I NCAE, a family of planar double-ring mechanisms is constructed. these mechanisms can transform their shapes between two specified polygons with equal number of sides.

Keywords: Scissor element, Morphing mechanism, Shape transformation

1 Introduction

Straight scissor element (SSE) and crossing angulated element (CAE) are two types of conventional scissor structural elements [1] [2]. A SSE is made from two straight rods crosswise interconnected by a hinge, while a CAE consists of two angulated rods crosswise interconnected by a hinge. Both elements are widely used in machines and mechanisms, such as Horberman's planar and spatial mechanisms [3], planar deployable objects [4], and deployable 3D linkages [5]. In addition to the two elements, there is another structural element, non-crossing angulated element (NCAE), that is less reported than the former two. An ordinary NCAE was first reported by Kempe [6]. Similar to CAE, NCAE also comprises two angulated rods interconnected by a hinge, but the two rods do not cross each other. This element was subsequently employed to construct planar double-ring mechanisms [7] and double-ring polyhedral linkages [8]. To investigate the potentialities of NCAE, this paper is devoted to the generalization and application of NCAE. Two types of NCAE assemblies are presented, termed Types I and II NCAE, which has a constant subtended angle during morphing. Based on Type I NCAE, a shape transformation method is further presented to endow planar double-ring mechanisms with the ability of transforming their shapes between two specified polygons with equal number of sides.

The paper is organized as follows: Section 2 presents two types of NCAE assemblies and the constructed mechanisms, respectively. Section 3 proposes the

shape transformation method of planar double-ring mechanisms. Finally draw a conclusion.

2   Two Types of NCAE Assemblies

An ordinary NCAE can be treated as a basic module to form more advanced mechanisms. After investigating this element, we propose two types of NCAE assemblies that can change their shapes while maintaining a **constant subtended angle**. The two NCAE assemblies are called Types I and II NCAE respectively and are useful for constructing more morphing mechanisms. The structural characteristics of both NCAE assemblies are as follows,

(1). **Type I NCAE**: This structure consists of a chain of an **arbitrary number** of parallelograms with two **isosceles triangles** connected at both flanks, see Fig.1. For example, every two NCAEs form a parallelogram $B_i E_i A_i E_{i+1}$ at the hinge joints B_i and A_i, and the two isosceles triangles are $\angle E_1 B_0 A_0$ and $\angle E_n B_n A_n$.

(2). **Type II NCAE**: This structure consists of a chain of an **odd number** of parallelograms with a pair of **similar triangles** connected at both flanks, see Fig.3. For example, every two NCAEs form a parallelogram $B_i E_i A_i E_{i+1}$ at the hinge joints B_i and A_i, the two similar triangles are $\angle E_1 B_0 A_0$ and $\angle E_n B_n A_n$, and the number of parallelogram must be odd.

The following sections will detail the geometric constraints of these two NCAE assemblies and prove that they have a constant subtended angle.
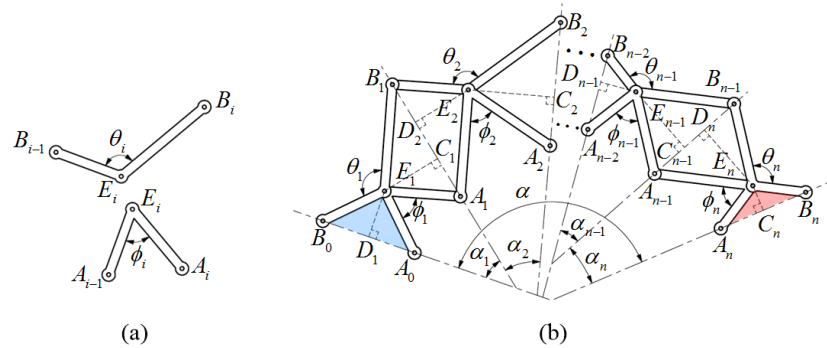

(a)   (b)

Fig. 1. Type I NCAE composed of several ordinary NCAEs and having an arbitrary number of parallelograms and two isosceles triangles. (a) Structure of NCAE; (b) Type I NCAE.

2.1   Analysis of Type I NCAE

Fig. 1 shows a Type I NCAE, which is composed of several ordinary NCAEs. In order to ensure subtended angle α keeps constant, we make the following geometry assumption.

(i) Every two adjacent NCAEs forms a parallelogram, and this leads to the following constraint,

$$\overline{A_i E_i} = \overline{B_i E_{i+1}}$$
$$\overline{B_i E_i} = \overline{A_i E_{i+1}} \tag{1}$$

(ii) $\Delta A_0 E_1 B_0$ and $\Delta A_n E_n B_n$ are isosceles triangles,

$$\overline{A_0 E_1} = \overline{B_0 E_1}$$
$$\overline{A_n E_n} = \overline{B_n E_n} \tag{2}$$

here, $i \in \mathbb{N}^*$, and the kink angles of rods $A_i E_i A_{i-1}$ and $B_{i-1} E_i B_i$ are respectively defined as ϕ_i and θ_i, $\overline{E_i D_i}$ and $\overline{E_i C_i}$ are respectively perpendicular to $\overline{A_{i-1} B_{i-1}}$ and $\overline{A_i B_i}$. Next, the results will show that angle α keeps constant when the end points A_0, B_0, A_n, and B_n moves along the radius direction of the sector. From Fig.1, it can be obtained that,

$$\alpha = \sum_{i=1}^{n} \alpha_i \tag{3}$$

$$\angle A_{i-1} E_i B_{i-1} + \phi_i + \angle A_i E_i B_i + \theta_i = 2\pi (i \in 1, 2, \ldots, n) \tag{4}$$

Since $\angle A_{i-1} D_i E_i = \angle A_i C_i E_i = \frac{\pi}{2}$, the angle α_i can be obtain as,

$$\alpha_i = \pi - (\angle A_{i-1} E_i D_i + \phi_i + \angle A_i E_i C_i) \tag{5}$$

According to condition (i),

$$\angle A_i E_i B_i = \angle A_i E_{i+1} B_i \tag{6}$$

$$\angle A_i E_i C_i + \angle A_i E_{i+1} D_{i+1} = \angle A_i E_{i+1} B_i \tag{7}$$

Substituting equation (6) into (4) gives,

$$\angle A_0 E_1 B_0 + \angle A_n E_n B_n + 2 \sum_{i=1}^{n-1} \angle A_i E_{i+1} B_i + \sum_{i=1}^{n} (\phi_i + \theta_i) = 2n\pi \tag{8}$$

Substituting equation (7) into (5) and the result into equation (3) gives,

$$\alpha = n\pi - \left(\angle A_0 E_1 D_1 + \angle A_n E_n C_n + \sum_{i=1}^{n-1} \angle A_i E_{i+1} B_i + \sum_{i=1}^{n} \phi_i \right) \qquad (9)$$

Because of condition (ii),

$$\angle A_0 E_1 B_0 = 2\angle A_0 E_1 D_1$$
$$\angle A_n E_n B_n = 2\angle A_n E_n C_n \qquad (10)$$

Substituting equation (10) into (8) and the result into equation (9) gives,

$$\alpha = \frac{(\theta - \phi)}{2} \qquad (11)$$

with $\theta = \sum_{i=1}^{n} \theta_i$ and $\phi = \sum_{i=1}^{n} \phi_i$. Namely, the **subtended angle** of Type I NCAE is **constant** whether this structure moves or not.

Especially, when $n = 1$, $\theta + \phi = \pi$, and $\overline{A_0 E_1} = \overline{B_0 E_1} = \overline{A_1 E_1} = \overline{B_1 E_1}$, Type I NCAE has the simplest configuration, and it can form a series of axisymmetric and rotationally symmetric double-ring mechanisms by connecting the terminal hinges together. In this configuration, it can be obtained that,

$$\alpha = \frac{\pi}{m_1} \, (m_1 \geq 2) \qquad (12)$$

where m_1 is the pair number of Type I NCAEs, and $m_1 \in \mathbb{N}^*$.

When $m_1 = 5$, the corresponding mechanism is shown in Fig. 2. Due to the geometrical condition, both the fully folded configurations in Fig. 2 are exactly the same.
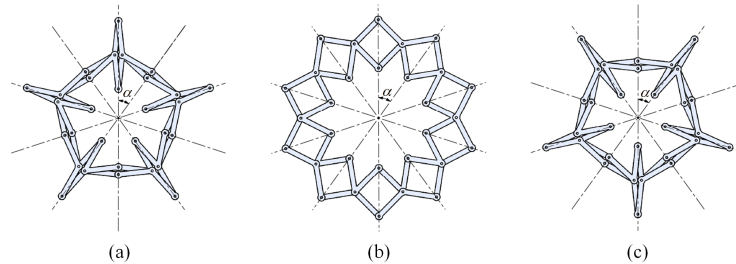

Fig. 2. Double-ring mechanism formed by 10 identical Type I NCAEs. (a) Fully folded configuration; (b) Expanded configuration with each closed-loop being square; (c) Another fully folded configuration.

2.2   Analysis of Type II NCAE

Fig. 3 shows the configuration of Type II NCAE, and the geometrical constraints are as follows,

(i) Every two adjacent NCAEs forms a parallelogram, and this leads to the constraint as shown in (1);

(ii)$\Delta A_0 E_1 B_0$ and $\Delta A_n E_n B_n$ are similar triangles, which leads to,

$$\frac{\overline{A_0 E_1}}{\overline{B_n E_n}} = \frac{\overline{B_0 E_1}}{\overline{A_n E_n}}$$
$$\angle A_0 E_1 B_0 = \angle A_n E_n B_n \tag{13}$$

(iii) The number of parallelograms is odd.

Here demonstrates that Type II NCAE has a constant subtended angle α. The equation (3) to (9) is also valid for Type II NCAE according to above condition (i). Meanwhile, due to the similar triangle constraint of condition (ii),

$$\angle A_0 E_1 B_0 = \angle A_n E_n B_n \tag{14}$$

$$\angle A_0 E_1 D_1 + \angle A_n E_n C_n = \angle A_0 E_1 B_0 \tag{15}$$

Substituting equations (14), (15) into (8), and the result into (9) gives equation (11). Thus, the **subtended angle** of Type II NCAE is also **constant**.

Furthermore, substituting equation (6) into (4) also gives,

$$\angle A_n E_n B_n = \begin{cases} 2\pi - \angle A_0 E_1 B_0 + \sum_{i=1}^{n} \left[(-1)^i (\theta_i + \phi_i) \right] & n = 2k - 1 \\ \\ \angle A_0 E_1 B_0 + \sum_{i=1}^{n} \left[(-1)^{i-1} (\theta_i + \phi_i) \right] & n = 2k \end{cases} \tag{16}$$

Substituting equation (14) into (16) gives,

$$\angle A_0 E_1 B_0 = \pi + \frac{1}{2} \sum_{i=1}^{n} \left[(-1)^i (\theta_i + \phi_i) \right], n = 2k - 1 \tag{17}$$

$$\sum_{i=1}^{n} \left[(-1)^{i-1} (\theta_i + \phi_i) \right] = 0, n = 2k \tag{18}$$

Because of ϕ_i and θ_i are constant parameters and the left side of equation (17) stay constant, while $\angle A_0 E_1 B_0$ is a variable and changes when the structure moves. Therefore, equation (17) is not always workable, while equation (18) is true and leads to,

$$\sum_{i=1}^{k} (\theta_{2i-1} + \phi_{2i-1}) = \sum_{i=1}^{k} (\theta_{2i} + \phi_{2i}), n = 2k, k \in \mathbb{N}^* \tag{19}$$
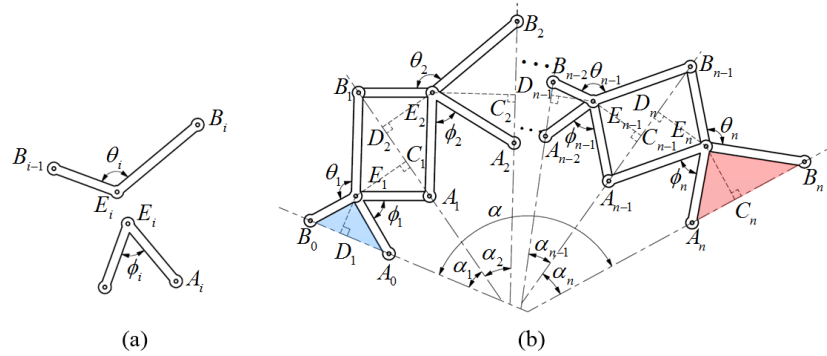
Fig. 3. Type II NCAE composed of several ordinary NCAEs and having an odd number of parallelograms and a pair of isosceles triangles. (a) Structure of NCAE; (b) Type II NCAE.

Therefore, the condition (iii) is necessary for defining Type II NCAE in order to maintain a constant subtended angle.

Especially, when $n = 2$, $\theta_1 + \phi_1 = \pi$, $\theta_2 + \phi_2 = \pi$, $\overline{A_0 E_1} = \overline{B_1 E_1} = \overline{A_1 E_2} = \overline{B_2 E_2}$, and $\overline{B_0 E_1} = \overline{A_1 E_1} = \overline{B_1 E_2} = \overline{A_2 E_2}$, any number of identical Type II NCAEs can form a series of rotationally symmetric double-ring mechanisms by connecting the terminal hinges. In such case, it can be obtained that,

$$\alpha = \frac{2\pi}{m_2}, m_2 \geq 3 \tag{20}$$

where m_2 is the number of Type II NCAEs.

When $m_2 = 5$, the corresponding mechanism is shown in Fig. 4. Similar phenomenon can be observed that the fully folded configuration in Fig. 4(a) is exactly the same as the shape in Fig.4(c), and the difference between Fig. 4 and Fig. 2 is that the shape of closed-loop degenerates from rectangle (see Fig. 4) into square (see Fig. 2).
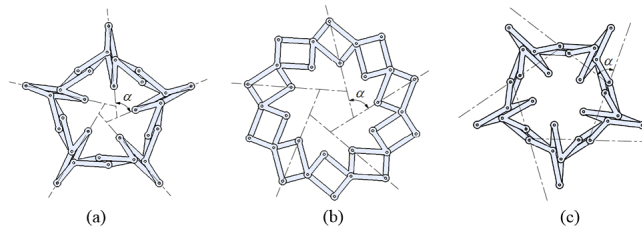
Fig. 4. Double-ring mechanism formed by 5 identical Type II NCAEs. (a) Fully folded configuration; (b) Expanded configuration with each closed-loop being rectangle; (c) Another fully folded configuration.

3 Planar Shape Transformation Method

By using the proposed Type I NCAE, we propose a shape transformation method to treat planar double-ring mechanisms. The proposed mechanisms are capable of transforming their shapes between two specified polygons with equal number of sides. Next, we will detail the method to use the Type I NCAE with $n = 1$ and $\theta + \phi = \pi$ to construct the mechanisms.
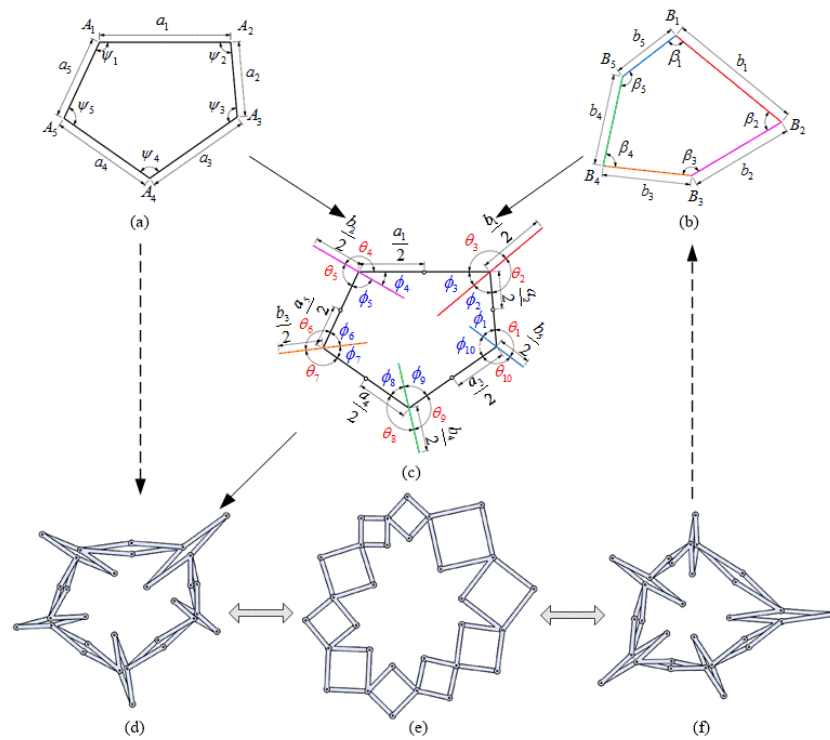

Fig. 5. Shape transformation method between two pentagons. (a) Initial pentagon; (b) Final pentagon; (c) Description of design parameters; (d) Initial shape configuration; (e) Transition configuration; (f) Final shape configuration.

Fig. 5 illustrates an example of how to construct a double-ring mechanism transforming the shape between two specified polygons. Fig. 5(a) and (b) shows two pentagons that represents a initial shape and a final shape. Fig. 5(c) shows the design parameters of the Type I NCAEs. Based on Fig. 5(c), the mechanism is constructed in Fig. 5(d) and (f). Fig. 5(e) shows the transition state of the mechanism. During morphing of the mechanism, the vertices in Fig. 5(a) are expanded into the sides in Fig. 5(b) and the sides in Fig. 5(a) degrade into the vertices in Fig. 5(b).

Step 1: The side number of two polygons is N, the ith side length of start shape is a_i and the jth side length of the target shape is b_j and clockwise numbered. ψ_i refers to the interior angle embraced by the sides a_{i-1} and a_i, and β_j refers to the interior angle embraced by b_{j-1} and b_j.

Step 2: Decompose the final shape at vertices to form a sequence of multiple individual segments $\mathbf{b} = \{b_1, b_2, \ldots, b_N\}$.

Step 3: Insert the segment sequence $\mathbf{b}$ at the vertices of the initial shape, and there are $2N$ possible solutions. We can use $A_{i_0}\mathbf{b}$ represents the shape of that $\mathbf{b}$ is inserted at vertex A_{i_0} clockwise and $\mathbf{b}A_{i_0}$ for counterclockwise. If $\mathbf{b}$ is inserted from A_1 to A_N, we can use $\mathbf{A}_{i_0}\mathbf{b}$ to represent all the combined shapes that vertices are inserted clockwise, and $\mathbf{b}\mathbf{A}_{i_0}$ for counterclockwise. Further, set $\mathbf{A}_{i_0}\mathbf{b}$ is actually $\{A_1\mathbf{b}, A_2\mathbf{b}, \ldots A_N\mathbf{b}\}$. For example, we use the $\mathbf{b}A_2$ to represent shape of Fig. 5(c), since $\mathbf{b}$ is inserted from A_2 to A_3 counterclockwise.

Sequentially the corresponding subscript relationship of vertex A_i and segment b_j in a set $\mathbf{A}_{i_0}\mathbf{b}$ or $\mathbf{b}\mathbf{A}_{i_0}$ is,

$$\frac{\mathrm{sgn}(|\ (i_0 - i)\ |) + (-1)^k \mathrm{sgn}(i_0 - i)}{2} N + (-1)^k (i - i_0) = j - 1, k \in \mathbb{N}^* \quad (21)$$

where i_0 is the subscript of start vertex, and k is even number when $\mathbf{b}$ is clockwise inserted while k is odd number when counterclockwise inserted.

Moreover, two constraints must be taken into consideration, one is length constraint and the other is angular constraint,

1) Length constraints: Each segment from $\mathbf{b}$ is bisected by the corresponding vertex of the initial shape, as shown in Fig. 5(c).

2) Angle constraints: Each segment from $\mathbf{b}$ divides the corresponding interior angle of the initial pentagon into two sub-internal angles. Let ϕ_{2j-1} and ϕ_{2j} be the two sub-internal angles between the sides of lengths b_{j-1} and b_j. The sum of two sub-internal angles ϕ_{2j-1} and ϕ_{2j} must equal the internal angle β_j for the preparation of constructing the proposed mechanism, as given by (22). Based on (21), the sum of the two sub-internal angles ϕ_{2j} and ϕ_{2j+1} equals the internal angle $\psi_{i_0+(-1)^k(j-1)}$, as given by (23). Moreover, the supplementary angle of each sub-internal angle ϕ_{2j-1} and ϕ_{2j} is denoted as θ_{2j-1} and θ_{2j}, as illustrated in Fig. 5(c).

$$\phi_{2j-1} + \phi_{2j} = \beta_j \quad (22)$$
$$\phi_{2j} + \phi_{2j+1} = \psi_{i_0+(-1)^k(j-1)} \quad (23)$$

where k is even number if clockwise and k is odd number if $\mathbf{b}$ is inserted counterclockwise.

Step 4: Insert two Type I NCAEs at each vertex of the initial shape, connect the two adjacent Type I NCAEs at the terminal hinges, and then the proposed mechanism is synthesized and can transform between the two shapes, as shown in Fig. 5(d-f). According to (21) and (23), the relationship between the design parameters of two Type I NCAEs and the interior angle of the vertex can be

Table 1. Parameters of all Type I NCAEs

Direction	Clockwise	Counterclockwise
Interior angle of the vertex where inserted	$\psi_{i_0+(j-1)}$	$\psi_{i_0-(j-1)}$
Design parameters of the first Type I NCAE	$\phi_{2j}, \theta_{2j}, a_{i_0+(j-2)}/2, b_j/2$	$\phi_{2j}, \theta_{2j}, a_{i_0-(j-1)}/2, b_j/2$
Design parameters of the second Type I NCAE	$\phi_{2j+1}, \theta_{2j+1}, a_{i_0+(j-1)}/2, b_j/2$	$\phi_{2j+1}, \theta_{2j+1}, a_{i_0-j}/2, b_j/2$

Table 2. Simulation results of the mechanism for two pentagons

ψ_1	ψ_2	ψ_3	ψ_4	ψ_5	β_1	β_2	β_3	β_4	β_5
$115°$	$95°$	$120°$	$110°$	$100°$	$103°$	$70°$	$143°$	$84°$	$140°$

ϕ_1	ϕ_2	ϕ_3	ϕ_4	ϕ_5	ϕ_6	ϕ_7	ϕ_8	ϕ_9	ϕ_{10}
$48°$	$55°$	$40°$	$30°$	$85°$	$58°$	$42°$	$42°$	$68°$	$72°$

θ_1	θ_2	θ_3	θ_4	θ_5	θ_6	θ_7	θ_8	θ_9	θ_{10}
$132°$	$125°$	$140°$	$150°$	$95°$	$122°$	$138°$	$138°$	$112°$	$108°$

obtained and is shown in Table 1. Relying on Table 1, we can design all Type I NCAEs for constructing the mechanism.

Step 5: For one of the solutions, we can uniquely determine the other sub-internal angles relying on (22) and (23) if the sub-internal angle ϕ_2 shown in Fig. 5(c) is given, while ϕ_2 can actually be the arbitrary angle value between zero and the smaller value in ψ_{i_0} and β_1, namely

$$0 \leq \phi_2 \leq \min(\psi_{i_0}, \beta_1) \tag{24}$$

As a result, the possible solutions for constructing the mechanism that transforms the shape between the two pentagons are infinite. According to the practical experience, when the kink angles of two inner rods of the mechanism at each vertex bisect the corresponding interior angle of the two pentagons, the results usually has special properties, such as the mechanism illustrated in Fig. 2. Based on this, an optimal objective function can be given by,

$$\phi^* = \mathrm{argmin} \sum_{j=1}^{N} \left(\frac{\mid \phi_{2j-1} - \phi_{2j} \mid}{\beta_j} + \frac{\mid \phi_{2j} - \phi_{2j+1} \mid}{\psi_{i_0+(-1)^k(j-1)}} \right) \tag{25}$$

where ϕ^* is the optimal set of all sub-internal angles, the first terms of the right-hand side means that each final shape vertex β_j is divided as evenly as possible into two sub-internal angles ϕ_{2j-1} and ϕ_{2j} , and the second terms means that each initial shape vertex $\psi_{i_0+(-1)^k(j-1)}$ is divided as evenly as possible into two sub-internal angles ϕ_{2j} and ϕ_{2j+1}. Based on the constraints in (22-24), an optimal solution for constructing the mechanism can be derived through (25).

Three configurations of the optimal mechanism are shown in Fig. 5(d-f), and its optimal set ϕ^* is listed in Table 2.

The above method is also applicable to the construction of double-ring mechanism that can transform the shape between any two specified polygons with equal number of sides.

4   Conclusion

This paper presented two types of NCAE assemblies. The analysis of the geometrical constraints showed that both NCAE assemblies can maintain the subtended angle constant when these structures moves. By using these NCAE assemblies, several planar double-ring mechanisms were builded. The paper also proposed a shape transformation method to endow planar double-ring mechanisms with the ability of transforming their shapes between two specified polygons with equal number of sides. Further research will focus on building more detail and intact framework for the NCAE assemblies and promoting their applications.

5   Acknowledgements

References

1. Yang, Y., Peng, Y., Pu, H., et al: Deployable parallel lower-mobility manipulators with scissor-like elements. Mechanism and Machine Theory. 135, 226-250 (2019). doi:10.1016/j.mechmachtheory.2019.01.013
2. Luo, Y.D., Zhao, N., Kim, K. J., Yi, J., Shen, Y.T.: Inchworm Locomotion Mechanism Inspired Self-Deformable Capsule-Like Robot: Design, Modeling, and Experimental Validation. In: IEEE International Conference on Robotics and Automation, pp. 6800-6805. IEEE Press, New York (2018).
3. Hoberman C.: Radial expansion/retraction truss structures. US Patent 5,024,031.
4. Zhang, R., Wang, S., Chen, X., et al.: Designing Planar Deployable Objects via Scissor Structures. IEEE Transactions on Visualization and Computer Graphics. 22(2), 1051-1062 (2016).
5. Zheng, C., Sun, T., Chen, X.: Deployable 3D linkages with collision avoidance. In: Acm Siggraph/eurographics Symposium on Computer Animation, Eurographics Association (2016). doi:10.2312/sca.20161235
6. Kempe, A.B.: On conjugate four-piece linkages. In: Proceedings of the London Mathematical Society. 9, 133-147 (1878).
7. Wohlart, K.: Double-chain mechanism. In: Proceedings of the IUTAM-IASS Symposium on Deployable Structures: Theory and Application. 457C466 (2000).
8. Wohlhart, K.: Double-ring polyhedral linkages. In: Interdisciplinary Applications of Kinematics. Springer, Dordrecht. 1-17 (2012).

A Quasi Rigid Constant Curvature Model for Inverse Kinematics of a Soft Panel Continuum Robot

Wenbin Wang[1], Xiangping Yu[2], Yingzhong Tian[2]*, Yinjun Zhao[2], Hanbin Jiang[2] and Yuwen Li[2], Fengfeng Xi[3]

[1] School of Mechanical and Electrical Engineering, Shenzhen Polytechic, China
[2] School of Mechatronic Engineering and Automation, Shanghai University, China
Corresponding author email: troytian@shu.edu.cn.
[3] Department of Aerospace Engineering, Ryerson University, Canada

Abstract. Due to the coupled problem between kinematics and statics, the inverse kinematics of continuum robots is highly nonlinear, posing a challenging problem to solve. This paper presents a simplified approach to solve the inverse kinematics of a flexible panel continuum robot. The proposed method is based on a constant curvature model. Through experiment, two approximate relationships are observed. First, the arc length of the middle backbone can be estimated from the arc lengths of the two panels; second, the length difference between the two panels can be related to the tip angle. Based on these two approximate relationships, a simple inverse kinematics method is proposed. The proposed method has been validated by the experiment data with less than 2% of error, thereby demonstrating the effectiveness of the proposed method.

Keywords: Inverse kinematics, continuum robot, mechanism simplification, effectiveness analysis.

1 Introduction

Continuum robots have become a subject of intensive research mainly thanks to their ability to reproduce certain animals' movement, such as snakes, elephant trunks and octopus tentacles. They are made up of flexible materials possessing good ability of bending and dexterity, enabling them to maneuver in congested environments. Specific applications such as minimally invasive surgery, nuclear reactor maintenance, disaster

relief and many other places have proved their universal use.

Continuum robots are often kinematically redundant and highly nonlinear. The lack of sufficient discrete joints renders their kinematic analysis more complex than their rigid-link counterparts. Unlike of rigid robots where the pose of any point in the robot workspace can be fully defined by links lengths and joint angles, the kinematic of continuum robots remains difficult to obtain with high accuracy, because they are under-determined systems with a high number of parameters.

In the past, Jones and Walker [1, 2] used a modified homogenous transformation matrix in terms of Denavit-Hartenberg (D-H) approach to develop and analyze the kinematic model of the continuum robot. Godage et al. [3] presented a new three-dimensional kinematic model for multisection continuum arms using a novel shape function-based approach [4], which incorporates geometrically constrained structure of the arm. Another interesting approach is the one presented in [5], where the authors used torus segments to represent the sections of the bionic handling assistant (BHA) manipulator. Escande et al. [6] developed the forward kinematic model of the compact bionic handling assistant (CBHA) based on the constant curvature assumption. However, the above methods mentioned have a common problem of being difficult to derive the inverse kinematics directly from the forward kinematics. Usually, we make the use of numerical methods (least squares, Newton–Raphson methods, etc.), which are computationally intensive. On the other side, qualitative methods have become a popular method to solve inverse kinematics problems. Giorelli et al. [7] approximated the inverse kinematic model (IKM) of a soft manipulator using a feed-forward neural networks. Rolf et al. [8] introduced a goal babbling approach to solve the IKM of the bionic handling assistant robot. Melingui et al. [9] used NN in a distal supervised learning scheme to approximate the IKM of the CBHA robot. Although qualitative methods are more accurate than quantitative methods in solving inverse kinematics problems, they are still time-consuming and computationally expensive. For this reason, we are exploring a simple approach to solving the inverse kinematics problem.

The rest of this paper is arranged as follows. Section 2 describes the Structure of the soft panel continuum robot. In section 3, we propose a quasi-rigid model for inverse kinematics of the planar soft parallel robot based on the recent experimental study results and the conclusions of previous work. At last, we conduct a number of case studies to show the effectiveness of the model.
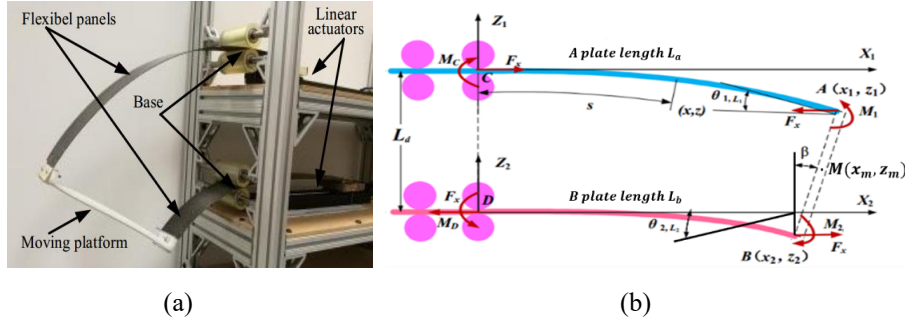
2 Structure Description

Fig. 1. Structure of the soft panel continuum robot

As shown in Figure 1(a), the continuum robot consists of two flexible panels made of carbon fibers. Each panel is connected to a linear actuator on one end and runs through the gap between two sets of rollers to connect to the moving platform on the other end. Both linear actuators and rollers are mounted on a frame. The two sets of rollers form the bases of the flexible panels. Since the panels are mainly subject to bending, their deformations are directional, very flexible in the length direction yet very rigid in the width direction. Due to this directionality, they are naturally constrained only to deform along the length direction, i.e. in the *X-Z* plane as shown in Figure 1(b), which shows the simplified model of this continuum robot. As the two linear actuators move back and forth, the panel lengths changes to cause the robot to curve up or down, depending on the direction of the length difference between the two panels.

Kinematically, this continuum robot is formed by four points: *A* and *B* for the moving platform, *C* and *D* for the fixed base. There are two sets of the coordinate frames: (x_1, z_1) for top plate *A* and (x_2, z_2) for bottom plate *B*. The distance between these two coordinate frames is L_d along the common *Z* axis. The top panel length is denoted by L_a and the bottom one by L_b. L_a and L_b are the changing variables controlled by the respective linear actuators. x_1, z_1 represent the coordinates of the end point of the top panel (point *A*) and x_2, z_2 the coordinates of the end point of the bottom panel (point *B*), in their respective coordinate frames.

The positions of the end point $A(x_1, z_1)$ and $B(x_2, z_2)$ can be solved according to [10]. The position and orientation (also called tip angle) of the moving platform can be calculated from these two points as

$$x_M = \frac{x_1 + x_2}{2}, z_M = \frac{z_1 + z_2}{2} \tag{1}$$

$$\beta = \tan^{-1}\frac{x_1 - x_2}{z_1 - z_2} \tag{2}$$

As described in [10], the forward kinematics of the continuous robot is solved. In actual applications, however, a desired tip posture is specified, and the inverse problem becomes more important in order to determine the actuator lengths that correspond to the desired tip posture. There are too many implicit parameters in forward kinematics modeling, which makes the inverse kinematics a very challenging problem. For this reason, we are exploring a simple method for solving this problem.

3 A Quasi Rigid Model for Inverse Kinematics

We propose a quasi-rigid model for solving its inverse kinematics. First, we conducted a serial of experiments by inputting the panel lengths and then measuring the end positions of the two panels by an optical coordinated machine measurement (CMM) device. These two end points are $A(x_1, z_1)$ and $B(x_2, z_2)$ as shown in Figure 2(a), from which we can calculate the middle point of the moving platform and its orientation as defined before as x_M, z_M and tip angle β (Eq. (1) and (2)). Table 1 presents the experiment data in increments of panel lengths La and Lb.

Table 1. Experimental results unit: mm

Series1: Lb=150;	x_M	z_M	$\beta_{rea}(deg)$
La=200;	174.06	-120.79	13.38
La=250;	193.98	-145.74	27.55
La=300;	210.10	-175.54	40.71
La=350;	219.17	-208.68	54.26
La=400;	219.87	-239.81	66.56
Series2: Lb=200;	x_M	z_M	$\beta_{rea}(deg)$
La=250;	222.91	-128.43	13.95
La=300;	243.26	-155.72	28.06
La=350;	255.21	-191.32	41.41
La=400;	262.07	-227.22	54.62
Series3: Lb=250;	x_M	z_M	$\beta_{rea}(deg)$

La=300;	271.85	-135.51	14.01
La=350;	289.41	-171.09	27.71
La=400;	300.26	-209.69	40.88
Series4: Lb=300;	x_M	z_M	$\beta_{rea}(deg)$
La=350;	319.96	-142.68	14.06
La=400;	336.88	-183.78	27.82
Series5: Lb=350;	x_M	z_M	$\beta_{rea}(deg)$
La=400;	370.91	-150.14	14.25

(a)   (b)
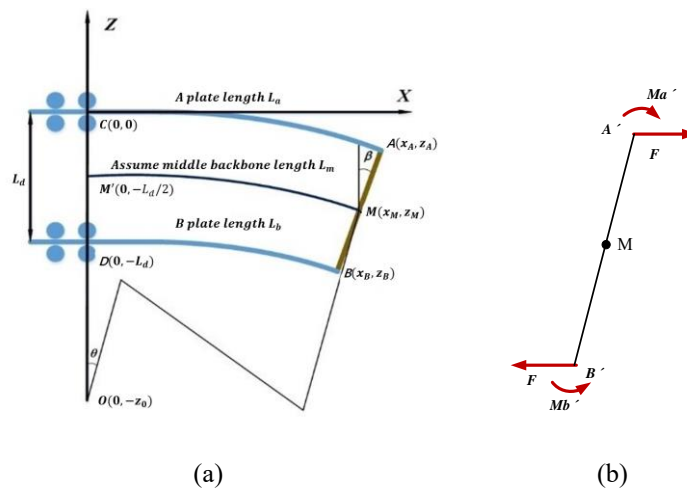
Fig. 2. continuum robot and coordinate and static analysis of configuration rigid bar

To develop a quasi-rigid model, a virtual backbone is assumed that runs through the middle of the two panels, as shown in Figure 2(a). In terms of internal forces, there is a pushing force at point A and a pulling force at point B, so forces are balanced on the moving platform but with moments, as shown in Figure 2(b). According to the Bernoulli–Euler beam theory, a beam with a pure-moment load will resemble a purely circular arc. The obtained loading condition under a pure-moment scenario suggests that the middle backbone would bend into a perfectly circular shape. Therefore we assume the shape of middle backbone is arc. Since the arc is perpendicular to the Z axis at the start point, the center coordinate of the arc is 0 in X direction and z_0 in Z direction. In other words, the middle backbone has the start point at $M'(0, -L_d/2)$ and the end point at $M(x_M, z_M)$. Therefore, a circle equation can be written as

$$(L_d/2 - z_o)^2 = {x_M}^2 + (z_M + z_o)^2 \tag{3}$$

from which Z_o can be determined for given x_M and z_M

$$z_o = \frac{x_M^2 + z_M^2 - \frac{L_d^2}{4}}{2z_M + L_d} \tag{4}$$

To this end, we have found the center of the circle. The next step is to determine the radius of the circle. This can be readily obtained by adding z_o and half of the distance between the two panels as

$$r = -(z_o + \frac{L_d}{2}) \tag{5}$$

Based on the circle center, we can obtain the following relation

$$tan\theta = \frac{x_M}{(z_M - z_o)} \quad , \theta \in [0, \frac{\pi}{2}] \tag{6}$$

leading to the angle θ as

$$\theta = arctan \frac{x_M}{(z_M - z_o)} \tag{7}$$

Based on this angle, the arc length of the middle backbone can be determined as

$$L_m = \theta \cdot r \tag{8}$$

Now let us look at the experiment data in order to draw certain useful relationships. Table 2 shows the measured length of the middle backbone under different panel lengths. In this table, ΔL represents the difference between two panels. The initial lengths of the two panels were both at 0.15m, and panel A is put forward by 0.05m for each increment. By using the previously mentioned 3D optical device, the end coordinates of the two panels were measured and the position of the moving platform x_M and z_M were calculated by using Eq. (1) and (2). We further determined the center of the middle backbone and the radius by Eq. (4) and (5), and angle θ and the middle backbone length L_m by Eq. (8) and (9). Table 2 to 6 repeated the same experiments but with different start length of panel B in order to cover the entire motion range for our study. According to Eq. (5) (7) and (8), the arc length of the middle backbone can be expressed in terms of (x_M, z_M), β and L_d as

$$L_m = (\frac{L_d}{2} - \frac{x_M^2 + z_M^2 - L_d^2/4}{2z_M + L_d}) \cdot arctan(\frac{2x_M z_M + L_d}{z_M(z_M + L_d) - x_M^2 + L_d^2/4}) \tag{9}$$

Table 2. The length of assumed backbone in difference ΔL(Data from experiment, Lb=0.15m)

$\Delta L: (m)$	$x_m: (m)$	$z_m: (m)$	$L_m: (m)$	$\frac{(L_a + L_b)}{2}: (m)$	$e_L = L_m - \frac{(L_a + L_b)}{2}$

$\Delta L:(m)$	$X_m:(m)$	$Z_m:(m)$	$L_m:(m)$	$\frac{(L_a+L_b)}{2}:(m)$	$e_L=L_m-\frac{(L_a+L_b)}{2}$
0.05	0.1741	-0.1208	0.1750	0.1750	0.000
0.10	0.1940	-0.1457	0.1996	0.2000	-0.0004
0.15	0.2101	-0.1755	0.2255	0.2250	0.0005
0.20	0.2201	-0.2087	0.2513	0.2500	0.0013
0.25	0.2199	-0.2398	0.2714	0.2725	-0.0011

Table 3. The length of assumed backbone in difference ΔL(Data from experiment, Lb=0.20m)

$\Delta L:(m)$	$X_m:(m)$	$Z_m:(m)$	$L_m:(m)$	$\frac{(L_a+L_b)}{2}:(m)$	$e_L=L_m-\frac{(L_a+L_b)}{2}$
0.05	0.2229	-0.1284	0.2245	0.2250	-0.0005
0.10	0.2433	-0.1557	0.2503	0.2500	0.0003
0.15	0.2552	-0.1913	0.2742	0.2750	-0.0008
0.20	0.2621	-0.2272	0.2983	0.3000	-0.0017

Table 4. The length of assumed backbone in difference ΔL(Data from experiment, Lb=0.25 m)

$\Delta L:(m)$	$X_m:(m)$	$Z_m:(m)$	$L_m:(m)$	$\frac{(L_a+L_b)}{2}:(m)$	$e_L=L_m-\frac{(L_a+L_b)}{2}$
0.05	0.2718	-0.1355	0.2741	0.2750	-0.0005
0.10	0.2894	-0.1710	0.2994	0.3000	0.0003
0.15	0.3003	-0.2097	0.3242	0.3250	-0.0009

Table 5. The length of assumed backbone in difference ΔL(Data from experiment, Lb=0.30 m)

$\Delta L:(m)$	$X_m:(m)$	$Z_m:(m)$	$L_m:(m)$	$\frac{(L_a+L_b)}{2}:(m)$	$e_L=L_m-\frac{(L_a+L_b)}{2}$
0.05	0.3200	-0.1427	0.3226	0.3250	-0.0024
0.10	0.3369	-0.1838	0.3488	0.3500	-0.0012

Table 6. The length of assumed backbone in difference ΔL(Data from experiment, Lb=0.35 m)

$\Delta L:(m)$	$X_m:(m)$	$Z_m:(m)$	$L_m:(m)$	$\frac{(L_a+L_b)}{2}:(m)$	$e_L=L_m-\frac{(L_a+L_b)}{2}$
0.05	0.3709	-0.1501	0.3745	0.3750	-0.0005

The proposed inverse kinematics is based on the observation from Table 2 to 6. It was found from these tables that L_m and $(L_a+L_b)/2$ have very closed values, from

which the first approximate relation is assumed to relate the panel lengths to L_m as

$$L_m = \frac{L_a + L_b}{2} \tag{10}$$
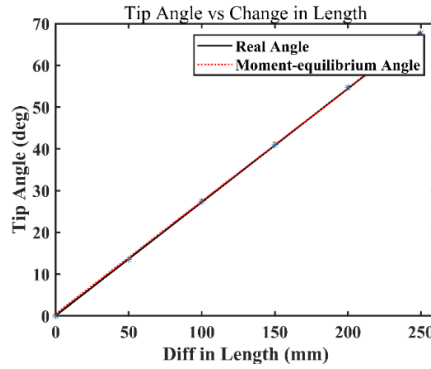
Fig. 3. Tip angle vs change in length

Furthermore, Figure 3 is the experiment data showing that the tip angle β is linearly proportional to the length difference of the two panels ΔL. The moment-equilibrium Angle is obtained by forward kinematics analysis [10]. From which the second approximate relationship is assumed as

$$L_a - L_b = \Delta L = k\beta \tag{11}$$

where β is the tip angle defined before and k is the constant coefficient depending on the material of the two panels. From Eq. (10) and (11), we can now solve the panel lengths as

$$L_a = L_m + \frac{k\beta}{2} \tag{12}$$

$$L_b = L_m - \frac{k\beta}{2} \tag{13}$$

To summarize, the inverse kinematic problem can be solved as follows. For given (x_M, z_M) and β, Eq. (9) is first used to determine L_m and then Eq. (12) and Eq. (13) are used to determine the panel lengths L_a and L_b that will drive the robot to reach the given position (x_M, z_M) with given orientation angle β. Apparently this is a much simple way of solving the inverse kinematics problem.

4　Effectiveness Analysis of The Method

To validate the proposed method, we use the experiment data recorded in Tables 2 to

6. In this validation, the original lengths of the two panels are taken as the actual lengths. As explained before, the original lengths were used to input to the robot and then the position and orientation of the robot were measured. For comparison, the measured robot position and orientation were used to solve the lengths using the steps described in the proceeding section. The comparison results are given in Figure 4, where the X label is L_a / L_d with the length of $L_d = 0.21\text{m}$, and the Y label represents the error of panel length A and B. Figure 4 has four small figures covering four cases of different L_b. It can be seen from Figure 4 that the maximum error of the simplified method is less than 2% compared to the actual input values. Therefore, we can claim our inverse kinematic method is valid and effective.
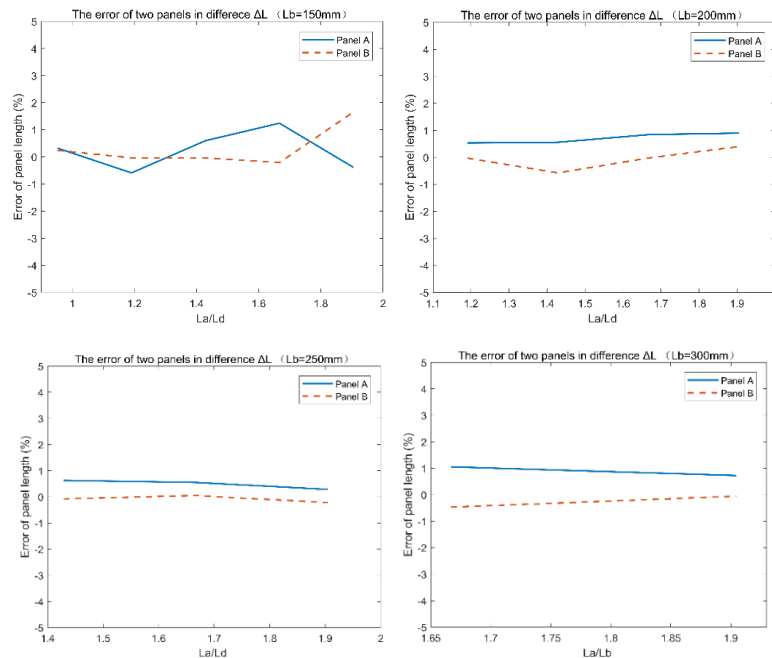
Fig. 4. Error analysis of the method

5   Conclusions

This paper presents a quasi-rigid model for solving the inverse kinematics of a continuum robot driven by flexible panels. It is shown that the planar panel continuum robot under study, though having two actuators, can control fully the position and orientation of the robot. Through experiment, two approximate relationships are

observed. First, the arc length of the middle backbone can be estimated from the arc lengths of the two panels; second, the length difference between the two panels can be related to the tip angle. Based on these two approximate relationships, a simple inverse kinematics method is proposed. The proposed method has been validated by the experiment data with less than 2% of error, thereby demonstrating the effectiveness of the proposed method.

References

1. B. A. Jones and I. D. Walker, "Practical kinematics for real time implementation of continuum robots," IEEE Transactions on Robotics, vol. 22, no. 6, pp. 1087–1099, 2006.
2. B. A. Jones and I. D. Walker, "Kinematics for multi-section continuum robots," IEEE Transactions on Robotics, vol. 22, no.1, pp. 43–55, 2006.
3. I. S. Godage, E. Guglielmino, D. T. Branson, G. A. Medrano-Cerda, and D. G. Caldwell, "Novel modal approach for kinematics of multisection continuum arms," in Proc. IEEE Int. Conf. Intell. Robots Syst., 2011, pp. 1093–1098.
4. I. S. Godage, D. T. Branson, E. Guglielmino, G. A. Medrano-Cerda, and D. G. Caldwell, "Shape function-based kinematics and dynamics for variable length continuum robotic arms," in Proc. IEEE Int. Conf. Robot.Autom., 2011, pp. 452–457.
5. M. Rolf and J. J. Steil, "Constant curvature continuum kinematics as fast approximate model for the bionic handling assistant," in Proc. IEEE Int. Conf. Intell. Robots Syst., 2012, pp. 3440–3446.
6. C. Escande, R. Merzouki, P. M. Pathak, and V. Coelen, "Geometric modelling of multisection bionic manipulator: Experimental validation on robotinoxt," presented at the IEEE Int. Conf. Robotics Biomimetics, Guangzhou, China, Dec. 2012.
7. M. Giorelli, F. Renda, G. Ferri, and C. Laschi, "A feed-forward neural network learning the inverse kinetics of a soft cable-driven manipulator moving in three-dimensional space," in Proc. IEEE Int. Conf. Intell. Robots Syst., 2013, pp. 5033–5039.
8. M. Rolf and J. J. Steil, "Efficient exploratory learning of inverse kinematics on a bionic elephant trunk," IEEE Trans. Neural Netw. Learn. Syst., vol. 25, no. 6, pp. 1147–1160, Jun. 2014.
9. T. Mahl, A. Hildebrandt, and O. Sawodny, "Forward kinematics of a compliant pneumatically actuated redundant manipulator," in Proc. IEEE 7th Ind. Electron. Appl. Conf., 2012, pp. 1267–1273.
10. Li Y, Zhao Y, Tian Y, Xi F, Wang W. Modeling and Analysis of a Planar Soft Panel Continuum Mechanism. Journal of Mechanisms and Robotics. 2020;12(4).

Foldable 3-UPU parallel mechanism

Zheng Zhang[1,2], An Yin[1,2], Nianlong Chen[1,2], Haijiao Jia[1,2], Ziming Chen[1,2,*]

[1] School of Mechanical Engineering, Yanshan University, Qinhuangdao, Hebei 066004, China
[2] Parallel Robot and Mechatronic System Laboratory of Hebei Province, Yanshan University, Qinhuangdao, Hebei 066004, China
`chenzm@ysu.edu.cn`

Abstract. Parallel mechanisms have undergone many years of development, and many types of parallel mechanisms have been derived. Although the components of the parallel mechanism are relatively compact. However, it occupies a large space, which is not conducive to the transport and handling of the parallel mechanism. Therefore, the text intends to design a folding mechanism, so that the parallel mechanism can change its own space occupation while maintaining the original degree of freedom. As the platform size changes, the workspace of the mechanism will also change accordingly. It can increase the effective working space of the parallel mechanism.

This paper takes 3-UPU parallel mechanism as an example. A 3-UPU parallel mechanism with variable platform is proposed. The degree of freedom of the mechanism is analyzed by using the helix theory. According to the distribution of the constraint line vector, the properties of the degree of freedom of the mechanism are two rotations and one movement. The full circumferential properties of the degree of freedom are proved by means of spatial analytic geometry. Based on Herve and Bricard overconstrained mechanism designs, the platform deformation method with the platform changing and the degree of freedom invariable was deduced.

The characteristics of the triple symmetric Bricard mechanism were analyzed, and the relationship between the shape of the fully expanded mechanism and the parameters of the mechanism was obtained by D-H method. Based on the triple symmetric Bricard mechanism, a folding 3-UPU parallel mechanism is designed, which greatly reduces the space consumption of the mechanism and is convenient for transportation and handling.

Keywords: Deformation platform, Parallel mechanism, Folding, Triple symmetric Bricard mechanism.

1 Introduction

The parallel mechanism has always been unable to apply its advantages to different scenarios due to its small workspace, low flexibility and narrow application range. However, in recent years, with the development of intelligent devices and communication networks, the traditional media industry, TV and movies and other industries have gradually created a new demand for devices: more stable, more

portable devices. Therefore, it is a trend to design a parallel mechanism with strong bearing capacity, large stiffness, and portable flexibility at the same time.For these demands, there have been many successful commercial products based on series mechanism in the market. However, parallel platform structure is more stable, but the related product is not found.

The 3-UPU parallel mechanism was first proposed by Tsai [1] in 1996, which is a 3-UPU mechanism with three spatial mobility degrees of freedom. Subsequently, many scholars have done a lot of research on the freedom properties, workspace, Jacobian and statics of this mechanism [2−5].

Mohamed, Lambert, Li Ruiming and others have done a lot of significant studies on such institutions to varying degrees. On the basis of the research on the deformation platform 3-UPU parallel mechanism, this paper attempts to design the foldable 3-UPU parallel mechanism, which contributes to the lightweight, miniaturization and portability of the parallel mechanism. Deformation platform parallel mechanism is a kind of reconfigurable mechanism, which can change the size and shape of the platform under the condition that the branch chains and degrees of freedom of the mechanism remain unchanged.

With 3-UPU parallel mechanism as an example, this paper analyses the platform changes affect the performance of organization, because of the freedom of 3-UPU institutions of UPU branched chain and connection way of the platform and the axis of rotation of the relationship is very sensitive, different ways of connection and axis relationship can make a great difference to the overall degree of freedom, also because of the characteristics of 3-UPU parallel mechanism has been the attention of many scholars, and produced a large number of related research literature.

2   Deformation factors of UPU variable platform

2.1   DOF analysis of 3-UPU mechanism

The angles between the slides of the moving and fixed platform are θ_1 and θ_3. The distance between the center of the U pair of the fixed platform and the central axis of the fixed platform is R_1, R_2 and R_3 respectively. The distance between the center of the U pair of the moving platform and the central axis of the moving platform is r_1, r_2 and r_3 respectively. In each U pair, the rotating pair connected with the fixed and moving platform is called the first rotating pair, and the rotating pair connected with P pair is called the second rotating pair. The first rotating pair of moving platform U intersects with the first rotating pair of fixed platform U at point P. The mechanism takes three P pairs as driving pairs, whose lengths are L_1, L_2 and L_3 respectively.

Taking the θ_1 and θ_3 as 120° as the research object. According to the screw theory, the degree of freedom and the character of freedom of 3-UPU mechanism in the initial condition can be obtained. The mechanism posture of the initial position is shown in Fig. 1. According to the screw theory, three coplanar disjoint binding forces can be obtained. Fig. 2

The freedom of this platform is z-axis movement, and rotation around the x-axis and y- axis.
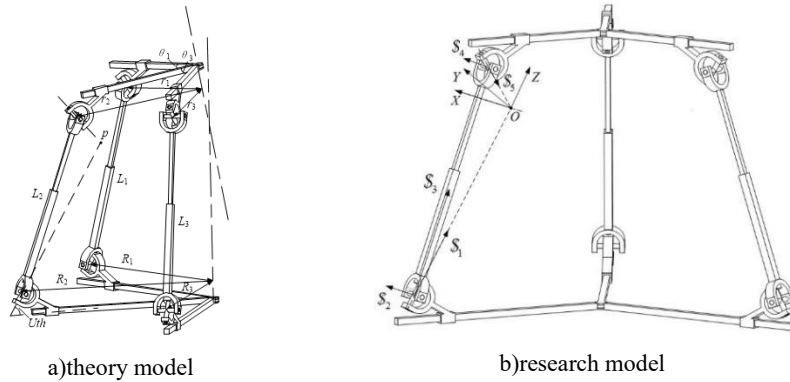

a)theory model   b)research model

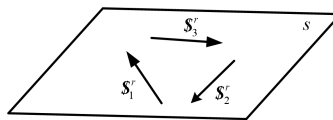**Fig. 1.** Initial position and attitude of mechanism

Fig. 2. Distribution of constrained linear vectors of the mechanism

2.2   Deformation of mechanism

The deformation of the mechanism means that the degree of freedom and the nature of degree of freedom of the mechanism will not change when the relevant parameters of the mechanism are changed. According to the conclusion in Section 1.1, as long as the binding force of the three branches can coplanar disjoint, the property of the degree of freedom of the mechanism will not change. Unfold the axis of the upper and lower platforms and the rods of the branch chains into a plane.

As shown in Fig. 3 As long as the lines formed by the intersections are parallel to the lines m and b, the three binding forces can be guaranteed to be coplanar. The second is to study the conditions that the structural parameters of the mechanism should be satisfied when the three binding forces are coplanar and the three binding forces do not intersect. As shown in Fig. 4
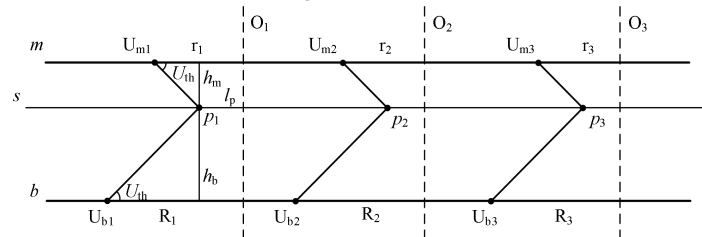
Fig. 3. Planar transformation of axis intersection points

a) Three-line interchange   b) Three parallel to the line
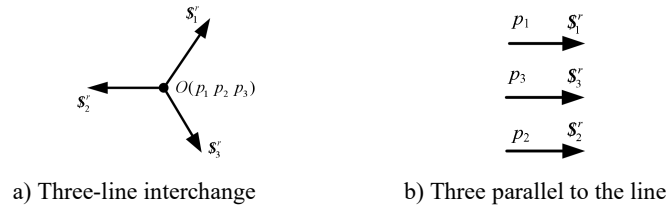
Fig. 4. Collinear or parallel of the three binding line vectors

Therefore, as long as the binding force is satisfied and there is no collinearity or parallelism, and the coplanar condition is satisfied, the degree of freedom of the mechanism will not be changed.

3   The design of auxiliary deformation mechanism

3.1   Triple symmetric Bricard mechanism

A single degree of freedom mechanism was designed to assist the 3-UPU mechanism to realize platform deformation. In order to reduce the complexity of the mechanism and control difficulty. Bricard mechanism was first proposed by French engineer and mathematician Raoul Bricard [1,7]. It is a spatial over-constrained closed-loop mechanism composed of 6 bars connected by 6 rotating pairs. Since all the links are connected in series, the D-H link coordinate system can be used to represent the structure and parameter relations, as shown in Fig. 4.

In Fig. 5, α represents the length of the connecting rod; α_I represents the deflection Angle between the axis of the rotating pair at the connecting end of the same connecting rod; d_I represents the distance between the two connecting rods on the axis of the rotating pair connecting them; α is the rotation deformation of the mechanism; represents the included Angle between the two connecting rods connected by the rotating pair. Different α will make the three-fold symmetry Bricard mechanism have different properties, but each mechanism can be fully expanded into an equilateral triangle. Fig. 6 shows a three-fold symmetric Bricard mechanism when $\alpha = 90°$.
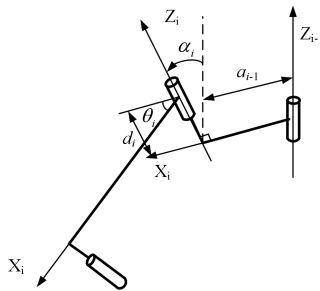
Fig. 5. Bricard linkage coordinate system

a) Equilateral triangle shape   b) General form
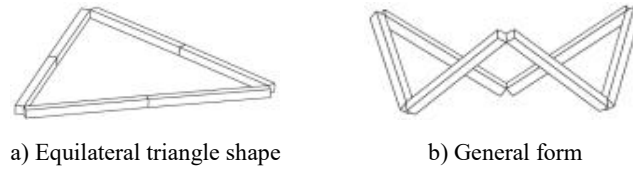
Fig. 6. Triple symmetric Bricard mechanism in $\alpha = 90°$

3.2 Triple symmetric Bricard mechanism for auxiliary deformation device

Since different values of α will make the three-fold symmetric Bricard mechanism have different motion properties. Triple symmetric Bricard mechanism must be selected according to the requirements of deformation assist device. Conditions to be met by the deformation assist device: the degree of freedom of the mechanism is 1, and the size of the equilateral triangle can be changed while the platform can be controlled to maintain the equilateral triangle.

For the degree of freedom of Bricard mechanism, Zhen Huang has proved in his book [8] that the degree of freedom of Bricard mechanism is 1 by using the screw theory. Since the six-connecting link of the tripartite symmetric Bricard mechanism are equal in length and have tripartite symmetric properties, the three points of the six non-adjacent endpoints of the mechanism constitute an equilateral triangle, and the dimensions change with the movement of the mechanism, which meets the requirements of the deformation auxiliary device. However, for different α values, the size of the equilateral triangle formed by the end points of the mechanism is different. When α = 60° or α = 120°, the mechanism can control the endpoint equilateral triangle to produce the maximum size variation, as shown in Fig. 7

A) Maximum equilateral   B) Size of middle   C) Minimum equilateral
triangle size   equilateral triangle   triangle size
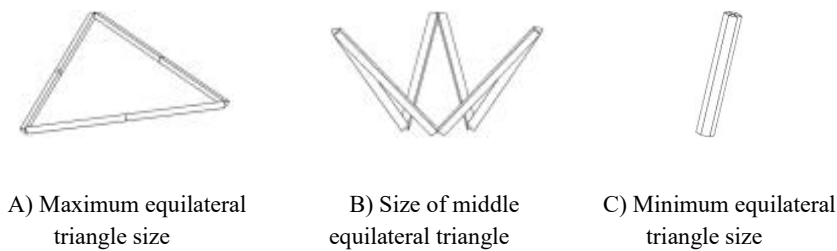
Fig. 7. Size variation of equilateral triangle at the end of the mechanism

By observing Fig. 6, it can be found that the mechanism can control the equilateral triangle of the endpoint to produce the maximum size variation range if and only if the six connecting rods of the mechanism can be folded into a bundle. In this case, the included Angle between each connecting rod of the mechanism is 180°, and the corresponding connecting rod parameters of the mechanism are:

$$\begin{cases} \theta = 180° \\ \varphi = 180° \end{cases} \tag{1}$$

Chen gave the closed-loop equation of the tripartite symmetric Bricard mechanism in reference [9].

$$\cos^2\alpha(\cos\theta - 1)(1 - \cos\varphi) + 2\cos\alpha\sin\theta\sin\varphi - \cos\theta - \cos\theta\cos\varphi - \cos\varphi = 0 \quad (2)$$

Solution:

$$\alpha = 60° \text{ or } \alpha = 120° \quad (3)$$

The institutions corresponding to $\alpha = 60°$ and $\alpha = 120°$ are exactly the same, and the proof is completed. Therefore, we choose the triple symmetry Bricard mechanism when $\alpha = 60°$ (120°) as the original mechanism configuration of the 3-UPU parallel mechanism platform deformation auxiliary device.

4 The design of the collapsible parallel mechanism

4.1 Equivalent mechanism of triple symmetric Bricard mechanism

Gan and Pellegrino [1] found the equivalent mechanism of the tripartite symmetric Bricard mechanism, which could make the connecting rod of the tripartite symmetric Bricard mechanism no longer perpendicular to the axis of the rotating pair. As shown in Fig. 8. The dotted line represents a triplicard mechanism. Keep the rotating pair axis fixed, so that the connecting rod and the intersection of the rotating pair axis in the direction of the rotating pair axis to produce a certain distance of movement. Then the mechanism formed by the moving solid lines is the equivalent mechanism of the tripartite symmetric Bricard mechanism.
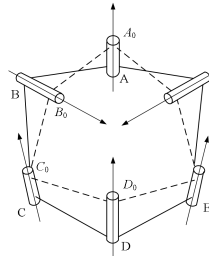
Fig. 8. Equivalent mechanism of tripartite symmetric Bricard mechanism.

4.2 Complete folding conditions of the equivalent mechanism

In order to make the folding conditions of the triple symmetric Bricard mechanism also apply to the equivalent mechanism. The folding condition of the supplementary triple symmetric Bricard mechanism is: The Angle formed by the projection of the axis of the rotating pairs at both ends of the linkage on the plane perpendicular to the linkage is $\gamma = 60°$. A regular prism is used to denote their relationship. As shown in Fig. 9., the projection Angle between axis AC and AD at both ends of connecting rod AD on plane ABC is 60°. Therefore, the equivalent mechanism of the triple

symmetric Bricard mechanism constituted by the new rotating pair axis of the mechanism can still be fully folded.
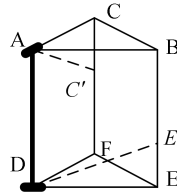
Fig. 9. Equivalent folding conditions of tripartite symmetric Bricard mechanism

4.3   Design of foldable 3-UPU parallel mechanism Subsection Sample

When $\gamma = 60°$, $\lambda = 90°$, the mechanism can be completely folded into a bundle. The structural characteristics are very similar to those of fixed and moving platforms of the 3-UPU mechanism studied in this paper. Therefore, a collapsible 3-UPU parallel mechanism is designed according to this mechanism. As shown in Fig. 10, making the axis of rotation pair of the foldable mechanism coincide with the axis of the first rotating pair of U pair of the moving platform. The two rotational axes intersect at point P. This is the foldable 3-UPU parallel mecha-nism Fig. 11.
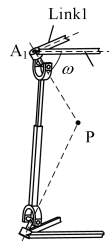
Fig. 10. Connection mode of equivalent mechanism and UPU branch chain

A) Fully expanded state   B) Folding process   C) Fully folded state
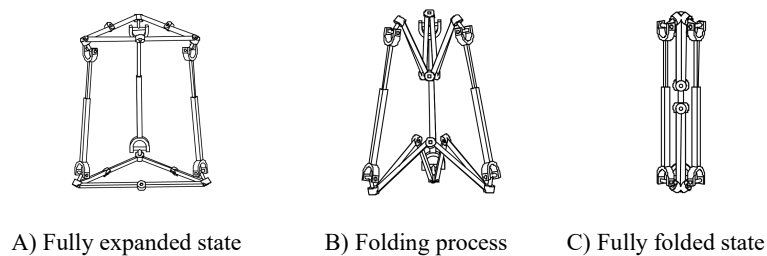
Fig. 11. Foldable 3-UPU Parallel Mechanism

The realization of foldable parallel mechanism will bring great application value to the parallel mechanism. It can directly reduce the space occupation of the organization, Easy to transport, handling, reduce the cost of mass transport. It can also

8

be applied to aerospace and other applications with strict requirements on space occupation.

Conclusion

(1) The degree of freedom and the nature of degree of freedom of 3-UPU mechanism are analyzed. Then we get the conditions that the parameters of the mechanism need to meet when the degree of freedom of the mechanism is unchanged.
(2) Research on the Bricard mechanism and obtain the conditions that the parameters of the maximum expansion of the Bricard mechanism should meet.
(3) The equivalent mechanism of the Bricard mechanism was studied to make it have the same expansion characteristics with the Bricard mechanism, and it was applied to the 3-UPU mechanism without affecting the degree of freedom and the nature of degree of freedom of the mechanism.

References

1. Lung-Wen Tsai. Kinematics of a Three-DoF Platform with Three Extensible Limbs[C]. Recent advances in robot kinematics, Springer, 401-410(1996).
2. Raffaele Di Gregorio, Vincenzo Parenti Castelli. A Translational 3-DoF Parallel Manipulator[M]. Springer Netherlands, 49-58 (1998).
3. Raffaele Di Gregorio, Vincenzo Parenti Castelli. Mobility Analysis of the 3-UPU Parallel Mechanism Assembled for a Pure Translational Motion[J]. Journal of mechanical Design, 124(2):259-264 (2002).
4. Sameer Alpana Joshi, Lung-Wen Tsai. Jacobian Analysis of Limited-DoF Parallel Manipulators[J]. Journal of Mechanical Design, 124(2):254-258 (2002).
5. Liwen Guan, Jinsong Wang, Liping Wang. Mobility Analysis of the 3-UPU Parallel Mechanism Based on Screw Theory[C]. International Conference on Intelligent Mechatronics and Automation, 309-314 (2004).
6. Xiangzhou Zheng, Zhiyong Deng, Yougao Luo, et al. Static Analysis of Translational 3-UPU Parallel Mechanism Based on Principle of Virtual Work[J]. Global Design to Gain A Competitive Edge, 681-690 (2008).
7. Raoul Bricard. Mémoire Sur La Théorie De L'octaèdre Articulé[J]. Journal de Mathématiques pures et appliquées, 3:113-148 (1897).
8. Raoul Bricard. Leçons Des Cinematique, Vol. 2[J]. Gauthier-Villars et cie, Paris, (1927).
9. Yan Chen, Zhong You, Tibor Tarnai. Three fold-Symmetric Bricard Linkages for Deployable Structures[J]. International journal of solids and structures, 42(8):2287-2301 (2005).
10. W.W. Gan, Sergio Pellegrino. Closed-Loop Deployable Structures[C]. Aiaa /asme /asce /ahs /asc Structures, Structural Dynamics, and Materials Conference, 2323-2330 (2003).

Design and Testing of a New Cell Microinjector by Combining Positive-Stiffness with Negative-Stiffness Mechanisms

Yuzhang Wei[1] and Qingsong Xu[2]

[1] University of Macau, Macau, China,
yb77450@um.edu.mo,
[2] University of Macau, Macau, China,
qsxu@um.edu.mo,
WWW home page: https://www.fst.um.edu.mo/people/qsxu/

Abstract. Microinjection with force sensing plays an important role in biomedical domain. However, most of microinjectors with force sensors lack enough load-bearing ability to support a pipette holder, which is needed to inject foreign materials into cells. In this paper, a new force-sensing cell microinjector with novel compliant small-stiffness mechanism is presented. It maintains large load-bearing ability and meanwhile high sensitivity. The small-stiffness is realized by the combination of a positive-stiffness and a negative-stiffness mechanisms, both generated from a constant-force mechanism. The output force of the microinjector is the force difference of these two mechanisms. When the microinjector moves forward, the forces of these two mechanisms are both increased, and hence the difference will be extremely small. The positive- and negative-stiffness mechanisms are designed and calibrated. A prototype microinjector is fabricated and tested. Experimental results show that the sensitivity has been improved more than twice that of the previous work, verifying its effectiveness in force-sensing microinjection.

Keywords: Microinjection, compliant mechanism, constant-force mechanism

1 Introduction

Microinjection is a process that uses a fine needle to inject small quantitative volume of materials into living cells [1]. The microinjection has many meaningful applications in genetics, molecular biology, and other biomedical areas [2,3]. As the manual microinjection is low efficient and inconsistent, robotic assisted microinjection has been a hot topic in last decades. At present, the robotic assisted microinjection is mainly depends on pure vision-based method [4]. However, the pure vision-based method is hard to judge whether the microinjection is successful or not [5]. Moreover, the huge computation of image processing requires relatively long time and high-performance equipment [6]. On the contrary, microinjection with force feedback can prevent cells from damage with

accurate control [7]. Currently, there are mainly three types of force sensors, that is, piezoresistive force sensors [8, 9], piezoelectric force sensors [10, 11], and capacitive force sensors [12, 13]. Although the resolution is quite high with low-stiffness, these force sensors are normally fragile or too soft to bear the weight of an air/liquid tube, which is necessary in injecting foreign materials into cells. Usually, the pipette needle is directly attached to the force sensor, making the microinjector manipulate cells to obtain the mechanical properties of cells.

In order to equip the microinjector with compressed air, a pipette holder (connecting a compressed air tube and a pipette needle as shown in Fig. 2) is normally used in microinjection. The microinjector should also have a certain load-bearing ability and relatively high sensitivity. To solve this problem, several previous work has been done [7, 14]. Specially, in our previous work [14], a constant-force mechanism and a positive-stiffness mechanism have been combined to achieve a novel small-stiffness mechanism. This previously designed microinjector can support the pipette holder and maintain a sensitivity of 1.24 mN. However, the property of the constant-force mechanism is extremely sensitive to parameter variation [14], and ideal property of constant force is hard to be obtained through the current limited machining accuracy. Fortunately, the properties of positive stiffness and negative stiffness are easier to be gained. The negative-stiffness mechanism in this work is defined as a mechanism which shows negative stiffness at certain range of displacement. Likewise, the positive-stiffness mechanism will show positive stiffness at certain range of displacement. Thus, the opposite combination of positive-stiffness mechanism and negative-stiffness mechanism has been proposed to obtain an extremely small stiffness mechanism in this paper.

As shown in Fig. 1(a), the start point is the initial position of the combined small-stiffness mechanism. When the small-stiffness mechanism moves from its initial position in the direction of +X axis, these two mechanisms will show force-displacement relationship in the directions of +X axis and -X axis starting from the start point, respectively. As the force direction is opposite for the opposite placement, the resultant force is the difference value of the forces of these two mechanisms, as shown in Fig. 1(b). In order to make the difference be small enough, the slope of the absolute value for these two straight line should be close. To keep the stroke of small-stiffness mechanism as large as possible, the start point should be at the middle of those straight lines. In this way, the requirement of the machining accuracy can be reduced and the sensitivity would also be increased.

The main contribution of the paper is the design and development of a new cell microinjector based on small-stiffness mechanism. The novelty of the design lies in that a small-stiffness mechanism is presented by combining a postive-stiffness mechanism and a negative-stiffness mechanism for microinjection. Compared with our previous work [14], this new design can reduce the requirement of machining accuracy and improve its sensitivity.
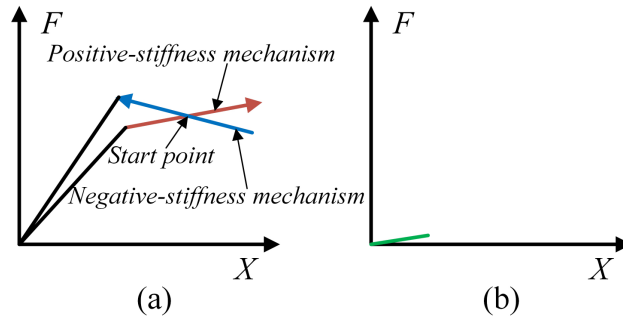
Fig. 1. Working principle of the proposed small-stiffness structure. (a) The small-stiffness mechanism is realized by combining a positive-stiffness mechanism with negative-stiffness mechanism oppositely. When the small-stiffness mechanism moves from the start point, theses two mechanisms will show force-displacement relationship in the arrow directions; (b) as these two mechanisms are placed oppositely, the resultant force will be the difference value of these two forces, which is extremely small.

2 Design and Analysis of a New Small-Stiffness Microinjector

The proposed small-stiffness microinjector is used to inject zebrafish, as it is a common biological model [4]. Thus, the microinjector should be able to release materials at the center of zebrafish and the minimum stroke is about 400 μm, which is the average radius of yolk for a zebrafish. Similarly, the force sensor attached to the microinjector should be able to deform more than 400 μm in the working direction. As the microinjector is used to inject zebrafish, the microinjection force should be sensed obviously and stably. Thus, the minimum requirement of resolution is about 20% of puncture force with specific micropipette needle.

2.1 Conceptual Design

In our previous work [14], a small-stiffness microinjector made up of a constant-force mechanism and a small positive-stiffness mechanism with intercept had been proposed. The previous microinjector obtained by the combination method overcomes the contradiction between the sensitivity and load-bearing ability to some extent. That is, the designed microinjector has relatively high sensitivity and meanwhile large load-bearing ability. Moreover, the microinjector only uses the motion range of constant force, reducing the requirement of material's property. However, the constant-force mechanism is extremely sensitive to the parameter variation, and hence the property of constant-force deteriorates, resulting in relatively low sensitivity of the previous microinjector.

In order to obtain pure constant-force property, the resolution of 0.01 mm is necessary [14], which is unrealistic for almost all common machining methods.
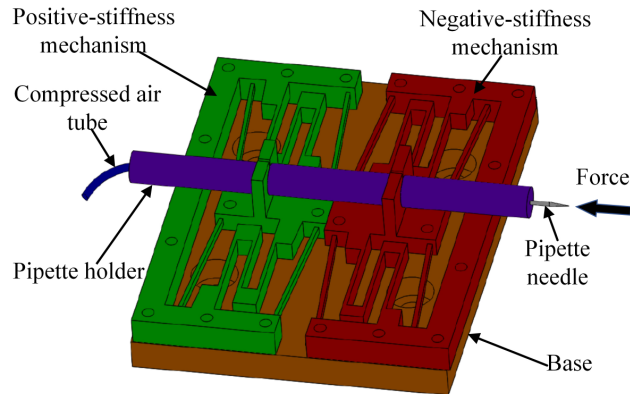
Fig. 2. 3D model of designed microinjector without pre-deformation. The microinjector is composed of positive stiffness mechanism with opposite negative stiffness mechanism. These two mechanisms support the pipette holder together. The pipette holder connects the pipette needle with the compressed air tube.

Actually, the properties of positive stiffness and negative stiffness are easier to be obtained. Thus, a new microinjector composed of positive-stiffness mechanism and positive-mechanism is presented, as shown in Fig. 2. These two mechanisms are placed oppositely with pre-deformation to make them be at the middle point, i.e., the start point in Fig. 1. In this configuration, when the microinjector moves in the force direction, the resultant force is the difference of the positive- and negative-stiffness mechanisms. Specially, when the microinjector moves in the force direction, the forces of these two mechanisms will increase together. Consequently, the difference is extremely small and the sensitivity of the microinjector with attached force sensor will be higher than that of the previous work, whose difference is between a small-stiffness and zero-stiffness mechanisms. It is noted that the 3D model in Fig. 2 is not pre-deformed for simplification. The two mechanisms support the pipette holder and the pipette holder connects the pipette needle with the compressed air tube. However, most of the current microinjectors with force sensors cannot inject materials, due to lacking compressed air to inject external materials [11–13, 15].

According to former design experience, the small positive-stiffness mechanism can be obtained by machining a constant-force mechanism via 3D printing using PC-ABS material. In other words, the small positive stiffness is generated by the machining error. Thus, a constant-force mechanism is firstly designed and tested, and then, the negative-stiffness mechanism will be designed according to the test result of the machined positive-stiffness mechanism. The PC-ABS is a popular and outstanding material with good mechanical property for 3D printing. Hence, in this work, the prototype is manufactured using PC-ABS for rapid prototyping.
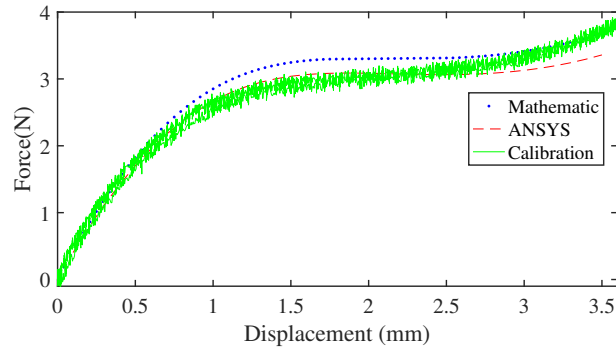
Fig. 3. Force-displacement relationship of the constant-force mechanism obtained by mathematic model, ANSYS simulation, and experimental calibration result. The small positive-stiffness mechanism is obtained by the machining error, as shown in the calibration result, although the mathematic model and ANSYS simulation results show excellent constant-force property, i.e., 3.3 N and 3.1 N, with the same constant-force motion range of 1.1 mm.

2.2 Calibration of Constant-Force Mechanism

The results of mathematic model and ANSYS simulation are shown in Fig. 3. These two results show excellent constant-force property, i.e., 3.3 N and 3.1 N, with 6.5% deviation in force, caused by simplification in the mathematic model [16]. The constant-force motion range is the same as 1.1 mm. Furthermore, the static stress simulation has been performed and the maximum stress is obtained as 16.66 MPa. Thus, the safety factor is 2.47 with the yield strength of 41 MPa for PC-ABS. In conclusion, the optimization result is satisfactory.

The prototype is manufactured with PC-ABS through 3D printing. As the negative-stiffness mechanism should be matched with positive-stiffness mechanism, the positive-stiffness mechanism should be calibrated first. It is noted again that the positive-stiffness mechanism is generated by the machining error of the constant-force mechanism. For clear explanation, the machined constant-force mechanism is called positive-stiffness mechanism. For calibration, an XYZ stage is used to carry and drive the force sensor to push the positive-stiffness mechanism. The laser-displacement sensor (model: LK-H055, resolution: 1 μm, from Keyence Corp.) and force sensor (model: LSB200-25lb, resolution: 0.1 N, from FUTEK Advanced Sensor Technology, Inc.) are used to collect the displacement and force signals of the positive-stiffness mechanism, respectively. The signals are collected by NI CRIO (model: 9022, from National Instruments Corp) and processed through LABVIEW. The whole setup is fixed on a vibration isolation platform. The calibration result can be seen in Fig. 3. A small-positive stiffness is generated during the constant-force motion range in mathematic and ANSYS results. It also should be noted that the relatively large fluctuation of calibration results is caused by hysterisis of back and forth movement, and the relatively large noise of calibrated force sensor. Fortunately, this fluctuation has

Table 1. Main Parameters of the Designed Nagative-Stiffness Mechanism

Componet	Parameter	Value
Positive-stiffness beam	l	21.5 mm
	h	1 mm
	b	5 mm
Negative-stiffness beam	L	34 mm
	γ	$5°$
	h	1.2 mm
	t	2 mm

insignificant effect on designing combined negative-stiffness mechanism. Since the positive stiffness has been obtained, a matched negative stiffness should be designed, as shown in Fig. 1.

2.3 Design of the Negative-Stiffness Mechanism

The negative-stiffness mechanism is obtained by increasing the output force and reducing the stiffness value of the positive-stiffness mechanism simultaneously. In this way, the force-displacement curve of negative stiffness could be similar as shown in Fig. 1. On the basis of previous work [14, 17], the value of the output force is of positive correlation with the in-plane width (h), inclined angle (γ), and out-of-plane thickness (t), but of negative correlation with the length of beam (L). Specially, the influence of inclined angle (γ) is too big to modulate, as the stiffness only needs fine tuning. For convenience, the in-plane width (h) and length (L) have been selected as variables to tune the curve of the negative-stiffness mechanism. The in-plane width has larger effect on the curve and the effect of length parameter is smaller.

Moreover, there are two important points from experience to regulate the curve. Firstly, the value from the mathematic model is a bit bigger than that of ANSYS simulation. Secondly, the slope from the calibration result of the negative-stiffness mechanism will be larger than that of mathematic model and ANSYS simulation results. These two points can be found in Figs. 3 and 4. Therefore, during the searching process, a little smaller slope and larger force should be added when matching the curves. After searching parameters in the mathematic model and ANSYS simulations by trial and error, the parameters are determined as shown in Table. 1. In this configuration, the start point in Fig. 1 is put a little further and the slope is a little smaller.

By using the searched parameters, the prototype of negative-stiffness mechanism is machined by the same 3D printing method and material. Then, the negative-stiffness mechanism is calibrated and the calibration result is given in Fig. 4. In order to verify the concept in Fig. 1, the calibration results of positive-stiffness mechanism and negative-stiffness mechanism are put together. As shown in Fig. 5, the calibration results are nearly consistent with the concept in Fig. 1, although there is hysterisis phenomenon in both results.
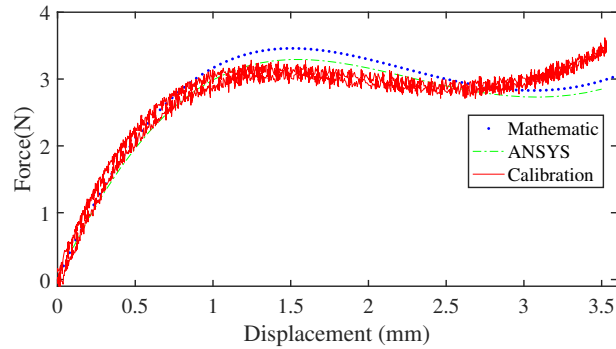
Fig. 4. Force-displacement relationship of the negative-stiffness mechanism obtained by mathematic model, ANSYS simulation and calibration result.
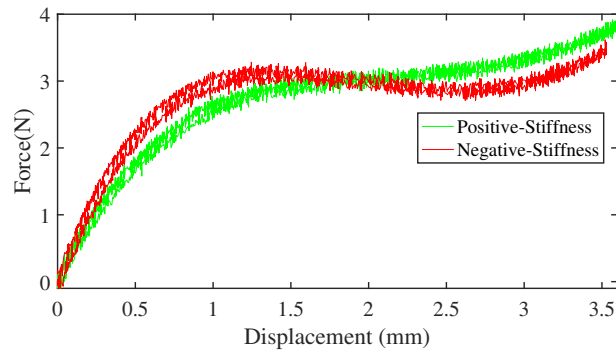

Fig. 5. Calibration results of positive-stiffness mechanism and negative-stiffness mechanism, which be nearly consistent with the concept in Fig. 1.

To conclude, the calibration results of the proposed positive-stiffness mechanism and negative-stiffness mechanism meet the requirement of Fig. 1. Therefore, the microinjector can be assembled as shown in Fig. 2. As the cross point is located at 1.7 mm in displacement, the pre-deformation of 3.4 mm is set on the base.

3   Experimental Results of the Small-Stiffness Cell Microinjector

The assembled microinjector and experimental setup are shown in Fig. 6. The experimental result can be seen in Fig. 7. Obviously, the curve can be divided into two parts, i.e., linear part and nonlinear part. The microinjector has a linear stroke of 0.65 mm, half of constant-force motion range in both positive- and negative-stiffness motion range in Figs. 3 and 4, corresponding with force
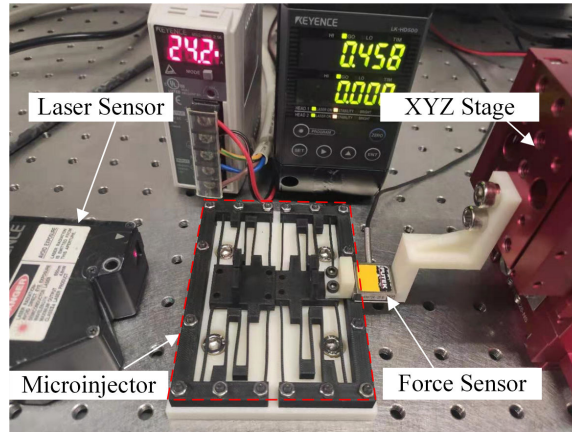
Fig. 6. Experimental calibration setup for the constant-force mechanism and small-stiffness mechanism.

range of 450 mN. Moreover, the stroke is actually larger than the average radius of zebrafish embryo, i.e., 500 μm, satisfying the motion range target.

The linear part of the curve in Fig. 7 is fitted well with a linear factor of 0.6955. Compared with our previous work, the sensitivity increases almost twice, where the linear factor is 1.37 within 0.7 mm stroke. The microinejctor can sense the injection force with piezoresistive strain gauges attached at the end of the positive-stiffness beam. In our previous work [14], the resolution is 1.24 mN and hence the resolution in this new design will be about half of the resolution, i.e., 0.62 mN, if the same strain gauges are used. It also should be noted that the resolution of the microinjection is related to two aspects, i.e., the stiffness of microinjector and the resolution of the force sensor. To conclude, the concept of combining positive-stiffness and negative-stiffness mechanisms has been verified for improving the sensitivity. In future work, specially designed capacitive force sensor is promising to improve the resolution of microinjector.

As compared with the available microinjectors, the proposed microinjector has three distinctive advantages. Firstly, the design reduces the requirement of materials and machining accuracy by only adopting the difference between relatively small positive-and negative-stiffness mechanisms during the constant-force motion range. In this motion range, the influences of the materials and machining error on force-displacement relationship are reduced by the difference between the positive-stiffness beam and negative-stiffness beam. Secondly, the microinjector has a large load-bearing ability to support the pipette holder (see Fig. 1), connecting pipette needle and compressed air tube, which is necessary to inject materials into cells. However, most of the current microinjectors with force sensor cannot support the pipette holder [5, 13, 15]. Thirdly, the stroke is relatively large, in comparison with several μm to tens of μm in [3, 8, 9, 12].
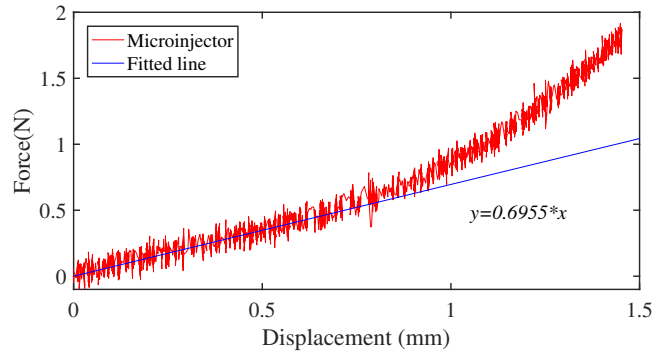
Fig. 7. Resultant force-displacement relationship of the microinjector and its fitted line.

Meanwhile, there are also two obvious disadvantages. Firstly, the microinjector is relatively bulky and heavy. Secondly, although the influence of machining error has been reduced by the designed configuration, there is still uncontrollable factors in manufacture, deteriorating the performance of the microinjector.

4 Conclusion

In this paper, a new microinejector based on small-stiffness mechanism is proposed. The presented small-stiffness mechanism is completed by combining positive- and negative-stiffness mechanisms. The positive-stiffness mechanism is obtained by making use of the machining error of the designed constant-force mechanism. The negative-stiffness mechanism is finely designed to reduce the positive stiffness from the middle point of constant-force motion range. A prototype microinjector is fabricated for experimental testing. Results indicate that the microinjector provides a linear range of 0.65 mm with the force range of 450 mN. The sensitivity has been improved twice in comparison with the previous work, which verifies the effectiveness of the designed small-stiffness mechanism. Moreover, the stroke is large enough to inject the targeted zebrafish embryo. In future work, design improvement will be conducted to further enhance its performance.

Acknowledgement

References

1. Y. Zhang, K. K. Tan, and S. Huang, "Vision-servo system for automated cell injection," *IEEE Transactions on Industrial Electronics*, vol. 56, no. 1, pp. 231–238, 2009.
2. D. Desmaële, M. Boukallel, and S. Régnier, "A planar structure sensitive to out-of-plane forces for the force-controlled injection of suspended and adherent cells," in *Proc. of 2011 Annual International Conference of the IEEE Engineering in Medicine and Biology Society (EMBC)*, 2011, pp. 8420–8423.
3. T. Beutel, N. Ferreira, A. Balck, M. Leester-Schadel, and S. Buttgenbach, "Cell manipulation system based on a self-calibrating silicon micro force sensor providing capillary status monitoring," *IEEE Sensors Journal*, vol. 12, no. 10, pp. 3075–3081, 2012.
4. Y. Wei and Q. Xu, "A survey of force-assisted robotic cell microinjection technologies," *IEEE Transactions on Automation Science and Engineering*, 2018.
5. Y. Xie, D. Sun, H. Y. G. Tse, C. Liu, and S. H. Cheng, "Force sensing and manipulation strategy in robot-assisted microinjection on zebrafish embryos," *IEEE/ASME Transactions on Mechatronics*, vol. 16, no. 6, p. 1002, 2011.
6. Z. Nan, Q. Xu, Y. Zhang, and W. Ge, "Force-sensing robotic microinjection system for automated multi-cell injection with consistent quality," *IEEE Access*, vol. 7, pp. 55 543–55 553, 2019.
7. Y. Wei and Q. Xu, "Design of a pvdf-mfc force sensor for robot-assisted single cell microinjection," *IEEE Sensors Journal*, vol. 17, no. 13, pp. 3975–3982, 2017.
8. V. T. Stavrov, A. A. Shulev, C. M. Hardalov, V. M. Todorov, and I. R. Roussev, "All-silicon microforce sensor for bio applications," in *Smart Sensors, Actuators, and MEMS VI*, vol. 8763, 2013, p. 87630Y.
9. Z. Lu, P. C. Chen, J. Nam, R. Ge, and W. Lin, "A micromanipulation system with dynamic force-feedback for automatic batch microinjection," *Journal of micromechanics and microengineering*, vol. 17, no. 2, p. 314, 2007.
10. A. Pillarisetti, M. Pekarev, A. D. Brooks, and J. P. Desai, "Evaluating the effect of force feedback in cell injection," *IEEE Transactions on Automation Science and Engineering*, vol. 4, no. 3, pp. 322–331, 2007.
11. Y. Xie, D. Sun, C. Liu, H. Y. Tse, and S. H. Cheng, "A force control approach to a robot-assisted cell microinjection system," *International Journal of Robotics Research*, vol. 29, no. 9, pp. 1222–1232, 2010.
12. Y. Sun, B. J. Nelson, D. P. Potasek, and E. Enikov, "A bulk microfabricated multi-axis capacitive cellular force sensor using transverse comb drives," *Journal of Micromechanics and Microengineering*, vol. 12, no. 6, p. 832, 2002.
13. Y. Sun and B. J. Nelson, "MEMS capacitive force sensors for cellular and flight biomechanics," *Biomedical Materials*, vol. 2, no. 1, p. S16, 2007.
14. Y. Wei and Q. Xu, "Design and testing of a new force-sensing cell microinjector based on small-stiffness compliant mechanism," *IEEE/ASME Transactions on Mechatronics*, 2020.
15. H. Huang, D. Sun, J. K. Mills, W. J. Li, and S. H. Cheng, "Visual-based impedance control of out-of-plane cell injection systems," *IEEE Transactions on Automation Science and Engineering*, vol. 6, no. 3, pp. 565–571, 2009.
16. Q. Xu, "Design of a large-stroke bistable mechanism for the application in constant-force micropositioning stage," *Journal of Mechanisms and Robotics*, vol. 9, no. 1, p. 011006, 2017.
17. P. Wang and Q. Xu, "Design and modeling of constant-force mechanisms: A survey," *Mechanism and Machine Theory*, vol. 119, pp. 1–21, 2018.

A Multi-mode Spatial Variable Geometry Truss Manipulator for Morphing Wings

Jieyu Wang[1], Yinjun Zhao[2*], and Jingjun Yu[1]

[1] Beihang University, Beijing, China, 100191
[2] Shanghai University, Shanghai, China, 200444
zhaoyj@shu.edu.cn

Abstract. Proposed in this paper is a method for constructing a multi-mode variable geometry truss manipulator (VGTM) with applications to morphing wings. The conventional wingbox structure is replaced by two planar VGTMs to obtain wing shape morphing. Each planar VGTM can be used to realize airfoil-level morphing while the combined spatial VGTM can be controlled to realize wing-level morphing including span, sweep, twist, dihedral and wingtip morphing. Essentially, the VGTMs are adopted to replace the conventional fixed wing structure including spars and ribs. Variable-length limbs are utilized instead, along with lockable joints to allow geometry morphing yet maintaining structural stability and reduce the number of actuators. In our design, only six actuators are used to drive the VGTM. By locking specific joints, the spatial VGTM can operate in different motion modes to have distinct morphing motions. In these modes, the VGTM all have low degrees-of-freedom (DOFs) and high stiffness and when locking all the joints, the VGTM turns into a statically indeterminate truss and can withstand large loadings.

Keywords: VGTM, Multi-mode, Morphing wing, Lockable joints, Under-actuation.

1 Introduction

The adoption of morphing wings can improve the efficiency of the aircraft significantly. Morphing concepts can be categorized into [1-6]: i) airfoil-level including thickness, camber, chord and reflex and ii) wing-level including span, sweep, twist, dihedral. These morphing motions can be achieved using smart materials such as shape-memory polymers [7] and piezoelectric [8]. These designs are flexible but their load-carrying ability is low. Therefore, there are a lot of researches that apply mechanisms to the morphing wing, including compliant mechanisms and rigid mechanisms. Compliant structures like chiral, hexagonal honeycombs, lattice, cellular and tensegrity structures [9-13] are difficult to meet the requirement of large load-carrying capacity as well as large-scale shape morphing. Hence, only rigid-link mechanisms are considered in this paper. Usually, mechanisms can be classified into serial mechanisms, parallel mechanisms (PMs) and hybrid mechanisms. For example, Neal [14] built a 7-DOF serial mechanism that can morph the aircraft wing to undergo span, sweep, twist and extend motions. Nevertheless, compared with PMs or hybrid

mechanisms, serial mechanisms have lower stiffness, and concentrating the load on the base of the mechanism results in a bulky system.

In order to have both shape-changing and load-carrying abilities, variable geometry truss manipulators (VGTM) have been applied. Trusses are composed of two-force members in the form of a parallel structure therefore are lightweight, stiff and capable of carrying large loads. In a VGTM, truss members are replaced by linear actuators or telescopic bars. Several morphing systems have been designed based on VGTMs, for antennas [15, 16] and morphing wings [17].

In our previous work, we have proposed a planar VGTM for airfoil morphing [18, 19], as shown in Fig. 1(a). The mechanism is actually a 4-RPR parallel mechanism and has three degrees-of-freedom (DOFs). It has one redundant limb and can be turned into a statically indeterminate truss. The function of the additional limb is to increase the stiffness of the mechanism and reduce the number of actuators. Only two actuators are utilized to drive the 3-DOF mechanism. The under-actuation is achieved by adopting lockable joints, as described in [18-19]. To achieve the other morphing motions, we applied the Gough-Stewart parallel mechanism [20] as shown in Fig. 1(b). Additional two limbs are assembled to the Gough-Stewart parallel mechanism to have a spatial VGTM. Reference [20] used multiple Gough-Stewart parallel mechanism connected in serial to have multiple morphing motions. This paper will investigate to use only one mechanism to accomplish six distinct morphing motions by locking specific joints and transiting among different motion modes. The purpose of this paper is to propose a method for constructing multi-mode VGTM that can accomplish all the morphing motions, including airfoil-level morphing and wing-level morphing. Structurally speaking, the method is to combine a planar VGTM and a parallel VGTM to obtain a spatial loop-coupled VGTM.
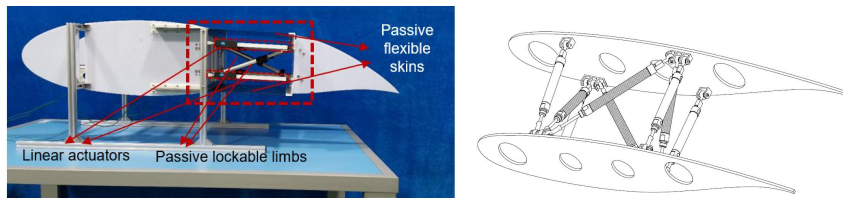
Fig. 1. VGTMs in the previous work: (a) planar VGTM; (b) parallel VGTM

2 Mechanism description
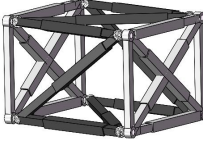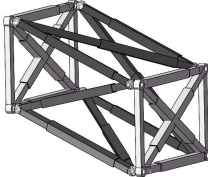
2.1 Objective determination

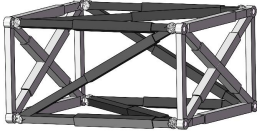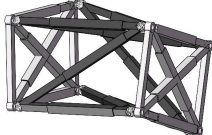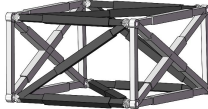To design a mechanism that can realize an aircraft morphing wing, the relationship between the morphing motion and the motion of the mechanism needs to be investigated first, as shown in Table 1. If a span motion is required, the right-side platform of the parallel mechanism should translate along z-axis. If a sweep motion is required, the right-side platform should translate along x-axis. If a dihedral motion is required, the right-side platform should translate along y-axis. If a twist motion is

required, the right-side platform should rotate around z-axis. If a wingtip motion is required, the right-side platform should rotate about y-axis or x-axis

2.2   Mechanism design

Table 1. The relationship between the morphing motion of the aircraft wing and the motion of the mechanism.

Morphing motion	Span	Sweep	Dihedral
Moving motion	Translating along z-axis	Translating along x-axis	Translating along y-axis
Morphing motion	Twist	Wingtip	Airfoil adjustment
Moving motion	Rotating around z-axis	Rotating around x-axis	Planar mechanism morphing

From Table 1, it can be seen that the Gough-Stewart parallel mechanism can accomplish wing-level morphing but not for airfoil-level morphing. In order to morph the airfoil shape, the two platforms of the Gough-Stewart parallel mechanism are replaced by a planar VGTM with additional two limbs to form a spatial loop-coupled

4

VGTM, as shown in Fig. 2. The proposed mechanism is comprised of two 3-DOF planar mechanisms with eight RPR limbs, connected by eight SPS limbs. To avoid interference, the two diagonal limbs in a planar VGTM will be arranged with an offset, as in our previous work.
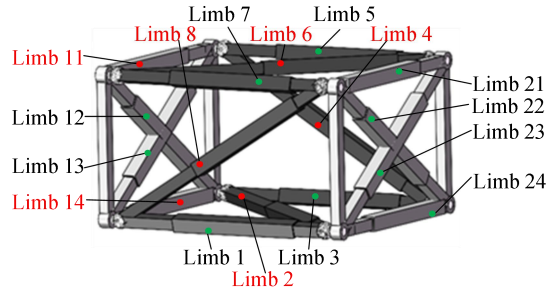

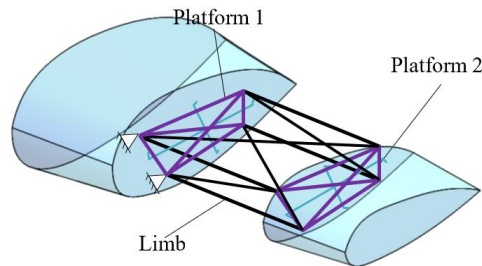Fig. 2 The proposed VGTM for the morphing wing

Fig. 3 The locked VGTM

When all the P joints are locked, the mechanism is equivalent to the truss shown in Fig. 3. The structural stability should be checked to see whether the truss composed of two-force members can withstand loadings. This stability depends on the number and the arrangement of members and joints. Mathematically, the degree of static indeterminacy is calculated as [21]

$$m + r - 3j = 20 + 8 - 3 \times 8 = 4 \tag{1}$$

where m, j and r are the number of members, joints and reaction components respectively.

The calculated results mean the truss has four redundant members, which can be released during the morphing motion, while the structure can still be statically determinate.

3   Motion modes analysis

To reduce the number of actuators and the weight of the mechanism, only six actuators are adopted and assembled on the P joints of limbs 11, 14, 2, 4, 6 and 8, as shown in Figs. 2 and 4. The other prismatic joints are designed to be lockable. The design of lockable joints has been discussed in our previous work [22]. In this section,

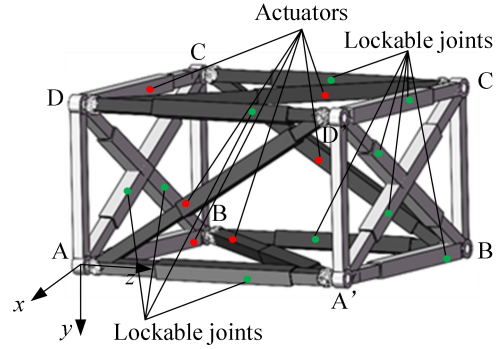it will be verified that this type of under-actuated mechanism can still accomplish all the motions desired.

Fig. 4 The actuated VGTM

3.1   Parallel mechanism morphing

First, we will introduce the morphing motions except for airfoil-level morphing. In this case, all the limbs (limbs 11, 12, 13, 14, 21, 22, 23 and 24) in the two planar mechanisms are locked.

To calculate the DOF of the mechanism in each mode, the screw theory is applied. Suppose the position of A' (in Fig. 4) is ($a2x$, $a2y$ $a2z$). In line of the coordinate system with A as the origin, the limb twist system of the limb is expressed as

$$
\begin{aligned}
\$_{11} &= (0 \quad 0 \quad 1; 0 \quad 0 \quad 0) \\
\$_{12} &= (0 \quad 1 \quad 0; 0 \quad 0 \quad 0) \\
\$_{13} &= (1 \quad 0 \quad 0; 0 \quad 0 \quad 0) \\
\$_{14} &= (0 \quad 0 \quad 1; a2y \quad -a2x \quad 0) \\
\$_{15} &= (0 \quad 1 \quad 0; -a2z \quad 0 \quad a2x) \\
\$_{16} &= (1 \quad 0 \quad 0; 0 \quad a2z \quad -a2y)
\end{aligned}
\tag{1}
$$

When locking the prismatic joint, the limb constraint system can be obtained as:

$$
\$_1^r = (\tfrac{a2x}{a2z} \quad \tfrac{a2y}{a2z} \quad 1; 0 \quad 0 \quad 0)
\tag{2}
$$

Equation (2) shows that a single limb exerts a constraint force along the limb on the end-effector. When locking all the limbs in the planar mechanisms and limbs 1, 3, 4, 5, 7 and 8, the total constraints on the right platform are two forces along y-axis and z-axis, and torques around x-axis, y-axis and z-axis. Therefore, the mechanism can only achieve one translation motion along x-axis. Driving limbs 2 and 6 synchronously, the mechanism can accomplish a translation along the x-axis, as shown in Fig. 5(a). When locking limbs 1, 2, 3, 5, 6 and 7, the total constraints on the right platform are two forces along x-axis and z-axis, and torques around x-axis, y-axis and z-axis. Actuating limbs 4 and 8 synchronously, the mechanism can translate along y-axis, as shown in Fig. 5(b).
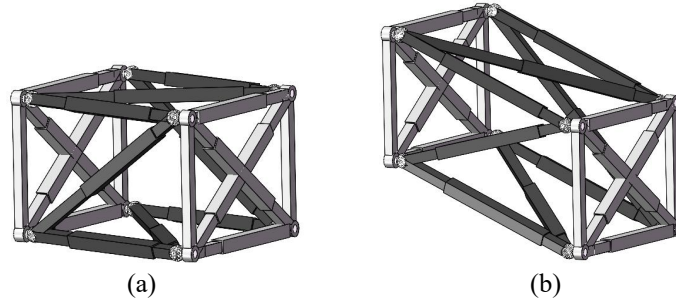
(a)   (b)

Fig. 5 Translation motions along *x*-axis and *y*-axis: (a) translation motion along *x*-axis; (b) translation motion along *y*-axis
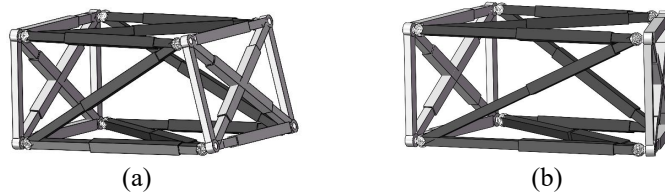

(a)   (b)

Fig. 6 Rotation motions around *x*-axis and *y*-axis: (a) rotation motion along *x*-axis; (b) rotation motion along *y*-axis

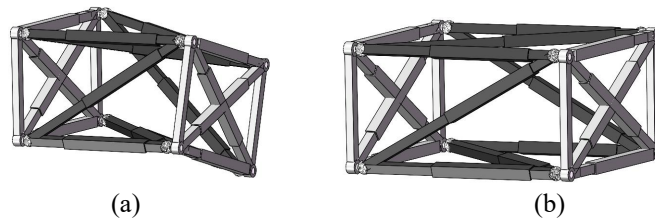(a)   (b)

Fig. 7: Rotation and translation motions about *z*-axis (a) rotation motion along *z*-axis; (b) translation motion along *z*-axis

When locking limbs 5, 6, 7 and 8 or 1, 2, 3 and 4, the total constraints on the right platform are three forces along *x*-axis, *y*-axis and *z*-axis, and one torque around *y*-axis, and the mechanism can rotate around *x*-axis and *z*-axis (Fig. 7(a)). (1) locking limbs 5, 6, 7 and 8, releasing limbs 1 and 3 and actuating limbs 2 and 4 synchronously, or (2) locking limbs 1, 2, 3 and 4, releasing limbs 5 and 7 and actuating limbs 6 and 8 synchronously, the mechanism can rotate around *x*-axis. When locking limbs 1, 2, 7 and 8 or 3, 4 and 5 and 6, the total constraints on the right platform are three forces along *x*-axis, *y*-axis and *z*-axis, and one torque around *x*-axis, and the mechanism can rotate around *y*-axis and *z*-axis (3) Locking limbs 1, 2, 7 and 8, releasing limbs 3 and 5 and actuating limbs 4 and 6 synchronously, or (4) locking limbs 3, 4, 5 and 6, releasing limbs 1 and 7 and actuating limbs 2 and 8 synchronously, the mechanism can rotate around y-axis. More importantly, when combining approaches (1) and (2), or (3) and (4), the mechanism can translate along *z*-axis, as shown in Fig. 7(b).

3.2   Planar mechanism morphing

When performing the airfoil-level morphing, at least six limbs of the Gough-Stewart parallel mechanism should be locked. In this way, two platforms morph synchronously. As shown in Fig. 8(a), to rotate the end-effectors AD and A'D' of the two planar mechanisms around z-axis, we need to lock limbs 1, 3, 4, 5, 6, 7, 8, 11 and 12, release limb 13 and actuate limbs 2 and 14, so that the positions of A and A', which are the left bottom vertices of the two platforms, can be adjusted. Locking limbs 1, 2, 3, 4, 5, 7, 8, 13 and 14, release limb 12 and actuate limbs 6 and 11, the positions of D and D', which are the left top vertices of the two platforms, can be changed. Besides, combining these two steps, the end-effectors AD and A'D' can achieve translation along x-axis.

In the above morphing motions, the two platforms have the same shape and morph synchronously. Actually, the shapes of two platforms can be different. In this case, to change the shape of one of the platforms, the other platform should be locked. For example, if the shape of the right platform needs to be changed, all the limbs of the left platform (limbs 11, 12, 13 and 14) should be locked. Locking limbs 1, 3, 5 and 7, and two of the limbs in the right platform, e.g. limbs 13 and 14, and actuating limbs 2, 4, 6 and 8, the right platform can deform while rotating, as shown in Fig. 9.
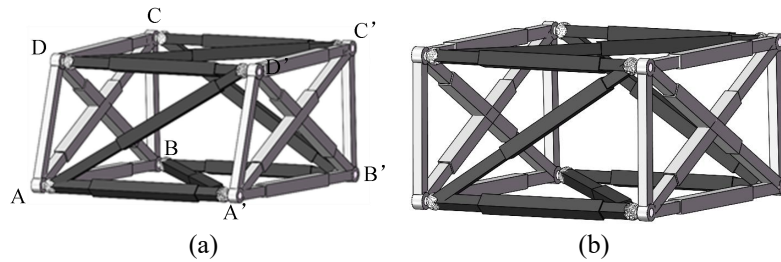

Fig. 8 Airfoil morphing (two platforms morph synchronously): (a) rotate around z-axis; (b) translate along x-axis
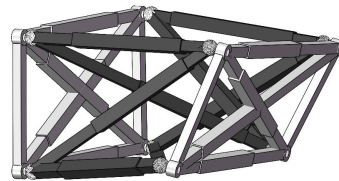

Fig. 9 Airfoil morphing with one platform locked

It can be seen that in each mode, the number of released limbs is less than four, which means the VGTM is statically indeterminate and has high stiffness and great load-carrying ability. However, the number of actuators is larger than the DOF in several cases, so a precise control strategy with inverse kinematic analysis will be needed for the prototype of the VGTM.

8

4　Conclusion

In this paper, a novel method has been proposed to obtain a multi-mode VGTM that can accomplish all the morphing motions, including span, sweep, twist, dihedral, wingtip morphing, and airfoil-level morphing. Planar VGTM and spatial VGTM are combined to form a loop-coupled VGTM. By using additional limbs and lockable joints, the number of actuators has been reduced to six. The VGTM can operate in different motion modes to have distinct morphing motions separately.

In the future, modes analysis using the approach of Euler parameter quaternions will be conducted to explore more motion modes, the inverse kinematic analysis will be carried out, and prototypes will be fabricated for the application of morphing wings.

Acknowledgement

References

1. Barbarino, S., Bilgen, O., Ajaj, R.M., Friswell, M.I. and Inman, D.J.: A review of morphing aircraft. Journal of Intelligent Material Systems and Structures 22(9), 823-877 (2011).
2. Sofla, A.Y.N., Meguid, S.A., Tan, K.T. Yeo, W.K.: Shape morphing of aircraft wing: Status and challenges. Materials & Design 31(3), 1284-1292 (2010).
3. Bae, J.S., Seigler, T.M., Inman, D.J.: Aerodynamic and static aeroelastic characteristics of a variable-span morphing wing. Journal of aircraft 42(2), 528-534 (2005).
4. Mattioni, F., Gatto, A., Weaver, P., Friswell, M., Potter, K.: The application of residual stress tailoring of snap-through composites for variable sweep wings. In: 47th AIAA/ASME/ASCE/AHS/ASC Structures, Structural Dynamics, and Materials Conference, pp. 1972. Newport (2006).
5. Mistry, M., Gandhi, F., Nagelsmit, M., Gurdal, Z.: Actuation requirements of a warp induced variable twist rotor blade. Journal of Intelligent Material Systems and Structures 22(9) 265-285 (2010).
6. Zhao, K., Schmiedeler, J.P., Murray, A.P.: Design of planar, shape-changing rigid-body mechanisms for morphing aircraft wings. Journal of Mechanisms and Robotics 4(4) 041007 (2012).
7. Manzo, J., Garcia, E.: Demonstration of an in situ morphing hyperelliptical cambered span wing mechanism. Smart Materials and Structures 19(2) 025012 (2010).
8. Pinkerton, J.L.: A feasibility study to control airfoil shape using THUNDER, NASA, Langley Research Center 4767 (1997).
9. Heo, H., Ju, J., Kim, D.M.: Compliant cellular structures: application to a passive morphing airfoil. Composite Structures 106 560-569 (2013).
10. Bettini, P., Airoldi, A., Sala, G., Di Landro, L., Ruzzene, M., Spadoni, A.: Composite chiral structures for morphing airfoils: numerical analyses and development of a manufacturing process. Composites Part B: Engineering 41(2) 133-147 (2010).

11. Vigliotti, A. and Pasini, D.: Analysis and design of lattice materials for large cord and curvature variations in skin panels of morphing wings. Smart Materials and Structures 24(3) 037006 (2015).
12. Ramrakhyani, D.S., Lesieutre, G.A., Frecker, M.I., Bharti, S.: Aircraft structural morphing using tendon-actuated compliant cellular trusses. Journal of Aircraft 42(6) 1614-1620 (2005).
13. Moored, K.W., Bart-Smith, H.: The analysis of tensegrity structures for the design of a morphing wing. Journal of Applied Mechanics 74(4) 668-676 (2007).
14. Neal, D., Farmer, J., Inman, D.: Development of a morphing aircraft model for wind tunnel experimentation. In: 47th AIAA/ASME/ASCE/AHS/ASC Structures, Structural Dynamics, and Materials Conference, pp. 2141. Newport (2006).
15. Xu, Y., Chen, Y., Liu, W., Ma, X., Yao, J., Zhao, Y.: Degree of freedom and dynamic analysis of the multi-loop coupled passive-input overconstrained deployable tetrahedral mechanisms for truss antennas. Journal of Mechanisms and Robotics 12(1) 1-19 (2020).
16. Yang, H., Guo, H., Wang, Y., Liu, R., Deng, Z.: Configuration synthesis of planar folded and common overconstrained spatial rectangular pyramid deployable truss units. Chinese Journal of Aeronautics 32(07) 1772-1787 (2019).
17. Austin, F., Rossi, M. J., Van Nostrand, W., Knowles, G., Jameson, A.: Static shape control for adaptive wings. AIAA Journal 32(9) 1895–1901 (1994).
18. Wang, J., Zhao, Y., Xi, F., Tian, Y.: Design and analysis of a configuration-based lengthwise morphing structure. Mechanism and Machine Theory 147 103767 (2020).
19. Xi, F., Zhao, Y., Wang, J., Tian, Y., Wang, W.: Two Actuation Methods for a Complete Morphing System Composed of a VGTM and a Compliant Parallel Mechanism, Journal of Mechanisms and Robotics 13(2) 021020 (2021).
20. Moosavian, A., Xi, F., Hashemi, S.M.X.: Design and Motion Control of Fully Variable Morphing Wings. Journal of Aircraft 50(4) 1189-1201 (2021).
21. McCormac, J.C.: Structural Analysis: using classical and matrix methods. John Wiley & Sons (2006).
22. Moosavian, A., Rizoiu, M., Xi, F.: Design of a multifunctional flow control valve for self-circulating hydraulic cylinders. Journal of Pressure Vessel Technology 139(2) 025001 (2017).

Optimization Design of 3UPS-2UPU Parallel Manipulator used for Loading Device

Bin Zhu[1,2], Liping Wang[1,2] and Jun Wu [1,2]

[1] State Key Laboratory of Tribology and Institute of Manufacturing Engineering, Department of Mechanical Engineering, Tsinghua University, Beijing 100084, China.
[2] Beijing Key Lab of Precision/Ultra-precision Manufacturing Equipment and Control, Beijing 100084, China.
jhwu@mail.tsinghua.edu.cn

Abstract. The reliability is very important for computer numeral control (CNC) machine tools in the industrial application. To avoid lots of waste of materials, the loading device which can output multi-axis force to simulate the cutting force is important for reliability study of machine tools. In this paper, a 5 degrees of freedom (DOFs) parallel manipulator with 3UPS-2UPU chains is proposed, which can generate all motion except for the rotation with the rotating axis normal to the moving platform. Workspace, payload uniformity and stiffness indexes are defined for loading device, and corresponding performance atlases of 3UPS-2UPU parallel manipulator are represented. Based on performance atlases, the geometrical parameters of 3UPS-2UPU parallel manipulator are optimized. The 3UPS-2UPU parallel manipulator with optimum geometric parameters is used to develop loading device. This study is of great significance for designers to find a suitable parallel manipulator for loading device and to optimize the parallel mechanism to obtain better performance.

Keywords: Loading Device, Parallel Manipulator, Payload Uniformity, Stiffness, Workspace.

1   Introduction

The 5-axis computer numeral control (CNC) machine tools are satisfied with the complex and precision parts machining and have important applications [1]. The reliability is very important performance for CNC machine tools in the industrial application and has attracted more and more attention [2,3]. In general, the reliability is analyzed based on the field failure records which need track a machine tool for a long time [4,5]. In fact, there is a high failure rate during early failure period [6]. Thus, run-in test is usually necessary, and it can expose early failure of machine tool. However, the ex-factory run-in test requires continuously cutting raw materials for several weeks, which cause plenty of waste of materials and high test cost [7,8]. Loading device which can output the same force as cutting force, is a great substitute for run-in test [7]. However, unfortunately, the report about loading devices for the whole machine tools is rare, especially for 5-axis machine tools.

The loading device that is used for 5-axis machine tools should need the follows requirements: 1). The loading device need output 5-axis forces/moments to spindle to simulate the real loading condition [7]; 2). The loading device need five axis motion to track spindle, which include translation along three Cartesian axes and rotation along x-axis and y-axis; 3) The volume of loading device is small enough to ensure that it can be mounted on worktable of 5-axis machine tool. Parallel manipulators possess several advantages such as high payload to weight ratio, high stiffness and excellent dynamics [9,10], therefore, a 5-DOF parallel manipulator is a good choice for developing 5-axis loading device.

In order to better performance, parallel manipulator should be optimized, which is a quite important and challenging issue [11]. In general, there are lots of performance requirements put forward by practical engineering applications, but these requirements can't be established a comprehensive objective function [12]. The multi-objective optimization design method for parallel manipulators can mainly be classified into two categories, algorithm-based and atlas-based ones [13]. The algorithm method need establish objective function and search for optimization results based on optimization algorithms [14]. Although the optimal solutions can be obtained, it is not clear how the design variable affect the object function [13]. The atlas-based method can give designers a global and visual information on with what kind of design variable the mechanism can have good or best performance. Liu et al. [15] have contributed in this method and use it to optimize several parallel manipulators [16,17].

In this paper, 3UPS-2UPU parallel manipulator used to develop 5-axis loading device is proposed. P, U and S denote the prismatic, universal and spherical joint, respectively, and _ presents the actuated joint. In order to better loading performance, the performance atlas for workspace, payload uniformity and stiffness indices are drawn and the optimum geometric parameters of parallel manipulator are obtained from performance atlas. The 3UPS-2UPU parallel manipulator with optimum geometric parameters has higher payload uniformity and stiffness, and its workspace also meets requirements for loading device.

2   Structure description and kinematic analysis

2.1   Structure Description

As shown in Fig.1, The loading device is fixed on worktable of machine tool and connected to the machine tool spindle by a connector. To track the spindle motion, the loading device is required for five axis motion. As shown in Fig.2, 3UPS-2UPU parallel manipulator is composed by moving platform, base platform and five chains. The two U joints in UPU chains connected to the moving platform have a collinear axis and the two U joints connected the fixed base platform have a collinear axis, which leads to two UPU chains with same force wrench. The force wrench causes 3UPS-2UPU parallel manipulator generate all the motion except for the rotation with the rotating axis normal to the moving platform. The schematic diagram of 3UPS-2UPU parallel manipulator is shown in Fig. 3.
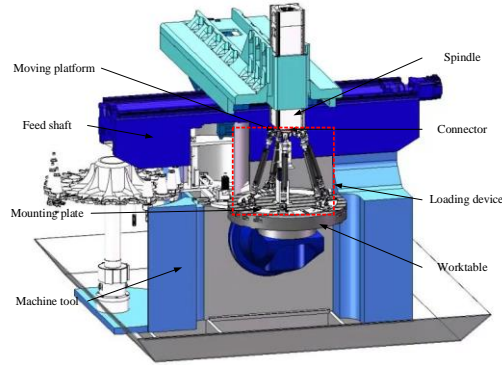
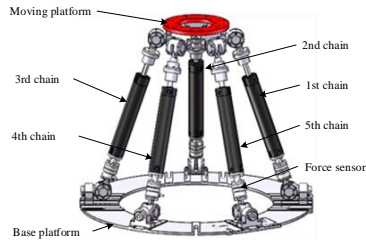**Fig. 1.** CAD model of 5-axis loading device and 5-axis machine tool
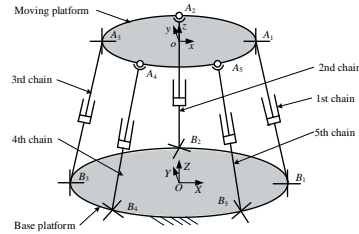

Fig. 2. 3D model

Fig. 3. Schematic diagrams

3 **2.2   Inverse Kinematics**

4 In order to analyze the inverse kinematics of 3UPS-2UPU parallel manipulator, two
5 coordinate system are established, as shown in Fig.3. The base coordinate system *O-*
6 *XYZ* is attached to the base platform and the moving coordinate system *o-xyz* is attached
7 to the moving platform. 3UPS-2UPU parallel manipulator is lack of the rotation with
8 the rotating axis normal to the moving platform. Hence, the orientation of *o-xyz* with
9 respect to *O-XYZ* can be expressed by Euler angle $[\alpha \quad \beta \quad \gamma]^{\mathrm{T}}$ as

10
$$^{B}\boldsymbol{R}_{A}=\boldsymbol{R}_{x}(\alpha)\boldsymbol{R}_{y'}(\beta)\boldsymbol{R}_{x''}(\gamma) \tag{1}$$

11 As shown in Fig. 4, the body fixed coordinate system $B_i\text{-}x_iy_iz_i$ is attached to joint
12 point B_i. The rotation matrix of $B_i\text{-}x_iy_iz_i$ with respect to *O-XYZ* can be written as

13
$$^{B}\boldsymbol{R}_{i}=\boldsymbol{R}_{Z}(\psi_{i})\boldsymbol{R}_{x_{i'}}\left(\phi_{i}\right)\boldsymbol{R}_{y_{i''}}(\theta_{i}) \tag{2}$$

14 where θ_i and ϕ_i are associated with the rotations about the two axes of the U joints,

15 and ψ_i is the angle between line OB_i and *X*-axis.

16 As shown in Fig.4, the closed-loop constraint equation associated with each chain
17 can be written as

$$\boldsymbol{b}_i + q_i\boldsymbol{e}_i = \boldsymbol{r} + \boldsymbol{a}_i \quad i=1,\ 2,\ 3,\ 4,\ 5 \tag{3}$$

where $\boldsymbol{b}_i$ is the position vector of point B_i in base coordinate system $O\text{-}XYZ$, $\boldsymbol{b}_i = [Rc\psi_i \quad Rs\psi_i \quad 0]^{\mathrm{T}}$, R is the radius of base platform, $c = \cos()$, $s = \sin()$, q_i is the length of each chain, $\boldsymbol{e}_i$ is the unit vector of the axial axis of the ith chain, $\boldsymbol{e}_i = {}^B\boldsymbol{R}_i \, {}^i\boldsymbol{e}_i$, ${}^i\boldsymbol{e}_i = [0 \quad 0 \quad 1]^{\mathrm{T}}$, $\boldsymbol{r}$ is the position vector of point o, $\boldsymbol{r} = [x \quad y \quad z]^{\mathrm{T}}$, $\boldsymbol{a}_i = {}^B\boldsymbol{R}_A\boldsymbol{a}_i'$, $\boldsymbol{a}_i'$ is the position vector of joint point A_i in coordinate system $o\text{-}xyz$, $\boldsymbol{a}_i' = [rc\zeta_i \quad rs\zeta_i \quad 0]^{\mathrm{T}}$, ζ_i is the angle between line $\boldsymbol{a}_i'$ and x-axis, r is the radius of moving platform.

Let $\boldsymbol{r}_p$ and $\boldsymbol{r}_p'$ be the position vectors of a random point P on the moving platform in coordinate systems $O\text{-}XYZ$ and $o\text{-}xyz$, respectively. It can be obtained that

$$\boldsymbol{r}_p = {}^B\boldsymbol{R}_A \cdot \boldsymbol{r}_p' \tag{4}$$

Taking the time derivative of Eq. (4) leads to

$$\dot{\boldsymbol{r}}_p = {}^B\dot{\boldsymbol{R}}_A\boldsymbol{r}_p' = \begin{vmatrix} 0 & -\omega_z & \omega_y \\ \omega_z & 0 & -\omega_x \\ \omega_y & \omega_x & 0 \end{vmatrix} \boldsymbol{r}_p \tag{5}$$

where $\boldsymbol{\omega} = [\omega_x \quad \omega_y \quad \omega_z]^{\mathrm{T}}$ is the angular velocity of the moving platform, and $\omega_x = \dot{\alpha} + c\beta \cdot \dot{\gamma}$, $\omega_y = c\alpha \cdot \dot{\beta} + s\alpha s\beta \cdot \dot{\gamma}$, $\omega_z = s\alpha \cdot \dot{\beta} - c\alpha s\beta \cdot \dot{\gamma}$. Taking the time derivative of the left side of Eq. (3) yields leads to

$$\dot{q}_i = \boldsymbol{e}_i^{\mathrm{T}}\dot{\boldsymbol{r}}_{A_i} \tag{6}$$

Taking the time derivative of the right side of Eq. (3) yields leads to

$$\dot{\boldsymbol{r}}_{A_i} = \boldsymbol{J}_{A_i}\dot{\boldsymbol{x}} \tag{7}$$

where $\boldsymbol{J}_{A_i} = \begin{vmatrix} 1 & 0 & 0 & 0 & a_{iz} & -a_{iy} \\ 0 & 1 & 0 & -a_{iz} & 0 & a_{ix} \\ 0 & 0 & 1 & a_{iy} & -a_{ix} & 0 \end{vmatrix}$ and $\dot{\boldsymbol{x}} = [\dot{\boldsymbol{r}}^{\mathrm{T}} \quad \boldsymbol{\omega}^{\mathrm{T}}]^{\mathrm{T}}$ is the twist of moving platform. Combining Eqs. (6) and (7) leads to

$$\dot{q}_i = \boldsymbol{e}_i^{\mathrm{T}}\boldsymbol{J}_{A_i}\dot{\boldsymbol{x}} \tag{8}$$

Eq. (8) can be written in matrix form as

$$\dot{q} = J\dot{x} \tag{9}$$

where, $\dot{q}=[\ \dot{q}_1 \quad \dot{q}_2 \quad \dot{q}_3 \quad \dot{q}_4 \quad \dot{q}_5\ ]^{\mathrm{T}}$, and J is a 5×6 matrix which is called Jacobian matrix of the parallel manipulator, $J = \begin{bmatrix} J_{A_1}^{\mathrm{T}}e_1 & J_{A_2}^{\mathrm{T}}e_2 & J_{A_3}^{\mathrm{T}}e_3 & J_{A_4}^{\mathrm{T}}e_4 & J_{A_5}^{\mathrm{T}}e_5 \end{bmatrix}^{\mathrm{T}}$.

In fact, the six components in $\dot{x}$ is not independent because of the force wrench of two U$\underline{P}$U chains, and the parasitic motion can be expressed as

$$\alpha = \arctan(-\,y/z) \tag{10}$$

Therefore, the relationship between the input velocities and the velocities of the moving platform can be expressed as

$$\dot{q} = J'\dot{X} \tag{11}$$

where $\dot{X}=\begin{bmatrix} \dot{x} & \dot{y} & \dot{z} & \dot{\beta} & \dot{\gamma} \end{bmatrix}^{\mathrm{T}}$ is the velocity of moving platform.

3   Optimum design

3.1   Development of Design Space

As shown in Fig. 5, considering symmetry of 3U$\underline{P}$S-2U$\underline{P}$U parallel manipulator, the geometric parameters θ_1, θ_2, R, r and the initial length of chain L are variables for optimum design. Besides, according to configuration analysis, the influence of R, r and L versus θ_1 and θ_2 for optimization indexes is independent. Thus, they can be respectively optimized. Obviously, the range of θ_1 and θ_2 are limited, while R, r and L are not limited, and they should be normalized. The dimensional factor is defined as $D = (R + r + L)/3$ and the Non-dimensional optimization variable r_1, r_2 and l can be written as:

$$r_1 = R/D,\ r_2 = r/D,\ l = L/D \tag{12}$$

They are not independent, r_1 and r_2 are considered as independent optimization variable. It obvious that all optimum variables are positive, and assuming that the radius of base platform is larger than moving platform. Therefore, variation range of four optimization variable $r_1 \in (0,1.5)$, $r_2 \in (0,1.5)$, $\theta_1 \in (0,\pi/2)$ $\theta_2 \in (0,\pi/2)$.
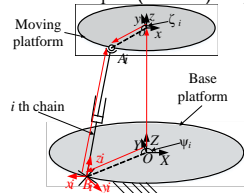

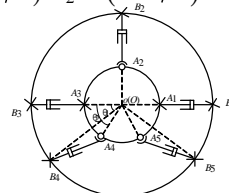**Fig. 4.** Closed-loop constraint of the ith chain

Fig. 5. Top view of schematic diagrams of 3U$\underline{P}$S-2U$\underline{P}$U parallel manipulator

3.2 Performance Indexes

Workspace index. Workspace of parallel manipulator should be optimized to ensuring enough workspace for loading device to track the spindle. As shown in Fig. 6, workspace of loading device is defined as the set of points where the moving platform can reach when moving platform satisfies the prescribed orientation. However, in order to make workspace index more universal, it should be dimensionless. Thus, workspace index ξ is defined as

$$\xi = V_w / V \tag{13}$$

where V_w is the volume of desired workspace of 3UPS-2UPU parallel manipulator, and V is the volume of 3UPS-2UPU parallel manipulator, which can be calculated from

$$V = \pi \left(r_1^2 + r_2^2 + r_1 r_2 \right) \left(\sqrt{l^2 - (r_1 - r_2)^2} \right) \Big/ 3 \tag{14}$$

When the orientation of moving platform is prescribed that β and γ ranges in $\left[-\pi/9,\ \pi/9 \right]$. The workspace index is shown in Fig. 7, when $\theta_1 = 1.1\ rad$ and $\theta_2 = 0.3\ rad$, the smaller r_1 and r_2 are, the larger the workspace is. When $r_1 = 0.9$, $r_2 = 0.35$, $l = 1.75$, the closer $(\theta_1,\ \theta_2)$ is to (0.4, 0), the larger the workspace index is.

Fig. 6. Workspace of 3UPS-2UPU parallel manipulator

(a) $\theta_1 = 1.1\ rad$, $\theta_2 = 0.3\ rad$ (b) $r_1 = 0.9$, $r_2 = 0.35$, $l = 1.75$
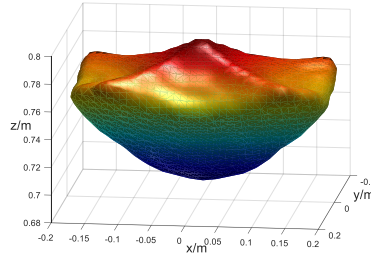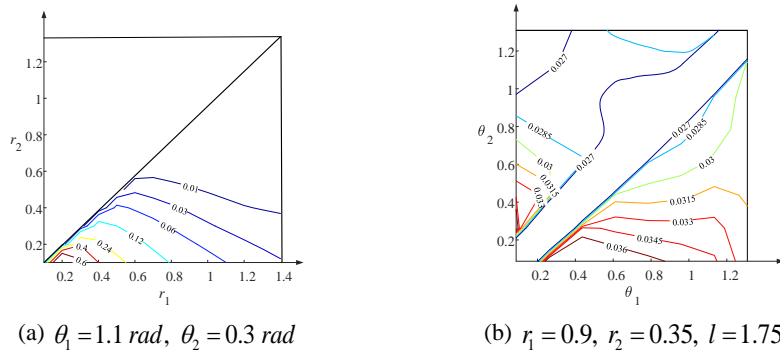
Fig. 7. Atlas of the workspace index

Payload uniformity index. Payload capability is salient feature of loading device which is different from other robotics. Based on the principle of virtual displacement, the relationship between output loads F and driving forces τ can expressed as

$$\tau = J'^{-T} F \tag{15}$$

Let the driven force τ be one unit, namely, it can be obtained that $\|F\|_{\max} = \sqrt{\max(|\lambda_{Fi}|)}$, $\|F\|_{\min} = \sqrt{\min(|\lambda_{Fi}|)}$, where λ_{Fi} is the eigenvalues of the matrix $J'^{-1}J'^{-T}$. Loading device need simulate cutting force in multiple working conditions, therefore, the payload capability of loading device should be uniform in different direction. Payload uniformity index can be defined as

$$\eta_1 = \int_{V_w} \|F\|_{\min} \big/ \|F\|_{\max} \, dv \bigg/ \int_{V_w} dv \tag{16}$$

The payload uniformity index atlas is shown in Fig. 8. when $\theta_1 = 1.1 \, rad$, $\theta_2 = 0.3 \, rad$ and $r_1 < 1.1$ and $r_2 < 0.4$, the larger r_1 is, the larger η_1 is. When $r_1 = 0.9$, $r_2 = 0.35$ and $l = 1.75$, the larger $|\theta_1 - \theta_2|$ is, the larger η_1 is.

Stiffness index. Enough stiffness is necessary for loading device, because the deformation of moving platform have an effect on loading device. It is assumed that stiffness of the ith kinematic chain is k_i. Thus, the relationship between the force and deformation can be expressed as

$$\tau_i = k_i \delta q_i \ \ i = 1,2,3,4,5 \tag{17}$$

Based on Eqs. (11) and (16), it can be obtained that

$$\delta X = K^{-1} F \tag{18}$$

where $K = J'^T K_p J'$ is the stiffness matrix. In this study, the factors of size and material are not investigated, so let $k_i = 1$, and $K = J'^T J'$. Let the F be unit, $\|\delta X\|_{\max} = \sqrt{\max(|\lambda_{Xi}|)}$. The large deformation means that the manipulator has bad stiffness along this deformation direction with large deformation. Therefore, stiffness index η_2 can be expressed as

$$\eta_2 = \int_{V_w} \|\delta X\|_{\max} \, dv \bigg/ \int_{V_w} dv \tag{19}$$

The stiffness atlas is shown in Fig.9. When $\theta_1 = 1.1 \, rad$, $\theta_2 = 0.3 \, rad$ and $r_1 < 1.1$ and $r_2 < 0.4$, the larger r_1 is, the larger η_2 is. When $r_1 = 0.9$, $r_2 = 0.35$ and $l = 1.75$, the larger $|\theta_1 - \theta_2|$ is, the larger η_2 is.
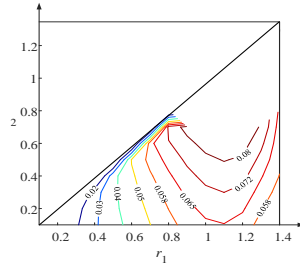
(a) $\theta_1 = 1.1\,rad$, $\theta_2 = 0.3\,rad$ (b) $r_1 = 0.9$, $r_2 = 0.35$, $l = 1.75$
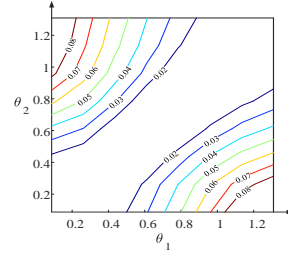
1   **Fig. 8.** Atlas of the payload uniformity index

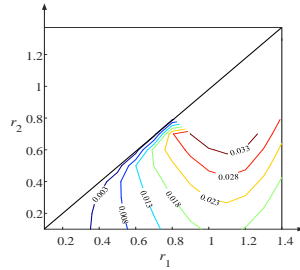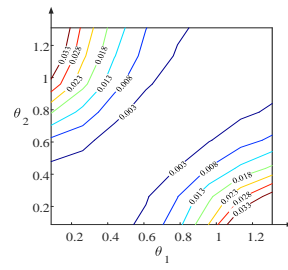(a) $\theta_1 = 1.1\,rad$, $\theta_2 = 0.3\,rad$ (b) $r_1 = 0.9$, $r_2 = 0.35$, $l = 1.75$

2   **Fig. 9.** Atlas of the stifness index

3   **3.3**   Optimum Design Based on the Atlas.

4   From Fig. 7, 8 and 9, a region with desired performance can be discovered, which is
5 called optimum region. Taking the optimization indexes, $\xi \geq 0.04$, $\eta_1 \geq 0.065$,
6 $\eta_2 \geq 0.02$ into account, the optimum region can be obtained in Fig. 10. In fact, anyone
7 in optimum region can be selected as final design, however, considering some condi-
8 tions for engineering application, a group of optimum variable is obtained from Fig.10,
9 and r_1=0.9, r_2=0.35, $l = 1.75$, $\theta_1 = 1.1$, $\theta_2 = 0.3$. According to limits of machine tool, the
10 dimensional factor is specified as $D = 0.362$. Therefore, a group of real geometric pa-
11 rameter of 3U<u>P</u>S-2U<u>P</u>U parallel manipulator is obtained as $R = 0.326$m , $r = 0.127$m ,
12 $L = 0.634$m .
13   After optimization, the volume of 3U<u>P</u>S-2U<u>P</u>U parallel manipulator's desired work-
14 space is $0.0028 m^3$, and workspace index ξ=0.037 . The payload uniformity and stiff-
15 ness indexes on plane $Z = 0.680 m$ are shown in Fig. 11 and Fig. 12, respectively. The
16 payload uniformity index in whole workspace is 0.068, and the stiffness index is 0.022.
17   Based on the optimization design, the 3U<u>P</u>S-2U<u>P</u>U parallel manipulator is used to
18 develop multi-axis loading device, as shown in Fig.13. The loading device can track
19 the spindle motion and output multi-axis force to spindle, which is great helpful to the
20 reliability study.
21

(a) $\theta_1 = 1.1\ rad$, $\theta_2 = 0.3\ rad$

(b) $r_1 = 0.9$, $r_2 = 0.35$, $l = 1.75$
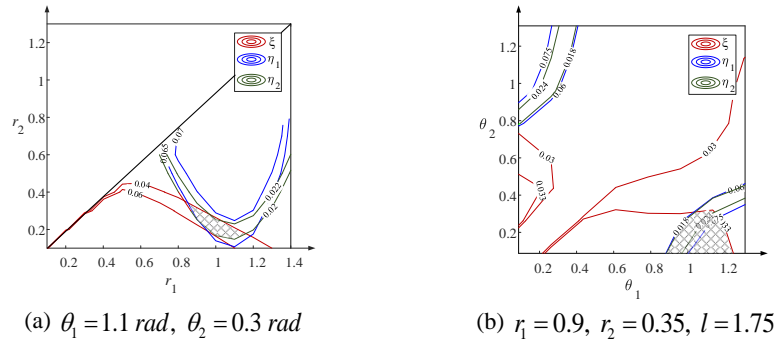
Fig. 10. Optimum region
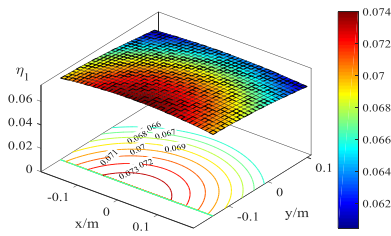
Fig. 11. Payload uniformity index
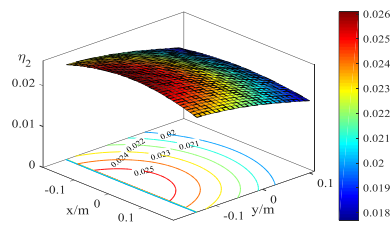
Fig. 12. Stiffness index
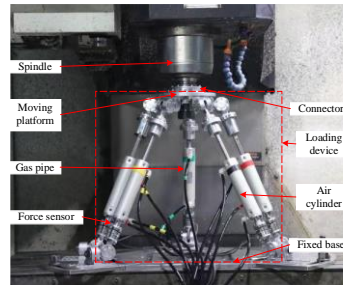
Figure 13. Multi-axis loading device

4 Conclusion

According to requirements for developing loading device, the workspace, payload uniformity and stiffness indexes are defined and corresponding performance atlases of 3UPS-2UPU parallel manipulator are drawn. Based on performance atlas, the optimum region with desired performance is obtained, and geometrical parameters without dimension are determined in optimum region. The optimum dimensional parameters are achieved based on the non-dimensional parameters. After optimized, 3UPS-2UPU parallel manipulator has higher payload uniformity and stiffness and its workspace also meets requirements for loading device. Then, a loading device is developed.

References

1. Wang P, Huo X, Wang Z. Topology design and kinematic optimization of cyclical 5-DoF parallel manipulator with proper constrained limb. Advanced Robotics, 31(4):204-219 (2017).
2. P. F. Mcgoldrick, H. Kulluk, Machine tool reliability—A critical factor in manufacturing systems, Reliability Engineering, 14(3):205-221 (1986).
3. Z. J. Yang, C. H. Chen, F Chen, G. F. Li. Progress in the research of reliability technology of machine tools. Journal of Mechanical Engineering, 49(20):130-139 (2013).
4. B. Cai, Y. Liu, Z. Liu, X. Tian, X. Dong, and S. Yu, Using Bayesian networks in reliability evaluation for subsea blowout preventer control system, Reliability Engineering & System Safety, vol. 108, 32-41 (2012).
5. B. Cai, Y. Liu, Y. Ma, Z. Liu, Y. Zhou, and J. Sun, Real-time reliability evaluation methodology based on dynamic Bayesian networks: a case study of a subsea pipe ram BOP system, ISA ISA Transactions, vol. 58, 595-604 (2015).
6. Y. Wang, Y. Jia, and W. Jiang, Early failure analysis of machining centers: a case study, Reliability Engineering & System Safety, vol. 72, no.1, 91-97, (2001).
7. J. Guo, D. Wang, T. Li, et al, Triaxial loading device for reliability tests of three-axis machine tools, Robotics & Computer Integrated Manufacturing, 49:398-407 (2018).
8. J. Guo, D. Wang, T. Li, et al, Multi-Axis Loading Device for Reliability Tests of Machine Tools, IEEE/ASME Transactions on Mechatronics, 1-1 (2018).
9. J. Wu, G. Yu, Y. Gao et al, Mechatronics modeling and vibration analysis of a 2-DOF parallel manipulator in a 5-DOF hybrid machine tool, Mechanism & Machine Theory, 121:430-445 (2018).
10. D. Wang, L. Wang, J. Wu, et al. An experimental study on the dynamics calibration of a 3-DOF parallel tool head. IEEE/ASME Transactions on Mechatronics, 24(6): 2931-2941 (2019).
11. P. Wang, X. Huo, Z. Wang, Topology design and kinematic optimization of cyclical 5-DoF parallel manipulator with proper constrained limb, Advanced Robotics, 31(4):204-219 (2017).
12. Y. Zhao. Dimensional synthesis of a three translational degrees of freedom parallel robot while considering kinematic anisotropic property, Robotics and Computer-Integrated Manufacturing, 29(1):169-179 (2013).
13. L. Wang, Z. Zhang, Z. Shao et al, Analysis and optimization of a novel planar 5R parallel mechanism with variable actuation modes, Robotics & Computer Integrated Manufacturing, 56:178-190 (2019).
14. A. N. Chaudhury, A. Ghosal. Optimum design of multi-degree-of-freedom closed-loop mechanisms and parallel manipulators for a prescribed workspace using Monte Carlo method, Mechanism and Machine Theory, 118:115-138 (2017).
15. X. J. Liu, J. Wang. A new methodology for optimal kinematic design of parallel mechanisms, Mechanism & Machine theory, 42(9):1210-1224 (2007).
16. F. Xie, X J Liu, C. Wu, P. Zhang, A novel spray painting robotic device for the coating process in automotive industry, ARCHIVE Proceedings of the Institution of Mechanical Engineers Part C Journal of Mechanical Engineering Science 1989-1996 (vols 203-210), 229(11):2081-2093 (2015).
17. F. Xie, X. J. Liu. Design and Development of a High-Speed and High-Rotation Robot With Four Identical Arms and a Single Platform, Journal of Mechanisms & Robotics, 7(4):041015 (2015).

Kinematic Analysis and design of a cable-driven parallel robot with a self-deformable end-effector

Kun Zhao [1,2], Nan Li [1,2], Wenjiang Yan [1,2], Zixuan Liu [1,2], Ziming Chen [1,2,*]

[1] School of Mechanical Engineering, Yanshan University, Qinhuangdao, Hebei 066004, China
[2] Parallel Robot and Mechatronic System Laboratory of Hebei Province, Yanshan University, Qinhuangdao, Hebei 066004, China
chenzm@ysu.edu.cn

Abstract. Based on the analysis and summary of previous research results, this paper presents a cable-driven parallel robot which is driven by 8 cables, has 6 degrees of freedom, and the end-effector can be deformed. First, the structure of the mechanism is briefly introduced, and a simplified mechanism model is obtained. Then the kinematics of the end-effector is established, and the kinematics results are verified by MATLAB software. Finally, it is verified by experiment.

Keywords: Cable-driven parallel mechanism, Actuator deformation, Kinematics establishment, Experimental verification.

1 Introduction

Cable-Driven Parallel Robots(CDPRs) are a device that connects the driver and the actuator with a flexible cable, and transmits movement through the flexible cable. CDPRs have the advantages of simple structure, large working space, fast response speed and low cost. It has great application prospects in wind tunnel tests, storage handling, motion simulation and so on.

At present, the research on CDPRs is also relatively extensive. Zheng has made a comprehensive and in-depth study on the 6-DoF CDPR from the aspects of robot kinematics, trajectory planning, optimization algorithm for cable tension, etc. She has conducted in-depth research in the direction of motion control schemes based on task space [1]. Qiu et al, proposed a generalized Stewart platform design scheme for suspension cable traction for a project based on Five-hundred-meter Aperture Spherical radio Telescope. and then carried out the system modeling, the derivation of the equilibrium equation, and the elimination of force singularity [2]. BenHamida Ines designed a CDPR, and applied it to medical rehabilitation [3]. Xiao designed a cord-driven exoskeleton with seven degrees of freedom, and evaluated its performance [4]. Patyt Thibau considers pulley kinematics and cable elasticity to model a cable-driven parallel robot [5]. A new mechanism was proposed by Ding from Beijing Jiaotong University, which consists of two identical space folding platforms [6]. Wang et al., proposed a new type of cable-driven remote actuator mechanism [7]. Rushton Mitchell

et al. studied the variable structure CDPR [8]. Sun proposed a solution to suppress vibration by using CDPR [9]. Li proposed a cable-driven three-rotation parallel mechanism [10]. Patrice Lambert and Just L Herder designed a deformable parallel mechanism with end effectors [11]. Xu et al, designed a real-time path planning algorithm for CDPRs in a dynamic environment based on artificial potential guided RRT [12]. Mottola Giovanni et al, proposed a kind of dynamic feasible motion of a purely translational CDPR [13]. However, the cable-driven parallel robot's end-effector is generally rigid or integral structures, and there is still a lack of research on deformable end-effector. The end-effector is designed as a deformable structure, and the actuator can be used to directly clamp the object, thereby expanding the function of the cable-driven mechanism, which has extremely important significance for the application of this technology.

This paper presents a cable-driven parallel robot which is driven by 8 cables, has 6 degrees of freedom, and the end-effector can be deformed. The end-effector of the mechanism can grip objects through deformation, which greatly expands the scope of application of the cable traction device. The kinematics of the end-effector is established and verified by experiments.

2 The configuration of CDPR with a self-deformable end-effector

The structure diagram of the CDPR designed in this paper is shown in Fig. 1. The outer frame of the device is a cuboid, and the end-effector at the initial moment is a cube. The attachment points of the outer frame and the end-effector are respectively connected to $C_1 \cdots C_8$ and $d_1 \cdots d_8$. The device transmits the power on the outer frame to the end-effector through 8 cables, and then the end-effector realizes movement and deformation. By changing the deformation degree of the end-effector according to the size of the object, the object can be grasped and moved.
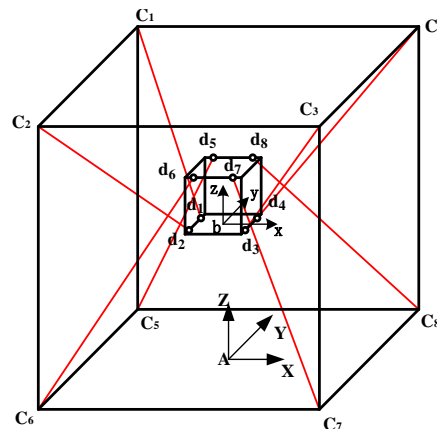

Fig. 1. The structure diagram of the CDPR

The end-effector is a cube structure and adopts a double-layer planar four-bar mechanism. The joints of two planar four-bar mechanisms can be rotated. Because the rotation axes of the double-layer four-bar mechanism are all coincident, the end-effector has only one degree of freedom, as shown in Fig. 2. Through the cooperation of the cables, the shape of the four-bar mechanism is changed, that is, the size of the internal space is changed. For a specific object, the object can be grasped and moved.
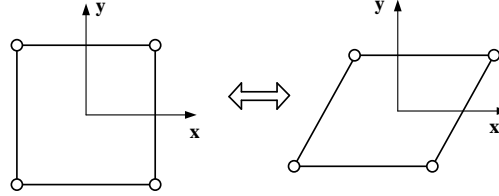
Fig. 2. The structure of four-bar mechanism

3   Kinematic Analysis

3.1   Translation and rotation

Establish a fixed reference frame at the geometric center of the bottom surface of the outer frame as {A-XYZ}，The fixed reference frame is fixedly connected to the earth. The vertex coordinates of the outer frame are $C_i(i = 1, 2, \cdots, 8)$. Establish a moving reference frame at the geometric center of the end-effector {b-xyz}, as shown in Fig. 1. The moving reference frame moves with the end-effector. The attachment points coordinates on the end-effector are $d_i(i = 1, 2, \cdots, 8)$.

Note that $\mathbf{P}=[\mathbf{P}_b \quad \mathbf{P}_{ang}]^T$ is the pose of the moving coordinate {b} frame relative to the fixed coordinate {A} frame.

Among them, $\mathbf{P}_b = [X_b \quad Y_b \quad Z_b]^T$ is the coordinate of origin of the {b} frame in the {A} frame. $\mathbf{P}_{ang} = [\varphi_\alpha \quad \varphi_\rho \quad \varphi_\gamma]^T$ is the posture coordinate of the {b} frame in the {A} frame. φ_α、 φ_ρ and φ_γ are respectively the rotation angles of {b} frame around the X-axis, Y-axis and Z-axis of {A} frame [14].

The coordinates of the attachment point between the outer frame and the cables in frame {A} are:

$$\mathbf{C}_i = [C_{ix} \quad C_{iy} \quad C_{iz}]^T (i = 1, 2, \cdots, 8) \tag{1}$$

The coordinates of the attachment point between the actuator and the cables in the frame {*b*} are:

$$\mathbf{d}_i^b = [d_{ix} \quad d_{iy} \quad d_{iz}]^T (i = 1, 2, \cdots, 8) \tag{2}$$

The coordinates of the attachment point between the actuator and the cables in the frame {A} are:

$$\mathbf{D}_i = {}_b^A \mathbf{R} \cdot \mathbf{d}_i^b + \mathbf{P}_b \tag{3}$$

Where $^A_b\mathbf{R}$ is the rotation matrix mapped from the local coordinate system to the global coordinate system.

$$^A_b\mathbf{R} = \begin{bmatrix} \cos\beta\cos\alpha & -\sin\alpha\cos\beta & \sin\beta \\ \sin\gamma\sin\beta\cos\alpha + \cos\gamma\sin\alpha & -\sin\alpha\sin\gamma\sin\beta + \cos\gamma\cos\alpha & -\sin\gamma\cos\beta \\ -\sin\beta\cos\gamma\cos\alpha + \sin\gamma\cos\alpha & \sin\alpha\sin\beta\cos\gamma + \sin\gamma\cos\alpha & \cos\gamma\cos\beta \end{bmatrix} \quad (4)$$

Regardless of the influence of the cable's own weight, the 8 effective cables length can be obtained

$$\mathbf{L}_i = \|\mathbf{C}_i - \mathbf{D}_i\|(i = 1, 2\cdots, 8) \quad (5)$$

3.2   Deformation of the end-effector

The end-effector is divided into two plane four-bar mechanisms, each of which has four attachment points. The attachment points of the four-bar mechanism on the upper surface are distributed on the sides AB and CD. The attachment points of the four-bar mechanism on the lower surface are distributed on the sides of EH and FG. The distance from each attachment point to the adjacent vertex is equal, as shown in Fig. **3**.
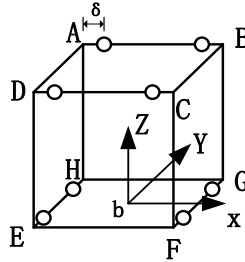
Fig. 3. Attachment points and vertexs relationship graph

The end-effector is square before deformation, and the attachment points on the two sides of the square are represented by $d_i(i = 1, \cdots, 4)$, and after deformation, it becomes a rhombus, the attachment points on the two sides of the rhombus are represented by $d_i(i = 1, \cdots, 4)$, And suppose the side length of the cube actuator is $2l$, the angle between the rhombus side and the X-axis is θ, and the distance from each attachment point to the adjacent vertex is δ, as shown in Fig. 4.
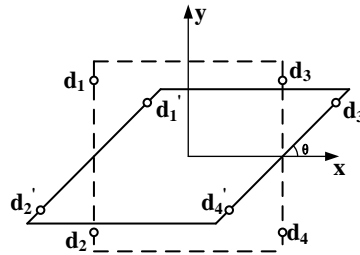

Fig. 4. End-effector deformation diagra

The coordinates of all attachment points before and after the deformation of the end-effector are shown in the following Table 1.

Table 1. The coordinates of the attachment points before and after deformation

d_i	coordinate	d'_i	coordinate
d_1	$(-l, l - \delta, 0)$	d'_1	$(-l + (l - \delta)\cos\theta, (1 - \delta)\sin\theta, 0)$
d_2	$(-l, -l + \delta, 0)$	d'_2	$(-l - (l - \delta)\cos\theta, -(l - \delta)\sin\theta, 0)$
d_3	$(l, l - \delta, 0)$	d'_3	$(l + (l - \delta)\cos\theta, (l - \delta)\sin\theta, 0)$
d_4	$(l, -l + \delta, 0)$	d'_4	$(l - (l - \delta)\cos\theta, -(l - \delta)\sin\theta, 0)$
d_5	$(-l + \delta, l, 2l)$	d'_5	$(-l + l\cos\theta + \delta, l\sin\theta, 2l)$
d_6	$(-l + \delta, -l, 2l)$	d'_6	$(-l - l\cos\theta + \delta, -l\sin\theta, 2l)$
d_7	$(l - \delta, -l, 2l)$	d'_7	$(l - l\cos\theta - \delta, -l\sin\theta, 2l)$
d_8	$(l - \delta, l, 2l)$	d'_8	$(l + l\cos\theta - \delta, l\sin\theta, 2l)$

The coordinates of the attachment point between the deformed end-effector and the cables in the {A} frame are:

$$\mathbf{D}'_i = {}^A_b\mathbf{R} \cdot \mathbf{d}'_i + \mathbf{P}_b \qquad (6)$$

Regardless of the influence of the weight of the cable, the 8 effective cables length can be obtained at this time:

$$\mathbf{L}'_i = \|\, \mathbf{C}_i - \mathbf{D}'_i \,\| \, (i = 1, 2, \cdots, 8) \qquad (7)$$

4 Simulation and Experiment

The experimental prototype is shown in Fig. 5. Its outer frame is cuboid with a size of 1000mm×1000mm×800mm. The cables and the end-effector are fixed with a simple design of an L-shaped fixing ring. Put one side of the L-shaped fixing ring into the profile groove, and fix it with screws. There is a round hole on the other side and the cables can be fixed through the hole. The end-effector adopts a cube frame structure with a size of 150mm×150mm×150mm. According to the height of the object to be clamped, it adopts a double hinged construction, as shown in Fig. 6.
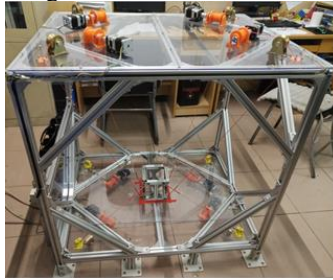
Fig. 5. Prototype overall

Fig. 6. End-effector

The movement of the end-effector before deformation (its initial shape is cube). The given trajectory is: the end-effector moves from the origin (0,0,0) to the position (0,0,300), and then moves to (0,150,300), Then move to (0,0,300), and then rotate 30° around the X-axis forward and backward, and finally return to (0,0,0). In the process of motion, the quintic polynomial interpolation method is used to plan the velocity and acceleration to make the end-effector run smoothly. The movement trajectory obtained through MATLAB simulation is shown in Fig. 7.

A) Initial position   B) Translational motion   C) Rotational motion
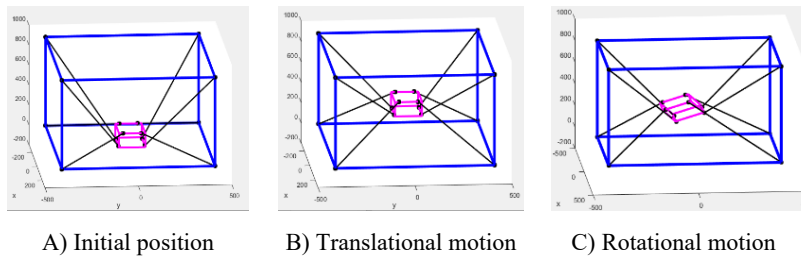
Fig. 7. Translational and rotational motion in MATLAB

The trajectory of the prototype experiment is shown in Fig. 8.

A) Initial position   B) Translational motion   C) Rotational motion
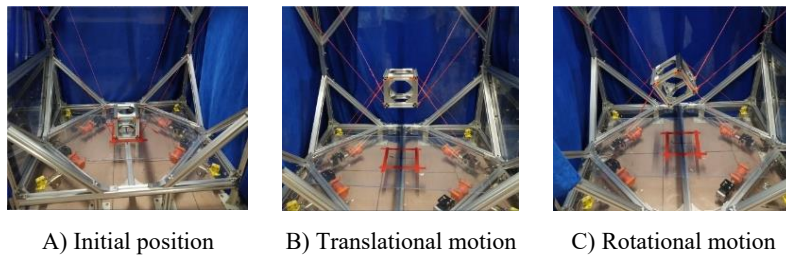
Fig. 8. Translational and rotational motion of prototype

The movement of end-effector after deformation. The given trajectory is the same as the undeformed, except that the end-effector is deformed at the initial moment, and the deformation angle θ is 30°. The trajectory of MATLAB simulation is shown in Fig. 9.

A) Initial position	B) Deformable motion	C) The motion of deformation
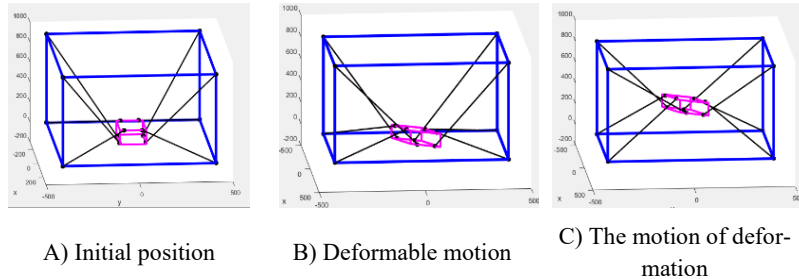
Fig. 9. The motion of deformation in MATLAB

The movement process of the prototype is shown in Fig. 10.

A) Initial position	B) Deformable motion	C) The motion of deformation
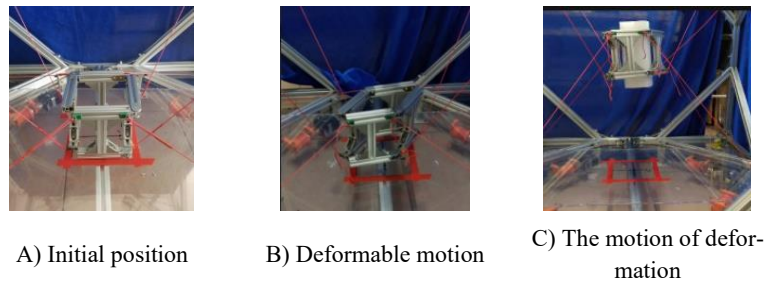
Fig. 10. Deformable motion of prototype

5 Conclusion

(1) Due A cable-driven parallel robot with a self-deformable end-effector is proposed. The end-effector is designed as a deformable structure, which greatly enriches the functions of the cable traction device.

(2) The kinematics of the end-effector is analyzed and calculated, and the inverse kinematic of the mechanism is carried out, then variation of the cable length during the end-effector movement is obtained.

(3) A prototype was built, and MATLAB was used to calculate the motion trajectory of the end-effector, and the correctness of the calculation was verified with the prototype.

Acknowledgements

References

1. Yaqing Zhang. Modeling of wire-driven parallel crane robot for containers handling[J]. Natural Science News 4(5),496-501(2009).
2. Yuanying Qiu, Qiang Wei, Baoyan Duan.et al. Redundant general stewart platform for the large radio telescope[J]. Mechanism and Machine Theory3(12),7-15(2001).
3. Benhamida Ines, Laribimed Amine, Mlika Abdelfattah.et al. Multi-Objective optimal design of a cable driven parallel robot for rehabilitation tasks. Mechanism and Machine Theory 4(5),496-501(2009).
4. Feiyun Xiao, Yongsheng Gao, Yong Wang.et al. Design and evaluation of a 7-DOF cable-driven upper limb exoskeleton[J]. Journal of Mechanical Science and Technology32(2), 855-864(2018).
5. Paty Thibaut, Binaud Nicolas, Caro Stéphane. et al. Cable-driven parallel robot modelling considering pulley kinematics and cable elasticity[J]. Mechanism and Machine Theory159(2021).
6. Wan Ding, Yan-an Yao. Self-crossing Motion Analysis of a Novel Inpipe Parallel Robot with Two Foldable Platforms[M]. Springer International Publishing,2-3(2015).
7. Yizhao Wang, Qixin Cao, Xiaoxiao Zhu. et al. A cable-driven distal end-effector mechanism for single-port robotic surgery[J]. International Journal of Computer Assisted Radiology and Surgery, 1-9(2021).
8. Rushton Mitchell, Khajepour Amir. Planar Variable Structure Cable-Driven Parallel Robots for Circumventing Obstacles[J]. Journal of Mechanisms and Robotics, 13(2), 5-6(2021).
9. Haining Sun, Senhao Hou, Qunzh Li. et al. Research on the configuration of cable-driven parallel robots for vibration suppression of spatial flexible structures[J]. Aerospace Science and Technology, 109(2021).
10. Yao Xiang, Qinchuan Li, Xiaoling Jiang. Dynamic rotational trajectory planning of a cable-driven parallel robot for passing through singular orientations[J]. Mechanism and Machine Theory, 158(2021).
11. Patrice Lambert, Just L Herder. Parallel robots with configurable platforms: Fundamental aspects of a new class of robotic architectures[J]. Proceedings of the Institution of Mechanical Engineers, Part C: Journal of Mechanical Engineering Science230(3) ,463-472(2016).
12. Jiajun Xu, Kyoung Supark. A real-time path planning algorithm for cable-driven parallel robots in dynamic environment based on artificial potential guided RRT[J]. Microsystem Technologies26(prepublish),1-14(2020).
13. Mottola Giovanni, Gosselin Clément, Carricato Marco. Dynamically feasible motions of a class of purely-translational cable-suspended parallel robots[J]. Mechanism and Machine Theory132, 193-206(2019).
14. Xiongwei Liu, Yaqing Zhang. Kinematic analysis of 6-DOF wire-driven parallel kinematic manipulator[J]. Mechanism and Machine Theory 38, 17(2002).

A morphing structure covered with panels inspired by fish scales

Jieyu Wang[1,2], Fengfeng Xi[2*], Yinjun Zhao[3]

[1] Beihang University, Beijing, China, 100191
[2] Ryerson University, Toronto, Canada, M5B 2K3
fengxi@ryerson.ca
[3] Shanghai University, Shanghai, China, 200444

Abstract. Inspired by fish scales driven by bones and muscles, this paper proposes a morphing structure consisting of a multi-loop mechanism covered by scaled panels. A combinatory design method is put forward to design a mechanism with consideration of a cover enclosing it. For the mechanism design, the tracer points of the mechanism are required to follow three different curves mimicking fish morphing shapes. The key design variables and constraints are defined to determine the degrees-of-freedom (DOFs) and the module type of the morphing structure. For the cover design, the dimensions and placement of the panels are investigated for interference avoidance. At the end, the two designs are combined to realize a complete morphing structure. Based on the proposed method, a final system is developed capable of morphing through three different curves.

Keywords: Morphing structure, Fish scales, Bioinspired mechanism, Multiple loops, Morphometry.

1 Introduction

In recent years, biological principles started to be transferred to engineering applications for innovative product design. In the area of morphing structure research that aims to accomplish shape morphing, animal skin epidermis and dermis driven by bones and muscles have been studied and applied to various industrial applications spanning from architecture to automotive and aerospace. Various shape morphing materials, including shape memory alloys, piezoelectric materials and self-shaping materials, have been investigated [1-3]. Continuum robots have been proposed for continuous shape changing of surface. These robots usually have a central backbone surrounded by large flexible parts, such as panels [4-6], to form an enclosed morphing system.

By examining nature, a large number of animals have evolved to obtain armored skins in order to protect from predatory attacks. The armors possess the function of distributing loadings, reduction of friction, regulation of body temperature, improvement of concealment and water tightness. To apply the principle of the animal armors to morphing skins, the structure of armors needs to be translated for proper modeling. In [7-9], armors are designed using flexible materials with segmented scales fixing to a

surface. However, compliant materials are easy to wrinkle, difficult to control surface shapes, and with little load bearing capability.

In this paper, an underlying rigid continuum mechanism will be applied to replace the flexible materials and compliant structures in the literature for shape changing and load bearing. Sliding panels will be designed to serve as fish scales providing protections. Mechanism theory will be applied to find the solutions for the tracer points following the morphing surfaces, the solutions for the scales attached to the tracer points without interference and a minimum number of actuators required for morphing. The bioinspired multi-loop morphing structure works as dermis with the tracer points as control points of epidermis covered by overlapped scales. The degrees of freedom (DOFs) and the module type of the structure will be determined, the fish scale directions will be calculated and the dimensional synthesis will be conducted.

This paper is organized as follows: Section 2 focuses on the problem statement. In Section 3, DOFs are determined and a mechanism is designed. Section 4 provides the dimensional synthesis to compute the link lengths. Finally, conclusions are drawn.

2   Problem statement

This section addresses how to transfer a fish structure with scales to a mechanism design problem. The idea is to replace the flexible materials (epidermis and dermis) as shown in Figs. 1(a-b) by a rigid multi-loop mechainsm as shown in Fig. 1(c). Fig. 1(b) is a kinematic representation of the fish scales (dentine) attached to the epdiermis and dermis which are modeled by a morphing curve (dash line in Fig 1(c)). This problem is stated as designing a multi-loop mechanism with panels attached to follow a morphing curve.
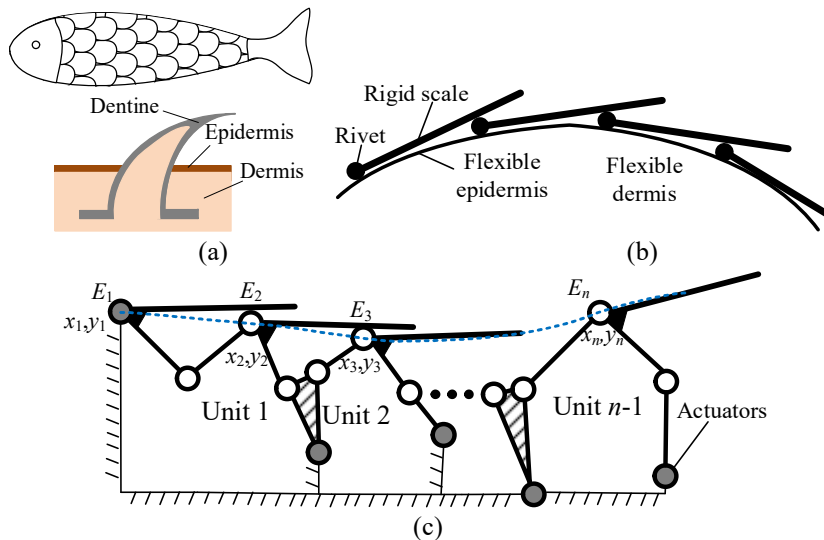
Fig. 1 Fish structure: (a) fish scale; (b) kinematic modeling; (c) substituting mechanism.

This design problem falls under mechanism type and dimensional synthesis with the following requirements. First, fish scales are segmented and fixed to individual connection points. This requires a mechanism be of multiple loops to provide multiple tracer points as indicated by E_i (i is the number of tracer points) in Fig. 1(c). Second, the scale connection points move with the fish epidermis. This requires that the tracer points follow the morphing curve defined by the fish epidermis. Third, fish scales are fixed to the connection points in specific directions. This requires that the coupler links where the scales are attached have prescribed angles with respective to the scales.

3   Mechanism design

Figure 2 translates the afore-mentioned requirements to a schematic for mechanism design. Three morphing curves are given presenting the shape change, and the objective is to design a mechanism whose tracer points (E_i) can arrive at points on the three curves with the scales along specific directions. First, type synthesis is carried out to determine the basic unit type and DOFs of the mechanism based on the number of variables and constraints.
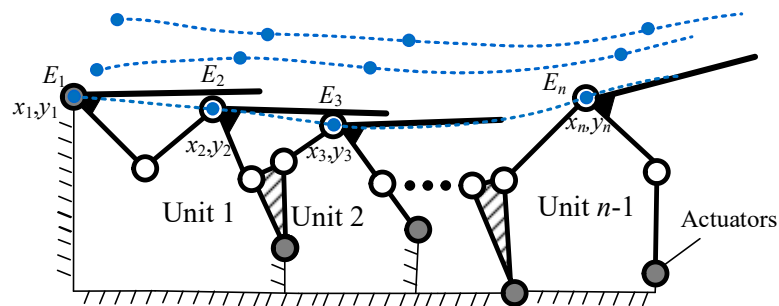
Fig. 2 Three desired curves
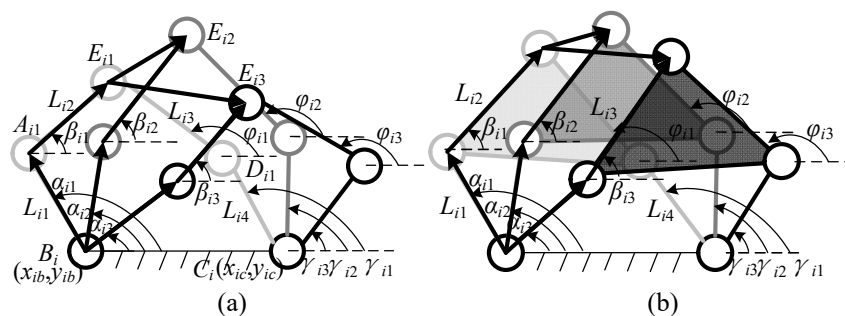
Fig. 3 The parameters in a loop: (a) 5R linkage; (b) 4R linkage

To reduce the DOFs and the number of actuators for structure compactness, we investigate 4R and 5R linkages as two basic module units, which have 1-DOF and 2-DOF respectively. It can be seen from Fig. 3(a) that the 5R linkage is formed by 5 points

4

A_i, B_i, C_i, D_i, and E_i. In total, there are 18 variables for a 5R linkage including: four link lengths, 12 link angles and four coordinates of base B_i and C_i, i.e., $L_{i1}, L_{i2}, L_{i3}, L_{i4}, \gamma_{i1}$, $\varphi_{i1}, \alpha_{i1}, \beta_{i1}, \gamma_{i2}, \varphi_{i2}, \alpha_{i2}, \beta_{i3}, \gamma_{i3}, \varphi_{i3}, \alpha_{i3}, \beta_{i3}, xb_i, yb_i, xc_i$ and yc_i. To let the tracer point E_{i1} move from the first desired curve to the other two desired curves E_{i2} and E_{i3}, there exist three sets of dyad equations expressed in 12 constraints equations as below.

$$xb_i + L_{i4}\cos\gamma_{i1} + L_{i3}\cos\varphi_{i1} = x_{i1} \tag{1a}$$
$$yb_i + L_{i4}\sin\gamma_{i1} + L_{i3}\sin\varphi_{i1} = y_{i1} \tag{1b}$$
$$xb_i + L_{i4}\cos\gamma_{i2} + L_{i3}\cos\varphi_{i2} = x_{i2} \tag{1c}$$
$$yb_i + L_{i4}\sin\gamma_{i2} + L_{i3}\sin\varphi_{i2} = y_{i2} \tag{1d}$$
$$xb_i + L_{i4}\cos\gamma_{i3} + L_{i3}\cos\varphi_{i3} = x_{i3} \tag{1e}$$
$$yb_i + L_{i4}\sin\gamma_{i3} + L_{i3}\sin\varphi_{i3} = y_{i3} \tag{1f}$$
$$xb_{i-1} + L_{i1}\cos\alpha_{i1} + L_{i2}\cos\beta_{i1} = x_{i1} \tag{1g}$$
$$yb_{i-1} + L_{i1}\sin\alpha_{i1} + L_{i2}\sin\beta_{i1} = y_{i1} \tag{1h}$$
$$xb_{i-1} + L_{i1}\cos\alpha_{i2} + L_{i2}\cos\beta_{i2} = x_{i2} \tag{1i}$$
$$yb_{i-1} + L_{i1}\sin\alpha_{i2} + L_{i2}\sin\beta_{i2} = y_{i2} \tag{1j}$$
$$xb_{i-1} + L_{i1}\cos\alpha_{i3} + L_{i2}\cos\beta_{i3} = x_{i2} \tag{1k}$$
$$yb_{i-1} + L_{i1}\sin\alpha_{i3} + L_{i2}\sin\beta_{i3} = y_{i3} \tag{1l}$$

where x_{ij} and y_{ij} (j=1, 2, 3) represent three positions of the tracer point on three curves.

It is noted that joint B of each unit is coincident with joint C in the preceding unit. To connect two adjacent units together, we have the following constraint equations.

$$(\gamma_{(i-1)1} - \alpha_{i1}) - (\gamma_{(i-1)2} - \alpha_{i2}) = 0 \tag{2a}$$
$$(\gamma_{(i-1)3} - \alpha_{i3}) - (\gamma_{(i-1)2} - \alpha_{i2}) = 0 \tag{2b}$$

For the first unit, link 1 is fixed to the first scale instead of the preceding unit, there are

$$(\arctan k_{11} - \alpha_{21}) - (\arctan k_{12} - \alpha_{22}) = 0 \tag{3a}$$
$$(\arctan k_{13} - \alpha_{23}) - (\arctan k_{12} - \alpha_{22}) = 0 \tag{3b}$$

The scales of the system should be along a specific direction, so there should be

$$(\arctan k_{i1} - \varphi_{i1}) - (\arctan k_{i2} - \varphi_{i2}) = 0 \tag{4a}$$
$$(\arctan k_{i3} - \varphi_{i3}) - (\arctan k_{i2} - \varphi_{i2}) = 0 \tag{4b}$$

Therefore, there are 16 equations for each 5R linkage and there are always solutions in this case.

In the case of a 4R linkage as shown in Fig. 3(b), the angle between links 2 and 3 is constant, so there are two additional constraints.

$$\varphi_2 - \beta_2 = \varphi_1 - \beta_1 \tag{5a}$$
$$\varphi_3 - \beta_3 = \varphi_1 - \beta_1 \tag{5b}$$

The number of constraints is increased to 18. There is only one solution in this case. It is noted that there are inequality constraints apart from the equality constraints mentioned above. For example, the links must translate beneath the scale; the x coordinate of C_i should be larger than that of B_i (the detailed inequation will be presented in Section 4). Since the 4R linkage cannot satisfy the requirement, the 5R linkage is adopted for our system design. The DOF of the first 5R linkage is 2 and each subsequent 5R linkage adds 1-DOF. Suppose that there are n tracer points, the number of add-on units is n-2, so the total DOF of the system is

$$M = 2 + (n - 2) = n \tag{6}$$

4   Objective determination and dimensional synthesis

In this section, the target parameters, including the desired positions of the tracer points and the directions of the scales are determined first, then dimensional synthesis is conducted to determine the link lengths of the mechanism. The first step is to define morphing curves. This definition is inspired by fish, so the moving curve of the fish is used as the objective of our study. Three fish curves are considered as shown in Fig. 4, representing three shape morphing cases.

Fig. 4 The fish morphing curves

Through digitizing the fish shapes and curve fitting, the following three curves of the fish epidermis can be obtained as

$$y_1 = -1.487 \times 10^{-6}x_1^3 + 0.001419x_1^2 - 0.3226x_1 + 83.18 \qquad (7a)$$
$$y_2 = -4.816 \times 10^{-6}x_2^3 + 0.001801x_2^2 - 0.05914x_2 + 83.18 \qquad (7b)$$
$$y_3 = -7.761 \times 10^{-6}x_3^3 + 0.002095x_3^2 + 0.2054x_3 + 83.18 \qquad (7c)$$

The second step is to determine n tracer points, i.e., separating each curve into (n-1) segments equally. In this study, the three curve lengths are equaled to be 350mm. The even segment length of 50mm is used, leading to 7 segments for each curve and in total 21 points for three curves as given below.

$$x_1 = [\, 0, 48.3929, 97.8882, 147.8280, 197.7909, 247.5980, 297.2495] \qquad (8a)$$
$$y_1 = [83.18\,, 70.7230\,, 63.8035, 61.6965, 63.3796, 67.7253, 73.6115] \qquad (8b)$$
$$x_2 = [\, 0, 49.9480, 99.5428, 148.8958, 198.4832, 248.4295, 297.7452] \qquad (8c)$$
$$y_2 = [83.18\,, 84.1191\,, 90.3885, 98.4047, 104.7351, 105.7999, 98.1119] \qquad (8d)$$
$$x_3 = [\, 0, 48.0084, 94.7199, 141.5893, 189.9799, 239.7893, 287.2819] \qquad (8e)$$
$$y_3 = [83.18\,, 97.0107, 114.8361, 132.2323, 144.5996, 145.8872, 131.0795] \qquad (8f)$$

The third step is to determine the fish scale directions. Since the panels are overlapped, we need to ensure that the gaps between the scales are as small as possible yet without interference.
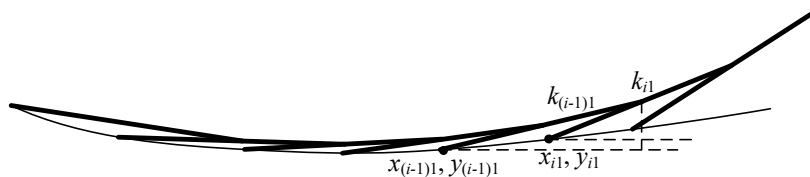
Fig. 5 Scale direction calculation of curve 1

6

When the curve is concave, the interference occurs when the end of each scale contacts the following scale, as shown in Fig. 5. To avoid interference and minimize the gap, scale directions are calculated as

$$k_{i1} = \frac{l\sin k_{(i-1)1} - (y_{i1} - y_{(i-1)1})}{l\cos k_{(i-1)1} - (x_{i1} - x_{(i-1)1})} \qquad (9)$$

where l is the length of the scale. Furthermore, in considering link width, as shown in Fig. 6, we should decrease the angle by δ, which is equal to $\arcsin \left(\dfrac{s}{\sqrt{[l\sin k_{(i-1)1} - (y_{i1} - y_{(i-1)1})]^2 + [l\cos k_{(i-1)1} - (x_{i1} - x_{(i-1)1})]^2}} \right)$. s is the distance between the endpoint of the first scale and the central line of the second scale, and is always smaller than $2h$, which is the width of the link. Manufacture and assembly errors (0.02) are also considered, so the scale direction formula is modified as

$$k_{i1f} = \tan\left(\arctan k_{i1} - \arcsin \frac{2h}{\sqrt{[l\sin k_{(i-1)1} - (y_{i1} - y_{(i-1)1})]^2 + [l\cos k_{(i-1)1} - (x_{i1} - x_{(i-1)1})]^2}} - 0.02\right)$$

$$(10)$$
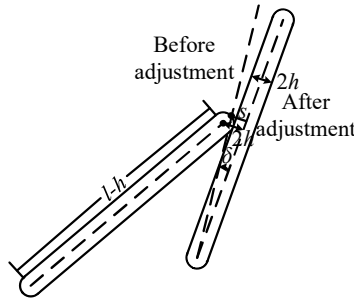
Fig. 6 Modified angle when considering link width and error

In case that the curve is convex, like the segments of curve 2 between the third and the last tracer points, the interference happens when the scale is in contact with the next revolute joint, as shown in Fig. 7. To avoid interference and minimize the gap, the scale direction is calculated as

$$k_{i2f} = \tan\left(\arctan \frac{y_{i1} - y_{(i-1)1}}{x_{i1} - x_{(i-1)1}} + \arcsin \frac{r+h}{\sqrt{(x_{i1} - x_{(i-1)1})^2 + (y_{i1} - y_{(i-1)1})^2}}\right) + 0.02 \quad (11)$$

It is noted that the segment of curve 2 between the first and the third tracer points is concave, so the direction of the first scale is obtained using the method for the concave curve.

To reduce the gap between the last and the second last scales, the direction of the last scale is also calculated using the method for the concave curve, as shown in Fig. 7. Similarly, we can yield the scale directions for the third curve, as shown in Fig. 8.
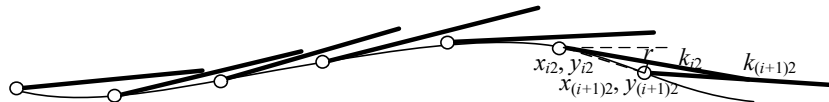
Fig. 7 Scale direction calculation of curve 2
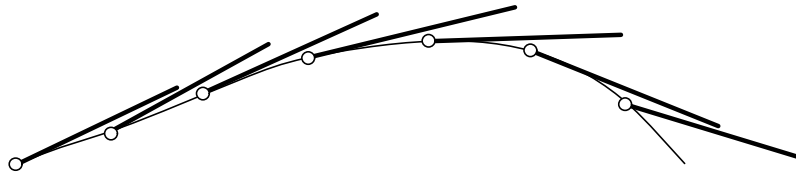
Fig. 8 Scale direction calculation of curve 3

The final results of the scale direction of three curves are shown in Fig. 9 and given as.

$$k_1 = [-0.08, 0.0174, 0.1015, 0.1763, 0.2532, 0.3586, 0.5565] \qquad (12a)$$
$$k_2 = [0.1571, 0.2274, 0.2606, 0.2249, 0.1168, -0.0596, -0.0156] \qquad (12b)$$
$$k_3 = [0.4295, 0.4903, 0.4792, 0.3574, 0.1215, -0.2108, -0.1655] \qquad (12c)$$

(a)

(b)

(c)
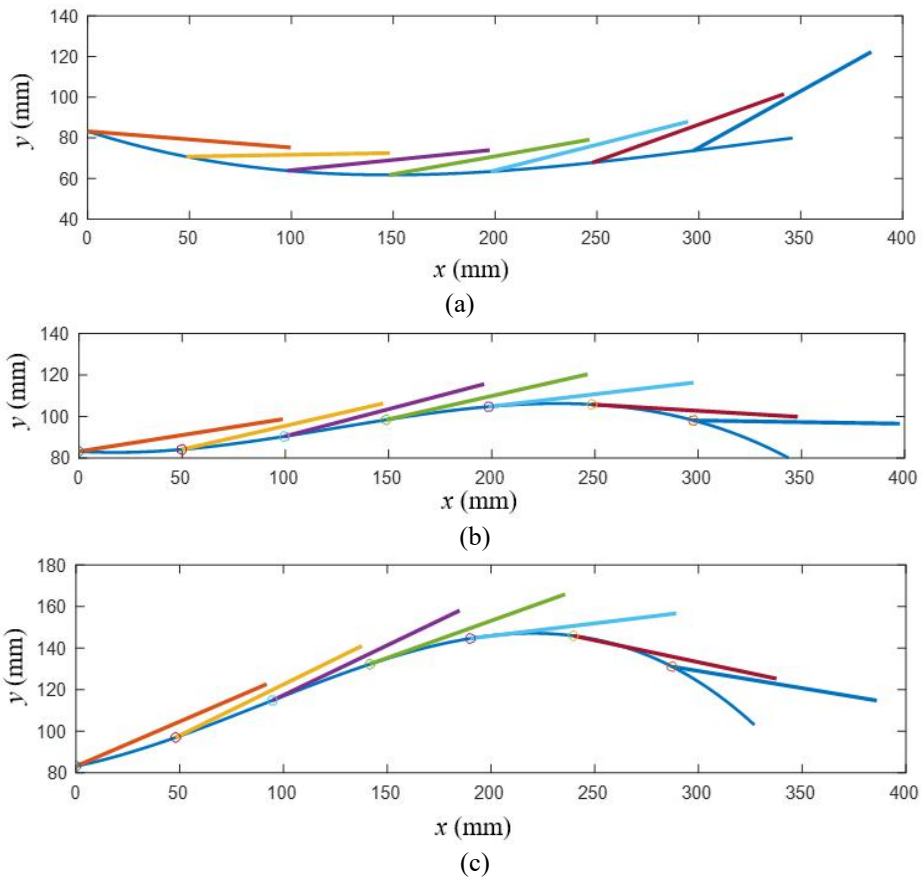
Fig. 9 The direction of scales: (a) curve 1; (b) curve 2; (c) curve 3

8

The final step is to obtain the link lengths of the mechanism through morphometry using an optimization method. The objective is to minimize the distance between the actual and the desired position of the tracer points. The constraints include: the links should be below the scale; the length of the links and the position of the base should be in a reasonable range. The optimization problem is represented by

$$\text{Minimize } T = (xb_i + L_{i4}\cos\gamma_{i1} + L_{i3}\cos\varphi_{i1} - x_{i1})^2 + (yb_i + L_{i4}\sin\gamma_{i1} + L_{i3}\sin\varphi_{i1} - y_{i1})^2 + (xb_i + L_{i4}\cos\gamma_{i2} + L_{i3}\cos\varphi_{i2} - x_{i2})^2 + (yb_i + L_{i4}\sin\gamma_{i2} + L_{i3}\sin\varphi_{i2} - y_{i2})^2 + (xb_i + L_{i4}\cos\gamma_{i3} + L_{i3}\cos\varphi_{i3} - x_{i3})^2 + (yb_i + L_{i4}\sin\gamma_{i3} + L_{i3}\sin\varphi_{i3} - y_{i3})^2 + (xb_{i-1} + L_{i1}\cos\alpha_{i1} + L_{i2}\cos\beta_{i1} - x_{i1})^2 + (yb_{i-1} + L_{i1}\sin\alpha_{i1} + L_{i2}\sin\beta_{i1} - y_{i1})^2 + (xb_{i-1} + L_{i1}\cos\alpha_{i2} + L_{i2}\cos\beta_{i2} - x_{i2})^2 + (yb_{i-1} + L_{i1}\sin\alpha_{i2} + L_{i2}\sin\beta_{i2} - y_{i2})^2 + (xb_{i-1} + L_{i1}\cos\alpha_{i3} + L_{i2}\cos\beta_{i3} - x_{i2})^2 + (yb_{i-1} + L_{i1}\sin\alpha_{i3} + L_{i2}\sin\beta_{i3} - y_{i3})^2$$

$$\text{Subject to } \begin{cases} (\gamma_{(i-1)1} - \alpha_{i1}) - (\gamma_{(i-1)2} - \alpha_{i2}) = 0 \\ (\gamma_{(i-1)3} - \alpha_{i3}) - (\gamma_{(i-1)2} - \alpha_{i2}) = 0 \\ (\arctan k_{i1} - \varphi_{i1}) - (\arctan k_{i2} - \varphi_{i2}) = 0 \\ (\arctan k_{i3} - \varphi_{i3}) - (\arctan k_{i2} - \varphi_{i2}) = 0 \\ \frac{x_{i1}+x_{i2}+x_{i3}}{3} - 100 < xb_i < \frac{x_{i1}+x_{i2}+x_{i3}}{3} + 100 \\ -100 < yb_i < 10 \\ 10 \le L_{ij} \le 250 \quad i = 2,4 \dots 7, j = 1, 2, 3 \text{ and } 4 \\ 0 \le \varphi_{ij} \le \pi \quad i = 2,4 \dots 7, j = 1, 2 \text{ and } 3 \\ 0 \le \beta_{ij} \le \pi \quad i = 2,4 \dots 7, j = 1, 2 \text{ and } 3 \end{cases} \quad (13)$$

Table 1 The obtained results of the parameter of the system

| i	Link 1	Link 2	Link 3	Link 4	xb_i	yb_i
2	32.8284	79.9984	73.1603	100.6387	-28.7195	-48.5247
3	104.5811	115.2401	136.8919	72.0886	25.3267	-57.4918
4	73.8289	176.5031	179.9010	120.0408	130.4703	-65.1759
5	115.3264	210.8621	224.2030	133.3963	268.9419	-68.2264
6	117.2682;	211.1432	186.7089	88.4375	332.6531	1.9045
7	64.4767	139.6586	196.0895	73.9157	383.7559	-14.8563

Using the optimization method, the link lengths and the coordinates of the base are obtained, as listed in Table 1. Fig. 10 illustrates the final system able to follow three different curves, thereby demonstrating the effectiveness of the proposed method.

5   Conclusion

In this paper, it is shown that fish with elasmoid scales can be mathematically modeled. By curve fitting of fish morphing shape, a set of digitized points can be selected as the tracer points for the design of a multi-loop mechanism. Through proper type synthesis, a basic unit type can be found and the overall DOFs of the mechanism can be determined. Subsequently, by formulating the constraint equations, an optimization method can be applied to solve the link lengths and the base coordinates. With a

combination of type and dimensional synthesis, a final system can be obtained capable of morphing between given shape changing curves. Currently, a prototype is being fabricated and the applications in the field of morphing wings will be explored.

(a)

(b)

(c)
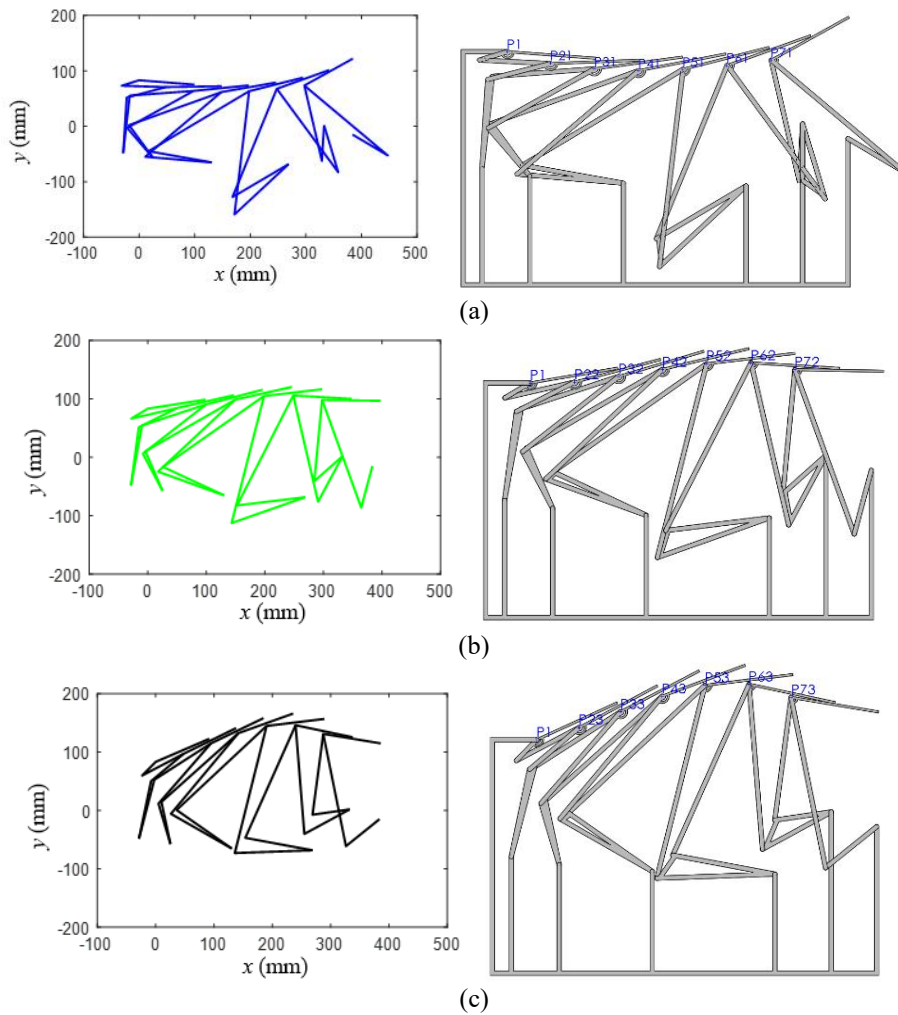
Fig. 10 The comparison between the theoretical and practical models

Acknowledgement

10

References

1. Jani, J.M., Leary, M., Subic, A., Gibson, M.A.: A review of shape memory alloy research, applications and opportunities. Materials & Design (1980-2015) 56 1078-1113 (2014).
2. Irschik, H.: A review on static and dynamic shape control of structures by piezoelectric actuation. Engineering Structures 24(1) 5-11 (2002).
3. Oliver, K., Seddon, A., Trask, R.S.: Morphing in nature and beyond: a review of natural and synthetic shape-changing materials and mechanisms. Journal of Materials Science 51(24) 10663-10689 (2016).
4. Lock, J., Laing, G., Mahvash, M., Dupont, P.E.: Quasistatic Modeling of Concentric Tube Robots with External Loads. Rep U S 2325-2332 (2010).
5. Till, J., Rucker, D.C.: Elastic Stability of Cosserat Rods and Parallel Continuum Robots. IEEE Transactions on Robotics 33(3) 718-733 (2017).
6. Kang, B., Kojcev, R., Sinibaldi, E.: The First Interlaced Continuum Robot, Devised to Intrinsically Follow the Leader. Plos One 11(2) e0150278 (2016).
7. Porter, M.M., Ravikumar, N., Barthelat, F., Martini, R.: 3D-printing and mechanics of bio-inspired articulated and multi-material structures. Journal of the mechanical behavior of biomedical materials 73 114-126 (2017).
8. Chintapalli, R.K., Mirkhalaf, M., Dastjerdi, A.K., Barthelat, F.: Fabrication, testing and modeling of a new flexible armor inspired from natural fish scales and osteoderms. Bioinspiration & biomimetics 9(3) 036005 (2014).
9. Yang, W., Chen, I.H., Mckittrick, J., Meyers, M.A.: Flexible dermal armor in nature. Jom 64(4) 475-485 (2012).

Practical Investigation of Modern Bird Flight Evolution from Arboreal Ancestors

Farzeen Shahid[1] and Jing-Shan Zhao[2]

[1,2] State Key Laboratory of Tribology, Department of Mechanical Engineering, Tsinghua University, Beijing 100084, China.

Abstract. Bioinspired and Biomimetic mechanisms is a merging concept that helps us to comprehend the performance and behavior of different creatures. Particularly bird-inspired structure such as Flapping flight robots, fixed-winged flying robots, Unmanned Aerial Vehicles (UAV) and Micro Aerial Vehicle (MAV) plays an important role in conceptual understanding of Evolution of Flight. In this paper, a bioinspired wing mechanism is proposed that evolved into a gliding robot. The developed system is based on an important flight evolution hypothesis i.e., Arboreal Hypothesis and helps to investigate the behavioral aspect of winged dinosaurs. Bioinspired reconstructions of basal birds will help in understanding the evolution of avian flight. While developing this wing, several different prototypes were generated to ensure an accurate and precise folding and unfolding motion. The prototype was built using a 3D printer and then feathers were attached to the linkage system giving the mechanism a perfect chambered shape. The surface area is constructed with real feathers to evaluate the performance of the proposed mechanism. The extension and relaxation of a bird's wing play a significant role during different flight activities, combining it with the flapping mechanism will help a lot in building a competent air vehicle.

Keywords: Evolution, Bio-inspired, Arboreal, Foldable Wing Mechanism, Flying Robot.

1   Introduction

The concept of Bio-inspired and Biomimetic models dates back to the 15th century, back then it was anticipated that flight was probable if the behavioral aspect and performance of birds could get mimicked. Sir George Cayley was the pioneer in the field of aviation who was among the first few individuals to develop the design of fixed-wing aircraft [1]. The design of an aircraft can be categorized into two main forms, fixed-winged aircraft and rotary-wing aircraft. The fixed-wing aircraft have high load-bearing capacity but requires sufficient space or area to attain a certain velocity, needed to take-off from the ground. The rotary-wing aircraft, on the other hand, can hover in the air and is capable enough to fly at low speed.

Over the last few years, Unmanned Aerial Vehicle has been an important prospect in commercial and military areas because of their effective aerodynamic surfaces and ability to passively produce lift. The new conceptual design of UAV's can be projected

by studying the behavioral characteristics of bird's flight. Pelagornis sandersi, an extinct flying specie, had a wingspan of 6.4 meters and a weight of about 40.1 kg, which is almost double to that of modern Albatross' wingspan, approaching the size of small aircraft [2]. To achieve a stable, sound and systematized design of UAV, it is important to discover the flight capabilities of birds with large payloads, from evolutionary, biophysical and bio-inspirational perspectives.

Presently, UAVs are mostly rotary aircraft that are proficient in low-speed flight, easy maneuverability and hovering. All these features require an extensive amount of energy, while on the other hand, the distance covered is fairly short especially when carrying some payload. The fixed-winged ones can cover longer distances but they need more space as compared to rotary ones. Aeronautical research contributed a lot to the UAVs industry, but we still lack a successful and beneficial flying device used for commercial purposes. Bio-inspired or Biomimetic flying robots provide a huge investigative area to study the dynamic behavior of flying creatures [3]. The experimental data of actual birds is inadequate due to the complication involved in measuring their motion during different flying modes. By taking inspiration from the bird's wing and reconstructing the biomechanical aspects will lead to a better understanding.

Bird wings are capable of generating lift and thrust and a substantial amount of research study has been conducted concerning the airfoil shape of the bird's wing [4], aerodynamic properties and morphological parameters. The wing comprises four main bones, humerus, ulna, radius and metacarpals. The feathers attached to the bird's wing can be classified into primaries, secondaries and tertiaries. Primaries, the outermost feathers attached to the carpometacarpus and digits, play a significant role in generating forward thrust during the downward stroke and lift during gliding. Secondaries, connected to the Ulna, build a smooth surface essential for lift. The tertiaries are located behind the humerus and serve as a defensive shield for the primaries and secondaries.

In this paper, a brief investigation has been made in connection to the origin and early evolution of flight both from an engineering and paleontological viewpoint. The aerodynamical and experimental evaluation is based on the 3D printed prototypes. These assessments will help in understanding the flight origin of paravian dinosaurs as well as provide enlightenment for the design of modern bird-inspired aircraft. A theoretical and experimental foundation for the design and manufacturing of a wing mechanism can be obtained by exploring the origin of bird's flight, wing kinematics and structural dynamic.

2 Flight Evolution

Archaeopteryx, the oldest known feathered fossil that was discovered in Germany in 1861, caused a disputable debate about the origin of flight among palaeontologists [5,6]. It is now a fact that birds have an ancestral association with paravian dinosaurs, especially around 1998, when well preserved feathered dinosaur's fossils were discovered in China. It exhibits how progressively the paravian dinosaurs have been transformed into modern birds [7,8]. Since the discovery of feathered dinosaurs, palaeontologists have found more than fifty non-flying paravian dinosaurs' fossils with extensive diversity in size, osteology, limb proportions and integumentary covering. Primarily, fuzzy proto-feathers cover the body of a basal dinosaur and serve the purpose of heat

insulation [9]. Later on, longer and more complex feathers evolved in feathered thero-pods, probably for visual display [10]. Although it is assumed that initially feathers were not developed for flight purposes [11], it is undeniable that they provided aerody-namic control for gliding and then powered flight, later in the evolution of paravian dinosaurs as well as modern birds [11,12].

Powered flight is an unusual locomotory behavior in vertebrates, contrary to gliding flight. Gliding evolved independently in more than 30 theropod lineages and is difficult to understand because of the complex morphology, physiology and behavioral adaption required to accomplish it. Late Jurassic basal paravian from China, indicates that the-ropod dinosaurs used the air in two different ways during the Mesozoic era, implying that aerial niches might have been occupied by more than one theropod lineage [7].

Several theories have been put forward to explain the origin of avian flight. The cursorial model proposed by Williston in 1879 and the arboreal model proposed by Marsh in 1880 remain the most reasonable hypotheses. The ability of a bird to flap its wings has evolved from gliding, according to the arboreal hypothesis [13,14]. As a result, it's fair to assume that avian ancestors lived in trees and were capable of gliding. However, to live in an elevated area, the birds' ancestors had to first learn to ascend the trees and then glide using the gravitational potential energy. The climbing skills of non-avian dinosaurs have never been documented precisely [15], that's why palaeontolo-gists have not yet accepted the arboreal hypothesis [11,16]. Contrastingly, the cursorial hypothesis states that flight abilities of paravian theropods developed from active run-ning [17]. The hypothesis indicates that many basal paravians had elongated feathers along their forelimbs and possibly even along their hindlimbs. The hindlimb feathers were likely to be a hurdle in their running abilities, making it difficult for them to glide and take off from the ground [18,19]. To summarize, the fossil evidence shows that both the cursorial and arboreal hypotheses fail to justify the origin of flight in birds.

3 Mechanism Development

Birds and their ancestors require a well-arranged and effective mechanism to perform various flight activities. During the flight, the birds fold their wings to provide the re-quired surface area for getting the necessary lift and the ancestors might have followed a similar pattern. This paper focuses on the folding and unfolding motions of the flying feathered creatures. The four-bar linkage system was chosen to develop a folding and unfolding mechanism, due to its simple structure, ease in manufacturing and high per-formance.

3.1 Conceptual Design

A four-bar mechanism consists of four members linked together by a revolute joint. The inter-connecting of these four-bar links in a plane creates a robust framework that permits movements within the plane. The length and position of the links are very im-portant in producing a specific motion, which in this case is the folding and unfolding motion of the wing. There has been a lot of research conducted on the aerodynamics and kinematics of flapping motion [20]. However, only a small percentage of them concentrate on folding movement. The primary goal is to create a mechanism and pro-totype that is light in weight and can produce lift effectively. The initial design concept

of the bio-inspired foldable mechanism is illustrated in **Fig. 1**. The links or elements represent the humerus, ulna, radius and metacarpals. The rope provided is designed to imitate the tendon, so when the string is pulled the wing is completely folded. The rope started from the first pulley loop over the second and finally passes through the last one. This is an underactuated system that possesses three degrees of freedom and is designed in such a manner that it can fold and unfold up to the maximum possible limit.
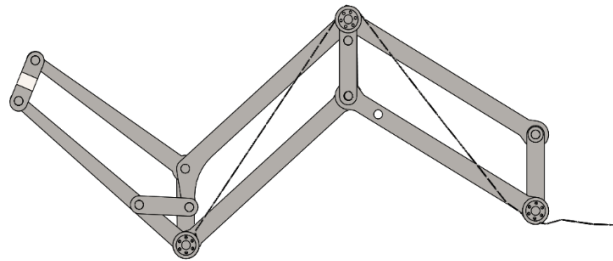
Fig. 1. Preliminary Framework of the Bio-Inspired Four-Bar Mechanism

This preliminary version lacks a proper system to integrate the airfoil and feathers. The primary and secondary feathers move in a particular fashion and play an important role in the aerodynamic performance of the wing so to incorporate these and the airfoil, the second version of the prototype is designed. Moreover, this underactuated system leads to the uncontrollable movement of the mechanism.

The approach to the second prototype is shown in **Fig. 2**. As compared to the previous version, the number of links in this mechanism are doubled to increase the strength. The airfoil is also incorporated to give the mechanism a proper shape and dimension. The string is supposed to pass through the pulleys and then through the slots provided in the last individual links which help the primary feathers to move accordingly. A prototype using a 3D printer was created to evaluate its performance, which showed that when the wing is completely unfolded, the rope experienced a force but when the force is released it folds up.
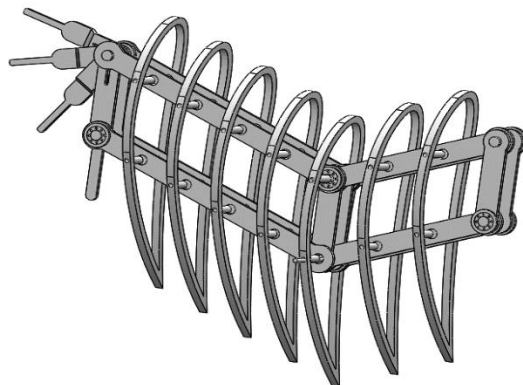
Fig. 2. Second Version of Bio-Inspired Mechanism Incorporating Airfoils

3.2 First Complete Version

The mechanism intended to attached primary feathers, in the preliminary designed system, didn't work properly because when the primaries were attached, they overlapped each other and produced a lot of friction. Another shortcoming was that the mechanism was built with many small components that needed to be joined together with the help of glue, which added extra weight. To mimic the motion of primary feathers properly, there is a requirement to design an appropriate mechanism, which provides sufficient space to attach the feathers as well as hold them tightly so that they don't lose their original position.

The updated version of the prototype was the first fully developed version of the bird robot, modelled in SolidWorks to assess its performance. The real-sized primary and secondary eagle feathers, as well as the coverts, were attached to the mechanism. The benefit of using real feathers, in comparison to artificial feathers, is that it would add less weight to the overall structure and save the effort of designing and cutting them precisely. The torso was also created to match the wing configuration. The positioning of motors, batteries, and other electronic components was taken into consideration while designing the torso. The tail was a critical part and have a separate mechanism to connect the tail feathers as well as the specific movements to control the bio-inspired robot's stability. The design concept of the prototype is illustrated in **Fig. 3**.
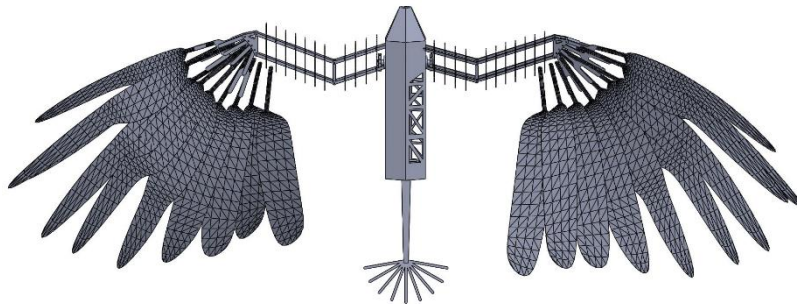
Fig. 3. Fully Developed Prototype of The Bioinspired Wing with Feathers and Torso

3.3 Airfoil Selection

The design of the wing profile is critical because to produce enough lift the wing transition from root to tip has to be smooth and chambered. For this purpose, airfoil selection is an important step. The two main concerns or constraints for the airfoil selection are that it should be closer to the shape of the bird's wing and also get appropriately attached to the designed mechanism. A wide range of airfoils are available that can mimic the bird shape e.g., S1223, GOE464 etc.

Gottingen 464 – The first airfoil that is taken into consideration was GOE 464. Its profile looks similar to the shape of the bird's wing and has high values of lift coefficient (CL) and lift to drag ratio (L/D). The high L/D means that a high lift can be produced with less dimension.

Selig S1223 – The bio-inspired flying robot is designed to operate at low altitude and not at high speed, the next airfoil considered is S1223, which is a high lift and low

Reynold number airfoil. Although the shape of GOE 464 is closer to the bird's profile, it's relatively thin and cambered while S1223 can produce more lift at a low angle of attack.

Liebeck LNV109A – This airfoil also comes under the category of high lift producing airfoils. The maximum value of CL is lower than that of S1223.

There is some limitation with this and the above-mentioned airfoils. The thickness of the profile is not suitable and compatible with the linkage mechanism. If the thickness and chord of the airfoil shape are adjusted according to the designed system then it completely distorts the shape and efficiency of the airfoil.

Due to the size and shape limitation of the already existed airfoils. A new airfoil is proposed which not only looks closer to the bird's profile but is suitable for the mechanism. The evolution process of the airfoil developed is shown in **Fig. 4**. The profile at the extreme left is the airfoil shape Lnv109-A, which has a smaller chord and shorter chamber. Both these parameters are not suitable for the mechanism. The profile next to the Lnv109-A is the new proposed airfoil whose length and chord are optimized according to the mechanism. The chord length of the proposed airfoil is 135mm with 30mm of camber length. The holes and slots are created for assembly purposes.

Fig. 4. Shape Optimization of the Airfoil

3.4 Numerical Investigation of Airfoil

The proposed airfoil is numerically investigated by using ANSYS18. The investigation is used to evaluate the coefficients and aerodynamic forces. The investigation parameters are summarized in **Table 1**.

Table 1. Fluent Analysis Parameters

Parameters	Values
Chord length of Airfoil	135 mm
Camber length	30 mm
Analysis Velocity	10 m/s
Turbulence Model	K-epsilon
Temperature	288 K
Maximum No. of iteration	1000
Residual criteria	1x10-6

The contours obtained after the analysis are shown in **Fig. 5**. The velocity contour obtained shows that the higher value of velocity is at the maximum camber of the airfoil which makes the value of the pressure decrease in the same area. The value of pressure is higher at the lower region of the airfoil as compare to the upper region which creates the lift force. The results obtained are at the zero angle of attack. The results can be improved further by increasing the number of iteration and grid resolution.

(a)

(b)
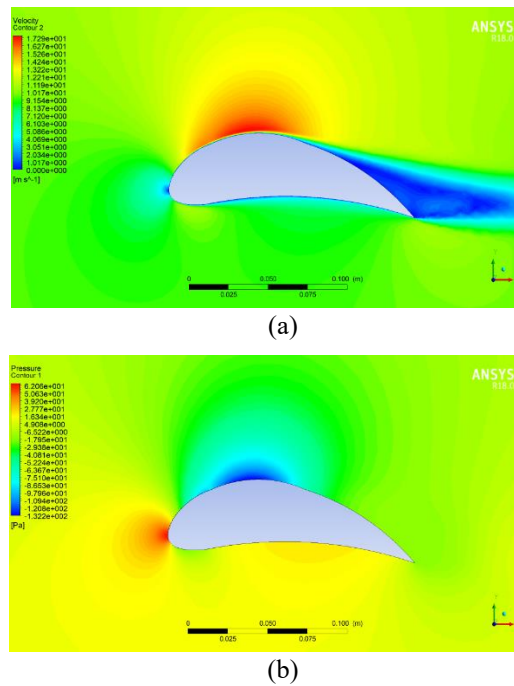
Fig. 5. (a) Velocity Contours around the airfoil, (b) Pressure Contours around the airfoil

4   Fabrication Procedure

Recently, 3D printing has become an efficient and productive method for creating prototypes. To evaluate the performance of the designed and purposed mechanism prototypes can be generated and analyzed using the aforementioned technique. The bio-inspired robot was manufactured using carbon fibre, as it is light in weight. The individual parts have to be assembled precisely with the help of bearing and screws to make the system stable and frictionless. The batteries, motors and propeller were attached in such a way that the whole mechanism is well-balanced. The robot can fold and unfold its wing and can change the angle of attack. The tail has four degrees of motion, it can move up and down and also move to the right and left. The manufactured carbon fibre prototype is shown in **Fig. 6**.
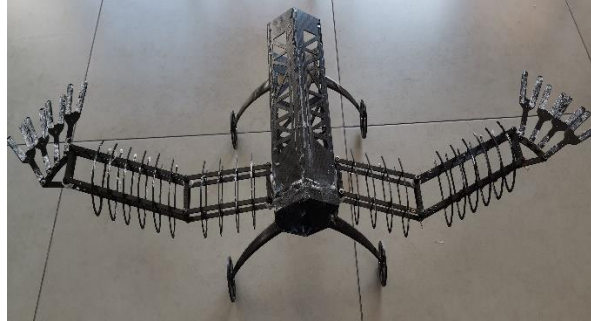
Fig. 6. Fully Assembled Bird's robot

To evaluate the output of folding and unfolding motion with feathers, real primaries and secondary feathers were integrated. The feathers needed to be assembled accurately and form a curvature similar to that of a real bird. The primaries have a specific angle between them which prevent them to overlap with the adjacent feathers and the secondaries were fixed with the linkage mechanism. The coverts were also attached to the mechanism to smooth out the airflow. The design parameters for the prototype are summarized in **Table 2**.

Table 2. Design Parameters of Bio-Inspired Robot

Design Parameters	Values
Total Wing Span (w. feathers)	160 cm
Wing Span	75 cm
Airfoil Chord	12 cm
Estimated Area	6660 cm^2
Closest Airfoil	Archer A18 F1C
Weight	1.6 Kg

The robot axis was kept at an angle that allows and help it to take off from the ground when the thrust is generated. The torso was designed to be aerodynamically efficient and it provides more resistance to the incoming air. A tunnel was made specially, to assemble the propellers with the prototype. The summary of electrical equipment used to set up the control of the Bio-inspired robot is given in **Table 3**.

Table 3. Electrical Equipment and it's Specification

Electrical Equipment	Specification
Propellers	50 mm Ducted Fan (11 Blades)
Electronic Speed Control	55 A
Batteries	1300 mAh (3S 35C)
Remote Control set	RC Controller

The weight of the prototype was also measured at each phase, with just the carbon fibre framework the prototype weighs almost 652 grams. The weight of the prototype

with the primaries was 811.1 grams and with all the feathers, tail, motor and battery it weighs 1214 grams. The bio-inspired bird robot with real feathers is shown in **Fig. 7**.

Fig. 7. The Bio-Inspired Bird Robot with Torso and Feathers

The experiment was conducted in the natural environment and it was observed that since the resultant force is dependent on the surface area of a paravian's body, the creation of more aerodynamic limb feathers was a key factor in gliding down the trees. Paravians learned to adjust the direction of their wings later in the evolution process to achieve higher lifts. It is observed that as the speed of the wind increases, more lift is generated which comes in handy for the flying creatures to descend from an elevated area or a higher branch of a tree. To cover longer distances or glide down to a distant branch of a tree the paravian may have used the potential energy.

5 Conclusion

A highly efficient flapping-wing aircraft is developed based on the wing design and aerodynamic effects of flight feathers on the limbs in non-avialan paravians and basal birds. A crucial factor in gliding down the trees was the creation of aerodynamic limb feathers. Later in the evolution process, paravians learned to change the trajectory of their wings to reach higher lifts. Since more lift is provided as the wind speed increases, the animal may glide to an elevated place. Using the energies, the winged paravian glide from a high enough altitude over a long distance. Early birds became semi-arboreal at this time. The arboreal theory and the findings of this study can be used to better predict the aerodynamic behavior of extinct species and to design a more effective and beneficial framework for future flying robots. The basic design and manufacturing theory for the industrialization of the wing robots, includes airfoil mechanism design, material selection, flapping and gliding motion dynamics studies, wing kinematics, control to flight experiment calculation and data acquisition.

6 References

1. Ackroyd, J.A.D. Sir George Cayley, the father of aeronautics part 2. Cayley's aeroplanes. *Notes Rec. R. Soc.* **2002**, *56*, 333–348.
2. Ksepka, D.T. Flight performance of the largest volant bird. **2014**, *111*.
3. Webb, B. Can robots make good models of biological behaviour? *Behav. Brain Sci.* **2001**.
4. Withers, B.Y.P.C. An Aerodynamic Analysis of Bird Wings as Fixed Aerofoils. *J. Exp. Biol.* **1981**, *90*, 143–162.
5. Ostrom, J.H. Archaeopteryx: Notice of a "New" Specimen. *Science* **1970**, *170*, 537–8.
6. Gibbons, A. New Feathered and Dinosaurs Fossil Birds Brings Closer. *Am. Assoc. Adv. Sci.* **1996**, *274*, 720–721.
7. Zhang, F.; Zhou, Z.; Xu, X.; Wang, X.; Sullivan, C. A bizarre Jurassic maniraptoran from China with elongate ribbon-like feathers. *Nature* **2008**, *455*, 1105–1108.
8. Xu, X.; Zhou, Z.; Wang, X.; Kuang, X.; Zhang, F.; Du, X. Four-winged dinosaurs from China. *Nature* **2003**, *421*, 335–340.
9. Pascal, G.; Danielle, D.; Mcnamara, M.E. Dinosaur evolution. A Jurassic ornithischian dinosaur from Siberia with both feathers and scales. **2014**.
10. Clarke, J. Feathers before flight. *Science* **2013**, *340*, 690–692.
11. Prum, R.O. Dinosaurs take to the air. *Nature* **2003**, *421*, 323–324.
12. Lewin, R. How Did Vertebrates Take to the Air? *Am. Soc. Nat.* **1983**, *221*, 38–39.
13. Garner, J.P.; Taylor, G.K.; Thomas, A.L.R. On the origins of birds: The sequence of character acquisition in the evolution of avian flight. *Proc. R. Soc. B Biol. Sci.* **1999**, *266*, 1259–1266.
14. Chatterjee, S.; Templin, R.J. The flight of Archaeopteryx. *Naturwissenschaften* **2003**, *90*, 27–32.
15. Feduccia, A. Evidence from Claw Geometry Indicating Arboreal Habits of Archaeopteryx. *Science* **1993**, *259*, 790–793.
16. Zhou, Z. The origin and early evolution of birds: Discoveries, disputes, and perspectives from fossil evidence. *Naturwissenschaften* **2004**, *91*, 455–471.
17. Shahid, F.; Zhao, J.; Godefroit, P. Aerodynamics from Cursorial Running to Aerial Gliding for Avian Flight Evolution. *Appl. Sci.* **2019**, *9*, 649.
18. Zhang, F.; Zhou, Z. Leg feathers in an early cretaceous bird. *Nature* **2004**, *431*, 925.
19. Shahid, F.; Zhao, J.S.; Godefroit, P. Design of flying robots inspired by the evolution of avian flight. *Proc. Inst. Mech. Eng. Part C J. Mech. Eng. Sci.* **2019**.
20. McDonald, M.; Agrawal, S.K. Design of a Bio-Inspired Spherical Four-Bar Mechanism for Flapping-Wing Micro Air-Vehicle Applications. *J. Mech. Robot.* **2010**, *2*, 021012.

Trajectory Planning of Controllable Metamorphic Palletizing Robot Based on Optimal Time

Yichen Dong, Rugui Wang*, Huiqing Chen

College of Mechanical Engineering, Guangxi University, Nanning 530004, China

Abstract. To improve the efficiency of the controllable metamorphic palletizing robot, a trajectory planning algorithm based on optimal time is proposed. Taking the joint angle of the metamorphic position as the design variable, combined with the joint angle of the grasping point and the placement point, the joint space trajectory planning is carried out by cubic spline interpolation. Considering the metamorphic palletizing trajectory in three segments, and according to the nature of the spline curve, the shortest time for each segment to meet the motion restriction conditions can be obtained, and the time optimal objective function is established based on the sum of the shortest time of three segments. The forward and inverse kinematics solution combined with particle swarm optimization are used to solve the time optimization problem. Finally, an example is given to prove the effectiveness of the trajectory planning algorithm.

Keywords: Controllable Metamorphic Palletizing Robot, PSO, Time Optimal, Trajectory Planning

1   Introduction

Metamorphic mechanism was first proposed by Dai and Ree Jones [1] at the 25th ASME biennial meeting of mechanism and robotics in 1998 and has been widely concerned and studied by the international institutional circles since then. Zhao et al. [2] proposed a kind of metamorphic mobile robot with multiple motion modes, which can adapt to different terrain. Cui et al. [3] proposed a new planar reconfigurable metamorphic manipulator with flexible palm, which has the advantages of dexterity and strong adaptability. Nurahmi and Gan [4] constructed a kind of parallel metamorphic mechanism by using a reconfigurable rotational joint and analyzed its workspace under different configurations. Wei and Dai [5] proposed a method to analyze the configuration synthesis of parallel metamorphic mechanisms based on group theory. In short, metamorphic mechanisms have made a lot of achievements in the field of mechanical design, but most of these achievements stay in the conceptual design, and few of them are applied to industrial robots.

2

Time optimal trajectory planning is a method to improve the work efficiency of robots, and it is also an important research content of industrial robots. Trajectory planning of industrial robot can be divided into joint space trajectory planning and Cartesian space trajectory planning. Interpolation function is often used in joint space trajectory planning [6-9]. Li and Kim [10-12] applied the method of cubic interpolation function for trajectory planning, whose expression is simple and easy to implement. Fang and Zhang [13-15] used the method of quintic interpolation function to further improve the stability of joint angular acceleration. Zhu et al. [16] proposed the method of fifth-order B-spline curve, which improved the controllability of trajectory. However, the working conditions of the metamorphic mechanism in each configuration will affect its motion constraints, and metamorphosis positions are also important parameters that influence the running time of the trajectory. Therefore, the traditional trajectory planning algorithm cannot be used, and a new trajectory planning algorithm for the metamorphic robot is needed.

According to the above research status, based on the controllable metamorphic palletizing robot [17] developed by this experimental team, combined with cubic interpolation function, this paper proposes a time optimal trajectory planning method of metamorphic mechanism, and uses this method to determine the time optimal palletizing trajectory meeting the motion constraints, which provides a reference for practical engineering application.

2 Kinematics Analysis of Metamorphic Palletizing Mechanism

2.1 Controllable Metamorphic Palletizing Robot

The controllable metamorphic palletizing robot is an industrial robot based on the metamorphic palletizing mechanism. The mechanism can realize the mutual conversion of two configurations in the metamorphic plane. The prototype of the controllable metamorphic palletizing robot is shown in Fig.1.

The metamorphic palletizing robot uses a combination of clutch and plug to metamorphose, as shown in Fig.1 (b) and Fig.1 (c). In the 2-DOF configuration, the plug is pulled out and the clutch is closed, point B and point N of the mechanism are separated to form a five-bar mechanism, and the driving members are rod AB (1-axis) and

The plug hole
The plug housing
The clutch

(a) 2-DOF state   (b) Single-DOF state

(c) The clutch (open state) (d) The plug (inserted state)

Fig.1. The controllable metamorphic palletizing robot

(a) Schematic diagram of
2-DOF configuration
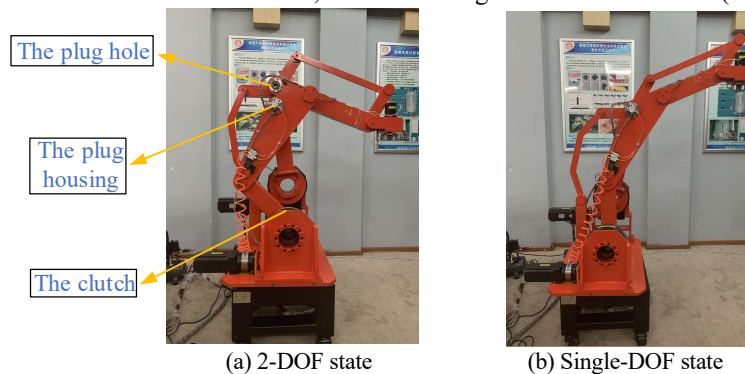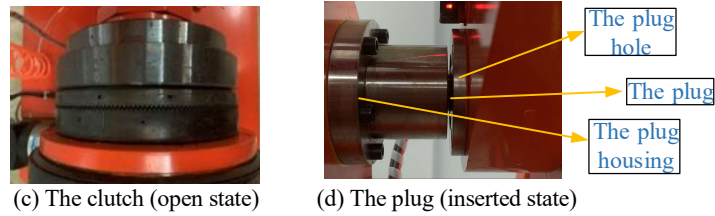
(b) Schematic diagram of
Single-DOF configuration
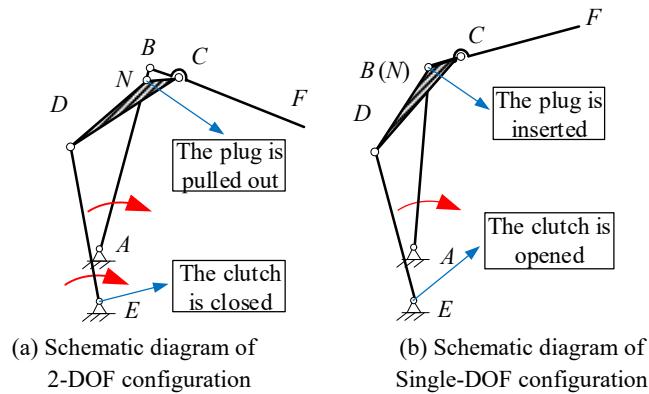
Fig.2. The schematic diagram of metamorphic palletizing mechanism

rod DE (2-axis), as shown in the Fig.1(a) and Fig.2(a). In the single-DOF configuration, the plug is inserted, and the clutch is opened, point B and point N of the mechanism are merged to form a four-bar mechanism, and the driving member is the rod AB, as shown in the Fig.1(b) and Fig.2(b). Point F is selected as the end effector in both configurations.

Because the metamorphic palletizing mechanism moves relatively stable in the single-DOF configuration, it can realize fast long-distance handling, while the mechanism needs to be flexibly grasped and placed in the 2-DOF configuration, and the movement is required to be relatively smooth. The operating conditions of the robot in different configurations are different, and the joint motion constraint conditions are also different accordingly. In the process of trajectory planning, the metamorphic position should be allocated reasonably to give full play to the advantages of each configuration.
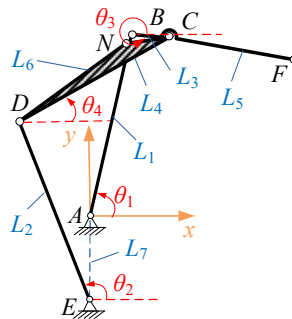
Fig.3. Dimension parameter of mechanism

4

2.2 Forward Kinematics Analysis of Single-DOF Configuration

As shown in Fig.3, with point A as the origin, establishes a rectangular coordinate system for the plane where the metamorphic mechanism is located (hereinafter referred to as the metamorphic plane). The lengths of rods and the angles between rods of the mechanism are shown in Fig.3. Then the coordinates of the four points B, C, D, and F are:

$$\begin{cases} x_B = x_A + L_1 \cos\theta_1 \\ y_B = y_A + L_1 \sin\theta_1 \\ x_C = x_B + L_3 \cos\theta_3 = x_D + L_4 \cos\theta_4 \\ y_C = y_B + L_3 \sin\theta_3 = y_D + L_4 \sin\theta_4 \\ x_D = x_E + L_2 \cos\theta_2 \\ y_D = y_E + L_2 \sin\theta_2 \\ x_F = x_C + L_5 \cos\theta_3 \\ y_F = y_C + L_5 \sin\theta_3 \end{cases} \tag{1}$$

The function expression of the angle of 2-axis relative to active angle can be obtained by closed loop vector method, which is:

$$\theta_2 = 2\arctan(U) \tag{2}$$

where: $\quad U = \dfrac{C_0 \pm \sqrt{C_0^2 - A_0^2 + B_0^2}}{A_0 + B_0}$,

$A_0 = \left(L_1 \cos\theta_1\right)^2 + \left(L_1 \sin\theta_1 + L_7\right)^2 + L_2^2 - L_6^2$, $B_0 = 2L_1 L_2 \cos\theta_1$, $C_0 = 2(L_1 \sin\theta_1 + L_7)L_2$

2.3 Inverse Kinematics Analysis of 2-DOF Configuration

According to formula (1), it can be obtained that:

$$\begin{aligned} &\left(x_F - x_A\right)^2 + \left(y_F - y_A\right)^2 + L_1^2 - \left(L_3 + L_5\right)^2 \\ &-2L_1\left(x_F - x_A\right)\cos\theta_1 - 2L_1\left(y_F - y_A\right)\sin\theta_1 = 0 \end{aligned} \tag{3}$$

From formula (3), it can be obtained that:

$$\theta_1 = 2\arctan(V) \tag{4}$$

where: $\quad V = \dfrac{C_1 \pm \sqrt{C_1^2 - A_1^2 + B_1^2}}{A_1 + B_1}$,

$A_1 = \left(x_F - x_A\right)^2 + \left(y_F - y_A\right)^2 + L_1^2 - \left(L_3 + L_5\right)^2$, $B_1 = 2L_1\left(x_F - x_A\right)$, $C_1 = 2L_1\left(y_F - y_A\right)$

In the same way:

$$\begin{aligned} &\left(x_F - x_E\right)^2 + \left(y_F - y_E\right)^2 + L_2^2 - \left(L_3 + L_5\right)^2 \\ &-2L_1\left(x_F - x_E\right)\cos\theta_2 - 2L_1\left(y_F - y_E\right)\sin\theta_2 = 0 \end{aligned} \tag{5}$$

It can be found that:

$$\theta_2 = 2\arctan(W) \tag{6}$$

where: $\quad W = \dfrac{C_2 \pm \sqrt{C_2^2 - A_2^2 + B_2^2}}{A_2 + B_2}$;

$$A_2 = (x_F - x_E)^2 + (y_F - y_E)^2 + L_E^2 - (L_3 + L_5)^2, \, B_2 = 2L_2(x_F - x_E), \, C_2 = 2L_2(y_F - y_E)$$

3   Trajectory Planning Based on Time Optimal

3.1   Establishment of the optimization model

Since the other axes of the controllable metamorphic palletizing robot run faster except for the 1-axis and 2-axis, they can move synchronously with the handling process, which has less impact on the overall robot's time-optimal trajectory planning. Therefore, in the process of trajectory planning, the spatial metamorphic palletizing trajectory is simplified to the motion trajectory in the metamorphic plane. Its general form is shown in Fig.4, the robot passes through P_0 to P_5 in turn and returns to P_0. Among them, point P_0 is the grasping point, point P_3 is the placement point, and the remaining points are metamorphic points. This article divides the entire trajectory into two parts, where $\overset{\frown}{P_0 P_1 P_2 P_3}$ is the load part and $\overset{\frown}{P_3 P_4 P_5 P_0}$ is the part without load.
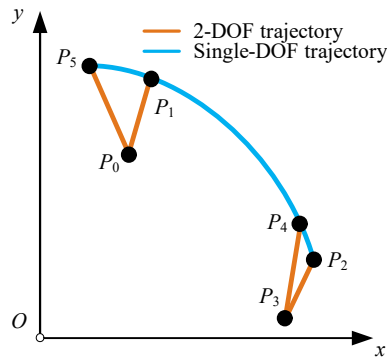
Fig.4. Schematic diagram of metamorphic palletizing trajectory in metamorphic plane

As the two parts of the trajectory differ only in motion constraints and the trajectory planning algorithm is the same, this article only studies the load part trajectory. The load part trajectory is divided into three sections, namely $\overset{\frown}{P_0 P_1}$, $\overset{\frown}{P_1 P_2}$ and $\overset{\frown}{P_2 P_3}$. The robot undergoes a configuration transformation at the metamorphosis point.

The displacement before and after the process of metamorphosis is the same, but acceleration can be changed. Therefore, this paper uses a cubic spline curve to ensure the continuous speed and acceleration in each trajectory, and the displacement between the two trajectories continuous. Considering the different restriction conditions of the three trajectories, this paper takes the angle of the 1-axis as the design variable when the robot is in the metamorphic position (P_1 and P_2) and takes the total time of the three trajectories as the optimization objective and establishes the optimization problem.

3.2   Cubic Spline Curves and Motion Constraints

The general expression of joint cubic spline curve is as follows:

6

$$q(t) = a_3t^3 + a_2t^2 + a_1t + a_0 \tag{7}$$

Due to there are four coefficients in this formula, the only cubic curve expression can be obtained if the displacement and velocity of any two points are known. Set the initial time t_0 to 0, the total time be t_f. Set the initial displacement be q_0, and the final displacement be q_f.

So as to ensure reliability of the metamorphism, the metamorphic palletizing robot stay still while grasping, placing, and metamorphosing, so the initial and final velocity of each trajectory is 0. That is, the expression of the cubic curve in joint space can be obtained by substituting it into the general formula of the cubic curve. The expression of velocity curve and acceleration curve can be obtained at the same time.

$$\begin{cases} q(t) = -\dfrac{2(q_f - q_0)}{t_f^3}t^3 + \dfrac{3(q_f - q_0)}{t_f^2}t^2 + q_0 \\[3mm] \dot{q}(t) = -\dfrac{6(q_f - q_0)}{t_f^3}t^2 + \dfrac{6(q_f - q_0)}{t_f^2}t \\[3mm] \ddot{q}(t) = -\dfrac{12(q_f - q_0)}{t_f^3}t + \dfrac{6(q_f - q_0)}{t_f^2} \end{cases} \tag{8}$$

It can be obtained from formula (8) that the velocity curve is a quadratic function, so the maximum absolute value of velocity is obtained when $t = t_f / 2$. The maximum value of absolute velocity is:

$$\left| \dot{q}(t)_{\max} \right| = \left| \dot{q}(\frac{t_f}{2}) \right| = \frac{3\left| q_f - q_0 \right|}{2t_f} \tag{9}$$

Similarly, the acceleration curve is a linear function, so the maximum absolute value of acceleration is obtained at both ends of its domain. The maximum value of absolute acceleration is:

$$\left| \ddot{q}(t)_{\max} \right| = \left| \ddot{q}(0) \right| = \frac{6\left| q_f - q_0 \right|}{t_f^2} \tag{10}$$

Since the physical limits of the kinematics and dynamic performance of the motor and the actual work requirements, each joint has corresponding speed and acceleration limits in each trajectory, namely:

$$\begin{cases} \left| \dot{q}(t)_{\max} \right| = \dfrac{3\left| q_f - q_0 \right|}{2t_f} \leq V_{\max} \\[3mm] \left| \ddot{q}(t)_{\max} \right| = \dfrac{6\left| q_f - q_0 \right|}{t_f^2} \leq A_{\max} \end{cases} \tag{11}$$

Among them, $V_{\max}$ and $A_{\max}$ are respectively the maximum speed and maximum acceleration limits of motor shaft joint.

3.3 Fitness Function and Constraint Equation

Since the three trajectories are independent of each other, the total time of three segment trajectories can be obtained only by calculating the shortest time of the three segment trajectories satisfying the corresponding motion restriction conditions, and the total time is chosen as the optimization object. Therefore, the fitness function can be written as:

$$f = \sum_{i=1}^{3} t_{i\min} \tag{12}$$

Where, $t_{i\min}$ is the shortest time of the i-segment trajectory.

$$t_{i\min} = \max\{\frac{3|q_{ijf} - q_{ij0}|}{2V_{ij\max}}, \sqrt{\frac{6|q_{ijf} - q_{ij0}|}{A_{ij\max}}}\}, j = 1, 2$$

Among, q_{ij0} and q_{ijf} are the initial displacement and final displacement of j-axis in the i-segment trajectory; $V_{ij\max}$ and $A_{ij\max}$ are the maximum velocity limit and maximum acceleration limit of j-axis in the i-segment trajectory. The constraint equations of the optimal problem are the range of design variables (1-axis angle).

$$\begin{cases} 0 \le \theta_{p1} \le \pi \\ 0 \le \theta_{p2} \le \pi \end{cases} \tag{13}$$

Where θ_{p1} and θ_{p2} are the joint angles of 1-axis angular of point P_1 and P_2, respectively.

3.4 Algorithm for Solving Optimization Problem

Particle swarm optimization (PSO), also known as particle swarm optimization, is an effective algorithm to solve multi-dimensional optimization problems. The number of design variables of optimization design problems are directly used as the dimension of particles [18-20]. In this paper, the 1-axis angles of the metamorphic points P_1 and P_2 are taken as the design variables, and PSO is used to solve the two-dimensional optimization problem. The flow chart is shown in Fig.5.
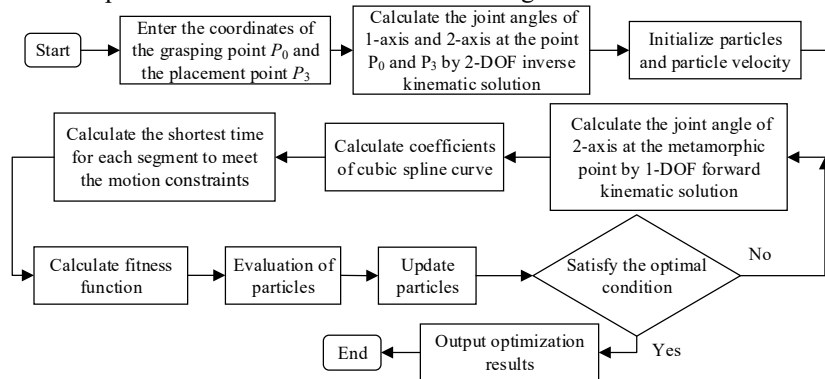
Fig.5. Flow Chart of Particle Swarm Optimization Algorithm

8

4 Calculation Example of Metamorphic Trajectory Planning

The values of the length and position parameters of each link in the metamorphic plane of the Metamorphic palletizing robot are $L_1 = 0.6$m, $L_2 = 0.35$m, $L_3=0.2$m，$L_4=0.608$m，$L_5=0.6$m，$L_6=0.455$m，$L_7=0.196$m. The coordinates (unit: m) of the grasping point and the placing point are set as: (0.700,0.800) and (1.067, - 0.056). Considering the motor performance and operating conditions, the motion constraints of the driving axes of each section are shown in Table1.

<p style="text-align:center">Table1. Motion constraints</p>

Degree of Freedom	Driving axis	$V_{max}/[(°) \cdot s^{-1}]$	$A_{max}/[(°) \cdot s^{-2}]$
1-DOF	1-axis	32.0	150
2-DOF	1-axis	19.3	100
2-DOF	2-axis	19.3	100

Using particle swarm algorithm to solve the optimization problem, the shortest time to obtain the three segments are 0.563s, 2.392s and 0.659s. Considering the response time of the clutch and plug, this paper takes that the metamorphic time is 0.2s, so the shortest total time is 4.014s. At the same time, the driving functions of the joint angular displacement (unit: °) of the driving members for the three segments of trajectory are obtained:

$$\begin{cases} \theta_{011}(t) = -66.65t^3 + 56.23t^2 + 97.03, \quad t \in [0, 0.563) \\ \theta_{012}(t) = 81.62t^3 - 68.86t^2 + 118.67, \quad t \in [0, 0.563) \\ \theta_{121}(t) = 7.46(t-0.763)^3 - 26.75(t-0.763)^2 + 102.96, \quad t \in [0.763, 3.155) \\ \theta_{231}(t) = 50.13(t-3.355)^3 - 49.56(t-3.355)^2 + 51.95, \quad t \in [3.355, 4.014] \\ \theta_{232}(t) = -59.04(t-3.355)^3 + 58.37(t-3.355)^2 + 82.09, \quad t \in [3.355, 4.014] \end{cases} \quad (14)$$

Among them, θ_{ijk} represents the trajectory function of the k-axis from point P_i to point P_j. The optimal trajectory of the robot is shown in Fig.6, where the 2- axis is only active in the first and third segments of the three curves.

(a) Time optimal trajectory graph
(b) Active joint angular displacement
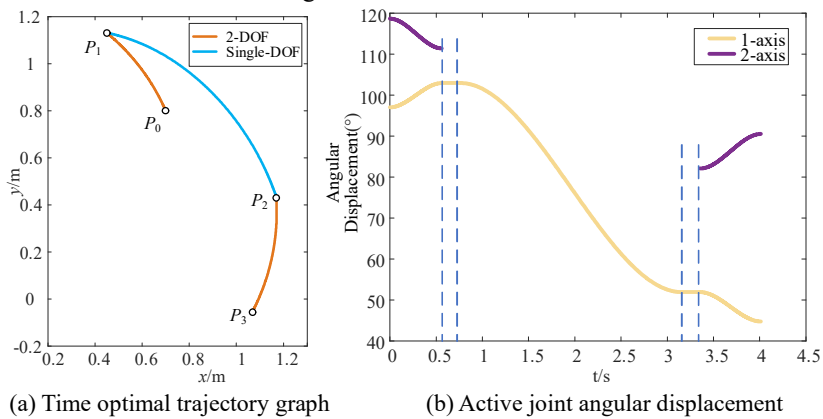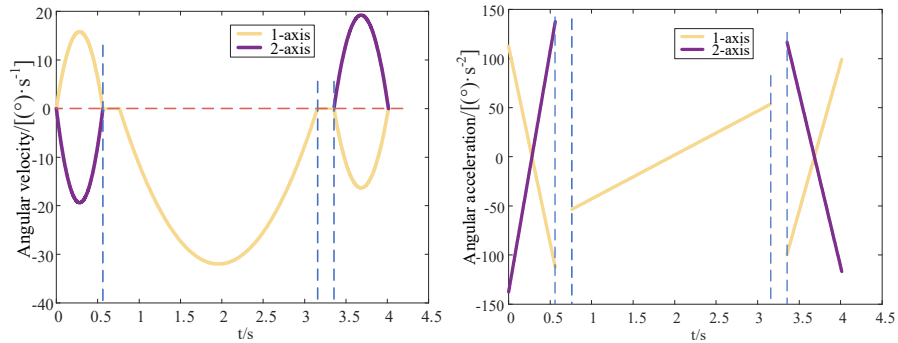
(c) Angular velocity curve of active joint   (d) Angular acceleration curve of active joint

Fig.6. Time optimal trajectory and active joint angular displacement, angular velocity, angular acceleration curve

5   Conclusion

This paper discussed the working condition and metamorphic process of the metamorphic palletizing mechanism. On this foundation, the forward kinematics of the Single-DOF configuration as well as the inverse kinematics of the 2-DOF configuration based on the controllable metamorphic palletizing robot are analyzed.

The time optimal trajectory planning model was established, and a cubic spline curve was selected as a displacement function to keep the continuity of velocity and acceleration of each trajectory segment and the calculation is simplified. A time optimal trajectory algorithm based on metamorphic palletizing mechanism was proposed on the basis of them. The optimal time and joint driving function were obtained by using this algorithm.

The work of this paper provides a reference for the trajectory planning algorithm of metamorphic robots and the application of metamorphic mechanisms to practical engineering problems.

Acknowledgment

References

1. J. S. Dai and J. Rees Jones.: Mobility in metamorphic mechanisms of foldable/erectable kinds. J. Mech. Design 121(3), 375–382 (1999).
2. T. J. Zhao, Y. W. Wang and M. J. Sun.: Structure Design and Analysis of Metamorphic Mobile Robot Based on Screw Theory. In: International Conference on Intelligence and Safety for Robotics (ISR), pp. 50-55. IEEE, Shenyang, China (2018).

3. X. Cui, J. Sun, X. S. Zhang, S. J. Xu and J. S. Dai.: A Metamorphic Hand with Coplanar Reconfiguration. In: 2018 International Conference on Reconfigurable Mechanisms and Robots (ReMAR), pp. 1-7. IEEE, Delft, Netherlands (2018).

4. L. Nurahmi and D. Gan.: Operation Mode and Workspace of a 3-rRPS Metamorphic Parallel Mechanism with a Reconfigurable Revolute Joint. In: 2018 International Conference on Reconfigurable Mechanisms and Robots (ReMAR), pp. 1-9. IEEE, Delft, Netherlands (2018).

5. J. Wei and J. S. Dai.: Reconfiguration-aimed and manifold-operation based type synthesis of metamorphic parallel mechanisms with motion between 1R2T and 2R1T. Mechanism Mach. Theory 139, 66–80 (2019).

6. S. J. Han et al.: Industrial robot trajectory planning based on improved pso algorithm. In: Journal of Physics: Conference Series, 1820 012185 (2021).

7. X. Y. He et al.: Research on trajectory planning of dual-arm cooperative robot. Journal of Physics: Conference Series, 1820: 012025 (2021).

8. C. Zhang and Z. Zhang.: Research on Joint Space Trajectory Planning of SCARA Robot Based on SimMechanics. In: IEEE 3rd Information Technology, Networking, Electronic and Automation Control Conference (ITNEC), pp. 1446-1450. IEEE, Chengdu, China (2019).

9. R. Zhao and S. Ratchev.: On-line Trajectory Planning with Time-variant Motion Constraints for Industrial Robot Manipulators. In: IEEE International Conference on Robotics and Automation, pp. 3748-3753. IEEE, Singapore (2017).

10. G. Li and Y. Wang.: Industrial Robot Optimal Time Trajectory Planning Based on Genetic Algorithm. In: IEEE International Conference on Mechatronics and Automation (ICMA), pp. 136-140. IEEE, Tianjin, China (2019).

11. K. W. Kim, H. S. Kim and Y. K. Choi.: Optimization of cubic polynomial joint trajectories and sliding mode controllers for robots using evolution strategy. In: International Conference on Industrial Electronics, pp. 1465-1477. New Orleans (2012).

12. S. Klemens, G. Hubert, S. Peter.: On time-optimal trajectory planning for a flexible link robot. Journal of Systems and Control Engineering 227(10): 752-763 (2013).

13. S. Fang, X. Ma, Y. Zhao, Q. Zhang and Y. Li.: Trajectory Planning for Seven-DOF Robotic Arm Based on Quintic Polynormial. In: 11th International Conference on Intelligent Human-Machine Systems and Cybernetics (IHMSC), pp. 198-201. IEEE, Hangzhou, China (2019).

14. Q. Zhang, M. Yuan and R. Song.: Robot trajectory planning method based on genetic chaos optimization algorithm. In: 18th International Conference on Advanced Robotics (ICAR), pp. 602-607. IEEE, Hong Kong, China (2017).

15. Y. Li and B. Mo.: The trajectory planning of spacecraft based on optimal quintic polynomial. In: Proceedings of 2013 2nd International Conference on Measurement, Information and Control, pp. 865-868. IEEE, Harbin, China (2013).

16. Y. F. Zhu, W. B. Zha and P. Zhou.: Trajectory Planning and Dynamics Simulation of a 6-DOF Dual-Arm Robot. Mechanical Research & Application 33,187-191 (2020).

17. H. Chen, N. Zhou and R. Wang.: Design and Dimensional Optimization of a Controllable Metamorphic Palletizing Robot. IEEE Access 8, 123061-123074 (2020).

18. J. Wang and X. Lei.: On-Line Kinematical Optimal Trajectory Planning for Manipulator. In: 10th International Conference on Intelligent Human-Machine Systems and Cybernetics (IHMSC), pp. 319-323. IEEE, Hangzhou, China (2018).

19. S. Ziadi, M. Njah and M. Chtourou.: PSO optimization of mobile robot trajectories in unknown environments. In: 13th International Multi-Conference on Systems, Signals & Devices (SSD), pp. 774-782. IEEE, Leipzig, Germany (2016).

20. Q. Lv and D. Yang.: Multi-target path planning for mobile robot based on improved PSO algorithm. In: 5th Information Technology and Mechatronics Engineering Conference (ITOEC), pp. 1042-1047. IEEE, Chongqing, China (2020).

Design of deployable mechanisms based on Wren parallel mechanism units

Jieyu Wang[1], Xianwen Kong[2], and Jingjun Yu[1*]

[1] Beihang University, Beijing, China, 100191
[2] Heriot-Watt University, Edinburgh, UK, EH14 4AS
jjyu@buaa.edu.cn

Abstract. This paper proposes a series of deployable mechanisms based on n-UU (universal joint) Wren parallel mechanism (PM) units, which undergo one degree-of-freedom (DOF) Borel-Bricard motion. First, the PM unit is developed into ortho-planar mechanisms by adopting a variation of U joint. The link parameters of the mechanism are optimized to maximize the folding ratio while avoiding interference. Then, the optimized PM units are connected to construct the novel 1-DOF multi-layer mechanism which has the larger folding ratio than those in the literature. Finally, polyhedral deployable mechanisms are also obtained by connecting the PM unit using special U joints. Apart from saving space, the polyhedral mechanisms can transform among different polyhedrons.

Keywords: Deployable mechanisms, Wren parallel mechanism, Ortho-planar mechanisms, Polyhedral mechanisms, Optimization.

1   Introduction

Deployable/foldable mechanisms have drawn great attention of researchers in centuries due to their advantage of facilitating transportation and storage. There are several approaches to increase the deploying/folding ratio. The first one is connecting large amounts of deployable units and extending the units in the axial direction. Lu et al. [1] designed a family of one degree-of-freedom (DOF) deployable prism mechanisms, which can be folded and deployed. The deployable unit can also be extended in the radial direction to build a polyhedral mechanism. Chen et al. [2] proposed a kinematic method to design 1-DOF polyhedral deployable mechanisms, which can transit between two polyhedrons. By embedding deployable units into faces or edges of polyhedrons, 1-DOF deployable polyhedral mechanisms were constructed in our previous work [3-5]. The same approach was also adopted in [6-9].

Apart from extending the deployable unit, the deploying/folding ratio can also be increased by optimizing the structures and parameters of the mechanisms. One of the approaches is to offset panels away from the plane that is defined by two joints on the panels, to allow mechanisms to be fully folded [10-13]. Lamina emergent mechanisms (which belong to ortho-planar mechanisms [14]) were also designed, which can be spread onto a plane and have motions emerging out of the plane [15].

This paper will focus on a deployable Wren parallel mechanism (PM) unit [16-22], which can undergo 1-DOF Borel-Bricard motion. The units will be first modified into ortho-planar mechanisms, then parameters of the structures are optimized to maximize the folding ratio. Multi-layer and polyhedral deployable mechanisms will also be obtained by connecting the PM unit.

This paper is organized as follows: the PM unit in the literature is introduced in Section 2. In Section 3, the unit is optimized to avoid interference at the stowed configuration and to maximize the folding ratio. A multi-layer mechanism is also proposed. Section 4 investigates the extensions of the PM unit, which can deploy and transform among different polyhedrons. Finally, conclusions are drawn.

2   Description of the PM unit in the literature

The Wren mechanisms that can achieve 1-DOF Borel-Bricard motion are composed of two platforms and several UU (universal joint), SS (spherical joint) or US limbs which have equal length and are arranged symmetrically [23, 24]. The two joint axes within the U joints are always vertical and horizontal respectively. A 4-UU PM unit is shown in Fig. 1.

| (a) | (b) | (c) |
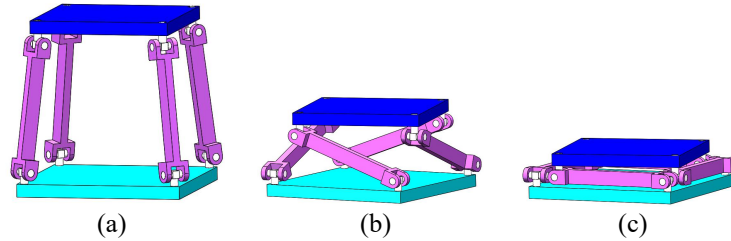
Fig. 1 n-UU Wren mechanism: (a) fully deployed; (b) under Borel-Bricard motion; (c) fully folded

3   Ortho-planar mechanism based on the PM unit

For easier fabrication, transportation, and storage, and to increase the folding ratio, the mechanism in Fig. 1 is developed into an ortho-planar mechanism by offsetting the centers of the U joints, as shown in Fig. 2. Although the two axes of the U joints do not intersect anymore, the ortho-planar mechanism can still have 1-DOF Borel-Bricard motion. When fully folded, the limbs and platforms are all located in a plane [Fig. 2(c)], and the height of the mechanism in this configuration is equal to the thickness of the platform.

Then, the folding ratio will be maximized. The objective is deriving the link parameters of the mechanism to maximize the height in the fully deployed configuration. The height of the mechanism when fully deployed is calculated as:

$$h = \sqrt{(a - 2k)^2 - (\tfrac{L}{2} - 2k - b)^2} \qquad (1)$$

where a, b, L and k denote the limb length (link length plus $2k$), the circumradius of the upper platform, the distance between two vertical joints of the lower platform, and the distance between the two joint axes of the U joint respectively (Fig. 3).

(a) (b) (c)
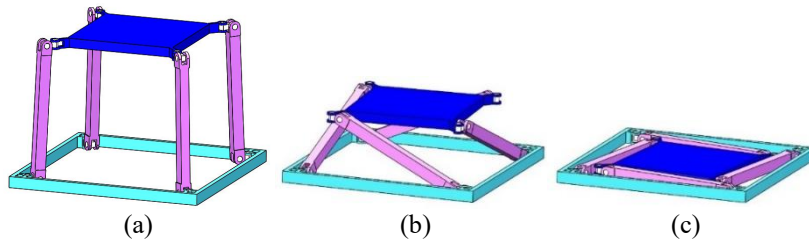
Fig. 2 4-UU ortho-planar mechanism: (a) fully deployed; (b) under Borel-Bricard motion; (c) fully folded

(a) (b)
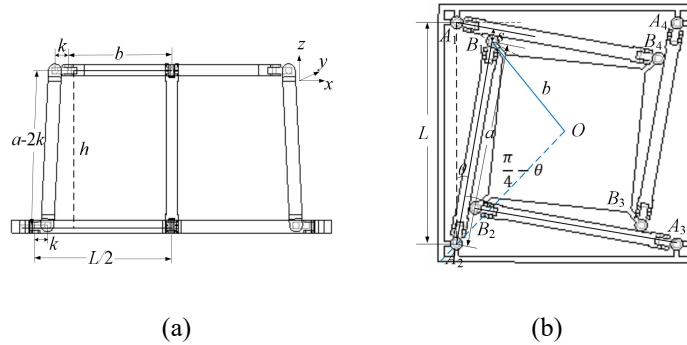
Fig. 3 Optimization of the 4-UU ortho-planar mechanism: (a) projection in the O-xz plane when fully deployed; (b) projection in the O-xy plane when fully folded

The constraint condition is that there is no interference between the limbs and the platforms when the mechanism is fully folded. When projected onto the O-xy plane, as shown in Fig. 3(b), the distance between the vertical joint axis of the U joint on the upper platform (B_1) and the central line of limb A_1B_3 should be equal to or longer than s, which is the sum of the radius of the vertical R joint within the U joint on the upper platform and half the width of the limb. We have

$$t\sin(\frac{\pi}{2} - \theta - \gamma) \geq s \tag{2}$$

where t is the length of A_1B_1, θ and γ represent the angles between A_2A_1 and A_2B_1, and A_1B_1 and A_1A_2 respectively.

In triangle A_2B_1O, we have

$$b^2 = a^2 + (\frac{L}{\sqrt{2}})^2 - 2a\frac{L}{\sqrt{2}}\cos\left(\frac{\pi}{4} - \theta\right) \tag{3}$$

θ can be yielded as:

$$\theta = \frac{\pi}{4} - \arccos[\frac{a^2 + \frac{L^2}{2} - b^2}{\sqrt{2}aL}] \tag{4}$$

4
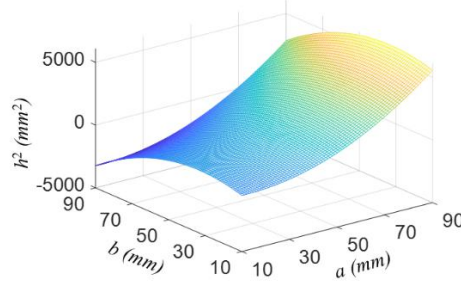
Fig. 4 The variation of the squared height of the mechanism in the fully deployed configuration
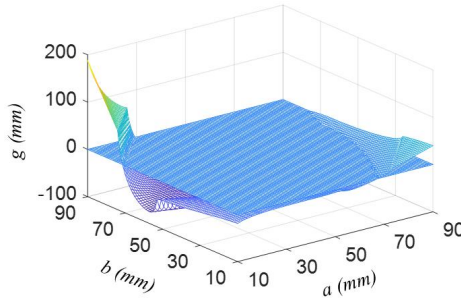
Fig. 5 The constraint condition of the 4-UU mechanism

Let $s = 5\text{mm}$, $k = 6\text{mm}$ and $L = 90\text{mm}$, the plot of the squared height of the mechanism in the fully deployed configuration associated with a and b is given in Fig. 4. Let $g = s - t\sin\left(\frac{\pi}{2} - \theta - \gamma\right)$, g should be equal to or less than zero to avoid interference. When $g = 0$, the joint and the limb contact. The variation of g with a and b is plotted in Fig. 5.

The optimization problem is represented by

$$\text{Minimize T} = -h^2$$

$$\text{Subject to } \begin{cases} 0 \leq a \leq 90 \\ 0 \leq b \leq 90 \\ g \leq 0 \end{cases} \tag{5}$$

The optimal a and b are obtained as:

$$\begin{cases} a = 83.6338\text{mm} \\ b = 48.2211\text{mm} \end{cases} \tag{6}$$

h is calculated as 70.00mm. Suppose that the thickness of the platforms is $p = 5\text{mm}$ (p can be arbitrary), the folding ratio is

$$f = \frac{h+p}{p} = \frac{70+5}{5} = 15 \tag{7}$$

The above analysis and optimization method can be extended to n-UU Wren mechanisms. It is noted the lengths of the limbs and the folding ratio decrease with the increase of the number of limbs, considering the interference between the limbs. The n-UU Wren mechanisms can be optimized subject to the constraint condition of

$$t\sin\left(\frac{\pi(n-2)}{n} - \theta - \gamma\right) \geq s \tag{8}$$

where

$$\theta = \frac{\pi(n-2)}{n} - \arccos[(a^2 + \left(\frac{L}{2\cos\left(\frac{\pi(n-2)}{2n}\right)}\right)^2 - b^2)/2a\frac{L}{2\cos\left(\frac{\pi(n-2)}{2n}\right)}] \quad (9)$$

Using Eq. (9), Wren PMs with an arbitrary number of limbs can be readily optimized to have the maximum folding ratio. The height equation of the mechanism when fully deployed is the same as the 4-UU mechanisms. The folding ratio is

$$f = \frac{h+p}{p} = \frac{\sqrt{(a-2k)^2 - (\frac{L}{2}-2k-b)^2}+p}{p} \quad (10)$$

where a and b are obtained using the optimization method.

The PM unit can be extended into multi-layer mechanisms for applications such as aerospace. The variation of U joint is used to connect two PMs. The designed U joint has three joint axes, including a vertical one and two horizontal ones. In this way, the limb in the first PM and the corresponding one in the second PM rotate synchronously along the vertical direction, and the obtained mechanism has only 1-DOF and can deploy. The shapes of the platforms of the 4-UU ortho-planar mechanism are modified into a circular ring to keep the mechanism as a cylinder, then multiple 4-UU ortho-planar mechanisms are connected to obtain a multi-layer deployable mechanism, as shown in Fig. 6. The adjacent PMs are symmetrically connected, which means one deploys clockwise while the other anticlockwise. The obtained deployable mechanism also has 1-DOF and can be folded [Fig. 6(c)] and deployed [Fig. 6(a)].

(a)

(b)   (c)
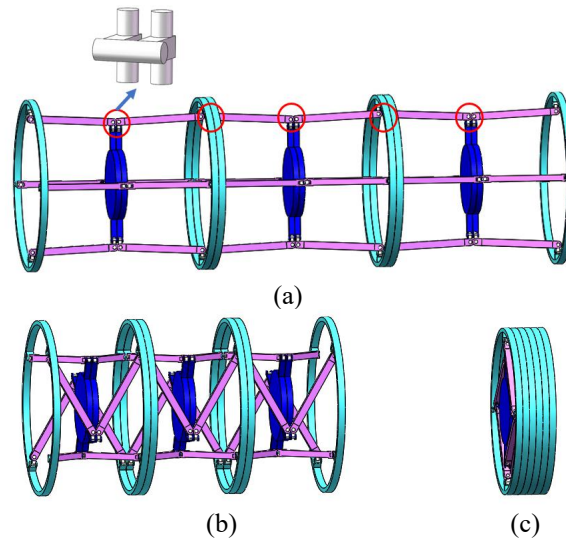
Fig. 6 The multi-layer mechanism: (a) fully deployed; (b) under Borel-Bricard motion; (c) fully folded

4 Polyhedral mechanisms based on the deployable PM unit

The *n*-UU PM can also be used to construct deployable polyhedral mechanisms that can transform among different polyhedrons, which have the potential application on education. As shown in Fig. 7, four 3-UU PMs are used to obtain a tetrahedron mechanism [Fig. 7(c)]. To construct the deployable mechanism, four upper platforms are fastened and form a tetrahedron. Since there are four PMs, three U joints are used to connect adjacent PMs, as shown in Fig. 8. In this way, the DOF of the tetrahedron mechanism is reduced to one.
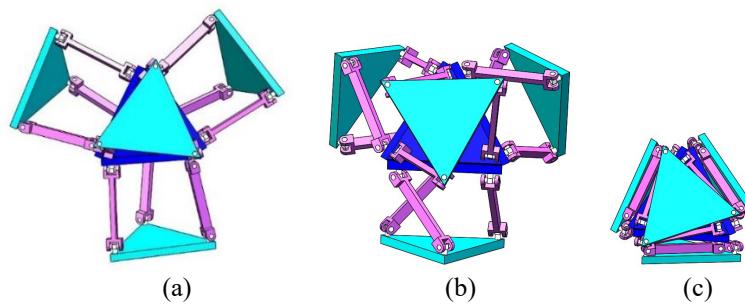
Fig. 7 The tetrahedron mechanism: (a) deployed; (b) under Borel-Bricard motion (truncated tetrahedron); (c) folded (tetrahedron)
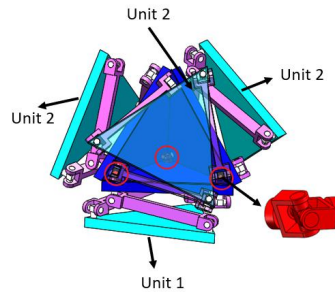
Fig. 8 The construction of the tetrahedron mechanism

To make four PMs deploy towards the same direction, the two PMs connected by a U joint should be symmetrical about the middle plane of the two planes defined by the two upper platforms. Therefore, two types of units are used, with the same configuration while unit 1 deploys clockwise and unit 2 anticlockwise. In this tetrahedral mechanism, one unit 1 and three unit 2 are adopted.

When deployed, the mechanisms can transform into a truncated tetrahedron as shown in Fig. 7(b). Different from the polyhedral mechanisms in the literature, the polyhedral mechanisms in the paper can deploy along specific directions [Fig. 7(a)].

Similarly, a cube mechanism can also be obtained by connecting six 4-UU PMs using five UU chains, as shown in Fig. 9. Since the upper platforms of adjacent PMs are perpendicular to each other, the U joints used in the above tetrahedral mechanism

are in the singular position since the two shafts are perpendicular. Therefore, UU chain is used in the cube mechanism as shown in Fig. 10. The distance between the vertical axes of the two U joints is constant and the two horizontal axes are on the same plane, perpendicular to each other and intersect at the center of the UU chain.

| (a) | (b) | (c) |
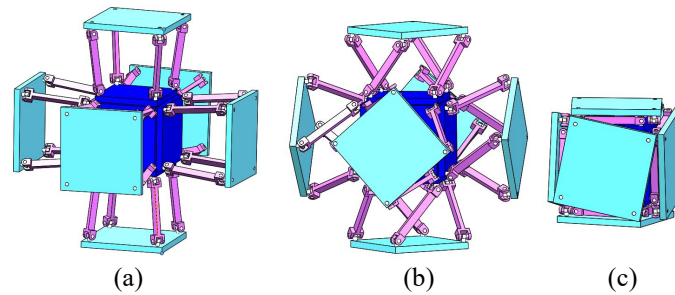
Fig. 9 The cube mechanism: (a) deployed (rhombicuboctahedron); (b) under Borel-Bricard motion I (truncated octahedron); (c) folded (cube)
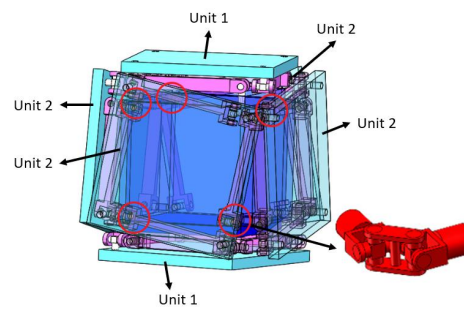
Fig. 10 Construction of the cube mechanism

To ensure all the PMs deploy towards the same direction, two unit 1 and four unit 2 are used to construct the mechanism. It is noted that the UU chain can also be utilized in the tetrahedral mechanism. However, this paper still uses the normal U joint to save space.

The mechanism is in the shape of a cube [Fig. 9(c)] when folded and transforms into a truncated octahedron [Fig. 9(b)] during the Borel-Bricard motion. When fully deployed, it turns into a rhombicuboctahedron [Fig. 9(a)]. This mechanism and the two following mechanisms can transform into more shapes than the ones in [4], which only have two states.

Similarly, by connecting multiple identical n-UU Wren mechanisms, or different types of Wren PMs, a large number of polyhedral mechanisms can be obtained. The number of the U joints (UU chains) required is one less than the number of faces of the polyhedron. For example, when connecting 12 5-UU mechanisms using 11 U joints, a dodecahedron mechanism can be constructed [Fig. 11(c)], which can deform into a truncated icosahedron [Fig. 11(b)] during the Borel-Bricard motion and become a rhombicosidodecahedron [Fig. 11(a)] when fully deployed.

8

The octahedron mechanism [Fig. 12(c)] composed of eight 3-UU PMs can transit into a truncated cube [Fig. 12(b)] during the Borel-Bricard motion and a rhombicuboctahedron [Fig. 12(a)] when fully deployed.

| (a) | (b) | (c) |
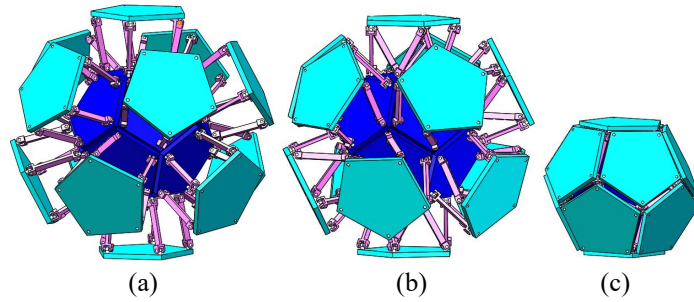
Fig. 11 The dodecahedron mechanism: (a) deployed (rhombicosidodecahedron); (b) under Borel-Bricard motion I (truncated icosahedron); (c) folded (dodecahedron)

| (a) | (b) | (c) |
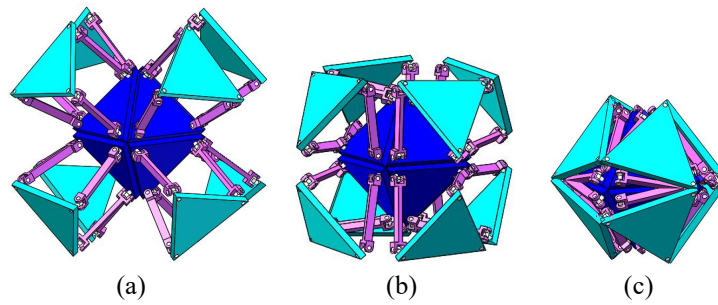
Fig. 12 The octahedron mechanism: (a) deployed (rhombicuboctahedron); (b) under Borel-Bricard motion I (truncated cube); (c) folded (octahedron)

5   Conclusion

This paper has proposed a family of deployable mechanisms based on a Wren parallel mechanism unit which undergoes the Borel-Bricard motion. Ortho-planar mechanisms have been obtained based on the unit, which have the maximum folding ratio by using optimization. Multi-layer mechanisms and polyhedral mechanisms which can transform among different polyhedrons have also been constructed using this PM unit. The multi-layer mechanism could be applied to the area of aerospace and the polyhedral mechanisms can serve as a protective cage when using compliant joints.

In the future, kinematic and mobility analysis for these mechanisms will be conducted using screw theory, and prototypes will be fabricated using 3D printing technology to verify the constructing approach.

Acknowledgement

References

1. Lu, S., Zlatanov, D., Ding, X., Molfino, R.: A new family of deployable mechanisms based on the Hoekens linkage. Mechanism and Machine Theory 73, 130-153 (2014).
2. Chen, Y., Yang, F., You Z.: Transformation of polyhedrons. International Journal of Solids and Structures 138, 193-204 (2018).
3. Wang, J., Kong X.: A novel method for constructing multi-mode deployable polyhedron mechanisms using units. Journal of Mechanisms and Robotics 11(2), 020907 (2019).
4. Wang, J., Kong X.: Deployable polyhedron mechanisms constructed by connecting spatial single-loop linkages of different types and/or in different sizes using S joints. Mechanism and Machine Theory 124, 211-225 (2018).
5. Wang, J., Kong X.: Deployable mechanisms constructed by connecting orthogonal Bricard or extension using S joint. Mechanism and Machine Theory 120, 178-191 (2018).
6. Wei, G., Chen, Y., Dai J.: Synthesis, mobility, and multifurcation of deployable polyhedral mechanisms with radially reciprocating motion. Journal of Mechanical Design 136(9), 091003 (2014).
7. Kiper, G., Söylemez, E., Kişisel A.Ö.: A family of deployable polygons and polyhedral. Mechanism and Machine Theory 43(5), 627-640 (2008).
8. St-Onge, D., Gosselin, C.: Synthesis and design of a one degree-of-freedom planar deployable mechanism with a large expansion ratio. Journal of Mechanisms and Robotics 8(2), 021025 (2016).
9. Li, R., Yao, Y., Kong, X.: A class of reconfigurable deployable platonic mechanisms. Mechanism and Machine Theory 105, 409-427 (2016).
10. Chen, Y., Peng, R., You Z.: Origami of thick panels. Science 349(6246), 396-400 (2015).
11. Wang, J., Bai, G., Kong, X.: Single-loop foldable 8R mechanisms with multiple modes. In: New Trends in Mechanism and Machine Science, pp. 503-510. Springer International Publishing, Nantes (2016).
12. Morgan, J., Magleby, S.P., Howell, L.L.: An approach to designing origami adapted aerospace mechanisms. Journal of Mechanical Design 138(5), 052301 (2016).
13. Deng, Z., Huang, H., Li, B., Liu, R.: Synthesis of deployable/foldable single loop mechanisms with revolute joints. Journal of Mechanisms and Robotics 3(3), 031006 (2011).
14. Parise, J.J.: Ortho-planar mechanisms. Doctoral dissertation, Brigham Young University (1999).
15. Jacobsen, J.O., Winder, B.G., Howell, L.L., Magleby, S.P.: Lamina emergent mechanisms and their basic elements. Journal of Mechanisms and Robotics 2(1), 011003 (2010).
16. Wohlhart, K.: Kinematotropic linkages. In: Recent Advances in Robot Kinematics, pp. 359-368. Dordrecht (1996).
17. Douglas, M.V.: Module for an articulated stowable and deployable mast. U.S. Patent 5,267,424 (1993).
18. Kiper, G.: Design methods for planar and spatial deployable structures. Doctoral dissertation, Middle East Technical University (2011).

10

19. Nawratil, G.: Congruent Stewart Gough platforms with non-translational self-motions. In: 16th International Conference on Geometry and Graphics, pp. 4-8. Innsbruck (2014),

20. Zhao, L., Wang, H., Chen, G., Huang, S.: Sequentially assembled reconfigurable extended joints: self-lockable deployable structure. Journal of Aerospace Engineering 31(6), 04018103 (2018).

21. Zhang, K., Dai, J.S.: Reconfiguration analysis of wren platform and its kinematic variants based on reciprocal screw systems. In: Proceedings of the 14th IFToMM World Congress, pp. 237-242.Taipei (2015).

22. Lee, C.C., Hervé, J.M.: Bricard one-DoF motion and its mechanical generation. Mechanism and Machine Theory 77, 35-49 (2014).

23. Yang, Y., Zhen, C., Hou, Y., Zeng, D.: Type synthesis of structural symmetry one degree-of-freedom of helical motion parallel mechanisms (in Chinese), Chinese Journal of Mechanical Engineering 55(3), 27-33 (2019).

24. Zeng, Q., Ehmann, K.F.: Design of parallel hybrid-loop manipulators with kinematotropic property and deployability. Mechanism and Machine Theory 71, 1-26 (2014).

Error-Space-Oriented Tolerance Design for a Deployable Mechanism with Multiple Clearances

Jianzhong Ding[1], Yang Dong[1], and Chunjie Wang[2]

[1] School of Mechanical Engineering and Automation, Beihang University, Beijing, 100191, China,
`jianzhongd@buaa.edu.cn`
[2] State Key Laboratory of Virtual Reality Technology and Systems, Beihang University, Beijing, 100191, China

Abstract. This paper presents a geometric alternative to estimate the accuracy of a deployable mechanism equipped on space satellite. The deployable mechanism is simplified into a planar mechanism and error space of the outer panel in its deployed state is modeled concerning multiple revolute joint clearances and link length tolerances. Compared to the existing methods, advance of the geometric approach discussed in this paper lies in that it gives expressions of all possible error mobility that the end-effector may have. After deducing the expressions, the final error space is visualized and evaluated numerically with discrete sampling points. Finally, based on the error space and maximum errors, effects of tolerances on accuracy are studied and optimal accuracy design of tolerances are obtained. The result reveals that, for the deployable discussed in this paper, effects of tolerances can be eliminated by optimized tolerance design.

Keywords: deployable mechanism, tolerance design, clearance

1 Introduction

Panels of a satellite antenna are stowed to take rocket to space and deployed to work in orbit. Generally, panels are extended and supported by deployable mechanisms for better accuracy and higher stiffness. Deployable mechanism is usually a linkage and its accuracy is affected by joint clearances and link length tolerances.

Clearances lead uncertain behaviors to the end-effector and the problem of error modeling concerning clearances is being studied persistently. Early in 2000, Ting et al. [1] studied the effects of multiple clearances in a closed loop on the final output using a virtual-link model. Then, they further developed kinematic models for revolute joint and spherical joint clearance to estimate the angular error of a 3-RPR mechanism [2] and spatial four,five-bar linkage [3], respectively. Tsai et al. [4, 5] modeled the closed-loop constraint using screws and analyzed the positioning error of planar mechanisms concerning clearances. Huang et al. [6] presented the error model for lower-mobility parallel mechanisms with screws

and distinguished the compensable and uncompensable errors, and applied this method to accuracy analysis of a parallel machine tool [7]. For closed-loop mechanisms, modeling with screws has the advantage of succinct expression over the other methods and therefore screw-based methods are widely used in error modeling of mechanisms with clearances, such as those discussed by Frisoli [8], Cammarata [9] and Simas [10].

Apart from the well-appraised screw methods, many other methods were also developed. Li et al. [11] studied the angular output uncertainty of a planar linkage with multiple clearances via a Lie-group-based approach. Zhao [12] also provided the error space analysis method with the help of Lie group. The above-mentioned methods conducted probability analysis with Lie group computations given proper distributions for clearances. Since clearances are bounded error sources, direct optimization methods [13, 14] and interval analysis methods [15, 16] were also developed for maximum errors estimation. Though plenty of error modeling methods regarding clearances have been developed, they focused on limited information of the final output errors, such as probability and maximum, and they are not capable of or efficient in entire error space analysis. In view of this, geometric methods [17, 18] were proposed for entire error mobility analysis and illustrated with planar 3-RPR mechanisms.

Besides joint clearances, link length deviations are also inevitable and bring in output errors of end-effector. Kumaraswamy et al.[19] applied the screws to model the clearances and tolerances, and studied their effects on path generation. Huang et al. [20] improved the accuracy of lower-mobility parallel mechanisms considering tolerances by optimizing assembly process. Most of the existing tolerance design methods aim to optimize tolerances to compromise accuracy and manufacturing cost [21]. Coupled effects of clearances are not included. Therefore, in this paper, for a deployable mechanism used to unfold and support satellite antenna panels, a geometrical method is introduced to give the error space of the mechanism regarding both clearances and tolerances. Compared with the existing methods, the proposed geometrical method studies the positioning and orientating errors simultaneously, and it gives the expression of the entire error space. Effects of tolerance allocations on accuracy are studied aiming to improve the accuracy of the antenna mechanism by optimizing tolerance allocation without increasing the manufacturing cost.

The rest of the paper is organized as follows. In the next section, the deployable mechanism is introduced and its planar representation is given, following which the error space of the mechanism considering multiple clearances and tolerances is defined and deduced using a proposed geometrical method. Section 3 presents the study on effects of various tolerance designs on the accuracy of the mechanism. Finally, we conclude this study in Section 4.

2   Error Space Modeling

2.1   Deployable Mechanism Modeling

The deployable mechanism discussed here is used to deploy and support antenna panels of a Synthetic Aperture Radar (SAR) and its deployed structure is charactered in Fig.1.
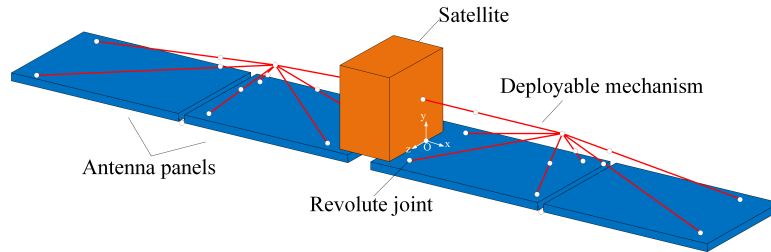
Fig. 1. Schematic Diagram of the deployed supporting mechanism in SAR

As shown in Fig.1, the deployable mechanism is an articulated space linkage that is symmetric in the $O - xy$ plane. Moreover, its unfolding motion is also constrained in the same plane. We care about its angular accuracy about the $o - z$ axis most. Therefore, it is convenient to study its kinematics performance in a plane and its planar representation is give in Fig.2.
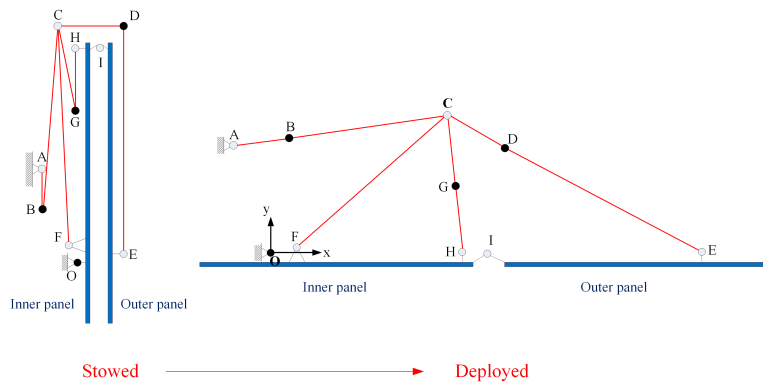
Fig. 2. Planar representation of the deployable mechanism

In Fig.2, capital letters denote revolute joints. In order to have determined motion, the mechanism is actuated by a motor at O and three auxiliary torsional

springs at B, D and G, respectively, and they are locked after deployment to support the deployed panels. Two panels are designed to be coplanar when they are completely unfolded. However, in practice, the outer panel can still move freely in a small range after the mechanism is locked due to passive joint clearances and the gravity-free working condition in orbit. Error model of the deployable mechanism regarding revolute clearances in its deployed state is depicted in Fig 3.
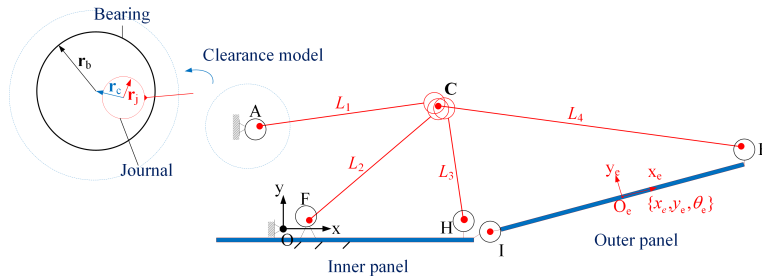
Fig. 3. Error model of the deployable mechanism

Clearances of the locked joints are not included in the error model. Therefore, we simplified links AB and BC into a single link AC with length L_1, and analogously, we obtain the equivalently simplified links CH and CE. No penetration is considered and the clearance is modeled with the commonly-used virtual link. Length of the virtual link is computed as

$$r_c = x, \quad x \in [0, r_b - r_j], \tag{1}$$

where r_b and r_j are the radii of bearing and journal, respectively.

In the error model, the inner panel is error-free due to the locked O and the outer panel may locate randomly within a small range. The midpoint O_e of IE and the body coordinate system $O_e - x_e y_e$ are used to indicate the pose of the outer panel. Given that the error-free pose and the real pose of the outer panel in global frame $O - xy$ are g_0 and g_e, respectively, we have

$$g_e = g_0 \circ \exp \begin{pmatrix} 0 & -\theta_e & x_e \\ \theta_e & 0 & y_e \\ 0 & 0 & 0 \end{pmatrix}. \tag{2}$$

where g_0 and g_e are elements of Lie group SE(2), and $[x_e, y_e]^\top$ and θ_e are the positioning error and orientation error, respectively. And the error space of the deployable mechanism is defined as the set of all $[x_e, y_e, \theta_e]^\top$.

2.2   Error Space Estimation

Apart from the revolute joint clearances, link length tolerances are also considered to estimate the error space. A geometric approach is discussed here for error propagation and accumulation analysis.

As discussed previously, the clearance can be represented by a virtual link with maximum length of $r = r_b - r_j$. Therefore, geometrically, the journal can move freely inside a disk region. Then it is convenient to use the disk of radius r to represent the error space of a revolute joint. In this way, taking joint F and link FC for example, the error propagation and accumulation are modeled, as shown in Fig.4.
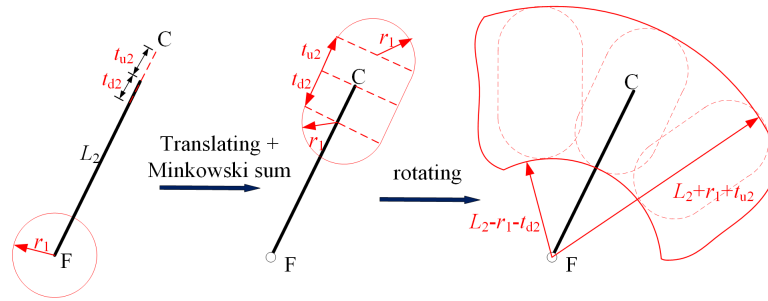
Fig. 4. Error propagation and accumulation in an open loop

In Fig.4, the error space of joint F due to clearance is represented by a disk with radius r_1, the length of link FC regarding tolerance is in the interval $[L_2 - t_{d2}, L_2 + t_{u2}]$. The error space at C can be obtained by translating disk from F to C and Mincowski adding with vector t_d and t_u. In a plane, the sum of a region $\mathcal{M}$ with a vector $\mathbf{t}$ is defined as

$$\mathcal{M} + \mathbf{t} \doteq \begin{pmatrix} x_m \\ y_m \end{pmatrix} + \mathbf{t}, \tag{3}$$

where $(x_m, y_m)^\top$ is any point in $\mathcal{M}$.

Since the mobility of revolute joint F is not constrained in an open loop, the final error space of C is obtained by rotating the error region generated previously, and finally a ring region is got, suggesting that point C can locate at any position in that ring region. The quadric expression of a planar circle is used to define $\mathcal{C}_{\mathbf{x}_0, R}$, as

$$\mathcal{C}_{\mathbf{x}_0, R} \doteq (\mathbf{x} - \mathbf{x}_0)^\top \mathbf{Q}(\mathbf{x} - \mathbf{x}_0) - 1 \tag{4}$$

where $\mathbf{x}$ is any point in a plane, $\mathbf{x}_0$ is the center of a circle, R is the radius of a circle, and $\mathbf{Q}$ is a 2×2 diagonal matrix, as

$$\mathbf{Q} = \begin{pmatrix} \dfrac{1}{R^2} & 0 \\ 0 & \dfrac{1}{R^2} \end{pmatrix}. \tag{5}$$

Then the error space of C considering clearance at F and tolerance can be expressed as

$$\mathcal{M}_C = \{\mathcal{C}_{\mathbf{x}_C, L_2 - r_1 - t_{d2}} \geq 0\} \cap \{\mathcal{C}_{\mathbf{x}_C, L_2 + r_1 + t_{u2}} \leq 0\} \tag{6}$$

where $\mathbf{x}_c$ denotes the error-free coordinates of C.

Now that the geometric expression of clearance and tolerance propagating and accumulating in the open loop is obtained, the error space in the closed loop is to be derived next. As shown in Fig.3, the deployable mechanism owns a multi-closed-loop structure, and the error propagation path should be studied before estimating the final error space of panel IE. Obviously, for the deployable mechanism, error spaces at joints A, F, H and I are only decided by their own clearances, error space of C is decided in multiple loops ACF and FCH, and error space of E is decided by joint C, link CE and its own clearance. Then, the error space of C is geometrically modeled, as shown in Fig.5.
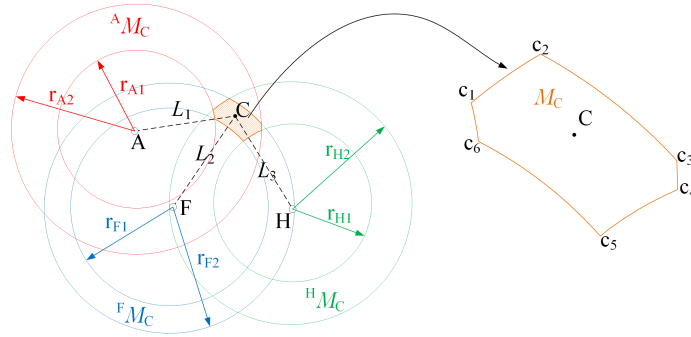
Fig. 5. Error space of joint C

In Fig.5, $\{r_{A1}, r_{A2}\}$, $\{r_{F1}, r_{F2}\}$ and $\{r_{H1}, r_{H2}\}$ are radii of rings representing the error spaces of A, F and H, respectively. As discussed previously, error spaces at C in open loops AC, FC and HC can be represented by rings denoted as $^A\mathcal{M}_C$, $^F\mathcal{M}_C$ and $^H\mathcal{M}_C$, respectively, as shown in Fig.5. Given that all joints are of the same size r_1 and complex revolute joints at C share the common journal that is fixed with link CE, referring to Eq.(6), the propagated error spaces are

expressed as

$$
\begin{aligned}
{}^{A}\mathcal{M}_C &= \{\mathcal{C}_{\mathbf{x}_A, r_{A1}} \geq 0\} \cap \{\mathcal{C}_{\mathbf{x}_A, r_{A2}} \leq 0\} \\
{}^{F}\mathcal{M}_C &= \{\mathcal{C}_{\mathbf{x}_F, r_{F1}} \geq 0\} \cap \{\mathcal{C}_{\mathbf{x}_F, r_{F2}} \leq 0\} \quad, \\
{}^{H}\mathcal{M}_C &= \{\mathcal{C}_{\mathbf{x}_H, r_{H1}} \geq 0\} \cap \{\mathcal{C}_{\mathbf{x}_H, r_{H2}} \leq 0\}
\end{aligned}
\tag{7}
$$

where

$$
\begin{aligned}
r_{A1} &= L_1 - 2r_1 - t_{d1} \\
r_{A2} &= L_1 + 2r_1 + t_{u1} \\
r_{F1} &= L_2 - 2r_1 - t_{d2} \\
r_{F2} &= L_2 + 2r_1 + t_{u2} \\
r_{H1} &= L_3 - 2r_1 - t_{d3} \\
r_{H2} &= L_3 + 2r_1 + t_{u3}
\end{aligned}
\tag{8}
$$

where L_1, L_2 and L_3 are lengths of links AC, FC and HC, respectively, and their tolerances are $[-t_{d1}, t_{u1}]$, $[-t_{d2}, t_{u2}]$ and $[-t_{d3}, t_{u3}]$, respectively.

Therefore, when considering closed-loop constraints, the error space indicating all the positions journal C can locate is expressed as

$$
\mathcal{M}_C = {}^{A}\mathcal{M}_C \cap {}^{F}\mathcal{M}_C \cap {}^{H}\mathcal{M}_C,
\tag{9}
$$

suggesting the intersection region of three rings. Generally, three rings can intersect at up to 24 individual points and the shape of the error space depends on the intersection situation. However, the points used for error space computation must satisfy the Eq.(7). As shown in Fig.5, the error region of C has 6 intersection points.

As discussed previously, error space of E is computed in the open loop CE, and it consists of the error space propagated from C, error space arisen from length tolerance of L_4 and its sole clearance. The propagated part is modeled first, as shown in Fig.6.
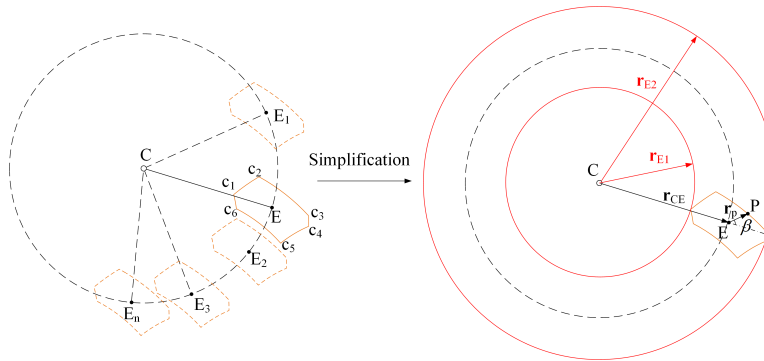
Fig. 6. Error space of joint E

Despite of closed-loop constraint, the trajectory of E is a circle with radius L_3 and center $\mathbf{C}$. When the error space of C is considered, the error space of E

arisen from C can be obtained by translating (without rotation) $\mathcal{M}_C$ to every position on the trajectory of E. The region enclosing all translated $\mathcal{M}_C$ is the error space of E propagated from C, denoted as $^C\mathcal{M}_E$. However, the contour of $^C\mathcal{M}_E$ is difficult to express with equations. Then a simplified ring is used to substitute the $^C\mathcal{M}_E$. Using the $\mathcal{M}_C$ translated to the error-free position of E, the radii of the substituting ring are computed. Given that P is an arbitrary point on $\mathcal{M}_C$ at E, $\mathbf{r}_P$ is a vector from E to P and $\mathbf{r}_{CE}$ is a vector from C to E, then the projection of $\mathbf{r}_P$ on CE is computed as

$$\mathbf{r}_{P1} = \frac{(\mathbf{r}_P \cdot \mathbf{r}_{CE})\mathbf{r}_{CE}}{|\mathbf{r}_{CE}|} \tag{10}$$

Then the radii of the ring are computed as

$$\begin{aligned} r_{E1} &= L_3 + \min(\mathbf{r}_{P1}) \\ r_{E2} &= L_3 + \max(\mathbf{r}_{P1}) \end{aligned} \tag{11}$$

When the length tolerance $[-t_{d4}, t_{u4}]$ and clearance of E are included, the finale error space of E is expressed as

$$\mathcal{M}_E = \{\mathcal{C}_{\mathbf{x}_C, r_{E1}-r_1-t_{d4}} \geq 0\} \cap \{\mathcal{C}_{\mathbf{x}_C, r_{E1}+r_1+t_{u4}} \leq 0\} \tag{12}$$

Since joint I is fixed to the error-free inner panel, the error space of I is a disk with radius r_1, denoted as $\mathcal{M}_I$. Then, error space estimation of the outer panel is to find all the possible mobilities of $O_e - x_e y_e$ when two ends of segment IE are strictly restrained in $\mathcal{M}_I$ and $\mathcal{M}_E$, respectively, as shown in Fig.7.
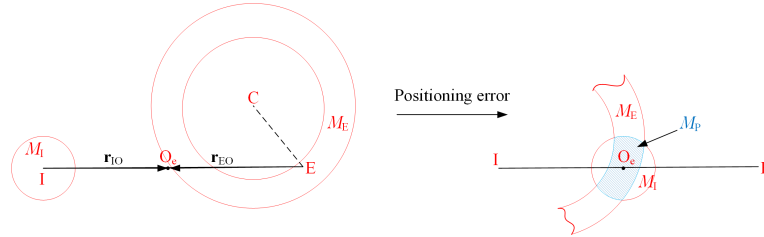
Fig. 7. Positioning error space of the outer panel

The positioning error space of the outer panel is obtained by translating $\mathcal{M}_I$ and $\mathcal{M}_E$ to the common point O_e and computing the intersected region. A planar disk translated by a vector is expressed as

$$\mathcal{C}_{\mathbf{x}_0, R} + \mathbf{t} \doteq \mathcal{C}_{\mathbf{x}_0+\mathbf{t}, R} \tag{13}$$

Then the position error space of the outer panel is expressed as

$$\mathcal{M}_P = \{\mathcal{C}_{\mathbf{x}_C+\mathbf{r}_{EO}, r_d} \geq 0\} \cap \{\mathcal{C}_{\mathbf{x}_C+\mathbf{r}_{EO}, r_u} \leq 0\} \cap \{\mathcal{C}_{\mathbf{x}_I+\mathbf{r}_{IO}, r_1} \leq 0\} \tag{14}$$

Referring to Eq.(12), $r_d = r_{E1} - r_1 - t_{d4}$ and $r_u = r_{E1} + r_1 + t_{u4}$. When angular error is considered, the final error space of the outer panel is given as

$$\mathcal{M} = \bigcup_{\mathbf{R}_\theta \in SO(2)} \{\mathcal{C}_{\mathbf{x}_C + \mathbf{R}_\theta \mathbf{r}_{EO}, r_d} \geq 0\} \cap \{\mathcal{C}_{\mathbf{x}_C + \mathbf{R}_\theta \mathbf{r}_{EO}, r_u} \leq 0\} \cap \{\mathcal{C}_{\mathbf{x}_I + \mathbf{R}_\theta \mathbf{r}_{IO}, r_1} \leq 0\},$$

(15)

where $\mathbf{R}_\theta$ denotes the planar rotation and is expressed as

$$\mathbf{R}_\theta = \begin{pmatrix} \cos\theta & -\sin\theta \\ \sin\theta & \cos\theta \end{pmatrix}.$$

(16)

It is noteworthy that the angular error θ is usually rather small. When $|\theta|$ is large, we have $\mathcal{M} = \emptyset$. It is difficult to evaluate Eq.(15) and it can be approximated numerically, as

$$\begin{cases} \mathcal{M} = \sum_{i=1}^{N} [\{\mathcal{C}_{\mathbf{x}_C + \mathbf{R}_{\theta_i} \mathbf{r}_{EO}, r_d} \geq 0\} \cap \{\mathcal{C}_{\mathbf{x}_C + \mathbf{R}_{\theta_i} \mathbf{r}_{EO}, r_u} \leq 0\} \cap \{\mathcal{C}_{\mathbf{x}_I + \mathbf{R}_{\theta_i} \mathbf{r}_{IO}, r_1} \leq 0\}] \\ \theta_i = -\pi + \dfrac{2\pi i}{N} \end{cases},$$

(17)

where N is the number of slices that represent positioning errors under certain orientations.

Given that tolerances are 1/1000 of link lengths. Parameters used for error space estimation of the deployable mechanism are presented in Table 1.

Table 1. Parameter settings

Labels	Meaning	Values (mm)
$\mathbf{x}_A$	error-free coordinate of A	$(0, 300)^\top$
$\mathbf{x}_F$	error-free coordinate of F	$(100, 0)^\top$
$\mathbf{x}_H$	error-free coordinate of H	$(500, 0)^\top$
$\mathbf{x}_I$	error-free coordinate of I	$(600, 0)^\top$
$\mathbf{x}_E$	error-free coordinate of E	$(1100, 0)^\top$
$L_1{}^{+t_{u1}}_{-t_{d1}}$	length of AC with tolerance	$500^{+0.25}_{-0.25}$
$L_2{}^{+t_{u2}}_{-t_{d2}}$	length of FC with tolerance	$500^{+0.25}_{-0.25}$
$L_3{}^{+t_{u3}}_{-t_{d3}}$	length of HC with tolerance	$300^{+0.15}_{-0.15}$
$L_4{}^{+t_{u4}}_{-t_{d4}}$	length of CE with tolerance	$670.82^{+0.34}_{-0.34}$
r_1	joint clearance	0.5

We sample on x with increment of $0.02mm$, y with increment of $0.2mm$ and θ with increment of $0.02°$, and the error space of the outer panel is visualized in the 3-dimensional Euclidean frame $\{x, y, \theta\}$, as shown in Fig.8.(a). It is noteworthy that the $x-$axis, y-axis and θ-axis are not in the same scale, so the shape displayed in Fig.8.(a) is deformed.

The error-free pose of the outer panel is given as $(850, 0, 0)$. It can be observed in Fig.8 that the positioning error in the x-direction is restrained in

a. view in 3D

b. projection in xy plane

c. projection in $x\theta$ plane

d. projection in $x\theta$ plane

d. zoom out positive maximum angular error

e. zoom out negative maximum angular error

f. zoom out maximum positioning error

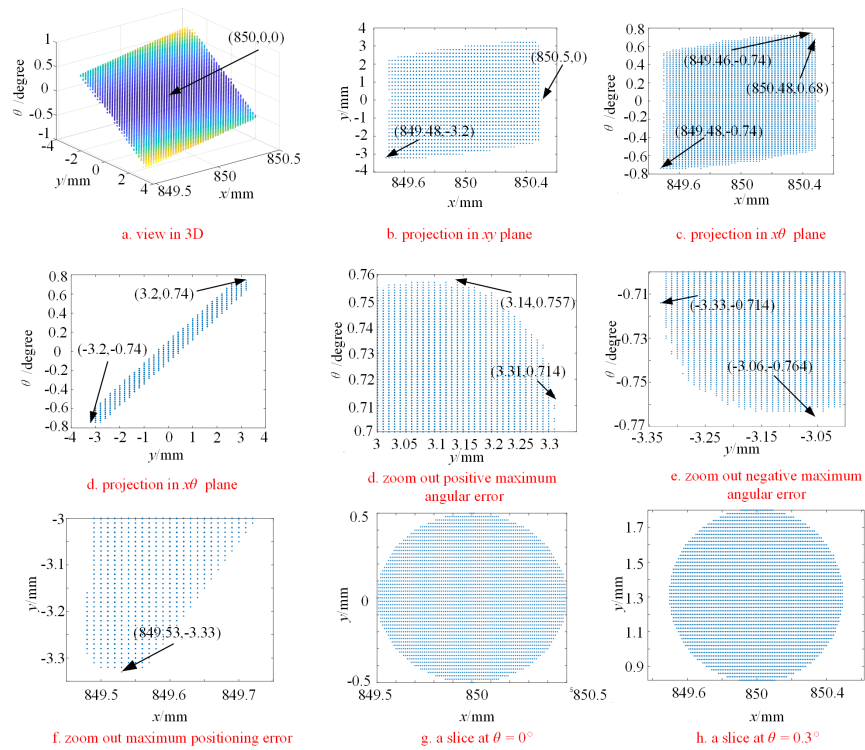g. a slice at $\theta = 0°$

h. a slice at $\theta = 0.3°$

Fig. 8. Visualization of the final error space

$[-0.52mm, 0.5mm]$, the positioning error projected in the x-direction is restrained in $[-3.33mm, 3.31mm]$ and angular error is restrained in $[-0.764°, 0.757°]$. Moreover, the maximum positioning error is $3.36mm$ at $(849.53, -3.33, -0.714)$. Since the error space of I (represented by a disk with radius $0.5mm$) is much smaller than that of E (represented by a ring with width $4.94mm$), the positioning error is coupled with the angular error, and the translational mobility is mainly determined by $\mathcal{M}_I$ when angular is fixed, as shown in Fig.8.(g) and Fig.8.(h). The error space of the outer panel is like a cylinder subjected to shear deformation in shape, two ends of which converge to two individual points. In Figure 8, the translational mobility at any given rotation can be obtained, which gives a deep insight of the accuracy performance of the outer panel.

3   Accuracy Analysis with Various Tolerance Design

This section aims to research into the effects of tolerances on the final accuracy. Here, tolerances are restrained $1/1000$ of link lengths. Three limited cases for each link tolerance allocation are considered, as shown in Table 2.

Table 2. Tolerance Allocation

Labels	Meaning	Levels (mm)
$[-t_{d1}, t_{u1}]$	tolerance of L_1	$[-0.25, 0.25], [0, 0.5], [-0.5, 0]$
$[-t_{d2}, t_{u2}]$	tolerance of L_2	$[-0.25, 0.25], [0, 0.5], [-0.5, 0]$
$[-t_{d3}, t_{u3}]$	tolerance of L_3	$[-0.15, 0.15], [0, 0.3], [-0.3, 0]$
$[-t_{d4}, t_{u4}]$	tolerance of L_4	$[-0.34, 0.34], [0, 0.68], [-0.68, 0]$

There are 81 combinations in total and the maximum y_e and θ_e are computed as they have great influence on the planarity of the two panels. The results are presented in the Appendix A.

It can be observed from Tables 3 and 4 in the appendix that tolerance design ($[-t_{d2}, t_{u2}]$) of link FC (L_2) makes no difference on the maximum positioning error y_e and angular error θ_e, suggesting that the tolerance of link FC has no contribution to the radii of $^C\mathcal{M}_E$. The optimal situation occurs at $[-0.5, 0]$ for L_1, $[0, 0.3]$ for L_3, $[-0.68, 0]$ for L_4, and maximum positioning error in y-direction and maximum angular error are $2.62mm$ and $0.601°$, respectively. In this situation, tolerances of L_1 and L_4 take the lower boundaries and tolerance of L_3 takes the upper boundary, suggesting shorter L_1, L_4 and longer L_3 benefit the accuracy. Conversely, when tolerances of L_1 and L_4 take the upper boundaries and tolerance of L_3 takes the lower boundary as $[500^{+0.5}_0]$, $[670.82^{+0.68}_0]$ and $[300^0_{-0.3}]$, respectively, it gives the worst situation with maximum positioning error $y_e = 4.04mm$ and maximum angular error $\theta_e = 0.927°$.

Moreover, the accuracy without tolerances are computed for comparison. The maximums considering clearances are $y_e = 2.62mm$ and $\theta_e = 0.601°$ and they are same with those computed with the optimal tolerance design, suggesting that

the errors brought by tolerances can be eliminated by proper tolerance design for this specific deployable mechanism.

4   Conclusion

The error space of the deployable mechanism concerning revolute joint clearances and link tolerances is derived using a geometric approach and estimated numerically with discrete sampling points. The maximum positioning error and angular error are therefore obtained. In this numerical way, precision of the result depends on the distances between sample points. It is noteworthy that points on the boundaries of the error space can also be obtained directly by solving equations. For the deployable mechanism discussed in this paper, positioning error of outer panel in the x-direction is mainly determined by the clearance of joint I. Error in y-direction and angular error are coupled. When the angular error is fixed, the translational mobility of the outer panel is determined by the clearance of joint I.

Effects of tolerances on the accuracy are studied. It can be concluded from the results that tolerances of link FC make no difference to the final error when tolerance range is restrained to be 1/1000 the link length. The reason is that the position of C is redundantly determined by three links, among which AC and HC contribute most in propagation. Through the comparison with clearances-only result, it reveals that the effects of tolerances on final error can be eliminated by proper tolerance design.

Acknowledgement

Reference

1. Kwun-Lon Ting, Jianmin Zhu, and Derek Watkins. The effects of joint clearance on position and orientation deviation of linkages and manipulators. *Mechanism and Machine Theory*, 35(3):391–401, 2000.
2. Kwon-Lon Ting, Kuan-Lun Hsu, and Jun Wang. Clearance-induced orientation uncertainty of spherical linkages. *Journal of Mechanisms and Robotics*, 9(6):061001, 2017.
3. Cody Leeheng Chan and Kwun-Lon Ting. Clearance-induced orientation uncertainty of spherical linkages. *Journal of Mechanisms and Robotics*, 13(2):021021, 03 2021.
4. Ming-June Tsai and Tien-Hsing Lai. Kinematic sensitivity analysis of linkage with joint clearance based on transmission quality. *Mechanism and Machine Theory*, 39(11):1189–1206, 2004.
5. Ming-June Tsai and Tien-Hsing Lai. Accuracy analysis of a multi-loop linkage with joint clearances. *Mechanism and Machine Theory*, 43(9):1141–1157, 2008.

6. Haitao Liu, Tian Huang, and Derek G Chetwynd. A general approach for geometric error modeling of lower mobility parallel manipulators. *Journal of Mechanisms and Robotics*, 3(2):021013, 2011.
7. Wenjie Tian, Weiguo Gao, Dawei Zhang, and Tian Huang. A general approach for error modeling of machine tools. *International Journal of Machine Tools and Manufacture*, 79:17–23, 2014.
8. Antonio Frisoli, Massimiliano Solazzi, D Pellegrinetti, and Massimo Bergamasco. A new screw theory method for the estimation of position accuracy in spatial parallel manipulators with revolute joint clearances. *Mechanism and Machine Theory*, 46(42):1929–1949, 2011.
9. Alessandro Cammarata. A novel method to determine position and orientation errors in clearance-affected overconstrained mechanisms. *Mechanism and Machine Theory*, 118:247–264, 2017.
10. Henrique Simas and Raffaele Di Gregorio. Geometric error effects on manipulators' positioning precision: A general analysis and evaluation method. *Journal of Mechanisms and Robotics*, 8(6):061016, 2016.
11. Xin Li, Xilun Ding, and Gregory S Chirikjian. Analysis of angular-error uncertainty in planar multiple-loop structures with joint clearances. *Mechanism and Machine Theory*, 91:69–85, 2015.
12. Qiangqiang Zhao, Junkang Guo, and Jun Hong. Closed-form error space calculation for parallel/hybrid manipulators considering joint clearance, input uncertainty, and manufacturing imperfection. *Mechanism and Machine Theory*, 142:103608, 2019.
13. Jian Meng and Zexiang Li. A general approach for accuracy analysis of parallel manipulators with joint clearance. In *2005 IEEE/RSJ International Conference on Intelligent Robots and Systems*, pages 2468–2473. IEEE, 2005.
14. Jian Meng, Dongjun Zhang, and Zexiang Li. Accuracy analysis of parallel manipulators with joint clearance. *Journal of Mechanical Design*, 131(1):011013, 2009.
15. Sébastien Briot and Ilian A Bonev. Accuracy analysis of 3t1r fully-parallel robots. *Mechanism and Machine Theory*, 45(5):695–706, 2010.
16. Rui Yao, Wenbai Zhu, and Peng Huang. Accuracy analysis of stewart platform based on interval analysis method. *Chinese Journal of Mechanical Engineering*, 26(1):29–34, 2013.
17. Genliang Chen, Hao Wang, and Zhongqin Lin. A unified approach to the accuracy analysis of planar parallel manipulators both with input uncertainties and joint clearance. *Mechanism and Machine Theory*, 64:1–17, 2013.
18. Jianzhong Ding, Shengnan Lyu, Ting Da, Chunjie Wang, and Gregory S Chirikjian. Error space estimation of 3-dof planar parallel mechanisms. *Journal of Mechanisms and Robotics*, 11(3):031013, 2019.
19. U Kumaraswamy, MS Shunmugam, and S Sujatha. A unified framework for tolerance analysis of planar and spatial mechanisms using screw theory. *Mechanism and Machine Theory*, 69:168–184, 2013.
20. Huang. Tian, Whitehouse David J., and Chetwynd Derek G. A unified error model for tolerance design, assembly and error compensation of 3-dof parallel kinematic machines with parallelogram struts. *CIRP Annals*, 51(1):297–301, 2002.
21. Hallmann Martin, Schleich Benjamin, and Wartzack Sandro. From tolerance allocation to tolerance-cost optimization: a comprehensive literature review. *The International Journal of Advanced Manufacturing Technology*, 107(1):1–54, 2020.

A   Results of the Tolerance Design

Table 3. Tolerance Analysis Results-1

Case	$[-t_{d1}, t_{u1}]$	$[-t_{d2}, t_{u2}]$	$[-t_{d3}, t_{u3}]$	$[-t_{d4}, t_{u4}]$	$\max |y_e|$	$\max |\theta_e|$
1	$[-0.5, 0]$	$[-0.5, 0]$	$[-0.3, 0]$	$[-0.68, 0]$	2.77	0.636
2	$[-0.5, 0]$	$[-0.5, 0]$	$[-0.3, 0]$	$[-0.34, 0.34]$	3.15	0.723
3	$[-0.5, 0]$	$[-0.5, 0]$	$[-0.3, 0]$	$[0, 0.68]$	3.53	0.811
4	$[-0.5, 0]$	$[-0.5, 0]$	$[-0.15, 0.15]$	$[-0.68, 0]$	2.69	0.618
5	$[-0.5, 0]$	$[-0.5, 0]$	$[-0.15, 0.15]$	$[-0.34, 0.34]$	3.07	0.706
6	$[-0.5, 0]$	$[-0.5, 0]$	$[-0.15, 0.15]$	$[0, 0.68]$	3.46	0.794
7	$[-0.5, 0]$	$[-0.5, 0]$	$[0, 0.3]$	$[-0.68, 0]$	2.62	0.601
8	$[-0.5, 0]$	$[-0.5, 0]$	$[0, 0.3]$	$[-0.34, 0.34]$	3.00	0.688
9	$[-0.5, 0]$	$[-0.5, 0]$	$[0, 0.3]$	$[0, 0.68]$	3.38	0.777
10	$[-0.5, 0]$	$[-0.25, 0.25]$	$[-0.3, 0]$	$[-0.68, 0]$	2.77	0.636
11	$[-0.5, 0]$	$[-0.25, 0.25]$	$[-0.3, 0]$	$[-0.34, 0.34]$	3.15	0.723
12	$[-0.5, 0]$	$[-0.25, 0.25]$	$[-0.3, 0]$	$[0, 0.68]$	3.53	0.811
13	$[-0.5, 0]$	$[-0.25, 0.25]$	$[-0.15, 0.15]$	$[-0.68, 0]$	2.69	0.618
14	$[-0.5, 0]$	$[-0.25, 0.25]$	$[-0.15, 0.15]$	$[-0.34, 0.34]$	3.07	0.706
15	$[-0.5, 0]$	$[-0.25, 0.25]$	$[-0.15, 0.15]$	$[0, 0.68]$	3.46	0.794
16	$[-0.5, 0]$	$[-0.25, 0.25]$	$[0, 0.3]$	$[-0.68, 0]$	2.62	0.601
17	$[-0.5, 0]$	$[-0.25, 0.25]$	$[0, 0.3]$	$[-0.34, 0.34]$	3.00	0.688
18	$[-0.5, 0]$	$[-0.25, 0.25]$	$[0, 0.3]$	$[0, 0.68]$	3.38	0.777
19	$[-0.5, 0]$	$[0, 0.5]$	$[-0.3, 0]$	$[-0.68, 0]$	2.77	0.636
20	$[-0.5, 0]$	$[0, 0.5]$	$[-0.3, 0]$	$[-0.34, 0.34]$	3.15	0.723
21	$[-0.5, 0]$	$[0, 0.5]$	$[-0.3, 0]$	$[0, 0.68]$	3.53	0.811
22	$[-0.5, 0]$	$[0, 0.5]$	$[-0.15, 0.15]$	$[-0.68, 0]$	2.69	0.618
23	$[-0.5, 0]$	$[0, 0.5]$	$[-0.15, 0.15]$	$[-0.34, 0.34]$	3.07	0.706
24	$[-0.5, 0]$	$[0, 0.5]$	$[-0.15, 0.15]$	$[0, 0.68]$	3.46	0.794
25	$[-0.5, 0]$	$[0, 0.5]$	$[0, 0.3]$	$[-0.68, 0]$	2.62	0.601
26	$[-0.5, 0]$	$[0, 0.5]$	$[0, 0.3]$	$[-0.34, 0.34]$	3.00	0.688
27	$[-0.5, 0]$	$[0, 0.5]$	$[0, 0.3]$	$[0, 0.68]$	3.38	0.777
28	$[-0.25, 0.25]$	$[-0.5, 0]$	$[-0.3, 0]$	$[-0.68, 0]$	3.02	0.693
29	$[-0.25, 0.25]$	$[-0.5, 0]$	$[-0.3, 0]$	$[-0.34, 0.34]$	3.40	0.781
30	$[-0.25, 0.25]$	$[-0.5, 0]$	$[-0.3, 0]$	$[0, 0.68]$	3.78	0.869
31	$[-0.25, 0.25]$	$[-0.5, 0]$	$[-0.15, 0.15]$	$[-0.68, 0]$	2.94	0.676
32	$[-0.25, 0.25]$	$[-0.5, 0]$	$[-0.15, 0.15]$	$[-0.34, 0.34]$	3.33	0.764
33	$[-0.25, 0.25]$	$[-0.5, 0]$	$[-0.15, 0.15]$	$[0, 0.68]$	3.71	0.852
34	$[-0.25, 0.25]$	$[-0.5, 0]$	$[0, 0.3]$	$[-0.68, 0]$	2.87	0.659
35	$[-0.25, 0.25]$	$[-0.5, 0]$	$[0, 0.3]$	$[-0.34, 0.34]$	3.25	0.747
36	$[-0.25, 0.25]$	$[-0.5, 0]$	$[0, 0.3]$	$[0, 0.68]$	3.63	0.834
37	$[-0.25, 0.25]$	$[-0.25, 0.25]$	$[-0.3, 0]$	$[-0.68, 0]$	3.02	0.693
38	$[-0.25, 0.25]$	$[-0.25, 0.25]$	$[-0.3, 0]$	$[-0.34, 0.34]$	3.40	0.781
39	$[-0.25, 0.25]$	$[-0.25, 0.25]$	$[-0.3, 0]$	$[0, 0.68]$	3.78	0.869
40	$[-0.25, 0.25]$	$[-0.25, 0.25]$	$[-0.15, 0.15]$	$[-0.68, 0]$	2.94	0.676
41	$[-0.25, 0.25]$	$[-0.25, 0.25]$	$[-0.15, 0.15]$	$[-0.34, 0.34]$	3.33	0.764
42	$[-0.25, 0.25]$	$[-0.25, 0.25]$	$[-0.15, 0.15]$	$[0, 0.68]$	3.71	0.852
43	$[-0.25, 0.25]$	$[-0.25, 0.25]$	$[0, 0.3]$	$[-0.68, 0]$	2.87	0.659
44	$[-0.25, 0.25]$	$[-0.25, 0.25]$	$[0, 0.3]$	$[-0.34, 0.34]$	3.25	0.747
45	$[-0.25, 0.25]$	$[-0.25, 0.25]$	$[0, 0.3]$	$[0, 0.68]$	3.63	0.834

Table 4. Tolerance Analysis Results-2

Case	$[-t_{d1}, t_{u1}]$	$[-t_{d2}, t_{u2}]$	$[-t_{d3}, t_{u3}]$	$[-t_{d4}, t_{u4}]$	$\max |y_e|$	$\max |\theta_e|$
46	$[-0.25, 0.25]$	$[0, 0.5]$	$[-0.3, 0]$	$[-0.68, 0]$	3.02	0.693
47	$[-0.25, 0.25]$	$[0, 0.5]$	$[-0.3, 0]$	$[-0.34, 0.34]$	3.40	0.781
48	$[-0.25, 0.25]$	$[0, 0.5]$	$[-0.3, 0]$	$[0, 0.68]$	3.78	0.869
49	$[-0.25, 0.25]$	$[0, 0.5]$	$[-0.15, 0.15]$	$[-0.68, 0]$	2.94	0.676
50	$[-0.25, 0.25]$	$[0, 0.5]$	$[-0.15, 0.15]$	$[-0.34, 0.34]$	3.33	0.764
51	$[-0.25, 0.25]$	$[0, 0.5]$	$[-0.15, 0.15]$	$[0, 0.68]$	3.71	0.852
52	$[-0.25, 0.25]$	$[0, 0.5]$	$[0, 0.3]$	$[-0.68, 0]$	2.87	0.659
53	$[-0.25, 0.25]$	$[0, 0.5]$	$[0, 0.3]$	$[-0.34, 0.34]$	3.25	0.747
54	$[-0.25, 0.25]$	$[0, 0.5]$	$[0, 0.3]$	$[0, 0.68]$	3.63	0.834
55	$[0, 0.5]$	$[-0.5, 0]$	$[-0.3, 0]$	$[-0.68, 0]$	3.27	0.752
56	$[0, 0.5]$	$[-0.5, 0]$	$[-0.3, 0]$	$[-0.34, 0.34]$	3.65	0.839
57	$[0, 0.5]$	$[-0.5, 0]$	$[-0.3, 0]$	$[0, 0.68]$	4.04	0.927
58	$[0, 0.5]$	$[-0.5, 0]$	$[-0.15, 0.15]$	$[-0.68, 0]$	3.20	0.734
59	$[0, 0.5]$	$[-0.5, 0]$	$[-0.15, 0.15]$	$[-0.34, 0.34]$	3.58	0.822
60	$[0, 0.5]$	$[-0.5, 0]$	$[-0.15, 0.15]$	$[0, 0.68]$	3.96	0.910
61	$[0, 0.5]$	$[-0.5, 0]$	$[0, 0.3]$	$[-0.68, 0]$	3.12	0.716
62	$[0, 0.5]$	$[-0.5, 0]$	$[0, 0.3]$	$[-0.34, 0.34]$	3.50	0.805
63	$[0, 0.5]$	$[-0.5, 0]$	$[0, 0.3]$	$[0, 0.68]$	3.89	0.893
64	$[0, 0.5]$	$[-0.25, 0.25]$	$[-0.3, 0]$	$[-0.68, 0]$	3.27	0.752
65	$[0, 0.5]$	$[-0.25, 0.25]$	$[-0.3, 0]$	$[-0.34, 0.34]$	3.65	0.839
66	$[0, 0.5]$	$[-0.25, 0.25]$	$[-0.3, 0]$	$[0, 0.68]$	4.04	0.927
67	$[0, 0.5]$	$[-0.25, 0.25]$	$[-0.15, 0.15]$	$[-0.68, 0]$	3.20	0.734
68	$[0, 0.5]$	$[-0.25, 0.25]$	$[-0.15, 0.15]$	$[-0.34, 0.34]$	3.58	0.822
69	$[0, 0.5]$	$[-0.25, 0.25]$	$[-0.15, 0.15]$	$[0, 0.68]$	3.96	0.910
70	$[0, 0.5]$	$[-0.25, 0.25]$	$[0, 0.3]$	$[-0.68, 0]$	3.12	0.716
71	$[0, 0.5]$	$[-0.25, 0.25]$	$[0, 0.3]$	$[-0.34, 0.34]$	3.50	0.805
72	$[0, 0.5]$	$[-0.25, 0.25]$	$[0, 0.3]$	$[0, 0.68]$	3.89	0.893
73	$[0, 0.5]$	$[0, 0.5]$	$[-0.3, 0]$	$[-0.68, 0]$	3.27	0.752
74	$[0, 0.5]$	$[0, 0.5]$	$[-0.3, 0]$	$[-0.34, 0.34]$	3.65	0.839
66	$[0, 0.5]$	$[0, 0.5]$	$[-0.3, 0]$	$[0, 0.68]$	4.04	0.927
76	$[0, 0.5]$	$[0, 0.5]$	$[-0.15, 0.15]$	$[-0.68, 0]$	3.20	0.734
77	$[0, 0.5]$	$[0, 0.5]$	$[-0.15, 0.15]$	$[-0.34, 0.34]$	3.58	0.822
78	$[0, 0.5]$	$[0, 0.5]$	$[-0.15, 0.15]$	$[0, 0.68]$	3.96	0.910
79	$[0, 0.5]$	$[0, 0.5]$	$[0, 0.3]$	$[-0.68, 0]$	3.12	0.716
80	$[0, 0.5]$	$[0, 0.5]$	$[0, 0.3]$	$[-0.34, 0.34]$	3.50	0.805
81	$[0, 0.5]$	$[0, 0.5]$	$[0, 0.3]$	$[0, 0.68]$	3.89	0.893

Dynamic Modeling of Folding Bundling Mechanism

Jinzhu Zhang[1], Zepeng Lu[1], Tao Wang[2], Wei Shi[1], Ziliang Li[1] and Jiang Li[3]

[1] Taiyuan University of Technology, Taiyuan, Shanxi 030024, PR China

[2] Engineering Center of Ministry of Education of Metal Composites Taiyuan University of Technology, Taiyuan, Shanxi 030024, PR China

[3] Sino-Australian Joint Research Centre, Australian Embassy, Beijing 100020, PR China

zhangjinzhu@tyut.edu.cn

Abstract. Large energy consumption of steel production has been one of the important factors affecting global ecological governance. This paper attempts to apply the folding mechanism to the design of steel bar binding robot to reduce the energy consumption of the binding robot. Based on the bar bundling process to determine the trajectory of the bundling mechanism, a new type of binding robot is designed and its three-dimensional modeling is carried out, the position inverse solution and positive solution models of baling mechanism are established respectively, the forward and inverse solution model is verified by the results of the forward and inverse solution, and the dynamic analysis of the baling mechanism is carried out based on Newton Euler method, and the simulation verification is carried out. The dynamic model established in this paper provides a theoretical basis for energy consumption analysis and optimization design of baling robot.

Keywords: Baler robot, Discount institutions, Kinematics, Dynamics.

1   Introduction

At the moment of the outbreak of COVID-19, environmental issues are more important than ever in the minds of people around the world. There are many environmental problems, such as acid rain, global warming, species extinction, land desertification, etc. However, the causes of environmental problems are complex and diverse, such as industrial energy consumption, fossil fuel combustion and so on [1].

As we all know, industrial production is highly dependent on energy and almost occupies the vast majority of energy consumption. As the basis of industry, iron and steel production is the field with the largest energy consumption in all aspects of industrial production. For example, steel and other metal products are the main raw materials of mechanical equipment such as nuclear power industry, intelligent equipment and automobile manufacturing. Their production capacity will increase with the increase of market demand of equipment manufacturing industry, so that the annual increase of steel production capacity will bring great challenges to global ecological governance and recovery. Therefore, it is crucial to improve the energy efficiency utilization rate of various equipment on the steel production line [2].

Mechanism is the skeleton of equipment, good mechanism is an important guarantee for high energy efficiency of steel production equipment. Therefore, steel equipment also needs to keep pace with the development of institutional innovation theory. The folding mechanism has the characteristics of variable working trajectory, high action accuracy and small volume after folding. Compared with the traditional mechanism, the ratio of the number of connecting rods to the number of configurations is large, and it has strong adaptability to the operation with variable processes. The energy utilization efficiency can be optimized according to the task folding.

With more and more scholars engaged in the research of folding mechanism, it not only enriches the configuration library of folding mechanism, but also promotes the development of the basic theory of folding mechanism. For example, Japanese experts such as Miura and Tachi put forward the concept of rigid folding paper and folding paper mosaic[3]; Professor Z.Q. Deng summarized and elaborated the basic theory and design method of large space folding mechanism[4]; The metamorphic mechanism proposed by Professor J.S. Dai and its comprehensive theoretical basis also provide specific ideas for folding mechanism[5];Professor X.L. Ding proposed a shear fork bending and folding metamorphic mechanism unit based on the shear fork

mechanism unit, which effectively combines the metamorphic mechanism and the folding mechanism[6];Professor Y. Chen, in cooperation with British scholars, creatively proposed the theoretical model of thick plate folding mechanism[7]; At present, some folding mechanisms have achieved good application effects in aerospace and space communication[8];Such as deployable antennas, spacecraft solar wings, and giant space telescopes developed and manufactured by NASA[9]; Based on the increasingly rich and mature theory of folding mechanism, scholars began to explore the application of folding mechanism in industries such as steel.

Bundling is an important process in the production process of Special Steel. The operation process includes five links: preload, wire feeding, shearing, retracting and knotting. The position of different links is also different, and the force is different. Therefore, based on the motion and force characteristics of the baling mechanism in each link of the baling operation, this paper explores the application of the folding mechanism in the baling operation, so as to apply the folding mechanism to the production field of special steel and reduce the energy consumption of the baling equipment. The content of this paper is of great significance to expand the application field of folding mechanism and promote the development of folding mechanism.

2   Overall layout and working process of the bundling robot

2.1   Overall layout of baling robots

The baling robot is mainly composed of pre-tightening device, wire feeding device, shearing device, integrated retracting device and baling device. The overall structure of the baling robot is shown in Figure 1.
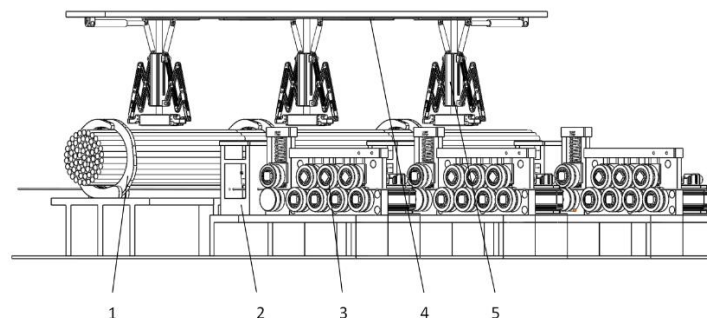
1.Pre-tightening device 2. Shearing device 3. Wire feeding device 4. Integrated receiving and discharging device 5. Binding device

From the overall structure of the bundling robot, it can be seen that the above five parts are independent of each other in structural arrangement. In the working process, the five components of the bundling process cooperate to complete the bundling task according to certain rules. The bundling device is the core component of the bundling robot. This bundling device is designed based on two symmetrically arranged folding mechanisms with the same degree of freedom characteristics. This paper mainly studies the folding baling mechanism.

2.2 Working process of folding bundling mechanism

The operation process of the folding bundling mechanism can be decomposed into four sub-states, namely, initial state, expansion state, envelope state and recovery state, as shown in Fig. 2.

1. Wire binding 2. Clamp 3. Electric clamp 4. Slider 5. Single degree of freedom folding telescopic frame
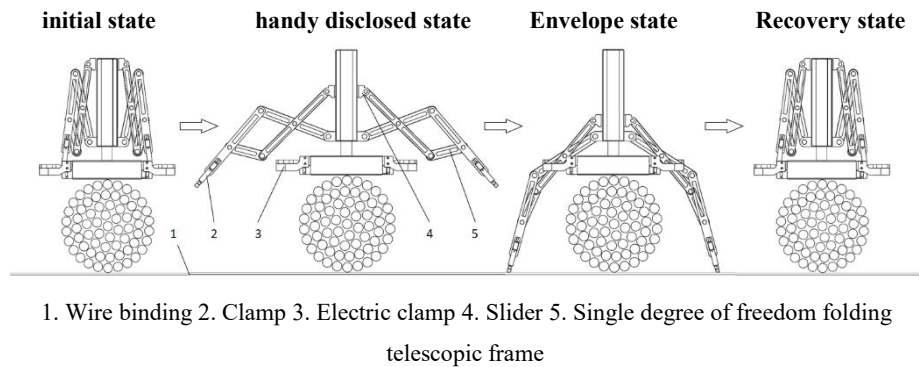
Fig. 2. Bundling process diagram

The initial state is the state of the bundling device without working tasks, and is also the installation and detection state of the bundling device ; The envelope state is that after entering the working state, the slider moves downward along the sliding track, and the end of the single-degree-of-freedom deployable telescopic frame moves along the established parabolic trajectory to the wire binding place [10]. At this time, the bundling mechanism and the bundling wire form a closed loop to completely envelope the bar ; the expansion state is a state between the initial state and the included state ; The recovery state is that the end of the bundling mechanism reaches the clamp position at both ends of the torsion mechanism by clamping the bundling wire through the clamp at both ends ; Rotating mechanism has only one rotational

degree of freedom, through its rotation to achieve binding, and complete the binding action. Go round and round, the pre-tightening device, wire feeding device, shearing device, integrated retracting device and baling device cooperate with each other for the next round of baling operation.

3　Kinematics analysis of folding bundling mechanism

3.1　Introduction of folding mechanism and establishment of coordinate system

The folding bundling mechanism is derived from the traditional scissors and forks mechanism by changing the length of bars at different positions. The schematic diagram of the mechanism is shown in Fig. 3, where A, B, C, E, F and G represent the center of each rotational pair in the mechanism, D represents the end point of the mechanism, and B represents the centroid of the slider. Let the rod length of AC, CD, BF, FG, AE, EC, CG be $L_1, L_2, L_3, L_4, L_5, L_6, L_7, L_8$, and the angle between the connecting rod AC, CD, BF, FG and the lines of point A and B be $\alpha_1, \alpha_2, \alpha_3$.

The coordinate system is established as shown in Figure 3. Taking A as the origin, the plane fixed coordinate system A-xy, x axis along the horizontal direction, y axis along the vertical direction is established. The position vector of point D is set as $D[x_D,\ y_D,\ \theta]^T$,where x_D and y_D represent the position coordinates of D, respectively, θ is the angle between AD and x axis, and the position vector of slider centroid B is set as $B[0,\ y_B, 0.5\pi]^T$.
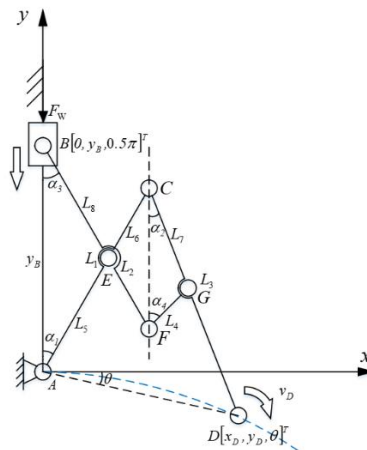

Fig. 3. A sketch of unfolding baling mechanism

3.2 Position inverse solution

Reverse motion is the process of solving all joint variables through the end posture of the mechanism, that is, when the position vector of the end D of the mechanism is determined, the position vector and angle α_i of the slider B are obtained. According to the geometric relationship expressed in Figure 3, The vector closed-loop equations between end D and bars can be written as:

$$AC + CD = AD \tag{3-1}$$

Equation (3-1) is expressed in component form :

$$x_D = L_1 \sin\alpha_1 + L_2 \sin\alpha_2 \tag{3-2}$$

$$y_D = L_1 \cos\alpha_1 - L_2 \cos\alpha_2 \tag{3-3}$$

The square sum of equations (3-2) and (3-3) is calculated to obtain the relationship between L1, L2 and angle α_1, α_2:

$$\alpha_1 + \alpha_2 = \arccos \frac{x_D{}^2 + y_D{}^2 - L_1{}^2 - L_2{}^2}{2L_1 L_2} \tag{3-4}$$

Determined by Equations (3-5) α_1, y_B can be derived by cosine theorem :

$$\alpha_1 = \frac{\pi}{2} - \left(\arccos \frac{x_D{}^2 + y_D{}^2 + L_1{}^2 - L_2{}^2}{2L_1 \sqrt{x_D{}^2 + y_D{}^2}} - \theta \right) \tag{3-5}$$

$$y_b = \sqrt{L_8{}^2 - L_5{}^2 - L_5{}^2 \sin^2\alpha_1} + L_5 \cos\alpha_1 \tag{3-6}$$

Therefore, the inverse position solution of the folding bundling mechanism is solved.

3.3 Position positive solution

Forward kinematics is the process of calculating the position and attitude of the end of the mechanism given all joint variables, that is, the position vector of the end of the mechanism D is obtained when the initial position vector of the slider B and the α_i angle are determined. Because each member parameter is known, α_1 in $\triangle$ ABE by cosine theorem:

$$\alpha_1 = \arccos \left(\frac{y_b{}^2 + L_5{}^2 - L_8{}^2}{2y_b L_5} \right) \tag{3-7}$$

The distance between points C and F is obtained by the similarity between $\triangle$ ABE and $\triangle$ CFE, α_2 is obtained by the law of cosines:

$$CF = \frac{y_b L_6}{L_5} \tag{3-8}$$

$$\alpha_2 = \arccos\frac{y_b{}^2 L_6{}^2 - L_5{}^2 L_7{}^2 - L_4{}^2 L_5{}^2}{2 y_b L_5 L_6 L_7} \tag{3-9}$$

Similarly, α_3, α_4 are respectively

$$\alpha_3 = \arccos\left(\frac{y_b{}^2 + L_8{}^2 - L_5{}^2}{2 y_b L_8}\right) \tag{3-10}$$

$$\alpha_4 = \arccos\frac{y_b{}^2 L_6{}^2 - L_4{}^2 L_5{}^2 - L_5{}^2 L_7{}^2}{2 y_b L_4 L_5 L_6} \tag{3-11}$$

$\alpha_1, \alpha_2, \alpha_3, \alpha_4$ determines the pose state of the whole mechanism, obtain x_D, y_D by formula 3-2 and 3-3. Therefore, each determined slider B has a unique end D corresponding to it.

3.4 Verification of position positive and negative solution calculation example

In this paper, an example is given to verify the correctness of the positive and negative solutions of the position of the folding baling mechanism, and the length of each rod of the whole mechanism is set as shown in table 3-1

Table 3-1 Parameter setting of each member

structural parameter	numerical value	structural parameter	numerical value
L_1	150mm	L_6	75mm
L_2	200mm	L_7	100mm
L_3	190mm	L_8	95mm
L_5	75mm	y/x^2	a mm^{-1}

According to the structural parameters given in Table 3-1, Equations 3-4 to 3-6 are combined to obtain the inverse position solutions α_1, α_2. The obtained inverse position solution data are brought into Equations 3-2 to obtain the forward position solutions x_D and y_D of the folding bundling mechanism. The calculation results are shown in Table 3-2. The unit of all angles in the table is degree and the unit of length is millimeter.

Table 3-2. A positive and negative calculation example of the position of the folding baling mechanism

Terminal reference point	Calculation results of	Calculation results of positive solution

coordinates			inverse solution		of backward position		
x_D	y_D	θ	α_1	α_2	x_D	y_D	θ
250	225	41.987	113.375	34.163	249.999	225.001	41.987
235	215	42.455	103.925	26.554	234.999	215.000	42.455
225	200	41.633	95.699	22.253	224.999	200.000	41.633
210	190	39.806	84.056	17.700	210.000	174.999	39.806
200	175	41.186	82.971	14.811	200.000	174.999	41.186

By comparing the calculation results, it can be seen that the error of the positive and negative solutions is less than 0.001 mm, which belongs to the allowable range of computer error. Therefore, the calculation results verify the correctness of the positive and negative solutions of the position of the folding bundling mechanism [11].

4   Kinetic analysis

4.1   Dynamic modeling

In section 2.2 of this paper, the working process of the folding baling mechanism is analyzed in detail. Through the qualitative analysis of the force at the end of the folding mechanism in the working process, that is, the interaction force between the folding mechanism and the wire, it can be seen that the force of the folding mechanism is small in the deployment state, and the force gradually increases with the gradual recovery of the mechanism. However, at this time, as the stiffness of the mechanism recovery mechanism increases, it is not easy to deform. Based on this, this paper considers all the components of the mechanism as rigid components. It can be seen from Fig. 3 that the whole mechanism is asymmetric. It is necessary to analyze the force of AC, CD, BF and FG, and obtain the dynamic equation of each member according to the Dalembert principle [12].

$$\begin{cases} F_i - m_i \ddot{O}_i = 0 \\ M_i - J_i \ddot{\alpha}_i = 0 \end{cases} \tag{4-1}$$

Where F_i is the resultant external force of rod i;m_i is the mass of member i;$\ddot{O}_i$ is the vector acceleration at the center of mass of member i;$M_i$is the external force moment of member i;Ji is the moment of inertia at the center of mass of bar i;$\ddot{\alpha}_i$ is the vector

angular acceleration of member i. The force analysis of each rod is shown in Figure 5, where Gm is the weight of each rod (m=AC, CD, BF, FG), FL is the pulling force of the rod end on the bundle wire, and the direction is along the tangential direction of the movement.
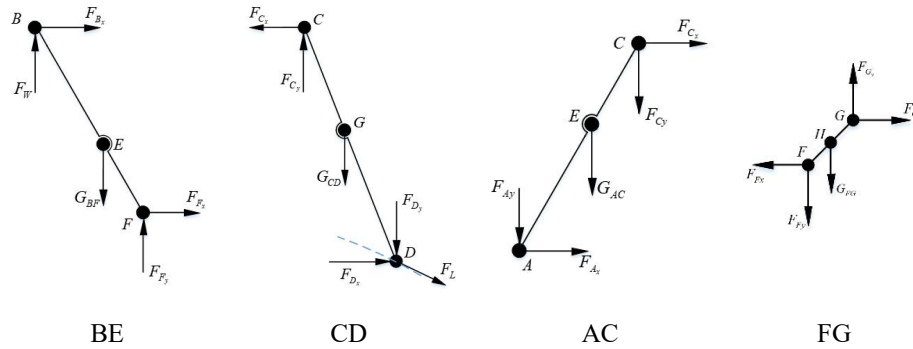

BE	CD	AC	FG

Fig. 4. Force analysis of each member

The coordinates of the center of mass of each member are as follows:

$$E = O_{BF} = O_{AC} = \begin{cases} x_E = \dfrac{L_1 sin\alpha_1}{2} \\ y_E = \dfrac{L_1 cos\alpha_1}{2} \end{cases} \tag{4-2}$$

$$G = O_{CD} = \begin{cases} x_G = L_3 sin\alpha_3 + L_4 sin\alpha_4 \\ y_G = y_b - L_3 cos\alpha_3 + L_4 cos\alpha_4 \end{cases} \tag{4-3}$$

$$O_{FG} = \begin{cases} x_H = L_3 sin\alpha_3 + \dfrac{L_4 sin\alpha_4}{2} \\ y_H = y_b - L_3 cos\alpha_3 + \dfrac{L_4 cos\alpha_4}{2} \end{cases} \tag{4-4}$$

The vector velocity and acceleration at the centroid can be obtained by the first and second derivation of the centroid coordinate position O_i, and the angular velocity and angular acceleration at the corresponding position can be obtained by the first and second derivation of the angle α_i. According to the force analysis diagram shown in Figure 5, the dynamic model of AC,CD,BF,FG rod in plane is established, and the

equilibrium equations of force and moment are listed based on Newton Euler method [13].

$$\begin{cases} -F_{A_y} - F_{C_y} + m(\ddot{y}_E - g) = 0 \\ -F_{A_x} - F_{C_x} + m\ddot{x}_E = 0 \\ 0.5L_1\left(F_{A_y}\cos\alpha_1 - F_{A_x}\cos\alpha_1 + F_{C_y}\sin\alpha_1 - F_{C_x}\cos\alpha_1\right) - J_1\ddot{\alpha}_1 = 0 \end{cases} \tag{4-5}$$

$$\begin{cases} F_{C_y} - F_{D_y} + m(\ddot{y}_G - g) = 0 \\ F_{C_x} - F_{D_x} + m\ddot{x}_G = 0 \\ 0.5L_2\left(F_{C_y}\sin\alpha_2 - F_{C_x}\cos\alpha_2 - F_{D_y}\sin\alpha_2 + F_{D_x}\cos\alpha_2\right) - J_2\ddot{\alpha}_2 = 0 \end{cases} \tag{4-6}$$

$$\begin{cases} F_w + F_{F_y} + m(\ddot{y}_E - g) = 0 \\ -F_{B_x} - F_{F_x} + m\ddot{x}_E = 0 \\ 0.5L_3\left(F_w\sin\alpha_3 - F_{B_x}\cos\alpha_3 + F_{F_y}\sin\alpha_3 + F_{F_x}\cos\alpha_3\right) - J_3\ddot{\alpha}_3 = 0 \end{cases} \tag{4-7}$$

$$\begin{cases} F_{G_y} - F_{F_y} + m(\ddot{y}_H - g) = 0 \\ F_{F_x} - F_{G_x} + m\ddot{x} = 0 \\ 0.5L_4\left(F_{F_y}\sin\alpha_4 - F_{F_x}\cos\alpha_4 - F_{G_y}\sin\alpha_4 + F_{G_x}\cos\alpha_4\right) - J_4\ddot{\alpha}_4 = 0 \end{cases} \tag{4-8}$$

When the parabolic trajectory and the load of all external forces are known [14], 12 equations can be obtained by simultaneous equations 4-5 to 4-8. The number of unknowns is also 12, and the equation can be solved. Finally, the force and torque of four joints A, E, C and F are obtained.

4.2   Dynamic simulation

Let each bar be a uniform bar, density $\rho = 790\text{kg/m}^3$, the bar parameter table 3-1 shows. According to the actual production situation of a steel enterprise in China, the most common bundle diameter is selected, and the length of rod 4 is set to be 73.25 mm.

Given the external load and driving force are FL = 50N and FW = 100N, the force of each joint is calculated based on the dynamic modeling results of section 4.1, as shown in Figure 5 and Figure 6. In order to verify the correctness of the dynamic modeling results, the dynamic simulation of the folding bundling mechanism is carried out by using the simulation software. The force and torque of the joint A,E,C,F are collected in the simulation environment, and compared with the theoretical calculation results. The comparison results are shown in Table 4-1.
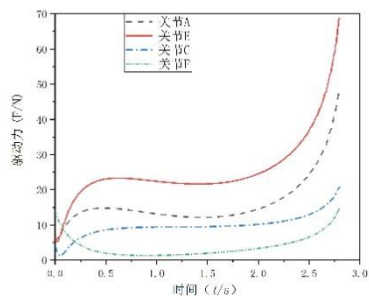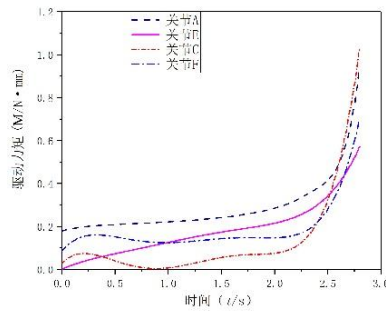

Fig. 5. Driving force F

Fig. 6. Driving torque M

Table 4-1 Data Comparison between Theoretical Calculation and Simulation Results

Joint	Theoretical results				Simulation result				Maximum error
	A	E	C	F	A	E	C	F	
Power (N)	48.31	68.68	20.81	14.57	48.33	68.70	20.84	14.58	0.03
Moment (N·m)	0.99	0.63	1.27	0.85	1.01	0.63	1.29	0.86	0.02

Based on the results of table 4-1, it can be seen that the maximum error between the theoretical calculation results and the simulation results is less than 3%, and the error is within a reasonable range [15], which further shows that the theory is consistent with the simulation model, thus proving the correctness of the dynamic model.

As can be seen from figure 5 and figure 6, the simulation movement of the folding baling mechanism is realized from envelope state to recovery state in 2.8s, and the force and torque of each joint increase slowly in 0~2.5s; In 2.5~2.8s, the force and

torque of each joint increase sharply, which is especially obvious in joint A and E. Therefore, the strength check of these two joints should be paid special attention in engineering. In addition, the image analysis can also be designed by extending the length of the electric clamp to find the best matching position of the recovery state as shown in Figure 2, that is, the ideal position of the clamp and the electric clamp to connect the binding wire, which can effectively reduce the adverse effects of the folding baler due to excessive force in the recovery process.

5   Conclusion

(1) Based on the bar baling process, the trajectory of the baling mechanism is determined, and a new type of baling robot is designed and its three-dimensional modeling is carried out.

(2) The forward and inverse kinematics model of the folding bundling mechanism is established and its correctness is verified, which provides a new idea for the structural design optimization of the bundling machine.

(3) Based on Newton-Euler method, the dynamic model of the folding bundling mechanism was established. The correctness of the dynamic model was verified by the force and torque images obtained by simulation analysis, and the force of the joint was clarified, which laid a theoretical foundation for the strength design of the joint. At the same time, the dynamic calculation results can provide guidance for the selection of the optimal matching position of the recovery state of the binding mechanism.

Acknowledgment

References

1. B. Wang, G.T. Liu: Energy conservation and emission reduction and China 's green economic growth Based on the perspective of total factor productivity [J]. China 's industrial economy,57-69(2015).

2. J.M. Hu, H. Xiang: Special steel rod finishing production line process configuration and new technology application [J]. Modern metallurgy 44(06),42-43(2016).

3. Kroyo Miura: Method of Packaging and Deployment of Large Membranes in Space[C]. In: 31th international conference of Asrtonautics federation,22-28(1980).

4. R.Q. Liu, D.K. Tian, Z.Q. Deng. Research status and prospect of space deployable antenna structure [J]. Mechanical design 27(09), 1-10(2010).

5. J.S. Dai, X.L. Ding, H.J. Zou. Principles and types of metamorphic mechanisms [J]. Journal of Mechanical Engineering 41(6),7-12(2005).

6. K. Xu, A.W. Qiao, X.L. Ding. Design and analysis of shear fork bending and unfolding metamorphic mechanism [J]. Mechanical Engineering Journal 56 (05),55-62(2020).

7. Y. Chen, R. Peng, Z. You. Origami of thick panels[J]. Science 6246,349(2015).

8. S.Y. Liu, L.W. Wang. The application and development of folding paper technology in spatial structure [J]. Aerospace return and remote sensing 41(06),114-128(2020).

9. X.L. Ding. Foundation for future large spacecraft: space deployable mechanism [J]. Science and technology report 32(23),84(2014).

10. Y Sun, G.K. Shi, M.F. Dong, Y.L. Mao. Design and implementation of parabolic shaped planar multi-link folding mechanism [J]. Mechanical design 26(02),46-48(2009).

11. J.Z. Zhang, Z.L. Jin, H.B. Feng. Type synthesis of a 3-mixed-DOF protectable leg mechanism of a firefighting multi-legged robot based on G F set theory[J]. Mechanism and Machine Theory,130(2018).

12. Y.Q. Li, Y. Guo, Y. Zhang. A dynamic modeling method for spatial passive over constrained parallel mechanisms based on Newton-Euler method [J]. Journal of Mechanical Engineering 56(11),48-57 (2020).

13. X.X. Chai, Y. Yang, M. Xu. Dynamic modeling and performance analysis of 2-UPR-RPU parallel robot [J]. Journal of Mechanical Engineering 56 (13),110-119(2021).

14. Z. Zhang, B.Y. Chang, X.N. Li. Dynamic analysis of planar two-dimensional mobile deployable mechanism [J]. Mechanical design and research 35(05),50-55(2019).

15. J.Z. Zhang, Z.J Jin, Y.M. Zhao. Dynamics analysis of leg mechanism of six-legged firefighting robot[J]. Journal of Mechanical Science and Technology 32(1),(2018).

Kinematics Analysis of the Over-constrained 7R Pyramid Deployable Truss Structures

Hui Yang[1] and Dongtian Wu[1]

[1] School of Electrical Engineering and Automation, Anhui University, Hefei 230601

Abstract. In the context of space exploration, the existence of space satellites is indispensable. Antennas are an important part of satellites to meet future requirements for new trusses for space antennas. This paper analyzes the kinematics of an over-constrained seven-rotation Pyramid deployable truss structure (7R-PDTS). The degree of freedom is calculated by the screw theory and the degree of freedom calculation formula for the closed-loop over-constrained mechanism based on the loop theory. Using the Product-of Exponentials Formula (POE) to solve the variation on the pose angle of the mechanism and establish the error model of the rotation angle of each joint. The mechanism spaced motion trajectory is converted into a plane motion trajectory by the characteristics of the mechanism and the motion screw. Finally, the closed vector polygon method is used to complete the kinematic analysis of the mechanism. After the mechanism parameters are given, the ADAMS software simulation is used to complete the above-mentioned kinematic analysis.

Keywords: Deployable truss structures, Kinematics analysis, Screw theory, Product-of Exponentials Formula.

1   Introduction

The deployable space truss structures is an important research project in the aerospace field. In the construction of satellites, space stations, and space telescopes, the space deployment mechanism has become a key research object of the aerospace industry due to its large diameter, high rigidity, stable structure, and large folding ratio.

The single-loop over-constrained space mechanism proposed by You and Chen[1-3] as a unit of developable mechanism has received widespread attention. They have conducted research based on Bennett, Myard, and Bricard institutions. In turn, many spatial closed-loop over-constrained foldable mechanisms had been obtained, and related networking and kinematics characteristics have also been studied. In the research process of many scholars on the related problems of deployable mechanism, the screw theory is mostly used for kinematic analysis. Viquerat AD[4] designed a plane symmetrical mechanism linked by Bricard mechanism, and its internal mechanism was described by the D-H coordinate method. B. Siriguleng[5] meet the higher performance requirements of satellite operators at present, a large ring truss deployable antenna is adopted. The ring truss mechanism is composed of 18 parallelogram mechanisms with a diameter of 1.8m in the contracted state and the expanded state. The height is 0.4m.

Huang[6] based on the configuration synthesis method of the spiral theory, studied the curved support structure adopting the tetrahedral unit configuration, and obtained various configurations of large antennas. Shi[7]proposed an over-constrained expandable unit based on the spiral theory and the description of the topological structure of the expandable antenna. Cheng[8] conducted related research on umbrella-shaped deployable mechanisms and obtained a large number of new umbrella-type mechanisms. Wei[9] proposed a reconfigurable deployable Platonic mechanism and a deployable polyhedron mechanism. Dai[10] used the decomposition principle and screw-loop equation to study the flexion and expansion of complex spheres. Wang [11-12] adopted a new construction method, using the Bricard orthogonal mechanism to construct another type of over-constrained closed-loop mechanism. Wu[13]deals with the dynamic modeling and design optimization of a three Degree-of-Freedom spherical parallel manipulator by using the position relation among the bars. Tao[14] analyzed singularities and interfered areas of the spherical parallel mechanism. Li[15]uses a novel numerical algorithm to solve the inverse kinematics for 6-DOF robot. Yu[16] adopted the twist coordinates and the POE improved the efficiency and accuracy of error calculation. Wang[17] constructed a Satellite synthetic aperture radar (SAR) antenna using a quadrangular pyramid expandable mechanism.

According to the theme of the 5th IEEE/IFToMM International Conference on Reconfigurable Mechanisms and Robots, an over-constrained 7R-PDTS was proposed for kinematic analysis. The screw theory and the calculation formula for the degree of freedom are used to verify that the mechanism is a single-freedom over-constrained mechanism. Then the pose change matrix of the mechanism is established through POE. The spatial motion analysis of this mechanism is transformed into plane motion analysis, and the simulation modeling on position analysis further verifies the feasibility of the theoretical model.

2   Introduction of 7R-PDTS

The over-constrained 7R Pyramid deployable truss structure is composed of seven rotation pairs, two triangles $\triangle CDE$ and $\triangle CBD$ at the bottom of the isosceles triangle $\triangle ADE$, and two corresponding folding rods. The seven rotation axes of the mechanism are all parallel to the bottom. The configuration diagram and topology diagram of the mechanism is shown in Fig.1.
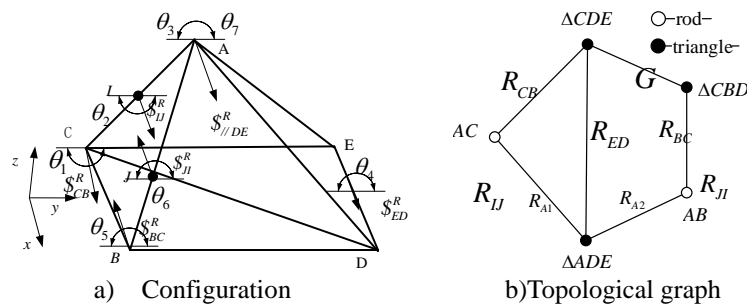

a)   Configuration   b)Topological graph
Fig.1 Pyramid deployable truss structures of 7R

The reference coordinate system *B-xyz* established according to the PDTS shown in Fig.1, and then gives the variation of each point. Figure.1 reveals that the coordinates of the following points are $A(0,a_1,a_2)$,$B(l_2/2,0,0)$,$C(-l_2/2,0,0)$,$D(l_2/2,l1,0)$,$E(-l_2/2,l_1,0)$,$I(-l_2/4,a_1/2)$.

3 The mobility of structures

3.1 DOF-based Screw

From the over-constrained 7R-PDTS configuration diagram and its coordinates in the reference coordinate system, the rotation axis of the two loops of the mechanism can be expressed in the form of rotation according to the screw theory, and then two the screw system of the loop uses the calculation of the reciprocal spiral to find the common constraints contained in the mechanism loop and then uses the degree of freedom calculation formula to solve the degree of freedom of the mechanism.

According to the calculation of the screw theory, the motion screw of the two-loop shafts of the mechanism can be obtained as shown in Table 1.

Table 1. The screw systems of the two loops shown in Fig.1

Loop-1	Loop-2
$\$_{ED}^{R} = \begin{pmatrix} 1 & 0 & 0 & 0 & 0 & 0 \end{pmatrix}^{T}$	$\$_{ED}^{R} = \begin{pmatrix} 1 & 0 & 0 & 0 & 0 & 0 \end{pmatrix}^{T}$
$\$_{A1}^{R} = \begin{pmatrix} 1 & 0 & 0 & 0 & a_2/2 & l_3 \end{pmatrix}^{T}$	$\$_{A2}^{R} = \begin{pmatrix} -1 & 0 & 0 & 0 & -a_2/2 & -l_3 \end{pmatrix}^{T}$
$\$_{IJ}^{R} = \begin{pmatrix} 1 & 0 & 0 & 0 & a_2 & -a_1 \end{pmatrix}^{T}$	$\$_{JI}^{R} = \begin{pmatrix} 1 & 0 & 0 & 0 & a_2 & -a_1 \end{pmatrix}^{T}$
$\$_{CB}^{R} = \begin{pmatrix} 1 & 0 & 0 & 0 & 0 & l_1 \end{pmatrix}^{T}$	$\$_{BC}^{R} = \begin{pmatrix} -1 & 0 & 0 & 0 & 0 & -l_1 \end{pmatrix}^{T}$

Further calculation of the motion screw system of the loops can be obtained, the motion spirals system of loop-1 and loop-2 have the same motion screw base, and the motion screw basis of the mechanism is shown in the figure below.

$$\begin{vmatrix} 1 & 0 & 0 & 0 & 0 & 0 \\ 0 & 0 & 0 & 0 & 1 & 0 \\ 0 & 0 & 0 & 0 & 0 & 1 \end{vmatrix}$$

Fig.2 Motion screw basis of 7R-PDTS

Then three sets of solutions can be obtained by solving the anti-screws by screw theory, which means that the mechanism contains three public constraints. Taking into account the influence of public constraints, the calculation of the degree of freedom of the mechanism adopts the calculation formula of the degree of freedom of the deployable truss structures based on the loop theory

$$F = (3S + 2U + R) - (6 - d)l + u$$
$$= 7 - (6 - 3) \times 2 = 1 \tag{1}$$

In the formula, *F* is the number of degrees of freedom, *S* is the number of ball pairs, *U* is the number of universal pairs, *R* is the number of rotation pairs, *d* is the number of

public constraints of the mechanism, and u is the number of redundant constraints after the public constraints are released.

3.2   Mobility-based POE

There are two loops in the over-constrained 7R-PDTS. The corresponding inertial coordinate system $\{S\}$ and the tool coordinate system $\{T\}$ are established for loop 1 and loop 2, respectively, and based on the Lie group, Lie algebra and screw theory, respectively. The two loops establish a spinner coordinate system. The establishment of the coordinate system is shown in Fig.3.
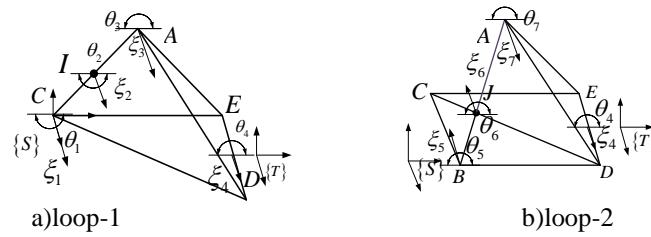

a)loop-1   b)loop-2

Fig.3 Coordinate system of loops

When the rotation angle of each joint of the two loops is 0, the change of angle between the inertial coordinate system of loop 1 and the tool coordinate system is $g_{ST}(0)$, and its value is shown in Eq.(2).

$$g_{ST}(\boldsymbol{0}) = \begin{vmatrix} 1 & & & l_2/2 \\ & 1 & & l_1 \\ & & 1 & 0 \\ & & & 0 \end{vmatrix} \tag{2}$$

Judging from the motion torque of the two loops of the over-constrained 7R-PDTS and the construction of its configuration, the motion trajectories of the two loops are completely equal, so analyze loop 1 by the POE. For each joint in the mechanism loop, a unit motion screw ξ_i can be constructed, which represents the motion of the i-th joint. At this time, all joints except this joint are fixed in the initial position. Then for the rotating pair, it can be expressed as

$$\boldsymbol{\xi}_i = \begin{bmatrix} \boldsymbol{\omega}_i & \boldsymbol{r}_i \times \boldsymbol{\omega}_i \end{bmatrix}^T \tag{3}$$

Then the position is established by the inertial coordinate system in loop 1 of Fig. 3-a, and the rotation calculation result of each joint position according to Eq.(3) is shown in the following formula

$$\begin{cases} \boldsymbol{\xi}_1 = \begin{bmatrix} 1 & 0 & 0 & 0 & 0 & 0 \end{bmatrix}^T \\ \boldsymbol{\xi}_2 = \begin{bmatrix} 1 & 0 & 0 & l_2 & a_1/2 & a_2/2 \end{bmatrix}^T \\ \boldsymbol{\xi}_3 = \begin{bmatrix} 1 & 0 & 0 & l_2/2 & a_1 & a_2 \end{bmatrix}^T \\ \boldsymbol{\xi}_4 = \begin{bmatrix} 1 & 0 & 0 & l_2/2 & l_1 & 0 \end{bmatrix}^T \end{cases} \tag{4}$$

According to the obtained moving screw in Eq.(4), it can be solved according to Rodriguez formula (5), where I is the identity matrix

$$e^{\theta\hat{\omega}} = I + \frac{\hat{\omega}}{\|\omega\|}\sin\theta + \frac{\hat{\omega}^2}{\|\omega\|^2}(1-\cos\theta) \tag{5}$$

Where $\widehat{\omega}$ represents the three-dimensional vector ω antisymmetric matrix, which can be expressed as Eq.(6)

$$\hat{\omega} = \begin{vmatrix} 0 & -x_3 & x_2 \\ x_3 & 0 & -x_1 \\ -x_2 & x_1 & 0 \end{vmatrix} \tag{6}$$

Then POE can be expressed as Eq.(7)

$$e^{\theta\hat{\xi}} = \begin{vmatrix} e^{\theta\hat{\omega}} & (I - e^{\theta\hat{\omega}})(\omega \times v) + \theta\omega\omega^T v \\ \mathbf{0} & 1 \end{vmatrix}, \quad \omega \neq 0 \tag{7}$$

Therefore, the forward kinematic of POE in 7R-PDTS loop 1 is solved as follows

$$g_{ST}(\theta) = e^{\theta_1\hat{\xi}_1}e^{\theta_2\hat{\xi}_2}e^{\theta_3\hat{\xi}_3}e^{\theta_4\hat{\xi}_4}g_{ST}(\mathbf{0})$$

$$= \begin{bmatrix} 1 & 0 & 0 & l_2(\theta_2 + 2\theta_3 + 2)/4 \\ 0 & c\beta & -s\beta & n_y \\ 0 & s\beta & c\beta & n_z \\ 0 & 0 & 0 & 1 \end{bmatrix} \tag{8}$$

where $\beta = \sum \theta_i$ ($i=1,2,3,4$),

$$n_y = \frac{2l_1(c\beta + s\beta) - a_2c(\theta_1 + \theta_2) - a_1s(\theta_1 + \theta_2) - a_2c\theta_1 - a_1s\theta_1}{2} + a_2c(\beta - \theta_4) + a_1s(\beta - \theta_4) - l_1s(\beta - \theta_4)$$

$$n_z = \frac{l_1(s\beta - c\beta) - a_1c(\theta_1 + \theta_2) + a_2s(\theta_1 + \theta_2) + a_1c\theta_1 - a_2s\theta_1}{2} - a_1c(\beta - \theta_4) + l_1c(\beta - \theta_4) + a_2s(\beta - \theta_4)$$

For the over-constrained 7R-PDTS, the key joints in the process of folding and stretching are I and J, The joint points directly connected with the two joints are A, B, and C, so in the process of inverse solution, the focus is on solving the rotation angles of ξ_2 and ξ_3. Give θ_1 as an input rotating pair, note that the principle of keeping the position unchanged , then choose the point of ξ_4 is taken as q.

$$e^{\theta_4\hat{\xi}_4}q = q \tag{9}$$

Integrated Eq.(8) and Eq.(9) are available

$$e^{\theta_2\hat{\xi}_2}e^{\theta_3\hat{\xi}_3}q = g_{ST}(\theta)g^{-1}{}_{ST}(\mathbf{0})e^{-\theta_1\hat{\xi}_1}q \tag{10}$$

Let $g_{ST}(\theta)g_{ST}^{-1}(0)e^{-\theta1\xi1}q = q_w$, and $q_w = [q_x\ q_y\ q_z]$. The ξ_2 and ξ_3 are shown in Fig.4

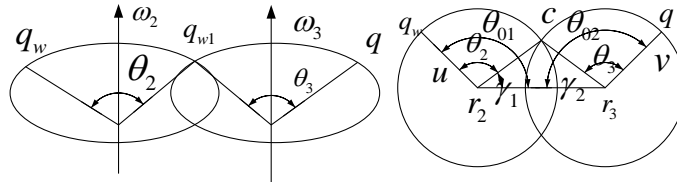**Fig.4** The spiral motion and plane projection of ξ_2 and ξ_3

The defined vector is shown in the following formula

$$\begin{cases} \boldsymbol{u} = \boldsymbol{q}_w - \boldsymbol{r}_2 & \boldsymbol{v} = \boldsymbol{q} - \boldsymbol{r}_3 \\ \boldsymbol{r}_{23} = \boldsymbol{r}_2 - \boldsymbol{r}_3 & \boldsymbol{r}_{32} = \boldsymbol{r}_3 - \boldsymbol{r}_2 \end{cases} \tag{11}$$

Then θ_{01} can be obtained as follows

$$\begin{aligned} \theta_{01} &= a\tan 2(\boldsymbol{\omega}^T(\boldsymbol{u}\times\boldsymbol{r}_{32}), \boldsymbol{u}^T\boldsymbol{r}_{32}) \\ &= a\tan(\frac{8(a_2 \cdot q_y - a_1 \cdot q_z)}{(l_1 - l_2) \cdot (q_x - \dfrac{l_2}{4}) - a_1(a_1 - 2q_y) + a_2(a_2 - 2q_z)}) \end{aligned} \tag{12}$$

According to the law of cosines, γ_1 can be computed.

$$\begin{aligned} \gamma_1 &= a\arccos(\frac{\|\boldsymbol{u}\|^2 + \|\boldsymbol{r}_{23}\|^2 - \|\boldsymbol{v}\|^2}{2\|\boldsymbol{u}\|\|\boldsymbol{r}_{23}\|}) \\ &= a\cos(\frac{(\dfrac{a_1 - 2q_y}{2})^2 + (\dfrac{a_2 - 2q_z}{2})^2 - (\dfrac{l_1 - 2l_2}{4})^2 + (\dfrac{l_1 - l_2}{4})^2 + (\dfrac{l_2 - 4q_x}{4})^2 + \dfrac{a_1^2 - 3a_2^2}{4} - (a_1 - l_1)^2}{2\sqrt{((\dfrac{a_1 - 2q_y}{2})^2 + (\dfrac{a_2 - 2q_z}{2})^2 + (\dfrac{l_2 - 4q_x}{4})^2) \cdot ((\dfrac{l_1 - 2l_2}{4})^2 + \dfrac{a_1^2 + a_2^2}{4})}}) \end{aligned} \tag{13}$$

Then the value of θ_2 can be obtained

$$\theta_2 = \theta_{01} \pm \gamma_1 \tag{14}$$

Taking Eq.(12) and Eq.(13) for example, θ_3 can be derived

$$\begin{aligned} \theta_{02} &= a\tan 2(\boldsymbol{\omega}^T(\boldsymbol{v}\times\boldsymbol{r}_{23}), \boldsymbol{v}^T\boldsymbol{r}_{23}) \\ &= a\tan(-\frac{4a_2 l_1}{2a_2^2 + (l_1 - 2l_2)(l_1 - l_2) + a_1(a_1 - l_1)}) \end{aligned} \tag{15}$$

$$\begin{aligned} \gamma_2 &= a\cos(\frac{\|\boldsymbol{v}\|^2 + \|\boldsymbol{r}_{23}\|^2 - \|\boldsymbol{u}\|^2}{2\|\boldsymbol{v}\|\|\boldsymbol{r}_{23}\|}) \\ &= \frac{(\dfrac{l_1 - 2l_2}{4})^2 - (\dfrac{a_2 - 2q_z}{2})^2 - (\dfrac{a_1 - 2q_y}{2})^2 + (\dfrac{l_1 - l_2}{4})^2 - (\dfrac{l_2 - 4q_x}{4})^2 + \dfrac{a_1^2 + 5a_2^2}{4} + (a_1 - l_1)^2}{2\sqrt{(\dfrac{l_1 - 2l_2}{4})^2 + a_2^2 + (a_1 - l_1)^2}\sqrt{(\dfrac{l_1 - l_2}{4})^2 + \dfrac{a_1^2 + 5a_2^2}{4}}} \end{aligned} \tag{16}$$

$$\theta_3 = \theta_{02} \pm \gamma_2 \tag{17}$$

3.3   Closed vector solution

3.3.1   Pose analysis of *IC* and *AE*
The configuration of the 7R-PDTS is completely symmetrical, and the position and posture of loop 1 of the 7R-PDTS mobile on the *yoz* plane, and the directions of the rotation axes of the joints of each loop are parallel. The screw movement relationship

is also symmetrical. Therefore, the kinematics analysis of 7R-PDTS can be simplified to the kinematics analysis of loop 1. At this point, the 7R-PDTS loop 1 mechanism can be equivalent to a plane four-bar mechanism for related analysis. The simplified process is shown in Fig.5.Establish the coordinate system for the simplified planar four-bar mechanism as shown in Fig.6, and use the closed vector polygon rule to solve the kinematics of this mechanism.
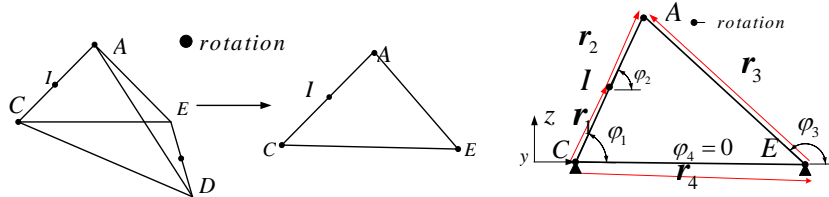

Fig.5 Simplified structure diagram   **Fig.6** The model coordinate system of loop-1

According to Fig.6, it can be obtained according to the closed vector polygon rule

$$\vec{r}_1 + \vec{r}_2 = \vec{r}_3 + \vec{r}_4 \tag{18}$$

Two formulas can be obtained by solving the real and imaginary parts of the vector

$$\begin{cases} r_2 c\varphi_2 = r_3 c\varphi_3 + r_4 - r_1 c\varphi_1 \\ r_2 s\varphi_2 = r_3 s\varphi_3 - r_1 s\varphi_1 \end{cases} \tag{19}$$

Simplify Eq.(19) to get the equation of φ_3 and φ_2 with φ_1 as the variation

$$\begin{cases} (c\varphi_1 - h_1)c\varphi_3 + s\varphi_1 s\varphi_3 = -h_3 c\varphi_1 + h_5 \\ h_1 = \dfrac{r_4}{r_1} \quad h_3 = \dfrac{r_4}{r_3} \quad h_5 = \dfrac{r_4^2 + r_1^2 - r_2^2 + r_3^2}{2r_1 r_3} \end{cases} \tag{20}$$

The half-angle formula $x=\tan(\varphi_3/2)$ can also be identified with the Eq.(20),It's transformed into the form of a quadratic polynomial, namely

$$Ax^2 + Bx + C = 0 \tag{21}$$

In the Eq.(21), $A=-h_1+(1-h_3)c\varphi_1+h_5$、 $B=-2s\varphi_1$、 $C=h_1-(1+h_3)c\varphi_1+h_5$. Finally can be solved

$$\varphi_3 = 2\arctan\left(\frac{-B \pm \sqrt{B^2 - 4AC}}{2A}\right) \tag{22}$$

In the same way, φ_2 can be obtained

$$\begin{cases} \varphi_2 = 2\arctan\left(\dfrac{-B \pm \sqrt{B^2 - 4DE}}{2D}\right) \\ h_2 = \dfrac{r_4}{r_2} \quad h_4 = \dfrac{-r_4^2 - r_1^2 - r_2^2 + r_3^2}{2r_1 r_3} \end{cases} \tag{23}$$

Where $D=-h_1+(1+h_2)c\varphi_1+h_4$,$E=h_1-(1-h_2)c\varphi_1+h_4$.

4.2.2 Angular velocity of *IC* and *AE*

The input rod is set to *IC*, then φ_1 is a known angle, so the Eq.(19) is used to differentiate φ_1, and the transformation matrix form can be obtained as the following equation

$$\begin{bmatrix} -r_2 s\varphi_2 & r_3 s\varphi_3 \\ r_2 c\varphi_2 & -r_3 c\varphi_3 \end{bmatrix} \begin{bmatrix} \dfrac{d\varphi_2}{d\varphi_1} \\ \dfrac{d\varphi_3}{d\varphi_1} \end{bmatrix} = \begin{bmatrix} r_1 s\varphi_1 \\ -r_1 c\varphi_1 \end{bmatrix} \tag{24}$$

Then $\boldsymbol{\omega}_2$ and $\boldsymbol{\omega}_3$ as shown in

$$\begin{cases} \omega_2 = \dfrac{d\varphi_2}{d\varphi_1} = -\dfrac{r_1 s(\varphi_1 - \varphi_3)}{r_2 s(\varphi_2 - \varphi_3)} \omega_1 \\ \omega_3 = \dfrac{d\varphi_3}{d\varphi_1} = -\dfrac{r_1 s(\varphi_1 - \varphi_2)}{r_2 s(\varphi_2 - \varphi_3)} \omega_1 \end{cases} \tag{25}$$

4.2.3 Angular acceleration of *IC* and *AE*

Find the second-order differential of Eq.(22) and Eq.(23) with respect to *t*, where $\varphi_1 = \mathrm{atan}(a_2/a_1)$-*t*.

$$\begin{cases} \varepsilon_2 = \dfrac{d^2\varphi_2}{dt^2} = J_{b1} + J_{b2} - J_{b3} + J_{b4} + J_{b5} \\ \varepsilon_3 = \dfrac{d^2\varphi_3}{dt^2} = J_{c1} + J_{c2} + J_{c3} \end{cases} \tag{26}$$

4   Simulation of 7R-PDTS

Establishing the model of a_1=169.708,a_2=492.679,l_1=800,l_2=600 in ADAMS, given a drive at *C*. The folding process is shown in Fig.7. The angle value of the rotation pair can be obtained as shown in Fig.8 . Extract the value of parameter θ_1=70.9 in Fig.8, that is, the output angle values of the rotation pair at point *I* and the rotation pair at point *A* in the closed position, The inverse solution of the POE the error results can be obtained as shown in Table 2. The data diagram of the pose angles φ_2 and φ_3 is shown in Fig.9. In the simulation, the rod *AI* and rod *AE* are shown in Fig.7, the angular velocity φ_2 and φ_3 is shown in Fig.10 and the angular acceleration φ_2 and φ_3 is shown in Fig. 11. The kinematic characteristics of the mechanism theory verified by simulation results and demonstrates the movement characteristics of the mechanism.

Table.2 POE value of the PDTS

	θ_1	θ_2	θ_3	θ_4
Simulation value	70.9	179.7906	-70.9452	-37.9454
Theory value	-	174.5396	-77.0865	-
Error value	-	-0.0292	0.0866	-
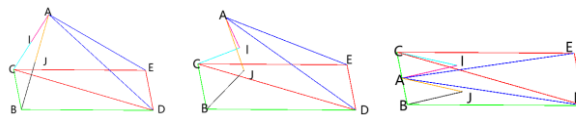
a)Deployed state b)mid state c)Folded state
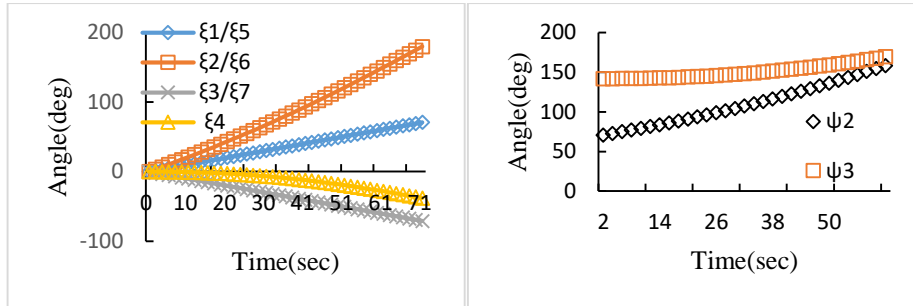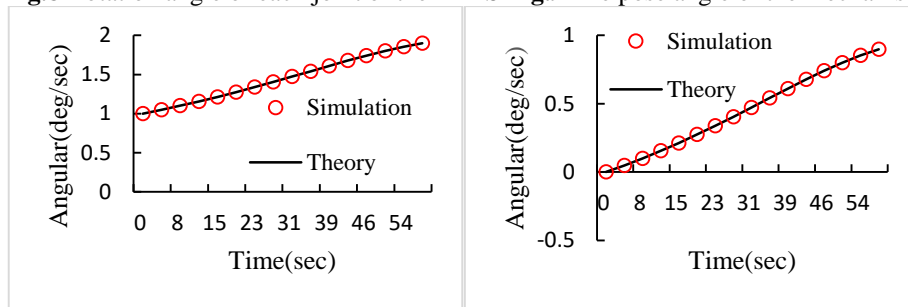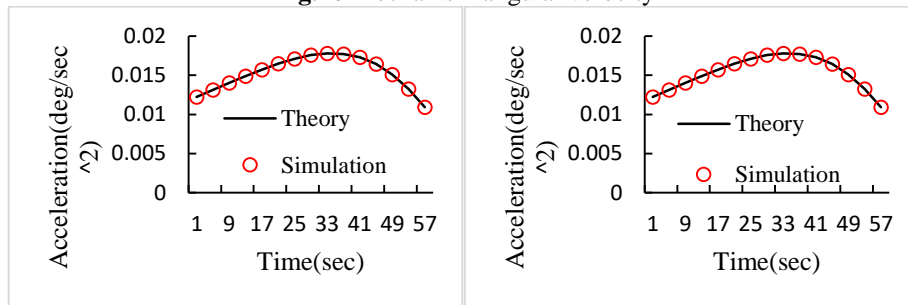**Fig.7** The movement process of the 7R-PDTS

Fig.8 Rotation angle of each joint of the PDTS **Fig.9** The pose angle of the mechanism

a)Angular velocity of φ_2 b)Angular velocity of φ_3
Fig.10 Mechanism angular velocity

a)Angular acceleration of φ_2 b)Angular acceleration of φ_3
Fig.11 Angular acceleration of mechanism

5   Conclusion

1) An over-constrained 7R-PDTS is proposed. Based on the analysis of its configuration, the screw theory is used to analyze that it is an over-constrained mechanism with a single degree of freedom and symmetrical loop motion trajectory.

2) Calculate the position transformation in the loop based on the POE, and further obtain the rotation angle of each joint of the mechanism through the inverse POE solution, and the inverse solution to analyze the error of the mechanism movement process.

3) Through the configuration analysis of the mechanism and the establishment of the motion screw, the motion analysis process of the over-constrained 7R-PDTS as a space mechanism is transformed into a plane mechanism for analysis, and its kinematics related analysis is completed.

Appendix

Parameters of Eq.(31) as shown in

$$J_{b1} = \frac{(2J_6((4\sqrt{J_1}J_3^4 c\rho + 4J_4 J_7 a_1^2 + 4J_4 J_7 a_2^2 - 16J_3 J_7 a_1 s\rho + 8J_3 a_1^2 l_1 s\rho + 8J_3 a_2^2 l_1 s\rho)))}{\sqrt{J_1} J_2 J_3^4}$$

$$J_{b2} = (2J_6 J_8 s\rho(2J_3 + 4l_1))/J_3)(J_3 J_5 J_8 J_2^3 + 2J_3 J_6 s\rho + 4J_6 l_1 s\rho)))/(J_2^3 J_4 (J_8 J_6^2 + 1)^2)$$

$$J_{b3} = (4s\rho - (32J_7 a_1^2 (2c^2\rho - 1) + 32J_7 a_2^2 (2c^2\rho - 1) + 32J_3 a_1 l_1 c\rho + 32J_3 a_2 l_1 c\rho$$
$$-64J_3 J_7 a_1 c\rho))/\sqrt{J_2} J_3^4$$

$$J_{b4} = (128(J_4 J_7 a_1^2 + J_4 J_7 a_2^2 - 4J_3 J_7 a_1 s\rho + 2J_3 a_1^2 l_1 s\rho + 2J_3 a_2^2 l_1 s\rho)^2/(\sqrt[3]{J_1} J_3^8)/J_2$$

$$J_{b5} = (2J_5 J_8 s\rho(4J_3 + 8l_1))/J_3 + (16J_6 s^2\rho(J_3 + 2l_1)^2)/(J_2^3 J_3^2))/(J_8 J_6^2 + 1)$$

$$J_{c1} = ((16J_{13} J_{15}^2 s^2\rho)/J_{10}^3 - (4s\rho + (\sqrt{2}J_{11}^2/2J_9^{3/2}) + (\sqrt{2}(4s^2\rho - 4c^2\rho$$
$$-(c\rho(J_{12}l_1 + 1)(4J_{14}l_1 + 4J_{15}c\rho - J_{C12}))/\sqrt{J_9}))/J_{10}$$

$$Jc_{12} = J_{12} J_{14}(2a_2^2 + 2l_1^2 + 2(a_1 - l_1)^2 + 4J_{15} s^2\rho(J_{12}c\rho + 1) + 2J_{15}c\rho(J_{14}l_1 - c\rho(J_{12}c\rho + 1)$$
$$+(J_{12} J_{14}(a_2^2 + l_1^2 + (a_1 - l_1)^2))/2)$$

$$J_{c2} = (4J_{13} J_{15}c\rho)/J_{10}^2 + (8J_{15} J_{16} s\rho/J_{10}^2)/(J_{13}^2/J_{10}^2 + 1)$$

$$J_{c3} = \frac{(((4c\rho + \sqrt{2}J_{11}/\sqrt{J_9})/J_{10} + (4J_{13} J_{15} s\rho)/J_{10}^2)(2J_{13} J_{16}/J_{10}^2 + 4J_{13}^2 J_{15} s\rho/J_{10}^3)}{(J_{13}^2/J_{10}^2 + 1)^2}$$

$$J_1 = 4s^2\rho - (2l_1/J_3 + (a_1^2 - 4l_1 a_1 + a_2^2)/(a_1^2 + a_2^2) + (c\rho(2l_1 - J_3))/(a_1^2 + a_2^2))$$
$$((4a_1^2 - 16l_1 a_1 + 4a_2^2)/(a_1^2 + a_2^2) - 8l_1/J_3 + (c\rho(8l_1 + 4J_3))/J_3$$

$$J_2 = (2a_1^2 - 8l_1 a_1 + 2a_2^2)/(a_1^2 + a_2^2) - 4l_1/J_3 + (c\rho(4l_1 + 2J_3))/J_3$$

$$J_3 = \sqrt{a_1^2 + a_2^2}, \quad J_4 = s(2t - 2\operatorname{atan}(a_2/a_1))$$

$$J_5 = 2c\rho + (8J_4 a_1^2 l_1^2 + 16J_3 a_1^2 l_1 s\rho - 32J_3 a_1^2 l_1 s\rho + 8J_4 a_2^2 l_1^2 + 16J_3 a_2^2 l_1^2 s\rho)/(\sqrt{J_1} J_3^4)$$

$$J_6 = 2s\rho + \sqrt{J_2}, \quad J_7 = l_1^2, \quad J_8 = 1/\sqrt{J_2}$$

$$J_9 = 2s^2\rho + ((l_1\sqrt{a_1^2/4 + a_2^2/4} - c\rho(l_1/\sqrt{a_2^2 + (a_1 - l_1)^2} + 1) + (a_2^2 + l_1^2 + (a_1 - l_1)^2)$$
$$/(2\sqrt{a_2^2 + (a_1 - l_1)^2}\sqrt{a_1^2/4 + a_2^2/4})(4c\rho(l1/\sqrt{a_2^2 + (a_1 - l_1)^2} - 1) + 4l_1/\sqrt{a_1^2/4 + a_2^2/4})$$
$$-(2a_2^2 + 2l_1^2 + 2(a_1 - l_1)^2)/(\sqrt{a_2^2 + (a_1 - l_1)^2}\sqrt{a_1^2/4 + a_2^2/4}))/2$$

$$J_{10} = 2c\rho \frac{l_1}{(\sqrt{a_2^2 + (a_1 - l_1)^2} - 1)} + \frac{2l_1}{\sqrt{a_1^2/4 + a_2^2/4}} - \frac{(a_2^2 + l_1^2 + (a_1 - l_1)^2)}{\sqrt{a_2^2 + (a_1 - l_1)^2}\sqrt{a_1^2/4 + a_2^2/4}}$$

$$J_{10} = 2c\rho(l_1/(\sqrt{a_2^2 + (a_1 - l_1)^2} - 1) + \frac{2l_1}{\sqrt{a_1^2/4 + a_2^2/4}} - \frac{a_2^2 + l_1^2 + (a_1 - l_1)^2}{\sqrt{a_2^2 + (a_1 - l_1)^2}\sqrt{a_1^2/4 + a_2^2/4}}$$

$$J_{11} = 4c\rho s\rho - 2s\rho(\frac{l_1}{\sqrt{a_2^2 + (a_1 - l_1)^2} - 1)(l_1/\sqrt{a_1^2/4 + a_2^2/4})} - c\rho(\frac{l_1 - \sqrt{a_2^2 + (a_1 - l_1)^2}}{\sqrt{a_2^2 + (a_1 - l_1)^2}})$$

$$+ \frac{(a_2^2 + l_1^2 + (a_1 - l_1)^2)}{2\sqrt{a_2^2 + (a_1 - l_1)^2}\sqrt{a_1^2/4 + a_2^2/4}} + (\frac{s\rho}{2}(\frac{l_1}{\sqrt{a_2^2 + (a_1 - l_1)^2}} + 1)(4c\rho(l_1\sqrt{a_2^2 + (a_1 - l_1)^2} - 1)$$

$$+ \frac{4l_1}{\sqrt{a_1^2/4 + a_2^2/4}} - \frac{2(a_2^2 + l_1^2 + (a_1 - l_1)^2)}{\sqrt{a_2^2 + (a_1 - l_1)^2}\sqrt{a_1^2/4 + a_2^2/4})/2})$$

$$J_{12} = \left(a_2^2 + (a_1 - l_1)^2\right)^{-\frac{1}{2}}, J_{13} = 2s\rho + \sqrt{2J_9}, J_{14} = \left(a_1^2/4 + a_2^2/4\right)^{-\frac{1}{2}}, J_{15} = J_{12}l_1 - 1$$

$$J_{16} = 2c\rho + \frac{\sqrt{2}J_{11}}{2\sqrt{J_9}}$$

Where $\rho = t\text{-atan}(a_2/a_1)$.

References

1. Chen Y, You Z . Spatial 6 R linkages based on the combination of two Goldberg 5R linkages. Mechanism and Machine Theory 42(11) :1484-1498(2007).
2. Chen Y, You Z . An Extended Myard Linkage and its Derived 6R Linkage. Journal of Mechanical Design, 130(5):680-682(2008).
3. Yang F.F, You Z ,Chen Y. Mobile assembly of two Bennett linkages and its application to transformation between cuboctahedron and octahedron. Mechanism and Machine Theory, 145:(2020).
4. Viquerat A D , Hutt T , Guest S D . A plane symmetric 6R foldable ring. Mechanism & Machine Theory, 63:73-88(2013).
5. Siriguleng B, Zhang W. Liu T. Liu Y.Z.. Vibration modal experiments and modal interactions of a large space deployable antenna with carbon fiber material and ring-truss structure. Engineering Structures, 207:(2020).
6. Huang Z , Ma X , Hu F ,. Synthesis and networking of tetrahedral deployable mechanism based on screw theory. IOP Conference Series Materials Science and Engineering, 892:012-097(2020).
7. Shi C , Guo H , Zhang S , et al. Configuration synthesis of linear foldable over-constrained deployable unit based on screw theory – Science Direct. Mechanism and Machine Theory, 156（2021）
8. Cheng P ,H Ding, Cao W A . A novel family of umbrella-shaped deployable mechanisms constructed by multi-layer and multi-loop spatial linkage units. Mechanism and Machine Theory, 161:(2020).
9. Wei G ,Dai J . Reconfigurable and Deployable Platonic Mechanisms with a Variable Revolute Joint. In: Lenarčič J., Khatib O.(eds) Latest Advances in Robot Kinematics. Springer, Dordrecht, (2014).
10. Dai J S , Li D , Zhang Q . Mobility analysis of a complex structured ball based on mechanism decomposition and equivalent screw system analysis. Mechanism & Machine Theory, 39(4):445-458(2004).

11. Wang J ,Kong X . Deployable polyhedron mechanisms constructed by connecting spatial single-loop linkages of different types and/or in different sizes using S joints. Mechanism & Machine Theory, 124:211-225(2018).
12. J Wang, Kong X .A novel method for constructing multi-mode deployable polyhedron mechanisms using symmetric spatial RRR compositional units. In: Computers and Information in Engineering Conference, ASME,(2018).
13. Wu, S. Caro, S.-P. Bai, J. Kepler, Dynamic modeling and design optimization of a 3-DOF spherical parallel manipulator, Robot. and Autonomous Systems.62(10):1377-1386(2014).
14. Tao Z ,Qi A . Interference analysis and workspace optimization of 3-RRR spherical parallel mechanism. Mechanism and Machine Theory, 69:62-72(2013).
15. Li J ,Yu H , Shen N Y , et al. A novel inverse kinematics method for 6-DOF robots with non-spherical wrist. Mechanism and Machine Theory, 157(2021).
16. Yu J , Zhao Y , Wang H , et al. Tolerance analysis of mechanical assemblies based on the product of exponentials formula. Proceedings of the Institution of Mechanical Engineers Part B Journal of Engineering Manufacture 232(14):2616-2626 (2018).
17. Wang Y , Guo H , Yang H . Deployment analysis and optimization of a flexible deployable structure for large synthetic aperture radar antennas. Proceedings of the Institution of Mechanical Engineers Part G Journal of Aerospace Engineering, 230(4):212-213 (2016).

Singularity Crossing of Various Configurations of a 3-(rR)PS Metamorphic Parallel Mechanism Through Dynamics Modelling and Trajectory Planning

Latifah Nurahmi[1] and Dongming Gan[2]

[1] Department of Mechanical Engineering, Institut Teknologi Sepuluh Nopember,
60111 Surabaya, Indonesia
latifah.nurahmi@me.its.ac.id,
[2] Polytechnic Institute, Purdue University, West Lafayette,
IN 47907, USA,
dgan@purdue.edu

Abstract. This paper presents dynamic models of 3-(rR)PS metamorphic parallel mechanism to pass through singularities. The dynamic models are established by using Lagrange formulation and two conditions to cross singularities are presented. The first condition is based on the consistency condition where the uncontrollable motion should be reciprocal to the wrench matrix. The denominator of inverse Jacobian is its determinant whose value is zero at singularities. This singularity can be removed by compensating the numerator to be zero. Both numerator and denominator are null and this indeterminate form becomes the second condition. Finite input forces are obtained by computing second time-derivative of Lôpital's rule over the indeterminate form.

Keywords: singularities, dynamic, L'Hopital rule, reconfiguration

1 Introduction

When parallel mechanisms are subjected to singularities, their performance in terms of motion transmission and stiffness degenerates which consequently reduces their payload capacity. Hence, it is also necessary to investigate the singularities from dynamic point of view.

By taking into account Type 2 singularities, path planning for both rigid and flexible 5-bar linkages were analysed in [1–3]. Forces discontinuity can be avoided by computing the consistency condition, namely reciprocal product between the uncontrollable motion and the wrench matrix. The numerical results were verified by conducting some experiments in [4]. The consistency condition alone, however, was not sufficient for the inverse dynamics near singularities to be finite, therefore a new criterion was added in [5], namely the vanishing conditions of time derivative of consistency condition. In addition to the consistency condition, the time derivative of determinant of Jacobian was defined to be the

second condition in [6]. In this paper, this approach is extended up to second time derivative and kinematics properties at singularity are determined.

This paper focuses on the formulation of singularity-free dynamic models of the 3-(rR)PS metamorphic parallel mechanism shown in Fig. 1 [7–9]. The consistency condition that the uncontrollable motion should be reciprocal to the wrench, will still be respected in this paper. In forward Jacobian, its determinant becomes denominator and it vanishes at singularities. Fortunately, this singularity is removable by compensating the numerator to be zero and it is called the indeterminate form of zero [10]. This form becomes the second condition to be respected to pass through singularities. At this instant, the first time-derivative of L'Hôpital's rule is applied, however this is not sufficient to determine finite values of input torques for few manipulators. Therefore, the second time-derivative should be computed and the kinematic properties (velocities, accelerations and jerks) are introduced for trajectory planning.

Fig. 1: 3-(rR)PS Metamorphic Parallel Mechanism

2   Types of configurations

The 3-(rR)PS metamorphic parallel manipulator shown in Fig. 1 is composed of three (rR)PS legs where (rR) is called metamorphic joint having $\mathbf{m}_i$ and $\mathbf{n}_i$ axes $(i = 1, 2, 3)$. Both axes are orthogonal to each other. Worm gear system is used to reconfigure (rR) joint. Thanks to this reconfiguration system, axis $\mathbf{n}_i$ can be discreetly orientated.

Figure 2(a) and 2(b) respectively show fix $\mathcal{A}(x, y, z)$ and moving $\mathcal{B}(u, v, w)$ coordinate systems. The origins of fix and moving coordinate systems are re-

spectively O and O'. The (rR) joint is attached to the base and is denoted by point A_i. The spherical joint is mounted to the moving platform and is denoted by point B_i. The base and moving platform are equilateral triangles of circum-radius a and b, respectively. The change of axis $\mathbf{n}_i$ of (rR) joint yields the change of angle α. This paper considers only at $\alpha = 0$ deg when all axes $\mathbf{n}_i$ intersect at point Q. The design parameter β can also be modified, such that $\beta \in [0, 90]$ and three configurations will be investigated in more details in this paper, as follows:

- Configuration 1: $\beta = 30$ deg
- Configuration 2: $\beta = 54.7$ deg
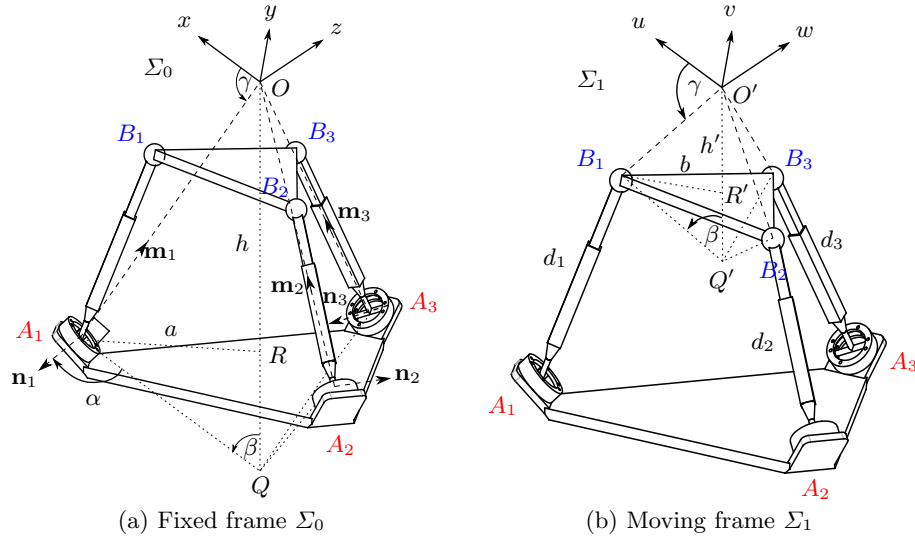- Configuration 3: $\beta = 60$ deg

(a) Fixed frame Σ_0 (b) Moving frame Σ_1

Fig. 2: Mechanism Architecture

3   Kinematic Analysis

Algebraic geometry approach is used to derive the kinematic model of the manipulator under study. For this purpose, transformation matrix for any value of angle β is initially determined, as follows:

$$\mathbf{M} = \begin{bmatrix} c_\phi c_\psi - s_\phi c_\theta s_\psi & -c_\phi s_\psi - s_\phi c_\theta c_\psi & s_\phi s_\theta & \sigma_1 \\ s_\phi c_\psi + c_\phi c_\theta s_\psi & -s_\phi s_\psi + c_\phi c_\theta c_\psi & -c_\phi s_\theta & \sigma_2 \\ s_\theta s_\psi & s_\theta c_\psi & c_\theta & \sigma_3 \\ 0 & 0 & 0 & 1 \end{bmatrix} \tag{1}$$

Matrix $\mathbf{M}$ is a homogeneous transformation that consists of Euler angles (ϕ, θ, ψ) and point displacement vector ρ_1, ρ_2, ρ_3. ρ_1, ρ_2, ρ_3 are completely expressed in terms of (ϕ, θ, ψ) and design parameter β. Their expressions cannot be shown here because they are very lengthy. However, ρ_1, ρ_2, ρ_3 for Configuration 2 can be simplified as follows:

$$
\begin{aligned}
\rho_1 &= -\frac{\sqrt{6}b}{2}\big(s_\phi c_\theta c_\psi + c_\phi s_\psi - s_\phi s_\theta\big) \\
\rho_2 &= \frac{\sqrt{6}b}{2}\big(c_\phi c_\theta s_\psi + s_\phi c_\psi - c_\phi s_\theta\big) \\
\rho_3 &= \frac{\sqrt{6}b}{2}s_\theta\big(c_\psi + s_\psi\big)
\end{aligned}
\tag{2}
$$

Let the angular velocity of a rigid body be described by a vector $\omega^T = \begin{bmatrix} \omega_x\ \omega_y\ \omega_z \end{bmatrix}$. Their values are determined from a velocity matrix $\mathbf{\Omega}$ which are derived from the transformation matrix $\mathbf{M}$, as follows:

$$
\mathbf{\Omega} = \dot{\mathbf{M}}\mathbf{M}^{-1} = \begin{bmatrix} 0 & -\omega_z & \omega_y & v_x \\ \omega_z & 0 & -\omega_x & v_y \\ -\omega_y & \omega_x & 0 & v_z \\ 0 & 0 & 0 & 0 \end{bmatrix}
\tag{3}
$$

Hence, velocities of point B_i in the moving platform is obtained as: ${}^{\mathcal{A}}\mathbf{v}_{b_i} = \mathbf{\Omega}\,{}^{\mathcal{A}}\mathbf{b}_i$.
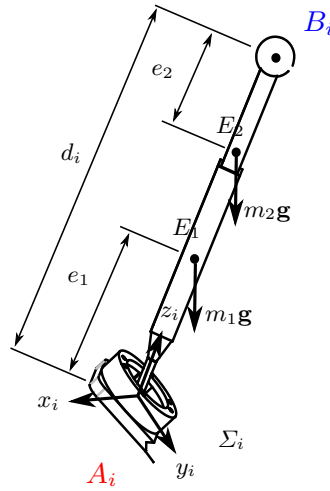

Fig. 3: Free body diagram

Local coordinate system of each leg $\Sigma_i(x_i, y_i, z_i)$ is shown in Fig. 3. The axis z_i is pointing from A_i to B_i. Therefore, velocities of point B_i can be transformed into the local coordinate system by matrix ${}^i\mathbf{M}_{\mathcal{A}}\ {}^{\mathcal{A}}$.

Center of gravity of piston and cylinder are denoted by points E_1 and E_2, respectively. The velocities at E_1 and E_2 are obtained by initially computing leg angular and linear velocities (${}^i\omega_i$ and $\dot{d}_i$), as follows:

$$
\begin{aligned}
{}^i\omega_i &= \frac{1}{d_i}({}^i\mathbf{s}_i \times {}^i\mathbf{v}_{b_i}) \\
\dot{d}_i &= {}^i\mathbf{v}_{b_i}\ {}^i\mathbf{s}_i \\
{}^i\mathbf{v}_{g_{1i}} &= e_1\left({}^i\omega_i \times {}^i\mathbf{s}_i\right) \\
{}^i\mathbf{v}_{g_{2i}} &= (d_i - e_2)\left({}^i\omega_i \times {}^i\mathbf{s}_i\right) + \dot{d}_i\ {}^i\mathbf{s}_i
\end{aligned}
\tag{4}
$$

where ${}^i\mathbf{s}_i = \begin{bmatrix} 0\ 0\ 1 \end{bmatrix}$. These velocities are important to formulate the dynamic model hereafter.

3.1   Singularities

The 3-(rR)PS metamorphic parallel manipulator has equal number of degree-of-freedom (DOF), actuators and legs, which yields symmetrical 3×3 matrices of forward and inverse Jacobian. To determine these Jacobian, the inverse kinematics should be initially obtained. Let prismatic joints be the actuators. Hence the inverse kinematics are:

$$
f_i : \|{}^{\mathcal{A}}\mathbf{b}_i - {}^{\mathcal{A}}\mathbf{a}_i\| - d_i^2 = 0, \quad i = 1, 2, 3
\tag{5}
$$

Let $\mathbf{x} = \begin{bmatrix} \phi, \theta, \psi \end{bmatrix}$ and $\mathbf{d} = \begin{bmatrix} d_1, d_2, d_3 \end{bmatrix}$ be the vectors of output and input variables, respectively. Then the forward and inverse Jacobian can be obtained from first-order partial derivative of f_i with respect to vector $\mathbf{x}$ and $\mathbf{q}$, as follows:

$$
\mathbf{J}_x = \left(\frac{\partial f_1}{\partial \phi}, \frac{\partial f_2}{\partial \theta}, \frac{\partial f_3}{\partial \psi}\right) \quad \text{and} \quad \mathbf{J}_d = \left(\frac{\partial f_1}{\partial d_1}, \frac{\partial f_2}{\partial d_2}, \frac{\partial f_3}{\partial d_3}\right)
\tag{6}
$$

where

$$
\mathbf{J}_x \mathbf{x} + \mathbf{J}_d \mathbf{d} = 0
\tag{7}
$$

Parallel mechanism is said to be in an actuation singularity when determinant of forward Jacobian vanishes, such that:

$$
\det(\mathbf{J}_x) = 0
\tag{8}
$$

For any values of β, the actuation singularity occurs at home position, namely $\phi = \theta = \psi = 0$. The readers may refer to [11] for complete analysis of actuation singularity of 3-(rR)PS metamorphic parallel mechanism. Let the circumradius of the base and moving platform be $a = 0.25$ and $b = 0.125$. Then Jacobian matrices at singularity position are as follows:

Configuration 1: $\mathbf{J}_x = \begin{bmatrix} 0 & 54 & 54 \\ 108 & -108 & -108 \\ -108 & 0 & 0 \end{bmatrix}$, $\mathbf{J}_d = \begin{bmatrix} -2304d_1 & 0 & 0 \\ 0 & -4608d_2 & 0 \\ 0 & 0 & -4608d_3 \end{bmatrix}$

Configuration 2: $\mathbf{J}_x = \begin{bmatrix} 0 & 6 & 6 \\ 6 & -6 & -6 \\ -6 & 0 & 0 \end{bmatrix}$, $\mathbf{J}_d = \begin{bmatrix} -256d_1 & 0 & 0 \\ 0 & -256d_2 & 0 \\ 0 & 0 & -256d_3 \end{bmatrix}$

Configuration 3: $\mathbf{J}_x = \begin{bmatrix} 0 & 36 & 36 \\ 108 & -108 & -108 \\ -108 & 0 & 0 \end{bmatrix}$, $\mathbf{J}_d = \begin{bmatrix} -1536d_1 & 0 & 0 \\ 0 & -4608d_2 & 0 \\ 0 & 0 & -4608d_3 \end{bmatrix}$

$$\tag{9}$$

At given singular position, the Jacobian rank degenerates by one and a non-zero vector of null-space $\mathbf{x}_s$ can be determined, such that:

$$\mathbf{J}_x \mathbf{x}_s = \mathbf{x}_s^T \mathbf{J}_x^T = 0 \tag{10}$$

$\mathbf{x}_s$ provides the direction of an infinitesimal motion gained by the moving platform. It turns out that Configurations 1, 2, and 3 have the same null-space, as follows:

$$\mathbf{x}_s^T = \begin{bmatrix} 0 & -1 & 1 \end{bmatrix} \tag{11}$$

4   Dynamic Analysis

Lagrange formulation is used to derive the dynamic models of the 3-(rR)PS metamorphic parallel mechanism, as follows:

$$\tau = \mathbf{W}_b - \mathbf{J}_d \lambda, \quad \mathbf{W}_b = \frac{d}{dt}\left(\frac{\partial L}{\partial \dot{\mathbf{d}}}\right) - \frac{\partial L}{\partial \mathbf{d}} \tag{12a}$$

$$\mathbf{J}_x \lambda = \mathbf{W}_p, \quad \mathbf{W}_p = \frac{d}{dt}\left(\frac{\partial L}{\partial \dot{\mathbf{x}}}\right) - \frac{\partial L}{\partial \mathbf{x}} \tag{12b}$$

where $\mathbf{J}_x$ and $\mathbf{J}_d$ are forward and inverse Jacobian from Eq. (6), λ is the Lagrange multiplier, and L is the Lagrangian function. Lagrangian function L is the energy difference between kinetic energy T and potential energy V, such that:

$$L = T - V \tag{13}$$

where

$$V = mgh_{R'} + \sum_{i=1}^{3}(m_1 g h_{E_{1i}} + m_2 g h_{E_{2i}}) \tag{14a}$$

$$T = \frac{1}{2}m\mathbf{v}_{R'}^2 + \frac{1}{2}\omega^T \mathbf{I}_{R'}\omega + \sum_{i=1}^{3}\Big(\frac{1}{2}m_1\mathbf{v}_{E_{1i}}^2 + \frac{1}{2}m_2\mathbf{v}_{E_{2i}}^2 + \frac{1}{2}{}^i\omega_i^T(\mathbf{I}_{E_{1i}} + \mathbf{I}_{E_{2i}})^i\omega_i\Big)$$

(14b)

The consistency condition of dynamic model based on [4] is the first condition to fulfil hence the mechanism may pass through singularity. This condition describes that the null-space from Eq. (11) should be orthogonal to the wrench $\mathbf{W}_p$ from Eq. (12b) at singular configuration, such that:

$$\mathbf{x}_s^T \mathbf{J}_x^T \lambda = \mathbf{W}_p \mathbf{x}_s = 0 \tag{15}$$

The second condition to ensure that the input torque to be finite is necessary and will be described hereafter.

Let the Lagrange multiplier from Eq. (12b) be defined as a function of time t, as follows:

$$\lambda(t) = \big(\mathbf{J}_x(t)\big)^{-1}\mathbf{W}_p(t) = \frac{1}{\det(\mathbf{J}_x(t))}\,\mathrm{Adj}\big(\mathbf{J}_x(t)\big)\,\mathbf{W}_p(t) \tag{16}$$

The numerator and denominator from Eq. (16) are denoted as $\eta(t)$ and $\delta(t)$ to simplify the following derivation. When the mechanism is approaching singularity, Eq. (16) can be expressed as a limit of singularity time t_s, as follows:

$$\lim_{t \to t_s}\lambda(t) = \lim_{t \to t_s}\frac{\eta(t)}{\delta(t)} \tag{17}$$

The denominator will vanish when the time t is exactly at the singularity time i.e. $\delta(t_s) = 0$ and Eq. (17) becomes undefined. This problem can be solved by applying L'Hôpital's rule if and only if the numerator also vanish, hence the indeterminate form of type $0/0$ is achieved. Then, the first-time derivative is performed as follows:

$$\lim_{t \to t_s}\lambda(t) = \lim_{t \to t_s}\frac{\eta'(t)}{\delta'(t)} \tag{18}$$

Let the motion parameters $\phi(t)$ and $\psi(t)$ be null and the moving platform be designed to move only with a single parameter $\theta(t)$. By satisfying Eq. (15) and Eq. (18), the velocity and acceleration of moving at singularity are found for Configurations 1, 2, and 3, as follows:

$$
\begin{array}{llll}
\text{Configuration 1}: & \dot{\theta}(t_s) = 2.64 & \ddot{\theta}(t_s) = 4.89 & \\
\text{Configuration 2}: & \dot{\theta}(t_s) = 2.46 & \ddot{\theta}(t_s) = 3.86 & (19)\\
\text{Configuration 3}: & \dot{\theta}(t_s) = 2.31 & \ddot{\theta}(t_s) = 3.39 &
\end{array}
$$

The above properties become the boundary conditions of trajectory generation. The initial and final positions, velocities and accelerations are planned to be the same for Configurations 1, 2, and 3, namely:

$$
\begin{array}{ll}
\theta(t_i) = -\pi/2 & \theta(t_f) = \pi/2 \\
\dot{\theta}(t_i) = 0 & \dot{\theta}(t_f) = 0 \\
\ddot{\theta}(t_i) = 0 & \ddot{\theta}(t_f) = 0
\end{array}
\tag{20}
$$

By considering all boundary conditions, the 8-th degree polynomial trajectory of $\theta(t)$ is planned as follows:

$$\text{Configuration } 1: -1.6 + 25.9t^3 - 77.6t^4 + 99t^5 - 63.3t^6 + 19.9t^7 - 2.5t^8$$
$$\text{Configuration } 2: -1.6 + 23.2t^3 - 66.4t^4 + 82.5t^5 - 51.5t^6 + 16t^7 - 1.9t^8$$
$$\text{Configuration } 3: -1.6 + 22.6t^3 - 63.2t^4 + 76.5t^5 - 46.8t^6 + 14.2t^7 - 1.7t^8$$

$$(21)$$

The distribution of input forces while executing 8-th degree polynomial trajectory for Configurations 1, 2, and are shown respectively in Figs. 4(a), 4(c), and 4(e). Blue curves show finite input force for the first leg since the first-time derivative is fulfilled. However, the input forces for second and third legs (denoted by red and green curves, respectively) are unbounded. It occurs because the denominator of the first-time derivative of Eq. (18) is still null.

Additional condition of second-time derivative of L'Hôpital's rule is proposed, such that:

$$\lim_{t \to t_s} \lambda(t) = \lim_{t \to t_s} \frac{\eta''(t)}{\delta''(t)} \tag{22}$$

For fulfilling Eq. (22), both numerator and denominator of the first-time derivative should be indeterminate form, i.e. $\dfrac{\eta'(t)}{\delta'(t)} = \dfrac{0}{0}$. This introduces a new kinematic property to the boundary conditions, namely a jerk at singular configuration, as follows:

$$\text{Configuration } 1: \quad \dddot{\theta}(t_s) = 37.78$$
$$\text{Configuration } 2: \quad \dddot{\theta}(t_s) = -5.19 \tag{23}$$
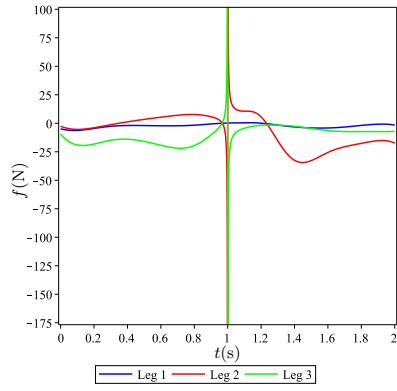$$\text{Configuration } 3: \quad \dddot{\theta}(t_s) = 31.32$$

Let the initial and final jerks of the moving platform be zero. The 11th-degree polynomial trajectory of $\theta(t)$ can be formulated as follows:

$$\text{Configuration } 1: -1.6 - 46t^4 + 321t^5 - 800t^6 + 1020t^7 - 740t^8 + 310t^9 - 70t^{10} + 6.6t^{11}$$
$$\text{Configuration } 2: -1.7 + 91.8t^4 - 355t^5 + 560t^6 - 542t^7 + 298t^8 - 74.6t^9 + 24.2t^{10} - 1.5t^{11}$$
$$\text{Configuration } 3: -1.6 - 14t^4 + 161t^5 - 450t^6 + 610t^7 - 460t^8 + 195t^9 - 44t^{10} + 4.2t^{11}$$

$$(24)$$

Figs. 4(b), 4(d), and 4(f) show the distribution of input forces when following 11th-degree polynomial trajectory. The input forces are now finite which means that all Configurations 1, 2, and 3 can pass through singularity continuously.
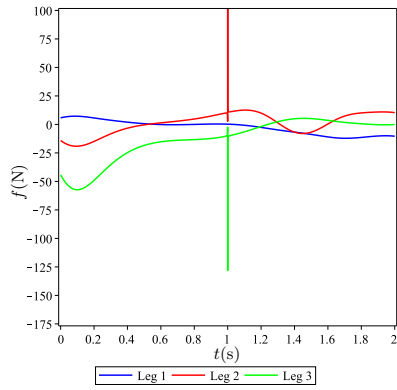
5   Conclusions

This paper discussed dynamic models of the 3-(rR)PS metamorphic parallel mechanism to cross singularities. Three types of configurations were analysed.
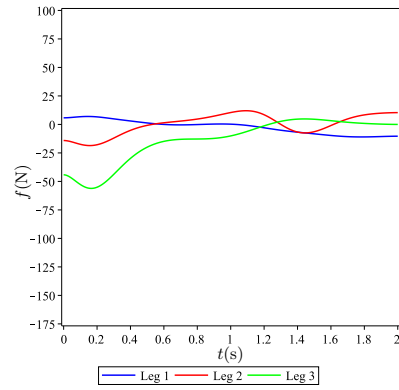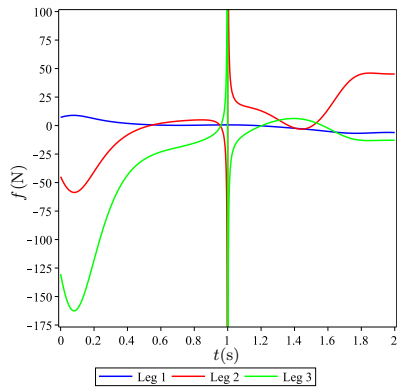
(a) Configuration 1: 8th-degree
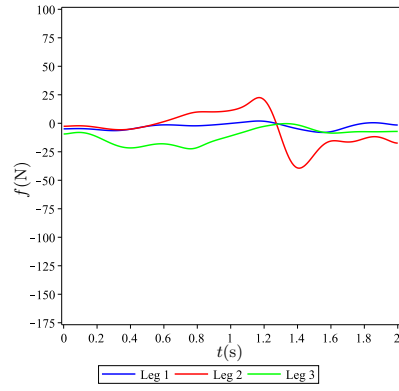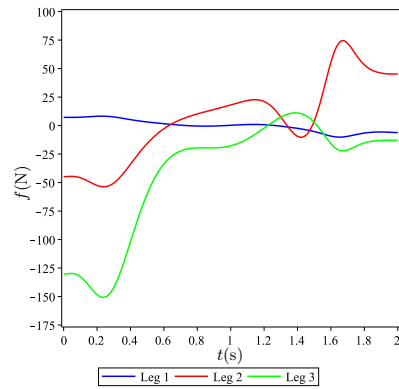
(b) Configuration 1: 11th-degree

(c) Configuration 2: 8th-degree

(d) Configuration 2: 11th-degree

(e) Configuration 3: 8th-degree

(f) Configuration 3: 11th-degree

Fig. 4: Distribution of input forces

Upon fulfilling the first and second conditions, the input forces still tend to infinity. It is caused by the zero denominator that appeared although the first time-derivative was performed. As a consequence, the second time-derivative should be computed which introduced jerk to the system. This computation led to 11th-degree polynomial trajectory and the results showed that the mechanism can pass through singularities without infinite forces. Experimental tests of the proposed algorithm will be the subject of future researches.

References

1. S. Briot, V. Arakelian: On the Dynamic Properties of Flexible Parallel Manipulators in the Presence of Type 2 Singularities, *Journal of Mechanisms and Robotics* **3** (2011), 031009-1–8.
2. S. Briot, V. Arakelian: On the Dynamic Properties of Rigid-Link Flexible-Joint Parallel Manipulators in the Presence of Type 2 Singularities, *Journal of Mechanisms and Robotics* **3** (2010), 021004-1–6.
3. D. Six , S. Briot , A. Chriette , P. Martinet: A Controller Avoiding Dynamic Model Degeneracy of Parallel Robots During Singularity Crossing, *Journal of Mechanisms and Robotics* **9**(5) (2017), 051008-1–8.
4. S. Briot, G. Pagis, N. Bouton, P. Martinet: Degeneracy conditions of the dynamic model of parallel robots, *Multibody System Dynamics* **37** (2016), 371—412.
5. G. Pagis, N. Bouton, S. Briot, P. Martinet: Enlarging parallel robot workspace through type-2 singularity crossing, *Control Engineering Practice* **39** (2015), 1—11.
6. M. Özdemir: Removal of singularities in the inverse dynamics of parallel robots, *Mechanism and Machine Theory* **107** (2017), 71–86.
7. L. Nurahmi, D. Gan: Reconfiguration of a 3-(rR)PS Metamorphic Parallel Mechanism Based on Complete Workspace and Operation Mode Analysis, *Journal of Mechanisms and Robotics* **12**(1) (2020), 0110021–15.
8. X. Chai, L. Nurahmi, J. S. Dai, D. Gan Kinematic Calibration of a 3rRPS Metamorphic Parallel Mechanism, *ASME 2020 International Design Engineering Technical Conferences and Computers and Information in Engineering Conference* (2020).
9. L. Nurahmi, D. Gan Dynamic analysis of the 3-RRPS metamorphic parallel mechanism based on instantaneous screw axis, *ASME 2019 International Design Engineering Technical Conferences and Computers and Information in Engineering Conference* (2019), vol. 59230, V05AT07A064.
10. P. Dyke: Advanced Calculus, *Macmillan Press Ltd, London* (1998).
11. L. Nurahmi, M. Husty, D. Gan: Forward Kinematics and Singularities of a 3-(rR) PS Metamorphic Parallel Mechanism, *USCToMM Symposium on Mechanical Systems and Robotics* (2020), 68–77.

Design of Deployable Mechanisms Based on Single-Vertex Multi-crease Origami Patterns

Chenhan Guang and Yang Yang(✉)

School of Mechanical Engineering and Automation, Beihang University, XueYuan Road No.37, HaiDian District, Beijing 100191,China,
`yang_mech@126.com`

Abstract. Inspired by the single-vertex multi-crease origami pattern, a method to design deployable mechanisms to be used for solar arrays, diffraction mirrors and reflectors on spacecrafts is presented. Firstly, four types of single-vertex multi-crease origami patterns are constructed by differently arranging mountain and valley creases. After thickness added, virtual experiments on synchronously folding thick-panel patterns are conducted to find the constraint planes. Secondly, the restrained sub-panels are selected to be the minimal repeating units to analyze, and transformed into single-mobility unit mechanisms with through equivalent substitution method and screw theory. Finally, single-mobility deployable mechanisms composed of unit mechanisms are built and motion simulations are conducted to confirm the correctness for the configurations of the mechanisms and the characteristic of single mobility.

Keywords: design, deployable mechanism, single-vertex multi-crease origami pattern

1 Introduction

Based on the shape-changing characteristic, origami has merged with other fields, and been a hot topic in technology recently. Researchers have done innovative works related with origami applying. Taghavi et al. [1] introduced an electrostatic active origami to be used for adaptive grippers, self-packing deployable structures, and origami artificial muscles. Miyashita et al. [2] presented an approach to extending and changing the capabilities of a robot by enabling metamorphosis using self-folding origami exoskeletons. Li et al. [3] proposed an architecture for fluid-driven origami-inspired artificial muscles which was able to be programed to achieve multiaxial motions including contraction, bending, and torsion. The full-diamond origami pattern was implemented in the design of pre-folded carbon fiber reinforced plastics tubes with the aim of improving the energy absorption performance under axial compression [4].

In this study, inspired by the single-vertex multi-crease origami pattern, we present a method to design deployable mechanisms to be used for solar arrays, diffraction mirrors and reflectors on spacecrafts. Different from existing studies

that construct large origami patterns or deployable mechanisms with single-mobility patterns [5–8], the single-vertex multi-crease origami pattern usually has more than one mobility. Therefore, a distinct method should be applied to transform the patterns into mechanisms.

Firstly, we construct four types of single-vertex multi-crease origami patterns by differently arranging mountain and valley creases. Then thickness is added to these patterns, and virtual experiments folding the origami patterns synchronously are conducted to find the constraint planes. Secondly, the restrained subpanels are treated as the minimal repeating units to be analyzed, and transformed into unit mechanisms with single mobility through equivalent substitution method and screw theory. Finally, two single-mobility deployable mechanisms composed of unit mechanisms are built in three-dimensional computer aided design software and motion simulations are conducted to confirm the correctness for the configurations of the mechanisms and the characteristic of single mobility.

2   Single-vertex Multi-crease Origami Patterns and Their Thickness Adding Based on Axis-shift Method

Vertex is the point where creases meet. If all the creases intersect, and meet at only one vertex in flattened (unfolded) state, this kind of pattern is named single-vertex multi-crease origami pattern.

As shown in Fig. 1, a piece of circular material is equally divided into several parts by the same number of creases, and distinct single-vertex multi-crease origami patterns (type I, type II, type III and type IV) are constructed by differently arranging mountain and valley creases.
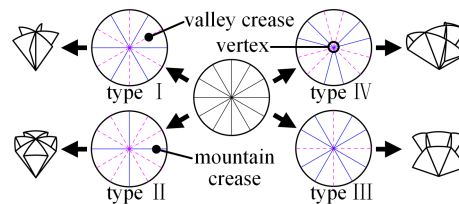
Fig. 1. Single-vertex multi-crease origami patterns

To evaluate the folding efficiency for these types of patterns after folded, these patterns with the same diameter should be divided into the same number of parts. The number of creases in a repeating unit of type I is two, three for type II and type III, and four for type IV. The number of creases for type II should be less than eighteen, therefore twelve, the common multiple of 2, 3 and 4, is the most appropriate choice.

Obviously, there are other type of patterns, but their folded configurations are over complex, so not in consideration.

After synchronously folded, these two-dimensional origami patterns are folded into three-dimensional rotational symmetric objects, and the radial dimensions of them reduce.

With the characteristics of structure transforming and radial dimension reducing, these origami patterns can inspire the design of deployable mechanisms. Thickness should be added to origami patterns, because the mechanisms are designed for solar arrays, diffraction mirrors and reflectors used in space whose thickness cannot be ignored. To increase the effective area of the deployed mechanisms, the axis-shift method is applied [9]. The thickness-added origami pattern can be named thick-panel origami pattern, the portion between two adjacent creases as is named subpanel [10].

The thick-panel origami patterns for type I, type II, type III and type IV are respectively illustrated in Fig. 2, Fig. 3, Fig. 4 and Fig. 5. The sector angle of a subpanel is denoted by α. H is the height of the folded configuration from the front view, R is the radius of the circular nonzero thickness panel, h is the thickness of the thick panel, r_{in} is the apothem of the regular polygon cavity, and r_{out} is the circumradius of the folded configuration from the top view. H, r_{in} and r_{out} can be calculated by equations which are unlisted for conciseness. The equations of type I can be seen in Ref. [11], and the equations of the other types will be presented in extended virsion soon.

Fig. 2. Thick-panel origami pattern of type I: (a) deployed configuration, (b) middle configuration, (c) folded configuration

Fig. 3. Thick-panel origami pattern of type II: (a) deployed configuration, (b) middle configuration, (c) folded configuration

It is observed that for each type of origami pattern, some of the creases or the symmetry axes of subpanels are always on several planes dividing the space into several equal parts. We build three-dimensional models and restrain
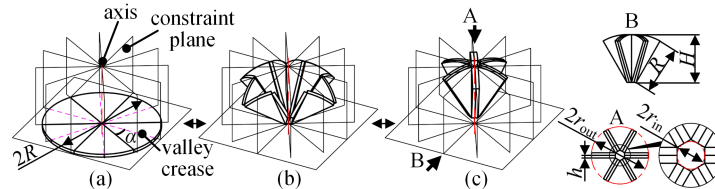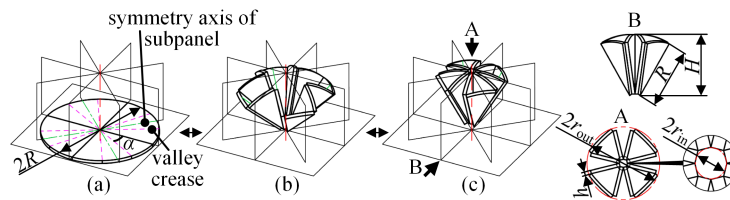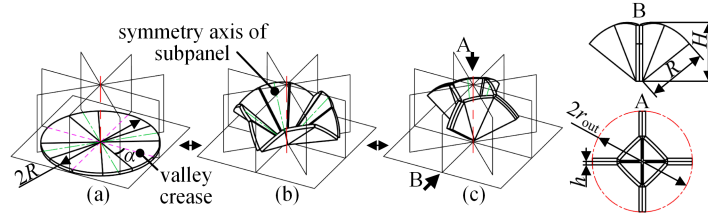
Fig. 4. Thick-panel origami pattern of type III: (a) deployed configuration, (b) middle configuration, (c) folded configuration
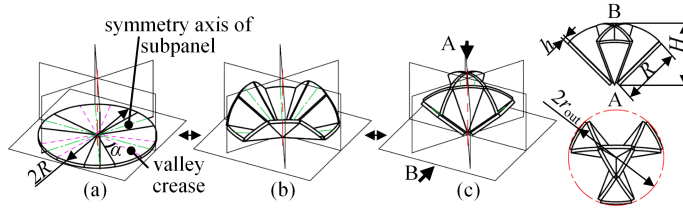

Fig. 5. Thick-panel origami pattern of type IV: (a) deployed configuration, (b) middle configuration, (c) folded configuration

the corresponding creases or symmetry axes of subpanels on the planes. When dragging a subpanel for each pattern, we find that the whole pattern can fold and deploy synchronously. It is likely that the constrained thick-panel origami patterns have single mobility. We prove this conclusion in the next section.

3   Transformation from Thick-panel Origami to Deployable Mechanisms

Because of their rotationally symmetric configurations for the thick-panel origami patterns, one subpanel or a group of subpanels can be treated as the minimal repeating unit to be analyzed.

For the type I origami pattern, one subpanel is selected to be analyzed. As shown in Fig. 6, A_1, A_2, B_1, B_2, E_1 and O_1 are the six vertices of the subpanel. The points O, O_1, and B_1 are collinear and on the plane xOz (xOz plane is also a constraint plane). The points A_2, E_1, and E_2 are collinear and on the constraint plane, meanwhile the point E_2 is on the z axis. The angle between the line $\overline{OB_1}$ and the x axis is θ. The angle between the line $\overline{E_2A_2}$ and the plane xOy is φ_1. The dihedral angle between the plane $A_2B_2E_1$ and the constraint plane is ψ_1. The dihedral angle between the plane xOz and the plane $A_1B_1O_1$ is ψ_2.

When α and h are fixed, the parameters φ_1, ψ_1, ψ_2, $\left|\overline{OO_1}\right|$, $\left|\overline{E_1E_2}\right|$, and $\left|\overline{OE_2}\right|$ describing position and orientation of the subpanel are only related with θ, and the variation of the parameters is continuous as shown in Fig. 6. Therefore the mobility of the constrained subpanel should be one.

Then to transform the constrained subpanel into a mechanism, linkages and joints are introduced to represent the parameters and to equivalently replace the
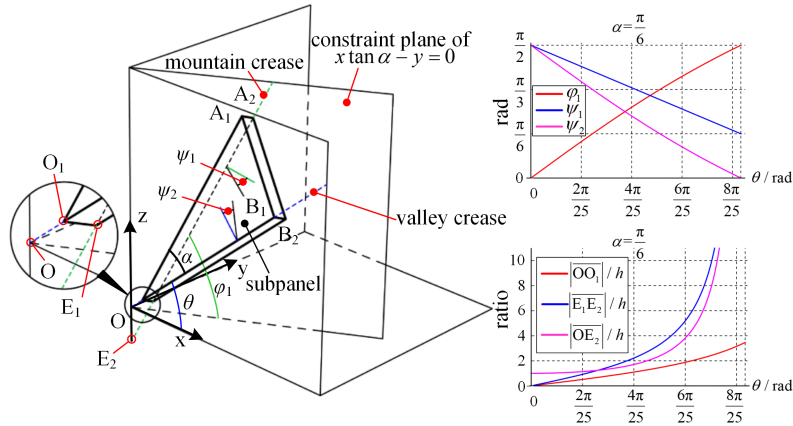
Fig. 6. Analysis of a subpanel of type I and variation of parameters with changing θ

constraint planes and to mimic the motion. The screw theory is used to analyze the mobility of the mechanisms.

As shown in Fig. 7(a), the linkage 1 which represents the subpanel rotates about the lines $\overline{E_2A_2}$ and $\overline{OB_1}$, and the rotation angles are ψ_1 and ψ_2, respectively. Simultaneously, the linkage 1 slides along the lines $\overline{E_2A_2}$ and $\overline{OB_1}$, and the displacements are $\left|\overline{E_1E_2}\right|$ and $\left|\overline{OO_1}\right|$, respectively. The linkage 1 can be joined by the linkage 2 and the linkage 3 with two cylindrical joints described as two pairs of screws, $\mathbf{\$}_1$, $\mathbf{\$}_2$ and $\mathbf{\$}_4$, $\mathbf{\$}_5$, respectively. The linkage 3 is the fixed linkage. The linkage 2 is hinged with the linkage 3, and the joint can be described as $\mathbf{\$}_3$ to represent θ. The linkage 4 is connected with the linkage 3 by a revolute joint and a prismatic joint which can be described as $\mathbf{\$}_6$ and $\mathbf{\$}_7$ to represent φ_1 and $\left|\overline{OE_2}\right|$, respectively.
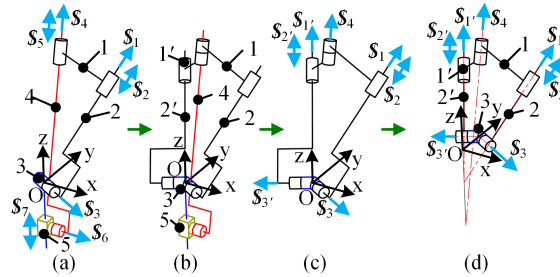
Fig. 7. Transformation from a subpanel of type I

The mobility of this unit mechanism can be calculated by modified G-K equation and screw theory [12], and the mobility of it is one. When θ approaches to $\pi/2 - \alpha$, $\left|\overline{E_1E_2}\right|$ tends to infinity. It means that the displacement of the prismatic joint between linkage 4 and linkage 5 should be infinity, which in practice is impossible. We add the linkage 1' and linkage 2', remove the linkage

3, the linkage 4, and the linkage 5 to simplify the mechanism, as shown in Fig. 7(b) and (c). After the calculation of the mobility, it is proved that the unit mechanism in Fig. 7(c) has two DoFs (degrees of freedom).

It is significant that a satisfactory deployable mechanism has only one degree-of-freedom, meanwhile there is not enough space for several hinges arranged near the point O as shown in Fig. 7(c). The hinge axis intersection shifted from the point O to another point on the y axis, as shown in Fig. 7(d). Through this method, the mobility of this new unit mechanism is one. Then we circularly align enough units to construct a close-loop deployable mechanism in which every adjacent units share a linkage (such as the linkage 2 shown in Fig. 7(d)). Each unit has one DoF, therefore, the whole deployable mechanism composed of several identical units has one DoF. When the unit mechanism is deployed ($\theta = 0$), the mobility becomes two, so the mobility of the whole deployable mechanism will be more than one. However, this disadvantage in its deployed configuration can be ignored in practice, because usually the deployable mechanism is not to be folded again once deployed in orbit.

As for the other types of thick-panel origami patterns, the same method can be applied. In this paper, we only present the results shown in Fig.8 - Fig. 12, and the detailed processes of analysis and transformation are omitted.

Two panels are selected to be the minimal repeating unit for type II and type III. Although the folded configurations of the type II and the type III are different shown in Fig. 8 and Fig. 9, the configurations of the transformed unit mechanisms are the same illustrated in Fig. 10. The unit mechanism shown in Fig. 10 has single mobility, so it can be used to construct deployable mechanisms whose mobility are one. The constructed deployable mechanism also has single mobility when in its deploying state.
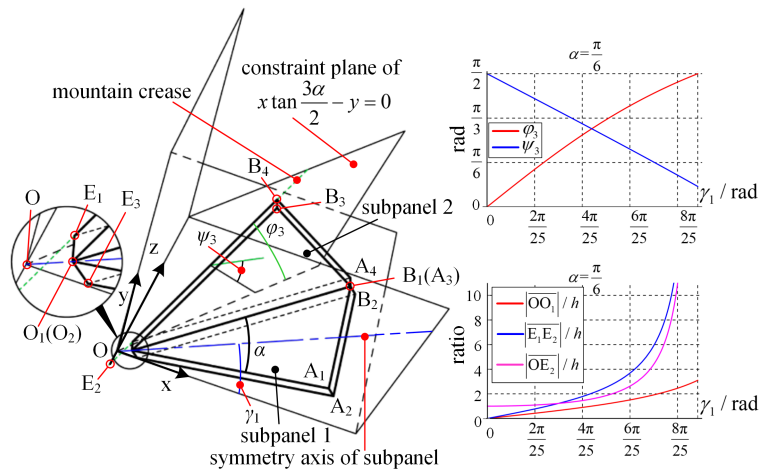

Fig. 8. Analysis of subpanels of type II and variation of parameters with γ_1
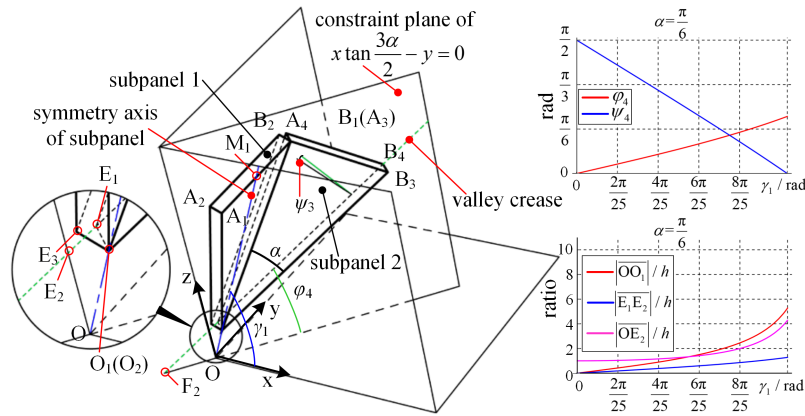
Fig. 9. Analysis of subpanels of type III and variation of parameters with γ_1
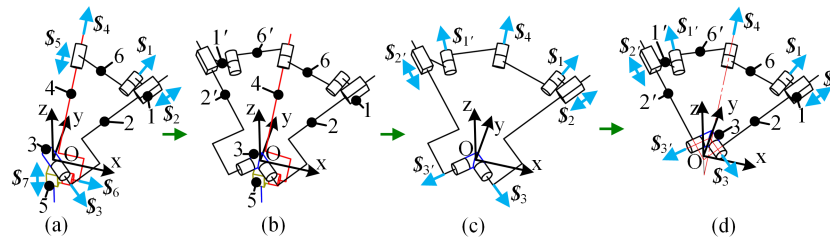
Fig. 10. Transformation from subpanels of type II and type III

Three panels are selected to be the minimal repeating unit for type IV. After analysis, the mobility of the transformed unit mechanism is two, which means that this type of thick origami pattern cannot be transformed into the deployable mechanism.

4 Results for The Designing of Deployable Mechanisms

The results for the designing of deployable mechanisms are listed in Table 1. Two kinds of unit mechanism configurations with single DoF are transformed from the minimal repeating units of type I, type II and type III. The minimal repeating unit of type IV is transformed into a two-DoF unit mechanism which can not be used to construct deployable mechanisms with single mobility.

With different relative positions of the kinematic pairs, two kinds of deployable mechanisms whose folded configurations are distinct can be built by the unit mechanism configuration transformed from type II and type III.

According to the configurations shown in Fig. 7(d), Fig. 10(d) and Table 1, we constructed three-dimensional models of deployable mechanisms transformed form type I and type II respectively in computer aided design software, and conduct the motion simulations to conform their single mobility during their deployment, as shown in Fig. 13.

Fig. 11. Analysis of subpanels of type IV and variation of parameters with γ_1

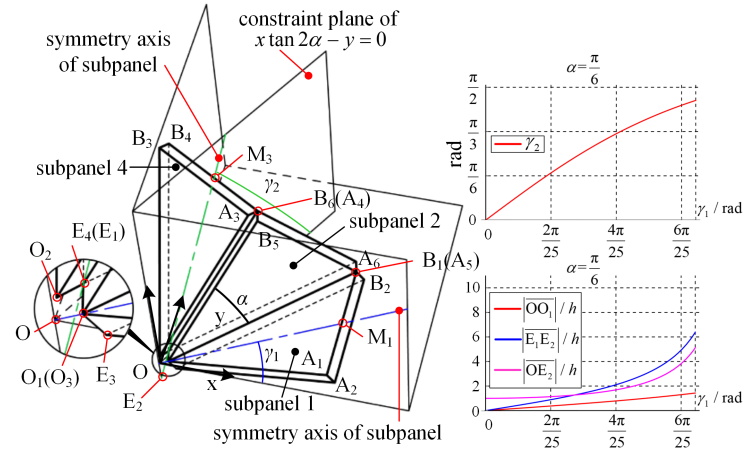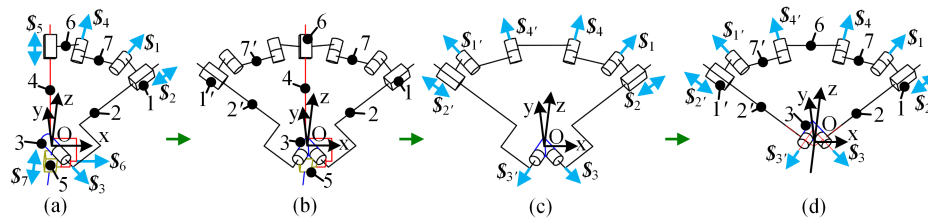**Fig. 12.** Transformation from subpanels of type IV
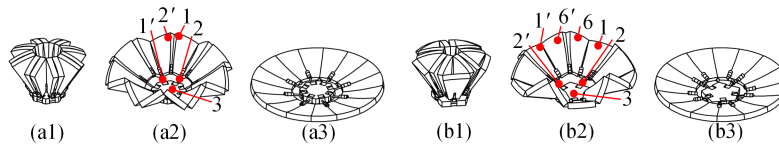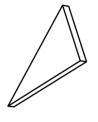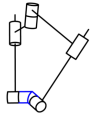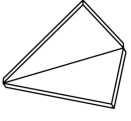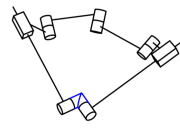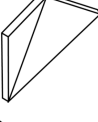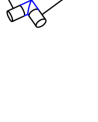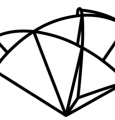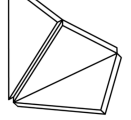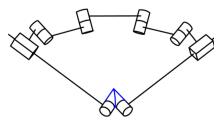
Fig. 13. Deployable mechanism transformed from the type I and the II and their deployment

Table 1. Results

Pattern with zero thickness	Pattern with thickness	Minimal repeating unit	Configuration of unit mechanism	Degree(s) of freedom
				1
				1
				2

5   Conclusions and Future Work

In this study, four types of origami patterns are constructed by differently arranging mountain and valley creases. Based on axis-shift method, their thick-panel forms are also built. Through virtual experiments, the characteristic of being restrained by planes when being synchronously folded is found, which can help to design deployable mechanisms with single mobility.

Then, one subpanel or a group of subpanels are treated as the minimal repeating unit, and the motion parameters are analyzed. It is proven that the four types of plane-restrained thick-panel origami patterns can be folded and unfolded with single mobility. Subsequently, the minimal repeating units of type I, type II and type III are transformed into deployable unit mechanisms with single mobility during deployment. Finally, three-dimensional models are built and the motion simulations are conducted to confirm the correctness for the constructed deployable mechanisms and the characteristic of single mobility.

This is a preliminary study, and a series of work can be done in the future. The universal kinematic model of the restrained subpanels needs to be built to systematacially synthesize thick-panel origami patterns which can inspire the design of deployable mechanisms. The constructing method of the unit mechanism can be further studied, for the deployable mechanism only containing revolute pairs is more practical.

Bibliography

[1] Taghavi, M., Helps, T., Rossiter, J.: Electro-ribbon actuators and electro-origami robots. Sci. Robot., 3(25), p. eaau9795 (2018).doi:10.1126/scirobotics.aau9795

[2] Miyashita, S., Guitron, S., Li, S., Rus, D.: Robotic metamorphosis by origami exoskeletons. Sci. Robot., 2(10), p. eaao4369 (2017).doi:10.1126/scirobotics.aao4369

[3] Li, S., Vogt, D. M., Rus, D., Wood, R. J.: Fluid-driven origami-inspired artificial muscles. Proc. Natl. Acad. Sci. U. S. A., 114(50), pp. 13132-13137 (2017). doi:10.1073/pnas.1713450114

[4] Ye, H., Ma, J., Zhou, X., Wang, H., You, Z.: Energy absorption behaviors of pre-folded composite tubes with the full-diamond origami patterns. Compos. Struct., 221, p. 110904 (2019). doi:10.1016/j.compstruct.2019.110904

[5] Guest, S. D., Schenk, M.: Geometry of Miura-folded metamaterials. Proc. Natl. Acad. Sci. U. S. A., 110(9), pp. 3276-3281 (2013). doi:10.1073/pnas.1217998110

[6] Liu, S., Lv, W., Chen, Y., Lu, G.: Deployable prismatic structures with rigid origami patterns. J. Mech. Robot., 8(3), p. 031002 (2016). doi:10.1115/1.4031953

[7] Feng, H., Peng, R., Zang, S., Ma, J., Chen, Y.: Rigid foldability and mountain-valley crease assignments of square-twist origami pattern. Mech. Mach. Theory, 152, p. 103947 (2020).doi:10.1016/j.mechmachtheory.2020.103947

[8] Zhang, X., Chen, Y.: Vertex-splitting on a diamond origami pattern. J. Mech. Robot., 11(3), p. 031014 (2019). doi:10.1115/1.4043214

[9] Tachi, T.: Rigid-foldable thick origami. In: 5th International Meeting of Origami Science, Mathematics and Education, pp. 253–264. CRC Press, U. S. A. (2011).

[10] Chen, Y., Peng, R., You, Z.: Origami of thick panels[J]. Science, 349(6246), pp: 396-400 (2015). doi:10.1126/science.aab2870

[11] Guang, C., and Yang, Y.: Single-vertex multicrease rigid origami with nonzero thickness and its transformation into deployable mechanisms. ASME J. Mech. Rob., 10(1), p. 011010 (2018). doi:10.1115/1.4038685

[12] Huang, Z., Zhao, Y., and Zhao, T.: Advanced Spatial Mechanism. Higher Education Press, Beijing, China, (2014).

Design and analysis of a new deployable and foldable mechanism

Runhao Xu, Rugui Wang*, Yi Zhang

College of Mechanical Engineering, Guangxi University, Nanning 530004, China

Abstract. By modifying the link length relation of the scissors mechanism, an offset scissors mechanism is obtained, and an offset deployable mechanism unit composed of offset scissors mechanism is designed. Next, using spinor method to obtain the degree of freedom of the offset deployable mechanism unit as 1, and the kinematics of this mechanism unit is analyzed to prove that the movement of the mechanism will produce offset. Using nested structural hinges, the offset deployable mechanism unit can be connected in series, and it can work under the control of a single prime mover. Finally, the kinematics simulation of the mechanism unit is carried out by programming, and the relationship between the offset and the scale parameter of the mechanism is discussed. The offset deployable mechanism can be applied in emergency bridge and other engineering applications.

Keywords: Deployable And Foldable Mechanism, Scissors Mechanism, Kinematics Analysis, Applied Research.

1 Introduction

The deployable and foldable mechanism is a kind of mechanisms with large folding ratio. Compared with the working state, the volume in the folding state is very small, which is convenient for machine transportation or rapid deployment, so that it can adapt to the working conditions with limited mechanism size.

The deployable and folding mechanism is mostly composed of some large folding ratio units that can be connected in series. The scissors mechanism is widely used in industrial production and life because of its large folding ratio and simple series relationship. Xu[1] proposed a scissor-bending deployable and foldable mechanism. Li[2] proposed a deployable spherical mechanism composed of spherical scissors mechanism units. Ref[3]-[4], based on the deformation characteristics of the scissors mechanism, the construction method of reconfigurable parallelogram mechanism unit is discussed. Garc í-Mora[5] proposed a method of constructing unfolding surface by scissors mechanism units. Ref [6][8], a kind of large deployable manipulators consisting of scissors mechanism units are designed to realize accurate objects grasping. Yang[9]-[10] proposed a two degree of freedom parallel mechanism with a

---

* Corresponding author.
 E-mail addresses: rugui@gxu.edu.cn (R. Wang).

series scissors structure as a branch chain. Nizami[11] use the variant scissors as the legs of a quadruped robot. Afshar[12] designed a variant scissors mechanism with spherical workspace. Ref[13]-[15], a kind of parallel mechanisms with large fold-expansion ratio are constructed by taking the series scissors mechanism as the branch chain. Ref[16]- [18], a kind of lifting platforms with scissors branched chain are designed. Ref[19][20] , the dynamic analysis of the scissors mechanism is carried out, and the driving method of the scissors mechanism is discussed. Sun[21]-[22] proposed a kinematics and position analysis method of scissors mechanism according to screw theory, which provided a theoretical basis for the design and manufacture of scissors mechanism.

In this paper, based on the general scissors mechanism, an offset scissors mechanism is designed. This mechanism retains the above advantages of the scissors mechanism, and makes it possible to produce controllable lateral offset in the process of stretching. Based on the offset scissors mechanism, a spatial offset deployable mechanism unit is proposed. This unit can be arbitrarily connected in series to form a deployable and foldable mechanism, and the mechanism is only controlled by a single motor. During the operation of the mechanism, each unit has complete controllable lateral displacement in the specified direction. In section 2, the concept of offset scissors mechanism is proposed, and the kinematics analysis of the offset scissors mechanism is carried out by vector method. In section 3, the offset deployable mechanism is designed. it is proved that the degree of freedom of the mechanism is 1 through the screw theory. And the kinematics analysis of this mechanism is carried out. In section 4, the relationship between the length of each link and the offset is analyzed. In section 5, the application prospect of the mechanism is discussed.

2   Analysis of offset scissors mechanism unit

The scissors mechanism is a combination mechanism with large folding ratio. As shown in Fig. 1(a), the conventional scissors mechanism obtained by hinged four connecting links with equal length, where M and N are the midpoints of AD and BC, CF and DE. Make AM, BM, CM, DM, CN, DN, EN, FN eight links equal in length. A significant advantage of the scissor mechanism is that the distance x_1 from A to B is equal to the distance x_2 from E to F during the operation of the mechanism. The transverse distance of each unit connection is constant, so that the width and fold ratio of each scissor mechanism units are kept constant after series connection, which provides convenience for the assembly and connection of the scissor mechanism.

(a) Scissors mechanism unit (b) Offset scissors mechanism unit
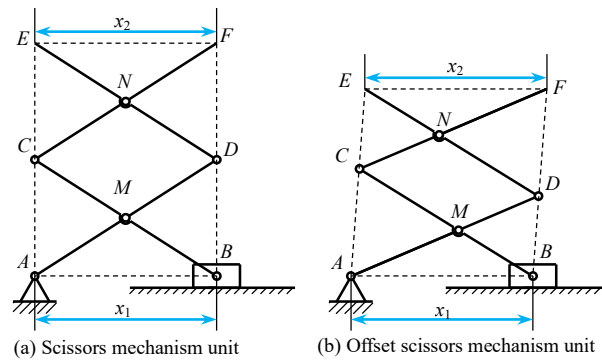
Fig. 1. Scissor mechanism unit and offset scissors mechanism unit

Fig. 1(b) is a variant of scissors mechanism unit. The difference between Fig. 1(a) and Fig. 1(b) is that the hinges M and N in Fig. 1(b) are not located at the midpoint of AD, BC, CF and DE, but the lengths of the four bars are still equal, and meet the requirements of $l_{AM} = l_{CM} = l_{DN} = l_{FN}$ and $l_{BM} = l_{DM} = l_{CN} = l_{EN}$. In this paper, the variant scissors mechanism is defined as a offset scissors mechanism. The freedom degree of the mechanism is calculated according to the freedom degree formula of the mechanism.

$$M = 3n - 2p_l - p_h \tag{1}$$

where M is the degree of freedom of the mechanism, n is the number of active components of the mechanism, p_l is the number of low pairs in the mechanism, and p_h is the number of high pairs in the mechanism. The degree of freedom $M = 1$ is obtained by substituting $n = 5$, $p_l = 7$, $p_h = 0$.
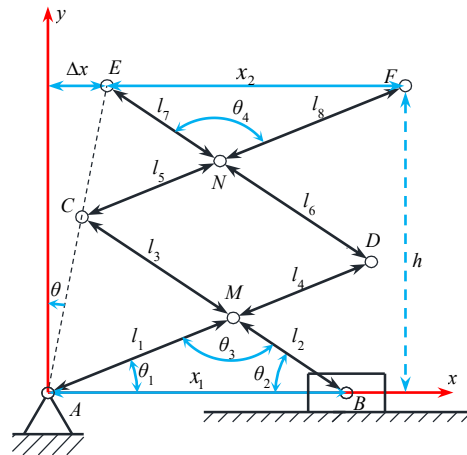
Fig. 2. Schematic diagram of offset scissors mechanism

According to the knowledge of plane geometry, $CMDN$ is a parallelogram in Fig. 2. Because of $\theta_3 = \theta_4$, $l_{AM} = l_{FN}$ and $l_{BM} = l_{EN}$, $\triangle_{AMB} \cong \triangle_{ENF}$ and $x_1 = x_2$ are proved. Therefore, the distance of A and B is always equal to the distance of E and F during the movement of the mechanism. Three points A, C, E and three points B, D, F are located in the same straight line, respectively. However, with the movement of the mechanism, the front end will shift perpendicular to the extension direction of the mechanism, and the quadrilateral formed by the six points is a parallelogram.

In order to determine the offset $\triangle x$ of offset scissors mechanism, the coordinate system is established with point A as the origin. The length of AM link is set to l_1, the length of BM link is set to l_2, and the space of A and B is x_1. The angle θ between AC and y-axis is known as the offset angle of the mechanism, and h is the height of the mechanism. According to the cosine theorem

$$\theta_1 = \frac{l_2^2 + x_1^2 - l_1^2}{2l_2 x_1} \tag{2}$$

$$\theta_2 = \frac{l_1^2 + x_1^2 - l_2^2}{2l_1 x_1} \tag{3}$$

The relationship between θ and θ_1, θ_2 is

$$\theta = \frac{\pi}{2} - \frac{\pi - (\theta_1 + \theta_2)}{2} - \theta_2 = \frac{\theta_1 - \theta_2}{2} \tag{4}$$

The height h of the offset scissors mechanism unit is the sum of the ordinates of C and D

$$h = (l_1 + l_2)(\sin \theta_1 + \sin \theta_2) \tag{5}$$

The offset $\triangle x$ is calculated by the height h and offset angle θ

$$\triangle x = h \sin \theta \tag{6}$$

According to the above conditions, the coordinate vector of each point in the Fig. 2 can be obtained, where $E = (\triangle x, h)^T$, $F = (\triangle x + x_1, h)^T$.

Furthermore, when $l_1 > l_2$, $\triangle x > 0$, indicating that the offset scissors mechanism migrates to the positive direction of x-axis. When $l_1 < l_2$, $\triangle x < 0$, the mechanism migrates to the opposite direction of x-axis. When $l_1 = l_2$, $\triangle x = 0$, the mechanism becomes a general scissors mechanism, and there is no lateral migration.

3 Design and analysis of offset deployable and foldable mechanism

3.1 Design of offset deployable mechanism unit

(a) Structure of the mechanism   (b) Schematic diagram of the mechanism
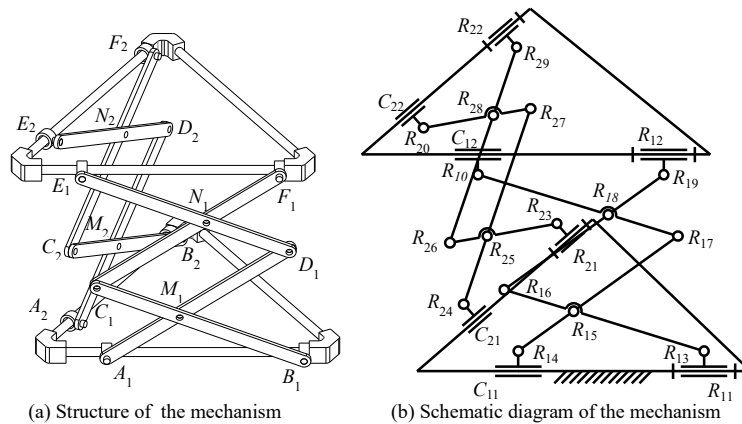
Fig. 3. Structure design of offset deployable mechanism units

The mechanism shown in Fig. 3(a) is obtained by the combination of two offset scissors mechanism and two platforms. One platform is used as a frame, the other is a moving platform. The offset scissor mechanism is connected with the platforms through a revolute pair and a cylindrical pair, so that B_1, B_2, F_1 and F_2 hinges in the offset scissors mechanism can rotate around the axis where they are located, and A_1, A_2, E_1 and E_2 hinges can rotate around the shaft and move along the shaft. The schematic diagram of the mechanism is shown in Fig. 3(b).

Similar to the offset scissors mechanism unit, the offset deployable mechanism unit still has the characteristics of easy series connection, and the offset deployable mechanism unit can produce a displacement parallel to the moving platform direction during the stretching process. This displacement is called the offset of the offset deployable mechanism, which is determined by the parameters of each link length in the offset deployable mechanism unit. By connecting the offset deployable mechanism units with different offset in series, a new type of deployable and foldable mechanism can be obtained, and the attitude of the mechanism after deployment will be determined by the offset of each offset deployable mechanism unit.

3.2 Degree of freedom analysis and kinematics analysis of offset deployable mechanism unit
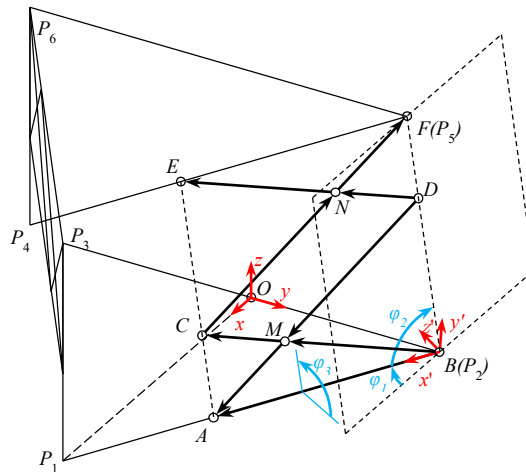
Fig. 4. The lateral schematic diagram of offset deployable mechanism

As shown in Fig. 4, with the midpoint of P_2P_3, O as the origin, OP_1 is x-axis positive direction, OP_2 is y-axis positive direction to establish a rectangular coordinate system, known as the main coordinate system $\{\alpha_1\}$.

In order to determine the degree of freedom and the displacement of the moving platforms, the offset scissors mechanism on one side are discussed. Taking P_2 as the

origin, P_2P_1 is x-axis to establish another coordinate system, so that the offset scissors mechanism is located in the xy-plane of the coordinate system which is called $\{\alpha_2\}$. In Fig. 4, φ_1 is the angle between the xz-plane of $\{\alpha_1\}$ and the x-axis of $\{\alpha_2\}$, φ_2 is the angle between AB link and BF link, and φ_3 is the angle between the xy-plane of $\{\alpha_1\}$ and the xy-plane of $\{\alpha_2\}$.

In the coordinate system a2, the screw system composed of pairs on the left side is

$$\{S_{a2b1}\} = \begin{cases} S_{R10} = \begin{pmatrix} 1 & 0 & 0 & p_{R10} & q_{R10} & 0 \end{pmatrix}^T \\ S_{R11} = \begin{pmatrix} 1 & 0 & 0 & 0 & 0 & 0 \end{pmatrix}^T \\ S_{R12} = \begin{pmatrix} 1 & 0 & 0 & p_{R12} & q_{R12} & 0 \end{pmatrix}^T \\ S_{R13} = \begin{pmatrix} 0 & 0 & 1 & 0 & 0 & 0 \end{pmatrix}^T \\ S_{R14} = \begin{pmatrix} 0 & 0 & 1 & p_{R14} & 0 & 0 \end{pmatrix}^T \\ S_{R15} = \begin{pmatrix} 0 & 0 & 1 & p_{R15} & q_{R15} & 0 \end{pmatrix}^T \\ S_{R16} = \begin{pmatrix} 0 & 0 & 1 & p_{R16} & q_{R16} & 0 \end{pmatrix}^T \\ S_{R17} = \begin{pmatrix} 0 & 0 & 1 & p_{R17} & q_{R17} & 0 \end{pmatrix}^T \\ S_{R18} = \begin{pmatrix} 0 & 0 & 1 & p_{R18} & q_{R18} & 0 \end{pmatrix}^T \\ S_{R19} = \begin{pmatrix} 0 & 0 & 1 & p_{R19} & q_{R19} & 0 \end{pmatrix}^T \\ S_{C11} = \begin{pmatrix} 1 & 0 & 0 & p_{C11} & 0 & 0 \end{pmatrix}^T \\ S_{C12} = \begin{pmatrix} 1 & 0 & 0 & p_{C12} & q_{C12} & 0 \end{pmatrix}^T \end{cases} \tag{7}$$

It is easy to obtain that the constraint screw system is

$$\{S_{a2b1}^r\} = \begin{cases} \begin{pmatrix} 0 & 0 & 0 & 0 & 1 & 0 \end{pmatrix}^T \\ \begin{pmatrix} 0 & 0 & 1 & 0 & 0 & 0 \end{pmatrix}^T \end{cases} \tag{8}$$

The constraint screw system $\{S_{a2b1}^r\}$ in the main coordinate system a1 is obtained by multiplying the left coordinate transformation matrix N.

$$S_{a1b1}^r = N S_{a2b1}^r \tag{9}$$

$$N = \begin{bmatrix} R & 0 \\ AR & R \end{bmatrix} \tag{10}$$

Coordinate a1 can be transformed into coordinate a2 by two rotations and one translation. Firstly, it rotates φ_1 around the z-axis of the coordinate system a1, and then rotates θ_3 around the x-axis of the coordinate system after rotation. Finally, it moves r_y along the y-axis of the coordinate system a1 to obtain the rotation matrix.

$$R = R_z R_x \tag{11}$$

of which

$$R_x = \begin{vmatrix} 1 & 0 & 0 \\ 0 & \cos\varphi_3 & -\sin\varphi_3 \\ 0 & \sin\varphi_3 & \cos\varphi_3 \end{vmatrix} \tag{12}$$

$$R_z = \begin{vmatrix} \cos\varphi_1 & -\sin\varphi_1 & 0 \\ \sin\varphi_1 & \cos\varphi_1 & 0 \\ 0 & 0 & 1 \end{vmatrix} \tag{13}$$

The displacement matrix is

$$A = \begin{vmatrix} 0 & 0 & r_y \\ 0 & 0 & 0 \\ -r_y & 0 & 0 \end{vmatrix} \tag{14}$$

The constraint screw system of this side is obtained as

$$\{S^r_{a1b1}\} = \begin{cases} \left(\sin\varphi_3\sin\varphi_1 \quad -\sin\varphi_3\cos\varphi_1 \quad \cos\varphi_3 \quad r_y\cos\varphi_3 \quad 0 \quad -r_y\sin\varphi_3\sin\varphi_1\right)^T \\ \left(0 \quad 0 \quad 0 \quad \cos\varphi_3\sin\theta_1 \quad -\cos\varphi_3\cos\varphi_1 \quad \sin\varphi_3\right)^T \end{cases} \tag{15}$$

Similarly, the constraint screw system of the other side in the coordinate system a1 can be deduced. Since the other side and the current side are symmetrical along the xy-plane of the coordinate system a1, the coordinate system of the other side can be obtained by rotating the coordinate system a1 around the z-axis $-\varphi_1$, and then around the x-axis of the coordinate system after rotation $-\varphi_3$, and finally moving $-r_y$ along the y-axis of the coordinate system a1. The derivation process is omitted.

$$\{S^r_{a1b2}\} = \begin{cases} \left(\sin\varphi_3\sin\varphi_1 \quad \sin\varphi_3\cos\varphi_1 \quad \cos\varphi_3 \quad -r_y\cos\varphi_3 \quad 0 \quad r_y\sin\varphi_3\sin\varphi_1\right)^T \\ \left(0 \quad 0 \quad 0 \quad -\cos\varphi_3\sin\varphi_1 \quad -\cos\varphi_3\cos\varphi_1 \quad -\sin\varphi_3\right)^T \end{cases} \tag{16}$$

The constraint screw system of the moving platform is a union of $\{S^r_{a1b1}\}$ and $\{S^r_{a1b2}\}$, consisting of four linearly independent screws

$$\{S^r\} = \begin{cases} \left(a_1 \quad 0 \quad b_1 \quad 0 \quad 0 \quad 0\right)^T \\ \left(0 \quad a_2 \quad 0 \quad b_2 \quad 0 \quad c_2\right)^T \\ \left(0 \quad 0 \quad 0 \quad a_3 \quad 0 \quad b_3\right)^T \\ \left(0 \quad 0 \quad 0 \quad 0 \quad 1 \quad 0\right)^T \end{cases} \tag{17}$$

By calculating the reciprocal screw of $\{S^r\}$, the basis of the motion screw of a moving platform can be obtained

$$\{S^f\} = \left\{ \left(0 \quad 0 \quad 0 \quad b_1 \quad 0 \quad -a_1\right)^T \right\} \tag{18}$$

of which

$$\frac{a_1}{b_1} = -\sin\varphi_1 \tan\varphi_3 \tag{19}$$

The analysis of $\{S^f\}$ shows that the moving platform has only one degree of freedom.

According to the conclusions in section 2, the offset angle θ, height h and offset $\triangle x$ can be obtained. Where φ_1 and $\boldsymbol{P_2} = (0, y_{P_2}, 0)^T$ are known. φ_2 is the complementary angle of offset angle θ, and φ_3 is calculated by φ_1 and φ_2.

$$\varphi_2 = \frac{\pi}{2} - \theta \tag{20}$$

$$\varphi_3 = \cos^{-1}\frac{\tan\varphi_1}{\tan\varphi_2} \tag{21}$$

Coordinate $\{\alpha_2\}$ can be obtained by translating coordinate $\{\alpha_1\}$ vector $\boldsymbol{P_2}$. For point coordinate vector $\boldsymbol{F}$ analysis

$$\boldsymbol{F}_{\{\alpha_1\}} = \boldsymbol{P_2} + \boldsymbol{RF}_{\{\alpha_2\}} \tag{22}$$

The point coordinate vector $\boldsymbol{F}$ in the coordinate system $\{\alpha_2\}$ is

$$\boldsymbol{F}_{\{\alpha_2\}} = (x, h, 0)^T \tag{23}$$

The point coordinate vector $\boldsymbol{F}$ in the coordinate system $\{\alpha_1\}$ is

$$\boldsymbol{F}_{\{\alpha_1\}} = (\triangle x\cos\varphi_1 - h\cos\varphi_3 \sin\varphi_1, y_{P_2}, h\sin\varphi_3)^T \tag{24}$$

The relative displacement of the upper and lower surfaces can be obtained

$$\boldsymbol{P_2P_5} = \boldsymbol{F}_{\{\alpha_1\}} - \boldsymbol{P_2} = (\triangle x\cos\varphi_1 - h\cos\varphi_3 \sin\varphi_1, 0, h\sin\varphi_3)^T \tag{25}$$

3.3 Engineering accomplishment of offset deployable mechanism unit

The offset deployable mechanism unit retains the characteristics of constant transverse spacing at the joint of the scissors and forks, so the offset deployable mechanism unit can be in series like the scissors mechanism. According to the engineering needs, the length of the link should be adjusted to make each unit have different transverse displacements.
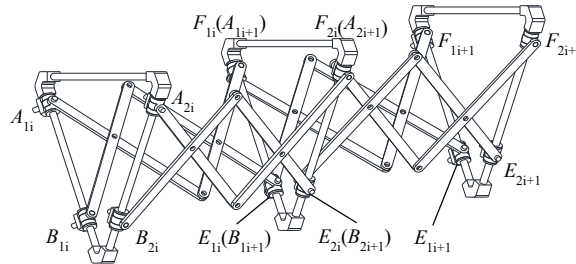
Fig. 5. Connection between offset deployable mechanisms unit

Let the upper and lower surface of the former unit merge with the lower surface of the next unit. The former unit F_{1i} and F_{2i} overlap with the B_{1i+1} and B_{2i+1} of the next unit, and the former unit E_{1i} and E_{2i} overlap with the A_{1i+1} and A_{2i+1} of the next unit. These points are connected by hinges. In order to achieve this function, this paper designs the nested hinge structure as shown in Fig. 6.
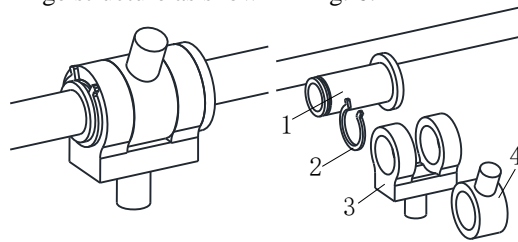
Fig. 6. Nested hinge structure

Among them, the internal rotation shaft 4 and the external rotation shaft 3 are nested on the linear bearing 1, and their positions are fixed by the retaining ring 2. The internal rotation shaft and the external rotation shaft can independently rotate around the linear bearing. At the same time, the linear bearing can slide along the assembled shaft. The hinge exists as the connection unit between the two offset deployable mechanisms units. It makes serial multiple units a deployable and folding mechanism.

4   Simulation verification of offset deployable mechanism unit
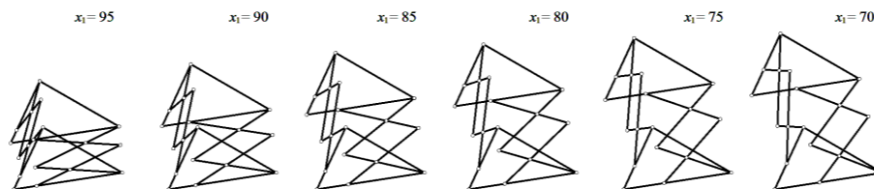
Fig. 7. Kinematics simulation of offset deployable mechanism unit

In Fig. 4, the length of AM link is $l_1 =60$, the length of BM link is $l_2 =40$, the upper and lower surfaces are equilateral triangles with side length of 100, and the distance of A and B is x_1. The kinematics simulation of the offset deployable mechanism is carried out by programming. The simulation result is shown in Fig. 7.
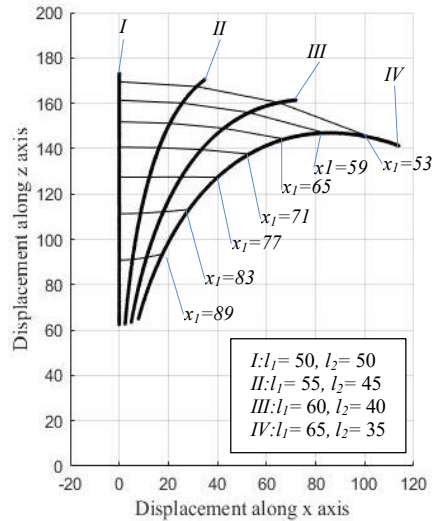
Fig. 8. The trajectory diagram of moving platform under different link lengths

In order to study the influence of link length in the process of mechanism movement, the displacement curves of the moving platform along x-axis and z-axis with different link lengths are shown in Fig. 8. Both platforms are equilateral triangles with sides of 100.

By comparing the displacement curves of four calculation example with different link lengths, it can be seen that when the link length is $l_1 = l_2$, the side of the offset deployable mechanism unit becomes a general scissor mechanism, and the offset deployable mechanism unit loses lateral offset. With the increase of the difference between the link length l_1 and l_2, the offset also increases.

5 Application of offset deployable and foldable mechanism

Emergency bridges are of great significance in extreme environments such as emergency rescue and disaster relief or battlefield. Mechanized emergency bridges can be rapidly deployed at designated locations to help personnel and vehicles quickly cross rivers, valleys, damaged roads and other complex terrain. The existing emergency bridges are mainly divided into two types: the assembly type and the folding type. The former is mostly composed of portable assembled units, which has the advantages of large span, flexible and reliable structure. However, the installation and disassembly rate is slow, and it is difficult to cope with emergency situations. The latter relies on the linkage mechanism or rope to complete the rapid shrinkage and extension of the bridge deck, but limited by the mechanism configuration and the strength of the material, the bearing capacity is insufficient.

The arch structure has better bearing capacity than the linear structure. The traditional folding emergency bridge is often a linear telescopic mechanism. Relying

on the offset deployable and foldable mechanism, an emergency bridge with arch structure shown in the Fig. 9 can be constructed. The offset deployable and foldable mechanism has the advantages of large folding ratio and less freedom, which makes the bridge span larger and the control simpler. At the same time, the offset deployable and foldable mechanism is only controlled by a single prime mover, which makes the bridge contraction and extension process simple and rapid.

(a) Unfolding state of the bridge   (b) Folding state of the bridge
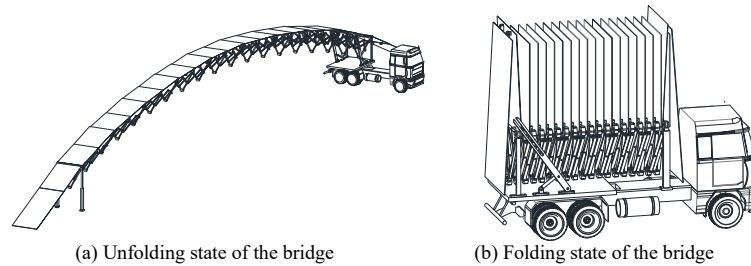
Fig. 9. Vehicle emergency arch bridge

6   Conclusion

In this paper, an offset scissors mechanism is proposed, and an offset stretch mechanism unit is proposed based on the offset scissors mechanism. The mechanism retains the large folding ratio of the scissors mechanism and the invariance of the distance during the operation, and can produce controllable lateral offset during the stretching process. The relationship between the lateral offset of the mechanism and the length of each connecting link is determined through the kinematic analysis of the offset deployable mechanism unit. The lateral offset in the offset scissors mechanism is positively correlated with the extension length. The larger the gap between the length of the long link and the short link is, the larger the lateral offset is.

The three-dimensional model of the mechanism is designed, and a nested hinge is proposed to realize the series connection between the offset deployable mechanism units. The mathematical model of offset deployable mechanism unit is established by programming, and its kinematics simulation is carried out to verify the feasibility of the above design.

Acknowledgment

References

[1] K. Xu, A.W. Qiao, X.L. Ding: Design and analysis of a Scissor-bending deployable and foldable mechanism. Journal of mechanical engineering 56(05), 55-62 (2020).

[2] D.L. Li, Z.H. Zhang, Z. YU: Kinematic characteristic analysis of spherical scissors deployable mechanisms. Journal of mechanical engineering 49(13), 1-7 (2013).

[3] X.M. Sun, R.M. Li, Z.Y. Xun, et al: A multiple-mode mechanism composed of four antiparallelogram units and four revolute joints. Mechanism and Machine Theory 155,104-106 (2021).

[4] R. Li, Y.A. Yao, X. Kong: Reconfigurable deployable polyhedral mechanism based on extended parallelogram mechanism. Mechanism and Machine Theory 116, 467-480 (2017).

[5] C.J. Garcḯa-Mora, J. Sánchez-Sánchez: Geometric method to design bistable and non-bistable deployable structures of straight scissors based on the convergence surface. Mechanism and Machine Theory 146, 103720 (2020).

[6] G. Li, H. Huang, H. Guo, et al: Design, analysis and control of a novel deployable grasping manipulator. Mechanism and Machine Theory 138, 182-204 (2019).

[7] C.Q. Gao, H.L. Huang, B. Li, et al: Design of a truss-shaped deployable grasping mechanism using mobility bifurcation. Mechanism and Machine Theory 139, 346-358 (2019).

[8] W.H. Lee, A.C. Sanderson: Dynamic analysis and distributed control of the tetrobot modular reconfigurable robotic system. Autonomous Robots 10(1), 67-82 (2001).

[9] Y. Yang, T. Lei, H.Y. Zheng, et al: Kinematic stability of a 2-DOF deployable translational parallel manipulator. Mechanism and Machine Theory 160, 104261 (2021).

[10] Y. Yang, L. Hu, H.Y. Zheng, et al: Two types of remote-center-of-motion deployable manipulators with dual scissor-like mechanisms. Mechanism and Machine Theory 160(2), 104274 (2021).

[11] M. Nizami, Z.A. Shah, Y. Ayaz, et al: Proximal Actuation of an Elastically Loaded Scissors Mechanism for the Leg Design of a Quadruped Robot. IEEE Access, pp. 208240-208252. IEEE (2020).

[12] M. Afshar, J. Carriere, T. Meyer, et al: Optimal Design of a Novel Spherical Scissor Linkage Remote Center of Motion Mechanism for Medical Robotics. 2020 IEEE/RSJ International Conference on Intelligent Robots and Systems (IROS). pp. 6459-6465. IEEE, USA (2020).

[13] Y. Yang, Y. Peng, H.Y. Pu, et al: Deployable parallel lower-mobility manipulators with scissor-like elements. Mechanism and Machine Theory 135, 226-250 (2019).

[14] D.J. Gonzalez, H.H. Asada: Design and Analysis of 6-DOF Triple Scissor Extender Robots with Applications in Aircraft Assembly. IEEE Robotics & Automation Letters, PP: 1420-1427. IEEE (2017).

[15] D.J. Gonzalez: Triple Scissor Extender: A 6-DOF lifting and positioning robot. IEEE International Conference on Robotics & Automation, ICRA, pp. 847-853, Stockholm, Sweden (2016).

[16] L. Zhang, Y. Li: Synchronous control of double hydraulic cylinders of scissors aerial work platform based on Fuzzy PID. 2020 5th International Conference on Electromechanical Control Technology and Transportation, ICECTT (2020).

[17] N. Shrivastava, A. Pande, J. Lele, et al: Embedded Control System for Self Adjusting Scissor Lift. 2018 Fourth International Conference on Computing Communication Control and Automation (ICCUBEA), pp. 1-5. IEEE, India (2018).

[18] S. Santhosh: Innovative methodology and designing of intelligent mobile robots computer vision with genetic algorithm SLE mechanism and advanced sensors in managing disaster. 2014 International Conference on Circuits, Power and Computing Technologies [ICCPCT-2014], pp. 1692-1697. IEEE, India (2014).

[19] M. T. Islam, C. Yin, S. Jian, et al: Dynamic analysis of Scissor Lift mechanism through bond graph modeling. 2014 IEEE/ASME International Conference on Advanced Intelligent Mechatronics, pp. 1393-1399. IEEE, France (2014).

[20] J.G. Grijalva, R. Edson. D. Pieri, et al: Robust control of scissor-like elements based systems. Mechanism and Machine Theory 150, 103849 (2020).

[21] Y.T. Sun, S.M Wang, J.K Mills, et al: Kinematics and dynamics of deployable structures with scissor-like-elements based on screw theory. Chinese Journal of Mechanical Engineering 27(4), 655-662 (2014).

[22] Y.T. Sun, S.M Wang, J.F Li, et al: Mobility analysis of the deployable structure of SLE based on screw theory. Chinese Journal of Mechanical Engineering 26(4), 793-800 (2013).

[23] J.S. DAI: Geometrical foundations and screw algebra for mechanisms and robotics. Higher Education Press, Beijing (2014).

[24] R.Q. Liu, C. Shi, H.W. Guo, et al: Review of space deployable antenna mechanisms. Journal of mechanical engineering 56(05), 1-12 (2020).

[25] J.S. Dai, J.R. Jones: Mobility in metamorphic mechanisms of foldable/erectable kinds. Journal of Mechanical Design 121(3), 375-382 (1999).

[26] R.G. Wang, J.X Sun, J.S. Dai: Design analysis and type synthesis of a petal-inspired space deployable-foldable mechanism. Mechanism and Machine Theory 141, 151-170 (2019).

Design and Analysis of a Passive Lockable Prismatic Joint for Reconfigurable Mechanisms

Yingzhong Tian[1,2], Zhenyu Tian[1,2], Yinjun Zhao[1,2], Long Li[1,2*], Fengfeng Xi[3]

[1] School of Mechatronic Engineering and Automation, Shanghai University,
Shanghai 200444, China
[2] Shanghai Key Laboratory of Intelligent Manufacturing and Robotics,
Shanghai 200444, China
[3] Department of Aerospace Engineering, Ryerson University,
Toronto ON M5B 2K3, Canada
Corresponding author email: lil@shu.edu.cn

Abstract. Reconfigurable mechanisms have a wide range of applications in aerospace. One of the ways to achieve reconfiguration is to use the lockable joints to merge the adjacent components to change the topological structures and mobility. In actual engineering applications, this lockable device needs to be designed with a compact, light-weight structure as well as has a good load-bearing ability. Focus on this, a passive lockable prismatic joint based on the ratchet mechanism is proposed in this paper. The proposed joint can lock and resist high force from two directions under normal conditions and unlock quickly in any of the two directions when necessary. The wedge unlocking mechanisms arranged in the axial direction make the design relatively lightweight, compact, and effortless. By controlling two sets of locking modules, this joint can achieve four motion modes, including unlockable, bilateral lockable, and unidirectional locking. The static force analysis of the lockable devices is conducted, and corresponding experiments were taken to validate the correctness of the theoretical model. Furthermore, an application in a morphing wing to change its chord length and camber is proposed to further demonstrate the effectiveness and functions of the design.

1   Introduction

Reconfigurable mechanisms can rearrange and change the components to adapt to different requirements and environments [1, 2]. A simple way to realize the reconfiguration is to use lockable joints to merge the adjacent components to change the topological structures and mobility [3-5].

In general, the common locking joints are categorized into four main locking principles including singularity locking, friction-based locking, mechanical locking[4], and material-based locking[6]. Singularity locking mechanisms can achieve high locking

force in a singular position and little power consumption when unlocking. Van Oort et al. presented a knee locking mechanism by using the singularity of a four-bar linkage to lock the knee in a specific position[7]. However, these mechanisms based on singularity locking have only one locking position and need large design space.

Friction-based locking joints can achieve infinite locking positions by engaging the two friction surfaces. Therefore, the corresponding locking force is determined by the normal force and the friction coefficient. Aghili et al. [8] proposed a lockable telescopic joint and applied it in a reconfigurable space robot to change the DH parameters and fold the robots into a small space. Similarly, Hebert et al. [9] presented a 3-degree-of-freedom (DOF) reconfigurable robotic arm equipped with passive telescopic joints according to the friction locking. In Ref. [10], the authors proposed a novel concept of a reconfigurable fixture using stepless active revolute lockable joints to resist high torque in both directions. The friction-based locking joints need high energy consumption although can be realized by equipped with a force amplifier, the design becomes bulk.

In order to increase the locking force by changing the normal force, an extra force amplifier needs to be arranged in the locking joint which makes the design bulky.

With the development of material science, many researchers use smart materials to lock, for instance, shape memory polymer composites (SMPCs). Zhang et al.[11] presented an ultra-light release device by using the SMPCs to lock. Lan et al.[6] proposed the SMPC releasing mechanism and used it to lock and release the rolled flexible solar array. Material-based locking mechanisms have satisfactory reusability and limited locking capacity and are suitable for miniaturized hold-release environments.

Mechanical locking mechanisms limit the motion of two parts by the blocking part such as solid component and incompressible liquid. The locking force is determined by the strength of the material. Mechanical locking mechanisms are compact and have low energy consumption and weight when compared to other locking principles. Chung Deok Gyoon et al.[12] presented the shape-locking flexible joint based on latches and applied them into the flexible surgical robots to improve the rigidity. Zuo et al.[13] proposed the "Dragon skin" mechanical locking structure to switch between the rigid and flexible modes. Guo et al.[14] proposed a self-locking structure based on ratchet-and-pawl to change the stiffness of the soft gripper. Besides, Moosavian and Xi [15] designed a multifunctional flow control valve for self-circulating hydraulic cylinders which can generate four positions, and discussed the application of the morphing wings to restore the required stiffness and providing additional structural support.

Focus on aerospace applications, we propose a passive lockable joint with a light-weight and compact structure. The mechanism is designed with two-direction controllable spring-ratchet mechanisms and is controlled by two wedge unlocking mechanisms to release the two directions. The static force analysis and experiments are also conducted to evaluate the function and performance of the proposed design.

The following of this paper is organized as follows. Section 2 discusses the design of the lockable joint and its working principles. Section 3 presents the fabrication and statics modeling of the passive lockable joint. Section 4 carries out relevant mechanics experiments and applies them in an airfoil-morphing wing.

2 Design and Working Principle

2.1 Conceptual Design

The ratchet mechanisms, allowing the motion of one direction and prohibiting the reversed, have been widely used to transmit motion in engineering [16-18]. Figure 1 shows the configuration of the lockable joint that consists of two locking modules, tube, inner and outer pipe.
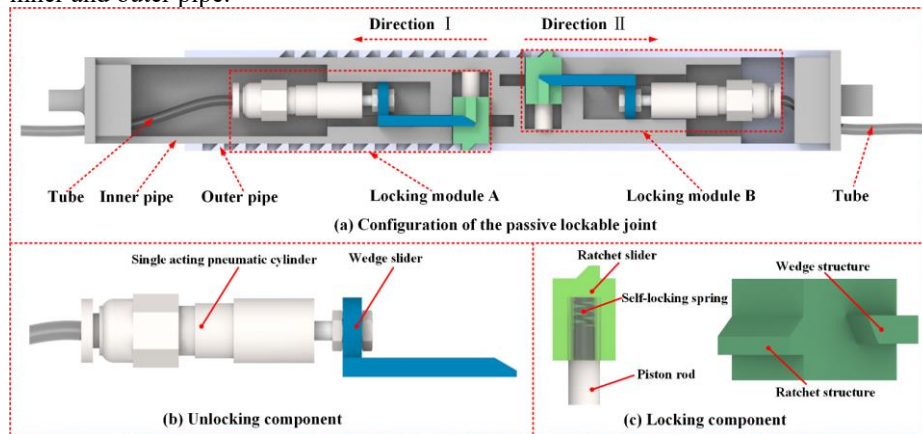
Fig. 1. The structure design of the passive lockable joint

As is shown in Fig. 1, the locking module is composed of a spring-ratchet locking component and a wedge unlocking component. The locking component contains a ratchet slider, a self-locking spring, and a piston rod. Under the action of the self-locking spring, the ratchet slider can lock in a stable position and bear the external load of one direction. The slider slides freely in the other direction with little driving force.

The lockable joint needs to unlock quickly and effortlessly when performing unlocking tasks. According to the excellent performance of pneumatic cylinders, which are lightweight, clean, large power output, and fast response, the lockable joint adapts it to act as an unlocking driver [19-21]. Besides, to increase the force of unlocking, the unlocking component takes the design of the wedge structure. Wedge mechanism, not only can change the direction of force transmission but also can amplify the output force. The wedge unlocking mechanism arranged in the axial direction reduces the design space in case of effective unlocking.

This paper takes the single-acting pneumatic cylinder to push the wedge slider to resist the spring force and push the ratchet teeth slider out away from the cogging when needed to perform unlocking tasks. Without air pressure input, the single-acting pneumatic cylinder returns to the normal position by spring and the joint can lock in the scheduled position.

The inner and outer pipe are both square, where the inner pipe has circuits for installing locking modules and the inner wall of the outer pipe has arrayed cogging which acts as different locking positions.

2.2 Working Principle

The working principle of the passive lockable joint is illustrated in Fig. 2. Four positions are generated by the passive lockable joint and presented in Table 1 (The direction is the inner pipe relative to the outer pipe). Terms A and B correspond to the two locking modules, while terms 1 and 0 represent the on and off working status of the single-acting pneumatic cylinder, respectively.

In normal instances, the ratchet sliders are locked by the self-locking spring and limit to two directions. When the joint needs to perform tasks, the cylinder works, and the ratchet slider moves back so that the inner pipe can slide freely. When the inner pipe moves to the targeted position, the air pressure inside the cylinder is interrupted to stop the movement.

Since the load-bearing capacity of the passive lockable joint is not only related to the manufacturing material but also related to the unlocking mechanisms generated by the pneumatic cylinder. Hence the extreme value of the unlocking capacity can be adjusted by changing the working pressure.
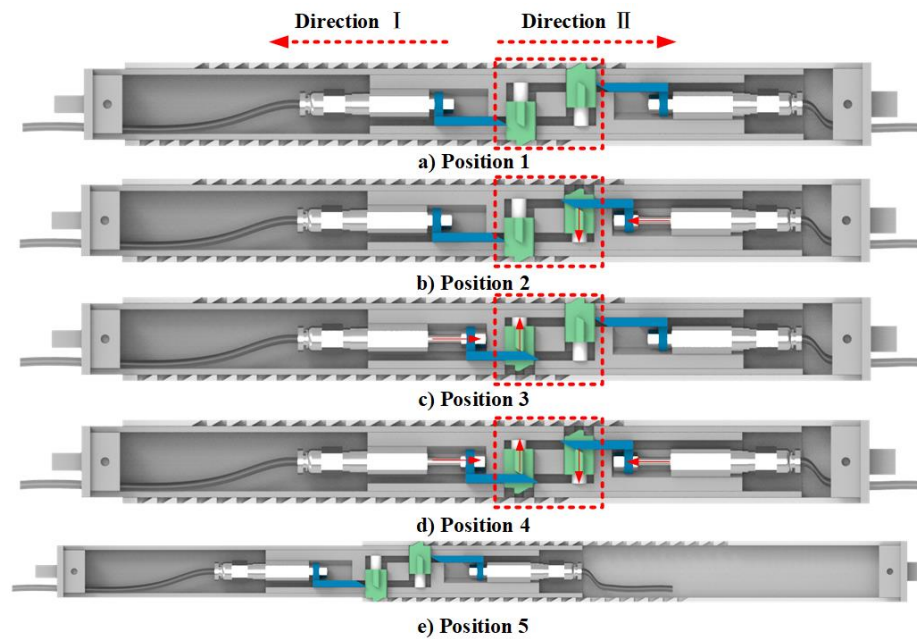
Fig. 2. Operation principle of the passive lockable joint. (a)The joint is locked in normal positions. (b)When the locking module B works, the inner pipe is free in Direction II and limited in Direction I. (c) When the locking module A works, the inner pipe is free in Direction I and limited in Direction II. (d) When the locking module A and B work at the same time, the inner pipe is free in Direction I and II. (e) The extreme working position of the lockable joint is shown in Fig. 2(e).

Table 1 Four positions generated by controlling two locking modules

Position	Locking module A	Locking module B	Direction I	Direction II
1	0	0	locked	locked
2	0	1	locked	unlocked
3	1	0	unlocked	locked
4	1	1	unlocked	unlocked

3   Fabrication and Modeling

3.1   Fabrication

Figure 3 illustrates the system composition of the passive lockable joint. The main components of the lockable joint are made possible by a 3D printer. The actual locking and unlocking parts are shown in Fig. 3(b) and Fig. 3(c). The pneumatic controller board is used to control the two solenoid valves and responsible for switching the work modes according to various situations.
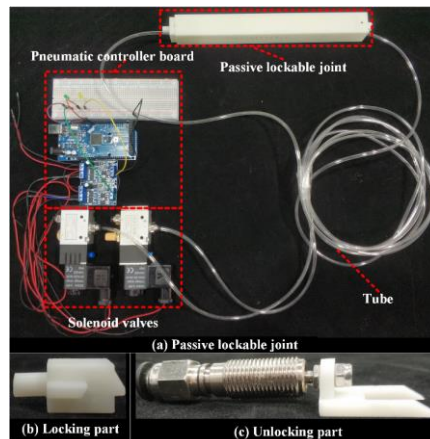
Fig. 3. Fabrication of the passive lockable joint. (a) The components of the joint. (b)The 3D-printed locking part. (c)The 3D-printed wedge slider and pneumatic cylinder.

3.2   Modeling

The ratchet slider determines the load-bearing capacity of the passive lockable joint and the wedge slider takes the responsibility for the unlocking. This section provides the static force analysis to guarantee that the joint can function normally and ensure the effective working range according to the unlocking capacity.

Load-Bearing Capacity

In the lockable state, the ratchet teeth sliders are pushed to the cogging of the outer pipe by the self-locking spring to limit the relative movement between the outer and

inner pipe. Therefore, the slider supports the shear force from the pipes, and the corresponding shear strength and cross-sectional area determine the load-bearing capacity of the joint. Accordingly, the formula of bearing external force is as follows:

$$F_{load} \leq A\tau \tag{1}$$

As is shown in Fig. 4, $A(A = a*b)$ is the cross-sectional area of the ratchet teeth slider and a, b is the cross-sectional geometric parameters of the slider, w is the height of the slider, and the τ is the shear modulus of the manufacturing material. This paper chooses the resin material to manufacture and the load-bearing force of the joint can achieve $1500N$ where A is $50mm^2$.
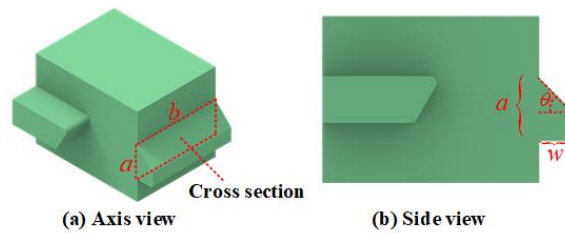
Fig. 4. Ratchet slider

Force Analysis of Unlocking Process

The wedge slider, driven by a single-acting pneumatic cylinder, pushes the ratchet teeth slider to move back from the cogging. In this circumstance, the pipes slide freely and the joint unlocks to move to the targeted position. This chapter calculates the relationship between the input force F_i provided by the pneumatic cylinder and the external load F_{load}.
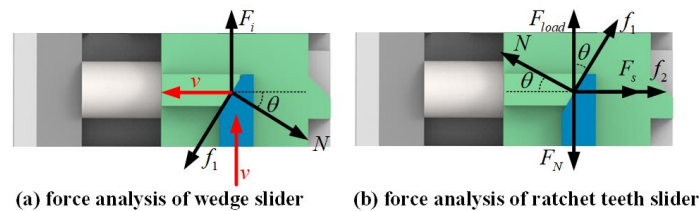
Fig. 5. Force analysis of the unlocking process

As is shown in Fig. 5, the wedge unlocking component not only changes the direction of the force but also increases the output force by changing the wedge angle. The single-acting pneumatic provides the input force F_i to drive the ratchet slider to overcome the existed resistance. The input force F_i can be written as

$$F_i = PS \tag{2}$$

where P represents the air pressure of the pneumatic actuator, S denotes the cross-sectional area of the pneumatic cylinder. And N represents the support force generated

by the input force F_i and drives the ratchet slider to move back. As seen in Fig. 5(a), the relationship between support force (N) and input force (F_i) can be written as

$$N = \frac{F_i}{(\sin\theta + \mu\cos\theta)} \tag{3}$$

where θ is the friction coefficient of the manufacturing material (Resin), θ denotes the angle of the wedge slider. As shown in Fig. 5(b), support force (N) overcomes the existed resistance, including the spring force F_s generated by self-locking spring, the friction force f_1 between the wedge and ratchet slider, and the friction f_2 between the ratchet slider and inner pipe, so that the joint can unlock freely and perform other work. The statics balance analysis of ratchet slider in unlocking process can be obtained as

$$N\cos\theta = f_1\sin\theta + F_s + f_2 \tag{4}$$

Where $f_1 = \mu N$, $F_s = kx$ (k represents the spring stiffness and x denotes the compressed displacement), F_N is the supporting force provided by the inner pipe, and $f_2 = \mu(N\sin\theta + f_1\cos\theta + F_{load})$ (F_{load} is the external load). According to equations (3)-(4), the relationship between the input force F_i and external force can be written as

$$F_i = (F_s + \mu F_{load})\frac{(\sin\theta + \mu\cos\theta)}{(\cos\theta - 2\mu\sin\theta - \mu^2\cos\theta)} \tag{5}$$

According to Eq. 5, the joint can achieve a larger output force by decreasing the wedge angle θ and increasing the input working pressure.

Analysis of Sliding Process

One side of the ratchet slider can undertake the external loads, while the other side begins to slide freely when applied the external force. Figure 6 shows the mechanics analysis of the free sliding process. This chapter calculates the minimum external load to ensure that the inner pipe can slide freely.

(a) force analysis of outer pipe   (b) force analysis of ratchet slider
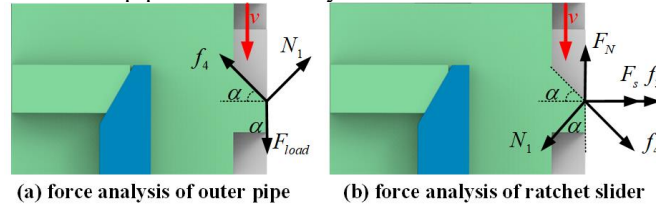
Fig. 6. Force analysis of the sliding process

As seen in Fig. 6, the external load F_{load} needs to overcome the existed resistance, including elastic force F_s, f_3 and f_4 that the friction force between the ratchet slider and the outer, inner pipe respectively. The statics balance analysis of the ratchet slider in the sliding process can be obtained as

$$N_1\sin\alpha = f_3 + f_4\cos\alpha + F_s \tag{6}$$

where α denotes the ratchet angle, N_1 represents the support force generated by F_{load} and $N = F_{load} / (\cos\alpha + \mu\sin\alpha)$, $f_4 = \mu N_1$, $f_3 = \mu F_N (F_N = N_1 \cos\alpha + f_4 \sin\alpha)$. According to Eq. (6), the relationship between the external force and the resistance can be described as

$$F_{load} = F_s \frac{(\cos\alpha + \mu\sin\alpha)}{(\sin\alpha - 2\mu\cos\alpha - \mu^2 \sin\alpha)} \qquad (7)$$

As calculated by Eq. (7), the minimum external load F_{load} that drives the inner pipe to slide is 1.07N in this prototype. Ensure that the inner pipe can slide smoothly, the actual external load needs to be larger than the calculated value.

4 Validation and Application

4.1 Experimental Validation

To validate the functionality of the passive lockable joint, an experimental setup was designed and shown in Fig. 7(a). The stepper motor was driven at a rated speed, while the load was measured on a dynamometer fixed on the stepper motor. Due to the modular design of the locking module, this paper focuses on the experiments of the compressed state and verifies the accuracy of the model.

Through the experiments, the passive lockable joint can overcome more than 100N but is limited by the range of the dynamometer. Besides the reliable locking, the joint needs to unlock in time to complete related work. The unlocking capacity deserves the actual effective working range. Relevant experiments validate the theoretical model with the actual unlocking. Figure 7(b) shows the experimental results and the theoretical predictions of the load-bearing force. It can be observed that experimental results are similar to the theoretical predictions. And actual load-bearing force is lower than the theoretical due to the influence of various existed frictions.

(a) Experimental Setup   (b) Comparision
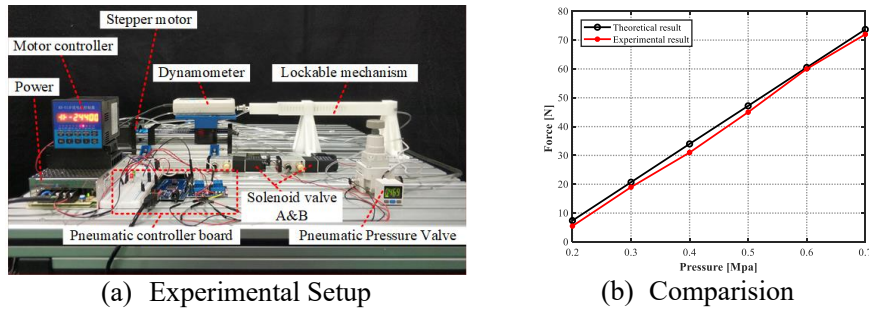
Fig. 7. The experimental setup and comparison

4.2 Application

Xi et al.[22, 23] proposed the design of an underactuated parallel mechanism that is applied in the morphing wing. As shown in Fig. 8, this design is composed of active linear actuators and passive lockable limbs. Through locking specific lockable joints,

the motion modes of the mechanism can be changed. Through a multi-step control strategy with topology changing, this morphing mechanism can achieve planar 3-DOF morphing using 2 actuators. Hence, the mechanism could be used to change the wing airfoil. Besides, the proposed joints can ensure that the wing can morph in the targeted direction(released direction of lockable joints) and limit the motion of the opposite direction when faced with gust loads in each step motion.
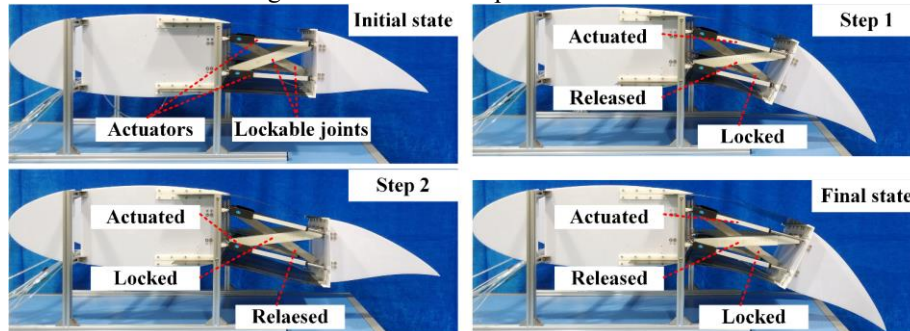
Fig. 8. Application on a morphing wing

5 Conclusion

This paper presents a novel passive lockable joint based on the spring-ratchet mechanism and wedge unlocking mechanism, which can lock in normal conditions to undertake the external load from two directions and unlock quickly when needed. By controlling the locking modules, the joint has four operation modes including unlockable, bilateral lockable, and unidirectional lockable.

Statics model is proposed to evaluate the performance of its load-carrying ability and the unlocking actuation force. The experiment results on the prototype validate the functions of the joints and the correctness of the relationship between the input force and external load. Finally, we apply the passive lockable joint in an underactuated parallel mechanism to show its potential applications in aerospace.

References

[1] D. Li, P. Jia, J. Li, D. Zhang, X. Kong, Constraint and Mobility Change Analysis of Rubik's Cube-inspired Reconfigurable Joints and Corresponding Parallel Mechanisms, Chinese Journal of Mechanical Engineering, 33 (1) (2020).

[2] R.M. Setchi, N. Lagos, Reconfigurability and reconfigurable manufacturing systems state-of-the-art review, (2004) 529-535.

[3] W. Zhang, S. Lu, X. Ding, Recent development on innovation design of reconfigurable mechanisms in China, Frontiers of Mechanical Engineering, 14 (1) (2018) 15-20.

[4] M. Plooij, G. Mathijssen, P. Cherelle, D. Lefeber, B. Vanderborght, Lock Your Robot: A Review of Locking Devices in Robotics, IEEE Robotics & Automation Magazine, 22 (1) (2015) 106-117.

[5] D. Wang, J. Dai, Theoretical foundation of metamorphic mechanism and its synthesis, Chinese Journal of Mechanical Engineering, 43 (8) (2007) 32-42.

[6] X. Lan, L. Liu, F. Zhang, Z. Liu, L. Wang, Q. Li, F. Peng, S. Hao, W. Dai, X. Wan, Y. Tang, M. Wang, Y. Hao, Y. Yang, C. Yang, Y. Liu, J. Leng, World's first spaceflight on-orbit demonstration of a flexible solar array system based on shape memory polymer composites, Science China Technological Sciences, 63 (8) (2020) 1436-1451.

[7] G. van Oort, R. Carloni, D.J. Borgerink, S. Stramigioli, An Energy Efficient Knee Locking Mechanism for a Dynamically Walking Robot, 2011 Ieee International Conference on Robotics and Automation (Icra), (2011) 2003-2008.

[8] F. Aghili, K. Parsa, Ieee, Design of a reconfigurable space robot with lockable telescopic joints, Ieee, New York, 2006.

[9] P. Hebert, C. Tatossian, M. Cairns, F. Aghili, K. Parsa, A. Morozov, Toward the design and simulation of a new generation of reconfigurable space manipulators using telescoping passive joints, Trans. Can. Soc. Mech. Eng., 31 (4) (2007) 535-545.

[10] S.N. Lu, M. Zoppi, D. Zlatanov, Z. Ahamad, R. Molfino, Design And Testing Of a Novel Stepless Lockable Joint for Use In Reconfigurable Fixtures, Proceedings Of the Asme International Design Engineering Technical Conferences And Computers And Information In Engineering Conference, 2014, Vol 5b, (2014).

[11] D. Zhang, L. Liu, J. Leng, Y. Liu, Ultra-light release device integrated with screen-printed heaters for CubeSat's deployable solar arrays, Composite Structures, 232 (2020).

[12] D.G. Chung, J. Kim, D. Baek, J. Kim, D.-S. Kwon, Shape-Locking Mechanism of Flexible Joint Using Mechanical Latch With Electromagnetic Force, IEEE Robotics and Automation Letters, 4 (3) (2019) 2661-2668.

[13] S. Zuo, K. Iijima, T. Tokumiya, K. Masamune, Variable stiffness outer sheath with "Dragon skin" structure and negative pneumatic shape-locking mechanism, Int J Comput Assist Radiol Surg, 9 (5) (2014) 857-865.

[14] X.-Y. Guo, W.-B. Li, Q.-H. Gao, H. Yan, Y.-Q. Fei, W.-M. Zhang, Self-locking mechanism for variable stiffness rigid–soft gripper, Smart Materials and Structures, 29 (3) (2020) 035033.

[15] A. Moosavian, M. Rizoiu, F. Xi, Design of a Multifunctional Flow Control Valve for Self-Circulating Hydraulic Cylinders, Journal of Pressure Vessel Technology, 139 (2) (2017) 025001.

[16] P.H. Pham, D.V. Dao, A micro gearing system based on a ratchet mechanism and electrostatic actuation, Microsystem Technologies, 19 (2) (2012) 261-267.

[17] D.V. Dao, P.H. Pham, S. Sugiyama, Multimodule Micro Transportation System Based on Electrostatic Comb-Drive Actuator and Ratchet Mechanism, Journal of Microelectromechanical Systems, 20 (1) (2011) 140-149.

[18] D.V. Dao, P.H. Pham, S. Sugiyama, A novel micro transportation system with fast movement of a micro container based on electrostatic actuation and a ratchet mechanism, Journal of Micromechanics and Microengineering, 20 (11) (2010).

[19] B. Taheri, D. Case, E. Richer, Force and Stiffness Backstepping-Sliding Mode Controller for Pneumatic Cylinders, IEEE/ASME Transactions on Mechatronics, 19 (6) (2014) 1799-1809.

[20] M.E. Giannaccini, C. Xiang, A. Atyabi, T. Theodoridis, S. Nefti-Meziani, S. Davis, Novel Design of a Soft Lightweight Pneumatic Continuum Robot Arm with Decoupled Variable Stiffness and Positioning, Soft Robot, 5 (1) (2018) 54-70.

[21] H.I. Ali, S. Noor, S. Bashi, M. Marhaban, A review of pneumatic actuators (modeling and control), Australian Journal of Basic and Applied Sciences, 3 (2) (2009) 440-454.

[22] F. Xi, Y. Zhao, J. Wang, W. Wang, Y. Tian, Two Actuation Methods for a Complete Morphing System Composed of a VGTM and a Compliant Parallel Mechanism, Journal of Mechanisms and Robotics, (2021) 1-39.

[23] J. Wang, Y. Zhao, F. Xi, Y. Tian, Design and analysis of a configuration-based lengthwise morphing structure, Mechanism and Machine Theory, 147 (2020).

Considering Thickness-Accommodation, Nesting, Grounding and Deployment in Design of Miura-ori Based Space Arrays

Diana Bolanos[1], Nathan Brown, Collin Ynchausti, Hunter Pruett, Jared Hunter, Brooklyn Clark, Terri Bateman, Larry L. Howell, and Spencer P. Magleby

Brigham Young University, Provo UT 84602, USA

Abstract. *Miura-ori is a commonly used origami pattern in the field of aerospace design. The pattern exhibits favorable qualities needed for deployable space arrays. However, it is important to understand the limitations of the Miura-ori before selecting it as the pattern of choice. The goal of the paper is to build on previous work regarding applications of the Miura-ori pattern. The challenges associated with thickness-accommodation, nesting, grounding and deployment of the Miura-ori are addressed. Recommendations are provided on ways to mitigate such challenges.*

1 INTRODUCTION

Deployable space arrays, whether they be used as a solar panel [1], reflectarray [2], sunshield [3], or telescope [4], are designed to achieve a high ratio of deployed area to stowed volume. This is necessary to maintain spatial efficiency in the payload area of the spacecraft the array launches in. Maximizing this ratio is difficult, as larger deployed sizes pose complications with stowing the array within the spacecraft prior to deployment. One solution to this challenge is the use of origami-based design [5].

Traditional origami is created using paper and other materials that effectively have zero-thickness. Origami-based design utilizes origami patterns and principles with engineered materials and applies them to applications such as space arrays.

One particular origami pattern that has caught the attention of the aerospace industry is the Miura-ori [6]. This pattern is attractive because it can deploy from a relatively small stowed volume to a large deployed area using a one degree-of-freedom actuation system [7], as seen in Fig. 1. The Miura-ori pattern has other favorable qualities - such as simplicity of structure resulting from the repetition of its basic unit cell. This allows rows of cells to be added or removed from the pattern for a given design, allowing designers to modify the deployed to stowed ratio. While these qualities are attractive for a deployable space array design,

(a) Stowed paper Miura-ori.
(b) Partially-deployed paper Miura-ori.
(c) Mostly-deployed paper Miura-ori.
(d) Fully deployed paper Miura-ori.

(e) Stowed metal Miura-ori.
(f) Partially-deployed metal Miura-ori.
(g) Mostly-deployed metal Miura-ori.
(h) Deployed metal Miura-ori.
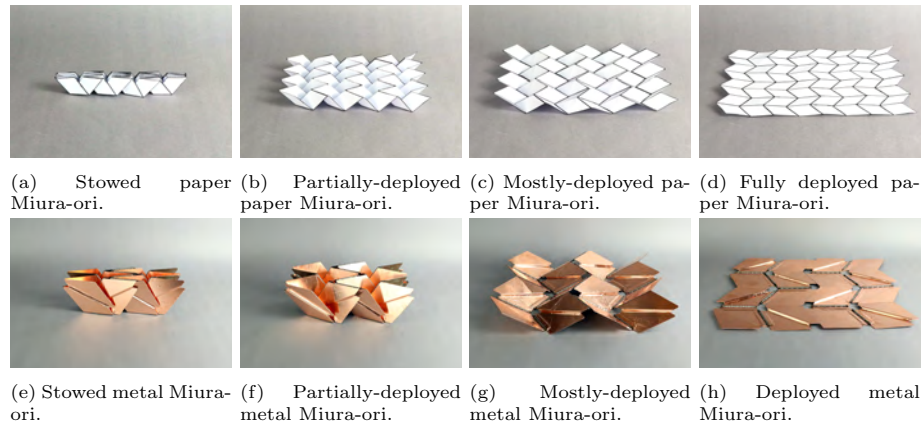
Fig. 1: The evolution of Miura-ori from paper origami to a metal prototype. a-d) The deployment of a paper origami Miura-ori, e-h) The deployment of a metal, thickness-accommodated, real-world applicable Miura-ori.

other challenges arise. Careful consideration must be made to avoid issues caused by panel thickness [8], deployment [9], and nesting to create a viable Miura-ori origami-inspired mechanism. The evolution of the Miura-ori origami pattern to an application using such considerations can be seen in Fig. 1.

This paper acknowledges the Miura-ori as a favorable pattern to be used in deployable space arrays, but also presents the challenges that must be considered when designing a Miura-ori array. Potential solutions are also introduced. While this paper focuses on space array applications, it is important to note that such methods can be adapted to aid in the design and development of other thick Miura-ori applications.

2   BACKGROUND

Deployable origami is seen in bellows [10], sound barriers [11], and space telescopes [3]. Characterizations between types of active and passive deployment have been developed to help designers distinguish different methods of actuation and better understand their principles [12]. One common approach for deploying origami systems is to use strain energy [13]. This method of deployment is favorable for space applications because it avoids the need for external energy sources or actuators like motors. Strain energy is an efficient way to create deployment in space systems [14]. However, other mechanisms such as trusses and booms exist for deployment. These methods may also be considered to converge on an optimal deployment method dependant on the needs of the mission.

The Miura-ori is one of many deployable origami patterns. This pattern was first developed by Koryo Miura [15]. One attractive quality of the pattern is its flat-foldability, meaning that the pattern can be continuously folded from 0 to
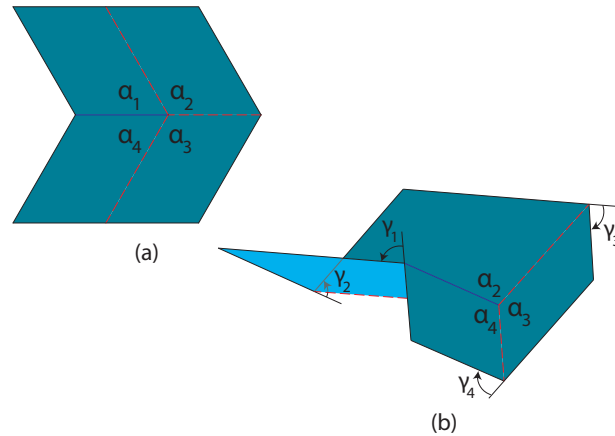
Fig. 2: (a) Angle parameters of the Miura-ori unit-cell. $\alpha_1 = \alpha_4$ and $\alpha_2 = \alpha_3$. (b) γ_i is the deployment angle of each panel and shows the angle of each panel from flatness with the previous panel. The dark blue is the top of each panel and the light blue shows the bottom of the panel.

+/- 180 degrees without requiring deformation of the panels. In addition, it has rigid-foldability, which stems from a single vertex that is repeated throughout the pattern [16]. The Miura-ori pattern occurs naturally in the deformation of an elastic plate of infinite length under compression, as it is the lowest energy manner in which this plate can deform [17]. This is comparable to the relationship between the Yoshimura pattern and axial buckling on cylindrical shells.

The Miura-ori pattern has been used in applications as diverse as architecture [18], biomedical devices [19], and energy absorption on rotorcraft [20]. The folding of the Miura-ori pattern has been studied in detail through methods such as finite element analysis [21]. Folding, in the context of returning the pattern to its flat state for uses in space arrays, is of particular interest. The pattern is often modelled as a single degree of freedom (DOF) mechanism. However, this is difficult to achieve in real world prototypes because the pattern is overconstrained.

The benefits and challenges of the Miura-ori in space arrays will now be further discussed, specifically in the areas of thickness accommodation, nesting, and deployment.

(a)   (b)
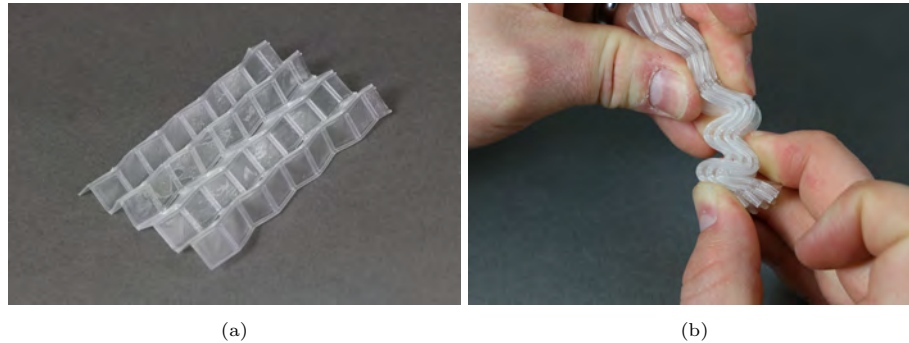
Fig. 3: (a) Polypropylene Miura-ori with $\alpha = 85^o$ and lacking thickness accommodation. (b) Folded state of the Miura-ori prototype undergoing thickness and nesting complications. Panels and joints must deform and bend to accommodate for nesting.

3   THICKNESS ACCOMMODATION AND NESTING

3.1   Motivation

To maximize the surface area of a space array in the deployed state, it is generally desirable to reduce panel thickness and use as much of the payload volume as possible (neglecting any mass constraint). The type of array will dictate other desired properties of the deployed state, such as aspect ratio and flatness (considered as a variation of the dihedral angles between adjacent panels). For example, the surface area and aspect ratio of a deployable sunshield are important parameters, while flatness is not. As such, material and form selection for such a mechanism may include thin Kapton® films, which can be efficiently stowed in cylindrical form by taking advantage of the compliance of the material with techniques such as slip-wrapping [22]. The compliant nature of the film, residual stresses in creases, and difficulty in uniformly flattening the structure with tensile stress may result in a less-flat deployed state in comparison with thick rigid-foldable mechanisms [22]. Where flatness is thin, compliant films have the greatest potential to maximize surface area and may therefore be the most desirable option. For applications where flatness is paramount, however, thick rigid-foldable structures may be more desirable.

3.2   Challenges

Lang et al. compiled a review of thickness-accommodation techniques used to convert zero-thickness origami into rigid-foldable structures [23]. Another method proposed by Ku uses an axially volume trimming technique to achieve precise folds [24]. These methods serve as stepping stones to be adapted for specific thick-origami needs.
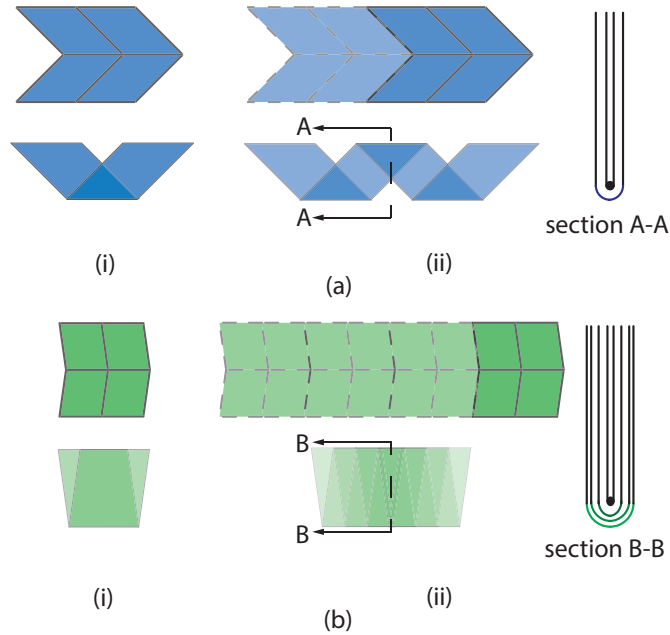
Fig. 4: (a) Miura-Ori with $\alpha_1 = 45^o$. (b) Miura-Ori with $\alpha_1 = 82^o$. Column (i) shows the unit cell of each pattern in the flat and folded configurations. The 82° Miura-Ori nests more of the panel than does the 45° Miura-Ori. Column (ii) shows each unit cell being arrayed in the horizontal direction. Added unit cells are shown with dashed lines. The 45° pattern only nests one set of panels (degree-1 fold), while the 82° pattern nests 3 sets of panels (degree-3 fold). The nesting is shown in the folding version as the colors/shade of the pattern becomes darker in the figure. The section view shows the number of panels nested in each pattern. As thick materials are used in these patterns, the required panel thicknesses of the 82° pattern increase very quickly.

An important phenomenon related to these thickness-accommodation techniques is referred to as nesting. Fig. 3 shows a polypropylene Miura-ori array undergoing nesting complications as a result of using a thick material. In general, nesting refers to having folds within folds in the flat-folded state. When this occurs in thick rigid-folding structures, it requires some form of thickness accommodation. In rigid-folding arrays, nesting may more generally be thought of as portions of pairs of panels resting within portions of other pairs of panels in the flat-folded state, where every "fold" represents two panels linked at their edges by a revolute joint.

The degree to which an array requires nesting is defined as the maximum number of folds that rest within folds in the flat-folded state. A simple mountain-valley fold is considered a degree-0 fold, as no nesting occurs. A degree-4 vertex

(a)

(b)
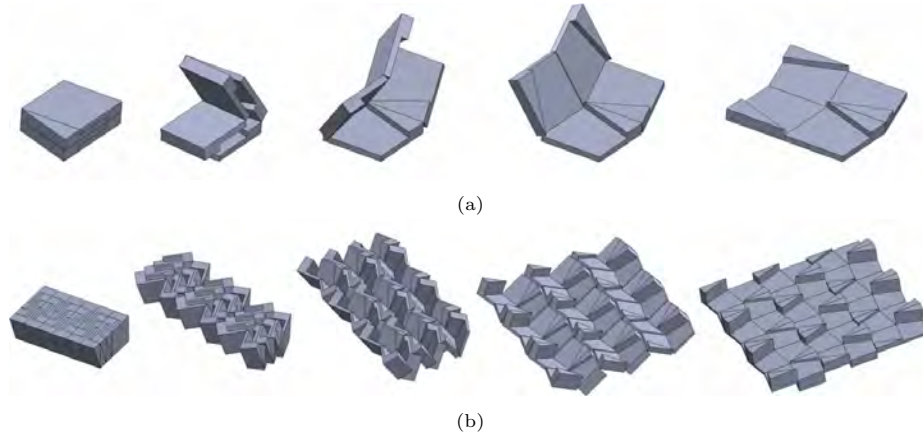
Fig. 5: (a) Single unit using Hoberman's offset hinge technique from fully stowed to deployed. (b) A 6x6 modified Miura-ori from fully stowed to deployed, using the same approach.

is considered a degree-1 fold, as some portion of the interior fold must rest within the exterior fold in the flat-folded state regardless of the parameters of the vertex (see Fig. 4). Increasing α, increasing the length of the minor fold (l_{min}), or decreasing the length of the major fold (l_{maj}) increases the degree of nesting in integer increments (see Fig. 4).

Two types of nesting are discussed. Parameter nesting refers to nesting occurring exclusively due to the choice of the Miura-ori parameters, α, (l_{maj}), or (l_{min}). The degree of nesting of such a pattern is simply

$$DoN = ceil\left(\frac{l_{maj}}{2l_{min}cos(\alpha)}\right) \qquad (1)$$

To introduce the second type of nesting, some terminology must be established. The minor direction is herein defined as the direction of the parallel lines formed by the minor folds of a Miura-ori array in the deployed state. The major direction is herein defined as perpendicular to the minor direction and in the plane of the deployed Miura-ori state. Values "m" and "n" refer to the number of panels in a Miura-ori array propagating in the major and minor directions respectively. Propagation nesting then refers to nesting occurring exclusively due to the propagation of panels in the minor direction. The degree of nesting for propagation nesting is simply n-1.

Three types of propagation-nesting Miura-ori patterns have been identified and are discussed; offset hinge, map fold, and modified tapered map fold.

The concept of an offset hinge was formalized by Hoberman in 1988 [25]. Hoberman later generalized a propagation-nesting pattern using the offset hinge technique [26]. A degree-4 vertex and 6-by-6 array using this technique is shown in Fig. 5. The models shown in Fig. 5 can propagate indefinitely in the major

direction, but is fixed to propagate n number of units in the minor direction. These units are therefore only modular in the major direction; more or less propagation in the minor direction requires an entirely different and unique set of units. With no modifications, this pattern requires n number of unique units.

The map fold is a special case of the Miura-ori, in which $\alpha = 90^o$. A rigid-foldable map fold was demonstrated by Zirbel in 2014 [27]. The map fold also requires n number of unique units, though it also requires either an elastic membrane [27] or gaps in the hinging to accommodate for thickness and achieve a fully-dense fully-folded form. One negative aspect of the map fold is that it has $m + n - 2$ degrees of freedom, and would require at least two external actuators in perpendicular directions to range from folded to unfolded states.

The modified tapered map fold alters the map fold such that the map fold becomes a one-DoF mechanism [27]. This pattern also requires either an elastic membrane or gaps in the hinging to achieve a fully-dense fully-folded form. This pattern requires $n + 1$ number of unique units.

One notable drawback of the map fold patterns is the hinge gaps. Such gaps substantially decrease the stiffness of the patterns, and would likely make any form of internal actuation difficult. Such patterns would likely need to be externally actuated.

The above propagation-nesting patterns are potentially good solutions for stowage in rectangular prisms, and may therefore be useful in CubeSat applications. One drawback of propagation-nesting patterns is that the thickness of all the regular panels (as opposed to "spacer panels" [27]) stack in one direction. Depending on the dimensions of the prescribed rectangular prism, this may require a significant decrease in volume efficiency to achieve a desired aspect ratio.

Parameter-Nesting Patterns Two types of parameter-nesting patterns have been identified and are discussed; tapered-panel, and origami-based cylindrical structures (OCSs).

The tapered-panel Miura-ori has been investigated by Lang et. al [23]. The tapered-panel Miura-ori retains the kinematics of the zero-thickness model, thereby simplifying analysis of the pattern. The main difference between this pattern and the zero-thickness model is that it cannot fold completely flat; in the stowed state, the panels will rest in some position that is partially unfolded. While tapered panels enable a much more compact state than untapered models, there is still a notable gap between succeeding minor folds (see [23]), indicating that it is not the most volumetrically-efficient model.

OCSs were developed by Wang et. al [28] and are related to Hoberman's initial formalization of the hinge shift [25]. The basis of these designs is to incorporate axis shifts on every fold. This is to say that one pair of major and minor folds are shifted relative to the other pair for every quadrilateral unit. Wang et al. join the shifted axis at an angle, enabling curvature such that the propagation of these units flatly folds into a cylindrical or otherwise-curved shape (see [28]). This may be a good solution for payloads using a cylindrical volume. A drawback of this pattern is that to continuously fill the volume of a cylinder would require

Fig. 6: Carbon Fiber prototype of a single degree-four vertex undergoing folding motion showing simplicity as a result of minimizing the structure to a single unit cell.

a spiraling flat-folded state, which requires a large multiplicity of unique units, thereby increasing manufacturing complexity. Yet another drawback is that because these units are at an angle and must accommodate for subsequent units, a significant portion of the panels is twice the thickness of the mating portion of the panels. These regions yield that portion of the panel half as efficient as the rest, thereby lowering the overall volume efficiency of the array.

3.3   Solutions

The challenges of accommodating for thickness, preventing nesting propagation, and maximizing volume efficiency of space array are key topics that should be addressed before pursuing the Miura-ori. The following sections build on published work to provide innovative solutions for deployable space array applications.

Single Degree-Four Vertex As seen in Fig. 4, as the number of panels increase, the amount of nesting follows in accumulation. When the defining α is below 60° and assuming equal side lengths (Fig. 4a), a degree-1 nest occurs every other duplex of facets. As alpha grows beyond 60° (Fig. 4b), more facets begin to nest, creating a degree-n nest. Therefore, reducing the amount of facets to a single unit cell is one approach for mitigating nesting to a single degree-four vertex. In addition, this method proves favorable for missions that require the array to stow in thin spaces. As seen in Fig. 6, a single degree-four vertex array is capable of deploying to about four times its stowed areal dimension if alpha is near 90 degrees - often a favorable approach for approaching square apertures. It is important to note that this design still requires the use of one thickness accommodating technique to allow for a single nest of two facets.

Double-Hinge Offset The double-hinge offset (DHO) Miura-ori may be thought of as a special case of the OCS; when $\alpha_i = \alpha_{i-1}$ [28]. This case may be thought of as an OCS array attempting to achieve a cylinder with an infinite radius in the flat-folded state. DHO may also be thought of as a generalization of Hoberman's work from 1988 [25]. Hoberman's original "reversibly expandable

(a) Fully stowed DHO D4V. (b) Partly-deployed DHO D4V. (c) Mostly-deployed DHO D4V. (d) Deployed DHO D4V.

(e) Fully stowed DHO 6-by-6 array. (f) Partly-deployed DHO 6-by-6 array. (g) Mostly-deployed DHO 6-by-6 array. (h) Deployed DHO 6-by-6 array.
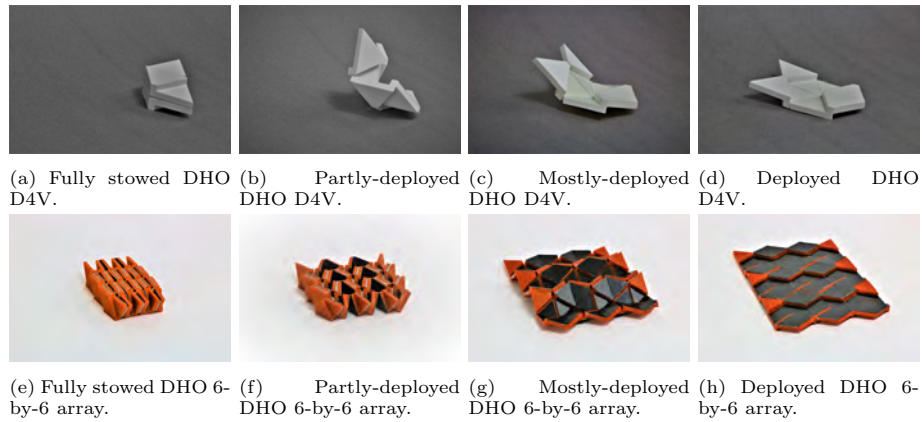
Fig. 7: a-d) A DHO degree-4 vertex at various stages of deployment, e-h) a 6-by-6 DHO array at various stages of deployment.

three-dimensional structure" was specific to 45°, 90°, and 135° angles, and portrayals of the units exhibited large doubly-thick regions [25]. The DHO seeks to minimize the doubly-thick region, and spans $0 < \alpha < 90^o$. A DHO degree-4 vertex and 6-by-6 array can be seen in Fig. 7.

This method is not amenable to cylindrical payload volumes, but is very amenable to rectangular prism stored volumes, as the profile of the flat-folded state is linear, not curved. Furthermore, because $\alpha_i = \alpha_{i-1}$, the doubly-thick less efficient portions of the panels are minimized, making DHO more volumetrically efficient. One major benefit of the DHO method is that it requires a single repeating unit cell.

From Fig. 7, there are apparent gaps in the flat-folded state at the edges propagating in the minor direction. Left alone, these gaps render any implementation of the DHO method less volumetrically efficient. One method (not shown) to fill this gap is to slice one of the unit cells along the height of the isosceles triangle that are the interior facets. Doing so creates "1/4 units" and "3/4 units". Such units can form a degree-4 vertex independent of the repeating degree-4 vertices of the rest of the array, and render the method nearly fully-dense in filling a rectangular prism.

Tapered Gaps In cases where the allocated stowing compartment of the array is a rectangular prism, tapered offsets can serve as a favorable method of modifying the Miura-ori. This idea follows the method presented by Zirbel in [27], however this time allowing for panels where α does not equal 90°. Figure 8 shows the tapered gap method presented on facets with $\alpha = 82^o$. The most beneficial aspect of this design is the volume efficiency of its stowed state.

It is important to understand the tradeoffs that arise from using this method. One notable drawback is the propagating gaps that exist in order to accommodate for stacking of facets. This may not be favorable if rigid panels are necessary

<center>(a)   (b)</center>
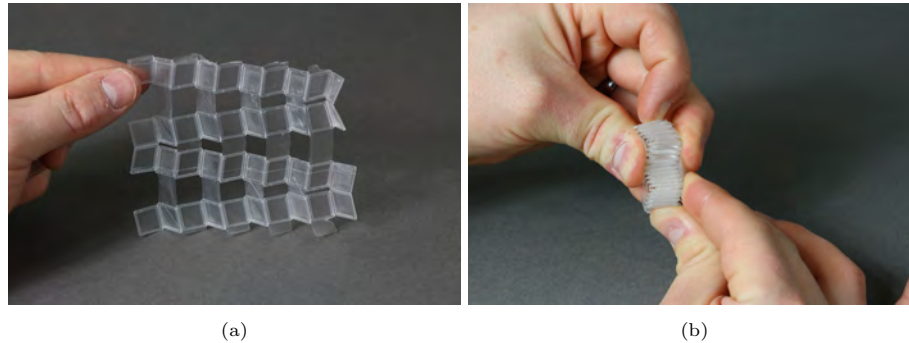
Fig. 8: (a) Polypropylene Miura-ori with $\alpha = 85^o$ and propagating tapered gaps used to accommodate for thickness. (b) Folded state of the Miura-ori without nesting complications.

across the entire array. Additionally, the lack of fully rigid facets ultimately decreases the stiffness, and thereby flatness, of the array, which may pose issues if deflection angles are critical in the deployed state.

Such growth in gap propagation may also be unfavorable due to the wasted space exhibited in the deployed state. Similar to the tapered map fold, this can be mitigated by filling the gaps with a rigid panel and encompassing the array in an elastic membrane.

Cylindrical The last modification we present stems from the aforementioned method of introducing gaps. However, rather than propagating the width of each gap, this method retains a constant gap width measuring twice the thickness of the panels. As seen in Fig. 9, by introducing gaps, and therefore removing a hinge of each Miura-ori unit cell, the structure collapses into a cylindrical state. However, this method still retains a rigid-foldable structure, therefore not needing to compromise panel rigidity to achieve pseudo curved folding. This method is most favorably used when a cylindrical volume is required for the stowed state, such as stowing the structure within a rocket payload.

Another favorable quality of this method is its high deployment ratio. In the example shown in Fig. 9, the array is capable of deploying to seven times its stowed cylindrical diameter. As a reference, if the diameter of the cylinder is 1 meter, then the circumference is 3.14 meters. However, the deployed length of the structure is 7 meters. This is nearly 2.25 times the length of if a flat sheet were wrapped within the cylinders. It is important to note that the height of the structure remains nearly the same in both states.

Since we are not removing a significant amount of material within the gaps, the resultant reduction in stiffness can be minimized. However, concerns may arise as a result of introducing gaps and therefore reducing the effective area of the structure. Depending on the need for such array, it may be possible to fill the gaps with a membrane containing the technology used on the rigid facets.
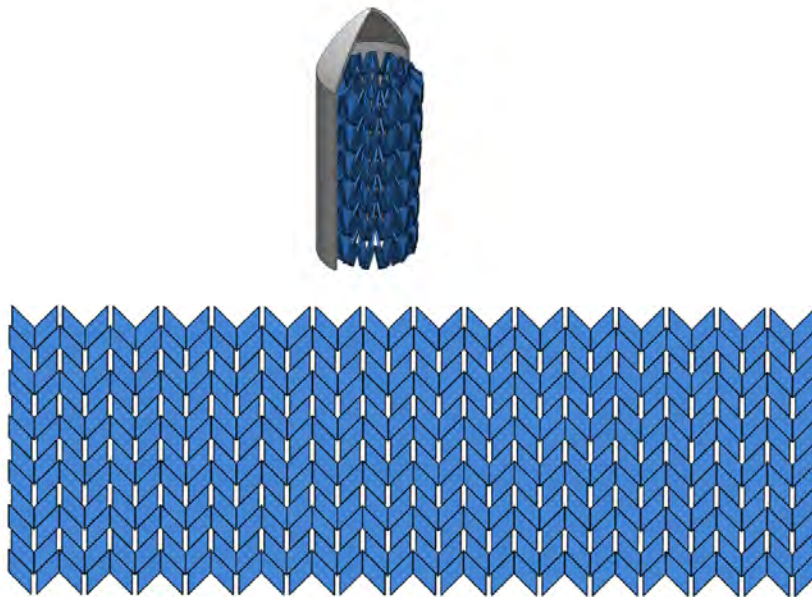
Fig. 9: Stowed and deployed states of the cylindrical modified Miura-ori.

4   DEPLOYMENT

4.1   Motivation

As discussed previously in this work, space arrays must generally achieve a large and flat area. Origami pattern tessellations are attractive for achieving large apertures for telescopes or antennas, however, deploying such arrays poses difficulties. In this paper, deployment will refer to grounding or attaching the array to the base system, and actuating the pattern to and from a flat state (flat-foldability). This leads to at least four important questions:

1. Where or how can the pattern be grounded or "held onto"?
2. Where is the pattern actuated from?
3. How is the pattern actuated into (and out of) the flat state?
4. How do we ensure smooth deployment?

These questions are not too applicable when folding a paper Miura-ori model. As shown in Fig. 10, we usually grab one end of the paper array with one hand (ground a corner vertex or edge), grab the opposite end with the other hand and pull (actuation of another corner vertex or edge). Near the end of deployment (flat), the array is pressed against a table and "smashed" flat with our hands. Folding the paper pattern back up from this flat state also requires making sure that creases "pop" at specific locations to facilitate a resistance-free folding
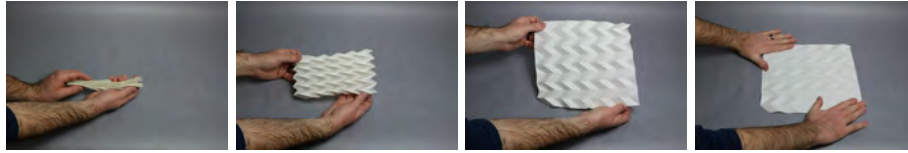
Fig. 10: Deployment method of a Miura-ori pattern from stowed to deployed by hand while using a table top to guide the deployment.

motion. While this is a relatively simple motion for human arms and hands, this motion becomes difficult to achieve remotely. These questions are especially important if you have a specific design requirement or need, such as having a deployable feed that always needs to point at the center of the array or if the array needs to face a predetermined direction.

When discussing origami pattern designs, the grounding and actuation methods are often omitted. Specifically for the Miura-ori pattern, Papa and Pellegrino [29] and Cai et al. [30] studied the deployment of Miura-ori patterns in membranes. Papa and Pellegrino [29] noted the membrane initially deployed to an equilibrium position. They then applied corner forces to fully deploy the pattern, however, no discussion of how to attach or actually deploy the membrane was presented. Cai et al. [30] suggest that the smoothness, meaning how close each panel of the membrane truly forms a "flat plane" between 3 points of the panel of the pattern is better with more attachment points on the edges of the pattern, however, no specific mention of how to ground the pattern was made.

Moving specifically into antenna design cases, Lynd and Harne [31] looked at the Miura-ori for beam folding in transducers and Seiler et al. [32] used Miura-ori to create a patch antenna. In both cases, the main discussion was on the benefit of the Miura-ori design to the electromagnetic properties of the design and no discussion was made on how the actual grounding and actuation would occur.

4.2   Challenges

Prior work has shown that the Miura-ori pattern can be very beneficial to various applications. However, the problems of grounding, actuating, and fully "folding" space arrays have not been fully researched. Looking at the four main challenges separately will allow more insight into why each is particularly difficult.

Grounding The Miura-ori pattern is auxetic, meaning that it expands in both of the in-plane directions as it is unfolded (see Fig 11). While this is great for increasing the exposed or visible area, this means that to hold onto the edges of the array, a mechanism that can expand in 2 directions is needed.

Additionally, the unfolding direction (the x-y plane in Fig 11) is perpendicular to the most compact folded direction (the x-z plane in the figure). This means that if we want the surface of the system (ground) that the array is attached to to be the x-y plane in the figure, to compactly stow the array and then deploy
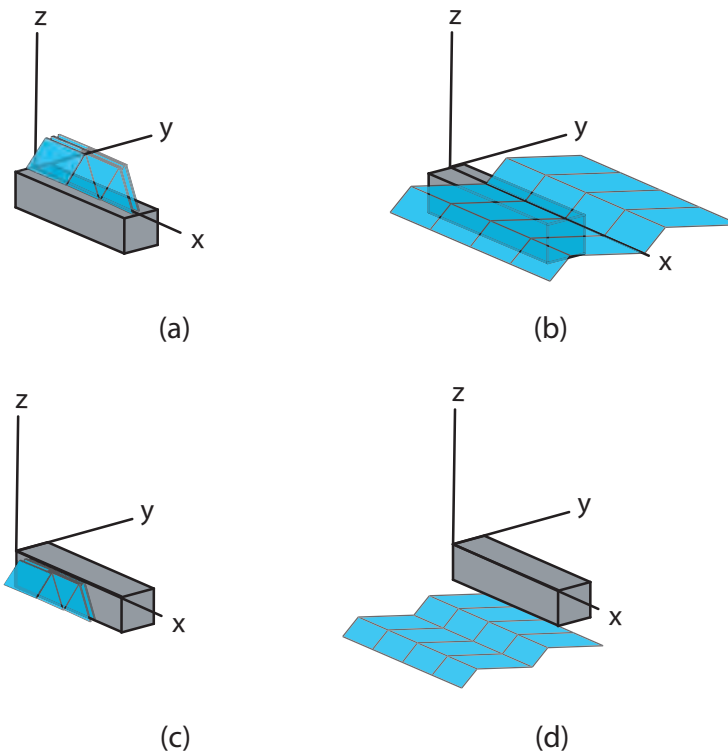
Fig. 11: A symmetric Miura-ori pattern (a) stowed on the x-y plane of the gray box representing a CubeSat or other space system. (b) The deployed pattern in the x-y plane. Attachment would occur at the central vertex. (c) The same symmetric pattern stowed on the x-z plane of the CubeSat. (d) The deployed pattern from the x-z plane resides in a plane parallel to the x-y plane when fully deployed. Attachment to the "ground" could be via vertex or edge.

it along the x-y plane, we would need the array to first rotate around the x-axis and then unfold. This would allow the array to stow compactly and be, at least partially, supported by the "ground" when it is deployed; however, it does add an extra required input motion for the array. In contrast, if we attach the array on the x-z plane of the system, then the pattern stows compactly. However, as the array deploys, it extends away from the system, making it hard, if not impossible, to use the system as a "ground" for additional support on the extended pattern.

An additional consideration and challenge with grounding a vertex is all the panels (and their corresponding vertices) rotate with respect to each other during deployment; the system lacks a convenient center panel that remains in place while all other panels move around it. While there is a vertex that stays in the center of the pattern, this would require a complex mechanical joint
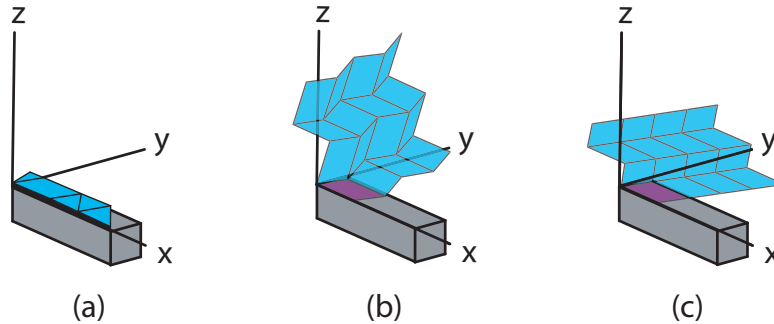
Fig. 12: A symmetric Miura-Ori pattern that is grounded to a CubeSat (gray box) by an edge panel in the (a) stowed, (b) partially deployed, and (c) deployed states. The darker panel is the panel that is grounded to the CubeSat. Unlike the deployments from a vertex or edge, as shown in Fig. 11, the deployment is asymmetric with respect to the x-y plane.

with additional hardware to symmetrically deploy the structure and connect the system to the vertex to the ground structure. Grounding to a crease line presents a problem as none of the crease lines start on the x-y plane. This would require another complex mechanism to allow for a symmetric deployment.

If instead of trying to ground a vertex or crease, an entire panel is grounded, the pattern does not deploy symmetrically, as shown in Fig. 12, as only one of the corner panels would be grounded due to the deployment of the other panels and potential interference with the space system it is attached to.

In many space-array design situations, the equivalent design methodology to hands pulling the array apart (see Fig. 10) has been accomplished by using extra-array parts or mechanisms that are attached to the exterior points of the array and expand the array, such as trusses or booms. These work well to deploy the pattern, however, the disadvantage is that they add additional pieces to the overall design, which increases weight and utilizes valuable space. Essentially, this is placing an extra mechanism between the array and the space structure and allowing such a mechanism to facilitate actuation and grounding. This method also does not guarantee flatness in the center of the pattern, especially if the pattern is large. Additional mechanisms or structures must be added to fully support the structure.

Actuation The actuation of the pattern relies directly upon how the pattern is grounded, the overconstraints and hinges of the pattern, the thickness accommodation technique used, and the desired deployment scheme (symmetric in-plane or out-of-plane). Most actuation of a Miura-ori array has occurred using booms and trusses, allowing a symmetric deployment in the plane. The need for
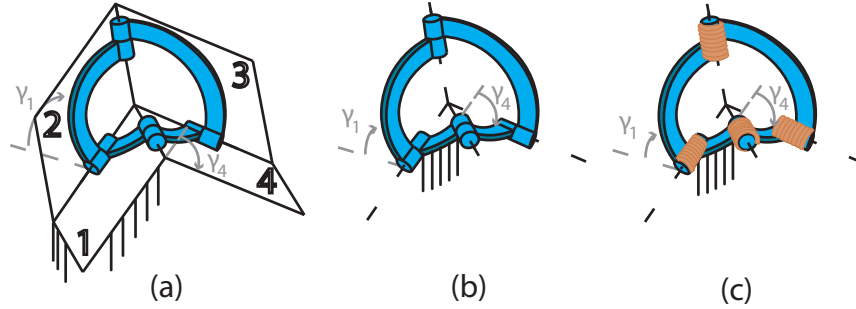
Fig. 13: (a) A unit Miura-ori represented as a spherical four-bar mechanism. Panel/link 1 is the ground link. (b) The rigid mechanical advantage of the mechanism. (c) Incorporation of the idea of compliance by modeling springs at each joint. The springs are shown in orange. Additional losses will occur and the mechanical advantage will be decreased.

multiple actuation points due to binding and desired full deployment is also an issue. This challenge will be discussed in detail in Section 4.3. Horner and Elliot designed a Miura-ori solar sail, but needed to attach rings along the length of the edges, that were allowed to slide, to allow the pattern to extend during actuation of inflatable trusses [33]. This highlights this design challenge perfectly.

Achieving Flat-Foldability For many types of deployable space arrays, the array is desired to be flat at the stowed and fully deployed positions. This is considered flat-foldability in zero-thickness origami models. As this is still relevant to create a highly compact stowed package and highly deployed pattern in space applications, we will refer to this as achieving flat-foldability of the array. A mechanical principle to think about with this desired deployment is the mechanical advantage. Mechanical advantage is the ratio of output motion or force to input motion or force. This is important because with higher mechanical advantage, the array is easier to fold and unfold (less input motion or force produces greater output motion or force).

Figure 13 shows a unit Miura-ori as a spherical four-bar mechanism. Butler et al. [34] determined the mechanical advantage of origami mechanisms with the consideration of the mechanism being rigid as well as incorporating compliance. Looking first at only the mechanical advantage of the rigid mechanism, using the equation provided in [34], and tailoring it to the Miura-ori, the equation becomes

$$MA_R = \frac{[\cos(\alpha)cos(\gamma_1) - \cot(\pi - \alpha)\sin(\alpha)]^2 + sin^2(\gamma_1)}{-2\cos(\alpha) + 2\cos(\gamma_1)\cot(\pi - \alpha)\sin(\alpha)} \qquad (2)$$

The mechanical advantage of the Miura-ori with different "Miura Angles" (α) is shown in Fig. 14. It can be seen that in the range of desired α ($45^o - 89^o$) the
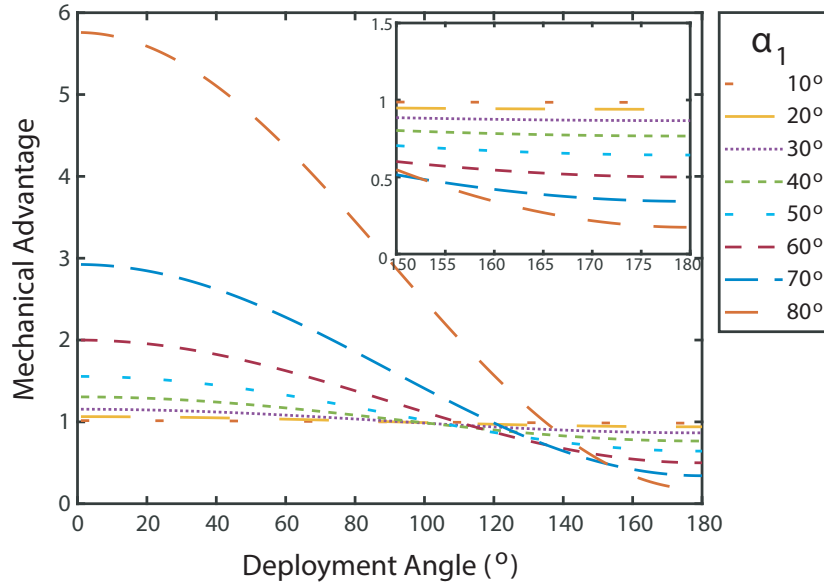
Fig. 14: The mechanical advantage throughout the deployment from folded to flat for different angles of Miura-ori. Note, deployment angle is $\pi - \gamma$ in the figure.

mechanical advantage starts high. For cases close to 45°, the mechanical advantage stays relatively close to 1, meaning that the force input into folding will be output on the output crease. However, with higher deployment angles, the mechanical advantage approaches zero. These higher deployment angles correspond to the flat, deployed state of the array.

It is important to note regarding the plot of mechanical advantage throughout the deployment shown in Fig. 14 that this is for a single unit cell Miura-ori. As the unit cell is multiplied to create an array, the mechanical advantage of the end panel is the initial rigid mechanical advantage raised to the power of the number of unit cell arrays that the end panel is away $(MA_{Rp} = (MA_{R1})^p)$. This effectively drives all mechanical advantage to zero, especially at the edges of the array, near the end of deployment.

The previous discussion only considers rigid mechanical advantage. When considering the compliance in the system (the right figure in Fig. 13, where springs simulate the flexibility of the creases), Butler et al. [34] showed that the mechanical advantage is

$$MA_C = MA_R\left(1 - \frac{\delta U_c}{\delta W_{in}}\right) \qquad (3)$$
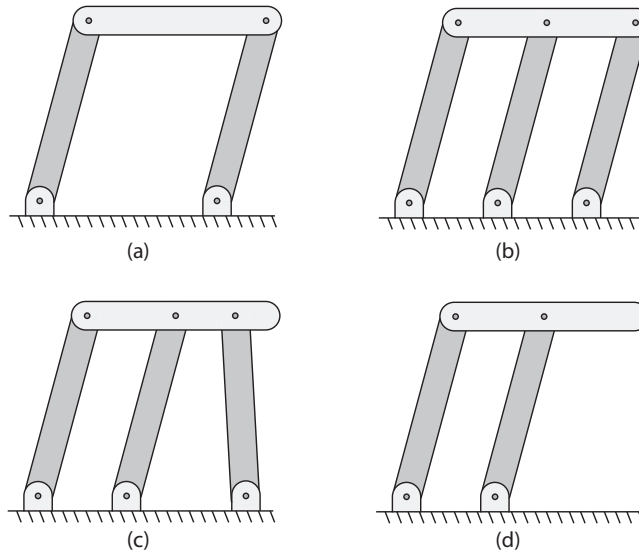
Fig. 15: (a) A parallelogram four bar mechanism with one degree of freedom. (b) Additional parallel link adds constraints, but symmetry preserves the single degree of freedom. (c) Misaligned links turn redundant constraints into conflicting constraints and can cause loss in mobility. (d) Removal of redundant constraints does not affect motion of the coupler.

As some of the energy used in the deployment will be transferred into potential energy in the compliance of the system (the U_c term), the mechanical advantage will decrease even more than that shown in Fig. 14, which makes the mechanical advantages even closer to zero. All these added together create a system where it becomes very challenging to precisely actuate to the flat state.

Another potential problem to consider here is that when the pattern is flat, the mechanism reaches a change-point and there may be a bifurcation point, where the creases can change orientation (from mountain to valley folds, or vice-versa). This would cause the array to fold in a different direction, or possibly just bind and completely prohibit folding. In one-time deployment, this is not an issue, however, for multiple deployments, this challenge also needs to be addressed.

Ensuring Smooth and Defined Motion During deployment and stowage, fully defined, smooth motion is important to ensure full motion of the panels. Due to non-ideal conditions, it is possible for an "ideal" design to have incomplete or choppy motion during actuation.

Binding Due to Overconstraint An overconstrained system is one that has more degrees of freedom than is predicted by its mobility equation. For example,

the degrees of freedom of the planar linkage system, shown in Fig. 15(a), can be calculated as...

$$DoF = 3(n - 1) - 2 * j_1 - j$$
$$= 3(4 - 1) - 2 * 4 - 0 \qquad (4)$$
$$= 1$$

where n is the number of links, j_1 is the number of lower pairs, and j_2 is the number of higher pairs.

This is defined as an exactly-constrainted system, where it is predicted to have 1 DoF and is observed to have 1 DoF.

Now consider the system in Fig. 15(b) where a link is added and is parallel to the other vertical links. Here the Grublers equation predicts the DoF to be 0, however due to special geometry we know that this system still has 1 DoF. This then becomes an overconstrained system. By adding more parallel links to the system in the same manner, the predicted DoF would decrease, while increasing the issue of overconstraint.

Due to special geometry (symmetry and repeatability), the mobility of the mechanism is not affected. However, if one link of this was to be slightly misaligned as shown in Fig. 15(c) (exaggerated for illustration), the mechanism would bind on itself and no longer move. This would then turn the redundant constraint into a conflicting constraint. While potential conflicting constraints (such as the misalignment of parallel links) are not seen during kinematic analysis, they can become a apparent once the mechanism is physically constructed. When constructed, the before ideal kinematic system becomes non-ideal through simple geometric imperfections such as hinge misalignment, tolerances and thermal expansion differences. These changes can turn redundant constraints into conflicting constraints. Conflicting constraints can limit motion (by locking or binding), cause choppy motion, and induce undesirable internal loads [35]. The more redundant constraints a system has, the more opportunities there are for non-ideal conditions to turn them into conflicting constraints.

Although more complicated, the mobility of a Miura-ori based mechanism can be defined very similarly. The Miura-ori is made up of many degree-4 vertices with repeating geometry. Each vertex can be viewed as a spherical mechanism with $m - 1$ degrees of freedom where m is the degree of the vertex [36]. The larger tessellation can then be seen as a system of linked spherical mechanisms. Symmetry and periodicy give the Miura-ori "special geometry" that allow it to have more degrees of freedom than predicted by its general mobility equation. A Miura-ori-based mechanism is greatly overconstrained, as there are many redundant constraints. Hinge misalignment, too much or too little backlash in the joints, uneven deployment, or poor tolerances can cause the Miura-ori mechanism to bind, cause choppy motion, and/or induce internal loads.

When designing for space applications, reliability, repeatability, and low-force actuation is important for design success. For a deployable array this means
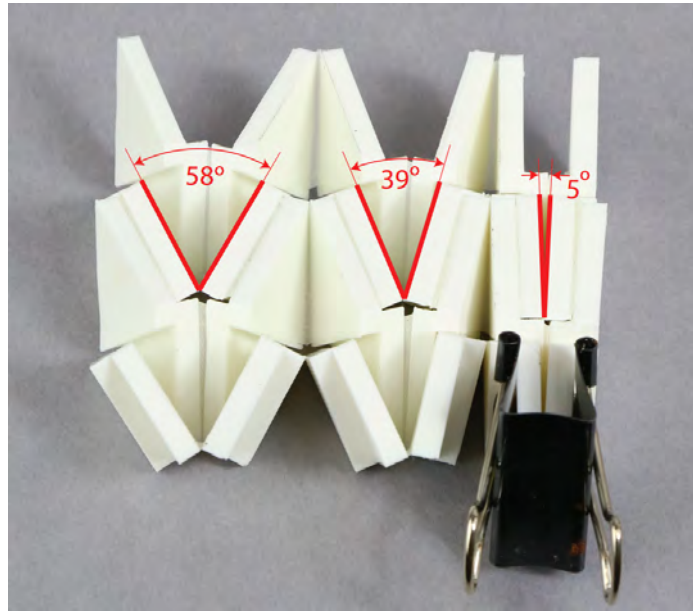
Fig. 16: Miura-ori prototype with the same geometry and behavior as that shown in Fig. 7. Fully closed at a corner with a clamp, the Miura-ori array shows uneven stowage. It can be seen that further away from the actuation point less of the closing force is distributed, despite being a one degree-of-freedom system. The result is the same whether stowing or deploying.

smooth, defined motion requiring low-force actuation. The overconstraint in a Miura-ori-based deployable array could make these hard to attain.

Uneven Deployment and Stowage When actuating the Miura-ori under ideal conditions, any input to two panels would result in uniform motion throughout the 1 DoF system. However under non-ideal conditions, joints can have "slop" and cause uneven deployment across the array. This can cause the system to have more than 1 DoF. This becomes a problem particularly when there are long chains of consecutively linked panels, causing many panels and hinges to be far away from the actuation point. Under non-ideal conditions, panels farther away from the point of actuation can "lag" or not follow the same motion due to the "slop" in the joints. This is illustrated in Fig. 16, where the clamped bottom right vertex acts as the single actuation point. The "slop" in each joint accumulates as you move across the array, and the motion becomes poorly defined. Whether stowing or deploying the array, the same inconsistency in defined motion is observed. This accumulation of "slop" causes misalignment of redundant hinges, and can cause binding.
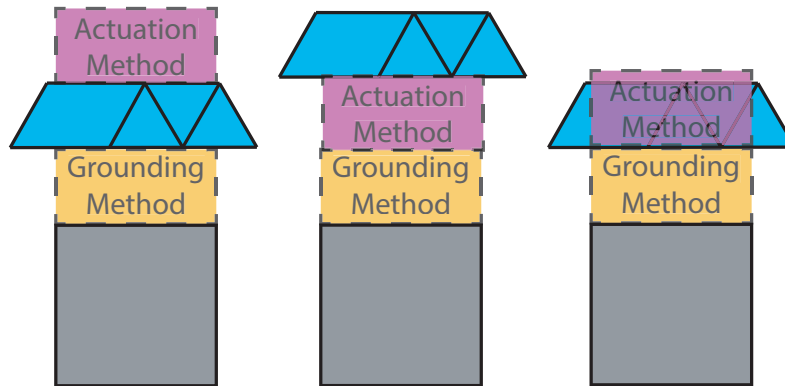
Fig. 17: A systems diagram showing the overall different configurations of the Miura-ori array and the actuation and grounding mechanisms. For example, the grounding method in the right figure could be grounding to the panel, as in Fig. 12 with the actuation method being strain energy, which is inherent to the pattern.

4.3   Solutions

The following sections present some current and proposed methods that may assist in overcoming the challenges of ground, actuating the array and ensuring smooth actuation and deployment.

Grounding As discussed, the current methods of deploying Miura-ori arrays utilize trusses surrounding the pattern that expand with the pattern. Booms provide a similar scheme to deployment. This is essentially connecting the pattern to a mechanism and that serves as a deployment actuator and a grounding scheme. This could also be accomplished with a slider mechanism (trusses, booms, or other sliding mechanism), or with a variation of mechanisms, as shown in Fig 17.

As described above, if asymmetric deployment is suitable for a particular application, grounding to a corner panel could serve as a potential solution. This solution also allows a potential "locking" of a crease, as a portion of 2 panels would be grounded if the grounding structure is large enough. This would theoretically lock the entire pattern in the state where the second panel contacts the structure, as the array is one DoF. Even with the compliance in the system, a greater portion of the pattern would be stabilized using this method.

For either case discussed above, to increase the stability of the center of the array (in the first deployment case) and the stability of the edge of the array (in the panel grounding case), hard stop mechanisms that deploy out the of the system could be implemented, such as the ones developed by Andrews et al. [37].

Actuation Actuation solutions are linked to the analysis of pattern grounding. Grounding the structure to a corner, face, or an "intermediate mechanism" (Int.Mech.) allows different methods of actuation to be used. For our purposes, the terms "actuation" and "deployment" both convey the meaning of a complete opening of the Miura-ori pattern. To optimize the deployment and minimize required actuation forces, one should select an actuation method that complements the corners, faces, or mechanisms to which the pattern is grounded.

Several mechanisms and techniques have been put forth as solutions for deploying complex arrays in space: internal strain energy [38], an external truss [14], telescoping booms [39], cables [40], magnets embedded between panels [41], or torsional springs on the pattern's creases [42]. This list is not comprehensive. However, each method has amassed prior research sufficient to justify their mention in this discussion. A plethora of actuation methods is not only helpful from a design engineer's standpoint, but necessary to the system's success. Each method exists on a spectrum of relative strengths and weaknesses. The selected actuation method should be tailored to the requirements and environment of the specific Miura-ori configuration and its real-world application.

Actuation methods exist as either "internal" (within the volume of the pattern when stowed) or "external" (situated outside the structure/folds of the pattern when stowed). These internal/external actuation methods can be further organized by identifying the grounding methods to which they are best suited (see Table 1).

Bowen et al. [43] demonstrates the implementation of magnetic actuation in a waterbomb pattern mechanism. Magnets are oriented on the panels in such a way that repelling magnetic fields cause the waterbomb to fully open. One panel is used as the mechanism's ground. Similarly, Cowan and Von Lockette have illustrated the feasibility of Miura Ori magnetic actuation [41].

A perimeter truss is a clean deployment solution for high panel number origami arrays. Zirbel et al. [14] introduced a perimeter truss with serpentine flexures that deploy a flasher pattern solar array. The serpentine flexures exert outward tension, pulling the pattern open, whilst undergoing a 90° torsion and

Table 1: Internal and external methods of actuation with their complementary grounding methods.

	Actuation Method	**Grounding Method**	Cit.
	Torsional Springs	Vertices/Int.Mech.	[42]
Internal	Embedded Magnets	Panel	[41]
	Strain Energy	Panel/Vertices	[38]
	Cables	Int.Mech.	[40]
External	Perimeter Truss	Vertices	[14]
	Telescoping Booms	Vertices	[39]

90° bend [14]. Similar compliant linkages would aid in attaching a perimeter truss to the Miura-ori.

In summary, the challenge of grounding and deploying the Miura-ori pattern can be solved in a variety of ways. Several actuation methods can be coupled with various grounding locations to produce a desirable result that satisfy project constraints.

Achieving Flat-Foldability After discussing solutions for attaching and deploying the pattern from a structure, the next discussion will focus on transitioning the pattern to and from a flat state. A possible solution to the challenge of achieving flatness is to bias the pattern's minimum energy state to be at or past the desired flat state. Thickness accommodation techniques or other hard stops can be used to stop the pattern in the desired flat state in cooperation with the method.

To solve the second challenged of leaving the flat state, additional mechanisms could be added to move the stowing force out of the plane of the flat pattern. This would increase the mechanical advantage of the pattern and allow less needed force to actuate the array. Additionally, certain thickness accommodating techniques move hinges off the neutral axis of the pattern. These could be used to move the forces out of the plane of the pattern and increase the mechanical advantage of the system.

Instead of having the minimum energy state be at the flat configuration, the array could be designed to have the minimum energy state at the stowed configuration. This would cause bias the array toward a stowed position and prevent the need for an external folding force. However, this would require a determination of an actuation method for the deployment of the array and that mechanism would also have to resist the loads introduced by the strain energy stored in the creases.

Actuation Point Placement It was shown that under non-ideal conditions, joints can have "slop" that causes uneven deployment and stowage when actuated from one point. The inconsistency in progression can first be minimized by centralizing the actuation point. A more central location for the driving actuation point would minimize overall distance between it and the most distal panels. In addition to centralized placing, having multiple actuation points would further minimize the inconstant motion. Instead of having the entire pattern actuated by only one driven location, multiple points spread throughout the pattern would encourage uniform deployment of the Miura-ori array.

Strain Energy As stated previously, stored strain energy could be used to assist in opening the array. Instead of binding and resisting the opening motion, stored strain energy within the joints of the array would assist the actuator in opening the array. Instead of an single actuator acting at a single location on the array, each location of stored strain energy becomes a point of actuation and
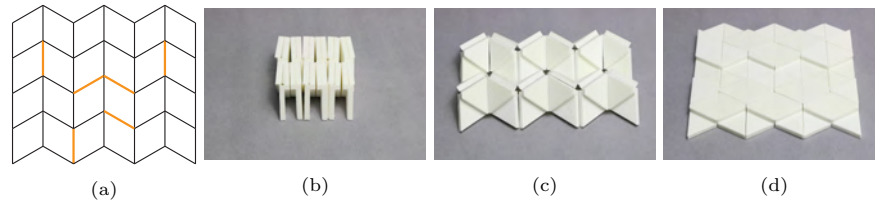
Fig. 18: (a) A diagram of Miura-ori prototype with several membrane hinges removed. Locations of removed hinges are shown in orange. The prototype is shown through deployment in its (b) stowed, (c) partially deployed, and (d) fully deployed states.

helps the array open uniformly. Pehrson et al. showed that the incorporation of lamina emergent torsion joints into a modified flasher patterned array yields easier actuation [38]. However, it is important to note that this works more effectively for one-time deployment designs as the strain energy is used to assist the opening motion. If an array were needed to be closed, such as in a multiple deployment application, the strain energy would resistant the closing motion and increase the likelihood of binding.

Eliminate Redundant Constraints In an overconstrained system, redundant constraints could be removed while still maintaining fully defined motion. Consider the overconstrained mechanism in Fig. 15(b). If any of the redundant vertical parallel linkages are removed, the motion of the coupler is still fully defined (as shown in Fig. 15(d)). Likewise, in an overconstrained Miura-ori system, redundant constraint (such as joints) could be removed while preserving the same defined motion. Removing redundant hinges eliminates the overconstraints, thereby reducing the chance for binding and reduces friction. In addition, it decreases the amount of needed hinges, thus simplifying manufacturing and assembly.

A demonstration of this is shown in Fig. 18. Membrane joints shown in blue have been severed, thus removing the joint. It can be seen that the motion is still fully defined throughout its motion.

5   CONCLUSIONS

While several methods exist for designing origami-inspired tessellations, a set of methods have been presented to show the special considerations needed to design a Miura-ori space array.

Thickness accommodation is critical when creating origami-inspired mechanisms for real world applications. The Miura-ori is often infamous for its propagation of nesting, especially when thick facets are required. As such, new methods have been introduced to offer alternative solutions to utilize the Miura-ori in de-

ployable space arrays. These methods offer varying solutions depending on the array's stowed and deployed needs.

The motion of the Miura-ori makes it an attractive mechanism for space arrays, specifically due to its one degree of freedom deployment from small-to-large sizes. However, these same factors can make it difficult to deploy. Deployment encompasses many different aspects: grounding, actuation, smooth movement, and achieving flat-foldabilty, which are all inter-connected. As such, deployment scheme (symmetric or asymmetric) affects which deployment mechanisms and grounding to use. In addition, mechanical advantage is very low near the ends and potential bifurcation can occur when flat. While these concerns may lead to difficulties in full deployment or actuation from a flat state, this paper presents a set of methods to aid in the development of robust Miura-ori deployment.

As a result of this work, engineers and designers should have an understanding of Miura-ori limitations within the areas of thickness, nesting, and deployment motion. With this foundation, the Miura-ori can be properly modified to suit different needs. Future work should be directed towards finding suitable applications of the Miura-ori in aerospace and non-aerospace design alike.

6   ACKNOWLEDGMENT

References

1. Zirbel, S. A., Trease, B. P., Thomson, M. W., Lang, R. J., Magleby, S. P., and Howell, L. H., 2015. "Hanaflex: a large solar array for space applications". In Micro-and Nanotechnology Sensors, Systems, and Applications VII, Vol. 9467, International Society for Optics and Photonics, p. 94671C.
2. Velez, C. A., Kaddour, A.-S., Georgakopoulos, S. V., Bolanos, D. S., Ynchausti, C., Magleby, S., and Howell, L. L., 2021. "Reconfigurable and deployable miura-ori ra analysis for satellite applications". In 2021 IEEE 21st Annual Wireless and Microwave Technology Conference (WAMICON), IEEE, pp. 1–3.
3. Wilson, L., Pellegrino, S., and Danner, R., 2013. "Origami sunshield concepts for space telescopes". In 54th AIAA/ASME/ASCE/AHS/ASC Structures, Structural Dynamics, and Materials Conference, p. 1594.
4. Lang, R. J., 2008. "From flapping birds to space telescopes: the modern science of origami.". In NPAR, p. 7.
5. Natori, M., Katsumata, N., Yamakawa, H., Sakamoto, H., and Kishimoto, N., 2013. "Conceptual model study using origami for membrane space structures". In International Design Engineering Technical Conferences and Computers and Information in Engineering Conference, Vol. 55942, American Society of Mechanical Engineers, p. V06BT07A047.
6. Nishiyama, Y., 2012. "Miura folding: Applying origami to space exploration". *International journal of pure and applied mathematics,* **79**(2), pp. 269–279.
7. Miura, K., 1994. "Map fold a la miura style, its physical characteristics and application to the space science". *Research of pattern formation*, pp. 77–90.

8. Tachi, T., 2011. "Rigid-foldable thick origami". *Origami,* **5**, pp. 253–264.

9. Zhang, Z., Ma, W., Wu, H., Wu, H., Jiang, S., and Chai, G., 2018. "A rigid thick miura-ori structure driven by bistable carbon fibre-reinforced polymer cylindrical shell". *Composites Science and Technology,* **167**, pp. 411 – 420.

10. Butler, J., Morgan, J., Pehrson, N., Tolman, K., Bateman, T., Magleby, S. P., and Howell, L. L., 2016. "Highly compressible origami bellows for harsh environments". In ASME 2016 International Design Engineering Technical Conferences and Computers and Information in Engineering Conference.

11. Yu, X., Fang, H., Cui, F., Cheng, L., and Lu, Z., 2019. "Origami-inspired foldable sound barrier designs". *Journal of Sound and Vibration,* **442**, pp. 514–526.

12. Wilson, M., Magleby, S., Howell, L., and Bowden, A., 2019. "Characteristics of self-deployment in origami-based systems".

13. Howell, L. L., 2001. *Compliant mechanisms.* John Wiley & Sons.

14. Zirbel, S. A., Trease, B. P., Magleby, S. P., and Howell, L. L., 2014. "Deployment methods for an origami-inspired rigid-foldable array".

15. Miura, K., 1969. *Proposition of pseudo-cylindrical concave polyhedral shells.* Institute of Space and Aeronautical Science, University of Tokyo Tokyo.

16. Tachi, T., 2009. "Generalization of rigid-foldable quadrilateral-mesh origami". *Journal of the International Association for Shell and Spatial Structures,* **50**(3), pp. 173–179.

17. Miura, K., and Lang, R., 2009. "The science of miura-ori: A review". *Origami,* **4**, pp. 87–99.

18. Gioia, F., Dureisseix, D., Motro, R., and Maurin, B., 2012. "Design and analysis of a foldable/unfoldable corrugated architectural curved envelop". *Journal of Mechanical Design,* **134**(3).

19. Johnson, M., Chen, Y., Hovet, S., Xu, S., Wood, B., Ren, H., Tokuda, J., and Tse, Z. T. H., 2017. "Fabricating biomedical origami: A state-of-the-art review". *International journal of computer assisted radiology and surgery,* **12**(11), pp. 2023–2032.

20. Sareh, P., Chermprayong, P., Emmanuelli, M., Nadeem, H., and Kovac, M., 2018. "Rotorigami: A rotary origami protective system for robotic rotorcraft". *Science Robotics,* **3**(22).

21. Liu, S., Lu, G., Chen, Y., and Leong, Y. W., 2015. "Deformation of the miura-ori patterned sheet". *International Journal of Mechanical Sciences,* **99**, pp. 130–142.

22. Arya, M., Hodges, J. S. R. E., and Pellegrino, S., 2019. "Large-area deployable reflectarray antenna for".

23. Lang, R. J., Tolman, K. A., Crampton, E. B., Magleby, S. P., and Howell, L. L., 2018. "A review of thickness-accommodation techniques in origami-inspired engineering". *Applied Mechanics Reviews,* **70**(1).

24. Ku, J. S., 2017. "Folding thick materials using axially varying volume trimming". In ASME 2017 International Design Engineering Technical Conferences and Computers and Information in Engineering Conference, American Society of Mechanical Engineers Digital Collection.

25. Hoberman, C. S., 1988. Reversibly expandable three-dimensional structure, Oct. 25. US Patent 4,780,344.

26. Hoberman, C., 2010. Folding structures made of thick hinged sheets, Sept. 14. US Patent 7,794,019.

27. Zirbel, S. A., 2014. "Compliant mechanisms for deployable space systems".

28. Wang, F., Gong, H., Chen, X., and Chen, C., 2016. "Folding to curved surfaces: A generalized design method and mechanics of origami-based cylindrical structures". *Scientific reports,* **6**(1), pp. 1–10.

29. Papa, A., and Pellegrino, S., 2008. "Systematically creased thin-film membrane structures". *Journal of Spacecraft and Rockets,* **45**(1), pp. 10–18.
30. Cai, J., Ren, Z., Ding, Y., Deng, X., Xu, Y., and Feng, J., 2017. "Deployment simulation of foldable origami membrane structures". *Aerospace Science and Technology,* **67**, pp. 343–353.
31. Lynd, D. T., and Harne, R. L., 2017. "Strategies to predict radiated sound fields from foldable, miura-ori-based transducers for acoustic beamfolding". *The Journal of the Acoustical Society of America,* **141**(1), pp. 480–489.
32. Seiler, S. R., Bazzan, G., Fuchi, K., Alanyak, E. J., Gillman, A. S., Reich, G. W., Buskohl, P. R., Pallampati, S., Sessions, D., Grayson, D., et al., 2017. "Physical reconfiguration of an origami-inspired deployable microstrip patch antenna array". In 2017 IEEE International Symposium on Antennas and Propagation & USNC/URSI National Radio Science Meeting, IEEE, pp. 2359–2360.
33. Horner, G., and Elliott, M., 2002. "A fabrication and deployment approach for a miura-ori solar sail model". In 43rd AIAA/ASME/ASCE/AHS/ASC Structures, Structural Dynamics, and Materials Conference, p. 1708.
34. Butler, J., Bowen, L., Wilcox, E., Shrager, A., Frecker, M. I., von Lockette, P., Simpson, T. W., Lang, R. J., Howell, L. L., and Magleby, S. P., 2018. "A model for multi-input mechanical advantage in origami-based mechanisms". *Journal of Mechanisms and Robotics,* **10**(6).
35. Nijenhuis, M., Meijaard, J., and Brouwer, D., 2020. "Misalignments in an overconstrained flexure mechanism: A cross-hinge stiffness investigation". *Precision engineering,* **62**, pp. 181–195.
36. Lang, R. J., 2017. *Twists, tilings, and tessellations: mathematical methods for geometric origami.* CRC Press.
37. Andrews, D. W., Magleby, S. P., and Howell, L. L., 2020. "Thickness-utilizing deployable hard stops for origami-based design applications". *Mechanical Sciences,* **11**(2), pp. 395–410.
38. Pehrson, N. A., Ames, D. C., Smith, S. P., Magleby, S. P., and Arya, M., 2020. "Self-deployable, self-stiffening, and retractable origami-based arrays for spacecraft". *AIAA Journal*, pp. 1–8.
39. McEachen, M. E., 2018. "Compact telescoping array: Advancement from concept to reality". In 2018 AIAA Spacecraft Structures Conference, p. 1945.
40. Liu, R., Guo, H., Liu, R., Wang, H., Tang, D., and Song, X., 2017. "Shape accuracy optimization for cable-rib tension deployable antenna structure with tensioned cables". *Acta Astronautica,* **140**, pp. 66–77.
41. Cowan, B., and Von Lockette, P. R., 2017. "Fabrication, characterization, and heuristic trade space exploration of magnetically actuated miura-ori origami structures". *Smart Materials and Structures,* **26**(4), p. 045015.
42. Xia, Y., and Wang, K.-W., 2019. "Dynamics analysis of the deployment of miura-origami sheets". In International Design Engineering Technical Conferences and Computers and Information in Engineering Conference, Vol. 59247, American Society of Mechanical Engineers, p. V05BT07A026.
43. Bowen, L., Springsteen, K., Frecker, M., and Simpson, T., 2016. "Trade space exploration of magnetically actuated origami mechanisms". *Journal of Mechanisms and Robotics,* **8**(3).

Robust 3D Printed Modular Soft Pneumatic Actuator using Origami Concept for High Contraction Soft Systems

X. Y. Sandoval-Castro[1], D. S. Garcia Morales[2], E. Castillo-Castaneda, and A. Raatz

[1] CONACYT-IPN, Mechatronics Department, Queretaro 76090, Mexico,
`yamile_catedraqro@ipn.mx`,
[2] Leibniz University Hannover, Institute of Assembly Technology, Garbsen 30823, Germany

[1] [2]These authors contributed equally in this paper

Abstract. Soft Robotics offers an opportunity to fabricate more adaptable systems to be used outside industrial areas. For practical applications of soft robots, their active parts should achieve high forces and considerable displacements keeping the structures lightweight, modular, and easy to fabricate. Consequently, robust and predictable motion actuators with easy manufacture are required. This paper applies the origami concept to address a 3D printed low-weight modular soft pneumatic linear actuator denoted ORI-Structure. The presented structure has a high contraction rate (up to 52.5%) and can lift 1161.64× its weight. Additionally, we present a more complex module with 3 DOF formed with the ORI-Structure. The module can displace linearly with a high-contraction rate (up to 52.5%), and it can rotate in two axes up to 42°. In both cases, the module exhibits high-lifting capabilities (611.53× its weight). In both cases, simulation and experiments are introduced to describe the design parameters and their performances.

Keywords: Soft robotics, Soft actuators, Origami, 3D printing, Robust actuator, High contraction, Modularity

1 Introduction

Soft Robotics is an interdisciplinary area that aims to develop more compliant robotics systems by shifting the material from which traditional robots are made [1]. Soft actuators, which are the active part of a soft robot, are crucial to achieving robust systems which can handle additional weight while keeping a compliant body for high energy absorption. This active component can be generally categorized according to their stimuli, e.g., electro-driven, thermo-driven, magneto-driven, light-driven, and pressure-driven [2]. Generally, the performance constraints are dictated by their stimuli, affecting their contraction rate, robustness, fabrication process, durability, cost, among other aspects [3]. Pressure-driven actuators are one of the most commonly use actuation method

for soft actuators. Motion can be achieved by applying positive or negative (vacuum) pressure. Numerous upgrades like in [4] and [5] showed good performance producing robust pneumatic systems with considerable contraction ratio. Nevertheless, their design is made to deform their structure to achieve movement, making them energy deficient and difficult to predict their displacement for the application of control techniques [6]. Alternative designs such as [7] introduce high-displacement pneumatic actuators made of textiles shaped in small rectangular sections that can contract up to 40–65% its original length avoiding high material deformation but also with a more complex fabrication process. Moreover, designs that combine more complex geometries with accessible and considerable easier fabrication steps have been already addressed. Such as [8] where a soft pneumatic actuator can contract up to 64.7% with a maximum force of 295.2 N, and it can be 3D printed with an additional coating step. Still, these soft pneumatic actuators present safety concerns due to possible leakage causing malfunctions. However, alternatives like soft vacuum actuators have the advantage of providing a fail-safe feature in contrast to positive pressure-driven actuators shrinking upon activation, improving the lifetime and durability of the actuators [9]. Though soft pneumatic actuators generally require high-pressure inputs to achieve motion, and a compromise between easy fabrication, contraction rate, robustness, and low-pressure inputs persist in the current state of the art.

On the other hand, origami, the art of paper folding, allows creating soft structures that are stimulated by vacuum inputs, providing inspirations for deployable and robust structures [10]. These origami structures are defined by their crease pattern [11]. The most common foldable patterns are Yoshimura, Miura, Waterboom, Kresling, and Resch [12]. The origami patterned towers have been used to design soft pneumatic linear actuators that exhibit high contraction and high force at low-pressure input [13]. A variety of origami-inspired tubular structures have been proposed, including the Yoshimura [14], Miura–Tachi polyhedron [15], and Miura-ori patterns. In [14] developed pseudo cylindrical concave polyhedral shell (PCCP) from diamond and hexagonal Yoshimura pattern, demonstrating develop-ability of its mid-surface and intrinsically high circumferential bending rigidity. Yoshimura pattern is the exactly isometric, axially, and uniformly shortened surface indefinitely close to an arbitrary circular cylindrical surface. More specifically, in this paper, we address the benefit of using the origami concept in soft robotics by designing and evaluating a 3D printed origami tubular structure (ORI-Structure) with one degree of freedom (DOF). Additionally, we assess its modularity through a final development of a multi-degree freedom module creating a high strength system with low input pressure and high contraction.

2   ORI-Structure Design

The ORI-Structure is based on the Yoshimura pattern, the crease pattern is composed of equilateral trapezoids (Fig. 1A), when the closure condition is satisfied, the pattern forms a closed structure, [16], as shown in Fig. 1B. The pattern is
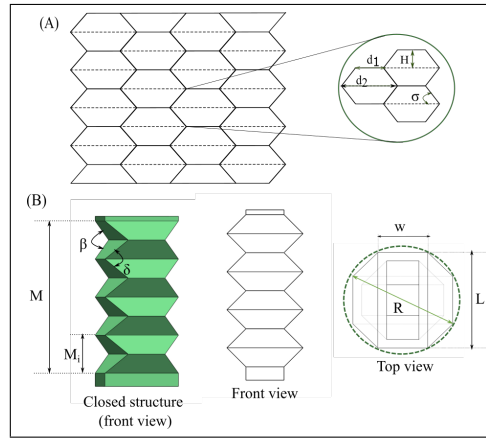
Fig. 1. (A) The origami pattern with equilateral trapezoid; (B) The closed structure, lateral, front, and top view.

composed of 4-array equilateral trapezoids (horizontal axis) with parallel sides d_1 y d_2, height H, and base angle σ. In addition, the closed tube has 4 levels represented by M_i, τ_i describes the $i-th$ trapezoid horizontally. When τ_i=4, an approximately square cross-section is obtained, similarly, τ_i=6 and τ_i=8 for hexagonal and octagonal cases, respectively. The closure equation of the pattern [17], is described by

$$tan(\sigma)cos(\beta/2) = tan(\pi/\tau_i). \tag{1}$$

Where β is the dihedral angle between the two panels connected by valley fold when the pattern closed, σ is the angle between two oblique hill folds at any vertex. The length, width, and cross-sectional diameter of the structure are L, w y R, respectively. Each level's height is described as $M_i = M/i$, where i corresponds to the number of levels. Thus, the relationship between M_i, $M_i = M/i$, and H is described by (2). The geometric parameters of the closed structure are: M=80 mm, wall thickness 2.5 mm, $\beta=\delta=90°$, M_i=20 mm.

$$H = M_i/2cos((\pi - \beta)/2) \tag{2}$$

3   ORI-STRUCTURE FEM ANALYSIS

Initially, we processed different FEM simulations to evaluate the ORI-Structure performance, using ABAQUS CAE 2017. We evaluated relevant design parameters to observe the relationship between the performance under compression and load to define the suitable design dimensions and the unitary section's capabilities. The material adopted was the silicone AR-G1L with Mooney-Rivlin parameters reported in [18]. For geometric evaluation and load tests, the hexahedral element was used for the meshing the structure.
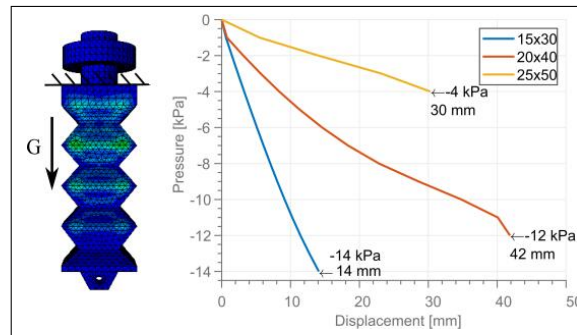
Fig. 2. Influence of the variation of the geometrical parameters L and w.

3.1 Geometric Parameters

We analyzed the cross-sectional diameter (R) influence on the unitary structure's axial displacement under vacuum (contraction). Since (R) is denoted by the parameters (L) and (w), which have a relationship of 2:1, the proposed dimensions in millimeters were: A) 30 mm x 15 mm, B) 40 mm x 20 mm y C) 50 mm x 25 mm. In this case, Fig. 2 reports the performance of each variant, where a significant variation of cross-sectional diameter changes the actuator's displacement. As a result, B) 40 mm x 20 mm presented the best contraction-pressure ratio, obtaining 42 mm at -12 kPa (52.5% of actuator's length).

3.2 Compression Test FEM Simulation

Once we defined the suitable parameters for the actuator (40 mm x 20 mm), we performed a compression test to determine the contraction of the ORI-Structure as a function of an external homogeneous applied force. This simulation allowed us to evaluate the origami structure's maximum contraction value without losing the geometry properties. It can also be repeated in experiments with accurate information for further evaluations (Sect. 4). In the simulation, to mesh the ORI-Structure, a 4-node bilinear axisymmetric quadrilateral element C4X4 was used. The structure was fixed from the bottom cover, as shown in Fig 3. A quasi-static procedure was used with a crushing distance of 50% of the origami tube length (M). The tube was compressed freely and axially, considering self contact constrain. We obtained a maximum displacement of 35 mm at 8 kPa.

3.3 Load Test FEM Simulation

We investigated the load capabilities of the structure through a weight lifting simulation. The actuator was suspended as shown in Fig. 4A. The test considers lifting the load at 40% of the ORI-structure's length (M); we varied the load from 100 g to 800 g. As a result, at 40%, 512 g were successfully lifted; however, the actuator maximum lifted load was 792 g, reaching 37% of actuator contraction. With a higher load than 800g, the structure loses its geometry.
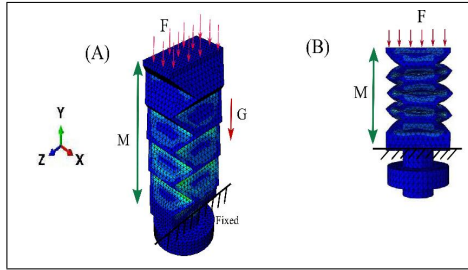
Fig. 3. (A) Boundary conditions of the compression test; (B) Compressed origami tube.
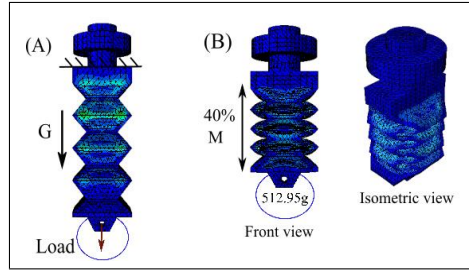
Fig. 4. (A) Boundary conditions of the load test simulation; (B)The actuator lifting 512.95g.

4 ORI-Structure Evaluation

A 3D printed version of the design is tested to verify the simulation results for further design adjustments. Two tests were performed, compression tests and load tests.

4.1 Compression Test

This section describes the verification of the simulation values obtained in Sect. 3.3 to verify the simulation accuracy. In this way, a compression test of the ORI-Structure was performed using the zwickiLine test machine. The machine was configured with a pre-load of 0.1Pa, 0.05 mm/sec velocity, and a maximum force of 9 kPa on a surface of 40 mm x 20 mm (ORI-Strcutre's size). Two support were 3D printed to fix the actuator (see Fig. 5). Two sessions of experiments were carried, producing 16 tests. As a result, in Fig. 5, the test is compared to the simulation in terms of displacement vs pressure. A maximum displacement of up to 52.5% with a maximum force of 9 kPa was observed in both cases. Compared to the simulation, the data remains between the tolerance indicated by the tests' standard deviation. Thus, the simulation is considered accurate enough to provide relevant values, and the maximum displacement of the ORI-Structure is defined as 52.5%.

4.2 Load Test

Following the design's evaluation, a load test was performed where the actuator was suspended, and a hook was added to the top surface (see Fig. 6). The actuator lifted six different weights from 380 g to 1000 g to observe whether the weight could be lifted or not. During this process, the pressure of the actuator was measured. We observed good performance up to 700 g; at this weight, the actuator could contract and keep the structural integrity achieving a maximum pressure of -42 kPa. For loads greater than 800 g, the actuator's behavior was observed to lose its geometry completely and suck instead of contract concluding that the ORI-Structure could lift 1161.64× its weight (60 g).
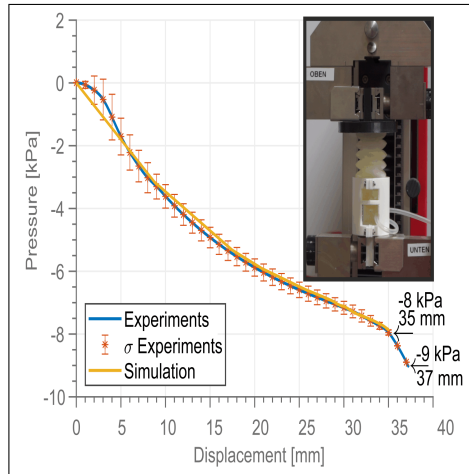
Fig. 5. Pressure vs Displacement of the simulation and the experiments, including the actuator fixation for the experiments.
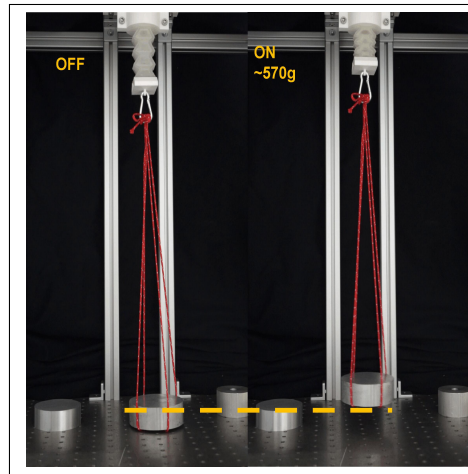
Fig. 6. Load test of the ORI-Structure with an extra weight of 570 g. Left side vacuum off and right side vacuum on.

5   Modular Soft Pneumatic Actuator

An important part of this research is to emphasise the concept's modularity by developing a multi-degree of freedom module. We propose a module based on the ORI-Structure reported in this paper. The module is conformed of three parallel ORI-Structure denoted A1, A2 and A3 distributed 120° around Z-axis separate from each other (Fig. 7). It has 3 DOF, one translational (along Z-axis) denoted by Δ, and two rotational (around X and Y axes, denoted by α and Ψ, respectively). The module's base has a triangular shape with rounded corners; the base's dimension is 126 mm x 126 mm.
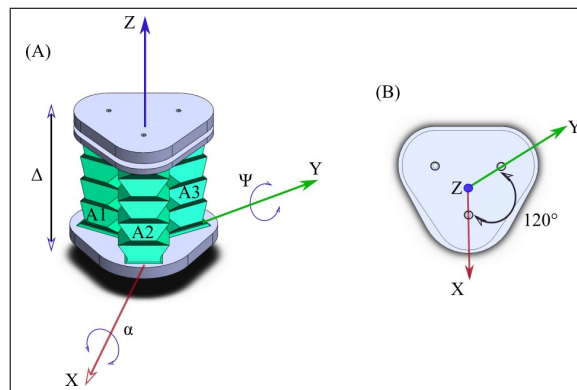
Fig. 7. CAD design of the 3 DOF module. (A) Top-front view; (B) Top view.

5.1 Module FEM Simulation

This section demonstrates the module performance similarity with the unitary structure and its mobility using a FEM simulation. The configuration is similar to section 3, and the boundary conditions without considering additional load are displayed in Fig. 8A. Due to the individual actuators' arrangement, the module can achieve two different motions linear and bending.

When three actuators are activated simultaneously, the module displaces on Z-axis, as is shown in Fig. 8B. Likewise, when one actuator is activated independently (A1, A2, A3) or two actuators are activated simultaneously (A1+A2, A2+A3, A3+A1), the module bends in several directions as shown in Fig. 8C and D.
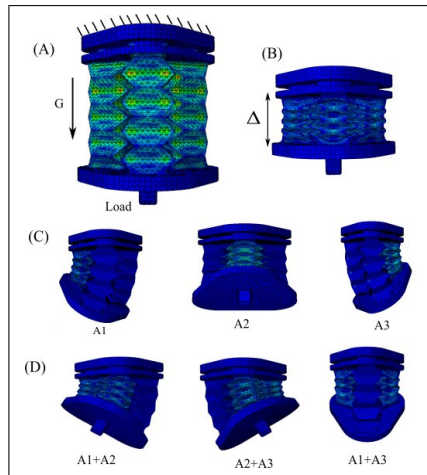
Fig. 8. Module FEM simulation results with different views of the motion. (A) Boundary conditions and gravity applied; (B) Negative pressure applied to actuators A1, A2, A3; (C) Negative pressure applied to individual actuators; (D) Negative pressure applied to two actuators at the same time.
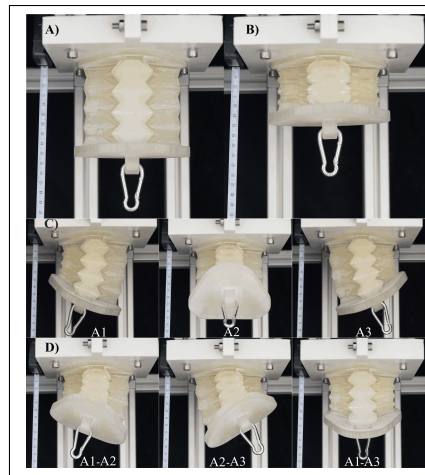
Fig. 9. 3D printed soft pneumatic module with different views of the motion. (A) Boundary conditions and gravity applied; (B) Negative pressure applied to actuators A1, A2, A3; (C) Negative pressure applied to individual actuators; (D) Negative pressure applied to two actuators at the same time.

Furthermore, the simulation results shown in Fig. 10 reports the linear displacement of the actuator (blue line), reaching 42 mm (52.5%) similar to the ORI-Structure, presenting no changes in the performance when more than two structures are in parallel. Also, in the solid red line, the maximum angular displacement when an ORI-Strcutre is activated independently is 42°, and in the red dotted line, the activation of two ORI-Strcutres simultaneously reached a maximum of 40°. In all the possible combinations, similar behaviour where observed.
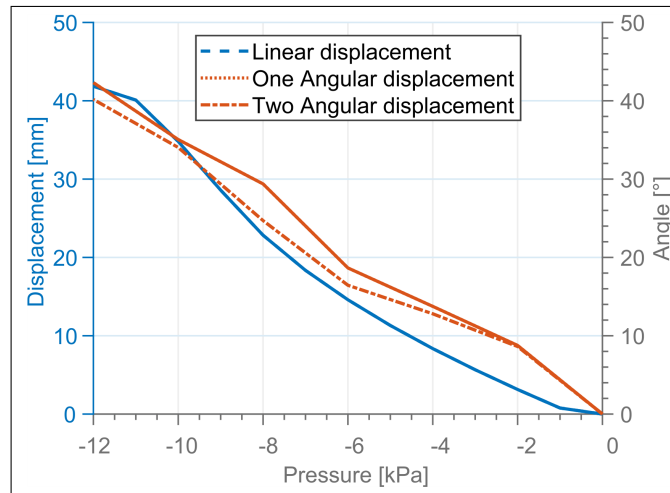
Fig. 10. Simulation results of the module motion, including a relationship between pressure and displacement and pressure and bending angle activating individual actuators, two combined actuators and all.

Additionally, in the simulation, we performed a load test to evaluate the maximum load that the actuator theoretically can lift, considering the boundary conditions showed in Fig. 8A. We varied the load from 100 g to 2500 g, observing that the actuator has a good performance when lifting a load of 2000 g contracted at 40% of the modules' length. However, with a more significant load, the module's base starts to bend, creating undesired stresses on the surface.

5.2   Module Evaluation

Following the results from the previous section, in this section, we prove the robustness and mobility of the actuator. Figure 9 visualize the possible combinations of the actuators to achieve different positions, which agrees with the simulation results (Fig. 10), demonstrating that original ORI-Strcutre can be configured to achieve more than one degree of freedom. Likewise, we perform a lifting test with different weights from 300 g to 2600 g and measured the displacement using a ruler mounded next to the module. As a result, the module's displacement with a load of up to 2000 g was 52.5% carrying 611.53× its weight (327 g). Additionally, we found that the displacement decreased significantly for weight greater than 2400 g, and deformation on the base was observed. We observed greater contraction in the evaluation than in the simulation since the maximum pressure applied in the simulation was lower than the one applied during the experiments because of the computational cost.

6   Conclusion

This paper introduced a 3D printed robust unitary structure denoted ORI-Structure inspired by the Yoshimura pattern variation with a high contraction and low-pressure input. We reported the design, FEM analysis and hardware evaluation of the ORI-Structure, showing that the cross-sectional diameter denoted by the tube base's length and width significantly influences the pressure-contraction ratio. The FEM simulations showed that the parameters L=40 mm and w=20 mm have a dramatic increment in the contraction compared to the other two variations. Furthermore, through the FEM simulation and experiments, we defined the ORI-Structure maximum displacement of 52.5% of its length showing lifting capabilities with a maximum of 700 g at -41 kPa or 1161.64× its weight. We conclude that the simulation agrees with our experiments and accurately predict the performance.

Furthermore, the modular system was manufactured using a 3D printer with only one material, which allows a quick and mass production fabrication of actuators with predictable behaviour. Besides, the system does not increase or decrease its radius, improving the working area's use. Additionally, we proposed a modular soft pneumatic actuator using three ORI-Structures separated 120°around the Z-axis. This configuration has 3 DOF allowing 1 DOF of pure translation and 2 DOF of rotation. Its motion was evaluated by means FEM simulations reached a contraction of 52.5% of the actuators' length, which implies that the unitary structure simulation provides enough information to create more complex and functional modules. Likewise, the maximum module angle obtained when a single unitary structure is activated independently and when two structures are activated simultaneously are 42°and 40°, respectively. The module exhibits rotation in several directions with excellent mobility using linear actuators. Besides, the module lifted 2000 g at full contraction (52.5%), corresponding to 611.53× its weight without any observable problems. The maximum load that the module can lift is 2400 g; however, significant deformations on the base are presented. All in all, the module exhibits high dexterity and a high contraction even under load conditions.

For future work, we propose a robotic arm that can be used in health care assistance. This future work will understand the module kinematics exploiting the origami structure to define its movement accurately. Also, we will work on the dynamics of the modules working together as a system and the definition of suitable mechanisms for the modules' connection.

ACKNOWLEDGMENT

References

1. C. Lee, M. Kim, Y.J. Kim. "Soft robot review." Int. J. Control Autom. Syst. vol. 15, pp.3–15, 2017.
2. N. El-Atab, R.B. Mishra, F. Al-Modaf, L. Joharji, A.A. Alsharif, H. Alamoudi, M. Diaz, N. Qaiser and M.M. Hussain. "Soft Actuators for Soft Robotic Applications: A Review." Adv. Intell. Syst., 2: 2000128, 2020.
3. J. Kim, J.W. Kim, H.C. Kim. "Review of Soft Actuator Materials." Int. J. Precis. Eng. Manuf. 20, 2221–2241, 2019.
4. K. T. Yoshida, X. Ren, L. H. Blumenschein, A. M. Okamura and M. Luo, "AFREEs: Active Fiber Reinforced Elastomeric Enclosures," 2020 3rd IEEE International Conference on Soft Robotics (RoboSoft), New Haven, CT, USA, pp.305-311, 2020.
5. Y. Yamada, A. Kojima, Y. Higashi, M. Okui and T. Nakamura, "Hollow Pneumatic Artificial Muscles with Air Cylinder: Improvement for compatibility of high durability and high efficiency." International Conference on Biomedical Robotics and Biomechatronics (Biorob), Enschede, pp. 865-870, 2018.
6. J. Ch. Krause, S. Ibrahim and A. Raatz. "Evaluation Environment for Control Design of Soft Pneumatic Actuators." Tagungsband des 4. Kongresses Montage Handhabung Industrieroboter, pp.74–83, 2019.
7. H. D. Yang, B. T. Greczek and A. T. Asbeck. "Modeling and Analysis of a High-Displacement Pneumatic Artificial Muscle With Integrated Sensing." Frontiers in Robotics and AI, vol. 5, pp. 136, 2019.
8. K. Han, N. Kim, and D. Shin. "A Novel Soft Pneumatic Artificial Muscle with High-Contraction Ratio." Soft Robotics, 5:5, pp.554-566, 2018.
9. Ch. Tawk, G. M. Spinks, M. Panhuis, and G. Alic. "3D Printable Linear Soft Vacuum Actuators:Their Modeling, Performance Quantification and Application in Soft Robotic Systems." Transactions on Mechatronics, 24(5). 2019.
10. Xu S, et al. "Assembly of micro/nanomaterials into complex, three-dimensional architectures by compressive buckling". Science 347:154–159. 2015.
11. J. Mitani. "A method for designing crease patterns for flat-foldable origami with numerical optimization." Journal for Geometry and Graphics, 15(2), 195-201. 2011.
12. M. R. Gardiner, "ORI* On the Aesthetics of Folding and Technology (Thesis or Dissertation style)." Ph.D. dissertation, University of Newcastle, Australia, 2018.
13. S. Li, D M. Vogt, D. Rus and R. J. Wood. "Fluid-driven origami-inspired artificial muscles." National Academy of Sciences, vol. 114, num. 50, pp. 13132–13137, 2017.
14. K. Miura. "Proposition of pseudo-cylindrical concave polyhedral shells." Proc. of IASS Symposium on Folded Plates and Prismatic Structures, 1969.
15. Yasuda H, Yein T, Tachi T, Miura K, Taya M. "Folding behaviour of Tachi-Miura polyhedron bellows." Proc. R. Soc. A 469, 20130351. 2013.
16. P. Wang-Iverson, R. Lang, M. YIM. "Origami 5." New York: A K Peters/CRC Press, 2017.
17. J. Song, Y. Chen, G. Lu. "Axial crushing of thin-walled structures with origami patterns." Thin-Walled Structures, Vol. 54, 65-71. 2012.
18. D.S Garcia Morales, S. Ibrahim, BH. Cao, A. Raatz. "Design and Characterization of a 3D Printed Soft Pneumatic Actuator." Mechanisms and Machine Science, vol 89., 2020.

Characterization of Multistable Self-Folding Origami Architectures

Salvador Rojas, Katherine S. Riley, and Andres F. Arrieta

Programmable Structures Lab, School of Mechanical Engineering, Purdue University,
585 Purdue Mall, West Lafayette IN 47907, USA
`rojas23@purdue.edu`
home page: `https://engineering.purdue.edu/ProgrammableStructures/`

Abstract. We propose a method for designing self-folding, multistable origami structures based on bioinspired spring origami theory and bilayer crease architectures. An analytical model based on bilayer theory is developed to predict the self-folding angles of such origami systems. We extend this self-folding model from traditional origami-based theory with straight creases to bioinspired spring origami theory with missing angle (β) creases, in order to generate bistable origami structures with programmable energy landscapes. Integrating bioinpsired spring origami theory and 4D printing, a flat sheet with arranged facets and mountain-valley crease assignments can be actuated to trigger localized, programmable folding which results in global shape shifting. By prescribing origami crease patterns with straight and β creases we demonstrate bistable, self-folding structures that can be manufactured and stored as 2D sheets and deployed into structures with useful applications in engineering, biological systems, and arts.

Keywords: multistable, self-folding, 4D printing, origami,bioinpsired

1 Introduction

Origami inspired principles are attractive in areas where shape transformation, morphing, and reconfigurable structures are advantageous. However, shape transformation and reconfigurabilty of structures introduce automation challenges [1]. Active origami [2], the ability of objects to fold upon actuation of a stimulus, has emerged as a promising solution to meet the needs of shape transformation and morphing. Most active origami structures are designed by locating environmentally responsive materials, such as shape memory materials, at the creases leveraging stimuli such as changes in light [3], temperature [4], or hydration [5] to induce local deformation at the folds. Current active folding technologies have successfully achieved complex 3D shapes but their ability to reconfigure is limited as only one shape can be attained in response to a given stimulus. By harnessing geometric buckling instability, it is possible to generate new solution branches associated with multiple stable configurations in origami systems [6, 7]. The effect of global buckling in self-foldable origami-inspired structures has been explored by localized heating of single shape memory polymers

(SMPs) such as prestressed polystyrene (PSPS). The shape adaptation occurs due to strain mismatch creating local and global bending behavior yielding 3D shapes [8].

Nature provides intriguing examples for designing programmable matter that self-folds into complex shapes, thereby reducing the need for constant actuation. Earwig wings [9, 10] offer interesting examples in which material architectures are leveraged to store energy for self-locking multiple stable shapes, and enabling shape reconfiguration that requires only a triggering stimulus, as opposed to the constant supply of energy needed in most active origami examples. Recently, a new theory—bioinspired spring origami—explained the bistable self-folding process of the mid-wing mechanism [10]. Concretely, spring origami captures the Earwig's mid-wing behavior by introducing extensible creases that stretch, thus avoiding the singularities found when using rigid origami theory [11]. It is desirable to translate the material system architectures observed in nature to fully synthetic systems to obtain self-folding and achieve multiple configurations, thereby extending the origami design space.

In this work, we design a method for reconfiguring the encoded multiple shapes of spring origami structures by imposing different folding angles after printing. Specifically, we utilize a 4D printing method demonstrated in [12, 13] to pre-stress the printing material via the stretching of the polymer chains during the directional deposition and rapid cooling. We develop a model to predict the folding behavior of angles in origami systems with straight ($\beta = 0°$) and β angle ($\beta \neq 0°$) effects in a bilayer crease system. We validate our results with tests of folding systems with straight and β creases and compare their shapes to the analytical and Finite Element Analysis (FEA). By utilizing the bilayer model with β angle effects, we enable the design of programmable multistable origami structures with adaptable stable states after manufacturing.

2   Programmable folding angle

Multistable origami structures offer the possibility of attaining a richer set of functional shapes. Most multistable origami structures leverage facet flexibility to generate coexisting solution branches [6, 7]. We focus on using crease stretching in combination with geometrical constraints to generate multistable origami systems. This is exemplified by the central mechanism of the Earwig wing, shown in Fig. 1a. This features facets with angles δ_i for $i = 1, .., n$, where n is the number of facets surrounding a single vertex that add up to $\delta_1 + ... + \delta_n < 360°$. This generates a strain mismatch that would result in ripping or tearing if inextensibility was enforced when the object is subjected to flattening. Enabling crease stretching gives rise to the effect of a missing angle, β angle, Fig. 1a, which allows the structure to switch from one energy potential to another. To program multiple statically stable states, a method to introduce pre-stress into the folds is necessary. To achieve this, we use differential cross-sectional straining in the crease induced by the stretching of polymer chains during printing, as shown in Fig. 1c. We enable rapid cooling to minimize polymer chain mobility,

thus freezing the material in a stretched state. These strains are subsequently released by heating the print above the polymer's glass transition temperature, T_g resulting in directional shrinkage of the polymer chains, causing a macroscopic pre-strain across the crease, Fig. 1d. We leverage this pre-strain to induce folding angles, which alongside the programmed β angle results in a multistable origami structure with programmable energy landscapes offering new associated stable shapes.
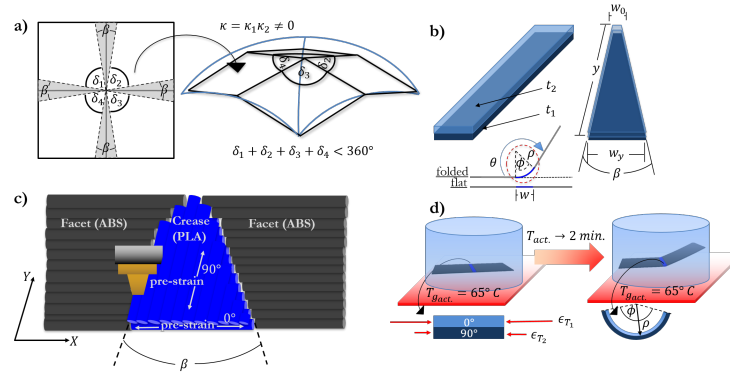
Fig. 1. Programmable folding angles: a) Integrating β (missing) angle geometry and the sum of the facet angles $\delta_i < 360°$ introduces multistability. b) Geometrical definitions of the crease angle in relation to the width (w) for straight and β creases. c) 4D printing of a multi-material folding sheet with PLA and ABS using an Ultimaker S3. d) After the structure in c) is printed, it is submerged in a heated water tank at the activation temperature $T_{g_{act.}}$ for 2 minutes.

To predict the obtained folding angle θ, we draw from a simplified bilayer model [14] which assumes the crease curvature is obtained from a thermally activated bilayer beam in plain-strain state. Thus, we can indirectly relate the folding angle θ to the active crease geometrical parameters exemplified in Eq. 1 below [5, 8]:

$$\frac{1}{\rho} = \frac{6\Delta\epsilon_T(1+m)^2}{\frac{t}{2}(3(1+m)^2 + (1+mn)(m^2 + \frac{1}{mn}))} \tag{1}$$

where $\Delta\epsilon_T = \Delta\alpha\Delta T$ represents the product between the difference in layer thermal expansion coefficients $\Delta\alpha$ and the change in temperature ΔT, t is the overall thickness, $m = \frac{t_1}{t_2}$ represents the thickness ratio, and $n = \frac{E_1}{E_2}$ represents the modulus ratio. The ratios n and m, play a vital role in determining the fold angle of an active bilayer crease and its dependence on the geometrical and material properties. Although it is possible to develop a purely geometrical analytical model as shown in [15, 16], the model presented here proves parameters such as stiffness cannot be neglected.

The bilayer model can thus be utilized to relate the folding angle θ to the width w of the crease as shown in Fig. 1b. We begin considering the straight crease ($\beta = 0°$) with folding angle θ. The inscribed angle ϕ along side arc parameters w and curvature $\frac{1}{\rho}$ are related by

$$\phi = \frac{w}{\rho} \tag{2}$$

the folding angle θ is the supplementary of angle ϕ and is computed as

$$\theta = \pi - \phi = \pi - \frac{w}{\rho} \tag{3}$$

Next, we extend the bilayer beam model to the geometry of the β angle, where $\beta \neq 0$, Fig. 1b. This is done by approximating the average of the width of the newly created β crease in order to find the inscribed angle ϕ_β and the folding angle θ_β between the facets that follows. Starting with an initial crease width as before, w now becomes w_0, and by defining a β angle to be used we can compute the width w_y at the end of the length of the crease and find the average width value of the crease w_β to use in the kinematics equations as follows:

$$\phi_\beta = \frac{w_\beta}{\rho} \tag{4}$$

where $w_\beta = \frac{w_0 + w_y}{2}$, thus

$$\theta_\beta = \pi - \phi_\beta = \pi - \frac{w_\beta}{\rho} \tag{5}$$

Thus, substituting the curvature equation, Eq. 1, in Eq. 3 for straight creases ($\beta = 0°$), and Eq. 5 for β ($\beta \neq 0°$) creases, we can model the folding behavior of straight and β crease systems. Fig. 2a is used as a design source for determining possible curvatures based on the effect of the ratios m and n [17, 18], and thermal strain ϵ_T, and is useful in applications where certain curvatures are desired or when some design parameters are limited and compensation is necessary. For instance, printing parameters were found to manipulate the resulting pre-strain [12, 13, 19]. Studies with a larger pre-strain $\epsilon_T = 0.087$ corresponding to a printing layer height of 0.05 mm can achieve larger curvatures overall for each modulus ratio n ranging from $1 \to 10$ compared to a smaller pre-strain $\epsilon = 0.054$ corresponding to a printing layer height of 0.1 mm.

3   Experimental methods

In order to experimentally validate the bilayer beam model, we manufacture a representative amount of straight and $\beta = 3.75°$ folding samples using 4D printing with fused deposition modeling (FDM). During FDM printing (Fig. 1c), pre-strain can be encoded by carefully controlling print direction and settings to leverage the shape memory effect of polymer filaments.
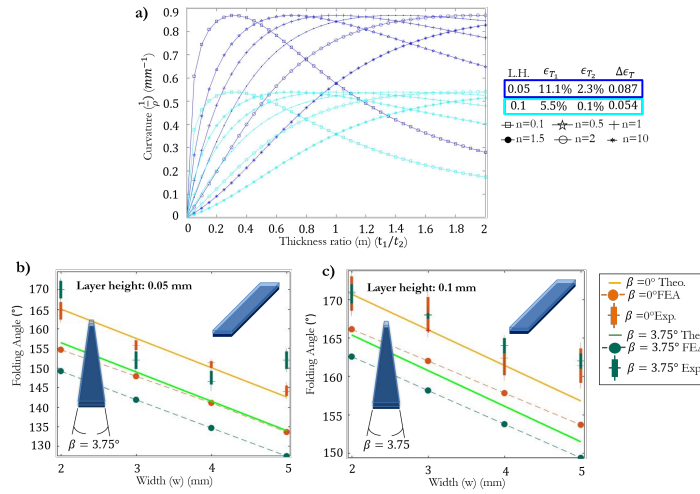
Fig. 2. a) Two scenes for the effect of Layer Heights $L.H. = 0.05$ mm and $L.H. = 0.1$ mm in 4D printing of folding sheets with programmable curvatures $(1/\rho)$, with different Young's Modulus ratio (n), as a function of the thickness ratio (m). b) Straight and missing angle crease folding angles for varying widths (w) for layer height 0.05 mm. c) Straight and missing angle crease folding angles for varying widths (w) for layer height 0.1 mm.

For the manufactured creases, we use Ultimaker Polylactic Acid (PLA), which has a nominal T_g of 60° C [20]. We assume linear, elastic isotropic material properties. The pre-strain in each layer is dictated by the specified print direction as shown in Fig. 1c, and can be 0° along the x-axis or 90° along the y-axis. The level of pre-strain can be controlled by the activation temperature, activation time, and layer height. For this set of experiments, we fix the activation temperature, $T_{g_{act.}}$, to 65° C and time at $T_{act.}$ to 2 minutes, Fig. 1d. The layer heights used are 0.05 mm and 0.1 mm, resulting in the pre-strains shown in Fig. 2a, where ϵ_{T_1} is in the 0° direction and ϵ_{T_2} is in the perpendicular 90° in-plane direction [12]. The out-of-plane strain is considered to be negligible for these experiments.

Because the pre-strain occurs principally along the print direction, a locally [0/90] or [90/0] layup may be used to induce a mountain or valley (M-V) fold, respectively. The 0° layer will shrink significantly perpendicular to the length of the crease, causing folding in that direction. This is illustrated in Fig. 1d. It is worth mentioning that the 90° constraining layer introduces longitudinal shrinkage, thus it may cause some anticlastic bending. However, for the dimensions studied here, this is found to be minimal.

In order to approximate rigid facets and constrain deformation to the creases, as in bioinspired spring origami, we print them primarily using Ultimaker Acrylonitrile Butadiene Styrene (ABS), which has a softening temperature of 97° C. Therefore, at $T_{g_{act.}} = 65°$ C, the ABS retains its glassy state stiffness of $E = 2030$

MPa, 128 times greater than the PLA rubbery state stiffness of $E = 15.8$ MPa [12, 20]. The facets are printed with a 0.1 mm thin initial layer of PLA for print continuity and uniform build plate adhesion. The remaining 0.7 mm are printed with ABS, which dominates the facet properties.

We verify the validity of the bilayer beam model with several straight and $\beta = 3.75°$ crease samples over a representative range. Five models of each width, $2, 3, 4,$ and 5 mm were printed and compared to the theoretical model and FEA models, as shown in Fig. 2 b,c. The comparison of the straight and β crease folding systems between theoretical, FEA, and experimental yielded results within 10% difference as shown in Table 1 for the majority of the experiments, providing an effective prediction for the self-folding angles. The outliers can be found between the 5 mm theoretical-experimental, 2 mm and 5 mm FEA-experimental for layer height 0.05 mm.

	Layer Height 0.05 mm					
	Theo-FEA		Theo.-Exp.		FEA-Exp.	
Width (w)	Straight	$\beta = 3.75°$	Straight	$\beta = 3.75°$	Straight	$\beta = 3.75°$
2	6.28	4.64	0.27	8.64	6.41	13.92
3	6.12	4.75	1.19	2.01	5.25	7.11
4	5.98	4.81	0.49	3.97	6.89	9.2
5	6.26	4.86	1.09	13.39	7.85	19.18
	Layer Height 0.1 mm					
	Theo-FEA		Theo.-Exp.		FEA-Exp.	
Width (w)	Straight	$\beta = 3.75°$	Straight	$\beta = 3.75°$	Straight	$\beta = 3.75°$
2	2.67	1.70	0.04	3.14	2.80	4.93
3	2.44	1.62	1.21	4.37	3.75	6.09
4	2.24	1.50	0.59	4.79	2.90	6.39
5	1.98	1.38	2.93	6.94	5.01	8.45

Table 1. Percent Differences for straight and $\beta = 3.75°$ folding systems for layer heights 0.05 mm and 0.1 mm.

It is worth noting that for $\beta = 3.75°$, the experimental missing angle width and thus folding angle does not differ much from the straight crease folding systems for both layer heights 0.05 mm and 0.1 mm as shown in Fig. 2b and Fig. 2c, respectively. In order to capture the β angle effect in which $\sum \delta_i < 360°$ thus enabling multistability, it is important that β creases deviate from straight crease geometry. To better distinguish β and straight creases, we increase the angle to $7.5°$, $15°$, and $30°$. By increasing the β angle we increase the total width of the crease, and thus the folding angle decreases leading to larger folding capabilities, as shown in Fig. 3 a,b for theoretical and FEA values. It is shown in Fig. 3 a,b that certain β angle and width combinations yield $< 10\%$ difference (*green*) providing an effective prediction while manipulating β crease geometry. On the other hand, there are combinations which yield $> 10\%$ difference (*red*); this indicates significant errors for higher β angle values and thus modifications to the model are necessary; this and additional experiments are left to future work.
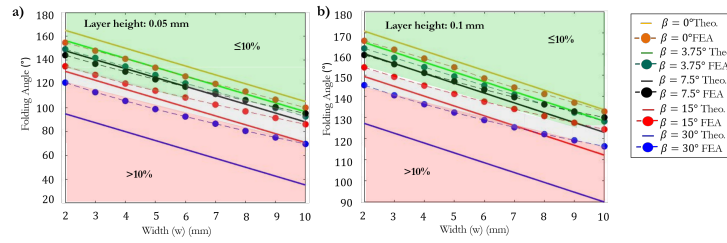
Fig. 3. Self-folding origami structures with the effect of crease angles $\beta = 0°, \beta = 3.75°, \beta = 7.5°, \beta = 15°$, and $\beta = 30°$ and percent difference map. a) Straight and missing angle crease folding angles for varying widths (w) for layer height 0.05 mm. b) Straight and missing angle crease folding angles for varying widths (w) for layer height 0.1 mm.

4   Results and Discussion

To capture the self-folding actuation of monostable and bistable origami systems, we transfer the design principles into fully synthetic demonstrators by preprogramming M-V assignments. To reproduce straight creases, we set a width w for the entire length of the crease and assign a local [0/90] or [90/0] layup. In the case of multistable origami crease patterns, we set w_0 and provide an angle β for the length of the crease.

Straight Folds: We aim to design a self-folding box with straight creases each targeted at 90° which corresponds to a width $w \rightarrow$ 12 mm. The self-folding
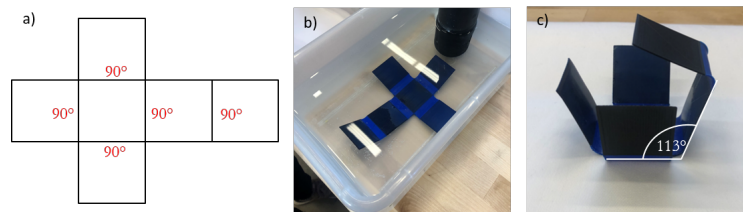
Fig. 4. a) 2D crease pattern for a box with predicted 90° angles at each crease. b) Submerged box in water heated above T_g. c) Experimental result for a 4D printed box based on bilayer crease pre-stressing

box proved to reach 75% of the predicted fold angle. In this experiment, we believe the discrepancy is due to the pressure of the water on the facets, which had a larger surface area than in the test subjects in Sec. 3, which creates an obstacle for the crease to overcome. To remedy this, we propose facets with holes in future experiments such that the pressure of the water on the surface of the facets decreases.

β Folds: Origami patterns with facet angles $\sum \delta_i < 360°$ at a single vertex will result in ripping or tearing when subjected to flattening if the system is restricted to rigid origami theory. The effect of β creases as presented here, enables reconfigurability in origami structures with such crease patterns. These particular types of geometrical structures would otherwise rip or tear if they were flattened, but by allowing the creases to stretch, while having stiff facets, we can pass the structure through the flat state and into another potential well as theorized in [10]. In the case of the Miura-ori unit cell, a single crease is
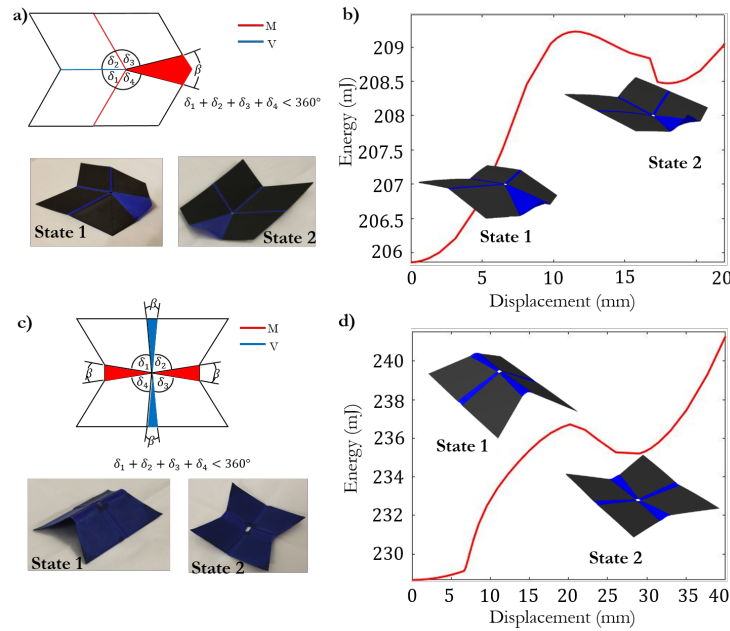
Fig. 5. Origami crease patterns with incorporated β angle a) Experimental Miura-ori, 3M-1V, crease pattern and included β angle enabling bistability. b) FEA simluation of a). c) Experimental pyramid-like, 2M-2V, crease pattern and included β angles enabling bistability. d) FEA simluation of the energy wells of c).

assigned a β angle, thus $\sum \delta_i$ around the vertex is $< 360°$ leading to a structure with multiple stable states. Upon thermal activation at $T_{g_{act.}}$, the experimental Miura-ori unit cell folds into its predicted initial folding configuration and can be manipulated, while still at $T_{g_{act.}}$ where the creases are in their rubbery state, to pass through the flat state into its second stable state as shown in Fig. 5a. We inspect the energy landscape of the bistable Miura-ori unit cell with FEA by a displacement-controlled deflection of the central vertex. While initiating a downward displacement at the central vertex, energy increases until reaching a

maximum (unstable equilibrium) near the flat state. After passing this point, the structure morphs into its second stable state as shown in Fig. 5b.

We modify the facet angles of the Miura-ori unit cell to resemble an hourglass with multiple β angle creases. Upon thermal activation, the encoded pre-stress and geometry yield a pyramid-like shape: one of its two stable states. Subsequently, we reconfigure the origami design into its second stable state, as shown in Fig. 5c. This behavior was validated through FEA revealing the expected double-well energy landscape with two minima each associated to the pyramid-like shapes, as can be seen in Fig. 5d. As expected, the Miura-ori unit cell and modified pyramid-like unit exhibit bistability with the implemented β angle effect.

5   Conclusion

In conclusion, we developed a model that enables reconfigurability in multistable origami systems by enabling crease pre-stressing upon thermal activation. We introduce a crease pre-stressing method that in combination with β angles enables an adaptable initial stable state. This method allows for modifying the as printed energy landscape and the associated stable states. We develop an analytical model allowing for rapid programming of the folding angles as a function of the crease bilayer microstructure. The analytical model is validated with FEA and experimental results revealing the range of crease parameters for which good agreement is obtained; defined as $< 10\%$ error. We also indicate the crease parameters for which the analytical model predictions exceed the 10% error boundary. We modeled and experimentally developed multistable self-folding systems by incorporating the β angle effect into Miura-ori based crease patterns. The printed unit cells revealed the expected double-well energy landscapes achieving two stable configurations while being manipulated at $T_{g_{act.}}$. This work provides a methodology for designing self-folding origami structures with adaptable energy landscapes, thereby enabling a route to changing the available coexisting configurations after manufacturing. This method allows for leveraging geometrically induced multistability with thermally programmable folding angles to obtain reconfigurable systems with multiple energy landscapes, thus allowing far greater functional shapes with applications in shape transforming and morphing structures.

References

1. Qi Ge, Conner K. Dunn, H. Jerry Qi, and Martin L. Dunn. Active origami by 4D printing. *Smart Materials and Structures*, 23(9), 2014.
2. Edwin A. Peraza-Hernandez, Darren J. Hartl, Richard J. Malak, and Dimitris C. Lagoudas. Origami-inspired active structures: A synthesis and review. *Smart Materials and Structures*, 23(9), 2014.
3. Yonghee Lee, Hyeok Lee, Taesoon Hwang, Jong Gu Lee, and Maenghyo Cho. Sequential Folding using Light-activated Polystyrene Sheet. *Scientific Reports*, 5:1–9, 2015.

4. Yiqi Mao, Kai Yu, Michael S. Isakov, Jiangtao Wu, Martin L. Dunn, and H. Jerry Qi. Sequential Self-Folding Structures by 3D Printed Digital Shape Memory Polymers. *Scientific Reports*, 5:1–12, 2015.

5. Anna B. Baker, Simon R.G. Bates, Thomas M. Llewellyn-Jones, Laurie P.B. Valori, Michael P.M. Dicker, and Richard S. Trask. 4D printing with robust thermoplastic polyurethane hydrogel-elastomer trilayers. *Materials and Design*, 163:107544, 2019.

6. Jesse L. Silverberg, Arthur A. Evans, Lauren McLeod, Ryan C. Hayward, Thomas Hull, Christian D. Santangelo, and Itai Cohen. Using origami design principles to fold reprogrammable mechanical metamaterials. *Science*, 345(6197):647–650, 2014.

7. Scott Waitukaitis, Rémi Menaut, Bryan Gin Ge Chen, and Martin Van Hecke. Origami multistability: From single vertices to metasheets. *Physical Review Letters*, 114(5):2–6, 2015.

8. Qiuting Zhang, Jonathon Wommer, Connor O'Rourke, Joseph Teitelman, Yichao Tang, Joshua Robison, Gaojian Lin, and Jie Yin. Origami and kirigami inspired self-folding for programming three-dimensional shape shifting of polymer sheets with light. *Extreme Mechanics Letters*, 11:111–120, 2017.

9. Fabian Haas. Geometry and mechanics of hind-wing folding in Dermaptera and Coleoptera Submitted by Fabian Haas to the University of Exeter Master of Philosophy in the Faculty of Science. (April), 1994.

10. Jakob A. Faber, Andres F. Arrieta, and André R. Studart. Bioinspired spring origami. *Science*, 359(6382):1386–1391, 2018.

11. F Haas, S Gorb, and R J Wootton. Elastic joints in dermapteran hind wings : materials and wing folding. 29:137–146, 2000.

12. Katherine S. Riley, Karl Jin Ang, Katie A. Martin, Wan Kyn Chan, Jakob A. Faber, and Andres F. Arrieta. Encoding multiple permanent shapes in 3D printed structures. *Materials and Design*, 194:108888, 2020.

13. Teunis Van Manen, Shahram Janbaz, and Amir A. Zadpoor. Programming 2D/3D shape-shifting with hobbyist 3D printers. *Materials Horizons*, 4(6):1064–1069, 2017.

14. S Timoshenko. ANALYSIS OF BI-METAL THERMOSTATS The following investigation contains a general theory of bending of a bi-metal strip submitted to a uniform heating . This theory is applied in analysis of operation of a bi-metal strip thermostat . The equations are obtai. (l):233–255.

15. Byoungkwon An, Ye Tao, Jianzhe Gu, Tingyu Cheng, Xiang Chen, Xiaoxiao Zhang, Wei Zhao, Youngwook Do, Shigeo Takahashi, Hsiang Yun Wu, Teng Zhang, and Lining Yao. Thermorph: Democratizing 4D printing of self-folding materials and interfaces. *Conference on Human Factors in Computing Systems - Proceedings*, 2018-April:1–12, 2018.

16. Ying Liu, Russell Mailen, Yong Zhu, Michael D. Dickey, and Jan Genzer. Simple geometric model to describe self-folding of polymer sheets. *Physical Review E - Statistical, Nonlinear, and Soft Matter Physics*, 89(4):1–8, 2014.

17. Marc Christophersen, Benjamin Shapiro, and Elisabeth Smela. Characterization and modeling of PPy bilayer microactuators. Part 1. Curvature. *Sensors and Actuators, B: Chemical*, 115(2):596–609, 2006.

18. Fuqian Yang and J. C.M. Li. Diffusion-induced beam bending in hydrogen sensors. *Journal of Applied Physics*, 93(11):9304–9309, 2003.

19. Wei Wang, Chenzhe Li, Maenghyo Cho, and Sung Hoon Ahn. Soft Tendril-Inspired Grippers: Shape Morphing of Programmable Polymer-Paper Bilayer Composites. *ACS Applied Materials and Interfaces*, 10(12):10419–10427, 2018.

20. Ultimaker. Technical data sheet - Ultimaker PLA. pages 1–3, 2018.

Design Development of Flexible Aircraft Furniture

Aditya Venkatesh[1], Dr. Fengfeng (Jeff) Xi[1] and Dr. Joon Chung[1]

[1]Ryerson University, Department of Aerospace Engineering, Toronto ON M5B 2K3, Canada
avenkatesh@ryerson.ca
fengxi@ryerson.ca
j3chung@ryerson.ca

Abstract. The purpose of this paper is to express a design development process aimed at multi-functional aircraft cabin furniture to improve passenger comfort. The multi-functional furniture will allow users to modify the existing furniture pieces found within a cabin to their liking, thereby customizing their overall travel experience. The flexible furniture will be developed using Multidisciplinary Design Optimization (MDO) techniques to arrive at a holistic and airworthy solution. Geometry, structures, actuation, ergonomics, aesthetics, and certification are the different elements considered during the design development process. The design development process will include individual systems optimized using continuous and discrete optimization techniques while the whole system will be analyzed using Interval Analysis (IA). This study considers business jets as the environment for the application of the furniture folding concepts. Business jets are designed for flexible uses, which make them an ideal testbed to validate and iterate new cabin interior concepts.

Keywords: Flexible Cabin, Multi-functional Furniture, Open space, Reconfiguration, Design Development

1   Introduction

An aircraft's interior is a traditionally rigid environment. Bouwens et al. reported that passengers find the take-off and arriving at the destination are the most comfortable phases of air travel while the cruise phase is lease comfortable [1]. Research by Hiemstra-van Mastrigt shows that interaction with other passengers or even walking around the aircraft improved the on-board experience of the passengers [2]. The cabin's rigidity inhibits the passengers from taking full advantage of their surrounding space. Vink et al. suggest that passenger experience can be improved with careful attention to aircraft interior design and the passenger flight experience [3]. Currently, any changes within an aircraft's cabin requires it to be grounded before undergoing an expensive and time-consuming retrofitting and recertification process. The purpose of this paper is to introduce the process of designing multi-functional furniture for aircraft cabins, increasing the passenger's ability to interact with their environment and reconfigure it to their purpose and liking.

Space-saving multi-functional furniture provide cabins with the advantage of increased functionality without the space limitations for passenger activities. Stowing tray tables when not in use is an existing application of the space-saving multi-functional concept. There are various organizations that are currently investigating the use of flexible aircraft cabins in different capacitates. Airbus announced their Transpose concept, a modular approach to replace entire sections of the fuselage with different passenger centric design based on the liking of the operator [4]. The ULTRAFLEX concept by Aim Altitude and the Space For All (SFA) concept by Adient Aerospace offer simpler multi-functional space solutions that do not interfere with the exterior structure of the aircraft [5,6]. The interior of the Flying V, developed by Vink et al., includes a 3-seat bench that transforms into a collapsible bed [7].

Stacking, implosion, bundling, and folding are examples of different space-saving techniques, with folding being the most common [8]. This paper considers an optimized furniture folding process developed by Li et al. called foldabilization. Foldabilization is defined as "Given a 3D object O representing a piece of furniture, our goal is to apply a minimum amount of modification to O to allow its parts to be folded flatly onto themselves or each other" [9]. This technique can be translated to the furniture pieces found within an aircraft. This paper presents a process to design flexible furniture based on the furniture folding methodology introduced by Venkatesh et al. [10].

2   Folding Application within Aircraft Cabins

Open-on-Demand and Reconfiguration are applications of folding concepts based on the general furniture methodology introduced by Venkatesh et al. [1]. The Open-on-Demand concept is aimed at stowing the furniture pieces away while they are not in use. This opens a multi-functional space that the passenger can use as desired. Meanwhile, the application of the Reconfiguration concept is to transform any furniture piece into a new form as chosen by the passenger. The transformation of any furniture piece is dictated by its original modular combination, orientation, and layout. The application of the two concepts within a business jet offer a quick, low-cost, and low-effort solution to modify a cabin interior on the fly.

The following section explores the different aspects that need to be considered during the development process of novel furniture designs that are capable of achieving the applications described in this section.

3   Furniture Design development

The design for a multi-functional furniture piece needs to be developed through the lens of various disciplines to result in an airworthy product, as seen Figure 1. This iterative process involves optimizing the individual streams while balancing the trade-offs between the streams to achieve a comprehensive solution.
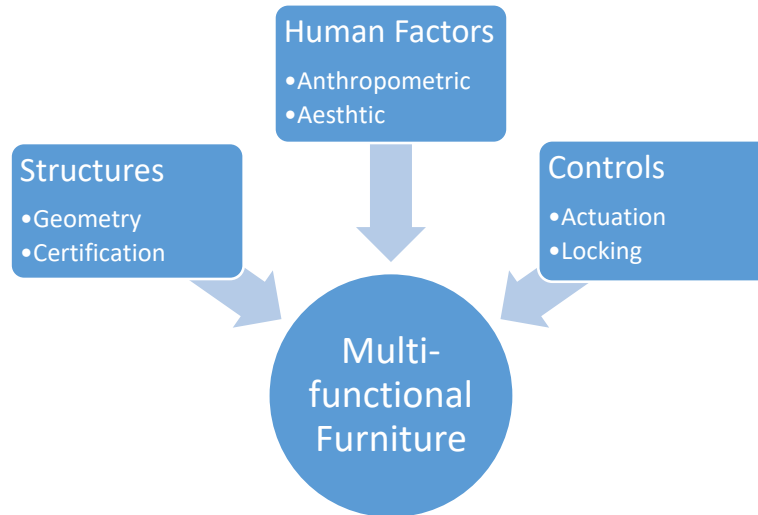
Fig. 1. Design considerations for a multi-functional furniture piece.

3.1 Structures

The geometric transformation of the furniture piece can be quantified using Equation (1)[10],

$$L_1\, W_1\, H_1 = x L_2\, y W_2\, z H_2 \tag{1}$$
$$\text{Form (1)} \qquad \text{Form (2)}$$

where $L,\ W,\ and\ H$ are the respective length, width, and height measurements of a furniture piece. Equation (2) depicts another technique to analyse the transformation of furniture pieces by comparing the change in surface area geometry while maintaining its material volume [10].

$$Surface\ Area(SA) : Volume(V) \tag{2}$$

In the event of folding, the objective is to minimize the occupied volume of the folded furniture piece. This is achieved minimizing the overall dimensions, $L_2\,, W_2, \& H_2$ of the furniture piece in its folded form, Equation (3). Meanwhile, during the expansion process, having a large surface area allows for increased functionality. This means maximizing the extended dimensions, $L_1\,, W_1, \& H_1$ of the furniture piece, Equation (4). A continuous system optimization process can be employed to calculate the ideal value for the dimensions.

$$Folding\,(\,L, W, H)_{min} = L_1\, W_1\, H_1 \tag{3}$$
$$Extending\,(\,L, W, H)_{max} = L_2\, W_2 \tag{4}$$
$$= W_2\, H_2$$
$$= H_2 L_2$$

Based on the choice of initial and final form of the furniture piece, the Folding Module Ratio (FMR), seen in Equation (5), can be used to determine the ideal position of the necessary folding lines [10]. A furniture piece's panel length-width, width-height or

length-height dimensions affect the FMR as they dictate its surface area. The ideal folding line location can be calculated using a continuous system optimization process by maximizing FMR for folding and minimizing FMR for extending, seen in Equation (6) and Equation (7) respectively.

$$Folding\ Module\ Ratio\ (FMR) = \frac{Initial\ Module\ Aspect\ Ratio}{Final\ Module\ Aspect\ Ratio} \tag{5}$$

$$Folding\ (FMR)_{max} = \frac{(Surface\ Area)_{intial}}{(Surface\ Area)_{final}} \tag{6}$$

$$Extending\ (FMR)_{min} = \frac{(Surface\ Area)_{intial}}{(Surface\ Area)_{final}} \tag{7}$$

It is necessary to consider the furniture piece's original geometry and potential transformations, as it will dictate the skeletal frame of the foldable furniture. Structural analysis of the design, conducted using a NASTRAN solver, will indicate the different aspects of the skeleton frame that will need to be redesigned to withstand the operations of the transformation process.

This section will focus on the material selection, module thickness, and joint and lock placement to help develop a furniture design that is not only functional but also secure enough to pass its certification requirements. The new furniture design will have to have minimum weight, minimum deformation, and maximum tensile strength. This is achieved through the right material selection, appropriate volume of the design, and ideal placement of the locks and hinges. These aspects are dictated by the thickness, t, length, L, and width, W, of the panels and location of the locks and hinges.

A discrete system optimization can be employed for the choice of material, while a continuous system optimization process can be used to determine the ideal panel surface area and thickness, and the locks and hinges placement.

$$Material\ Weight_{min} = Material\ Density\ \times\ Material\ Volume \tag{8}$$

$$f\big(weight_{min}, deformation_{min,}\ tesile\ strength_{max}\big) \tag{9}$$
$$\rightarrow choice\ of\ material$$

$$f(L, W, t) \rightarrow volume, locks\ and\ hinges\ placement \tag{10}$$

Certification is the most important aspect in developing an airworthy multi-functional furniture piece. It is imperative that the new design of the furniture can withstand the various operational loads without failing when in use within a cabin. Regulatory agencies have specific requirements for aircraft components, so the multi-functional furniture will be designed to address those requirements based on the purpose and application for it to be considered airworthy [11, 12]. This integral aspect is considered as a constraint to the design development process.

3.2 Controls

The transformation of the furniture piece will need to be driven by an actuation system that is automatic, manual, or a combination of both. The automated version will be electrically powered and can employ gesture control techniques to control the folding operation. The manual version will require a human to actively control and modify the

furniture piece to transform it. This system will also control a push-button that systematically influences the engagement of micro-pin locks that hold the joints in its rigid place.

Aircraft regulations require that any item of mass be secured in place and not be operated during take-off, landing, and in-flight turbulence [13, 14]. So, any furniture modifications will be undertaken during the cruise phase of the flight. The automated actuation is a gesture based non-intrusive process, but will add more complexity to the furniture piece, hence increasing the risk of failure along with increased equipment cost and frequent maintenance. Manual actuation is a simple lower-risk method of implementation, but it is an involved process that requires active physical interaction with the furniture. Ideally, a combination of the two methods would be employed, with the automatic method providing a laid-back control and the manual method acting as redundancy control in the event of the automated system failing.

This aspect involves minimizing the cost of the actuation system. The cost is driven by the type of actuation, automatic or manual, this is expressed in Equations (11)-(13). This choice is in turn driven by the initial and final forms of the furniture piece along with the quantity and placement of the lock. A discrete system optimization process can be employed to calculate the minimum cost of the actuation system.

$$f(Cost)_{min} \rightarrow Operation\ Type \qquad (11)$$

$$Operation\ Type \rightarrow Ease\ of\ operation_{max} \qquad (12)$$

$$f(Ease\ of\ Operation)_{max} \rightarrow Initial\ \&\ Final\ form, \qquad (13)$$
$$quantity\ and\ placement\ of\ locks$$

3.3 Human Factors (HF)

A multi-functional furniture piece needs to cater to the needs of a diverse audience when operated on-board an aircraft. A HF analysis allows the furniture piece to account for the Ergonomic aspect of the new design.

While there are no set average body-dimensions to design for, anthropometrics will significantly impact of design of the furniture piece since it will consider user ranges that fit and reach-the 95th percentile of men and the 5th percentile of women in the given population. This will include an anthropometric fit/reach consideration for each function of the multi-functional furniture piece along with force considerations required for the manual actuation of the transformation [15, 16]. This provides the design with a range of spatial constraints to fit/reach within.

The final design element will consider the overall aesthetics of the furniture piece. A consumer's response to a product has a deep impact on how the product is interpreted, approached, and used [17]. Consumers make subjective judgments based on elegance, functionality and social significance of product [18]. Since a multi-functional furniture piece is a product design for an aircraft cabin, its aesthetic impression is very important for the user's overall perceived comfort within the cabin. The aesthetic parameters will include discrete choices such edge and corner types, color, finish, to name a few. Such The aesthetics qualities can be assessed using the survey technique described by Antal

et al. [19]. The aesthetic parameters and choices will need to be reassessed and updated periodically based on current market trends and regular user feedback.

4 Case Study

Consider an OnD credenza frame transformation, depicted in Figure 2. A manually operated foam-board prototype was designed and modeled based on the credenza transformation. This prototype is displayed in the CS100 mock-up in the Ryerson Aerospace Engineering Centre(RAEC), seen in Figure 3. The foam board prototype depicts the folded form of the credenza being contracted by a factor of 3 in the depth dimension and is 66.7% more compact than in its extended form. The credenza frame in Figure 3 illustrates the difference in occupied space and usability in an extended and stowed form.
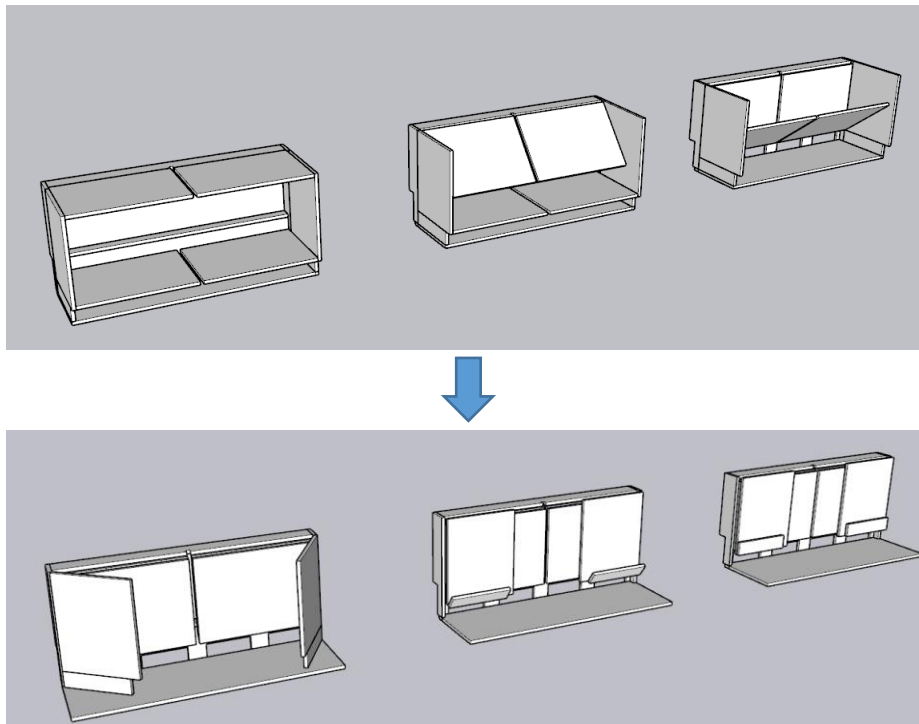
Fig. 2. OnD credenza transformation.

Fig. 3. A partially stowed credenza frame displayed in the RAEC cabin mock-up.

5 Conclusion

This paper introduces a design development process for multi-functional furniture aimed at improving the on-board experience for passengers. The furniture folding methodology applications introduced by Venkatesh et al., is further explored as a solution to maximize the functionality of an aircraft cabin while minimizing the footprint of existing furniture pieces.

The design development process considers various disciplines to arrive at a well-rounded final product. The individual aspects of the development will be optimized using continuous and discrete system optimization techniques while Interval analysis (IA) will be used to study the overall design. By developing such furniture pieces, aircraft passengers can add a personal touch to their otherwise rigid environment, thereby improving their on-board experience.

Future work will entail the realization of the initial theoretical process that is outlined in this paper and a Human Factors (HF) evaluation of the novel furniture design. The proposed flexible furniture pieces and their applications are aimed at aircraft interiors, but they can be retooled and expanded to consider operation in any given environment.

References

1. Bouwens, J. M., Tsay, W. J., & Vink, P.: The high and low comfort peaks in passengers' flight. Work, 58(4), 579-584 (2017). https://doi.org/10.3233/wor-172637

2. Hiemstra-van Mastrigt, S.: Comfortable passenger seats: Recommendations for design and research. Delft University of Technology, Netherlands (2015). https://doi.org/10.4233/uuid:eedd25e6-c625-45e9-9d32-f818aa89c19d

3. Vink, P., Overbeeke, C., & Desmet, P.: Comfort experience. Comfort and Design, 1-12 (2004). https://doi.org/10.1201/9781420038132

4. Aerospace Innovation Project – Transpose, https://acubed.airbus.com/projects/transpose/, last accessed 2021/01/19.

5. Ultraflex. (2019, April 03), https://www.aimaltitude.com/ultraflex, last accessed 2021/01/19.

6. UKi Media & Events, The 2020 crystal cabin awards finalists. (2020, February 24), https://www.aircraftinteriorsinternational.com/features/the-2020-crystal-cabin-awards-finalists.html, last accessed 2021/01/19.

7. Vink, P., Rotte, T., Anjani, S., Percuoco, C., & Vos, R.: Towards a hybrid comfortable passenger cabin interior for the flying V aircraft. International Journal of Aviation, Aeronautics, and Aerospace, 7(1) (2020). https://doi.org/10.15394/ijaaa.2020.1431

8. Mollerup, P.: Collapsible: The genius of space-saving design. San Francisco: Chronicle (2001).

9. Li, H., Hu, R., Alhashim, I., & Zhang, H.: Foldabilizing furniture. ACM Transactions on Graphics, 34(4), 1-12 (2015). https://doi.org/10.1145/2766912

10. Venkatesh, A., Xi, F., & Chung, J.: Folding Methodology for Flexible Aircraft Interiors. *International Journal of Aviation, Aeronautics, and Aerospace, 8*(1) (2021). Retrieved from https://commons.erau.edu/ijaaa/vol8/iss1/

11. Federal Aviation Administration: 14 CFR Part 25 airworthiness standards: Transport category airplanes (1972). https://www.ecfr.gov/cgibin/retrieveECFR?gp=&SID=bafc792f8722c29c2f52e7af95799b9b&mc=true&n=pt14.1.25&r=PART&ty=HTML, last accessed 2021/01/19.

12. Transport Canada: CAR SOR/96-433, Part V: Airworthiness manual chapter 525 - transport category aeroplanes (2012), https://tc.canada.ca/en/corporate-services/acts-regulations/list-regulations/canadian-aviation-regulationssor-96-433/standards/part-v-airworthiness-manual-chapter-525-transportcategory-aeroplanes-11, last accessed 2021/01/19.

13. Federal Aviation Administration: 14 CFR Part 25.789 Retention of items of mass in passenger and crew compartments and galleys (1972), https://www.ecfr.gov/cgi-bin/text-idx?node=14:1.0.1.3.11#se14.1.25_1789, last accessed 2021/01/19.

14. Transport Canada: CAR SOR/96-433, Part VI: Subpart 2: Division IV: 602.86 Carry-on baggage, equipment and cargo (1996), https://loislaws.justice.gc.ca/eng/regulations/SOR-96-433/FullText.html#s-602.86, last accessed 2021/01/19.

15. Deneau, J., Wyk, P. M., Mallender, M., & Duquette, A.: Anthropometry of the Canadian adult population: Developing comprehensive, updated normative-reference standards. International Journal of Industrial Ergonomics, 68, 199-204 (2018). doi:10.1016/j.ergon.2018.08.001

16. Behara, D. N., & Das, B.: Structural anthropometric measurements of the Canadian adult population: The fallacy of the 'average person' concept. Theoretical Issues in Ergonomics Science, 13(3), 380-392 (2012). doi:10.1080/1463922x.2010.505271

17. Crilly, N., Moultrie, J., Clarkson, P.J.: Shaping things: intended consumer response and the other determinants of product form. Des. Stud. 30(3), 224–254 (2009)

18. Mono, R.: Design for Product Understanding Liber. Stockholm, Sweden (1997)

Antal, M. R., Domljan, D., & Horváth, P. G. (2017). Functionality and aesthetics of furniture - numerical expression of subjective value. *Drvna Industrija*, *67*(4), 323–332. https://doi.org/10.5552/drind.2016.1544

The Design of a Twisting Origami Robot Inspired by Resch Triangular Tessellation

Haitong Liang[1,2], Oskar Z. Olszewski[1], Alex Pentek[3] and Guangbo Hao[1,2*]

[1] Tyndall National Institute, Lee Maltings Complex, Dyke Parade, Cork, Ireland, T12R5CP
[2] School of Engineering and Architecture, University College Cork, College Road, Cork, Ireland, T12K8AF
[3] National Sculpture Factory, Albert Road, Cork, Ireland.
G.Hao@ucc.ie

Abstract. Inspired by the twisting behavior of the minimum unit in Resch Triangular Tessellation, a twisting robot based on Origami principles was proposed and characterized. The geometric and kinematic features of this twisting motion were analyzed. With specially designed connecting joints, this twisting Origami robot could be fabricated from a sheet of paper simply by folding. Due to its 3 degrees of freedom (DoF), diverse transforming configurations with different settings of actuating angles were presented based on the 3D model created. Taking this twisting robot as a module, an integrated robot was developed by connecting several modules in series through well-designed origami joints. The twisting behavior and screw-like motion are verified with a preliminary prototype. The potential application scenarios include minimally invasive surgery, space exploration, search and rescue, micro-machining systems, micro-positioning stages, etc.

Keywords: Origami, Twisting Motion, Resch Triangular Tessellation, Robot.

1   Introduction

Origami is the art of folding a sheet of paper into various forms without stretching, cutting, or gluing other pieces of paper to it [1]. It derived its name from the Japanese words 'oru', which means 'to fold', and 'kami', which refers to 'paper' [2]. Originally, origami was developed more for artistic purposes, folding sheets of paper into various shapes, either in abstract forms or mimicking certain objects [3]. Enabling complex 3D structures from a 2D plane simply by folding, Origami has attracted attention from various areas such as architecture [4-6], mathematics [7-9], engineering[10, 11], etc.

In the field of Origami, some terms are widely accepted and used [12, 13]. A *Mountain fold* is where the crease line forms the crest of a mountain, which is represented by an alternate dot-dashed or solid line. A *Valley fold* is where the crease line forms a valley, which is represented by a regular dotted line. A *Crease pattern* is composed of crease

lines when the paper is fully unfolded. There are four basic crease patterns: the *Miura-ori pattern*, the *Waterbomb pattern*, the *Yoshimura pattern*, and the *Diagonal pattern* respectively. These crease patterns all belong to tessellation origami, where both the unfolded and folded states use repeated elements to form a two-dimensional pattern [14, 15].

Transforming between 2D patterns and 3D structures through simple folding and unfolding, Origami shows great application value in the area of robotics. Particularly, because both mountain fold and valley fold can be seen as rotational joints from the aspect of robotics, further highlighting the possibility to combine Origami with robotics. There has been a variety of types of origami-based robots reported in the literature [16-18]. To achieve desired tasks, appropriate actuators are critical for origami-based robots. Various actuating methods have been reported in literature and they include traditional motors, piezoelectric effect, pneumatic pressure, thermal expansion, magnetic force, optically-induced deformation etc. Belke et al. published a robotic platform based on Origami theories and reconfigurable modular robots [17]. Driven by micro stepper motors, different spatial configurations and functions could be achieved through folding motions among robotic modules. McClintock et al. reconstruct the Delta robot with Origami techniques in millimeter-scale [19]. Actuated with three individual piezoelectric bending actuators, this milliDelta Origami robot presented micrometer-level operation precision. Li et al. developed a light-weight, soft robotic gripper, which is composed of an origami structure based on a Waterbomb pattern and a flexible thin membrane [20]. Driven by vacuum, this Origami gripper could lift a large variety of objects, showing great adaptability and robustness. Hao et al. proposed a deployable stent inspired by the non-monotonic characteristics of a Waterbomb pattern [21]. Actuated and controlled by memory alloy wire, this design presented good bi-stability and deployability. Miyashita etc. developed a self-foldable Origami device which could transform from a tiny sheet into a 3D functional structure under the remote control of alternating external magnetic field [18]. Tasks and behaviors, including swimming, delivering blocks, climbing a slope, and digging can be achieved by this miniature device. Advantages shared by these origami-inspired robots include ultra-compact footprint, reduced weight, low cost, good manufacturability, free friction, etc.[22]

In this article, a twisting robot inspired by Resch Triangular Tessellation is proposed by following Origami principles, which was not reported yet. This paper is organized as fellows. Section 2 introduces the geometric theory behind twisting behavior. The primary design and optimization of the twisting Origami robot are presented in section 3. Section 4 provides expanded discussion on diverse transformation modes of this

twisting robot with 3D examples. This is followed by the introduction of an integrated robot proposed by connecting twisting robots as modules in series. A preliminary prototype of this twisting robot is presented for verification of the twisting behavior and the screw-like motion in section 5. Conclusions and prospects are drawn in section 6.

2   The Twisting Behavior of the Unit of Resch Triangular Tessellation

Resch Triangular Tessellation (RTT), presented in Fig. 1, is a typical example of origami tessellation design. It was patented by Ronald Resch, an artist, computer scientist and applied geometrist in the 1960s [23]. The crease pattern of this tessellation is composed of identical minimum units repeating in a certain order, which is illustrated in Fig. 1(a). During the transformation process from a 2D sheet gradually into a 3D structure (from the state in Fig. 1(a) to 1(e)), the triangular block in the center of each minimum unit twisted 30 degrees, as shown separately below each graph. This twisting behavior can be observed on every triangular minimum unit of Resch Triangular Tessellation during the folding process. Each minimum unit is composed of four parts, one central plane and three identical external planes, as illustrated in Fig. 1(a). Since both the unit itself and the central place are all triangular, their tip angles are all 60 degrees. The boundaries of these components are solid lines which all become origami mountain folds. Rotating three external planes about the solid boundary (simultaneously at the same rotational speed during the folding process) causes the central plane to twist.
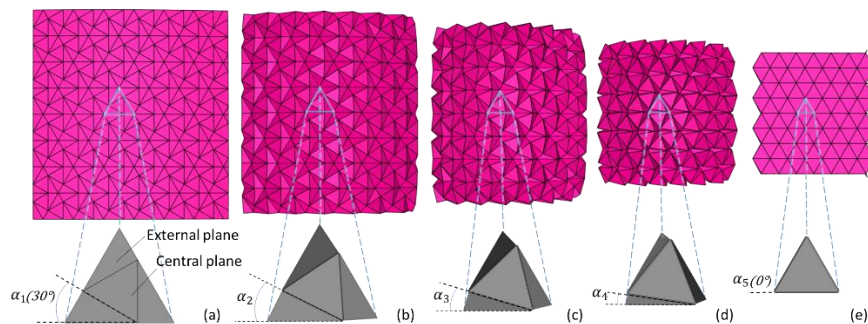
Fig. 1. The folding process of RTT and the twisting behaviour of the minimum unit [24].

To release the geometric theory behind this twisting behavior, a further discussion is carried out which is based on a single minimum unit as shown in Fig. 2. In the

coordinate system created, a minimum unit is in a certain folding condition where external planes rotate with angle θ at an angular speed ω. In x-y plane, the projective regular triangle ABC turns into A′B′C′ when the external planes rotate, while the central triangle plane is fixed in x-y plane. α represents relative angle between the central triangle DEF and the changing projective triangle A′B′C′. α_C indicates the angular displacement of the triangle A′B′C′ relative to the initial position ABC, which is the twisting angle of the minimum unit. Height h represents the increase in the size of this unit in the z-direction. According to geometric knowledge, their relationship can be easily derived and described by the equations below:

$$\alpha = \arctan\left(\frac{2\cos\theta + 1}{\sqrt{3}}\right) - 30° \tag{1}$$

$$h = l \cdot \sin\theta \tag{2}$$

Rotational angle θ can be replaced by ωt, indicating the dynamic folding process. Therefore, the twisting angle of the central plane relative to the reference line, α_C, is:

$$\alpha_c = 60° - \arctan\left(\frac{2\cos\theta + 1}{\sqrt{3}}\right) \tag{3}$$

According to the equations (2) and (3), the twisting motion and the increase of the height in the z-direction are coupled with each other and are determined by the rotation of three external planes. From this aspect, the minimum unit of Resch Triangular Tessellation behaves in a screw-like manner and its equivalent pitch is:

$$P = \frac{360°}{\alpha_{C\max}} \cdot h = 12h \tag{4}$$
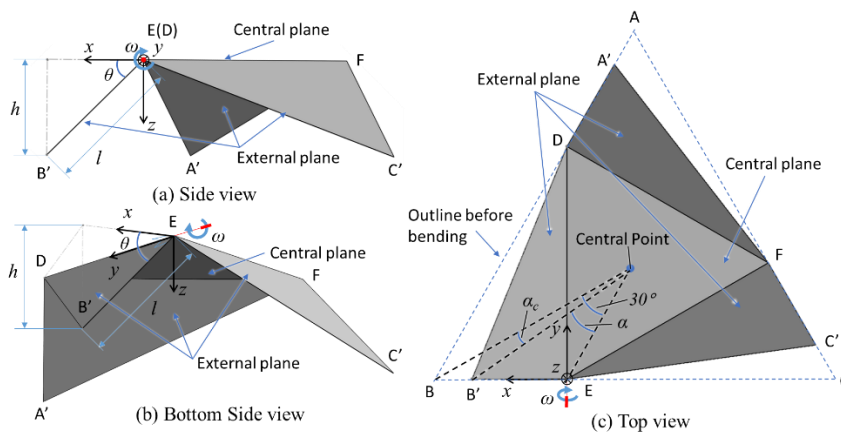
Fig. 2. Geometric parameters of the minimum unit of RTT in different views.

3　Design and Modelling of the Twisting Robot Based on Origami Principles

Inspired by the twisting behaviour of the folding process of RTT, a twisting robot based on the minimum triangular unit of RTT is proposed in this section.

3.1　The Primary Construction of the Twisting Robot

A twisting robot is created primarily by arranging two identical minimum units face to face and connecting their three tip points correspondingly. The expected twisting motion is obtained when these two minimum units fold towards each other during transformation. A 3D model of this twisting Origami robot is created with Solidworks shown in Fig. 3. To investigate the feasibility of the twisting function, spherical joints were adopted in this model to connect the upper and bottom units, as illustrated in Fig. 3(b). The transformation process is presented separately from Fig. 3(a) to 3(d), corresponding to the actuation angle θ of 0°, 30°, 60°, and 90°, respectively. The twisting angle, α_C', changes from 0° to 60° considering two identical unites are contained. It should be pointed out that all three external planes of the bottom unit act simultaneously with the same angular pace. For the convenience of modelling, a larger thickness of all the components was used. For real origami works, the relative thickness is very small.
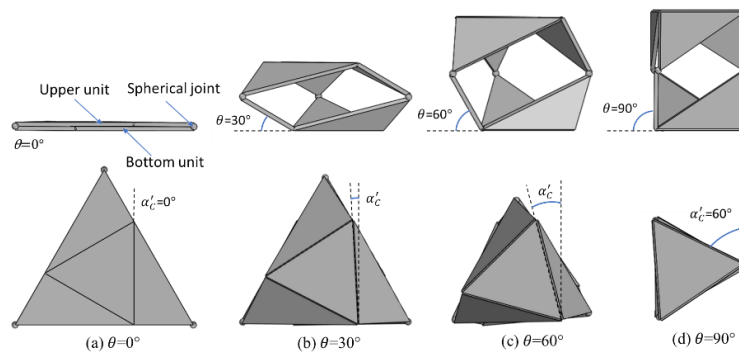
Fig. 3. The primary design of the twisting robot and its transformation process with different actuation angle θ.

The number of total components of this structure (N) is 8. Crease lines are replaced by equivalent rotational joints and the number of rotational joints (i) is 6. The number of

spherical joints (j) is 3. Thus, *DoF* of this twisting robot with three spherical joints can be calculated as below:

$$DoF = 6 \times (N-1) - i \times (6-1) - j \times (6-3) = 3 \qquad (5)$$

Unfortunately, in the field of Origami spherical joints do not exist. While spherical joints enable the desired twisting function, it is not practical for fabrication with origami methodology and alternative joints replacing spherical joints are needed.

3.2 Alternative Connecting Joints Based on Origami Principles

Considering that a spherical joint validates three rotational motions that are perpendicular to each other, a connecting joint can be achieved through connecting three rotational joints in series following origami principles. This is illustrated in Fig. 4. In this way, the function of spherical joints is achieved in a purely-origami way. For each connecting position however, two extra planes have to be introduced and the total number of components is increased. The twisting Origami robot with optimized connecting joints and its transformation process with different actuation angle θ is illustrated in Fig. 5.

Replacing spherical joints with the optimized origami connecting joints, the number of total components (N) is 14. All joints here are rotational and the number (i) is 15. With the equation below, the *DoF* is still 3, while this optimized twisting robot can be fabricated in a pure Origami manner.

$$DoF = 6 \times (N-1) - i \times (6-1) = 3 \qquad (6)$$

As shown in Fig. 5, the effective twisting angle of this Origami robot (α_C') is 60°, due to the two minimum units arranged in a stack. In the meantime, the increase of the height (h_O) also doubles. They can be calculated with the functions below:

$$\alpha_c' = 120° - 2\arctan\left(\frac{2\cos\omega t + 1}{\sqrt{3}}\right) \qquad (7)$$

$$h_o = 2l \cdot \sin\omega t \qquad (8)$$

In terms of the screw behavior in the overall scale, the pitch keeps the same value given in equation (4). It should be noted that the screw behavior here is different from that of general screws. The ratio between the increase of height (h_O) and the twisting angle

(α'_C) is not constant during the twisting process, and it changes along with the actuating angle (θ), which is verified with the ratio between equation (7) and (8).
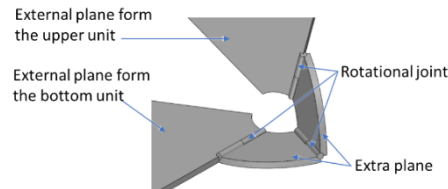
Fig. 4. Optimized connecting joint following Origami principles with three rotational joints and two extra planes.
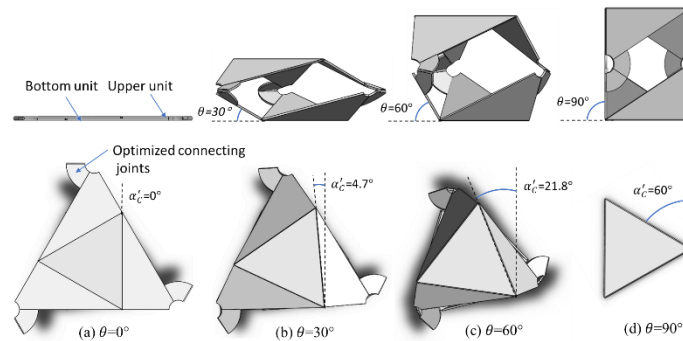
Fig. 5. The twisting Origami robot with optimized connecting joints and its transformation process with different actuation angle θ.
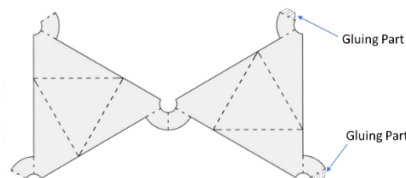
Fig. 6. Outline and crease pattern of the twisting Origami robot.

By completely unfolding the proposed twisting robot, one possible outline and its corresponding crease pattern is obtained to resemble a butterfly shape shown in Fig. 6. The dotted lines represent valley folds. Based on this pattern, we can easily make a twisting robot from only a piece of paper. Gluing operation is still required in certain positions to complete the fabrication as indicated in Fig. 6. This monolithic character highly reduces fabrication time and cost. It is noteworthy that the outline pattern shown in Fig. 6 is one of many possible solutions. It is not necessary to follow this pattern only to fabricate the twisting Origami robot. In addition, various materials in sheet form such

as steel, plastic, carbon fiber plastic composites, etc. provide more choices for different application scenarios.

After fabrication, actuation is required to realize the desired motion. As discussed earlier, 3 actuation angles of external planes of the bottom unit determine the twisting behavior and three corresponding actuators are needed to validate the folding process, which is equivalent to the rotation around the crease lines. Fig. 7 indicates the distribution of actuators and related parameters for actuation. Because of the physical restrictions to avoid interference, the angular range for each actuating angle is [0°, 90°]. Different from the case of traditional mechanisms, driving origami robots should show some of the following principles, e.g. maintaining the compact volume, self-folding, reliability in special conditions, etc. Traditional Motors are applicable, but this will increase the size and volume of the device and special interfaces will have to be designed. Actuating methods based on other principles, such as piezoelectric effect, shape memory alloy, pneumatic press, magnetic forces, etc. have better compatibility to Origami robots, as they enable self-folding in both macro and micro scales for different application conditions. The disadvantages of these approaches lay in limited bearing capability and reduced precision control.
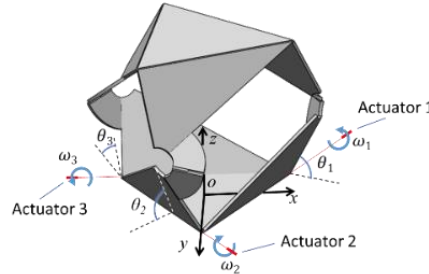
Fig. 7. Distribution positions of actuating motors in the twisting origami robot.

4 Extended Discussion on Possible Forms Based on 3 DoF

As calculated with equation (6), the Origami robot proposed has three DoF. Twisting motion around the z-axis (in the coordinate system in Fig. 7), is achieved with three identical actuation angles changing simultaneously at the same speed. This is just one of the three possible motions but with different sets of actuation angles diverse deformation modes can be achieved.

4.1 Diverse Deformation Modes Based on 3 DoF

Several transformation modes with different combinations of actuating angles are illustrated in the following figures as examples of possible spatial configurations and reachable positions.

| (a) Front view | (b) Left side view |
| (c) Top view | (d) Isometric side view |
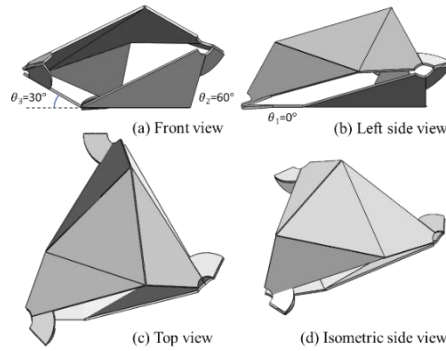
Fig. 8. Transformation mode of the twisting robot with actuating angles $\theta_1=0°$, $\theta_2=30°$, $\theta_3=60°$.

| (a) Front view | (b) Left side view |
| (c) Top view | (d) Isometric side view |
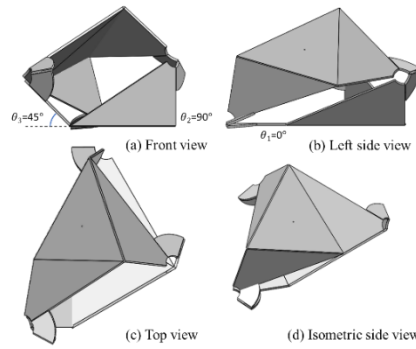
Fig. 9. Transformation mode of the twisting robot with actuating angles $\theta_1=0°$, $\theta_2=45°$, $\theta_3=90°$.

| (a) Front view | (b) Left side view |
| (c) Top view | (d) Isometric side view |
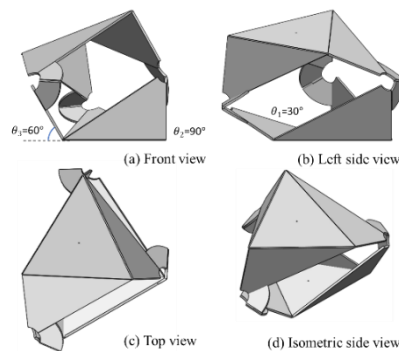
Fig. 10. Transformation mode of the twisting robot with actuating angles $\theta_1=30°$, $\theta_2=60°$, $\theta_3=90°$.
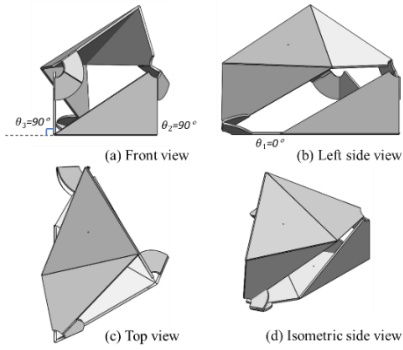
Fig. 11. Transformation mode of the twisting robot with actuating angles $\theta_1=0°$, $\theta_2=90°$, $\theta_3=90°$.
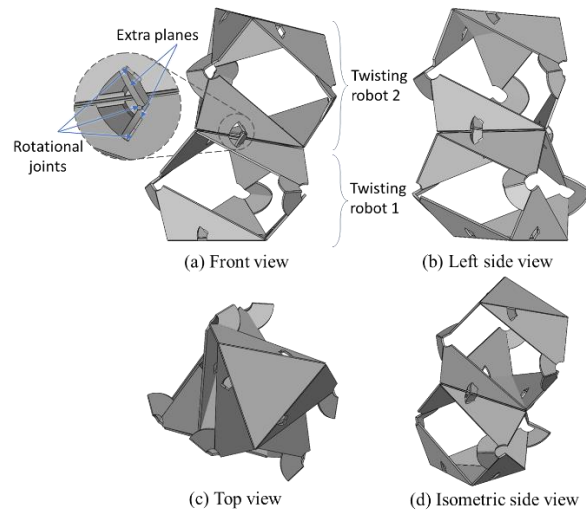
Fig. 12. Integrated Origami robot connecting two twisting robots in series and its transformation mode from different perspectives.
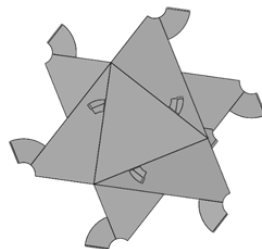
Fig. 13. Top view of the integrated robot in its unfolded mode.

4.2 An integrated Robot Connecting Twisting Robots in Series

In this section, considering a single twisting Origami robot as a single module, an integrated Origami robot is proposed. This is achieved by connecting several modules in series for a larger twisting angle and a wider operating range. The main challenge here is how to actuate the complex device with just a few actuators. This problem can be solved mechanically by using well-designed origami links as indicated in Fig. 12(a). Each Origami link contains two extra planes and three rotational joints, forming a four-bar link together with one external plane from the upper unit of the bottom twisting robot 1 and another external plane from the bottom unit of the upper twisting robot 2. In this way, only three actuators will be enough to control the new integrated robot that still has 3 DoF. One transformation mode of this integrated robot from different perspectives is shown in Fig. 12. Its unfolded mode, where all three actuating angles are zero, is shown from the top view in Fig. 13. In this mode, the robot has a minimum volume.

5 Prototype

A prototype of this twisting Origami robot is fabricated with the assistance of 3D printing and the material used is PLA. Every two adjacent plates are connected with adhesive tapes and then rotational joints (i.e. mountain fold and valley fold) are naturally formed. The prototype and its transformation process with the actuation angle θ of 0°, 30°, 60° and 90° respectively are shown in Fig. 14. In this primary prototype, the transformation is achieved manually and actuators are not considered and utilized. The twisting angle, α'_c, of the top plane of the Origami structure was roughly measured and compared with the theoretical value based on the equation (7), which is presented as a chart in Fig. 15. It is shown that the experimental results reasonably meet the theoretical values. The maximal error is about 4.2° when the actuation angle is 45° and 75° respectively. The average error rate is about 21%. Errors are mainly from measurement inaccuracy while other factors include fabrication, actuation, material defects etc. In addition, the height of the Origami structure increases along with the twisting process as indicated in Fig. 14. The twisting behaviour of the top plate and the overall screw-like motion, which are theoretically analysed in section 2, are experimentally verified.
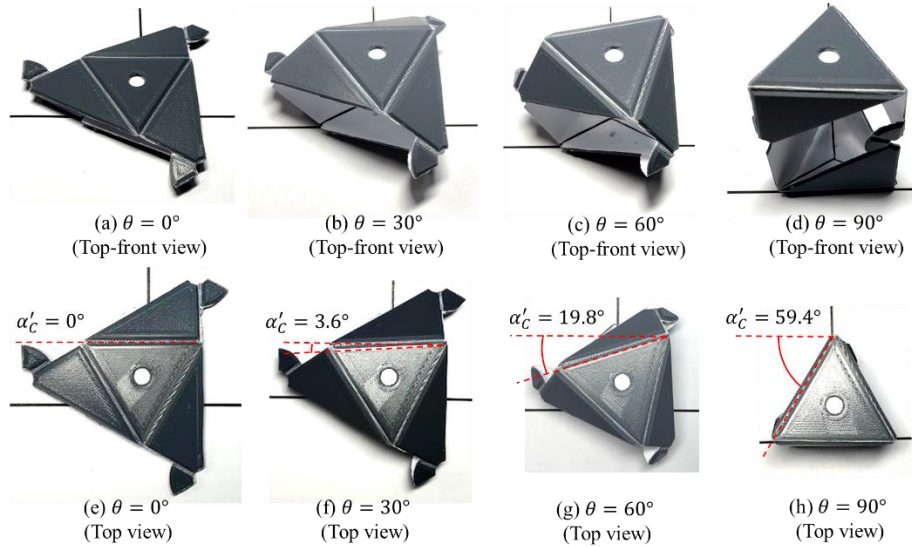
Fig. 14. Prototype of the twisting Origami robot and its transformation process
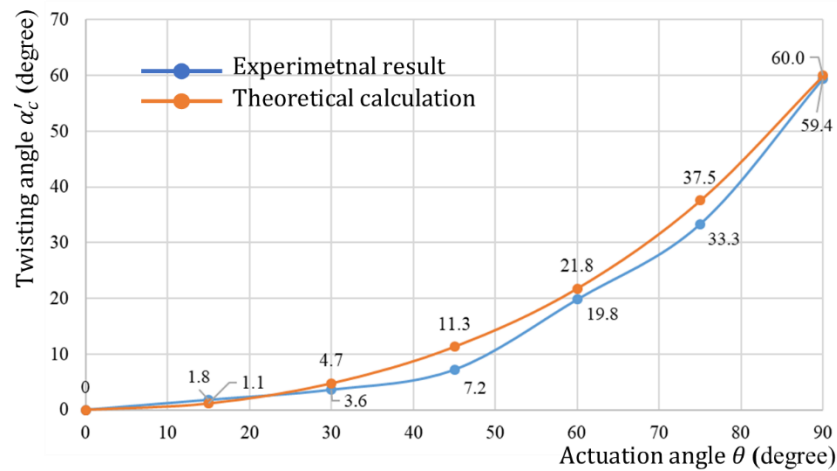
Fig. 15. Actuation angle (θ) – twisting angle (α'_c) curves

6   Conclusions and Prospects

The minimum units of Resch Triangular Tessellation show twisting behaviour during the folding process. Inspired by this twisting behaviour, a twisting robot was proposed by connecting two minimum units in a stack. Specially designed connecting joints,

following Origami principles and techniques, enabled the desired twisting function to be successfully achieved. According to the geometric analysis, equations describing the twisting motion and the increase of the height subject to the actuating angle, were derived. Due to the coupling between these two motions, the twisting robot presented a nonlinear screw-like motion. The actuating method was also discussed. The twisting behaviour and the screw-like motion were experimentally verified with a preliminary prototype.

The twisting Origami robot demonstrated in this paper owns 3 DoF and twisting is just one of three available motions that are determined by three actuating angles. Based on the 3D model created, examples of possible deformation modes corresponding to different settings of actuating angles were presented from multiple perspectives. Taking the twisting robot as a module, an integrated robot connecting twisting robots in series was proposed. By adopting well-designed Origami connecting joints, the number of required actuators still remains to be three. Constructed from twisting origami modules, the integrated robot amplified the twisting angles and reachable range.

Providing controllable twisting motion and diverse deformation modes through simple folding operations together with its ultra-compact original volume, this origami robot shows great application value. Potential application scenarios include surgical manipulators in minimally invasive surgery, operators for space exploration, 3-DoF operation platforms, search and rescue, scenarios where twisting or screw-like motions are needed, etc. Based on its scalable character this twisting origami robot can also be fabricated with the MEMS process and it can be utilized as micromachining systems, micromanipulators, micro-positioning stages, etc. Future research and development will focus on the following aspects: accurate kinematic analysis, motion characterization, modelling of effective workspace, development of an integrated robot with more twisting modules, actuating and prototyping of devices.

References

1.	Tachi, T. *Freeform origami tessellations by generalizing Resch's patterns*. in *ASME 2013 International Design Engineering Technical Conferences and Computers and*

Information in Engineering Conference. 2013. American Society of Mechanical Engineers Digital Collection.

2. Debnath, S. and L. Fei, *Origami theory and its applications: a literature review.* World Academy of Science, Engineering and Technology, 2013: p. 1131-1135.

3. Demaine, E.D. *Folding and unfolding linkages, paper, and polyhedra.* in *Japanese Conference on Discrete and Computational Geometry*. 2000. Springer.

4. Buri, H. and Y. Weinand, *ORIGAMI-folded plate structures, architecture.* 2008.

5. Sorguç, A.G., I. Hagiwara, and S. Selcuk, *Origamics in architecture: a medium of inquiry for design in architecture.* Metu Jfa, 2009. **2**: p. 235-247.

6. Thrall, A. and C. Quaglia, *Accordion shelters: A historical review of origami-like deployable shelters developed by the US military.* Engineering structures, 2014. **59**: p. 686-692.

7. Hull, T., *Project origami: activities for exploring mathematics*. 2012: CRC Press.

8. Hull, T., *On the mathematics of flat origamis.* Congressus numerantium, 1994: p. 215-224.

9. Santangelo, C.D., *Theory and practice of origami in science.* Soft matter, 2020. **16**(1): p. 94-101.

10. Zirbel, S.A., et al., *Accommodating thickness in origami-based deployable arrays.* Journal of Mechanical Design, 2013. **135**(11).

11. Edmondson, B.J., et al. *Oriceps: Origami-inspired forceps.* in *ASME 2013 conference on smart materials, adaptive structures and intelligent systems*. 2013. American Society of Mechanical Engineers Digital Collection.

12. Lang, R.J., *Origami design secrets: mathematical methods for an ancient art*. 2011: AK Peters/CRC Press.

13. Kanade, T., *A theory of origami world.* Artificial intelligence, 1980. **13**(3): p. 279-311.

14. Davis, E., et al., *Reconstructing David Huffman's origami tessellations.* Journal of Mechanical Design, 2013. **135**(11).

15. Chen, Y., J. Yan, and J. Feng, *Geometric and Kinematic Analyses and Novel Characteristics of Origami-Inspired Structures.* Symmetry, 2019. **11**(9): p. 1101.

16. Faber, J.A., A.F. Arrieta, and A.R. Studart, *Bioinspired spring origami.* Science, 2018. **359**(6382): p. 1386-1391.

17. Belke, C.H. and J. Paik, *Mori: a modular origami robot.* IEEE/ASME Transactions on Mechatronics, 2017. **22**(5): p. 2153-2164.

18. Miyashita, S., et al. *An untethered miniature origami robot that self-folds, walks, swims, and degrades.* in *2015 IEEE International Conference on Robotics and Automation (ICRA)*. 2015. IEEE.

19. McClintock, H., et al., *The milliDelta: A high-bandwidth, high-precision, millimeter-scale Delta robot.* Science Robotics, 2018. **3**(14): p. eaar3018.

20. Li, S., et al. *A Vacuum-driven Origami "Magic-ball" Soft Gripper.* in *2019 International Conference on Robotics and Automation (ICRA)*. 2019. IEEE.

21. Hao, G., J. Yu, and H. Li, *A brief review on nonlinear modeling methods and applications of compliant mechanisms.* Frontiers of Mechanical Engineering, 2016. **11**(2): p. 119-128.

22. Peraza-Hernandez, E.A., et al., *Origami-inspired active structures: a synthesis and review.* Smart Materials and Structures, 2014. **23**(9): p. 094001.

23. Resch, R.D., *Self-supporting structural unit having a series of repetitious geometrical modules*. 1968, Google Patents.

24. Ghassaei., A. *Origami Simulator*. 2017; Available from: http://apps.amandaghassaei.com/OrigamiSimulator/.

Vectorised Formulation of Newton-Euler Dynamics for Efficiently Computing 3D Multibody Chains

T. H. Fass[1,2], Guangbo Hao[1,2]

and Pádraig Cantillon-Murphy[1,2]

[1] Tyndall National Institute, University College Cork, Cork, T12 R5CP, Ireland
[2] School of Engineering and Architecture, University College Cork, Cork, Ireland

Abstract. Within the wide field of self-assembly, the self-folding chain has unique potential for reliable and repeatable assembly of 3-dimensional structures as demonstrated by protein biosynthesis. This potential could be translated to self-reconfiguring robots by utilizing magnetic forces between the chain components as a driving force for the folding process. Due to the constraints introduced by the joints between the chain components, simulation of the dynamics of longer chains is computationally intensive and challenging. This paper presents a novel analytical approach to formulate the *Newton-Euler* dynamics of a self-reconfiguring chain in a single vectorised differential equation. The vectorised differential equation allows for a convenient implementation of a parallel processing architecture using *Single Instruction Multiple Data* (SIMD) or *Graphical Processing Unit* (GPU) computation and as a result can improve simulation time of rigid body chains. Properties of existing interpretations of the *Newton-Euler* and *Euler-Lagrange* algorithms are discussed in their efficiency to compute the dynamics of rigid body chains. Finally, GPU and SIMD supported simulation, based on the vectorised *Newton-Euler* equations described in this paper, are compared, showing a significant improvement in computation time using GPU architecture for long chains with a certain chain geometry.

Keywords: Multi-Body System Dynamics, Self-Assembly, Newton-Euler Dynamics, Magnetic Self-Reconfiguration

1   Introduction

Self-assembly, as a branch of robotics, seeks to enable machines and devices to assemble themselves to allow for improved assembly methods or a flexible change of functionality [1]. Self-folding and self-reconfiguring chains belong to a subgroup of self-assembly, where a chain of components folds to specific 3-dimensional shapes [2]. The biological model par excellence for this self-folding is protein biosynthesis.

The protein biosynthesis is a process in every living cell in which a chain of amino acid molecules folds into complex 3D structures called proteins [3]. The process can produce a wide range of shapes, depending on the sequence of amino acids along the chain. Understanding and predicting the principle of self-reconfiguring chains, such as

proteins, could not only lead to engineering of proteins, but the process could be translated to origami or reconfigurable robots [4] across multiple scales, capable of mimicking a wide range of shapes and tools.

One application of interest is to apply self-reconfiguring chains, with magnetism as the driving force, in minimally invasive surgery, exploiting the property of magnetic self-reconfiguring chains to pass through narrow deployment ports. During surgery, a chain of magnetic components could be fed through a catheter [5] to be deployed in an otherwise difficult-to-reach orifice. After deployment, the chain can reconfigure itself due to magnetic interaction between chain components, to be used as a surgical tool or therapeutic device larger than the catheter or port used to deploy it [6]. The magnetic properties of the self-reconfiguring tools might be further used in applications such as magnetic anastomoses creation [7], or magnetic anchoring [8]. A concept for a self-reconfiguring magnetic anchor for minimally invasive surgery is displayed in Figure 1.
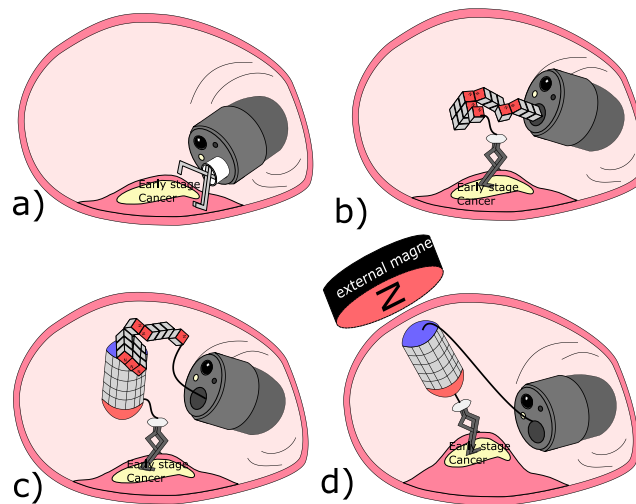
Fig. 1. Concept for a magnetic self-reconfiguring anchor for minimally invasive surgery. Showing the inside of the stomach where the anchor is deployed through an endoscope and anchors cancerous stomach tissue before removal. The target is anchored a), then the chain components are deployed b) and self-reconfigure c) into a magnetic anchor d) to lift target tissue.

Figure 2 shows the concept of a self-reconfiguring magnetic voxel that folds from a chain of magnetic components into a cube. The final folding shape and overall magnetic polarization is similar to the individual building block it is made of and therefore itself could act as a building block for larger and complex structures. However, the longer the chain is, the more possible states of configuration the chain might assume and the more difficult to design a self-reconfiguring process that folds the chain into a desired configuration. Therefore, in order to fold the chain into a specific shape, reliable prediction of the folding process is necessary to enable a repeatable and reliable self-reconfiguration of the desired shape [6].

Many mathematical approaches for the prediction of self-reconfiguring multibody chains and rigid body dynamics exist. The current work presents a novel algorithm that allows for a convenient implementation of *Single Instruction Multiple Data* (SIMD) and *Graphical Processing Unit* (GPU) architecture supported simulation of self-reconfiguring chains and seeks to offer an alternative to existing rigid body dynamics algorithms.
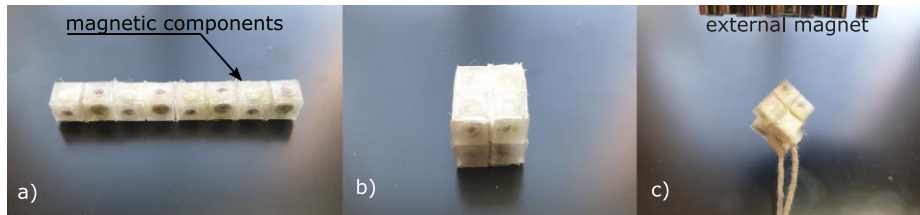
Fig. 2. Concept of a self-reconfiguring magnetic voxel. A chain of magnetic components a) can self-reconfigure into a cube b) that is capable of magnetic interaction c).

The majority of modern *Central Processing Units* (CPU) in computer systems support with the SIMD architecture, a method to compute a limited number of operations at the same time. A GPU, in contrast, is a hardware specialized in parallel computing and allows for the fast computation of compatible algorithms.

The dynamics of a system are commonly characterised by the *Newton-Euler* equation [9] or the *Euler-Lagrange* equation [10].

Silver 1982 [11] attempted a comparison between the *Euler-Lagrange* and the *Newton-Euler* approach and shows that both are comparable in the possible representation of rotation in the system, and both may potentially be used recursively to compute the dynamics of a system.

The system dynamics can be efficiently computed recursively with the *Articulated-Body Algorithm* [12][13] by computing the forces in the links, component by component. Due to the use of GPU, multi core processors and the SIMD model [14] modern computers can process multiple operations simultaneously and significantly increase computational speed. A different class of algorithms is necessary to utilise this potential for parallel computation architectures, such as with the *Divide and Conquer algorithm* [15] that is based on the *Newton-Euler* equations. *Chadaj 2017* [16] presents an implementation of *Divide and Conquer algorithm* for the *Hamilton* equations and uses parallel computation. These algorithms separate the chain in segments that are computed simultaneously. Another possibility is the vectorisation of the algorithm, where the dynamics of the system are represented in a set of vector equations that allow for the computation of dynamics for all components of the system simultaneously. GPUs and the SIMD model are particularly efficient in regard to vector computations [14].

A. Stokes 1996 [17] and *P.C. Müller 1992* [18] describe two vectorised approaches to the *Euler-Lagrange* kinematics. This work seeks to present a vectorised approach based on the *Newton-Euler* Equations.

In the Sections 2.1 and 2.2 we will demonstrate how to acquire the vectorised forward dynamics from the *Newton-Euler* equations for a given set of constraints. Section 2.3 details the implementation in a numerical simulation, as it was done for this work.

Finally, the results of the simulation will be discussed in Section 3 to estimate precision and computation speed of the proposed algorithm.

2 Principals and Methods

This work seeks to analyse the forward dynamics of folding chains. As such, to make use of parallel computation, a vectorised differential equation was devised that would express angular acceleration of all chain components in the form;

$$\dot{\vec{\omega}} = F(\vec{\omega}, \vec{f}, \vec{r}) \tag{1}$$

where $F(\vec{\omega}, \vec{f}, \vec{r})$ is the desired function that describes the angular acceleration of all components as a function of angular velocity $\vec{\omega}$, forces acting on the system $\vec{f}$ and system sate and geometry $\vec{r}$. Expressing the dynamics in such a form allows for a convenient implementation with common vector computation libraries, enabling a convenient use of parallel computation architecture, including SIMD and GPU architectures.

2.1 Newton-Euler Formulation for Folding Chains

This section shows how Equation (1) might be acquired from the *Newton-Euler* equations to express the dynamics of a chain with *n* components. Each component of the chain, with index $i \in [1, .., n]$ is characterised as one rigid body with a mass m_i and $\mathbf{I}_{0\,i}$ is the mass moment of inertia with respect to the center of mass. The components are linked at the points $\bar{\mathbf{p}}_{a\,i}$ by rotational joints, which transmit force between the components but do not transmit torque. A corresponding rotation matrix $\mathbf{Q}_i$ describes the orientation of each component with respect to the world frame. Therefore, the inertia at a specific rotation is given as $\mathbf{I}_i = \mathbf{Q}_i \mathbf{I}_{0\,i} \mathbf{Q}_i^{\mathrm{T}}$.
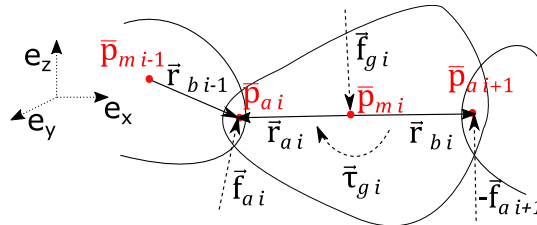
Fig. 3. Free-force diagram of ith chain component.

The geometry of each component is defined by the joint position $\vec{\mathbf{r}}_{a\,i} = \bar{\mathbf{p}}_{a\,i} - \bar{\mathbf{p}}_{m\,i}$ linking to the previous component and $\vec{\mathbf{r}}_{b\,i} = \bar{\mathbf{p}}_{a\,i+1} - \bar{\mathbf{p}}_{m\,i}$ linking to the next component, relative to the components center of mass as seen in Figure 3. The constraints acting on the first component and the last component define the constraints acting on the system. We assume that the first component is connected to the world frame and the last component is free to move, as seen in Figure 4.

Applying the *Newton-Euler* Equations [9] the dynamics of each individual body is described as:

$$m_i \, \vec{\mathbf{a}}_{m\,i} = \vec{\mathbf{f}}_{g\,i} + \vec{\mathbf{f}}_{a\,i} + \vec{\mathbf{f}}_{b\,i} \tag{2}$$

and

$$\mathbf{I}_i \frac{d\vec{\boldsymbol{\omega}}_i}{dt} + \vec{\boldsymbol{\omega}}_i \times (\mathbf{I}_i \vec{\boldsymbol{\omega}}_i) = \vec{\boldsymbol{\tau}}_{g\,i} + \vec{\mathbf{r}}_{a\,i} \times \vec{\mathbf{f}}_{a\,i} + \vec{\mathbf{r}}_{b\,i} \times \vec{\mathbf{f}}_{b\,i} \tag{3}$$

where $\vec{\mathbf{f}}_{a\,i}$ and $\vec{\mathbf{f}}_{b\,i}$ are the forces acting on the joints induced from the neighboring components. Therefore $\vec{\mathbf{f}}_{b\,i} = -\vec{\mathbf{f}}_{a\,i+1}$. $\vec{\boldsymbol{\tau}}_{g\,i}$ is the generalised torque and $\vec{\mathbf{f}}_{g\,i}$ is the generalized force acting on its center of mass, such as gravity or forces resulting from magnetic interaction.
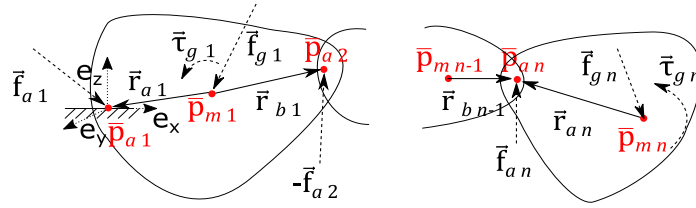
Fig. 4. Free-force diagram of chain start, fixed to world frame (left) and chain end, free (right).

As $|\vec{\mathbf{r}}_{a\,i}|$ and $|\vec{\mathbf{r}}_{b\,i}|$ are constant in time, the second derivative of $\vec{\mathbf{r}}_{a\,i}$ and $\vec{\mathbf{r}}_{b\,i}$ describes the acceleration of the components around their center of mass as [9];

$$\vec{\mathbf{a}}_{a\perp\,i} = \frac{\partial^2 \vec{\mathbf{r}}_{a\,i}}{\partial t^2} = \ddot{\vec{\mathbf{r}}}_{a\,i} = \vec{\boldsymbol{\omega}}_i \times (\vec{\boldsymbol{\omega}}_i \times \vec{\mathbf{r}}_{a\,i}) + \dot{\vec{\boldsymbol{\omega}}}_i \times \vec{\mathbf{r}}_{a\,i} \tag{4}$$

$$\vec{\mathbf{a}}_{b\perp\,i} = \frac{\partial^2 \vec{\mathbf{r}}_{b\,i}}{\partial t^2} = \ddot{\vec{\mathbf{r}}}_{b\,i} = \vec{\boldsymbol{\omega}}_i \times (\vec{\boldsymbol{\omega}}_i \times \vec{\mathbf{r}}_{b\,i}) + \dot{\vec{\boldsymbol{\omega}}}_i \times \vec{\mathbf{r}}_{b\,i} \tag{5}$$

Note that the derivation with respect to time t of any vector $\vec{\mathbf{p}}$ is noted as $\frac{\partial \vec{\mathbf{p}}}{\partial t} = \dot{\vec{\mathbf{p}}}$ and $\frac{\partial^2 \vec{\mathbf{p}}}{\partial t^2} = \ddot{\vec{\mathbf{p}}}$. The cross product in Equation (4) and (5) is expressed by defining the *Skew-Symmetric* matrices [9];

$$[\vec{\mathbf{r}}_{a\,i}]_{\mathrm{X}} = \begin{bmatrix} 0 & -r_{az\,i} & r_{ay\,i} \\ r_{az\,i} & 0 & -r_{ax\,i} \\ -r_{ay\,i} & r_{ax\,i} & 0 \end{bmatrix} \tag{6}$$

$$[\vec{\mathbf{r}}_{b\,i}]_{\mathrm{X}} = \begin{bmatrix} 0 & -r_{bz\,i} & r_{by\,i} \\ r_{bz\,i} & 0 & -r_{bx\,i} \\ -r_{by\,i} & r_{bx\,i} & 0 \end{bmatrix} \tag{7}$$

$$[\vec{\boldsymbol{\omega}}_i]_{\mathrm{X}} = \begin{bmatrix} 0 & -\omega_{z\,i} & \omega_{y\,i} \\ \omega_{z\,i} & 0 & -\omega_{x\,i} \\ -\omega_{y\,i} & \omega_{x\,i} & 0 \end{bmatrix} \tag{8}$$

As seen in Figure 4, the position $\bar{\mathbf{p}}_{m\,i}$ of the ith components center of mass in relation to the previous components center of mass $\bar{\mathbf{p}}_{m\,i-1}$, for all $i \in [2, .., n]$, can be described as:

$$\bar{\mathbf{p}}_{m\,i} = \bar{\mathbf{p}}_{m\,i-1} + \vec{\mathbf{r}}_{b\,i-1} - \vec{\mathbf{r}}_{a\,i} \tag{9}$$

As seen in Figure 4, Equation (9) holds true for the last component $i = n$. For component $i = 1$ however this might be expressed under the chosen constraint conditions as

$$\bar{\mathbf{p}}_{m\,1} = -\vec{\mathbf{r}}_{a\,1} \tag{10}$$

Therefore, the acceleration of the center of mass can be expressed as the second derivative of the position with respect to time for $i \in [2,..,n]$

$$\frac{\partial^2 \bar{\mathbf{p}}_{m\,i}}{\partial t^2} = \vec{\mathbf{a}}_i = \vec{\mathbf{a}}_{i-1} - \frac{\partial^2 \vec{\mathbf{r}}_{a\,i}}{\partial t^2} + \frac{\partial^2 \vec{\mathbf{r}}_{b\,i-1}}{\partial t^2} \tag{11}$$

and for $i = 1$

$$\frac{\partial^2 \bar{\mathbf{p}}_{m\,1}}{\partial t^2} = \vec{\mathbf{a}}_1 = -\frac{\partial^2 \vec{\mathbf{r}}_{a\,1}}{\partial t^2} \tag{12}$$

Inserting (4) and (5) into Equation (11) as well as expressing the cross product with the respective matrices (6), (7) and (8) the difference in acceleration between component i and $i-1$ might be expressed as

$$\vec{\mathbf{a}}_i - \vec{\mathbf{a}}_{i-1} = -[\vec{\boldsymbol{\omega}}_i]_X \cdot ([\vec{\boldsymbol{\omega}}_i]_X \cdot \vec{\mathbf{r}}_{a\,i}) - [\vec{\mathbf{r}}_{a\,i}]_X \cdot \dot{\vec{\boldsymbol{\omega}}}_i \\ + [\vec{\boldsymbol{\omega}}_{i-1}]_X \cdot ([\vec{\boldsymbol{\omega}}_{i-1}]_X \cdot \vec{\mathbf{r}}_{b\,i-1}) + [\vec{\mathbf{r}}_{b\,i-1}]_X \cdot \dot{\vec{\boldsymbol{\omega}}}_{i-1} \tag{13}$$

2.2 Vectorised Formulation for a Chain of n Components

In order to express the whole system in a single equation we define the vectors

$$\vec{\mathbf{a}}_s = [a_{x\,1}, a_{y\,1}, a_{z\,1}, .., a_{x\,n}, a_{y\,n}, a_{z\,n}] \tag{14}$$
$$\vec{\boldsymbol{\omega}}_s = [\omega_{x\,1}, \omega_{y\,1}, \omega_{z\,1}, .., \omega_{x\,n}, \omega_{y\,n}, \omega_{z\,n}] \tag{15}$$
$$\vec{\mathbf{r}}_{as} = [r_{ax\,1}, r_{ay\,1}, r_{az\,1}, .., r_{ax\,n}, r_{ay\,n}, r_{az\,n}] \tag{16}$$
$$\vec{\mathbf{r}}_{bs} = [r_{bx\,1}, r_{by\,1}, r_{bz\,1}, .., r_{bx\,n}, r_{by\,n}, r_{bz\,n}] \tag{17}$$
$$\vec{\mathbf{f}}_{as} = [f_{ax\,1}, f_{ay\,1}, f_{az\,1}, .., f_{ax\,n}, f_{ay\,n}, f_{az\,n}] \tag{18}$$
$$\vec{\boldsymbol{\tau}}_{gs} = [\tau_{x\,1}, \tau_{y\,1}, \tau_{z\,1}, .., \tau_{x\,n}, \tau_{y\,n}, \tau_{z\,n}] \tag{19}$$
$$\vec{\mathbf{f}}_{gs} = [f_{gx\,1}, f_{gy\,1}, f_{gz\,1}, .., f_{gx\,n}, f_{gy\,n}, f_{gz\,n}] \tag{20}$$

Equation (13) might now be expressed as;

$$\mathbf{A}\,\vec{\mathbf{a}}_s = \mathbf{B}\,\mathbf{W}_s\,\mathbf{W}_s\,\vec{\mathbf{r}}_{bs} - \mathbf{W}_s\,\mathbf{W}_s\,\vec{\mathbf{r}}_{as} + (\mathbf{R}_{as} - \mathbf{B}\,\mathbf{R}_{bs})\,\dot{\vec{\boldsymbol{\omega}}}_s \tag{21}$$

With the unity matrix $\boldsymbol{\delta}_d$ of dimension d and the Block matrices;

$$\mathbf{B} = \begin{bmatrix} \mathbf{0} & \mathbf{0} & \mathbf{0} & & \mathbf{0} & \mathbf{0} & \mathbf{0} \\ \boldsymbol{\delta}_3 & \mathbf{0} & \mathbf{0} & \cdots & \mathbf{0} & \mathbf{0} & \mathbf{0} \\ \mathbf{0} & \boldsymbol{\delta}_3 & \mathbf{0} & & \mathbf{0} & \mathbf{0} & \mathbf{0} \\ & \vdots & & \ddots & & \vdots & \\ \mathbf{0} & \mathbf{0} & \mathbf{0} & & \mathbf{0} & \mathbf{0} & \mathbf{0} \\ \mathbf{0} & \mathbf{0} & \mathbf{0} & \cdots & \boldsymbol{\delta}_3 & \mathbf{0} & \mathbf{0} \\ \mathbf{0} & \mathbf{0} & \mathbf{0} & & \mathbf{0} & \boldsymbol{\delta}_3 & \mathbf{0} \end{bmatrix} \tag{22}$$

$$\mathbf{A} = (\boldsymbol{\delta}_{3n} - \mathbf{B}) \tag{23}$$
$$\mathbf{R}_{as} = \mathrm{diag}([[\vec{\mathbf{r}}_{a\,1}]_X, .., [\vec{\mathbf{r}}_{a\,n}]_X]) \tag{24}$$
$$\mathbf{R}_{bs} = \mathrm{diag}([[\vec{\mathbf{r}}_{b\,1}]_X, .., [\vec{\mathbf{r}}_{b\,n}]_X]) \tag{25}$$
$$\mathbf{W}_s = \mathrm{diag}([[\vec{\boldsymbol{\omega}}_1]_X, .., [\vec{\boldsymbol{\omega}}_n]_X]) \tag{26}$$

Note that the **0** entries in block matrix **A** represent zero matrices of dimension 3×3.

Equivalently the *Newton-Euler* equations for the system (2) and (3) can be expressed as vectorised equations describing the complete system as;

$$\mathbf{M}_s\,\vec{\mathbf{a}}_s = \vec{\mathbf{f}}_{gs} + \mathbf{C}\,\vec{\mathbf{f}}_s \tag{27}$$

and

$$\mathbf{I}_s\dot{\vec{\boldsymbol{\omega}}}_s + \mathbf{W}_s\mathbf{I}_s\vec{\boldsymbol{\omega}}_s = \vec{\boldsymbol{\tau}}_{gs} + (\mathbf{R}_{as} - \mathbf{R}_{bs}\mathbf{D})\,\vec{\mathbf{f}}_s \tag{28}$$

where we the block matrices $\mathbf{M} = \mathrm{diag}([m_1\boldsymbol{\delta}_3, .., m_n\boldsymbol{\delta}_3])$, $\mathbf{I}_s = \mathrm{diag}([\mathbf{I}_1, .., \mathbf{I}_n])$, describe the system properties and $\mathbf{C} = (\boldsymbol{\delta}_{3n} - \mathbf{B}^{\mathrm{T}}) = \mathbf{A}^{\mathrm{T}}$ and $\mathbf{D} = \mathbf{B}^{\mathrm{T}}$, describe system constraints.

The Equations (21), (27) and (28) describe the system dynamics and can be combined in a single equation. This might be achieved by substituting the force acting in the joint $\vec{\mathbf{f}}_s$ in Equation (28) with Equation (27) and finally by substituting the acceleration $\vec{\mathbf{a}}_s$ with Equation (21), resulting in the nonlinear differential equation describing the motion of a chain with n components;

$$(\mathbf{I}_s - \mathbf{R}_D\mathbf{E}\mathbf{R}_B)\,\dot{\vec{\boldsymbol{\omega}}}_s \qquad (29)$$
$$= \mathbf{R}_D\big(\mathbf{E}\mathbf{B}\mathbf{W}_s\mathbf{W}_s\vec{\mathbf{r}}_{bs} - \mathbf{E}\mathbf{W}_s\mathbf{W}_s\vec{\mathbf{r}}_{as} - \mathbf{C}^{-1}\vec{\mathbf{f}}_{gs}\big) + \vec{\boldsymbol{\tau}}_{gs} - \mathbf{W}_s\mathbf{I}_s\vec{\boldsymbol{\omega}}_s$$

For a convenient notation, the matrices $\mathbf{E}, \mathbf{R}_D$ and $\mathbf{R}_B$ are defined as $\mathbf{E} = \mathbf{C}^{-1}\mathbf{M}_s\,\mathbf{A}^{-1}$, $\mathbf{R}_D = \mathbf{R}_{as} - \mathbf{R}_{bs}\mathbf{D}$, $\mathbf{R}_B = \mathbf{R}_{as} - \mathbf{B}\,\mathbf{R}_{bs}$ and the inertia are defined as $\mathbf{I}_s = \mathbf{Q}_s\mathbf{I}_{0s}\mathbf{Q}_s^{\mathrm{T}}$, with $\mathbf{Q}_s = \mathrm{diag}([\mathbf{Q}_1, .., \mathbf{Q}_n])$ and $\mathbf{I}_{0s} = \mathrm{diag}([\mathbf{I}_{0\ 1}, .., \mathbf{I}_{0\ n}])$.

2.3 Numerical Solution

The non-linear differential Equation (29) describes the angular acceleration between the components as a function of angular velocity and their orientation. Equation (29) is solvable if the square matrices $\mathbf{A}, \mathbf{C}$ and $(\mathbf{I}_s + \mathbf{R}_D\mathbf{E}\mathbf{R}_B)$ are invertible. For the given constraint conditions $\mathbf{A}$ and $\mathbf{C}$ can be shown to be invertible. The left-hand side of Equation (39) $(\mathbf{I}_s + \mathbf{R}_D\mathbf{E}\mathbf{R}_B)$ is shown in simulation to be invertible for significant cases with $|\vec{\mathbf{r}}_{a\ i}|, |\vec{\mathbf{r}}_{b\ i}| > 0$ and $\vec{\mathbf{r}}_{a\ i} \neq \vec{\mathbf{r}}_{b\ i}$. The initial conditions are defined as $\vec{\mathbf{r}}_{as}(t = 0) = \vec{\mathbf{r}}_{as0}$, $\vec{\boldsymbol{\omega}}_s(t = 0) = \vec{\boldsymbol{\omega}}_{s0}$, $\vec{\mathbf{r}}_{bs}(t = 0) = \vec{\mathbf{r}}_{bs0}$, the constant matrices $\mathbf{E}, \mathbf{B}, \mathbf{D}, \mathbf{I}_s, \mathbf{C}^{-1}$ and time step Δt. The geometry at any given time t then is computed by solving $\vec{\mathbf{r}}_{as}(t) = \mathbf{Q}_s(t)\,\vec{\mathbf{r}}_{as0}$ and $\vec{\mathbf{r}}_{bs}(t) = \mathbf{Q}_s(t)\,\vec{\mathbf{r}}_{bs0}$.

A reduction of dimension is implemented by defining

$$\vec{\mathbf{z}} = [\mathbf{Q}_s, \mathbf{W}_s] \qquad (30)$$
$$\dot{\vec{\mathbf{z}}} = [\mathbf{W}_s\mathbf{Q}_s, [\dot{\vec{\boldsymbol{\omega}}}_s]_{\mathrm{X}}] \qquad (31)$$

where $\dot{\vec{\boldsymbol{\omega}}}_s$ is calculated solving Equation (29) and the system state $\vec{\mathbf{z}}(t)$ to a time t can be acquired by integrating Equation (31);

$$\vec{\mathbf{z}}(t) = \int_{t_0}^{t}\dot{\vec{\mathbf{z}}}\ dt \qquad (32)$$

In this work a fourth degree *Runge-Kutta* integration $\vec{\mathbf{z}}(t + \Delta t) = \mathrm{rk4}(\vec{\mathbf{z}}, \dot{\vec{\mathbf{z}}}, t, \Delta t)$ [19] is used to integrate Equation (32) and simulate the system.

The presented algorithm does not consider interaction between components other than in the joint and therefore collision handling has to be implemented with other algorithm and can be integrated by modeling the general forces $\vec{\mathbf{f}}_{gs}$ and torques $\vec{\boldsymbol{\tau}}_{gs}$ respectively. $\vec{\mathbf{f}}_{gs}$ and $\vec{\boldsymbol{\tau}}_{gs}$ can model constant forces such as gravity, as well as non-constant forces such as friction, magnetic interaction or collision forces. The non-constant forces are easily integrated by updating $\vec{\mathbf{f}}_{gs}$ and $\vec{\boldsymbol{\tau}}_{gs}$ with every time step. The algorithm has been tested by introducing torques resulting from friction as well as introducing magnetic forces between components. However, depending on the complexity to compute the non-constant forces the performance of the presented algorithm would be altered. Therefore, as this work seeks to analyse the computation time and error of the

presented algorithm, only gravity as a constant, conservative force is introduced in the following simulation.

3 Results and discussion

Equation (29) was applied using the numerical methods described in section 2.3 to simulate the dynamics of a chain of components with one end fixed to the world frame and the other end free. All computations were done in *Python* on a 64Bit *Windows* computer system with 2.5 GHz CPU, 16 GB internal memory and a *Nvidia GTX1080* GPU. For a meaningful comparison, the algorithm was applied for a 3D case of a pendulum with a varying number of components. The following system properties have been used for simulation: $m_i = 0.1$, $\mathbf{I}_{0\,i} = 4 \cdot 10^{-6}$, $\mathbf{W}_i(t = 0) = \mathbf{0}$, $\vec{\mathbf{r}}_{ai0} = -\vec{\mathbf{r}}_{bi0} = [0, 0, 0.2m\,]^{\mathrm{T}}$, $\vec{\mathbf{f}}_{gi} = m_i[0, 0, -9.807\text{ m/s}^2]^{\mathrm{T}}$ and $\mathbf{Q}_i(t = 0)$ representing a hanging chain with a deflection of $25°$. A total simulation time of 5 seconds have been chosen. In this time the simulated chain was swinging back and forth a total of 18 times.
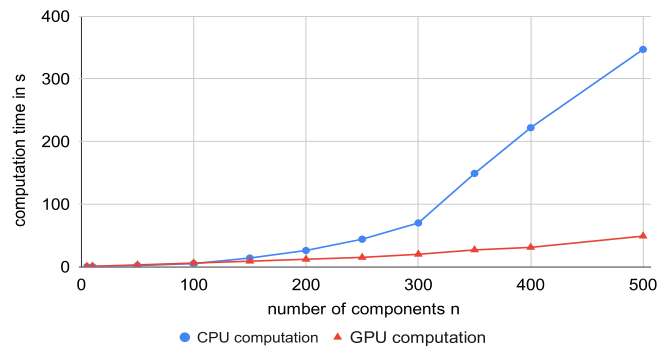
Fig. 5. Comparison of computation time utilizing SIMD architecture (CPU) vs. computation utilizing GPU architecture.

The algorithm was implemented twice, once using SIMD supported computation of vector equations and once using GPU supported computation. Computation with the *Numpy* library supporting SIMD architecture was compared in its average computation time against computation using the *Cupy* library supporting GPU architecture seen in Figure 5. The CPU calculation using the SIMD structure shows a significant rise in computation time for chains with more than 300 components. The presented algorithm uses square matrices with $(3n)^2$ entries. The increase in computation time could be explained by to large matrices for the SIMD structure to work efficiently. The GPU computation is slower for small numbers of components compared to the CPU computation. It is assumed that this is due to the overhead created by the implementation of the GPU architecture. However, for $n \geq 100$ components GPU computation of the chain dynamics clearly shows to take significantly less computation time than SIMD

calculation and displays a near linear relationship between number of chain components and computation time.

To estimate the error of the simulation the internal energy of the system was analysed for a chain length of n=10 components, over a simulated time of 5s, with varying Δt and containing multiple oscillation in which the chains swung back and forth. The results are shown in Figure 6.

All forces in the implemented simulation are conservative forces. As a result, in an ideal case scenario, there is no change in internal energy $U(t) = T(t) + V(t)$ in the system, the sum of kinetic energy $T(t)$ and potential energy $V(t)$. Therefore, any change to the internal energy $\|U(t) - U(t_0)\|$ is seen as the error of the numerical simulation. For ease of interpretation the error displayed in Figure 6 is expressed as;

$$\varepsilon = \frac{mean(\|U(t) - U(t_0)\|)}{U_{total} \cdot \Delta t} \tag{33}$$
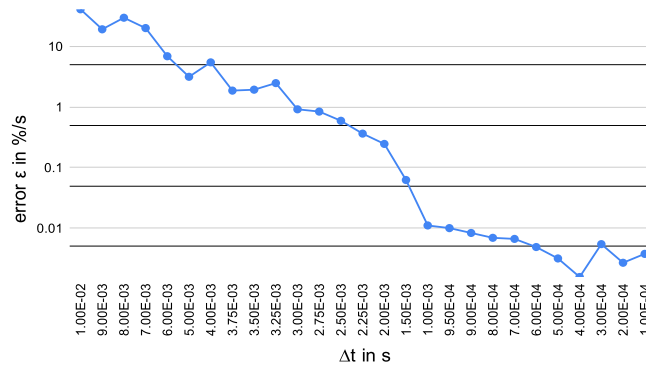
Fig. 6. Computational error per second of vectorised Newton-Euler equations, on the example of a swinging chain, over integration time step Δt.

As such the error ε can be interpreted as the average offset from a zero internal energy, that can accumulate over a second of simulation, in relation to the total energy available in the system U_{total}. For the given system the total available energy can be estimated as the maximum potential energy the system can release $U_{total} = max(\|V(t) - V(t_0)\|)$. Figure 6 shows that the error ε tends towards zero for small time steps Δt. This leads to the assumption that the error in simulation originates from the chosen numerical integration method, as it is the only part of the simulation that depends on Δt and the here presented interpretation of the *Newton-Euler* equation correctly represents the dynamics of a chain of components under the given constraints. Furthermore, it leads to the interpretation that for any system fulfilling the constraints a Δt can be chosen to adequately simulate the dynamics of the system.

The parallel *Newton-Euler* algorithm, however, relies on square matrices with a size of $(3n)^2$ entries. As a result, longer chains might generate matrices which are too large for the memory of the computer to process. This is expected to limit the efficient computation of very long chains depending on the available memory space.

4   Conclusion

The presented vectorised formulation of *Newton-Euler* dynamics offers an alternative to existing mathematical models and allows for a simulation of time varying forces and torques acting on the chain components. It can be applied for certain cases of self-reconfiguring chains to simulate the system dynamics. This work shows the implementation of the presented algorithm for non-linear chain dynamics which enables a convenient use of GPU computation architectures to significantly improve computational speed. As the relation between computation time and chain length is nearly linear, the presented algorithm is well suited to the computation of very long chains.

However, as the computation relies on large matrices the maximum chain length that allows for efficient calculation is expected to be limited by the used hardware. The exponential usage of memory however can be compensated for by intelligent memory management as frequently used for *Big-Data* computations, e.g. [20]. Furthermore, the algorithm needs to be further explored for different constraints of the system. This work seeks to enable the improved computation of chain dynamics in selected cases and a better understanding of one of the most versatile forms of self-assembly: the self-folding chain. The presented algorithm could potentially improve the simulation as well as enable the consequent folding prediction and construction of long self-folding chains of components such as self-reconfiguring chain shaped robots or proteins.

Acknowledgements

References

1. Grifith, S. T., Jacobson, J.: Growing Machines. Ph.D. dissertation. School of Architecture and Planning, Massachusetts Institute of Technology, Cambridge, MA, USA (2004).
2. Felton, S. M., Tolley, M. T., Shin, B., Onal, C. D., Demaine, E. D., Rus, D., Wood, R.J.: Self-folding with shape memory composites. Soft Matter, vol. 9, no. 32, pp. 7688–7694 (2013). doi:10.1039/c3sm51003d
3. Wei, L., Liao, M., Gao, X., Zou, Q.: Enhanced Protein Fold Prediction Method Through a Novel Feature Extraction Technique. IEEE Transactions on NanoBioscience, vol. 14, no. 6, pp. 649–659 (2015). doi:10.1109/TNB.2015.2450233
4. An, B., Rus, D.: Designing and programming self-folding sheets. Robotics and Autonomous Systems, vol. 62, no. 7, pp. 976–1001 (2014). doi:10.1016/j.robot.2013.06.015
5. Zimmermann, K., Naletova, V. A., Zeidis, I., Turkov, V. A., Kolev, E., Lukashevich M. V., Stepanov, G. V.: A deformable magnetizable worm in a magnetic field-A prototype of a mobile crawling robot. Journal of Magnetism and Magnetic Materials, vol. 311, no. 1, pp. 450–453 (2007). doi:10.1016/j.jmmm.2006.11.153

6. Fass, T. H., Hao, G., Cantillon-Murphy, P.: On planar self-folding magnetic chains: Comparison of Newton–Euler dynamics and internal energy optimization. Robotics and Autonomous Systems, vol. 132, Oct 2020, pp. 103601(2020). doi: 10.1016/j.robot.2020.103601

7. McEvoy, R.P., McMenamin, M., Ha, G., Lang, J. H., Cantillon-Murphy, P.: Self-deployed magnetic polygons: Design, construction, and application. IEEE Transactions on Magnetics, vol. 62, no. 7, pp. 976–1001 (2012). doi:10.1109/TMAG.2012.2205935

8. Tugwell, J., Brennan, P., O'Shea, C., O'Donoghue, K., Power, T., O'Shea, M., Griffiths, J., Cahill R., Cantillon-Murphy, P.: Electropermanent magnetic anchoring for surgery and endoscopy. IEEE Transactions on Biomedical Engineering, vol. 62, no. 3, pp. 842–848 (2015). doi:10.1109/TBME.2014.2366032

9. Aardema, M. D.: Newton-Euler Dynamics. 1st edn. Springer, Boston, MA (2005). doi:10.1007/b101082

10. Gregory, R. D.: Classical Mechanics. 1st edn. Cambridge University Press, Cambridge, United Kingdom (2006). isbn: 9780521826785

11. Silver, W.: On the Equivalence of Lagrangian and Newton-Euler Dynamics for Manipulators. The International Journal of Robotics Research, vol. 1, no. 2, pp. 60–70 (1982). doi:10.1177/027836498200100204

12. Featherstone, R.: Robot dynamics algorithms. Automatica, vol. 25, no. 5, pp. 785–786 (1989). doi:10.1016/0005-1098(89)90037-X

13. Mirtich, B. V.: Impulse-based Dynamic Simulation of Rigid Body Systems. Ph.D. dissertation. Dep. of Computer Science, University of California, Berkeley, CA, USA (1996).

14. Naishlos, D., Biberstein, M., Ben-David, S., Zaks, A.: Vectorizing for a SIMdD DSP architecture. In: Moreno, J., Muthy, P. (eds.) CASES 2003: International Conference on Compilers, Architecture, and Synthesis for Embedded Systems, pp. 2–11, CA, USA (2003). doi: 10.1145/951710.951714

15. Featherstone, R.: Divide-and-conquer articulated-body algorithm for parallel O(log(n)) calculation of rigid-body dynamics. Part 1: Basic algorithm. International Journal of Robotics Research, vol. 18, no. 9, pp. 867–875 (1999). doi:10.1177/02783649922066619

16. Chadaj, K., Malczyk, P., Fraczek, J.: A parallel recursive hamiltonian algorithm for forward dynamics of serial kinematic chains. IEEE Transactions on Robotics, vol. 33, no. 3, pp. 647–660 (2017). doi:10.1109/TRO.2017.2654507

17. Stokes, A., Brockett, R.: Dynamics of kinematic chains. International Journal of Robotics Research, vol. 15, no. 4, pp. 393–405 (1996). doi:10.1177/027836499601500406

18. Müller, P.: Robot dynamics and control. Automatica, vol. 28, no. 3, pp. 655–656 (1992). doi:10.1016/0005-1098(92)90197-N

19. Hairer, E., Norsett, S. P., Wanner, G.: Solving ordinary differential equations I. nonstiff problems. Mathematics and Computers in Simulation, vol. 29, no. 5, pp. 447 (1987). doi:10.1016/0378-4754(87)90083-8

20. Wang, Y., Goldstone, R., Weikuan, Y., Wang, T.: Characterization and Optimization of Memory-Resident MapReduce on HPC Systems. In: IEEE 28th International Parallel and Distributed Processing Symposium, vol. 28, pp. 799-808, Phoenix, AZ, USA (2014). doi: 10.1109/IPDPS.2014.87

Tendon-Actuated Miura-ori Bellows

Steven W. Grey, Fabrizio Scarpa, and Mark Schenk

Bristol Composites Institute, University of Bristol, Bristol BS8 1TR ,UK
m.schenk@bristol.ac.uk

Abstract. A tendon-actuated origami bellows is proposed as a reconfigurable robotic manipulator, which has the potential to be compactly stowed. A cylindrical Miura-ori fold pattern is selected which combines a high axial stiffness with low bending stiffness, to minimise coupling between the degrees of freedom of the end-effector. The structural properties of the origami bellows and the tendon actuation are modelled using finite element software. A prototype is constructed and tested to demonstrate the potential of tendon-actuated origami structures.

Keywords: engineering origami, origami bellows, tendon actuation

1   Introduction

Origami has been proposed for a range of deployable and reconfigurable structures and mechanisms, including compliant and soft robotics [4, 5, 9, 11]. In this work we investigate the properties of a robotic manipulator based on an origami bellows; using tendons or wires running along the length of the origami cylinder, the position and orientation of the end-effector can be controlled [7, 8]. The wires might connect discrete points on the folded structure [6] or run continuously through multiple attachment points on the structure to actuators placed at the base. The proposed concept is illustrated in Figure 1, which shows the combined retraction and tip rotation of an origami bellows as a result of actuating a single wire. Placing multiple wires around the circumference of the origami bellows would also enable axial compression of the manipulator for stowage.

At the core of the proposed manipulator is an origami bellows, which consists of a flat sheet folded into a closed cylindrical configuration. The tendon actuation relies on the interplay between the stiffness of the bellows and the displacements and forces imposed by the actuated wires. The structural properties of the bellows are determined by its material properties as well as the geometry of its fold pattern. Previous modelling of origami bellows has either focused on establishing its geometry [1, 12, 13] or used simplified models for its structural response [2, 3, 10]. In this work, the modelling of the origami bellows and its actuation using tendons is performed using commercial finite element analysis software.

The paper is laid out as follows. Section 2 outlines the geometric design space of a robotic manipulator based on the Miura-ori bellows. Section 3 describes the

structural modelling of the bellows using finite element analysis to identify designs that provide a high axial stiffness and low bending stiffness, which enables more effective control of the end-effector by reducing the coupling between tip rotation and axial translation. In Section 4 the actuation scheme is selected for the prototype structure described in Section 5.
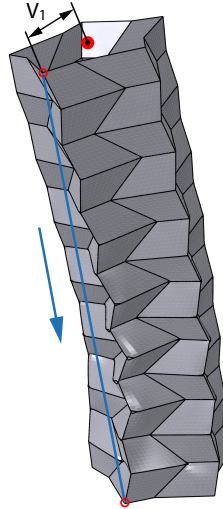
Fig. 1: A Miura-ori origami bellows is actuated by contracting a wire attached to the top and passing through a point at the base. Placing multiple actuated tendons or wires around the circumference enables control of orientation and position of an end-effector placed at the tip of the bellows.

2   Fold Pattern for Miura-ori Bellows

Origami bellows are formed by folding a flat sheet into a cylindrical configuration before joining the longitudinal edges. The geometric design space of origami bellows was outlined by Reid et al. [12]. It was shown that origami bellows can be designed with multiple geometrically compatible configurations; in absence of elastic strain energy at the folds, the cylinders would be undeformed (and thus unstressed) in those configurations. In this work we focus on a subset of origami bellows, namely Miura-ori patterns that have both a partially deployed and fully stowed compatible configuration [13]. For the cylinder to deform axially from one of the two compatible configurations, facet deformations (*i.e.* stretching, bending and twisting of the material between the folds) are required. These facet deformations, in combination with the stiffness of the folds, give rise to the structural response of the origami bellows.
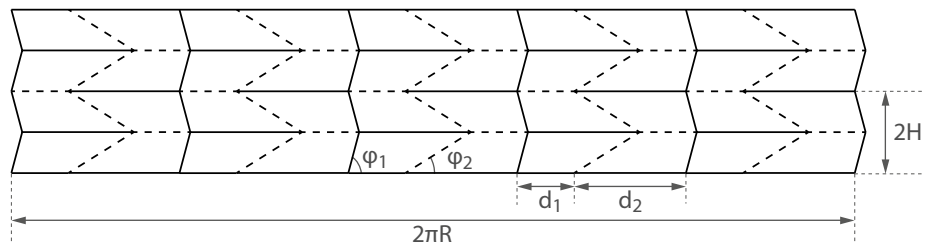
(a)
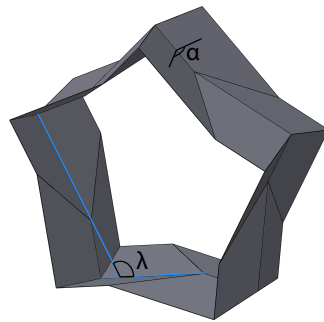
(b)

Fig. 2: Geometry of a Miura-ori bellows: (a) crease pattern with $n = 5$ circumferential unit cells and $m = 2$ layers; the unit cell is defined by sector angles φ_1 and φ_2 and non-dimensional parameter H/R; (b) assembled compatible configuration with dihedral angle α and unit cell enclosed angle λ.

The Miura-ori bellows pattern is defined in Figure 2a. The pattern consists of n repeating unit cells along the circumference, and m layers along the length of the cylinder. The pattern of a Miura-ori unit cell is described by sector angles φ_1 and φ_2 (with $\varphi_1 > \varphi_2$), and length:

$$d_1 + d_2 = \frac{2\pi R}{n}. \tag{1}$$

In a partly-folded configuration, the angle λ enclosed by a unit cell is given as:

$$\lambda = \pi - 2\arctan\left(\cos\frac{\alpha}{2}\tan\varphi_1\right) + 2\arctan\left(\cos\frac{\alpha}{2}\tan\varphi_2\right) \tag{2}$$

where $\alpha \in [0, \pi]$ is the dihedral angle between facets along the circumferential folds; see Figure 2b. In a compatible configuration the following must hold:

$$\lambda = \frac{n-2}{n}\pi \tag{3}$$

to form a closed cross-section. Imposing a flat-folded ($\alpha = 0$) compatible configuration provides a relationship between sector angles:

$$\varphi_1 - \varphi_2 = \frac{\pi}{n} \tag{4}$$

which allows the geometry to be defined in terms of φ_1. Combining these expressions provides a quadratic equation [13] in terms of $\cos(\alpha/2)$ which can be used to find the extended state for the compatible closed bellows:

$$\left(\tan^2\varphi_1 - \tan\varphi_1\tan\frac{\pi}{n}\right)\cos^2\frac{\alpha}{2} - \left(1 + \tan^2\varphi_1\right)\cos\frac{\alpha}{2} + \tan\varphi_1\tan\frac{\pi}{n} = 0 \tag{5}$$

Lastly, we ensure that all quadrilateral facets are identical:

$$\frac{d_1}{R} = \frac{\pi}{n} - \frac{H}{2R}\frac{(\tan\varphi_1 - \tan\varphi_2)}{\tan\varphi_1\tan\varphi_2}. \tag{6}$$

These expressions describe Miura-ori bellows with a compatible flat-folded configuration for compact stowage; additionally, the quadratic equation can yield a partly-folded solution ($\alpha \neq 0$) for a deployed origami bellows. It is assumed that the origami bellows are assembled in the extended compatible configuration; as a result of elastic strain energy stored in the folds, the stowed configuration is therefore not expected to be stable. Instead, the folded bellows prototypes are considered reconfigurable, where the geometric compatibility of the stowed configuration helps reduce the force required for stowage.

In order to construct a prototype of the origami bellows, the total height of the fold pattern ($2mH$) is limited to 300 mm for manufacturing reasons and a limit of $d_2/d_1 > 5$ rejects patterns with short folds which would be impractical to fold accurately. Further, for the origami bellows to be suitable for a robotic manipulator, the assembled height of the bellows is set to be at least double its assembled diameter. This leaves the following parameters to define suitable patterns: n unit cells, m layers (which define unit cell height H from the limit on size of flattened pattern), angle φ_1 and dimension R. Selected patterns for analysis are shown in Table 1; values of m, n and R were selected for ease of manufacture and φ_1 to provide representative range of responses.

3   Structural Analysis of Origami Bellows

The structural properties of the bellows directly affect its performance as a robotic manipulator: contracting a wire connected to the top of the cylinder will not only result in a rotation of the end-effector but also an axial compression of the cylinder. Therefore, a bellows pattern with a high axial stiffness and a low bending stiffness was sought to reduce the coupling between these deformation modes. It is recognised that an increased axial stiffness will impact the ability of the bellows to be stowed readily.

The axial and bending stiffness of the bellows are analysed using the commercial finite element analysis software Abaqus. The facets are meshed using shell elements (S4R) and the folds are modelled using connector elements (CONN3D2) with a linear-elastic fold stiffness. The material is a PET sheet with Young's modulus $E = 3.2$ GPa, Poisson's ratio $\nu = 0.43$, and thickness $t = 200$ μm. The torsional stiffness for the folds was set at $k_f = 0.05$ N/rad based on experimental measurements. The origami bellows is assumed to be unstressed in the extended compatible configuration. The boundary conditions are selected to reflect attachment of the bellows to a rigid base and end-effector. The nodes on the base of the bellows are constrained such that they have no displacement but are free to rotate. On the other end of the structure the nodes are constrained to remain planar and maintain a constant cross-section whilst allowing fold rotation relative to the end-effector. This is achieved using a combination of multi-point constraints that link the element nodes to a control point.

The bellows' axial stiffness is calculated from a compressive axial displacement of the control point. The force-displacement response is nonlinear and the axial stiffness is taken to be the tangent at the undeformed configuration. The bending stiffness is found by applying a rotation to the control point, whilst leaving the remaining degrees of freedom unconstrained. The axial and bending stiffness of the bellows strongly depends on the chosen boundary conditions, and the importance of edge effects is illustrated by the non-uniform deformations along the length of the bellows; see Figure 3.

Table 1: Miura-ori bellows designs selected for comparison in Figure 4.

Pattern No.	m [-]	n [-]	$\varphi_1[^\circ]$	R [mm]
Bending 1	7	7	65	55
Bending 2	7	5	80	45
Bending 3	5	6	75	65
Bending 4	7	7	80	65
Compression 1	6	6	70	65
Compression 2	7	5	80	45
Compression 3	6	7	80	65
Compression 4	5	5	80	65

(a)   (b)
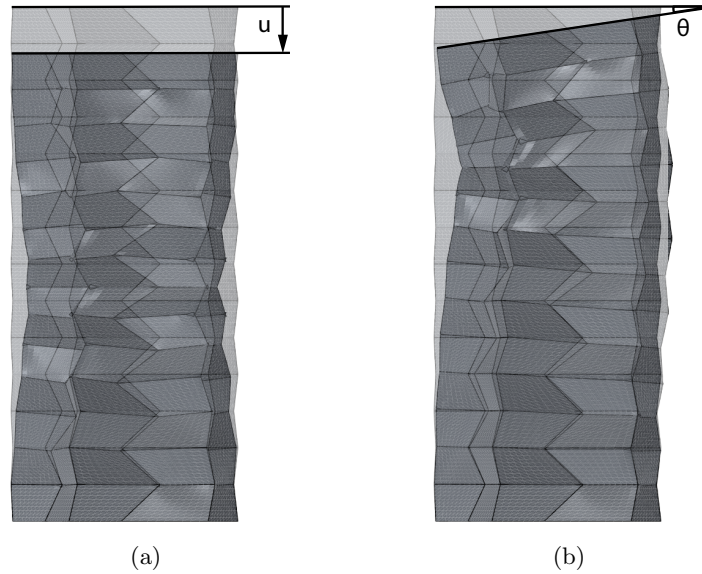
Fig. 3: Finite element simulations of a Miura-ori bellows under (a) axial compression and (b) tip rotation. Both ends are attached to rigid end plates which constrain the cross-sectional geometry; the effect of the boundary conditions is seen in the non-uniform deformations along the length of the bellows.

The investigated patterns in the feasible design space displayed significant differences in structural response, with up to an order of magnitude difference in stiffness between the most and least compliant designs. A representative selection of these responses is shown in Figure 4. Not only the axial stiffness, but also the magnitude of the peak force varies significantly with the fold pattern. Similar results are found for the bending stiffness. Attempts to link the axial stiffness to simple metrics of geometric incompatibility [13] were inconclusive, potentially due to the effect of the boundary conditions.

The ratio of the axial stiffness over the bending stiffness provides a metric for evaluating different Miura-ori bellows fold patterns for use as a tendon-actuated robotic manipulator. Further, dividing the stiffness ratio by the offset of the actuating wire from the centre of the bellows (V_1 in Figure 1) gives an estimate for the expected tip rotation for a given axial compression:

$$\text{stiffness ratio} = \frac{k_{\text{axial}} V_1}{k_{\text{bend}}} \tag{7}$$

where k_{axial} and k_{bend} are the axial and bending stiffness of the bellows. The pattern that displayed the largest stiffness ratio was selected for further analysis and prototyping (geometric parameters: $m = 7$, $n = 5$, $\varphi_1 = 80°$, and $R = 45$ mm).
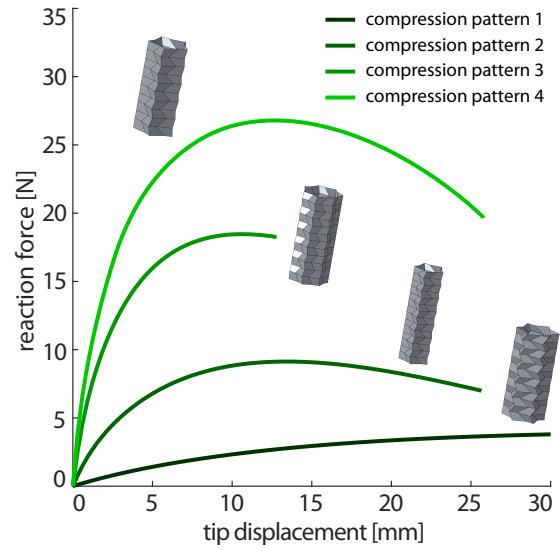
(a)
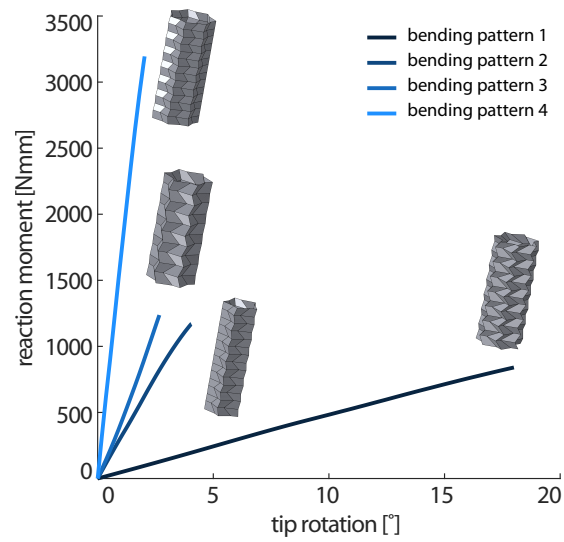
(b)

Fig. 4: The (a) force-displacement and (b) moment-angle responses of a representative subset of the design space. The geometric properties of the patterns selected are presented in Table 1. Inset are images of the undeformed Miura-ori bellows patterns selected.

4   Actuation Design

The Miura-ori bellows robotic manipulator is actuated by contracting wires connected to the top of the structure, as illustrated in Figure 5. These wires could pass through any combination of vertices along the length of the bellows, to provide more localised control over the deformed shape. To reduce the design space this is here limited to either: (i) a wire running straight from the top to the base without interacting with any vertices on its path; or (ii) a wire passing through every vertex on the way to the base. Next, the location where the wire feeds through at the base can be varied via an offset at radius $N \cdot V_1$ from the centre of the cylinder, where $N = 1$ means that it passes through bottom vertex.
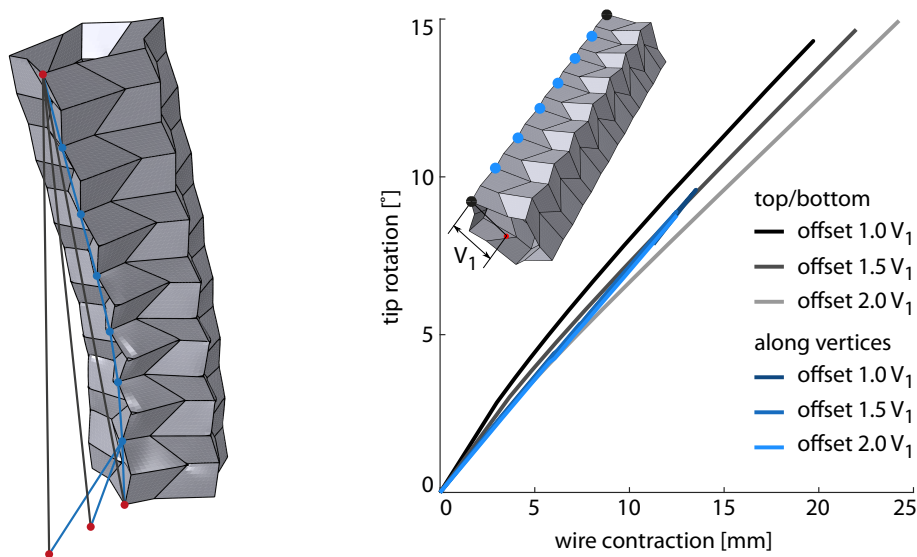
Fig. 5: End-effector rotation for different actuation schemes. Inset highlights where the wires interact with the bellows for each configuration and defines the distance V_1 from the centre of the bellows to the actuated node.

Physically, actuation is achieved by controlling the length of the actuating wire and the tension in the wire (which is assumed constant throughout) results in a force at the vertices it passes through to control the shape of the bellows. The actuation is modelled in Abaqus by applying a follower force to vertices connected by the wire. This is achieved using a user amplitude function (UAMP) in combination with 'sensors' that report the positions of each of the connected vertices throughout the deformation. This is different from the physical implementation, as the loading is force controlled rather than displacement controlled. Consequently, the analysis method cannot pass any potential force limit points, such as those seen in Figure 4.

Figure 5 shows the tip rotation of the origami cylinder as a function of the wire contraction. For wires running through multiple vertices along the length of the bellows, the offset at the base has minimal impact. The offset only significantly changes the direction of the load applied at the bottom vertex, which is itself constrained due to its proximity to the fixed boundary conditions at the base. In contrast, when the wire is attached only to the top of the bellows this offset has a much more pronounced effect. Interestingly, offsetting the base of the wire away from the bellows makes the wire a less effective actuator. The tip rotation due to cantilever deflection is less pronounced than due to the moment produced by the component of the wire tension along the length of the bellows. For the prototype, an actuation scheme with wires running from the tip directly to the base of the bellows was therefore selected.

5   Prototype Origami Bellows

A prototype of the actuated origami bellows was designed and constructed following the fold pattern and actuation scheme outlined in this work. The Miura-ori bellows is folded from $200\,\mu$m thick PET film with perforated fold lines (the fold stiffness was lower than that used in FE simulations to ensure precise folding). The Nylon wires which actuate the bellows are attached to stepper motors situated in the base of the robotic manipulator, and which are controlled using an Arduino micro-controller. The length of wire between the top and bottom of the bellows is contracted at 7.5 mm/s. The tip rotation and axial contraction of the bellows was measured from video recordings of the actuated structure; see Figure 6a. In both experiments and FE analyses, the deformation is localised in limited number of layers; however, in the experiments this is towards the centre of the bellows, whereas in the numerical analyses it is near the base. Figure 6b shows a good match between experimental and numerical results for tip rotation *vs* wire contraction. Although the FE analysis did not converge for the non-linear static analysis beyond an actuation of 20 mm, the modelling nonetheless enabled the preliminary design of a Miura-ori bellows based robotic manipulator.

6   Discussion

Using an origami bellows provides the opportunity to design a compliant robotic manipulator which is reconfigurable, enabling stowage and deployment, and combines both the structure and mechanism into a single system. Finite element modelling of the bellows enabled exploration of the mechanical properties of the structure as a function of its geometric parameters. Due to the actuation method of contracting a wire running up one side of the structure, the selected pattern maximises the ratio between the axial and bending stiffness. After constructing a prototype Miura-ori bellows robotic manipulator from a PET sheet, this was tested by tracking the tip rotation for a given actuation input. Comparison with the FE model shows a good correlation, giving confidence in the modelling techniques used in the development of the design.
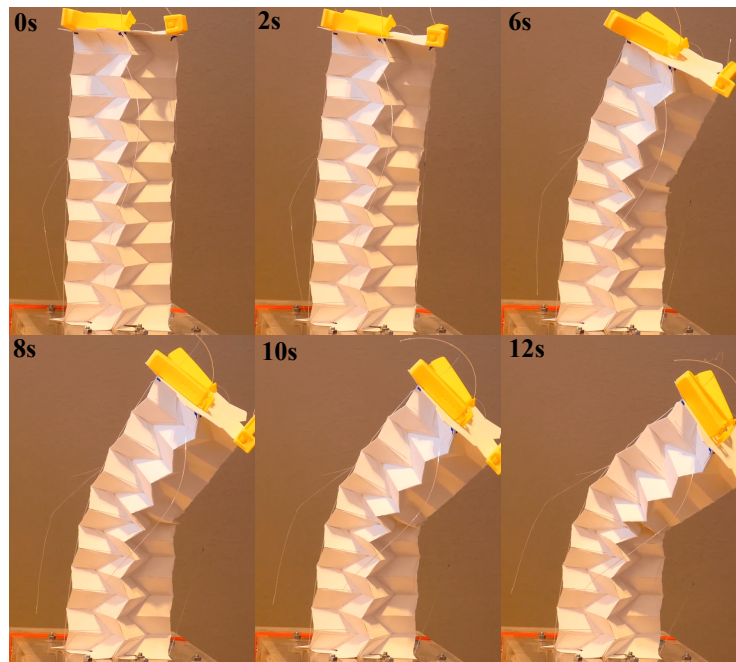
(a)
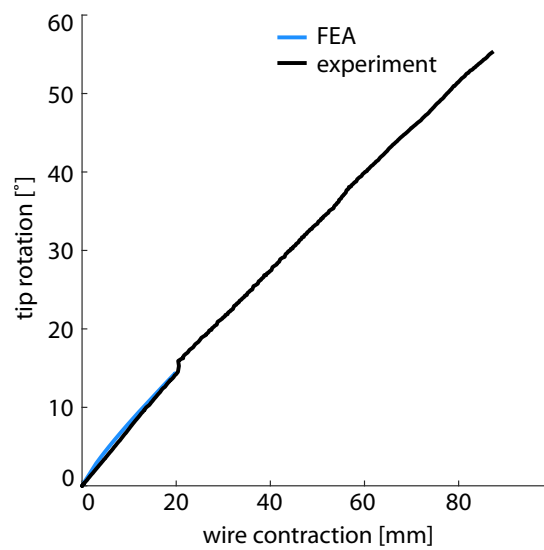
(b)

Fig. 6: Actuation of prototype Miura-ori bellows; (a) snap-shots of deformed configuration as wire is actuated; (b) comparison numerical and experimental results. The discontinuity in the experimental results at approximately 20 mm contraction corresponds to a slippage in an unactuated wire.

Bibliography

[1] S. D. Guest and S. Pellegrino. The Folding of Triangulated Cylinders, Part I: Geometric Considerations. *Journal of Applied Mechanics*, 61(4), December 1994. doi: 10.1115/1.2901553.

[2] S. D. Guest and S. Pellegrino. The Folding of Triangulated Cylinders, Part II: The Folding Process. *Journal of Applied Mechanics*, 61(4), December 1994. doi: 10.1115/1.2901554.

[3] S. D. Guest and S. Pellegrino. The Folding of Triangulated Cylinders, Part III: Experiments. *Journal of Applied Mechanics*, 63(1), March 1996. doi: 10.1115/1.2787212.

[4] K. Gustafson, O. Angatkina, and A. Wissa. Model-based Design of a Multistable Origami-enabled Crawling Robot. *Smart Materials and Structures*, 29(1):015013, nov 2019. doi: 10.1088/1361-665x/ab52c5.

[5] J. Hughes, U. Culha, F. Giardina, F. Guenther, A. Rosendo, and F. Iida. Soft Manipulators and Grippers: A Review. *Frontiers in Robotics and AI*, 3, 2016. doi: 10.3389/frobt.2016.00069.

[6] M. Kilian, A. Monszpart, and N. J. Mitra. String Actuated Curved Folded Surfaces. *ACM Transactions on Graphics*, 36(3), 2017. doi: 10.1145/3072959.3015460.

[7] K. Lee, Y. Wang, and C. Zheng. TWISTER Hand: Underactuated Robotic Gripper Inspired by Origami Twisted Tower. *IEEE Transactions on Robotics*, 2020. doi: 10.1109/TRO.2019.2956870.

[8] M. Luo, R. Yan, Z. Wan, Y. Qin, J. Santoso, E. H. Skorina, and C. D. Onal. OriSnake: Design, Fabrication, and Experimental Analysis of a 3-D Origami Snake Robot. *IEEE Robotics and Automation Letters*, 3(3):1993–1999, 2018. doi: 10.1109/LRA.2018.2800112.

[9] R. V. Martinez, C. R. Fish, X. Chen, and G. M. Whitesides. Elastomeric Origami: Programmable Paper-Elastomer Composites as Pneumatic Actuators. *Advanced Functional Materials*, 22(7):1376–1384, feb 2012. doi: 10.1002/adfm.201102978.

[10] R. Masana and M. F. Daqaq. Equilibria and bifurcations of a foldable paper-based spring inspired by Kresling-pattern origami. *Physical Review E*, 100(6), 2019. doi: 10.1103/physreve.100.063001.

[11] A. Pagano, T. Yan, B. Chien, A. Wissa, and S. Tawfick. A crawling robot driven by multi-stable origami. *Smart Materials and Structures*, 26(9), 2017.

[12] A. Reid, F. Lechenault, S. Rica, and M. Adda-Bedia. Geometry and design of origami bellows with tunable response. *Physical Review E*, 95(1), 2017. doi: 10.1103/PhysRevE.95.013002.

[13] M. Schenk, S. G. Kerr, A. M. Smyth, and S. D. Guest. Inflatable Cylinders for Deployable Space Structures. *First Conference Transformables 2013*, (September), 2013.

A snake-inspired swallowing robot based on Hoberman's linkages

Zeyu Qian, Hailin Huang and Bing Li[*]

School of Mechanical Engineering and Automation, Harbin Institute of Technology, Shenzhen, 518052, China
∗Contact Email: libing.sgs@hit.edu.cn

Abstract. This paper presents a snake-inspired swallowing robot (SSR) which can synchronously deploy and fold both axially and radially. For SSR, an end disk (ED) mechanism is designed based on Hoberman's linkages to achieve radial deployment and fold; as for the axial deployment and fold, three Connecting backbone (CBB) mechanisms are added between the adjacent ED mechanisms as connections to form a complete SSR model. With the goal of maximizing the deploy/fold ratio of SSR and meeting the requirements of assembly, the length of rods is optimized. Auxiliary propulsion mechanisms are added to CBB mechanisms, hence obtaining CBB-T mechanism and CBB-B mechanism. In addition, the forces of the auxiliary propulsion mechanisms on the prey are analyzed to explain their effects on propulsion during the swallowing process. In the end, a SSR is fabricated and experiment of swallowing a 20cm spherical object is conducted to verify the feasibility of the proposed robot.

Keywords: Snake-inspired Swallowing Robot, Deploy and Fold, Hoberman's Linkages, Connecting Backbone Mechanisms.

1   Introduction

The characteristics of Animal predation are fast, accurate and ruthless[1, 2]. Pelican eels first open their mouths when predation, and then expand their mouths with the water pressure to maximize the possibility of catching prey [3]. As for snakes, they will open their mouths as wide as possible to bite the large prey with the cooperation of upper and lower jaws, and then swallow it directly. Due to the connection of ligament tissue and jaws, snakes can capture the prey which is 2-3 times larger than the diameter of their head [4]. Moreover, it is worth noting that animals need to transport the prey from the mouth to the digestive cavity for digestion and absorption after hunting. For snakes, fish or some single-celled organisms, swallowing is their method for predation.

Therefore, some researchers focus their attention on the cavity that realizes the swallowing movement. Haili Li and others used a flexible guiding mechanism to imitate the muscles of the swallowing cavity, using air and water as the medium to achieve the

swallowing process of objects of different shapes [5]. Haihang Wang used McKibben hydraulic artificial muscles to form a multi-segment continuum manipulator which could swallow and disgorge like snake [6]. The swallowing device which was constructed from silicon rubber and pneumatically driven, developed by Weiliang Xu's team to simulate the esophagus of human [7]; there were 12 layers of air chambers on it, and each layer had four air chambers, by controlling the air inlet and outlet of which to swallow the objects [8]. In all, the swallowing robots mentioned above adopt flexible driving methods, because the swallowing process involves the simultaneous deployment and fold of the cavity in both radial and axial directions. However, some problems like insufficient driving force and poor control robustness cause the swallowing robot with flexible drive to have not enough force to swallow objects of large mass.

Deployable mechanism has excellent folding and deploying performance [9, 10]. Not only can it complete the needed motion, but also reduce the occupied area of the mechanism which improves the practicality of the mechanism. Therefore, it is often applied in the aerospace field, such as the design of satellite antennas, space grippers and so on [11-13]. The deployable mechanism that can achieve radial deployment and fold is represented by Hoberman's linkages which is originally designed as a closed scissor mechanism [14]. It consists of arc-type or angulated scissor rods, connected by hinges. For example, the angulated scissor mechanism was used as the end-face mechanism, supplemented by the spring spine connection in the middle, which formed a radially expandable continuous robot [15]. Saverio Iacoponi covered a MDPE plastic sheet on a Hoberman sphere to make up an underwater jet propulsion [16]. In order to realize stable swallowing movement, deployable mechanism is applied to the swallowing robot, which can not only realize the robot's axial and radial deployment and fold, but also greatly improve its stiffness and increase swallowing force.

Inspired by the mechanism of snake swallowing the prey and its movement pattern, we design a snake-inspired swallowing robot that can deploy and fold in both axial and radial directions. In the section 2, end disk mechanism and connecting backbone mechanisms, including CBB-T mechanism and CBB-B mechanism, are applied to form a swallowing robot model. And then we make a prototype with a flexible chamber. In the section 3, we optimize the length of rods to maximize the deploy/fold ratio of SSR and the workspace of a single-segment optimized robot is also calculated. In addition, we analyze the force of two types of CBB mechanisms on the prey during swallowing process. In the end, the swallowing robot is driven to capture and swallow a spherical object.

2   Design and Prototype of SSR

2.1   Design of SSR

After snake has captured the prey, the muscle group of the body and backbone will cooperate to push the prey inward, and finally transport it to the digestive area as shown in Fig.1. Thus, it is the basic requirement that the inner cavity of each segment of SSR

could complete radial deployment, while the connecting backbone between the segments achieve the axial deployment. The design process of SSR is shown in the Fig.1. Each unit can be divided into two parts including end disk mechanism and connecting backbone mechanism.
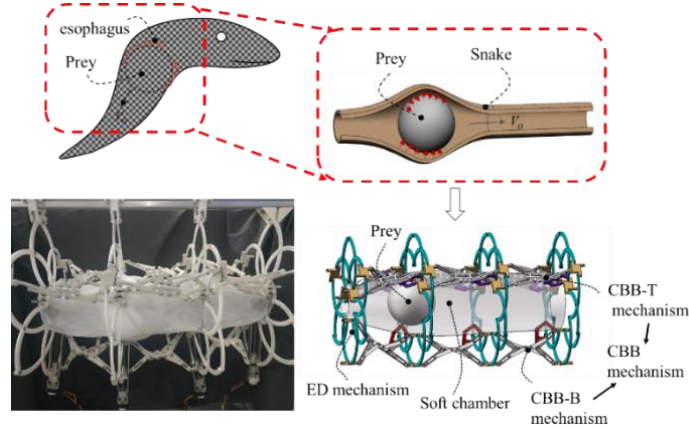
Fig. 1. Illustrations of the design of SSR.

Design of ED Mechanism. Hoberman's linkages are applied to form ED mechanism for achieving the radial deployment and fold. It is composed of arc-type rods as shown in Fig.2(a) and (b), where the radius of arc-type rod is r, and the central angle is $\theta = 120^o$ corresponding to the number of the rods as $n = 6$. The radius of the inner and outer connecting circle of Hoberman's linkages satisfies the following rule that with the increase of the inner one r_i, the outer one r_e has two different stages.[17]

In the first stage, r_e is increased with r_i, which can be expressed as

$$r_e = r_i \times cos \left(\frac{2\pi}{n}\right) + \sqrt{R^2 - r_i^2} \, sin \left(\frac{2\pi}{n}\right) \; (0 \leq r_i \leq R \, cos \left(\frac{2\pi}{n}\right)) \tag{1}$$

where R is the maximum radius of the outer connecting circle of Hoberman's linkages, which equals $2r$. r_e is calculated as in the range of $R sin(\frac{2\pi}{n}) \leq r_e \leq R$.

In the second stage, r_e is decreased with r_i, which can be expressed as

$$r_e = R \times cos \left(\frac{2\pi}{n} - arccos(\frac{r_i}{R})\right) \; (R \, cos \left(\frac{2\pi}{n}\right) \leq r_i \leq R \, cos \left(\frac{\pi}{n}\right)) \tag{2}$$

where r_e is calculated as in the range of $R sin(\frac{\pi}{n}) \leq r_e \leq R$.

As shown in Fig.2(c) and (d), ED mechanism adds three pairs of four-way connecting blocks (FWCBs) which act like a bridge connecting the ED mechanism to the CBB mechanisms, to Hoberman's linkages. In the mechanism diagram, it can be simplified as adding a straight rod every 120° between the arc-type rods. The distances between FWCBs and the center of ED mechanism O could be calculated as

$$d_i = r_i + \frac{l_0 tan30^0}{2} \; (0 \leq r_i \leq R \, cos \left(\frac{\pi}{n}\right)) \tag{3}$$

$$d_e = d_i + (r_e - r_i)\ \left(0 \leq r_i \leq R\ cos\left(\frac{\pi}{n}\right)\right) \tag{4}$$

where d_e is the distance between upper FWCB and point O while d_i turns to the distance between lower FWCB and point O.
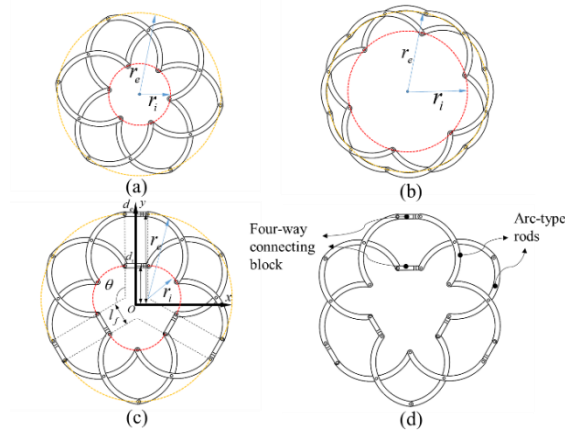
Fig. 2. Schematic diagrams of ED mechanism: (a) Fold of Hoberman's linkages, (b)Deployment of Hoberman's linkages, (c) Fold of ED mechanism, (d) Deployment of ED mechanism.

Design of CBB mechanisms. According to the different auxiliary propulsion mechanisms, CBB mechanisms can be divided into two types including CBB-T mechanism owning the top auxiliary mechanism and CBB-B mechanism having the bottom auxiliary mechanism as shown in Fig.3(a). As the distance d_i of ED mechanism increases, CBB mechanisms enable SSR to deploy and fold along the axial direction. And as shown in Fig.3(b), a segment of SSR has three stages including initial stage, middle stage and expanded stage.

As shown in Fig.3(c), we set the length of middle linkage as l_m, and l_d stands for length of end rod, and initial angle between middle linkage and end rod is θ_0, and the minimum angle is θ_{min}, and the maximum angle between C_1 and horizontal line is β_{max}, thus l_m and l_d should meet the requirements that

$$l_d \geq \frac{(d_e - d_i)_{max}}{2sin\theta_0} \tag{5}$$

$$l_m \geq \frac{(d_e + d_i)_{max} - (d_e + d_i)_{min}}{2sin\beta_{max}} \tag{6}$$

CBB-T mechanism consists of the basic mechanism and the top auxiliary mechanism as shown in the purple box in Fig.3(a). Four purple rods are added to the sliders and end linkages on two adjacent 3R1P mechanisms, which make up the top auxiliary mechanism. As the distance d_i of ED mechanism decreases, the end rod of CBB-T mechanism rotates toward the prey to force it inward at an angular velocity w_u.

CBB-B mechanism is different from CBB-T mechanism for its bottom auxiliary mechanism which is a ten-linkage mechanism as shown in the red box in Fig.3(a). As

the distance d_i of ED mechanism increases, the end rod of CBB-B mechanism rotates at an angular velocity w_D towards the prey to prevent it from escaping.
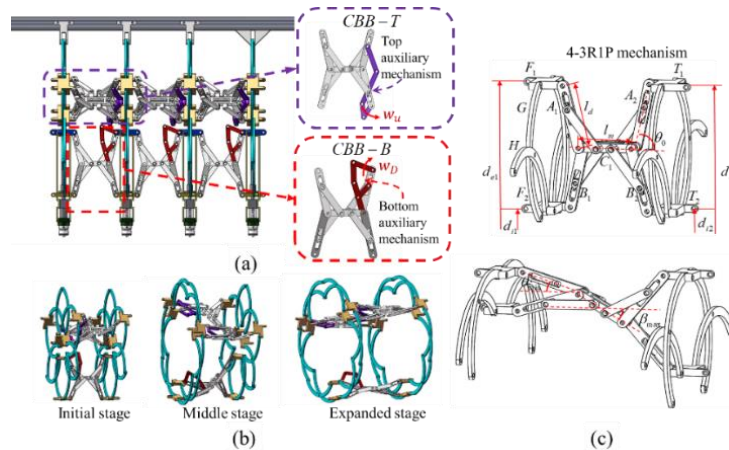
Fig. 3. Model of SSR: (a) 3D model of SSR, (b) three stages of a segment of SSR, (c) the basic mechanism of CBB mechanisms.

2.2   Prototype

As shown in Fig.4, SSR has three segments, which is suspended on an aluminum support frame. Both ED mechanism and CBB mechanisms are shaped by 3D printing, while the screw-nut drive mechanism is formed by milling. The inner cavity is made up of chemical fiber fabric. The robot is controlled by STM32F407, and driven by the DC motor and its corresponding ESC. In addition, we design a sliding platform based on an aluminum frame that allows SSR to be suspended for swallowing process in order to avoid damaging the mechanism by colliding with the ground.

Fig. 4. Prototype of SSR and its components.

3   Analysis and Experiment

3.1   Motion Analysis of SSR

Workspace. It could be calculated that the radius of circumscribed circle of ED mechanism is in the range of $\left[Rsin\left(\frac{2\pi}{n}\right), \quad R\right]$ by combining the Eqs.(1) and (2), which means that the radial deploy/fold ratio of SSR is $\psi_r = \frac{1}{sin(\frac{\pi}{3})} = \frac{2\sqrt{3}}{3}$. Therefore, it is necessary to increase the axial deploy/fold ratio by optimizing the length of middle linkage l_m and end linkage l_d. The overall deploy/fold ratio can be calculated as the ratio of the maximum and minimum of envelope volume of a single-segment SSR as

$$\psi = \frac{(V_e)_{max}}{(V_e)_{min}} \tag{7}$$

where V_e is the envelope volume of a single-segment SSR, expressing as

$$V_e = \frac{\pi h(d_{e1}^2 + d_{e2}^2 + d_{e1}d_{e2})}{3} \tag{8}$$

where h is the distance between the adjacent ED mechanism, which is derived as

$$h = \sqrt{l_d^2 - \left(\frac{d_{e1}-d_{i1}}{2}\right)^2} + \sqrt{l_m^2 - \left(\frac{d_{e2}+d_{i2}}{2} - \frac{d_{e1}+d_{i1}}{2}\right)^2} + \sqrt{l_d^2 - \left(\frac{d_{e2}-d_{i2}}{2}\right)^2} \tag{9}$$

Thus, we maintain the target of the optimization as

$$max(\psi)$$

The constraint conditions include $l_m \geq 67.8138mm$ and $l_d \geq 79.7219mm$ from the inequality (5) and (6). As shown in Fig.5(a), deploy/fold ratio ψ has a negative correlation with the length of middle linkage l_m and end linkage l_d. Moreover, decline of deploy/fold ratio with increase of middle linkage is larger than decline of that with same increase of end linkage. The folding ratio can reach up to 2.9153 when both the length of middle linkage and end linkage are the minimum. Taking the physical processing and assembly into account, the length of middle linkage and end linkage are set as $l_m = 70mm$ and $l_d = 85mm$, together with the deploy/fold ratio $\psi = 2.2459$.

Workspace of SSR is the volume of robot's inner cavity, a segment of which can be expressed as

$$WS = \frac{\pi h(d_{i1}^2 + d_{i2}^2 + d_{i1}d_{i2})}{3} \tag{10}$$

Due to the assembly and manufacture of robot, the distance d_{i1} vary from 40 mm to 160 mm, which means that diameter of the prey swallowed in the robot is limited to 80 mm to 320 mm. Sequentially, value of workspace of a single-segment optimized SSR is shown in Fig.5(b), and the ratio of the maximum volume to the minimum one of a single-segment SSR is 28.2754.
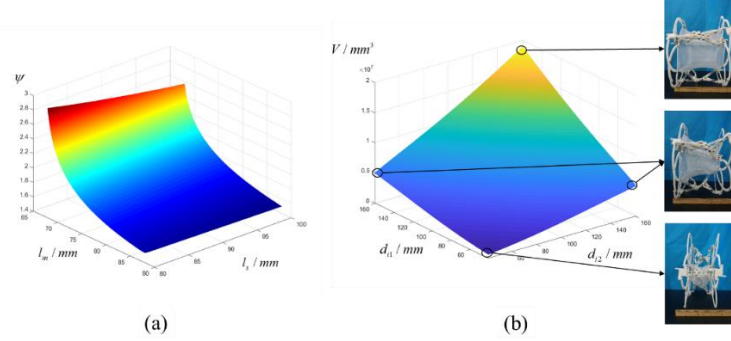
Fig. 5. Structure optimization of a single-segment SSR: (a) Folding ratio of SSR, (b)workspace of a single-segment optimized SSR.

Force analysis. When a snake is swallowing the prey as shown in Fig.6(a), the epaxial muscle will bend the backbone, which forces the prey to move continuously towards the digestive cavity along the esophagus on the one hand, and to prevent the prey from moving back on the other hand[18]. Fig.6(b) and (c) shows two stages in the process of swallowing.

As shown in Fig. 6(c), in the stage 1, the forces on the prey satisfy the follow equation

$$\overrightarrow{F_D} + \overrightarrow{F_{T_1}} + \overrightarrow{F_{I_1}} + \overrightarrow{f_{I_1}} - \overrightarrow{G_O} = 0 \tag{11}$$

where f_{I_1} is the force of the static friction on the surface of the prey and the inner cavity, and f_{T_1} is the force of FWCB T_1 on the prey, f_{I_1} stands for sum of distribution forces of inner cavity on the prey .

In the stage 2, the initial friction on the surface of the prey and the inner cavity is sliding friction which could be expressed as

$$\overrightarrow{f_{I_1}} = \mu(\overrightarrow{F_1^T} + \overrightarrow{F_3^T} - \overrightarrow{F_{U_1}} - \overrightarrow{F_{I_2}} - \overrightarrow{F_{T_2}} - \overrightarrow{G_O}) \tag{12}$$

where μ is the kinetic friction coefficient, $F_1{}^T$ and $F_3{}^T$ stand for force of the other two CBB mechanisms on the prey. Thus, the total force on the prey along Z_3 axis and Y_3 axis could be given as

$$\overrightarrow{F_{Z_3}} = (\overrightarrow{F_{U_1}})_Z + (\overrightarrow{F_{I_2}})_Z + (\overrightarrow{F_{T_2}})_Z + (\overrightarrow{F_1^T})_Z + (\overrightarrow{F_3^T})_Z - (\overrightarrow{f_{I_2}})_Z \tag{13}$$

$$\overrightarrow{F_{Y_3}} = (\overrightarrow{F_1^T})_Y + (\overrightarrow{F_3^T})_Y - (\overrightarrow{F_{U_1}})_Y - (\overrightarrow{F_{I_2}})_Y - (\overrightarrow{F_{T_2}})_Y - (\overrightarrow{f_{I_2}})_Y - \overrightarrow{G_O} \tag{14}$$

From the two equations above, at the beginning, the net force of the mechanisms and inner cavity on the prey is larger than force of sliding friction so that the prey has an acceleration in the swallowing direction, that is $F_{Z_3} > 0$. As ED mechanism folds to a certain range, the increase of friction is greater than that of the net force of the mechanisms. The prey will stay still in the position where the total force F_{Z_3} equals to zero,

when the sliding friction disappears and static friction occurs. So no matter how much force is added, the prey cannot be pushed forward.
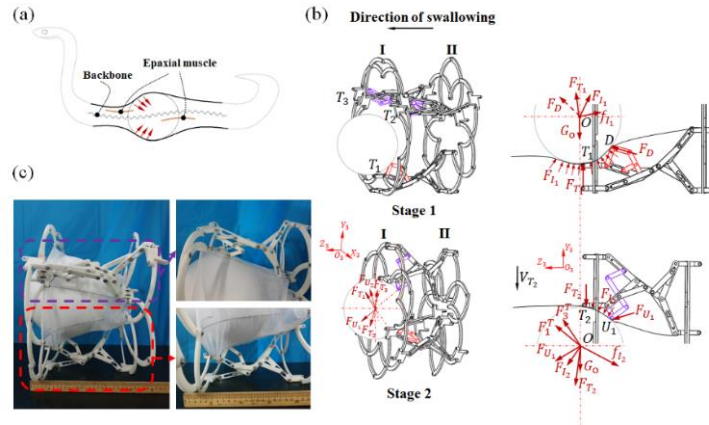
Fig. 6. Force analysis of the swallowing process: (a) Epaxial muscle and backbone of snake push the prey inward, (b) images of CBB-T mechanism and CBB-B mechanism, (c) two stages of the swallowing process and schematic diagrams of the forces on the prey.

3.2   Experiment

The process of SSR to swallow a 20cm spherical object is shown in Fig.7. After ED mechanism on the front face fit the ball, the swallowing process began. The swallowing strategy designed of SSR could be described as that ED mechanisms of Nth to $N+2$th would form the inner cavity like a sinusoidal wave through cooperation when the ball reached the Nth (N=1,2,..) end face. Due to the low friction coefficient between the ball and the internal cavity, the ball did not get stuck in a certain position for a long time. Eventually, the ball was swallowed and spit out in another side.
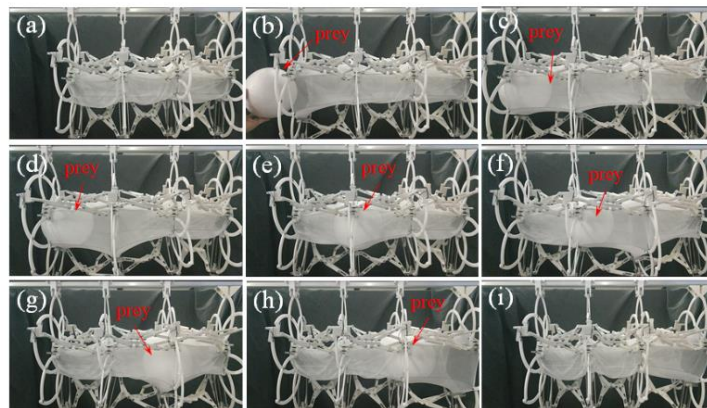
Fig. 7. Swallowing process of a 20cm spherical object.

4   Conclusion

This paper introduced a snake-inspired swallowing robot that consisted of end disk mechanisms and connecting backbone mechanisms, which could deploy and fold both axially and radially. ED mechanism was designed based on Hoberman's linkages, which could achieve the radial deployment and fold to act as an active mechanism. On the contrary, CBB mechanisms which acted as a passive axial deployed and folded mechanism was divided into two types including CBB-T mechanism and CBB-B mechanism. SSR was fabricated, and its soft chamber was constructed from chemical fiber fabric.

In order to maximize the deploy/fold ratio of SSR, we optimized the length of the middle rod and end rod of CBB mechanisms. Taking the requirement of assembly into consideration, the final deploy/fold ratio with the optimized rods was 2.2459. Meanwhile, workspace of a single-segment optimized SSR was calculated while the ratio of the maximum and minimum volume of its inner cavity was determined to be 28.2754. CBB-T mechanism was designed to push the prey inward efficiently while CBB-B mechanism was to prevent the prey from reciprocating motion. In the end, a SSR was driven to swallow a 20cm spherical object. As for the future work, control of SSR and the soft sensor using in the inner cavity will be the main targets for our further research, which will enable SSR to swallow the prey efficiently. It is expected that SSR could be used to fetch or transport items in narrow spaces, and disaster relief where useful items can be swallowed continuously on the spot to improve the efficiency of rescue.

References

1. Kane, S. A., M. Zamani: Falcons pursue prey using visual motion cues: new perspectives from animal-borne cameras. Journal of Experimental Biology 217(2), 225-234 (2014).
2. Olson, R.S., Knoester, D., Adami, C.: Evolution of swarming behavior is shaped by how predators attack. Artificial Life, 22, 299-318 (2016).
3. Kim, W., Byun, J., Kim, J. K., Choi, W. Y., Cho, K. J.: Bioinspired dual-morphing stretchable origami. Science Robotics, 4(36), eaay3493 (2019).
4. Frazzetta, T.: Studies on the morphology and function of the skull in the boidae (serpentes). part ii. morphology and function of the jaw apparatus in python sebae and python molurus. Journal of Morphology, 118(2), 217-295 (2010).
5. Li, H., Yao, J., Liu, C., Zhou, P., Xu, Y., Zhao, Y.: A Bioinspired soft swallowing robot based on compliant guiding structure. Soft Robotics (2020).

6. Wang, H., Xu, H., Yu, F., Li, X., Yang, C., Chen, S. Chen, J., Zhang, Y., Zhou, X.: Modeling and experiments on the swallowing and disgorging characteristics of an underwater continuum manipulator. In: 2020 IEEE International Conference on Robotics and Automation (ICRA), pp. 2946-2952, IEEE, Paris France (2020).

7. Dirven, S., W. Xu, L. Cheng: Sinusoidal peristaltic waves in soft actuator for mimicry of esophageal swallowing. IEEE/ASME Transactions on Mechatronics 20(3), 1331-1337 (2015).

8. Zhu, M., W. Xu, L. Cheng: Esophageal peristaltic control of a soft-bodied swallowing robot by the central pattern generator. IEEE/ASME Transactions on Mechatronics 22(1), 91-98 (2017).

9. Jia, G., Li, B., Huang, H., Zhang, D.: Type synthesis of metamorphic mechanisms with scissor-like linkage based on different kinds of connecting pairs. Mechanism and Machine Theory 151, 103848 (2020).

10. Wei, G., Y. Chen, J. Dai: Synthesis, Mobility, and multifurcation of deployable polyhedral mechanisms with radially reciprocating motion. Journal of Mechanical Design 136, 091003 (2014).

11. Araromi, O. A., Gavrilovich, I., Shintake, J., Rosset, S., Richard, M., Gass, V., et al.: Rollable multisegment dielectric elastomer minimum energy structures for a deployable microsatellite gripper. IEEE/ASME Transactions on Mechatronics 20(1), 438-446 (2014).

12. Finistauri, A.D., F. Xi: Type synthesis and kinematics of a modular variable geometry truss mechanism for aircraft wing morphing. In: 2009 ASME/IFToMM International Conference on Reconfigurable Mechanisms and Robots, pp. 478-485, IEEE, London (2009).

13. Qi, X., Deng, Z., Li, B., Liu, R., Guo, H.: Design and optimization of large deployable mechanism constructed by Myard linkages. CEAS Space Journal 5, 147-155 (2013).

14. You, Z., Pellegrino S.: Foldable bar structures. International Journal of Solids and Structures 34, 1825-1847 (1997).

15. Abah, C., A.L. Orekhov, N. Simaan: Design considerations and redundancy resolution for variable geometry continuum robots. In: 2018 IEEE International Conference on Robotics and Automation (ICRA), pp. 767-774, IEEE, Brisbane QLD (2018).

16. S. Iacoponi, G. Picardi, M. Chellapurath, M. Calisti, L. Cecilia: Underwater soft jet propulsion based on a Hoberman mechanism. In: 2018 IEEE International Conference on Soft Robotics (RoboSoft), pp. 449-454, IEEE, Livorno (2018).

17. Chen, B., Hu, J., Chen W., Qi, J.: Geometrical analysis of connecting beam mandala: A planar deployable mechanism. Journal of Mechanisms and Robotics 12, 011009 (2020).

18. Moon, B.R. The mechanics of swallowing and the muscular control of diverse behaviours in gopher snakes. The Journal of experimental biology 203 (17), 2589-601 (2000).

Inverse Dynamics Analysis of a New 2T1R Parallel Manipulator

Ju Li[*1]   Jinbo Zhou[1]   Jingjing You[2]   Huiping Shen[1]

[1] Research Center of Modern Mechanism, Changzhou University, Changzhou, Jiangsu 213016, P.R.China

[2] College of Mechanical and Electronical Engineering, Nanjing Forestry University, Nanjing, Jiangsu 210037, P.R.China

Abstract. In this paper, a symbolic solution of forward kinematics of a new 3-degree of freedom (DOF) parallel manipulator (PM) with two translations and one rotation (2T1R) is analyzed, and its inverse dynamic equation is established and solved. Firstly, using the kinematics modeling and solving method based on topological characteristics, the symbolic position direct solutions of the manipulator are given, and the velocity and acceleration equations are derived based on the direct position solutions. Secondly, the inverse dynamic equation of the manipulator is constructed and solved by Newton-Euler Formulation. Finally, the virtual prototype of the manipulator is designed by ADAMS, and the dynamics simulation is carried out. At the same time, the inverse dynamic equations are calculated by Matlab. The theoretical values and simulation values indicate the maximum driving force of each actuated pair is 4.71%, 2.87%, and 3.7% .This work lays a theoretical foundation for further study of the dynamic characteristics and motion control of the PM.

Keywords: Symbolic Solution, Forward Kinematics, Inverse Dynamics, Parallel Manipulator.

1   Introduction

In recent decades, the parallel manipulator (PM) with limited-degree of freedom (DOF) has a significant potential value due to its small number of actuated components, relatively simple structure and easily to be controlled. Many scholars have being studied 3-DOF PM by kinematics, dynamics and stiffness analysis etc. [1–3]. Simultaneously, dynamic analysis is the basis for the high-precision control of the PM. In most of the reported researches, dynamic analysis of such researches are usually using virtual work principle methods [4, 5], Lagrange [6, 7], Newton-Euler (N-E) formulation [8, 9], or Kane methods [10, 11]. Among them, the analysis of N-E formulation is relatively clear, and can derive easily the dynamic equations by eliminating the interaction force of each link.

At present, most of scholars use the N-E formulation to establish dynamic models, and generally derive the equations of velocity and acceleration based on inverse kinematics. In [8], the authors suggested a Stewart-Gough PM with a flexible platform

and developed dynamic analysis using Newton-Euler method. Li et al [9] proposed a 5-PSS/UPU PM used in the sea level recovery platform of spacecraft and established its dynamics model by Newton-Euler method. Nurahmi and Gan[12] presented the dynamic analysis of the 3-rRPS metamorphic parallel mechanism in both operation modes based on the Instantaneous Screw Axis (ISA).

This paper proposes a new 2T1R PM [13] according to design theory of PM based on Position and Orientation Characteristics equation (POC) [14–16]. Firstly, according to the kinematics modeling method based on topological characteristics, the symbolic direct position solutions are obtained, and the equation of the velocity and acceleration of each link are derived based on the direct kinematics. The symbolic direct kinematics can simplify and improve the efficiency and accuracy of the dynamic inverse solutions. Secondly, the forces of each link are obtained respectively, and the dynamics model of this PM is established by N-E method. Finally, the results are verified using ADAMS.

2 Manipulator Description

This 2T1R PM is illustrated in Figure 1, its topological architecture and geometric constraints are as follows.
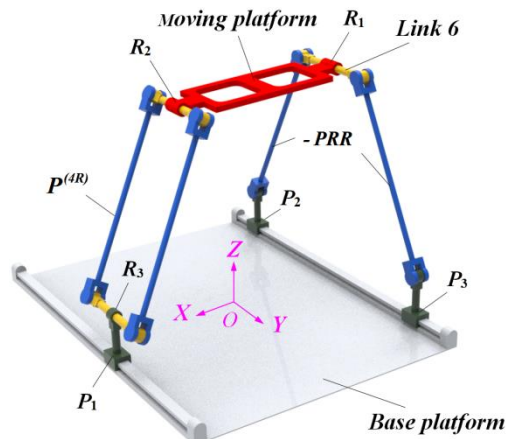
Fig. 1. CAD model of 2T1R parallel manipulator

The first hybrid branch I is composed of a planar six-bar linkage (abbreviation: 2P4R sub-PM) connected in series with a revolute joint R_1 which connects the moving platform. The output motion of branch I is two translations and two rotations (2T2R).

The second hybrid branch II is composed of a prismatic joint P_1, a revolute joint R_3, a 4R parallelogram linkage and a revolute joint R_2 connecting the moving platform in series. The output motion of branch II is three translations and one rotation (3T1R). The prismatic joints P_1, P_2 and P_3 are connected to the base platform; P_3 and P_2 are arranged coaxially, and prismatic P_1 is parallel to P_2. Thus the parallel manipulator

has two translations in the plane perpendicular to the X-axis and one rotation around the Y-axis.

3   Symbolic Solution of Forward Kinematics

As shown in Figure 2, the base platform of the 2T1R PM is a rectangle with a length of lp and a width of $2a$, and the positions of sliders on the base platform are respectively A_1, A_2, A_3. The frame coordinate system O-XYZ is established on the geometric center of the base platform, the X and Y axes of which are perpendicular and parallel to the line A_2A_3 respectively, and the Z axis is determined by the right hand Cartesian coordinate rule. The moving coordinate system O'-X'Y'Z' is established at the center of the moving platform, the X' and Y' axes of which are coincide and perpendicular to the line E_1D_1 respectively, and the Z' axis is determined by the right hand Cartesian coordinate rule. The angle between the vectors B_3C_3 and the positive Y axis is assigned as δ. The angle between the vectors E_1D_1 and the positive X axis is assigned as α, is shown in Figure 3.
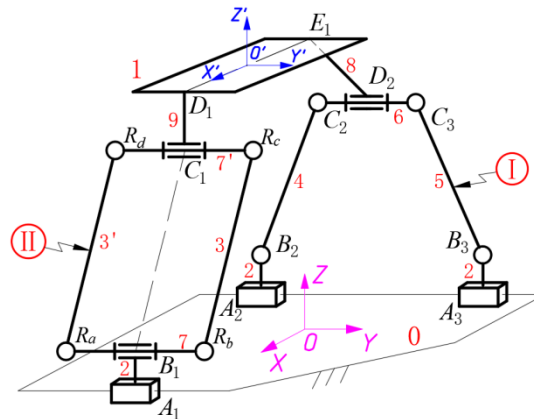
Fig. 2. Structural sketch of 2T1R PM
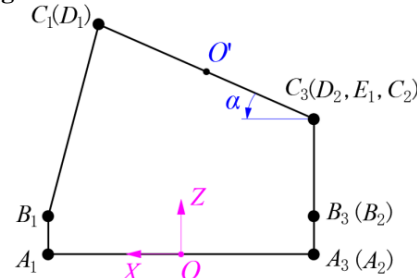
Fig. 3. Geometric relationship in the XOZ direction

The length of the line D_1E_1 on the moving platform is l_1, and the length of the three driving links 2 is l_2. The length of the connecting links 4, 5 of the hybrid chain I is l_4, and the lengths of the intermediate links 6, 8 are l_6, l_8 respectively, but l_8 is equal to 0.

The length of the parallelogram's short links 7, 7′ of the hybrid chain II is l_7, while the points B_1, C_1 are the midpoint of the short edge, and the length of the long links 3, 3′ is l_3. The length of the connecting link 9 is l_9 which is equal to 0.

3.1   Forward Kinematics

To solve the direct kinematics, i.e., to compute the position $O'(x_0, y_0, z_0)$ of the moving platform when setting the position values of the prismatic joints P_1, P_2 and P_3 (with the coordinates y_{A_1}, y_{A_2} and y_{A_3}).

In the first loop A_2-B_2-C_2-C_3-B_3-A_3, due to the special constrain of the PM, the movement of the component 6 of the 2P4R sub-PM is always parallel to the base platform, namely $C_2C_3 \| A_2A_3$, then we have $z_{C_2} = z_{C_3}$.

Therefore, the coordinates of the points C_2, C_3, and D_3 can be easily obtained. Due to the link length constraints defined by $B_2C_2 = l_4$, the constraint equation can be established as follows.

$$A\cos\delta + B = 0$$

Then, we have

$$\delta = 2\arctan\frac{\pm\sqrt{A^2 - B^2}}{A - B}$$

(1)

Where $A = 2l_5$, $B = y_{A_3} - 2l_6 - y_{A_2}$

In the second loop A_1-B_1-C_1-D_1-E_1-D_2, the coordinates of points E_1, C_1, and D_1 can be obtained from point D_2, and the coordinate of point O' can be calculated as follows.

$$\boldsymbol{O'} = \begin{bmatrix} x_0 \\ y_0 \\ z_0 \end{bmatrix} = \begin{bmatrix} x_{D_2} + l_1\cos\alpha/2 \\ y_{D_2} \\ z_{D_2} + l_1\sin\alpha/2 \end{bmatrix}$$

(2)

Due to the link length constraints defined by $B_1C_1 = l_3$, the constraint equation can be established below.

$$D\sin\alpha + E\cos\alpha + F = 0$$

We have

$$\alpha = 2\arctan\frac{D \pm \sqrt{D^2 + E^2 - F^2}}{E - F}$$

(3)

Where $D = 2l_1l_5\sin\delta$, $E = -4al_1$, $F = 4a^2 + l_1^2 - l_3^2 + (y_{C_1} - y_{A_1})^2 + l_5^2\sin^2\delta$

Finally, putting the values of δ and α obtained by Eqs. (1) and (3) into Eq. (2), the coordinate (x_0, y_0, z_0) of the point O' on the moving platform can be obtained. Therefore, there are four positive solutions theoretically.

3.2 Kinematic Equations

The coordinates of centroids of links 3, 4, 5, 6 and 7' are marked as $r_i (i = 3 \sim 7)$, and can be written by Section 3.1 as follows.

$$r_3 = \begin{bmatrix} (x_{B_1} + x_{C_1})/2 \\ (y_{B_1} + y_{C_1})/2 \\ (z_{B_1} + z_{C_1})/2 \end{bmatrix} r_4 = \begin{bmatrix} (x_{B_2} + x_{C_2})/2 \\ (y_{B_2} + y_{C_2})/2 \\ (z_{B_2} + z_{C_2})/2 \end{bmatrix}, \quad r_7 = \begin{bmatrix} x_{C_1}/2 \\ y_{C_1}/2 \\ z_{C_1}/2 \end{bmatrix}$$

$$r_5 = \begin{bmatrix} (x_{B_3} + x_{C_3})/2 \\ (y_{B_3} + y_{C_3})/2 \\ (z_{B_3} + z_{C_3})/2 \end{bmatrix}, \quad r_6 = \begin{bmatrix} (x_{C_2} + x_{C_3})/2 \\ (y_{C_2} + y_{C_3})/2 \\ (z_{C_2} + z_{C_3})/2 \end{bmatrix} \tag{4}$$

The velocity vector equations are found by time differentiating both sides of Eqs. (2) and (4) as follows.

$$v_{O'} = \begin{bmatrix} \dot{x}_0 \\ \dot{y}_0 \\ \dot{z}_0 \end{bmatrix}, \quad v_{l3} = \begin{vmatrix} \dot{x}_{r_3} \\ \dot{y}_{r_3} \\ \dot{z}_{r_3} \end{vmatrix}, \quad v_{l4} = \begin{vmatrix} \dot{x}_{r_4} \\ \dot{y}_{r_4} \\ \dot{z}_{r_4} \end{vmatrix},$$

$$v_{l5} = \begin{vmatrix} \dot{x}_{r_5} \\ \dot{y}_{r_5} \\ \dot{z}_{r_5} \end{vmatrix}, \quad v_{l6} = \begin{vmatrix} \dot{x}_{r_6} \\ \dot{y}_{r_6} \\ \dot{z}_{r_6} \end{vmatrix}, \quad v_{l7} = \begin{vmatrix} \dot{x}_{r_7} \\ \dot{y}_{r_7} \\ \dot{z}_{r_7} \end{vmatrix}$$

$$\tag{5}$$

Then by Eq. (5), the angular velocities of the moving platform and all links can be written as follows.

$$\omega_{l3} = \delta_3 \times (v_{l7} - v_{A1} e_{A1})/l_3 ; \quad \omega_{l4} = \delta_4 \times (v_{l6} - v_{A2} e_{A2})/l_4 ;$$

$$\omega_{l5} = \delta_5 \times (v_{l6} - v_{A3} e_{A3})/l_5 ; \quad \omega_{O'} = \omega_{l6} = \omega_{l7} = \begin{bmatrix} 0 \\ \dot{\alpha} \\ 0 \end{bmatrix} \tag{6}$$

Where $\omega_{O'}$ denotes the angular velocity of the moving platform; $\omega_{li}(i = 3 \sim 7)$ denotes the angular velocity of the links 3 to 7'; δ_3, δ_4 and δ_5 denote the unit vectors of the links 3, 4 and 5; e_{A1}, e_{A2} and e_{A3} denote the unit direction vectors of the prismatic joints P_1, P_2 and P_3.

Further, the second time derivative of Eq. (4), i.e. the accelerations of the moving platform and all links is given.

$$a_{O'} = \begin{bmatrix} \ddot{x}_0 \\ \ddot{y}_0 \\ \ddot{z}_0 \end{bmatrix}, \quad a_{l3} = \begin{vmatrix} \ddot{x}_{r_3} \\ \ddot{y}_{r_3} \\ \ddot{z}_{r_3} \end{vmatrix}, \quad a_{l4} = \begin{vmatrix} \ddot{x}_{r_4} \\ \ddot{y}_{r_4} \\ \ddot{z}_{r_4} \end{vmatrix},$$

$$\boldsymbol{a}_{l5} = \begin{vmatrix} \ddot{x}_{r_5} \\ \ddot{y}_{r_5} \\ \ddot{z}_{r_5} \end{vmatrix}, \quad \boldsymbol{a}_{l6} = \begin{vmatrix} \ddot{x}_{r_6} \\ \ddot{y}_{r_6} \\ \ddot{z}_{r_6} \end{vmatrix}, \quad \boldsymbol{a}_{l7} = \begin{vmatrix} \ddot{x}_{r_7} \\ \ddot{y}_{r_7} \\ \ddot{z}_{r_7} \end{vmatrix}$$

(7)

Then by Eq. (7), the angular accelerations of the moving platform and all links can be written as

$$\boldsymbol{\varepsilon}_{l3} = \boldsymbol{\delta}_3 \times \left(\boldsymbol{a}_{l7} - a_{A1}\boldsymbol{e}_{A1}\right)/l_3 \,; \boldsymbol{\varepsilon}_{l4} = \boldsymbol{\delta}_4 \times \left(\boldsymbol{a}_{l6} - a_{A2}\boldsymbol{e}_{A2}\right)/l_4 \,;$$

$$\boldsymbol{\varepsilon}_{l5} = \boldsymbol{\delta}_5 \times \left(\boldsymbol{a}_{l6} - a_{A3}\boldsymbol{e}_{A3}\right)/l_5 \,; \quad \boldsymbol{\varepsilon}_{O'} = \boldsymbol{\varepsilon}_{l6} = \boldsymbol{\varepsilon}_{l7} = \begin{pmatrix} 0 \\ \ddot{\alpha} \\ 0 \end{pmatrix}$$

(8)

Where $\boldsymbol{\varepsilon}_{O'}$ denotes the angular acceleration of the moving platform; $\boldsymbol{\varepsilon}_{li}(i = 3 \sim 7)$ denotes the angular accelerations of the links 3 to 7'.

4   Dynamic Equations

The N-E method can analyze the force of each link independently without considering the friction of each joint, and establish the N-E dynamic equation of each link respectively. Then by eliminating the internal force between each link, the dynamic model of 2T1R PM can be established. Finally, we can obtain the relationship between the actuated force and external force.

4.1   Dynamic Equations of Hybrid Chain I

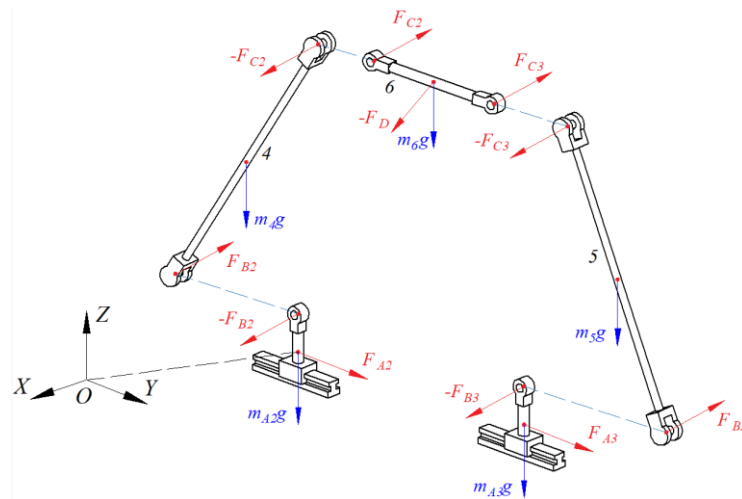The dynamic analysis of hybrid chain I is shown in Figure 4.

Fig. 4. Force diagram of hybrid chain I

The driving sliders 2, 3 are subject to the counter-forces $-\boldsymbol{F}_{Bi}$ (i=2, 3) of the corresponding rotating joints, their own gravity $m_{Ai}g$ (i=2, 3) and the counter-forces $\boldsymbol{F}_{Ai}$ (i=2, 3) of motors. The m_{Ai} (i=2, 3) denote the mass of sliders 2, 3, and the a_{Ai} (i=2, 3) denote the acceleration in their mass-centre respectively. Thus N-E's equations of the sliders 2, 3 are described by

$$-\boldsymbol{F}_{Bi} + \boldsymbol{F}_{Ai} + m_{Ai}g = m_{Ai}a_{Ai} \quad (i = 2, 3) \tag{9}$$

The links 4, 5 are subject to the counter-forces $-\boldsymbol{F}_{C2}$, $-\boldsymbol{F}_{C3}$ of the joints C_2 and C_3 of link 6, their own gravity m_4g, m_5g and the counter-forces $\boldsymbol{F}_{B2}$, $\boldsymbol{F}_{B3}$ of the driving sliders 2, 3. Thus the N-E's equations of the links 4, 5 are described by

$$-\boldsymbol{F}_{C2} + \boldsymbol{F}_{B2} + m_4 g = m_4 \boldsymbol{a}_{l4} \tag{10}$$

$$-l_4 \boldsymbol{\delta}_{l4} \times \boldsymbol{F}_{C2}/2 - l_4 \boldsymbol{\delta}_{l4} \times \boldsymbol{F}_{B2}/2 = {}^o\boldsymbol{I}_{l4}\boldsymbol{\varepsilon}_{l4} + \boldsymbol{\omega}_{l4} \times \left({}^o\boldsymbol{I}_{l4}\boldsymbol{\omega}_{l4}\right) \tag{11}$$

$$-\boldsymbol{F}_{C3} + \boldsymbol{F}_{B3} + m_5 g = m_5 \boldsymbol{a}_{l5} \tag{12}$$

$$-l_5 \boldsymbol{\delta}_{l5} \times \boldsymbol{F}_{C3}/2 - l_5 \boldsymbol{\delta}_{l5} \times \boldsymbol{F}_{B3}/2 = {}^o\boldsymbol{I}_{l5}\boldsymbol{\varepsilon}_{l5} + \boldsymbol{\omega}_{l5} \times \left({}^o\boldsymbol{I}_{l5}\boldsymbol{\omega}_{l5}\right) \tag{13}$$

Where, ${}^o\boldsymbol{I}_{lj} = {}^o\boldsymbol{R}_{lj}\boldsymbol{I}_{lj}{}^o\boldsymbol{R}_{lj}^T$ (j=4, 5); ${}^o\boldsymbol{I}_{lj}$ (j=4, 5) is the projection matrix of the links 4, 5 with respect to the inertia matrix of point O in the frame coordinate system; ${}^o\boldsymbol{R}_{lj}$ (j=4, 5) represents the transformation matrix of the links 4, 5 with respect to base coordinate system; $\boldsymbol{I}_{lj}$ (j=4, 5) is the projection matrix of the links 4, 5 in the coordinate system of links 4, 5 with respect to the inertia matrix of $\boldsymbol{r}_4$, $\boldsymbol{r}_5$.

The link 6 is subject to the counter-forces $\boldsymbol{F}_{C2}$, $\boldsymbol{F}_{C3}$ of the links 4, 5, its own gravity m_6g and the counter-forces $-\boldsymbol{F}_D$ of the moving platform. Hence,

$$\boldsymbol{F}_{C2} + \boldsymbol{F}_{C3} - \boldsymbol{F}_D + m_6 g = m_6 \boldsymbol{a}_D \tag{14}$$

Dot multiply the both sides of Eq. (9) to $\boldsymbol{e}_{A2}^T$

$$\boldsymbol{\tau}_2 = \boldsymbol{e}_{A2}^T \cdot \boldsymbol{F}_{A2} = \boldsymbol{e}_{A2}^T \cdot \boldsymbol{F}_{B2} + m_{A2}a_{A2} - m_{A2}g \tag{15}$$

Where $\boldsymbol{\tau}_2$ is an array of actuator force of the sliders 2.

Substituting Eq. (10) into Eq. (15), then

$$\boldsymbol{\tau}_2 = \boldsymbol{e}_{A2}^T \cdot \left(\boldsymbol{F}_{C2} + m_4 \boldsymbol{a}_{l4} - m_4 g\right) + m_{A2}a_{A2} - m_{A2}g \tag{16}$$

Eq. (11) can be rewritten as

$$l_4 \boldsymbol{\delta}_{l4} \times \boldsymbol{F}_{C2} = \boldsymbol{C}_2,$$

$$\boldsymbol{C}_2 = l_4 \boldsymbol{\delta}_{l4} \times \left(m_4 g - m_4 \boldsymbol{a}_{l4}\right)/2 - {}^o\boldsymbol{I}_{l4}\boldsymbol{\varepsilon}_{l4} - \boldsymbol{\omega}_{l4} \times \left({}^o\boldsymbol{I}_{l4}\boldsymbol{\omega}_{l4}\right) \tag{17}$$

Cross multiply the both sides of Eq. (17) to $\boldsymbol{e}_{A2}$

$$l_4 \boldsymbol{e}_{A2} \times \boldsymbol{\delta}_{l4} \times \boldsymbol{F}_{C2} = \boldsymbol{e}_{A2} \times \boldsymbol{C}_2$$

$$\Rightarrow \boldsymbol{F}_{C2} = \frac{\boldsymbol{\delta}_{l4}[\boldsymbol{e}_{A2}^T \boldsymbol{F}_{C2}]}{\boldsymbol{e}_{A2}^T \boldsymbol{\delta}_{l4}} - \frac{\boldsymbol{e}_{A2} \times \boldsymbol{C}_2}{l_4 \boldsymbol{e}_{A2}^T \boldsymbol{\delta}_{l4}} \tag{18}$$

Then Eq. (16) can be rewritten as

$$\boldsymbol{e}_{A2}^T \boldsymbol{F}_{C2} = \boldsymbol{\tau}_2 - \boldsymbol{e}_{A2}^T \left(m_4 \boldsymbol{a}_{l4} - m_4 g\right) - m_{A2}\boldsymbol{a}_{A2} + m_{A2}g \tag{19}$$

Substituting Eq. (19) into Eq. (18), then

$$F_{C2} = \frac{\delta_{l4}\left[\tau_2 - e_{A2}^T\left(m_4 a_{l4} - m_4 g\right) - m_{A2} a_{A2} + m_{A2} g\right]}{e_{A2}^T \delta_{l4}} - \frac{e_{A2} \times C_2}{l_4 e_{A2}^T \delta_{l4}} \tag{20}$$

Simultaneously,

$$F_{C3} = \frac{\delta_{l5}\left[\tau_3 - e_{A3}^T\left(m_5 a_{l5} - m_5 g\right) - m_{A3} a_{A3} + m_{A3} g\right]}{e_{A3}^T \delta_{l4}} - \frac{e_{A3} \times C_3}{l_5 e_{A3}^T \delta_{l5}},$$

$$C_3 = l_5 \delta_{l5} \times \left(m_5 g - m_5 a_{l5}\right)/2 - {}^o I_{l5} \varepsilon_{l5} - \omega_{l5} \times \left({}^o I_{l5} \omega_{l5}\right) \tag{21}$$

Substituting Eqs. (20), (21) into Eq. (14), then

$$F_D = F_{C2} + F_{C3} + m_6 g - m_6 a_D \tag{22}$$

4.2 Dynamic equations of hybrid chain II

The dynamic analysis of hybrid chain II is shown in Figure 5.

The N-E's equation of driving slider 1 is consistent with Eq. (9) in Section 4.1. Hence, we have

$$-F_{B1} + F_{A1} + m_{A1} g = m_{A1} a_{A1} \tag{23}$$

The link 7 is subject to the counter-forces $-F_{Ra}$, $-F_{Rb}$ of the rotating joints R_a, R_b of the links 3', 3, its own gravity $m_7 g$ and the counter-force F_{B1} of driving slider 1. Thus the N-E's equation of the links 7 is described by

$$F_{B1} - F_{Ra} - F_{Rb} + m_7 g = m_7 a_{A1} \tag{24}$$
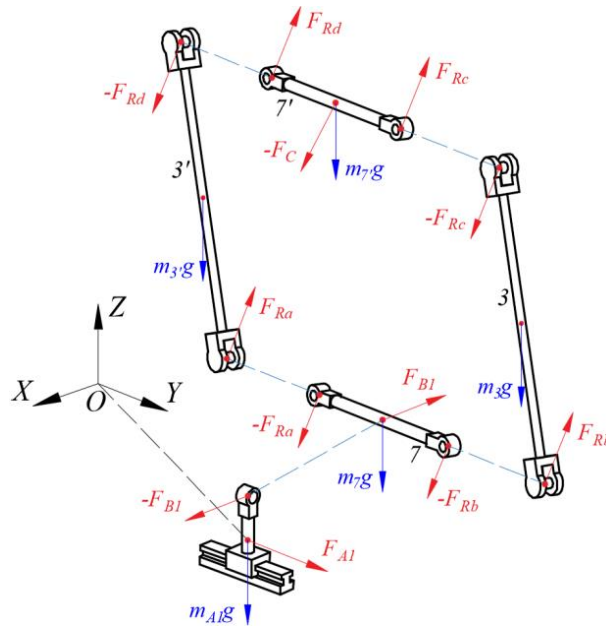

Fig. 5. Force diagram of hybrid chain II

The links 3', 3 are subject to the counter-forces $-\boldsymbol{F}_{Rd}$, $-\boldsymbol{F}_{Rc}$ of the link 7', their own gravity $m_3 g$ and the counter-forces $\boldsymbol{F}_{Ra}$, $\boldsymbol{F}_{Rb}$ of the link 7. Hence, we have

$$-\boldsymbol{F}_{Rd} + \boldsymbol{F}_{Ra} + m_3 g = m_3 \boldsymbol{a}_{l3} \tag{25}$$

$$-l_3 \boldsymbol{\delta}_{l3} \times \boldsymbol{F}_{Ra}/2 - l_3 \boldsymbol{\delta}_{l3} \times \boldsymbol{F}_{Rd}/2 = {}^o\boldsymbol{I}_{l3} \boldsymbol{\varepsilon}_{l3} + \boldsymbol{\omega}_{l3} \times \left({}^o\boldsymbol{I}_{l3} \boldsymbol{\omega}_{l3}\right) \tag{26}$$

$$-\boldsymbol{F}_{Rc} + \boldsymbol{F}_{Rb} + m_3 g = m_3 \boldsymbol{a}_{l3'} \tag{27}$$

$$-l_3 \boldsymbol{\delta}_{l3'} \times \boldsymbol{F}_{Rb}/2 - l_3 \boldsymbol{\delta}_{l3'} \times \boldsymbol{F}_{Rc}/2 = {}^o\boldsymbol{I}_{l3'} \boldsymbol{\varepsilon}_{l3'} + \boldsymbol{\omega}_{l3'} \times \left({}^o\boldsymbol{I}_{l3'} \boldsymbol{\omega}_{l3'}\right) \tag{28}$$

The link 7' is subject to the counter-forces $\boldsymbol{F}_{Rc}$, $\boldsymbol{F}_{Rd}$ of the links 3, 3', its own gravity $m_7 g$ and the counter-force $-\boldsymbol{F}_C$ of moving platform. Hence, we have

$$\boldsymbol{F}_{Rc} + \boldsymbol{F}_{Rd} - \boldsymbol{F}_C + m_7 g = m_7 \boldsymbol{a}_C \tag{29}$$

Dot multiply the both sides of Eq. (23) to $\boldsymbol{e}_{A1}^T$

$$\boldsymbol{\tau}_1 = \boldsymbol{e}_{A1}^T \cdot \boldsymbol{F}_{A1} = \boldsymbol{e}_{A1}^T \cdot \boldsymbol{F}_{B1} + m_{A1} a_{A1} - m_{A1} g \tag{30}$$

Substituting Eq. (24), (25) and (27) into Eq. (30), then

$$\boldsymbol{\tau}_1 = \boldsymbol{e}_{A1}^T \cdot [\boldsymbol{F}_{Rc} + \boldsymbol{F}_{Rd} - 2(m_3 g - m_3 \boldsymbol{a}_{l3})$$
$$- (m_7 g - m_7 \boldsymbol{a}_{A1})] - (m_{A1} g - m_{A1} a_{A1}) \tag{31}$$

Eq. (26) and (28) can be rewritten as

$$l_3 \boldsymbol{\delta}_{l3} \times \left(\boldsymbol{F}_{Rc} + \boldsymbol{F}_{Rd}\right) = \boldsymbol{C}_1 ,$$
$$\boldsymbol{C}_1 = l_3 \boldsymbol{\delta}_{l3} \times \left(m_3 g - m_3 \boldsymbol{a}_{l3}\right) - 2\left({}^o\boldsymbol{I}_{l3} \boldsymbol{\varepsilon}_{l3} - \boldsymbol{\omega}_{l3} \times \left({}^o\boldsymbol{I}_{l3} \boldsymbol{\omega}_{l3}\right)\right) \tag{32}$$

Cross multiply the both sides of Eq. (32) to $\boldsymbol{e}_{A1}$

$$l_3 \boldsymbol{e}_{A1} \times \boldsymbol{\delta}_{l3} \times \left(\boldsymbol{F}_{Rc} + \boldsymbol{F}_{Rd}\right) = \boldsymbol{e}_{A1} \times \boldsymbol{C}_1$$

$$\Rightarrow \boldsymbol{F}_{Rc} + \boldsymbol{F}_{Rd} = \frac{\boldsymbol{\delta}_{l3} [\boldsymbol{e}_{A1}^T \left(\boldsymbol{F}_{Rc} + \boldsymbol{F}_{Rd}\right)]}{\boldsymbol{e}_{A1}^T \boldsymbol{\delta}_{l3}} - \frac{\boldsymbol{e}_{A1} \times \boldsymbol{C}_1}{l_3 \boldsymbol{e}_{A1}^T \boldsymbol{\delta}_{l3}} \tag{33}$$

Substituting Eq. (33) into Eq. (31), then

$$\boldsymbol{F}_{Rc} + \boldsymbol{F}_{Rd} = -\frac{\boldsymbol{e}_{A1} \times \boldsymbol{C}_1}{l_3 \boldsymbol{e}_{A1}^T \boldsymbol{\delta}_{l3}} +$$
$$\frac{\boldsymbol{\delta}_{l3} [\boldsymbol{\tau}_1 - \boldsymbol{e}_{A1}^T \left(2 m_3 \boldsymbol{a}_{l3} - 2 m_3 g + m_7 \boldsymbol{a}_{A1} - m_7 g\right) + m_{A1} g - m_{A1} a_{A1}]}{\boldsymbol{e}_{A1}^T \boldsymbol{\delta}_{l3}} \tag{34}$$

Further, substituting Eq. (34) into Eq. (29), then we have

$$\boldsymbol{F}_C = \boldsymbol{F}_{Rc} + \boldsymbol{F}_{Rd} - m_7 \boldsymbol{a}_C + m_7 g \tag{35}$$

4.3   Dynamic equations of moving platform

The moving platform of the 2T1R PM is subject to its own gravity $m_1 g$ and the counter-forces $\boldsymbol{F}_D$ and $\boldsymbol{F}_C$ of hybrid chains I and II. The external force and external moment are defined as $\boldsymbol{F}_W$ and $\boldsymbol{M}_W$, as shown in Figure 6.
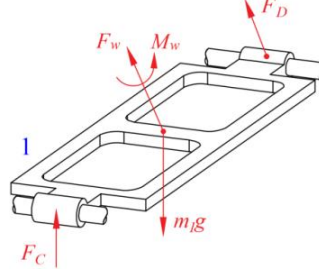
Fig. 6. Force analysis of moving platform

Therefore, the dynamic equations of the moving platform are given by

$$\boldsymbol{F}_w + \boldsymbol{F}_C + \boldsymbol{F}_D + m_1 g = m_1 \boldsymbol{a}_0 \tag{36}$$

$$\boldsymbol{M}_w + l_1 \boldsymbol{\delta}_{l1} \times \boldsymbol{F}_C / 2 - l_1 \boldsymbol{\delta}_{l1} \times \boldsymbol{F}_D / 2 = {}^o\boldsymbol{I}_{o'} \boldsymbol{\varepsilon}_{l1} + \boldsymbol{\omega}_{l1} \times \left({}^o\boldsymbol{I}_{o'} \boldsymbol{\omega}_{l1} \right) \tag{37}$$

Where ${}^o\boldsymbol{I}_{o'} = {}^o\boldsymbol{R}_{o'} \boldsymbol{I}_{o'} {}^o\boldsymbol{R}_{o'}^T$; ${}^o\boldsymbol{I}_{o'}$ is the projection matrix of the moving platform with respect to the inertia matrix of point O in the frame coordinate system; ${}^o\boldsymbol{R}_{o'}$ represents the transformation matrix of moving coordinate system with respect to base coordinate system; $\boldsymbol{I}_{o'}$ is the projection matrix of the moving platform with respect to the inertia matrix of point O' in the moving coordinate system.

Substituting Eqs. (22) and (35) into Eqs. (36) and (37), the complete dynamic equations of the 2T1R PM are written as follows in general form in the task-space.

$$\begin{vmatrix} \boldsymbol{D} \\ \boldsymbol{E} \end{vmatrix}_{6\times 1} = \boldsymbol{J}_\tau \cdot \boldsymbol{\tau} + \begin{vmatrix} \boldsymbol{F}_w \\ \boldsymbol{M}_w \end{vmatrix}_{6\times 1} \Rightarrow \boldsymbol{\tau} = \boldsymbol{J}_\tau^{-1} \cdot \begin{vmatrix} \boldsymbol{D} \\ \boldsymbol{E} \end{vmatrix} - \begin{vmatrix} \boldsymbol{F}_w \\ \boldsymbol{M}_w \end{vmatrix} \tag{38}$$

Where,

$$\boldsymbol{D} = \frac{\boldsymbol{\delta}_{l3}\left[\mathbf{e}_{A1}^T\left(m_7 a_{A1} - m_7 g + 2m_3 \mathbf{a}_{l3} - 2m_3 g\right) + m_{A1} g - m_{A1} a_{A1}\right]}{\mathbf{e}_{A1}^T \boldsymbol{\delta}_{l3}}$$

$$+ \frac{\mathbf{e}_{A1} \times \mathbf{C}_1}{l_3 \cdot \mathbf{e}_{A1}^T \boldsymbol{\delta}_{l3}} + \frac{\boldsymbol{\delta}_{l4}\left[e_{A2}^T\left(m_4 \mathbf{a}_{l4} - m_4 g\right) - m_{A2} g + m_{A2} a_{A2}\right]}{\mathbf{e}_{A2}^T \boldsymbol{\delta}_{l4}} + \frac{\mathbf{e}_{A2} \times \mathbf{C}_2}{l_4 \cdot \mathbf{e}_{A2}^T \boldsymbol{\delta}_{l4}}$$

$$+ \frac{\boldsymbol{\delta}_{l5}\left[e_{A3}^T\left(m_5 \mathbf{a}_{l5} - m_5 g\right) - m_{A3} g + m_{A3} a_{A3}\right]}{\mathbf{e}_{A3}^T \boldsymbol{\delta}_{l5}} + \frac{\mathbf{e}_{A3} \times \mathbf{C}_3}{l_5 \cdot \mathbf{e}_{A3}^T \boldsymbol{\delta}_{l5}}$$

$$+ m_3\left(\mathbf{a}_C - g\right) + m_6\left(\mathbf{a}_D - g\right) + m_1\left(\mathbf{a}_0 - g\right)$$

$$E = -\frac{1}{2} l_1 \boldsymbol{\delta}_{l1} \times \left\{ \frac{\boldsymbol{\delta}_{l4}\left[e_{A2}^T\left(m_4 \mathbf{a}_{l4} - m_4 g\right) - m_{A2} g + m_{A2} a_{A2}\right]}{\mathbf{e}_{A2}^T \boldsymbol{\delta}_{l4}} + \frac{\mathbf{e}_{A2} \times \mathbf{C}_2}{l_4 \cdot \mathbf{e}_{A2}^T \boldsymbol{\delta}_{l4}} \right\}$$

$$- \frac{1}{2} l_1 \boldsymbol{\delta}_{l1} \times \left\{ \frac{\boldsymbol{\delta}_{l5}\left[e_{A3}^T\left(m_5 \mathbf{a}_{l5} - m_5 g\right) - m_{A3} g + m_{A3} a_{A3}\right]}{\mathbf{e}_{A3}^T \boldsymbol{\delta}_{l5}} + \frac{\mathbf{e}_{A3} \times \mathbf{C}_3}{l_5 \cdot \mathbf{e}_{A3}^T \boldsymbol{\delta}_{l5}} \right\}$$

$$+ \frac{1}{2} l_1 \boldsymbol{\delta}_{l1} \times \left\{ \frac{\boldsymbol{\delta}_{l3}\left[e_{A1}^T\left(m_7 a_{A1} - m_7 g + 2m_3 \boldsymbol{a}_{l3} - 2m_3 g\right) + m_{A1} g - m_{A1} a_{A1}\right]}{\mathbf{e}_{A1}^T \boldsymbol{\delta}_{l3}} \right\}$$

$$+ \frac{1}{2} l_1 \boldsymbol{\delta}_{l1} \times \left[\frac{\mathbf{e}_{A1} \times \mathbf{C}_1}{l_3 \cdot \mathbf{e}_{A1}^T \boldsymbol{\delta}_{l3}} + m_6\left(g - \boldsymbol{a}_D\right) - m_3\left(g - \boldsymbol{a}_C\right) \right] + {}^o\boldsymbol{I}_{o'} \boldsymbol{\varepsilon}_{l1} + \boldsymbol{\omega}_{l1} \times \left({}^o\boldsymbol{I}_{o'} \boldsymbol{\omega}_{l1} \right)$$

$$
J_\tau = \begin{vmatrix}
\dfrac{\boldsymbol{\delta}_{l3}}{\boldsymbol{e}_{A1}^T \boldsymbol{\delta}_{l3}} & \dfrac{\boldsymbol{\delta}_{l4}}{\boldsymbol{e}_{A2}^T \boldsymbol{\delta}_{l4}} & \dfrac{\boldsymbol{\delta}_{l5}}{\boldsymbol{e}_{A3}^T \boldsymbol{\delta}_{l5}} \\[2mm]
\dfrac{l_1 \boldsymbol{\delta}_{l1} \times \boldsymbol{\delta}_{l3}}{2\boldsymbol{e}_{A1}^T \boldsymbol{\delta}_{l3}} & -\dfrac{l_1 \boldsymbol{\delta}_{l1} \times \boldsymbol{\delta}_{l4}}{2\boldsymbol{e}_{A2}^T \boldsymbol{\delta}_{l4}} & -\dfrac{l_1 \boldsymbol{\delta}_{l1} \times \boldsymbol{\delta}_{l5}}{2\boldsymbol{e}_{A3}^T \boldsymbol{\delta}_{l5}}
\end{vmatrix}_{6\times 3}
$$

$$
\boldsymbol{\tau} = \begin{bmatrix} \boldsymbol{\tau}_1 & \boldsymbol{\tau}_2 & \boldsymbol{\tau}_3 \end{bmatrix}_{3\times 1}^T
$$

When the motion law of the moving platform and the external force and torque are known, the driving force of each driving slider can be obtained from equation (38).

5   Example analysis and simulation

The process of establishing a dynamic model based on N-E method is shown in Figure 7.
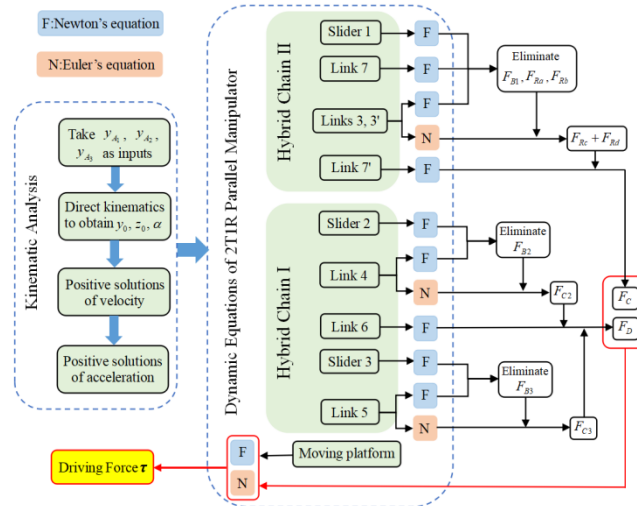
Fig. 7. Algorithm for solving the inverse dynamics of the PM

Taking the moving platform to perform 2T1R motion in a certain range as an example, let the motion law of driving sliders is

$$
\begin{cases}
y_{A1} = -80\sin(t) + 38 \\
y_{A2} = -40\sin(t) - 121 \\
y_{A3} = 20\sin(t) + 123
\end{cases}
\tag{39}
$$

The motions of all links of the PM can be naturally obtained by direct kinematics. Simultaneously, let each link is a rigid body with regular shape and uniform quality. The parameters of this PM are shown in Table 1.

By putting the values of the parameters in Table 1 into the dynamic model Eq. (38), the theoretical curve of the driving force with respect to time(s) can be obtained, as

shown by the line — in Figure 8. Then, a virtual prototype is established in ADAMS and set material properties of the each link, the constraint type of joints and gravity. This simulation step size and time are 0.01s and 10s respectively, and the dynamic simulation curve is shown as the line * in Figure 8.

As shown in Figure 8, the results of the analytical and commercial software are very close. The maximum relative errors of the driving forces of sliders are respectively 4.71% and 2.87%, 3.7%, which verify the correctness of the kinematic and dynamic model. The reason for the errors in each driving force is that joint friction is not considered.

Table 1. Parameters of 2T1R PM

Size parameters	Value
Moving platform length l_1	220 mm
Driving link 2 height l_2	37.5 mm
Links 3, 3' length l_3	180 mm
Links 4, 5 length l_4	180 mm
Link 6 length $2l_6$	2*45 mm
Links 7, 7' length l_7	80 mm
Distance between rails $2a$	2*125 mm
Rail length lp	300 mm
Moving platform mass m_1	0.9324 kg
Slider 1 mass m_{A1}	0.03234 kg
Slider 2 mass m_{A2}	0.03298 kg
Slider 3 mass m_{A3}	0.03298 kg
Links 3, 3'' mass m_3	0.08481 kg
Links 4, 5 mass m_4	0.08481 kg
Link 6 mass m_6	0.03678 kg
Links 7, 7' mass m_7	0.03377 kg
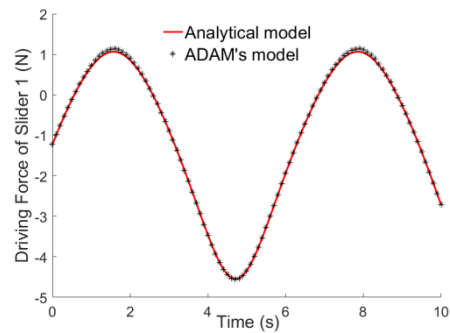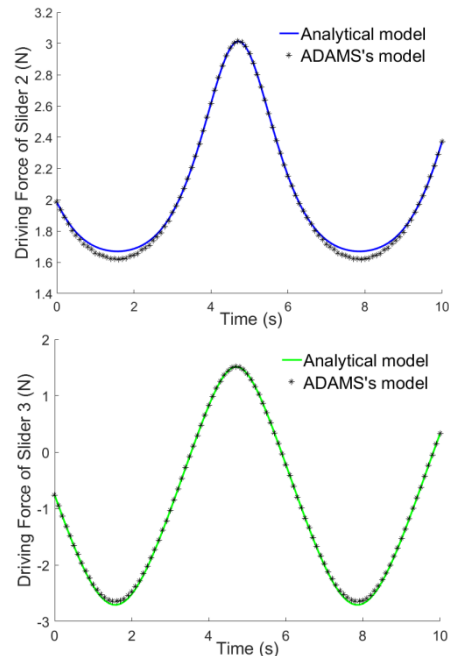
Fig. 8. Comparison of the analytical and ADAMS's model of each driving force

6   Conclusions

(1) According to the kinematics modeling and solving method based on topological characteristics, the symbolic direct position solution of the 2T1R PM is obtained, and the calculation formulas of the velocity and acceleration of each link are derived based on the direct kinematics.

(2) Using the hybrid chain as the unit, the N-E method is used to solve the inverse dynamic equations of the PM, and the result of the analytical and commercial software verifies the correctness of the dynamic analysis method. Dynamic results in this paper build a theoretical foundation for the design, manufacture and motion control of this PM.

(3) This paper deals with the dynamic analysis of the 2T1R PM based on the symbolic direct kinematics. Its advantage lies in simplifying the kinematics solution process and improving the efficiency of the inverse dynamics solution. The subsequent use of symbolic direct kinematics for error compensation of dynamics equations can greatly improve the accuracy of solving dynamic equations.

References

1. Refaat, S., Nahavandi, S., Trinh, H., et al..: Asymmetrical three-DOFs rotational-translational parallel-kinematics mechanisms based on Lie group theory. European Journal of Mechanics-A/Solids 25(3), 550-558 (2006).
2. Jiaming, D., Ke, X., Yingchun, Z.: Design and kinematics of an asymmetric 2T1R-type spatial parallel mechanism without parasitic motion. Transactions of the Chinese Society for Agricultural Machinery 49(6), 408-417 (2018).
3. Yimin, S., Xuedong, Z., Tao, S.: Stiffness analysis of a 3-DOF redundantly actuated parallel module. Journal of Tianjin University 48(1), 25-32 (2015).
4. Ziming, C., Xiaomeng, L., Yang, Z.: Dynamics analysis of a symmetrical 2R1T 3-UPU parallel mechanism. Journal of Mechanical Engineering 53(21), 46-53 (2017).
5. Xiangyang, W., Sheng, G., Haibo, Q.: Optimal allocation method of parallel mechanism and its application. Journal of Mechanical Engineering 55(1), 44-53 (2019).
6. Xiulong, C., Decai, S., Qing, W.: Rigid dynamics modeling of redundant actuation parallel mechanism based on lagrange method. Transactions of the Chinese Society for Agricultural Machinery 46(12), 329-336 (2015).
7. Guiyang, Xin., Hua, D., Guoliang, Z.: Closed-form dynamics of a 3-DOF spatial parallel manipulator by combining the Lagrangian formulation with the virtual work principle. Nonlinear Dynamics 86(2), 1329-1347 (2016).
8. Philip, L., Wisama, K., Philippe, M.: Dynamic modeling of parallel robots with flexible platforms. Mechanism and Machine Theory: Dynamics of Machine Systems Gears and Power Trandmissions Robots and Manipulator Systems Computer-Aided Design Methods 81, 21-35 (2014).
9. Yanbiao, L., Hang, Z., Peng S.: Dynamic modeling with joint friction and research on the inertia coupling property of a 5-PSS/UPU parallel manipulator. Journal of Mechanical Engineering 55(03), 43-52 (2019).
10. Ling, Lu., Jiantao, Y., Weidong, G.: Dynamics analysis of 5UPS/PRPU parallel machine tool with redundant actuation based on Kane Equation. Transactions of the Chinese Society for Agricultural Machinery 47(6), 366-372 (2016).
11. Gang, C., Xianlei, S.: Dynamics analysis of a parallel hip joint simulator with four degree of freedoms (3R1T). Nonlinear dynamics 70(4), 2475-2486 (2012).
12. Latifah, N., Dongming, G.: Dynamic analysis of the 3-RRPS metamorphic parallel mechanism based on instantaneous screw axis. In: International Design Engineering Technical Conferences and Computers and Information in Engineering Conference, Vol. 59230, pp. V05AT07A064, (2019).
13. Huiping, S., Jinbo, Z., Jingjing, Y.: A 2T1R parallel mechanism with analytic direct position solutions and its kinematic performance based optimization. Transactions of the Chinese Society for Agricultural Machinery 51(1), 398-409 (2020).
14. Tingli, Y., Anxin, L., Yufeng, L.: Theory and application of robot mechanism topology. Science Press, Beijing (2012).
15. Tingli, Y., Anxin, L., Huiping, S.: Topology design of robot mechanisms. Springer, Singapore (2018).
16. Tingli, Y.: Topology structure design of robot mechanisms. China Machine Press, Beijing (2004).

Robot station planning algorithm for high energy beam machining of large size workpiece

Xuewei Wang[1], Shijin Zhang[2*], Wenkang Zhou[1], Yue Zhao[2] and Kenji Yoshigoe[3]

[1] Shanghai Key Lab of Intelligent Manufacturing and Robotic, School of Mechatronic Engineering and Automation, Shanghai University, Shanghai, 200072, China
[2] School of Software, Northwestern Polytechnical University, Taicang, Jiangsu, 215400, China
[3] Department of Electrical Engineering and Computer Science, Embry-Riddle Aeronautical University, Daytona Beach FL, 32114, USA
*Corresponding author, Shijin Zhang: 1487383759@qq.com

Abstract. In order to further improve the flexibility of high energy beam (HEB) machining tools, the robotic arm (RA) has been applied in this field. Recently, the RA is installed upside down on the additional XY axis to machine the large size workpiece. However, the station planning of RA has become a difficult problem during sub-station machining. In this paper, a station planning method based on simulated annealing algorithm (SA) was proposed to solve it. First, the 3D feasible station space (FSS) of the RA is obtained by the Monte Carlo method after the DH inverse modeling. And the 2D feasible station area (FSA) at the height of the RA base plane is obtained by calculation. Second, by further reducing the set of 2D FSAs, the shrunken station areas to be selected are obtained. Finally, SA is used to select a specific station point from each shrunken FSA in the set. The simulation results show that this method significantly saves the time of station planning, improves the accuracy of the station, and successfully completes the HEB machining of the large size workpiece.

Keywords: High energy beam machining, robotic arm, station planning, large size.

1 Introduction

With the development of science and technology, the machining method evolves from the traditional turning, milling, grinding and boring to the HEB machining. The emergence of HEB machining solves the special machining problems of complex shape, small hole, narrow gap and the machining of high strength, high hardness, high toughness and high brittleness materials. However, most traditional HEB machining machines only have three degrees of freedom XYZ, which makes it difficult to compensate the errors caused by the characteristics of HEB machining, such as focus position error in laser cutting, taper error and drag error in abrasive water jet (AWJ) cutting. Nowadays, with the development of robotics technology, the application of RAs is more extensive. Therefore, some researchers studying HEB machining try to apply RAs to HEB machining.
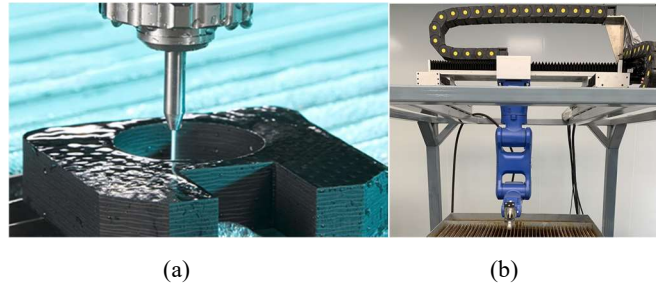
(a)   (b)

Fig. 1. Equipment: (a) AWJ cutting, (b) AWJ eight axis machine

However, the problem of the limited reach range of the RA exists during machining some large size workpieces. Therefore, Zhou et al. [1] proposes that the RA can be installed on a platform upside down, and the platform should be installed on two external XY axes, so that the position of the RA base can be changed by the external axes. In this method, the machining path needs to be segmented, and the RA is placed on a certain station to machine one or more segments of the machining path. The station position can be selected manually, but manual selection often results in high time cost of selection and the unreasonable segmentation of machining path. Generally, RA station points affect the machining efficiency and accuracy. Therefore, it is necessary to establish a RA station planning algorithm for HEB machining to select the reasonable and favorable station. There are two main problems. One is the selection of the search algorithm for the station planning, and the other is the selection of evaluation parameters for evaluating the station.

For the first problem, many scholars complete some researches, and use a variety of algorithms to select the best station. Carrikerp [2]et al. propose a direct search heuristic algorithm which takes the pose and force stability of the end effector as evaluation parameters. Afterwards, Carrikerp [3] use the SA for the selection of the optimal station point. R Raja [4] proposes a new method for motion planning of redundant mobile manipulators. Synodinos, Aris I [5] proposes a fuzzy system which is trained to approximate the manipulability index and the inverted condition number. Zeng Debiao [6] proposes a hybrid optimization algorithm for machining station setting.

For the second question, researchers use many evaluation parameters to select station, such as joint angle error[2], terminal stability [7, 8], stiffness and obstacle avoidance [9], operability [10, 11], robot running speed [12], execution efficiency optimization [13], environment perception online optimization [14], topology coverage efficiency optimization [15], and singularity avoidance [16].

Later, Ren [17] et al. introduce the concept of FSS of the base by re-establishing the DH coordinate system of the RA to determine the optional area. Also, Ren [18] establishes a numerical method to solve the intersection of the feasible position space of the foundation, and the maximum working area can be determined by solving the optimization problem. Afterwards, Yu Qiankun [19] proposes two effective base position optimization methods for mobile painting robot: one is based on the internal penalty function method to obtain the initial base position; the other is to obtain the approximate optimal base position based on the generalized Lagrange multiplier method. However,

most of the above studies are based on spraying and assembly RA, and there are few researches based on HEB machining. Due to some special requirements of HEB machining, such as machining continuity, machining accuracy, etc., evaluation parameters need to reconsider the stability and continuity. Therefore, theories proposed by the past scholars have some limitations when applied to the HEB machining. Moreover, the search algorithm in the past is inefficient due to the large search range, and the global optimal solution of the station position cannot be calculated due to local convergence.

Therefore, this work proposed a station planning method based on the SA. First, the machining path should be reasonably divided according to the machining feature points. Second, the intersection of the FSA was calculated by the Boolean operation to reduce the search range, which improved efficiency. At last, the stability of the RA was used as the evaluation parameter of the maximum weight to optimize the station.

2   Acquisition of base station area

2.1   Acquisition of 3D feasible station space

Due to the fact that some points to be machined cannot be machined at the station position selected manually, Ren [17] proposes the concept of FSS.

First, the wrist center is determined before the reverse modeling. Now most industrial RAs meet Pieper criterion, that is, three adjacent joint axes intersect at the same point or are parallel to each other. As long as one of the conditions is satisfied, the closed solution can be obtained. And the RA selected here meets the first condition. The 4, 5 and 6 axes intersect at A, which is defined as the wrist center. Therefore, in the space which is the reachable range of the wrist center in fact, the end of the RA can swing at any angle to compensate the taper error, drag error in AWJ cutting and focus position error in laser cutting.

Reverse DH modeling is designed based on forward DH model, as shown in Fig.2(b), taking the wrist center A as the new base and original base O as the end execution point of reverse DH model. The following description is based on Fig. 2(b).
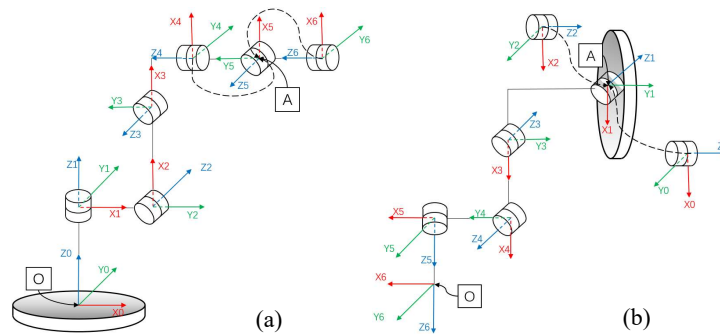

(a)   (b)

Fig. 2. DH coordinate system of RA: (a) forward DH, (b) inverse DH

4

Table 1. DH parameters of reverse model for YASAKAWA GP8/AR700 RA

i	Length of member a_i/mm	Torsion angle of member α_i/(°)	Joint distance d_i/mm	Joint angle θ_i/(°)
1	0	-90	0	θ_1
2	0	90	0	θ_2
3	40	-90	-340	θ_3
4	345	180	0	θ_4
5	40	-90	0	θ_5
6	0	0	330	θ_6

After the reverse modeling, Monte Carlo method is used to calculate the reachable space range of the reverse DH model as shown in Fig. 3, which is the FSS of the original RA base O. the method mainly consists of the following steps:

1. The rotation angle range of the 6 joint axes is continuously and evenly distributed to obtain the N ($N = 500000$) groups of rotation angle value of each joint. And the N possible values of each joint are shuffled and saved into a matrix of $N * 6$. This method can uniformly get all possible values in the angle range, and the probability density of every angle value is $\frac{1}{MAX-M}$, where MAX is the upper limit of the angle value, MIN is the lower limit of the angle value.

$$\theta = \begin{bmatrix} \theta_1(1) & \theta_2(1) & \dots & \theta_6(1) \\ \theta_1(2) & \theta_2(2) & \dots & \theta_6(2) \\ \dots & \dots & \dots & \dots \\ \theta_1(N) & \theta_2(N) & \dots & \theta_6(N) \end{bmatrix} \tag{1}$$

2. Based on the inverse DH model, the position of the end execution point O corresponding to the joint angle of each row is calculated by forward kinematics. Finally, according to the N groups of joint angle value, the positions of the end execution points are calculated.

Table 2. N groups of joint angle

n	θ_1/(°)	θ_2/(°)	θ_3/(°)	θ_4/(°)	θ_5/(°)	θ_6/(°)	θ_7/(°)
1	0	211.1328	-29.4465	-98.6785	15.5604	-130.0795	-17.4756
2	0	-294.631	-74.6079	120.1722	-3.4479	-72.1570	0.1601
				……			
N	0	130.8467	-11.0669	30.2862	93.8629	18.4620	141.8675

3. This method needs to extract the boundary of the point cloud and calculate the approximate envelope surface of the point cloud by the aggregation point method. Also, it creates a surface around the cluster of three or more points within the aggregation distance to envelope the point cloud and visualize it. The space within the envelope surface obtained through the above three steps is the FSS of the RA base.
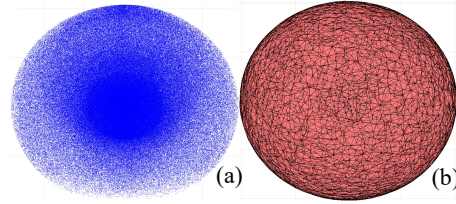
Fig. 3. Point cloud: (a) point cloud of FSS, (b) envelope of point cloud

2.2 Calculation of 2D feasible station area

A machining trajectory is composed of straight lines, arcs and splines. In the USMART® 3D CAM（3D CAM software）developed by our research group, some feature points, such as the end points of the straight line segment, the two end points and an intermediate point used to determine the shape of the arc and the control points of the spline curve, can be identified from the entire trajectory. Also, the position and posture parameters (RPY Euler angle) of the RA can be obtained by the software.

After that the position of the external axis used to install the RA base in the height direction of the Z axis is determined, the plane where external axes stay is used to cut the above FSS. As shown in Fig. 4(b), the 2D FSA of the base is obtained after it. The circle-like section corresponding to each feature point is the RA station area that can machine the feature point under the installation height of the base. In Fig. 4(c), the thickness of the workpiece to be machined is enlarged to indicate the size difference of 2D FSA caused by the height difference of Z-axis.
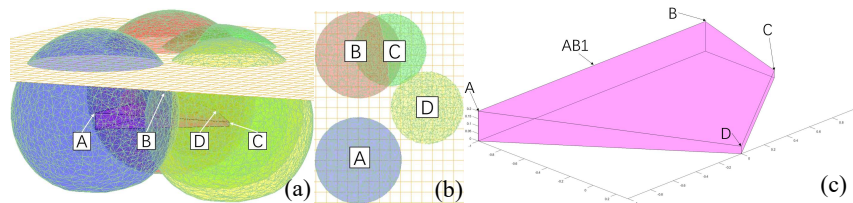
Fig. 4. Spatial section of feasible station: (a) 3D view, (b) 2D view, (c) workpiece

Since each feature point of the trajectory to be machined corresponds to a FSA, in order to facilitate the calculation of the search algorithm, our work fitted the edge of the circle-like FSA. Considering the accuracy of the fitting, our work used the least square method to fit it, the steps are as follows:

1. The formula of circular curve can be written as follows:

$$(x - x_c)^2 + (y - y_c)^2 = R^2 \tag{2}$$

Obviously, only if the center and radius of the circle are determined, the fitting of the point cloud is completed, and the least square fitting requires the sum of squares of the distance to be the smallest. Then, the following objective function is established.

6

$((x_i, y_i)$ $(i = 1,2, \cdots, \ n)$ is the point cloud coordinate data, (x_c, y_c) is the coordinate of the center of the circle)

$$f = \sum_{i=1}^{n}\left(\sqrt{(x_i - x_c)^2 + (y_i - y_c)^2} - R\right)^2 \tag{3}$$

2. In order to facilitate the calculation, the objective function is improved into the following formula:

$$f = \sum_{i=1}^{n}\left((x_i - x_c)^2 + (y_i - y_c)^2 - R^2\right)^2 \tag{4}$$

Expand it and substitute variables:

$$f = \sum_{i=1}^{n}(x_i^2 + y_i^2 + Ax_i + By_i + C)^2 \quad (A = -2x_c, B = -2y_c, C = x_c^2 + y_c^2 - r^2) \tag{5}$$

3. According to the method of least square, it is necessary to determine the parameters A, B, and C to ensure that the objective function f can get the minimum value. The partial derivative method is used to determine A, B, and C to obtain x_c、 y_c and r.

After the boundary of all FSAs are determined, it is necessary to further narrow the search range. Therefore, Boolean operations are performed on obtained FSA to find their intersection. Assuming that point A is the starting point of machining, the intersection of adjacent FSA is obtained in turn according to the machining direction of the trajectory. Obviously, there is no intersection between the two areas at some time. For example, the FSA corresponding to point A and point B do not intersect. At this time, an intermediate feature point $AB1$ needs to be added as shown in Fig. 4(c).

The new feature points are selected by default as the midpoint of the line segment intercepted by the feature points at both ends, the midpoint of the arc and the middle control point of the spline curve. As shown in Fig. 5, points 1 and 2 are the feature points corresponding to the two FSA without intersection.
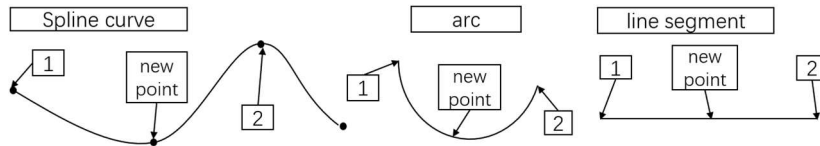
Fig. 5. Selection rules of new feature points

In Fig. 6, $ABCD$ represent the FSAs corresponding to feature points $ABCD$. Then a Boolean operation is performed between the FSA of the first feature point A and the FSA of the next feature point. That is, the FSA corresponding to A and the FSA corresponding to $AB1$ are combined to obtain the FSA $a2$. Here, the number following a in $a2$ represents the number of feature points that can be machined in this area, so the RA can machine the trajectory between A and B in area $a2$.

Clearly, there is no intersection between area $a2$ and the FSA corresponding to point B in Fig. 6. At this time, area $a2$ is saved as A_1 in the set $\sum A$ ($\sum A = \{A_1, A_2, \cdots, A_n\}$) which is used to store station areas to be selected.

$$A \cap AB1 = a2 \qquad a2 \cap B = \emptyset \qquad AB1 \cap B = b2 \qquad b2 \cap C = b3 \qquad b3 \cap D = \emptyset$$
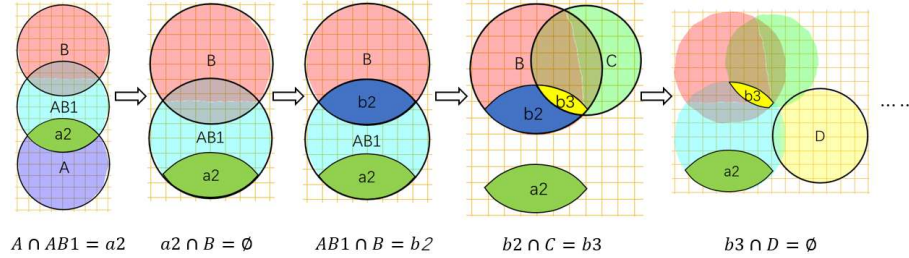
Fig. 6. Boolean operation diagram

Then, the intersection of the FSA corresponding to the point $AB1$ and the point B is calculated to obtain the area $b2$. Similarly, the area $b2$ is the station area where the RA can machine the trajectory between $AB1$ and B. At this time, the Boolean operation is performed between the area $b2$ and the FSA of the point C to get the new intersection area $b3$. In other words, the RA can machine the trajectory from $AB1$ to B and then to C in area $b3$. Obviously, there is no intersection between the area $b3$ and the FSA of the point D, so the area $b3$ is directly saved to the set $\sum A$ as A_2. And the process is repeated until the intersections of the FSA between all adjacent feature points are calculated to obtain final reduced FSA set $\sum A$.

Each element A_i represents a reduced FSA, such as the above area $A_1(a2)$ and $A_2(b3)$. The Boolean operation essentially merges the machining objects with the same feasible machining station.

3 Optimization algorithm for base station point

3.1 Determination of the optimal evaluation function

To get the set $\sum P$ of station points of the RA, it is necessary to further select a suitable station point in each reduced area A_i. That is to select optimal station points from $a2$, $b3$ and each subsequent area. This paper processes A_i based on the discretization strategy. And the method used to determine the coordinate of discrete point $p_{ij} = (x_{pij}, y_{pij})$ in the area A_i refers to the following formula:

$$\begin{cases} x_{p_{ij}} = x_{min}(i) + (x_{max}(i) - x_{min}(i)) * rand \\ y_{p_{ij}} = y_{min}(i) + (y_{max}(i) - y_{min}(i)) * rand \end{cases}, (0 < rand < 1) \qquad (6)$$

Among them, $rand$ is a random number generated by the program. The i in p_{ij} is the serial number of the area A_i. The j in p_{ij} represents the serial number of the discrete points in the area A_i. $x_{min}(i), x_{max}(i)$ represents the leftmost and rightmost X coordinates of the area A_i, $y_{min}(i), y_{max}(i)$ are the same rationale.

Obviously, the random point p_{ij} generated by this formula may does not fall in the area of A_i with a certain probability. Thus, this work used the ray method to judge it. If the point is not in the area, a new random point is generated. And the new random

point is judged whether it overlaps with other station points participating in the comparison before. If they overlap, a new random point is also generated.

In Fig.7, point M is the last feature point that the RA can machine in the station point p_{11}. At the same time, M is the first feature point that the RA can machine in the station point p_{21}. When the end execution point of the RA is located at the relay feature point M, θ_m is the mth joint angle value with the base of the RA located at p_{11} in A_1, and θ'_m is the mth joint angle value with the base of the RA located at p_{21} in A_2.
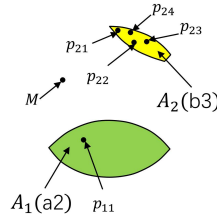

Fig. 7. The relay feature point M

According to the influence degree of each axis on the stability of the end execution point, the following weighted evaluation formula is determined:

$$D = k_1 D_1 + k_2 D_2 + k_3 D_3 + k_4 D_4 + k_5 D_5 + k_6 D_6 \qquad (7)$$

$$D_m = |\theta'_m - \theta_m|, \ (m = 1, 2, \cdots, 6) \qquad (8)$$

Where $k_1, k_2, \cdots, k_6$ are the weighting coefficients of the changes of the six joint angles, which satisfy the following relationships:

$$k_1 \geq k_2 \geq k_3 \geq k_4 \geq k_5 \geq k_6, k_1 + k_2 + k_3 + k_4 + k_5 + k_6 = 1 \qquad (9)$$

For the field of HEB machining, $k_1 = 0.35, k_2 = k_3 = 0.25, k_4 = k_5 = k_6 = 0.05$.

The premise of optimization is to determine an evaluation function as a reference. Due to the HEB's requirements for continuity, stability, etc., it is necessary to ensure that the rotation range of the end execution point of the RA is small. And the method of transferring station without shutdown is adopted. The stability of the RA has a direct impact on whether the end execution point can be stably located at the last feature point during transferring station. Therefore, this paper takes the sum D of the variation differences of each joint angle θ_m as the standard to compare the station points. Also, the smaller the D is, the more stable the RA is during transferring station. While calculating the angle change of each joint during moving, the inverse solution of each RA joint can be calculated by using the numerical method of 6R RA.

3.2 Simulated annealing optimization algorithm

Because each area A_i has many discrete station points p_{ij}. If the exhaustive method is used, the calculation amount is large and the speed is slow, also the general hill climbing algorithm is easy to fall into the local optimum. So this paper used the SA, which is essentially a random search algorithm. During the search process, the Metropolis

criterion which have a relatively high efficiency is used to judge whether to jump out the current optimal solution and to continue to search a global optimal solution.

The algorithm has three elements: solution space, initial solution, and evaluation function. The solution space is the discrete station point p_{ij} in each area A_i. The initial solution is the first randomly station point in the area A_i, such as the point p_{21} in A_2 in Fig. 7, and the evaluation function is D. The specific steps are as follows:

1. Determine the station of the robotic arm in the first area A_1. As the first station, there is no object that can be used for comparison. Therefore, the station of the robotic arm in A_1 is discretized by using the formula (6) and randomly selected.
2. Continue to carry out the optimization operation on the second FSA A_2, randomly select a point p_{21} in area A_2 as the initial solution of SA, and then select the randomly generated point p_{22} in area A_2 to compare with p_{21}. If the current random point p_{22} is better, select the random point as the current optimal station point. Otherwise, Metropolis criterion is used to judge whether to jump out of the current optimal station point and continue to search for the next station point p_{23}.
3. Metropolis criterion: It is explained that $D(ij)$ is the evaluation function of the current optimal station point p_{ij} in A_i, $D(i(j+1))$ is corresponding to the next randomly generated station point $p_{i(j+1)}$, $\Delta D = D(i(j+1)) - D(ij)$. If $\Delta D > 0$, a random number $\alpha(0 < \alpha < 1)$ is generated and compared with $exp(-\Delta D/T)$. If $\alpha < exp(-\Delta D/T)$, the station point $p_{i(j+1)}$ is accepted as the new station point used for next comparison, otherwise, it is rejected. Because the parameter T used to control the probability gradually decreases with time, the probability of accepting the deteriorated solution also decreases, so as to ensure the efficiency of the algorithm.
4. Repeat Step 2 and 3, calculate the optimal station point p_i corresponding to each area A_i, and save these station points into the set $\sum p = \{p_1, p_2, \cdots, p_n\}$. $\sum p$ is the set of RA station points that are ultimately used for complete path machining.

4 Experimental verification

Limited by the travel range of the laboratory platform is, it is difficult to conduct experiments using real machine. Thus, we used simulation method to verify the feasibility of the algorithm. The graph of simulation verification is shown in Fig. 8.
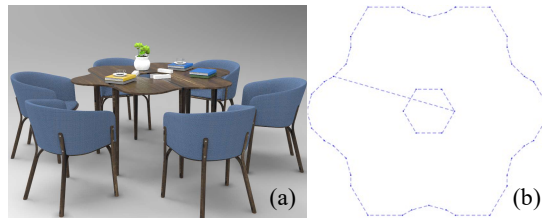

Fig. 8. Model: (a) conference table, (b) line diagram of feature points

Firstly, the model was imported into 3D CAM software to get feature points. Secondly, after calculating by the above optimization algorithm, the three RA machining station areas A_1, A_2 and A_3 were obtained as shown in Fig. 9(a). Thirdly, the three station points p_1, p_2, and p_3 were calculated iteratively. The method of judging whether the machining point was reachable was used to verify the correctness of the station. the three circles in Fig. 9(b) were the reachable range of the end execution point when the RA base was in the station points p_1, p_2, and p_3. It can be seen in Fig. 9(b) that the three stations are able to complete the machining of the entire path.
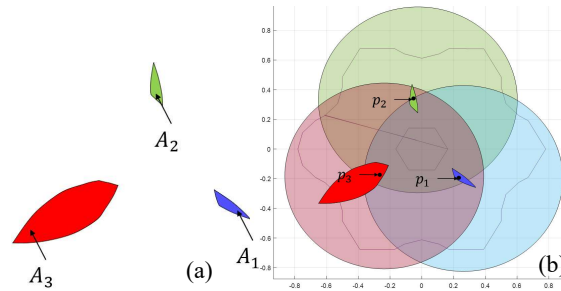
Fig. 9. Feasible station areas and points: (a) feasible station areas, (b) feasible station points

Obviously, because there was no reference target for the station point in the initial FSA A_1, p_1 was obtained randomly. Afterwards, the point p_2 was selected from the area A_2 after 58 iterations, and the point p_3 was selected from the area A_3 after 131 iterations. Finally, the whole optimization algorithm cost 7.85 seconds, which demonstrated that the algorithm was efficient. The Y-axis value in Fig. 10 omits two decimal places, and if a deteriorated station point is accepted in one iteration, the figure only shows the D corresponding to the current local optimal station point.
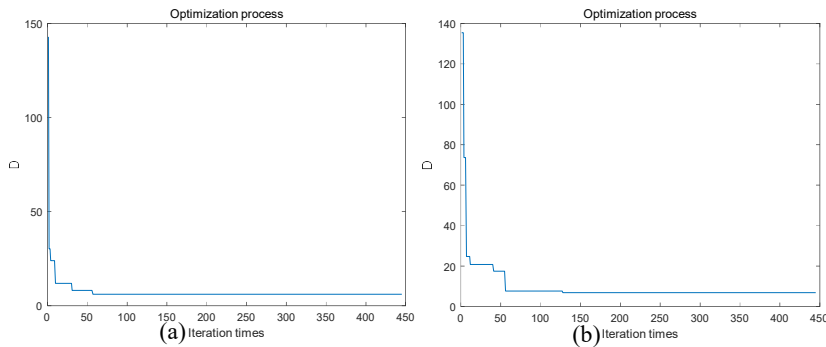
Fig. 10. Times of iterations: (a) p_2 iteration times, (b) p_3 iteration times

5   Conclusions

This work proposed a RA station optimization algorithm based on SA. This algorithm addressed the problem that HEB machine tools using multi-degree-of-freedom RAs

cannot automatically complete the station planning during machining large size work-pieces. According to the special characteristics of HEB machining, this work took the machining stability as the evaluation function, and used DH inverse modeling method to determine the 3D FSS to carry out the station planning. The method can ensure the machining accuracy and the validity of the station. Finally, our simulation results verified the feasibility and the high efficiency of the algorithm. Also, with some adjustments, the algorithm can also be applied to non-HEB machining scenarios, such as spraying or assembly robot station planning.

Acknowledgement

References

[1] W. Zhou, S. Zhang, and J. Xue, "A method to generate AWJ cutting path for a large-size part without well-defined location characteristics," *The International Journal of Advanced Manufacturing Technology,* vol. 108, no. 11, pp. 3807-3818, 2020.

[2] W. F. Carriker, P. K. Khosla, and B. H. Krogh, "An approach for coordinating mobility and manipulation," in *Proceedings of the International Conference on Systems Engineering*, 1989, pp. 59-63.

[3] W. F. Carriker, P. K. Khosla, and B. H. Krogh, "Path planning for mobile manipulators for multiple task execution," *IEEE Transactions on Robotics and Automation,* vol. 7, no. 3, pp. 403-408, 1991.

[4] R. Raja and A. Dutta, "Motion planning of a mobile manipulator using fuzzy controller to dexterity measures," in *2015 IEEE Workshop on Computational Intelligence: Theories, Applications and Future Directions (WCI)*, 2015, pp. 1-6: IEEE.

[5] A. I. Synodinos, V. C. Moulianitis, and N. A. Aspragathos, "A fuzzy approximation to dexterity measures of mobile manipulators," *Advanced Robotics,* vol. 29, no. 12, pp. 753-769, 2015.

[6] Z. Debiao, W. Shiming, L. Yingguang, L. Yong, and L. Dongming, "Hybrid optimization algorithm for processing station setting of assembly robot," *Journal of graphics,* vol. 37, no. 4, pp. 496-501, 2016.

[7] K. Alipour and S. A. A. Moosavian, "Dynamically stable motion planning of wheeled robots for heavy object manipulation," *Advanced Robotics,* vol. 29, no. 8, pp. 545-560, 2015.

[8] Q. Huang, S. Sugano, and K. Tanie, "Motion planning for a mobile manipulator considering stability and task constraints," in *Proceedings. 1998 IEEE International Conference on Robotics and Automation (Cat. No. 98CH36146)*, 1998, vol. 3, pp. 2192-2198: IEEE.

[9] F. G. Pin, J.-C. Culioli, and D. B. Reister, "Using minimax approaches to plan optimal task commutation configurations for combined mobile platform-manipulator systems," *IEEE Transactions on Robotics and Automation,* vol. 10, no. 1, pp. 44-54, 1994.

[10] D. H. Shin, B. S. Hamner, S. Singh, and M. Hwangbo, "Motion planning for a mobile manipulator with imprecise locomotion," in *Proceedings 2003 IEEE/RSJ International*

12

Conference on Intelligent Robots and Systems (IROS 2003)(Cat. No. 03CH37453), 2003, vol. 1, pp. 847-853: IEEE.

[11] D. Bing and Z. Jing, "Position optimization and motion planning of mobile manipulator platform," *High tech communication,* vol. 23, no. 5, pp. 546-552, 2013.

[12] A. Nektarios and N. A. Aspragathos, "Optimal location of a general position and orientation end-effector's path relative to manipulator's base, considering velocity performance," *Robotics and Computer-Integrated Manufacturing,* vol. 26, no. 2, pp. 162-173, 2010.

[13] Q.-V. Dang and L. Nguyen, "A heuristic approach to schedule mobile robots in flexible manufacturing environments," *Procedia Cirp,* vol. 40, pp. 390-395, 2016.

[14] Z. Qin, P. Wang, J. Sun, J. Lu, and H. Qiao, "Precise robotic assembly for large-scale objects based on automatic guidance and alignment," *IEEE Transactions on Instrumentation and Measurement,* vol. 65, no. 6, pp. 1398-1411, 2016.

[15] S. Seriani, P. Gallina, and A. Gasparetto, "A performance index for planar repetitive workspace robots," *Journal of Mechanisms and Robotics: Transactions of the ASME,* vol. 6, no. 3, 2014.

[16] S. Mitsi, K.-D. Bouzakis, D. Sagris, and G. Mansour, "Determination of optimum robot base location considering discrete end-effector positions by means of hybrid genetic algorithm," *Robotics and Computer-Integrated Manufacturing,* vol. 24, no. 1, pp. 50-59, 2008.

[17] R. Shunan, X. Yang, G. Wang, J. Lu, and K. Chen, "Station planning of mobile manipulator in large parts spraying," *Journal of Jilin University: Engineering Edition,* vol. 46, no. 6, pp. 1995-2002, 2016.

[18] S. Ren, X. Yang, J. Xu, G. Wang, Y. Xie, and K. Chen, "Determination of the base position and working area for mobile manipulators," *Assembly Automation,* 2016.

[19] Q. Yu, G. Wang, X. Hua, S. Zhang, L. Song, J. Zhang, and K. Chen, "Base position optimization for mobile painting robot manipulators with multiple constraints," *Robotics and Computer-Integrated Manufacturing,* vol. 54, pp. 56-64, 2018.

Kinematics of Hybrid Machining Robot Based on Screw Theory

Xin Tian[1,2] Tieshi Zhao[1,2*] Xiaoxiao Peng[1,2]

[1] Laboratory of Parallel Robot and Mechatronic System, Yanshan University, Qinhuangdao 066004, China
[2] Key Laboratory of Advanced Forging & Stamping Technology and Science （Yanshan University）, Ministry of Education of China, Qinhuangdao 066004, China
tszhao@ysu.edu.cn

Abstract. The application of hybrid machining robot has been more and more widely at present. This paper deals with the complete kinematics of hybrid machining robot based on screw theory. In order to establish the complete kinematics mapping relationship, the hybrid machining robot is modular disassembly by modular analysis method. Establish the equivalent relationship between the parallel module and the generalized screw series drive joints, so that the hybrid machining robot is treated as an equivalent series robot composed of drivers. According to such concept, two analysis examples of hybrid machining robots are given to verify the feasibility of this method. This method can be applied to solve a kind of hybrid mechanism.

Keywords: Hybrid machining robot, Kinematics, Screw theory.

1   Introduction

Compared with series mechanism, the parallel mechanism has the advantages of compact structure, high stiffness and large carrying capacity, but the working space is relatively small.[1] The hybrid mechanism can combine the advantages of the series mechanism and the parallel mechanism to meet the comprehensive performance needs of the working space and high stiffness of the processing robot. The Tricept [2,3] and the Exechon [4,5] processing robots and TriVariant hybrid robots [6,7] have achieved good results by using the mixed form of two rotations one translation(2R1T) three degree-of-freedom(DOF) parallel mechanism series multiple axes rotary spindle head. Hybrid robots in the form of parallel machining head in series with mobile slideways, such as ECOSPEED hybrid processing robots equipped with Sprint Z3 heads [8,9], have their own stiffness more secure, and easy to obtain a larger direction of mobile workspace.

The kinematics analysis of machining robot is an important prerequisite for studying its performance. With the application of the hybrid mechanism, scholars [10,11] have carried out the analysis of hybrid mechanisms. Liu et al. [12] proposed a 5-DOF hybrid machining robot, which is a 2-DOF parallel spherical mechanism serially

connected with a 3-DOF open loop kinematic chain via a prismatic joint. The speed mapping model is established for its 2- DOF parallel mechanism. Zhang et al. [13] proposed a new type of hybrid processing robot based on 2R1T 2UPU/SP parallel mechanism, and carried out the kinematics and dynamics analyses of the parallel mechanism. Tang et al. [14] proposed a novel hybrid processing robot, through the consideration of the parallel mechanism and the series mechanism respectively, the whole Jacobian matrix is established. At present, the analysis of hybrid machining robots is mainly aimed at the parallel mechanisms with relatively complex computational models or the simple linear superposition, and does not realize the decoupling between drivers and the end. In fact, it is very important to get the kinematics and dynamics model of the robot to reflect its performance.

This paper deals with the complete kinematics of hybrid machining robot based on screw theory. The kinematics analysis method is illustrated in section 2. The hybrid machining robot is modular disassembly by modular analysis method first. Establish the equivalent relationship between the parallel module and the generalized screw series drive joints, so that the hybrid machining robot is treated as an equivalent series robot composed of drivers. In section 3 and section 4, two analysis examples of hybrid machining robot P(2-PRU/2-PUS) and (R(2-PRR)/2-PUS)R are given to verify the feasibility of this method.

2   Kinematics analysis method based on screw theory

The overall kinematics mapping relationship of the hybrid mechanism can reflect its kinematics characteristics more directly, and is conducive to the subsequent research on the overall performance of the hybrid mechanism.

Based on the screw theory, adopt the modular analysis method to conduct modular disassembly of the hybrid mechanism, which divides the parallel mechanism and series mechanism into different modules. In this way, the hybrid mechanism can be regard as series mechanism series with every module. Establish the equivalent relationship between the parallel module and the generalized screw series drive joints, define the parallel module equivalent to generalized series screw joints. So that the hybrid mechanism is treated as an equivalent series mechanism composed of drivers.

The kinematics mapping relationship about the hybrid mechanism can be obtained by study of the equivalent series mechanism. The analysis method of hybrid mechanism is shown in the Fig.1.
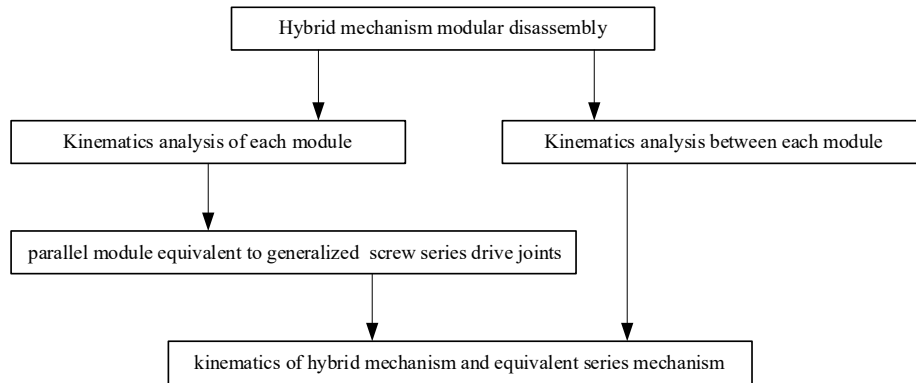
Fig. 1. Flowchart of analysis method

3 Analysis of P(2-PRU/2-PUS) hybrid machining robot

Literature [15] proposed 5-DoF hybrid machining robot, which is composed of a 4-DoF parallel robot (cross-arranged 2-PRU/2-PUS) plus an X table, as shown in Fig.2.
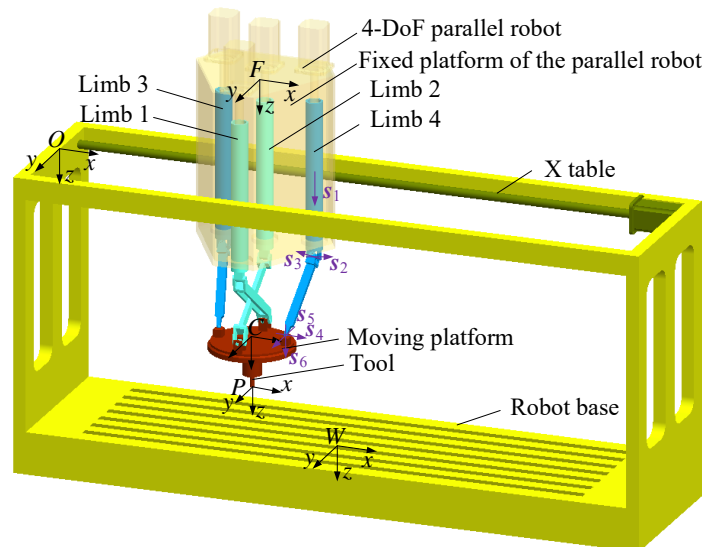
Fig. 2. P (2-PRU/2-PUS) hybrid machining robot

In order to calculate conveniently, the coordinate system is established: the workpiece frame $\{W\}$, the base frame $\{O\}$, the fixed platform frame $\{F\}$, the moving platform frame $\{C\}$, the tool frame $\{P\}$. $\boldsymbol{V}_P$ ($\boldsymbol{A}_P$) is the velocity (the acceleration) six-dimensional vector containing $\boldsymbol{\omega}_P$ and $\boldsymbol{v}_P$ ($\boldsymbol{\varepsilon}_P$ and $\boldsymbol{a}_P$) of the end in

the workpiece frame $\{W\}$ and the base frame $\{O\}$, because the axes between frame $\{W\}$ and frame $\{O\}$ are in the same directions. The screw velocity ${}^O V_{OP}$ and the screw acceleration ${}^O A_{OP}$ described in the frame $\{O\}$ can be obtained as:

$$
{}^O V_{OP} = \left| \begin{array}{c} \boldsymbol{\omega}_P \\ \boldsymbol{v}_P - \boldsymbol{\omega}_P \times {}^O \boldsymbol{P} \end{array} \right| \tag{1}
$$

$$
{}^O A_{OP} = \left| \begin{array}{c} \boldsymbol{\varepsilon}_P \\ \boldsymbol{a}_P - \boldsymbol{\varepsilon}_P \times {}^O \boldsymbol{P} - \boldsymbol{\omega}_P \times \boldsymbol{v}_P \end{array} \right| \tag{2}
$$

The hybrid machining robot can be divided into two modules: 2-PRU/2-PUS parallel module and P module. The kinematics relationship of this hybrid robot between each module can be obtained as:

$$
{}^O V_{OP} = {}^O V_{OF} + {}^O V_{FP} = {}^O V_{OF} + \mathrm{Adg}_{OF} \, {}^F V_{FP} \tag{3}
$$

$$
{}^O A_{OP} = {}^O A_{OF} + {}^O A_{FP} + \left[{}^O V_{OF}, {}^O V_{FP} \right] = {}^O A_{OF} + \mathrm{Adg}_{OF} \, {}^F A_{FP} + \left[{}^O V_{OF}, {}^O V_{FP} \right] \tag{4}
$$

As for the P module, ${}^O V_{OF}$ is affected by the driver joint q_1 and satisfied as:

$$
{}^O V_{OF} = \left| \begin{array}{c} \boldsymbol{0} \\ \left[\dot{q}_1 \quad 0 \quad 0 \right]^{\mathrm{T}} \end{array} \right| = \$_1 \dot{q}_1 \tag{5}
$$

$$
{}^O A_{OF} = \left| \begin{array}{c} \boldsymbol{0} \\ \left[\ddot{q}_1 \quad 0 \quad 0 \right]^{\mathrm{T}} \end{array} \right| = \$_1 \ddot{q}_1 \tag{6}
$$

As for the 2-PRU/2-PUS parallel module, ${}^F V_{FP}$ is affected by the drivers q_2, q_3, q_4, q_5. The parallel module is equivalent to 4-PUS parallel mechanism, and the axis of each joint is shown in fig.2, so the twist of every joint is defined as:

$$
\$_1^i = \left[\boldsymbol{0}; \boldsymbol{s}_1^i \right], \$_2^i = \left[\boldsymbol{s}_2^i; A_i \times \boldsymbol{s}_2^i \right], \$_3^i = \left[\boldsymbol{s}_3^i; A_i \times \boldsymbol{s}_3^i \right],
$$

$$
\$_4^i = \left[\boldsymbol{s}_4^i; B_i \times \boldsymbol{s}_4^i \right], \$_5^i = \left[\boldsymbol{s}_5^i; B_i \times \boldsymbol{s}_5^i \right], \$_6^i = \left[\boldsymbol{s}_6^i; B_i \times \boldsymbol{s}_6^i \right]
$$

The velocity and acceleration mapping relationship between the joints and the end of limb i is:

$$
{}^F V_{FP}^i = \left[\boldsymbol{G}_\phi^{P(i)} \right]_{\mathrm{P}} \dot{\boldsymbol{\phi}}^{(i)} \tag{7}
$$

$$
{}^F A_{FP}^i = \dot{\boldsymbol{\phi}}^{(i)\mathrm{T}} \left[\boldsymbol{H}_\phi^{P(i)} \right]_{\mathrm{P}} \dot{\boldsymbol{\phi}}^{(i)} + \left[\boldsymbol{G}_\phi^{P(i)} \right]_{\mathrm{P}} \ddot{\boldsymbol{\phi}}^{(i)} \tag{8}
$$

Inverse the Eqs (7, 8), and extract four drive joints and two dummy joints, the velocity and acceleration mapping from the end to drivers are:

$$\dot{\boldsymbol{q}}_{P6} = \left[\boldsymbol{G}_P^q\right]_{P6} {}^F\boldsymbol{V}_{FP} \tag{9}$$

$$\ddot{\boldsymbol{q}}_{P6} = \left[\boldsymbol{G}_P^q\right]_{P6} {}^F\boldsymbol{A}_{FP} - \dot{\boldsymbol{q}}_{P6}{}^{\mathrm{T}}\left[\boldsymbol{H}_P^q\right]_{P6}\dot{\boldsymbol{q}}_{P6} \tag{10}$$

Inverse the Eqs (9,10), and reserve the drive joints q_2, q_3, q_4, q_5, the velocity and acceleration mapping from the drivers to the end are:

$$^F\boldsymbol{V}_{FP} = \left[\boldsymbol{G}_q^P\right]_{\mathrm{P}}\dot{\boldsymbol{q}}_{\mathrm{P}} \tag{11}$$

$$^F\boldsymbol{A}_{FP} = \dot{\boldsymbol{q}}_{\mathrm{P}}{}^{\mathrm{T}}\left[\boldsymbol{H}_q^P\right]_{\mathrm{P}}\dot{\boldsymbol{q}}_{\mathrm{P}} + \left[\boldsymbol{G}_q^P\right]_{\mathrm{P}}\ddot{\boldsymbol{q}}_{\mathrm{P}} \tag{12}$$

Where $\left\lfloor\boldsymbol{G}_q^P\right\rfloor_{\mathrm{P}}$, $\left\lfloor\boldsymbol{H}_q^P\right\rfloor_{\mathrm{P}}$ are the Jacobian matrix and the Hessian matrix of the hybrid module.

The 2-PRU/2-PUS parallel module is equivalent to the HHHH series module according to its drivers, the twists of the drive joints q_2, q_3, q_4, q_5 should be

$$\$_2 = \left[\left[\boldsymbol{G}_q^P\right]_{\mathrm{P}}\right]_{:,1}, \$_3 = \left[\left[\boldsymbol{G}_q^P\right]_{\mathrm{P}}\right]_{:,2}, \$_4 = \left[\left[\boldsymbol{G}_q^P\right]_{\mathrm{P}}\right]_{:,4}, \$_5 = \left[\left[\boldsymbol{G}_q^P\right]_{\mathrm{P}}\right]_{:,5}$$

The PPPP series module of the parallel module satisfies

$$^F\boldsymbol{V}_{FP} = \$_2\dot{q}_2 + \$_3\dot{q}_3 + \$_4\dot{q}_4 + \$_5\dot{q}_5 \tag{13}$$

$$^F\boldsymbol{A}_{FP} = \$_2\ddot{q}_2 + \$_3\ddot{q}_3 + \$_4\ddot{q}_4 + \$_5\ddot{q}_5 + \dot{\$}_2\dot{q}_2 + \dot{\$}_3\dot{q}_3 + \dot{\$}_4\dot{q}_4 + \dot{\$}_5\dot{q}_5 \tag{14}$$

So, to sum up, substitute the Eqs (5,13 and 6,14) to Eqs (3 and 4) respectively, the velocity and acceleration of the hybrid machining robot should be

$$^O\boldsymbol{V}_{OP} = \$_1\dot{q}_1 + \mathrm{Adg}_{OF}\left(\$_2\dot{q}_2 + \$_3\dot{q}_3 + \$_4\dot{q}_4 + \$_5\dot{q}_5\right) \tag{15}$$

$$^O\boldsymbol{A}_{OP} = \$_1\ddot{q}_1 + \mathrm{Adg}_{OF}\left(\$_2\ddot{q}_2 + \$_3\ddot{q}_3 + \$_4\ddot{q}_4 + \$_5\ddot{q}_5 + \dot{\$}_2\dot{q}_2 + \dot{\$}_3\dot{q}_3 + \dot{\$}_4\dot{q}_4 + \dot{\$}_5\dot{q}_5\right)$$
$$+ \left[\$_1\dot{q}_1, \mathrm{Adg}_{OF}\left(\$_2\dot{q}_2 + \$_3\dot{q}_3 + \$_4\dot{q}_4 + \$_5\dot{q}_5\right)\right] \tag{16}$$

Extract the joint vector $\boldsymbol{q} = \left[q_1, q_2, q_3, q_4, q_5\right]^{\mathrm{T}}$, Eq (15) can also be written in matrix form as

$$^O\boldsymbol{V}_{OP} = \left[\$_1 \quad \mathrm{Adg}_{OF}\$_2 \quad \mathrm{Adg}_{OF}\$_3 \quad \mathrm{Adg}_{OF}\$_4 \quad \mathrm{Adg}_{OF}\$_5\right]\dot{\boldsymbol{q}} = \left[\boldsymbol{G}_q^P\right]\dot{\boldsymbol{q}} \tag{17}$$

So,

$$^{O}A_{OP} = \dot{q}^{\mathrm{T}} \left[H_q^P \right] \dot{q} + \left[G_q^P \right] \ddot{q} \qquad (18)$$

$\left\lfloor G_q^P \right\rfloor$ and $\left\lfloor H_q^P \right\rfloor$ are the Jacobian matrix and the Hessian matrix of the hybrid robot,

where
$$\left[H_q^P \right] = \begin{bmatrix} 0 & [\$_1, \ \mathrm{Adg}_{OF}\$_2] & [\$_1, \ \mathrm{Adg}_{OF}\$_3] & [\$_1, \ \mathrm{Adg}_{OF}\$_4] & [\$_1, \ \mathrm{Adg}_{OF}\$_5] \\ 0 & 0 & [\mathrm{Adg}_{OF}\$_2, \ \mathrm{Adg}_{OF}\$_3] & [\mathrm{Adg}_{OF}\$_2, \ \mathrm{Adg}_{OF}\$_4] & [\mathrm{Adg}_{OF}\$_2, \ \mathrm{Adg}_{OF}\$_5] \\ 0 & 0 & 0 & [\mathrm{Adg}_{OF}\$_3, \ \mathrm{Adg}_{OF}\$_4] & [\mathrm{Adg}_{OF}\$_3, \ \mathrm{Adg}_{OF}\$_5] \\ 0 & 0 & 0 & 0 & [\mathrm{Adg}_{OF}\$_4, \ \mathrm{Adg}_{OF}\$_5] \\ 0 & 0 & 0 & 0 & 0 \end{bmatrix}.$$

4   Analysis of (R(2-PRR)/2-PUS)R hybrid machining robot

Another 5-DoF (R(2-PRR)/2-PUS)R hybrid machining robot [16] is shown in Fig.3, which is composed of a 4-DoF R(2-PRR)/2-PUS parallel robot plus a single swing head.
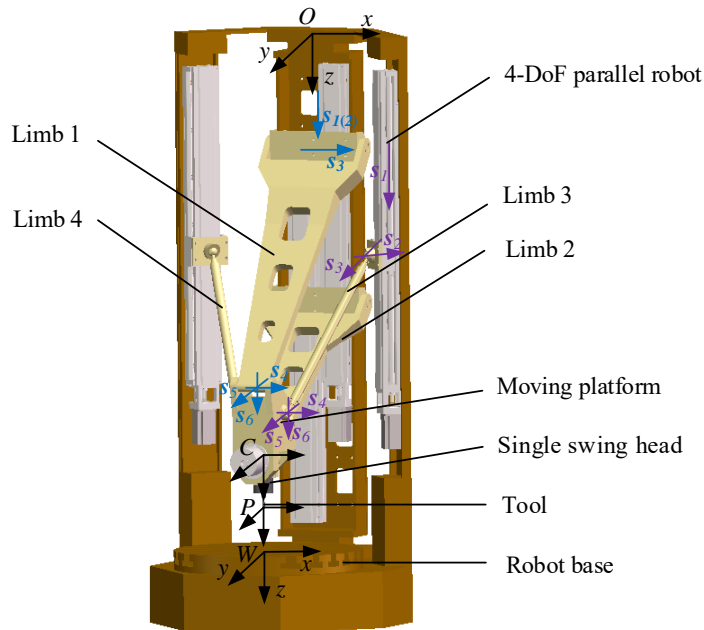

Fig. 3. P (2-PRU/2-PUS) hybrid machining robot

The coordinate system is established as: the workpiece frame $\{W\}$, the base frame $\{O\}$, the moving platform frame $\{C\}$, the tool frame $\{P\}$. As mentioned in the section 3, V_P (A_P) is the velocity (the acceleration) six-dimensional vector of the

end in the workpiece frame $\{W\}$ and the base frame $\{O\}$, and $^{O}V_{OP}(^{O}A_{OP})$ is the screw velocity (the screw acceleration) described in the frame $\{O\}$.

This hybrid machining robot can be divided into two modules: R(2-PRR)/2-PUS parallel module and R module.

The kinematics relationship of this hybrid robot between each module can be obtained as:

$$^{O}V_{OP} = {^{O}V_{CP}} + {^{O}V_{OC}} = \mathrm{Adg}_{OC}{^{C}V_{CP}} + {^{O}V_{OC}} \tag{19}$$

$$^{O}A_{OP} = {^{O}A_{CP}} + {^{O}A_{OC}} + \left[{^{O}V_{OC}}, {^{O}V_{CP}}\right] = \mathrm{Adg}_{OC}{^{C}A_{CP}} + {^{O}A_{OC}} + \left[{^{O}V_{OC}}, {^{O}V_{CP}}\right] \tag{20}$$

As for the R(2-PRR)/2-PUS parallel module, $^{O}V_{OC}$ is affected by the drivers q_1, q_2, q_3, q_4. The parallel module is equivalent to R(2-PRS)/2-PUS parallel mechanism, and the axis of each joint is shown in fig.3, so the twist of every joint in limb $i(i = 1, 2, 3, 4)$ is defined as:

$$\$_1^i = \left[s_1^i; A_i \times s_1^i\right], \$_2^i = \left[0; s_2^i\right] \text{ (while } i = 1, 2)$$

$$\$_1^i = \left[0; s_1^i\right], \$_2^i = \left[s_2^i; A_i \times s_2^i\right] \text{ (while } i = 3, 4)$$

$$\$_3^i = \left[s_3^i; A_i \times s_3^i\right], \$_4^i = \left[s_4^i; B_i \times s_4^i\right], \$_5^i = \left[s_5^i; B_i \times s_5^i\right], \$_6^i = \left[s_6^i; B_i \times s_6^i\right]$$

The velocity and acceleration mapping relationship between the joints and the end of limb i is:

$$^{O}V_{OC}^{i} = \left[G_{\phi}^{P(i)}\right]_{\mathrm{P}} \dot{\phi}^{(i)} \tag{21}$$

$$^{O}A_{OC}^{i} = \dot{\phi}^{(i)\mathrm{T}} \left[H_{\phi}^{P(i)}\right]_{\mathrm{P}} \dot{\phi}^{(i)} + \left[G_{\phi}^{P(i)}\right]_{\mathrm{P}} \ddot{\phi}^{(i)} \tag{22}$$

Inverse the Eqs. (21,22), and extract four drive joints and two dummy joints, the velocity and acceleration mapping from the end to drivers are:

$$\dot{q}_{\mathrm{P6}} = \left[G_{P}^{q}\right]_{\mathrm{P6}} {^{O}V_{OC}} \tag{23}$$

$$\ddot{q}_{\mathrm{P6}} = \left[G_{P}^{q}\right]_{\mathrm{P6}} {^{O}A_{OC}} - \dot{q}_{\mathrm{P6}}^{\mathrm{T}} \left[H_{P}^{q}\right]_{\mathrm{P6}} \dot{q}_{\mathrm{P6}} \tag{24}$$

Inverse the Eqs (23,24), and reserve the drive joints q_2, q_3, q_4, q_5, the velocity and acceleration mapping from the drivers to the end are:

$$^{O}V_{OC} = \left[G_{q}^{P}\right]_{\mathrm{P}} \dot{q}_{\mathrm{P}} \tag{25}$$

$$^{O}A_{OC} = \dot{q}_{\mathrm{P}}^{\mathrm{T}} \left[H_{q}^{P}\right]_{\mathrm{P}} \dot{q}_{\mathrm{P}} + \left[G_{q}^{P}\right]_{\mathrm{P}} \ddot{q}_{\mathrm{P}} \tag{26}$$

Where $\left\lfloor \boldsymbol{G}_q^P \right\rfloor_{\mathrm{P}}$, $\left\lfloor \boldsymbol{H}_q^P \right\rfloor_{\mathrm{P}}$ are the Jacobian matrix and the Hessian matrix of the parallel module.

The R(2-PRR)/2-PUS parallel module is equivalent to the HHHH series module according to its drivers, the twists of the drive joints q_1, q_2, q_3, q_4 should be

$$\$_1 = \left\lfloor \left[\boldsymbol{G}_q^P \right]_{\mathrm{P}} \right\rfloor_{:,1}, \$_2 = \left\lfloor \left[\boldsymbol{G}_q^P \right]_{\mathrm{P}} \right\rfloor_{:,2}, \$_3 = \left\lfloor \left[\boldsymbol{G}_q^P \right]_{\mathrm{P}} \right\rfloor_{:,3}, \$_4 = \left\lfloor \left[\boldsymbol{G}_q^P \right]_{\mathrm{P}} \right\rfloor_{:,4}$$

The HHHH series module of the parallel module satisfies

$$^O\boldsymbol{V}_{OC} = \$_1 \dot{q}_1 + \$_2 \dot{q}_2 + \$_3 \dot{q}_3 + \$_4 \dot{q}_4 \tag{27}$$

$$^O\boldsymbol{A}_{OC} = \$_1 \ddot{q}_1 + \$_2 \ddot{q}_2 + \$_3 \ddot{q}_3 + \$_4 \ddot{q}_4 + \dot{\$}_1 \dot{q}_1 + \dot{\$}_2 \dot{q}_2 + \dot{\$}_3 \dot{q}_3 + \dot{\$}_4 \dot{q}_4 \tag{28}$$

As for the R module, $^C\boldsymbol{V}_{CP}$ is affected by the driver joint q_1 and satisfied as:

$$^C\boldsymbol{V}_{CP} = \left[\boldsymbol{s}_R ; \boldsymbol{P}_{CP} \times \boldsymbol{s}_R \right] = \$_5 \dot{q}_5 \tag{29}$$

$$^C\boldsymbol{A}_{CF} = \$_5 \ddot{q}_5 + \dot{\$}_5 \dot{q}_5 \tag{30}$$

So, to sum up, substitute the Eqs (27,29 and 28,30) to Eqs (19 and 20) respectively, the velocity and acceleration of the hybrid machining robot should be

$$^O\boldsymbol{V}_{OP} = \$_1 \dot{q}_1 + \$_2 \dot{q}_2 + \$_3 \dot{q}_3 + \$_4 \dot{q}_4 + \mathrm{Adg}_{OC} \left(\$_5 \dot{q}_5 \right) \tag{31}$$

$$\begin{aligned} ^O\boldsymbol{A}_{OP} &= \$_1 \ddot{q}_1 + \$_2 \ddot{q}_2 + \$_3 \ddot{q}_3 + \$_4 \ddot{q}_4 + \dot{\$}_1 \dot{q}_1 + \dot{\$}_2 \dot{q}_2 + \dot{\$}_3 \dot{q}_3 + \dot{\$}_4 \dot{q}_4 \\ &+ \mathrm{Adg}_{OC} \left(\$_5 \ddot{q}_5 + \dot{\$}_5 \dot{q}_5 \right) + \left[\$_1 \dot{q}_1 + \$_2 \dot{q}_2 + \$_3 \dot{q}_3 + \$_4 \dot{q}_4 , \mathrm{Adg}_{OC} \left(\$_5 \dot{q}_5 \right) \right] \end{aligned} \tag{32}$$

Extract the joint vector $\boldsymbol{q} = \left[q_1, q_2, q_3, q_4, q_5 \right]^{\mathrm{T}}$, Eq(31) can also be written in matrix form as

$$^O\boldsymbol{V}_{OP} = \begin{bmatrix} \$_1 & \$_2 & \$_3 & \$_4 & \mathrm{Adg}_{OC} \$_5 \end{bmatrix} \dot{\boldsymbol{q}} = \left[\boldsymbol{G}_q^P \right] \dot{\boldsymbol{q}} \tag{33}$$

So,

$$^O\boldsymbol{A}_{OP} = \dot{\boldsymbol{q}}^{\mathrm{T}} \left[\boldsymbol{H}_q^P \right] \dot{\boldsymbol{q}} + \left[\boldsymbol{G}_q^P \right] \ddot{\boldsymbol{q}} \tag{34}$$

$\lfloor \boldsymbol{G}_q^P \rfloor$ and $\lfloor \boldsymbol{H}_q^P \rfloor$ are the Jacobian matrix and the Hessian matrix of the hybrid robot,

where
$$
\left[\boldsymbol{H}_q^P \right] = \begin{bmatrix}
0 & [\$_1,\$_2] & [\$_1,\$_3] & [\$_1,\$_4] & [\$_1, \ \mathrm{Ad}g_{OC}\$_5] \\
0 & 0 & [\$_2,\$_3] & [\$_2,\$_4] & [\$_2, \ \mathrm{Ad}g_{OC}\$_5] \\
0 & 0 & 0 & [\$_3,\$_4] & [\$_3, \ \mathrm{Ad}g_{OC}\$_5] \\
0 & 0 & 0 & 0 & [\$_4, \ \mathrm{Ad}g_{OC}\$_5] \\
0 & 0 & 0 & 0 & 0
\end{bmatrix} .
$$

5   Conclusion

This paper deals with the complete kinematics of hybrid machining robot based on screw theory. Establish the equivalent relationship between the parallel module and the generalized screw series drive joints, so that the hybrid machining robot is treated as an equivalent series robot composed of drivers. And give two types of hybrid machining robot to verify the feasibility of this method.

This method can be applied to solve a kind of hybrid mechanism, and it is more convenient and easier to understand.

References

1. Merlet J P., Parallel robots, Springer Science & Business Media, 2005.
2. J.L. Olazagoitia, S. Wyatt, New PKM Tricept T9000 and Its Application to Flexible Manufacturing at Aerospace Industry, Sae Tech. Pap. 2142 (2007) 37–48.
3. Y.Y. Wang, T. Huang, X.M. Zhao, J.P. Mei, S.J. Hu, Finite Element Analysis and Comparison of Two Hybrid Robots-the Tricept and the TriVariant, in: Intell. Robot. Syst. 2006 IEEE/RSJ Int. Conf., 2006.
4. Z.M. Bi, Y. Jin, Kinematic modeling of Exechon parallel kinematic machine, Robot. Comput. Integr. Manuf. 27 (2011) 186–193.
5. Y. Jin, Z.M. Bi, H.T. Liu, C. Higgins, M. Price, W.H. Chen, T. Huang, Kinematic Analysis and Dimensional Synthesis of Exechon Parallel Kinematic Machine for Large Volume Machining, J. Mech. Robot. 7 (2015) 41004.
6. T. Huang, M. Li, X.M. Zhao, J.P. Mei, D.G. Chetwynd, S.J. Hu, Conceptual design and dimensional synthesis for a 3-DOF module of the TriVariant-a novel 5-DOF reconfigurable hybrid robot, IEEE Trans. Robot. 21 (2005) p.449-456.
7. Meng, Li, Tian, Huang, Derek, G., Chetwynd, S., Jack, Hu, Forward Position Analysis of the 3-DOF Module of the TriVariant: A 5-DOF Reconfigurable Hybrid Robot, J. Mech. Des. 128 (2005) 319–322.

8. N. Hennes, D. Staimer, Application of PKM in aerospace manufacturing-high performance machining centers ECOSPEED, ECOSPEED-F and ECOLINER, Proc. 4th Chemnitz Parallel Kinemat. Semin. (2004) 557–577.

9. L. Uriarte, M. Zatarain, D. Axinte, J. Yagüe-Fabra, S. Ihlenfeldt, J. Eguia, A. Olarra, Machine tools for large parts, CIRP Ann. - Manuf. Technol. 62 (2013) 731–750.

10. K. Etemadi-Zanganeh, J. Angeles, Instantaneous Kinematics of General Hybrid Parallel Manipulators, J. Mech. Des. (1995).

11. D. Pisla, B. Gherman, C. Vaida, N. Plitea, Kinematic modelling of a 5-dof hybrid parallel robot for laparoscopic surgery*, Robotica. 30 (2012) 1095–1107.

12. H. Liu, H. Tian, J. Mei, X. Zhao, S.J. Hu, Kinematic design of a 5-DOF hybrid robot with large workspace/limb-stroke ratio, Chinese J. Mech. Eng. 129 (2007) 530.

13. D. Zhang, Y. Xu, J. Yao, Y. Zhao, Design of a novel 5-DOF hybrid serial-parallel manipulator and theoretical analysis of its parallel part, Robot. Comput. Integr. Manuf. 53 (2018) 228–239.

14. T. Tang, H. Fang, J. Zhang, Hierarchical design, laboratory prototype fabrication and machining tests of a novel 5-axis hybrid serial-parallel kinematic machine tool, Robot. Comput. Integr. Manuf. 64 (n.d.).

15. Tian X., Zhao T., Li E. (2019) A Novel 5-DOF Hybrid Robot Without Singularity Configurations. In: Yu H., Liu J., Liu L., Ju Z., Liu Y., Zhou D. (eds) Intelligent Robotics and Applications. ICIRA 2019. Lecture Notes in Computer Science, vol 11742. Springer, Cham.

16. Tieshi Zhao, Xin Tian, inventor. China patent CN209140511U; 07.23 (2019)

A Novel 6-DOF Wearable Ankle Exoskeleton Mechanism

Jiaxu Han[1], Zhibin Song[1,2,*], Paolo Dario[1,3,4], Jian S. Dai[5]

[1] School of Mechanical Engineering, Tianjin University, China

[2] Key Laboratory of Mechanism Theory and Equipment Design of the Ministry of Education, Centre for Advanced Mechanisms and Robotics, Tianjin University, China

[3] The BioRobotics Institute, Scuola Superiore Sant'Anna, Pisa Italy

[4] Department of Excellence in Robotics and AI, Scuola Superiore Sant'Anna, Pisa Italy

[5] King's College London, University of London, United Kingdom

Abstract. Most of existed designs of lower limb exoskeleton (LLE) did not take into account the misalignment between LLE and wearer, and misalignment will cause disturbance forces on the wearer which may make wearer discomfort, pain and even injury. According to the human ankle skeleton, the ankle part of LLE must has 6 degree of freedom (DOF) to achieve wearer-LLE coherence perfectly. This paper proposes a novel 6-DOF ankle exoskeleton which is made of SPU mechanism to fit the motion of human ankle. The serial mechanism is chosen because of the limited space and portable requirement. The DOF of exoskeleton mechanism is 6 which is analyzed based on the screw theory. The prototype of the mechanism is printed by 3D printer and the motion of exoskeleton mechanism matches the ankle movement smoothly through the test result.

Keywords: Ankle wearable exoskeleton, degree of freedom, screw theory.

1   Introduction

With the rapid development of lower limb exoskeleton (LLE) robotic technology from the 21st century, the LLE has a board application that can summarized as three aspects: performance augmentation, rehabilitation and assistance[1]. As for LLE is a type of wearable robotic device, if human and machine are not perfectly aligned, misalignment between the human and LLE movement causes disturbance forces on the wearer, may make wearer discomfort, pain, and even injury[2]. However, nowadays

only few LLEs were able to accomplish the complex movement to achieve human-LLE coherence actually. In order to improve the man-machine synchrony, the LLE should has the same kinematic characteristic to human lower limb[3]. There are two ways to fit the human movement, one is to use the misalignment compensation method[4], the other is to design the full-DOF LLE[5] (that is, the DOF of LLE joint is equal to the DOF of human joint).

Recently some researchers have pay attention to this problem that man-machine out of coherence. Bruening et al.[6] presented the ankle joint center has six degree-of-freedom translations during normal gait proved by 30 groups experiments, and the correction of ankle joint center may prove beneficial in kinematic and kinetic applications. Girone et al.[7] constructed a 6-DOF stewart parallel platform for ankle rehabilitation to adapt to the 6-DOF movement of ankle. Jamwal et al.[8] proposed a 4-UPS parallel mechanism which has 4-DOF for ankle rehabilitation, to decrease the ankle center error by using modified fuzzy inference control strategy. Zanotto et al.[9] stated that powered exoskeletons are prone to human-robot misalignments and these induce undesired interaction forces that may jeopardize safe operation. Hong et al.[10] presented a novel 3-DOF sensorized remote-center-of-motion (RCM) ankle module for a military-purpose lower-limb exoskeleton which is located close to the rotation center of the wearer's ankle. Hunt[11] introduce a 3-rotational-DOF parallel exoskeleton based on three 4 bar substructures that can be used for multiple-DOF biological joints. This new design can be described as a type of spherical parallel manipulator. Hyun et al.[3] proposed the design of a lower-limb exoskeleton called Human Universal Mobility Assistance (HUMA) which was developed as a research platform with the objective of providing its wearer with weight-bearing assistance for human strength/endurance augmentation. It has 2-DOF on ankle part that contain inversion/eversion and plantarflexion/dorsiflexion by using passive spring. Wang et al.[12] designed an adaptive mechanism with a slider/cam as an alternative to pin joints for the knee exoskeleton, and illustrated the application of the model for designing an adaptive mechanism that minimizes internal joint forces due to a human-exoskeleton interaction.

The human joint cannot be simply regarded as spherical pair or revolute pair, because of the complex human anatomy that the human joint axes change all the time on the motion process[13]-[15]. If the simple pairs above are used to fit the human joint, we need to compensate the misalignment between exoskeleton and human[16]-[18]. The misalignment compensation method would have errors between human and LLE[19]. The 6-DOF LLE can solve the problem fundamentally[20]. Among the

lower-limb joints, the ankle joint is major and complex joint that play an important role in stabilizing walking motion during the stance phase. This paper will focus on the preservation of natural biomechanics without restricting motion of the ankle. Only a few research groups have already focused on 6-DOF mechanisms to simulate the ankle complex movement, but they used parallel mechanisms on ankle rehabilitation, which are bulky and not portable. As for the compact space and portable requirement of wearable ankle exoskeleton, we proposed a serial mechanism with 6-DOF to match the human ankle movement.

The structure of this article is shown below. The motion of human ankle is analyzed on the perspective of mechanism theory in Section 2. To fit the motion of human ankle, a novel wearable exoskeleton mechanism is presented in Section 3. The DOF of ankle exoskeleton is analyzed based on the screw theory. The structure of ankle exoskeleton mechanism is designed and the prototype is printed by 3D printer. Finally, conclusion is presented in Section 4.

2 Motion of Ankle

The motion of human ankle can be generally described as three motions: Dorsiflexion/Plantarflexion, Abduction/Adduction, Inversion/Eversion, as shown in Figure 1. In fact, the joint motion between foot and leg is very complex, because the axis of every motion is not fixed owing to the indeterminate curvature of the ankle anatomy surface. In other words, the exoskeleton mechanism needs to adapt to the change of the human ankle joint axis. The three rotational-DOF mechanism cannot match the complex motion with the variable axis.

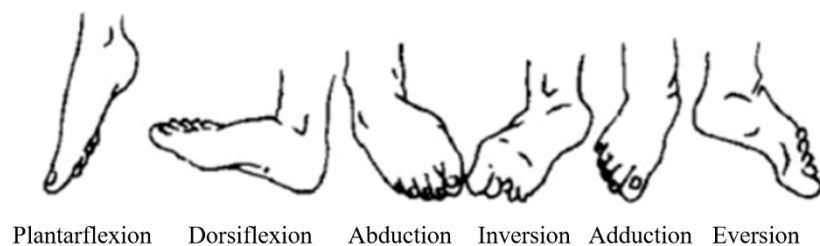Plantarflexion   Dorsiflexion   Abduction   Inversion   Adduction   Eversion

Fig. 1. Human ankle movement form

There are 6-DOF in space that can decompose three rotational-DOF around three coordinate axes and three translational-DOF along three coordinate axes respectively.

To achieve the man-machine synchrony that is to fit the ankle movement, considering the axis of the ankle rotation is not fixed, the highest DOF (6) is chosen for the DOF of ankle exoskeleton based on the analysis of the ankle anatomy above. As shown in above, the constraint screw system is an empty set that represents the exoskeleton has no constraint forces to human ankle movement. The exoskeleton mechanism is a passive mechanism without actuator. When the ankle joint is fixed, the exoskeleton should also be fixed. Therefore, the exoskeleton mechanism cannot have redundant degrees of freedom.

3   Ankle exoskeleton mechanism

The exoskeleton mechanism is fastened to the leg by flexible bandage, so it is not allowed to arrange complex kinematic pairs on the leg position. The mechanism on the foot position has more space and stiffness to arrange complex kinematic pair. The multiple-DOF pair is arranged on the foot position, the less-DOF pair is arranged on the leg position. In order to keep the mechanism integrated in the sagittal plane, prismatic pair is used in the middle position. Based on the principle above, the SPU mechanism is proposed in this article. The coordinate system and dimension parameter are established as shown in Figure 2.
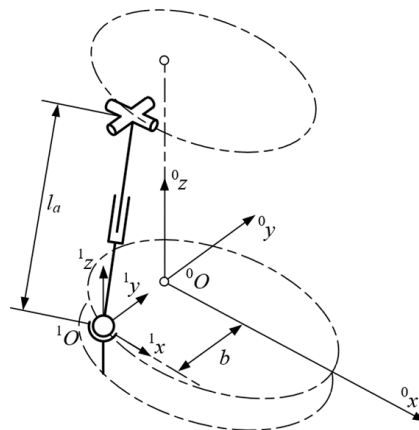

Fig. 2. Schematic diagram of SPU mechanism

The foot is seen as base platform, the leg is seen as moving platform. To define the local coordinate system, the center position O_1 of spherical pair is taken as the origin

point in local coordinate system; the sagittal axis is denoted as the ^1x axis; the coronal axis is denoted as the ^1y axis; and the vertical axis is denoted as the ^1z axis. The initial direction of prismatic pair is along the positive direction of the ^1z axis, and the translational displacement from the center of universal pair to the center of spherical pair is denoted as l_a. The initial directions of the rotational axis of the universal pair are parallel along the ^1x axis and ^1y axis respectively. So the initial unit orientation vector of the prismatic pair with the respect to local coordinate system $^1\boldsymbol{p}_0$ is given as $^1\boldsymbol{p}_0 = \begin{pmatrix} 0 & 0 & 1 \end{pmatrix}^{\mathrm{T}}$.

The screw system $^1\mathbb{S}_s$ of spherical pair with the respect to local coordinate system can be described as

$$^1\mathbb{S}_s = \begin{cases} ^1\boldsymbol{S}_{s1} = \begin{pmatrix} 1 & 0 & 0 & 0 & 0 & 0 \end{pmatrix}^{\mathrm{T}} \\ ^1\boldsymbol{S}_{s2} = \begin{pmatrix} 0 & 1 & 0 & 0 & 0 & 0 \end{pmatrix}^{\mathrm{T}} \\ ^1\boldsymbol{S}_{s3} = \begin{pmatrix} 0 & 0 & 1 & 0 & 0 & 0 \end{pmatrix}^{\mathrm{T}} \end{cases} \tag{1}$$

According to *Z-Y-X* Euler coordinate transformation, the orientation matrix $^1\boldsymbol{R}_{ZYX}$ of the spherical pair can be expressed as follows,

$$\begin{aligned} ^1\boldsymbol{R}_{ZYX} = {}^1\boldsymbol{R}_Z(\alpha)\,{}^1\boldsymbol{R}_Y(\beta)\,{}^1\boldsymbol{R}_X(\gamma) &= \begin{bmatrix} c\alpha & -s\alpha & 0 \\ s\alpha & c\alpha & 0 \\ 0 & 0 & 1 \end{bmatrix} \begin{bmatrix} c\beta & 0 & s\beta \\ 0 & 1 & 0 \\ -s\beta & 0 & c\beta \end{bmatrix} \begin{bmatrix} 1 & 0 & 0 \\ 0 & c\gamma & -s\gamma \\ 0 & s\gamma & c\gamma \end{bmatrix} \\ &= \begin{bmatrix} c\alpha c\beta & c\alpha s\beta s\gamma - s\alpha c\gamma & c\alpha s\beta c\gamma + s\alpha s\gamma \\ s\alpha c\beta & s\alpha s\beta s\gamma + c\alpha c\gamma & s\alpha s\beta s\gamma - c\alpha s\gamma \\ -s\beta & c\beta s\gamma & c\beta c\gamma \end{bmatrix} \end{aligned} \tag{2}$$

After the spherical pair orientation transformation, the direction vector of the prismatic pair can be calculated as follows:

$$^1\boldsymbol{p}_p = {}^1\boldsymbol{R}_{ZYX}\,{}^1\boldsymbol{p}_0 = \begin{pmatrix} c\alpha s\beta c\gamma + s\alpha s\gamma \\ s\alpha s\beta s\gamma - c\alpha s\gamma \\ c\beta c\gamma \end{pmatrix} \tag{3}$$

The screw system of prismatic pair can be obtained as:

$$^1\mathbb{S}_p = \left\{ {}^1\boldsymbol{S}_{p1} = \begin{pmatrix} 0 & 0 & 0 & c\alpha s\beta c\gamma + s\alpha s\gamma & s\alpha s\beta s\gamma - c\alpha s\gamma & c\beta c\gamma \end{pmatrix}^{\mathrm{T}} \right\} \tag{4}$$

The position vector of the universal pair ${}^1\boldsymbol{r}_u$ can be described as follows:

$$
{}^1\boldsymbol{r}_u = l_a \bullet {}^1\boldsymbol{p}_0 = \begin{pmatrix} l_a \left(\mathrm{c}\alpha\mathrm{s}\beta\mathrm{c}\gamma + \mathrm{s}\alpha\mathrm{s}\gamma \right) \\ l_a \left(\mathrm{s}\alpha\mathrm{s}\beta\mathrm{s}\gamma - \mathrm{c}\alpha\mathrm{s}\gamma \right) \\ l_a \mathrm{c}\beta\mathrm{c}\gamma \end{pmatrix} \tag{5}
$$

The motion screw system of universal pair can be calculated as:

$$
{}^1\mathbb{S}_u = \begin{cases} {}^1\boldsymbol{S}_{u1} = \begin{pmatrix} 0 & 1 & 0 & l_a\mathrm{c}\beta\mathrm{c}\gamma & 0 & -l_a\left(\mathrm{c}\alpha\mathrm{s}\beta\mathrm{c}\gamma+\mathrm{s}\alpha\mathrm{s}\gamma\right) \end{pmatrix}^{\mathrm{T}} \\ {}^1\boldsymbol{S}_{u2} = \begin{pmatrix} 1 & 0 & 0 & 0 & -l_a\mathrm{c}\beta\mathrm{c}\gamma & l_a\left(\mathrm{s}\alpha\mathrm{s}\beta\mathrm{s}\gamma-\mathrm{c}\alpha\mathrm{s}\gamma\right) \end{pmatrix}^{\mathrm{T}} \end{cases} \tag{6}
$$

The motion screw system of SPU mechanism in local coordinate system can be obtained as:

$$
{}^1\mathbb{S}_{SPU} = \begin{cases} {}^1\boldsymbol{S}_{s1} = \begin{pmatrix} 1 & 0 & 0 & 0 & 0 & 0 \end{pmatrix}^{\mathrm{T}} \\ {}^1\boldsymbol{S}_{s2} = \begin{pmatrix} 0 & 1 & 0 & 0 & 0 & 0 \end{pmatrix}^{\mathrm{T}} \\ {}^1\boldsymbol{S}_{s3} = \begin{pmatrix} 0 & 0 & 1 & 0 & 0 & 0 \end{pmatrix}^{\mathrm{T}} \\ {}^1\boldsymbol{S}_{p1} = \begin{pmatrix} 0 & 0 & 0 & \mathrm{c}\alpha\mathrm{s}\beta\mathrm{c}\gamma+\mathrm{s}\alpha\mathrm{s}\gamma & \mathrm{s}\alpha\mathrm{s}\beta\mathrm{s}\gamma-\mathrm{c}\alpha\mathrm{s}\gamma & \mathrm{c}\beta\mathrm{c}\gamma \end{pmatrix}^{\mathrm{T}} \\ {}^1\boldsymbol{S}_{u1} = \begin{pmatrix} 0 & 1 & 0 & l_a\mathrm{c}\beta\mathrm{c}\gamma & 0 & -l_a\left(\mathrm{c}\alpha\mathrm{s}\beta\mathrm{c}\gamma+\mathrm{s}\alpha\mathrm{s}\gamma\right) \end{pmatrix}^{\mathrm{T}} \\ {}^1\boldsymbol{S}_{u2} = \begin{pmatrix} 1 & 0 & 0 & 0 & -l_a\mathrm{c}\beta\mathrm{c}\gamma & l_a\left(\mathrm{s}\alpha\mathrm{s}\beta\mathrm{s}\gamma-\mathrm{c}\alpha\mathrm{s}\gamma\right) \end{pmatrix}^{\mathrm{T}} \end{cases} \tag{7}
$$

By moving the distance b along the y-axis, it is transformed into the global coordinate system,

$$
\boldsymbol{S}_i = \left({}^1_0\boldsymbol{T} \right) {}^1\boldsymbol{S}_i \tag{8}
$$

Where ${}^1_0\boldsymbol{T}$ denotes the transformation matrix from local coordinate system to Cartesian coordinate system,

$$
{}^1_0 T = \begin{bmatrix} I_3 & 0 \\ A & I_3 \end{bmatrix}
\tag{9}
$$

Where

$$
A = \begin{bmatrix} 0 & 0 & -b \\ 0 & 0 & 0 \\ b & 0 & 0 \end{bmatrix}
\tag{10}
$$

The motion screw system of SPU mechanism in base coordinate system can be obtained as:

$$
\mathbb{S}_{SPU} = \left\{ \begin{array}{c}
S_{s1} = \begin{pmatrix} 1 & 0 & 0 & 0 & 0 & -b \end{pmatrix}^{\mathrm{T}} \\
S_{s2} = \begin{pmatrix} 0 & 1 & 0 & 0 & 0 & 0 \end{pmatrix}^{\mathrm{T}} \\
S_{s3} = \begin{pmatrix} 0 & 0 & 1 & b & 0 & 0 \end{pmatrix}^{\mathrm{T}} \\
S_{p1} = \begin{pmatrix} 0 & 0 & 0 & c\alpha s\beta c\gamma + s\alpha s\gamma & s\alpha s\beta s\gamma - c\alpha s\gamma & c\beta c\gamma \end{pmatrix}^{\mathrm{T}} \\
S_{u1} = \begin{pmatrix} 0 & 1 & 0 & l_a c\beta c\gamma & 0 & -l_a (c\alpha s\beta c\gamma + s\alpha s\gamma) \end{pmatrix}^{\mathrm{T}} \\
S_{u2} = \begin{pmatrix} 1 & 0 & 0 & 0 & -l_a c\beta c\gamma & l_a (s\alpha s\beta s\gamma - c\alpha s\gamma) - b \end{pmatrix}^{\mathrm{T}}
\end{array} \right\}
\tag{11}
$$

The rank of $\mathbb{S}_{SPU}$ can be calculated as:

$$
\mathrm{rank}\left(\mathbb{S}_{SPU} \right) = 6
\tag{12}
$$

The rank of motion screw system represents the DOF of SPU mechanism which is equal to 6. Therefore, the SPU mechanism comply with a request for human ankle movement. The model of the SPU mechanism is established in 3D modeling software. The prototype of exoskeleton mechanism is built by 3D printer as shown in Figure 3.
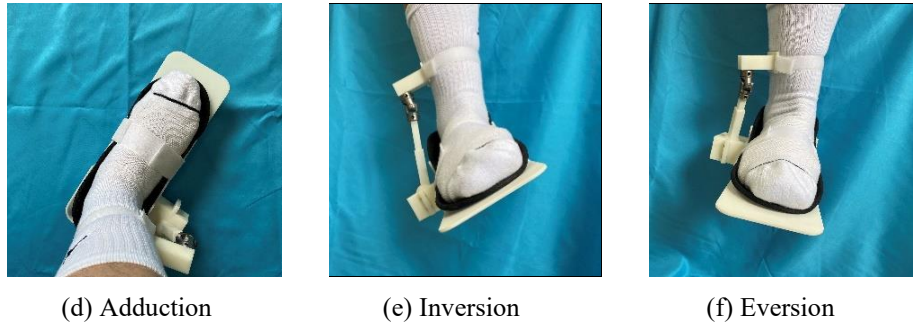

(a)Dorsiflexion   (b) Plantarflexion   (c) Abduction

| (d) Adduction | (e) Inversion | (f) Eversion |
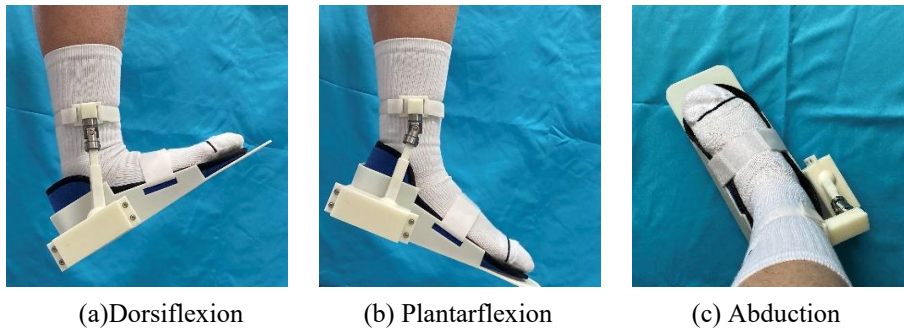
Fig. 3. Prototype test of ankle exoskeleton mechanism

4   Conclusion

This paper proposed a 6-DOF exoskeleton mechanism which can fit the complex motion of human ankle synchronously for full mobility. The kinematic analysis of the SPU mechanism for ankle exoskeleton is presented and the DOF of the mechanism is 6 which is calculated by the rank of motion screw system. This ankle mechanism displayed a compact, portable and wearable platform for improving wearer-exoskeleton adaptability. The prototype structure of the ankle mechanism is designed and printed by 3D printer. Experiment of the prototype has shown that the ankle moves smoothly while wearing the device. Above all, the request of wearer-exoskeleton synchronization is achieved through the theory analysis and experiment result.

Acknowledgment

References

[1]   Y. Lee, Y. J. Kim, J. Lee, M. Lee, B. Choi, J. Kim, Y. J. Park, and J. Choi, "Biomechanical Design of a Novel Flexible Exoskeleton for Lower Extremities," IEEE-ASME Transactions on Mechatronics, vol. 22, no. 5, pp. 2058-2069, Oct, 2017.

[2]   M. B. Naf, K. Junius, M. Rossini, C. Rodriguez-Guerrero, B. Vanderborght, and D. Lefeber, "Misalignment Compensation for Full Human-Exoskeleton Kinematic Compatibility: State of the Art and Evaluation," Applied Mechanics Reviews, vol. 70, no. 5, Sep, 2018.

[3]   D. J. Hyun, H. Park, T. Ha, S. Park, and K. Jung, "Biomechanical design of an agile, electricity-powered lower-limb exoskeleton for weight-bearing assistance," Robotics and Autonomous Systems, vol. 95, pp. 181-195, Sep, 2017.

[4]   J. Hunt, and H. Lee, "A New Parallel Actuated Architecture for Exoskeleton Applications Involving Multiple Degree-of-Freedom Biological Joints," Journal of Mechanisms and Robotics-Transactions of the ASME, vol. 10, no. 5, Oct, 2018.

[5]   K. Junius, M. Degelaen, N. Lefeber, E. Swinnen, B. Vanderborght, and D. Lefeber, "Bilateral, Misalignment-Compensating, Full-DOF Hip Exoskeleton: Design and Kinematic Validation," Applied Bionics and Biomechanics, vol. 2017, no. 5813154, 2017.

[6]   D. A. Bruening, A. N. Crewe, and F. L. Buczek, "A simple, anatomically based correction to the conventional ankle joint center," Clinical Biomechanics, vol. 23, no. 10, pp. 1299-1302, Dec, 2008.

[7]   M. Girone, G. Burdea, M. Bouzit, V. Popescu, and J. E. Deutsch, "A stewart platform-based system for ankle telerehabilitation," Autonomous Robots, vol. 10, no. 2, pp. 203-212, Mar, 2001.

[8]   P. K. Jamwal, S. Q. Xie, Y. H. Tsoi, and K. C. Aw, "Forward kinematics modelling of a parallel ankle rehabilitation robot using modified fuzzy inference," Mechanism and Machine Theory, vol. 45, no. 11, pp. 1537-1554, Nov, 2010.

[9]   D. Zanotto, Y. Akiyama, P. Stegall, and S. K. Agrawal, "Knee Joint Misalignment in Exoskeletons for the Lower Extremities: Effects on User's Gait," IEEE Transactions on Robotics, vol. 31, no. 4, pp. 978-987, Aug, 2015.

[10]   M. B. Hong, G. T. Kim, and Y. H. Yoon, "ACE-Ankle: A Novel Sensorized RCM (Remote-Center-of-Motion) Ankle Mechanism for Military Purpose Exoskeleton," Robotica, vol. 37, no. 12, pp. 2209-2228, Dec, 2019.

[11]   J. Hunt, and H. Lee, "A New Parallel Actuated Architecture for Exoskeleton Applications Involving Multiple Degree-of-Freedom Biological Joints," Journal of Mechanisms and Robotics-Transactions of the ASME, vol. 10, no. 5, Oct, 2018.

[12]   J. L. Wang, X. Li, T. H. Huang, S. Y. Yu, Y. J. Li, T. Y. Chen, A. Carriero, M. Oh-Park, and H. Su, "Comfort-Centered Design of a Lightweight and Backdrivable Knee Exoskeleton," IEEE Robotics and Automation Letters, vol. 3, no. 4, pp. 4265-4272, Oct, 2018.

[13] M. I. Awad, I. Hussain, S. Ghosh, Y. Zweiri, and D. M. Gan, "A Double-Layered Elbow Exoskeleton Interface With 3-PRR Planar Parallel Mechanism for Axis Self-Alignment," Journal of Mechanisms and Robotics-Transactions of the ASME, vol. 13, no. 1, Feb, 2021.

[14] H. C. Hsieh, D. F. Chen, L. Chien, and C. C. Lan, "Design of a Parallel Actuated Exoskeleton for Adaptive and Safe Robotic Shoulder Rehabilitation," IEEE-ASME Transactions on Mechatronics, vol. 22, no. 5, pp. 2034-2045, Oct, 2017.

[15] K. Junius, N. Lefeber, E. Swinnen, B. Vanderborght, and D. Lefeber, "Metabolic Effects Induced by a Kinematically Compatible Hip Exoskeleton During STS," IEEE Transactions on Biomedical Engineering, vol. 65, no. 6, pp. 1399-1409, Jun, 2018.

[16] A. S. Niyetkaliyev, E. Sariyildiz, and G. Alici, "Kinematic Modeling and Analysis of a Novel Bio-Inspired and Cable-Driven Hybrid Shoulder Mechanism," Journal of Mechanisms and Robotics-Transactions of the ASME, vol. 13, no. 1, Feb, 2021.

[17] S. V. Sarkisian, M. K. Ishmael, and T. Lenzi, "Self-Aligning Mechanism Improves Comfort and Performance With a Powered Knee Exoskeleton," IEEE Transactions on Neural Systems and Rehabilitation Engineering, vol. 29, pp. 629-640, 2021.

[18] Y. Y. Su, Y. L. Yu, C. H. Lin, and C. C. Lan, "A compact wrist rehabilitation robot with accurate force/stiffness control and misalignment adaptation," International Journal of Intelligent Robotics and Applications, vol. 3, no. 1, pp. 45-58, Mar, 2019.

[19] J. W. Sun, Y. Shen, and J. Rosen, "Sensor Reduction, Estimation, and Control of an Upper-Limb Exoskeleton," IEEE Robotics and Automation Letters, vol. 6, no. 2, pp. 1012-1019, Apr, 2021.

[20] J. S. Dai, T. Zhao, and C. Nester, "Sprained ankle physiotherapy based mechanism synthesis and stiffness analysis of a robotic rehabilitation device," Autonomous Robots, vol. 16, no. 2, pp. 207-218, Mar, 2004.

Urodela: Design of a Reconfigurable Robotic System for Landscapes Maintenance

A. A. Hayat, S. C. Eduardo, M. A. Viraj J. Muthugala, A. L. Pinxian, and M. R. Elara

Engineering Product Development Pillar, Singapore University of Technology and Design (SUTD), Singapore

Abstract. Landscapes, both vertical and horizontal, are being developed in numbers to maintain the greenery and food requirements given the limited availability of arable land in urban areas. This paper reports on the development of a reconfigurable robotic system for maintaining the vertical and horizontal landscape. The robotic system consists of three components: For vertical landscape, a track-rail system design, a reconfigurable and modular robot named *Urodela* with a manipulator arm traversing on the track rail and floor. The track design gives the ability to access sharp turns that are in-plane or out-of-plane. *Urodela* aimed at automating the gardening functionality of carrying plant pots, pruning, inspecting plants, among others. The design and system architecture of the robotic system is detailed, along with its static modeling. Furthermore, the demonstration of the locomotion and manipulation using the designed Urodela system is validated experimentally to showcase the scope for a robotic gardener.

Keywords: Vertical Landscape, Horizontal Landscape (plants nursery), Reconfigurable robot, Robotic gardener

1 Introduction

Vertical and horizontal landscapes are an emerging need for concrete vertical cities to maintain green and eco-friendly zones. Vertical landscape (VL) comprises units, such as vegetation mats, pots, and plantation racks, attached to the building walls whereas horizontal landscape (HL) refers to the plant nursery stretched over a horizontal area. Both VLs and HLs aid in improving the air quality, ambient cooling, apart from aesthetically pleasing. Nevertheless, regular maintenance work, such as pruning, watering, inspection, transfer, handling, and harvesting, by accessing high-rise areas is a monotonous, repetitive, risky, and labour-intensive task. Thus, there is immense scope for developing a robotic system to transform maintenance tasks for these landscapes and the present work's goal using robotic system.

In the present era, the emerging need for vertical farms is highlighted in the review works [1]. The detailed perspective of digital farming with the latest development in agricultural robotics, sensors, data analysis is surveyed in [2]. Developments of ground robots fixed with robotic manipulators to access plants above

the ground could be seen [3]. The work [4] proposed a robotic arm mounted on a vertical track rail to improve reachable height. However, the proposed mechanism could perform only vertical movements in the same plane, and the accessibility is still limited. Due to the limited accessibility of these ground robotic systems, the possibility of utilizing unmanned aerial vehicles for vertical landscape maintenance has also been studied [5]. Nevertheless, the maintenance abilities of an aerial vehicle-based mechanism are limited due to the inability to handle heavy payloads.

A climbing robot named Wallbot [6] has been proposed for vertical landscape maintenance since a robot with climbing ability could perform well. The Wallbot is hanged to a VL through four cables attached to the four corners of it. The robot can be moved to a position in a vertical plane by changing the distance of four cables through the hoist attached to them. The robot can move only in a single vertical plane, and the robot cannot be used with a VL that spreads in different planes of three-dimensional space. Furthermore, maintaining the four cables without tangling with plants becomes problematic when the size of the landscape increases. Therefore, the existing robots and systems designed for VLs require improvements. Moreover, novel practically integrated design solutions are required for VLs to overcome these challenges presented in this work.

The two major factors involved in the conception and design of vertical robots are their adhesion and locomotion methods. The design principles for adhesion and locomotion of these vertical robots are detailed in [7]. A noticeable trend in robotics research is on developing modular and self-reconfigurable robotic systems that can change their morphologies to overcome complexities in traversing environments [8–10]. The framework and principles to design reconfigurable robotic systems discussed in [11] are accounted in the present work.

According to the work [12], inbuilt grids/rails that use as supporting structures could often be found in vertical landscapes. Furthermore, such structural components could be arranged to improve the aesthetic appearance of landscapes. Therefore, a track-based modular reconfigurable robotic system has a great potential to overcome much of the limitations of robot-aided maintenance of VLs and HLs.

The rest of the paper is organized as follows. Section 2 presents design requirements, design and system architecture of robotic platform named as *Urodela* in detail. Section 3 presents the static analysis of the robot while climbing the track rail. Section 4 presents the experimental validation of locomotion and manipulation tasks. Finally, Section 5 concludes the paper with an outlook on future developments.

2   Conceptualization and Mechanical Layout

This section presents the VL and HL robotic system's essential design requirements, mainly the designed track rail, reconfigurable robot, and manipulator arm. The mechanical layout and system architecture are discussed in this section.

2.1   Design principles

Adopting a robotic solution for VL (here referring to vertical gardens and agricultural units) provides easy and safe access to the high-rise plantation area. Moreover, HL (here referring to horizontally laid plants nursery), robotic solution can assist in automated pick and place of plant pots, plants health monitoring, etc. For VL, the it has sharp corners, varying elevation angles, etc. And for HL, mainly with a plant nursery, has sharp corners and limited space to traverse. We used the design principles [13], which frame the design and realization of the robotic system as per the architectural requirements and constraints. The desired design features for the robotic system for the VL and HL are listed below:

- The robotic system can access the VL with the reconfigurable robot has HL mobility as well.
- Locomotion of the mobile platform should maneuver along curves, sharp angles both in-plane and out-of-plane of VL. Also, with HL, it can able manoeuvre in the narrow planting strip.
- For the VL robot should be in the state of static equilibrium at a given inclination and height without actuating the motors, which eventually makes the system energy efficient.
- Provision for the manipulation task essential for maintenance such as pot carriage and placement, seed planting, inspection, monitoring, etc., that a human gardener does for VL and HL.
- Can carry sensory units like camera, 3D scanner, humidity, temperature, air quality sensors for monitoring VL health.
- System should be scalable and reconfigurable for its deployment to VL and HL maintenance.

2.2   Mechanical layout

The reconfigurable and modular robot named *Urodela*, which is designed for reconfiguring its mobility according to VL and HL, is presented. The testbed is built for the VL system to demonstrate the robotic system's functional capabilities. The following section describes its features and technical details.

Reconfigurable Multi-functional Track Rail   The track rail (TR) system is a viable solution for accessing the vertical surface for maintenance. Therefore, an elevated track design that can be easily attached to VL surface is helpful. We have selected the dumbbell shape with two hollow circular pipes connected with a flat running plate made of steel AISI 1020 (Fig. 1a) and has the advantage and functionality as: ● Steel alloy, i.e., AISI 1020 hollow circular pipe is ferromagnetic, ductile, good weldability and is readily available, ● The two hollow pipe act functionally analogous to Xylem and Phloem in a plant. One side of the hollow circular pipe acts as a means for transporting the water (Xylem) for the plantation, and the other section can be used to take back the excess water ● The flat ferromagnetic running surface welded between the two hollow pipes in the middle is used to provide strong adherence by using permanent magnets on the robot.
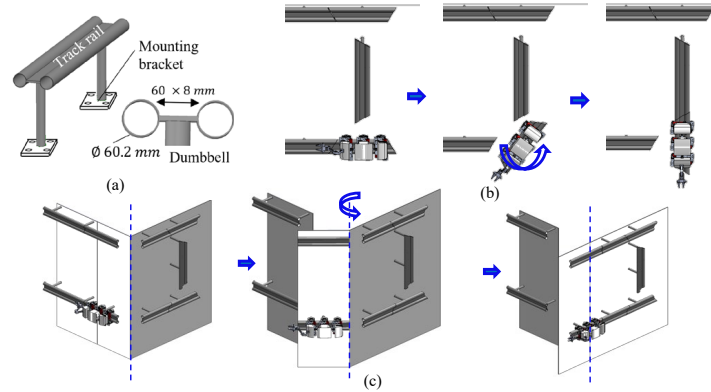
Fig. 1. Reconfigurable track design to enable track change. (a) Track rail (TR) design (b) In-plane transition (c) Out-of-plane scenario

The vertical landscape scheme for the reconfigurable TR layout is shown in Fig. 1b and Fig. 1c for in-plane and out-of-plane sharp turn, respectively. The robot's transition in an arbitrary direction or plane can be achieved by rotating a specific section of track rail as shown in Fig. 1. The design is generic and can attach to the vertical surface as per the structural need. The modular robot that is designed to move on the TR is discussed next.
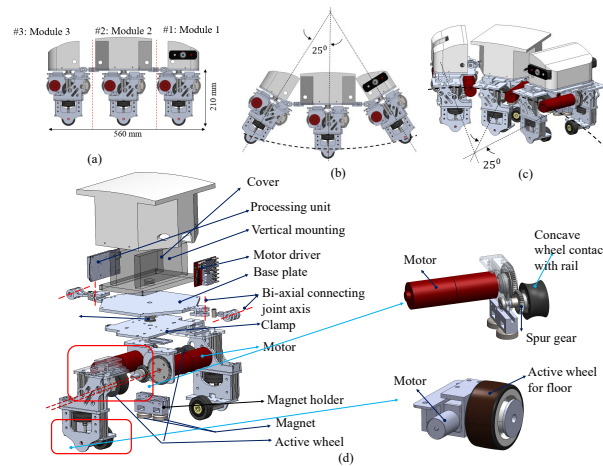
Fig. 2. Modular unit of *Urodela*. (a): Assembled unit, (b) curved in-plane freedom, (c) curved out-of-plane freedom, and (d) Exploded view with transmission system

Urodela Design and System Arhitecture   *Urodela* is a modular robot designed to traverse over the TR for VL and on a floor for HL as well. It has three major units, i.e., structural, adhesion, and locomotion unit. The structural unit or chassis is primarily made of machined Aluminum-6061 and supports wheels for locomotion, magnet holders for adhesion, control units, and an aesthetically

designed cover. Assembly of Urodela is shown in Fig. 2a. Individual modular units are connected using the biaxial passive joint connectors. The passive joint between the two modules of *Urodela* enables it to take a turn over a curved TR, which can be in-plane and out-of-plane as shown in Fig. 2b and c respectively. The exploded view shows the individual components and assembly along with the transmission for TR and horizontal surface wheels in Fig. 2d. The adhesion unit is designed to support the robot's weight against gravity on the vertical surface. Each module is assembled with the permanent Neodymium magnets (Lifton magnets, NA32) screwed to the holders. The statics and the Free Body Diagram (FBD) are presented in Section 3.

Each module's locomotion unit consists of two custom-designed rubber wheels having a concave outer surface instead of flat. The motion is transmitted from the motor to the wheel using a spur gear train, as shown in Fig. 2d. Additionally, two passive spring-loaded guiding wheels are provided on each side to ensure the clamping to the rail track and safety of the robot.

Manipulator and System Architecture   Vertical landscapes require the manipulation task to be carried out in the form of carrying a plant pot, seed-planting, inspection, etc., as discussed in motivation and design requirements. The selection of the manipulator arm for vertical landscape mainly depends upon the reachable workspace, joint and task space degrees of freedom (DOF), and the payload requirements. In this case, Module #3 of *Urodela* is mounted with five DOF manipulator arm having a two-finger gripper as depicted in 3a. The payload of the manipulator is approximately 0.5 kg, and the reachable workspace is overlaid on the robot and track in Fig. 3b. The gripper is made modular and can be attached with a custom-designed end-effector such as a nozzle or pruning or cutting unit, as shown in Fig. 3c.

The system architecture of *Urodela* is shown in Fig. 3d. The power to the actuators, sensors, and control unit is provided using a 24-volt battery place inside module #2. The weight of the battery is approximately 0.8 kg. The central mod-
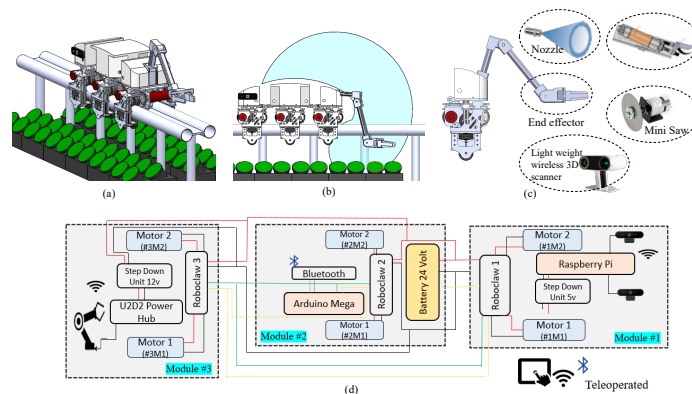

Fig. 3. Functionality of Urodela's manipulator. (a) Urodela with manipulator on the track rail, (b) Workspace of the arm, (c) Manipulator with reconfigurable option for end-efectors, and (d) System architecture of the three modules of Urodela

ule, i.e., #2, also has the microcontroller unit (Arduino Mega). Each module has two motors with encoders and is connected to one motor driver (RoboClaw) receiving signals from the microcontroller as per the command. Module #1 has two cameras placed on the left and right for monitoring the plants. The manipulator arm is also teleoperated using the camera feedback over the wifi, whereas the robot's locomotion is commanded using a Bluetooth module. The protocol used for communication is I2C for the manipulator arm and Universal asynchronous receiver-transmitter (UART) for the *Urodela* modules.

3   Modeling

The static modeling of the single module with the manipulator mounted is considered. The fundamental of robotic mechancial system like manipulator arms are explained in detail in [14]. The forces and torque are considered in the free body diagram (fbd), as in Fig. 4. Generally, the Center of Mass (COM) will vary as per the manipulator arm's configuration. The position of the COM l_{com} including the robot and arm,is given by:

$$l_{com} = \frac{1}{\sum m_i} \sum_{i=1}^{n} m_i l_i \qquad (1)$$

where m_i is the mass of each link, and the mobile base connected with the rail is assigned as link $\#L_1$ having mass as m_1, links $\#L_2, \cdots, \#L_n$ are generalized for the manipulator arm. The robot frame is assigned with XYZ- axes at point O_R along the inclination angle of α from the horizontal, as shown in Fig. 4b. The location of the two wheels is taken as offset with a distance a between the two along the $Y-$axis. Generally the left and right wheels are kept co-axial, but we have considered it to be with litttle offset. The static equilibrium condition that holds are listed given below:

$$\sum F_x : \sum_{w=1}^{2} F_{r,w} - W cos\alpha - F_M = 0 \qquad (2)$$

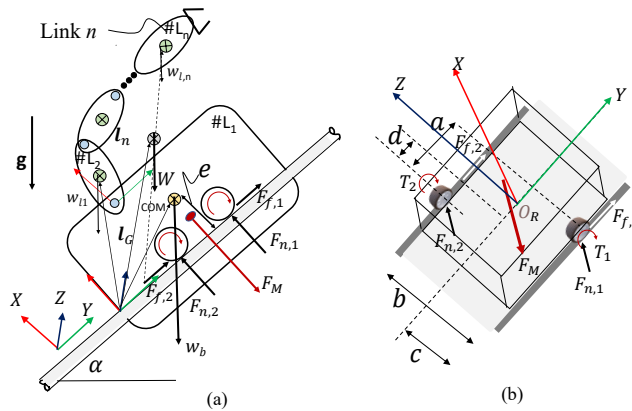$$\sum F_y :   \sum_{w=1}^{2} F_{f,w} - W sin\alpha = 0 \qquad (3)$$

Fig. 4. (a): Free body diagram of a single module with the manipulator arm and (b): Assignment of the robot frame.

where the magnetic adhesion force F_M, the weight of robot and manipulator arm W, normal reaction acting at the wheel point of contact with track rail as F_{n1}, F_{n2}, and friction forces F_{f1}, F_{f2} are taken into consideration. It is essential to determine the required magnetic force at an equilibrium condition and the wheel torque to overcome it. Then these forces and torques can be selected to climb the given scenario. The forces acting on the robot and wheels are shown with free body diagram (fbd) in Fig. 4. Also, the moment about the axes passing through the center of mass are considered to get the relationship between the design parameters and forces:

$$\sum M_x : c \times F_{f1} - ((b - c) \times F_{f2}) = 0 \tag{4}$$

$$\sum M_y : -c \times F_{n1} + ((b - c) \times F_{n2}) = 0 \tag{5}$$

$$\sum M_z : (\frac{a}{2} - d)F_M + \sum_{w=1}^{2} F_{f,w}(e) + F_{n,1}(a - d) - F_{n,2}a = 0 \tag{6}$$

where a, b, c, d and e are the distances denoting the spatial location of the COM given by Eq.1. The torque by the motor to the wheel and the traction forces for the non-slippage condition satisfies the following relation:

$$T_i = r_w \times F_{fi} \tag{7}$$

where r_w is the radius of the wheel, T_i is the torque at the wheel from the motor. For a certain pose of the manipulator, robot weight, and geometry, there are four unknowns, namely, F_{f1}, F_{f2}, F_{n1} and F_{n2}. There are assumptions for the analysis as: (a) It assumes non slip condition for the wheels; (b) wheels have the same size and material; and (c) the equilibrium is considered. The robot can be moved with a constant velocity or held at its position if the frictional force is less than the normal reaction force multiplied by the coefficient of static friction between the surface. The above system of equations can be used to check the variation of forces w.r.t., the inclination angle α. In the next section, experimental results are presented on the power consumed during the test run. The detailed analysis comparing the analytical formulation with experiments will be discussed in later communication due to space constraint.

4 Experiments and Discussion

Fig. 5a shows the experimental setup with the robot operating system (ROS) interface which was used to manipulate the arm in a teleoperated mode, and also the Urodela platform. To validate the locomotion and manipulation of the designed robotic system, a limited set of experiments were performed and are discussed below.

• **Urodela on a section of track rail**: First of all, the assembled robot *Urodela* is guided manually into the section of the designed Track Rail (TR) by powering the wheels. The track rail section mounted with the robot was inclined at an angle of 40° and 90° from horizontal, as shown in Fig. 5b and Fig. 5c respectively. The current drawn by each motor were logged using the Roboclaw for the commanded speed of 0.2 m/s. Fig. 5d shows the current variation of
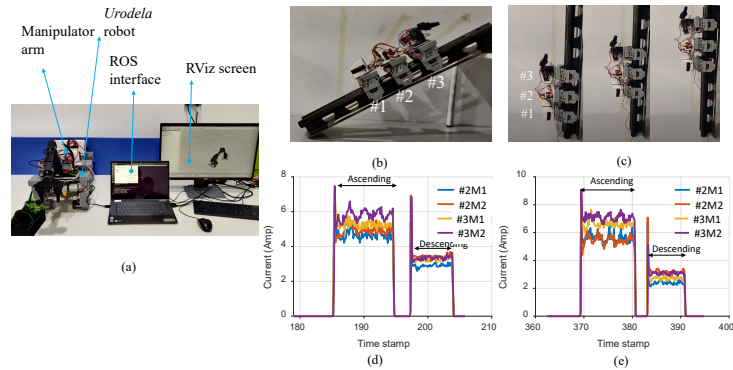
Fig. 5. (a) Experimental setup, Mobility of *Urodela* along with (b) 40° and (c) 90° inclined segments of TR. The plots of current drawn at an inclination of (d) 40° and (e) 90° of the track rail.

the two motors (M1 and M2) placed in Module #2 and #3 labelled as #2M1, #2M2, #3M1, and #3M2. It was observed that the current drawn by #3M1 and M2 is greater than #2 M1 and M2. This is because #3 was carrying a greater load due to the manipulator arm. Moreover, Fig. 5e shows the variation when the track rail is oriented vertically, and the average current drawn in this case is greatest. The power consumption of the robot was also computed for the test cases assuming a constant supply voltage. The amounts of average power consumed by the robot ascending on 40° and 90° were found to be approximately 28 and 24 W, respectively. This information is further useful for the passive control [15] of robot and manipulator arm robot to make it safe. The complete model for the power consumption and the study of the friction model will be detailed in a future publication.

• **Mobility and Manipulation**: Fig. 6a shows the mobility of the *Urodela* on a horizontal plane. The two wheels in contact with the ground were actuated using the servo motors. The differential action of the wheel makes the turning of the module around the pivot joint between the two modules. Moreover, the pickup of the plant pot in the teleoperated mode by an operator taking the video feedback was carried out and is shown in Fig. 6b. Our ongoing effort is towards 3D-reconstruction and health monitoring of the plants.

•*Urodela* **platform tested on vertical landscape testbed**: The vertical landscape testbed was built where the track rail was attached with the given dimension, and the turning radius is depicted in Fig. 6e (please zoom in or refer to the video link in the reference [1]). The *Urodela* robot was mounted on the TR from point (A) (Fig. 6d) (here manually, but with spatial designed track connecting floor to a vertical surface can result in a transition from floor to

---

[1] Video link: https://drive.google.com/file/d/1Hv3Ywzcw2NEczbz86z4g-7cdfjD_ge1Q/view?usp=sharing
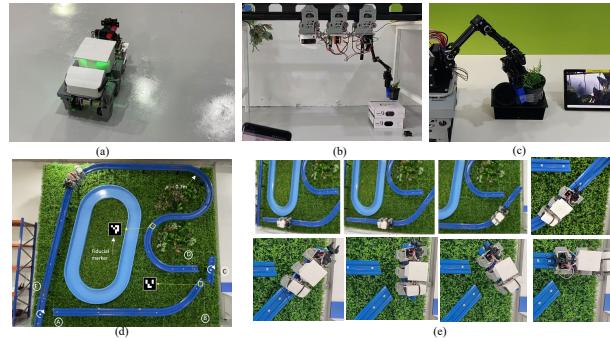
Fig. 6. Experimental setup for the vertical landscape maintenance. (a): Mobility of *Urodela* on ground, (b) and (c): Plant pot pickup, (d): VL testbed, (e): Snapshot sequence of *Urodela* moving on VL testbed including reconfiguration of the TR. Please refer the supplementary video link for more details.

vertical surface as well) and it traversed in the track rail section as shown in Fig. 6e. Once the *Urodela* robot reaches Ⓑ the Fiducial Makers (FM) are placed at the critical junctions to get the position of the robot on the TR using the camera detecting the FM. The average time taken in traversing the complete track is 160 seconds. All of the elementary locomotion and manipulation tasks, such as the motion of the robot along the section of the track, teleoperated manipulation of the plant pot by the manipulator arm, etc. are demonstrated in the supplementary video.

5   CONCLUSIONS

In this paper, we presented a robotic system for VL and HL maintenance. The modular and reconfigurable design of *Urodela* results in vertical and horizontal surface mobility, traversing over a curvature on VL, and also has the ability to carry different payloads like manipulator arm. The end effector of the manipulator arm can be made to reconfigure manually to accommodate different tools essential for gardening. The experiments were performed to show the essential capability of the robot along with the static modeling discussed. The proposed system is aimed at performing the task of a human gardener autonomously. The system kinematic and dynamic model, including the manipulator and end-effector design, will be investigated. Overall, the proposed system for vertical and horizontal landscape maintenance is modular and reconfigurable with scalable application as per the landscape conditions.

Acknowledgements

References

1. Al-Kodmany, K.: The vertical farm: A review of developments and implications for the vertical city. Buildings 8(2), 24 (2018)
2. R Shamshiri, R., Weltzien, C., Hameed, I.A., J Yule, I., E Grift, T., Balasundram, S.K., Pitonakova, L., Ahmad, D., Chowdhary, G.: Research and development in agricultural robotics: A perspective of digital farming (2018)
3. Lauguico, S.C., Concepcion, R.S., Macasaet, D.D., Alejandrino, J.D., Bandala, A.A., Dadios, E.P.: Implementation of inverse kinematics for crop-harvesting robotic arm in vertical farming. In: International Conference on Cybernetics and Intelligent Systems (CIS) and on Robotics, Automation and Mechatronics (RAM). pp. 298–303. IEEE (2019)
4. Nguyen, T.T., Kayacan, E., De Baedemaeker, J., Saeys, W.: Task and motion planning for apple harvesting robot. IFAC Proceedings Volumes 46(18), 247–252 (2013)
5. Kim, J., Kim, S., Ju, C., Son, H.I.: Unmanned aerial vehicles in agriculture: A review of perspective of platform, control, and applications. IEEE Access 7, 105100–105115 (2019)
6. Wilkinson, S., et al.: Wallbot: A must for green wall. Built Environment Economist: Australia and New Zealand (June/August 2020), 46 (2020)
7. Chu, B., Jung, K., Han, C.S., Hong, D.: A survey of climbing robots: Locomotion and adhesion. International journal of precision engineering and manufacturing 11(4), 633–647 (2010)
8. Muthugala, M.V.J., Vega-Heredia, M., Vengadesh, A., Sriharsha, G., Elara, M.R.: Design of an adhesion-aware façade cleaning robot. In: 2019 IEEE/RSJ International Conference on Intelligent Robots and Systems (IROS). pp. 1441–1447. IEEE (2019)
9. Hayat, A.A., Parween, R., Elara, M.R., Parsuraman, K., Kandasamy, P.S.: Panthera: Design of a reconfigurable pavement sweeping robot. In: 2019 International Conference on Robotics and Automation (ICRA). pp. 7346–7352. IEEE (2019)
10. Tan, N., Hayat, A.A., Elara, M.R., Wood, K.L.: A framework for taxonomy and evaluation of self-reconfigurable robotic systems. IEEE Access 8, 13969–13986 (2020)
11. Kalimuthu, M., Hayat, A.A., Elara, M.R., Wood, K.L.: Transformation design principles as enablers for designing reconfigurable robots. In: International Design Engineering Technical Conferences and Computers and Information in Engineering Conference. vol. 69373 (2021)
12. Özyavuz, M.: Advances in Landscape Architecture (2013)
13. Elara, M.R., Rojas, N., Chua, A.: Design principles for robot inclusive spaces: A case study with roomba. In: 2014 IEEE International Conference on Robotics and Automation (ICRA). pp. 5593–5599. IEEE (2014)
14. Angeles, J.: Fundamentals of robotic mechanical systems, vol. 2. Springer (2002)
15. Udai, A.D., Hayat, A.A., Saha, S.K.: Parallel active/passive force control of industrial robots with joint compliance. In: 2014 IEEE/RSJ International Conference on Intelligent Robots and Systems. pp. 4511–4516. IEEE (2014)

Robot with Reconfigurable Wheels for False-ceiling Inspection: Falcon

A. A. Hayat, Ramanan RKM, R. E. Abdulkader, B. Ramalingam, T. T. Tun,
and M. R. Elara

Engineering Product Development Pillar, Singapore University of Technology and
Design (SUTD), Singapore

Abstract. The inspection and surveillance of the false ceiling are vital for a safe, clean and healthy indoor environment for humans against the pest. The pest management industry is evolving and coming up with smart solutions. For the first time, we introduce the robotic solution for it. The robot named Falcon is designed to navigate efficiently in the false-ceiling environment. The wheels are designed for locomotion over the false ceiling and have the obstacle-negotiation capability at the same time. Also, the robot has a high definition night vision camera mounted on it, and the platform is teleoperated using the mobile application. The locomotion is verified with the experiments on the testbed and false ceiling.

Keywords: Compliant wheels, False ceiling, Inspection robot, Pest control

1 Introduction

False or suspended ceilings are a favorable place for rodents to seek refuge and build their habitat. These pests can wreak havoc in the buildings be it residential, commercial or industrial. Pests infestation is a major health hazard as well as [1]. For example, pests such as cockroaches and mosquitoes spread asthma, allergy, and food contamination illnesses. Rats are known for damaging building structures, chewing electrical wires (Fig. 1a), and transmitting diseases. They can get into tiny spaces, which is why even the smallest of holes is the potential entry point for rodents. Rodents are particularly harmful, in that they contaminate the areas in which they search for food. Rats fecal matter is laden with germs and can cause more than 20 diseases, spread through contact, inhalation of dried pellets (poop droppings), and ingestion. Salmonella, Hantavirus, and the plague are just a few examples of rat infestation [2].

The requirement of smoothly and implementing the autonomous task in uncertain environments with robust adaptive autonomous features is vital for the development of next-generation robots. Legged robots have higher adaptability to the different conditions of ground [3,4]. However, they are more complex and require high torque and power. A wheeled robot is comparatively simpler in structure, easier to control [5], and is efficient on moving a plane surface.

Nevertheless, it is inferior to adapt to obstacles or rough terrain. Subsequently, researchers are attempting to incorporate the advantages of legged types of the robot in wheeled mobile platform design as per the environmental needs.

Trackwheel robots have better ability to overcome obstacles and move on unstructured ground with the disadvantage of high power consumption. The special transformation mechanism from wheeled morphology to legged morphology was reported as Quattroped [6]. Bio-inspired design for the transformable leg-wheel robot was reported as TurboQuad [7]. Obstacle-negotiation can be attained using the mobility of wheel-legged type system. This combines the advantages of a leg and wheel mechanism. Both robots have a unique transformation mechanism that can switch the morphology of the driving mechanism between the wheels (i.e., a full circle) and 2 degrees of freedom leg (i.e., combining two half circles as a leg). The robot with the innovative design of claw-wheel transformation is reported in [8]. Here the robot switches between claw mode and wheel mode by folding and unfolding the front body and rear body with the help of actuators and hence the reconfiguration are using active motors. In this work, we present the novel wheel design which has the advantage of stable locomotion with full circle wheel with an advantage of transforming into claw shape passively to overcome an obstacle. Surveillance robot for the indoor environment for home security with hopping capabilities to crossover the obstacle is proposed in [9]. Self-propelled patrolling vehicle and an intelligent household surveillance robot were reported in [10, 11].

Self reconfigurational robots are classified in [12] with energy calculation during the shape change of reconfigurable tiling robot in [13]. In this paper in order to meet the terrains requirement of the false-ceiling inspection and surveillance task against the pest we present the robot named *Falcon* with self-reconfigurable compliant wheels. The active passive force control [14] can be applied to make the actuated system passive under given conditions. The design principles based on the induction approach [15] which are derived based on activity, observation, and accessibility discussed in the next section. The utility of the robot is immense for the pest identification and control task. As the use case the images taken by the on-board camera of Falcon robot fed into transfer learning models reported in [16] to identify the type of the pests by classifying dropping images into one of the trained categories of pests.

(a)   (b)   (c)

Fig. 1. Manual inspection and hazard of pests on false ceiling (source: Google images)

The rest of this paper is organized as follows. Section 2 explains the requirements for the design, mechanical layout and the system architecture of the designed robot *Falcon* in detail. The kinematics of the wheel is presented in Section 3. The experimental results and the used case for pest identification are outlined in Section 4. Finally Section 5 concludes the paper.

2   System Requirements and Realization

The existing inspection and surveillance task of the false ceiling is done manually (Fig. 1b). The observation made from the inspection task is that the human access is difficult due to the constraints and occluded environment due to presence of ducts and pipes over the false-ceiling. Moreover the alarming situation arrives when searching for dead pests or rodents over the suspended roof is done mainly by following the odour of dead pests. This is very hazardous for the environment and human occupants when left unnoticed for long.

2.1   Design Requirements

The observations made from the geometry of the false ceiling mainly conclude: a) The array of frame and ceiling-tiles (Fig. 2a-b) supported over the inverted T-section b) The average height of the obstacle posed by T-section is 3-9 cms (AS/NZS 2785:2000 [17] suspended ceilings Design and installation standard) c) The environment inside is mostly dark, d) The ceiling tiles conceal the heating ventilation and air-conditioning (HVAC) ducts, fire safety pipes, cables, etc. By these observations, the following features in the robot designed for the inspection and surveillance task will be of help:

- From the false-ceiling standards and observations, it was concluded that the channel height h (Fig. 2b) varies as $30 < h < 90$ mm. Hence the robot design should overcome this obstacle height.
- The platform must be lightweight and should generate less noise while moving over the false ceiling.
- The platform should be symmetric along the traverse plane which will allow it to move in an upright position.
- Fall recovery provision should be provided.
- Night vision camera mounted for the inspection task in the dark environment along with LED's to lighten up the localized region for further inspection.
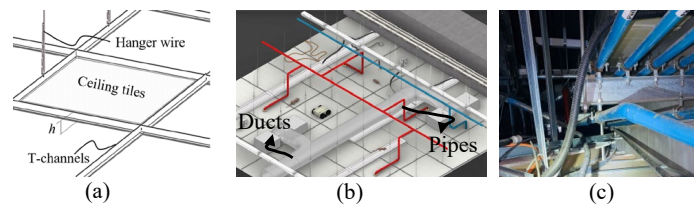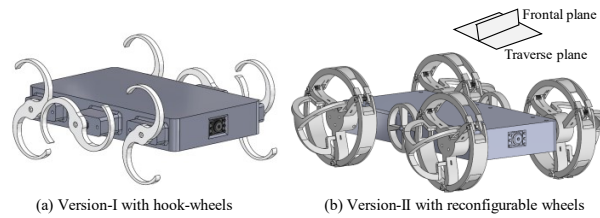

Fig. 2. False-ceiling environment

(a) Version-I with hook-wheels   (b) Version-II with reconfigurable wheels

Fig. 3. Arrangement of wheels and its design

2.2   Mechanical Design

Falcon is designed to move over the false-ceiling inspection robot. Fig. 3a shows the hooked shape wheel which is not a continuous circle. The obstacle with height less than the diameter of the wheel is easily crossover. The main drawback with these discontinuous wheels is the unstable trunk or the body of the robot while in locomotion which also results in the unstable or shaky vision feedback from the camera. To circumvent this issue, the wheels were modified and made continuous as shown in Fig. 3b. The mechanical design, prototyping and system architecture is deal in this section.
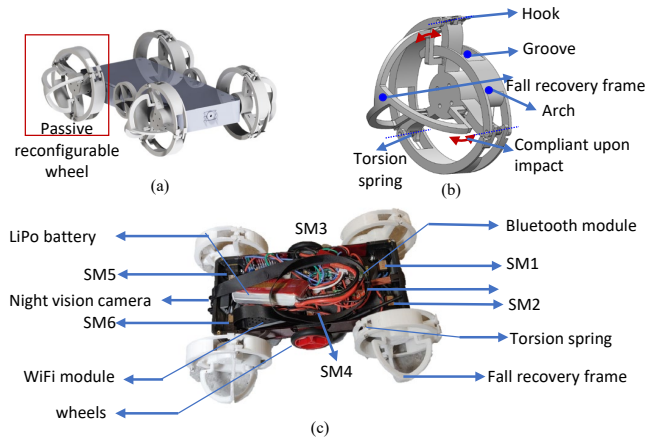

Fig. 4. Layout of the Falcon with passively reconfigurable wheels attached with fall recovery frames. The fall recovery frame with suitable stiffness and compliant design can assist in absorbing shock during fall

The *Falcon* robot is designed with symmetry about the traverse axis. Three wheels placed are placed along one side, and the rest three on the opposite face are equally protruded above and below the trunk. The rendered image of the *Falcon* is shown in Fig. 4a. The assembly of the passive reconfigurable wheel is shown in Fig. 4b. The novelty of its wheel serves the two purposes: a)It is

Table 1. Specifications for the Falcon

	Item name	Unit	
1	Net weight	g	310
2	Wheels	−	Compliant and reconfigurable
3	Wheel diameter	mm	100
4	Body ($l \times b \times h$)	mm	$250 \times 200 \times 40$
5	Continuous working time	s	1800
6	Working speed and Power source	m/s	1 and 12V LiPo battery
7	Payload and Sensors	g	200 and Nigh vision Camera

capable of changing its morphology based on the terrain in order to achieve better locomotion, and b) It prevents the shock to be directly transferred to the body in case of fall from a height. The details of the wheel kinematics are discussed in Section 3. To keep the body always parallel to the traverse plane, the fall-recovery frame is attached to the wheels as depicted in Fig. 4b. The systematic fall recovery frame in the wheel arrangement is meant for self-recovery action even when the robot topples down during locomotion.

The chassis of the robot is made up of Polylactic acid (PLA) having the density of 1.210-1.430 $g.cm^{-3}$ and has a melting point of $150 - 160°C$. Through fused deposit modeling (FDM) 3D printing process the body and the wheels were manufactured in-house. The infill density of the wheels was kept as high as 95%. This was because if the internal density of the arcs in reconfigurable wheels is low, then it will not withstand the stress of connection. As a result, it will snap off at its connecting point. For the body to keep the light weight the infill was kept between $20 - 30\%$. The fall recovery frame as shown in Fig. 4b is of softer stiffness which helps it to absorb the shock in case of fall. Fig. 5a shows the system assembly with the servo motors (M) labelled as M1 to M6 along with the power source and other components. The finite element analysis (FEM) analysis of the wheel assembly was done and will be reported in future communication.
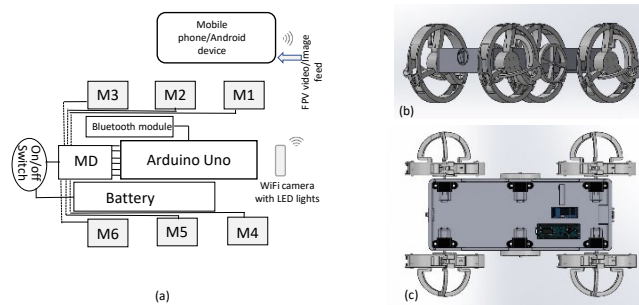

Fig. 5. System architecture with the camera and steering units, First person view (FPV), Motor driver (MD), and M(Servo motors)

Fig. 5 shows the line diagram for the Falcon system architecture. Six servo motors of Pololu micro metal gear (150:1 gear ratio) with encoders were used for the robot locomotion. The platform is controlled by onboard Arduino Uno microcontroller and powered through 12V Lithium Polymer battery. The wheels are controlled using an Arduino and Roboclaw motor controller. The device is connected to a mobile application through the Bluetooth transceiver with a range of 25 meters. Also, a night vision camera is positioned in the front of the body. The night vision camera provides a live stream of its recording onto the android application running on the mobile with the help of the WiFi module.

3   Wheel Kinetics

In this section, the analysis of the passive reconfigurable wheels is presented. The advantage of using the reconfigurable wheels especially for the false ceiling inspection task is:

- The circular wheel will provide the stable rolling motion while traversing on the plane surface. This will result in stable video feedback for the surveillance task.
- When the wheel goes over obstacles such as rough surfaces or small steps which are lesser than the diameter of the wheel, the mechanism will allow the wheel to overcome these obstacles.
- The fall recovery frame attached with the wheels will ensure the Falcon body to remain parallel to the traverse plane.
- The passive reconfigurable wheels will also be helpful while traversing over the rough surface like over the pebbles, etc.

The wheel consists of three spokes which are 120 degrees apart from each other. These three spokes connect the center hub. The passive revolute action is gained using the torsion spring which supports the circular arc beam at H_1, H_2 and H_3 as shown Fig. 6a. Fig. 4 shows the spokes are connected to the arch with a central shaft and torsional spring. The one end of the arch is attached using the prestressed coil spring, and the other end is supported with the hook acting as the stopper. The groove act as the guide while the arch pushes inward. The two-wheel states are discussed in this section:
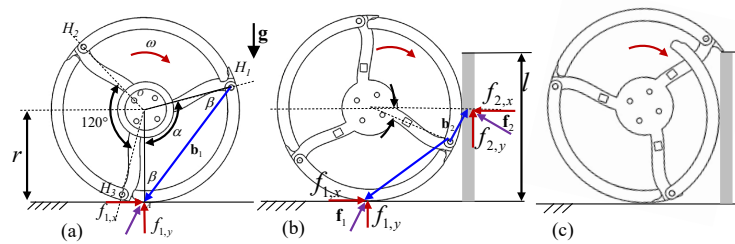

Fig. 6. Passive reconfigurable wheels while rolling on a plane surface and obstacle negotiation

Case: Rolling of wheels For rolling of wheels on the flat plane Fig. 6a shows the free body diagram of the wheels. Assuming the body to be symmetric the normal force on each wheel will be distributed equally on the four wheels in contact with the ground. Assuming the total mass of the robot as m_T, then the normal reaction force and the force of friction is given by:

$$f_{1,y} = m_T \mathbf{g}/4 \tag{1}$$
$$f_{1,x} \quad = \mu f_{1,y} \tag{2}$$

where μ is the co-efficient of friction of the rolling wheels and $\mathbf{g}$ is the gravity vector as shown in Fig. 6. The moment at the hinge having the torsion spring is given by the cross product as:

$$\mathbf{n_1} = \mathbf{b_1} \times \mathbf{f_1} \tag{3}$$

where $\mathbf{b_1}$ is the vector joining the hinge point (H_1) with the point of contact at the ground (A) as shown in Fig. 6a and $\mathbf{f_1}$ is the resultant force vector of $f_{1,x}$ and $f_{1,y}$. The magnitude of b_1 varies as the wheel rolls over the ground, and it can be easily calculated using the side angle side relation for the triangle formed as H_1OA. Hence, the maximum torque was used to select of the torsion spring. This will ensure that the arch does not bend due to the self-weight of the body as shown in Fig. 6b.

Case: Wheel at obstacle-negotiation To overcome the obstacle with the height of obstacle l in the range lesser than the diameter of the wheel the impact of the wheel with the obstacle will result in the impulsive force as:

$$f_{2,x} = m_T(\Delta\omega r) \tag{4}$$
$$f_{2,y} \quad = \mu_o f_{2,x} \tag{5}$$

where $\mathbf{f_{2,x}}$ is the impulsive force coming due to change in the angular velocity ω of the wheel after hitting the obstacle. Also the friction force between the wheel and obstacle denoted by μ_o is given by Eq.(5). Here the moment about the hinge due to contact with the obstacle is given by:

$$\mathbf{n_2} = \mathbf{b_2} \times \mathbf{f_2} \tag{6}$$

where $\mathbf{b_2}$ is the vector joining the hinge point with the point of contact at the obstacle as shown in Fig. 6c and $\mathbf{f_2}$ is the resultant force vector of $f_{2,x}$ and $f_{2,y}$.. Since the impulsive force due to hitting with the obstacle will be higher, it will result in the bending of arch about the hinge point. This will result in the expose of hook to the obstacle as shown in Fig. 6d which will aid the wheel to overcome the obstacle.

In the center of wheel the D-shape slot is provide to holds the wheels with the motor shaft. The spokes were provided with the slots for the snap fit of the fall-recovery frames. This resulted in easier assembly of the fall recovery frame with the wheel. Fig. 7 shows the fall recovery due to the moment created by the weight of the body and the spherical cage like frame provides the smoother transition.
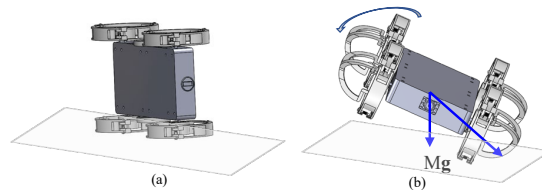
Fig. 7. Fall recovery due to the rim, i.e., cage like structure attached to the spokes

4   Experiments and Application

Fig. 8 depicted the scenario where the robot overcoming an obstacle with its reconfigurable wheel arrangement. The snapshot of these images is taken from the experimental video, where we set up the obstacle manually which is based on the false ceiling frame settings. The proposed mechanical design and suspension system can help the robot to access the obstacle in both forward and reverse mode of locomotion. The rubberized wheels which are in the center body of the robot help to overcome the wider frames. The fall recovery frames aides the robot to recover from any side of the fall, and it prevents the robot from structural damage.

The application of Falcon was done by taking the images using an onboard camera and fed to leaned model [16] developed for identification of the pests based on droppings images. The pre-trained model using the CNN architecture. The training was done using the images of droppings of commonly found household pest. Fig. 9 shows the utility of the trained model in the identification of pests.

5   Conclusions

In this paper, we described the false-ceiling inspection and surveillance that can be used to detect the abnormal activity on the false-ceiling for the pest control. The video feedback using a night-vision camera is used for the surveillance
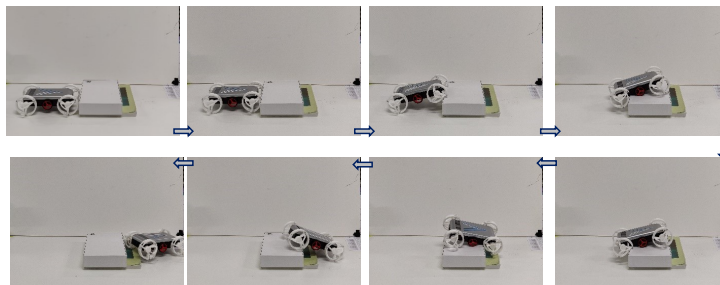

Fig. 8. Falcon obstacle negotiation with the passive reconfigurable wheels
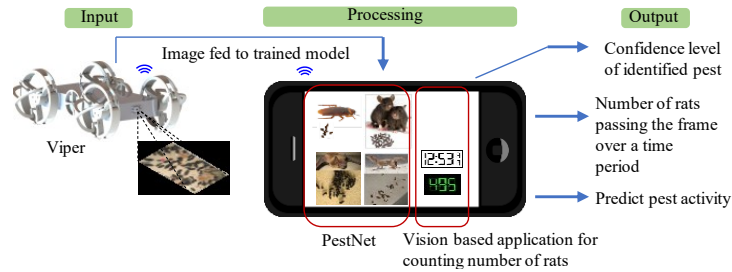
Fig. 9. Application of Falcon by processing the images with the trained model and developed application

of pest activities. Provision for LED lights is also made in the robot for lightning locally and taking the images. There are three main contributions in our work: a) The design of robot for the false-ceiling inspection; b) The passive reconfigurable wheels with three spokes passively act as claw for obstacle-negotiation; c) The fall recovery frame attached to the wheel spoke prevents the robot from getting stable in vertical pose. The learning based approach reported in [16], for the identification of pest using their excreta images. As a part of future work, we are testing for the power efficiency, autonomous docking of the platform on false ceiling for charging. The graphical user interface, along with the Android applications, is also under development for the analysis of pest activity based on their detection.

Acknowledgements

References

1. List of common household pests: [online] available at: https://en.wikipedia.org/wiki/list-of-common-household-pests [accessed: 20-04-2019]
2. Zamindar, H.: The effects of pest on human health: [online] available at: https://medicalwale.com/related-articles/blood/145 [accessed 5 apr. 2019]
3. Clark, J.E., Cham, J.G., Bailey, S.A., Froehlich, E.M., Nahata, P.K., Full, R.J., Cutkosky, M.R.: Biomimetic design and fabrication of a hexapedal running robot. In: Proceedings 2001 ICRA. IEEE International Conference on Robotics and Automation (Cat. No. 01CH37164). vol. 4, pp. 3643–3649. IEEE (2001)
4. Jha, R.K., Singh, B., Pratihar, D.K.: On-line stable gait generation of a two-legged robot using a genetic–fuzzy system. Robotics and Autonomous Systems 53(1), 15–35 (2005)

5. Caracciolo, L., De Luca, A., Iannitti, S.: Trajectory tracking control of a four-wheel differentially driven mobile robot. In: Proceedings 1999 IEEE International Conference on Robotics and Automation (Cat. No. 99CH36288C). vol. 4, pp. 2632–2638. IEEE (1999)
6. Chen, S.C., Huang, K.J., Chen, W.H., Shen, S.Y., Li, C.H., Lin, P.C.: Quattroped: a leg–wheel transformable robot. IEEE/ASME Transactions On Mechatronics 19(2), 730–742 (2014)
7. Chen, W.H., Lin, H.S., Lin, P.C.: Turboquad: A leg-wheel transformable robot using bio-inspired control. In: 2014 IEEE International Conference on Robotics and Automation (ICRA). pp. 2090–2090. IEEE (2014)
8. Chou, J.J., Yang, L.S.: Innovative design of a claw-wheel transformable robot. In: 2013 IEEE International Conference on Robotics and Automation. pp. 1337–1342. IEEE (2013)
9. Song, G., Yin, K., Zhou, Y., Cheng, X.: A surveillance robot with hopping capabilities for home security. IEEE Transactions on Consumer Electronics 55(4), 2034–2039 (2009)
10. Lee, H.T., Lin, W.C., Huang, C.H., Huang, Y.J.: Wireless indoor surveillance robot. In: SICE Annual Conference 2011. pp. 2164–2169. IEEE (2011)
11. Wu, X., Gong, H., Chen, P., Zhi, Z., Xu, Y.: Intelligent household surveillance robot. In: 2008 IEEE International Conference on Robotics and Biomimetics. pp. 1734–1739. IEEE (2009)
12. Tan, N., Hayat, A.A., Elara, M.R., Wood, K.L.: A framework for taxonomy and evaluation of self-reconfigurable robotic systems. IEEE Access 8, 13969–13986 (2020)
13. Hayat, A.A., Karthikeyan, P., Vega-Heredia, M., Elara, M.R.: Modeling and assessing of self-reconfigurable cleaning robot htetro based on energy consumption. Energies 12(21), 4112 (2019)
14. Udai, A.D., Hayat, A.A., Saha, S.K.: Parallel active/passive force control of industrial robots with joint compliance. In: 2014 IEEE/RSJ International Conference on Intelligent Robots and Systems. pp. 4511–4516. IEEE (2014)
15. Manimuthu, M., Hayat, A.A., Elara, M.R., Wood, K.: Transformation design principles as enablers for designing reconfigurable robots. In: International Design Engineering Technical Conferences and Computers and Information in Engineering Conference. pp. 1–12 (2021)
16. Balakrishnan, R., Thein, Than, T., Mohan, R.E., Braulio, Flix, G., Cheng, R., Selvasundari, B., Madan, Mohan, R., Hayat, A.A.: AI enabled IoRT framework for rodent activity monitoring in a false ceiling environment. Journal of Sensors 1 (2021)
17. AS/NZS 2785:2000. suspended ceiling design and installation: [online] //shop.standards.govt.nz/catalog/2785april 2019]
18. Robotic system with compliant wheels for suspended ceiling surveillance and inspection. https://bit.ly/3wZ8Z8c, accessed: 2021-07-05

Design and kinematic analysis of a novel dexterous hand

Kege Li, Rugui Wang[*], Haibo Huang

College of Mechanical Engineering, Guangxi University, Nanning 530004, China

Abstract. This paper presents a design of dexterous hand mechanism which imitates the motion characteristics of thumb and index finger. The dexterous hand mechanism not only can grasp the corresponding configuration deformation according to the shape of the object, but also can rotate the object. The D-H method and closed-loop vector method are used to analyze the kinematics of the palm mechanism and the finger mechanism of the dexterous hand. On this basis, the workspace of the palm mechanism is simulated and calculated to investigate the rotation ability of the novel dexterous hand to grasp the object for rotational motion, which provides a reference for further analysis of the dexterity of the dexterous hand.

Keywords: Dexterous Hand Mechanism, Kinematics, Workspace, Rotation Ability

1 Introduction

Dexterous hand is a widely used robot end-effector [1,2]. With the development of related technology and the demand of industrial production, dexterous hands with higher flexibility, carrying capacity and stronger adaptability have been studied extensively. There were many famous dexterous hands designed in the last century, such as Okada hand [3], Stanford / JP hand [4], Utah / MIT hand [5, 6] and Robonaut hand [7]. And some new designs have emerged in recent years. Dai et al. [8-10] presented a series of metamorphic anthropomorphic hands according to the metamorphic theory, which have the advantages of strong adaptability. Yamaguchi et al. [11]used link mechanism to make uGRIPP hand which has good rigidity, responds quickly to the bending and relaxation of fingers, and can give greater grasping force when grasping objects. Fang et al. [12] designed dexterous hands with parallel finger structures. Wang et al. [13] designed of a novel simulated "soft" mechanical grasper, which is able to drive and control with single-degree-of-freedom and automatically self-adapts to object's shape with uniform grasping force. Ref [14,15], a series of dexterous hands with strong sensing function are designed, providing accurate tactile feedback and position feedback. These existing dexterous hands show that they are similar to human hands in pinching, clamping and gripping the object [16-18].

---

[*] Corresponding author.
  E-mail addresses: rugui@gxu.edu.cn (R. Wang).

Kinematic analysis is essential for studying the relationship between joint space and end-effector space. Lu et al. [19] analyzed the kinematics of bionic finger hand rehabilitation robot mechanism via the D-H method. Shim and Kim [20] studied the kinematics of robotic gripper using closed-loop vector method. Li et al. [21] presented a systematic method for the kinematic design of the twisted and coiled polymers-actuated finger mechanism.

This paper presents a design of dexterous hand mechanism, which imitates the motion characteristics of thumb and index finger. The dexterous hand has the characteristics of the existing dexterous hand and increases the dexterity of rotation operation. Kinematics analysis of the palm and finger are presented to study the workspace performance, and the rotation ability of the dexterous hand is obtained through numerical example analysis, which provides a reference for further performance analysis of dexterous hand.

2   Design of the dexterous hand mechanism

Based on the fact that the motion of the human thumb and the index finger can be decomposed into horizontal motion along different directions, a novel dexterous hand which can rotate the object is designed, as shown in Fig. 1. The dexterous hand is equipped with a palm mechanism and two identical underactuated finger mechanisms, of which two fingers are arranged opposite. The palm mechanism consists of a flexible belt and a mechanism that rotates the object, and the finger mechanism consisting of five-bar linkage contains two knuckles.
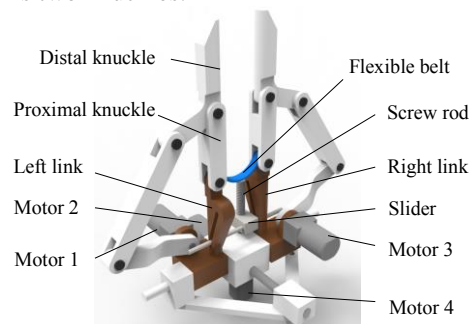

Fig. 1. The 3D model of dexterous hand

The slider, which is driven by motor 4 through the screw rod, drives the left link and the right link to rotate. The left link and the right link are respectively connected with the slider in a line tangent circle way. At this point, due to the limitation of torsion spring at the two knuckle units of the finger, the proximal knuckle and the distal knuckle are fixed as one. Fig. 2 shows the moving process of the fingers while rotating an object.
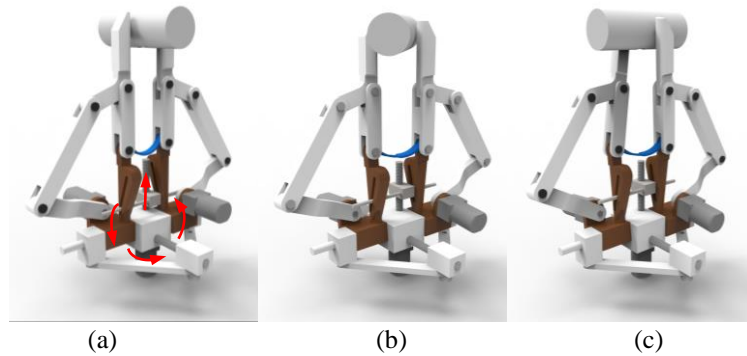
Fig. 2. An example of grasping the object and making it rotate counterclockwise, (a) Rotate the object 0 degrees counterclockwise; (b) Rotate the object 45 degrees counter-clockwise; (c) Rotate the object 90 degrees counterclockwise.

3 Kinematics analysis

3.1 Kinematics analysis of the palm mechanism

The model of the proposed dexterous hand is presented in Fig. 3, where $O-xyz$ is the global coordinate frame, $O_1 - x_1 y_1 z_1$ is the local coordinate frame which built on the O_1 joint.

The structure of dexterous hand is symmetrical, therefore, left branch chain is selected for kinematic analysis. In Fig. 4, a and b are separately for the driving parameters of slider A and slider D. Point U_1 and Point U_2 is the final output parameter, point E_1 is the line contact point connecting left link and slider D, e is the distance from the bottom of chute to y axis, θ denotes the angle between chute and left link, k is the distance from the bottom of chute to point E_1.
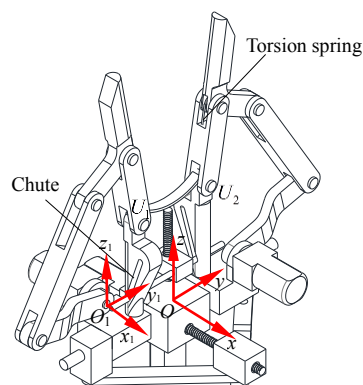
Fig. 3. Structure of dexterous hand

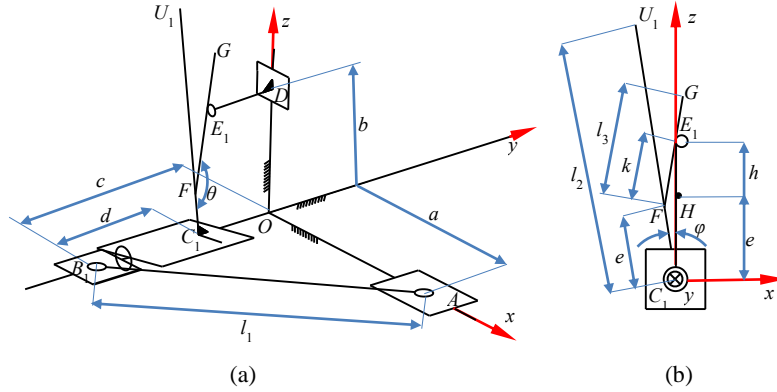(a)   (b)

Fig. 4. (a) The sketch of left branch chain of the palm mechanism; (b) The sketch of $O-xz$ plane structure of left branch chain of the palm mechanism

Suppose $U_1\left(x_{u1} \quad y_{u1} \quad z_{u1}\right)$ and the position coordinate of driving parameter is $\left(a \quad 0 \quad b\right)$. The mapping relationship between drive parameters and output parameters is established.

$$\begin{vmatrix} x_{u1} \\ y_{u1} \\ z_{u1} \\ 1 \end{vmatrix} = T \begin{vmatrix} a \\ 0 \\ b \\ 1 \end{vmatrix} \tag{1}$$

where T is the mapping matrix of driving parameter and output parameter.

Slider A moves along x axis and slider B_1 moves along y axis by connecting link AB_1. Since slider B_1 and slider C_1 are collinear, the point U_1 can only move along y axis as slider A moves. Then the mapping between drive parameters and output parameters is established.

$$\begin{vmatrix} 0 \\ y_{u1} \\ 0 \\ 1 \end{vmatrix} = T_A \begin{vmatrix} a \\ 0 \\ 0 \\ 1 \end{vmatrix} \tag{2}$$

where T_A is the mapping matrix of driving parameter of slider A and output parameter of point U_1.

According to the geometrical relations in Fig. 3, there are

$$y_{u1} = c - d \tag{3}$$

$$c = \sqrt{l_1^2 - a^2} \tag{4}$$

where c is the distance from slider B_1 to origin, d is the distance from slider B_1 to C_1, l_1 is the size of link AB_1.

Substituting Eqs. (3) and (4) into Eq. (2)

$$
\begin{vmatrix}
0 \\
-\sqrt{l_1^2 - a^2} + d \\
0 \\
1
\end{vmatrix}
= \boldsymbol{T}_A
\begin{bmatrix}
a \\
0 \\
0 \\
1
\end{bmatrix}
\tag{5}
$$

$$
\boldsymbol{T}_A =
\begin{vmatrix}
1 & 0 & 0 & -a \\
0 & 1 & 0 & -\sqrt{l_1^2 - a^2} + d \\
0 & 0 & 1 & 0 \\
0 & 0 & 0 & 1
\end{vmatrix}
\tag{6}
$$

Similarly, the slider D moves on the z axis, and the point of connecting link $C_1 U_1$ moves around the y axis on the $O - xz$ plane through the line contact method. Then the mapping between the slider D and the output point U_1 is

$$
\begin{vmatrix}
x_{u1} \\
0 \\
z_{u1} \\
1
\end{vmatrix}
= \boldsymbol{T}_D
\begin{vmatrix}
0 \\
0 \\
b \\
1
\end{vmatrix}
\tag{7}
$$

where $\boldsymbol{T}_D$ is the mapping matrix of driving parameter of slider D and output parameter of point U_1.

In Fig. 4, $l_{C_1 F} = l_{C_1 H} = e$, φ is the rotation angle of link $C_1 U_1$ around y axis, and its size is determined by the moving distance h of slider D on z axis. θ is the known parameter, l_2 is the length of left link, l_3 is the length of chute. According to the geometric relationship between Fig. 3 and Fig. 4,

$$
b = e + h
\tag{8}
$$

In $\Delta C_1 F E_1$, from the law of cosines

$$
\cos \theta = \frac{e^2 + k^2 - (e+h)^2}{2ek}
\tag{9}
$$

$$
\cos \varphi = \frac{e^2 + (e+h)^2 - k^2}{2e(e+h)}
\tag{10}
$$

With a similar calculation, the solution of k is listed below

$$
k = \pm \sqrt{(e+h)^2 - e^2 + (e\cos\theta)^2} + e\cos\theta
\tag{11}
$$

For $k \geq 0$

$$
k = \sqrt{(e+h)^2 - e^2 + (e\cos\theta)^2} + e\cos\theta
\tag{12}
$$

Substituting the value of k into Eq. (10) yields

$$
\varphi = \arccos\left(\frac{e^2 - (e\cos\theta)^2 - e\cos\theta\sqrt{(e+h)^2 - e^2 + (e\cos\theta)^2}}{e(e+h)} \right)
\tag{13}
$$

The locations between the projection of point U_1 on x axis and z axis are

$$x_{u1} = -l_2 \sin \varphi \qquad (14)$$

$$z_{u1} = l_2 \cos \varphi \qquad (15)$$

Substituting Eqs. (8), (14) and (15) into Eq. (7) yields

$$\begin{vmatrix} -l_2 \sin \varphi \\ 0 \\ l_2 \cos \varphi \\ 1 \end{vmatrix} = T_D \begin{vmatrix} 0 \\ 0 \\ b \\ 1 \end{vmatrix} \qquad (16)$$

$$T_D = \begin{vmatrix} 1 & 0 & -\dfrac{l_2 \sin \varphi}{b} & 0 \\ 0 & 1 & 0 & 0 \\ 0 & 0 & \dfrac{l_2 \cos \varphi}{b} & 0 \\ 0 & 0 & 0 & 1 \end{vmatrix} \qquad (17)$$

According to the principle of matrix operation,

$$T = T_A + T_D = \begin{vmatrix} 1 & 0 & \dfrac{l_2 \sin \varphi}{b} & -a \\ 0 & 1 & 0 & -\sqrt{l_1^2 - a^2} + d \\ 0 & 0 & \dfrac{l_2 \cos \varphi}{b} & 0 \\ 0 & 0 & 0 & 1 \end{vmatrix} \qquad (18)$$

By substituting Eq. (18) into Eq. (1), the relationship between the driving parameter coordinate $\begin{pmatrix} a & 0 & b \end{pmatrix}$ and the coordinate of point U_1 $\begin{pmatrix} x_{u1} & y_{u1} & z_{u1} \end{pmatrix}$ is obtained.

$$\begin{bmatrix} x_{u1} \\ y_{u1} \\ z_{u1} \\ 1 \end{bmatrix} = \begin{vmatrix} 1 & 0 & \dfrac{l_2 \sin \varphi}{b} & -a \\ 0 & 1 & 0 & -\sqrt{l_1^2 - a^2} + d \\ 0 & 0 & \dfrac{l_2 \cos \varphi}{b} & 0 \\ 0 & 0 & 0 & 1 \end{vmatrix} \begin{bmatrix} a \\ 0 \\ b \\ 1 \end{bmatrix} \qquad (19)$$

Similarly, the relationship between the driving parameter coordinate $\begin{pmatrix} a & 0 & b \end{pmatrix}$ and the position coordinate of point U_2 $\begin{pmatrix} x_{u2} & y_{u2} & z_{u2} \end{pmatrix}$ is used to define the output of the right branch chain.

$$
\begin{bmatrix} x_{u2} \\ y_{u2} \\ z_{u2} \\ 1 \end{bmatrix} = \begin{bmatrix} 1 & 0 & \dfrac{l_2 \sin\varphi}{b} & -a \\ 0 & 1 & 0 & \sqrt{l_1^2 - a^2} - d \\ 0 & 0 & \dfrac{l_2 \cos\varphi}{b} & 0 \\ 0 & 0 & 0 & 1 \end{bmatrix} \begin{bmatrix} a \\ 0 \\ b \\ 1 \end{bmatrix}
\tag{20}
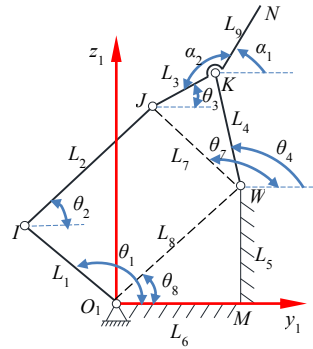$$

3.2   Kinematics analysis of the finger mechanism

Fig. 5. The sketch of $O_1 - y_1 z_1$ planar mechanism of left branch of finger

In Fig. 5, $L_i\, (i = 1, 2, ..., 6, 9)$ is the length of link, L_7 is the distance from point J to W, and L_8 is the distance from point O_1 to W. $\theta_i\, (i = 1, 2, ..., 8)$ is measured from y_1 axis, α_1 is the angle from y_1 axis to link KN, α_2 is the angle from link JK to link KN.

When the finger pinches the object, only the distal knuckle contacts with the object. The proximal knuckle and the distal knuckle are temporarily fixedly connected by the torsion spring. Since the distal knuckle and L_3 are on the same rigid link, the two knuckles and L_3 can be regarded as a whole, and the overall kinematic parameters can be consistent with the kinematic parameters of L_7. The finger mechanism can be considered as a combination of four-bar mechanism. An actuator for driving the linkage is installed to control the angle of L_1. θ_1 is treated as an input for kinematic analysis.

$$
L_7 = \sqrt{L_3^2 + L_4^2 - 2L_3 L_4 \cos\alpha}
\tag{21}
$$

$$
L_8 = \sqrt{L_5^2 + L_6^2}
\tag{22}
$$

$$
\theta_8 = \arctan\left(\frac{L_5}{L_6}\right)
\tag{23}
$$

To simplify calculations, the loop is composed of the kinematic chain of link 1-2-7-8. The vector-loop equation is written as follows [22].

$$L_1 + L_2 = L_7 + L_8 \tag{24}$$

$$L_1 e^{i\theta_1} + L_2 e^{i\theta_2} = L_7 e^{i\theta_7} + L_8 e^{i\theta_8} \tag{25}$$

To separate the real and imaginary parts of Eq. (25)

$$\begin{cases} L_1 \cos\theta_1 + L_2 \cos\theta_2 = L_7 \cos\theta_7 + L_8 \cos\theta_8 \\ L_1 \sin\theta_1 + L_2 \sin\theta_2 = L_7 \sin\theta_7 + L_8 \sin\theta_8 \end{cases} \tag{26}$$

In Eq. (26), the unknown angles θ_2 and θ_7 are obtained as follows.

$$\theta_2 = 2\arctan\left(\frac{P_1 + \sqrt{P_1^2 + Q_1^2 - R_1^2}}{Q_1 - R_1}\right) \tag{27}$$

$$\theta_7 = \arctan\left(\frac{L_1 \sin\theta_1 + L_2 \sin\theta_2 - L_8 \sin\theta_8}{L_1 \cos\theta_1 + L_2 \cos\theta_2 - L_8 \cos\theta_8}\right) \tag{28}$$

where

$$\begin{aligned} P_1 &= 2L_2\left(L_1 \sin\theta_1 - L_8 \sin\theta_8\right) \\ Q_1 &= 2L_2\left(L_1 \cos\theta_1 - L_8 \cos\theta_8\right) \\ R_1 &= \left(L_1 \cos\theta_1 - L_8 \cos\theta_8\right)^2 + \left(L_1 \sin\theta_1 - L_8 \sin\theta_8\right)^2 + L_2^2 - L_7^2 \end{aligned} \tag{29}$$

In ΔGKW,

$$\theta_3 = \arccos\left(\frac{L_3^2 + L_7^2 - L_4^2}{2L_3 L_7}\right) + \theta_7 - \pi \tag{30}$$

According to the angles above, the coordinates of joints of the linkage and the point N are calculated as follows:

$$\begin{cases} y_I = L_1 \cos\theta_1 \\ z_I = L_1 \sin\theta_1 \end{cases} \tag{31}$$

$$\begin{cases} y_J = L_1 \cos\theta_1 + L_2 \cos\theta_2 \\ z_J = L_1 \sin\theta_1 + L_2 \sin\theta_2 \end{cases} \tag{32}$$

$$\begin{cases} y_K = L_1 \cos\theta_1 + L_2 \cos\theta_2 + L_3 \cos\theta_3 \\ z_K = L_1 \sin\theta_1 + L_2 \sin\theta_2 + L_3 \sin\theta_3 \end{cases} \tag{33}$$

$$\begin{cases} \alpha_1 = \pi - \left(\alpha_2 - \theta_3\right) \\ y_N = y_K + L_9 \cos\alpha_1 \\ z_N = z_K + L_9 \sin\alpha_1 \end{cases} \tag{34}$$

4   Numerical example

According to the calculation results of the kinematic position of the palm, the workspace of point U_1 and point U_2 in the coordinate system can be obtained, as shown in Fig. 6 and Fig. 7. Mechanism parameter values are shown in Table 1.

Table 1. Parameters of finger structure

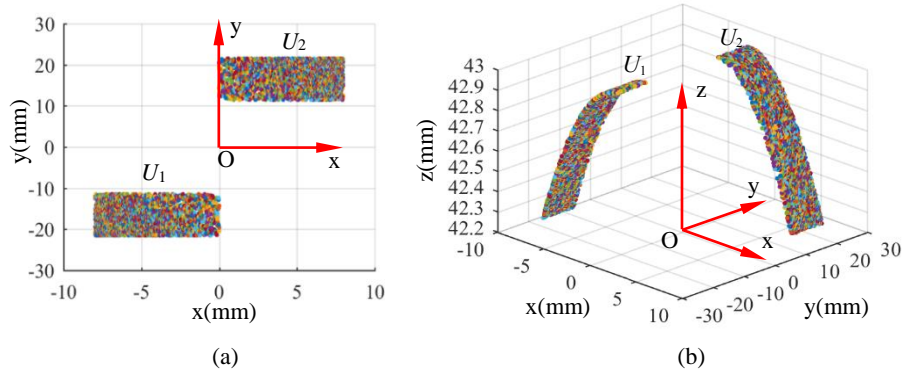| Parameter	l_1	l_3	d	e	a	h
Value(mm)	50	43	20.5	12	19.5~31	0~16

(a) (b)

Fig. 6. (a) Workspace of U_1 and U_2 in $O-xy$ plane; (b) Workspace of U_1 and U_2 in $O-xyz$ plane

In Fig. 6 and Fig. 7, when the slider drive parameter is in the range of 19.5 to 31mm, the point U_1 and point U_2 reach the workspace of ±10mm in the y axis. The minimum distance between U_1 and U_2 is 20mm, and the maximum distance is 40mm, indicating that the grasping hand has great grasping ability. When the slider drive parameter is in the range of 0 to 16mm, U_1 and U_2 rotate around the y axis, and the maximum stagger distance is 15mm, where the maximum rotation angle is 10.5°.
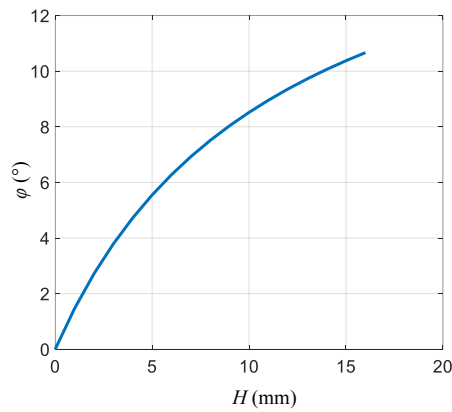

Fig. 7. The driving parameter H is related to φ

5   Conclusions

In this paper, based on the motion characteristics of human thumb and index finger, a novel of dexterous hand is designed. It has the ability to rotate objects while pinching the object. The kinematic equations of finger mechanism and palm mechanism are derived to calculate the coordinates of the terminal. Based on kinematic analysis, the simulation calculation of the workspace of the palm mechanism is carried out, and the maximum stagger distance of the palm mechanism is obtained.

This paper provides a theoretical basis for further performance analysis of dexterous hand, and also provides an important reference for the application of dexterous hand.

Acknowledgment

References

1. Piazza C, Grioli G, Catalano M G, et al.: A century of robotic hands. Annual Review of Control, Robotics, and Autonomous Systems 2, 1-32 (2019).
2. Li Z, Hou Z, Mao Y, et al.: The development of a two-finger dexterous bionic hand with three grasping patterns-NWAFU hand. Journal of Bionic Engineering 17(4), 718-731 (2020).
3. Okada T.: Computer Control of Multijointed Finger System for Precise Object-Handling. IEEE Transactions on Systems, Man, and Cybernetics 12(3), 289-299 (1982).
4. Franklin J A.: Robot hands and the mechanics of manipulation. In: Editor, M.T. Mason, Editor, J.K. Salisbury. Artificial Intelligence in Engineering, vol. 3(1), pp. 51-51 (1988).
5. Jacobsen S C, Wood J E, Knutti D F, et al.: The UTAH/MIT dextrous hand: Work in progress. The International Journal of Robotics Research 3(4), 21-50 (1984).
6. Jacobsen S, Iversen E, Knutti D, et al.: Design of the Utah/MIT dextrous hand. In: Proceedings. 1986 IEEE International Conference on Robotics and Automation, pp. 1520-1532. IEEE (1986).
7. Lovchik C S, Diftler M A.: The robonaut hand: A dexterous robot hand for space. In: Proceedings 1999 IEEE international conference on robotics and automation, pp. 907-912. IEEE, Detroit, MI, USA (1999).
8. Jian S. Dai, Delun Wang.: Geometric Analysis and Synthesis of the Metamorphic Robotic Hand. Journal of mechanical design 129(11), 1191-1197 (2007).
9. J. S. Dai, D. Wang and L. Cui.: Orientation and Workspace Analysis of the Multifingered Metamorphic Hand—Metahand. IEEE Transactions on Robotics 25(4), 942-947 (2009).
10. Wei G, Dai J S, Wang S, et al.: Kinematic analysis and prototype of a metamorphic anthropomorphic hand with a reconfigurable palm. International Journal of Humanoid Robotics 8(03), 459-479 (2011).
11. Yamaguchi K, Hirata Y, Kosuge K. Underactuated robot hand for dual-arm manipulation. In: 2015 IEEE/RSJ International Conference on Intelligent Robots and Systems (IROS), pp. 2937-2942. IEEE, Hamburg, Germany (2015).

12. Jin X, Fang Y, Zhang D, et al.: Design of dexterous hands based on parallel finger structures. Mechanism and Machine Theory, 152, 103952(2020).
13. Wang R, Huang H, Xu R, et al.: Design of a novel simulated "soft" mechanical grasper. Mechanism and Machine Theory 158(2), 104240 (2021).
14. Schmitz A, Pattacini U, Nori F, et al.: Design, realization and sensorization of the dexterous iCub hand. In: 2010 10th IEEE-RAS International Conference on Humanoid Robots, pp. 186-191. IEEE, Nashville, TN, USA (2010).
15. Wang L, DelPreto J, Bhattacharyya S, et al.: A highly-underactuated robotic hand with force and joint angle sensors. In: 2011 IEEE/RSJ International Conference on Intelligent Robots and Systems, pp. 1380-1385. IEEE, San Francisco, USA (2011).
16. Feix T, Romero J, Schmiedmayer H, et al.: The grasp taxonomy of human grasp types. IEEE Transactions on human-machine systems 46(1), 66-77 (2015).
17. Pozzi M, Sundaram A M, Malvezzi M, et al.: Grasp quality evaluation in underactuated robotic hands. In: 2016 IEEE/RSJ International Conference on Intelligent Robots and Systems (IROS), pp. 1946-1953. IEEE, Daejeon, Korea (South) (2016).
18. Kashef S R, Amini S, Akbarzadeh A.: Robotic hand: A review on linkage-driven finger mechanisms of prosthetic hands and evaluation of the performance criteria. Mechanism and Machine Theory 145, 103677 (2020).
19. G. Lu, N. An and Z. Liu.: Design and Kinematics Analysis of a Bionic Finger Hand Rehabilitation Robot Mechanism. In: 2019 34rd Youth Academic Annual Conference of Chinese Association of Automation (YAC), pp. 715-718. IEEE, Jinzhou, China (2019).
20. Shim M, Kim J H.: Design and optimization of a robotic gripper for the FEM assembly process of vehicles. Mechanism and Machine Theory 129, 1-16 (2018).
21. He J, Li J, Sun Z, et al.: Kinematic design of a serial-parallel hybrid finger mechanism actuated by twisted-and-coiled polymer. Mechanism and Machine Theory 152, 10395 (2020).
22. Norton R L, Institute W P.: Design of machinery: an introduction to the synthesis and analysis of mechanisms and machines. Mechanical Industry Press, China (2004).

Dimension Design of a Novel 2T2R-Type Rotary 3D Printer with Multi-mode for Flat and Curved Layer FDM

Donghua Zhao[0000-0002-6134-4929] Weizhong Guo[0000-0002-8982-7105]

State Key Laboratory of Mechanical Systems and Vibration, School of Mechanical Engineering, Shanghai Jiao Tong University, Shanghai, China
dongdong5212a@163.com;wzguo@sjtu.edu.cn

Abstract. Multi-degree-of-freedom (DOF) 3D printer is the precondition for curved layer fused deposition modeling (CLFDM) and also the promising direction of Additive Manufacturing (AM). Our previous research concerning the 2T2R rotary 3D printer with multi-mode has validated its feasibility for flat layer fused deposition modeling (FDM) and CLFDM. However, that printer's workspace is a cylindrical space with inhomogeneous print head swing capability, leading to complicated process planning and kinematics modeling. Hence, we proposed a novel 2T2R-type rotary 3D printer. This paper focuses on dimension design using performance-chart-based design methodology (PCbDM) to obtain homogeneous print head swing capability. Usually, PCbDM optimization parameters should be less than four. Here, the types of 4R1P five-bar have been investigated as an equivalent mechanism innovatively (virtual double-rocker, crank-rocker, and rocker-crank) to reduce the design space dimensionality. Meanwhile, the slider-crank has been optimized with PCbDM to obtain the dimensional global optimum solution of the 3D printer. Besides, the layout of the remote center of motion (RCM) mechanism has also been considered to avoid interference between the printed part and mechanical structures. This research can help people understand how to carry out the dimension design of 4R1P for specific applications with Grashof criteria and provide references for those interested in the dimensional synthesis of a novel mechanism with multi-chain.

Keywords: 3D printer, FDM, coordinated motion, dimension design, performance-chart-based design methodology (PCbDM).

1 Introduction

The existing AM process planning is classified into planar and non-planar slicing [1]. Non-planar slicing further breaks through the layer-wise framework with the aid of infinite directions, where the support structure could be avoided by conforming to the parts' geometric characteristics. The process planning of non-planar slicing calls for innovative machine design for multi-DOF 3D printers. Nowadays, on the one hand, multi-DOF 3D printers can manufacture smooth surfaces and complicated parts [1,2].

On the other hand, multi-DOF 3D printers with coordinated motion have the advantages of high stiffness (speed and accuracy), simple structure, and minor errors [3]. The 2T2R-type rotary 3D printer has been researched in our previous work [4]. However, there are problems mentioned in the Abstract. Therefore, we have dedicated ourselves to the dimension design of a novel 2T2R-type rotary 3D printer.

The multi-parameter optimization problem has been further researched in various research fields, such as PCbDM for the cantilever-type legged lander [5] and the investigation of the manufacturing elements-based AM process planning with compromise decision support problem (cDSP) [6]. The cDSP is applied in multi-objective design problems in the trade space [7]. For example, a multistage hot rod rolling system [8] and the corresponding integrated design exploration of materials-products-processes [9] have been investigated based on the application of cDSP. Based on the physical model theory, the PCbDM transforms the infinite-dimensional design space into the finite non-dimensional design space [5]. With the aid of performance atlases, which provide excellent global optimization and visualization for the optimum dimension design process, the designers can easily carry out the dimension design by comparing different performance indices.

In general, both PCbDM and cDSP are helpful for the multi-objective-function-based optimal design. Since the former is primarily used in the field of dimension synthesis of mechanisms, the design and optimization method for parameters described in Sec. 3 rely on the PCbDM, including the process of giving and reducing parameters, finding bounds of each parameter, defining the design space based on goals and minimizing optimal results.

There are many works of research concerning the five-bar mechanism's space model and dimensional types [10], 2-DOF RRRRP planar mechanism's workspace [11], optimum kinematic design of 2-DOF parallel manipulators with mirror-symmetrical geometry [12], and the symmetrical PRRRP's performance analysis and optimum design [13]. However, there are few research works concerning the dimension design of the 4R1P five-bar planar mechanism.

This paper is structured as follows: First, introduce the 3D printer's mechanism and design requirements. Second, derive the optimization parameters and optimization criteria. Then, implement the PCbDM for 4R1P, 3R1P and consider the layout of the RCM mechanism. Finally, obtain the 3D printer's optimum parameters.

2 The Mechanism of the 3D Printer

2.1 Structures and Mechanism

The cylindrical coordinates-based 3D printer has a larger build volume, fewer parts, and higher accuracy for the rotary part [1]. The 2T2R-type rotary 3D printer is shown in **Fig.** 1. The motion characteristic is $M=T(z)R(N,z)T(x)R(M,y')$. Here, T means translation and R means rotation.

The mechanism is (RRRRP&RRRP&P)-P $\oplus$ R in **Fig. 1**, where R, P, underline and $\oplus$ represent revolute joints, prismatic joints, the active joints, and two modules

working with coordinated motion. The 4R1P five-bar mechanism $A_1B_1C_1D_2$ has been applied to realize the rotation $R(M,y')$ and radial translation $T(x)$ of the print head, and it combines a parallelogram-based one-DOF planar RCM mechanism $D_1GG_1D_2$ and $G_1F_1F_2G_2$. A crank-slider mechanism (3R1P) $A_2B_2C_2$ is applied to keep the actuators close to the base, leading to lower inertia. The 4R1P mechanism and crank-slider mechanism (3R1P) share the same slider $C_2DD_1D_2$. Here, F_2P represents the axis of the print head. P means the nozzle tip of the print head, which is collinear with DD_1D_2. The parallelogram-based mechanism's layout is in **Fig. 1**.

(a) The 2T2R 3D printer   (b) The print head mechanism
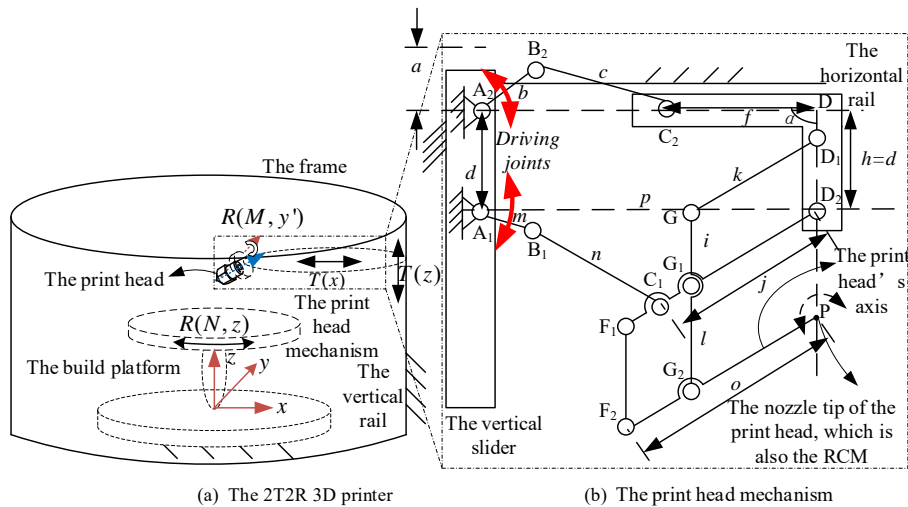
Fig. 1 The schematic diagram of the 2T2R-type 3D printer

For planar mechanisms, the Grübler–Kutzbach Criterion (G–K formula) [14,15] to analyze the 1T1R print head's mobility of mechanisms is 2. The DOFs of the 3D printer are equal to 4.

2.2 The Design Requirements

The PCbDM has the limitation mentioned in the Abstract. Hence, the 4R1P five-bar mechanism can be considered a four-bar mechanism with four optimization parameters for any slider's position. The structural dimensions should have a proper transmission angle and a constant common swing range when the slider moves. Under the structure limit, the print head's swing range is taken as [-30°,45°] around the horizontal. Here minus means the print head swings down. Besides, supposing the rotary build platform's diameter is 200mm, and the build volume height is 100mm. Hence, the print head mechanism's design goals are 1. Within the slider's larger stroke range of 100mm, the transmission angle is greater than the allowable value of 40°; 2. The output link has a large swing range of 75°.

3 Optimization Design of the 3d Printer

The vertical translation 1T is decoupled from the print head's radial translation 1T and rotation 1R. Therefore, the print head 1T1R mechanism's design procedure in **Fig. 2** is based on previous work on mobility and characteristics chart with Grashof criteria [12].
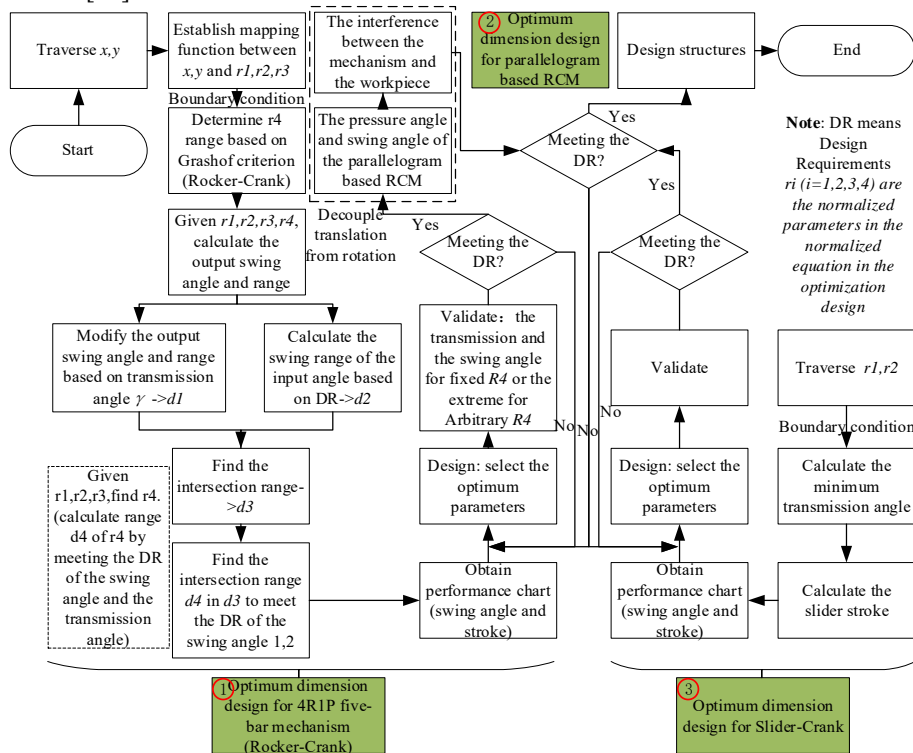

Fig. 2 The design procedure of the 1T1R print head mechanism based on rocker-crank

3.1 Brief Introduction of 4R1P Five-Bar's Classification based on Grashof Criterion

The 4R1P five-bar mechanism is regarded as a four-bar mechanism by introducing the virtual link with variable length d in **Fig. 3**, where the parameters of the remaining links determine the length d. Without considering the specific structure, the 4R1P five-bar mechanism must meet the assembly conditions to form a kinematic chain. In other words, the virtual four-bar mechanism should meet the quadrilateral closed condition: the length of the longest links should be less than the sum of the other three links($l_{max} \leqslant l_1+l_2+l_3$), where l_{max} is the longest bar of the virtual four-bar mechanism, and l_1, l_2, and l_3 are the lengths of the remaining three links.

In **Fig. 3** (a), the value range of the virtual link d is [0, $r_1+r_2+r_3$]. Specifically, if $d \in [0, r_{min}]$, d is the shortest link. $d \in [r_{min}, r_{max}]$, d is the middle link. $d \in [r_{max},$

$r_1+r_2+r_3$], d is the longest link, where $r_{max}=max(r_1, r_2, r_3)$, $r_{mid}= mid(r_1, r_2, r_3)$, $r_{min}= min(r_1, r_2, r_3)$. The reachable slider range is divided into three sub-sections in **Fig. 3**, respectively $r_{B1}=r_{min}$, $r_{B2}=r_{max}$ and $r_{B3}= r_{min}+r_{mid}+r_{max} =r_1+r_2+r_3$. Moreover, there will be a void area, which is not presented in **Fig. 3**, that the slider can not arrive in $r_{A1}= r_{max}-(r_{min}+r_{mid})$ if $r_{max}>(r_{min}+r_{mid})$. Based on the Grashof criterion to discuss whether the crank exists, the area divided by B_i could be further divided by $r_{C1}=r_{mid} +r_{min}-r_{max}$ if $r_{max}\leqslant(r_{min}+r_{mid})$, $r_{C2}= r_{min}+r_{max}-r_{mid}$ and $r_{C3}= r_{max}+r_{mid}-r_{min}$.
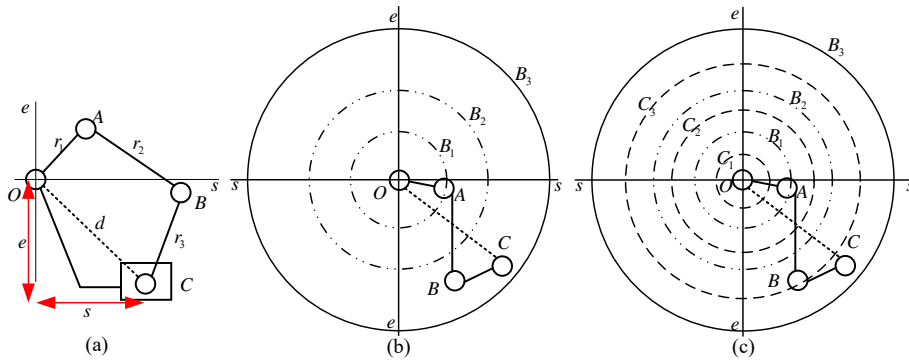

Fig. 3 (a) the scheme of 4R1P five-bar (b) the reachable slider range (c) Grashof division [16]

In general, it can be seen that the surrogate model (four-bar mechanism with the virtual link) of the 4R1P five-bar mechanism can be classified into four types: double-crank, double-rocker, double-crank, and crank-rocker. If $r_{max}<r_{mid}+ r_{min}$ is satisfied, the area of Grasshof is within r_{C1} and between r_{C2} and r_{C3}. The non-Grashof area is within $r_{C1}r_{C2}$ and within $r_{C3}r_{B3}$; if $r_{max}>r_{mid}+ r_{min}$ is satisfied, the Grashof area is between r_{C2} and r_{C3}. The non-Grashof area is within $r_{A1}r_{C2}$ and within $r_{C3}r_{B3}$; if $r_{max}>r_{mid}+ r_{min}$ is satisfied, the Grashof area is within $r_{C2}r_{C3}$. The non-Grashof area is within r_{C2} and between r_{C3} and r_{B2}.

3.2   Optimization Parameters

According to the 3D printer's radial stroke requirement (l=100mm), we should design $l\subseteq\Delta d$ ($\Delta d=d_{max}-d_{min}$), and then obtain the feasible regions of r_1, r_2, and r_3 of the virtual four-bar mechanism. At the same time, according to the limiting swing angle and its range (ψ_1, ψ_2 and $\psi=|\psi_1-\psi_2|$), and δ to describe the transmission angle, r_1, r_2, and r_3 are finally determined, as well as Δd, d_{max} and d_{min}.

According to **Fig. 1**, the critical dimension parameters determining the workspace for manufacturing capability are b, c, m, n and j. The parameter p depends on m, n, j, and the type of the 4R1P five-bar mechanism, affecting the existence of fully revolute joints.

3.3   Constraint Condition and Performance Indices

The stroke and pressure angles for slider-crank and rocker-crank are analyzed, not covering double-crank. Because in this case, the frame is the shortest bar, which

means the virtual link d is smaller than $r_{C1}= r_{mid}+r_{min}-r_{max}$ (if $r_{max}\leq r_{mid}+r_{min}$), leading to the difficulty in designing the slider stroke due to r_1, r_2, r_3 all larger than d. Therefore, a double-crank brings unreasonable structures to the 3D printer.

The mechanism works with the smaller the pressure angle α, reflecting the better force transmission characteristics of the planar multi-bar mechanism; The RCM mechanism [13] is incorporated to minimize the interference between the mechanical structure of the 3D printer and the printed part. The G1D2 swing range should be 75°, the same as the print head when the slider moves.

The parallelogram's output rod's swing angle range is [-50°, 50°] based on transmission angle requirement. Therefore, the parallelogram-based RCM mechanism's swing angle is taken as [-30°,45°] in **Fig. 1**. As a result, the print head can rotate around a fixed point P (the nozzle tip of the print head), also the RCM mechanism's remote center. Moreover, the axis of the print head is co-axial with the link G_1D_2.

3.4   Dimension Design of Slider-Crank

The design goals are slider stroke of 4R1P five-bar mechanism and the minimum transmission angle during AM. For unified expression, while obtaining the physical model of the design space and performance atlases of slider-crank and rocker-crank, R_i has been applied to represent the dimensional parameters. Supposing $R_1=b$, $R_2=c$, the normalization factor R is obtained by $R=(R_1+R_2)/2$, which means $R_1=R*r_1$, $R_2=R*r_2$. Then we can get the normalized equation $r_1 + r_2 = 2$.

The constraint inequations of normalized parameters are $0<r_1$, $r_2<2$, $r_1\leq r_2$ $(1< r_2<2)$. The minimum transmission angle is $\gamma_{min}=cos^{-1}(r_1/r_2)$. The slider's movement range is limited to the interior of the 3D printer when considering the 3D printer's structure. Hence, the rotation angle of r_1 is taken between ±90°. Under this circumstance, the change range of $r_{A_2C_{2\triangle}}$ is $[r_2 sin\gamma_{min}, r_1+r_2]$.

To select the optimum parameters of slider-crank easily, supposing the normalization factor $R=80mm$, the value of R_1 and R_2 meeting the design requirements could be obtained. The slider-crank mechanism's optimum dimension parameters are R1=68.8mm and R2=91.2mm to minimize the prototype's bounding box. The minimum transmission angle is 41.3°, and the slider stroke is 100.1mm.

3.5   Dimension Design of Rocker-Crank

Supposing $R_1=m$, $R_2=n$, $R_3=j$, the normalization factor R is obtained by $R=(R_1+R_2+R_3)/3$, which means $R_1=R*r_1$, $R_2=R*r_2$, $R3=R*r_3$. Then we can get the normalized equation $r_1+r_2 + r_3 = 1 (0 < r_1,r_2,r_3 < 3)$,

The constraint inequations of normalized parameters are ($r_3<r_2$, $r_3<r_1$, $0<r_3<1$, $1<r_2<2$, $1<r_1<2$, $r_{c2}<r_4<r_{c3}$). The parameter design space of rocker-crank is indicated with **Fig. 4**.
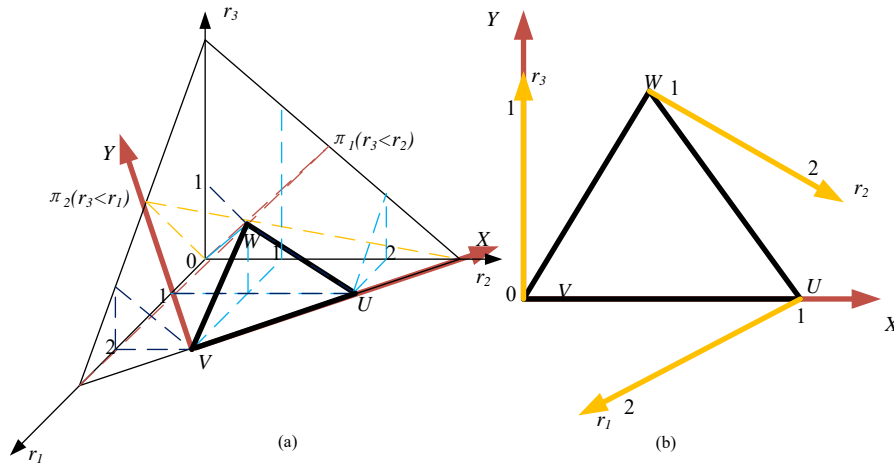
Fig. 4 Parameter design space of rocker-crank

The performance graphs of the output link's swing range and the slider stroke are in **Fig. 5**. The colored area meets the swing range requirement larger than 75° and the yellower means closing to 86°. A larger rotation capability of the print head is beneficial for CLFDM. Meanwhile, this area's slider stroke is minimal, close to zero and not acceptable. For slider stroke, the yellower is larger and suitable for dimensional parameters calculation.
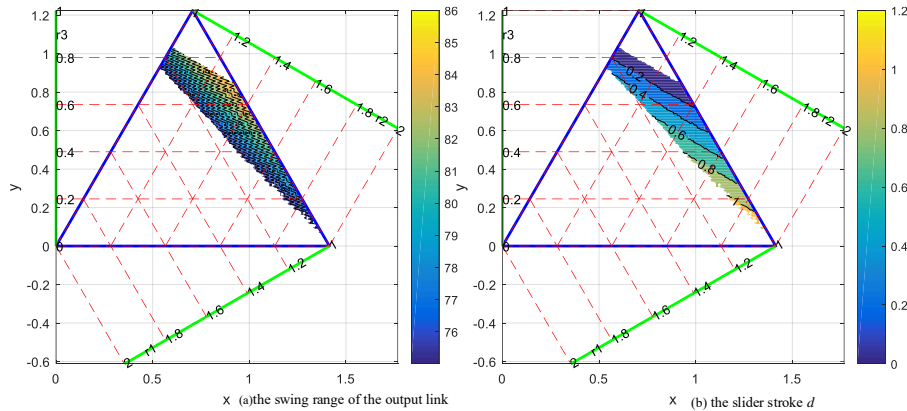

Fig. 5 The rocker-crank performance atlases: (a) the swing range (b) the slider stroke d

Furthermore, the double-rocker and crank-rocker dimension design results, which are not presented due to article length limitation, show that they do not meet the design requirements. Only the slider-crank and rocker-crank optimization results are given. The optimum dimension parameters of the slider-crank mechanism are $b=68.8mm$ and $c=91.2mm$. The minimum transmission angle is $41.3°$, and the slider stroke is $100.1mm$.
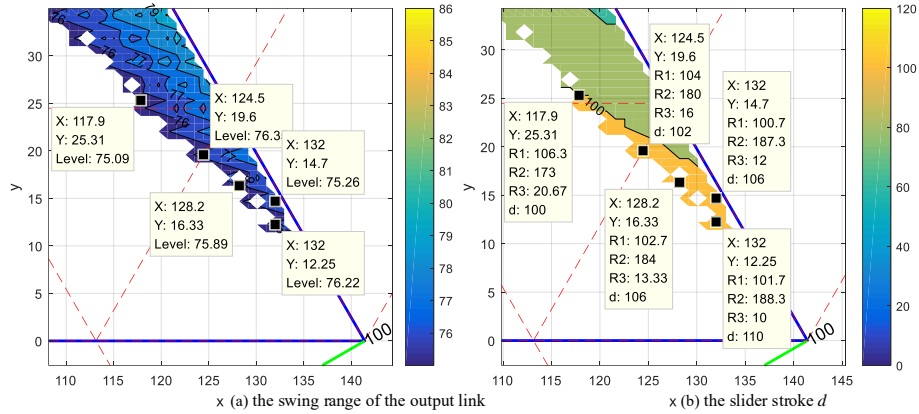
Fig. 6 Dimensional parameters selection based on the performance atlases of rocker-crank, (a) the swing range of the output link, and (b) the slider stroke d

To facilitate dimensional parameters selection of R_1, R_2, R_3, $R=100mm$ is taken, resulting in **Fig. 6**. The feasible region of R_1, R_2, R_3 with $d \geq l=100mm$ is the lower right corner area of the performance map, and the corresponding swing angle range of the output link exceeds 75°. Therefore, the farther to the lower right corner, the more significant the difference in R_1, R_2, R_3 is. Combined with design and manufacturing feasibility, let $R_1=m=106.3mm$, $R_2=n=173mm$, $R_3=j=20.67mm$, and the corresponding output bar's swing angle range is 75.09°. Hence, when $d=100mm$ and combined with d, it can be known that $A_1D_2=p=[158mm, 258mm]$.

4 The Virtual Prototype Structure Design and Workspace

The 3D printer's structure design is **Fig. 7**. Two groups of the print head have been applied for the pursuit of increasing printing speed. When the print head's gesture is fixed, the prototype functions with 2T1R mode, where the two driving joints in **Fig. 1** should work together. The prototype's 2T1R workspace for flat layer FDM and 2T2R workspaces for CLFDM is a $\phi200mm \times 100mm$ cylindrical space. The colors indicate the maximum value of the print head's upward and downward swing angles in the 2T2R mode. In other words, due to the difference in the radial position of the print head, the range of its upward and downward swing is also different. In the prototype design, both upward and downward shared swing ranges are taken as the print head's capacity space (from maximum upward swing angle 45° to maximum downward swing angle 30°). The working space validates the prototype design.
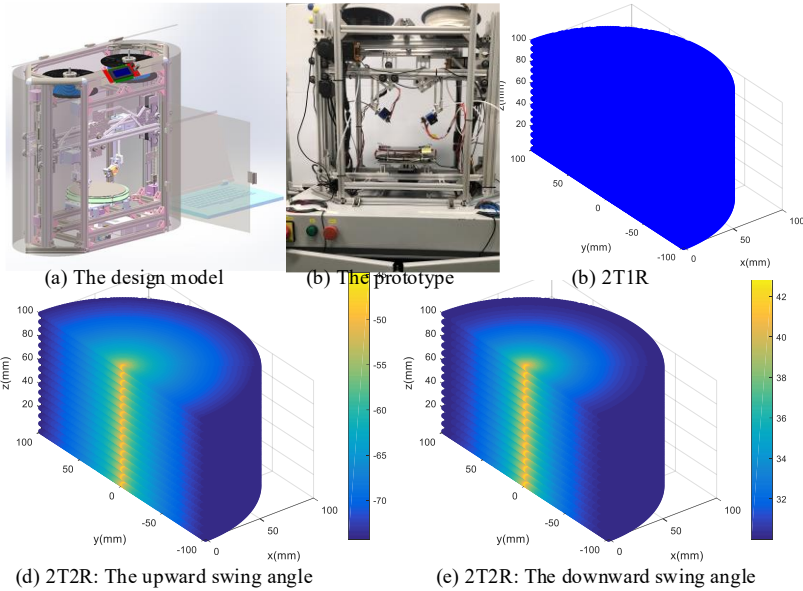
(a) The design model   (b) The prototype   (b) 2T1R

(d) 2T2R: The upward swing angle   (e) 2T2R: The downward swing angle

Fig. 7 The structure design of the prototype and workspaces for flat layer FDM and CLFDM

5   Conclusion

This paper presents a dimension design for the 2T2R-type rotary 3D printer. 4R1P, 3R1P, and RCM mechanisms have been considered simultaneously. Significantly, the classification of 4R1P five-bar based on the Grashof criterion has been applied to carry out PCbDM. This research provides a reliable, systematic, and comprehensive optimization design model for those interested in the 4R1P five-bar mechanism's dimension design and multi-chain mechanism. Finally, the results shown by the performance atlases are perceptual and reliable. Furthermore, a virtual prototype has been designed, and its kinematics and workspace have been obtained, which validate the dimension design.

References

1. Zhao, D., and Guo, W., 2020, "Shape and Performance Controlled Advanced Design for Additive Manufacturing: A Review of Slicing and Path Planning," J. Manuf. Sci. Eng. Trans. ASME, 142(1), pp. 1–23.

2. Gibson, I., Rosen, D., and Stucker, B., 2015, Additive Manufacturing Technologies: 3D Printing, Rapid Prototyping, and Direct Digital Manufacturing, Second Edition, Springer New York, New York, NY.

3. Wu, Y., Li, Z., Ding, H., and Lou, Y., 2011, "Quotient Kinematics Machines: Concept, Analysis and Synthesis," J. Mech. Robot., pp. 1964–1969.

4. Zhao, D., Li, T., Shen, B., Jiang, Y., Guo, W., and Gao, F., 2020, "A Multi-DOF Rotary 3D Printer: Machine Design, Performance Analysis and Process Planning of Curved Layer Fused Deposition Modeling (CLFDM)," Rapid Prototyp. J., 26(6), pp. 1079–1093.

5. Han, Y., Guo, W., Gao, F., and Yang, J., 2019, "A New Dimension Design Method for the Cantilever-Type Legged Lander Based on Truss-Mechanism Transformation," Mech. Mach. Theory, 142.

6. Xiong, Y., Tang, Y., Park, S. I., and Rosen, D. W., 2020, "Harnessing Process Variables in Additive Manufacturing for Design Using Manufacturing Elements," J. Mech. Des. Trans. ASME, 142(7).

7. 1993, "Compromise Decision Support Problem And The Adaptive Linear Programming Algorithm," Structural Optimization: Status And Promise, pp. 251–290.

8. Nellippallil, A. B., Song, K. N., Goh, C. H., Zagade, P., Gautham, B. P., Allen, J. K., and Mistree, F., 2017, "A Goal-Oriented, Sequential, Inverse Design Method for the Horizontal Integration of a Multistage Hot Rod Rolling System," J. Mech. Des. Trans. ASME, 139(3), pp. 1–16.

9. Nellippallil, A. B., Rangaraj, V., Gautham, B. P., Singh, A. K., Allen, J. K., and Mistree, F., 2018, "An Inverse, Decision-Based Design Method for Integrated Design Exploration of Materials, Products, and Manufacturing Processes," J. Mech. Des. Trans. ASME, 140(11), pp. 1–17.

10. Chi-Hou, Y., 1987, "The Space Model and Dimensional Types of the Four-Bar Mechanism," Mech. Mach. Theory, 22(1), pp. 71–76.

11. Bayram, A., and Kara, F., 2019, "The Workspace Optimization of a 2-DOF RRRPP Planar Mechanism Using Genetic Algorithm," VAN, TURKEY, pp. 49–61.

12. Huang, T., Li, M., Li, Z., Chetwynd, D. G., and Whitehouse, D. J., 2004, "Optimal Kinematic Design of 2-DOF Parallel Manipulators with Well-Shaped Workspace Bounded by a Specified Conditioning Index," IEEE Trans. Robot. Autom., 20(3), pp. 538–543.

13. Liu, X. J., Wang, J., and Pritschow, G., 2006, "On the Optimal Kinematic Design of the PRRRP 2-DoF Parallel Mechanism," Mech. Mach. Theory, 41(9), pp. 1111–1130.

14. Kutzbach, K., 1929, "Mechanische Leitungsverzweigung, Ihre Gesetze Und Anwendungen," Maschinenbau, 8(21), pp. 710–716.

15. Grübler, M., 1884, Allgemeine Eigenschaften Der Zwangläufigen Ebenen Kinematischen Ketten, L. Simion, L. Simion.

16. Guo, W. Z., Zou, H. J., Han, B., and Zhang, Q., 2004, "Mobility of 4R1P-Type Five-Bars Using Characteristics Charts," Proceedings of the ASME Design Engineering Technical Conference, pp. 627–634.

17. Guo, W. Z., and Gao, F., 2010, "Solution Space Atlases, Workspace Characteristics Charts and Joint Space Maps for the Design of Planar Serial Manipulators," Mech. Mach. Theory, 45(3), pp. 392–407.

18. Zong, G., Pei, X., Yu, J., and Bi, S., 2008, "Classification and Type Synthesis of 1-DOF Remote Center of Motion Mechanisms," Mech. Mach. Theory, 43(12), pp. 1585–1595.

19. Ye, W., Zhang, B., and Li, Q., 2020, "Design of a 1R1T Planar Mechanism with Remote Center of Motion," Mech. Mach. Theory, 149.

A 6-DOF Soft Robotic Joint with Tilt-arranged Origami Actuator

Sicong Liu[1,2,3], Jianhui Liu[1,2,3], Kehan Zou[1,2,3], Xiaocheng Wang[4], Juan Yi[1,2,3] and Zheng Wang*[1,2,3]

[1]Shenzhen Key Laboratory of Biomimetic Robotics and Intelligent Systems, Department of Mechanical and Energy Engineering, Southern University of Science and Technology, Shenzhen, China,

[2]Guangdong Provincial Key Laboratory of Human Augmentation and Rehabilitation Robotics in Universities, Southern University of Science and Technology, Shenzhen, China,

[3]Department of Mechanical and Energy Engineering, Southern University of Science and Technology, Shenzhen, China,

[4] the Center of Intelligent Control and Telescience, Tsinghua Shenzhen International Graduate School, Tsinghua University, Shenzhen, China

{liusc, Yji3, wangz}@sustech.edu.cn

Abstract. Soft manipulators attract increasing interests in robotic applications involving unstructured environment and human-robot interaction. The majority of the soft manipulator consists of joints that constructed by parallel actuators, achieving rotation and extension. The lack of twisting and lateral translations in the joints hinders the applications of the soft manipulators that require dexterous manipulation. In this work, we proposed a soft robotic joint with 6 soft origami actuators (SOAs) arranged in a tilted fashion, achieving 6 degree-of-freedom (DOF), i.e., 3 rotation and 3 translations. The actuation and passive section of the mass-production-ready SOA imitated the function of the hydraulic pump and universal joint of a conventional parallel mechanism, respectively. The 6-DOF joint maintains adaptivity, safety in the human-robot interaction and light weight (74.8g) due to the implementation of soft actuators and soft-rigid structure, while obtaining the superior dexterity. A 4-joint assembly have been produced to verify the practicality of the joint in constructing soft robotic systems. The investigation on the characteristics of the 4-joint assembly recorded maximum in-plane translations range over 70mm, axial translation over 50mm, and rotations over 120° in all three directions. FEM simulations have been carried out on the mechanical behavior of the joint. The simulation data show good agreement with the experimental results, which validate the simulation model. The proposed 6-DOF soft joint and simulation model showed the potential to be implemented in the design of the dexterous and light weight soft robotic system, with mass-production readiness.

Keywords: Soft origami actuator, soft-rigid mechanism, soft robotic joint, parallel mechanism.

1   INTRODUCTION

Soft robots receive significant interest in robotic applications involving unstructured environment and human-robot interaction, due to the merits in conformity to surfaces or objects, energy absorption to maintain stability, physical robustness and human-safe operation at potentially low cost [1].

The soft manipulators are essential when interacting with the environments and human. Substantial progresses in researches on soft manipulators have been presented. While the Active Hose[2] consists of spine structure and tube actuator wound around the hose, the majority of soft manipulators adopt the design with parallel arranged fluidic actuation chambers and multiple sections, achieving omnidirectional bending and elongation/shortening. The KSI tentacle[3] and Air-Octor[4] consist of pneumatic bladders and radially arranged cables. The McKibben-type artificial muscles are used in the continuum robot[5], the OctArm[6], the pneumatically actuated manipulator [7] and antagonistic actuation manipulator [8], drawing inspiration from the octopus tenacle. The Bionic Handling Assistant [9] and I-support soft arm [10] are actuated by Omega-shaped pneumatic chambers. The Robotic Tentacles [11], soft spatial fluidic manipulator [12], OBSS soft underwater manipulator [13] and the STIFF-FLOP manipulator [14] are based on flexible elastomers.

Modular designs are commonly used in the manipulators, for the advantage in customization, simplified fabrication and cost efficiency. Each module can be considered as a soft joint for the manipulator, consisting of multiple soft actuators. To enhance the load capacity and perception of soft robot, a series of soft joints have been proposed in [15,16,17], integrating pneumatic bellow actuators with soft-rigid approach, achieving omnidirectional bending and extension/shortening. Apart from composing the continuum manipulators, the soft joints also serve as the actuation modules for soft robotic arm [15] and gripper [18] with rigid linkages, as well as soft wearable devices [19,20].

While the state-of-the-arts soft manipulators and joints have shown mobility in bending and elongation, the lack of twist and lateral translation motions at the distal end, i.e., the rotation around its symmetrical axis and in-plane translations perpendicular to the axis, hinders its wider application, especially in dexterous manipulation. There are innovative approaches that have obtained twist motion inspired by origami patterns. The rotation around the axis of the triangulated cylindrical origami, also known as the Kresling pattern [21], have been investigated in [22] and [23], aiming for mechanical memory storage and impact mitigating applications, respectively. An 3D-printed origami soft robotic joint has been proposed in [24], consists of two origami pneumatic chambers, outputting rotation. However, adding such module dedicated to the twist motion onto the soft manipulator will increase the weight, body profile, control complexity and cost.

In developing soft joints, the general limitations of the soft actuators in the repeatability and complexity in fabrication significantly restrict the application. In order to further enhance the practicality and extend the application potential, a highly repeatable and mass-production-ready soft robotic actuator with linear mechanical behavior is required. The soft origami actuator (SOA), introduced in [19, 20] made by blow molding,

has shown the advantage in cost, repeatability, linear performance, high production-rate and mass-production potential, thus, meets the requirement.

In this work, to achieve dexterous movement, namely twisting, lateral translation, bending and extending, while maintaining a simple structure, we propose a soft robotic joint consisting of 6 origami patterned soft actuator in tilted arrangements between two rigid panels, outputting 6 degree-of-freedom (6-DOF). In comparison to the state-of-the-art soft joints, the proposed Tilted Actuator Soft Robotic (TASR) joint achieved the additional twisting and 2 translations without adding extra component, thus the weight and simplicity in the design will be retained. The main contributions are as follows:

1) A novel design of the soft robotic joint with tilted arrangement of actuators in between rigid panels was proposed, which enables the joint with 6-DOF mobility, namely twisting, bending around two directions and translation in three directions, without adding extra component or weight;

2) experimental investigation and simulation on the behavior of the proposed soft joint have been carried out, the validated Finite Element Method(FEM) simulation model can be used for customization and optimization of such joint, reducing the cost and time in the prototyping circle;

The concept of the joint is presented in Section 2, the design and fabrication are described in Section 3, Section 4 includes the experiments and simulations on the mechanical behavior of the actuator and joint. Section 5 concludes the paper with the future works proposed.

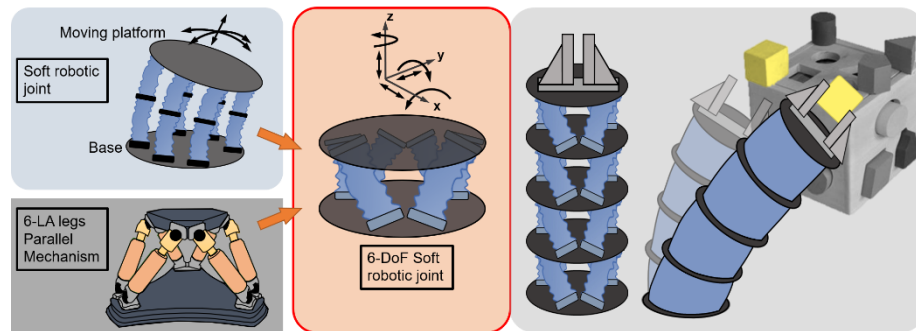## 2   Concept of the TASR joint

Fig. 1. The concept of the joint for dexterous application.

To find solution to the limitation in mobility, enabling the existing soft robotic joint with dexterous movement, the state-of-the-art parallel mechanisms were analyzed due to the modular structure and fluidic actuation method [21, 22]. The similarities between the soft joint and the parallel mechanism include the two panels, i.e., the base and the moving platform panels, and the translation-type actuators assembly in between, as shown in Fig. 1. By substituting the conventional fluidic pumps with soft pneumatic actuators, the resultant joint could achieve the desired mobility, while maintaining the merits of the soft robotic joints, hence obtaining the enhanced performance intended

for broaden application scenarios. To achieve superior dexterity in the moving platform and keep a compact structure, the tilted actuator arrangement of the 6-DOF parallel mechanism with 6 linearly actuated(6-LA) legs is adopted in the proposed soft robotic joint [23].

The soft origami actuator (SOA) is used to drive the platform, due to the versatility of the origami pattern. by changing the geometry of the origami facets and the combination of the mountain and valley folds, the actuator can be easily designated with three dedicated functional sections as shown in Fig. 2. In this way, the linear translation of the fluidic pump will be substituted by the elongation and contraction of the actuation section when pressurized and depressurized, respectively. The passive rotations of both universal joints during the movement of the platform will be accommodated by the deformation of the passive sections on the soft actuator, utilizing the compliance of the material and the purposeful design, see Fig. 2.
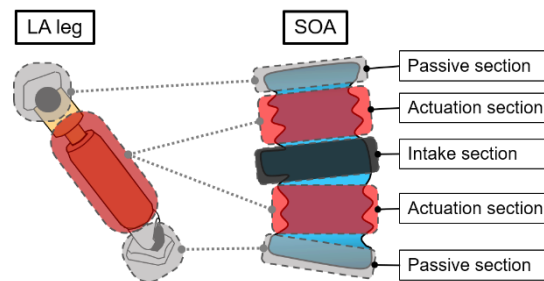

Fig. 2. Concept of the soft actuator comparing with the LA leg of the PM

The proposed joint is composed by 6 soft origami actuators in a tilted arrangement between two rigid panels, enabling 6-DOF mobility. The SOA is designed with dedicated functional sections to output extension and to accommodate passive deformation. In comparison with the existing soft robotic joints [5, 15-18], the proposed joint outputs 6-DOF mobility without adding extra component by utilizing 1) the SOAs of dedicated functional sections, 2) in a tilted arrangement.

3 Design and fabrication
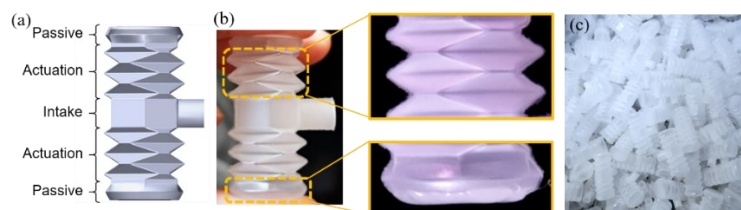
3.1 Production of SOA

Fig. 3. The design and fabrication of the actuator (a) the 3D model, (b) the SOA is fabricated by blow molding of EVA, (c) a batch of 500 pieces have been produced in one run.

To output extension, accommodate the passive deformation at both ends and consider the pneumatic input, the SOA is designed with three functional sections on the walls of the pneumatic chamber as shown in Fig. 3, namely, the Actuation, Passive and Intake section. The actuation sections implemented a variation of the Yoshimura origami pattern, with identical hexagonal facets. The hexagon facets effectively eliminate the extruding vertices formed by the triangular facets of the standard Yoshimura pattern, which fitted to the requirement of the blow molding fabrication process. In the passive section as shown in Fig.3, the prismatic origami pattern gradually transforms into a circular bottom, creating a flexible area tending to deform with the movement of the joint. The pneumatic intake section was placed between the actuation sections for compactness and as the reinforcement to the structure of SOA.

The geometric parameters of SOA are presented in [19]. The actuators were made of highly commercialized material Ethylene-Vinyl Acetate Copolymer (EVA) by FORMOSA. The SOAs have been produced in large quantity using blow molding. A batch of 500 pieces of SOA have been produced in one run. The investigation on the mechanical performance have been complete in [19].

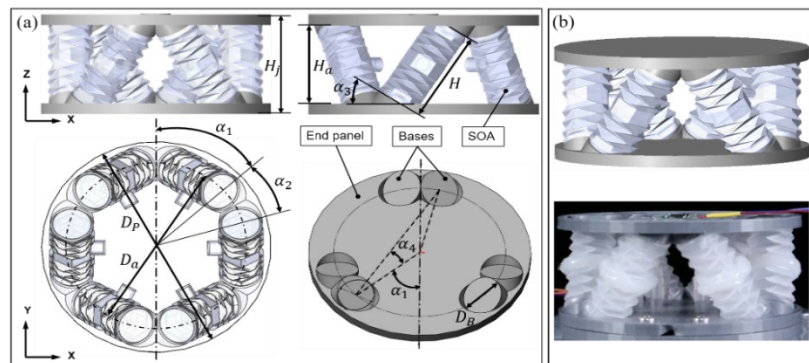## 3.2 Design and fabrication of the TASR joint

Fig. 4. The design and prototype of the 6-DOF soft robotic joint, (a) the design and geometric parameters of the TASR joint, (b) the 3D model and the prototype.

To achieve 6-DOF mobility and compactness, the design of the proposed TASR joint take inspiration from the state-of-the-arts soft joints and conventional 6 linearly-actuated-legs parallel mechanism. The TASR was composed of 2 rigid end panels and 6 SOAs using a soft-rigid design approach. The rigid panels were fabricated by FDM 3D-printing with PLA material. By assembling SOA in between the end panels in a tilted fashion (See Fig. 4), the joint is able to output 3 translations and 3 rotations along each axis of the datum. In order to minimize the profile of the joint, the actuators were assembled into a zigzag closed chain along the circumference of the end pFanels, with the adjacent bases closely positioned. The geometric parameters are listed in Table 1.

The prototype of the joint was produced as shown in Fig. 4. Each end of the actuator was fixed to the base on the panels using EVA based glue. Before assembling the SOA,

the pneumatic fittings were plugged into the actuator, and the tubes were routed through the designated channels on the panels. The resultant prototype, which was 74.8g in weight and 46.7mm in height, inherent the merits of soft robots, such as the safety in human-robot interaction, simplicity in design and easy-to-build, and achieved 6-DOF mobility.

Table 1. geometric parameters of the TASR joint

H	Height of SOA	42mm
H_j	Height of TASR	45.3mm
H_a	Initial height between two panels	35.3mm
D_a	Diameter of the base locations	77mm
D_P	Diameter of the end panels	100mm
D_B	Diameter of the base	19mm
α_1	Angular location 1 of the base	47.5°
α_2	Angular location 2 of the base	25.1°
α_3	Tilt angle of the base	33.1°
α_4	Twist angle of the base	17.2°

4 Experiments, kinematics and simulation

The TASR joint is capable of 6-DOF mobility. The movements are determined by the combination of the SOAs outputs. The range of motion and output force are investigated by experiments. The kinematic and simulation analysis were carried out.

4.1 The experiments on the TASR joint

The 6-DOF movements are presented in Fig. 5. In each axial view, the pressurized SOAs are marked as red, the depressurized are marked as blue and the non-pressurized remain blank. Due to the coupling motions of the SOAs, 3 translations and 3 rotations were obtained. The rotations X and Y are anisotropic due to the tilted arrangement of the SOAs. To output pure rotation Y, 3 adjacent SOAs are pressurized and the other 3 depressurized, while 2 neighboring SOAs were pressurized and the opposite 2 depressurized to derive pure rotation X. This is also the case in translation X and Y.

The anisotropic behaviors have been captured by the experiments, as shown in Fig. 6. Through the test setups, the angle of rotations and displacement of translations have been recorded by the IMU, 6-Axis motion tracking sensor MPU6050 (Gyro + Accelerometer, accuracy 0.1 degree, WitMotion, and the distance sensor, CMOS type Micro Laser Distance Sensor HG-C1100-P, respectively. The pneumatic pressures were recorded by sensor SSCDANN060PAAA5, 413kPa, Honeywell. The joint was controlled by the actuation box [20] as shown in Fig. 6a.

The angles and displacements were plotted against ΔP, which is the pressure difference between the pressurized and the depressurized SOAs. According to the experimental data, the TASR joint reached 15.4°, 20°, and 17.5° in rotations around axis X, Y and Z, respectively. The joint elongated 9.2mm and contract 11mm in Z direction,

while output 12.2mm and 10.3mm translational displacement in X and Y direction, respectively.
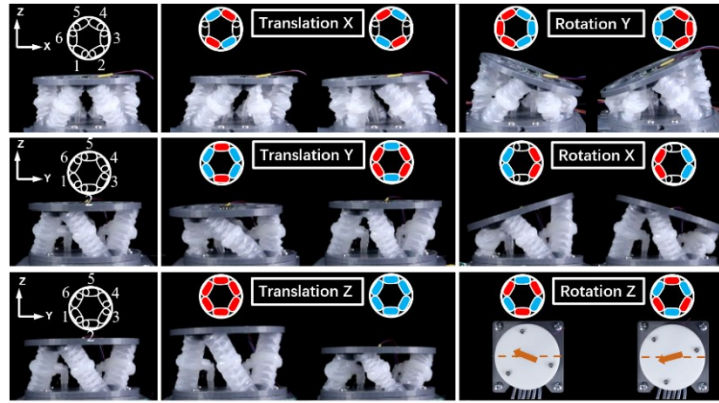

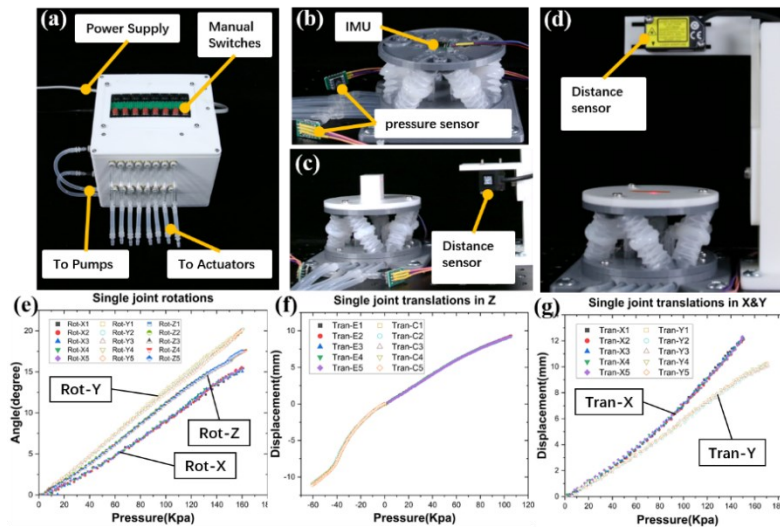**Fig. 5.** The actuation scheme and movements of the TASR joint

Fig. 6. The experiments on the TASR joint, (a) the actuation box, (b) the rotation angles were recorded by IMU sensor, (c) the translations in X, Y and (d) Z direction were captured by the distance sensor. (e) the angle-pressure relationships in three directions, (f) the displacement-pressure relationships in Z direction, (g) displacement-pressure relationships in X&Y direction.

4.2 Experiments on the 4-joint assembly

To further investigated the practicality of the TASR joint in constructing soft robots, an assembly of 4 TASR joints have been built as shown in Fig. 7. The joints were assembled by fixing the rigid panels with screws. The 4-joint assembly was 289.8g in weight, 185.4mm in height and 99.7mm in diameter. The 6-DOF mobility of the 4-joint

assembly has been obtained with the range of motions increased. The tests on the 4-joint assembly were carried out to measure the movements and force output as shown in Fig. 8. A force sensor, Allison, 3031-100N, was used to record the output force. The maximum displacement, angle and force are listed in Table 2.
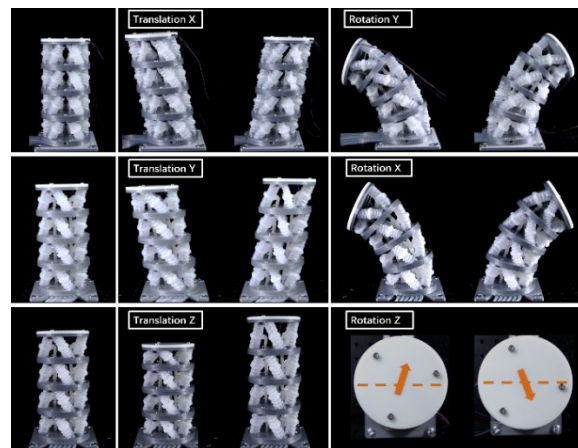
Fig. 7. Translations and rotations of the 4-joint soft arm
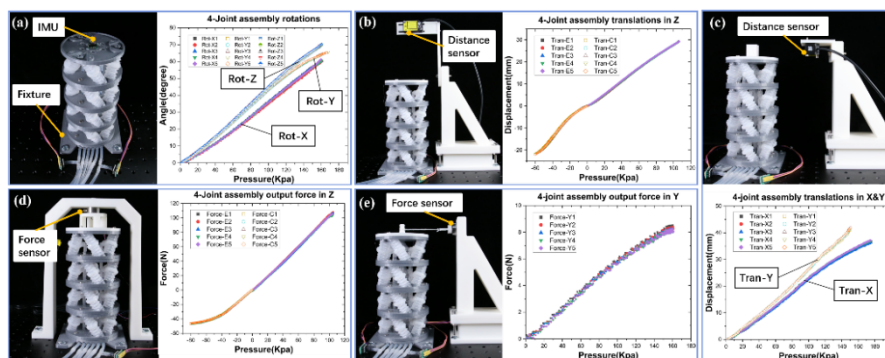
Fig. 8. The movements and force output of the 4-joint assembly were measured, (a) three rotations were measured by IMU, (b) the elongation and contraction in Z direction, (c) translation in X and Y direction, (d) the force output in Z direction and (e) in Y direction were measured.

Table 2. range of displacement

Direction	Displacement	Force
Translation X	37.2 mm	-
Translation Y	41.9 mm	8.5N
Elongation Z	29 mm	108N
Contraction Z	22 mm	46.3N
Rotation X	61°	-
Rotation Y	65°	-
Rotation Z	70°	-

4.3 Kinematics of TASR joint

To describe the movements of the joint, kinematic models of the TASR joint are derived using the geometric parameters defined in Fig. 4. The numbering for the SOAs is defined in Fig. 5. The kinematic model for translations is as following

$$l_i = \begin{cases} \sqrt{H_a^2 + \Delta_T^2 + R_a'^2 \pm 2R_a'\Delta_T \cos \alpha_T}, & \text{in translations;} \\ \sqrt{[H_a^2 \pm R_{sj}]^2 + R_{cj}^2 + R_a'^2 - 2R_a'R_{cj} \cos \alpha_R}, & \text{in rotation X and Y;} \\ \sqrt{2R_a^2[1 - \cos(\alpha_5 \pm \gamma)] + H_a^2}, & \text{in rotation Z,} \end{cases} \tag{1}$$

where $R_a' = R_a\sqrt{2(1 - \cos \alpha_5)}$, $R_{sj} = R_a \sin \alpha_j \sin \beta$, $R_{cj} = R_a \sin \alpha_j (1 - \cos \beta)$, $R_a = Da/2$, $\alpha_5 = \alpha_1 - \alpha_1/2$,

$$\alpha_T = \begin{cases} \alpha_1/2 + \alpha_2/4, & i = 1,2,4,5 \text{ in TX;} \\ \alpha_1 + \alpha_2/2, & i = 1,3,4,6 \text{ in TY;} \\ 0, & \text{other,} \end{cases}$$

$$\alpha_R = \begin{cases} \alpha_1/2 + \alpha_2/4, & i = 1,2 \text{ in RY;} \\ \pi - \alpha_1/2 - \alpha_2/4, & i = 4,5 \text{ in RY;} \\ \pm(\alpha_1 + \alpha_2/2), & i = 1,6 \text{ in RY;} \\ \mp(\alpha_1 + \alpha_2/2), & i = 3,4 \text{ in RY;} \\ \pi/2, & \text{other,} \end{cases} \quad \alpha_j = \begin{cases} \alpha_2/2, & i = 1,2 \text{ in RY;} \\ \pi - \alpha_5/2, & i = 3,6 \text{ in RY;} \\ \alpha_1, & i = 4,5 \text{ in RY;} \\ \alpha_1/2 + \alpha_2, & i = 1,3,4,6 \text{ in RX;} \\ \alpha_5/2, & i = 2,5 \text{ in RX,} \end{cases}$$

where TX, TY, RX, RY represent the translation X, Y, rotation X and Y, respectively. The deformations of the SOAs calculated from the kinematic models have been plotted in Fig. 9. The plots show that different SOAs output identical deformation in the same movement due to the rotational symmetric arrangements of the actuators, which could be used to simplify the control of the TASR joint.
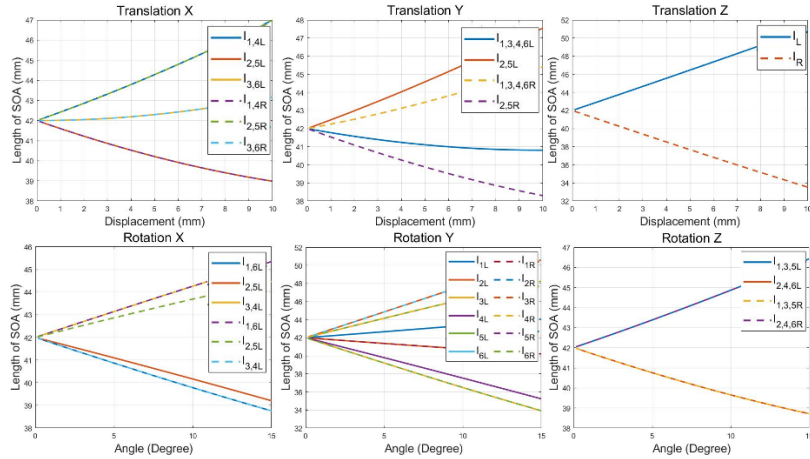

Fig. 9. The deformations of the SOAs calculated from the kinematic model.

4.4 Simulations of TASR joint

To investigate the deformation of the SOAs and the influence on the behavior of the TASR joint, a Finite Element Method (FEM) simulation model was developed, as shown in Fig. 10. The simulations on the 6-DOF movements of the TASR joint depends on the model of the SOA, thus, the pressure-displacement curve in [20] was used for validation of the SOA model.
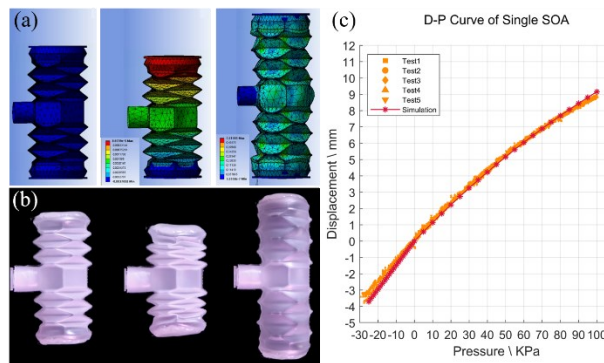

Fig. 10. The validation of the FEM model on the soft actuator, (a) the deformation of the SOA in simulations. (b) the contraction and elongation of the SOA captured by camera, (c) the simulation result shown good agreement with the experimental data.

The FEM simulations were carried out in ANSYS/Static Structure as shown in Fig. 10a and 10b. The SOA was meshed with solid Tet elements of minimum size 0.046mm. The EVA material for the SOA was given as elastic material with Young's modulus 15 MPa and Poison's ratio 0.35. To obtain the axial elongation and contraction of the SOA, the intake section was fixed and uniform pressure was applied to the inner surfaces. The simulation result is plotted in Fig. 10c, showing good agreement with the experimental data, hence, the FEM model for SOA was validated.

Base on the SOA model, the simulation for the TASR joint were carried out, as shown in Fig. 11. The PLA material (Young's modulus 3.45 GPa and Poison's ratio 0.39) was assigned to the rigid panels. The base panel were fixed while the moving panel were actuated by the coupling motions of the SOAs. The ends of the SOA were bonded with the bases on the rigid panels. The 6-DOF movements were obtained when the SOAs were actuated in the combinations as the schematics shown in Fig. 5. The simulation results were plotted in Fig. 11. The simulation data agree good with the experimental results in translation in X, rotations about X and Y and contraction in Z direction; while show disparities in rotation about X, translation in Y and elongation in Z direction.
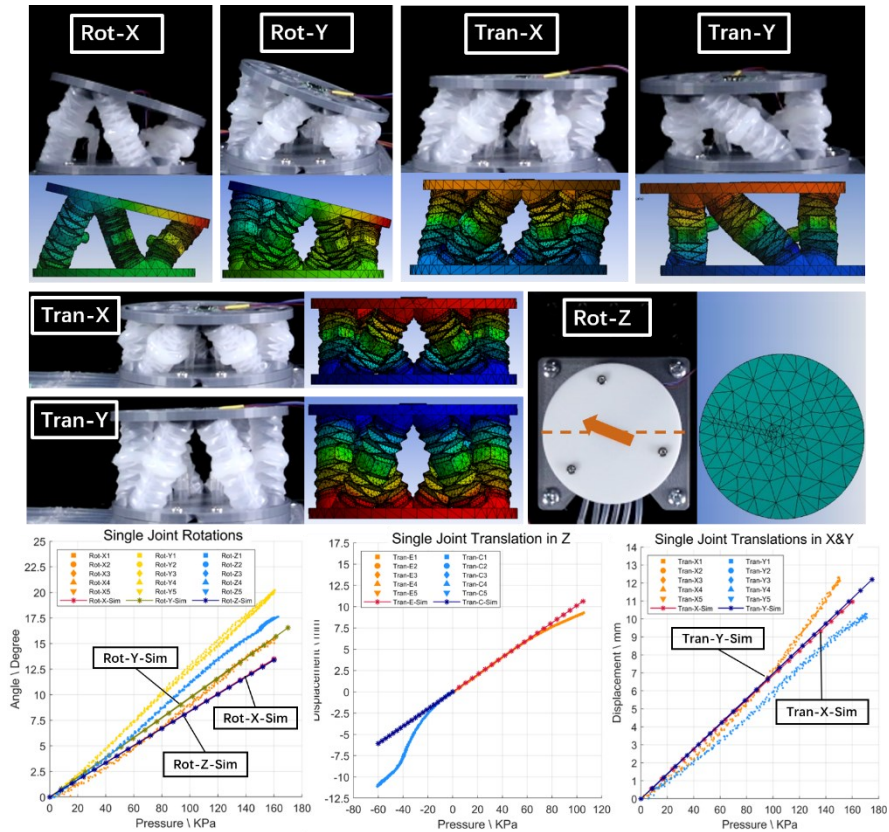
Fig. 11. Simulations on the TASR joint were compared with the experimental results.

5   Conclusion

The proposed TASR joint consists of 6 soft origami actuators in tilted arrangement and 2 rigid panels, achieving 6-DOF mobility. The additional twisting and in-plane translations at the moving panel were obtained without adding extra components or weights, in comparison to the state-of-the-art soft robotic joint. With the weight of 74.8g, the TASR joint was able to reach 15.4°, 20°, and 17.5° in rotations around axis X, Y and Z, respectively; elongated 9.2mm and contract 11mm in Z direction, translate 12.2mm and 10.3mm in X and Y direction, respectively. The practicality of the joint in constructing soft robots have been proved by the 4-joint assembly, which output maximum in-plane translations range over 70mm, axial translation over 50mm, and rotations over 120°. The FEM model of the SOA has been verified by the experimental data. The simulation on the TASR joint showed good agreements with the experimental results in translation in X, rotations about X and Y and contraction in Z direction. The TASR joint provides a dexterous, light-weight, simple structure and mass-production-ready solution to the soft robotic applications in unstructured environment and human-

robot interaction. The simulation model provides a design tool for the development of such soft robotic systems, reducing time and cost in the cycle of prototyping.

In the future works, the optimal design for the tilted arrangement, the joint integration in the soft robotic arms and the enhancement in rigidity and rapid response for the joint will be further studied.

References

1. Laschi, Mazzolai, Cianchetti, Soft robotics: Technologies and systems pushing the boundaries of robot abilities, Sci. Robot. 1, eaah3690 (2016)
2. Tsukagoshi H, Kitagawa A, Segawa M, et al. Active hose: an artificial elephant's nose with maneuverability for rescue operation. In: Robotics and automation, 2001. proceedings 2001 ICRA. IEEE international conference on, 2001, Vol. 3. IEEE.
3. Immega G and Antonelli K. The KSI tentacle manipulator. In: Proceedings of the IEEE International Conference on robotics and automation, 21 May 1995, Vol. 3, pp. 3149–3154. IEEE (1995).
4. McMahan W, Jones BA and Walker ID. Design and implementation of a multi-section continuum robot: Air-Octor. In: Intelligent Robots and Systems, 2005. (IROS 2005). 2005 IEEE/RSJ International Conference on, 2 August 2005, pp. 2578–2585. IEEE.
5. Pritts MB and Rahn CD. Design of an artificial muscle continuum robot. In: Robotics and automation, 2004, Proceedings. ICRA'04. 2004 IEEE International Conference on, 26 April 2004, vol. 5, pp. 4742–4746. IEEE.
6. McMahan W, Chitrakaran V, Csencsits M, et al. Field trials and testing of the OctArm continuum manipulator. In: Proceedings 2006 IEEE International Conference on Robotics and Automation, 2006. ICRA, 2006. IEEE.
7. Kang, R., Branson, D. T., Zheng, T., Guglielmino, E., & Caldwell, D. G. (2013). Design, modeling and control of a pneumatically actuated manipulator inspired by biological continuum structures. Bioinspiration & Biomimetics, 8(3), 036008.
8. Stilli A, Helge AW, Althoefer K, et al. Shrinkable, stiffness-controllable soft manipulator based on a bio-inspired antagonistic actuation principle. In: 2014 IEEE/RSJ International Conference on Intelligent Robots and Systems, 2014. IEEE.
9. Grzesiak A, Becker R and Verl A. The bionic handling assistant: a success story of additive manufacturing. Assem Autom 2011; 31(4): 329–333.
10. Arleo, L., Stano, G., Percoco, G. et al. I-support soft arm for assistance tasks: a new manufacturing approach based on 3D printing and characterization. Prog Addit Manuf 6, 243–256 (2021).
11. Martinez RV, Branch JL, Fish CR, Jin L, Shepherd RF, Nunes RM, Suo Z, Whitesides GM. Robotic tentacles with three-dimensional mobility based on flexible elastomers. Adv Mater. 2013 Jan 11;25(2):205-12.
12. Marchese AD, Rus D. Design, kinematics, and control of a soft spatial fluidic elastomer manipulator. The International Journal of Robotics Research. 2016;35(7):840-869.
13. Gong Z, Fang X, Chen X, et al. A soft manipulator for efficient delicate grasping in shallow water: Modeling, control, and real-world experiments. The International Journal of Robotics Research. 2021;40(1):449-469.
14. Ranzani T., Cianchetti M., Gerboni G., Falco I. D. and Menciassi A., "A Soft Modular Manipulator for Minimally Invasive Surgery: Design and Characterization of a Single Module," in IEEE Transactions on Robotics, vol. 32, no. 1, pp. 187-200, Feb. 2016

15. Chen X., Peng J., Zhou J., Chen Y., Wang M. Y. and Wang Z., "A robotic manipulator design with novel soft actuators," 2017 IEEE International Conference on Robotics and Automation (ICRA), Singapore, 2017, pp. 1878-1884.
16. Chen X., Yi J., Li J., Zhou J. and Wang Z., "Soft-Actuator-Based Robotic Joint for Safe and Forceful Interaction with Controllable Impact Response," in IEEE Robotics and Automation Letters, vol. 3, no. 4, pp. 3505-3512, Oct. 2018.
17. Chen, X., Duanmu, D. and Wang, Z. (2021) Model-Based Control and External Load Estimation of an Extensible Soft Robotic Arm. Front. Robot. AI 7:586490.
18. Su Y., Fang Z., Zhu W., Sun X., Zhu Y., Wang H., Huang H., Liu S. and Wang Z., "A Hybrid Robotic Gripper with High payload Soft Origamic Actuators and Proprioception," in Proc. IEEE Int. Conf. Robot. Automat. (ICRA), Paris, April 2020.
19. Liu S. et al., "Otariidae-inspired Soft-robotic Supernumerary Flippers by Fabric Kirigami and Origami," in IEEE/ASME Transactions on Mechatronics
20. Liu S., Fang Z., Liu J., Tang K., Luo J., Yi J., Hu X. and Wang Z. (2021) A Compact Soft Robotic Wrist Brace with Origami Actuators. Front. Robot. AI 8:614623.
21. Stewart, D. (1966), A Platform with Six Degrees of Freedom, Aircraft Engineering and Aerospace Technology, Vol. 38 No. 4, pp. 30-35.
22. Liu X., Wang J., Gao F. and Wang L., On the design of 6-DOF parallel micro-motion manipulators, Proceedings 2001 IEEE/RSJ International Conference on Intelligent Robots and Systems, 2001, pp. 343-348, vol.1.
23. Yang C., He J., Han J., Liu X. (2009). Real-time state estimation for spatial six-degree-of-freedom linearly actuated parallel robots. Mechatronics, 19(6), 1026–1033.
24. Cai J., Deng X., Zhang Y., Feng J., & Zhou Y. Folding Behavior of a Foldable Prismatic Mast with Kresling Origami Pattern. J. Mechanisms Robotics. 2016, 8(3): 031004.
25. Yasuda, H., Tachi, T., Lee, M. et al. Origami-based tunable truss structures for non-volatile mechanical memory operation. Nat Commun 8, 962 (2017).
26. Yasuda et al., Origami-based impact mitigation via rarefaction solitary wave creation, Sci. Adv. 2019; 5: eaau2835
27. Yi, J., Chen, X., Song, C., Zhou, J., Liu, Y., Liu, S., et al. (2018). Customizable three-dimensional-printed origami soft robotic joint with effective behavior shaping for safe interactions. IEEE Trans. Robotics 35 (1), 114–123.

Research on Path Planning Algorithm of Multi-Arm Collaborative Picking for Agaricus Bisporus Intelligent Picking Robot

Shuzhen Yang[1,2] and Bocai Jia [1] and Tao Yu[1]

[1] Shanghai University, Shangda Rd 99, Shanghai200444, China
[2] Shanghai Polytechnic University, Jinhai Rd 2360, Shanghai201209 ，China
szyang@sspu.edu.cn

Abstract. Based on the self-developed agaricus bisporus multi-arm picking robot, to optimize the the path planning problem with the difficulties such as equipartition of multi-arm tasks with Series Increasing Symmetric Shared (SISS) region, blanking point path, multi-arm avoidance and cluster-mushroom picking assignment, an improved stepwise algorithm combining Genetic Algorithm (GA) and Ant Colony Algorithm (ACO),which named GAAC,is proposed to achieve the optimal picking time. Firstly, GA is used to decompose the MTSP into m TSPs , and a DNA assignment rule is proposed for the SISS region so that each picking arm can achieve equal task under the constraints of the SISS region and the cluster-mushroom picking strategy. Then, ACO is used to get the shortest path of each TSP problem, meanwhile the avoidance problem of multi-arm cooperative picking was solved by combining auction mechanism. The experiment results show : GAAC can search for a relatively stable optimal solution in shorter time, and the optimal solution is improved by about 20% and 10%, respectively, compared with the Two-Chromosome Genetic Algorithm(TCGA) and stepwise algorithm combining Genetic Algorithm(GAGA). The hourly efficiency of a three-arm picking robot of agaricus bisporus,which be optimized by this algorithm,can reach manual level. It is the most efficient picking robot of Agaricus bisporus at present, which is of great significance to accelerate the practical process of picking robot of Agaricus bisporus and similar bed planting edible fungus.

Keywords: Agaricus Bisporus Picking Robot, Multi-arm Collaboration, Path Planning，MTSP，GAAC.

1   Introduction

Agaricus bisporus is one of the largest planting scale of edible fungi in the world. With the application of large-scale aseptic agaricus bisporus production workshops, Agaricus bisporus production has been greatly improved. However, its harvesting still relies on labor with high picking cost and difficult picking quality management. In addition, due to the poor environment, such as perennial low temperature and humidity, the danger of climbing to pick, and the difficulty in recruiting workers,the picking has become the main bottleneck affecting the further improvement of the output of Agaricus bisporus.

It is urgent to realize the automatic and efficient picking by the picking robot to adapt to its industrial production.

Scholars have carried out some research on Agaricus bisporus picking robot, but most of them using single picking arm, and the picking efficiency is generally low.For example,Yu Gaohong et al. [1] conducted a study on Agaricus bisporus picking robots, but their picking efficiency is much lower than manual picking, and it is impossible to realize true automation. Hu Xiaomei et al.[2] used the simulated annealing algorithm to optimize the Travelling Salesman Problem (TSP) of the Agaricus bisporus picking robot with a single picking arm, which improved the picking efficiency to a certain extent. It does not consider the specific picking strategy of gathering mushrooms, and the calculation time is too long,which will greatly affect the real-time performance of the control system. Therefore, in order to realize the practicality of the agaricus bisporus picking robot, the key point is to improve the picking efficiency of robot under the special requirements of picking.

A multi-arm picking robot of Agaricus bisporus is self-developed, which is equipped with multiple picking arms ,to improve the picking efficiency through the collaborative work of multiple arms, as shown in Fig.1.
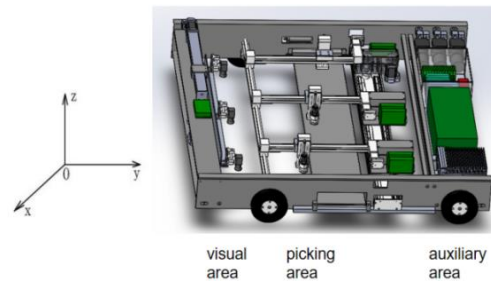

Fig. 1. Structure diagram of multi-arm picking robot of mushroom

The working principle is as follows: Firstly, the cameras in the visual area take pictures of Agaricus bisporus and identify the mature ones and their location that needs to be picked. Then, the control system of the auxiliary area intelligently optimizes all the picking tasks and assigns them to the three picking arms. Finally, the three picking arms in the picking area pick the mature agaricus bisporus and sends the picked ones to the conveyor belt, which transmits the Agaricus bisporus to the follow-up collection devicee.

In order to maximize the working efficiency of multi-arm picking robot, the keypoint is designing an appropriate assignment algorithm for multi-arm cooperative picking task to minimize the total picking time. The difficulties in solving this problem include:(1) To optimize the multi-arm cooperative picking path globally, both the equal distribution of picking tasks for each arm and the optimization of picking path for each arm should be considered; (2) Due to the phenomenon of multiple mushrooms clustering often occurs, as stated in section 2.2, the cluster mushrooms need to be picked from high to low to improve the success rate. This will make it harder to allocate picking

tasks to each arm equally; （3）For the size of the picking arm cannot be ignored compared with the narrow space of the mushroom bed, avoidance between arms should not be ignored,otherwise it will greatly affect the efficiency. This will increase the difficulty of optimizing the picking path of each arm; （4）The picking area is divided into exclusive area, partial shared area, and shared area. Mushrooms in different areas can only be picked by a certain number of picking arms, which will further increase the difficulty of even distribution of picking tasks and the picking path optimization.

According to the classification given in [3] and [4], this kind of multi-arm cooperative picking path planning problem of Agaricus bisporus generally belongs to the category of multi-task, multi-robot, and time-extended distribution, that is, it's a typical MTSP problem.

Common approaches to MTSP problem can be divided into two types [5]: precise algorithm and heuristic algorithm. The precise algorithmis is an early algorithm based on strict mathematical theory [6].Hermansson et al. [7] proposed a quasi-static planning algorithm when solving the path planning problem of an industrial robot performing welding work in a stud welding station.Spensieri et al. [8] used an accurate branch and bound method to solve the MTSP. Bektas et al. [9] used the cutting plane algorithm to solve the MTSP of vehicle path planning.Although precise algorithms have a strict mathematical foundation, their ability to solve problems depends entirely on the size of the problem. If there are too many Agaricus bisporus to be picked, the problem cannot be solved within an acceptable time.Therefore, more and more researchers turn to the study of heuristic algorithms, which can easily obtain the optimal, suboptimal or feasible solutions of large-scale MTSP [10-11]. The common strategy to solve MTSP in heuristic algorithm is to convert the problem into TSP, So that many methods used to solve TSP can be also used to solve MTSP [12]. The heuristic algorithms widely used to solve MTSP incude Genetic Algorithm(GA), Ant Colony Optimization(ACO) algorithm, Particle Swarm Optimization(PSO) algorithm and so on[13]. Sofge et al. [14] tried to use PSO to solve MTSP, and made some progress on the problem of small scale and small number of traveling merchants. But the approach can not work well if the problem is complicate,.Wei et al. [15] proposed a new multi-objective PSO to solve the MTSP of multi-robot collaborative work.The algorithm has fast convergence speed in the early stage, but it's easy to diverge in the later stage, so it is difficult to deal with MTSP which requires both balanced task distribution and the shortest total travel path.Liu et al. [16] used the maximum and minimum ant colony system combined with the local search algorithm to solve the MTSP, and obtained a better optimized solution for small-scale problems, but the global search ability of ACO was greatly weakened along with the increasing scale.Chen et al. [17] used ACO to solve the multi-robot patrol problem. The experiment proved that ACO has certain advantages in dealing with the MTSP with the shortest total travel path, but the uniform distribution of tasks is not considered. Wang et al. [18] used ACO in the logistics distribution problem,Considering the time constraints of modern commercial logistics and the impact of vehicle carrying capacity on logistics, but it did not study the problem of exclusive area and shared area of multi-traveling sales.Tang et al. [19] abstracted the hot rolling scheduling problem into MTSP model, decomposed the MTSP model into m TSP models, and used the improved GA to solve the problem. The scheduling quality is 20% improved than that

of traditional manual scheduling.Hu Shijuan [20] also used an improved GA to solve the MTSP, and obtained a more accurate optimization solution. Therefore, GA are getting more attention among the many heuristic algorithms used in MTSP[21].Due to the limitation of the mechanical structure, each picking arm has an unreachable area when multiple arms work together, that is, some cities can only be visited by a specific traveling agent. Li et al. [22] defined this type of MTSP with shared and exclusive areas as colored traveling salesman problem (CTSP), and the superiority of GA in solving this kind of problem has been proved by comparing several common algorithms. Dong et al. [23] used a new genetic algorithm with dual chromosome coding to solve the CTSP of resource and cargo scheduling. The experiment proved that the flexible coding method of GA is more suitable for such problems.General MTSP considers the optimal path problem only[24-26]. However, in some MTSP such as express delivery [27], transportation involving cargo handling [28] and workshop scheduling [29], traveling salesmen also need to spend extra time to work in each city.In this type of MTSP,the optimization goal of the problem is to minimize the total time which should consider not only the shortest distance, but also the traveling salesman's task banlance [30]. In the MTSP of multi-arm collaborative work in this paper, the time taken for the picking arm to perform picking in the position of the mushroom (city) is more than which taken for moving between citys. Therefore, to achieve optimal time of this MTSP, the problem of uniform assignment of tasks for traveling agents should be solved first, and then path optimization. For this kind of problem,the stepwise algorithm, which is easier to simplify the problem and achieve the shorter time, is more superior than the general algorithm[31].Xu et al. [32] used a stepwise algorithm combining clustering algorithm and genetic algorithm to deal with the MTSP, and achieved good results in terms of workload balance and overall travel minimum distance. Wang Mingjun [33] used a stepwise algorithm to study the MTSP of multi-UAV cooperative airport bird repelling. GA was used to decompose the MTSP into m TSPs to solve the task assignment of the UAV,and the experiment proved the superiority of GA in solving the task assignment problem of MTSP. Lu et al. [34] combined the K-means clustering algorithm and genetic algorithm to solve the multi-objective MTSP, and achieved a more uniform task distribution solution, avoiding the path crossing between traveling salesmen meanwhile, but its overall path search ability is poor.Luo zhiyuan et al. [35] used a stepwise algorithm to solve the MTSP of multiple unmanned cleaning vehicles area coverage path. The Fuzzy C-Means (FCM) clustering algorithm is used to decompose the MTSP into TSPs with multiple tasks balanced first, and then use GA to solve the TSP. Liu Wenbing et al. [36] proposed a stepwise combinatorial optimization algorithm based on clustering algorithm and genetic algorithm when studying the problem of multi-UAV collaborative search for multiple targets. Regrettably, neither of them has studied the collision problem when multi-robots work together.Although GA ,which has a strong global search ability in the early stage, can obtain better solutions and has certain advantages of dealing with CTSP, it is easy to fall into the local optimal solution in the later stage, the calculation time is also greatly increased meanwhile.So it is difficult to achieve good results for solving the avoidance problem of multi-arm cooperative work.

Aiming at the above problems of GA, this paper try to use the combination of GA and ant colony algorithm(ACO). ACO is a popular heuristic algorithm for solving discrete optimization problems in recent years.It has fast convergence and strong adaptability, and can be applied to any combinatorial optimization problem [37].ACO has been successfully applied in the fields of traveling salesman problem (TSP/MTSP), Sequential Ordering Problem (SOP),Multiple Knapsack Problem (MKP),Network Routing Problem (NRP), etc. Necula et al. [38] applied AC to the double standard surface of MTSP,Changdar et al. [39] applied ACO to the fixed-destination multi-station and multi-traveling salesman problem with non-random parameters, both got good result.

Therefore, to deal with the difficulties of exclusive area, partial shared area and shared area allocation, multi-arm avoidance, and cluster-mushrooms picking in the path planning problem of multi-arm picking robot, this paper combines the advantages of genetic algorithm and ant colony algorithm to design a stepwise algorithm based on GA and ACO (GAAC). Firstly, the MTSP problem is decomposed into m TSP problems by GA to get strong global optimization ability.Then, ACO is used to solve the single TSP problem to converge faster,at the same time,the auction mechanism is introduced into ACO to solve avoidance problem of the multi-arm collaborative picking. So,the performance of the GAAC algorithm to solve the MTSP in this paper is improved as a whole, which can not only overcome the shortcomings of the low global optimization efficiency of GA and the tendency to fall into local optimal solutions prematurely of ACO, but also improve the ability of general heuristic algorithms to solve the unique problem of avoidance between picking arms.

2   Description of Picking Path Planning Problem for Agaricus Bisporus Multi-Arm Robot

As described above, the multi-arm cooperative picking path planning problem of Agaricus bisporus picking robot studied in this paper is a typical MTSP problem. Its solution will be affected by the division of SSIS area and the constraint of cluster-mushrooms picking strategy,etc.

2.1   Description of Picking Area Division

As shown in Fig.1, the robot with M picking arms installed on the double beam structure.The picking arm can move freely in Y , while the movement in X will be limited by the adjacent arms, otherwise a collision may occur, so it is necessary to divide the cooperative picking area first, and then allocate picking task and plan path. The multi-arm cooperative work area is shown in Fig. 2. Set the length of the working area as L, the width of picking arm as W, the number of picking arms as M, and the starting points of each picking arm are 0,W,2W…(M-1)W. In this work area, there are not only exclusive areas S1 [1,1] and SM [M, M] with single arm working independently on both sides of the work area, which can only be picked by arm 1 and arm M respectively, but also a fully shared area s [1, M] which is located in the middle of the work area and can be picked by all arms. In addition, there are still some partial shared areas between the

exclusive area and the fully shared area, where the sharable picking arms increase in turn and symmetrically distributed from both sides to the middle. The entire work area is divided into 2M-1 picking areas in the X direction. In view of this, the shared area with above characteristic is called Serial Increasing Symmetric Shared (SISS) area in this paper, and the MTSP with SISS area is studied in the following.
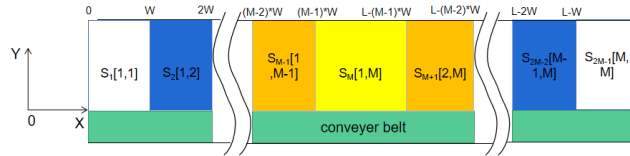

Fig. 2. Schematic diagram of picking area division

Now, define the SISS area.

The range of each picking area is determined by:

$$S_k=[X_{k-1}, X_k], \quad k\in\{1,2,\ldots,2M-1\} \tag{1}$$

$$X_k=\begin{cases} W\times k, & k\in\{1,2,\ldots M\} \\ L-(2M-1-k)\times W, & k\in\{M+1,M+2,\ldots,2M-1\} \end{cases} \tag{2}$$

Where S_k is the k-th picking area, X_k is the coordinate of the end point in the X direction of the k-th picking area;

The picking arms allowed to enter each area are determined by:

$$S_k[j1,j2]=\begin{cases} S_k[1,k], & k\in\{1,2,\ldots,M\} \\ S_k[k-M+1,M], & k\in\{M+1,M+2,\ldots,2M-1\} \end{cases} \tag{3}$$

Where [j1,j2] means the area can be picked by arms j1 to j2,$1\leqslant j1\leqslant j2\leqslant M$;

2.2 Picking Strategies for Cluster-Mushrooms

Due to the growth characteristics of mushroom, cluster-mushrooms often appear, as shown in Fig.3. A,B and C are clustered, and the height of A and C is higher than B. If they are picked in an random order as B-A(C)-C(A), the picking of B will fail and the A and C may be damaged as well, because the edge of B is partially covered by A and C.So cluster-mushrooms should be picked in the order from high to low.
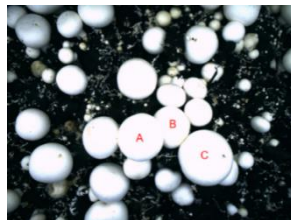

Fig. 3. Schematic diagram of cluster-mushrooms

In order to realize the aboved specific picking strategies for cluster-mushrooms,they are recognized and labeled in the visual recognition process in this paper.The method is as following: Expand and connect the mushroom region, and the region with cluster-mushrooms will be connected into a large region, then the mushrooms in this large connecting region should be marked with the same code, which called the cluster label,so that mushrooms with the same cluster label can be picked from high to low in turn.

2.3   Description of Path Planning for Multi-Arm Collaborative Picking

This paper aims to find the optimal path for each arm to pick mushrooms from their starting point,put them to the blanking area, and return to its original points after picking the last one. The optimal path should achieve the optimal total time T under the condition of meeting the actual picking constraints.

Suppose that the robot has M picking arms and N mushrooms to be picked in the work area. In this problem, each picking arm corresponds to the traveling salesman and the mushrooms corresponds to the city. That is, M traveling salesmen (picking arm) need to visit N cities (mushrooms) from M different original points and then return respectively. Each city (mushroom) can only be visited once by a traveling salesman (picking arm).

In addition, the traveling salesman (picking arm) needs to stay for a certain time (picking execution time) after arriving in a city (mushroom) before leaving. Moreover, every time the traveling salesman (picking arm) arrives in a city (mushroom), it needs to go to the conveyor belt(as shown in Fig.1) to drop materials before going to the next city (mushroom).

Therefore, the time T that needs to be optimized is the sum of the time traveled on the road and the time spent in each city (picking execution time for each mushroom).

The constraints are as follows:

— As described in section 2.2, the cluster-mushrooms should be picked in the order from high to low;
— A safety distance Dist is needed in the X direction between the picking arms to avoid collision. When the relative position of adjacent picking arms in the X direction is less than the safety distance Dist, avoidance between picking arms is required.
— The origin of each picking arm is (0,0), (W,0),...,((M-1)*W,0),each picking arm needs to return to the origin after completing all picking tasks.

Furthermore, some actual conditions of picking are assumed as follows:

— The picking time for each mushroom is the same. That is, when the picking arm moves to the (X, Y) coordinate position of the mushroom to be picked, it takes the same time for the Z direction to descend to pick and return to the Z=0 plane.
— The robot will take the same time(tp) to deal with each avoidance.

3 Mathematical Model of Path Planning for Multi-Arm Picking

3.1 Design Mathematical Model

Suppose the mushroom set is V = {1,2,...,N}, N is the number of mushrooms to be picked;U is the set of picking arms U={1,2,... ,M},$1 \leq M \leq N$; t_{jk} is the time taken by the picking arm to perform the task from mushroom j to mushroom k (j, k $\in$ V, j$\neq$ k);Let the number of mushrooms picked by the picking Arm i be Q_i,i$\in$U;Since the working range of each picking arm is limited, the set of mushrooms that can be picked by picking Arm i is $I_i \in V$; The picking Arm i needs to start from its original points d_i and finally return to the original points; Suppose there are e (e<N) groups of cluster mushrooms and each group is arranged from high to low, E = {1,2,...,e}, and the set of mushrooms in the u-th group is $C_u \in V$, u$\in$E; the total avoidance time is T_c, the total picking time is T. Thus, the objective function is :

$$\text{Min} \ \ T = \max (t\_ARM_i) + T_C, \ \ \forall i \in U \tag{4}$$

$$t\_ARM_i = \sum_{j=1}^{N}\sum_{k=1}^{N} t_{jk} x_{ijk} + \sum_{j=1}^{N} t_{d_i j} x_{id_i j} + \sum_{j=1}^{N} t_{jd_i} x_{ijd_i}, \ \ \forall i \in U \tag{5}$$

$$x_{ijk} = \begin{cases} 1, & \text{Arm i goes form mushroom j to k} \\ 0, & \text{other} \end{cases} \tag{6}$$

$$\sum_{j=1}^{N} t_{d_i j} x_{id_i j} = \frac{\sqrt{\left(X\_st_i - X_{d_i}\right)^2 + \left(Y\_st_i - 0\right)^2}}{v}, \ \ \forall i \in U \tag{7}$$

$$\sum_{j=1}^{N} t_{jd_i} x_{ijd_i} = \frac{\sqrt{\left(X\_end_i - X_{d_i}\right)^2 + \left(Y\_end_i - 0\right)^2}}{v}, \ \ \forall i \in U \tag{8}$$

Where,

$x_{id_i j}$ indicates that Arm i goes from the original points di to the mushroom j.

x_{ijd_i} indicates that Arm i goes from mushroom j to the original points d_i.

$(X_{d_i},0)$ indicates that the original point coordinates.

(X_st_i, Y_st_i) indicates that the coordinates of the first mushroom .

$(X\_end_i, Yend_i)$ indicates that the coordinates of the last mushroom .

The constraints are:

The sum of the number of mushrooms picked by all the picking arms should be equal to the total number of mushrooms N:

$$\sum_{i=1}^{M} Q_i = N \tag{9}$$

$$\sum_{j=1}^{N} y_{ij} = Q_i, \quad \forall i \in U \tag{10}$$

$$y_{ij} = \begin{cases} 1, & j \in I_i, \text{ when Arm i picks mushroom j} \\ 0, & \text{other} \end{cases} \tag{11}$$

Each mushroom can only be picked by one arm:

$$\sum_{i=1}^{M} y_{ij} = 1, \quad \forall j \in V \tag{12}$$

Each picking arm must start from its own original point and then come back after completing its picking task:

$$\sum_{j=1}^{N} x_{id_i,j} = \sum_{j=1}^{N} x_{ijd_i} = 1, \quad \forall i \in U \tag{13}$$

The same group of cluster-mushrooms should be picked by the same picking arm only, and they are picked in sequence in the order of the group:

$$\sum_{i=1}^{M} \prod_{j} y_{ij} = 1, \quad \forall j \in C_u, \ u \in E \tag{14}$$

$$\sum_{i=1}^{M} \prod_{j,k=j+1} x_{ijk} = 1, \quad \forall j, k \in C_u, \ u \in E \tag{15}$$

3.2   Determine the Optimal Blanking Point

The picking path of the Agaricus bisporus picking robot is different from the general path planning that only move from one object directly to next object. It also need to consider the blanking after the object is picked. So the blanking point C should be added into the picking path between the current object A and the next object B,as shown in Fig.5,and the picking path P_{AB} from one mushroom to another should be A-C-B. So it is the key to find a optimal blanking point C to get the shortest picking path P_{AB}.

As shown in Fig.4, Find the mirror point A' of A with respect to $y = 0$, then intersection point C of A'B and $y=0$ is the optimal blanking point.
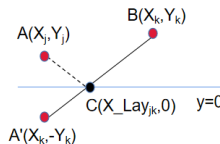

Fig. 4. The optimal path between two mushroom points

The X coordinate X_Lay_{jk} of C is calculated as:

$$X\_Lay_{jk} = \frac{Y_k\left(X_k - X_j\right)}{Y_j + Y_k}, \quad \forall j, k \in V \tag{16}$$

3.3 Caculate t_{jk} for Each Arm t-ARM$_i$

Picking Arm i picks mushroom j, and the next mushroom is k, j, k $\in$ V, the coordinates of mushroom j are (X_j, Y_j), the coordinates of k are (X_k, Y_k), the moving speed is v, and the actions can be divided into three phases:

Picking stage: The picking arm stops at the position to pick the mushrooms to pick them. At this time, the displacement $\Delta D1_{jk}$ is 0, $\Delta t1_{jk} = t_0$, and t_0 is the picking execution time, which is a constant.

Blanking stage: After the picking is completed, transport the mushroom j from the current position to the blanking point for blanking. The displacement is $\Delta D2_{jk}$ and the time is $\Delta t2_{jk}$.

Positioning stage: the picking arm moves from the blanking point $(X\_Lay_{jk}, 0)$ to the position of the next mushroom k to be picked. The displacement is $\Delta D3_{jk}$ and the time is $\Delta t3_{jk}$.

thus:

$$\Delta D2_{jk} = \sqrt{\left(X\_Lay_{jk} - X_j\right)^2 + \left(0 - Y_j\right)^2} \tag{17}$$

$$\Delta D3_{jk} = \sqrt{\left(X_k - X\_Lay_{jk}\right)^2 + \left(Y_k - 0\right)^2} \tag{18}$$

$$\Delta t2_{jk} = \frac{\Delta D2_{jk}}{v} \tag{19}$$

$$\Delta t3_{jk} = \frac{\Delta D3_{jk}}{v} \tag{20}$$

$$t_{jk} = \Delta t1_{jk} + \Delta t2_{jk} + \Delta t3_{jk} \tag{21}$$

3.4 Caculate Avoidance Time Tc

The picking arm does not interfere in the Y direction, so it is only possible to collide in the X direction. Then the picking arm i picks mushroom j, and the next mushroom is k, j, k $\in$ V, the coordinates of mushroom j are (X_j, Y_j), the coordinates of k are (X_k, Y_k), and its displacement in the X direction is D_x The function of time t is $D_x(t)$ as shown in Eq. (22):

$$D_x(t) = \begin{cases} X_j, t1_{jk} \leq t \prec t2_{jk} \\ X_j + v1_x *(t - t2_{jk}), t2_{jk} \leq t \prec t3_{jk} \\ X\_Lay_{jk} + v2_x *(t - t3_{jk}), t3_{jk} \leq t \prec t4_{jk} \end{cases} \tag{22}$$

$$v1_x = \frac{X\_Lay_{jk} - X_j}{\Delta t2_{jk}} \tag{23}$$

$$v2_x = \frac{X_k - X\_Lay_{jk}}{\Delta t3_{jk}} \tag{24}$$

where:

v1x represents the speed of the picking arm in the X direction during the blanking stage.

$v2_x$ represents the speed of the picking arm in the X direction during the positioning stage.

$t1_{jk} \leq t < t2_{jk}$ means that the picking arm is in the picking stage of picking j mushrooms, t2jk-t1jk=t0.

$t2_{jk} \leq t < t3_{jk}$ indicates that the picking arm is in the picking stage of picking the jth mushroom,t3jk-t2jk=$\Delta t2_{jk.}$

$t3_{jk} \leq t < t4_{jk}$ indicates that the picking arm is in the blanking stage of picking the jth mushroom,t4jk-t3jk=$\Delta t3_{jk}$.

Suppose the function of the X displacement of the i-th picking arm and the time is $D_x(t)\_Armi$, and the collision distance is Dist. Because the picking arms are arranged side by side in the X direction, when calculating the number of collisions of Armi $D_x(t)\_Armi$, only the number of collisions between Armi and Arm(i+1) is considered, that is, $D_x(t)$ when Armi is performing the picking task The number of times that $D_x(t)\_Armi+Dist$ is greater than $D_x(t)\_Arm(i+1)$, i∈{1,2,...,M-1}, then the number of times that the i-th arm needs to avoid is,

$$N\_Armi_{avoid} = \sum_{j=1}^{N}(a_{ij1} + a_{ij2} + a_{ij3}) \tag{25}$$

Where,

a_{ij} indicats the number of avoidances of Arm i when picking the jth mushroom.

a_{ij1} is 1 when Arm i collides with Arm i+1 in the positioning stage, otherwise it is 0.

a_{ij2} is 1 when Arm i collides with Arm i+1 in the picking stage, otherwise it is 0.

aij3 is 1 when Arm i collides with arm i+1 in the blanking stage, otherwise it is 0.

So the total avoidance times N_{avoid} of M picking arms is:

$$N_{avoid} = \sum_{i=1}^{M} N\_Armi_{avoid} \tag{26}$$

For every time the picking arm collides, the robot needs t_p time to adjust, the total avoidance time is:

$$T_c = N_{avoid} \times t_p \tag{27}$$

It can be seen from the above that the following two conditions needs to be met to achieve the optimal picking efficiency, that is, to minimize the value of T in Eq.(4):

— Reduce avoidance during picking as much as possible;
— The picking time for each picking arm t_Armi should be as short as possible;

4 GAAC for Multi-Arm Picking Path Planning and Optimization

To solve the MTSP problem of the path planning for multiple picking arms, both the uniform assignment of tasks and the path planning problem should be considered. This greatly increases the complexity of the problem, which makes it difficult for the general heuristic algorithm to find a better solution in a short time, and it is also difficult to deal with the avoidance problem between the travel agents under the special constraints in this paper.Therefore a stepwise combinatorial optimization algorithm is proposed to reduce the complexity of the problem by decomposing the MTSP into M TSPs [32]. The first step is to use the strong global optimization ability of GA[12] to decompose the MTSP into M independent TSPs to solve the difficulty of uniform distribution of the MTSP problem with the SISS area.The second step is to use the fast convergence speed of ACO [16] to get the minimum path in the shortest time for the above M TSPs to meet the real-time requirements, and combine the auction mechanism to solve the difficulty of avoid collision between picking arms under the constraints such as clus-tering-mushroom planning etc. The stepwise algorithm combining Genetic Algorithm and Ant Colony Optimization algorithm is called GAAC in this paper.

4.1 Genetic Algorithm

In the constraint condition (1), each arm has an unreachable area due to the limitation of the SISS area, so there are different constraint conditions for mushroom of allocation in different areas. The GA encoding has strong plasticity[21], and can satisfy all the constraints of the picking area by reasonable design so as to decompose the MTSP into M TSPs.

Step.1 Encoding. It can be seen from Fig. 2 that the working area is divided into 2M-1 SSIS areas, so this paper proposes to divide the gene sequence in GA into corre-sponding 2M-1 DNA segments, as shown in Fig. 5. A gene represents which picking arm the mushroom should be assigned to. DNA segment(DNA_k) corresponds to the picking area(S_k)in Fig. 2. The gene in the DNAK fragment can only take the code of picking arms allowed to enter the picking area S_k, which means that this area can only be picked by several designated picking arms.

S_1		...		S_M			...		S_{2M-1}		
1	1	...	...	1	2	M	...	...	M	M	...

Fig. 5. DNA sequence of genetic algorithm

Each element in the DNA segment (DNA_k) in Fig. 7 corresponds to each mushroom in the k-th area one-to-one, and $DNA_k[j]$ represents the assigned picking arm of the j-th mushroom in the k-th region. Then the assignment rule of $DNA_k[j]$ in population initialization is as shown in Eq.(28), corresponding to the picking arms allowed to enter each region of Eq. (3):

$$DNA_k[j] = \begin{cases} \text{random}[1, \text{ k}] , & k \in \{1, 2, \ldots, M-1\} \\ \text{random}[k-M+1, M] , & k \in \{M, M+1, \ldots, 2M-1\} \end{cases} \qquad (28)$$

Where: random[1,k] means random assignment of any integer in the closed interval 1 to k.

In addition, in particular, the constraint condition (2) requires mushrooms in the same cluster to be picked in order from high to low. In order to met this condition, this paper designs to assign the mushrooms in the same cluster to be picked by the same picking arm. All mushrooms in the same cluster are integrated into one element of the gene sequence, that is, the mushrooms in the same cluster appear as only one mushroom in the mushroom set, and other mushrooms in the cluster are put into a specific cluster mushroom set.

Step.2 Selection operator. In order to increase the optimization ability of the algorithm, a new selection operator is designed, which uses roulette to select two individuals every time, and then select the one has better fitness of the two individuals to survive.

Step.3 Crossover operator. Multi-point crossover method is used to randomly select multiple segments in the gene sequence for crossover to increase the global search ability of the algorithm.

Step.4 Mutation operator. As shown in Figure 7, the genes in each DNA segment need to comply with different mutation rules and can only mutate into the code of the picking arm that can enter the corresponding picking area of the segment.

After the first step of GA,all the mature mushrooms (n in total) in the working area are assigned to M groups according to the DNA sequence of the optimal individual in the population. The mushroom coordinate set of each group is named Arm_i, $i \in \{1, 2 \ldots M\}$, which represents the coordinate set of mushrooms that need to be picked by the i-th picking arm.

4.2 Ant Colony Optimization Algorithm Improvment

The MTSP problem of the multi-arm planning of the picking robot has been decomposed into M TSP problems through GA in section 4.1. In order to further improve the picking efficiency and consider the avoidance problem in the constraint condition (3) in Section 2.3, it is also necessary to solve the TSP problems, that is, the path planning of the mushroom sets to be picked for each of the three picking arms.

For dealing with the problem of avoidance among M picking arms, the path planning of each of the M picking arms should be carried out in parallel, so that it can be judged in real time whether there will be a collision between the picking arms. Because of its good parallelism and convergence in the later stage of the algorithm[37], ACO is choosen to approach to solve the path planning problem of the M picking arms, and the

auction mechanism,meanwhile, is combined to deal with the avoidance problem among arms . The auction mechanism is described as follows:

Determine whether the picking arm may collide with other picking arms when picking the current mushroom. If yes, delete the mushroom from the preliminary candidate mushroom set.

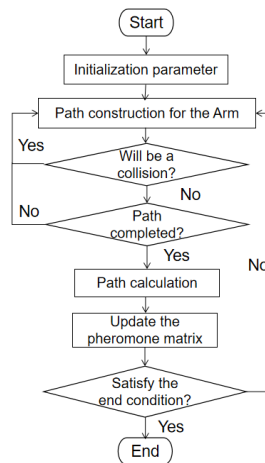The steps of the improved ant colony algorithm are as follows[39],and the flow chart is shown in Fig.6:

Fig. 6. Flow chart of picking optimal route planning for Armi

Step.1 Initialize. Initialize the pheromone matrix, the path taboo table, and the coordinate collection of each picking arm mushroom. In the process of initializing the mushroom coordinate set of picking arm, in order to ensure that the picking order ,where the mushrooms in the same cluster should be picked from high to low, is not disturbed, this paper regards all the mushrooms in the same cluster as a whole group to participate in the allocation.Therefore, only the first mushroom in the cluster is putted into the mushroom set to represent the whole cluster mushrooms for allocate, and other mushrooms in the cluster are placed in another specific clustering mushroom set.

Step.2 Construct path. The basic idea of path construction is that the ants construct the picking paths of the M picking arms in parallel. First, through the use of path taboo list, delete the mushrooms that have been picked from the mushroom coordinate set of the picking arm to form a preliminary candidate mushroom set,then determine the current candidate mushroom set for each ant by using the auction mechanism. Next, Select the next mushroom to be picked from the current candidate mushroom set according to the pheromone concentration for the picking arm. Finally, go to step.3 when all ants complete the path construction.

Step.3 Calculation path. Replenish the picking path completely which constructed by the ants for the M picking arms combined with the clustering mushroom set described in step (1), and then calculate the picking time.

Step.4 Update the pheromone matrix. The path with the shortest picking time is selected to update the pheromone matrix.

Step.5 Determine the number of iterations. If the maximum number of iterations is reached, go to step.6, otherwise go to step.1.

Step.6 End. Output the optimal path of M picking arms.

5 Experimental Verification and Result Analysis

5.1 Experimental Data

The three arm picking robot is taken as a typical example to verify GAAC.

All the mushroom data of this experiment are obtained from the field experiment of Agaricus bisporus planting base, as shown in Fig.7(a). Each layer of Agaricus bisporus cultivation rack is 1440 mm wide and 20 000 mm long, and each working area is set as 1440 mm * 180 mm. According to the actual measured data of dozens of layers of cultivation rack, most of the number of picking mushrooms in the working area is about 40 ~ 70. Therefore, three groups of mushrooms in the working area with the number of 41, 54 and 71 are selected for the experiment(Fig.7).
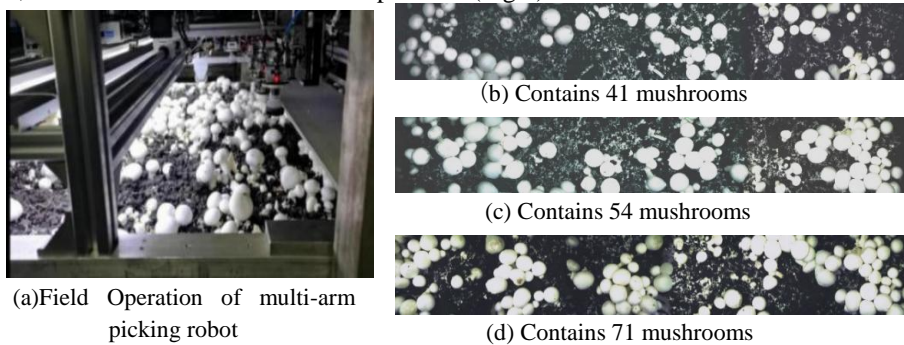

(a)Field Operation of multi-arm picking robot

(b) Contains 41 mushrooms

(c) Contains 54 mushrooms

(d) Contains 71 mushrooms

Fig. 7. Field operation of multi-arm picking robot and mushroom data

5.2 Experimental Verification and Result Analysis

The stepwise algorithm combining GA and ACO (GAAC) proposed in this paper is used to plan the picking path of the real mushroom data (Fig.7) obtained from the Agaricus bisporus planting base. The moving speed of picking arm(V) is 100 mm / s, the picking execution time(t1) is 5 s, There are 41 mature mushrooms in the first group, 60 mature mushrooms in the second group and 71 mature mushrooms in the third group. At the same time, c are used to plan the picking path of the experimental datas to compare with the results of GAAC.

The parameters of the algorithm in the experiment are set as follows :(1) The population of the genetic algorithm is 30, the crossover probability is 0.15, the mutation probability is 0.015 and the maximum number of iterations is 500. (2) In ant colony algorithm, the number of ants is 30, the important factor of pheromone is 1, the important factor of heuristic pheromone is 10, the intensity of pheromone is 5, the volatile factor is 0.1and the maximum number of iterations is 500.

The iteration process of the three algorithms is shown in Fig.8. When the number of mature mushrooms is 41, the number of iterations of GAAC is about 1/3 of DCGA, 2/5 of GAGA, and the optimal picking time of GAAC is 12% better than DCGA and 8% better than GAGA. When the number of mature mushrooms is 54, the iteration number of GAAC is about 1/4 of DCGA, 1/3 of GAGA, and the optimal picking time of GAAC is 16% better than DCGA, 9% better than GAGA. When the number of mature mushrooms is 71, the iteration number of GAAC is about 1/5 of GAGA, 2/7 of GAGA, and the optimal picking time of GAAC is 19% better than DCGA and 10% better than GAGA. It can be seen from the above that GAAC has the fastest convergence speed, followed by GAGA, and DCGA is the worst. Furthermore,with the increase of the number of mature mushroom, GAAC has more and more advantages in convergence speed and global search ability compared to DCGA and GAGA. This advantage makes the GAAC algorithm can get the optimization results quickly even when the mushroom is growing intensively, which improves the adaptability of the algorithm.
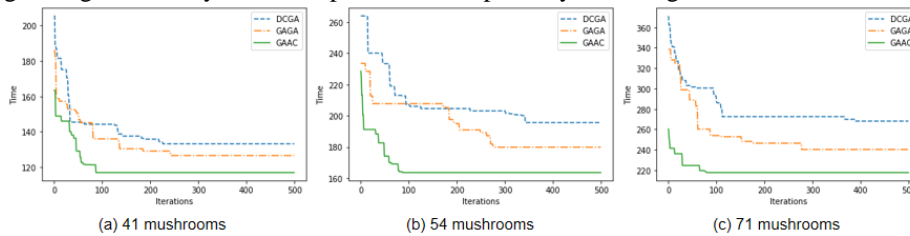

(a) 41 mushrooms   (b) 54 mushrooms   (c) 71 mushrooms

Fig. 8. Comparison of the iterative process of the three algorithms

The calculation results of the three algorithms are shown in table 1, on the one hand, due to the combination of ant colony algorithm and the auction mechanism,GAAC can greatly reduce the probability of a collision occurs and avoid the increased time caused by waiting for picking. Whereas the rest of the two algorithms is easier to fall into local optimal solution and optimization of picking path may produce more of the collision with the increase of the number of mature mushroom. On the other hand, the GAAC has the best uniformity of three-arm distribution. The picking path planned by the GAAC takes less time than the other two algorithms.

Table 1. Experiment results of the three algorithm

Algorithm	N	Avoid times	picking time(s)	Picking efficiency （pcs/h）	N1:N2:N3
DCGA	41	1	133.21	1108	11:14:16
	54	3	195.64	993	14:20:20
	71	6	268.09	953	25:19:27
GAGA	41	1	127.54	1157	10:16:15
	54	2	179.83	1081	16:19:19
	71	5	240.53	1062	22:27:22
GAAC	41	0	116.95	1262	14:13:14
	54	0	163.56	1188	16:19:19
	71	1	217.61	1174	22:24:25

The path diagrams of each picking arm optimized by GAAC for 41, 54 and 71 mushrooms are shown in Fig.9,10 and 11, respectively. It shows that picking paths planned according to the distribution of mushrooms have almost no redundant paths, and The workload distribution of each picking arm is also relatively uniform, which can meet the actual picking demand well.
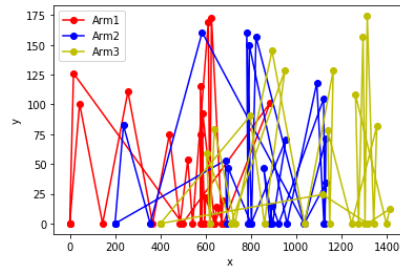

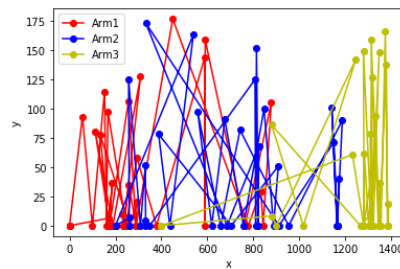**Fig. 9.** Trajectory diagram of GAAC（with 41 mushrooms）

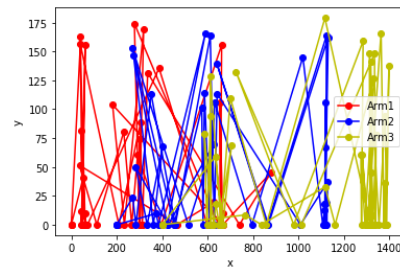**Fig. 10.** Trajectory diagram of GAAC（with 54 mushrooms）

Fig. 11. Trajectory diagram of GAAC（with 71 mushrooms）

It can be seen from the above that the GAAC can get the best picking efficiency besides having stronger convergence ability than the other two methods. In addition, for different quantities of mushrooms to be picked, the convergence ability and the calculated picking efficiency of the GAAC are not greatly affected, and the algorithm has good stability. It can better adapt to the problems of the density and distribution difference of mushrooms caused by natural growth.

In order to further verify the universal applicability of GAAC to solve the MTSP problem of picking path planning in the multi-picking arm system, this paper continued to conduct experiments on any 10 groups of mushroom data actually got from the mushroom planting base of Agaricus bisporus. The experimental results are shown in Table 3. After optimization, the picking efficiency of GAAC is about 20% higher than that of the DCGA and 10% higher than that of GAGA.the uniformity of the work distribution for each arm is also better than the other two algorithms, and the results are basically consistent with that in Table 2. It shows that the GAAC algorithm proposed in this paper can plan the optimal picking path well for multi-arm intelligent picking robot of Agaricus bisporus even for different mushroom quantities.

Table 2. Comparison among three algorim with 10 groups data

Group	N	picking time(s)			N1:N2:N3		
		DCGA	GAGA	GAAC	DCGA	GAGA	GAAC
1	51	181.77	164.94	152.47	15:20:16	16:16:19	17:16:18
2	51	185.71	165.83	148.23	19:16:16	18:15:18	18:17:16
3	37	113.21	112.25	102.54	11:14:12	11:13:13	13:12:13
4	53	198.01	175.48	156.41	19:20:14	19:15:19	17:18:18
5	59	218.77	202.87	180.45	24:16:19	18:19:22	20:18:21
6	48	165.90	150.48	142.38	18:14:16	14:17:17	16:17:15
7	55	203.26	184.16	166.65	21:16:18	20:18:17	19:19:17
8	41	131.52	124.84	118.91	12:16:13	13:13:15	14:14:13
9	50	175.48	165.09	149.44	15:19:16	16:16:18	17:17:16
10	65	242.35	221.20	200.42	20:25:20	22:24:19	23:22:20
Sum	510	1815.98	1667.1	1517.9			

In addition, the theoretical picking efficiency of Agaricus bisporus picking robot using GAAC is about 1209 pcs/h, basically reaching the artificial picking efficiency. Furthermore, because the working time of worker is 8 hours a day, while the picking robot can work 24 hours a day,except for the time needed for auxiliary work such as replacing batteries and changing layers,the working efficiency of a picking robot can be equal to at least 2 pickers every day. Therefore, the trajectory optimization of multi-picking arm robot with GAAC algorithm can meet the requirements of replacing picking workers well and adequate for the actual production need. Moreover, experiments also indicate that the proposed algorithm is an effective solution to the MTSP problem with SISS area.

6   Conclusion

Firstly, this paper introduces the structure of the multi-arm picking robot for Agaricus bisporus, analyzes the sharing characteristics of the cooperative working area, and defines the area with such characteristics as the series increasing symmetric sharing(SISS)

area. Secondly, the cooperative picking trajectory planning problem of Agaricus bisporus multi-arm picking robot is abstracted as MTSP problem, and the corresponding mathematical model is constructed to optimize the picking task of M-arm picking N mushrooms problem. Thirdly, the traditional genetic algorithm and ant colony algorithm are improved accordingly. A stepwise algorithm combining GA and ACO is designed to solve the MTSP of multi-arm collaborative picking with SISS area. By using genetic algorithm with strong global optimization ability,in which the DNA value rules for SISS area are designed, The MTSP problem of multi-arm collaborative picking is decomposed into m TSP problem and the picking task is evenly distributed; the improved ACO, which has the advantage of fast convergence, combined with auction mechanism is used to gain the shortest path of each TSP, which improves the global search ability and convergence ability of the algorithm, and effectively solves the avoidance problem for multiple picking arms. Known from the experimental results, when the number of coordinate points of Agaricus bisporus in the picking area is about 40-70, GAAC proposed in this paper can quickly find the shortest picking time solution, and is significantly better than the optimal solution obtained by DCGA and GAGA. The algorithm is suitable for the trajectory optimization of multi-arm collaborative picking of Agaricus bisporus. At the same time, through the comparison with the manual picking efficiency, the picking efficiency of the multi-arm robot optimized by GAAC can reach the manual picking efficiency, and the picking amount of the whole day can be approximately equivalent to two picking workers in theory, which can better meet the requirements of robot replacing manual picking in actual production. In order to better adapt to the requirements of real-time control, we can dynamically adjust the offspring individuals in the evolution process to prevent premature, improve the utilization rate of pheromone and other methods to enhance the convergence ability, so as to improve the stability and global optimization ability of the algorithm, and further reduce the operation time of the algorithm.

Acknowledgments

References

1. Yu, G.H, Zhao, Y., Li, G., Shi, H.: Mushroom monomer detection and location algorithm based on machine vision and its boundary description. Transactions of theChinese Society of Agricultural Engineering 2(6), 101–104 (2015).
2. Hu, X.M., Pan, Z.R., Lv, S.K.: Picking path optimization of agaricus bisporus picking robot. Mathematical Problems in Engineering 2019 (2019).
3. Seenu, N., Kuppan, R.M., Ramya, M.M.: Review on state-of-the-art dynamic task allocation strategies for multiple-robot systems.Industrial Robot47(6), 929–942 (2020).
4. Korsah, G.A., Stentz, A., Dias, M.B.: A comprehensive taxonomy for multi-robot task allocation.Int. J. Robot. 32(12), 1495–1512 (2013).

5. Lo, K.M., Yi, W.Y., Wong, P.K., Leung, K.S., Leung, Y., Mak, S.T.: A genetic algorithm with new local operators for multiple traveling salesman problems.International Journal of Computational Intelligence Systems 11(11), 692–705 (2018).

6. Wang, H.P., Wang, Z.C., Ding, S.Q.: Optimization of teaching management in colleges and universities based on dynamic programming.Cluster Computing 22(6),13731–13738 (2019).

7. Hermansson, T., Carlson, J.S., Linn, J., Kressin, J.: Quasi-static path optimization for industrial robots with dress packs. Robotics and computer-Integrated Manufacturing 68 (2021).

8. Spensieri,D., Carlson, J. S., Ekstedt, F., Bohlin,R.: An iterative approach for collision free routing and scheduling in multirobot station. IEEE Trans. Autom. Sci. Eng. 13(2), 950–962 (2016).

9. Tolga, B., Jens, L.: Optimal vehicle routing with lower and upper bounds on route durations. Networks 65(2), 166–179 (2015).

10. Trigui, S,. Cheikhrouhou, O., Koubaa,A., Baroudi, U., Youssef, H.: FL-MTSP: a fuzzy logic approach to solve the multi-objective multiple traveling salesman problem for multi-robot systems. Computers, Networks & Communications 21, (24), 7351–7362 (2017).

11. Lu, L.C., Yue, T.W.:Mission-oriented ant-team ACO for min–max MTSP. Applied Soft Computing Journal 76, 436–444 (2018).

12. Yu, Q., Lin, D., Wang, D.: A review of research on multiple traveling salesman problems. Value Engineering 31(2), 166–168 (2012).

13. Li, C.Z, Xu, B.: Optimal scheduling of multiple Sun-synchronous orbit satellites refueling. Advances in Space Research 66(2), 345–358 (2020).

14. Sofge, D., Schultz, A., Jong, K.D.: Evolutionary computational approaches to solving the multiple traveling salesman problem using a neighborhood attractor schema. Lecture notes in computer science2279151–160 (2002).

15. Wei, C.Y. Ji, Z., Cai, B.L.:Particle Swarm Optimization for Cooperative Multi-Robot Task Allocation: A Multi-Objective Approach. Ieee Robotics and Automation Letters 5(2), 2530–2537 (2020).

16. Liu, W., Li, S., Zhao, F., Zheng, A.: An Ant Colony Optimization Algorithm for the Multiple Traveling Salesmen Problem. In: The 4th IEEE Conference on Industrial Electronics and Applications, pp.1533–1537. IEEE Press, Xi'an (2009).

17. Chen, X.Y., Zhang, P., Du, G., Li, F.: Ant colony optimization based memetic algorithm to solve bi-objective multiple traveling salesmen problem for multi-robot systems. IEEE Access 6, 21745–21757 (2018).

18. Wang, M., Ma, T., Li, G., Zhai, X., Qiao, S.: Ant Colony Optimization With an Improved Pheromone Model for Solving Mtsp With Capacity and Time Window Constraint. Journal of Technology & Science 5, 1–1 (2020).

19. Tang, L., Liu, J., Rong, A., Yang, Z.: A multiple traveling salesman problem model for hot rolling scheduling in Shangai Baoshan Iron & Steel Complex. European Journal of Operational Research 124(2), 267–282 (2000).

20. Hu, S.J.: Research on multiple traveling salesman problem based on improved genetic algorithm.Master Thesis:Jiangnan University (2019).

21. Cai, W.Y., Zhang, M.Y., Zheng, Y.R.: Task Assignment and Path Planning for Multiple Autonomous Underwater Vehicles Using 3D Dubins Curves. Sensors17 (2017).

22. Li, J., Zhou, M.C., Sun, Q.R., Dai, X.Z., Yu, X.L.:Colored Traveling Salesman Problem. IEEE transactions on cybernetics 45(11), 2168–2267 (2015).

23. Dong, X., Cai, Y.: A novel genetic algorithm for large scale colored balanced traveling salesman problem. Future Generation Computer Systems 95,727–742 (2019).

24. Jiang, C., Wan, Z., Peng, Z.: A new efficient hybrid algorithm for large scale multiple traveling salesman problems. Expert Systems With Applications 139 (2020).
25. Maha, A., Zakir, H.: Experimental Study of a Hybrid Genetic Algorithm for the Multiple Travelling Salesman Problem. Mathematical Problems in Engineering 2020 (2020).
26. Chen, Y., Jia, Z., Ai, X., Yang, D., Yu, J.: A modified two-part wolf pack search algorithm for the multiple traveling salesmen problem. Applied Soft Computing 61,714–725 (2017).
27. Hu, S., Lu, H., Huang, Y., Xu, K.: Improved genetic algorithm to solve the multi-traveling salesman problem with workload balance. Computer Engineering and Applications 55, (17), 150–155 (2019).
28. Zhou, Z.Y.: Research on path planning simulation of warehouse handling robot. Master thesis: Xi'an University of Technology (2020).
29. B. He, J. Zhang, F. Zhang.: An improved genetic algorithm for solving job shop scheduling problem,"Manufacturing Automation 40(8), 113–117 (2018).
30. P，Venkatesh., A, Singh,: Two metaheuristic approaches for the multiple traveling salesperson problem. Applied Soft Computing 26, 74–89 (2018).
31. Yin, Y.M.: Research on warehouse robot path optimization based on improved genetic algorithm. Master thesis: Chengdu University of Technology (2019).
32. Xu, X.L., Yuan, H., Mark, L., Marcello, T.: Two phase heuristic algorithm for the multiple-travelling salesman problem. Soft Computing 22(19), 6567–6581 (2018).
33. Wang, M.J.: Task allocation and path planning of multi-UAV cooperative airport bird repelling system. Master thesis: Nanjing University of Aeronautics and Astronautics (2019).
34. Lu, Z.Q., Zhang, K., He, J.J., Niu, Y.Y.: Applying k-means clustering and genetic algorithm for solving MTSP. Bio-Inspired Computing-Theories and Applications .pp. 278–284. Springer, Singapore (2016).
35. Luo, Z.Y., Feng, S., Liu, X.F., Chen, J.F., Wang, R.: A multi-unmanned cleaning vehicle area coverage path planning method based on a step-by-step genetic algorithm. Journal of Electronic Measurement and Instrument 34(8), 43–50 (2020).
36. Liu, W.B., Wang, Y.D.: Research on path planning of multi-UAV collaborative search for multi-targets. Electro-Optics and Control 26(3), 35–38 (2019).
37. Kencana, E. N., Harini, I., Mayuliana, K.: The performance of ant system in solving multi traveling salResearch on path planning of multi-UAV collaborative search for multi-targetsesmen problem. Procedia Computer Science 124, 46–52 (2017).
38. Necula, R., Breaban, M., Raschip, M.: Tackling the bi-criteria facet of multipletraveling salesman problem with ant colony systems,"In 2015 IEEE 27th international conference on tools with artifificial intelligence (ICTAI), pp. 873–880, IEEE, Italy (2015).
39. Changdar, C., Pal, R. K., Mahapatra, G. S.: A genetic ant colony optimization based algorithm for solid multiple travelling salesmen problem in fuzzy rough environmen. Soft Computing 21(16), 4661–4675 (2017).

A Novel Ratchet and Pawl Lock Mechanism with Main and Auxiliary Pawls

Zhiyang Qu, Lubin Hang*, Qiansheng Wang, Chuanshuo Yin,

Chuanlei Zhong, Borui Wu

Shanghai University of Engineering Science, Shanghai 201620, China
`hanglb@126.com`

Abstract. A novel ratchet and pawl locking mechanism with main and auxiliary pawls is proposed in this paper. The novel mechanism adding the auxiliary pawl replaces the rigid impact of the conventional mechanism with flexible impact, such that lagged the time and reduce intensity of main pawl rigid impact. The singular configuration of the spring linkage mechanism enables rapid switching the contact states between the auxiliary pawls and ratchets to that of the main pawls and ratchets. Through the force transmission characteristic analysis, the hinge position of the pawl on the main pawl is ensured, the initial state and motion characteristics of the main and auxiliary pawls are guaranteed, and the influence of the stiffness of the auxiliary pawl spring on the contact force of the main pawl is discussed. Finally, the Adams simulation results show that the main pawl impact is 14.7% lower than the conventional lock mechanism.

Keywords: Auxiliary pawl, Flexible impact, Singular configuration.

1   Introduction

As an important accessory of the car body, the operability and reliability of the vehicle latch are related to the safety and performance of the car. The automobile side vehicle latch system mainly consists of the following five parts: locking mechanism, external opening mechanism, internal opening mechanism, external locking safety mechanism and internal locking safety mechanism. Facing the demand of 5G and pilotless automobile, the car vehicle latch system is becoming more intelligent and comfortable, the large sealing force between the door and vehicle body can pro-vide better noise reduction effect [1]. However, increasing the sealing force between the latch and the body will enlarge the impact and abrasion between the ratchet and pawl of the vehicle latch when the door is closed, which will affect the life span of the vehicle latch.

The main methods to reduce the impact and abrasion of ratchet and pawl mechanism are contact surface optimization design, material optimization, spring setting, etc. Quanmao He and Shunqiang Shang [2] found that if the end of the ratchet and the bottom of the ratchet slot is too sharp, it would reduce the bearing capacity of the mechanism and make it easy to abrasion. The contact surface of the ratchet and pawl was optimized, and the two contact surfaces were designed into circular arcs, and the radius

of the ratchet slot arc was greater than the radius of the end of the pawl. Through the analysis of ratchet and pawl mechanism and spring system in the circuit breaker [3-5], the relationship between pawl friction coefficient and eccentric shaft driving torque is parabolic, and the fatigue life of mechanism can be improved by reducing the friction coefficient and eccentricity of pawl and pressure angle. Darbit[6] analyzed the abrasion reason of ratchet and pawl by dynamic and static failure finite element model, optimized ratchet and pawl mechanism from material attribute and diameter. Chengjun Song et al. [7] established dynamic model of ratchet and pawl mechanism of automatic synchronous clutch, and proposed that the impact force is independent of absolute angular velocity, only depends on differential angular velocity; Deb and Sen [8-9] found that linkage kinematics and brake position play a leading role in the system, especially in the selection of spring and toggle position, and the spring layout helps to change the system performance. Gao et al. [10] found that a linear spring and a specific cam constitute a spring cam mechanism, and the desired motion of the follower can be obtained by designing the cam surface.

The above methods have certain effect in noise reduction and prolonging the life span of parts, and are mostly aimed at specified cases. It is worth furthering study to find the noise reduction methods [11-12]. In this paper, a novel ratchet and pawl mechanism with main and auxiliary pawls is proposed. The auxiliary pawl is composed of a spring connecting rod mechanism with cylindrical roller at the end. The singular configuration of the spring connecting rod realizes the fast switching from the auxiliary pawl to the main pawl. The auxiliary pawl contacts with the ratchet wheel by rolling, which effectively avoids the abrasion caused by the impact of sharp points and the contact of the surface, and makes the main pawl contact with the ratchet contact delay, reducing the contact time and abrasion of the main pawl [13-15]. The hinge point setting and auxiliary spring selection of the auxiliary pawl mechanism ensure the feasibility of the novel ratchet and pawl mechanism. Based on Adams dynamics simulation analysis, the contact force between the main and auxiliary pawls and the ratchet wheel of the novel mechanism is obtained, and the effectiveness of the novel ratchet and pawl mechanism is analyzed and verified.

2 Design and characteristics of novel ratchet and pawl mechanism

2.1 Basic idea of novel mechanism with Main and Auxiliary Pawls

The lock actuator can be view as ratchet and pawl mechanism, the general ratchet and pawl mechanism, as shown in Fig 1, has the functions of one-way locking and surface self-locking. The contact surface of ratchet and pawl mechanism is mainly in three ways: sharp point contact, curved surface contact and surface contact. When the ratchet shaft rotates at a high speed and the load is large, the relative motion between the ratchet and the pawl leads to a large noise and abrasion between the ratchet and the pawl.

In order to reduce the abrasion between the ratchets and pawls and ensure the locking reliability of the profile, an auxiliary pawl with spring linkage mechanism is constructed on the main pawl, and a novel ratchet and pawl mechanism is proposed by using the auxiliary pawl and the main pawl to contact with the ratchet wheel successively.
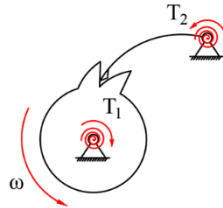

Fig. 1. General ratchet

The different states of the novel ratchet and pawl mechanism in motion are shown in Fig 2. In order to reduce the abrasion of ratchet and pawl and ensure the locking reliability of the mechanism, the basic idea of using two impacts to weaken one impact is to first use the roller at the end of auxiliary pawl to contact with ratchet to reduce the impact and abrasion; then use the lag contact ratchet of main pawl to reduce the impact and abrasion by reducing the contact time; and use the singular configuration of spring linkage mechanism switch the main pawl quickly, and the main pawl contacts and locks with the ratchet surface to ensure the reliability of the locking mechanism. The design idea and construction method of the novel ratchet and pawl are universal and reproducible, and can be extended to the application with ratchet and pawl locking mechanism.
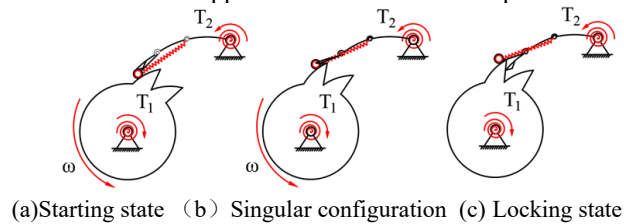

(a)Starting state （b）Singular configuration (c) Locking state

Fig. 2. Novel ratchet and pawl mechanism

2.2   Application of main and auxiliary pawl ratchet mechanism in vehicle latch

The locking mechanism of the vehicle latch is composed of ratchet and pawl mechanism.

The conventional ratchet and pawl locking mechanism (hereinafter referred to as the conventional locking mechanism) is shown in Fig 3. The ratchet is driven by the lock column to overcome the torsion spring force and rotate at a high speed. When it touches the ratchet, there will be greater impact and noise; when the ratchet is driven to rotate by the ratchet, the contact surface of the ratchet and pawl will slide relatively for a long time, resulting in more abrasion. In view of the above problems, a novel ratchet and pawl locking mechanism with main and auxiliary pawls is proposed, as shown in Fig 4.
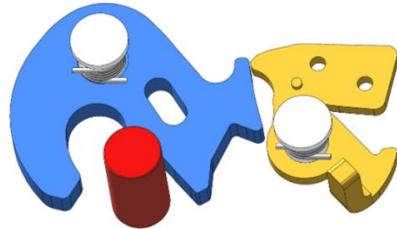
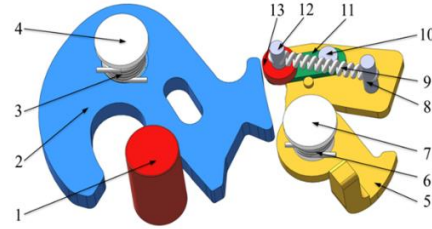**Fig. 3.** Conventional ratchet and pawl locking mechanism

Fig. 4. Novel ratchet and pawl locking mechanism

1-lock post 2-ratchet 3-ratchet spring 4-ratchet shaft 5-main pawl 6-main pawl spring
7-main pawl shaft 8-spring support 9-spring 10 - auxiliary pawl support 11 - auxiliary pawl
12 - roller shaft 13 - roller

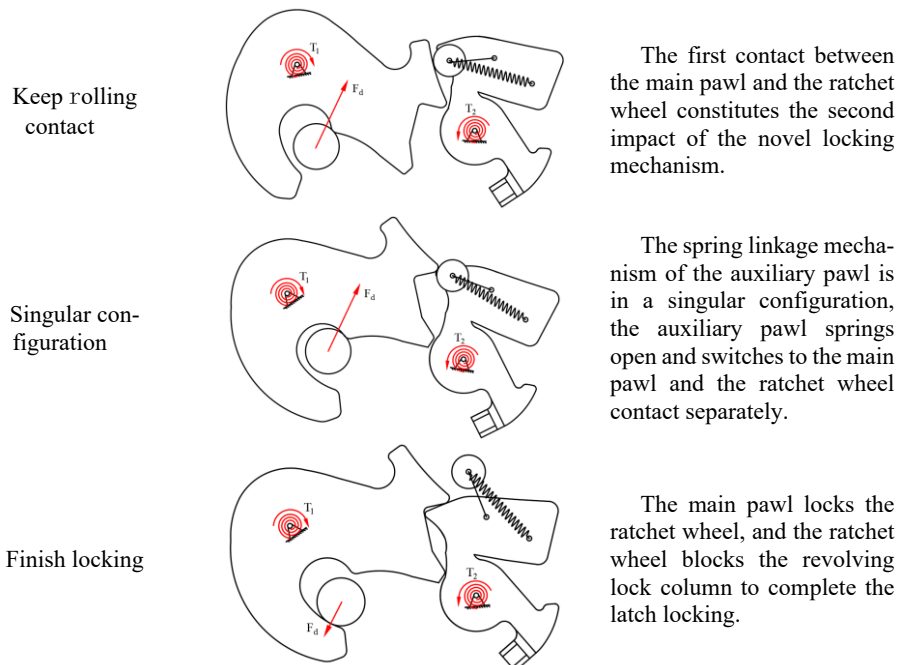The novel locking mechanism has the following characteristics:

1）The impact of the ratchet and pawl is reduced by using the wheel contact of the auxiliary pawl, and the quick switching of the main pawl is realized by the singular configuration of the spring linkage mechanism;

2）The external surface of the ratchet contacting with the roller on the auxiliary pawl should be close to the smooth curved surface, so as to ensure that the roller contacting with of the ratchet can roll around its contact curved surface flexibly and reduce the collision noise;

3）The contact time and force between the main pawl and the ratchet wheel are shortened to reduce the abrasion.

3   Movement of novel locking mechanism

The motion characteristics and states of the novel latching mechanism are that the auxiliary pawl and the main pawl contact with the ratchet successively, different movement stages have different contact states, and the movement states of each stage are shown in Table 1. The spring of the auxiliary pawl presents different states in the locking process.

Table 1. Motion state of novel locking mechanism

Movement stage of novel locking mechanism	Mechanism diagram of novel locking mechanism	Description of motion state
The first impact		The ratchet wheel is driven by the lock post to overcome its own torsion spring force; The first impact of the novel locking mechanism is caused by the first impact between the auxiliary pawl roller and the ratchet.

Keep rolling contact		The first contact between the main pawl and the ratchet wheel constitutes the second impact of the novel locking mechanism.
Singular configuration		The spring linkage mechanism of the auxiliary pawl is in a singular configuration, the auxiliary pawl springs open and switches to the main pawl and the ratchet wheel contact separately.
Finish locking		The main pawl locks the ratchet wheel, and the ratchet wheel blocks the revolving lock column to complete the latch locking.

According to the movement states in Table 1, the locking process of the novel latching mechanism can be detailed as follows: the door is closed and driven to the lock column, the ratchet wheel rotates under the driving force F_d to overcome the torsion spring T_1 force of the ratchet wheel, the first impact of the novel mechanism is formed by the first contact between the roller at the end of the auxiliary pawl and the ratchet wheel, and keep rolling contact of the novel mechanism is formed by the first contact between the roller and the ratchet wheel. Before the auxiliary pawl reaches the singular configuration, the ratchet wheel contacts with the main pawl and the auxiliary pawl together; the auxiliary pawl springs away after passing the singular configuration, and the ratchet wheel contacts with the main pawl separately until the torsion spring force T_2 potential energy of the main pawl is released; the main pawl rebounds to prevent the ratchet wheel from turning, and the ratchet wheel prevents the door from moving outward, and the latch is locked.

4   Key elements of auxiliary pawl mechanism design

The novel locking mechanism uses the auxiliary pawl to realize rolling contact instead of sliding contact, and the adding impact of the contact between auxiliary pawl and ratchet will reduce impact intensity and abrasion rate. Hinge point setting and auxiliary pawl spring stiffness selection are the key parameters of auxiliary pawl design.

4.1 Auxiliary pawl hinge point setting

The first impact of the novel locking mechanism is caused by the first contact of the auxiliary pawl with the ratchet wheel, and the first impact of the ratchet wheel is weakened by setting the contact angle of the auxiliary pawl mechanism to ensure the cutting angle, the balance equation of each driving force is obtained through force transmission, the contact angle is analyzed, the reasonable hinge points position of the auxiliary pawl mechanism is set, the switching point between the main pawl and the auxiliary pawl is ensured, and the spring stiffness of the auxiliary pawl is selected to realize the lag of the main pawl. The instantaneous force transfer analysis diagram between ratchet and pawl shown in Fig 5.
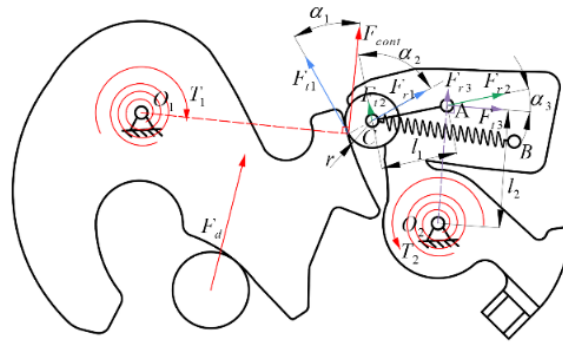

Fig. 5. Instantaneous analysis of force transfer between ratchet and pawl during the locking process

The transient force transfer between ratchet and pawl can be obtained from Fig 5 during the locking process:

$$F_d \to F_{cont} \to \begin{cases} F_{r1} \to \begin{cases} F_{r2} \to \begin{cases} F_{r3} \\ F_{t3} \end{cases} \\ F_{t2} \end{cases} \\ F_{t1} \end{cases} \tag{1}$$

Where: F_{t1} is the roller rotation driving force; F_{t2} is the auxiliary pawl rod rotation driving force; F_{t3} is the main pawl rotation driving force.

The instantaneous force balance equation of each member is obtained as follows:

$$\begin{cases} M_1 = F_n \cdot r = F_{cont} \cdot cos\alpha_1 \cdot r \\ M_2 = F_{t2} \cdot l_1 = F_{cont} \cdot sin\alpha_1 \cdot cos\alpha_2 \cdot r \\ M_3 = F_{t3} \cdot l_2 = F_{cont} \cdot sin\alpha_1 \cdot sin\alpha_2 \cdot cos\alpha_3 \cdot r \end{cases} \tag{2}$$

Where: M_1、M_2、M_3 are the rotation driving torque of roller, auxiliary pawl rod and main pawl respectively; α_1 is the angle between the rotation driving force F_{t1} of roller and the contact force F_{cont} of roller; α_2 is the angle between the rotation driving force F_{t2} of auxiliary pawl rod and the contact force F_{r1} of point C; α_3 is the angle between the rotation driving force F_{t3} of main pawl and the contact force F_{r2} of main pawl point A, r is the radius of roller; l_1 is the length of auxiliary pawl rod AC; l_2 is the length of main pawl rod AO_2.

From equation (2), it can be obtained:

$$\begin{cases} \alpha_1 = arccos\left[M_1 \middle/ (F_{cont} \cdot r) \right] \\ \alpha_2 = arccos\left[M_2 \middle/ (F_{cont} \cdot sin\alpha_1 \cdot l_1) \right] \\ \alpha_3 = arccos\left[M_3 \middle/ (F_{cont} \cdot sin\alpha_1 \cdot sin\alpha_2 \cdot l_2) \right] \end{cases} \qquad (3)$$

The motion characteristics of the novel locking mechanism are M_1、M_2、M_3. The parameters of r、 l_l and l_2 are selected. The contact angles α_1, α_2 and α_3 can be obtained by using equation (3). Finally, the hinge point of the auxiliary pawl on the main pawl is set.

4.2   Selection of auxiliary pawl spring

In addition to setting the hinge point, the auxiliary pawl mechanism also needs to select the appropriate auxiliary pawl spring stiffness to realize the motion state of the novel locking mechanism. The first and second impact of the novel locking mechanism and the fast switching of the main and auxiliary pawls will be affected by the spring linkage mechanism of the auxiliary pawl. As for the main pawl, it is necessary to ensure the potential energy of its locking spine and the stiffness of its torsion spring is consistent with that of the conventional locking mechanism. After setting the roller radius, it is necessary to select the stiffness of auxiliary pawl spring.

When the contact between the ratchet wheel and the auxiliary pawl roller reaches a stable state, the spring linkage mechanism also reaches a balanced state. This state is divided into two stages, the first stage is that the auxiliary pawl roller contacts with the ratchet wheel alone, and the second stage is that the auxiliary pawl roller and the main pawl contact with the ratchet wheel together. The spring force in the spring linkage mechanism is output by F_s, and the contact force between ratchet and roller is F_{cont}, as shown in Fig 6.
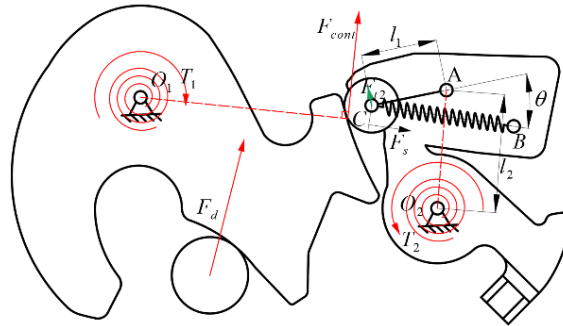

Fig. 6. Static balance mechanical analysis of spring linkage

Taking point A as the fulcrum, the transient force balance equation of the spring linkage with auxiliary pawl can be obtained

$$F_s \cdot l_1 \cdot sin\theta - F_{t2}l_1 = 0 \qquad (4)$$

Where θ is the angle between the spring force F_s and the auxiliary pawl lever F_s.

According to Hooke's law, the spring force F_s is satisfied

$$F_s = f \cdot \delta \qquad (5)$$

It can be seen from Fig 5 that the driving force F_{t2} of the auxiliary pawl lever is

$$F_{t2} = F_{cont} \cdot sin\alpha_1 \cdot cos\alpha_2 \qquad (6)$$

Simultaneous equations (4) to (6)

$$k = \frac{F_{cont} \cdot sin\alpha_1 \cdot cos\alpha_2}{\delta sin\theta} \qquad (7)$$

According to equation (7), the contact force on the end roller of the auxiliary pawl is proportional to the spring stiffness.

5 Simulation Research on novel locking mechanism

This paper studies the contact force between the main and auxiliary pawls and the ratchet wheel of the novel locking mechanism, analyzes the impact and abrasion between the main and auxiliary pawls and the ratchet wheel, and explores the influence of the spring stiffness of the auxiliary pawl on the novel mechanism. The Adams dynamic simulation model of the novel locking mechanism is established. The impact force of the novel locking mechanism is compared with that of the conventional locking mechanism.

5.1 Contact force analysis of novel locking mechanism

The simulation model of the novel locking mechanism is established as shown in Fig 7, the ratchet and pawl torsion spring parameters of the locking mechanism are set with reference to a certain type of vehicle latch as shown in Table 2, and the auxiliary pawl spring is set as 2.75N/mm. The auxiliary pawl spring make the contact force of ratchet and auxiliary pawl of novel mechanism is the half of the traditional one, which decrease the contact force but still promise the contact of the ratchet and pawl mechanism.
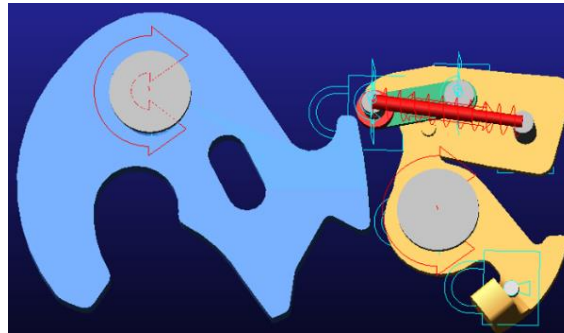

Fig. 7. Simulation model of novel locking mechanism

Table 2. Spring parameters of novel ratchet and pawl mechanism

Types of springs	Stiffness coefficient	Damping coefficient	Pretightening Force
Ratchet torsion spring	$0.5N \cdot mm/°$	$3.2 \times 10^{-4}N \cdot mm/°$	5N

Pawl torsion spring	0.5N · mm/°	3.2×10^{-4}N · mm/°	10N
Auxiliary pawl spring	2.75N · mm/°	6.4×10^{-4}N · mm/°	0N

The locking process of the locking mechanism is simulated according to the spring parameters in Table 2. The elongation of the auxiliary pawl spring of the novel locking mechanism is shown in Fig 8. The impact force of the novel locking mechanism is compared with that of the conventional locking mechanism through the peak value of the contact force, as shown in Fig 9.
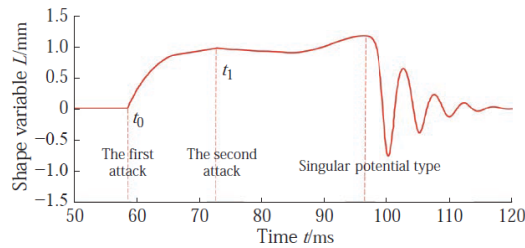

Fig. 8. Spring elongation of auxiliary pawl

The extension of auxiliary pawl spring in Fig 8 can reflect the first impact, second impact and singular configuration of the novel mechanism. According to the peak analysis of contact force between the novel locking mechanism and the conventional locking mechanism in Fig 9, it can be seen that the first and second impacts of the novel locking mechanism are at t_0 and t_1 respectively. The peak value of contact force F_{t0} and F_{t2} at these two times are lower than that of t_1' of conventional locking mechanism, indicating that the novel locking mechanism reduces the rigid impact, which can enhance the service life of the vehicle latch.

Compared with the conventional locking mechanism, the main pawl of the novel locking mechanism has lag characteristics. As can be seen from Fig 9, $t_1 > t_1'$, set the delay time of the main pawl $\Delta t_1 = (t_1 - t_1')(t_2' - t_1')$, set the impact reduction amplitude $\Delta F_{t_0} = \left(F_{t_1'} - F_{t_0} \right)/F_{t_1'}$, $\Delta F_{t_1} = \left(F_{t_1'} - F_{t_1} \right)/F_{t_1'}$ of the novel locking mechanism; calculate the lag $\Delta t_1 = 15.17\%$ of the main pawl, the impact reduction amplitude $\Delta F_{t_0} = 15.1\%$ of the auxiliary pawl, and the impact reduction amplitude $\Delta F_{t_1} = 14.7\%$ of the main pawl.
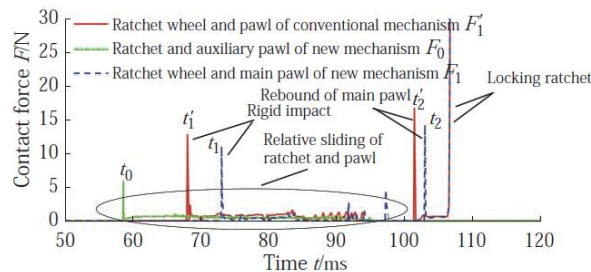

Fig. 9. Abrasion comparison between novel locking mechanism and

5.2   Stiffness setting of auxiliary pawl spring

The stiffness of auxiliary spring affects the impact force, contact force and main pawl lag of the novel locking mechanism. Choosing appropriate spring stiffness of auxiliary pawl can effectively reduce the impact force and abrasion between ratchet wheel and main pawl, and achieve the impact lag of main pawl. The different stiffness of auxiliary pawl spring is 2.55N/mm、2.65N/mm、2.75N/mm、2.85N/mm and 3.00 N/mm (0.00 N/mm refers to the conventional locking mechanism without auxiliary pawl). The contact force between auxiliary pawl roller and ratchet wheel under different spring stiffness is shown in Fig 10, and the contact force between main pawl and ratchet wheel under different spring stiffness is shown in Fig 11.
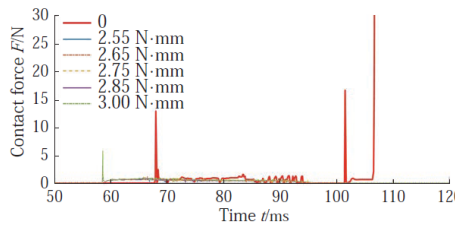

Fig. 10. Contact force between ratchet and auxiliary pawl under different spring
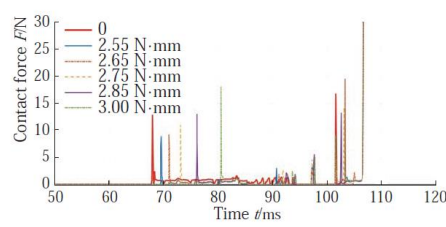
Fig. 11. Contact force between ratchet and main pawl with different spring stiffness

According to the analysis in Fig 10, the impact force and contact force between the auxiliary pawl and the ratchet wheel are less affected by the stiffness of the auxiliary spring; according to the analysis in Fig 11, the impact force and delay time of the main pawl increase with the increase of the stiffness of the auxiliary pawl spring.

The simulation results of the novel locking mechanism with different auxiliary pawl springs and the conventional locking mechanism are as follows: auxiliary pawl impact reduction ΔF_{t_0}, main pawl impact reduction ΔF_{t_1}, main pawl lag Δt_1 as shown in table 3.

Table 3. Comparison of simulation results of novel locking mechanism and conventional locking mechanism under different auxiliary pawl springs

Auxiliary spring stiffness/$(N \cdot mm^{-1})$	0	2.55	2.65	2.75	2.85	3.00
Impact reduction of auxiliary pawlΔF_{t0}/%	0	54.2	54.2	54.2	54.2	54.2
Impact reduction of main pawlΔF_{t1}/%	0	30.6	28.0	14.7	-1.1	-40.1
Main pawl lagΔt_1/%	0	4.8	9.0	15.2	24.1	37.5

It can be seen from table 3 that with the increase of the spring stiffness of the auxiliary pawl, the impact of the ratchet wheel of the novel locking mechanism on the auxiliary pawl is basically unchanged, and the impact force of the ratchet wheel on the main pawl becomes larger. The overall friction work of the novel locking mechanism is reduced, which indicates that the spring stiffness of the auxiliary pawl has a greater

impact on the abrasion between the ratchet and the main pawl, but has a smaller impact on the abrasion between the ratchet and the auxiliary pawl.

5.3 Application of novel locking mechanism in vehicle latch mechanism

At present, in the process of locking, the ratchet and pawl collide and contact, resulting in greater impact force. The sliding friction will cause greater abrasion and affect the service life. Changing the conventional locking mechanism into this novel locking mechanism can enhance the life span of the vehicle latch. The prototype of the novel locking mechanism is shown in Fig 12, the ratchet and pawl mechanism are made of Q235 steel, it's elasticity modulus $E=2 \times 10^5$MPa, Poisson's ratio $\mu=0.3$, and the condense $\rho =7850$kg/m^3. And the structure of the novel mechanism is applied in vehicle door Latch, shown in Fig 13. The novel locking mechanism provides a new idea for reducing the noise and abrasion of the vehicle latch when the latch is closed.

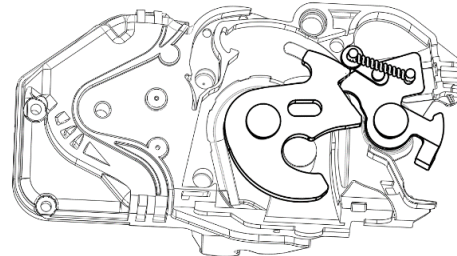**Fig. 12.** Physical drawing of novel ratchet and pawl mechanism

Fig. 13. Application of novel locking mechanism

6 Conclusion

- Based on adding auxiliary pawl, the novel ratchet-pawls locking mechanism uses the singular configuration of the spring linkage mechanism to realize the rapid switching from auxiliary pawls contact to main pawls contact with ratchet, and the auxiliary pawl uses the rolling contact at its end to replace the sliding contact of the profile to reduce abrasion and impact.
- The convention rigid impact of the conventional locking mechanism is replaced by the flexible impact of the auxiliary pawl and the rigid impact of the lagging main pawl, greatly reducing the impact and abrasion of the locking mechanism during the locking process.
- The spring stiffness of the auxiliary pawl has great influence on the impact and abrasion of the novel locking mechanism.

7   Reference

1. Li C F. Research on the mechanism of automobile door locks and its control system[D]. Nanjing: Nanjing University of Aeronautics and Astronautics, 2009 (in Chinese)
2. He Q M, Shang S Q. A novel dual-pawl drive geared ratchet mechanism[J]. Machine Design & Research, 2017, 33（2）: 33-35
3. Bagade V. Fatigue life enhancement of ratchet and pawl mechanism through dynamic analysis[C]//Proceedings of the 2nd International and 17th National Conference on Machines and Mechanisms. 2015
4. Deng H X. Analysis and automatic design study of circuit breaker spring operating mechanism[D]. Chengdu: Southwest Jiaotong University, 2015
5. Wang J, Hang L B, Huang X B, et al. Research on closing motion states of molded case circuit breaker operating mechanism based on singular configuration[J]. Machine Design and Research, 2016, 32（5）: 179-183
6. Darpit C P. Failure analysis & material optimization of ratchet and pawl mechanism-a review[J]. International Journal of Engineering Innovation and Scientific Research, 2015
7. Song C J, Wei J B, Gong L X, et al. Some observations concerning the collision of ratchet and pawl in an automatic synchronizing clutch[J]. Journal of Engineering for Thermal Energy and Power, 2003, 18（3）: 301-303
8. Deb M, Sen D. Parametric study of the behavior of double toggle switching mechanisms[J]. Mechanism and Machine Theory, 2013, 63: 8-27
9. Deb M, Sen D. Design of double toggle switching mechanisms[J]. Mechanism and Machine Theory, 2014, 71: 163-190
10. Gao F, Liu Y N, Liao W H. Cam profile generation for cam-spring mechanism with desired torque[J]. Journal of Mechanisms and Robotics, 2018, 10（4）: 1-7
11. Huang C Q, Zhao Y, Liu Y, et al. Design of a cam constant force mechanism[J]. Machinery Design & Manufacture, 2018,（2）: 178-181
12. Shen J F, Le Z, Xiang B, et al. Research on the equations of cam curve in main and auxiliary type of constant force spring hanger[J]. Machinery Design & Manufacture, 2019,（5）: 106-109, 113
13. Yu T X, Sun Y Q, Zhang Z M. Reliability computing new theory of mechanical elements with multi failure mode[J]. Chinese Journal of Mechanical Engineering, 2003, 39（3）: 134-138
14. Zhang M Z, Liu Y B, Yang X H. The progress in the tribologial investigation of automotive friction materials[J]. Tribology, 1999, 19（4）: 379-384
15. Ge S R, Zhu H. Complicate tribological systems and quantitative study methods of their problems[J]. Tribology, 2002, 22（5）: 405-408

Design and Analysis of a Novel Metamorphic RCM Mechanism

Zhi Wang[1], Wuxiang Zhang[1, 2] and Xilun Ding[1, 2]

[1]School of Mechanical Engineering and Automation, Beihang University, Beijing 100191, China
[2]Beijing Advanced Innovation Center for Biomedical Engineering, Beihang University, Beijing 100191, China
zhangwuxiang@buaa.edu.cn

Abstract. The remote centre-of-motion (RCM) mechanism could move through a fixed point of no physical joint, which plays an important role in minimally invasive surgery robotics to cause minimal pain and damage. Most of the existing RCM mechanisms only has one mobility and RCM point, which limits the applications for different motion requirements. This paper designs a novel parallel RCM mechanism with five configurations by considering the metamorphic mechanism method. Mobilities and motion characteristics of the multiconfiguration are proved by the varied constraint screw systems of its platform at different positions, two of which are instantaneous transient configurations and the rest are motion configurations. The kinematic models of the five configurations are established used the transformation matrix and the workspace of a point on the platform is shown. The novel mechanism could move as two rotational, one rotational or one translational DOF, three types of RCM. The changeable mobility of one RCM mechanism can make it have better adaption for different applications, such as foldable MIS end effector or multimode remote controller, which expands the application of both RCM and metamorphic mechanisms.

Keywords: Remote centre-of-motion, Metamorphic mechanism, Parallel mechanism.

1 Introduction

Recently, robotics has been used extensively in minimally invasive surgery (MIS) to improve safety and precision. A key problem for a surgery robot is to allow the operation end-effector to perform complex movements through a small incision, which makes the remote-centre-motion (RCM) mechanism attract more and more attention.

The end-effector of the RCM mechanism could rotate or translate through a fixed point without any physical joint at that point. The mechanism was classified into eight types by kinematic design[1]. Among them, the parallelogram mechanism is the most widely used and studies, for example, Da Vinci, the most famous commercial MIS robot system. Many other RCM mechanisms have been designed motivated by a par-

allelogram. By combining and expanding virtual centre mechanisms, two types of synthesis methods for one-degree-of-freedom (1-DOF) RCM were proposed[2]. Some novel 2-DOF RCM mechanisms were designed respectively based on the Peaucellier–Lipkin linkage[3], generalized parallelograms[4], N-parallelogram linkages[5] and a dual-triangular mechanism[6].

More than that, some parallel RCM mechanisms were studied to get larger stiffness, reduced inertia and higher precision. Wang et al. designed a novel 2-DOF parallel RCM mechanism by mapping the basic 1-DOF planar parallelogram to space[7]. Li et al. proposed a family of parallel RCM mechanisms based on intersecting motion plane[8]. Essomba et al. generated a new conceptual RCM mechanism by the origin five-bar linkage to achieve higher kinematic performance[9]. Kuo et al. presented a novel decouple RCM mechanism to simplify the control[10]. Bauman et al.[11] and Chen et al.[12] proposed parallel mechanisms composed of two limbs, one composed of 4R (R represents a revolute joint) limb and RPaRR(Pa represents a parallelogram compound joint) limb, another composed of two 4R1H (H represents a helical joint) limbs.

Most RCM mechanisms have specific mobility and motion characteristics. The function is unitary. Currently, a new type of mechanism named metamorphic mechanism, which could change the mobility during motion, have been developed. The mobility in metamorphic mechanisms of foldable/erectable kinds was analyzed by Dai and Jones[13]. A special classification approach of constraints based on the multiconfiguration characteristic was introduced by Zhang et al.[14] and Zhang et al.[15] designed a metamorphic mechanism for automated fibre placement. By combing the characteristics of metamorphic and RCM mechanisms, a novel metamorphic RCM mechanism is proposed in this study. It has varied mobility and RCM characteristic. The metamorphic RCM mechanism expands the function of one RCM mechanism, which can have better adaption for different applications, such as foldable MIS end effector or multimode remote controller.

2   Design of the Novel Metamorphic RCM Mechanism

2.1   Conceptual Design

Inspired by the existing parallel RCM mechanisms and basis parallelogram RCM mechanism, a novel parallel RCM mechanism is designed. As displayed in Fig. 1(a), the parallel mechanism is composed of two limbs. The basement is l_b and connects to limbs l_1 and l_2 by universal joints(two revolute joints intersecting vertically). Points A and B are the centres of the universal joints. The four revolute joints next to the universal joint form a parallelogram subloop and they have the same direction of the second revolute joint of the universal joint. At the end of the limb l_2, there is one more revolute joint connecting to the platform l_p than limb l_1. The axis of the end revolute joint alongside the platform l_p, intersects perpendicularly with the two close revolute joints. *Axis x* is the same as the axis of the revolute joint connecting the limb l_1 and the basement l_b. *Axis y* is the same as the axis of the revolute joint connecting l_2 and l_b. The origin of the coordinate system, O, is located at the intersection. The novel mech-

anism has different mobilities and motion characteristics when the platform l_p is at different positions, which means a metamorphic mechanism.
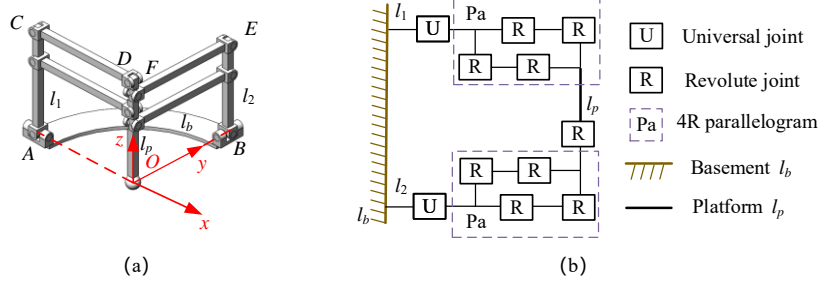

<div align="center">(a)　　　　　　　　　　(b)</div>

Fig. 1. (a) Novel parallel RCM mechanism; (b) Diagram of the mechanism.

2.2　Analysis of the Limbs

To analyze the motion characteristics of the parallel mechanism, it is necessary to use the screw theory to analyze the limbs firstly[16, 17]. A screw S is an element in a six-dimensional vector space. Two screws are reciprocal when

$$S_1 \circ S_2 = s_1 \cdot s_{20} + s_2 \cdot s_{10} = 0 \,, \tag{1}$$

where $S_1 = (s_1; s_{10})$ and $S_2 = (s_2; s_{20})$. The screw system S is a linear vector subspace. The motion screw system S is reciprocal to its corresponding constraint screw system S^r as follow:

$$\mathrm{S}^r \equiv \left\{ S_1^r, \cdots, S_{6-n}^r \left| \left(\left(S_i^r \circ S_j = 0, j = 1, \cdots, n \right), i = 1, \cdots, 6-n \right) \forall S_j \in \mathrm{S}, j = 1, \cdots, n \right\} \right. . \tag{2}$$

Different from the normal parallel mechanism, there are four revolute joints to form a subloop for each limb. The subloop is, essentially, a basic parallelogram mechanism, not a kinematic joint. As displayed in Fig. 2(a), the 4R parallelogram subloop could be equivalent to a compound kinematic joint connecting the two linkages[7]. The motion screw system of the compound joint could be expressed as:

$$S_{Pa} = \left(0; s_{Pa2} \times s_{Pa1} \right), \tag{3}$$

where S_{Pa} represents the equivalent motion screw of the 4R parallelogram subloop, s_{Pa1} is the unit vector of the direction of the revolute joint, s_{Pa2} is the unit vector alongside the linkage CD. As displayed in Fig. 2(b, c), the motion screw systems of limbs l_1 and l_2 are described by their basis as follows:

$$\mathrm{S}_1 = \begin{cases} S_{11} = (s_{11}; 0) \\ S_{12} = (s_{12}; l_{OA} s_{OA} \times s_{12}) \\ S_{13} = (0; s_{13} \times s_{12}) \end{cases}, \quad \mathrm{S}_2 = \begin{cases} S_{21} = (s_{21}; 0) \\ S_{22} = (s_{22}; l_{OB} s_{OB} \times s_{22}) \\ S_{23} = (0; s_{23} \times s_{22}) \\ S_{21} = (s_{24}; 0) \end{cases}, \tag{4}$$

where S_{ij} represents a motion screw associated with the jth joint of the ith limb, s_{ij} is the unit vector of the direction associated with the jth joint of the ith limb, l_{OA} is the length of $\overrightarrow{OA}$, s_{OA} is the unit vector of the direction of $\overrightarrow{OA}$ and so on for the rest. The non-unique bases for the constraint screw system of the two limbs can be easily calculated by the reciprocal product as follows:

$$\mathrm{S}_1^r = \begin{cases} \boldsymbol{S}_{11}^r = \left(\boldsymbol{0}; \boldsymbol{s}_{11} \times \boldsymbol{s}_{12}\right) \\ \boldsymbol{S}_{12}^r = \left(\boldsymbol{s}_{12}; \boldsymbol{0}\right) \\ \boldsymbol{S}_{13}^r = \left(\boldsymbol{s}_{13}; l_{OA}\boldsymbol{s}_{OA} \times \boldsymbol{s}_{13}\right) \end{cases}, \quad \mathrm{S}_2^r = \begin{cases} \boldsymbol{S}_{21}^r = \left(\boldsymbol{s}_{22}; \boldsymbol{0}\right) \\ \boldsymbol{S}_{22}^r = \left(\boldsymbol{s}_{23}; l_{OB}\boldsymbol{s}_{OB} \times \boldsymbol{s}_{23}\right) \end{cases}, \tag{5}$$

where S_{ij}^r represents the jth constraint screw of the ith limb. A spanning multiset $\langle \mathrm{S} \rangle$ is a collection of screws that span the screw system S, which may contain repeated elements[16]. The number of screws in a screw system S and a multiset $\langle \mathrm{S} \rangle$ is its cardinal number, written as $card\{\mathrm{S}\}$ and $card\langle \mathrm{S} \rangle$ respectively. They are always greater than or equal to the dimensional of the screw system, $card\langle \mathrm{S} \rangle \geq card\{\mathrm{S}\} = \dim \mathrm{S}$. The constraint screw multiset of the platform l_p combines the two constraint screw systems of limbs, Eq. (5),

$$\langle \mathrm{S}^r \rangle = \mathrm{S}_1 \ \hat{a} \ \mathrm{S}_2, \tag{6}$$

where $card\langle \mathrm{S}^r \rangle = 5$. However, there may be repeated linearly independent screws. As a metamorphic mechanism, there are changeable repeated linearly independent screws when the platform l_p locates at different positions or called varied configurations of the metamorphic mechanism.
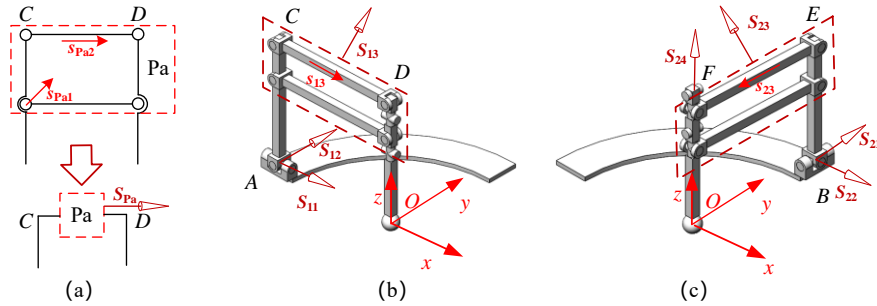

Fig. 2. Limbs of the mechanism. (a) Equivalent parallelogram joint; (b) Limb l_1; (c) Limb l_2.

3 Configurations Analysis

The novel mechanism has five configurations when the platform l_p locates at different positions. The mobilities and motion characteristics of varied configurations could be analysed by varied constraint screw systems. Of the five configurations, two are tran-

sient configurations, configuration 1 and 4. For the transient configurations, the mobilities and motion characteristics are instantaneous. Once the platform moves, the mechanism transforms from the transient configurations to motion configurations, configurations 2, 3 and 5.

3.1 Configuration 1

As in Fig. 1(a) and Fig. 2(b, c), the initial configuration is configuration 1. On configuration 1, the platform l_p, linkages AC, BE of limbs l_1 and l_2 are perpendicular to *plane O-xy*. The direction of the revolute joints on Pa and linkages CD, FE, s_{i1}, s_{i2} and s_{i3}, are in or parallel to *plane O-xy*. Some geometric relationships are satisfied as follows:

$$\begin{cases} s_{11}=s_{22}=s_{13}=s_{AO} \\ s_{21}=s_{12}=s_{23}=s_{BO} \end{cases}. \tag{7}$$

Substituting Eq. (7) to Eq. (6), $_1\langle S^r \rangle$ only contains there linearly independent screws, so a non-unique basis for the constraint screw system of the platform l_p on configuration 1 can be calculated as:

$$_1S^r = \begin{cases} _1S_1^r = (\boldsymbol{0}; s_{11} \times s_{12}) \\ _1S_2^r = (s_{21}; \boldsymbol{0}) \\ _1S_3^r = (s_{11}; \boldsymbol{0}) \end{cases}. \tag{8}$$

A non-unique basis for the motion screw system of the platform l_p can be calculated by the reciprocal product of Eq. (8):

$$_1S_f = \begin{cases} _1S_{f1} = (\boldsymbol{0}; s_{11} \times s_{12}) \\ _1S_{f2} = (s_{11}; \boldsymbol{0}) \\ _1S_{f3} = (s_{21}; \boldsymbol{0}) \end{cases}, \tag{9}$$

where $_1S_{f1}$ represents one translational DOF with direction $s_{11} \times s_{12}$, i.e. *axis z* on this configuration, $_1S_{f2}$ and $_1S_{f3}$ represent two rotational DOFs with direction s_{11} and s_{21}, i.e. *axis x* and *axis y*. The directions of two rotation DOFs and one translation DOF intersect at *origin O*, which fixed point the platform l_p rotates and translates through without any physical joint, i.e. the RCM point and it is a 3 DOF RCM mechanism on configuration 1. The geometric relationship Eq. (7) is instantaneous to satisfy. Once the platform l_p moves, the configuration and mobility change. Configuration 1 is a transient configuration. The mechanism transforms to configuration 2 when the platform l_p rotates around *origin O* and transforms to configuration 3 when it translates.

3.2   Configuration 2

When the platform l_p rotates around *origin O*, the mechanism transforms configuration 2 as displayed in Fig. 3(a). On configuration 2, the platform l_p is still through *origin O*, but its direction is not the same as the *axis z*. On the limbs l_1 and l_2, the directions of the linkages CD, EF, s_{i3} are still parallel to the *O-xy plane*, but the directions of the second revolute joints, s_{i2}, are not in or parallel to the same plane. Some geometric relationships are satisfied as follows:

$$\begin{cases} s_{11} = s_{13} = s_{AO} \\ s_{21} = s_{23} = s_{BO} \end{cases}.$$
(10)

Substituting Eq. (10) to Eq. (6), $_2\langle S^r \rangle$ contains four linearly independent screws, so a non-unique basis for the constraint screw system of the platform l_p on configuration 2 can be calculated as:

$$_2S^r = \begin{cases} _2S_1^r = (0; s_{11} \times s_{12}) \\ _2S_2^r = (s_{21}; 0) \\ _2S_3^r = (s_{11}; 0) \\ _2S_4^r = (s_{22}; 0) \end{cases}.$$
(11)

A non-unique basis for the motion screw system of the platform l_p can be calculated by the reciprocal product of Eq. (11):

$$_2S_f = \begin{cases} _2S_{f1} = (s_{11}; 0) \\ _2S_{f2} = (s_{12}; 0) \end{cases},$$
(12)

where $_2S_{f1}$ and $_2S_{f2}$ represent two rotational DOFs with direction s_{11} and s_{12}. The directions of two rotation DOFs intersect at *origin O*, an RCM point and it is a 2-DOF RCM mechanism on configuration 2. Different from transient configuration 1, it could maintain the motion characteristic in its spherical workspace.

3.3   Configuration 3

On configuration 1, when the platform l_p translates through *origin O*, the mechanism transforms configuration 3. On configuration 3, the platform l_p points at *origin O*. The directions of the second revolute joints and the linkages connecting the platform, s_{i2} and s_{i3}, are not in or parallel to *plane O-xy*. Some geometric relationships are always satisfied as follows:

$$\begin{cases} s_{11} = s_{AO} \\ s_{21} = s_{BO} \end{cases}.$$
(13)

All constraint screws of $_3\langle S^r \rangle$ are linearly independent and a non-unique basis for the constraint screw system of the platform l_p can be calculated as:

$$_3\mathbf{S}^r = {}_3\left\langle \mathbf{S}^r \right\rangle = \begin{cases} \mathbf{S}_1^r = \left(\mathbf{0}; \mathbf{s}_{11} \times \mathbf{s}_{12}\right) \\ \mathbf{S}_2^r = \left(\mathbf{s}_{12}; \mathbf{0}\right) \\ \mathbf{S}_3^r = \left(\mathbf{s}_{13}; l_{OA}\mathbf{s}_{11} \times \mathbf{s}_{13}\right) \\ \mathbf{S}_4^r = \left(\mathbf{s}_{22}; \mathbf{0}\right) \\ \mathbf{S}_5^r = \left(\mathbf{s}_{23}; l_{OB}\mathbf{s}_{21} \times \mathbf{s}_{23}\right) \end{cases}. \tag{14}$$

Notice that the direction of the platform l_p $\mathbf{s}_{24}$ is perpendicular to the directions of the second revolute $\mathbf{s}_{i2}$ on each limb. The directions of the first revolute joint $\mathbf{s}_{i1}$ and the linkages AC, BE are perpendicular to the second revolute joint $\mathbf{s}_{i2}$. For the direction vectors the relationships are satisfied as follows:

$$\begin{cases} \mathbf{s}_{11} \times \mathbf{s}_{13} = \mathbf{s}_{12} \\ \mathbf{s}_{21} \times \mathbf{s}_{23} = \mathbf{s}_{22} \\ \mathbf{s}_{12} \times \mathbf{s}_{22} = \mathbf{s}_{24} \end{cases}. \tag{15}$$

Considering Eq. (15), a non-unique basis for the motion screw system of the platform l_p can be calculated by the reciprocal product of Eq. (14):

$$_3\mathbf{S}_f = {}_3\mathbf{S}_{f1} = \left(\mathbf{n}; \mathbf{s}_{24}\right), \tag{16}$$

where $\mathbf{n}$ satisfies the relationships by reciprocal as follows:

$$\begin{cases} \mathbf{s}_{11} \times \mathbf{s}_{12} \cdot \mathbf{n} = 0 \\ l_{OA}\mathbf{s}_{11} \times \mathbf{s}_{13} \cdot \mathbf{n} = \mathbf{s}_{13} \cdot \mathbf{s}_{24} \\ l_{OB}\mathbf{s}_{21} \times \mathbf{s}_{23} \cdot \mathbf{n} = \mathbf{s}_{23} \cdot \mathbf{s}_{24} \end{cases}. \tag{17}$$

The unique solution of Eq. (17) could be solved as:

$$\mathbf{n} = x\mathbf{s}_{11} + y\mathbf{s}_{12}, \tag{18}$$

where

$$\begin{cases} x = \dfrac{l_{OA}\mathbf{s}_{24} \cdot \mathbf{s}_{13} - l_{OB}\mathbf{s}_{12} \cdot \mathbf{s}_{13}}{l_{OA}l_{OB}\mathbf{s}_{24} \cdot \mathbf{s}_{11}} \\ \\ y = \dfrac{\mathbf{s}_{13} \cdot \mathbf{s}_{24}}{l_{OA}} \end{cases}.$$

The motion screw on configuration 3 could be translated as:

$$\begin{aligned} _3\mathbf{S}_f = {}_3\mathbf{S}_{f1} &= \left(x\mathbf{s}_{11} + y\mathbf{s}_{12}; \mathbf{s}_{24}\right) \\ &= \left(x\mathbf{s}_{11} + y\mathbf{s}_{12}; \mathbf{0}\right) + \left(\mathbf{0}; \mathbf{s}_{24}\right) \end{aligned}, \tag{19}$$

which could be regarded as a compound motion with rotation and translation around the *O origin*. It is a 1-DOF RCM mechanism.

3.4 Configuration 4

As the platform l_p moving to *plane O-xy*, it transforms configuration 4. As displayed in Fig. 3(c), the platform l_p and all linkages of each limb are in *plane O-xy*. The directions of the all but first revolute joints are the same as *axis z*. The directions of the

linkages AC BE are the same as the platform l_p, s_{24} . $_4\langle S^r \rangle$ contains only four linearly independent screws, so a non-unique basis for the constraint screw system of the platform l_p on configuration 4 can be calculated as:

$$_4S^r = \begin{cases} S_1^r = (0; s_{11} \times s_{12}) \\ S_2^r = (s_{12}; 0) \\ S_3^r = (s_{13}; l_{OA}s_{OA} \times s_{13}) \\ S_5^r = (s_{23}; l_{OB}s_{OB} \times s_{23}) \end{cases}. \tag{20}$$

A non-unique basis for the motion screw system of the platform l_p can be calculated by the reciprocal product of Eq. (20):

$$_4S_f = \begin{cases} _4S_{f1} = (s_{11}; 0) \\ _4S_{f2} = (k; l_{OR}s_{OR} \times k) \end{cases}, \tag{21}$$

where $_4S_{f1}$ represents a rotation DOF with direction s_{11}, and $_4S_{f2}$ represents a rotation with the direction k , which is the direction of *axis z* and locates at the *R point*, $l_{OR}s_{OR} = (l_{OA}s_{OA} + l_{OB}s_{OB})$. Once the platform moves, the geometric relationships change, which means the mobility and motion characteristics change. Configuration 4 is a transient configuration. The mechanism turns back to configuration 3 when the platform rotates around *origin O* but transforms configuration 5 when it rotates around *point R*.

3.5 Configuration 5

When the platform l_p rotates around *point R* with the direction k on the transient configuration 4, it transforms to configuration 5. As displayed in Fig. 3(d) the directions of the revolute joints are still the same as the *z axis*. The directions of the linkages AC BE and the platform are the same too. But the axis of the platform l_p doesn't pass through *origin O*. The motion screw systems of the limb l_2 changes from Eq. (5) to Eq. (22)：

$$_5S_2 = \begin{cases} _5S_{21} = (s_{21}; 0) \\ _5S_{22} = (s_{22}; l_{OB}s_{OB} \times s_{22}) \\ _5S_{23} = (0; s_{23} \times s_{22}) \\ _5S_{21} = (s_{24}; (l_{OA}s_{OA} + l_{OB}s_{OB}) \times s_{24}) \end{cases}, \tag{22}$$

Some special geometric relationships are satisfied as follows:

$$\begin{cases} s_{12} = s_{22} = k \\ l_{ORy}s_{ORy} \times s_{24} = l_{OR}s_{OR} \times s_{24} \end{cases}, \tag{23}$$

where k is the direction of *axis z*, *point Ry* is the projection of *point R* at *axis y* with the direction of s_{24}, $l_{ORy}s_{ORy} = l_{OB}s_{24} \cdot s_{21} \cdot s_{21}$ .The constraint screw system could be calculated by the reciprocal product as follows:

$$\,_5\mathbf{S}_2^r = \left\{ \begin{matrix} \,_5\mathbf{S}_{21}^r = \left(\mathbf{s}_{22}; l_{ORy}\mathbf{s}_{ORy} \times \mathbf{s}_{22} \right) \\ \,_5\mathbf{S}_{22}^r = \left(\mathbf{s}_{23}; l_{OB}\mathbf{s}_{OB} \times \mathbf{s}_{23} \right) \end{matrix} \right\}. \tag{24}$$

$\,_5\langle \mathbf{S}^r \rangle$ contains five linearly independent screws, so a non-unique basis for the constraint screw system of the platform l_p can be calculated as:

$$\,_5\mathbf{S}^r = \,_5\langle \mathbf{S}^r \rangle = \left\{ \begin{matrix} \mathbf{S}_1^r = \left(\mathbf{0}; \mathbf{s}_{21} \right) \\ \mathbf{S}_2^r = \left(\mathbf{s}_{12}; \mathbf{0} \right) \\ \mathbf{S}_3^r = \left(\mathbf{s}_{13}; l_{OA}\mathbf{s}_{OA} \times \mathbf{s}_{13} \right) \\ \mathbf{S}_4^r = \left(\mathbf{s}_{22}; l_{ORy}\mathbf{s}_{ORy} \times \mathbf{s}_{22} \right) \\ \mathbf{S}_5^r = \left(\mathbf{s}_{23}; l_{OB}\mathbf{s}_{OB} \times \mathbf{s}_{23} \right) \end{matrix} \right\}. \tag{25}$$

A non-unique basis for the motion screw system of the platform l_p can be calculated by the reciprocal product of Eq. (23):

$$\,_5\mathbf{S}_f = \,_5\mathbf{S}_{f1} = \left(\mathbf{k}; l_{OR}\mathbf{s}_{OR} \times \mathbf{k} \right), \tag{26}$$

which represents one rotation DOF motion around the *R point*, an RCM point. It is a 1-DOF RCM mechanism on configuration 5.
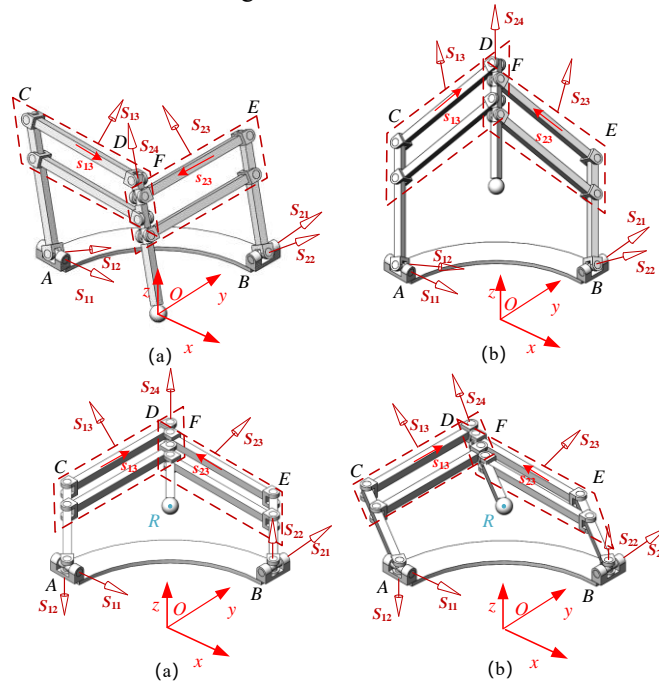

Fig. 3. (a)Configuration 2; (a)Configuration 3; (a)Configuration 4; (a)Configuration 5.

4   Kinematics and Simulation

4.1   Kinematics Analysis

The metamorphic RCM mechanism has five configurations, two of which are transient and they are instantaneous in a specific position. The kinematic models of the rest three configurations could be analyzed by a transformation matrix. As displayed in Fig. 4(a), the object coordinate system is based on *point R*, of the platform. The initial directions of the object coordinate system, *axis u, v, w* are the same as the *O* coordinate system. The orientation of the object coordinate is defined by two angles and expressed by rotation of *xy* angle, α and β. To simply the mechanism, let $l_{OA} = l_{OB} = l_1$. The configurations 2, 4 and 5 are 2-, 1- and 1-DOF motion mechanisms respectively in their workspace.
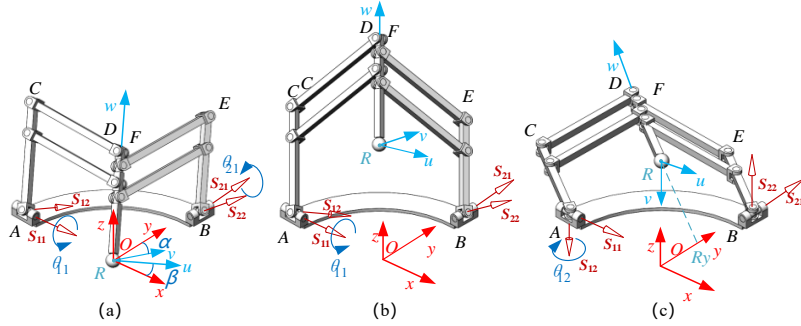

Fig. 4. Kinematics analysis; (a)Configuration 2; (b)Configuration 3; (a)Configuration 5.

Configuration 1. Configuration 1 is the initial configuration and transient configuration. The object coordinate system coincides with the base coordinate system so the rotation matrix $\boldsymbol{R}_R$ and translation vector $\boldsymbol{t}_R$ of the object coordinate system are zero:

$$\begin{cases} \boldsymbol{R}_R = [\boldsymbol{0}_{3\times 3}] \\ \boldsymbol{t}_R = (0,0,0) \end{cases}. \tag{27}$$

Configuration 2. As displayed in Fig. 4(a), the platform l_p and the linkages AC、BE point at the same direction on configuration 2, some equations as follows:

$$\boldsymbol{s}_w = \boldsymbol{s}_{AC} = \boldsymbol{s}_{BE} , \tag{28}$$

where

$$\begin{cases} \boldsymbol{s}_w = \boldsymbol{R}_x(\alpha)\boldsymbol{R}_{y'}(\beta)\boldsymbol{s}_{w0} \\ \boldsymbol{s}_{AC} = \boldsymbol{R}_x(\theta_{11})\boldsymbol{R}_{y'}(\theta_{12})\boldsymbol{s}_{AC0} \\ \boldsymbol{s}_{BE} = \boldsymbol{R}_y(\theta_{21})\boldsymbol{R}_{x'}(\theta_{22})\boldsymbol{s}_{BE0} \end{cases}, \ \boldsymbol{s}_{w0} = \boldsymbol{s}_{AC0} = \boldsymbol{s}_{BE0} = (0,0,1)^T,$$

$\boldsymbol{R}$ is a rotation matrix,

$$\boldsymbol{R}_x(\theta) = \begin{bmatrix} 1 & 0 & 0 \\ 0 & \cos\theta & -\sin\theta \\ 0 & \sin\theta & \cos\theta \end{bmatrix}, \ \boldsymbol{R}_y(\theta) = \begin{bmatrix} \cos\theta & 0 & \sin\theta \\ 0 & 1 & 0 \\ -\sin\theta & 0 & \cos\theta \end{bmatrix},$$

$\boldsymbol{s}_i$ represents the unit vector of the i direction, $\boldsymbol{s}_{i0}$ represents the initial unit vector of the i direction, θ_{ij} represents the rotation angle associated with the jth joint of the ith limb and so on. The orientation of the object coordinate could be expressed by:

$$
\begin{aligned}
\boldsymbol{R}_R &= \boldsymbol{R}_x(\alpha)\boldsymbol{R}_{y'}(\beta) \\
&= \begin{bmatrix} \cos\beta & 0 & \sin\beta \\ \sin\alpha\sin\beta & \cos\alpha & -\sin\alpha\cos\beta \\ -\cos\alpha\sin\beta & \sin\alpha & \cos\alpha\cos\beta \end{bmatrix},
\end{aligned} \tag{29}
$$

where

$$\begin{cases} \alpha = \theta_{11} \\ \beta = \arctan\left(\tan\theta_{21}\cos\theta_1\right) \end{cases}.$$

Configuration 3. As displayed in Fig. 4(b), when $l_{OA} = l_{OB}$, the mechanism could be regarded as symmetrical. Some equations are satisfied as follows:

$$\begin{cases} \boldsymbol{s}_w = \boldsymbol{s}_{AC} = \boldsymbol{s}_{BE} \\ \overrightarrow{OR} = \overrightarrow{OA} + \overrightarrow{AR} \end{cases}, \tag{30}$$

where

$$\begin{cases} \boldsymbol{s}_w = \boldsymbol{R}_x(\alpha)\boldsymbol{R}_{y'}(\beta)\boldsymbol{s}_{w0} \\ \boldsymbol{s}_{AC} = \boldsymbol{R}_x(\theta_{11})\boldsymbol{R}_{y'}(\theta_{12})\boldsymbol{s}_{AC0} \\ \boldsymbol{s}_{BE} = \boldsymbol{R}_y(\theta_{21})\boldsymbol{R}_{x'}(\theta_{22})\boldsymbol{s}_{BE0} \end{cases}, \quad \begin{cases} \boldsymbol{s}_{w0} = \boldsymbol{s}_{AC0} = \boldsymbol{s}_{BE0} = (0,0,1)^T \\ \theta_{11} = \theta_{21} \\ \theta_{12} = \theta_{22} \end{cases}, \quad \begin{cases} \overrightarrow{OR} \times \boldsymbol{s}_w = 0 \\ \overrightarrow{OA} = (-l_1, 0, 0) \\ |\overrightarrow{AR}| = l_1 \end{cases}.$$

The orientation of the object coordinate could be expressed by:

$$
\begin{aligned}
\boldsymbol{R}_R &= \boldsymbol{R}_x(\alpha)\boldsymbol{R}_{y'}(\beta) \\
&= \begin{bmatrix} \cos\beta & 0 & \sin\beta \\ \sin\alpha\sin\beta & \cos\alpha & -\sin\alpha\cos\beta \\ -\cos\alpha\sin\beta & \sin\alpha & \cos\alpha\cos\beta \end{bmatrix},
\end{aligned} \tag{31}
$$

where

$$\begin{cases} \alpha = \theta_{11} \\ \beta = \arctan\left(\sin\theta_{11}\right) \end{cases}.$$

The translation of the object coordinate could be expressed by:

$$\boldsymbol{t}_R = \overrightarrow{OR} = \left(2l_1\sin^2\beta, -2l_1\sin\alpha\sin\beta\cos\beta, 2l_1\cos\alpha\sin\beta\cos\beta\right)^T, \tag{32}$$

where

$$\begin{cases} \alpha = \theta_{11} \\ \beta = \arctan\left(\sin\theta_{11}\right) \end{cases}.$$

Configuration 4. Configuration 4 is a transient configuration and the object coordinate is instantaneous at two specific positions. It is an instantaneous position of configuration 3 when $\theta_{11}=\pm\pi/2$ and the two rotation matrix and translation vectors of the object coordinate system can be expressed by

$$
\begin{cases}
\boldsymbol{R}_{R1}=\begin{bmatrix} \sqrt{2}/2 & 0 & \sqrt{2}/2 \\ \sqrt{2}/2 & 0 & -\sqrt{2}/2 \\ 0 & 1 & 0 \end{bmatrix}, \boldsymbol{t}_{R1}=(l_1,-l_1,0) \\[4mm]
\boldsymbol{R}_{R2}=\begin{bmatrix} \sqrt{2}/2 & 0 & \sqrt{2}/2 \\ -\sqrt{2}/2 & 0 & \sqrt{2}/2 \\ 0 & -1 & 0 \end{bmatrix}, \boldsymbol{t}_{R2}=(-l_1,l_1,0)
\end{cases}
. \tag{33}
$$

Configuration 5. As displayed in Fig. 4(c), it is a 1 DOF RCM mechanism and the orientation of the object coordinate could be expressed by:

$$
\boldsymbol{R}_R = \boldsymbol{R}_x\left(\pi/2\right)\boldsymbol{R}_{y'}\left(\pi/4\right)\boldsymbol{R}_{y''}\left(\theta_{12}\right)
$$

$$
= \begin{bmatrix} \dfrac{\sqrt{2}}{2}\cos\theta_{12}-\dfrac{\sqrt{2}}{2}\sin\theta_{12} & 0 & \dfrac{\sqrt{2}}{2}\sin\theta_{12}+\dfrac{\sqrt{2}}{2}\cos\theta_{12} \\[3mm] \dfrac{\sqrt{2}}{2}\cos\theta_{12}+\dfrac{\sqrt{2}}{2}\sin\theta_{12} & 0 & \dfrac{\sqrt{2}}{2}\sin\theta_{12}-\dfrac{\sqrt{2}}{2}\cos\theta_{12} \\[3mm] 0 & 1 & 0 \end{bmatrix}. \tag{34}
$$

The fixed translation of the object coordinate could be expressed by:

$$
\boldsymbol{t}_R = \overrightarrow{OR} = \left(-\sqrt{2}l_1, \sqrt{2}l_1, 0\right)^T. \tag{35}
$$

4.2   Workspace

Based on the kinematics analysis above, the workspace for the metamorphic RCM mechanism could be described. Assumed $l_1=\left|\overline{PR}\right|=1$, the workspace of a *point p* on the platform l_p is shown used the Monte Carlo method on MATLAB, with five colour dots in Fig. 5, corresponding to five configurations. The configurations of the metamorphic mechanism are instantaneous on configurations 1 and 4. So they are points on the workspace. It is a two DOF RCM mechanism on configuration 2, shown as a sphere on the workspace and the RCM point is located at the centre of the sphere. As for the one DOF mechanism on configurations 3 and 5, they are curves. The RCM point on configuration 3 is the same as on configuration 2. The RCM point on configuration 5 is located at the centre of the circular curve. The black circle on the workspace is the singularity. The workspaces of all points on the platform l_p have a similar shape with *point p*, as shown in Fig. 5.
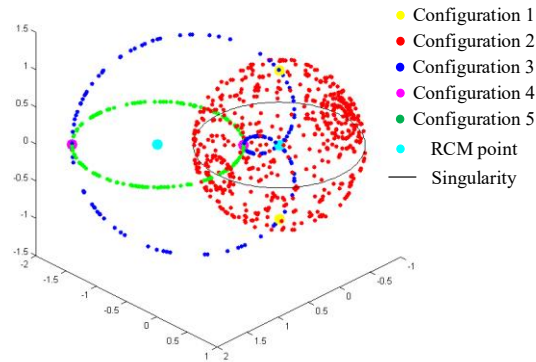
Fig. 5. Workspace of a point on the platform.

5 Conclusion

In this study, a novel metamorphic RCM mechanism composed of two limbs containing subloops, seen as compound joints was designed. The metamorphic mechanism has five configurations, two of which, configurations 1 and 4 were transient configurations and the rest three configurations, 2, 3, 5 were 2-, 1- and 1-DOF RCM mechanisms respectively. For the metamorphic mechanism, the constraint screw set is determinate and the varied constraint screw systems were analyzed to prove the mobilities and motion characteristics of the five configurations. The kinematic models were established used by the transformation matrix and the workspace of a point on the platform was presented by the Monte Carlo method on MATLAB.

Acknowledgement

References

[1] C.H. Kuo, J.S. Dai, P. Dasgupta, Kinematic design considerations for minimally invasive surgical robots: an overview, Int J Med Robot, 8 (2012) 127-145.

[2] G. Zong, X. Pei, J. Yu, S. Bi, Classification and type synthesis of 1-DOF remote center of motion mechanisms, Mechanism and Machine Theory, 43 (2008) 1585-1595.

[3] G. Chen, J. Wang, H. Wang, A New Type of Planar Two Degree-of-Freedom Remote Center-of-Motion Mechanism Inspired by the Peaucellier–Lipkin Straight-Line Linkage, Journal of Mechanical Design, 141 (2019).

[4] J. Li, G. Zhang, Y. Xing, H. Liu, S. Wang, A Class of 2-Degree-of-Freedom Planar Remote Center-of-Motion Mechanisms Based on Virtual Parallelograms, Journal of Mechanisms and Robotics, 6 (2014).

[5] F. Zhang, X. Zhang, L. Hang, C. Lu, T. Furukawa, Type Synthesis of N-Parallelogram-Based Surgical Arm with Remote Actuated Configuration, Mechanism and Machine Science, 2017, pp. 183-194.

[6] S.T. Liu, L. Harewood, B. Chen, C. Chen, A skeletal prototype of surgical arm based on dual-triangular mechanism, Journal of Mechanisms Robotics, 8 (2016).

[7] Z. Wang, W. Zhang, X. Ding, Design and analysis of a novel mechanism with a two-DOF remote centre-of-motion, Mechanism and Machine Theory, 153 (2020) 103990.

[8] J. Li, G. Zhang, A. Müller, S. Wang, A family of remote center of motion mechanisms based on intersecting motion planes, Journal of Mechanical Design, 135 (2013).

[9] T. Essomba, L. Nguyen Vu, Kinematic analysis of a new five-bar spherical decoupled mechanism with two-degrees of freedom remote center of motion, Mechanism and Machine Theory, 119 (2018) 184-197.

[10] C.-H. Kuo, J.S. Dai, Kinematics of a fully-decoupled remote center-of-motion parallel manipulator for minimally invasive surgery, Journal of Medical Devices, 6 (2012).

[11] R. Baumann, W. Maeder, D. Glauser, R. Clavel, The pantoscope: A spherical remote-center-of-motion parallel manipulator for force reflection, Proceedings of International Conference on Robotics and Automation, IEEE, 1997, pp. 718-723.

[12] G. Chen, J. Wang, H. Wang, C. Chen, V. Parenti-Castelli, J. Angeles, Design and validation of a spatial two-limb 3R1T parallel manipulator with remote center-of-motion, Mechanism and Machine Theory, 149 (2020).

[13] J.S. Dai, J. Rees Jones, Mobility in Metamorphic Mechanisms of Foldable/Erectable Kinds, Journal of Mechanical Design, 121 (1999) 375-382.

[14] W. Zhang, X. Ding, J.S.J.P.o.t.I.o.M.E. Dai, Part C: Journal of Mechanical Engineering Science, Morphological synthesis of metamorphic mechanisms based on constraint variation, 225 (2011) 2997-3010.

[15] W. Zhang, F. Liu, Y. Lv, X. Ding, Design and analysis of a metamorphic mechanism for automated fibre placement, Mechanism and Machine Theory, 130 (2018) 463-476.

[16] J.S. Dai, Z. Huang, H. Lipkin, Mobility of Overconstrained Parallel Mechanisms, Journal of Mechanical Design, 128 (2006) 220-229.

[17] J.S. Dai, Geometrical foundations and screw algebra for mechanisms and robotics, Higher Education Press, also Screw Algebra Kinematic Approaches for Mechanisms Robotics, Springer, London, 2014.

A Customized Multi-Size Egg Tart Carton Packaging Machine

Zhili Hou [1], Fengfeng Wu [1], Huibin Qin [2], Ruiqin Li [2]

[1] Taiyuan University of Technology, Taiyuan Shanxi 030024, China
[2] North University of China, Taiyuan Shanxi 030051, China

Abstract. Now the industries must respond proactively to meet rapid changing market demands. A packaging machine adapted to multi-size egg tart carton packaging was designed. The equivalent mechanism of carton folding is to be described the carton panels as links and carton crease lines as joints. Based on the folding procedure of the egg tart carton, there was a sequential motion between all the panels and the crease lines. Due to the diversity of motion trajectories and controllable motion of a coaxial layout 5R mechanism, which was chosen as a cover folding device to fold 2pcs, 3pcs, 4pcs, 6pcs egg trays carton. Moreover, the experimental validation system in a packaging robotic machine was developed to meet the demand of carton customization.

Keywords: Customized Egg Tart Carton, Multi-size, Packaging Machine, 5R mechanism

1   Introduction

The global food packaging is a USD 303.26 billion market which includes paper and cardboard, plastics, metal, glass, and the market demand for food packaging is rapidly growing [1]. In particular, the demand for paper packaging continues to grow, which provides consumers with a green, faster, and safer life services. The paper packaging materials account for more than 40% of the four major packaging materials, which are widely used in food packaging, home appliance packaging, and other fields [2-3].

At present, general food packaging is mainly manual operation in candy, pastries and other food retail industry. Existing food packaging production lines have a single packaging object, poor flexibility, cannot fully adapt to the needs of customization and other issues. In fact, demands for products are changing rapidly, various changes and innovations are proposed to deal with these changes. Therefore, some automated, intelligent and flexible packaging machines have yet to be developed. If there is no reconfigurable machine to join the work, this kind of business is not economically feasible. Further, a smart and reconfigurable machine with robotic fingers is needed in folding packaging which has a manipulator to adapt to various situations to meet customers' demand.

Literature [4] provided an overview of the cardboard packaging and the reconfiguration principles for packaging in the food industry, and motion analysis was the first

standard reconfiguration principle to be considered. The demonstration of this technology is very useful in origami-type cardboard packaging. Literature [5-8] studied the motion model and folding procedure of the carton folding, a new mechanism for the carton was presented and a reconfigurable packaging system for carton was developed. The experimental systems strongly supported the theories. These researches focused on kinematics and motion of carton folding with a aim to produce a multifunctional carton folding machine, and a packaging robot can reduce labor intensity and labor cost.

This paper takes the folding of egg tart cartons in multiple sizes as the research object and designs an automatic folding packaging machine. Egg tart is a pastry food that cannot be squeezed, its outer packaging must give the egg tart enough space to protect it from deformation. The parallel mechanism has good rigidity and strong carrying capacity. As a parallel manipulator, the 2-DOF 5R mechanism has the characteristics of controllable input movement, flexible output movement, and quick response to external functional requirements [9-10]. The folding motion of an egg tarts carton can be equivalent to a model in which the crease lines are used as the axis of rotation on the adjacent surfaces of the carton, and the motion can be equivalent to a rotating pair. In the paper, the folding packaging machine of various sizes egg tart cartons is designed, and the experimental verification is carried out.

This paper is organized as follows: the first part describes the size and the structure of customized egg tart carton and folding process. The next part shows the workflow and design scheme of the packing machine for different carton ranges, and the components of the packaging machine is introduced using folding principles. In the fourth part, the main components of egg tart carton packing machine are introduced, the 5R mechanism with coaxial layout [11-13] as the folding manipulator of cover panel, and a kind of tongue insert packaging robot is designed that can adapt to multi-size of shallow plate carton. In the fifth part, the experimental prototype system is designed, including the control model and experimental prototype. The last part shows the conclusion.

2　Customized Egg Tart Carton and Folding

Customized egg tart carton is usually made of white cardboard sheet, which applies to hold instant foods. Generally, there are diverse size as customers' requirements, which are ranging from 2pcs to 8pcs packing with different sizes. In the paper, the series sizes of egg tart cartons are as follows：

2pcs Packing: H35×W78×L145mm.
3pcs Packing: H35×W80×L220mm.
4pcs Packing: H37×W143×L143mm.
6pcs Packing: H37×W152×L230mm.

2.1　The structure of customized egg tart carton

Egg tart carton is a typical plate-shaped carton with crease lines, panels and tongue, which is composed of adjacent panels with crease lines folded sequentially. The flat

structure of the egg tart carton is shown in Fig.1. The flat and folded egg tart carton physical figure as shown in Fig.2.
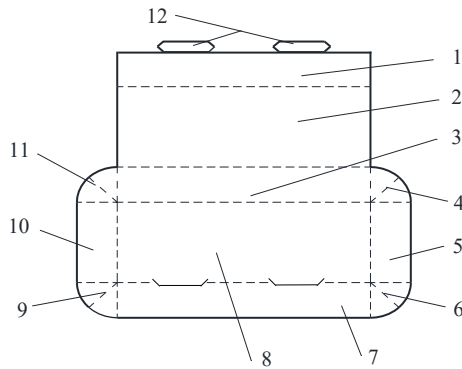

Fig. 1. The flat structure of customized egg tart carton（1. front panel, 2.cover panel, 3.rear panel, 4. right rear flap, 5.right panel, 6.right front flap, 7.front inner panel, 8.base panel, 9.left front flap, 10.left panel, 11.right rear flap, 12.tongue）

In Fig.1, the dotted lines represent crease lines, which can be viewed as the hinge joints of the kinematic mechanism. All panels implement the folding action of the carton along the crease lines. The four flaps fold to drive the adjacent panels to fold in order.

(a)   (b)

Fig. 2. Egg tart carton. (a) flat carton (b) folding carton.

2.2   Folding process

The egg tart carton folding begins with a flat cardboard, which performs crease lines folding, panels closure, tongue insertion and other motions to achieve the carton folding. The folding process of the egg tart carton is to indent crease lines, flaps, folding panels, tongues, and change the relative position between the covers and panels of the egg tart carton.

Fig.3 shows the egg tart carton folding process. Fig.3(a) is the initial flat carton unfolding, Fig.3(b) shows four flaps indentation and folding along the established trajectory of motion, Fig.3(c) shows flaps folded, Fig.3(d) shows the cover folding along the established trajectory of motion, Fig.3(e) shows the front panel folding along the cover crease line, Fig.3(f) shows the tongue folding along the crease into the carton and the carton packaging is completed.
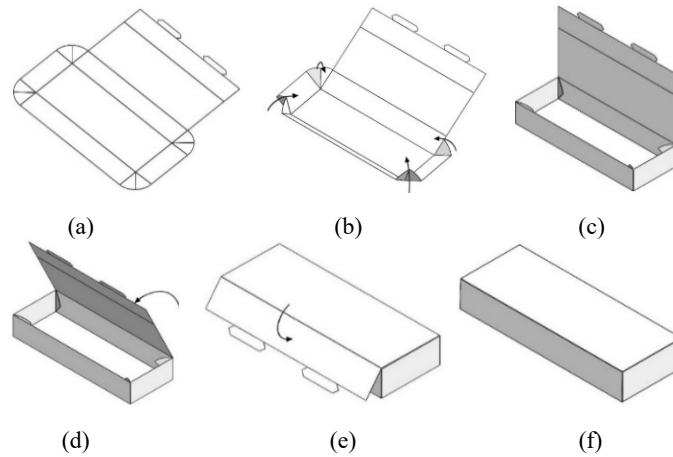
4

Fig. 3. Folding process of egg tart carton. (a) flat cardboard (b) folding four flaps (c) complete folding flaps(d) folding cover panel, (e) folding front panel (f) folding tongue.

3 Workflow and design scheme of the packing machine

Based on the folding process of egg tart carton, a tray carton packing machine with controllable 5R mechanism was designed to fold the egg tart carton. The workflow of the packaging machine is shown in Fig.4. The whole packaging machine is controlled by the sequential process program, and the position and posture of each assembly module can be adjusted.
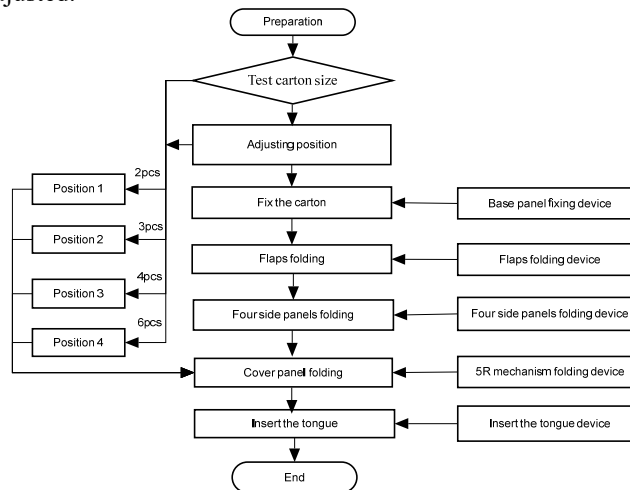
Fig. 4. The workflow of the packaging machine.

First, the carton is fixed to the workbench by suction cups. As the change of egg tart carton size (2pcs, 3pcs, 4pcas, 6pcs), the sensor feedback of adjustment device to select

the correspond working position. At the same time, the four flaps are folded by flaps folding device, which look like fingers, the process as shown in Fig.3(b). And the four side panels folding are folded by the four side panels folding device. So, the rear panel, right panel, front inner panel and left panel are folded, as shown in Fig.3(c).

A coaxial layout 5R mechanism is designed to fold cover panel. According to the position of the carton size, the end output trajectory of 5R mechanism is planned, and the positions of 2pcs, 3pcs, 4pcs and 6pcs egg tart carton with different specifications are adjusted to realize flexible control of the end output track. With the help of the 5R mechanism, the cover panel and front panel are folded, as shown in Fig.3(d) and Fig.3(e).

The packing machine is composed of base support, flap folding, panel folding, adapting and adjusting, cover folding and tongue guiding device. Three-dimensional model of egg tart carton packing machine is shown in Fig.5.
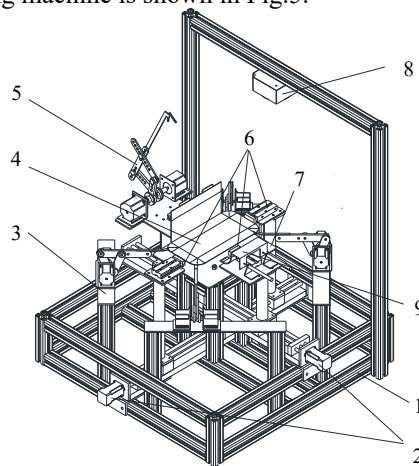
Fig. 5. Three-dimensional model of egg tart carton packing machine. (1. base support device, 2. adjustment device, 3. flaps folding device, 4. carton, 5. cover panel folding device-5R mechanism, 6. four side panels folding device, 7. cover panel folding device, 8. control system, 9. tongue guide device)

4 The main components of egg tart carton packing machine

4.1 Flap folding device

The four-corner flap of the carton rotates the origin with its corner vertex, moving along the arc trajectory, and the carton flaps are realized from flat to fold, as shown in Fig.3(d).

Four carton flaps folding devices with a certain elevation are designed and installed in the four positions of the front left, back left, front right and rear of the adjustment device, as shown in Fig.6. A folding mechanism consists of a U-shaped plate, an mounting plate, a miniature cylinder, a cylinder fixing plate, and a cylinder bend sheet metal.
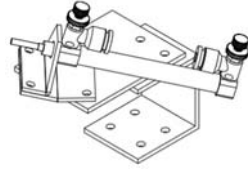
Fig. 6. Flap folding device.

When the carton is absorbed and secured, the miniature cylinder of the carton flap folding device protrudes and the flaps along the arc trajectory are folded, thus causing the side panel of the carton to rotate and fold along the crease.

4.2   Side panel folding device

The side panel folding motion is equivalent to a motion model in which the side panel of the carton rotates around the crease line, as shown in Fig.3 (c).

The side panel folding device, as shown in Fig.7. It is fixed to the slider of the package adaptation adjustment device and folds the four side panels of the paper tray with the help of the push bar of the four two-bar double-axis cylinders. When the four corners of the carton are folded, the four-position cylinders extend out to fold the side panels, thus the bottom of the carton tray is formed, as shown in Fig.3 (c).
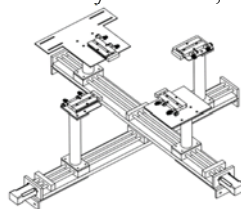

Fig. 7. Side panel folding device

4.3   5R Mechanism Kinematics and cover panel folding

5R Mechanism Kinematics Model. The 5R mechanism with symmetrical structure is shown in Fig.8(a). The linkage AE is the base, the linkage AB and linkage DE are the driving parts, the linkages AB and DE are the same length, and the linkage BC and CD are the same length. Currently, it is a two-degree-of-freedom symmetrical 5R mechanism. According to the rod length conditions, different types of 5R mechanisms can be obtained by adjusting the initial posture of the motor. When the axes of the driving joints A and E coincide collinearly, and the base length is 0, that is, $l_5=0$, it is transformed into a metamorphic 5R mechanism with the driving axes coincident, as shown in Fig.8(b).

Theoretical trajectory of cover panel. The cover panel folding motion includes continuous motion of cover panel, front panel and tongue. Different size cartons have a series of different size of theoretical trajectory. The folding motion of the carton is

regarded as a linkage mechanism of continuous rotation, that is, the crease line is regarded as the revolute pair, and the carton panel is regarded as the linkage, see Fig. 9(a). Linkage *OA* stands for rear panel, linkage *AB* stands for cover panel, linkage *BC* stands for cover panel linkage *CD* stands for tongue.
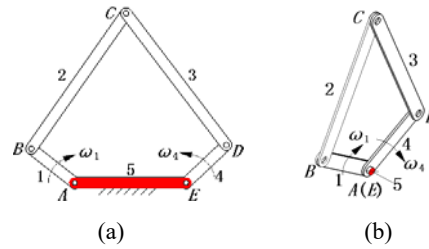

(a)　　　　　　(b)

Fig. 8. The symmetric 5R mechanism. (a) 5R mechanism (b) 5R mechanism of acuated layout with coincident axis.

Every 90° rotation of the linkage mechanism, the center of rotation is transformed once. The center of the rotation circle is O, A_{II}, B_{III}, C_{IV} in order, and the lengths of the rotation radii are OD_I, $A_{II}D_{II}$, $B_{III}D_{III}$, $C_{IV}D_{IV}$ in turn. Finally, it is folded into a carton $OA_{II}B_{III}C_{IV}D_V$. And the theoretical motion trajectory curve $D_ID_{II}D_{III}D_{IV}D_V$ of the end output is formed, which is the blue lines in Fig. 9(b).
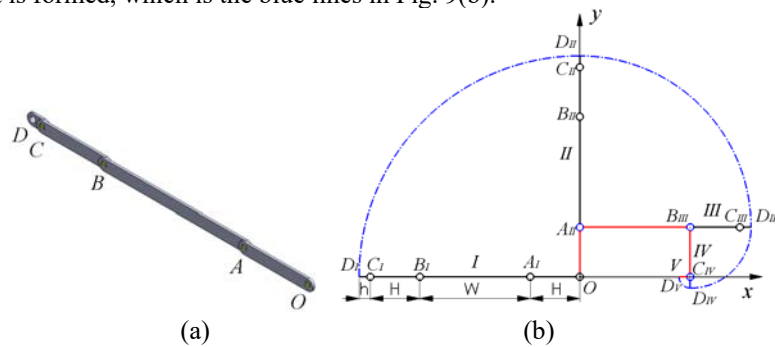

(a)　　　　　　(b)

Fig. 9. Theoretical trajectory of cover panel

The explicit equations of the theoretical motion trajectory are expressed as follows.

$$\text{I-II:} \quad y = \sqrt{(W + 2H + h)^2 - x^2} \qquad x \in [-(W+2H+h), 0] \qquad (1)$$

$$\text{II-III:} \quad y = \sqrt{(W + H + h)^2 - x^2} + H \qquad x \in [0, W+H+h] \qquad (2)$$

$$\text{III-IV:} \quad y = \sqrt{(H + h)^2 - x^2} + H \qquad x \in [W, W+H+h] \qquad (3)$$

$$\text{IV-V:} \quad y = -\sqrt{h^2 - (x - W)^2} \qquad x \in [W-h, W] \qquad (4)$$

The cover folding device. A 2-DOF coaxial planar 5R mechanism is selected as the cover folding mechanism, as shown in Fig.10(a). The drive axis of the two motors is collinear. A 60° L-shaped linkage is designed at the end of the 5R mechanism output rod as a finger to realize the motion of inserting tongue, as shown in Fig.10(b).
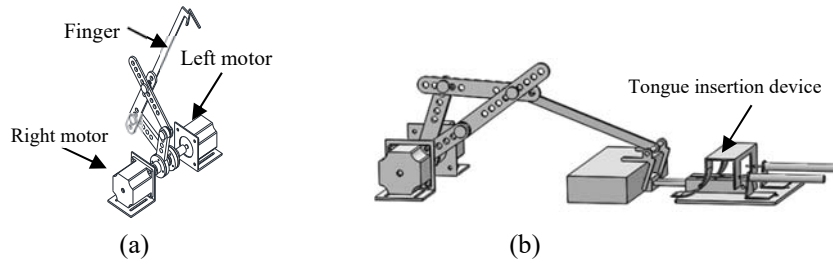

(a)   (b)

Fig. 10. Cover Folding Device. (a)5R Cover folding mechanism, (b) Cover folding and tongue insertion device.

Different angle displacement curves can be entered to achieve the diversity of motion trajectories of the plane 5R mechanism. The rigidity of the 5R mechanism is larger than that of the series mechanism, which can effectively reduce the weight of the end executor and reduce the inertia of the structure.

5 The experimental prototype

5.1 5R mechanism motion control

The process for achieving motion control of the 5R mechanism based on kinematic inverse solution is as follows:

Establish a working coordinate system and define the rotating center of the drive linkage as the origin.

Establish the motion trajectory of the carton folding process and motion simulation. According to the theoretical trajectory curve of cover panel, as shown in Fig.9, the angular velocity of input motors of 5R mechanism are inverse calculated, which through simulation software to track and fit the theoretical trajectory, so the angular velocity curve is obtained, as shown in Fig.11.

The equation of the motion trajectory curve is written to the motor control program, and the speed of input motors are reversed.

5.2 Control system

The control system is composed of pneumatic control system and motor control system. The pneumatic control system is composed of two two-way solenoid valve, two five-way solenoid valve, pressure reducing valve, vacuum generator, filter and air compressor. The motor control system consists of a motion control card, an I/O module, an adjustment driver module, a cover driver module, a flap driver module and a 5R cover

folding mechanism control module with coaxial layout. The control system connection diagram of packaging machine is shown in Fig.12.
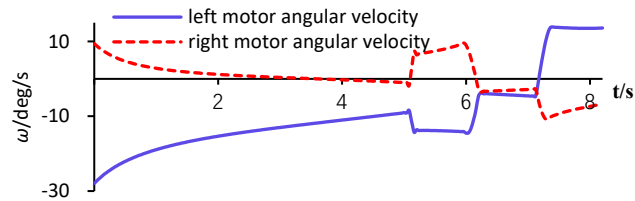

Fig. 11. Inverse solution of motor angular velocity curve of the controllable 5R mechanism

5.3   Experimental prototype machine

By executing control program to adjust the position and posture of 5R mechanism, the packing machine can quickly respond to customized packaging requirements and fold different specifications egg tart cartons.

The effective working space of the prototype is 300 mm×200 mm×50 mm. The carton packing machine can be used to pack 2pcs (145mm×78 mm×35mm), 3pcs (220 mm×80 mm×35mm), 4pcs (143 mm×143mm×37mm), and 6pcs (230 mm×152 mm×37 mm). The experimental prototype of carton packing machine is shown in Fig.13.
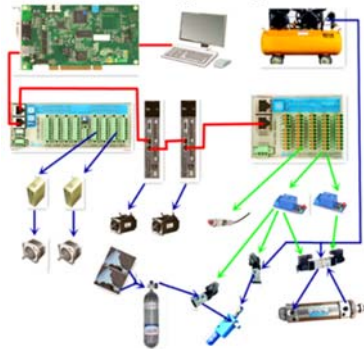

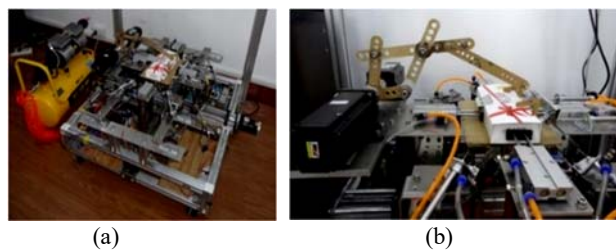**Fig. 12.** control system connection diagram of packaging machine.

(a)   (b)

Fig. 13. The prototype of carton packaging machine. (a)packaging machine, (b)cover folding device.
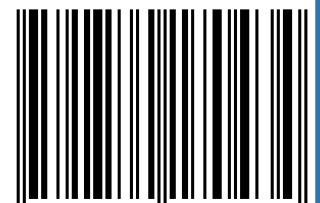
6   Conclusion

The paper shows a sequential procedure to fold the egg tart carton and a new reconfigurable folding mechanism to be developed. According to the carton folding process, the main component modules of the packaging machine are designed to fold different panels, and the experimental prototype can satisfy the multi-specification tray carton packaging. The coaxial layout of the 5R mechanism is used to control diversified cover motion trajectories. The folding packaging of the multi-standard tray carton has been verified by the experimental prototype, and it is flexible and controllable. Finally, the experimental prototype verifies the efficiency of the design.

References

1. Food Packaging Market Size, Share & Trends Analysis Report, https://www.grandviewre-search.com/industry-analysis/food-packaging-market, last accessed 2021/04/10.
2. Yao Quan Zhang: Development Status and Trend of Paper Packaging Industry in China in 2018. Printing Technology 06,39-40(2019).
3. Lin Liu, Kai-li Wang, Haihu Tan, et al: Research and Application Status of Green Packaging Materials in China. Packaging Engineering 37(05), 24-30 (2016).
4. J.S. Dai, D.G. Caldwell: Origami-based robotic paper-and-board packaging for food industry. Trends in Food Science & Technology 21(3), 153-157(2010).
5. Ferdinando Cannella, J.S. Dai: Origami-Carton Tuck–in with a Reconfigurable Linkage. Reconfigurable Mechanisms and Robots 233, 512-520(2009).
6. Wei Yao, F. Cannella, J.S. Dai: Automatic folding of cartons using a reconfigurable robotic system. Robotics and Computer-Integrated Manufacturing 27, 604-613(2011)
7. Wei Yao, J.S. Dai, Tony Medland: A reconfigurable robotic folding system for confectionery industry. Industrial Robot: An International Journal 37(6), 542-551(2010)
8. M. D'Imperio, D. Caldwell, F. Cannella and J. S. Dai.: Origami Carton Non Linear Multi-Body Simulation Towards Industry 4.0: Preliminary Study. In: 2018 International Conference on Reconfigurable Mechanisms and Robots (ReMAR), pp. 1-6. IEEE, Netherlands(2018).
9. Liping Wang, Zhaokun Zhang, Zhufeng Shao, et al.: Analysis and optimization of a novel planar 5R parallel mechanism with variable actuation modes. Robotics & Computer Integrated Manufacturing 56, 178-190(2019).
10. Mats Isaksson, Anders Eriksson, Matthew Watson, et al.: A method for extending planar axis-symmetric parallel manipulators to spatial mechanisms. Mechanism and Machine Theory 83, 1-13(2015).
11. Zhili Hou, Wenge Wu, Ruiqin Li, et al.: Design and experiment of maniphalanx type carton packing machine with controllable linkage mechanism. Packaging Engineering 38(3), 78-81(2017).
12. Zhili Hou, Wenge Wu, Rui-qin Li, et al.: Lectotype Design and Experiment of Variable Actuated Layout 5R Parallel Kinematic Mechanism. Transactions of The Chinese Society of Agricultural Machinery 48(2), 402-408(2017).
13. Zhili Hou, Fengfeng Wu, Huibin Qin, et al.: Design of Tongue-inserting Packaging Machine for Multi-specification Shallow Carton. Packaging Engineering41(9),199-204(2020).

Ryerson
University

IEEE

IFToMM